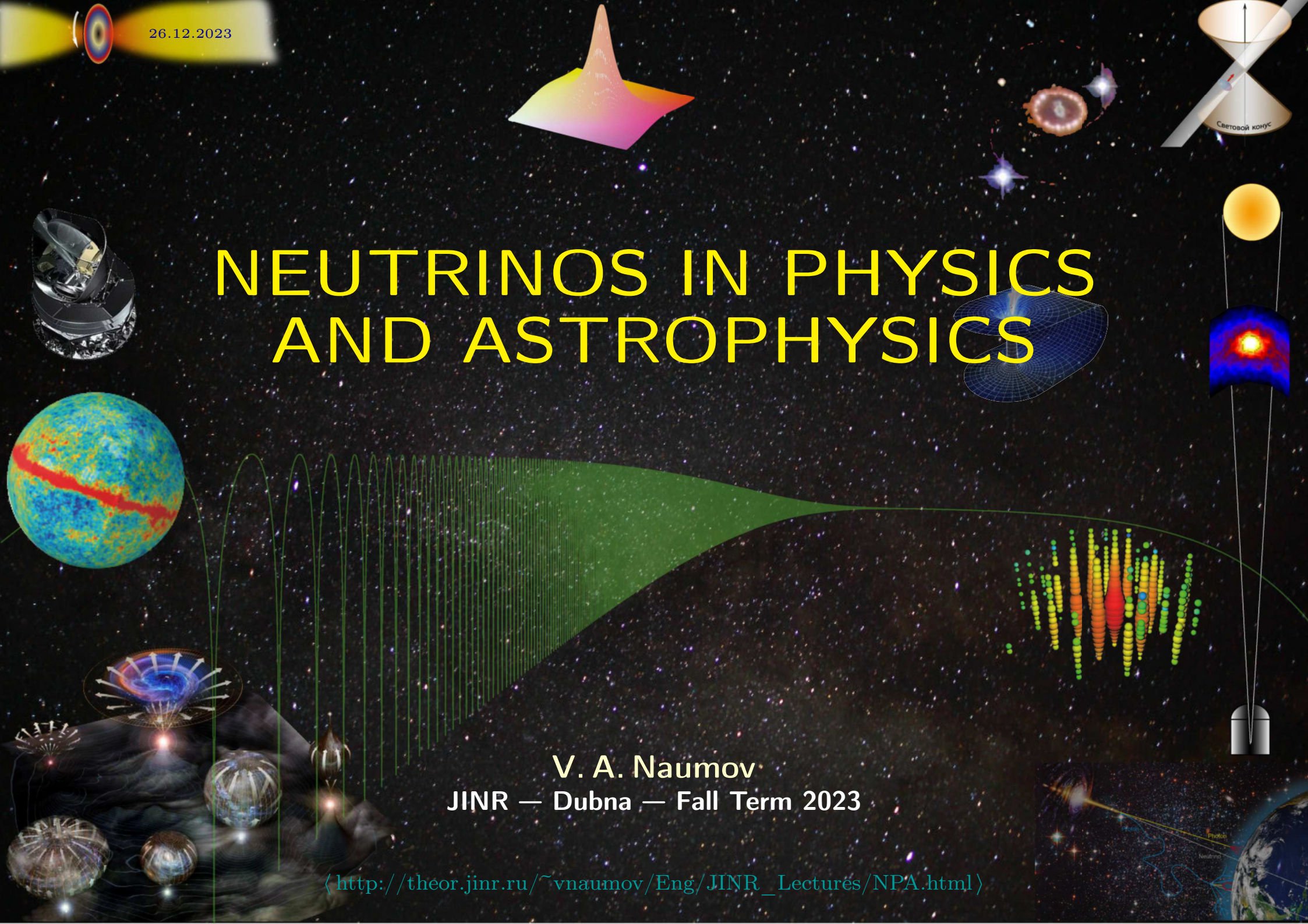

NEUTRINOS IN PHYSICS AND ASTROPHYSICS

V. A. Naumov
JINR — Dubna — Fall Term 2023

⟨http://theor.jinr.ru/~vnaumov/Eng/JINR_Lectures/NPA.html⟩

Contents

Part I

Neutrino Chronicles

(not-too-short history)

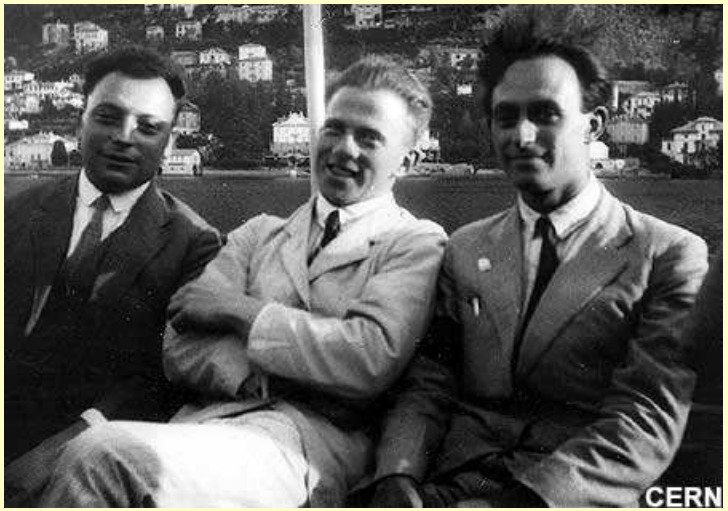

A particle linking physics, astrophysics, and more...

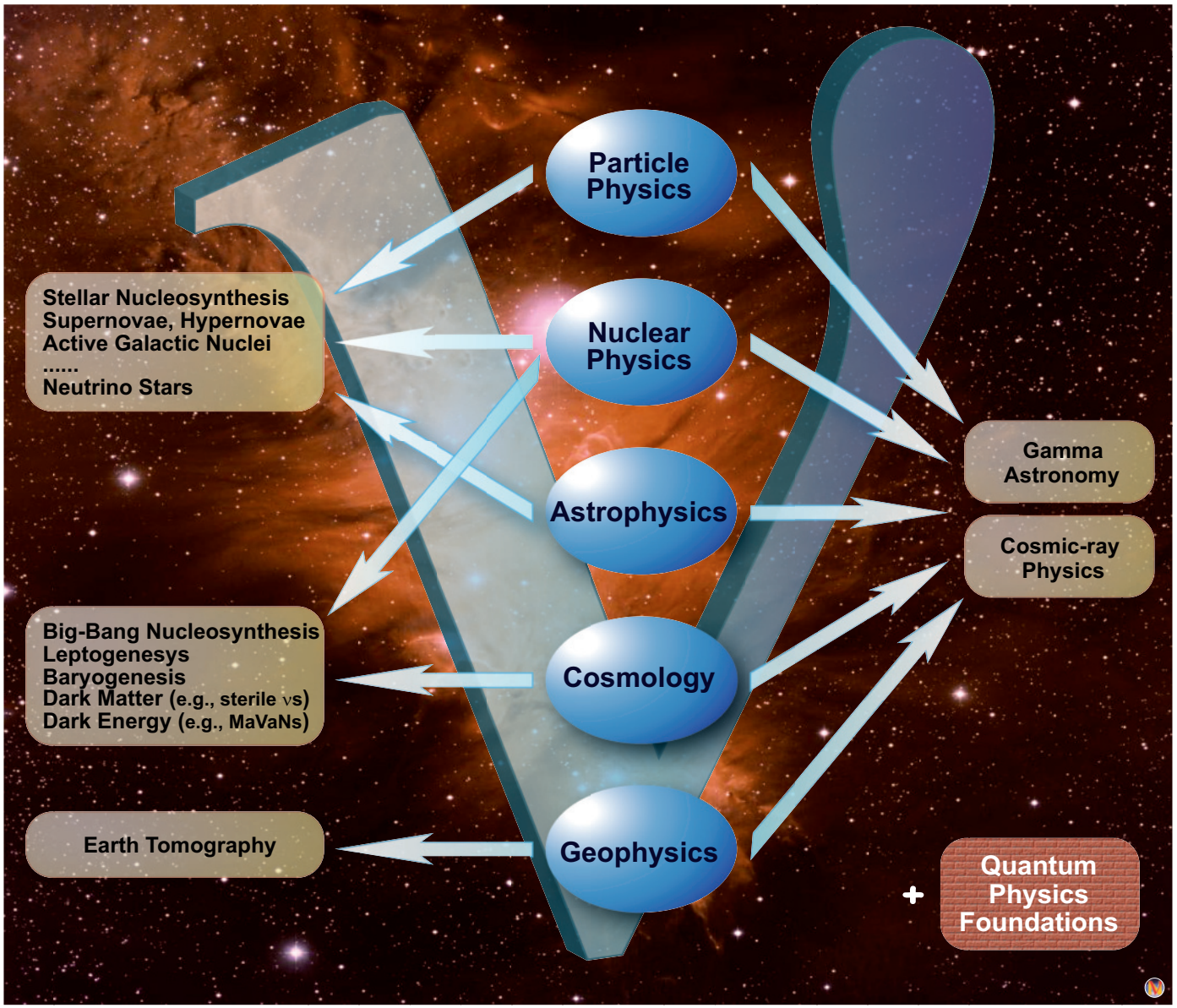

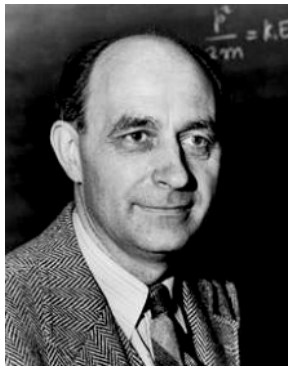

1914 James Chadwick discovers that the β^- spectrum of Ra (B+C) is continuous. [in today's terms, Chadwick studied the chain ${}^{214}_{82}\mathrm{Pb} \xrightarrow{\beta} {}^{214}_{83}\mathrm{Bi} \xrightarrow{\beta} {}^{214}_{84}\mathrm{Po}$].

1920–1929 Lise Meitner (author of many ideas in nuclear physics) and her team suggests various mechanisms whereby initially monoenergetic electrons might lose energy in the form of X rays. These were shown to be unsatisfactory.
Charles Drummond Ellis and William Wooster prove (1927) that the mean energy released in β decay is much less than the end-point energy of the β spectrum and thus clearly establish that the β spectrum is really continuous. This result (confirmed by Lise Meitner and Wilhelm Orthmann in 1929) ended all controversies but was in apparent contradiction to the energy conservation law.
Niels Bohr suggests that the conservation of energy may not hold.
The second problem with the nuclear models of the time was the belief that nuclei consisted of A protons and $A-Z$ electrons. The problem arouse when this model was applied to calculate the nuclear angular momentum ("wrong" spin of ${}^{14}\mathrm{N}$, $I_{\mathrm{exp}} = 1$).

1929-1930 Walter Heinrich Heitler and Gerhard Herzberg and then Franco Dino Rasetti (experiments on the Raman effect with N_2) show that N nuclei do not obey Fermi statistics but rather Bose statistics thus providing an experimental evidence that the atomic nucleus is not composed of protons and electrons.

1930 Wolfgang Pauli hypothesizes the existence of a spin-$\frac{1}{2}$ neutral particle "neutron" with mass $\lesssim 0.01 m_p$ inside the nucleus, which is emitted together with electron in the nuclear β decay. This hypothesis resolves both the "wrong spin-statistics" and energy nonconservation problems. Usually this idea is considered as the first invention of the neutrino.



Facsimile:

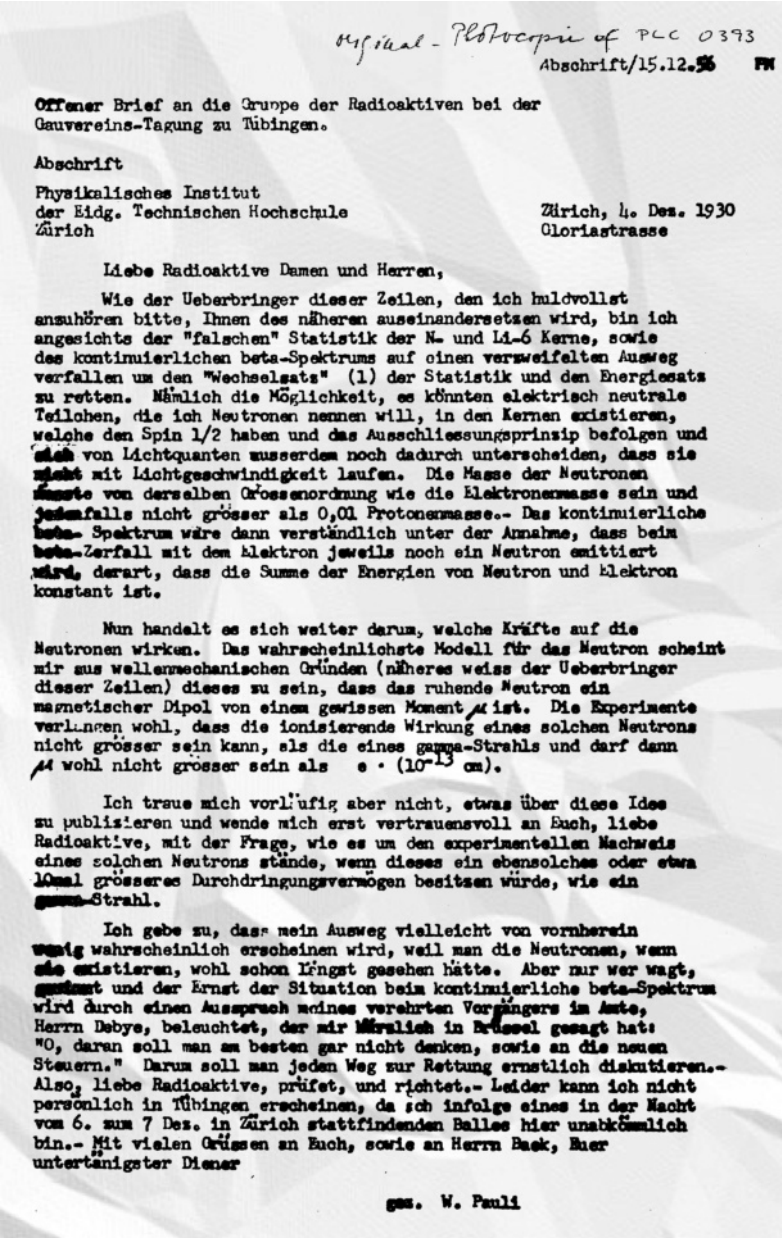

Original - Photocopie of PLC 0393

Abschrift/15.12.30 PM

Offener Brief an die Gruppe der Radioaktiven bei der Gauvereins-Tagung zu Tübingen.

Abschrift

Physikalisches Institut
der Eidg. Technischen Hochschule
Zürich

Zürich, 4. Dez. 1930
Gloriastrasse

Liebe Radioaktive Damen und Herren,

Wie der Ueberbringer dieser Zeilen, den ich huldvollst ansuhören bitte, Ihnen des näheren auseinandersetzen wird, bin ich angesichts der "falschen" Statistik der N- und Li-6 Kerne, sowie des kontinuierlichen beta-Spektrums auf einen verzweifelten Ausweg verfallen um den "Wechselsatz" (1) der Statistik und den Energiesatz zu retten. Nämlich die Möglichkeit, es könnten elektrisch neutrale Teilchen, die ich Neutronen nennen will, in den Kernen existieren, welche den Spin 1/2 haben und das Ausschliessungsprinzip befolgen und sich von Lichtquanten ausserdem noch dadurch unterscheiden, dass sie nicht mit Lichtgeschwindigkeit laufen. Die Masse der Neutronen müsste von derselben Grössenordnung wie die Elektronenmasse sein und jedenfalls nicht grösser als 0,01 Protonenmasse.- Das kontinuierliche beta- Spektrum wäre dann verständlich unter der Annahme, dass beim beta-Zerfall mit dem Elektron jeweils noch ein Neutron emittiert wird, derart, dass die Summe der Energien von Neutron und Elektron konstant ist.

Nun handelt es sich weiter darum, welche Kräfte auf die Neutronen wirken. Das wahrscheinlichste Modell für das Neutron scheint mir aus wellenmechanischen Gründen (näheres weiss der Ueberbringer dieser Zeilen) dieses zu sein, dass das ruhende Neutron ein magnetischer Dipol von einem gewissen Moment μ ist. Die Experimente verlangen wohl, dass die ionisierende Wirkung eines solchen Neutrons nicht grösser sein kann, als die eines gamma-Strahls und darf dann μ wohl nicht grösser sein als $e \cdot (10^{-13}$ cm).

Ich traue mich vorläufig aber nicht, etwas über diese Idee zu publizieren und wende mich erst vertrauensvoll an Euch, liebe Radioaktive, mit der Frage, wie es um den experimentellen Nachweis eines solchen Neutrons stände, wenn dieses ein ebensolches oder etwa 10mal grösseres Durchdringungsvermögen besitzen würde, wie ein gamma-Strahl.

Ich gebe zu, dass mein Ausweg vielleicht von vornherein wenig wahrscheinlich erscheinen wird, weil man die Neutronen, wenn sie existieren, wohl schon längst gesehen hätte. Aber nur wer wagt, gewinnt und der Ernst der Situation beim kontinuierliche beta-Spektrum wird durch einen Ausspruch meines verehrten Vorgängers im Amte, Herrn Debye, beleuchtet, der mir kürzlich in Brüssel gesagt hat: "O, daran soll man am besten gar nicht denken, sowie an die neuen Steuern." Darum soll man jeden Weg zur Rettung ernstlich diskutieren.- Also, liebe Radioaktive, prüfet, und richtet.- Leider kann ich nicht persönlich in Tübingen erscheinen, da ich infolge eines in der Nacht vom 6. zum 7 Dez. in Zürich stattfindenden Balles hier unabkömmlich bin.- Mit vielen Grüssen an Euch, sowie an Herrn Back, Euer untertänigster Diener

gez. W. Pauli

Some extractions:

- Dear Radioactive Ladies and Gentlemen!
- I have hit upon a desperate remedy to save ... the law of conservation of energy.
- ... there could exist electrically neutral particles, which I will call neutrons, in the nuclei ...
- The continuous beta spectrum would then make sense with the assumption that in beta decay, in addition to the electron, a neutron is emitted such that the sum of the energies of neutron and electron is constant.
- But so far I do not dare to publish anything about this idea, and trustfully turn first to you, dear radioactive ones, with the question of how likely it is to find experimental evidence for such a neutron ...
- I admit that my remedy may seem almost improbable because one probably would have seen those neutrons, if they exist, for a long time. But nothing ventured, nothing gained ...
- Thus, dear radioactive ones, scrutinize and judge.

Full English translation:

Open letter to the group of radioactive people
at the Gauverein meeting in Tübingen.

Copy

Physics Institute
of the ETH Zürich

Zürich, Dec. 4, 1930
Gloriastrasse

Dear Radioactive Ladies and Gentlemen,

As the bearer of these lines, to whom I graciously ask you to listen, will explain to you in more detail, because of the "wrong" statistics of the N- and Li-6 nuclei and the continuous beta spectrum, I have hit upon a desperate remedy to save the "exchange theorem" (1) of statistics and the law of conservation of energy. Namely, the possibility that in the nuclei there could exist electrically neutral particles, which I will call neutrons, that have spin 1/2 and obey the exclusion principle and that further differ from light quanta in that they do not travel with the velocity of light. The mass of the neutrons should be of the same order of magnitude as the electron mass and in any event not larger than 0.01 proton mass. – The continuous beta spectrum would then make sense with the assumption that in beta decay, in addition to the electron, a neutron is emitted such that the sum of the energies of neutron and electron is constant.

Now it is also a question of which forces act upon neutrons. For me, the most likely model for the neutron seems to be, for wave-mechanical reasons (the bearer of these lines knows more), that the neutron at rest is a magnetic dipole with a certain moment μ. The experiments seem to require that the ionizing effect of such a neutron can not be bigger than the one of a gamma-ray, and then μ is probably not allowed to be larger than $e \cdot (10^{-13}$ cm).
But so far I do not dare to publish anything about this idea, and trustfully turn first to you, dear radioactive people, with the question of how likely it is to find experimental evidence for such a neutron if it would have the same or perhaps a 10 times larger ability to get through [material] than a gamma-ray.
I admit that my remedy may seem almost improbable because one probably would have seen those neutrons, if they exist, for a long time. But nothing ventured, nothing gained, and the seriousness of the situation, due to the continuous structure of the beta spectrum, is illuminated by a remark of my honored predecessor, Mr. Debye, who told me recently in Bruxelles: "Oh, It's better not to think about this at all, like new taxes," Therefore one should seriously discuss every way of rescue. Thus, dear radioactive people, scrutinize and judge. – Unfortunately, I cannot personally appear in Tübingen since I am indispensable here in Zürich because of a ball on the night from December 6 to 7. With my best regards to you, and also to Mr. Back, your humble servant

signed W. Pauli

[From K. Riesselmann, "Logbook: Neutrino Invention," Symmetry. Dimensions of Particle Physics, Vol. 04, Iss. 02, March 2007, URL: ⟨https://www.symmetrymagazine.org/article/march-2007/neutrino-invention⟩. See also J. Steinberger, "The history of neutrinos, 1930–1985. What have we learned about neutrinos? What have we learned using neutrinos?" Ann. Phys. **327** (2012) 3182–3205.]

Полный русский перевод:

Открытое письмо группе радиоактивных, собравшихся в Тюбингене

Копия

Физический институт
Швейцарская высшая техническая школа Цюриха

Цюрих, дек. 4, 1930
Глориаштрассе

Дорогие радиоактивные дамы и господа!

Как подробно объяснит Вам предъявитель этих строк, которого я любезно прошу Вас выслушать, «неправильная» статистика ядер N- и Li-6 и непрерывный бета-спектр вынудили меня предпринять отчаянную попытку спасения «перестановочной теоремы» (1) статистики и закона сохранения энергии. Она заключается в возможности того, что в ядрах могут находиться электрически нейтральные частицы, которые я буду называть нейтронами, имеющие спин 1/2, удовлетворяющие принципу запрета и отличающиеся от световых квантов еще тем, что движутся они не со скоростью света. Масса нейтронов должна быть того же порядка величины, что и масса электрона; во всяком случае не больше, чем 0.01 массы протона. – Непрерывность бета-спектра станет понятной, если предположить, что при бета-распаде вместе с электроном испускается еще и нейтрон, причем сумма энергий нейтрона и электрона постоянна.

Теперь возникает вопрос о силах, действующих на нейтроны. На мой взгляд, по соображениям, основанным на волновой механике (предъявитель этих строк знает больше) наиболее приемлемая модель для нейтрона состоит в том, что покоящийся нейтрон является магнитным диполем с некоторым моментом μ. Похоже, эксперименты требуют, чтобы ионизационный эффект у такого нейтрона был не больше, чем у гамма-луча и поэтому μ вероятно не может превышать величину $e \cdot (10^{-13}$ см).
Пока я не рискую публиковать что-либо об этой идее и сперва доверчиво обращаюсь к Вам, дорогой радиоактивный народ, с вопросом о том можно ли было бы найти экспериментальные следствия существования такого нейтрона, если бы он обладал такой же как гамма-луч или, возможно, раз в 10 большей проникающей способностью.
Я признаю, что мое допущение может показаться почти невероятным, потому что эти нейтроны, если бы они существовали, пожалуй, давным давно были бы обнаружены. Однако, не рискнув, не выиграешь, а серьезность ситуации с непрерывной структурой бета-спектра проиллюстрировало замечание моего уважаемого предшественника г-на Дебая, который недавно сказал мне в Брюсселе: «Об этом лучше не думать вовсе, как о новых налогах». Поэтому необходимо серьезно обсудить любой путь к спасению. Итак, дорогой радиоактивный народ, проверяйте и судите. – Я сам, к сожалению, не смогу появиться в Тюбингене, так как необходим здесь, в Цюрихе из-за бала в ночь с 6 на 7 декабря. С наилучшими пожеланиями Вам и г-ну Бэку, Ваш покорный слуга

В. Паули.

↓ Радиоактивный народ идею не оценил...

Замечание: В том же 1930-м г. Виктор Амбарцумян и Дмитрий Иваненко высказали гипотезу о том, что β-частицы в ядре нет, а рождается она в самом процессе β-распада. ["Les électrons inobservables et les rayons β," Comptes Rendus Sci. Paris. **190** (1930) 582–584 (présentée par M. M. de Broglie).]

1932 James Chadwick discovers the "true" neutron (particle that Ernest Rutherford proposed in 1920), the proton's partner in the atomic nucleus, with a mass similar to that of the proton.

1932 Dmitri Ivanenko suggests that neutrons are the spin $\frac{1}{2}$ particles and that there were no electrons in the nucleus – only protons and neutrons. The proton-neutron model of the nucleus developed by Werner Heisenberg and, independently, by Ettore Majorana resolved the problem of the wrong spin of ^{14}N and other nuclei. The isospin concept is introduced.

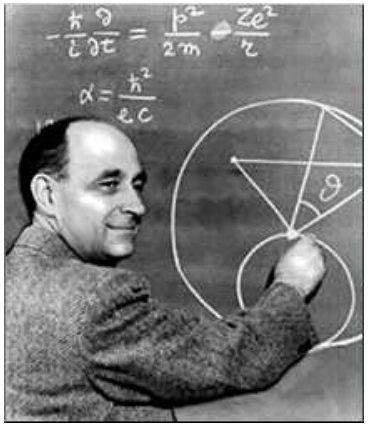

1933–1934 Enrico Fermi formulates the first correct and revolutionary theory of nuclear β-decay, incorporating both neutron and neutrino. Namely, Fermi suggested that the fundamental process underlying the β decay was $n \to p + e^- + \nu$ and wrote the basic $V \times V$ current interaction[a]

$$H_{\mathsf{F}} = G\,(\overline{p}\gamma_\mu n)\,(\overline{e}\gamma^\mu \nu) + \text{h.c.}, \quad G = G_F/\sqrt{2} \quad \text{[modern notation]}.$$

This interaction accounted for the continuous β spectrum, and from the measured shape at the endpoint Fermi concluded that m_ν is small and consistent with zero. Fermi's constant was estimated from the observed lifetimes of radioactive elements; its modern meaning and numerical value are $G_F/(\hbar c)^3 = g^2/(\sqrt{32}M_W^2 c^4) = 1.1663787(6)\times 10^{-5}$ GeV^{-2}.

The statement which can be found in many textbooks that Fermi (together with Amaldi) just *renamed* Pauli's "neutron" to "neutrino" ("little neutral one" in Italian) does not seem to be quite correct since Fermi's neutrino and his model of the nuclear β decay are completely different from those of Pauli. Despite this remark, the significance of Pauli's idea should not be underestimated.

[a] By analogy with $H_{\mathsf{QED}} = e\overline{\psi}\gamma_\mu\psi A^\mu$ and as the very first "beyond QED" extension of the QFT approach.

1934 Hans Bethe and Rudolf Peierls estimate the cross section for the "inverse beta decay" $\overline{\nu} + p \to n + e^+$ by applying the Fermi's Hamiltonian H_{F}. The result was $\sigma_\nu = (4/\pi) G_F^2 p_e^* E_e^* \simeq 2.3 \times 10^{-44}$ cm^2. They conclude: *"... This meant that one obviously would never be able to see a neutrino,"* Indeed, if one computes the (anti)neutrino mean free path in a matter with the proton number density $n = 10^{23}$ cm^{-3}, for $E_\nu = 2.5$ MeV (typical of a weak decay), one obtains $\lambda_\nu \equiv 1/n\sigma_\nu \approx 2.5 \times 10^{20}$ cm $\approx 10^7$ AU. This value is comparable to the thickness of the Galactic disk. Really, how can you catch such a ghost?!...

1935 Maria Göppert-Mayer predicts double β decay ($2\nu\beta\beta$ in modern notation).

1936 Georg Gamow and Edward Teller notice that the $V \times V$ Hamiltonian of Fermi is perhaps too restrictive; they offer an extension of Fermi's theory,

$$H_{\mathsf{GT}} = \sum_i G_i \left(\overline{p} O_i n\right) \left(\overline{e} O_i \nu\right) + \text{H.c.},$$

involving the matrices $O_i = 1,\ \gamma_\mu,\ \gamma_\mu\gamma_5,\ \gamma_5$, and $\sigma_{\mu\nu}$, corresponding to scalar (S), vector (V), axial vector (A), pseudoscalar (P), and tensor (T) currents. Assumed parity conservation suggests that A and P only appear as $A \times A$ or $P \times P$. This step was not the usual trend of theorists to generalize something. It was necessary because nuclear transitions prohibited by the Fermi interaction were observed. The GT Hamiltonian allows such transitions but the price is four more coupling constants.

1937 Ettore Majorana hypothesis that an electrically neutral fermion might be its own antiparticle ($\psi^c(x) = \psi(x)$). Giulio Racah proposes neutrinoless double β-decay ($0\nu\beta\beta$) as a test of Majorana's theory. The $0\nu\beta\beta$ decay (as opposed to $2\nu\beta\beta$ decay) still (2023) not discovered.

1937 Carl Anderson and Seth Neddermeyer and, independently, Jabez Street and Edward Stevenson discover mesotron (now known as muon) in cosmic rays.

Mesotron as the Name of the New Particle

After reading Professor Bohr's address at the British Association last September in which he tentatively suggested the name "yucon" for the newly discovered particle, I wrote to him incidently mentioning the fact than Anderson and Neddermeyer had suggested the name "mesotron" (intermediate particle) as the most appropriate name. I have just received Bohr's reply to this letter in which he says:

"I take pleasure in telling you that every one at a small conference on cosmic-ray problems, including Auger, Blackett, Fermi, Heisenberg, and Rossi, which we have just held in Copenhagen, was in complete agreement with Anderson's proposal of the name 'mesotron' for the penetrating cosmic-ray particles."

ROBERT A. MILLIKAN

California Institute of Technology,
Pasadena, California,
December 7, 1938.

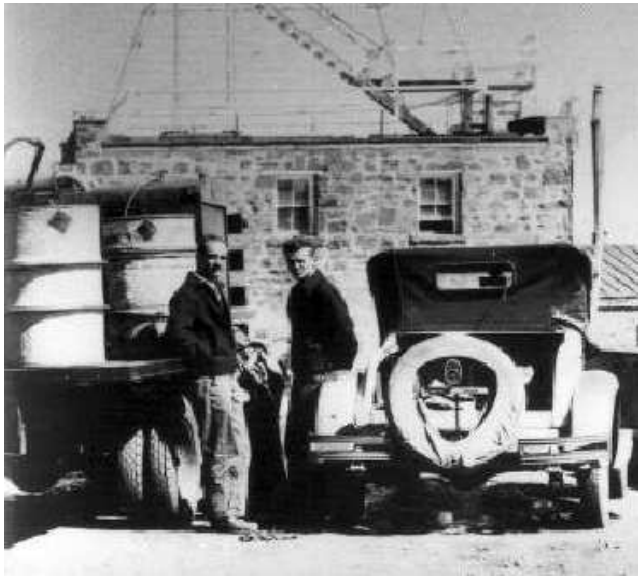

◁ [Phys. Rept. **55** (1939) 105 (a letter to the editor).]

An editorial problem has arisen with regard to the designation of the particle of mass intermediate between the electron and the proton. In the original papers and discussion no less than six different names were used. A vote indicated about equal choice between *meson* and *mesotron* with no considerable support for *mesoton*, *barytron*, *yukon* or *heavy electron*. Except where the authors have indicated a distinct preference to the contrary, we have chosen to use the term *mesotron*.

ARTHUR H. COMPTON

◁ [Rev. Mod. Phys. **11** (1939) 122 (from the foreword to the Proceedings of the Symposium on Cosmic Rays, held at the University of Chicago, June 1939).]

1937–1946 A big confusion:

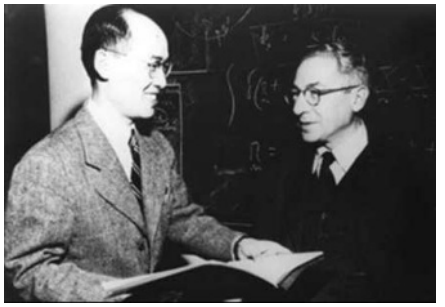

As long as 10 years since the muon was discovered, the physics community believed that it is just the particle predicted by Hideki Yukawa (1935) to account for the short-range strong force between protons and neutrons in nuclei.

From **1941** and through the years of World War II, Oreste Piccioni, Marcello Conversi and Ettore Pancini, carried on a series of observations of the mesotrons stopped in matter (Tomonaga-Araki experiment), which seemed at the beginning to support Yukawa's predictions. They were able to achieve a high level of precision and stability by innovating upon instruments and techniques of the Italian cosmic ray tradition. At the **end of 1946**, they reported that the rates of absorption of mesotrons in light materials were in catastrophic disagreement with the theory.

If mesotrons are not nuclear quanta, what are they? And what new kind of phenomenon was their β like decay? Well, we know that...

Famous exclamation by Isidor Isaac Rabi: "Who ordered that?" Strictly speaking, we still don't have an answer... But! It has long been recognized that mesotrons (muons) are just a gift from heaven.

Not to mention their many applications in physics, muons also have practical functions, namely in muon tomography or muography, a non-destructive technique that uses cosmic-ray muons to reconstruct 2D or 3D density maps of volumes (pyramids, tombs, dams, volcanic vents, glaciers, nuclear reactors, trucks, containers, and even extraterrestrial bodies).

1946 Shoichi Sakata and Takesi Inoue propose the $\pi - \mu$ scheme with a neutrino to accompany muon. They were the first to straighten out the confusion between the mesotron and Yukawa's meson. They
(a) get the spins right,
(b) write down the correct decay chain: $\pi \to \mu\nu_\mu$, $\mu \to e\nu_e\nu_\mu$,
(c) noticed that both ν_μ and ν_e are light neutral fermions, and
(d) suggested that ν_μ and ν_e might be different.

1956 Tsung-Dao Lee and Chen Ning Yang suggest that parity may be violated in weak interactions, which could explain the puzzles of the weak decays of particles called then Θ and τ (kaons). The suggested generalization of the Gamow-Teller Hamiltonian was

$$H_{\mathsf{LY}} = \sum_i \left(\overline{p}O_i n\right)\left[\overline{e}O_i\left(G_i + G_i'\gamma_5\right)\nu\right] + \text{H.c.}.$$

The terms like $V \times A$ or $P \times S$ allow the parity violation, but now we have already ten couplings (G_i and G_i') – they breed like rabbits. However, Lee and Young were fantastically lucky.

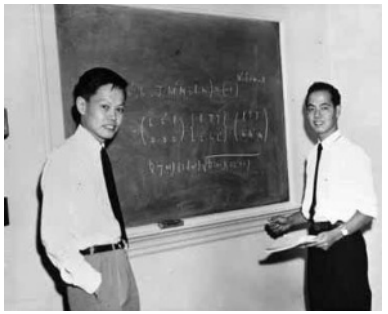

1957 Chien-shiung Wu and coauthors confirm the parity violation studying the direction of emission of the electrons emitted in the β decay of polarized Cobalt-60 [$^{60}\mathsf{Co}(J=5) \to {}^{60}\mathsf{Ni}^*(J=4) + e^- + \overline{\nu}_e$]. The decay rate is proportional to $1 + \alpha(\mathbf{P}\mathbf{n}_e)$, where $\mathbf{P}$ is the cobalt polarization vector and $\mathbf{n}_e$ is the unit vector along the electron velocity. Non–vanishing coefficient α would imply parity violation since $(\mathbf{P}\mathbf{n}_e)$ is a pseudoscalar. The result was that electrons preferred to be emitted in the direction opposite to $\mathbf{P}$ ($\alpha_{\mathsf{exp}} \simeq -0.7$).

1956 Fred Reines and Clyde L. Cowan, Jr. discover electron antineutrinos measuring an inverse β decay reaction $\overline{\nu}_e p \to e^+ n$ (IBD) in a reactor experiment. The IBD positron quickly finds an electron, and they annihilate each other. The two resulting γs are detectable. The neutron can be detected by its capture on a nucleus, releasing a γ. The coincidence of e^+e^- annihilation and neutron capture gives a unique signature of IBD.

1957 Bruno Pontecorvo proposes neutrino-antineutrino oscillations in analogy to $K^0 - \overline{K}^0$, leading to what is later called oscillations into sterile states.

1958 Maurice Goldhaber, Lee Grodzins and Andrew Sunyar found that neutrinos are left handed. The experiment consisted in observing the K-electron capture in ^{152}Eu $(I = 0)$ which produced ^{152}Sm* $(I = 1)$ plus a neutrino. The excited nucleus then decayed into ^{152}Sm $(I = 0) + \gamma$. Hence the measurement of the polarization of the photon gave the required information on the helicity of the neutrino emitted initially. The conclusion was that the results *"seem compatible with ... 100% negative helicity for the neutrinos"*, i.e. that the neutrinos are left handed particles.

1962 Ziro Maki, Masami Nakagawa and Shoichi Sakata introduce the concepts of neutrino flavor mixing and flavor oscillations based on the two-neutrino hypothesis.

1962 Leon Lederman, Mel Schwartz, Jack Steinberger and colleagues at Brookhaven National Laboratory discover muon neutrinos, ν_μ, and confirm that they are different from ν_e.

1964 John Bahcall and Ray Davis propose feasibility of measuring neutrinos from the Sun.

1965 The first naturally occurring neutrinos (actually atmospheric) were observed by Fred Reines with colleagues in the East Rand Proprietary Mine (ERPM, South Africa), and by Goku Menon with colleagues in the Kolar Gold Fields mine (KGF, India), setting first astrophysical limits.

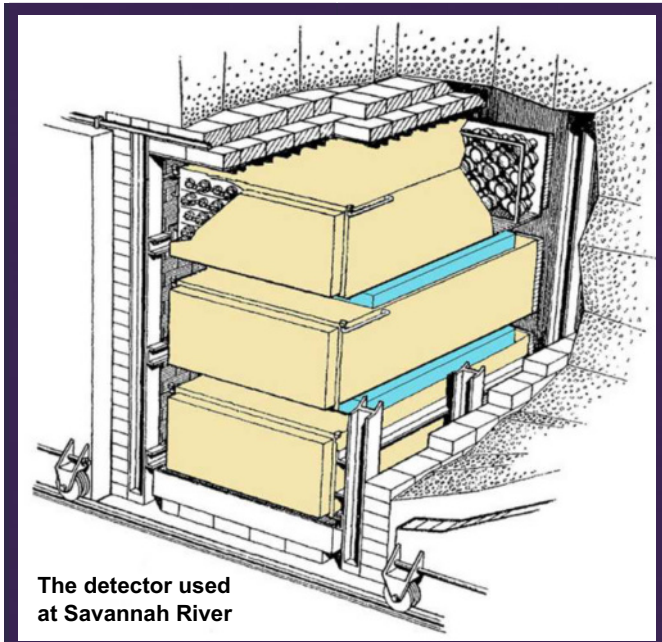

The detector used at Savannah River

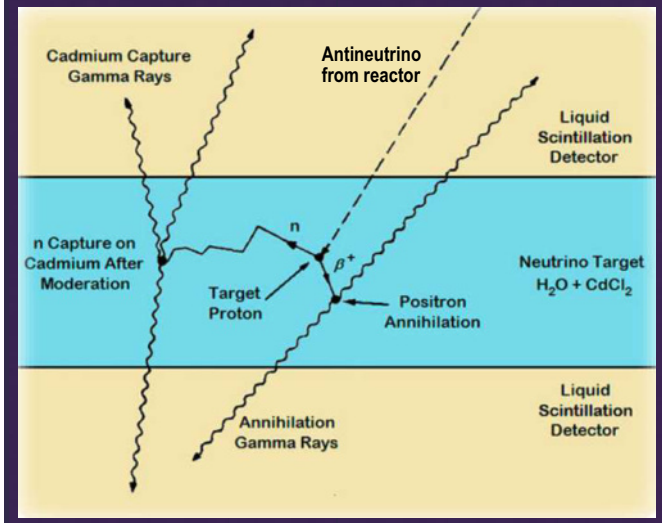

The principle of the delayed-coincidence method for detecting the electron antineutrino in the experiment

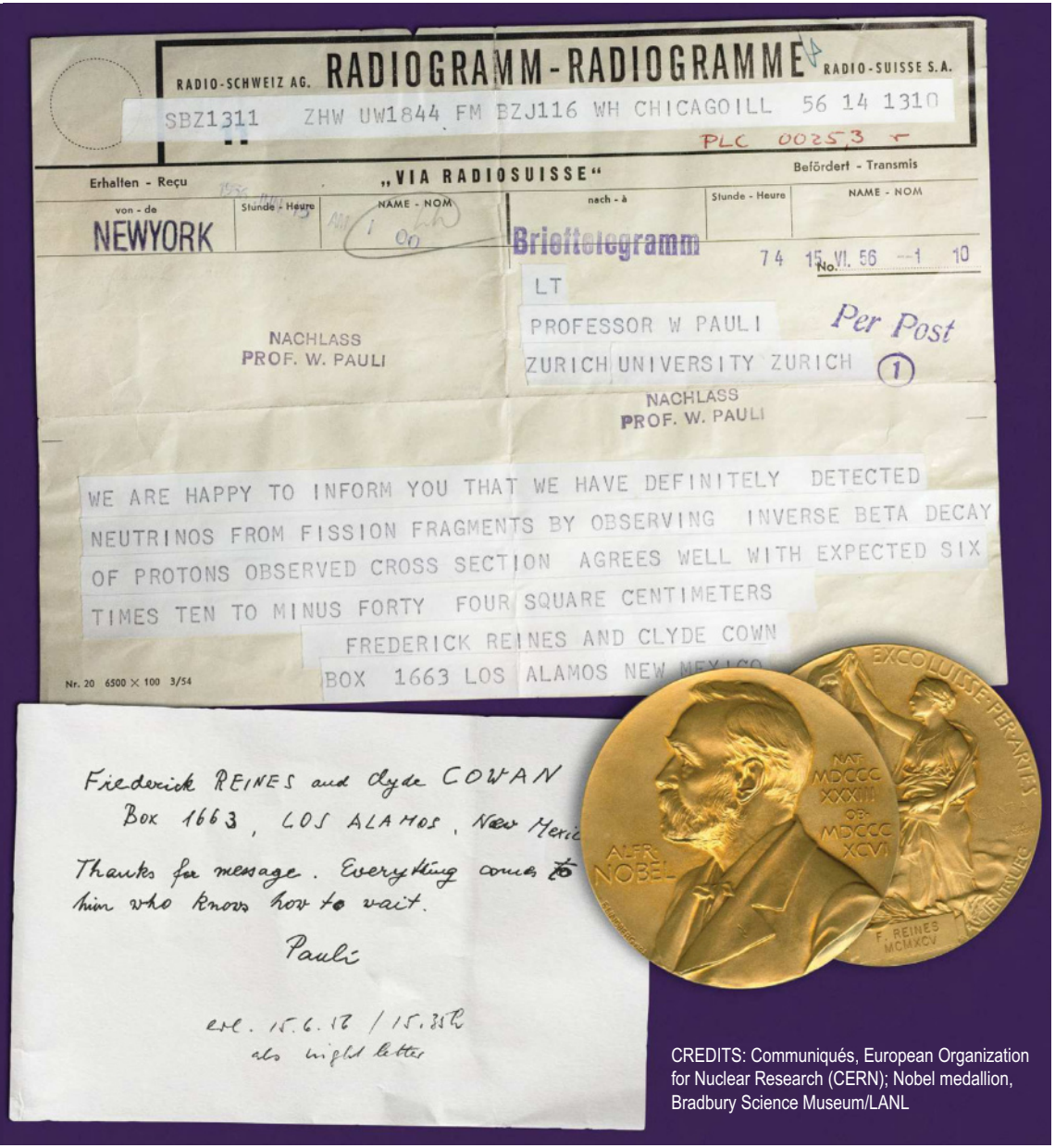

CREDITS: Communiqués, European Organization for Nuclear Research (CERN); Nobel medallion, Bradbury Science Museum/LANL

[From < https://neutrino-history.in2p3.fr/ > and < https://cdn.lanl.gov/files/1663-32-August2018.pdf >.]

The neutrino team at their relatively small detector at KGF in 1965.

Liquid scintillator detector Case-Witwatersrand-Irvine (CWI) at ERPM

The first atmospheric neutrinos were discovered 2 km underground in the Kolar Gold Fields mine (KGF) in Karnataka and 3.5 km underground in the East Rand Proprietary Mine (ERPM) , Witwatersrand Basin at Boksburg, to the east of Johannesburg.

The ERPM was the deepest and largest mine in the World until 2008.

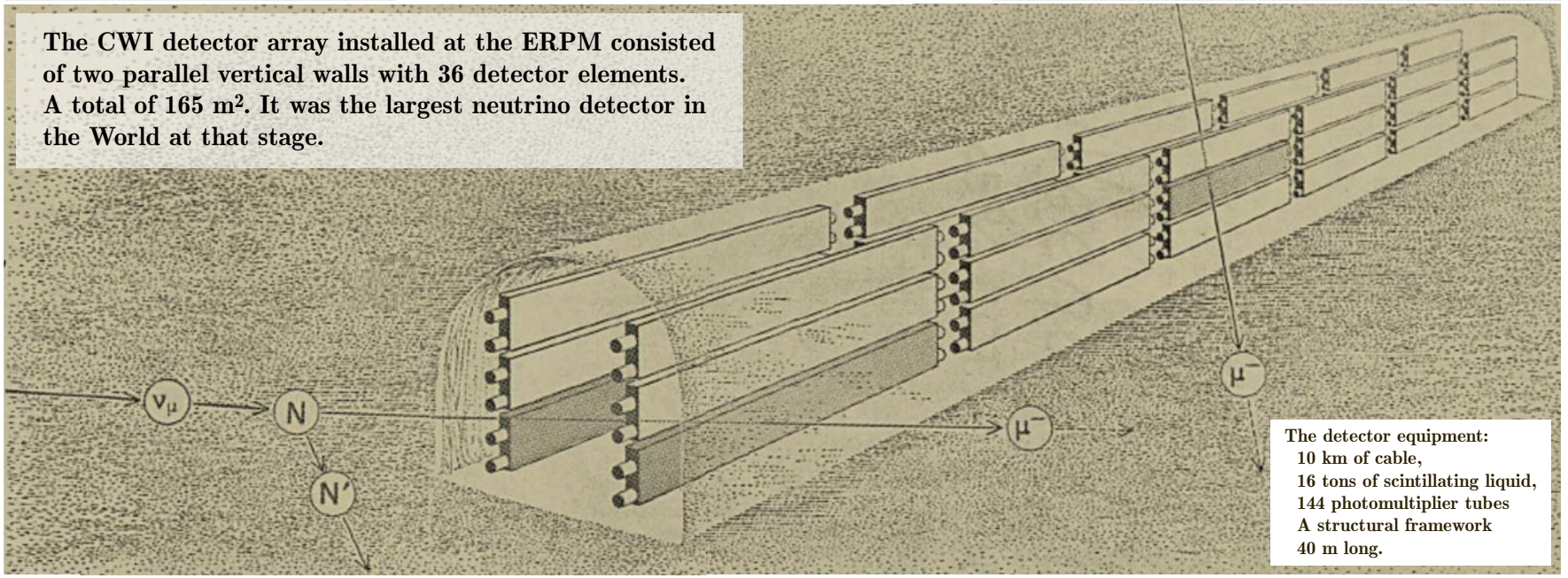

The CWI detector array installed at the ERPM consisted of two parallel vertical walls with 36 detector elements. A total of 165 m^2. It was the largest neutrino detector in the World at that stage.

The detector equipment:
10 km of cable,
16 tons of scintillating liquid,
144 photomultiplier tubes
A structural framework
40 m long.

1968 Ray Davis and his team get the first radiochemical solar neutrino results using a chlorine detector in the Homestake Gold Mine at Lead, South Dakota.

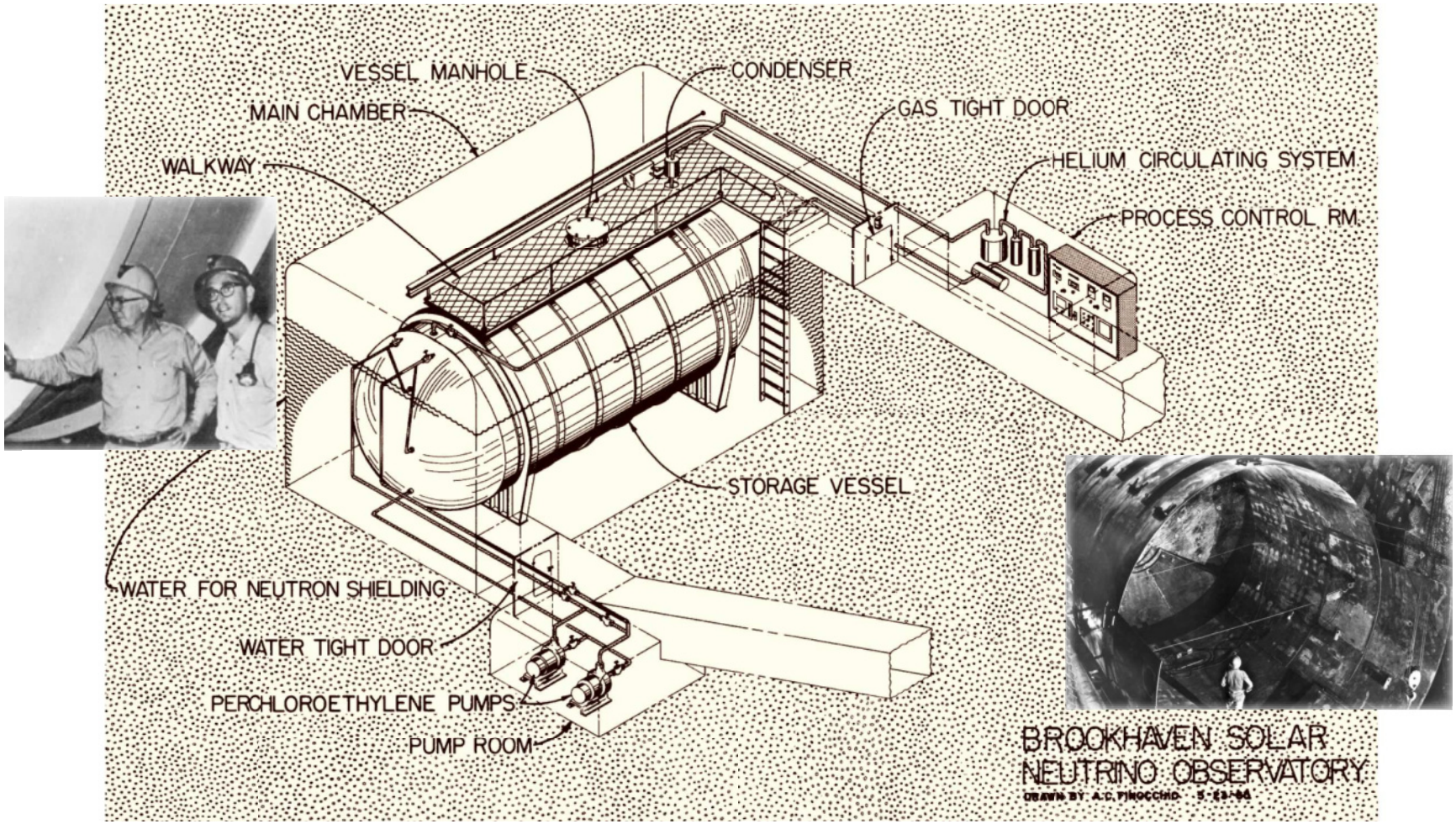

In two runs of the Homestake experiment it has been observed that the detector count rate was substantially smaller than the solar models of the day predicted. That was the first indication of the so-called "solar neutrino problem", see Sect. 33, p. 743.

1976 The tau lepton is discovered by Martin Perl and colleagues at SLAC (Stanford, California). After several years, analysis of τ decay modes leads to the conclusion that τ is accompanied by its own neutrino ν_τ which is neither ν_e nor ν_μ.

1980s The IMB and Kamiokande, the first massive underground nucleon decay search instruments and neutrino detectors are built in a deep Morton Salt mine near Cleveland, Ohio, USA and in Kamioka Zinc-Lead mine near Toyama city, Japan, respectively. Both detectors are huge water-Cherenkov tanks, based on the phenomena of Cherenkov radiation.

1986–1988 The first sign of the "atmospheric neutrino anomaly" (muon neutrino dissappearence) is observed by IMB and Kamiokande.

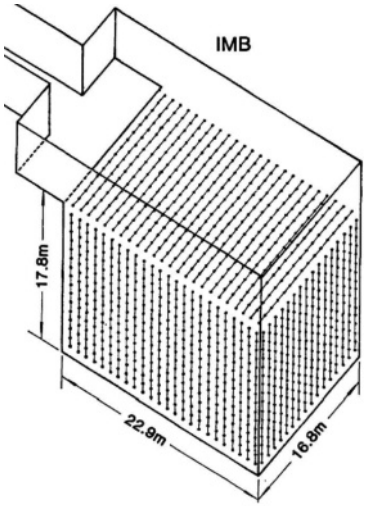

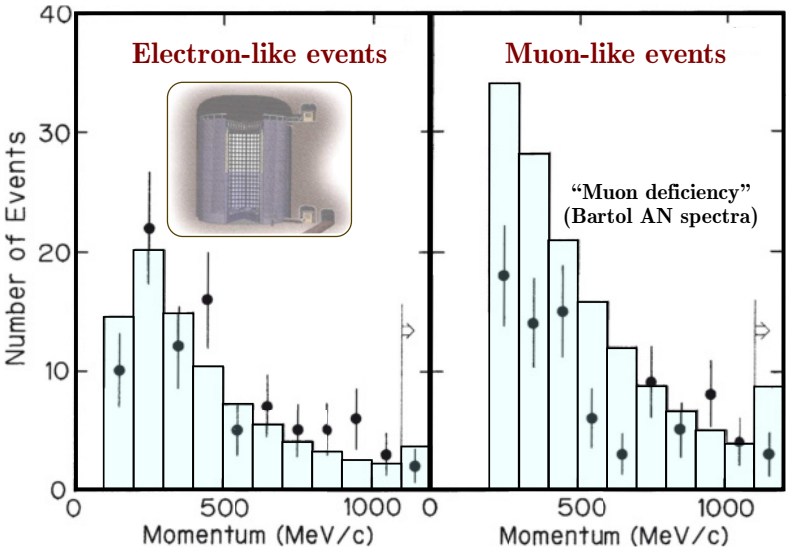

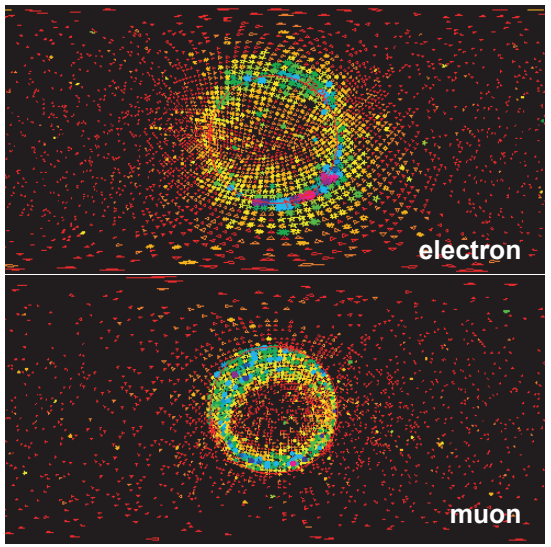

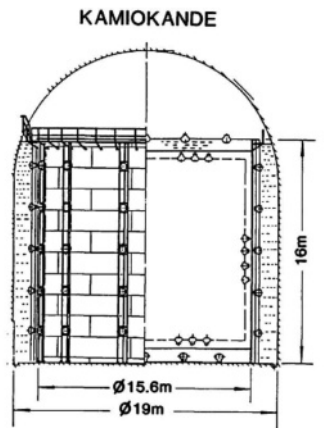

1987–1989 Kamiokande II collaboration performs the first directional counting observation in real time of solar neutrinos and confirms deficit of the ^{8}B neutrino flux.

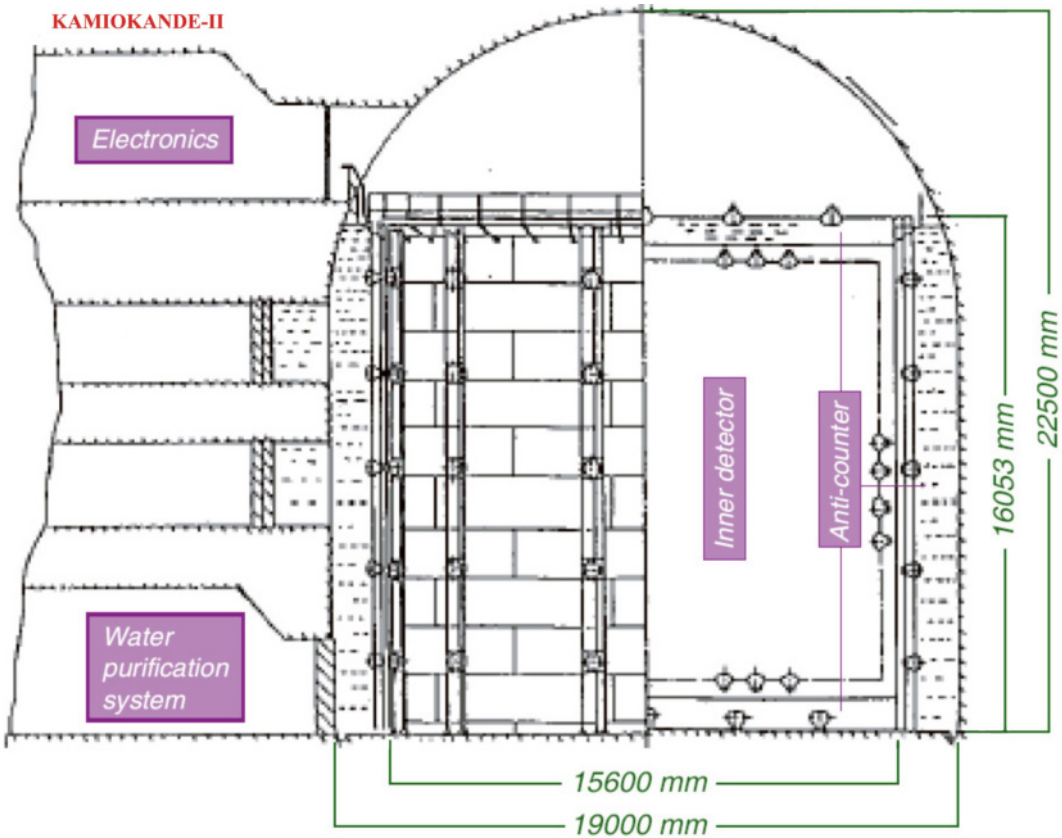

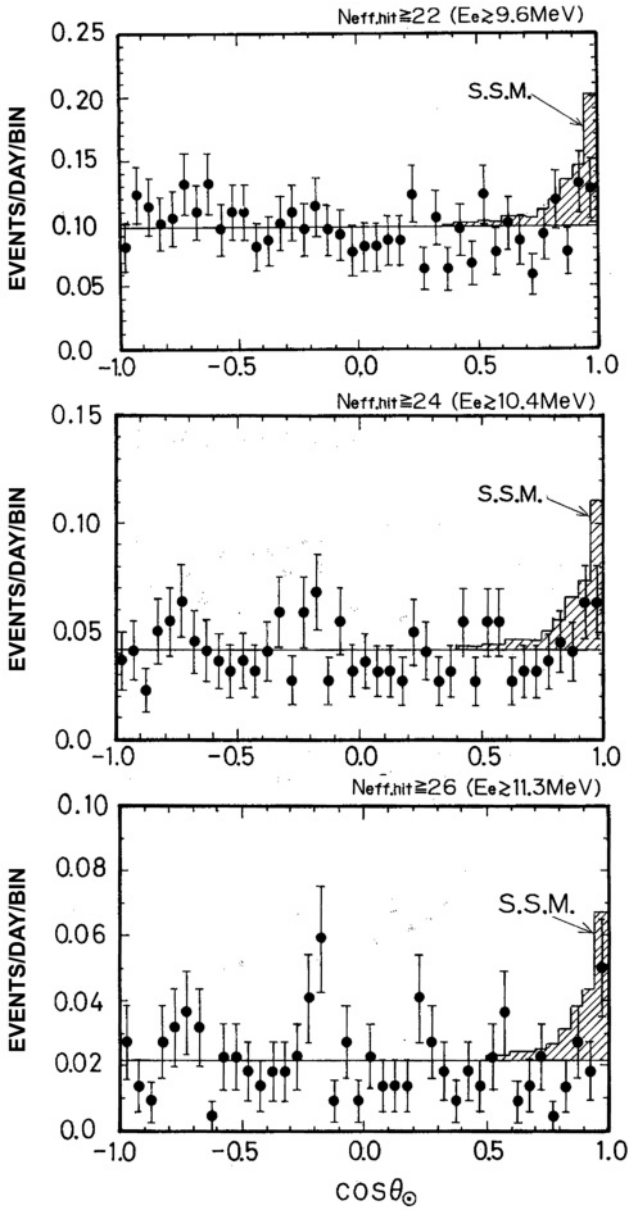

1987 Kamiokande, IMB and Baksan detectors detect burst of antineutrinos from SN 1987A in Large Magellanic Cloud (51.474 kpc), proclaiming the birth of neutrino astronomy, and setting strong limits on neutrino mass and velocity.

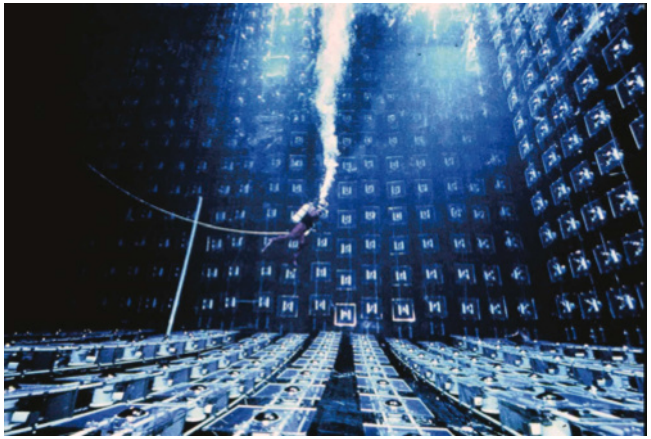

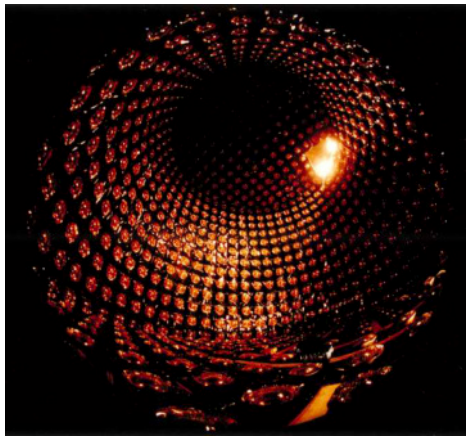

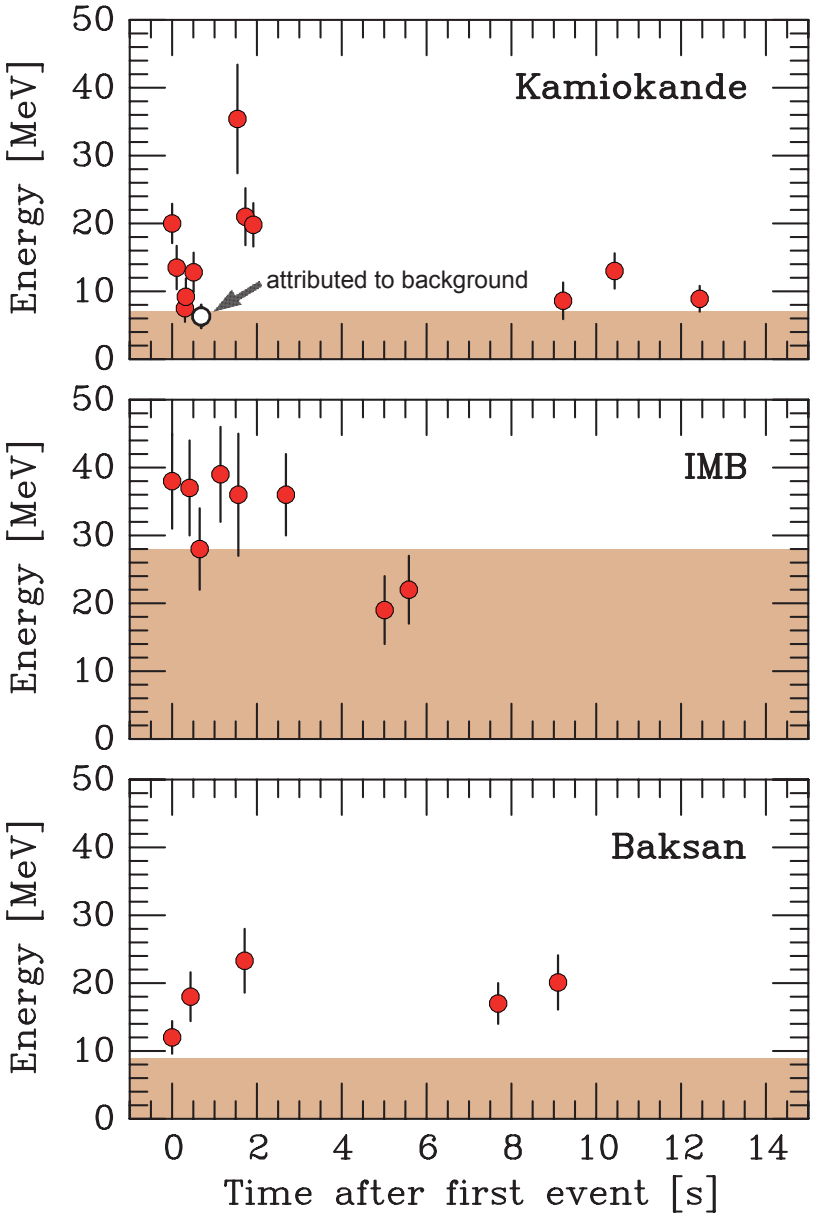

◁ SN 1987A antineutrino observations at Kamiokande, IMB and Baksan detectors. The energies refer to the secondary positrons from the reaction $\overline{\nu}_e p \to n e^+$. In the shaded area the trigger efficiency is less than 30%. The clocks have unknown relative offsets; in each case the first event was shifted to $t = 0$.
The signal does show a number of "anomalies".

- The average $\overline{\nu}_e$ energies inferred from the IMB and Kamiokande observations are quite different.
- The large time gap of 7.3 s between the first 8 and the last 3 Kamiokande events looks worrisome.
- The distribution of the positrons should be isotropic, but is found to be significantly peaked away from the direction of the SN.

In the absence of other explanations, these features are blamed on statistical fluctuations in the sparse data.

[From G. G. Raffelt, "Particle physics from stars," Ann. Rev. Nucl. Part. Sci. **49** (1999) 163–216, hep-ph/9903472.]

Kamiokande II result

TABLE I. Measured properties of the twelve electron events detected in the neutrino burst. The electron angle in the last column is relative to the direction of SN1987A. The errors on electron energies and angles are one-standard-deviation Gaussian errors.

Event number	Event time (sec)	Number of PMT's (N_{hit})	Electron energy (MeV)	Electron angle (degrees)
1	0	58	20.0 ± 2.9	18 ± 18
2	0.107	36	13.5 ± 3.2	15 ± 27
3	0.303	25	7.5 ± 2.0	108 ± 32
4	0.324	26	9.2 ± 2.7	70 ± 30
5	0.507	39	12.8 ± 2.9	135 ± 23
6	0.686	16	6.3 ± 1.7	68 ± 77
7	1.541	83	35.4 ± 8.0	32 ± 16
8	1.728	54	21.0 ± 4.2	30 ± 18
9	1.915	51	19.8 ± 3.2	38 ± 22
10	9.219	21	8.6 ± 2.7	122 ± 30
11	10.433	37	13.0 ± 2.6	49 ± 26
12	12.439	24	8.9 ± 1.9	91 ± 39

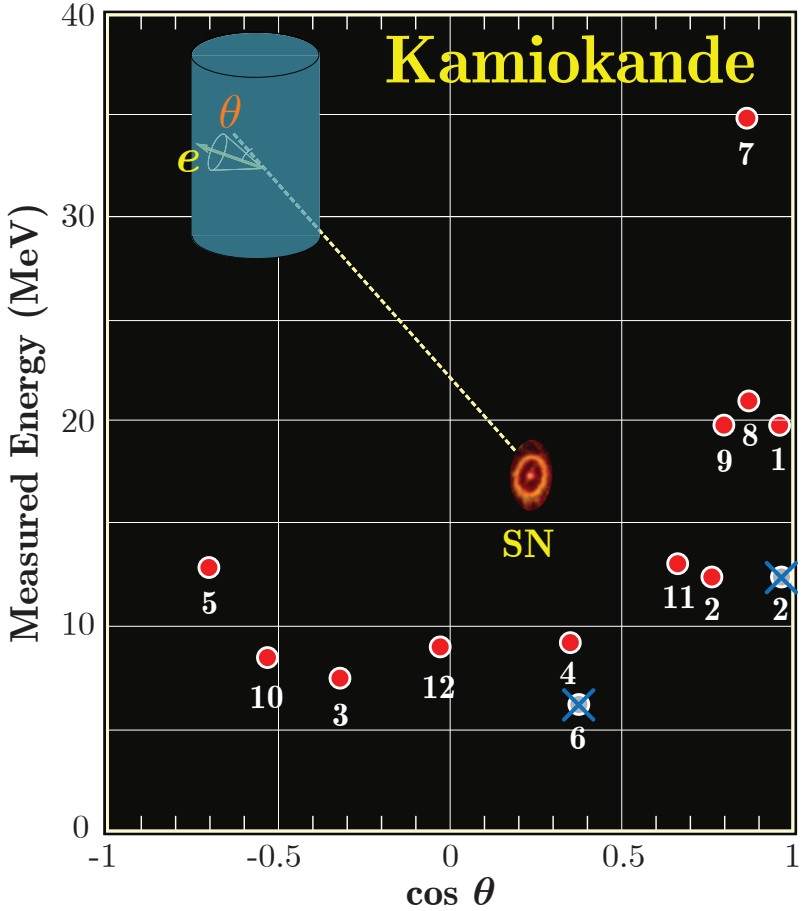

[K. Hirata *et al.* (Kamiokande-II Collaboration) "Observation of a neutrino burst from the supernovae SN 1987A," Phys. Rev. Lett. **58** (1987) 1490–1493; K. Hirata *et al.*, "Observation in the Kamiokande-II detector of the neutrino burst from supernova SN 1987A," Phys. Rev. D **38** (1988) 448–458.]

IMB result

TABLE III. Characteristics of the contained neutrino events recorded on 23 February.

Event No.[a]	Time (UT)	No. of PMT's	Energy[b] (MeV)	Angular distribution[c] (degrees)
33162	7:35:41.37	47	38	74
33164	7:35:41.79	61	37	52
33167	7:35:42.02	49	40	56
33168	7:35:42.52	60	35	63
33170	7:35:42.94	52	29	40
33173	7:35:44.06	61	37	52
33179	7:35:46.38	44	20	39
33184	7:35:46.96	45	24	102

[a]The event numbers are not sequential. Interspersed with the contained neutrino events are fifteen entering cosmic-ray muons.
[b]Error in energy determination is ±25% (systematic plus statistical).
[c]Individual track reconstruction uncertainty is 15°. Note that this angular distribution will be systematically biased toward the source because of the location of the inoperative PMT's.

[R. M. Bionta *et al.*, "Observation of a neutrino burst in coincidence with supernova 1987A in the Large Magellanic Cloud," Phys. Rev. Lett. **58** (1987) 1494–1496.]

TABLE I. Energies and angles of the eight events from supernova SN1987A. (a) Absolute UT is accurate to ±50 ms. Relative times are accurate to the nearest millisecond. (b) Additional systematic error in energy scale estimated to be ±10%. (c) Angle with respect to direction away from SN1987A. Angle errors include multiple scattering and event reconstruction. (d) assumes events are due to $\bar{\nu}+p\rightarrow e^{+}+n$ on free protons.

Event	(a) Time (UT) 23 Feb. 1987	(b) Measured energy (MeV)	(c) Polar angle (deg)	(d) Antineutrino energy (MeV)
1	7:35:41.374	38±7	80±10	41±7
2	7:35:41.786	37±7	44±15	39±7
3	7:35:42.024	28±6	56±20	30±6
4	7:35:42.515	39±7	65±20	42±7
5	7:35:42.936	36±9	33±15	38±9
6	7:35:44.058	36±6	52±10	38±6
7	7:35:46.384	19±5	42±20	21±5
8	7:35:46.956	22±5	104±20	24±5

[C. B. Bratton *et al.* (IMB Collaboration), "Angular distribution of events from SN 1987A," Phys. Rev. D **37** (1988) 3361–3363.]

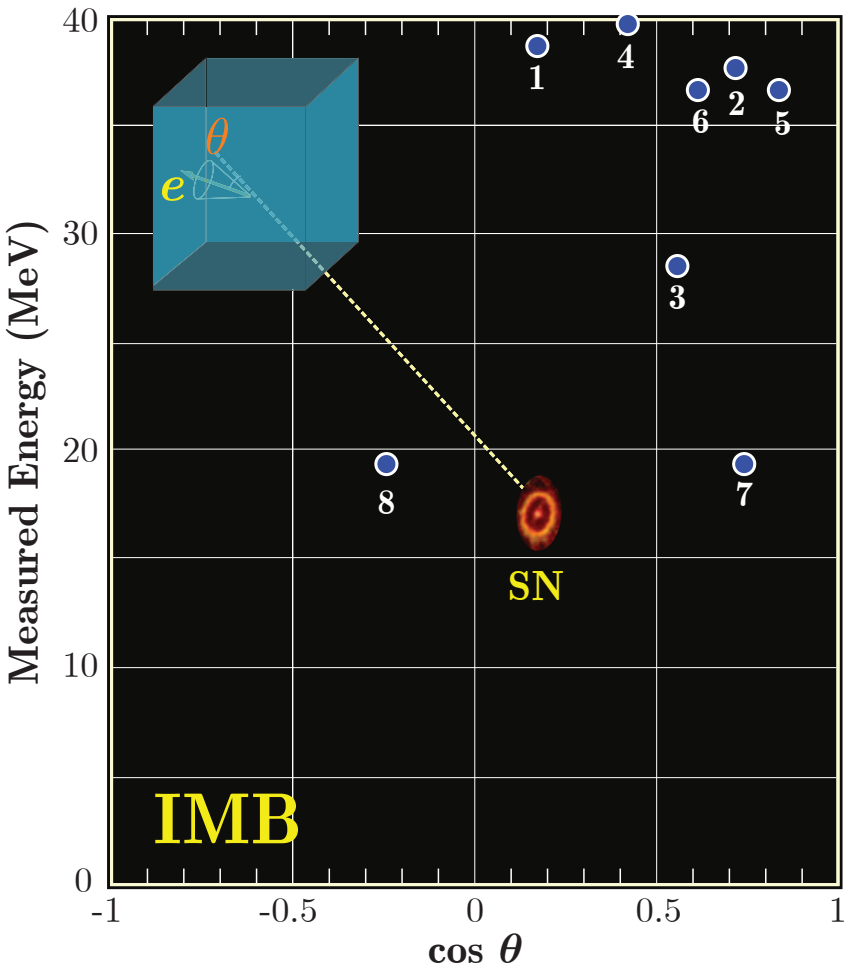

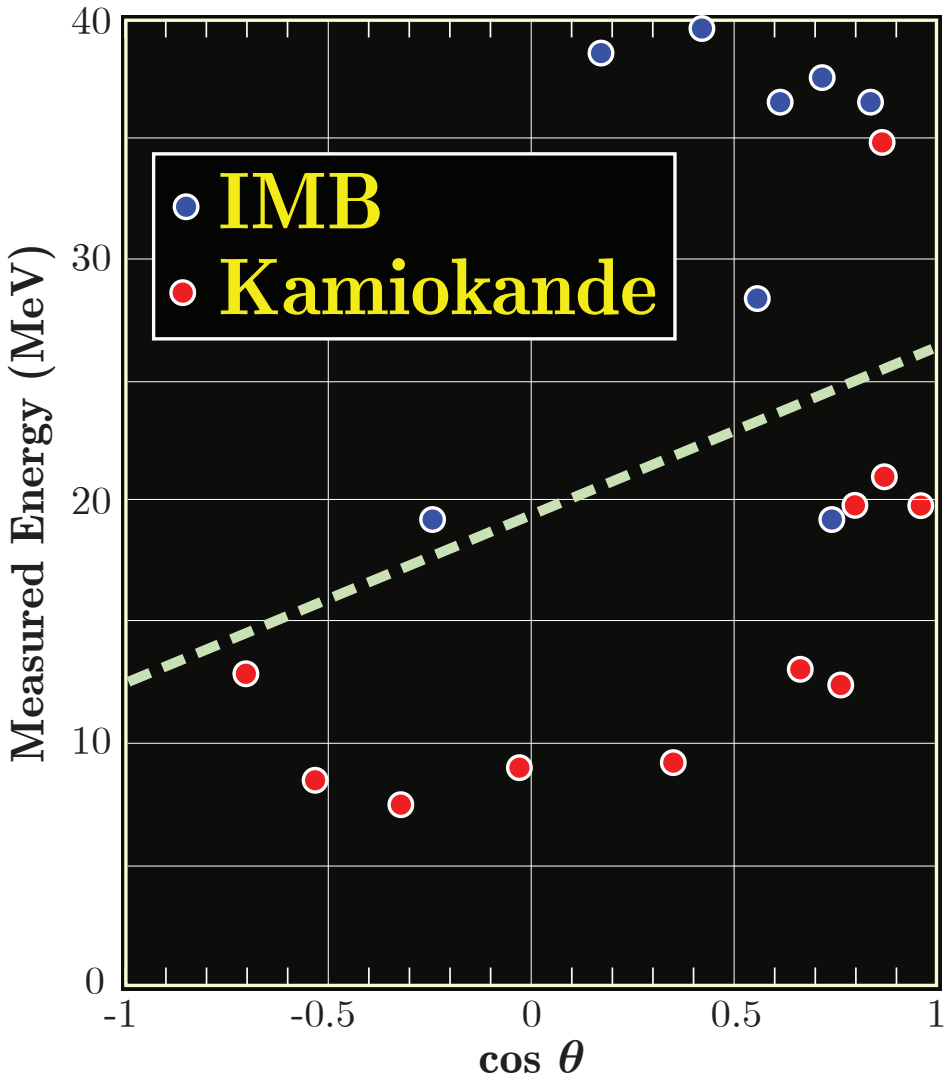

For other interesting facts about SN 1987A, see presentation "Cosmic rays" at ⟨http://theor.jinr.ru/~vnaumov/Eng/JINR_Lectures/NPA.html⟩.

We have to remember about the precursor low-energy antineutrino pulse ($E_{\overline{\nu}} = 7 - 11$ MeV) detected by LSD.[a] at 2:52:36 UT that is $4^{\mathrm{h}}44^{\mathrm{m}}$ earlier the second (Kamiokande-II-IMB-BUST) pulse.

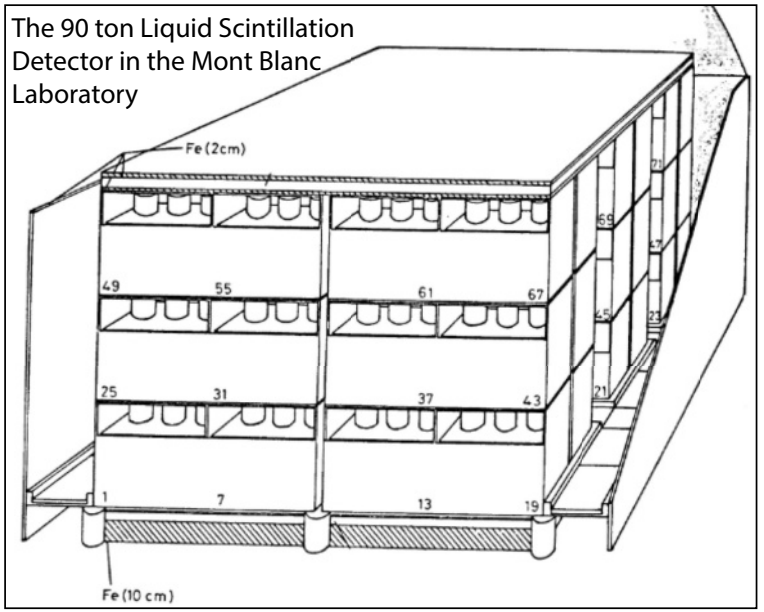

Unfortunately, this fact is often ignored by the community.

[a] V. L. Dadykin *et al.*, "Detection of a rare event on 23 February 1987 by the neutrino radiation detector under Mont Blanc," Pisma v Zh. Eksp. Teor. Fiz. **45** (1987) 464–466 [JETP Lett. **45** (1987) 593–595].

Kamiokande-II and IMB

August 11 – October 20, 1987

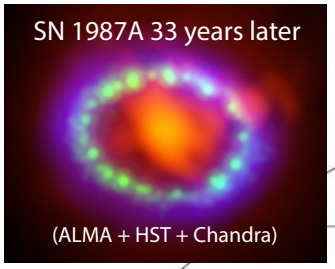

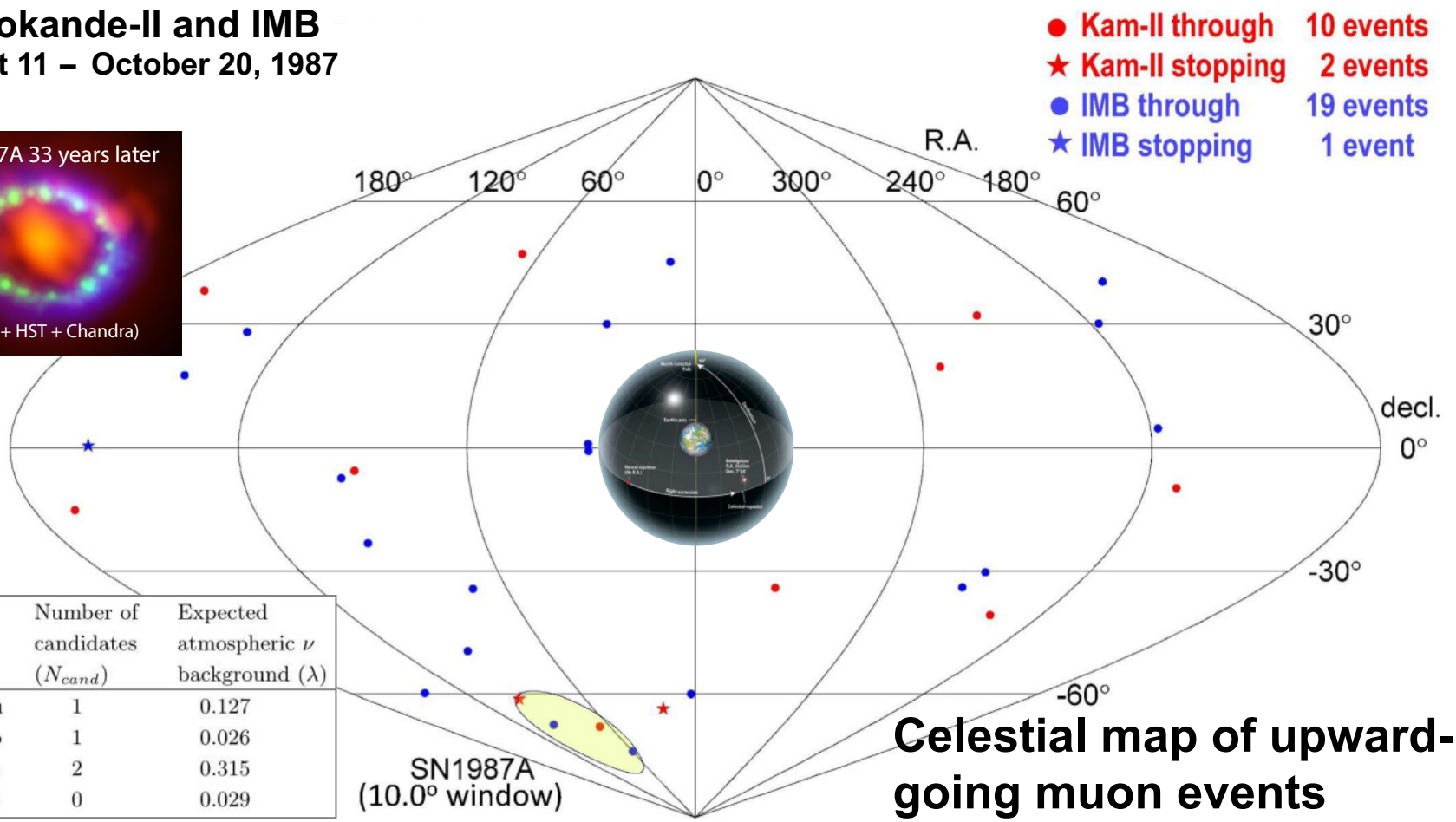

Event Category	Number of candidates (N_{cand})	Expected atmospheric ν background (λ)
Kam-thru	1	0.127
Kam-stop	1	0.026
IMB-thru	2	0.315
IMB-stop	0	0.029

Celestial map of upward-going muon events

Four upward-going muons by Kamiokande-II and IMB are observed between Aug. 11 and Oct. 20, 1987 within a 10.0° angular window around SN 1987A. The probability that these events can be explained by a chance coincidence of atmospheric neutrinos was estimated as 0.27%. These events might be the first (and yet the only) hint of high-energy ($\gtrsim 10$ GeV) νs from a supernova explosion.

[From Y. Oyama, "Evidence of high-energy neutrinos from SN1987A by Kamiokande-II and IMB," ApJ **925** (2022) 166, arXiv:2108.05347 [hep-ex].]

1989 Large Electron-Positron Collider (LEP) experiments in CERN and the SLAC Linear Collider (SLC) determine that there are only 3 light neutrino species (electron, muon and tau).

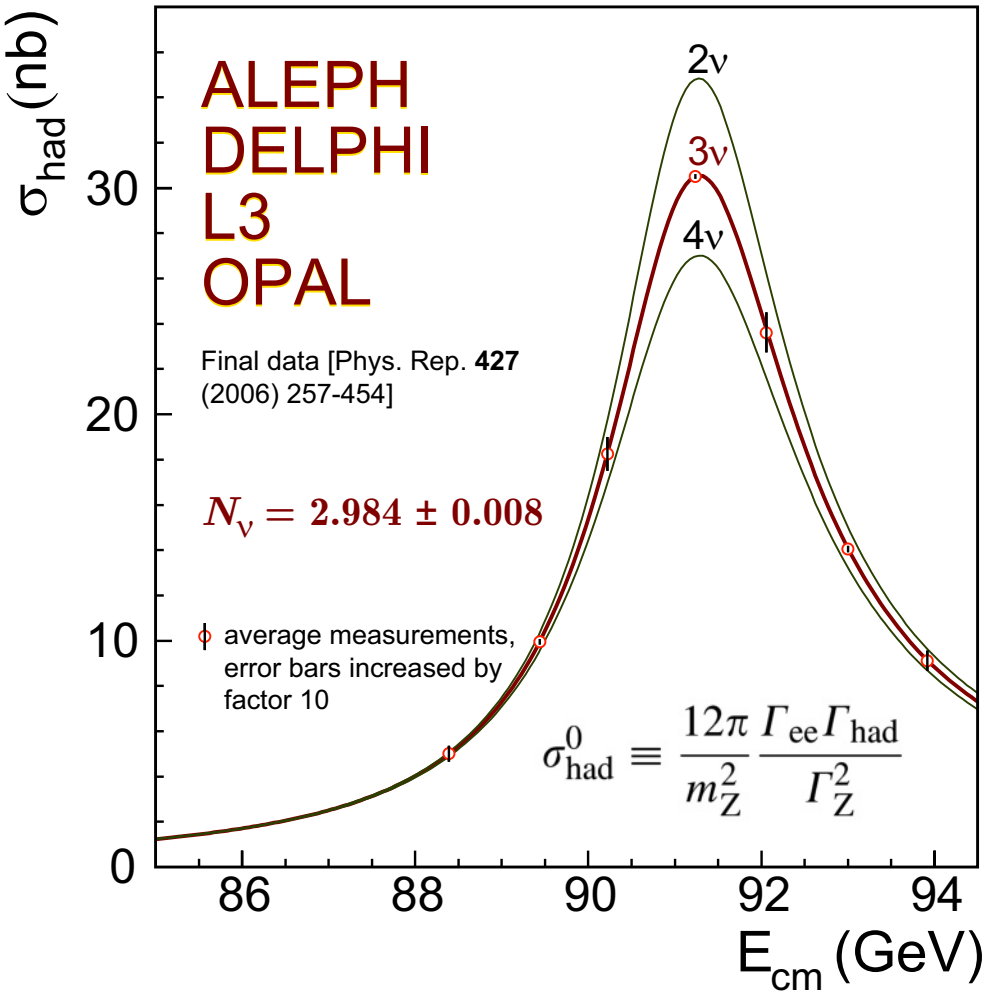

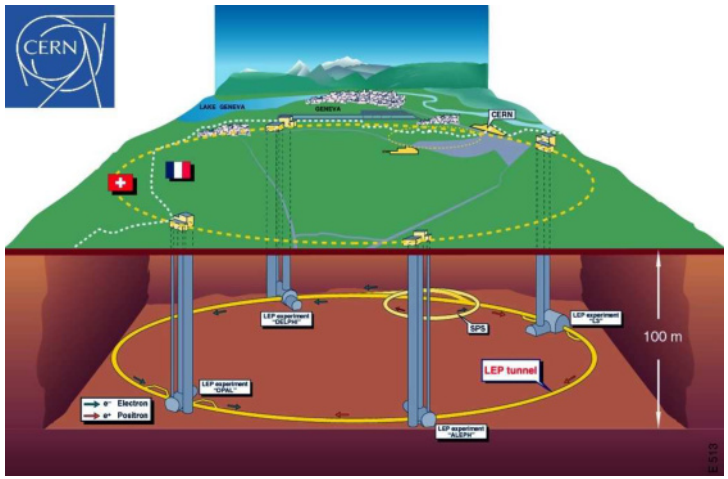

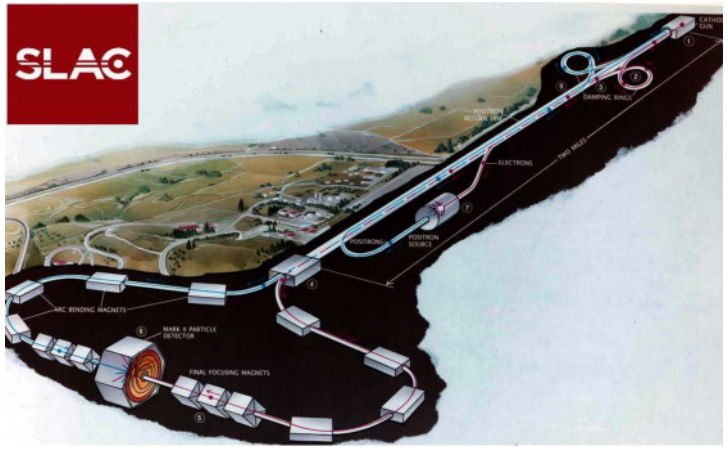

◁ The final combined result of the four LEP detectors on the annihilation cross section $\sigma(e^+e^- \to \text{hadrons})$ near m_Z.

1991–1995 SAGE (Baksan, Russia) and GALLEX (LNGS, Italy) confirm the solar neutrino deficit in Ga-Ge radiochemical experiments.

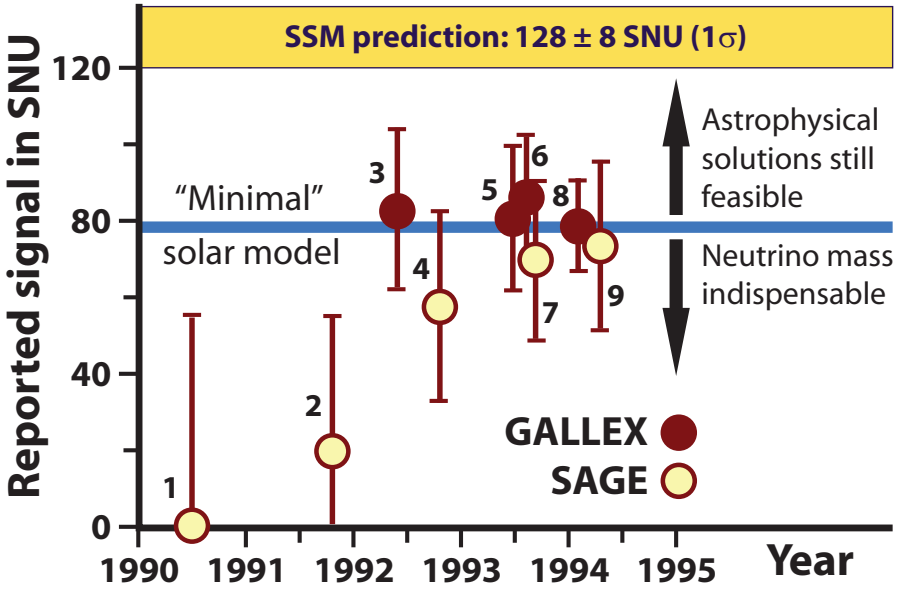

In fact the SAGE and GALLEX results constituted the first experimental observation of Hydrogen fusion in the solar interior. This is fundamental for the theory of stellar structure and evolution. At the same time, the deviation from 100% indicates a deficit of the beryllium and boron neutrinos.

1996 Super-Kamiokande, the largest ever underground neutrino detector, begins catching neutrinos on 1 April with Japan-US team led by Yoji Totsuka.

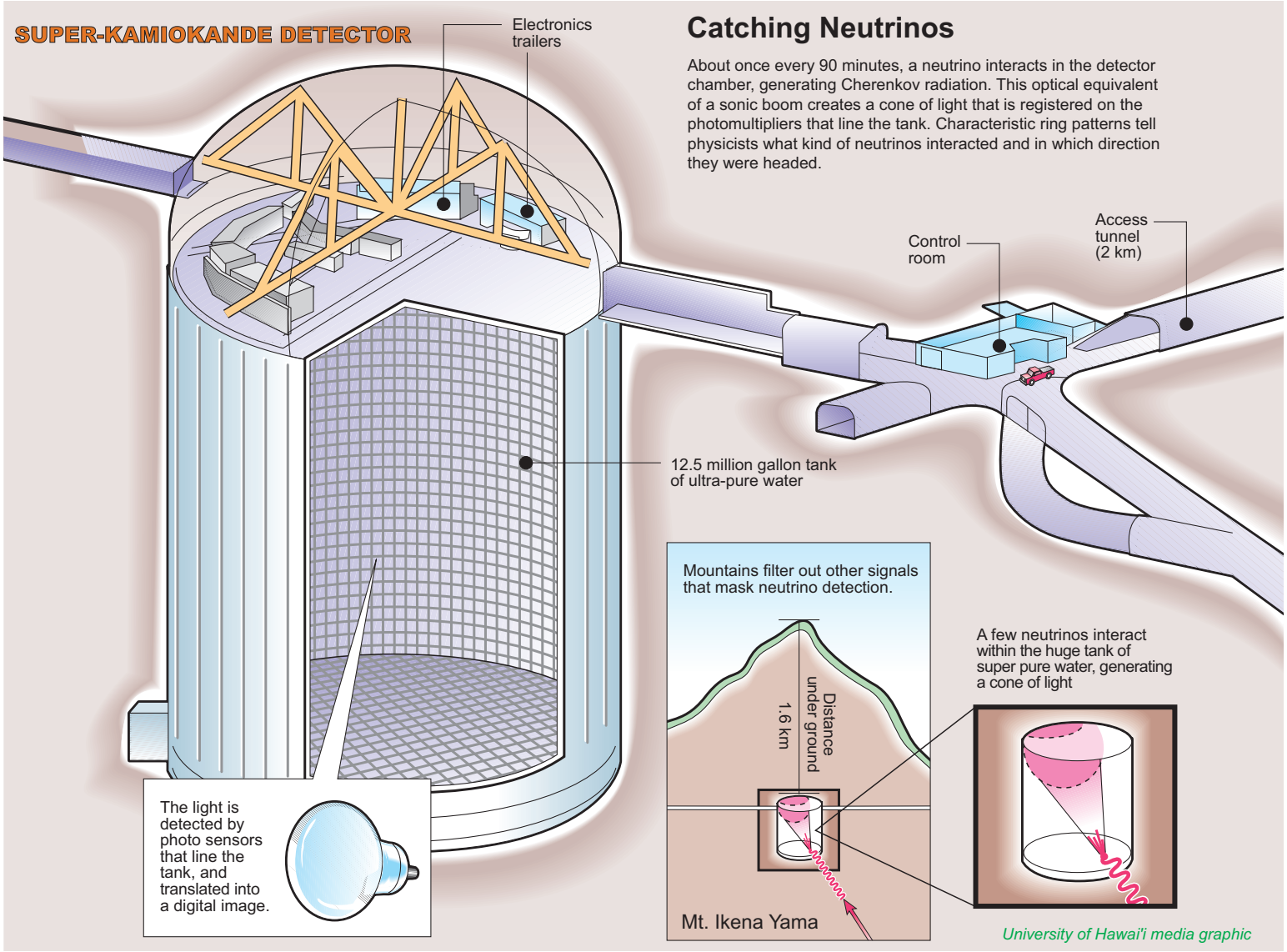

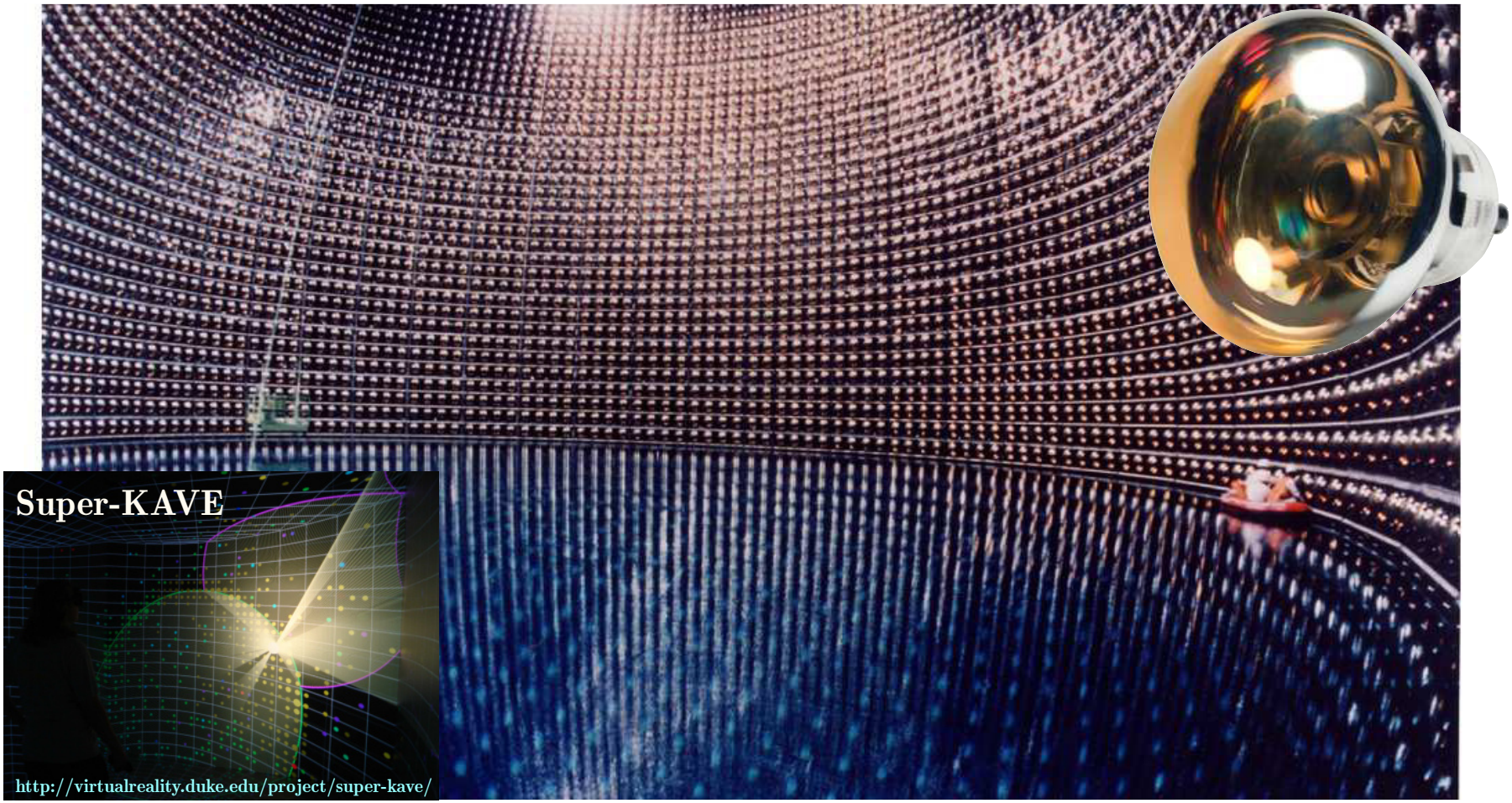

The Super-Kamiokande is located ~ 1 km underground in the Mozumi Mine in Hida's Kamioka area. It consists of a cylindrical stainless steel tank that is 41.4 m tall and 39.3 m in diameter holding 50,000 tons of ultrapure water. The tank volume is divided by stainless steel superstructure into an inner detector (ID) region, which is 36.2 m in height and 33.8 m in diameter, and outer detector (OD) which consists of the remaining tank volume. Mounted on the superstructure are 11,146 PMTs 50 cm in diameter that face the ID and 1,885 20 cm PMTs that face the OD for CR muon vetoing.

1998 After analyzing more than 500 days of data, the Super-Kamiokande team reports finding muon neutrino oscillations in atmospheric neutrinos. After several years these results are confirmed by several experiments and are widely accepted now.

2000 Super-Kamiokande announces that the oscillating partner to the muon neutrino is not a sterile neutrino, but the τ neutrino.

Model dependent ▷

Much less model dependent ▽

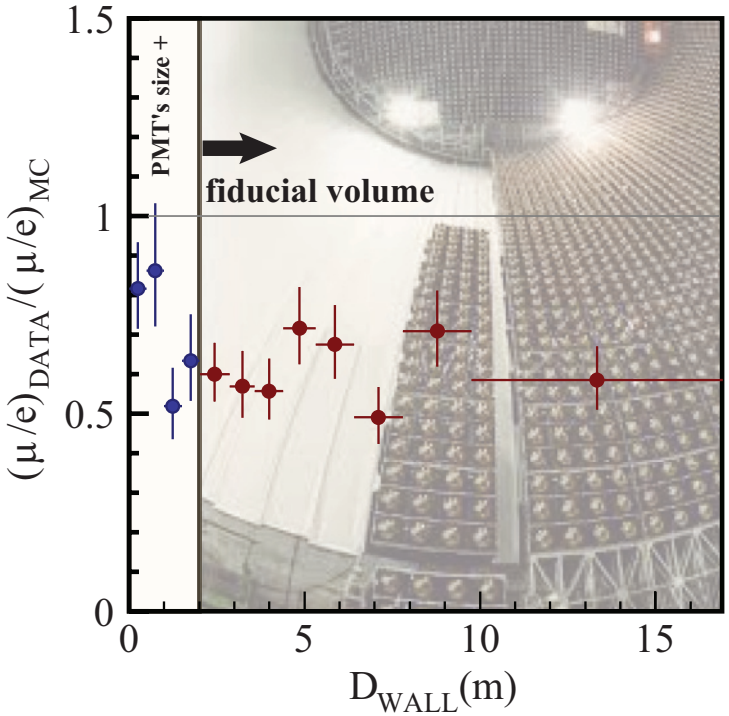

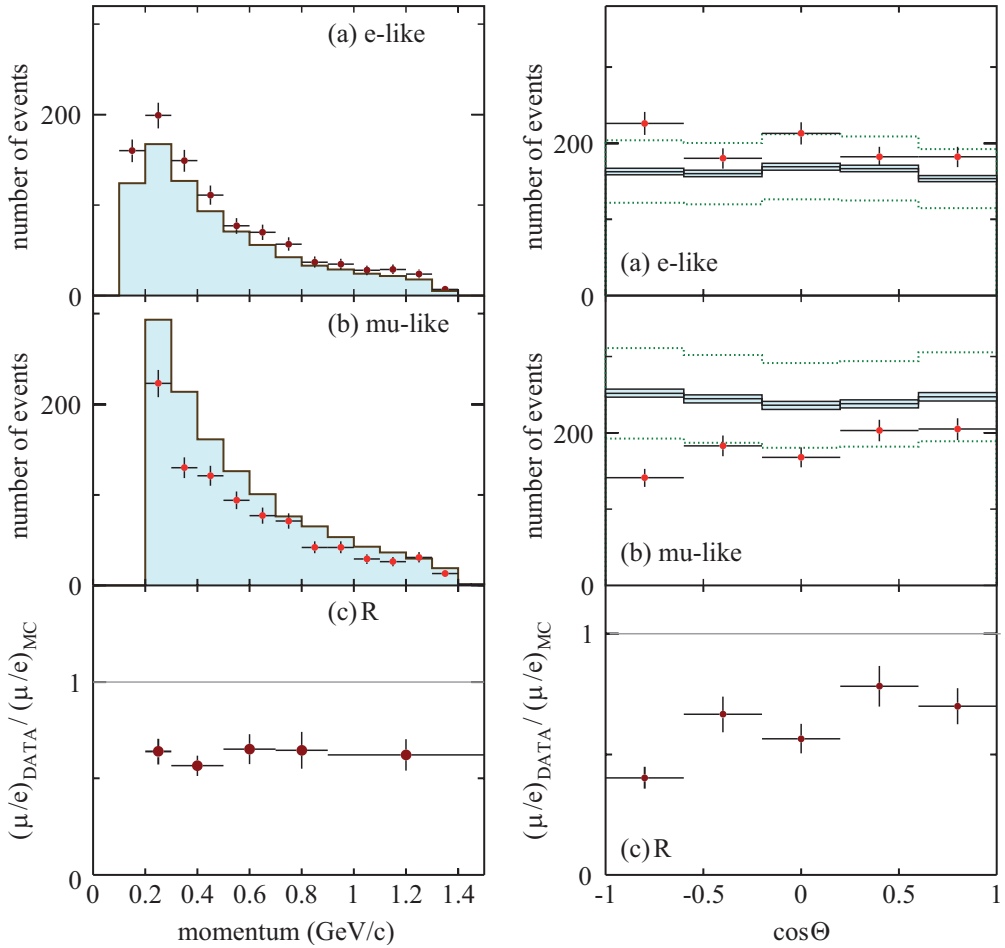

2000 The experiment DONUT (**D**irect **O**bservation of **NU** **T**au, Fermilab E872) announces observation of τ leptons produced by neutrinos, making the first direct observation of the τ neutrino. The signal (4 CC interaction events) was far in excess of the expected background of 0.34 ± 0.05 events.

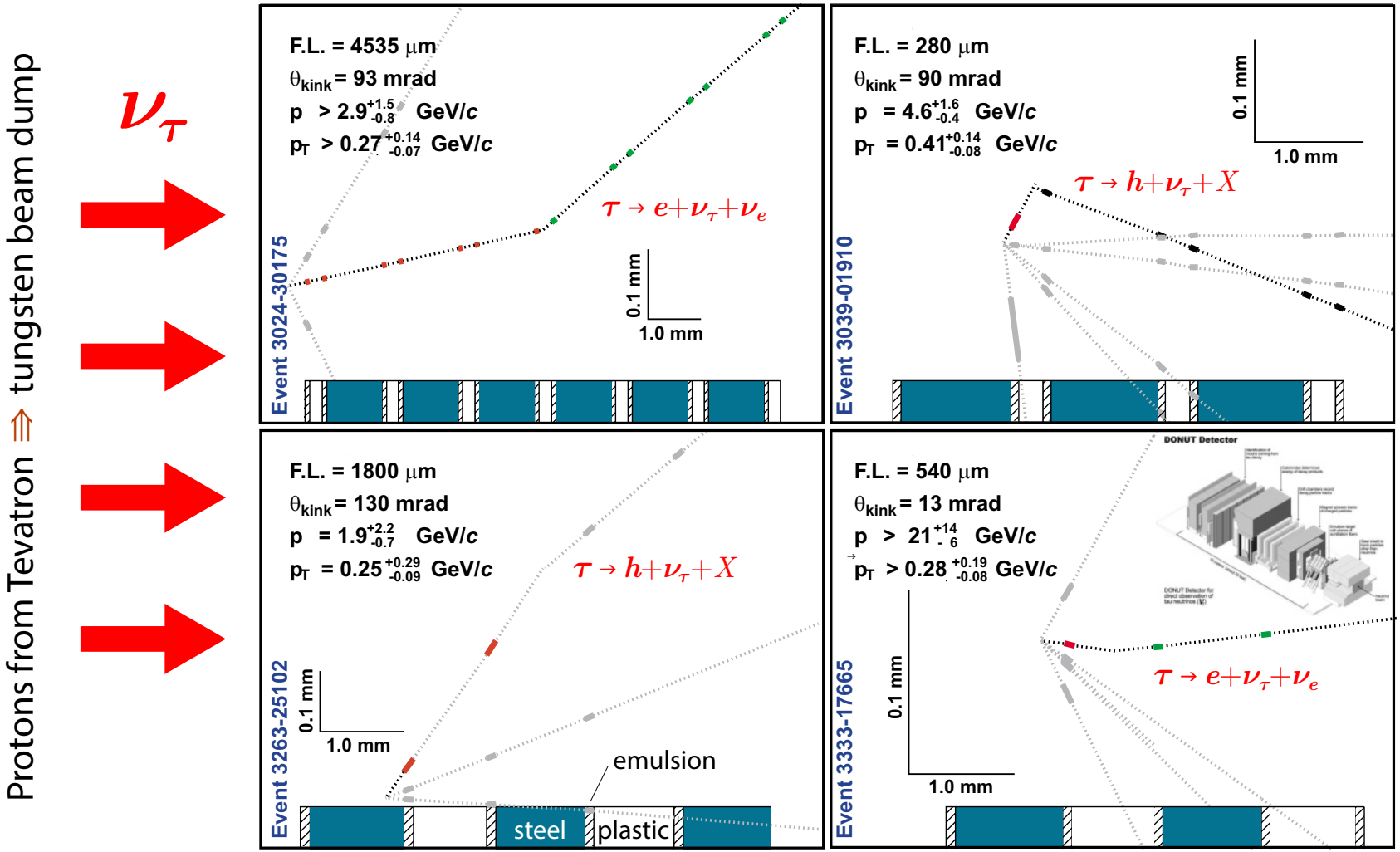

[From K. Kodama *et al.* (DONUT Collaboration), "Observation of tau neutrino interactions," Phys. Lett. B **504** (2001) 218–224, hep-ex/0012035. Note: The DONUT result is consistent with the Standard Model expectation.]

2001 SNO announces observation of neutral currents from solar neutrinos, along with charged currents and elastic scatters, providing convincing evidence that neutrino oscillations are the cause of the solar neutrino problem.

2002 KamLAND begins operations in January and in November announces detection of a deficit of electron antineutrinos from reactors at a mean distance of about 180 km in Japan. The results combined with all the earlier solar neutrino results, establish the correct parameters for the solar neutrino deficit (the LMA solution is preferred).

2004 Super-Kamiokande and KamLAND present firm evidences for neutrino disappearance and reappearance, fully eliminating non-oscillations models.

2005 KamLAND announces detection of electron antineutrino flux from Earth ("geoneutrinos") and makes the first measurements of the radiogenic heat production rate of the Earth.

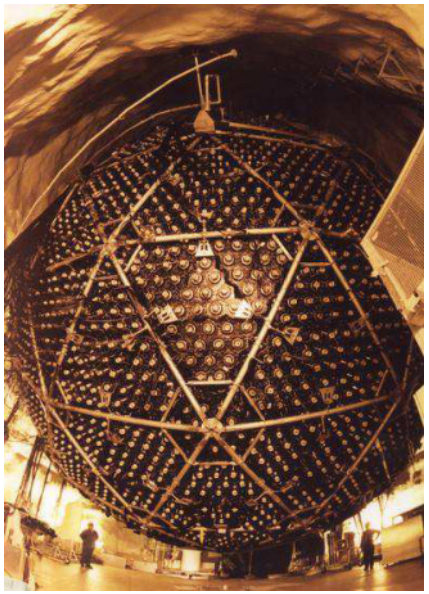

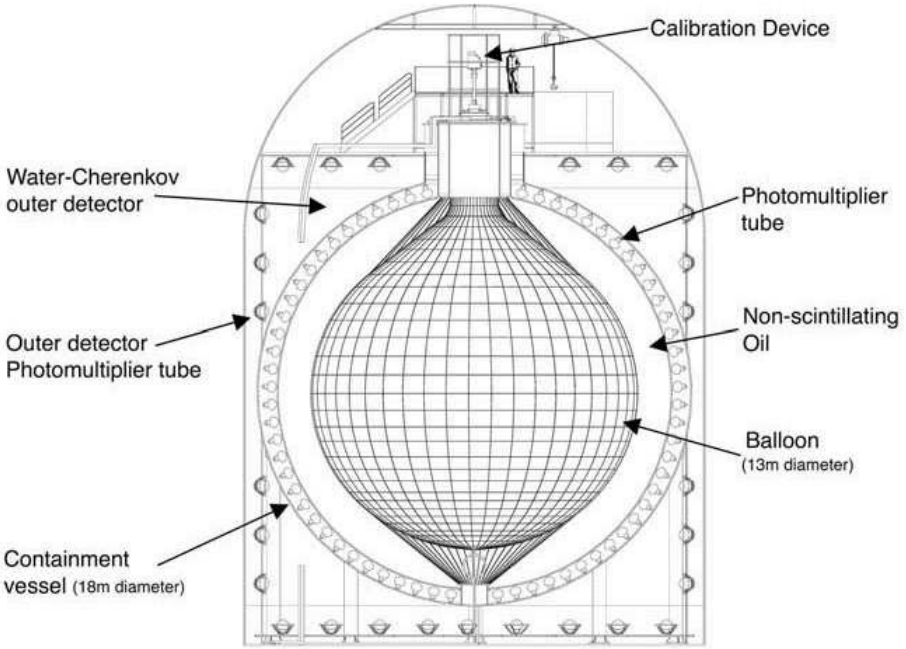

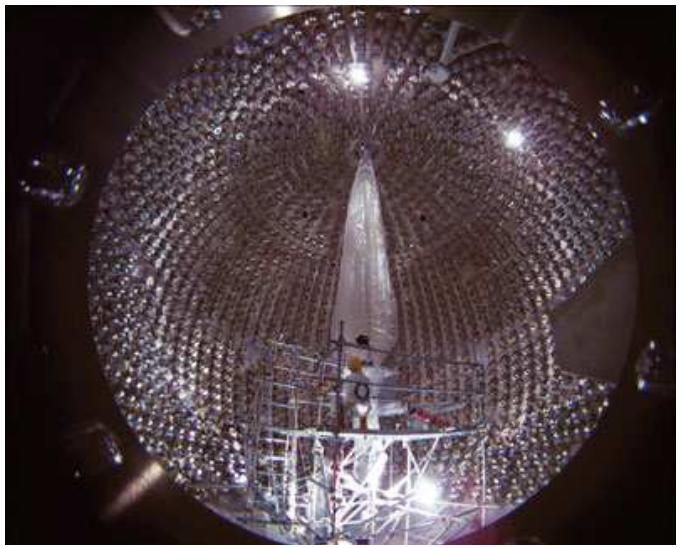

KamLAND is surrounded by 53 Japanese commercial power reactors, at a flux weighted average distance of about 180 km from the reactors.

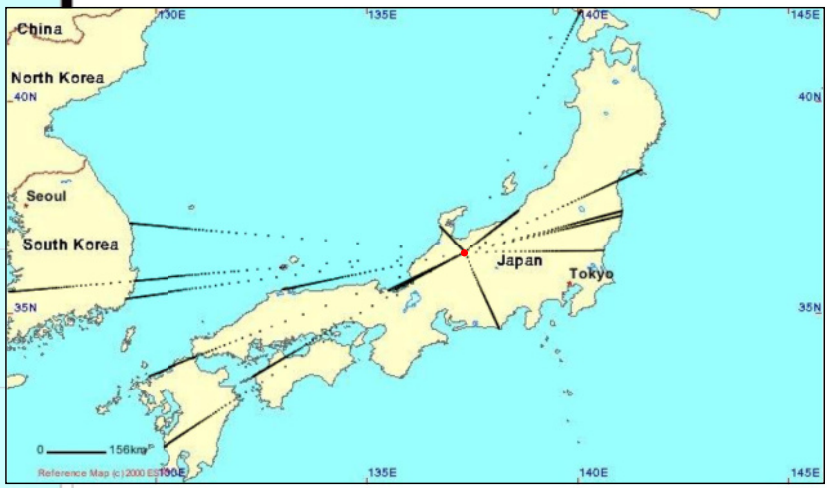

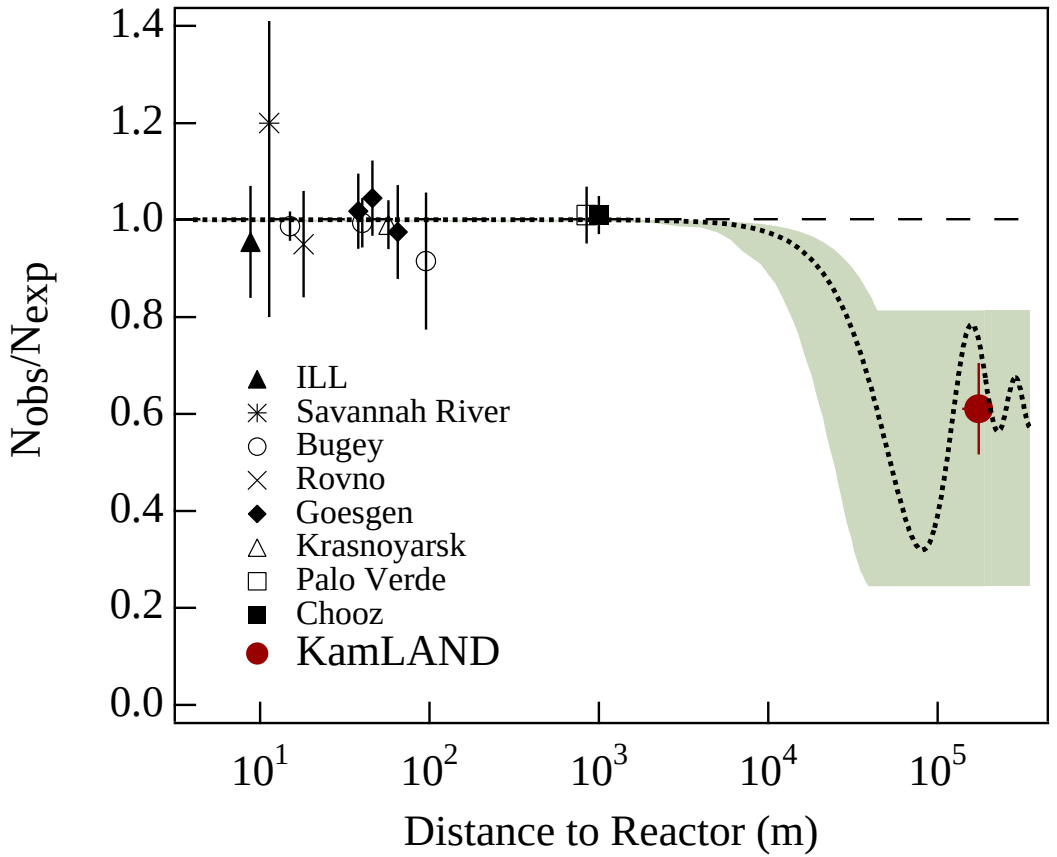

The ratio of measured to expected $\overline{\nu}_e$ flux from reactor experiments. The large solid circle is the KamLAND 2002 result plotted at a flux-weighted average distance of ~ 180 km. The shaded region indicates the range of flux predictions corresponding to the 95% C.L. large mixing angle (LMA) region from a global analysis of the solar neutrino data by G. L. Fogli *et al*. The dotted curve, $\sin^2 2\theta_{\mathsf{sol}} = 0.833$ and $\Delta m^2_{\mathsf{sol}} = 5.5 \times 10^{-5}$ eV^2, is representative of a best-fit LMA prediction and the dashed curve is expected for no oscillations.

[From K. Eguchi *et al*. (KamLAND Collaboration), "First results from KamLAND: Evidence for reactor antineutrino disappearance," Phys. Rev. Lett. **90** (2003) 021802, arXiv:0212021 [hep-ex].]

2010 The experiment OPERA (**O**scillation **P**roject with **E**mulsion-t**R**acking **A**pparatus) in the CNGS neutrino beam announces observation of the first ν_τ candidate event.

The figure on the right displays the event in two projections:

Top left: view transverse to the beam direction.

Top right: the same view zoomed on the vertices.

Bottom: longitudinal view.

Most probable reconstruction of the event is: $\nu_\tau N \rightarrow \tau^- X$, $\tau^- \rightarrow \rho^- \nu_\tau$, $\rho^- \rightarrow \pi^- \pi^0$. The oscillation hypothesis is in agreement with the observation.

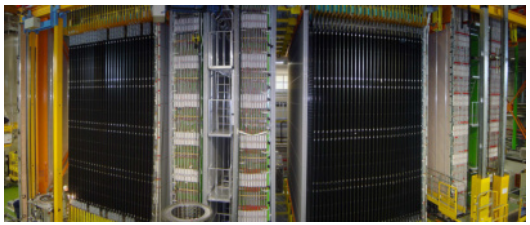

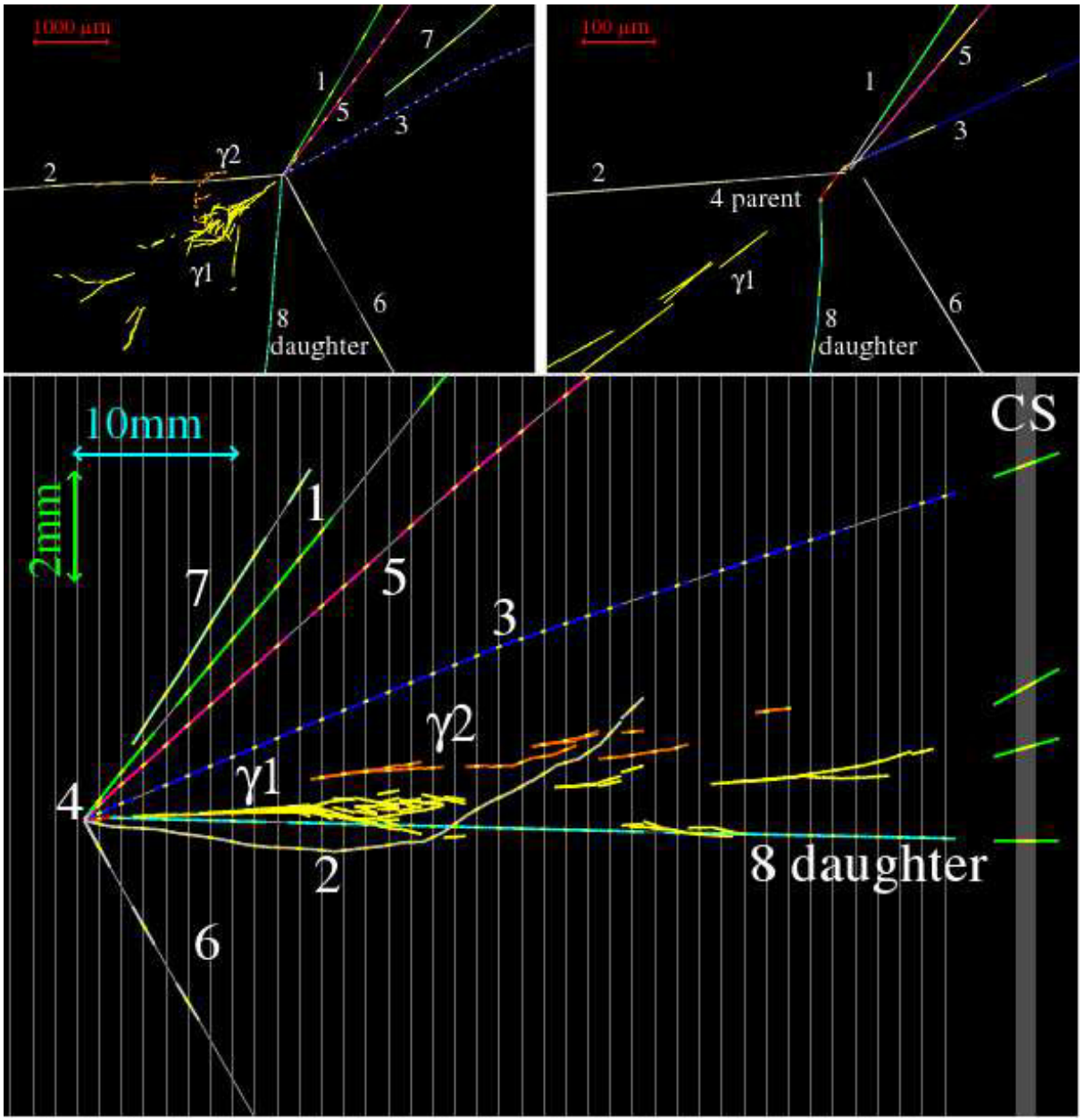

2011 Borexino experiment at LNGS reports a high-precision measurement of the interaction rate of 862 keV ^{7}Be solar νs and confirms the MSW-LMA solution of the solar neutrino problem.

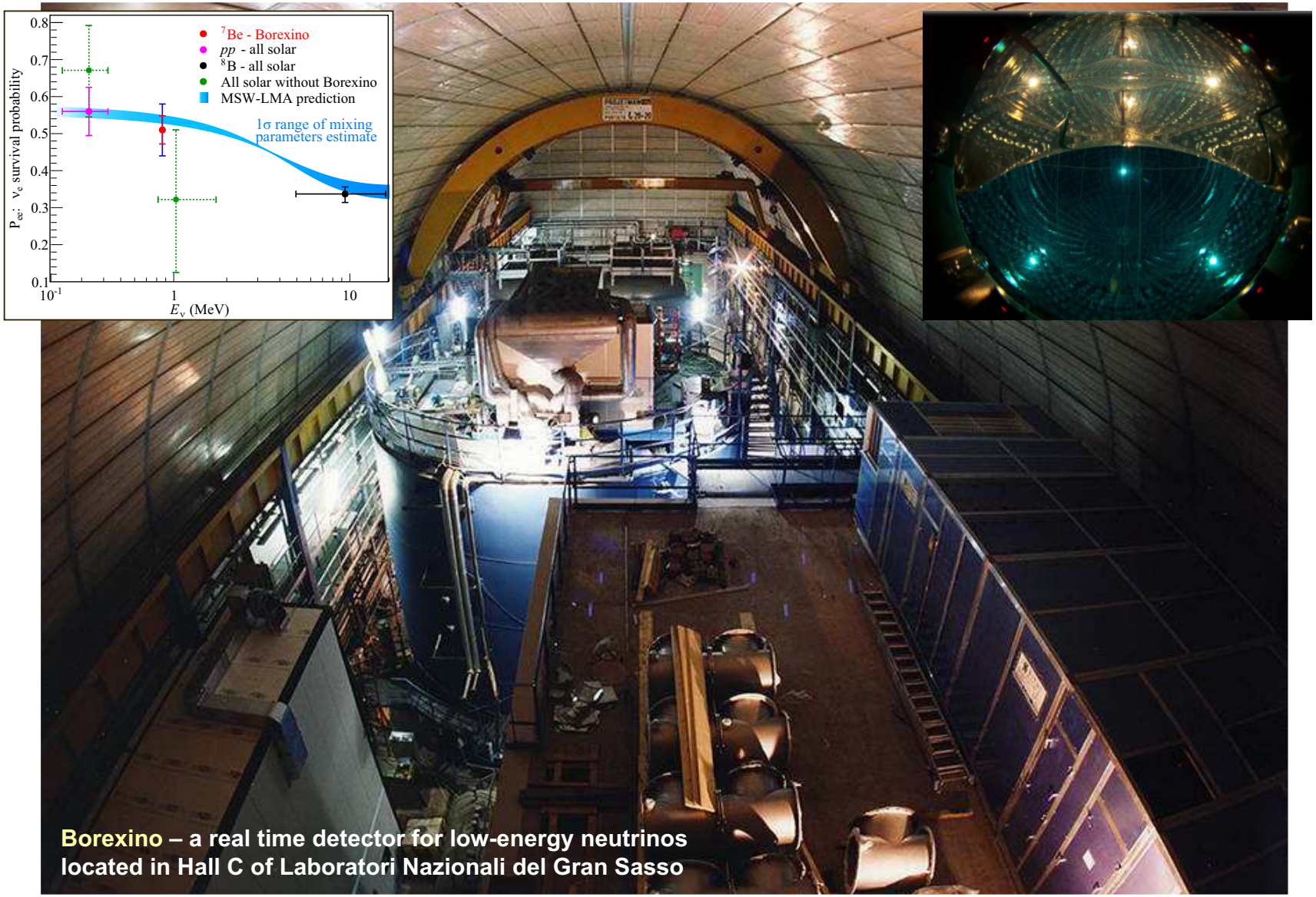

Borexino – a real time detector for low-energy neutrinos located in Hall C of Laboratori Nazionali del Gran Sasso

2011 [July 25] T2K collaboration announces first evidence for a nonzero mixing between the 1st and 3rd neutrino generations [$0.03(0.04) < \sin^2 2\theta_{13} < 0.28(0.34)$ (90% C.L.) for $\delta_{CP} = 0$ and a normal (inverted) hierarchy]. MINOS hastily confirms this clime.[a]

2011 [September 9] Super-Kamiokande collaboration disconfirms the MINOS $\nu\overline{\nu}$ anomaly by using the atmospheric neutrinos and antineutrinos.

For more details, see Appendix P, p. 936.

[a] For reviews, see, e.g., D. Karlen, "Progress on the neutrino mixing angle, θ_{13}," arXiv:1111.2397v1 [hep-ex]; S.-B. Kim & K.-B. Luk, "Measurement of θ_{13}," Ann. Rev. Nucl. Part. Sci. **65** (2015) 329-354.

2011 [November 9] The Double Chooz reactor experiment presents the first result on the $\nu_1 - \nu_3$ mixing. A *preliminary* rate + shape analysis indicated a hint for positive value of the θ_{13} neutrino mixing angle [$\sin^2 2\theta_{13} = 0.085 \pm 0.029\,(\text{stat}) \pm 0.042\,(\text{syst})$ (68% C.L.)].

Thanks to its simple site configuration, comprehensive set of calibration system and to its unique capability to measure the backgrounds in-situ during reactor Off-Off periods Double Chooz appeared to have played a leading role in the precise determination of the θ_{13} mixing angle, but the initiative was soon seized... And besides, the autumn news on θ_{13} faded somewhat against the background of the so-called "Opera Anomaly".

This image (© CBS Broadcasting Inc.) is from "The Speckerman Recurrence", Episode 11, Season 5 of the US sitcom (popular with physicists and beyond) **The Big Bang Theory**. In the background you can see the results of the aforementioned measurement by the Double Chooz experiment.

[Borrowed from LiveJournal, ⟨ https://wgseligman.livejournal.com/48050.html ⟩.]

2011 [September 23] OPERA collaboration announces an early arrival time of CNGS ν_μ with respect to the one computed assuming the speed of light in vacuum. The measured δt was $(60.7 \pm 6.9\,(\text{stat}) \pm 7.4\,(\text{syst}))$ ns. This anomaly corresponds to a relative difference of the ν_μ velocity with respect to the speed of light $(v-c)/c = (2.48 \pm 0.28\,(\text{stat}) \pm 0.30\,(\text{syst})) \times 10^{-5}$.

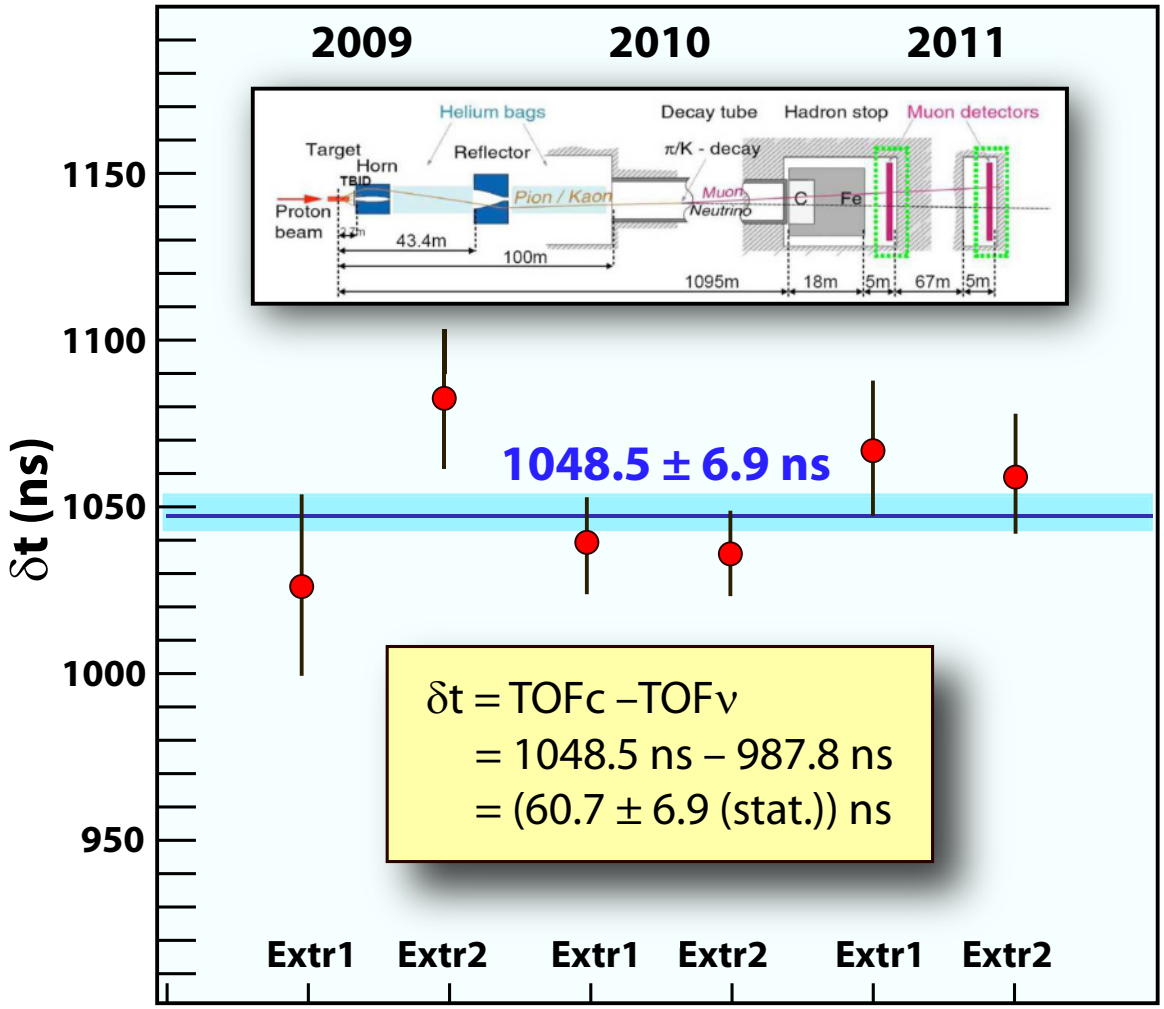

2011 [October 17] The next after OPERA experimental result concerning the "neutrino superluminality" is anounced by the ICARUS Collaboration.[a] The authors find that the neutrino energy distribution of the ICARUS events in LAr agrees with expectations from an unaffected energy distribution of the beam from CERN. This refutes a superluminal interpretation of the OPERA result in the spirit of Cohen and Glashow prediction[b] for a weak current analog to Cherenkov radiation.

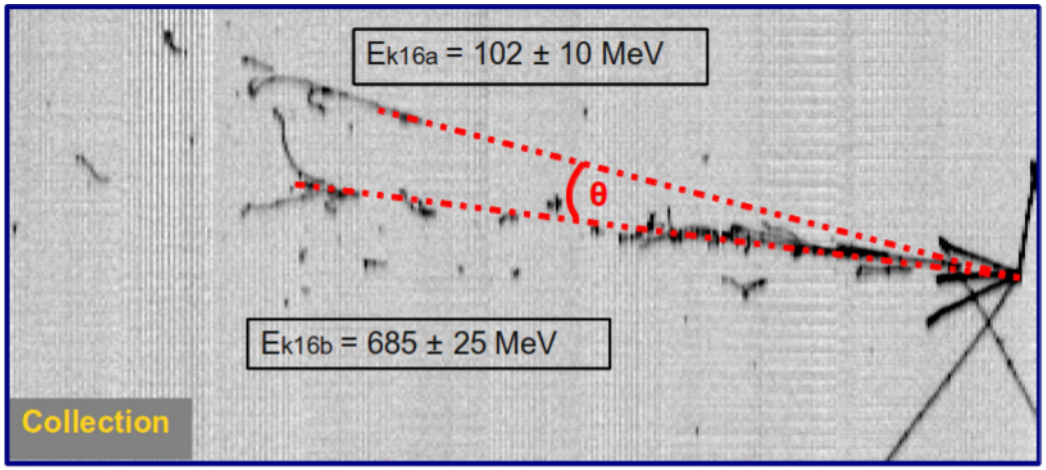

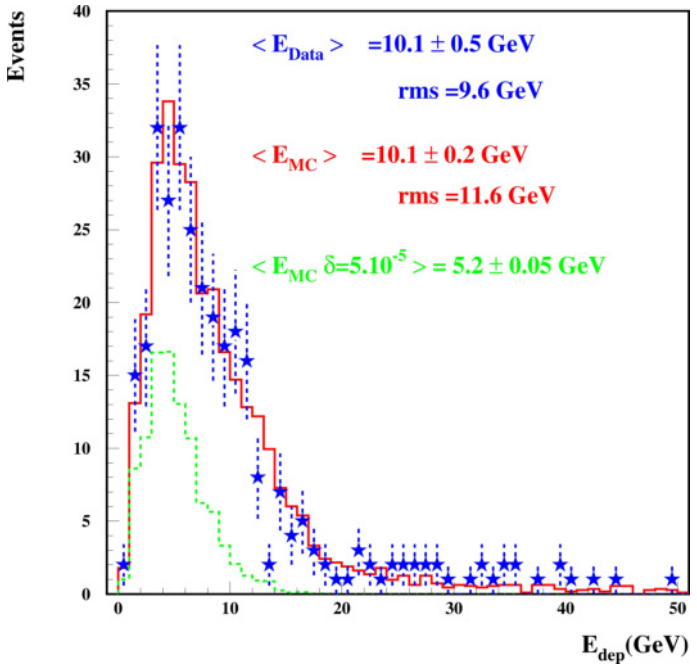

[a] M. Antonello *et al.* (ICARUS Collaboration), "A Search for the analogue to Cherenkov radiation by high energy neutrinos at superluminal speeds in ICARUS," Phys. Lett. B **711** (2005) 270–275, arXiv:1110.3763v3 [hep-ex].

[b] A. G. Cohen and S. L. Glashow, "Pair creation constrains superluminal neutrino propagation," Phys. Rev. Lett. **107** (2011) 181803, arXiv:1109.6562 [hep-ph].

2011 [November 18] The OPERA Collaboration rechecks many aspects of its September result[a] taking into account valuable suggestions from a wide range of sources. One key test was to repeat the measurement with very short beam pulses from CERN. This allowed the extraction time of the protons, that ultimately lead to the neutrino beam, to be measured more precisely. The measured time advance now is $\delta t = \left(57.8 \pm 7.8\,(\text{stat})\ {}^{+8.3}_{-5.9}\,(\text{syst})\right)$ ns. So the anomaly still exists and corresponds to a relative difference of the ν_μ velocity with respect to the speed of light

$$(v-c)/c = \left(2.37 \pm 0.32\,(\text{stat})\ {}^{+0.34}_{-0.24}\,(\text{syst})\right) \times 10^{-5}.$$

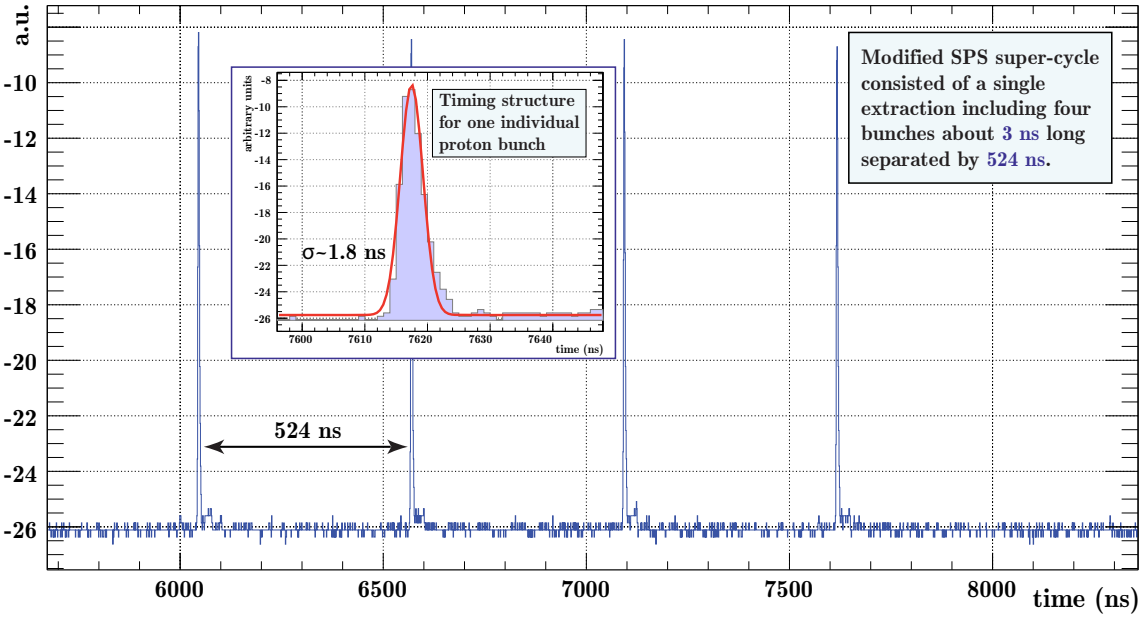

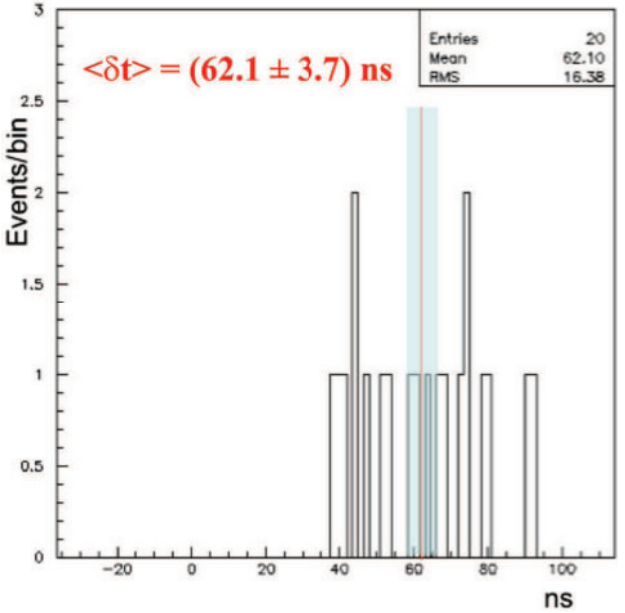

[a] T. Adam *et al.* (OPERA Collaboration), "Measurement of the neutrino velocity with the OPERA detector in the CNGS beam," arXiv:1109.4897v2 [hep-ex]. Figures shown are taken from arXiv:1109.4897v2 (right panel) and arXiv:1109.4897v3 (left panel). The 3rd version still does not complete the story... We'll devote a couple more slides to this anomaly, because it was an attack on the foundation of modern physics.

2012 [March 15] The ICARUS Collaboration performs the experiment quite similar to the OPERA one and disconfirms the OPERA result.[a]

2012 [June 12] Joint LVD and OPERA analysis closes the OPERA anomaly with the conclusion:[b]
"The result of this joint analysis is the first quantitative measurement of the relative time stability between the two detectors and provides a check that is totally independent from the TOF measurements of CNGS neutrino events and from the effect presented in arXiv:1109.4897, pointing to the existence of a possible systematic effect in the OPERA neutrino velocity analysis."

2012 [July 12] The very final OPERA result is (hurray!)[c]

$$\delta t = \left(6.5 \pm 7.4\,(\text{stat})\ {}^{+8.3}_{-8.0}\,(\text{syst})\right)\ \text{ns},$$

$$(v_\nu - c)/c = \left(2.7 \pm 3.1\,(\text{stat})\ {}^{+3.4}_{-3.3}\,(\text{syst})\right) \times 10^{-6}.$$

2012 [July 30] The measurement of the BOREXINO Collaboration seems to be even more expressive:[d]

$$\delta t = (0.8 \pm 0.7\,(\text{stat}) \pm 2.9\,(\text{syst}))\ \text{ns},$$

$$|v_\nu - 1|/c < 2.1 \times 10^{-6}\ 90\%\,\text{C.L.}$$

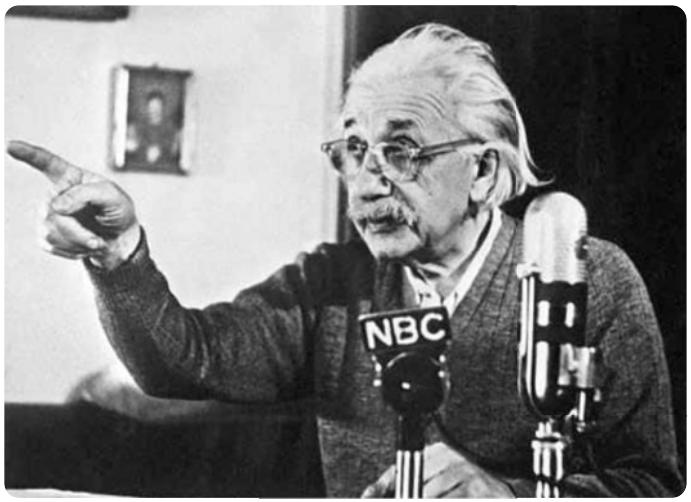

[a] M. Antonello *et al.* (ICARUS Collaboration), "Measurement of the neutrino velocity with the ICARUS detector at the CNGS beam," Phys. Lett. B **713** (2012) 17–22, arXiv:1203.3433v3 [hep-ex].

[b] N. Yu. Agafonova *et al.* (LVD & OPERA Collaborations), "Determination of a time-shift in the OPERA set-up using high-energy horizontal muons in the LVD and OPERA detectors," Eur. Phys. J. Plus **127** (2012) 071, arXiv:1206.2488v1 [hep-ex].

[c] T. Adam *et al.* (OPERA collaboration), "Measurement of the neutrino velocity with the OPERA detector in the CNGS beam," JHEP10(2012)093, arXiv:1109.4897v4 [hep-ex]; cf. with earlier versions of the eprint.

[d] P. Alvarez Sanchez *et al.* (Borexino Collaborations), "Measurement of CNGS muon neutrino speed with Borexino," Phys. Lett. B **716** (2012) 401–405, arXiv:1207.6860v1 [hep-ex].

2012 [August 3] One more result is obtained from an analysis of data from the experiment MACRO $|v_K - v_\pi| < 1.5 \times 10^{-4}$ (it is mainly of methodical interest).[a]

2012 [August 7] The next result comes from the LVD Collaboration:[b]

$$\delta t = (0.9 \pm 0.6\,(\text{stat}) \pm 3.2\,(\text{syst}))\ \text{ns},$$

$$-3.8 \times 10^{-6} < v_\nu - 1 < 3.1 \times 10^{-6}\ 99\%\,\text{C.L.}, \quad m_{\nu_\mu} < 47\ \text{MeV}/c^2\ 99\%\,\text{C.L.}.$$

2012 [August 13] The new result from ICARUS:[c] $\delta t = (-0.3 \pm 4.9\,(\text{stat}) \pm 9.0\,(\text{syst}))$ ns.

2012 [September 27] In the next (published) version of the eprint[d] the ICARUS result is significantly corrected and improved:

$$\delta t = (0.1 \pm 0.67\,(\text{stat}) \pm 2.39\,(\text{syst}))\ \text{ns}.$$

In terms of neutrino velocity it leads to the following (so far a record) upper limit:

$$|v_\nu - c|\,/c < 1.35 \times 10^{-6}\ 90\%\,\text{C.L.}.$$

To be continued with MINOS(+), T2K,...

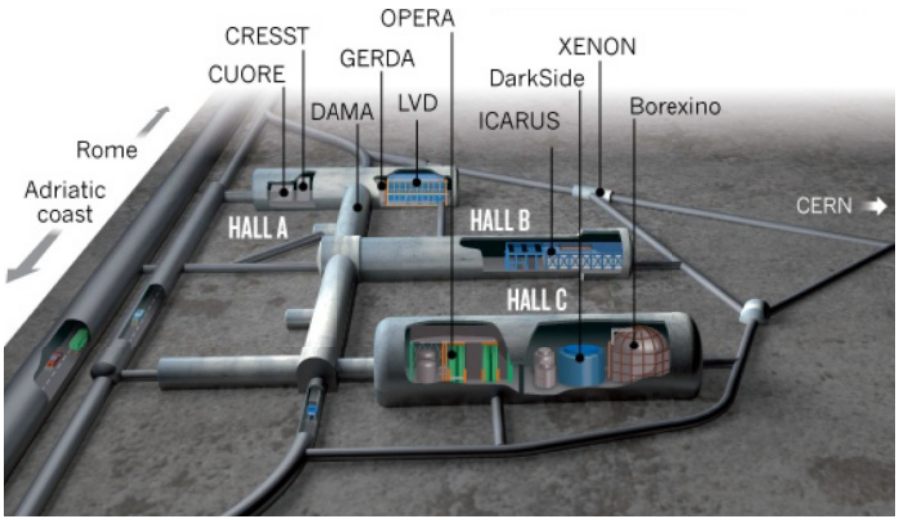

[a] F. Ronga, "Analysis of the MACRO experiment data to compare particles arrival times under Gran Sasso," arXiv:1208.0791v2 [hep-ex], unpublished.

[b] N. Yu. Agafonova *et al.* (LVD Collaboration), "Measurement of the velocity of neutrinos from the CNGS beam with the Large Volume Detector," Phys. Rev. Lett. **109** (2012) 070801, arXiv:1208.1392v2 [hep-ex].

[c] M. Antonello *et al.* (ICARUS Collaboration), "Precision measurement of the neutrino velocity with the ICARUS detector in the CNGS beam," arXiv:1208.2629v1 [hep-ex].

[d] M. Antonello *et al.* (ICARUS Collaboration), JHEP11(2012)049, arXiv:1208.2629v2 [hep-ex].

2012 [March] The Double Chooz Collaboration publishes their first official result:

$$\sin^2 2\theta_{13} = 0.086 \pm 0.041\,(\text{stat}) \pm 0.030\,(\text{syst})$$

and excludes the no-oscillation hypothesis at the 94.6% C.L.

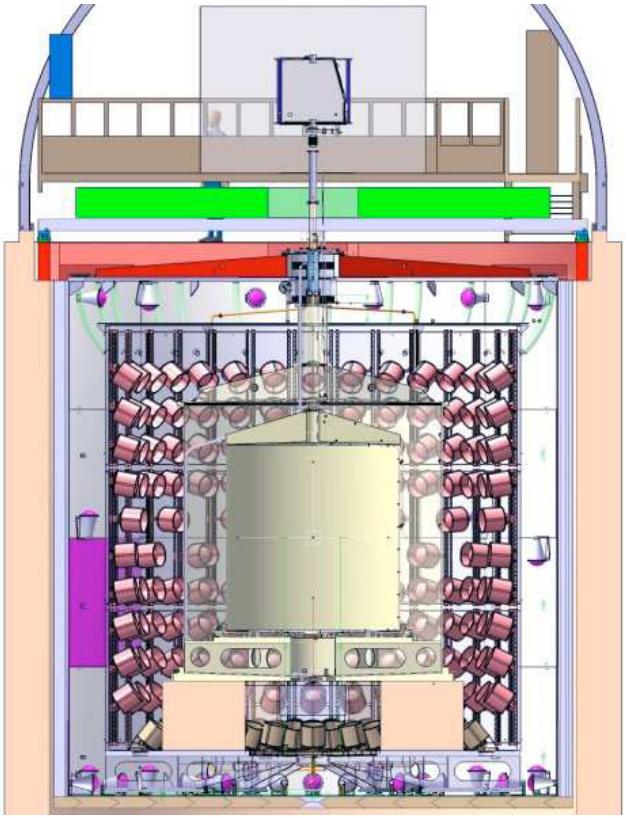

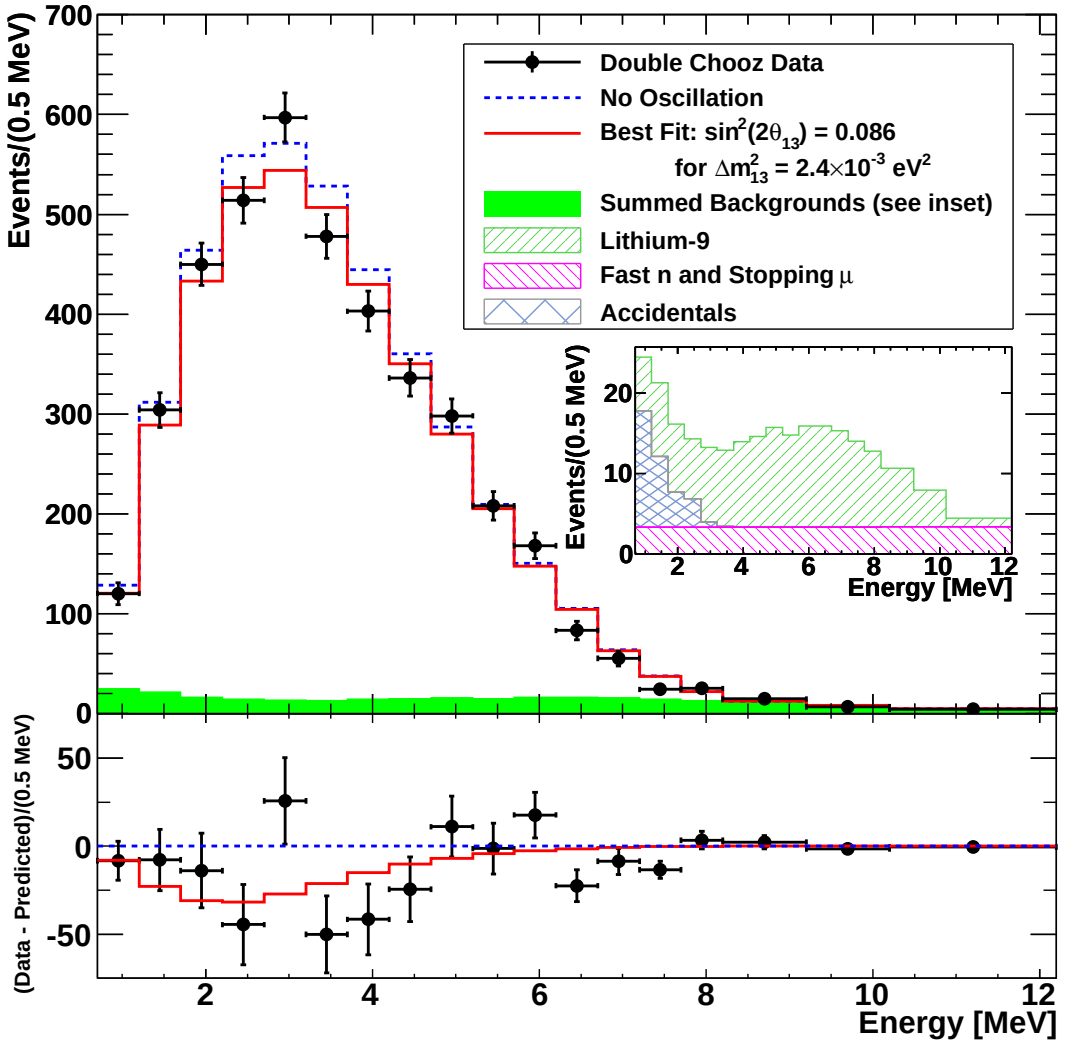

[From Y. Abe *et al.* (Double Chooz Collaboration), "Indication of reactor $\overline{\nu}_e$ disappearance in the Double Chooz experiment," Phys. Rev. Lett. **108** (2012) 131801, arXiv:1112.6353 [hep-ex].]

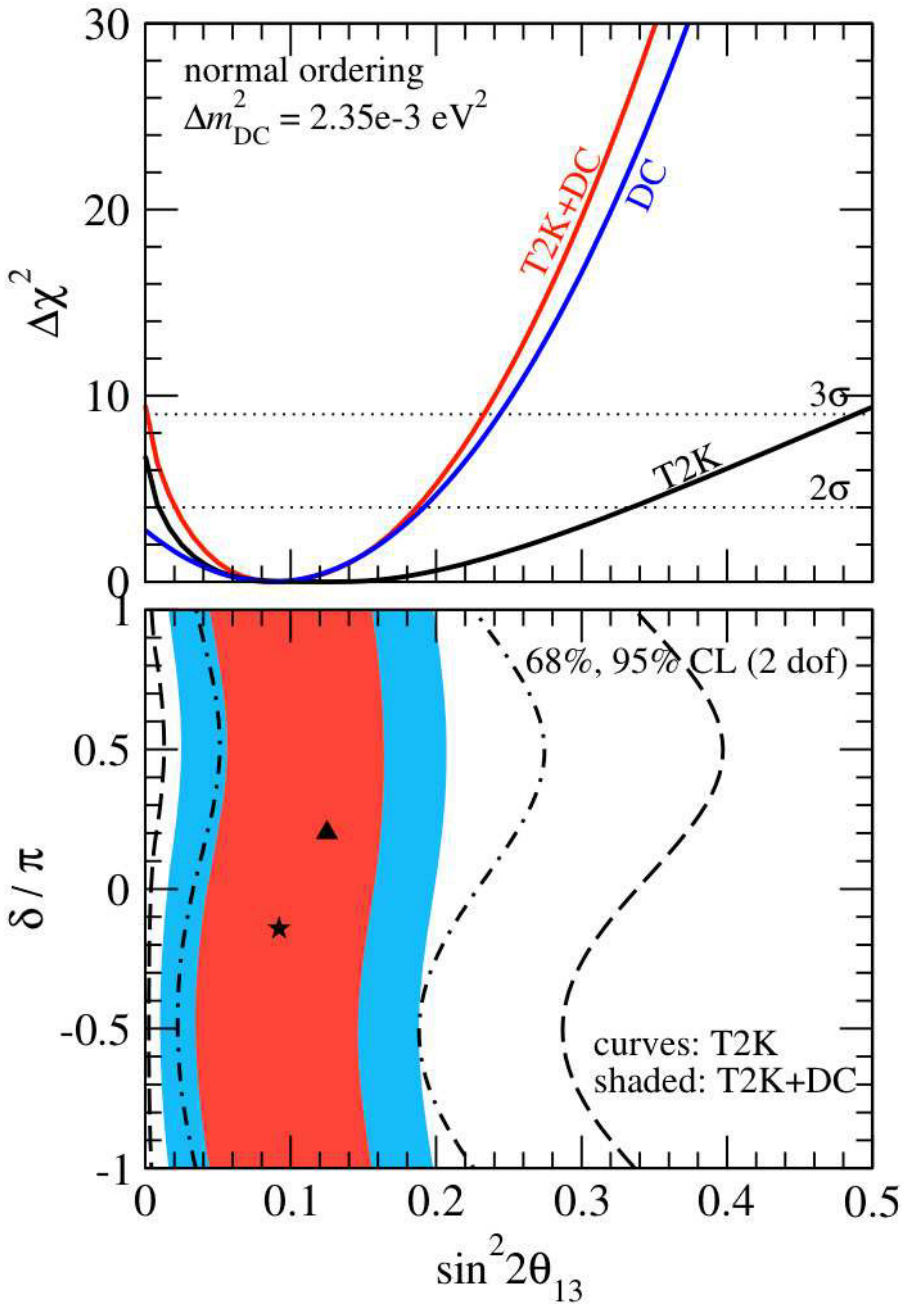

◁ Combined analysis of Double Chooz and T2K for normal neutrino mass ordering.

Top panel: shows the $\Delta\chi^2$ for the assumed normal neutrino mass ordering marginalized over the unknown CP-violating phase δ for T2K, Double Chooz alone and the combination (i.e., for each value of $\sin^2(2\theta_{13})$ the $\Delta\chi^2$ is minimized with respect to δ). Dotted horizontal lines indicate 2σ and 3σ.

Bottom panel: shows the allowed regions in the plane of $\sin^2(2\theta_{13})$ and the CP phase δ (in units of π) for T2K alone (curves) and the Double Chooz + T2K combination (colored region). The triangle (star) corresponds to the T2K (Double Chooz + T2K) best fit point.

For both neutrino mass orderings the Double Chooz + T2K combination excludes $\theta_{13} = 0$ at 3σ level.

2012 [April 27] The Daya Bay reactor neutrino experiment anounces the *precision* result on measuring a nonzero value of θ_{13} with a significance of 5.2 standard deviations. Antineutrinos from six 2.9 GW reactors were detected in six $\overline{\nu}$ detectors (AD) deployed in two near (flux-weighted baseline 470 m and 576 m) and one far (1648 m) underground experimental halls. The ratio of the observed to expected number of $\overline{\nu}$s at the far hall is $R = 0.940 \pm 0.011\,(\text{stat}) \pm 0.004\,(\text{syst})$. A rate-only analysis yields $\sin^2 2\theta_{13} = 0.092 \pm 0.016\,(\text{stat}) \pm 0.005\,(\text{syst})$ in a 3ν framework.

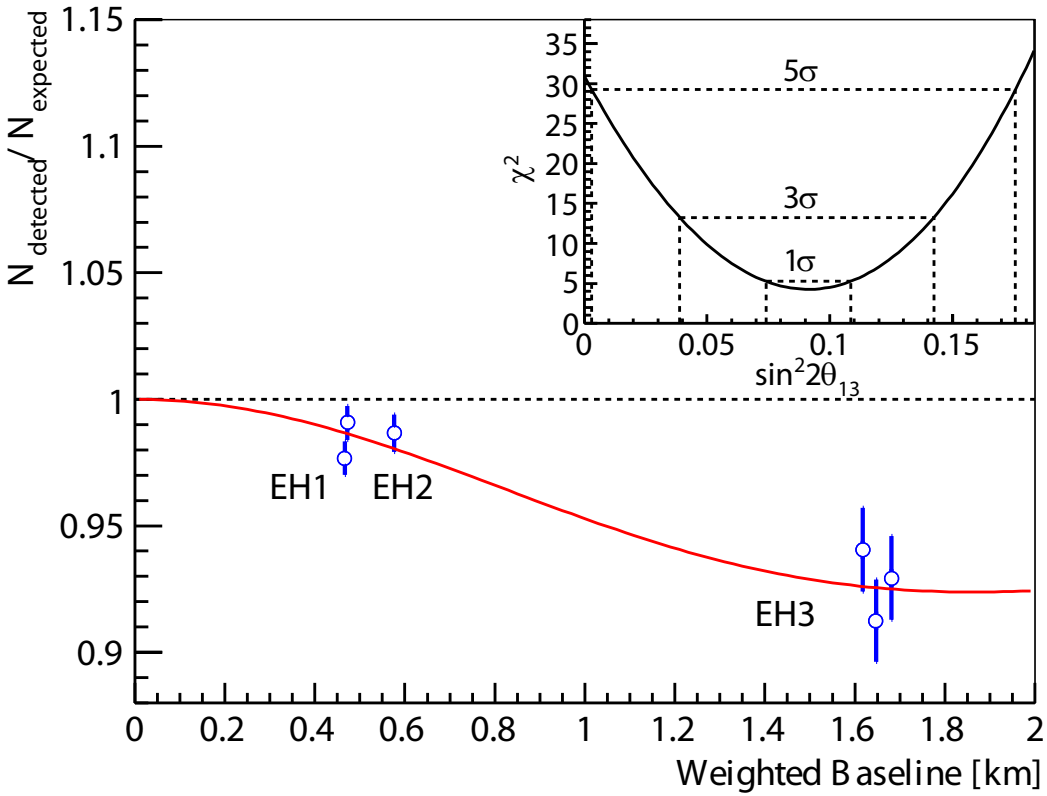

◁ Ratio of measured vs. expected signal in each detector, assuming no oscillation. The error bars are the uncorrelated uncertainties of each AD, including statistical, detector-related, and background-related uncertainties. The expected signal is corrected with the best-fit normalization parameter. Reactor and survey data were used to compute the flux-weighted average baselines. The oscillation survival probability at the best-fit value is given by the smooth curve. The AD4 and AD6 data points are displaced by -30 and +30 m for visual clarity. The inset shows χ^2 vs. $\sin^2 2\theta_{13}$.

[From F. P. An *et al.* (Daya Bay Collaboration), "Observation of electron-antineutrino disappearance at Daya Bay," Phys. Rev. Lett. **108** (2012) 171803, arXiv:1203.1669 [hep-ex].]

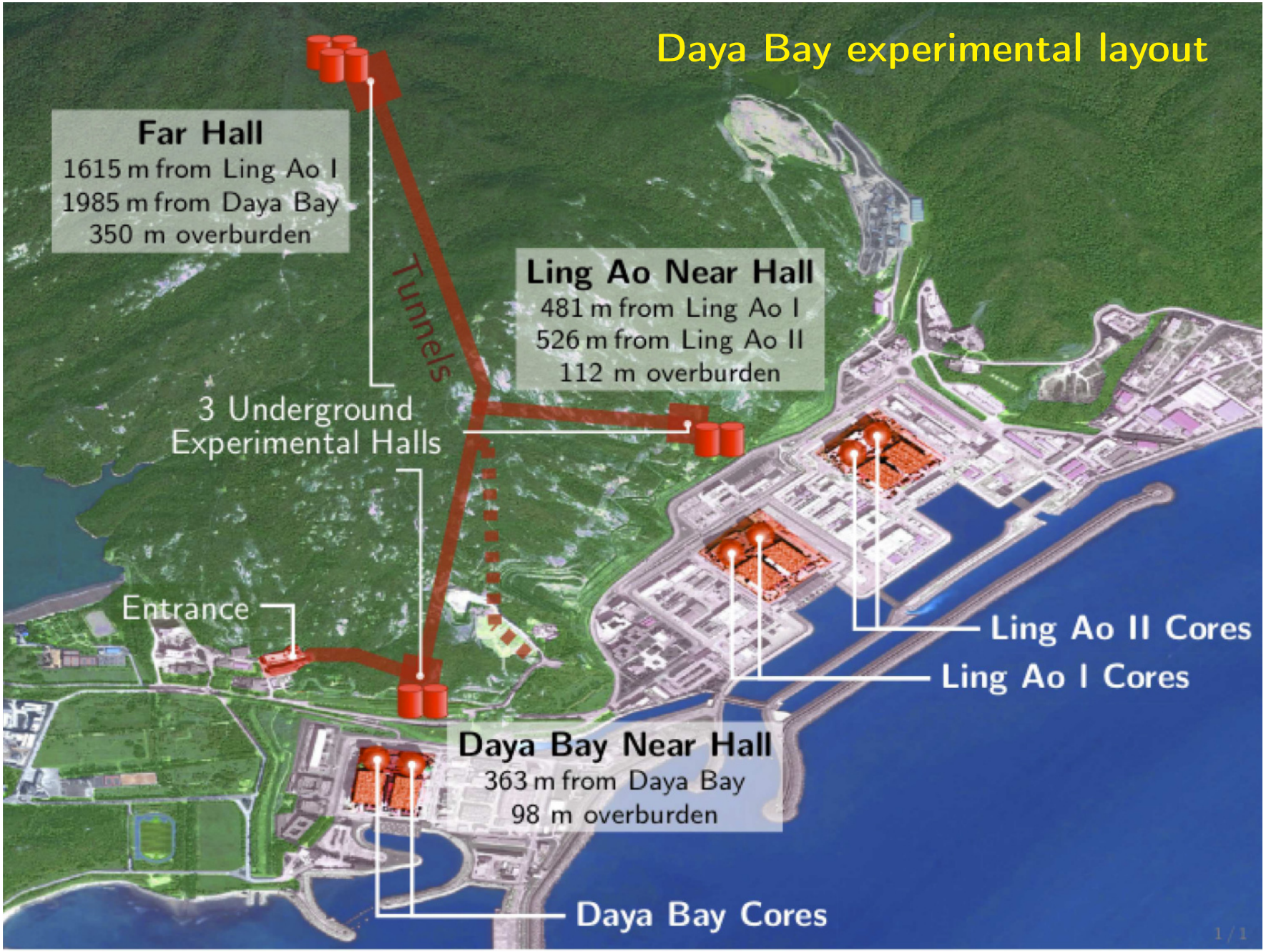
Daya Bay experimental layout
Far Hall
1615 m from Ling Ao I
1985 m from Daya Bay
350 m overburden
Tunnels
Ling Ao Near Hall
481 m from Ling Ao I
526 m from Ling Ao II
112 m overburden
3 Underground
Experimental Halls
Entrance
Ling Ao II Cores
Ling Ao I Cores
Daya Bay Near Hall
363 m from Daya Bay
98 m overburden
Daya Bay Cores
1/1

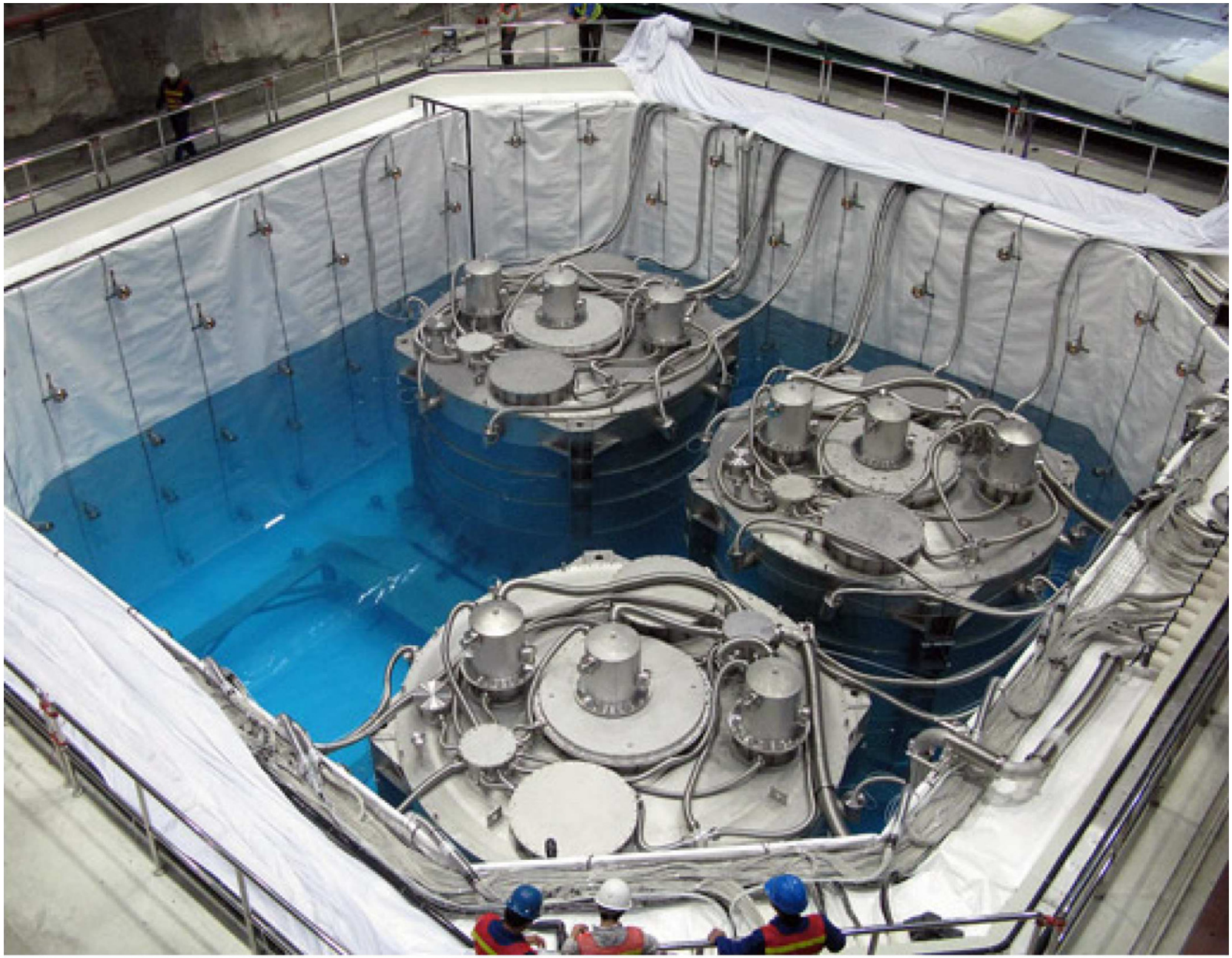

2012 [May 11] Almost simultaneously, the RENO reactor neutrino experiment anounces similar result. The RENO experiment has observed the disappearance of reactor $\overline{\nu}_e$s, consistent with neutrino oscillations, with a significance of 4.9 standard deviations. Antineutrinos from six 2.8 GW reactors at the Yonggwang Nuclear Power Plant in Korea, are detected by two identical detectors located at 294 and 1383 m from the reactor array center. The ratio of observed to expected numbers of $\overline{\nu}$s in the far detector is $R = 0.920 \pm 0.009\,(\text{stat}) \pm 0.014\,(\text{syst})$. A rate-only analysis finds

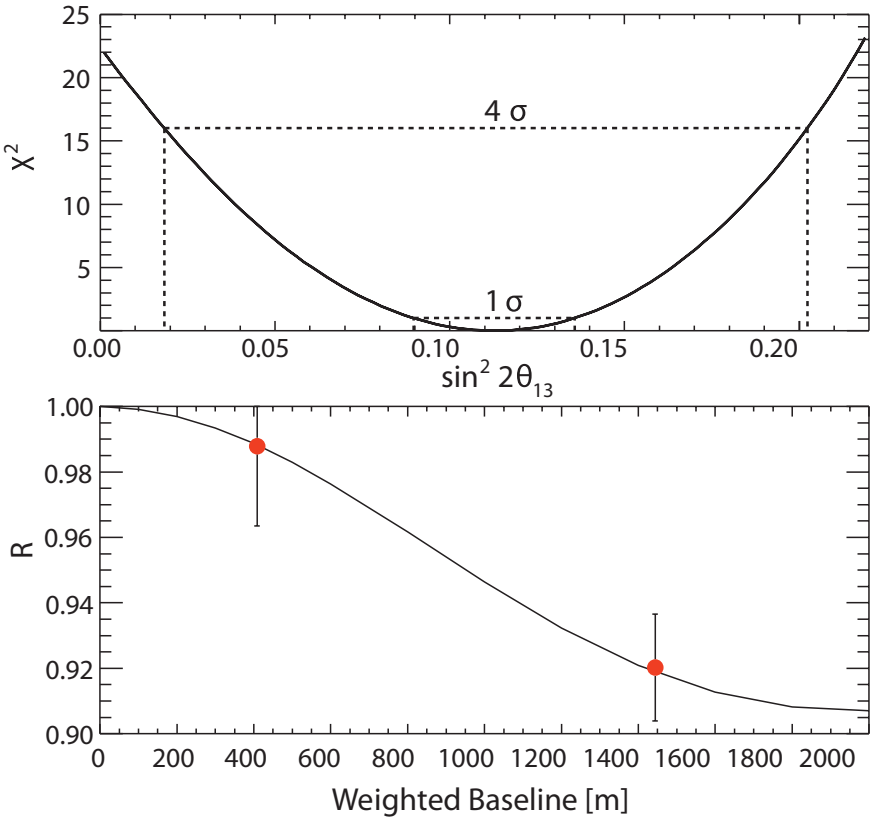

$\sin^2 2\theta_{13} = 0.113 \pm 0.013\,(\text{stat}) \pm 0.019\,(\text{syst})$.

◁ The χ^2 distribution as a function of $\sin^2 2\theta_{13}$ (*top panel*) and the ratio of the measured reactor neutrino events relative to the expected with no oscillation (*bottom panel*).
A clear deficit of 8.0% for the far detector, and of 1.2% for the near detector is observed, concluding a definitive observation of reactor $\overline{\nu}_e$ disappearance consistent with neutrino oscillations. The curve represents the oscillation survival probability at the best-fit, as a function of the flux-weighted baselines.

The Daya Bay and RENO results are in very good agreement.

[From J. K. Ahn *et al.* (RENO Collaboration), "Observation of reactor electron antineutrinos disappearance in the RENO experiment," Phys. Rev. Lett. **108** (2012) 191802, arXiv:1204.0626 [hep-ex].]

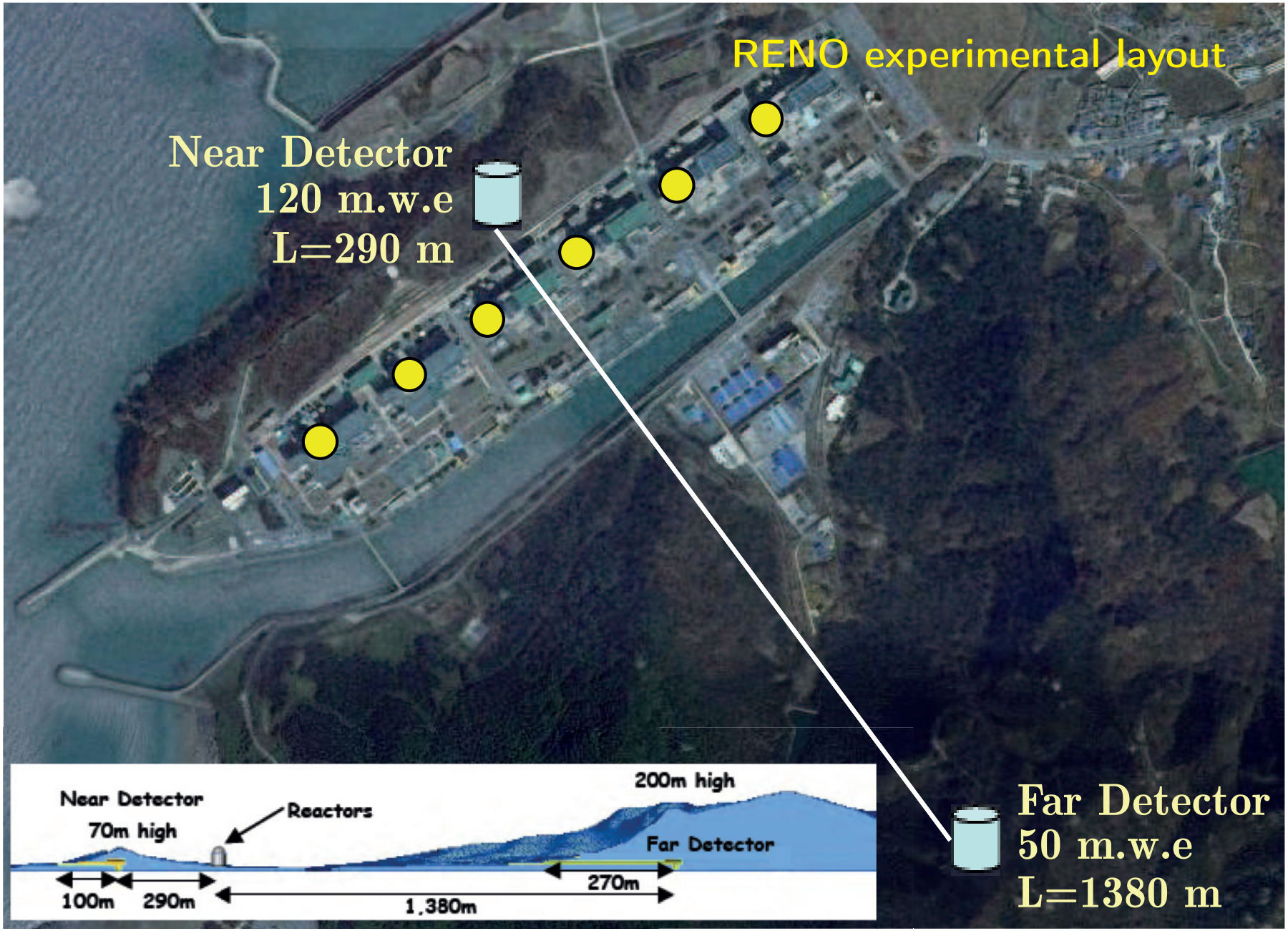
RENO experimental layout
Near Detector
120 m.w.e
L=290 m
Far Detector
50 m.w.e
L=1380 m
Near Detector
70m high
Reactors
200m high
Far Detector
100m
290m
270m
1,380m

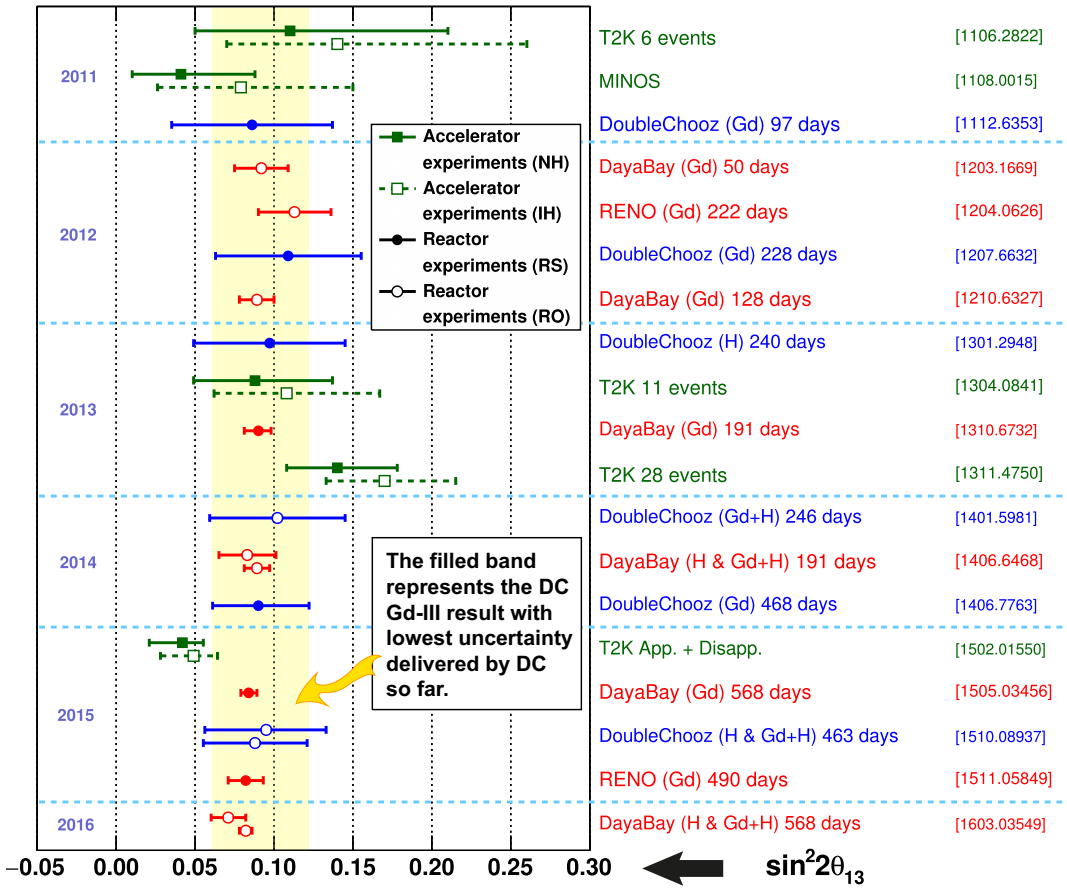

Reactor methods: The reactor $\overline{\nu}_e$ collides with a proton in a liquid scintillator and performs the inverse beta decay (IBD) reaction,

$$\overline{\nu}_e + p \rightarrow e^+ + n.$$

The e^+ emits scintillation light and slows down until it annihilates with an electron existing around. The $\overline{\nu}_e$ energy can be obtained from the e^+ energy,

$$E_{\overline{\nu}} \approx E_{e+} + 0.8 \text{ MeV}.$$

The produced neutron thermalizes quickly by colliding with protons around and absorbes by an embed nucleus (e.g., Gd) or Hydrogen. The γ(s) escaping from the target region are captured by the γ-catcher scintillator.

△ Figure provides a summary of the $\sin^2 2\theta_{13}$ main measurements released by reactor and accelerator experiments since 2011. The accelerator results are presented in Normal or Inverted Hierarchy (NH and NI respectively), while the reactor results are divided by Rate Only fit (RO), Spectral Shape and Rate fit (RS) or if the analysis is based on n-Gd, n-H or a combination of both (Gd + H). The number of days represents the live-time of each data-release and when the detectors have different live-time in a same release, the biggest value was taken. For each value, its arXiv number is given.
[From F. Suekane *et al.* (for the Double Chooz Collaboration), "Double Chooz and a history of reactor θ_{13} experiments," Nucl. Phys. B **908** (2016) 74–93, arXiv:1601.08041 [hep-ex].]

2013 [July 12] The IceCube Collaboration reports observation of two neutrino-induced events which have an estimated deposited energy in the detector of 1.04 ± 0.16 and 1.14 ± 0.17 PeV, respectively, the highest neutrino energies observed so far.

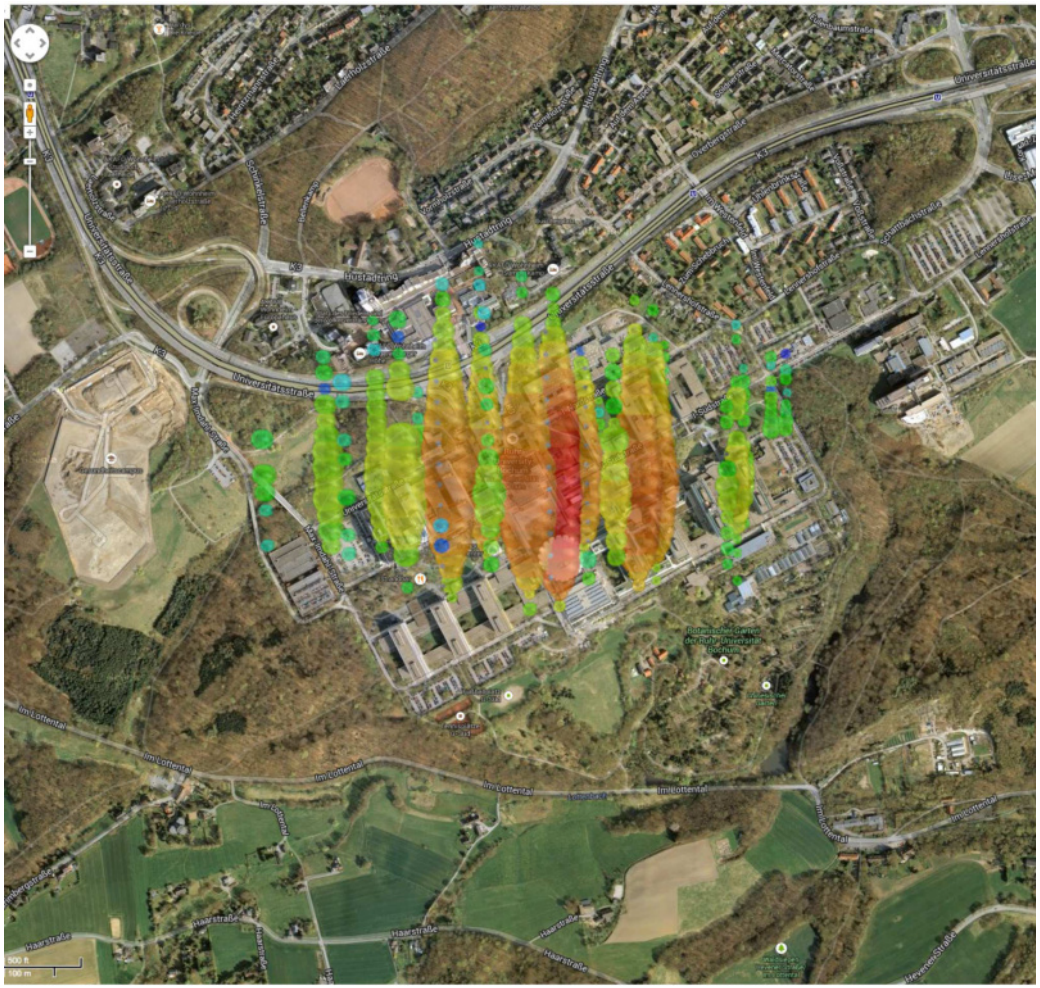

The two events are consistent with fully contained particle showers induced by NC $\nu_{e,\mu,\tau}$ ($\overline{\nu}_{e,\mu,\tau}$) or CC ν_e ($\overline{\nu}_e$) interactions within the detector. The events were discovered in a search for UHE neutrinos using data corresponding to 615.9 days effective live time.
The expected number of AN background is $0.082^{+0.004}_{-0.004}\,(\text{stat})\,^{+0.041}_{-0.067}\,(\text{syst})$.
The probability of observing two or more candidate events under the AN background-only hypothesis is 2.9×10^{-3} (2.8σ) taking into account the uncertainty on the expected number of background events. These two events could be a first indication of an astrophysical neutrino flux; the moderate significance, however, does not permit a definitive conclusion.

[From M. G. Aartsen *et al.* (IceCube Collaboration), "First observation of PeV-energy neutrinos with IceCube," Phys. Rev. Lett. **111** (2013) 021103, arXiv:1304.5356v2 [astro-ph.HE].]

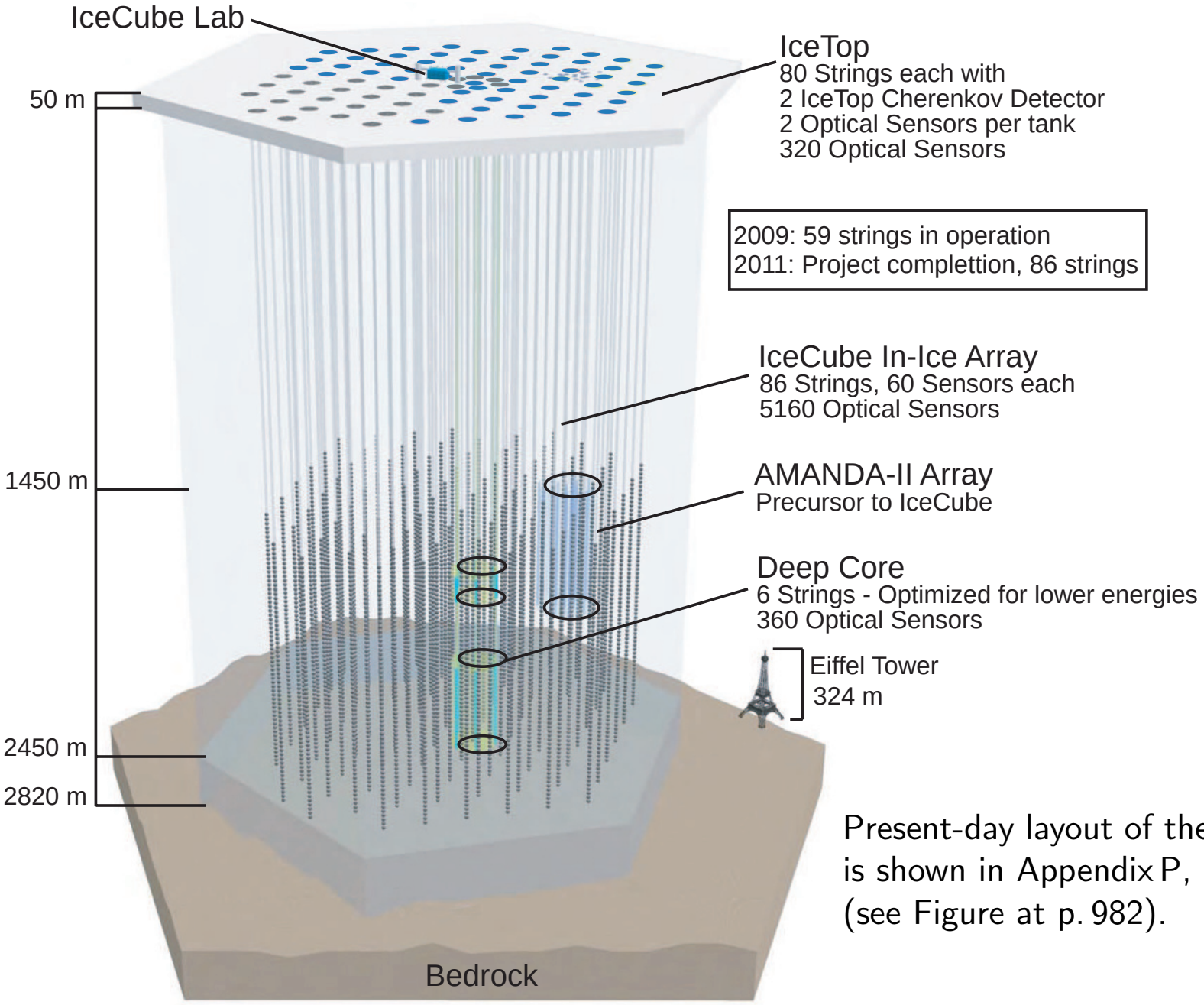

Present-day layout of the telescope is shown in Appendix P, p. 936 (see Figure at p. 982).

January 3, 2012 ("Ernie")

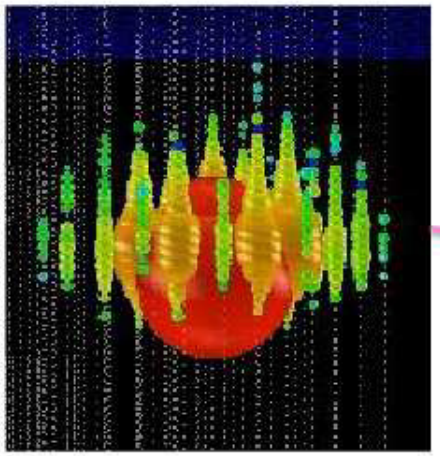

1.14±0.14 PeV
6.09 < log(E/GeV) < 8.65

August 9, 2011 ("Bert")

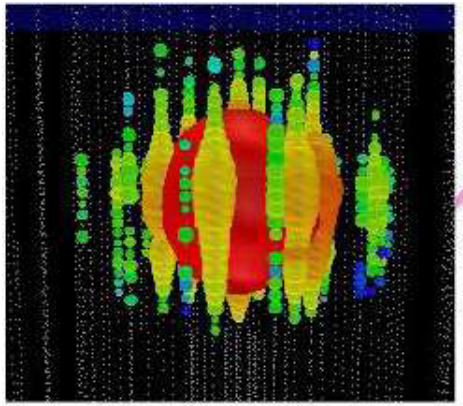

1.04±0.16 PeV
6.01 < log(E/GeV) < 8.03

IceCube-86 (78+8) intersections (surface) distances and closest string positions for the vertices

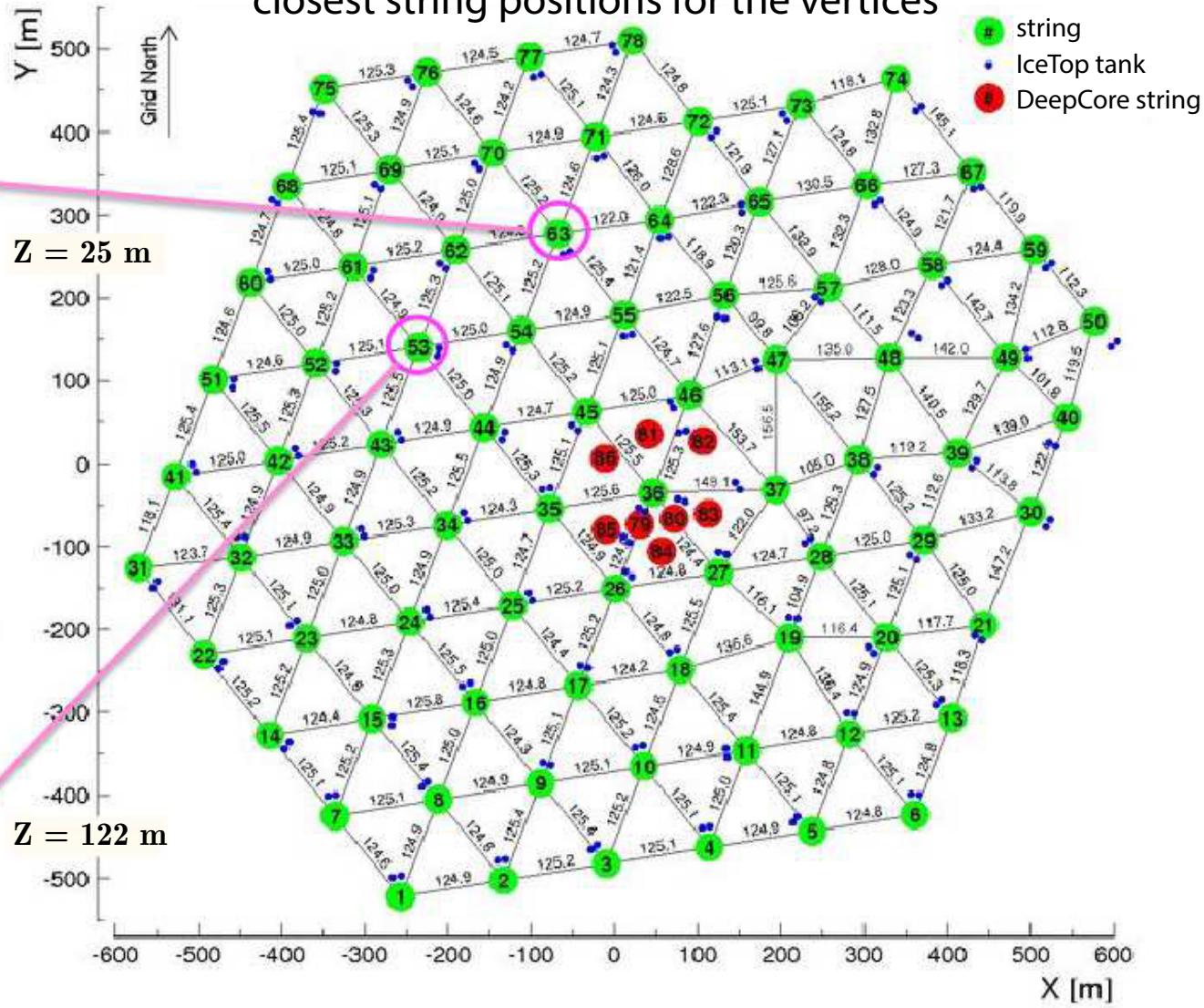

For more details on the IceCube data, see Section **7.8**, p. 315.

[From K. Mase, "A search for extremely high energy cosmogenic neutrinos with IceCube" (presentation).]

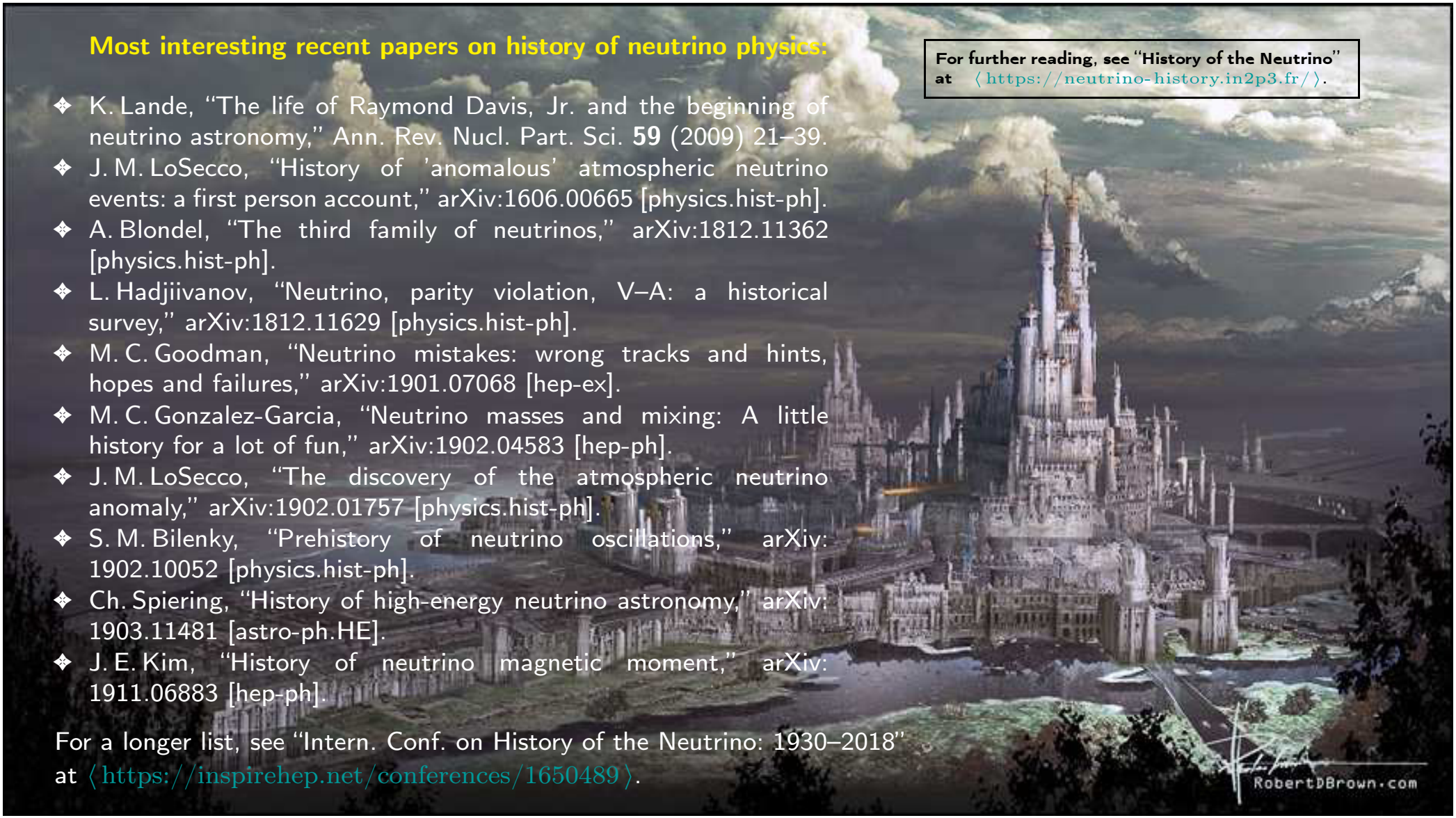

Most interesting recent papers on history of neutrino physics:

For further reading, see "History of the Neutrino" at ⟨https://neutrino-history.in2p3.fr/⟩.

- K. Lande, "The life of Raymond Davis, Jr. and the beginning of neutrino astronomy," Ann. Rev. Nucl. Part. Sci. **59** (2009) 21–39.
- J. M. LoSecco, "History of 'anomalous' atmospheric neutrino events: a first person account," arXiv:1606.00665 [physics.hist-ph].
- A. Blondel, "The third family of neutrinos," arXiv:1812.11362 [physics.hist-ph].
- L. Hadjiivanov, "Neutrino, parity violation, V–A: a historical survey," arXiv:1812.11629 [physics.hist-ph].
- M. C. Goodman, "Neutrino mistakes: wrong tracks and hints, hopes and failures," arXiv:1901.07068 [hep-ex].
- M. C. Gonzalez-Garcia, "Neutrino masses and mixing: A little history for a lot of fun," arXiv:1902.04583 [hep-ph].
- J. M. LoSecco, "The discovery of the atmospheric neutrino anomaly," arXiv:1902.01757 [physics.hist-ph].
- S. M. Bilenky, "Prehistory of neutrino oscillations," arXiv: 1902.10052 [physics.hist-ph].
- Ch. Spiering, "History of high-energy neutrino astronomy," arXiv: 1903.11481 [astro-ph.HE].
- J. E. Kim, "History of neutrino magnetic moment," arXiv: 1911.06883 [hep-ph].

For a longer list, see "Intern. Conf. on History of the Neutrino: 1930–2018" at ⟨https://inspirehep.net/conferences/1650489⟩.

The End of the Chronicles of Amber.

Part II

Neutrino Essays

(pell-mell)

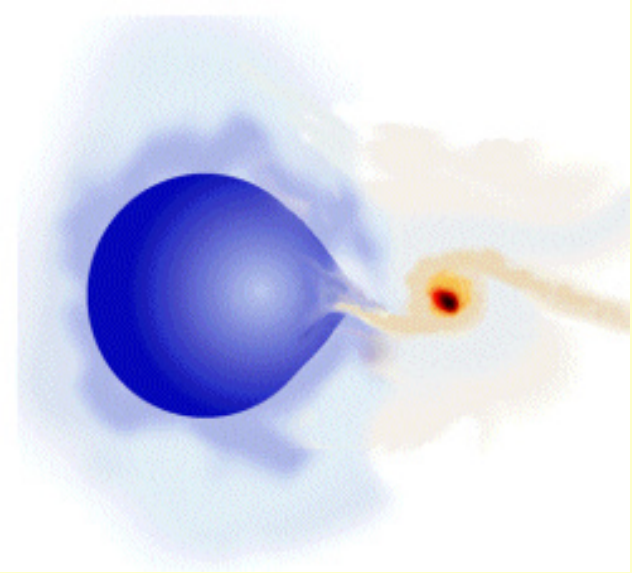

1 Multi-messenger astronomy

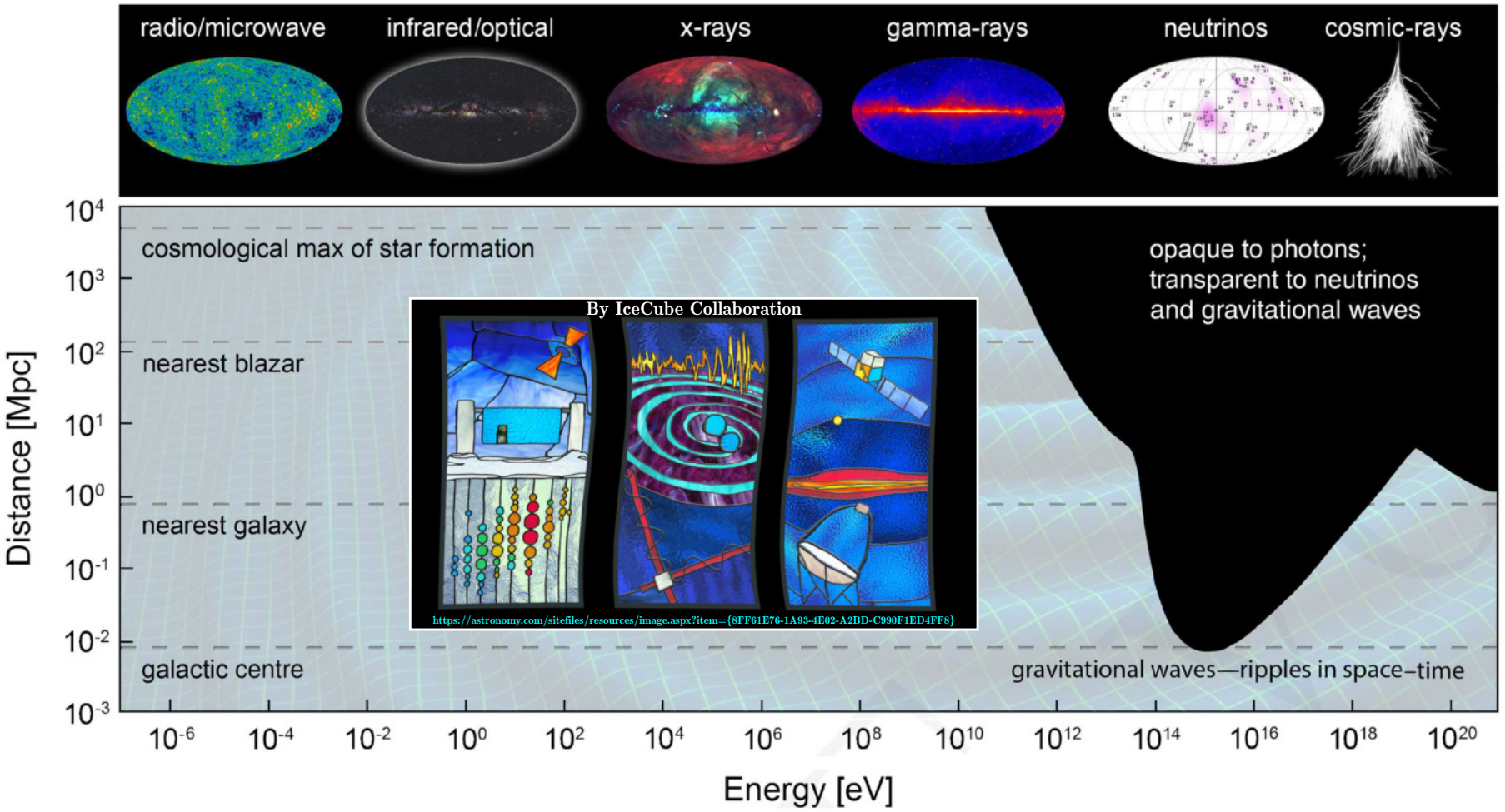

△ The distance horizon at which the Universe becomes optically thick to electromagnetic radiation. The highest-energy γs and CRs are attenuated after comparatively short distances, obscuring the view of the most energetic cosmic accelerators. The Universe is however transparent to GWs and νs.

[From I. Bartos & M. Kowalski, "Multimessenger Astronomy" (Physics World Discovery, IoP Publishing, Bristol, 2017).]

1.1 Neutrinos on Earth and in the Heavens.

Neutrino fluxes on Earth (tentative)

Energy range or average energy (eV)	Source	Local flux ($1/\mathrm{cm}^2\,\mathrm{s}$)
1.7×10^{-4}	Big Bang (relic)	10^{13}
$10^3 - 10^7$	Sun	6.5×10^{10}
$10^3 - 10^7$	Terrestrial radioactivity	7.5×10^6
$10^3 - 10^7$	Man-made nuclear reactors	7.5×10^6
$10^9 - 10^{12}$	Man-made accelerators	$<10^6$
$>10^8$	Cosmic rays (atmospheric)	$<10^6$
$>10^{12}$	Astrophysical objects (e.g. AGN)	$<10^{-6}$
$>10^{16}$	UHECR+ γ_{CMB} (cosmogenic)	10^{-12}

The table shows natural and artificial (man-made) fluxes of (anti)neutrinos near the Earth's surface. This is a preliminary and very approximate representation. Below we will study it all in more detail.

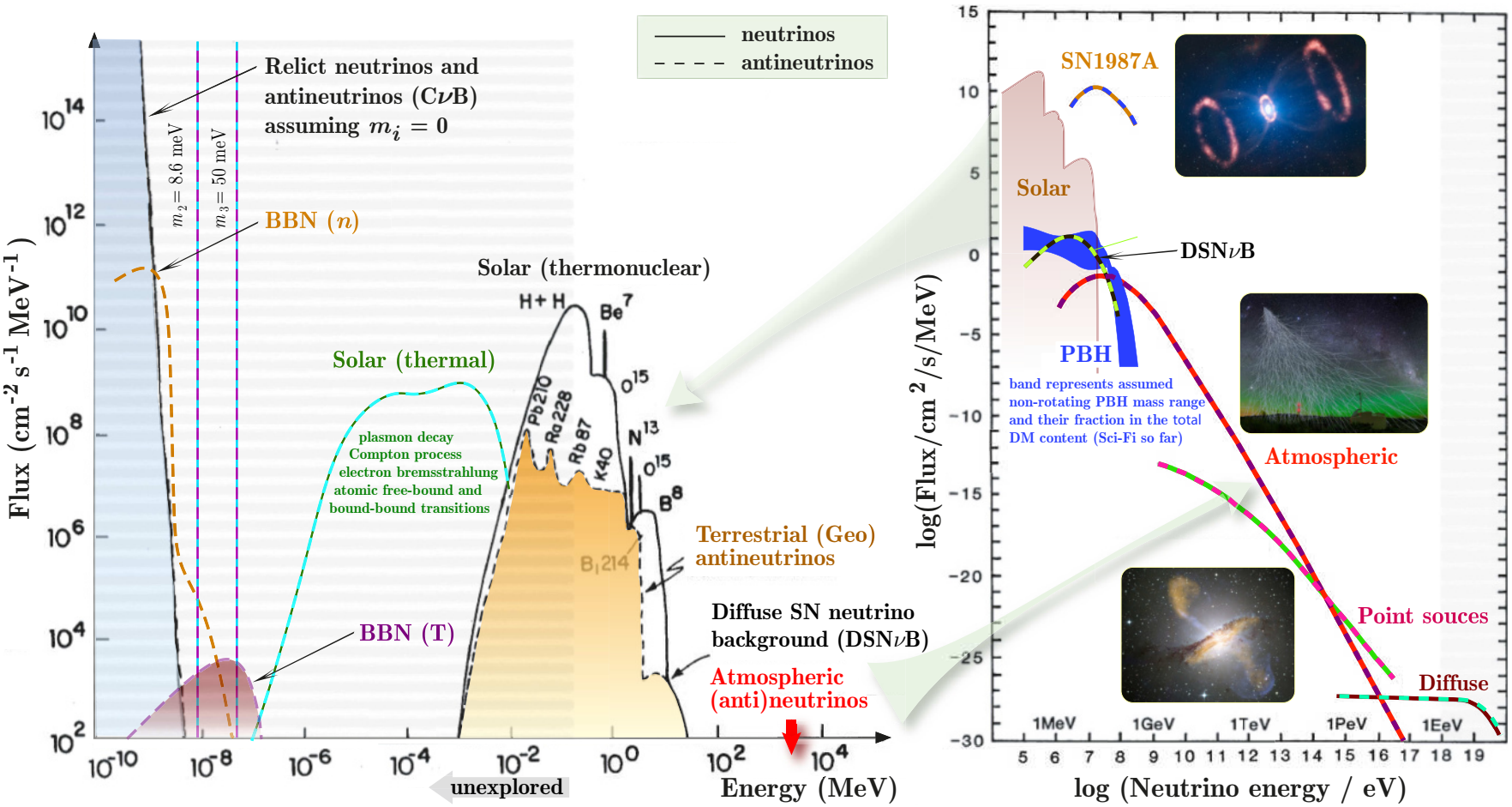

[Constructed from the data of L. M. Krauss *et al.*, "Antineutrino astronomy and geophysics," Nature **310** (1984) 191–198, E. Vitagliano *et al.*, "Grand unified neutrino spectrum at Earth: Sources and spectral components," Rev. Mod. Phys. **92** (2020) 45006, arXiv:1910.11878 [astro-ph.HE], and V. Yu. Yurchenko & A. V. Ivanchik, "Spectral features of non-equilibrium antineutrinos of primordial nucleosynthesis," Astropart. Phys. **127** (2021) 102537, arXiV:1911.03473 [hep-ph] (*left panel*) and A. M. Bakich, "Aspects of neutrino astronomy," Space Sci. Rev. **49** (1989) 259–310 and R. Calabrese *et al.*, "Primordial black hole dark matter evaporating on the neutrino floor," Phys. Lett. B **829** (2022) 137050, arXiv:2106.02492 [hep-ph] (*right panel*).]

Another representation of the natural fluxes of (anti)neutrinos (multiplied by E^3) on Earth. ▽

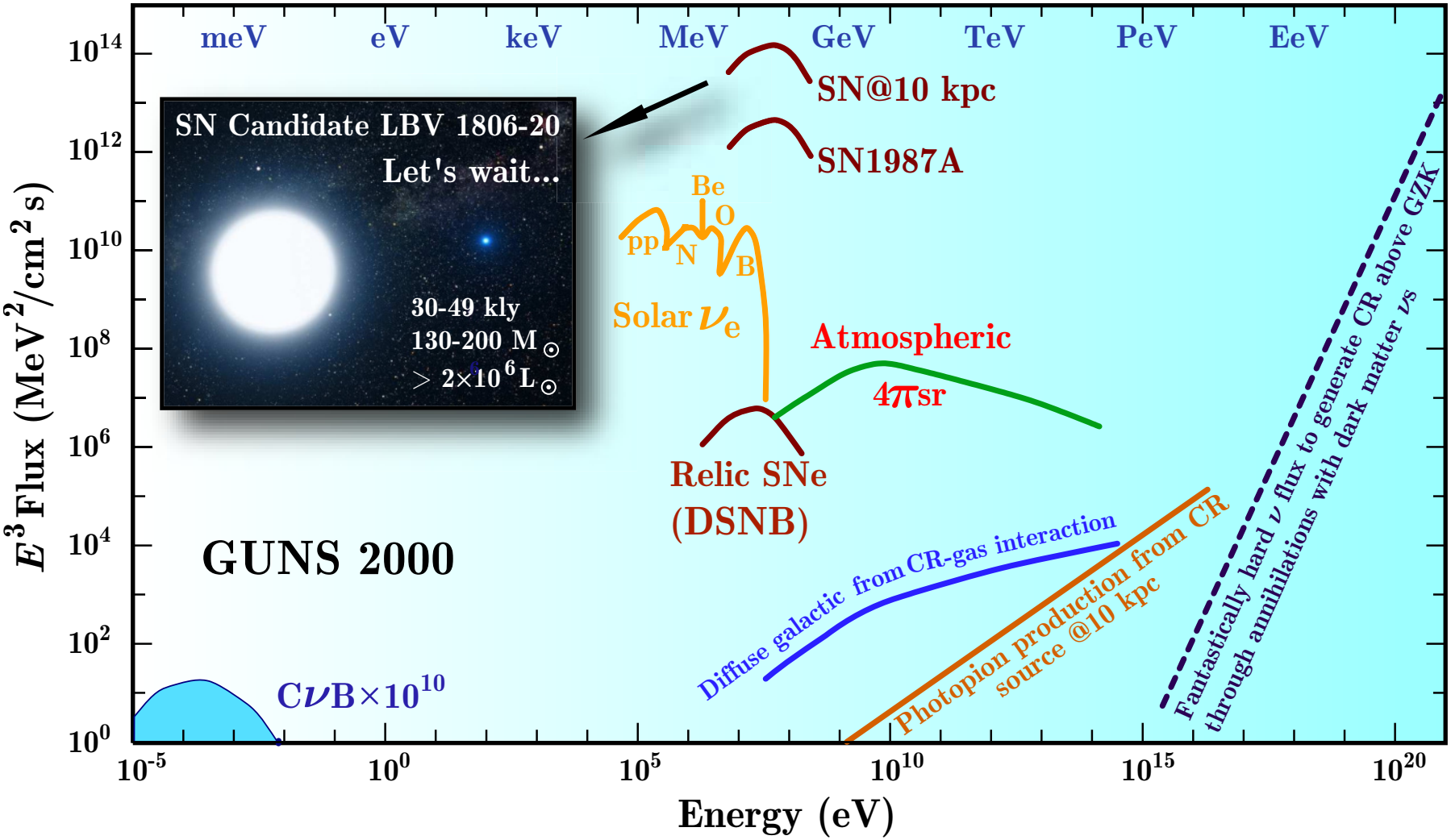

The spectra are integrated over directions and summed over flavors $\Longrightarrow$ flavor conversion between source and detector does not affect this plot. Monoenergetic spectra are in units of $\mathrm{cm}^{-2}\mathrm{s}^{-1}$.

[From E. Roulet, "Neutrinos in physics & astrophysics," Lect. Notes Phys. **556** (2000) 233–258, hep-ph/9910383.]

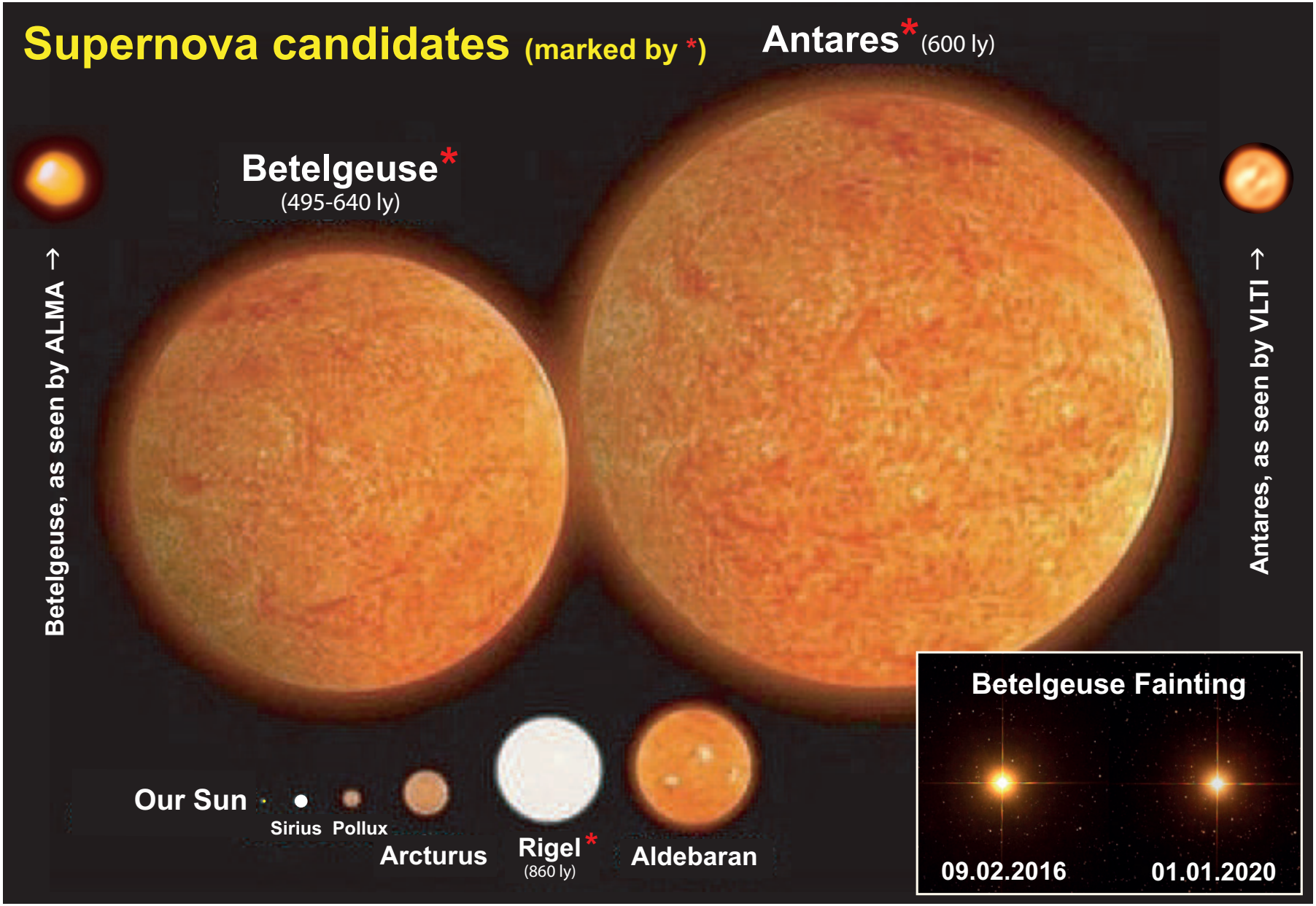

[See URL ⟨ https://en.wikipedia.org/wiki/List_of_supernova_candidates ⟩ for a longer list of SN candidates.]

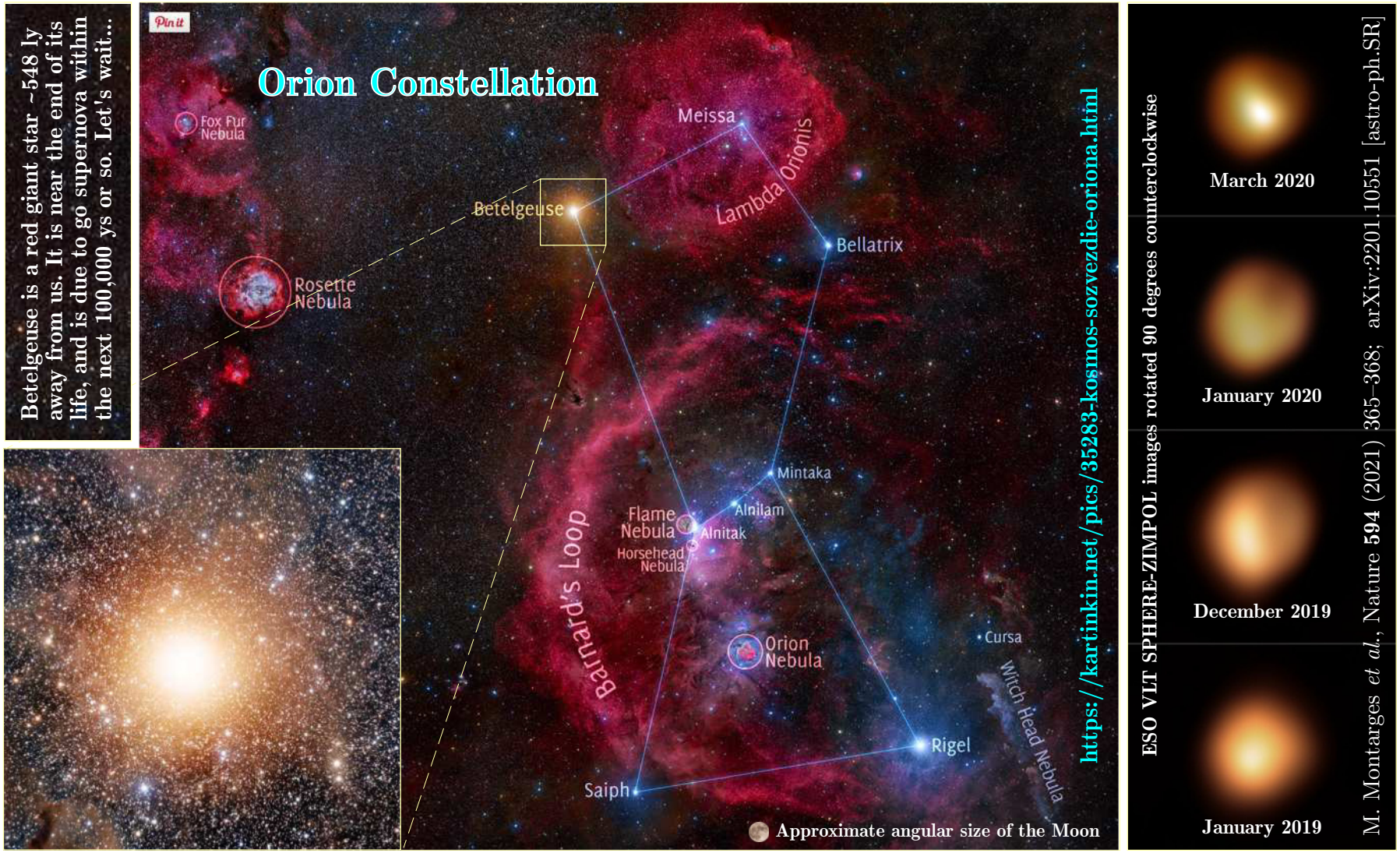

Betelgeuse and Rigel are located here △. ESO's VLT images (right) show Betelgeuse's surface during its dimming in 2019–2020. These events could occur due to stellar activity or just due to dust clouds. [By the way, the first very high-energy neutrino event ('IceCube-170922A') with a reliably identified γ source (blazar TXS 050+056) registered at IceCube occurred namely in this region of the sky, see p. 330.]

Modern collection of the dominant $\nu/\overline{\nu}$ fluxes ("Grand unified neutrino spectrum") on Earth. ▽

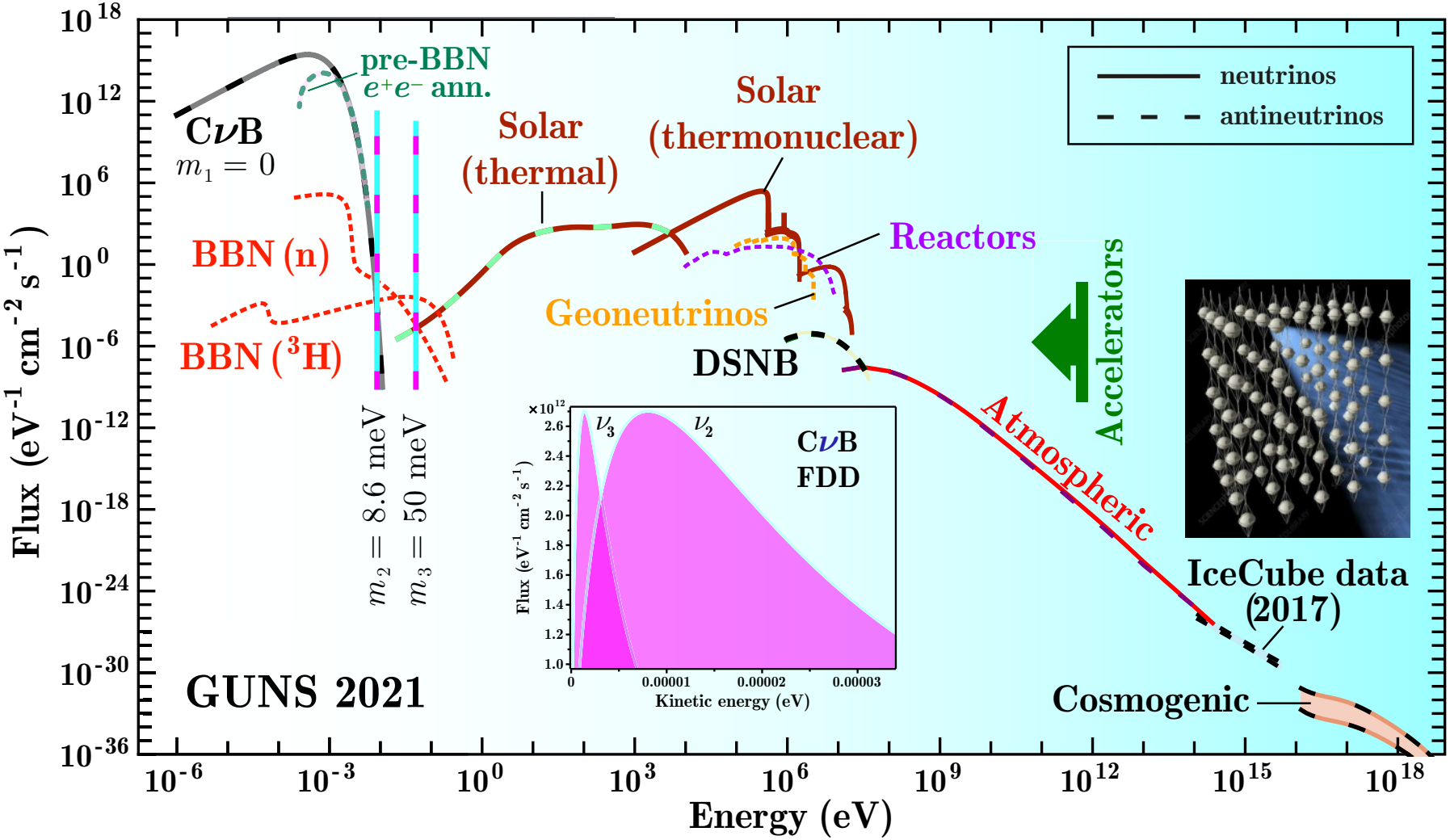

The continuous spectra are integrated over directions and summed over flavors $\Longrightarrow$ flavor conversion between source and detector does not affect the plot. "Monoenergetic" spectra are in $\mathrm{cm}^{-2}\mathrm{s}^{-1}$.

[Combined using the data of E. Vitagliano *et al.* (2020) and V. Yu. Yurchenko & A. V. Ivanchik (2021), see Refs. at p. 75.]

1.2 Electromagnetic wave spectrum.

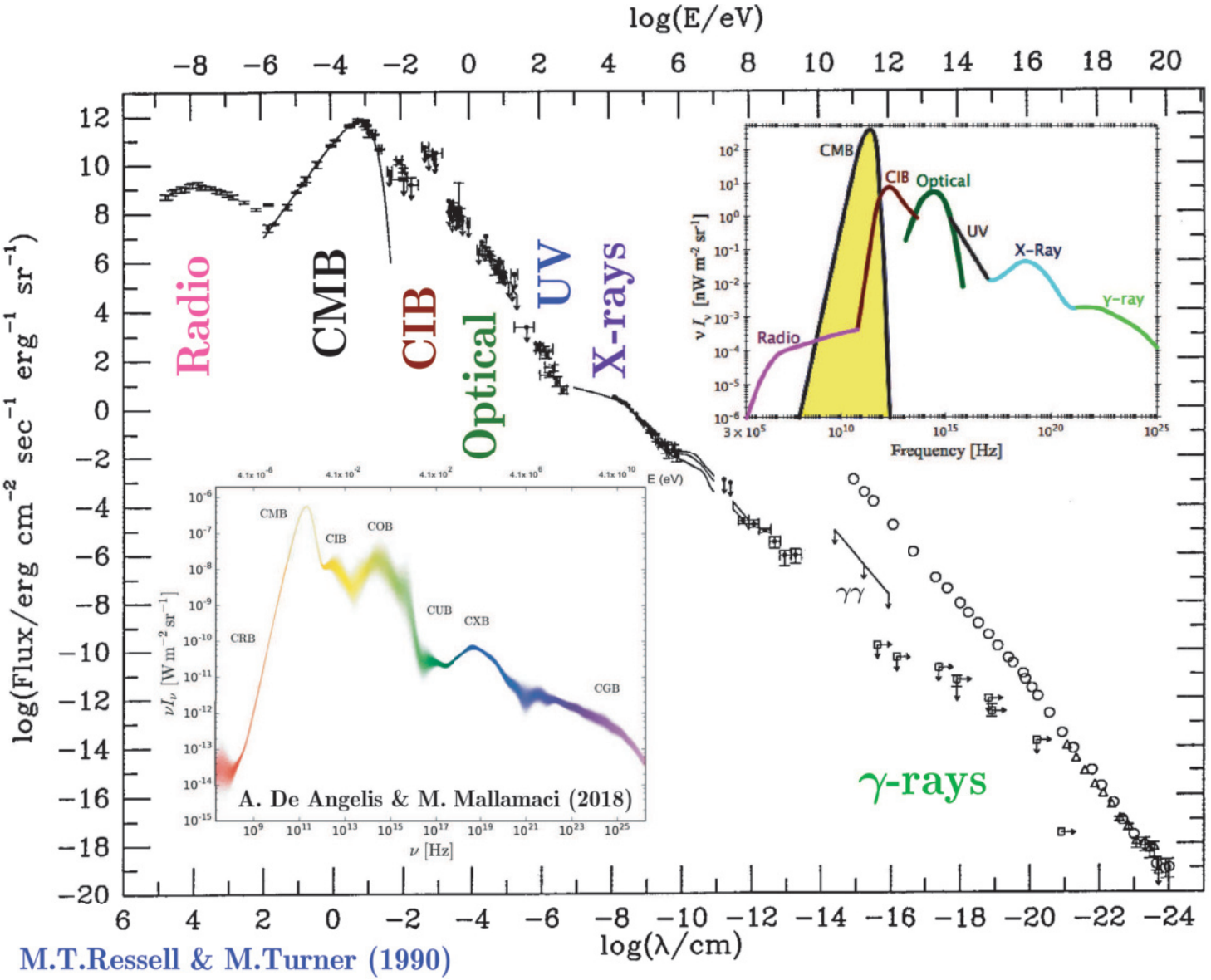

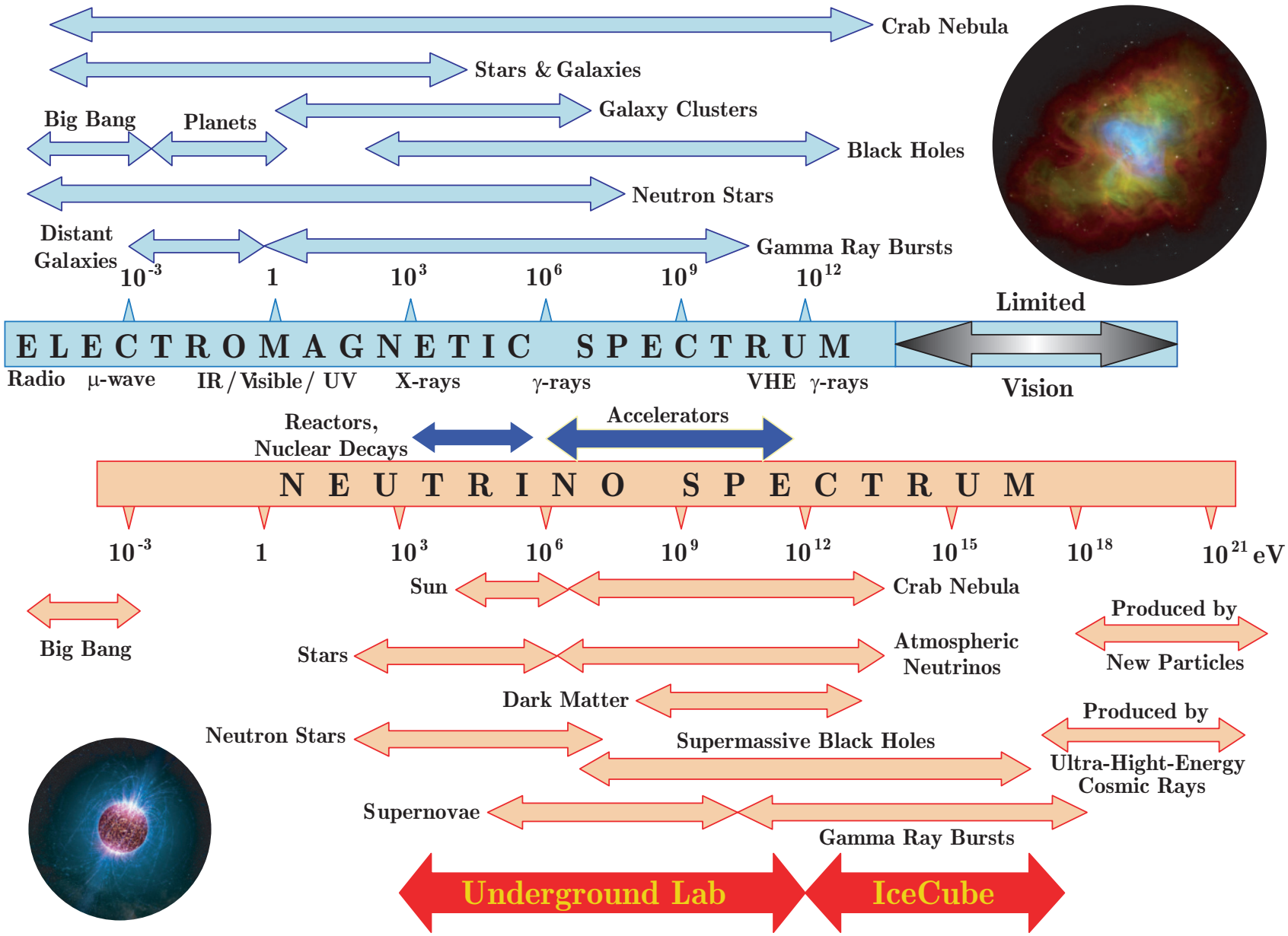

[From National Research Council of the National Academy, "Neutrinos and Beyond. New Windows on Nature".]

1.3 Cosmic microwave background (CMB).

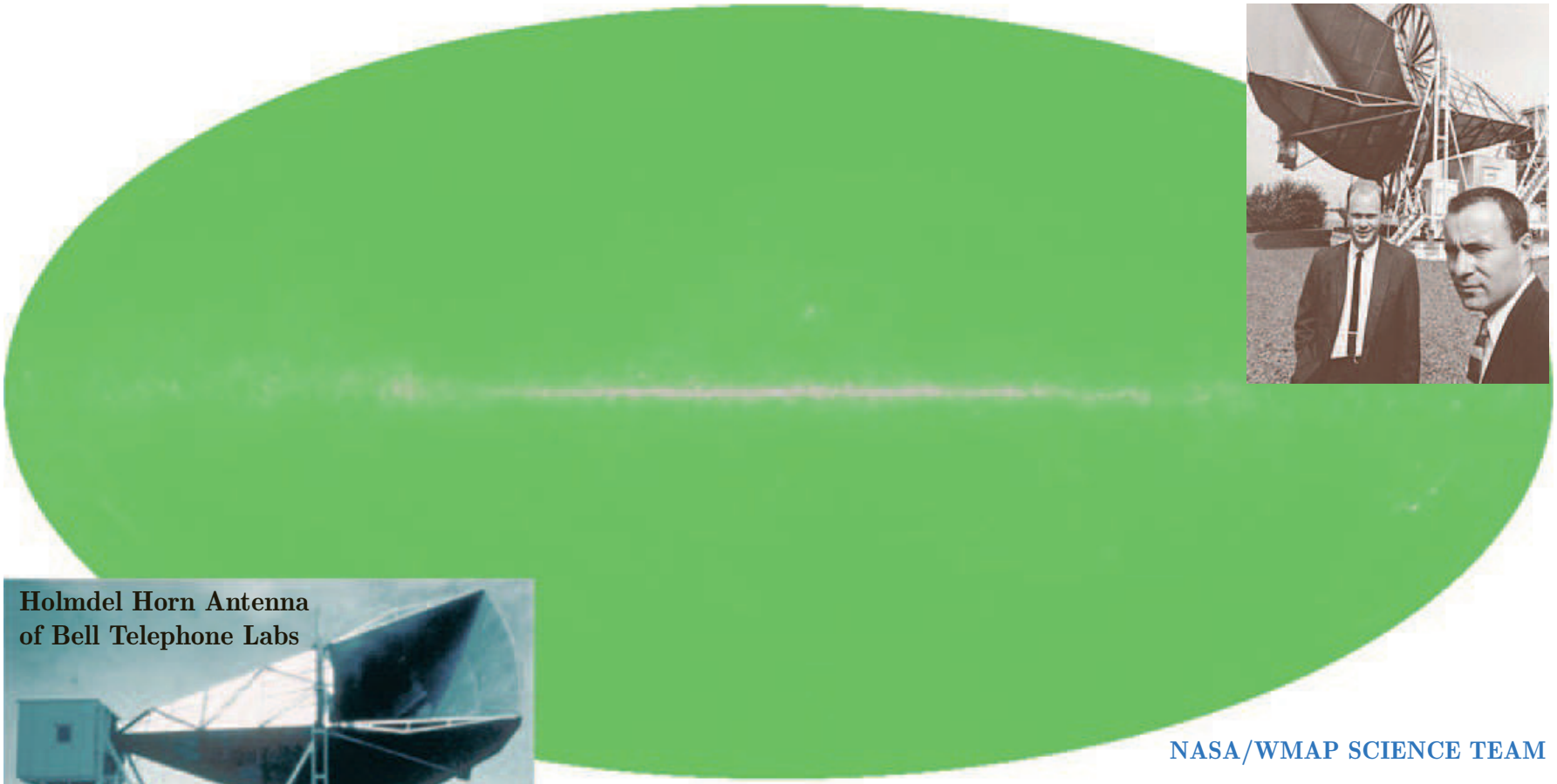

NASA/WMAP SCIENCE TEAM

Holmdel Horn Antenna
of Bell Telephone Labs

In 1964, Arno Penzias & Robert Wilson discovered the cosmic microwave background (CMB). Their giant but crude microwave receiver saw the radiation as being the same in all directions, occurring at 3.5 K.

[From URL: ⟨ http://www.nature.com/news/planck-snaps-infant-universe-1.12671 ⟩ (corrected).]

Note: The CMB was indirectly measured by Andrew McKellar in 1941 at an effective temperature of 2.3 K using CN stellar absorption lines (Walter S. Adams & Theodore Dunham, 1939–1941).

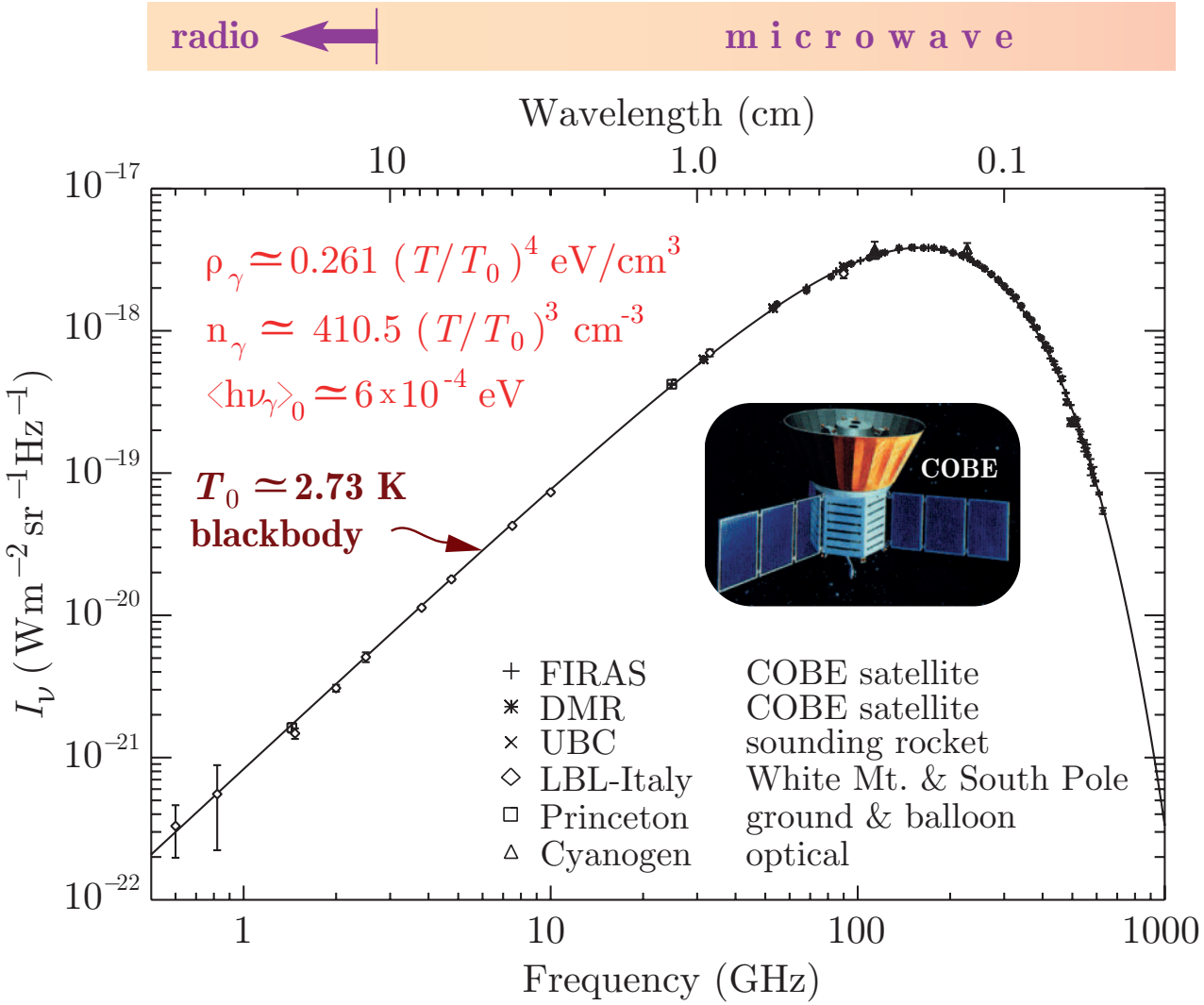

Precise measurements of the CMB (= CBR = RR) spectrum (after COBE). The curve represents a 2.73 K blackbody (present-day value), which describes the observed spectrum very well, especially around the peak of intensity. The spectrum is less well constrained at 10 cm and longer wavelengths.

When you tune your TV set between channels, *a few percent* of the "snow" that you see on your screen is noise caused by the CMB.

Velocity of the Sun with respect to CMB is 369.3 ± 2.5 km/s.

After many decades of experimental efforts, the CMB is known to be almost isotropic but having small temperature fluctuations called anisotropy with amplitude of order $10^{-5} - 10^{-3}$.

As is seen from the Figure at p. 83, the CMB spectrum follows with extraordinary precision the spectrum of a black body. The mean CMB temperature is

$$T_0 = 2.7255 \pm 0.0006 \text{ K}.$$

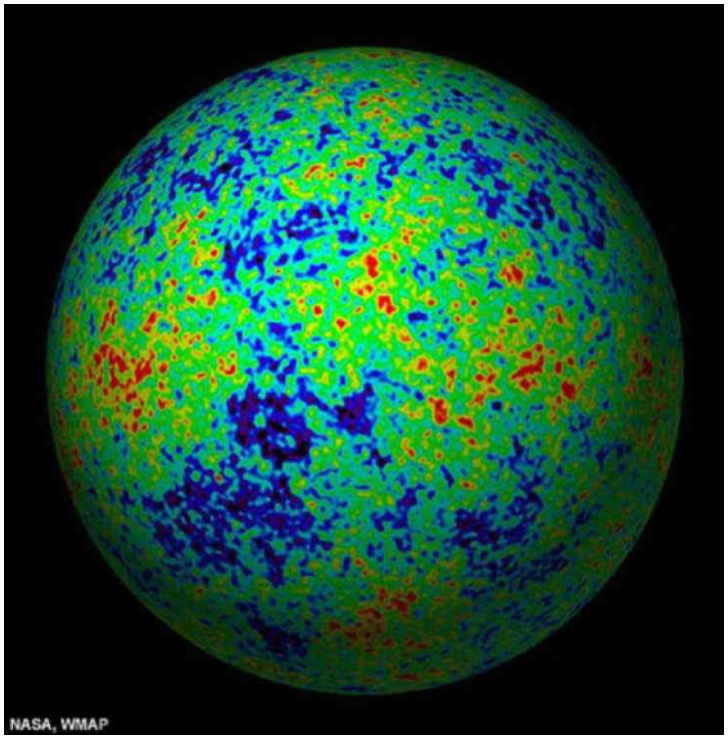

The variations of temperature of CMB, $\delta T(\theta, \phi)$ can be decomposed in a sum of spherical harmonics $Y_{lm}(\theta, \phi)$

$$\delta T(\theta, \phi) = \sum_{l=1}^{\infty} \sum_{m=-l}^{l} a_{lm} Y_{lm}(\theta, \phi).$$

The averaged squared coefficients a_{lm} give the variance

$$C_l = \langle |a_{lm}|^2 \rangle = \frac{1}{2l+1} \sum_{m=-l}^{l} |a_{lm}|^2.$$

If the temperature fluctuations are assumed to be Gaussian, as it appears to be the case, all of the information contained in the CMB maps can be compressed into the power spectrum, essentially giving the behavior of $l(l+1)C_l/(2\pi)$ as a function of l.

⋆ The observational data could map the universal fluctuations after removing the dipole anisotropy ($l = 1$), Doppler corrections, and galactic and extragalactic microwave contaminations (see p. 86).

⋆ The power spectrum profiles are shown in Figures at pp. 89 (after WMAP) and 98 (after *Planck*). Comparing the positions and heights of the peaks, one can deduce properties of the earlier Universe.

Digression: Physical meaning of the angular power spectrum.

Let's define the correlation function

$$C(\mu) = \langle \delta T(\mathbf{n}_1')\delta T(\mathbf{n}_2')\rangle \stackrel{\text{def}}{=} \frac{1}{(4\pi)^2}\int d^2 n_1' \int d^2 n_2' \delta T(\mathbf{n}_1')\delta T^*(\mathbf{n}_2') 2\delta(\mathbf{n}_1'\mathbf{n}_2' - \mu),$$

where $\mu = \mathbf{n}_1\mathbf{n}_2$ and $\mathbf{n}_i' = (\sin\theta_i\cos\phi_i, \sin\theta_i\sin\phi_i, \cos\theta_i)$. Then, taking into account the identities

$$\delta(\mu' - \mu) = \sum_{l=0}^{\infty} \frac{2l+1}{2} P_l(\mu)P_l(\mu'),$$

$$P_l(\cos\theta_1\cos\theta_2 + \sin\theta_1\sin\theta_2\cos(\phi_1 - \phi_2)) = \frac{4\pi}{2l+1}\sum_{m=-l}^{l} Y_{l_1 m_1}(\theta_1,\phi_1)Y^*_{l_2 m_2}(\theta_2,\phi_2),$$

and the spherical-harmonic decompositions for $\delta T(\mathbf{n}_i') \equiv \delta T(\theta_i,\phi_i)$, one obtains:

$$C(\mu) = \frac{1}{(4\pi)^2}\sum_{l=0}^{\infty}(2l+1)P_l(\mu)\int d^2 n_1' \int d^2 n_2' P_l(\cos\theta_1\cos\theta_2 + \sin\theta_1\sin\theta_2\cos(\phi_1-\phi_2))$$
$$\times \sum_{l_1,m_1} a^*_{l_1 m_1} Y^*_{l_1 m_1}(\theta_1,\phi_1) \sum_{l_2,m_2} a_{l_2 m_2} Y_{l_2 m_2}(\theta_2,\phi_2),$$

$$\Downarrow$$

$$C(\mu) = \frac{1}{4\pi}\sum_l a_l^2 P_l(\mu), \quad a_l^2 = \sum_{m=-l}^{l} |a_{lm}|^2.$$

The averaging of a_l^2 over the statistical ensemble yields the angular power spectrum $l(l+1)C_l/(2\pi)$.

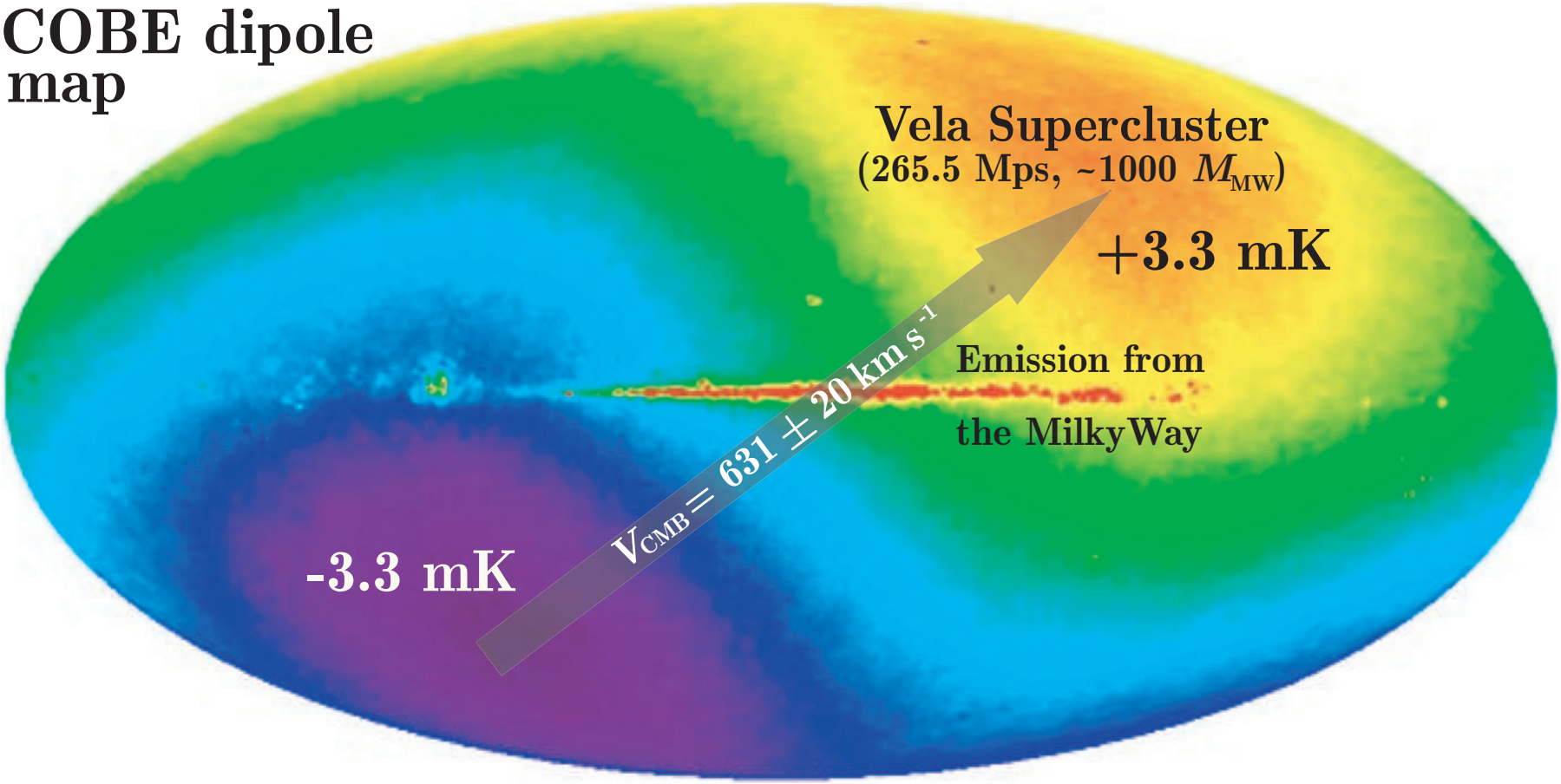

https://map.gsfc.nasa.gov/mission/observatory_cal.html

$$T_{\rm CMB}^{\rm mean} = 2.7255 \text{ K}$$

$$\delta T/T = V/c$$

Allowing for the Sun's orbital motion around the center of the Galaxy and the relative motion of the Milky Way and Andromeda within our Local Group, it is found that the barycenter of the Local Group is moving at a speed of about 631 km/s $\simeq 2.27 \times 10^6$ km/h with respect to the expanding Universe (modern data). [See M. J. Hudson, "Going with the flow," Nature Astron. **1** (2017) 0040 for relevant references.]

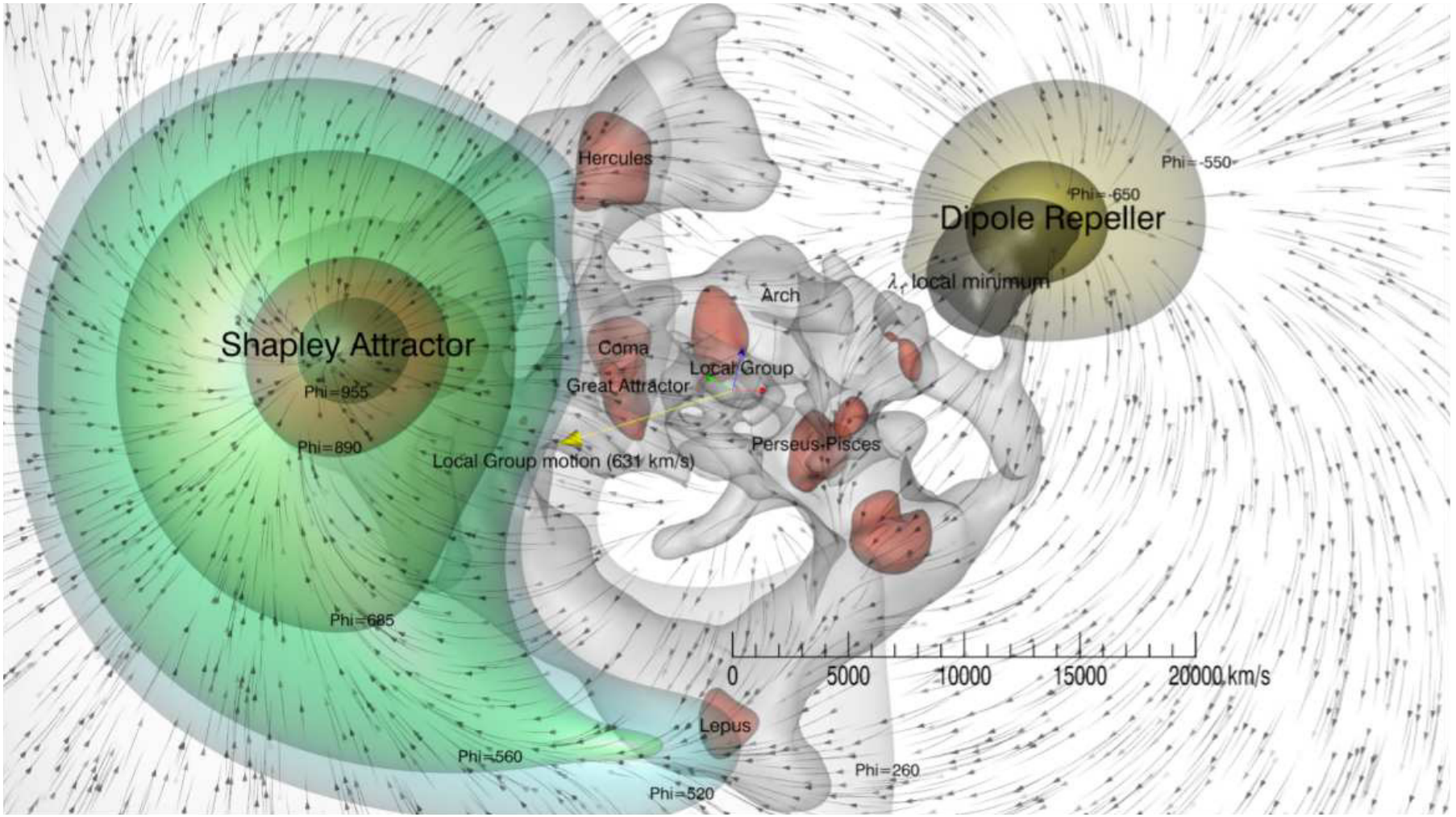

Local Group motion: The dominant influences causing the observed bulk flow are a single attractor (associated with the Shapley concentration) and a single dipole repeller (associated with a void or underdensity in the distribution of galaxies), which contribute 67 ± 27 and 59 ± 26 km/s, respectively, to the CMB dipole. The bulk flow is anti-aligned with the repeller out to $(16 \pm 4.5) \times 10^3$ km/s.

[From Y. Hoffman *et al.*, "The dipole repeller," Nature Astron. **1** (2017) 0036, arXiv:1702.02483 [astro-ph.CO].]

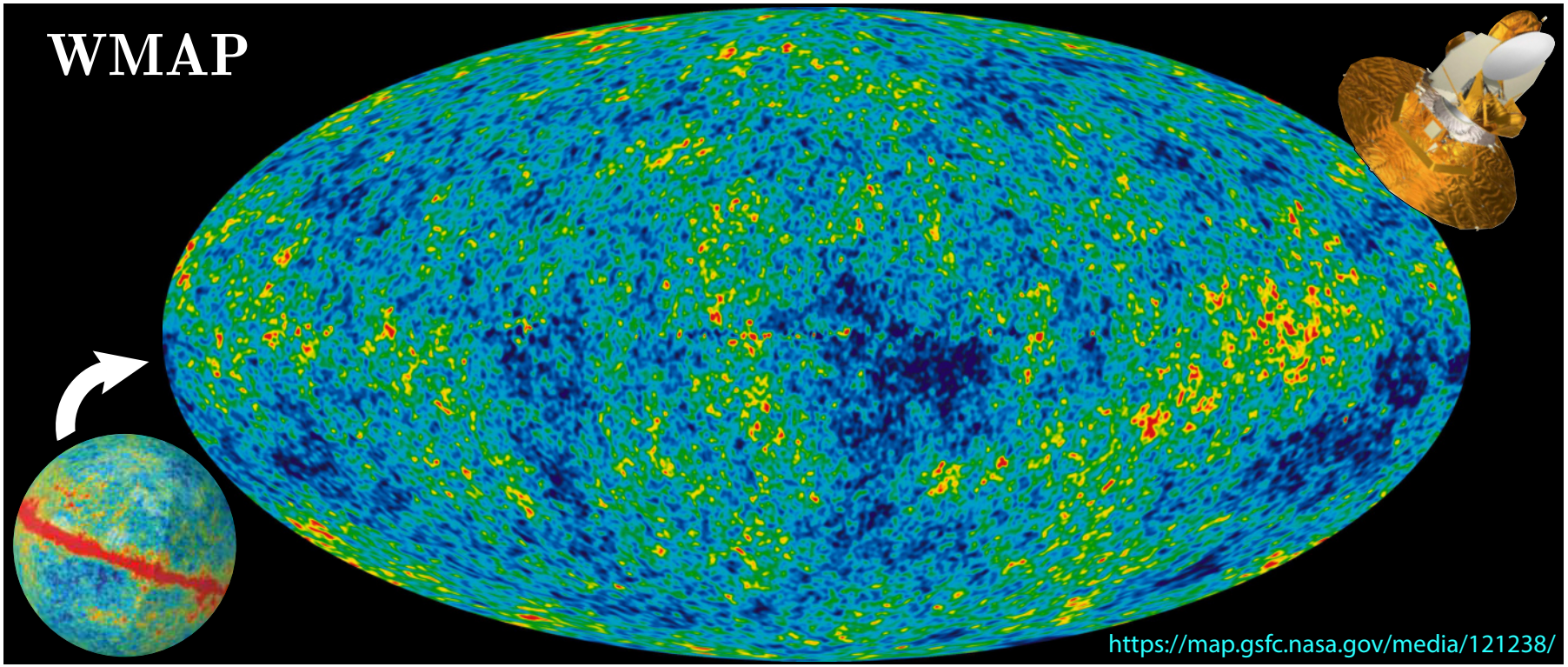

CMB anisotropy distribution after WMAP (Wilkinson Microwave Anisotropy Probe).
Doppler corrections and microwave radiation of Milky Way are subtracted.

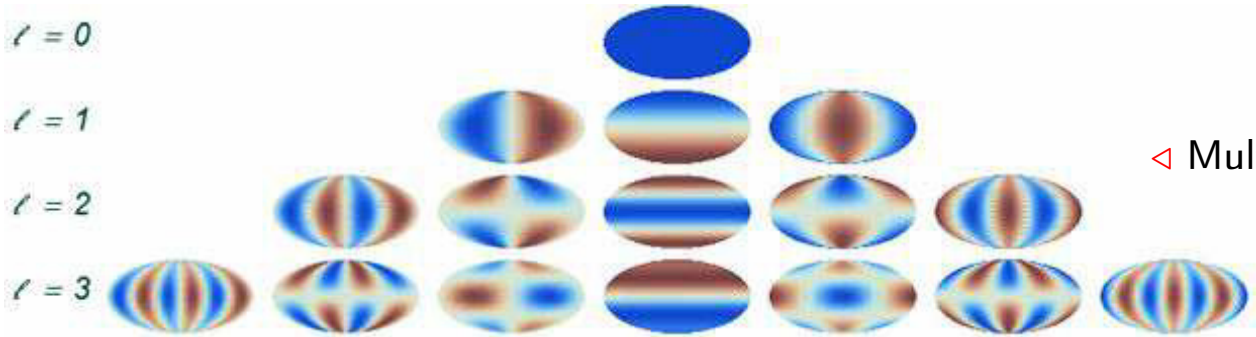

◁ Multipole expansion.

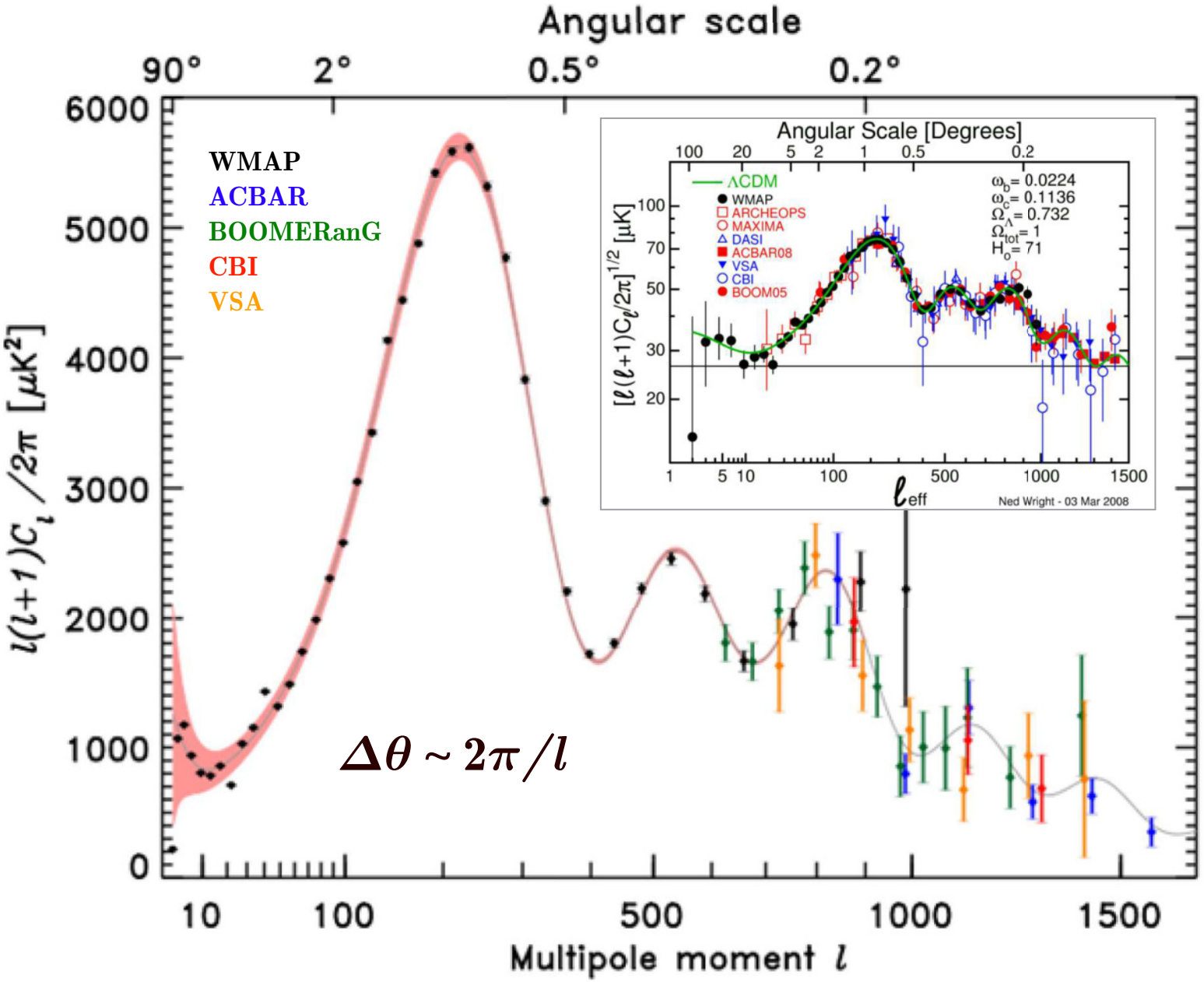
Angular scale
90°
2°
0.5°
0.2°
WMAP
ACBAR
BOOMERanG
CBI
VSA
$\Delta\theta \sim 2\pi/l$
$l(l+1)C_l/2\pi$ [μK^2]
Multipole moment l
Angular Scale [Degrees]
ΛCDM
WMAP
ARCHEOPS
MAXIMA
DASI
ACBAR08
VSA
CBI
BOOM05
ω_b= 0.0224
ω_c= 0.1136
Ω_Λ= 0.732
Ω_{tot}= 1
H_o= 71
$[l(l+1)C_l/2\pi]^{1/2}$ [μK]
l_{eff}
Ned Wright - 03 Mar 2008

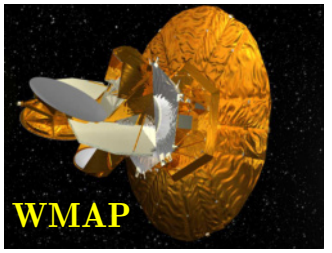
WMAP

ACBAR


BOOMERanG

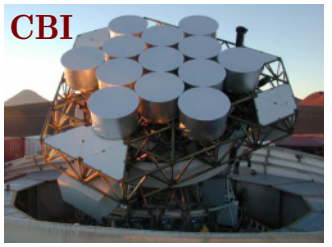
CBI

VSA

WMAP (**W**ilkinson **M**icrowave **A**nisotropy **P**robe) is a NASA Explorer mission that launched June 2001 to make fundamental measurements of cosmology. WMAP has been stunningly successful, producing our new Standard Model of Cosmology. WMAP's data stream has ended. Full analysis of the data is now complete.
⟨http://wmap.gsfc.nasa.gov/media/990307/index.html⟩.

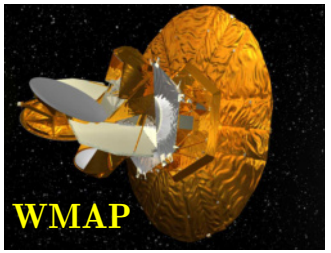

ACBAR (**A**rcminute **C**osmology **B**olometer **A**rray **R**eceiver) was an experiment (mounted on the Viper telescope at the South Pole to measure the anisotropy of the Cosmic microwave background. The ACBAR 145 GHz measurements were the most precise high multipole measurements of the CMB at the time.
⟨http://cosmology.berkeley.edu/group/swlh/acbar/⟩.

ACBAR

BOOMERanG (**B**alloon **O**bservations **O**f **M**illimetric **E**xtragalactic **R**adiation **AN**d **G**eophysics) was an experiment which measured the cosmic microwave background radiation of a part of the sky during three sub-orbital high altitude balloon flights.
⟨http://cmb.phys.cwru.edu/boomerang/⟩.

CBI (**C**osmic **B**ackground **I**mager) was a 13-element interferometer perched at an elevation of 5,080 m at Llano de Chajnantor Observatory in the Chilean Andes. It started operations in 1999 to study the CMB radiation and ran until 2008.
⟨http://www.astro.caltech.edu/~tjp/CBI/⟩.

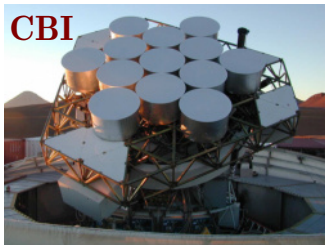

VSA (**V**ery **S**mall **A**rray) was a 14-element interferometric radio telescope operating between 26 and 36 GHz that is used to study the CMB radiation.
⟨http://www.jodrellbank.manchester.ac.uk/~mt/VSA.html⟩.

VSA

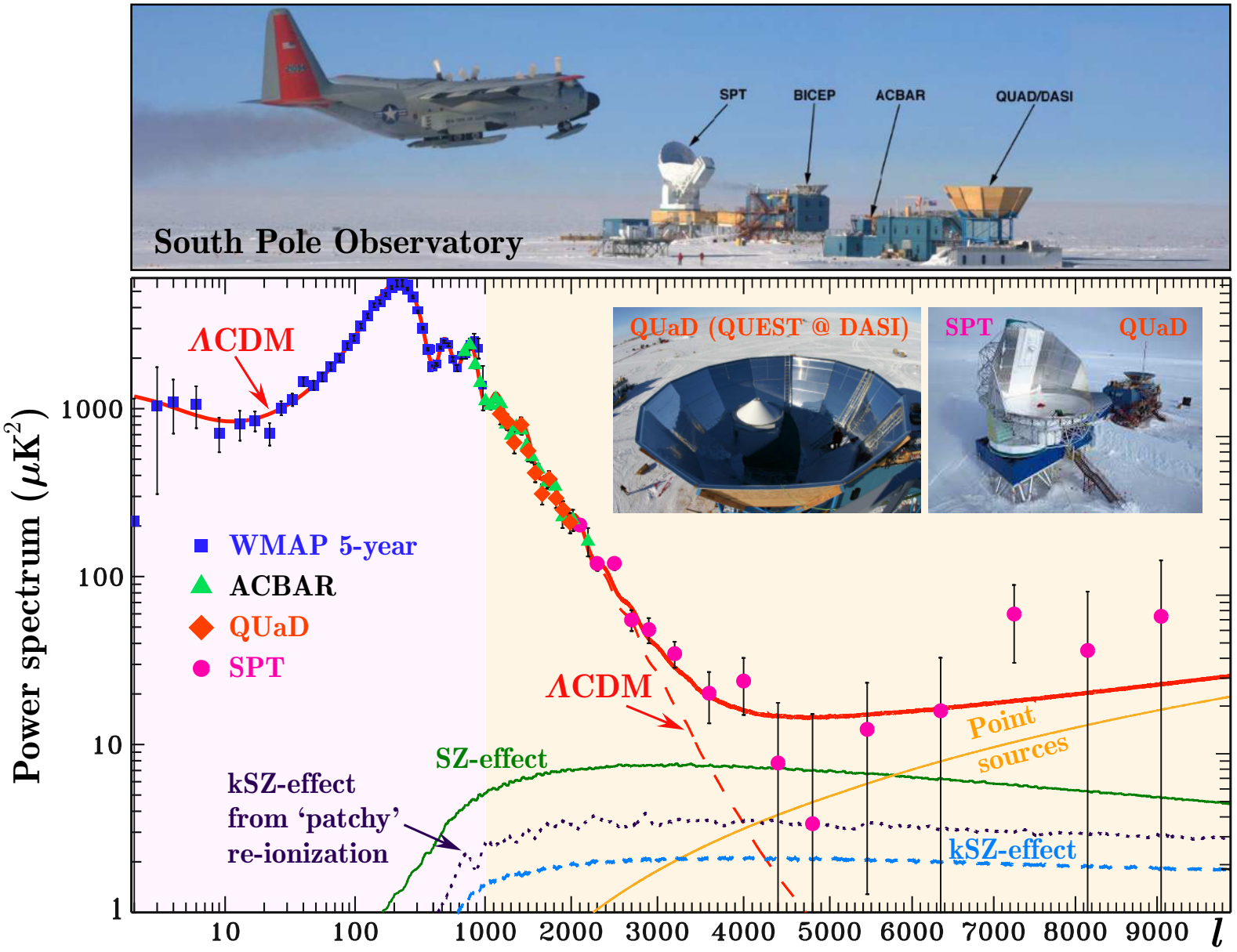

[Plot is taken from M. G. Burton, "Astronomy in Antarctica," Astron. Astrophys. Rev. **18** (2010) 417-469.]

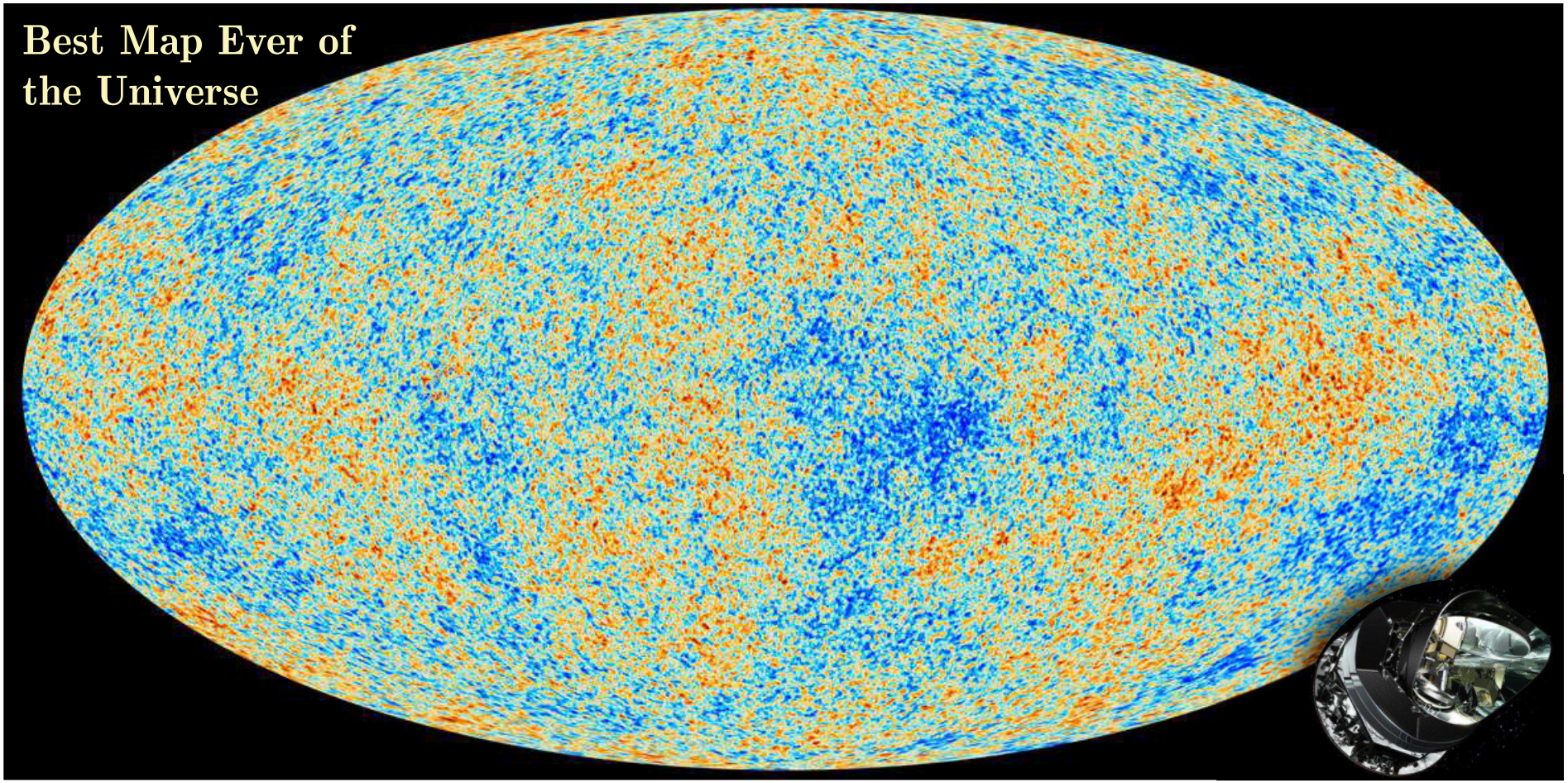

The map shows tiny temperature fluctuations in CMB as detected with the greatest precision yet by the *Planck*, a European Space Agency (ESA) mission, with significant participation from NASA's Jet Propulsion Laboratory (JPL). European, Canadian and U.S. *Planck* teams work together to analyze the *Planck* data. The results form the current **concordance model** which is the **ΛCDM** model.

[From URL: ⟨http://www.jpl.nasa.gov/spaceimages/details.php?id=PIA16873⟩.]

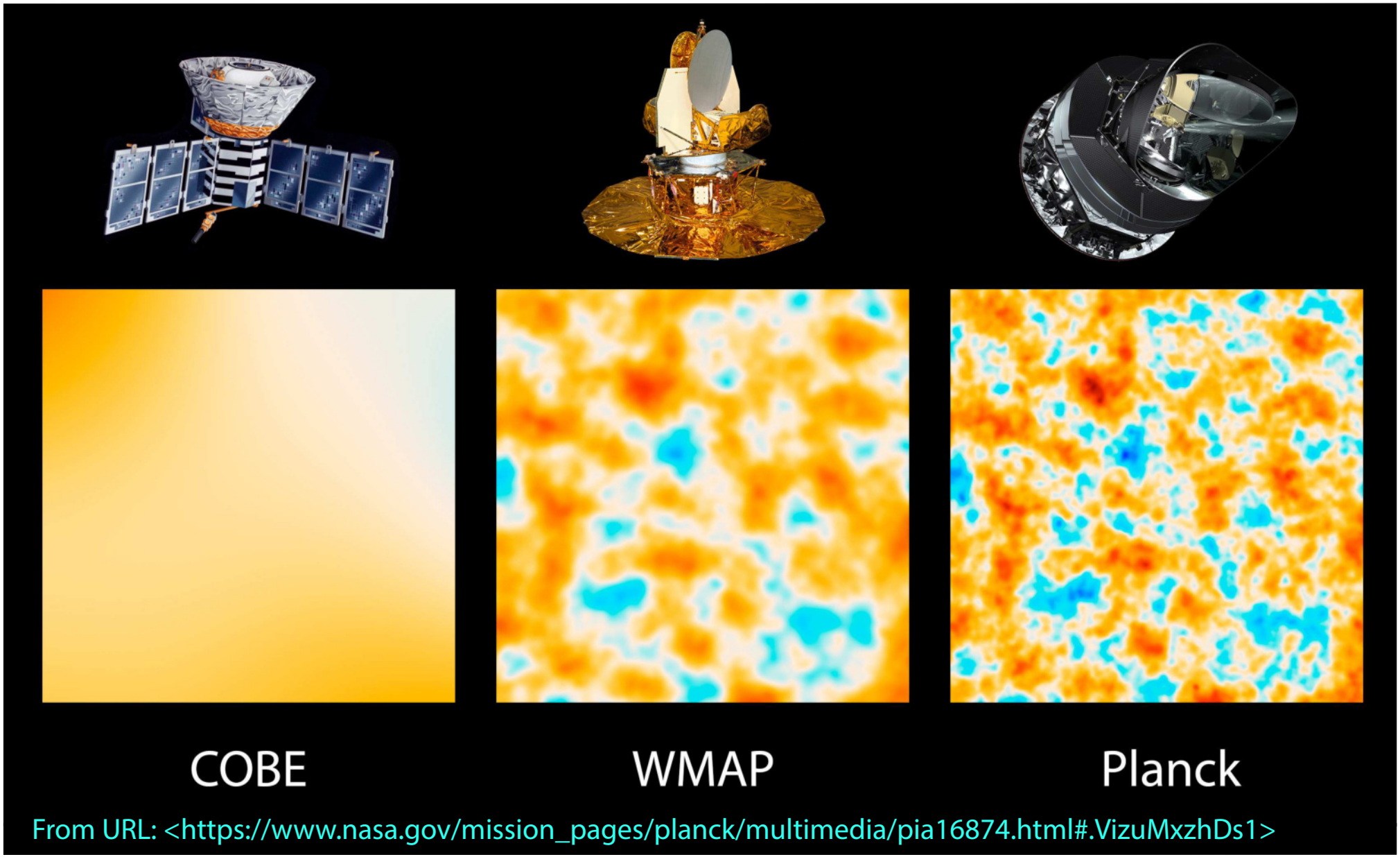
COBE
WMAP
Planck
From URL: <https://www.nasa.gov/mission_pages/planck/multimedia/pia16874.html#.VizuMxzhDs1>

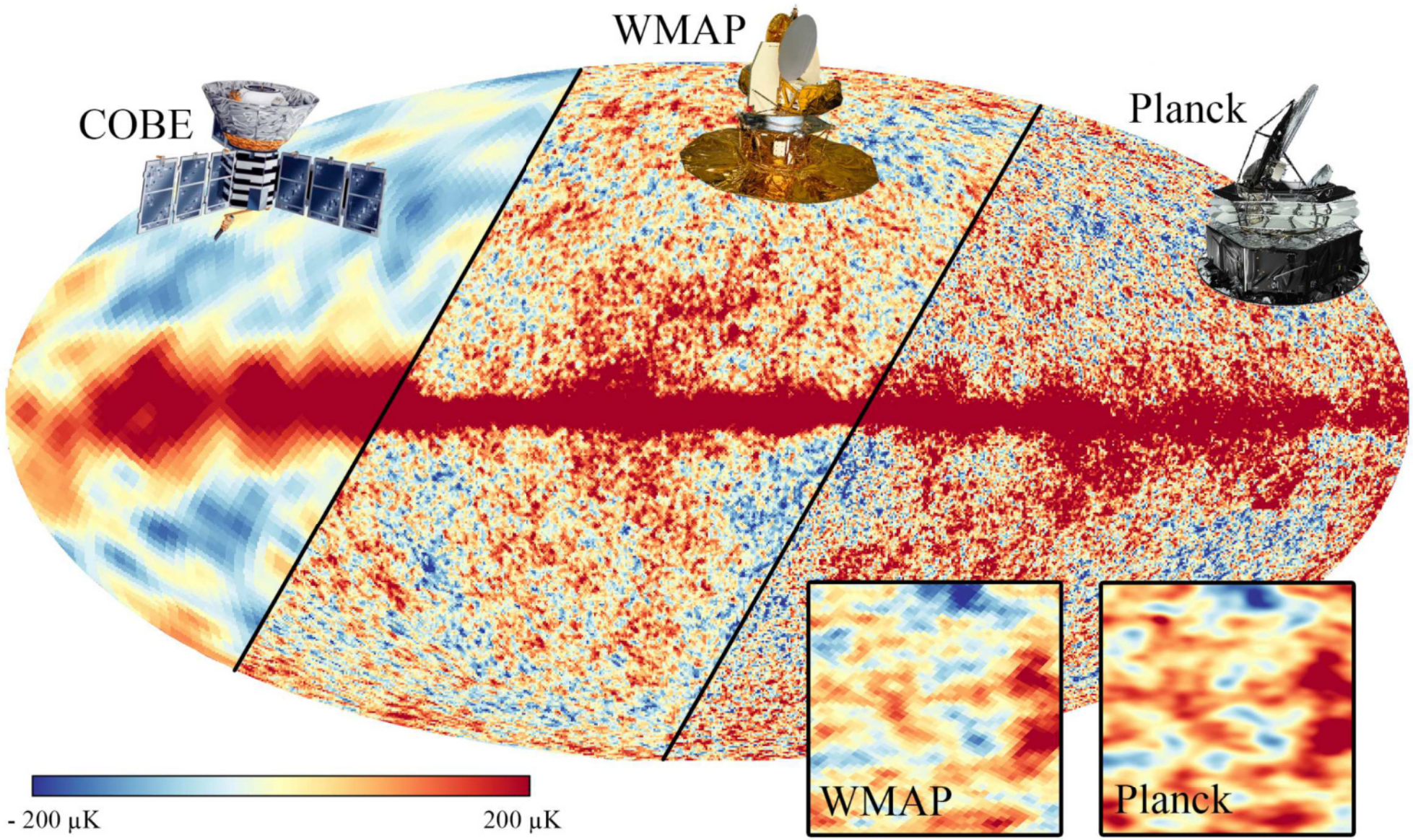

From URL: <https://jgudmunds.files.wordpress.com/2013/06/cobe_wmap_planck.png>

1.4 Selected results from Planck 2018.

Several conclusions:[a]

- *Planck* parameters reliable, no major change since 2015.
- Polarization now better understood (but not perfect; $\sim 0.5\sigma$ systematic uncertainty).
- *Planck* alone fits ΛCDM well: T, P + lensing all consistent.
- *Planck*+ΛCDM consistent with BAO (Baryon Acoustic Oscillations), SN, RSD (Redshift-space distortions), DES (Dark Energy Survey) lensing.
- *Planck*+ΛCDM moderate tension with DES joint probes.

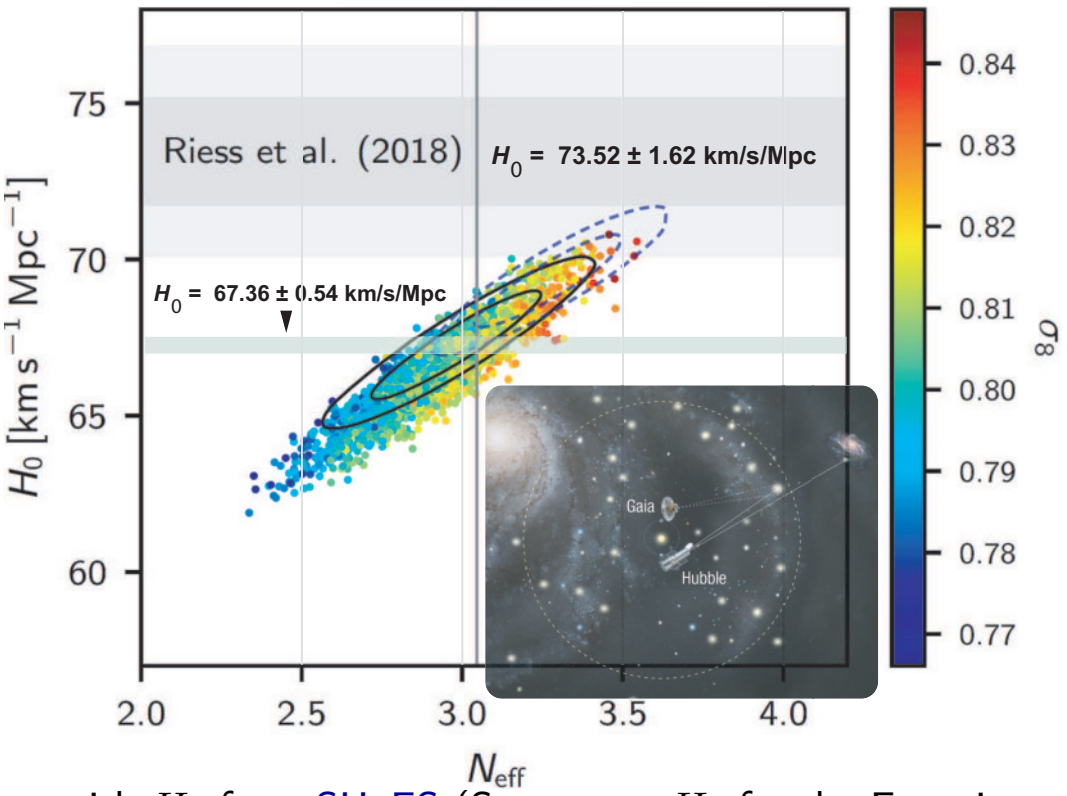

- *Planck*+ΛCDM in strong 3.6σ tension with H_0 from SHoES (Supernova H_0 for the Equation of State) team (see figure). It can be a problem with *Planck* or SHoES/Hubble+Gaia or ΛCDM.
- Some curiosities (like low-high features), but not more than $(2-3)\sigma$.
- If a new physics is the solution to the tensions, it does not have large signal in CMB.

[a] State of the art in 2019. For details see N. Aghanim *et al.* (*Planck* Collaboration), "*Planck* 2018 results. I. Overview and the cosmological legacy of *Planck*," Astron. Astrophys. **641** (2020) A1, arXiv:1807.06205 [astro-ph.CO]. Figure in this slide is an updated version of that from the report by Antony Lewis, "Planck 2018 – Cosmology & Parameters," Sesto Workshop, Italy 2018.

Situation with H_0 gets worse... [a]

Figure shows the inverse-distance-ladder (IDL) constraints on the Hubble parameter H_0 and Ω_m in the base-ΛCDM model, compared to the result from the full *Planck* CMB power-spectrum data. BAO data constrain the ratio of the sound horizon at the epoch of baryon drag and the distances; the sound horizon depends on the baryon density, which is constrained by the conservative prior of $\Omega_b h^2 = 0.0222 \pm 0.0005$, based on the measurement of D/H by Cooke *et al.* (2018) and standard BBN with modelling uncertainties.

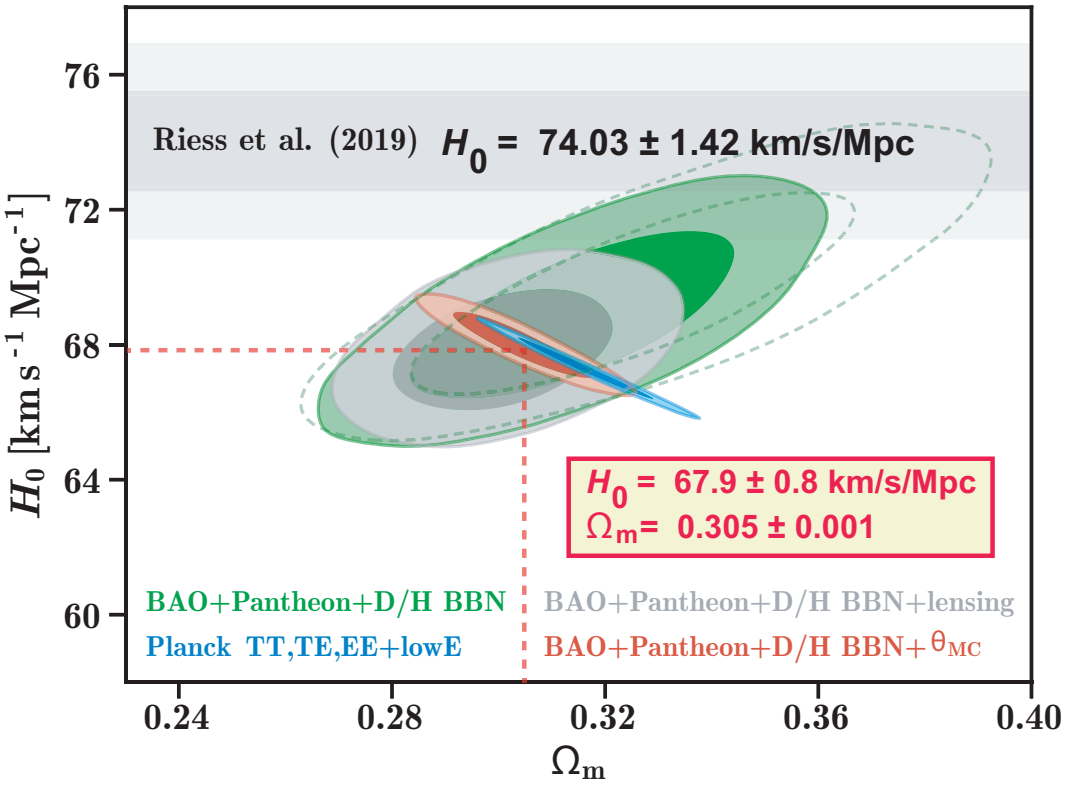

Adding *Planck* CMB lensing constrains the matter density, or adding a conservative *Planck* CMB "BAO" measurement ($100\theta_{MC} = 1.0409 \pm 0.0006$) gives a tight constraint on H_0, comparable to that from the full CMB data set. Grey bands show the local distance-ladder measurement of Riess *et al.* (2019). Contours contain 68% and 95% of the probability. Marginalizing over the neutrino masses or allowing dark energy equation of state parameters $w_0 > -1$ would only lower the IDL constraints on H_0. The dashed contours show the constraints from the data combination BAO+JLA+D/H BBN.

[a] See N. Aghanim *et al.* (*Planck* Collaboration), "*Planck* 2018 results. VI. Cosmological parameters," Astron. Astrophys. **641** (2020) A6, arXiv:1807.06209v4 [astro-ph.CO] and references therein.

Today (2021) the value of local Universe H_0 is known with an uncertainty of less than 10%. However, comparison of the current H_0 estimates with different methodologies, reveals the existence of a dichotomy: a first group of measures characterized by a central value below 70 km/(s Mpc) and a second one centered above 73 km/(s Mpc). The current "tension" is not only limited to CMB and Cepheid measurements but instead involves a dozen of different methods, mostly independent of each other.

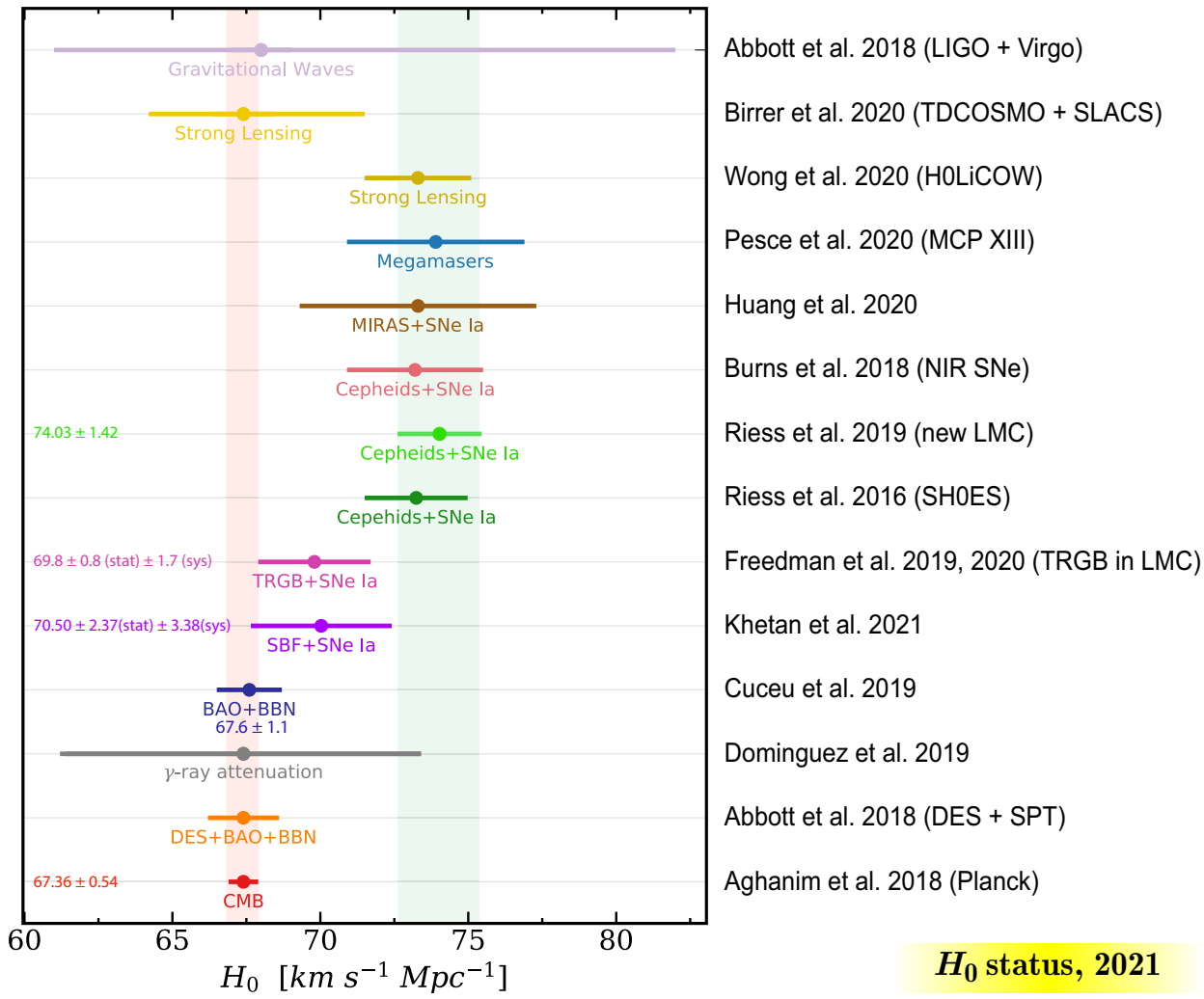

H_0 status, 2021

Recent results of N. Khetan *et al.* together with the other data suggest that there is a certain margin to interpret the discrepant results in terms of systematics while relaxing the quest for new physics.

[Taken with corrections from N. Khetan *et al.*, "A new measurement of the Hubble constant using Type Ia supernovae calibrated with surface brightness fluctuations," Astron. Astrophys. **647** (2021) A74, arXiv:2008.07754 [astro-ph.CO].]

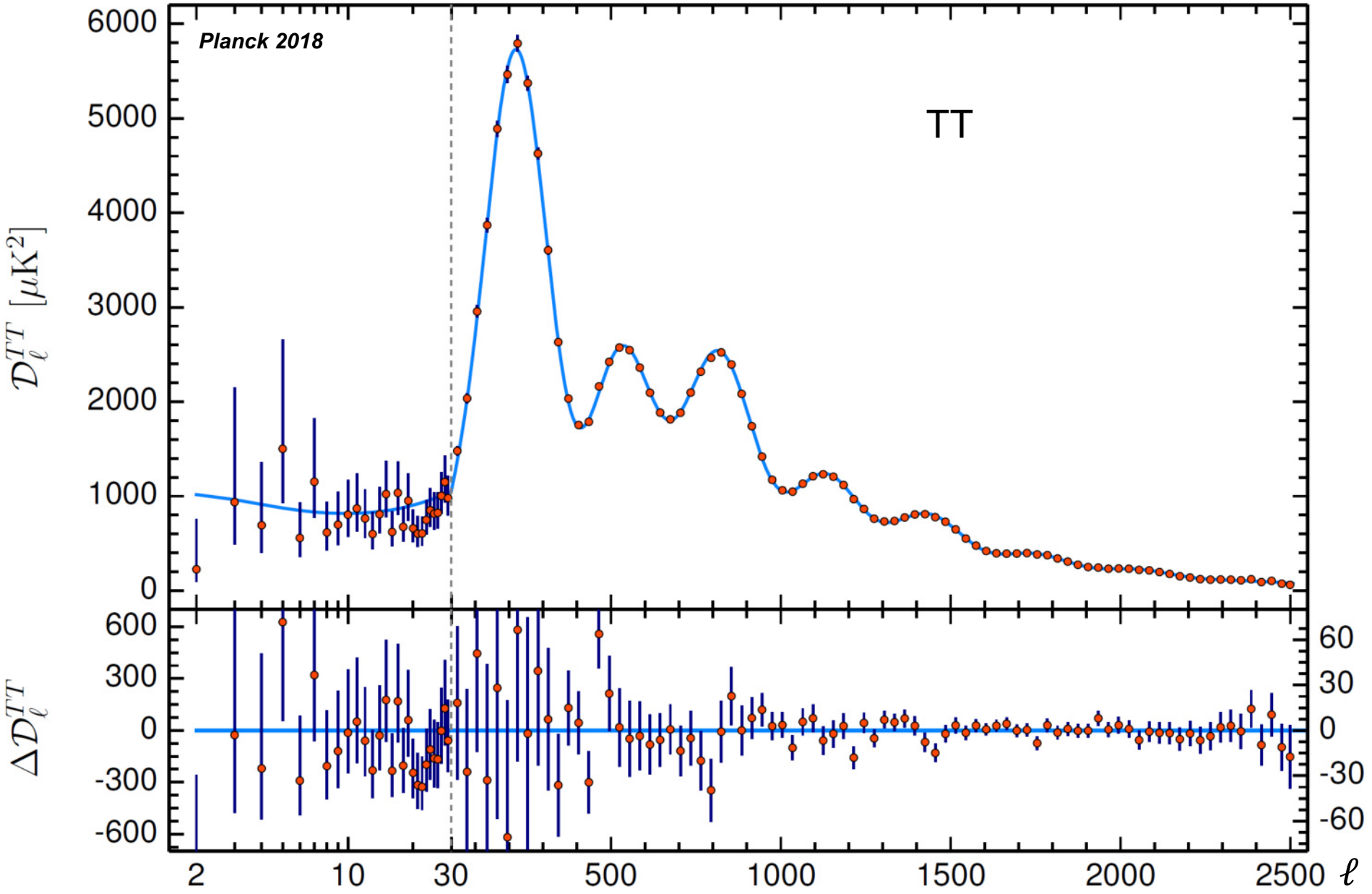
Planck 2018
TT
$\mathcal{D}_\ell^{TT}$ [μK^2]
$\Delta\mathcal{D}_\ell^{TT}$
6000
5000
4000
3000
2000
1000
0
600
300
0
-300
-600
60
30
0
-30
-60
2
10
30
500
1000
1500
2000
2500
ℓ

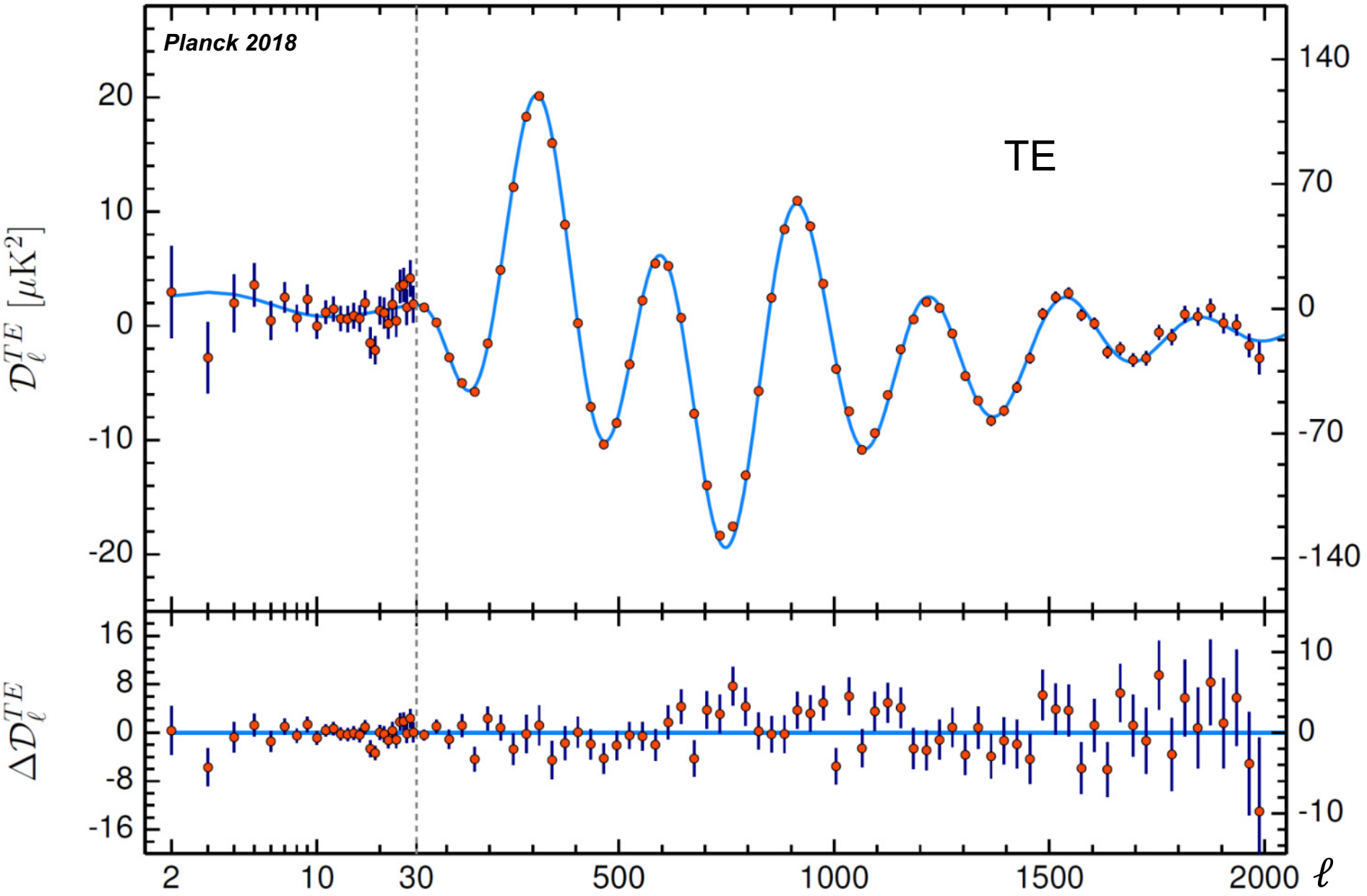
Planck 2018
TE
$\mathcal{D}_\ell^{TE}$ [μK^2]
$\Delta\mathcal{D}_\ell^{TE}$
20
10
0
-10
-20
140
70
0
-70
-140
16
8
0
-8
-16
10
0
-10
2
10
30
500
1000
1500
2000
ℓ

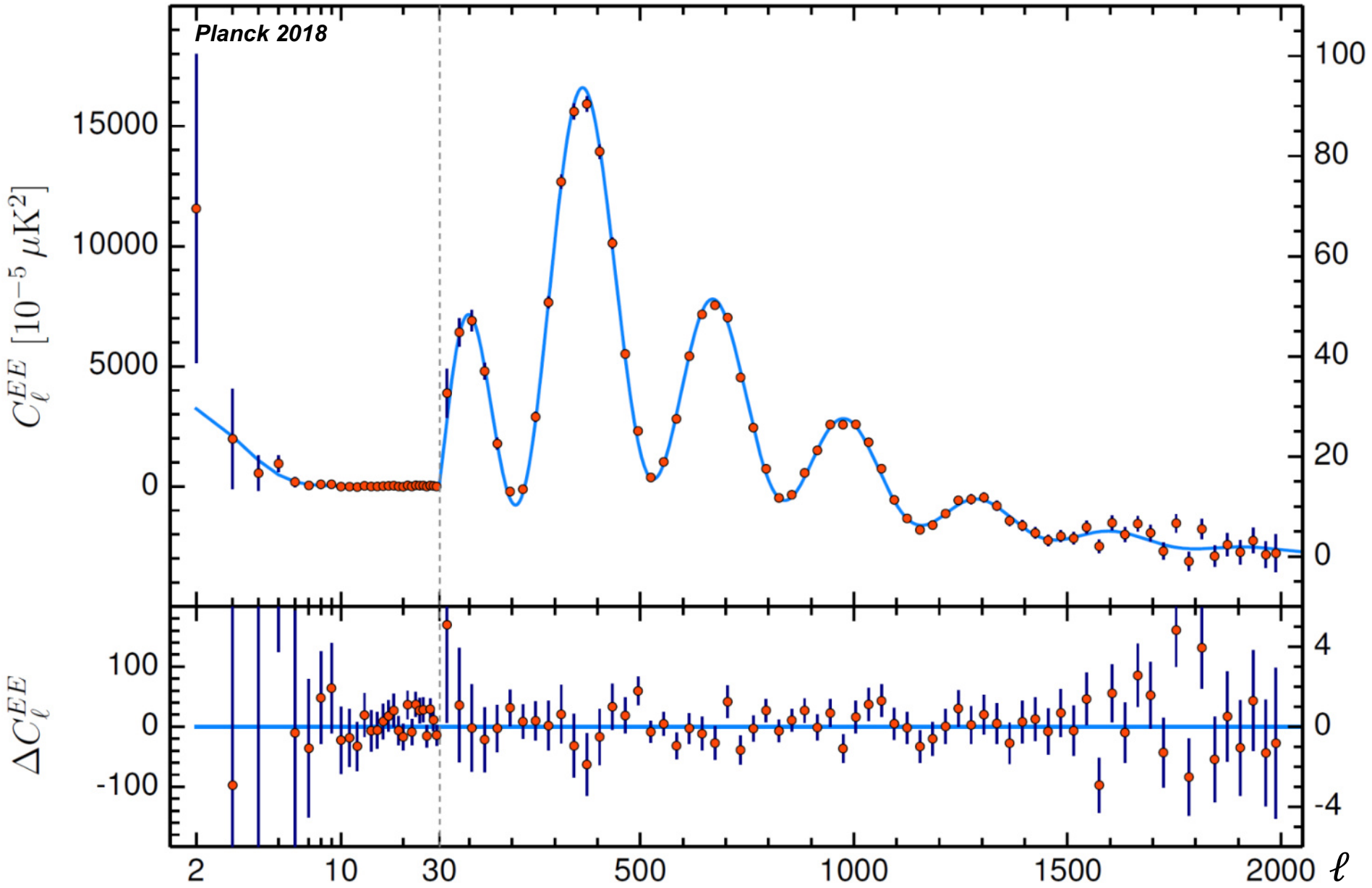
Planck 2018
C_ℓ^{EE} $[10^{-5}\ \mu\mathrm{K}^2]$
15000
10000
5000
0
100
80
60
40
20
0
ΔC_ℓ^{EE}
100
0
-100
4
0
-4
2
10
30
500
1000
1500
2000
ℓ

More details on the "Hubble tension":

In next slide, a comparison of some *Planck* 2015 and *Planck* 2018 neutrino results is shown.

Top panels: Samples from *Planck* TT+lowP chains in the $\sum m_\nu - H_0$ plane, colour-coded by σ_8. Solid black contours show the constraints from *Planck* TT,TE,EE+lowE+lensing, filled contours show the joint constraints from *Planck* TT+lowP+lensing+BAO, and the dashed green contours additionally marginalize over $N_{\rm eff}$. The olive vertical band in top *right panel* shows the region with $\sum m_\nu < 0.056$ eV ruled out by neutrino oscillation experiments. Mass splittings observed in the neutrino oscillation experiments (before 2018) also imply that the region left of the dotted vertical line can only be a normal hierarchy (NH), while the region to the right could be either normal or inverted hierarchy (IH); for more recent oscillation constraints, see Sect. **12.2.2**, p. 437.

Bottom panels: Samples from *Planck* TT+lowP chains in the $N_{\rm eff} - H_0$ plane, colour-coded by σ_8. Solid black contours show the constraints from *Planck* TT,TE,EE +lowE+lensing+BAO, dashed contours in *right panel* also include Riess *et al.* (2018) data. Notice that higher $N_{\rm eff}$ brings H_0 into better consistency (left) or decrease tension (right) with direct measurements, but increases σ_8. Dashed vertical lines in *left panel* correspond to specific fully-thermalized particle models, for example one additional massless boson that decoupled around the same time as the neutrinos ($\Delta N_{\rm eff} \approx 0.57$), or before muon annihilation ($\Delta N_{\rm eff} \approx 0.39$), or an additional sterile neutrino that decoupled around the same time as the active neutrinos ($\Delta N_{\rm eff} \approx 1$). Models with $N_{\rm eff} < 3.046$ (left of the solid vertical line) require photon heating after neutrino decoupling or incomplete thermalization.

In both *left panels*, the horizontal grey bands show the constraint from direct measurements $H_0 = (70.6 \pm 3.3)$ km s^{-1}Mpc^{-1}, namely the Cepheid data reanalysed by Efstathiou *et al.* (2014) using the revised geometric maser distance to NGC 4258 .

The horizontal grey bands on the bottom *right panel* show the local Hubble parameter measurement $H_0 = (73.45 \pm 1.66)$ km s^{-1} Mp^{-1} from Riess *et al.* (2018) [cf. with Riess *et al.* (2019), see p. 96].

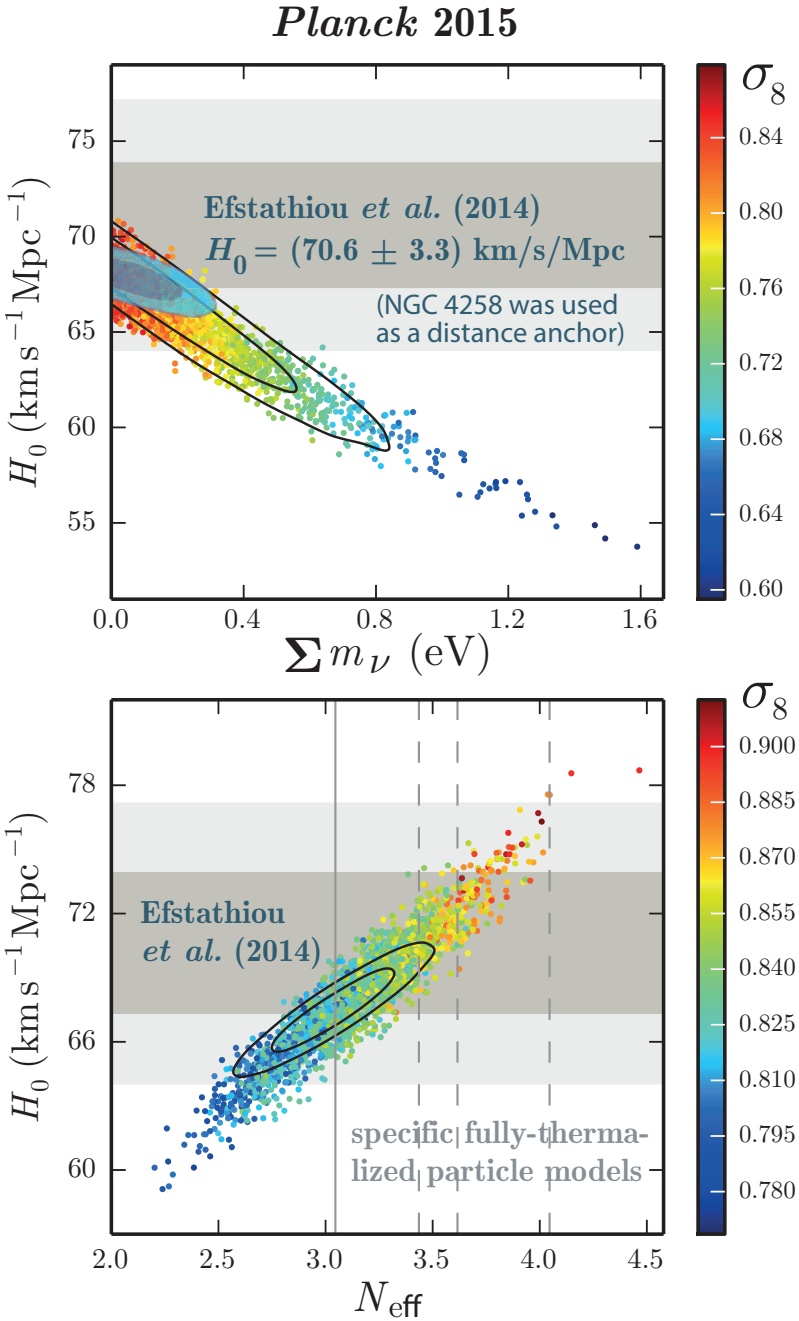
Planck 2015
Efstathiou et al. (2014)
$H_0 = (70.6 \pm 3.3)$ km/s/Mpc
(NGC 4258 was used as a distance anchor)
H_0 (km s^{-1} Mpc^{-1})
$\sum m_\nu$ (eV)
σ_8
Efstathiou et al. (2014)
specific | fully-therma-lized | particle models
$N_{\rm eff}$

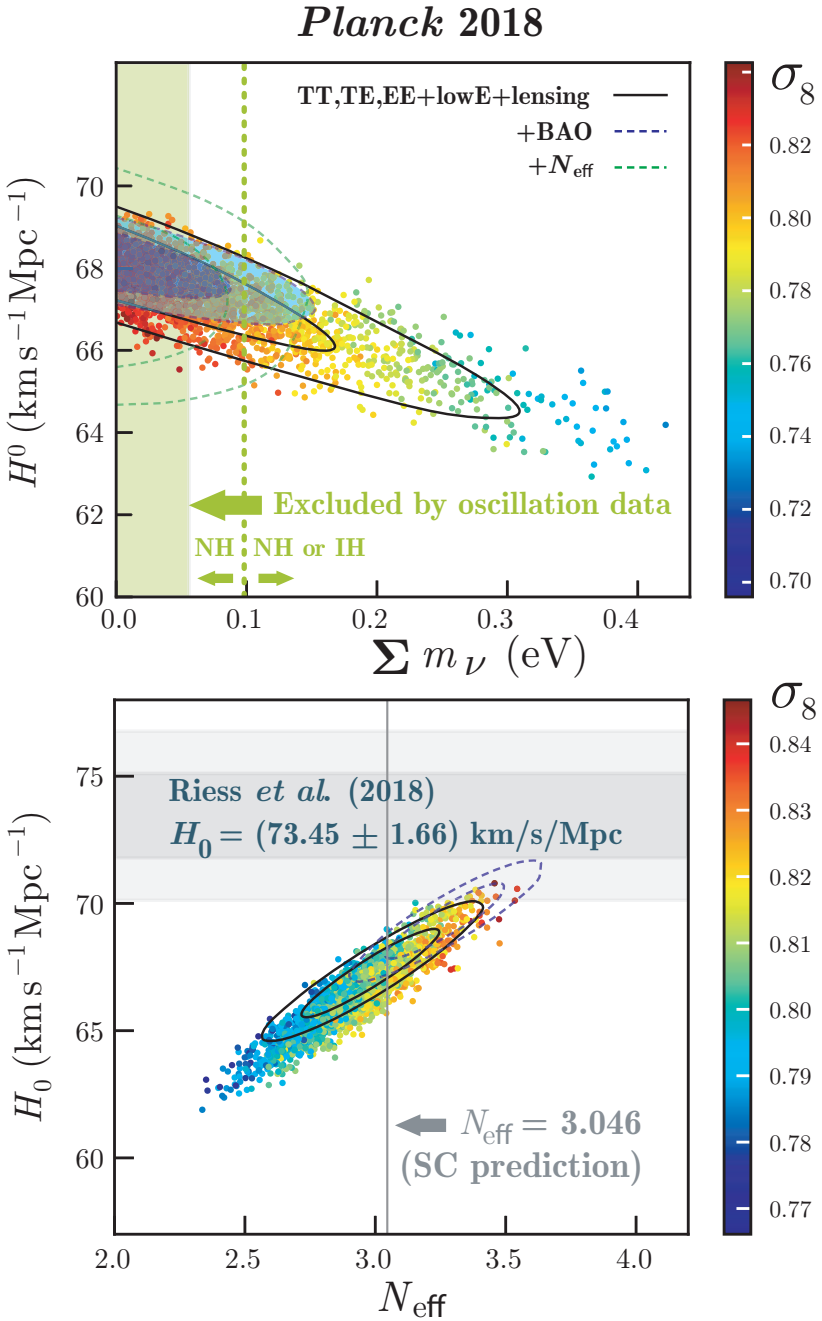
Planck 2018
TT,TE,EE+lowE+lensing
+BAO
+$N_{\rm eff}$
Excluded by oscillation data
NH | NH or IH
H^0 (km s^{-1} Mpc^{-1})
$\sum m_\nu$ (eV)
σ_8
Riess et al. (2018)
$H_0 = (73.45 \pm 1.66)$ km/s/Mpc
$N_{\rm eff} = 3.046$
(SC prediction)

1.5 Gravitational waves.

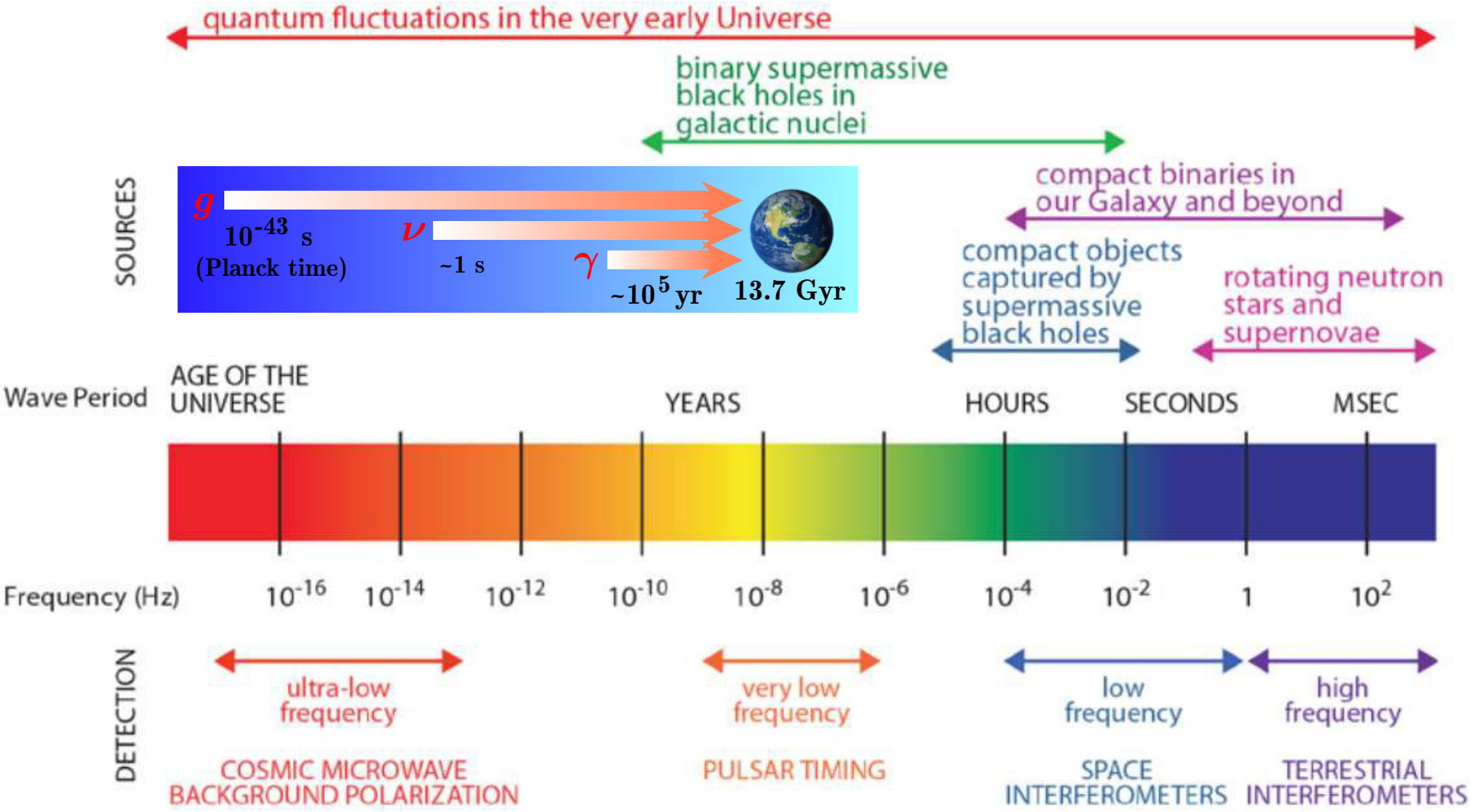

[From J. Centrella, "Gravitational wave astrophysics: opening the new frontier," AIP Conf. Proc. **1381** (2011) 98–116, arXiv:1109.3492 [astro-ph.HE].]

1.5.1 Birth of gravitational-wave astronomy (events GW150914 & GW151226).

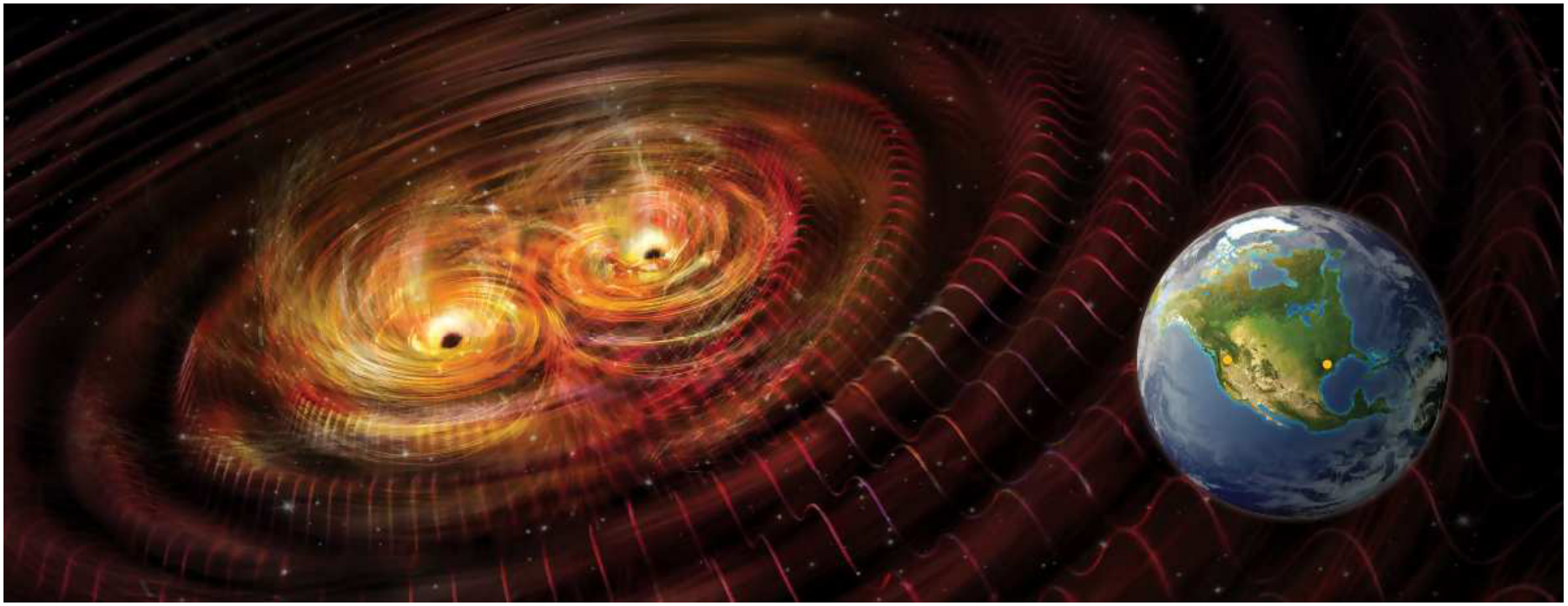

Cosmic shake-up: Colliding black holes send "ripples" through space-time that can be detected on Earth. The Advanced Laser Interferometer Gravitational-Wave Observatory (Advanced LIGO), which has detectors in Louisiana and Washington, has directly observed these gravitational waves at least twice (events GW150914[a], and GW151226[b]).

[a] B. P. Abbott *et al.* (LIGO & Virgo Collaborations), "Observation of gravitational waves from a binary black hole merger," Phys. Rev. Lett. **116** (2016) 061102, arXiv:1602.03837 [gr-qc].

[b] B. P. Abbott *et al.* (LIGO & Virgo Collaborations), "GW151226: Observation of gravitational waves from a 22-solar-mass binary black hole coalescence," Phys. Rev. Lett. **116** (2016) 241103, arXiv:1606.04855 [gr-qc].

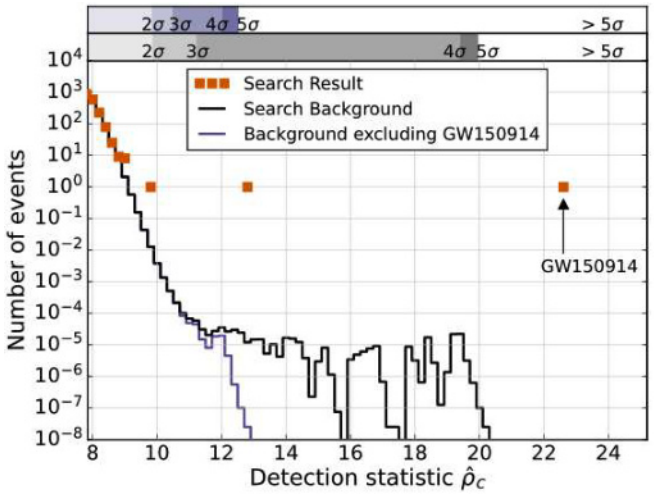

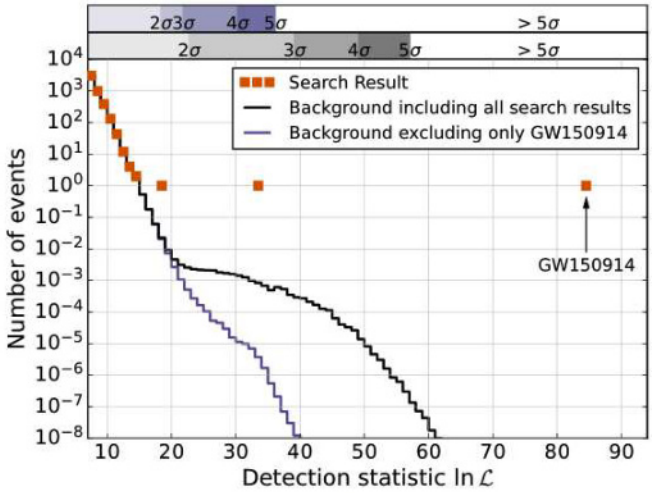

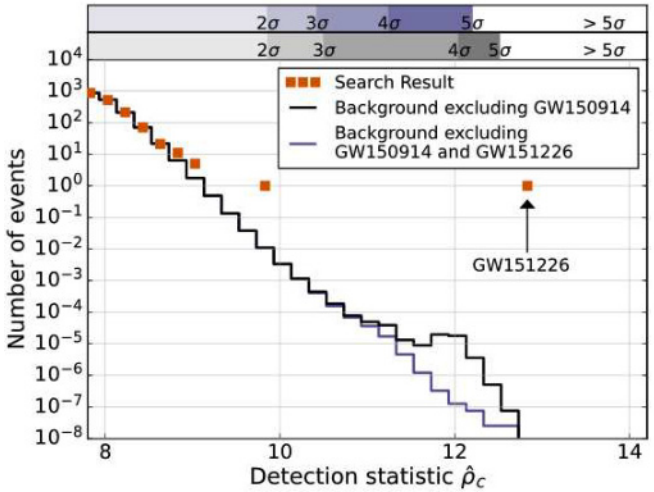

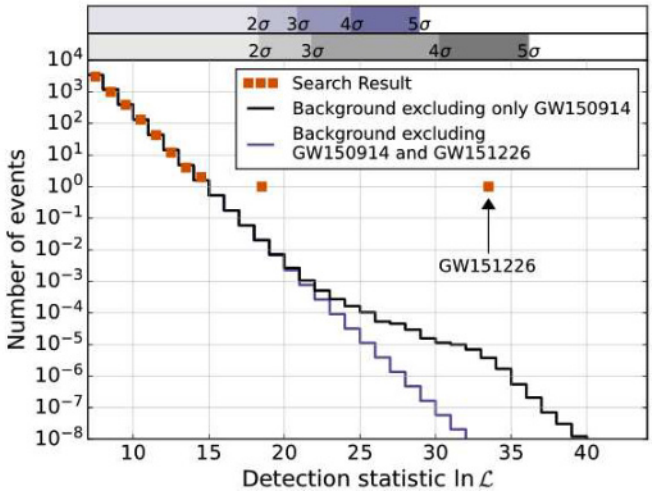

GW150914:

$M_1 = 36^{+5}_{-4} M_\odot$

$M_2 = 29^{+4}_{-4} M_\odot$

$M_f = 62^{+4}_{-4} M_\odot$

$E_{\rm GW} = 3.0^{+0.5}_{-0.5} M_\odot c^2$

$L_{\rm peak} = 3.6^{+0.5}_{-0.4} \times 10^{56}$ erg/s

$D = 410^{+160}_{-180}$ Mpc

$z = 0.09^{+0.03}_{-0.04}$

GW151226:

$M_1 = 14.2^{+8.3}_{-3.7} M_\odot$

$M_2 = 7.5^{+2.3}_{-2.3} M_\odot$

$M_f = 20.8^{+6.1}_{-1.7} M_\odot$

$E_{\rm GW} = 1.0^{+0.1}_{-0.2} M_\odot c^2$

$L_{\rm peak} = 3.3^{+0.8}_{-1.6} \times 10^{56}$ erg/s

$D = 440^{+180}_{-190}$ Mpc

$z = 0.09^{+0.03}_{-0.04}$

Advanced LIGO search results for two analyses of the events GW150914 (14 September, 2015) and GW151226 (26 December, 2015). The third most significant event in the search, LVT151012 (12 October, 2015) is identified with a significance of 1.7σ and 2.0σ in the two analyses respectively.

[From B. P. Abbott *et al.* (LIGO & Virgo Collaborations), "Binary black hole mergers in the first advanced LIGO observing run," Phys. Rev. X **6** (2016) 041015, arXiv:1606.04856v2 [gr-qc].]

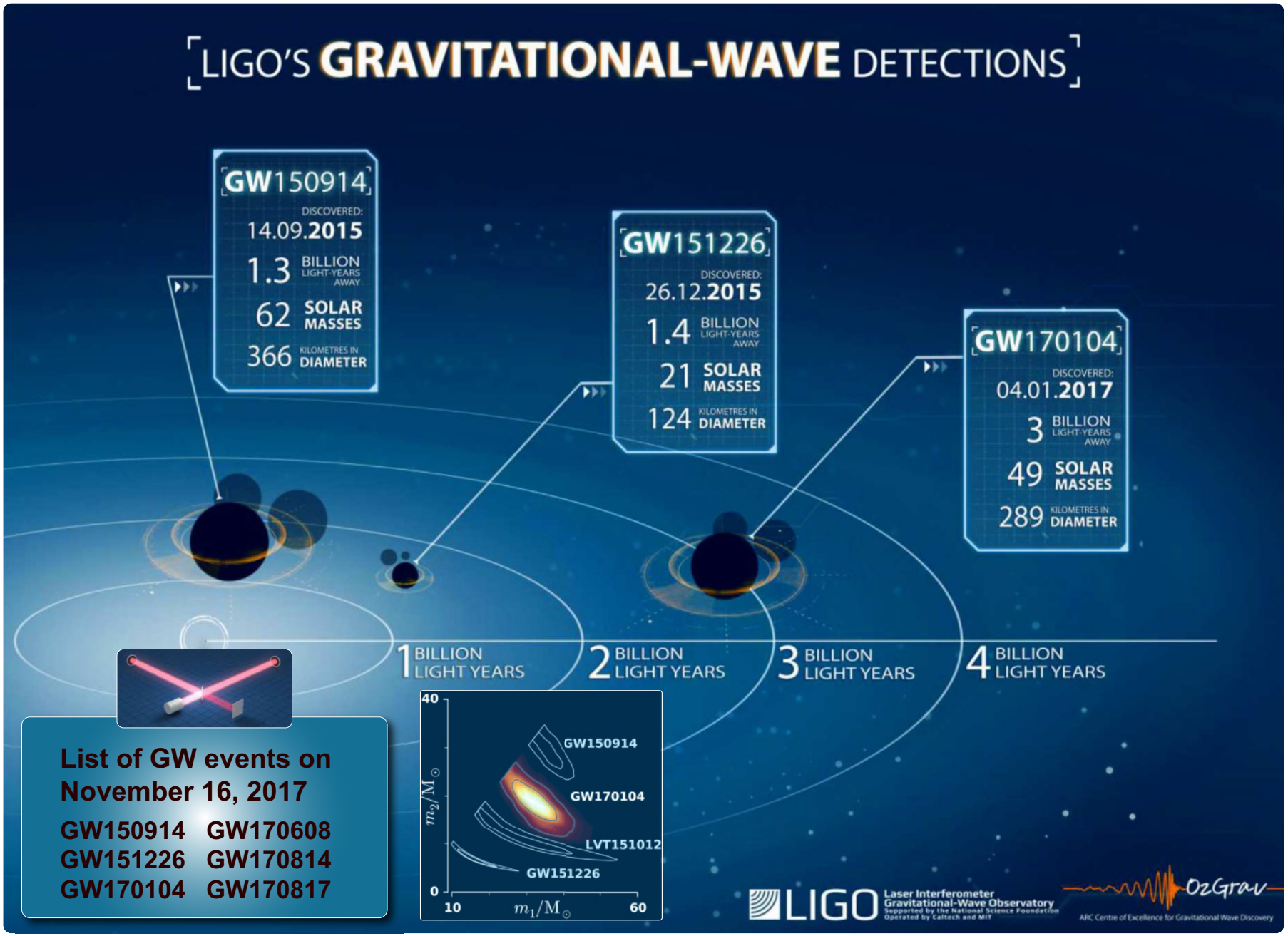
LIGO'S GRAVITATIONAL-WAVE DETECTIONS
GW150914
DISCOVERED: 14.09.2015
1.3 BILLION LIGHT-YEARS AWAY
62 SOLAR MASSES
366 KILOMETRES IN DIAMETER
GW151226
DISCOVERED: 26.12.2015
1.4 BILLION LIGHT-YEARS AWAY
21 SOLAR MASSES
124 KILOMETRES IN DIAMETER
GW170104
DISCOVERED: 04.01.2017
3 BILLION LIGHT-YEARS AWAY
49 SOLAR MASSES
289 KILOMETRES IN DIAMETER
1 BILLION LIGHT YEARS
2 BILLION LIGHT YEARS
3 BILLION LIGHT YEARS
4 BILLION LIGHT YEARS
List of GW events on November 16, 2017
GW150914 GW170608
GW151226 GW170814
GW170104 GW170817
40
0
10
60
$m_2/M_\odot$
$m_1/M_\odot$
GW150914
GW170104
LVT151012
GW151226
LIGO Laser Interferometer Gravitational-Wave Observatory
Supported by the National Science Foundation
Operated by Caltech and MIT
OzGrav
ARC Centre of Excellence for Gravitational Wave Discovery

1.5.2 The fourth GW detection: GW170814.

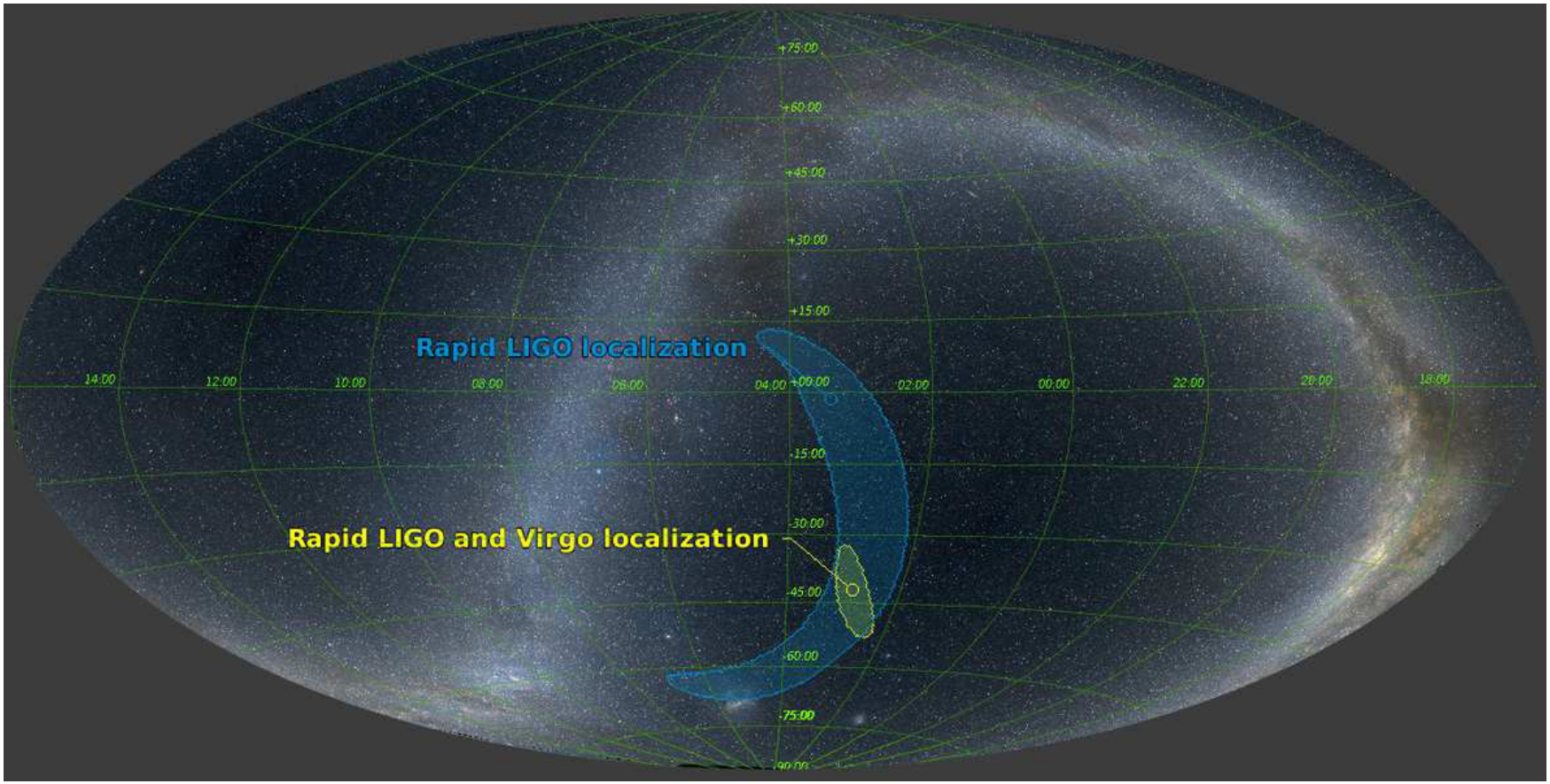

$$M_1 = 30.5^{+5.7}_{-3.0} M_\odot \qquad M_2 = 25.3^{+2.8}_{-4.2} M_\odot \qquad M_f = 55.9^{+3.4}_{-2.7} M_\odot$$
$$E_{\rm GW} = 2.7^{+0.4}_{-0.3} M_\odot c^2 \qquad L_{\rm peak} = 3.7^{+0.5}_{-0.5} \times 10^{56}\ {\rm erg/s} \qquad D = 540^{+130}_{-210}\ {\rm Mpc} \qquad z = 0.11^{+0.03}_{-0.04}$$

The GW170814 is the first event observed by the global 3-detector network, including not only the two twin Advanced LIGO detectors but the Advanced Virgo detector as well.

[From B. P. Abbott *et al.* (LIGO Scientific & Virgo Collaborations), "GW170814: A three-detector observation of gravitational waves from a binary black hole coalescence," Phys. Rev. Lett. **119** (2017) 141101, arXiv:1709.09660 [gr-qc].]

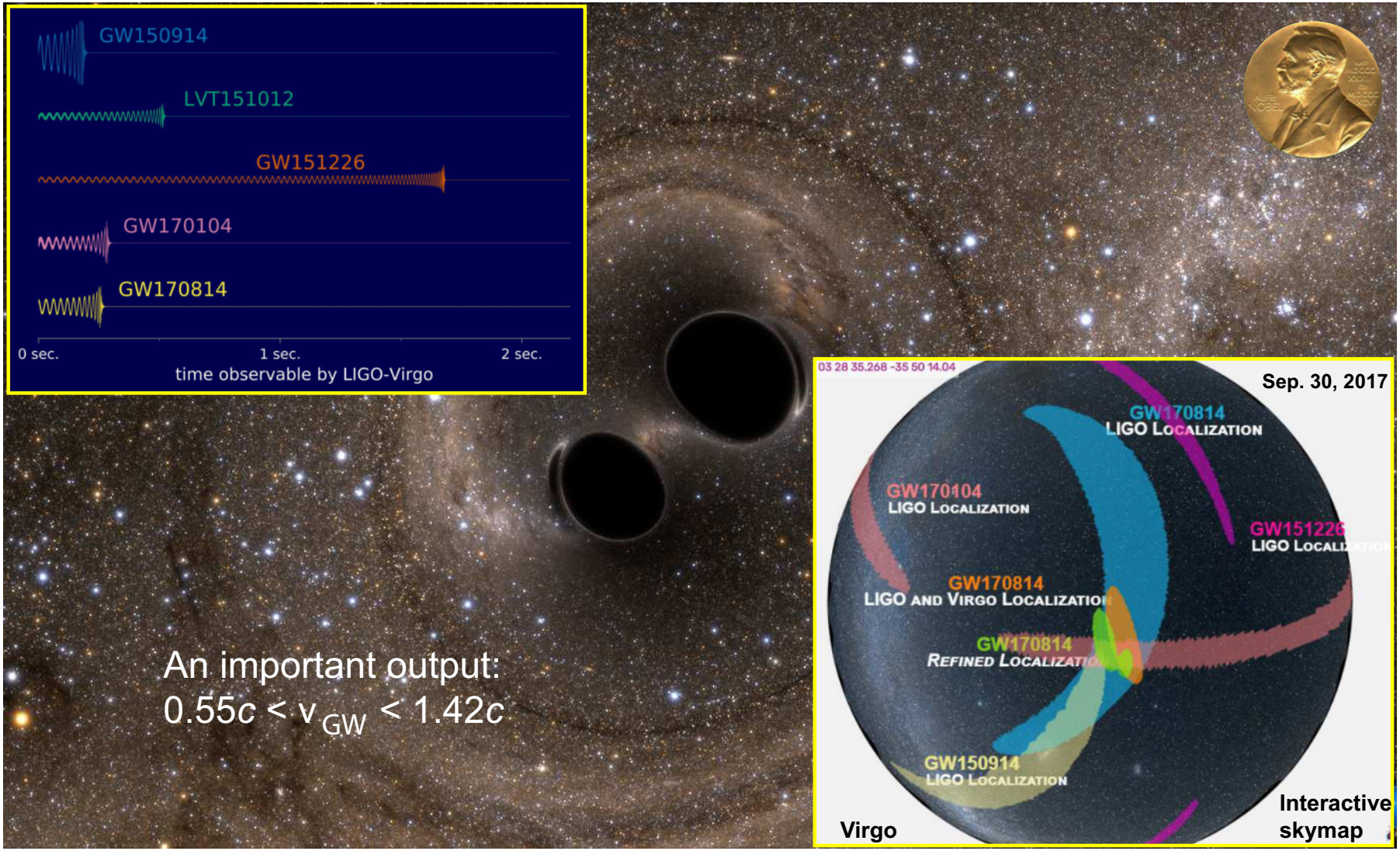

A nice popular explanation of the discovery of gravitational waves is given by Brian Greene, see URL: ⟨ https://www.youtube.com/watch?v=s06_jRK939I ⟩. For more special details, see LIGO's and Virgo's webpages ⟨ http://www.ligo.org/ ⟩ and ⟨ http://www.virgo-gw.eu/ ⟩.

1.5.3 Discovery of GW170817/GRB 170817A/SSS17a/AT 2017gfo

The next two slides show the time-line of the discovery of GW170817, and the follow-up observations are shown by messenger and wavelength relative to the time t_c of the gravitational-wave event.[a] Two types of information are shown for each band/messenger. First, the shaded dashes represent the times when information was reported in a GCN Circular. The names of the relevant instruments, facilities, or observing teams are collected at the beginning of the row. Second, representative observations in each band are shown as solid circles with their areas approximately scaled by brightness; the solid lines indicate when the source was detectable by at least one telescope. Magnification insets give a picture of the first detections in the gravitational-wave, gamma-ray, optical, X-ray, and radio bands.

[a] From B. P. Abbott *et al.* (LIGO Scientific Collaboration and Virgo Collaboration, *Fermi*-GBM, *INTEGRAL*, IceCube Collaboration, AstroSat Cadmium Zinc Telluride Imager Team, IPN Collaboration, The Insight-Hxmt Collaboration, ANTARES Collaboration, The Swift Collaboration, AGILE Team, The 1M2H Team, The Dark Energy Camera GW-EM Collaboration and the DES Collaboration, The DLT40 Collaboration, GRAWITA: GRAvitational Wave Inaf TeAm, The *Fermi* Large Area Telescope Collaboration, ATCA: Australia Telescope Compact Array, ASKAP: Australian SKA Pathfinder, Las Cumbres Observatory Group, OzGrav, DWF (Deeper, Wider, Faster Program), AST3, and CAASTRO Collaborations, The VINROUGE Collaboration, MASTER Collaboration, J-GEM, GROWTH, JAGWAR, Caltech-NRAO, TTU-NRAO, and NuSTAR Collaborations, Pan-STARRS, The MAXI Team, TZAC Consortium, KU Collaboration, Nordic Optical Telescope, ePESSTO, GROND, Texas Tech University, SALT Group, TOROS: Transient Robotic Observatory of the South Collaboration, The BOOTES Collaboration, MWA: Murchison Widefield Array, The CALET Collaboration, IKI-GW Follow-up Collaboration, H.E.S.S. Collaboration, LOFAR Collaboration, LWA: Long Wavelength Array, HAWC Collaboration, The Pierre Auger Collaboration, ALMA Collaboration, Euro VLBI Team, Pi of the Sky Collaboration, The Chandra Team at McGill University, DFN: Desert Fireball Network, ATLAS, High Time Resolution Universe Survey, RIMAS and RATIR, and SKA South Africa/MeerKAT) "Multi-messenger observations of a binary neutron star merger," ApJL **848** (2017) L12, arXiv:1710.05833 [astro-ph.HE]. Figure 2 from this paper is too large for a single slide and thus it is splitted into two parts shown below.

The insets are respectively illustrated by the combined spectrogram of the signals received by LIGO-Hanford and LIGO-Livingston, the *Fermi*-GBM and *INTEGRAL*/SPI-ACS lightcurves matched in time resolution and phase, $1'.5 \times 1'.5$ postage stamps extracted from the initial six observations of SSS17a/AT 2017gfo and four early spectra taken with the SALT (at $t_c + 1.4$ days), ESO-NTT (at $t_c + 1.4$ days), the SOAR 4 m telescope (at $t_c + 1.4$ days), and ESO-VLT-XShooter (at $t_c + 2.4$ days), and the first X-ray and radio detections of the same source by Chandra and JVLA. In order to show representative spectral energy distributions, each spectrum is normalized to its maximum and shifted arbitrarily along the linear y-axis (no absolute scale). The high background in the SALT spectrum below 4500 A prevents the identification of spectral features in this band.

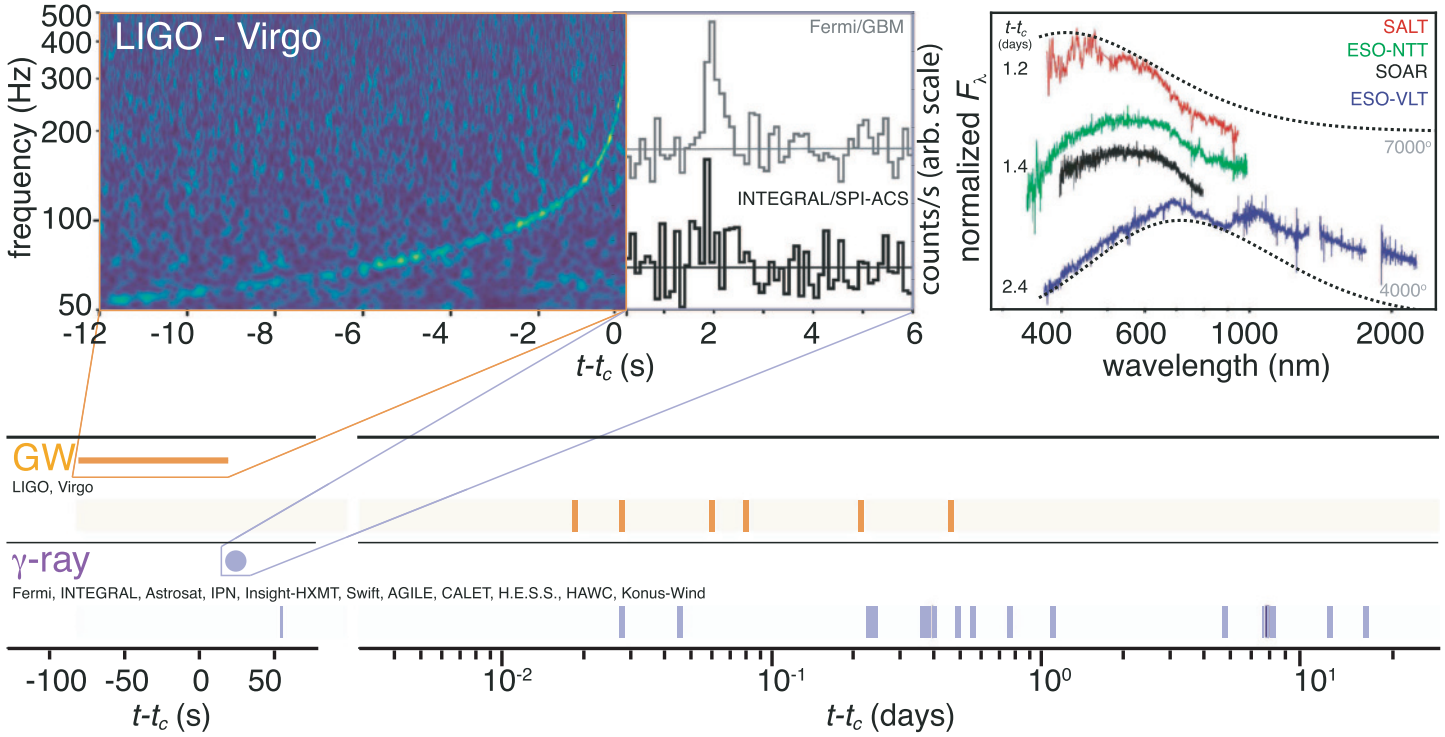

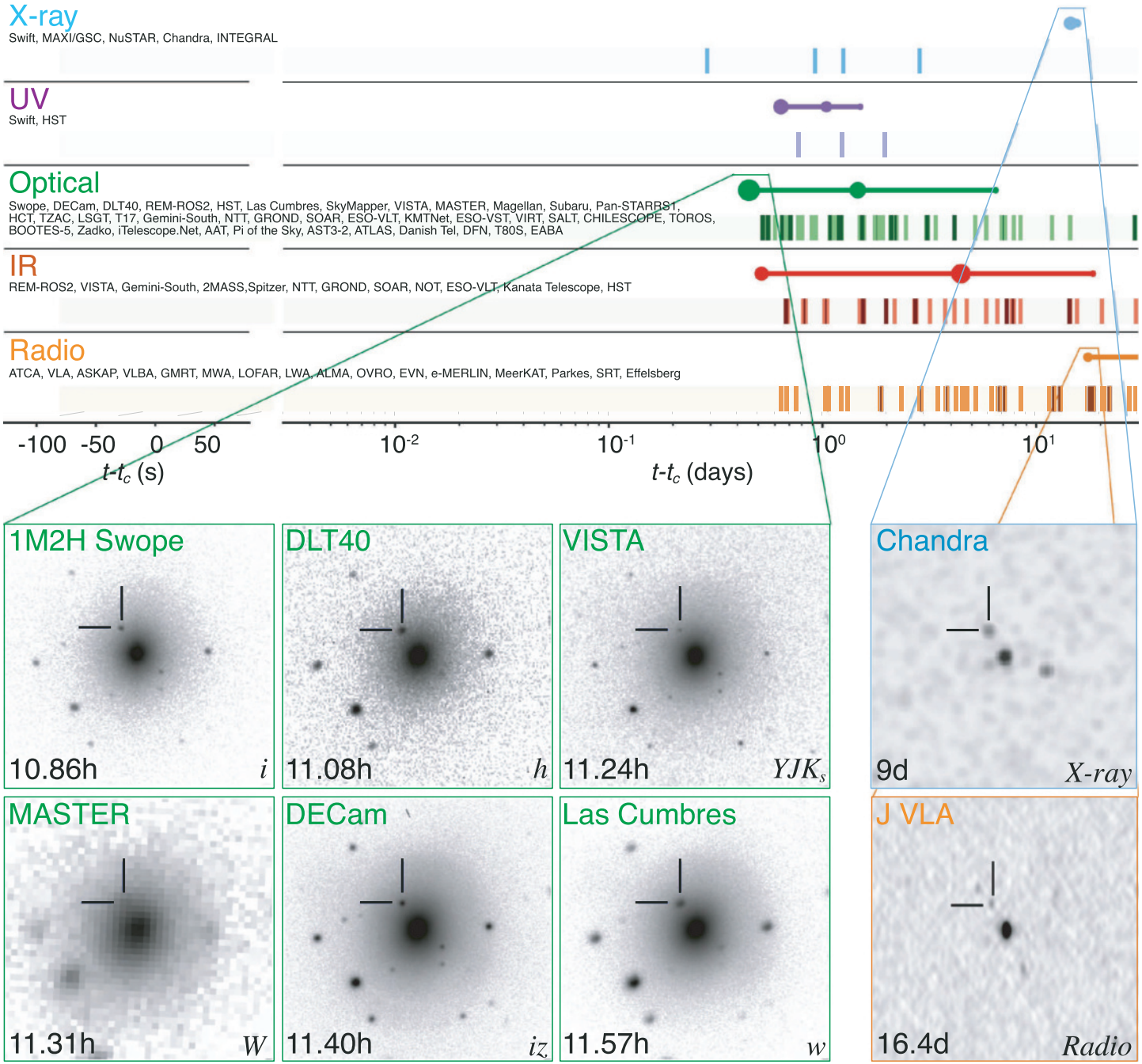
X-ray
Swift, MAXI/GSC, NuSTAR, Chandra, INTEGRAL
UV
Swift, HST
Optical
Swope, DECam, DLT40, REM-ROS2, HST, Las Cumbres, SkyMapper, VISTA, MASTER, Magellan, Subaru, Pan-STARRS1, HCT, TZAC, LSGT, T17, Gemini-South, NTT, GROND, SOAR, ESO-VLT, KMTNet, ESO-VST, VIRT, SALT, CHILESCOPE, TOROS, BOOTES-5, Zadko, iTelescope.Net, AAT, Pi of the Sky, AST3-2, ATLAS, Danish Tel, DFN, T80S, EABA
IR
REM-ROS2, VISTA, Gemini-South, 2MASS,Spitzer, NTT, GROND, SOAR, NOT, ESO-VLT, Kanata Telescope, HST
Radio
ATCA, VLA, ASKAP, VLBA, GMRT, MWA, LOFAR, LWA, ALMA, OVRO, EVN, e-MERLIN, MeerKAT, Parkes, SRT, Effelsberg
-100 -50 0 50
t-t_c (s)
10^-2 10^-1 10^0 10^1
t-t_c (days)
1M2H Swope
10.86h i
DLT40
11.08h h
VISTA
11.24h YJK_s
Chandra
9d X-ray
MASTER
11.31h W
DECam
11.40h iz
Las Cumbres
11.57h w
J VLA
16.4d Radio

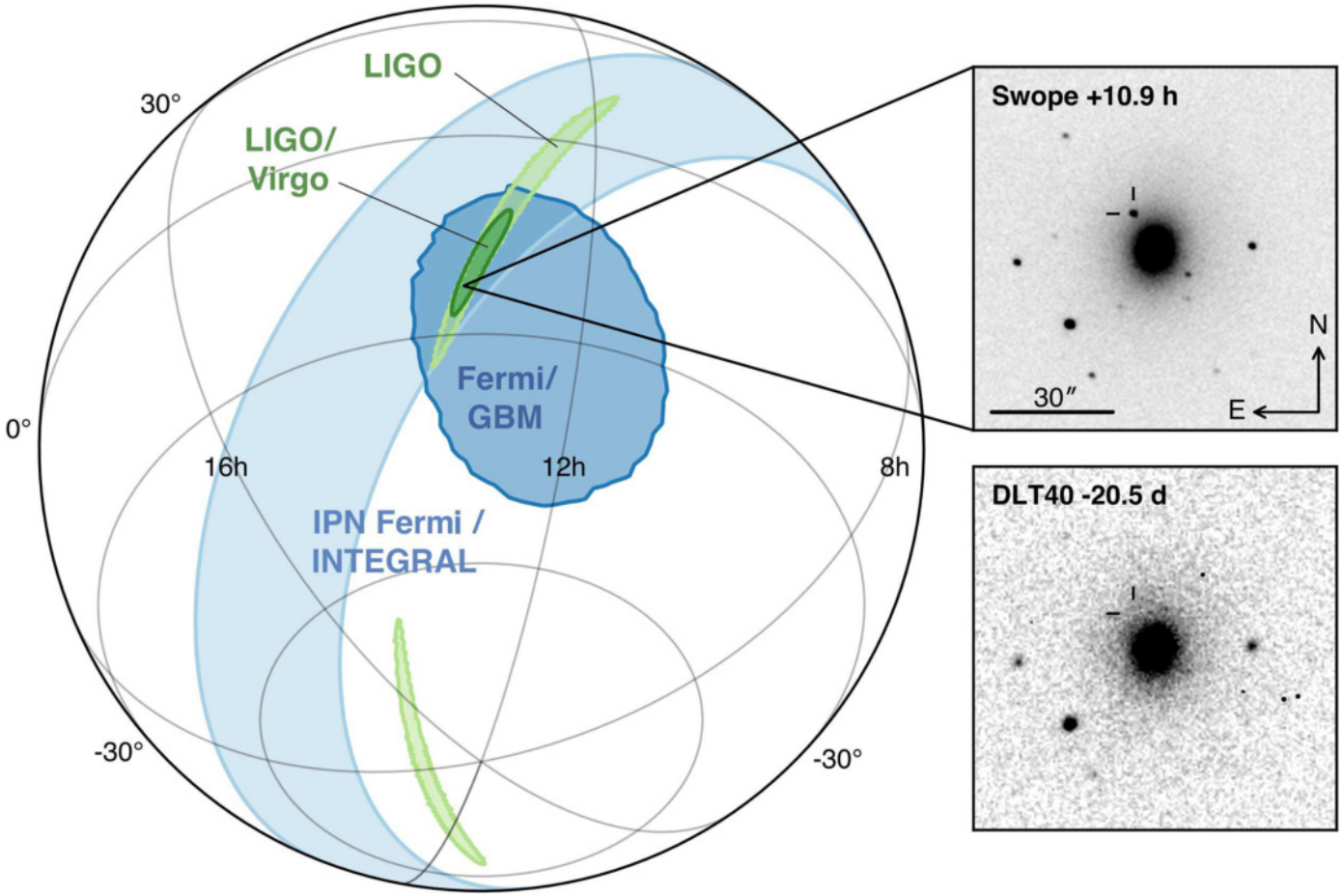

Localization of the gravitational-wave, gamma-ray, and optical signals. The *left panel* shows an orthographic projection of the 90% credible regions from LIGO (190 deg^2; light green), the initial LIGO-Virgo localization (31 deg^2; dark green), IPN triangulation from the time delay between *Fermi* and *INTEGRAL* (light blue), and *Fermi*-GBM (dark blue). The inset shows the location of the apparent host galaxy NGC 4993 in the Swope optical discovery image at 10.9 hr after the merger (top right) and the DLT40 pre-discovery image from 20.5 days prior to merger (bottom right). The reticle marks the position of the transient in both images. [Figure is taken from the same paper.]

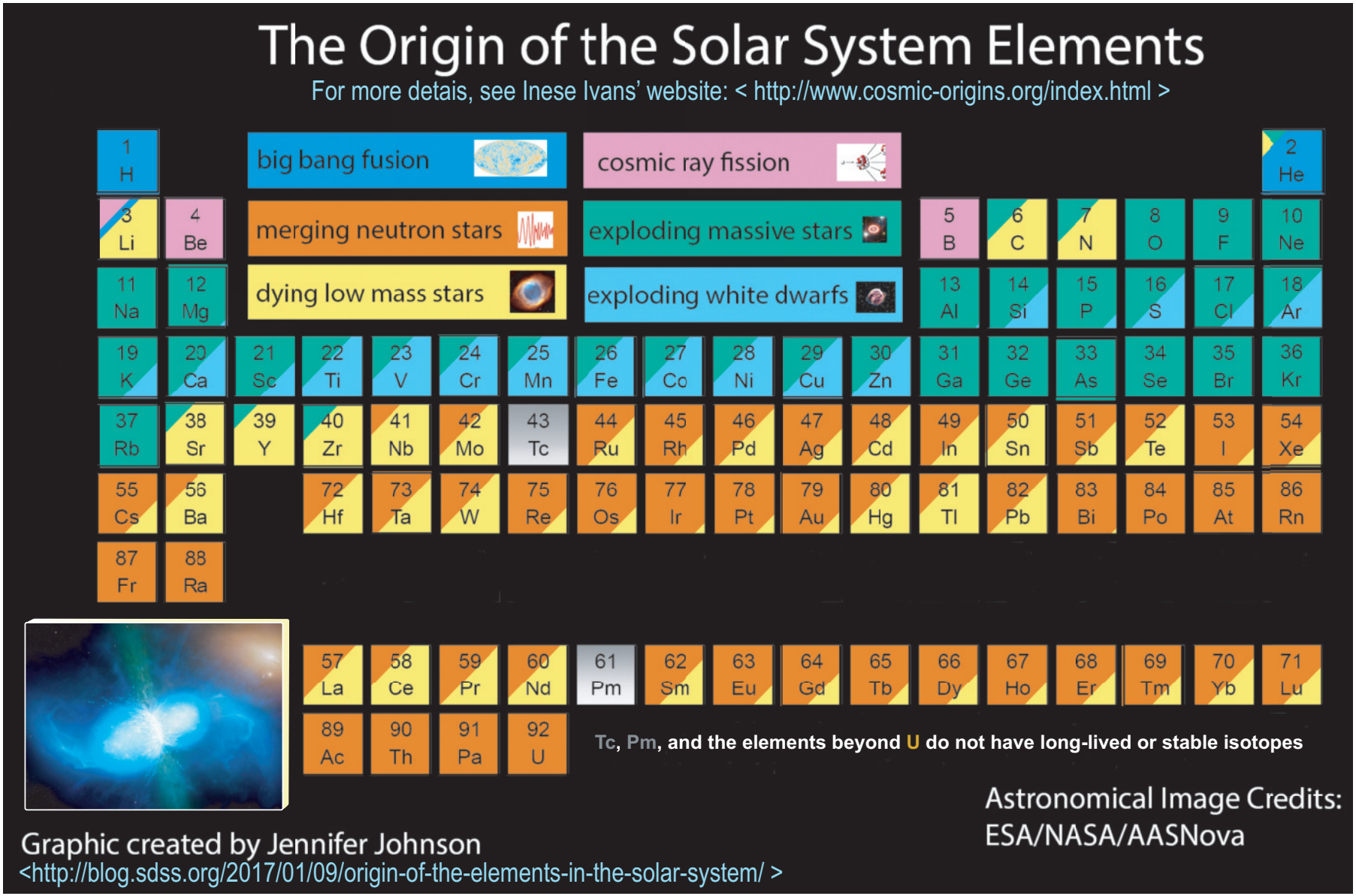

The electromagnetic radiation captured from GW170817 finally confirmed (among other things) that elements ranging from gold to uranium are synthesized in the aftermath of neutron star mergers.

Status on December 2018

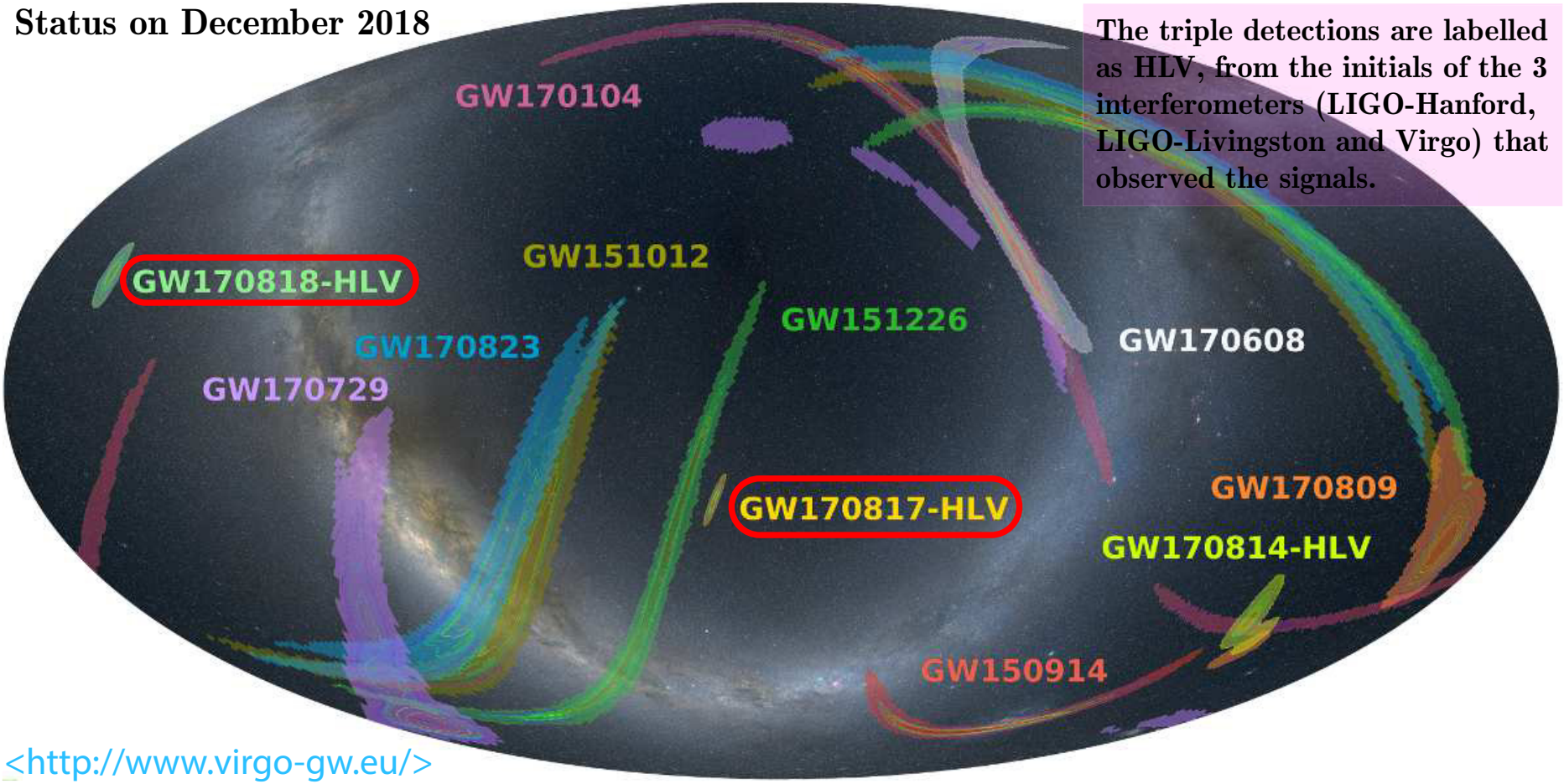

The triple detections are labelled as HLV, from the initials of the 3 interferometers (LIGO-Hanford, LIGO-Livingston and Virgo) that observed the signals.

<http://www.virgo-gw.eu/>

To the end of 2018, the LIGO and Virgo interferometers have confidently detected GWs from a total of ten stellar-mass binary black hole mergers and one merger of neutron stars, which are the dense, spherical remains of stellar explosions. One of the four new events, GW170818, detected by the global network formed by the LIGO and Virgo observatories, was precisely pinpointed in the sky. The sky position of the binary black holes, located $\sim 2.5 \times 10^6$ ly from Earth, was identified with a precision of 39 square degrees. That makes it the next best localized GW source after the GW170817.

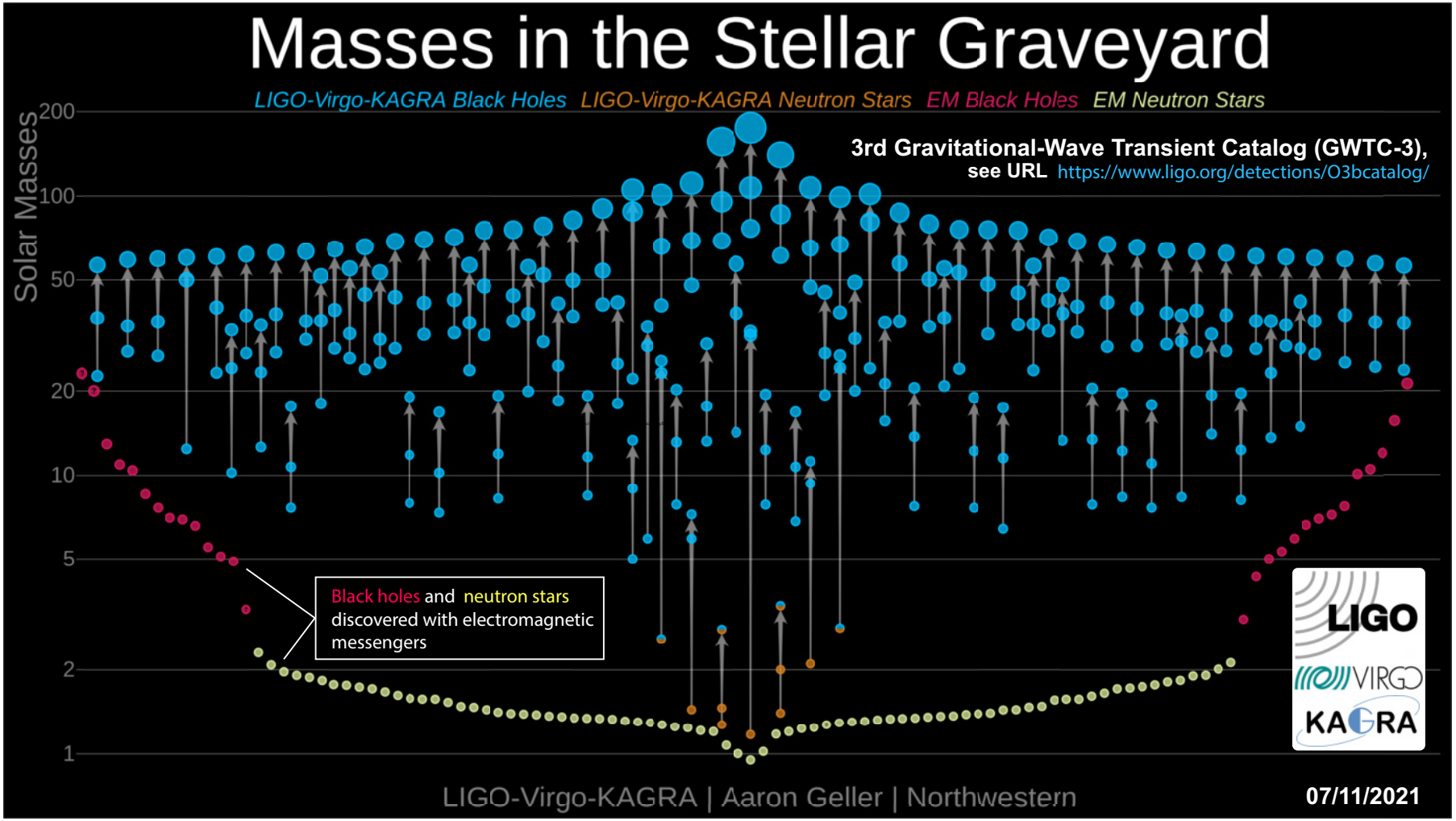

Masses of ninety compact objects. Each circle represents a different object and the vertical scale indicates the mass as a multiple of the solar mass. Blue (orange) circles represent black holes (neutron stars). Half-blue/half-orange mixed circles are objects whose classification is uncertain. Each merger involves three objects: two merging ones and the residue they formed. See also an interactive version of this figure: ⟨https://ligo.northwestern.edu/media/mass-plot/index.html⟩.

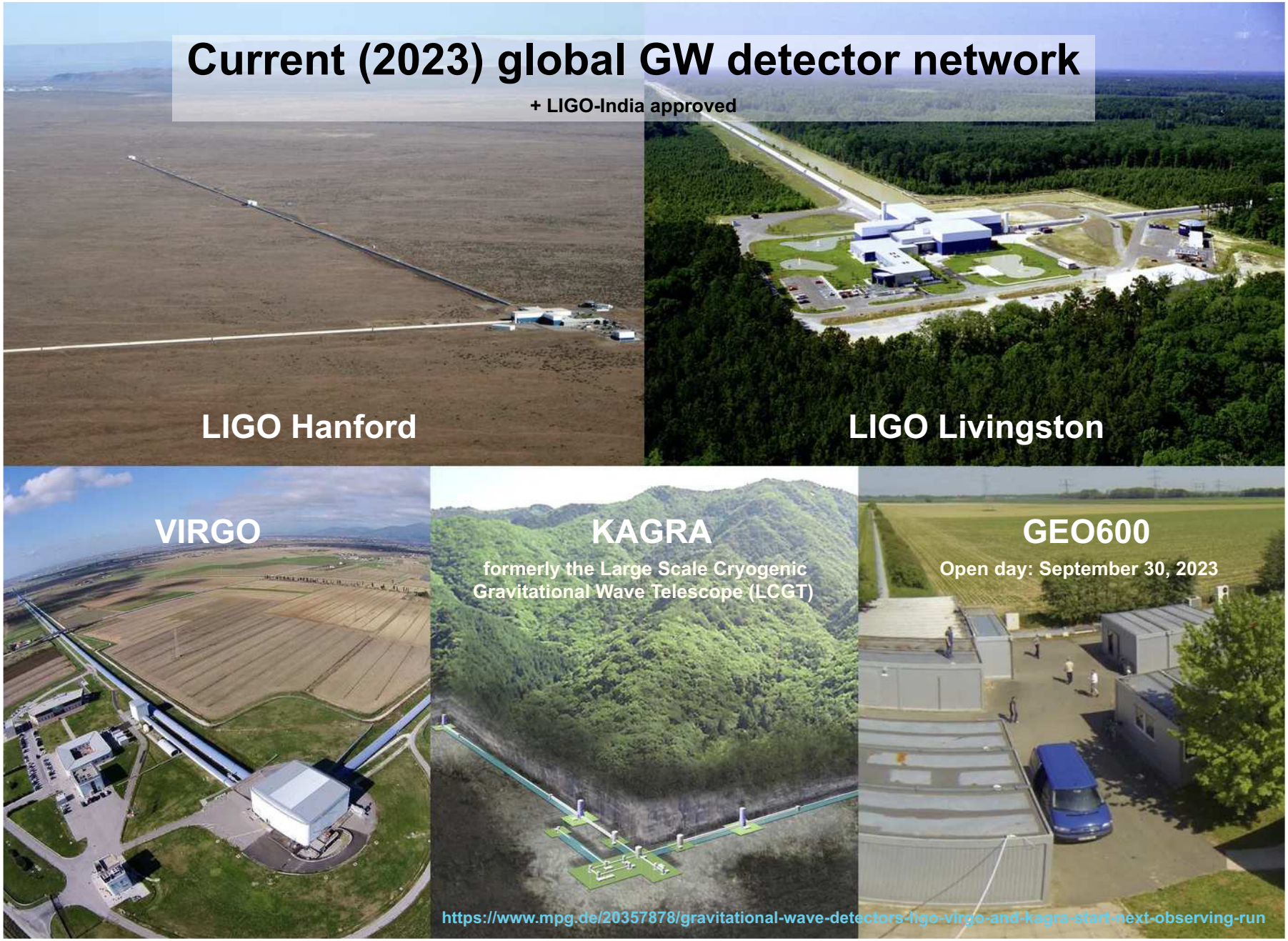
Current (2023) global GW detector network
+ LIGO-India approved
LIGO Hanford
LIGO Livingston
VIRGO
KAGRA
formerly the Large Scale Cryogenic Gravitational Wave Telescope (LCGT)
GEO600
Open day: September 30, 2023
https://www.mpg.de/20357878/gravitational-wave-detectors-ligo-virgo-and-kagra-start-next-observing-run

1.5.4 Searches (so far unsuccessful) for accompanying neutrino signals.

The search for matched neutrino candidates in the ANTARES and IceCube neutrino telescopes was conducted jointly with the Virgo Collaboration.[a]

Within ± 500 s of the gravitational wave event, the number of neutrino candidates detected by IceCube and Antares were three and zero, respectively. This is consistent with the expected atmospheric background, and none of the neutrino candidates were directionally coincident with GW150914.

The formal upper limit on the total energy radiated in neutrinos ($E_{\nu_\mu,\overline{\nu}_\mu} \gg 1$ GeV) is

$$E^{\mathsf{ul}}_{\nu,\mathsf{tot}} = \left(10^{52} - 10^{54}\right) \left(\frac{D_{\mathsf{gw}}}{410\,\mathsf{Mpc}}\right)^2 \text{ egr.}$$

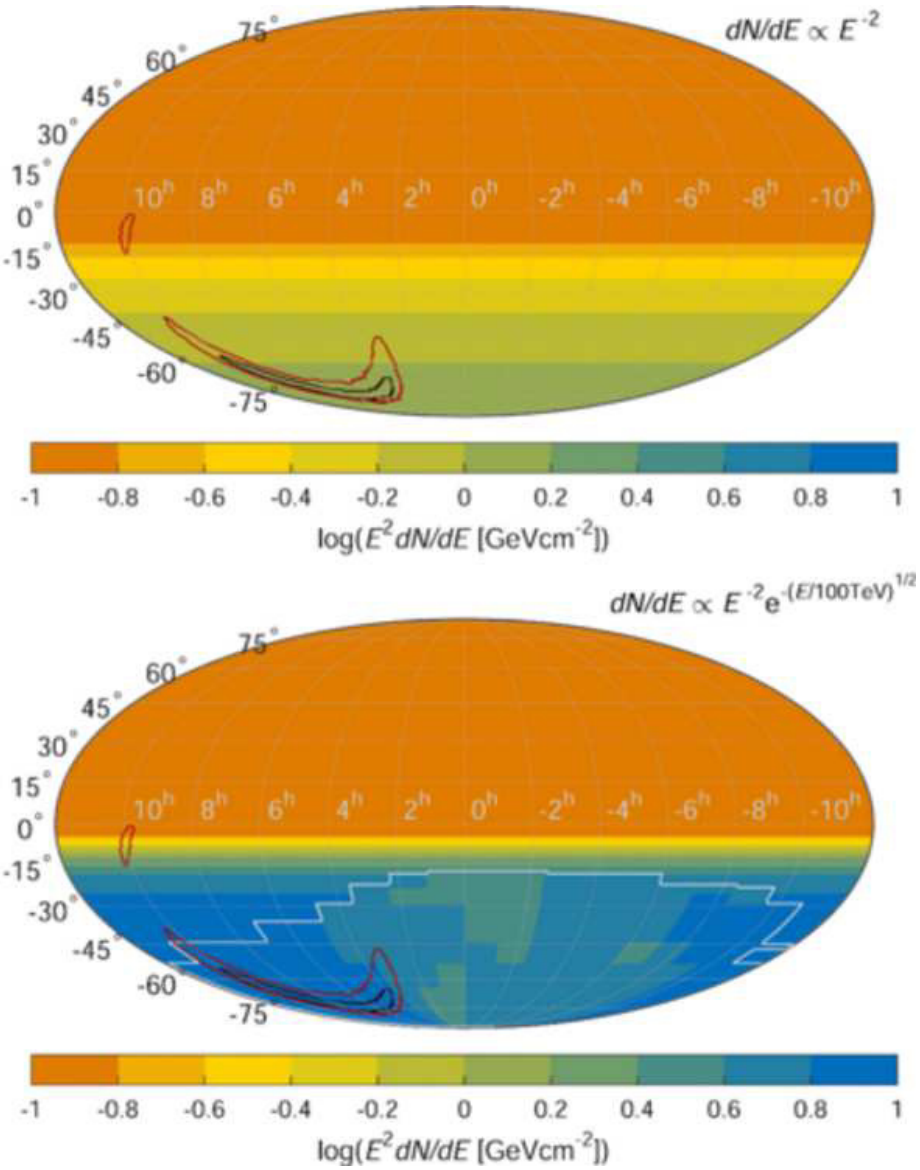

[a] S. Adrian-Martinez *et al.* (ANTARES, IceCube, and Virgo Collaborations), "High-energy Neutrino follow-up search of Gravitational Wave Event GW150914 with ANTARES and IceCube," Phys. Rev. D **93** (2016) 122010, arXiv:1602.05411 [astro-ph.HE].

KamLAND also finds no inverse beta-decay neutrino events within ± 500 s coincident with the gravitational-wave events GW150914 and GW151226, and the candidate event LVT151012.[a] This non-detection is used to constrain the electron anti-neutrino fluence and the total integrated luminosity of the astrophysical sources $E_{\overline{\nu}_e} = (1.8 - 111)$ MeV]:

$$F_{\overline{\nu}_e}^{\text{GW150914 \& LVT151012}} \leq 3.1 \times 10^{9}\ \text{cm}^{-2},$$
$$F_{\overline{\nu}_e}^{\text{GW151226}} \leq 3.6 \times 10^{10}\ \text{cm}^{-2}.$$

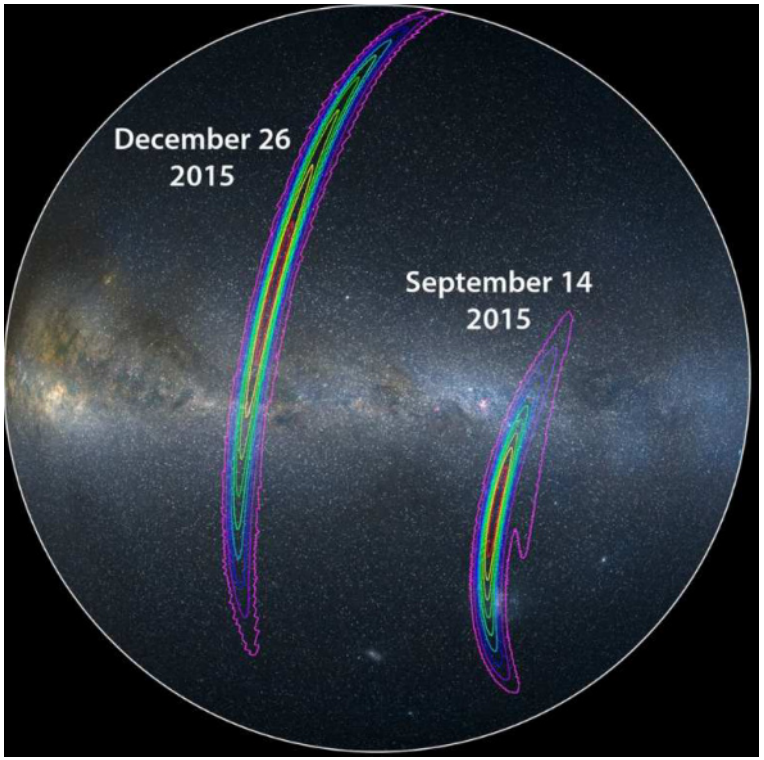

The electron antineutrino total energy upper limits without oscillation are thus given by

$$E_{\overline{\nu}_e}^{\text{GW150914}} \leq 1.25 \times 10^{60} \left(\frac{D_{\text{gw}}}{410\ \text{Mpc}} \right)^2\ \text{egr},$$
$$E_{\overline{\nu}_e}^{\text{GW151226}} \leq 1.71 \times 10^{60} \left(\frac{D_{\text{gw}}}{440\ \text{Mpc}} \right)^2\ \text{egr},$$
$$E_{\overline{\nu}_e}^{\text{LVT151012}} \leq 9.06 \times 10^{61} \left(\frac{D_{\text{gw}}}{1100\ \text{Mpc}} \right)^2\ \text{egr}.$$

The main papers on the search for electromagnetic counterparts to LIGO's gravitational-wave sources are collected at URL: ⟨http://iopscience.iop.org/2041-8205/focus/Focus_on_LIGO⟩.

[a] A. Gando *et al.* (The KamLAND Collaboration), "Search for electron antineutrinos associated with gravitational wave events GW150914 and GW151226 using KamLAND," ApJL **829** (2016) L34, arXiv:1606.07155v2 [astro-ph.HE].

No significant neutrino counterpart of the GW170817 event was found in any of the neutrino observatories, a result which is compatible with the expectations of a GRB observed off-axis.

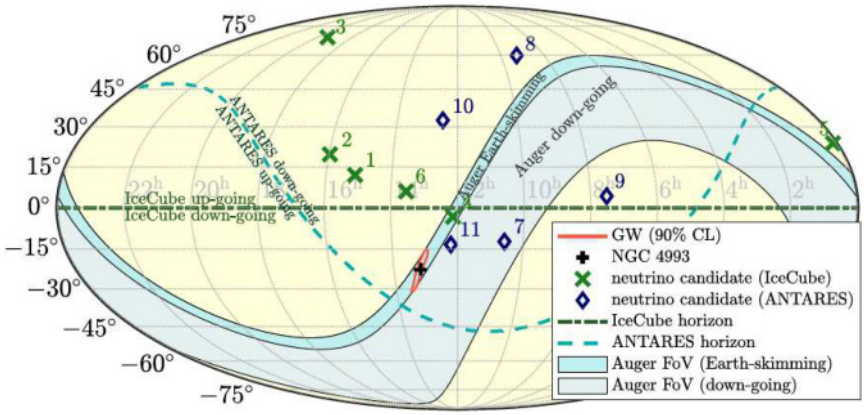

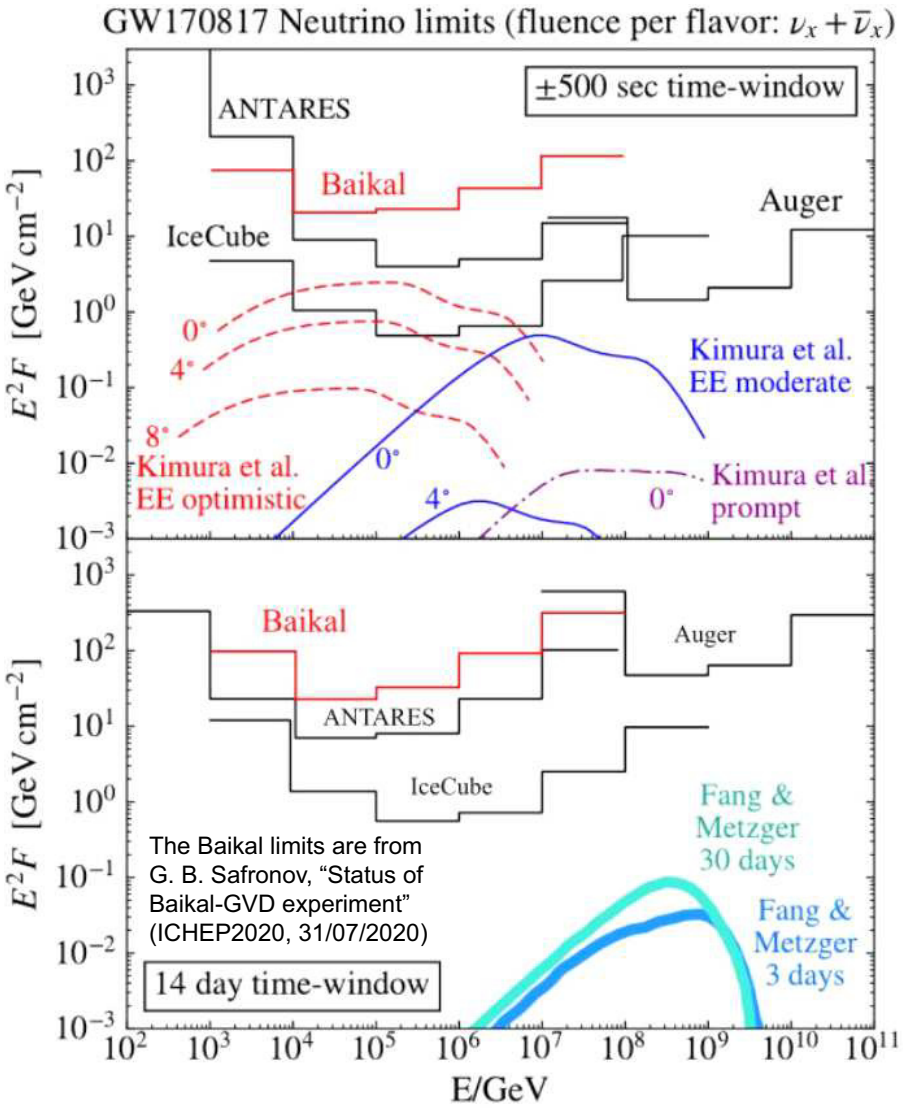

Left panel: Sensitive sky areas of the 3 most sensitive neutrino observatories, ANTARES, IceCube, and Pierre Auger at the time of the GW170817 event in Equatorial Coordinates (see p. 307).

Right panel: Upper limits at 90% C.L. of the neutrino spectral fluence from GW170817 event for a 500 s time window (top) and in the following 14 days after the trigger (bottom). No neutrino candidates were found in this time window either.

[Adapted from D. Gora (for the Pierre Auger Collaboration), "The Pierre Auger Observatory: review of latest results and perspectives," talk at ICNFP 2018, Universe **4** (2018) 128, arXiv:1811.00343v2 [astro-ph.IM].]

1.5.5 Discovery of very low-frequency stochastic gravitational waves.

Detection of low-frequency gravitational waves (GW) is possible by measuring the number of pulses per unit time (pulse rate) from many millisecond radio pulsars distributed throughout the Galaxy.[a]

Current technology is not sensitive enough to detect the minuscule changes. A workaround is to map the millisecond pulsars in the sky and calculate their pulsation times over a long enough time, to find out the average time it takes them to reach Earth. Deviations in this time will indicate interference from GWs or ... mimicking backgrounds...
A positive map will show a pattern of changes in many pulses, consistent with the expected stretch-squeeze template.

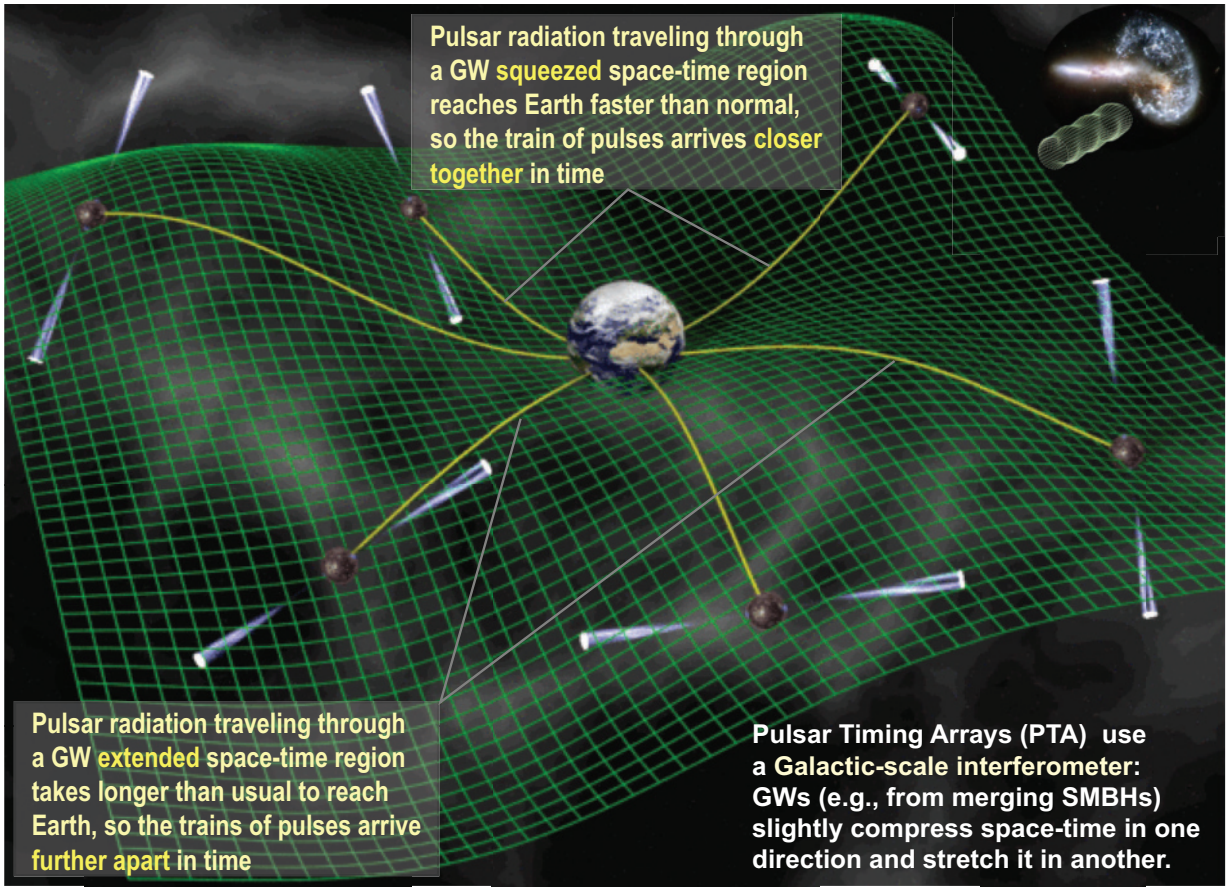

IPTA reports from 2023 seem to indicate that the Universe is (over)filled with stochastic GWs!

[a] M. V. Sazhin, "Opportunities for detecting ultralong gravitational waves," Sov. Astron. **22** (1978) 36–38.

NANOGrav, or the North American Nanohertz Observatory for Gravitational Waves, is a collaboration of astronomers and physicists from ~ 50 institutions across the U.S. and Canada.

NANOGrav cooperates with similar experiments in Australia (the Parkes Pulsar Timing Array), Europe (the European Pulsar Timing Array), and India (the Indian Pulsar Timing Array). Together, they make up the International Pulsar Timing Array, or IPTA.

The goal of the project is to directly detect GWs using an array of high-precision millisecond pulsars (Pulsar Timing Array), and then to characterize the sources of these GWs.

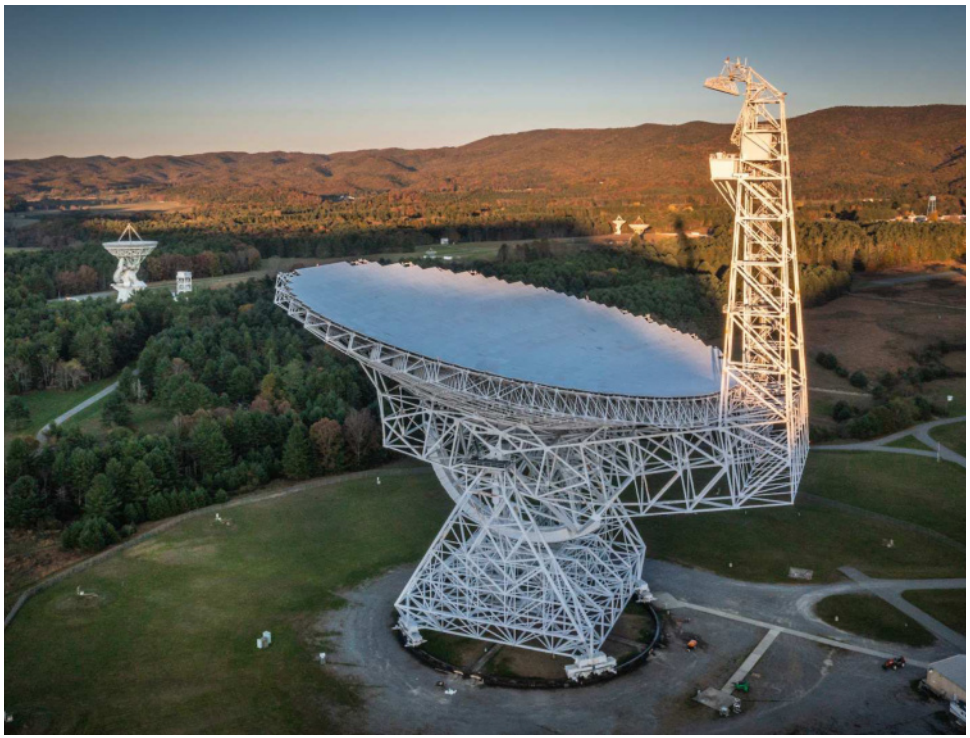

NANOGrav is sensitive to GWs with nHz frequencies, making it complementary to interferometers like LIGO, VIRGO, KAGRA that are sensitive to much higher frequencies, as well as to possible future space-based experiments like LISA.

◁ The 100-meter Green Bank Telescope (GBT), located in the National Radio Quiet Zone in Green Bank, West Virginia, U.S., is the world's largest fully-operated radio telescope and NANOGrav's primary instrument (after recently-collapsed Arecibo Observatory). Sixteen wheels carry 17 million pounds (7711 tons) on a steel track mounted on a concrete base. **Credit**: Jay Young.

The sources in the nHz GW spectrum are expected to be merging supermassive black holes (both individual sources and a stochastic background), cosmological phase transitions, relics from inflation (primordial black holes, cosmic strings), ultralight dark matter (e.g., axions), and so on.

The Very Large Array is a major radio astronomy facility located on the Plains of San Agustin about 50 miles (80 km) west of Socorro, New Mexico. It is remote from any habitation and the nearest conventional railways.

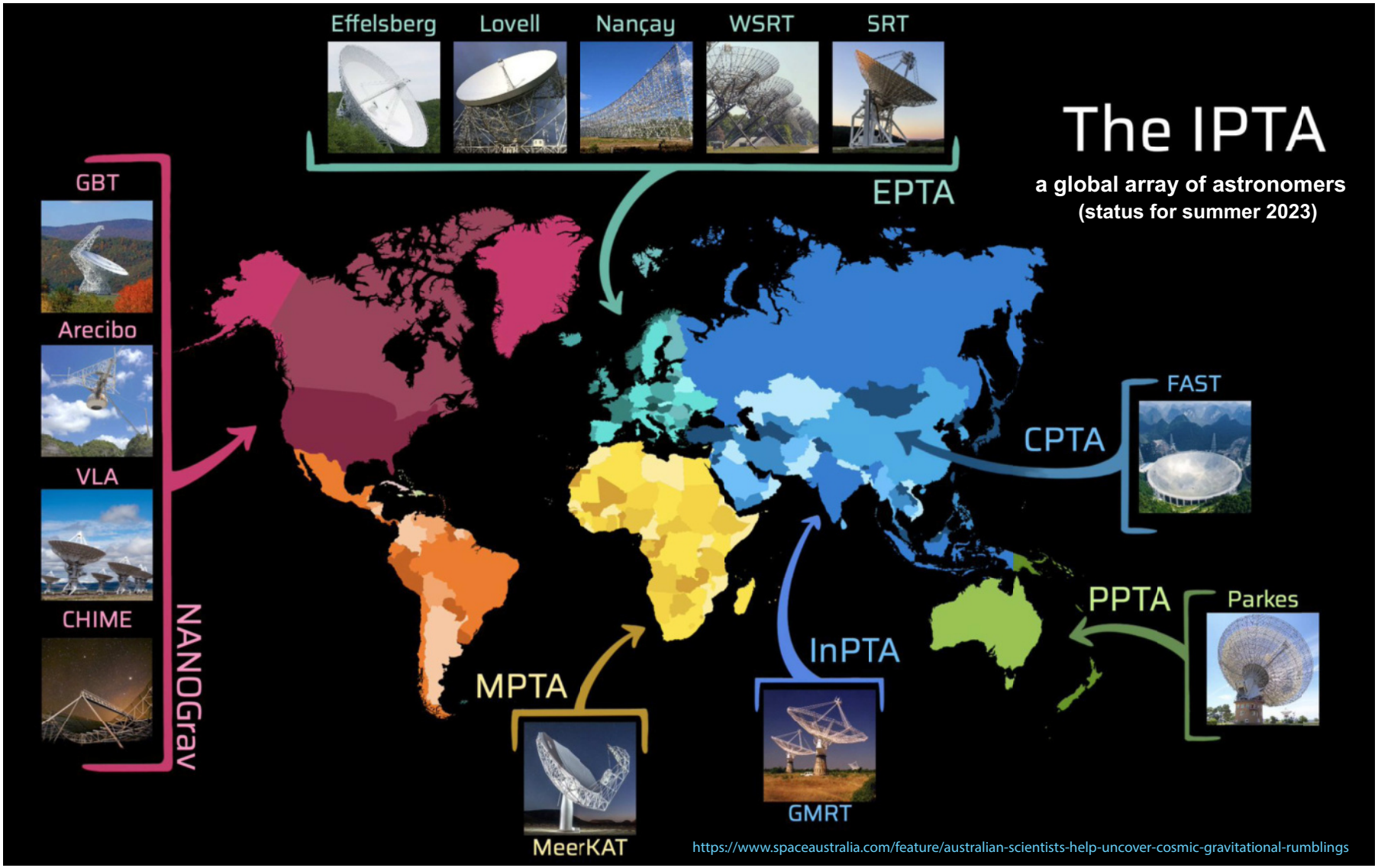

The IPTA telescopes from around the world with the members from North America, Australia, Europe, and India. New teams in Argentina, China, and South Africa have also begun timing millisecond pulsars.

Credit: Dr. Thankful Cromartie.

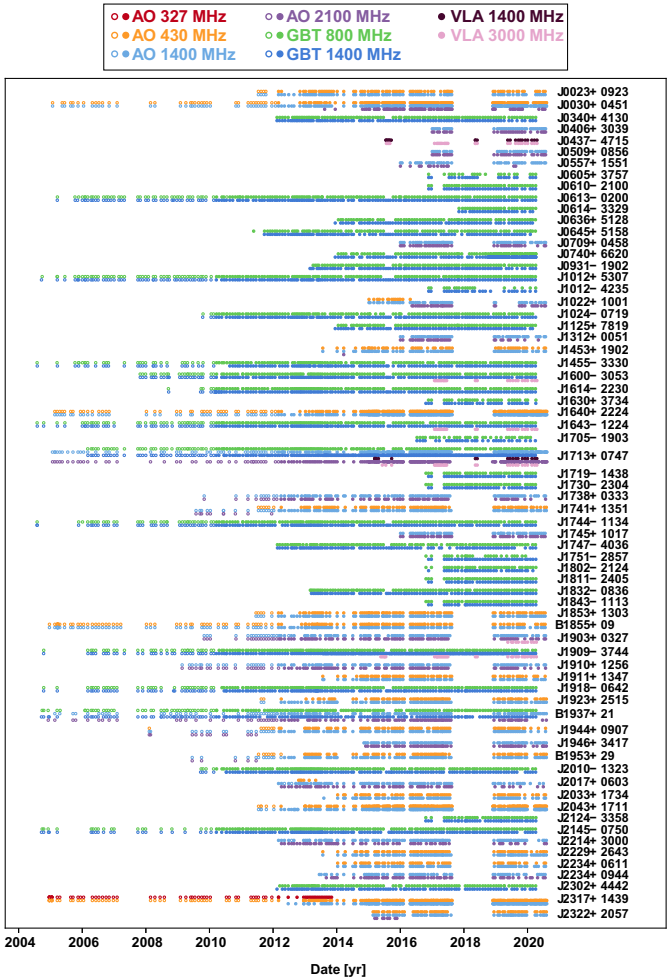

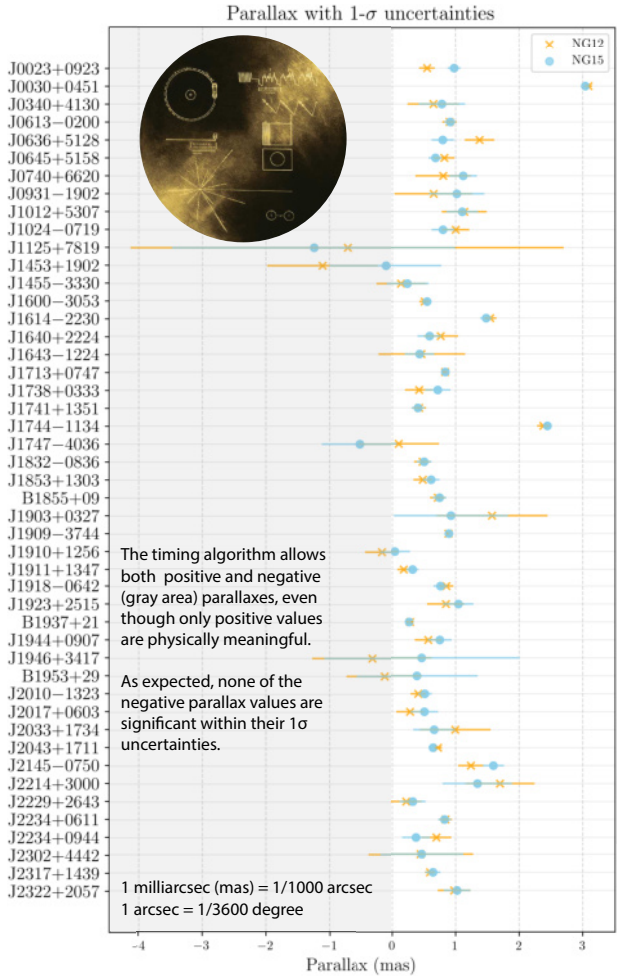

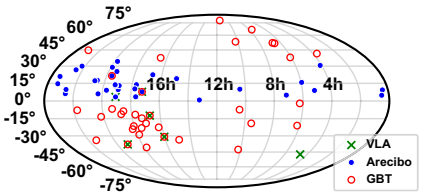

△ Sky locations of the pulsars used in the analysis (50 of 67 are binary).

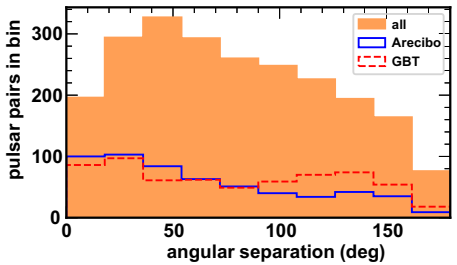

△ Distribution of angular separations probed by the pulsars in the full, Arecibo, and GBT datasets.

△ Epochs of all times of arrival (ToAs) in the NANOGrav 15-yr dataset. The observatory and observing frequency are indicated by color (*left panel*). Measurements and uncertainties of parallax from 12.5-yr and 15-yr data sets, showing the parallax values to be consistent across datasets (*middle panel*).

[From G. Agazie *et al.* (NANOGrav Coll.), "The NANOGrav 15 yr data set: Observations and timing of 68 millisecond pulsars," ApJL **951** (2023) L9, arXiv:2306.16217 [astro-ph.HE]; G. Agazie *et al.* (NANOGrav Coll.), "The NANOGrav 15 yr data set: Evidence for a gravitational-wave background," ApJL **951** (2023) L8, arXiv:2306.16213 [astro-ph.HE].]

1.6 Brief history of the Universe.

The three slides below outline the almost 14 billion year history of the Universe. They show the main events that occurred between the hypothetical structureless "quantum gravity era" to the rich variety of cosmic structure that we observe today. Early history is listed in the Table:

Epoch	**Time scale** (s)	**Temperature** (K)	**Energy** (eV)	**Physical characteristics**
Big Bang	0	**?**	**?**	Singularity / Vacuum fluctuation.
Planck	$0-10^{-43}$	$\gtrsim 10^{40}$	$\gtrsim 10^{36}$	Quantum gravity. Particle creation.
GUT	$10^{-43}-10^{-36}$	$10^{40}\longmapsto 10^{36}$	$10^{36}\longmapsto 10^{32}$	Gravity freezes out the GUT force.
Inflation	$10^{-32}\longmapsto 10^{-36}$	$10^{36}\longmapsto 10^{33}$	$10^{32}\longmapsto 10^{29}$	Expansion of space by a factor of $10^{\gtrsim 26}$. Strong force freezes out.
Electroweak (baryogenesis)	$10^{-12}\longmapsto 10^{-32}$	$10^{33}\longmapsto 10^{20}$	$10^{29}\longmapsto 10^{16}$	Weak force freezes out, GUT$\longmapsto$SM. Baryons & antibaryons annihilate.
Quark	$10^{-12}-10^{-6}$	$10^{20}\longmapsto 10^{16}$	$10^{16}\longmapsto 10^{12}$	Hot quark-gluon plasma, leptons, γs.
Hadron	$10^{-6}-1$	$10^{16}\longmapsto 10^{12}$	$10^{12}\longmapsto 10^{8}$	Quarks & gluons bind into hadrons.
Lepton	$1-3$	$10^{12}\longmapsto 10^{10}$	$10^{8}\longmapsto 10^{6}$	Universe contains γ, $e^{\pm}$, $\mu^{\pm}$, $\overset{(-)}{\nu}$.
Leptogenesis	~ 1	$\lesssim 10^{12}$	$\lesssim 10^{8}$	μ^+ & μ^- annihilate, $\overset{(-)}{\nu}$ decouple.
	~ 100	$\sim 10^{10}$	$\sim 10^{6}$	e^+ & e^- annihilate.

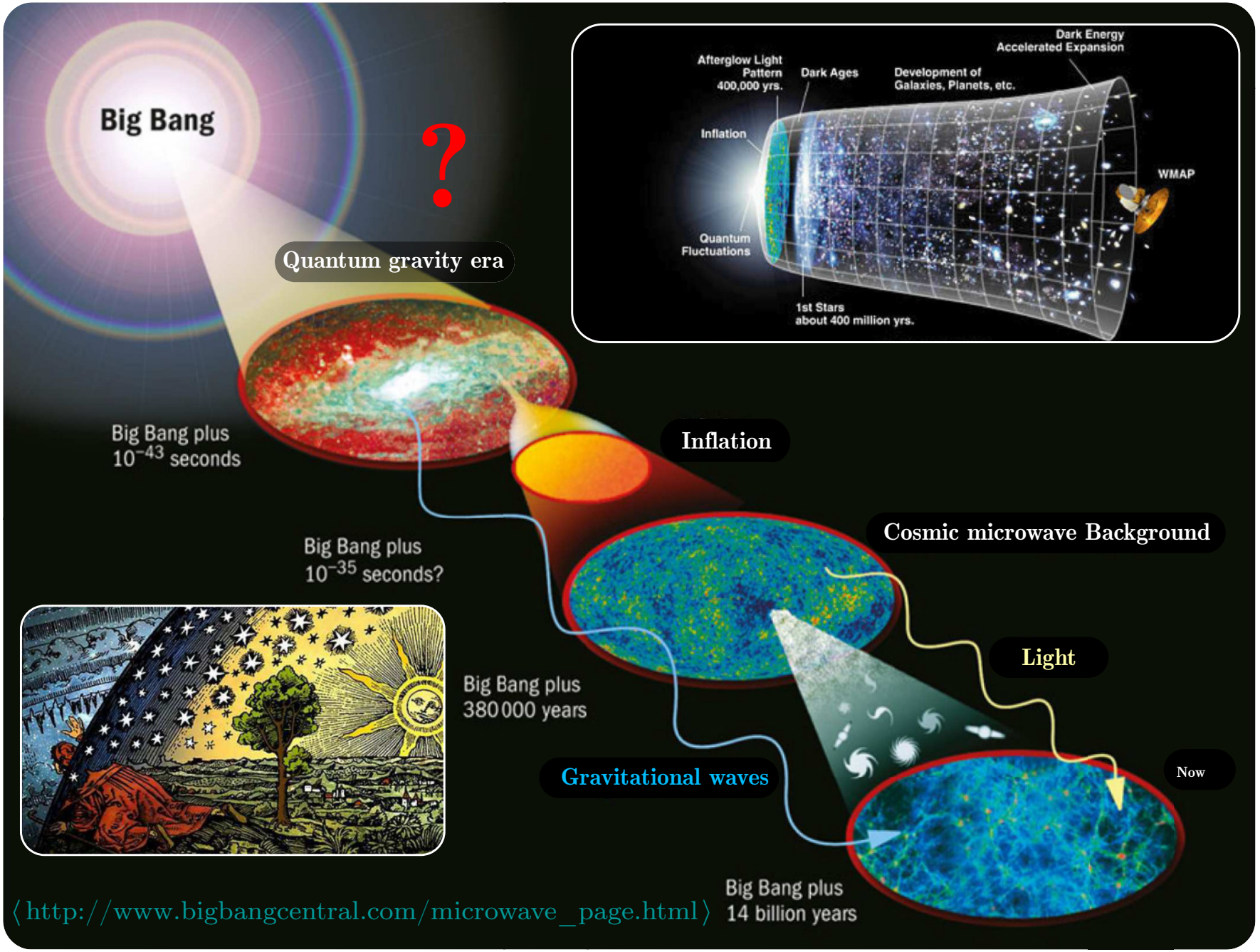
Big Bang
?
Quantum gravity era
Big Bang plus
10^-43 seconds
Big Bang plus
10^-35 seconds?
Inflation
Cosmic microwave Background
Light
Big Bang plus
380000 years
Gravitational waves
Now
Big Bang plus
14 billion years
⟨http://www.bigbangcentral.com/microwave_page.html⟩
Afterglow Light Pattern 400,000 yrs.
Dark Ages
Development of Galaxies, Planets, etc.
Dark Energy Accelerated Expansion
Inflation
WMAP
Quantum Fluctuations
1st Stars about 400 million yrs.

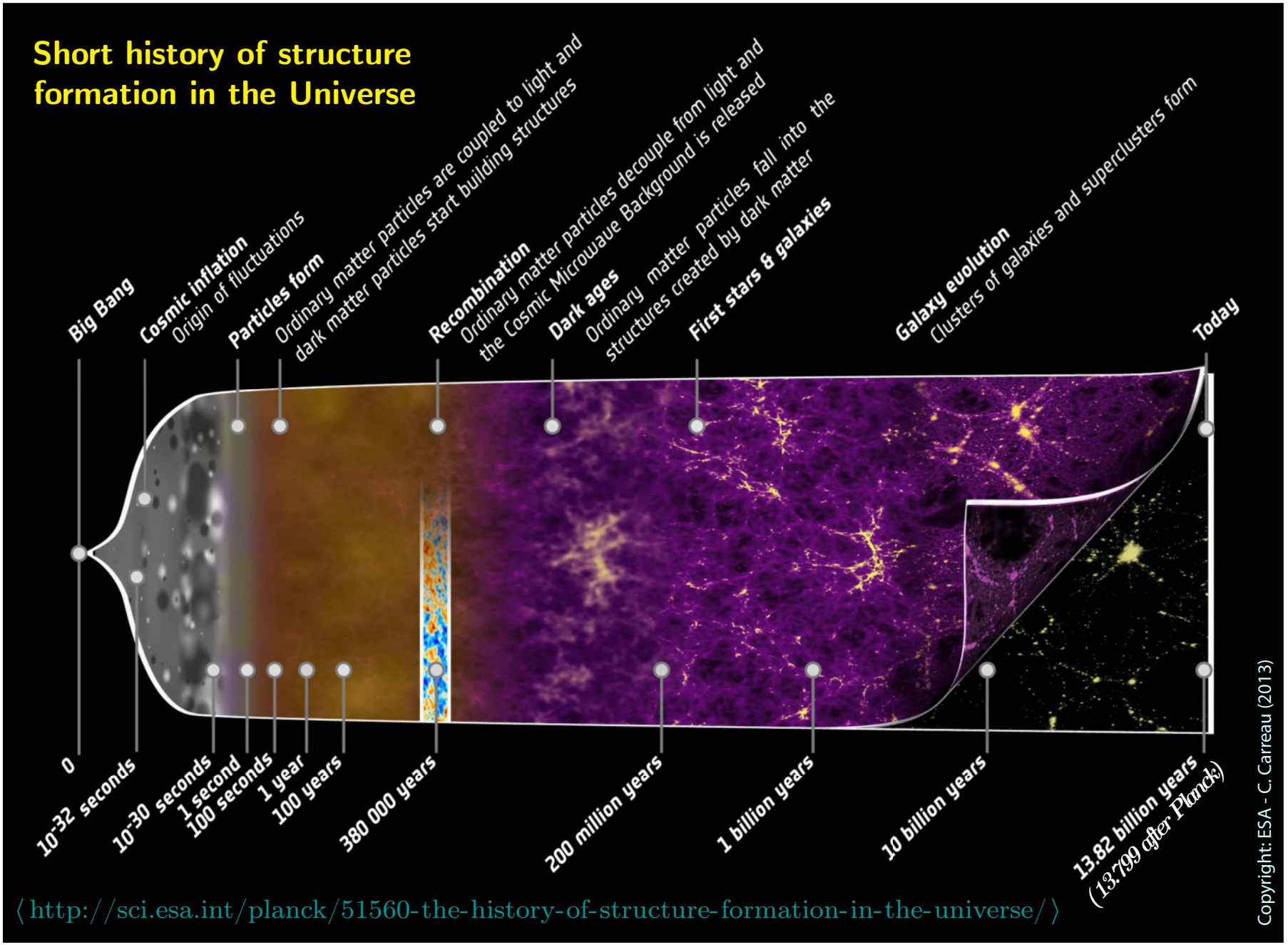
Short history of structure formation in the Universe
Big Bang
0
Cosmic inflation
Origin of fluctuations
10-32 seconds
Particles form
Ordinary matter particles are coupled to light and dark matter particles start building structures
10-30 seconds
1 second
100 seconds
1 year
100 years
Recombination
Ordinary matter particles decouple from light and the Cosmic Microwaue Background is released
380 000 years
Dark ages
Ordinary matter particles fall into the structures created by dark matter
200 million years
First stars & galaxies
1 billion years
Galaxy evolution
Clusters of galaxies and superclusters form
10 billion years
Today
13.82 billion years
(13.799 after Planck)
⟨ http://sci.esa.int/planck/51560-the-history-of-structure-formation-in-the-universe/ ⟩
Copyright: ESA - C. Carreau (2013)

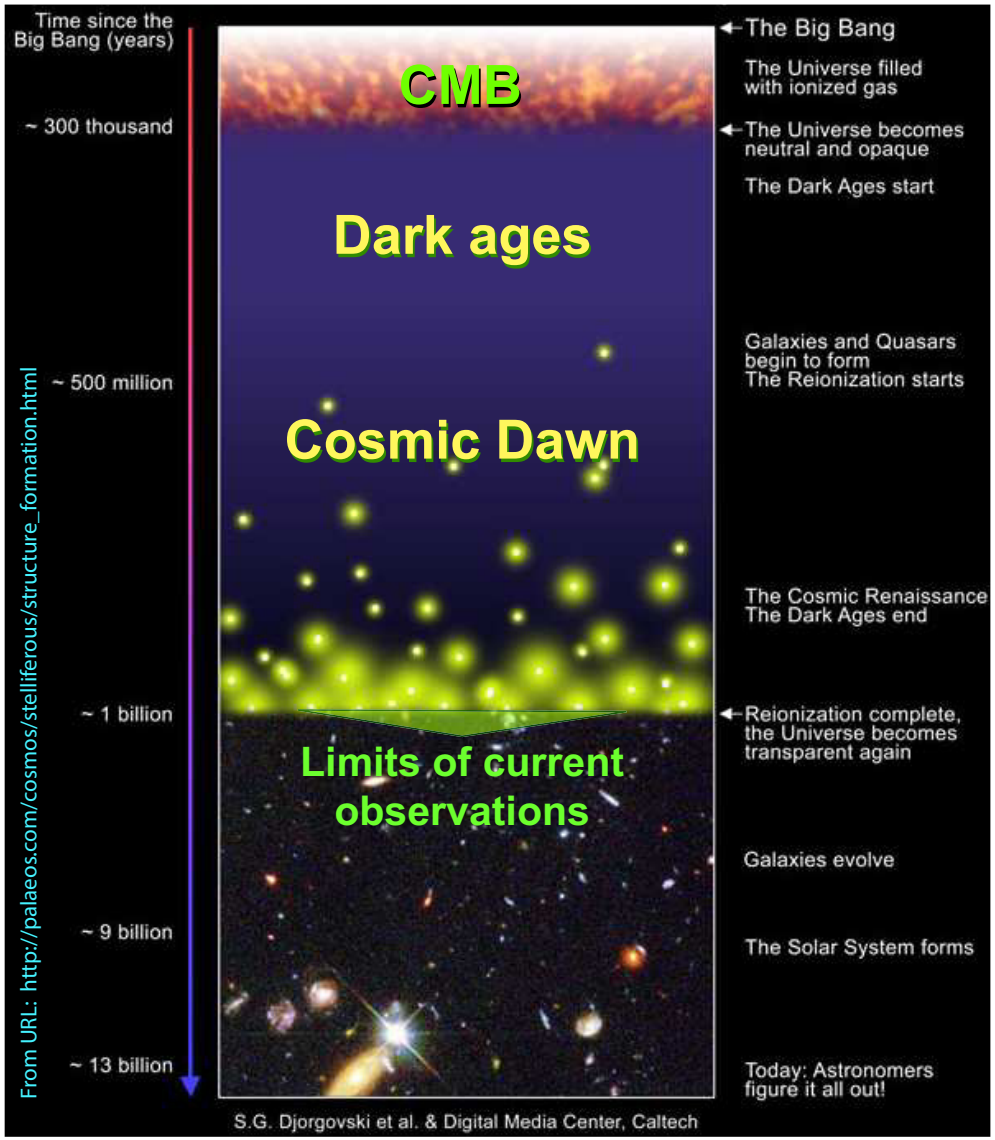

Hydrogen Reionization ($\sim 1.5 \times 10^8$ to 10^9 years): The intense radiation emitted by the first stars and quasars formed from gravitational collapse reionizes the Universe. Energy from the early massive stars ionized cold interstellar Hydrogen from the Big Bang. This epoch is called reionization because the Hydrogen nuclei were originally in an ionized state shortly after the Big Bang. From this point on, most of the universe is composed of plasma.

First Light (after a few $\times 10^8$ years of darkness): This first light is believed to have been captured in data from NASA's Spitzer Space Telescope, which detects infrared. The light detected by Spitzer would have originated as visible and ultraviolet light, then stretched, or redshifted, to lower-energy infrared waves during its long voyage to reach us across expanding space.

The CMB radiation detected by the Cosmic Background Explorer, Wilkinson Anisotropy Microwave Probe, and *Planck* traveled farther to reach us, and so stretched to even lower-energy microwaves.

Entire known Universe in single view.

M.C. Escher
Circle Limit IV

P.C. Budassi
Map of the Universe

The illustration by Pablo Carlos Budassi is based on Princeton's logarithmic map of the Universe which displays the entire range of astronomical scales from the Earth's neighborhood to the CMB sphere.[a]

The current measurement of the age of the Universe is (13.799 ± 0.021) Gy within the ΛCDM concordance model. According to modern calculations, the comoving distance (= current proper distance = radius of the visible Universe) to particles from which the CMBR was emitted, is about 14.0 Gps ≈ 45.7 Gly, while the comoving distance to the edge of the observable Universe is about 2% larger, 14.3 Gps ≈ 46.6 Gly. The total mass of ordinary matter in the Universe is estimated to be about 1.5×10^{53} kg.

[a] J. R. Gott III *et al.*, "A map of the Universe," ApJ **624** (2005) 463–484, arXiv:astro-ph/0310571v2; updated maps can be be found at URL: ⟨http://www.astro.princeton.edu/universe/⟩. The figure is taken from URL: ⟨https://www.inquisitr.com/2679749/pablo-carlos-budassi-logarithmic-map-of-the-universe/⟩.

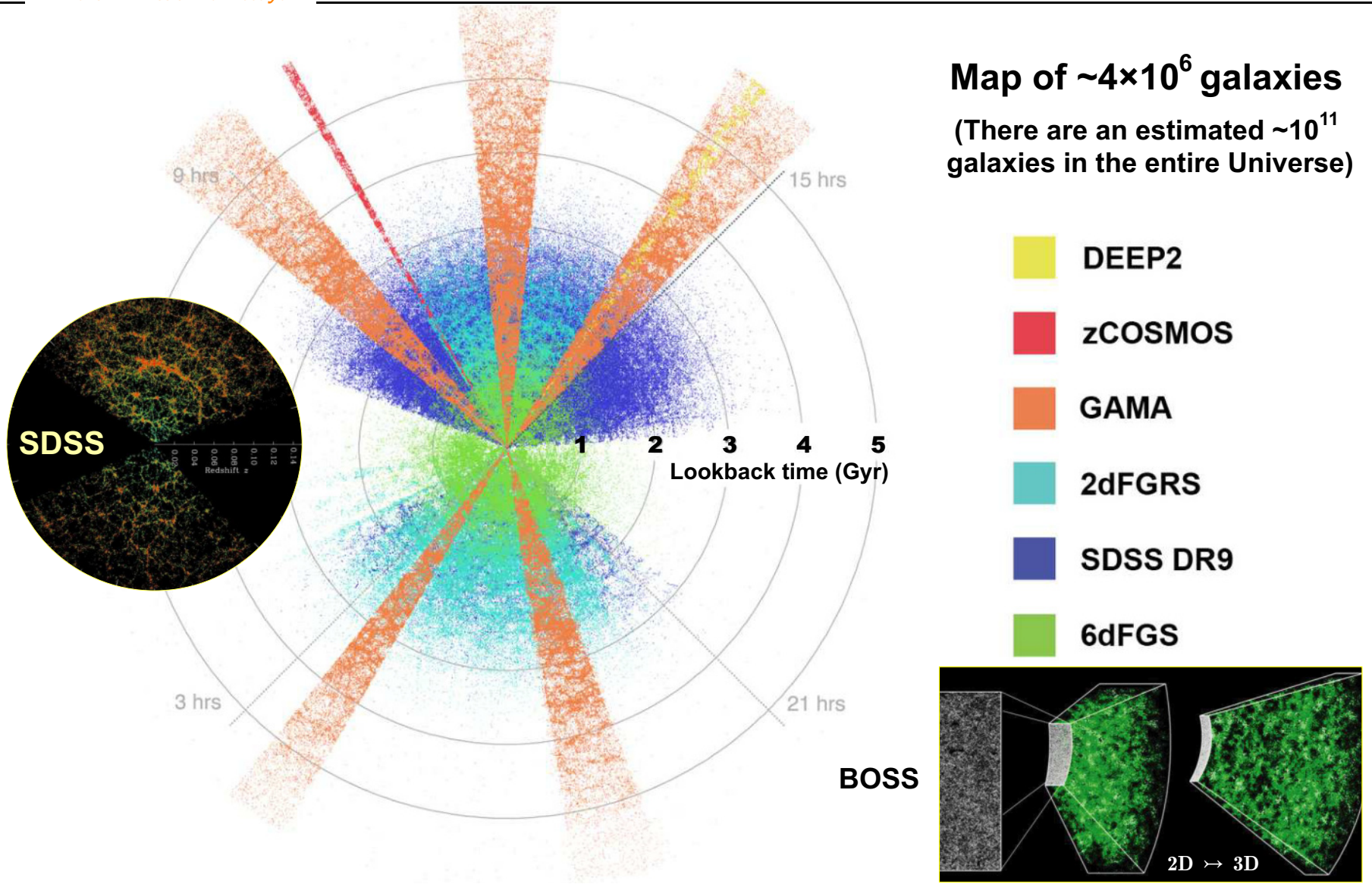

The distribution of galaxies as mapped by various Australia, US, and European survey teams. [From ⟨https://www.theregister.co.uk/2016/07/15/boffins_map_12_million_galaxies_in_3d_map/⟩ and ⟨https://phys.org/news/2015-08-death-universe.html⟩.]

Latest generation of SDSS.

The Sloan Digital Sky Survey (SDSS) has created the most detailed 3D maps of the Universe ever made. The Extended Baryon Oscillation Spectroscopic Survey (eBOSS), a SDSS phase, maps the distribution of galaxies and quasars from when the Universe was 3 to 8 billion years old, a critical time when dark energy started to affect the expansion of the Universe.

Key science questions:

- ⋆ How does the transition from deceleration to acceleration occur? Is it consistent with existing theories of dark energy?
- ⋆ How does structure grow during this epoch? Are there signs of violations of the general relativistic theory of gravity, which could be related to the acceleration?
- ⋆ Can we detect anomalies in the very largest scale clustering that could tell us about the earliest moments in the Universe's history?
- ⋆ Can we detect the effects of cosmic neutrinos, and thus pin down the neutrino mass scale?
- ⋆ What is the evolution of bright quasars of all luminosities out to redshift $z = 3$?

[From ⟨ http://www.sdss.org/surveys/eboss/ ⟩.]

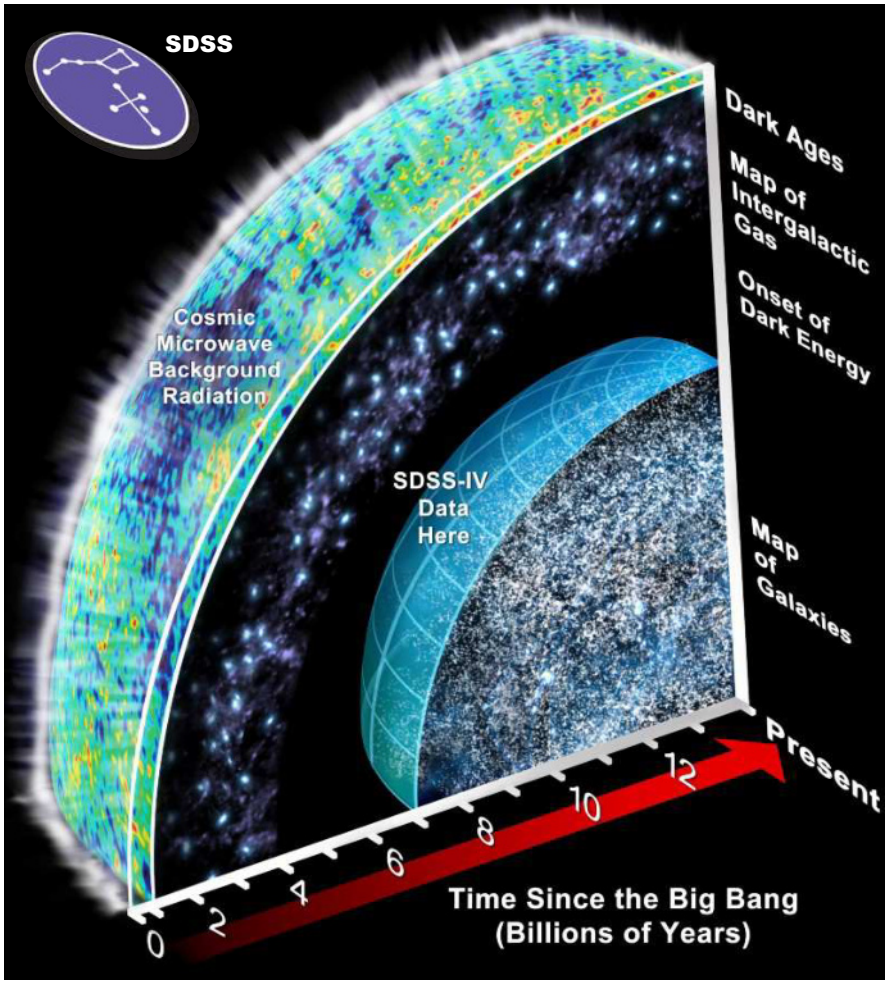

1.7 Galactic rotation curves.

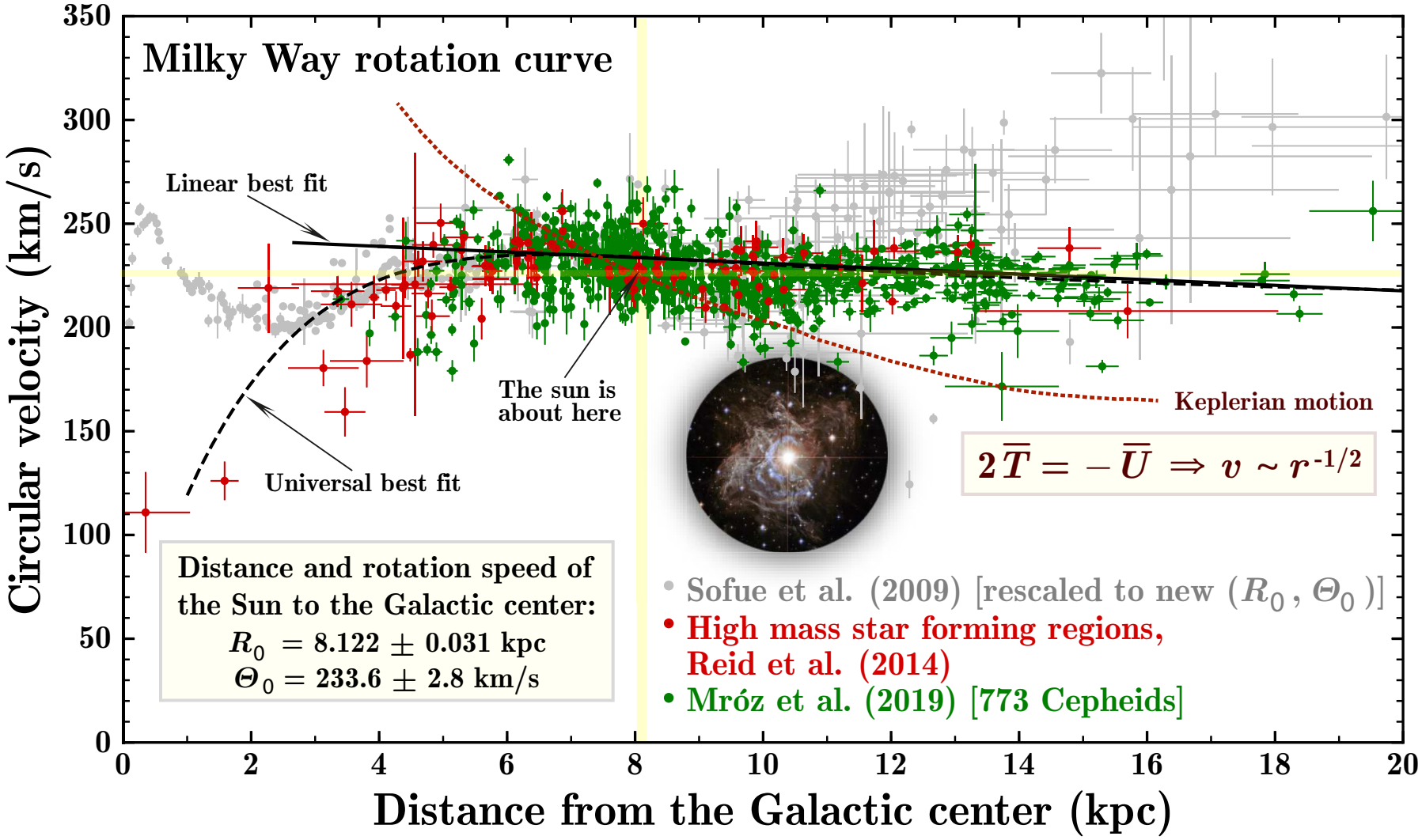

[Adapted from P. Mróz *et al.*, "Rotation curve of the Milky Way from classical cepheids," ApJL **870** (2019) L10, arXiv:1810.02131v2 [astro-ph.GA]; cf. arXiv:1810.02131v1 [astro-ph.GA] – this is interesting...]

More details: Expected spiral galaxy rotation curve.

For a spiral galaxy (like M31), the rotation speed of individual stars around its center is determined by the condition of constancy of orbits, i.e. equality of centrifugal and gravitational forces:

$$\frac{GmM(r)}{r^2} = \frac{mv^2}{r} \quad \Longrightarrow \quad v = v(r) = \sqrt{\frac{GM(r)}{r}},$$

where $M(r)$ is the total mass inside a sphere of radius r. In the case of perfect spherical or even cylindrical symmetry of the galaxy, the influence of masses outside the sphere is mutually compensated. In the first (very rough) approximation the central region of the galaxy can be considered spherical. Then for the stars located not too far from the galactic center we have

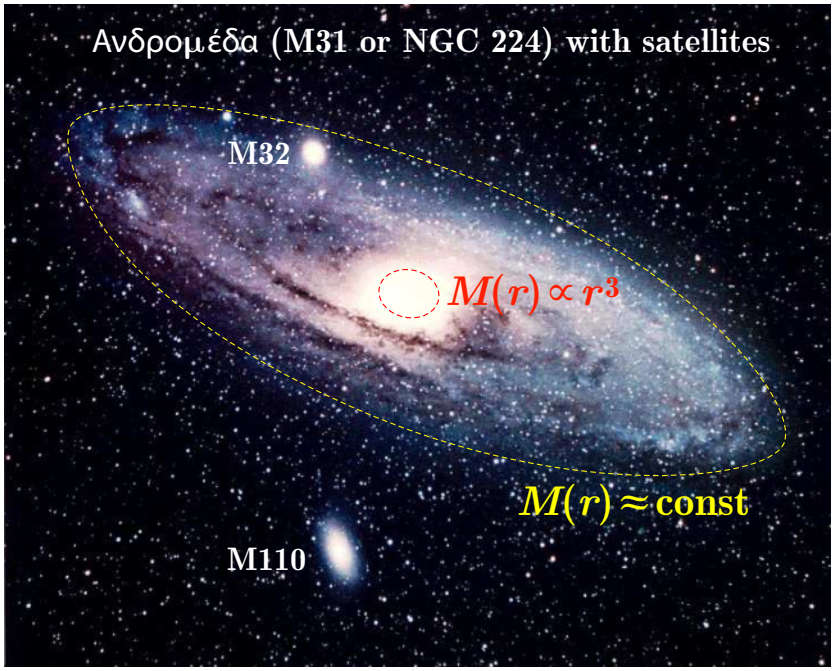

$$M(r) = \overline{\rho}\,\frac{4\pi r^3}{3} \quad \Longrightarrow \quad v(r) = \sqrt{\frac{4\pi G\overline{\rho}}{3}}\,r, \quad \Longrightarrow \quad v(r) \propto r.$$

In the outer region of the galaxy, the mass $M(r)$ is almost constant, $M(r) \approx M_g$. Therefore

$$v(r) = \sqrt{\frac{GM_g}{r}}, \quad \Longrightarrow \quad v(r) \propto \frac{1}{\sqrt{r}}.$$

However, we see that this is not the case.

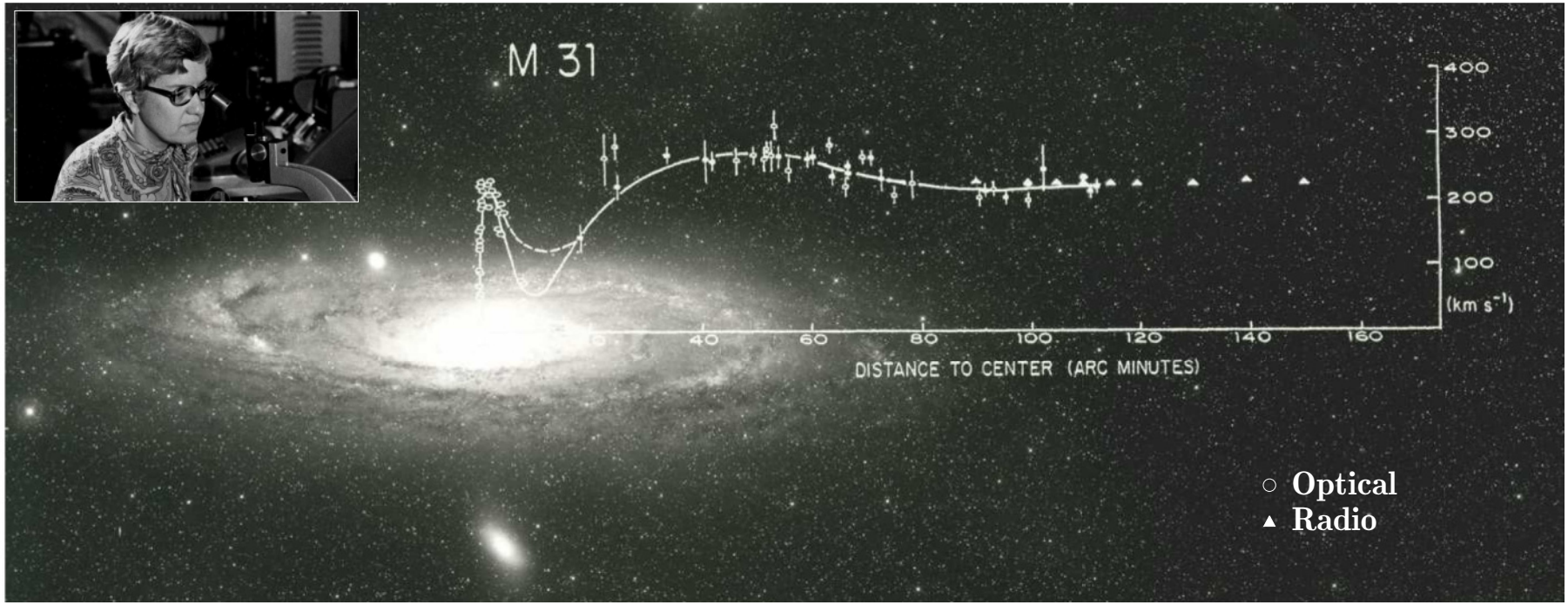

The M31 (Andromeda galaxy) major axis mean optical radial velocities and the rotation curve, $r < 120$ arcmin, superposed on the M31 image from the Palomar Sky Survey. Velocities from radio observations are indicated by triangles, $90 < r < 150$ arcmin. Rotation velocities remain flat well beyond the optical galaxy, implying that the M31 cumulative mass rises linearly with radius. (Image by Vera Rubin and Janice Dunlap.)

Vera Rubin writes:

> *The figure raises the questions: What's spinning the stars and gas around so fast beyond the optical galaxy? What's keeping them from flying out into space? The current answer is, "Gravity, from matter that has no light."*

[From V. Rubin, "Seeing dark matter in the Andromeda galaxy," Phys. Today **59**, No. 12 (2006) 8–9. See also J. R. Primack, "Dark matter and galaxy formation," AIP Conf. Proc. **1192** (2009) 101, arXiv:0909.2021 [astro-ph.CO].]

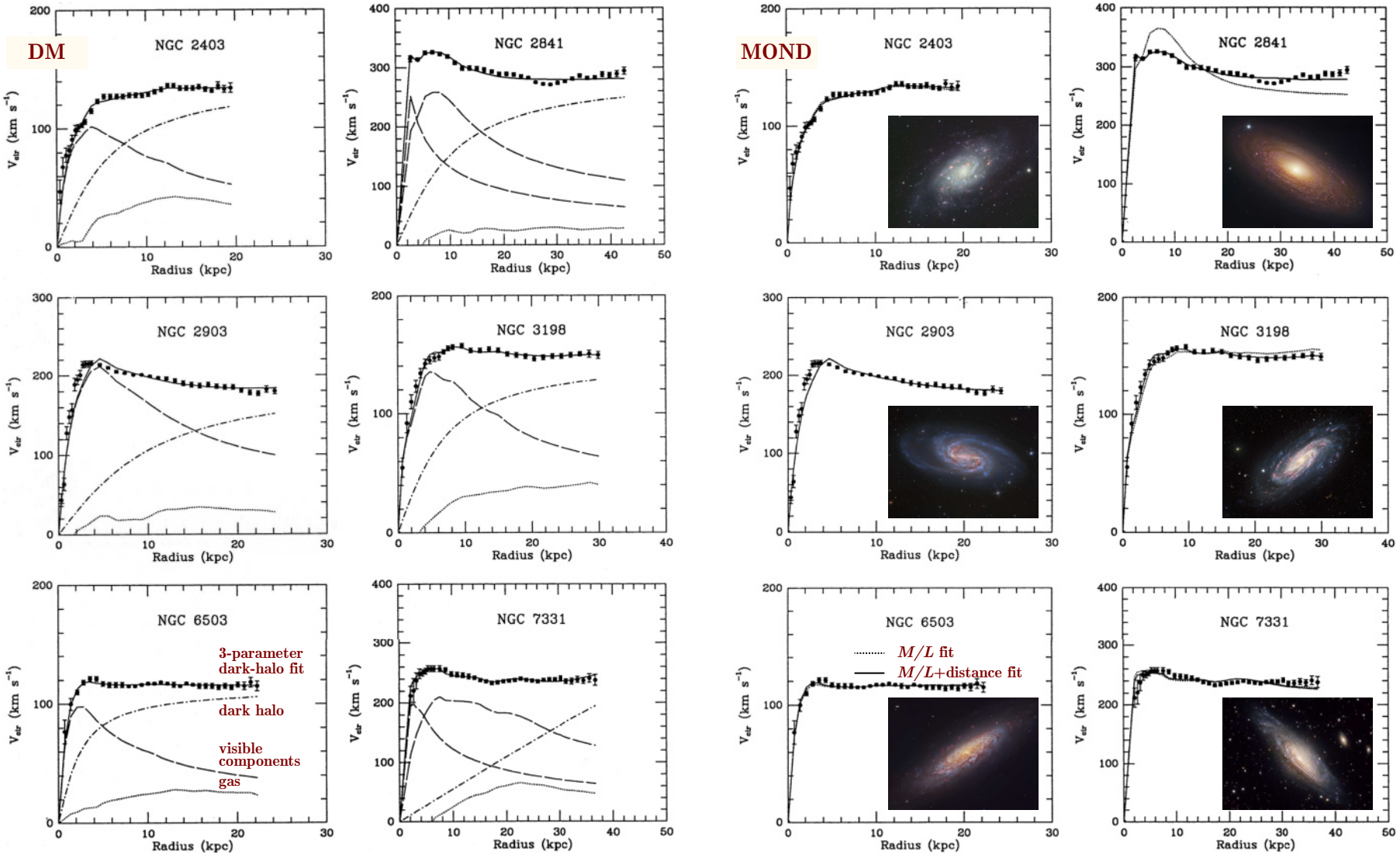

Dark-halo (6 left panels) and MOND (6 right panels) fits of rotation curves of ten spiral galaxies. The overall conclusion is that the MOND fits work usually better than 3-parameter dark-halo fits.

[From K. G. Begeman, A. H. Broeils, & R. H. Sanders, "Extended rotation curves of spiral galaxies – Dark haloes and modified dynamics," Mon. Not. Roy. Astron. Soc. **249** (1991) 523–537. Note: only Begeman's sample is shown here.]

A good argument in favor of DM is provided by ... galaxies without DM.

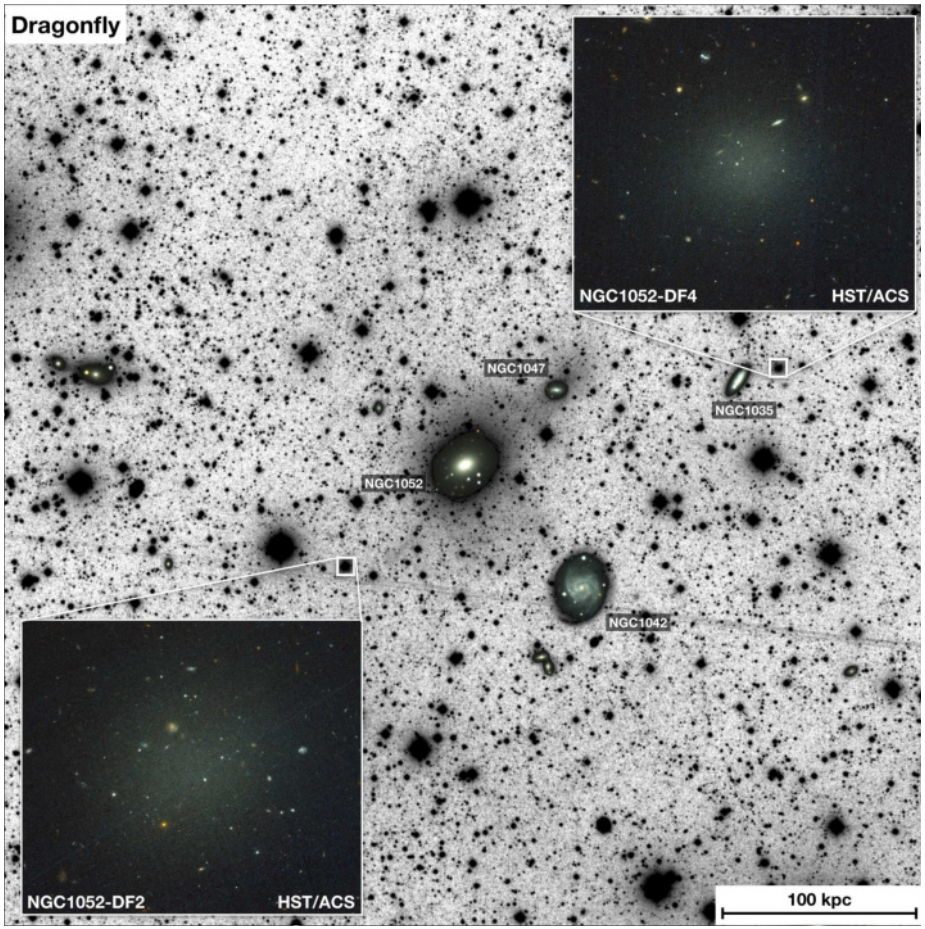

◁ The ultra-diffuse galaxies NGC1052-DF2 and NGC1052-DF4 have a very low velocity dispersion, indicating that they have little or no dark matter.[a] The galaxies have similar distances and similar (unusual) populations of luminous globular clusters.

Observations of the rotation curves in the high-redshift ($z \approx 0.6-2.6$, $\sim 10^{10}$ years old) massive ($\log(M/M_\odot) \gtrsim 9.6$) star-forming galaxies suggest that they have much smaller DM halos than galaxies in the local (low-redshift) Universe.[b]

Let's note in passing a remarkable hypothesis. If indeed our local neighborhood is not typical but crowded with dark matter, then the local value of the Hubble constant must be larger than the global one ($H_0 \propto \sqrt{\rho_\Lambda + \rho_c + \rho_b}$).[c]

[a] P. van Dokkum *et al.*, "A second galaxy missing dark matter in the NGC 1052 group," ApJ **874** (2019) L5, arXiv:1901.05973 [astro-ph.GA]. Several other candidates for the DM-poor galaxies have been discovered.

[b] R. Genzel *et al.*, "Strongly baryon-dominated disk galaxies at the peak of galaxy formation ten billion years ago," Nature **543** (2017) 397–401, arXiv:1703.04310 [astro-ph.GA].

[c] Yu. V. Dumin, "Can the dark-matter deficit in the high-redshift galaxies explain the persistent discrepancy in Hubble constants?" arXiv:1804.00562 [astro-ph.CO]. The hypothesis is somehow ignored by the community.

1.8 Dark-matter problem in the form of mind maps.

Some abbreviation:

CHAMP	=	**CH**arged **M**assive **P**article
CDM	=	**C**old **D**ark **M**atter
EWIP	=	**E**xtremely **W**eakly **I**nteracting **P**article
FIMP	=	**F**eebly **I**nteracting **M**assive **P**article
HDM	=	**H**ot **D**ark **M**atter
MaCHO	=	**Ma**ssive **C**ompact **H**alo **O**bject
MOG	=	**MO**dified **G**ravity
MoND	=	**Mo**dified **N**ewtonian **D**ynamics
MSSM	=	**M**inimal **S**upersymmetric **S**tandard **M**odel
SIDM	=	**S**elf-**I**nteracting **D**ark **M**atter
SIMP	=	**S**trongly **I**nteracting **M**assive **P**article
TeVeS	=	**Te**nsor-**Ve**ctor-**S**calar theory
WDM	=	**W**arm **D**ark **M**atter
WIMP	=	**W**eakly **I**nteracting **M**assive **P**article
WISP	=	**W**eakly **I**nteracting **S**ub-eV/**S**lim/Slender **P**article

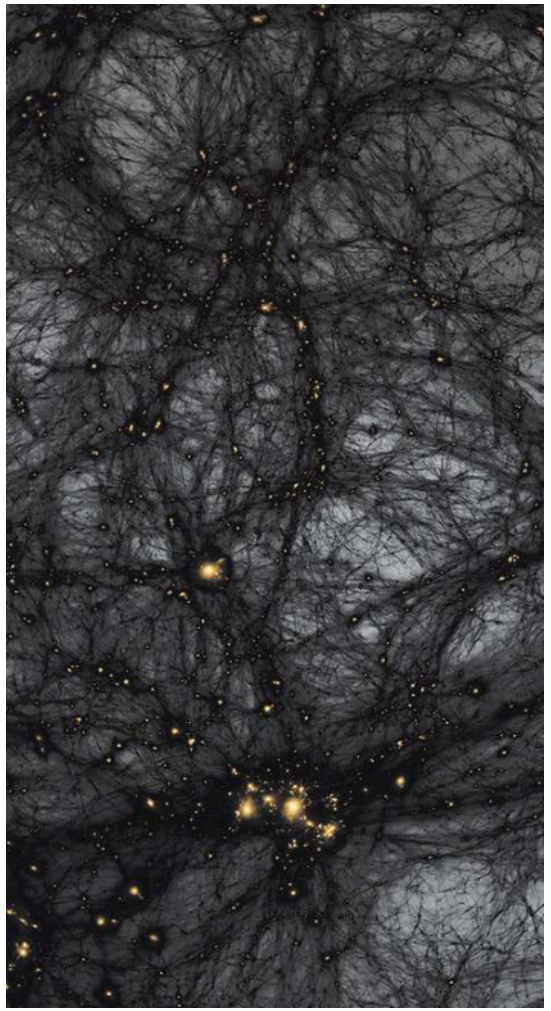

[The diagrams shown in next two slides are taken from T. M. P. Tait, "Dark Matter: Theoretical Overview," report at the Aspen Center for Physics, January 11, 2016 and G. Bertone & T. M. P. Tait, "A new era in the quest for dark matter," Nature **562** (2018) 51–56, arXiv:1810.01668 [astro-ph.CO].]

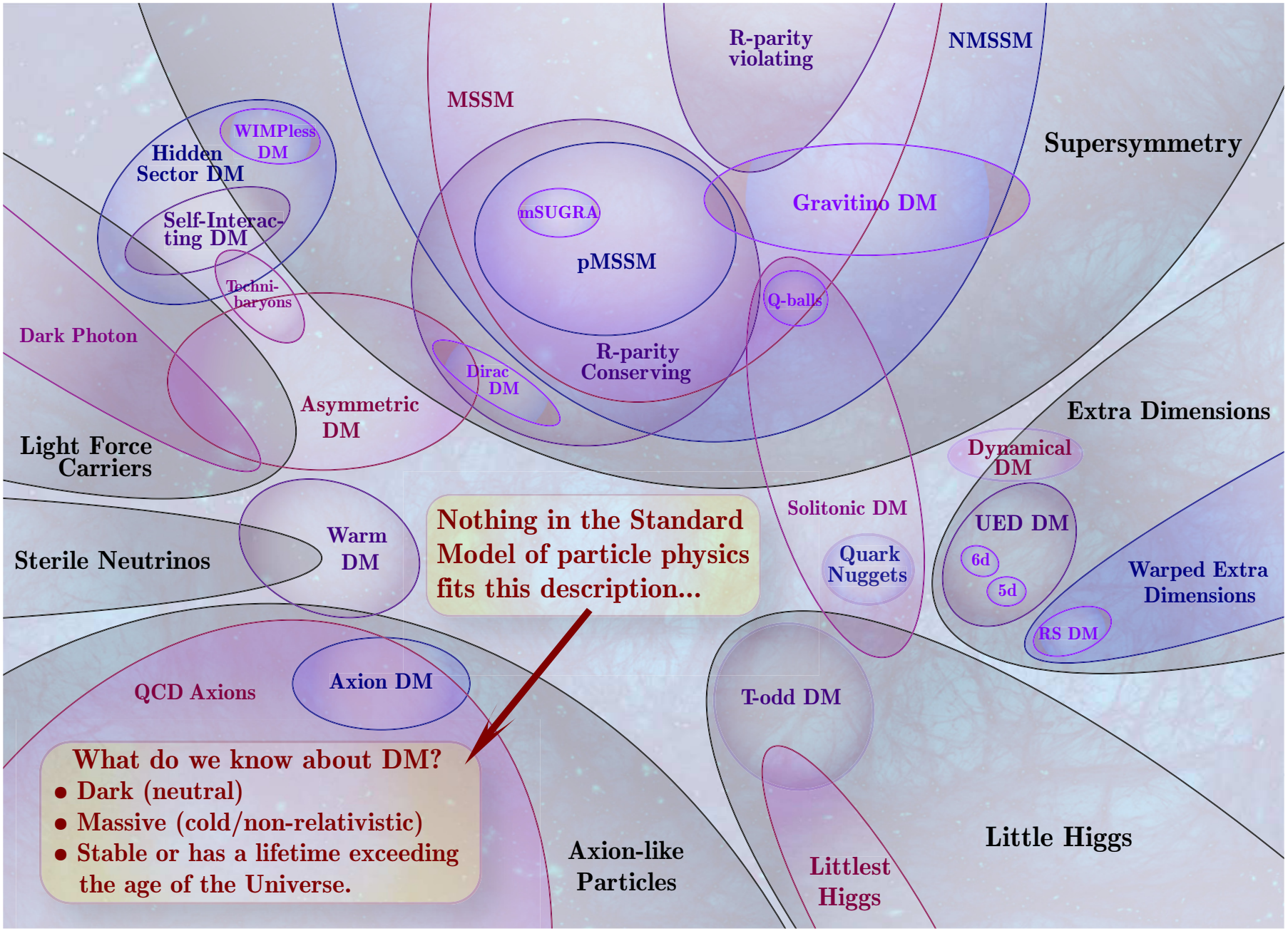
R-parity violating
NMSSM
MSSM
Supersymmetry
WIMPless DM
Hidden Sector DM
Self-Interac-ting DM
Techni-baryons
mSUGRA
pMSSM
Gravitino DM
Q-balls
Dark Photon
R-parity Conserving
Dirac DM
Asymmetric DM
Extra Dimensions
Light Force Carriers
Dynamical DM
Solitonic DM
UED DM
6d
5d
Quark Nuggets
Warped Extra Dimensions
RS DM
Sterile Neutrinos
Warm DM
Nothing in the Standard Model of particle physics fits this description...
QCD Axions
Axion DM
T-odd DM
What do we know about DM?
• Dark (neutral)
• Massive (cold/non-relativistic)
• Stable or has a lifetime exceeding the age of the Universe.
Axion-like Particles
Littlest Higgs
Little Higgs

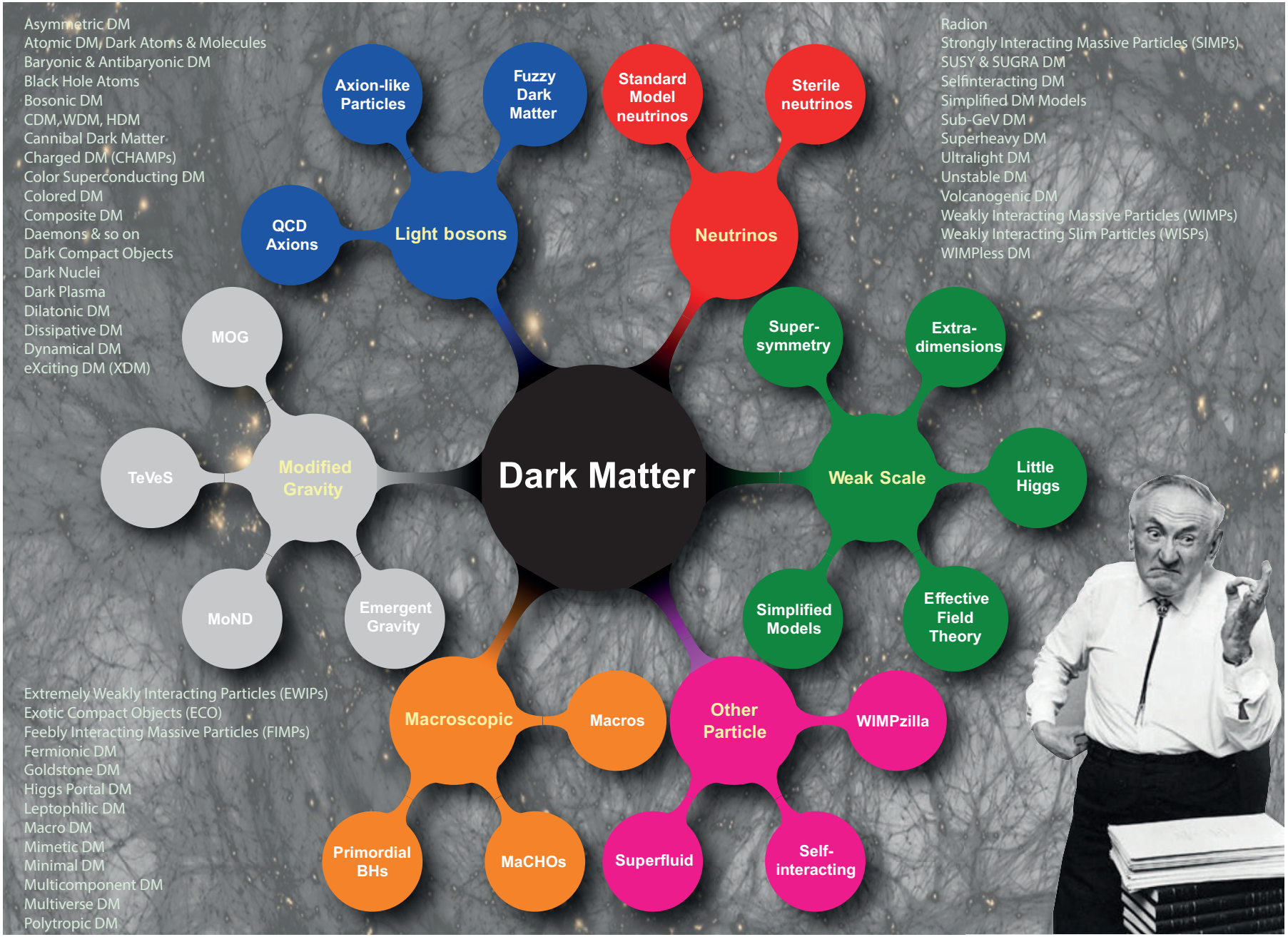
Asymmetric DM
Atomic DM, Dark Atoms & Molecules
Baryonic & Antibaryonic DM
Black Hole Atoms
Bosonic DM
CDM, WDM, HDM
Cannibal Dark Matter
Charged DM (CHAMPs)
Color Superconducting DM
Colored DM
Composite DM
Daemons & so on
Dark Compact Objects
Dark Nuclei
Dark Plasma
Dilatonic DM
Dissipative DM
Dynamical DM
eXciting DM (XDM)
Axion-like Particles
Fuzzy Dark Matter
QCD Axions
Light bosons
Standard Model neutrinos
Sterile neutrinos
Neutrinos
Radion
Strongly Interacting Massive Particles (SIMPs)
SUSY & SUGRA DM
Selfinteracting DM
Simplified DM Models
Sub-GeV DM
Superheavy DM
Ultralight DM
Unstable DM
Volcanogenic DM
Weakly Interacting Massive Particles (WIMPs)
Weakly Interacting Slim Particles (WISPs)
WIMPless DM
MOG
TeVeS
Modified Gravity
MoND
Emergent Gravity
Dark Matter
Super-symmetry
Extra-dimensions
Weak Scale
Little Higgs
Simplified Models
Effective Field Theory
Extremely Weakly Interacting Particles (EWIPs)
Exotic Compact Objects (ECO)
Feebly Interacting Massive Particles (FIMPs)
Fermionic DM
Goldstone DM
Higgs Portal DM
Leptophilic DM
Macro DM
Mimetic DM
Minimal DM
Multicomponent DM
Multiverse DM
Polytropic DM
Macroscopic
Macros
Primordial BHs
MaCHOs
Other Particle
WIMPzilla
Superfluid
Self-interacting

1.9 A mere mention of Multiverse.

2 Cosmic neutrino background (CνB).

Relict neutrinos (or Cosmic Neutrino Background, or CNB, or CνB) produce the largest neutrino flux on Earth, but compose only a very small fraction of invisible (non-luminous) matter in the Universe.

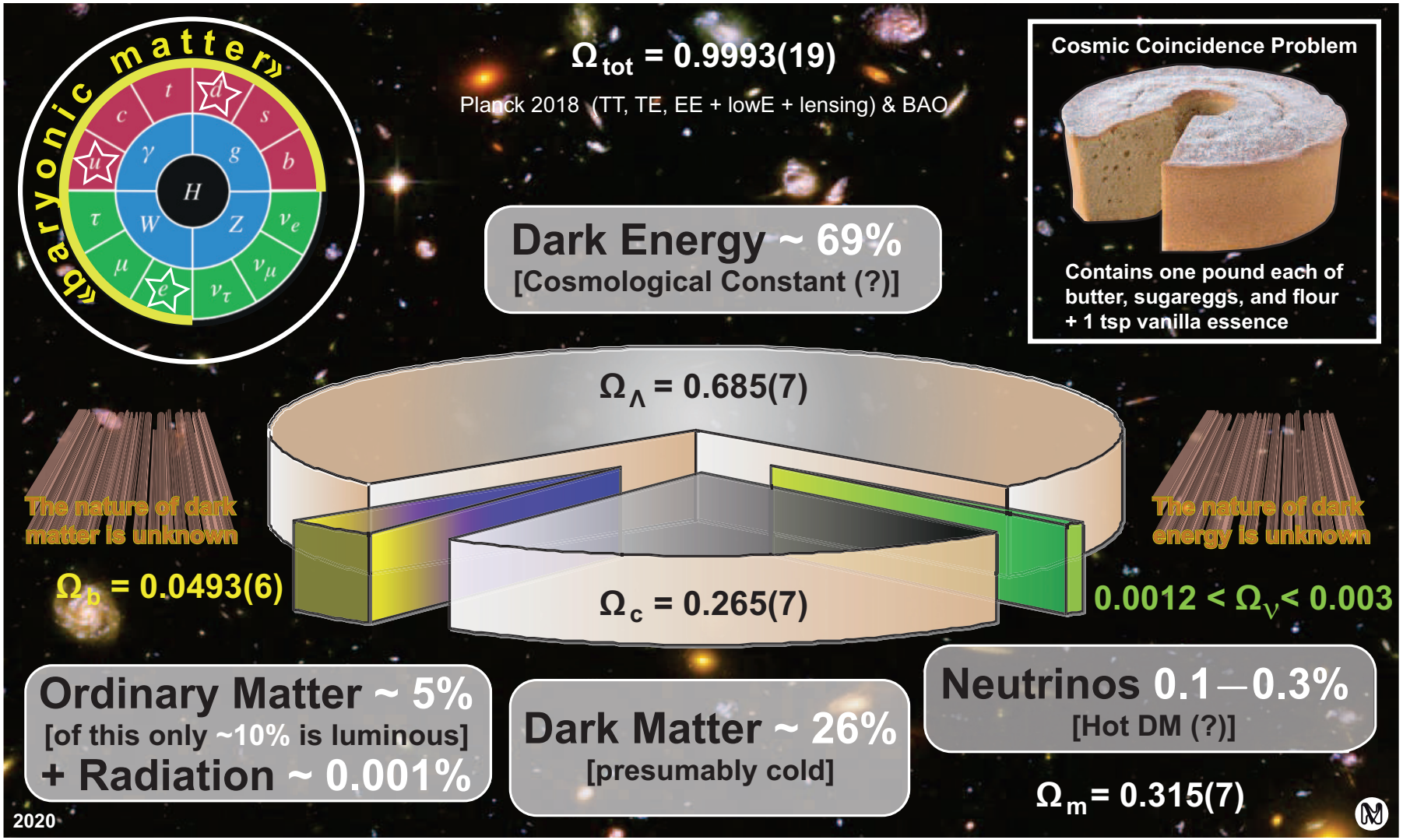

Baryon budget of the late-time Universe

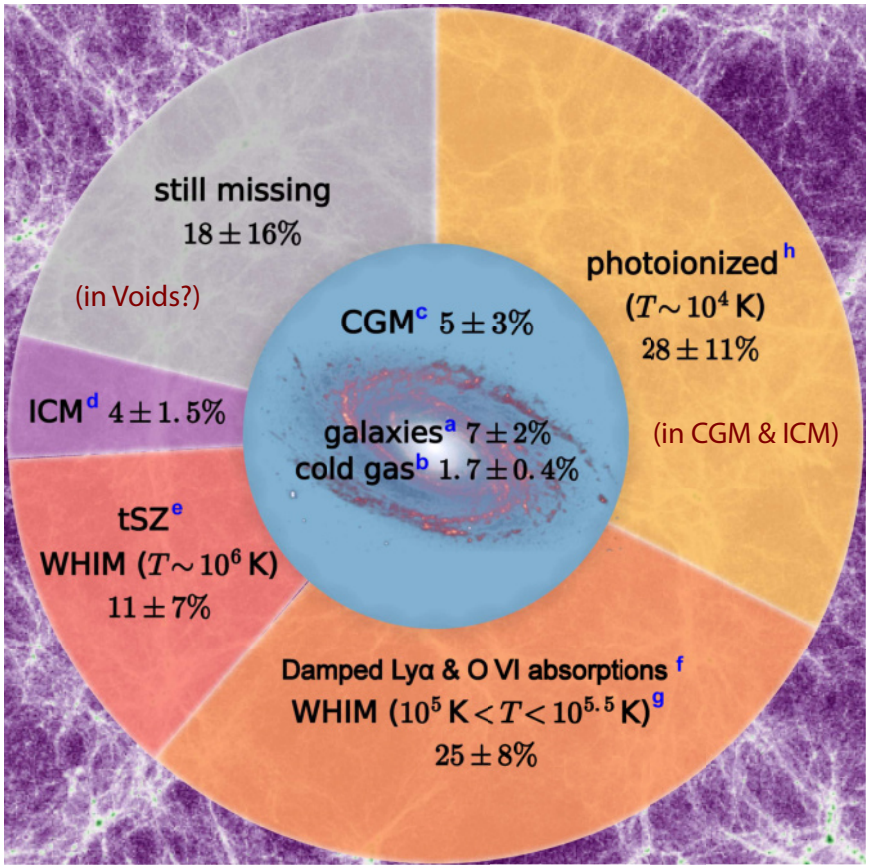

(a) Stellar component of galaxies.

(b) Cold gas in galaxies estimated from observation of HI and H_2.

(c) Circumgalactic medium (CGM) observed through Lyα and O VI absorptions.

(d) Intracluster medium (ICM) observed via X-ray emission. The recent detection of X-ray filaments near a massive nearby cluster, and Sunyaev-Zel'dovich (SZ) signal between interacting clusters measures hot gas in a similar phase as in this category.

(e) Warm-hot intergalactic medium (WHIM) detected via the thermal SZ (tSZ) effect; the value is estimated at $z \simeq 0.5$, which is consistent with the estimate by from the observation of two O VII absorbers.

(f,g) WHIM observed via Damped Lyα (DLA) and O VI absorptions. Note that there is some overlap between DLA and O VI – they trace the same gas. This is the biggest uncertainty for the amount of baryons which is still missing.

(h) Gas observed via photon-ionized Lyα absorbers. Relatively recent $(2015 - 2017)$ detection of the kinetic or kinematic SZ effect (kSZ) constrains the baryon content in and around collapsed objects, and therefore falls into the category of **(c)** and **(d)**.

[Adapted from A. de Graaff *et al.*, "Probing the missing baryons with the Sunyaev-Zel'dovich effect from filaments," Astron. Astrophys. **624** (2019) A48, arXiv:1709.10378v3 [astro-ph.CO].]

2.1 Planck 2018 neutrino probe.

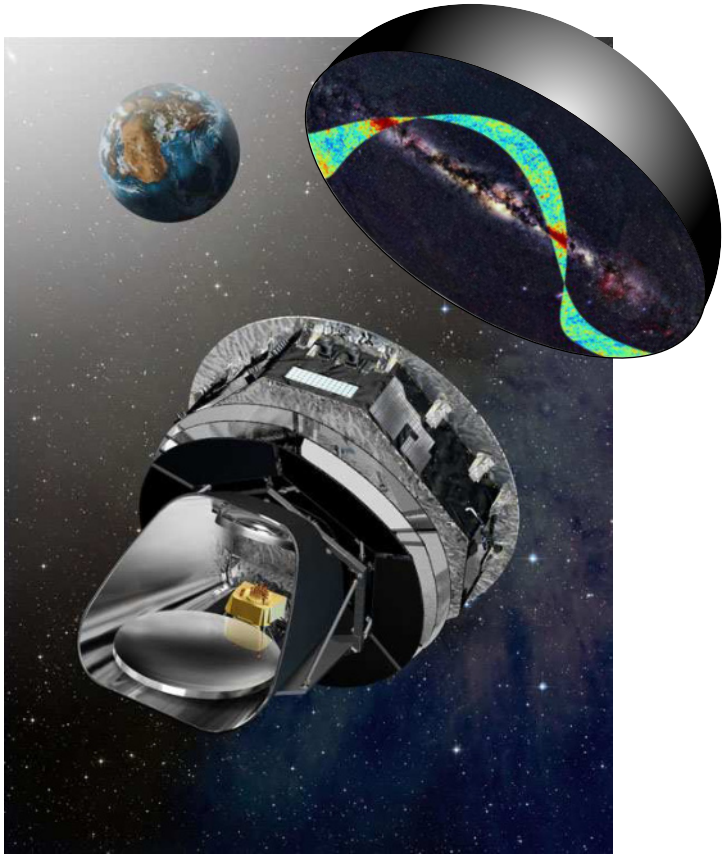

It is not yet realistic to directly detect the neutrinos, which were created within the first second after the Big Bang, and which have too little energy now. However, for the first time, *Planck* has unambiguously detected the effect these relic neutrinos have on relic radiation maps. The quality of these maps is now such that the imprints left by dark matter and relic neutrinos are clearly visible.[a] The relic neutrinos were released when the Universe was still opaque to light but already transparent to neutrinos, which can freely escape from environments that are opaque to photons. $\approx 380,000$ years later, when relic radiation was released, it bore the imprint of neutrinos because photons had gravitational interaction with these particles. Observing the oldest photons thus made it possible to confirm the properties of neutrinos.

Planck observations are consistent with the standard model of particle physics. They essentially exclude the existence of a fourth species of neutrinos, previously considered a possibility based on the final data from the WMAP satellite, the US predecessor of *Planck*.

Finally, *Planck* 2018 sets: $\sum m_\nu < \mathbf{0.12}$ eV, $N_{\text{eff}} = \mathbf{2.99 \pm 0.17}$.

[a] For details see N. Aghanim *et al.* (*Planck* Collaboration), "*Planck* 2018 results. VI. Cosmological parameters," Astron. Astrophys. **641** (2020) A6, arXiv:1807.06209v4 [astro-ph.CO].

2.2 Bit of theory: CνB temperature, number density, etc.

1. Entropy density. In thermal equilibrium, the total entropy density, s, of a multicomponent ideal gas mixture of elementary particles is

$$s = \sum_i \frac{\rho_i + p_i}{k_B T_i},$$

$t \approx 10^{-12} - 10^{-6}$ s $\qquad\qquad$ $t \gtrsim 10^{-6}$ s

$i \in \{q, \overline{q}, \ell^{\pm}, \nu_\ell, \overline{\nu}_\ell, \gamma, W^{\pm}, Z, H, g,$ God knows what else$\}$ or $i \in \{p, n, e^{\pm}, \nu_\ell, \overline{\nu}_\ell, \gamma \ldots\}$,

where ρ_i, p_i, and T_i are, respectively, the equilibrium energy density, pressure, and temperature of particles of type i, and k_B is the Boltzmann constant (hereafter we simply denote $k_B T_i = T_i$). The energy density for bosons (sign $-$) and fermions (sign $+$) is given by

$$\rho_i = \frac{g_i}{(2\pi)^3} \int_0^\infty \frac{E_i d\mathbf{k}}{\exp\left[\left(E_i - \mu_i\right)/T_i\right] \mp 1} = \frac{g_i}{2\pi^2} \int_0^\infty \frac{E_i k^2 dk}{\exp\left[\left(E_i - \mu_i\right)/T_i\right] \mp 1},$$

where g_i, $E_i = \sqrt{k^2 + m_i^2}$, m_i, and μ_i are, respectively, the number of the internal degrees of freedom, energy, mass, and chemical potential of the ith gas component; $k = |\mathbf{k}|$, $d\mathbf{k} = d^3k$.

- We'll consider a very early and hot Universe, when all particles are ultrarelativistic ($T_i \gg m_i$).
- Since the L and B asymmetries are $\sim 10^{-9}$, the chemical potentials are negligibly small. Then

$$\rho_i = \frac{g_i T_i^4}{2\pi^2} \int_0^\infty \frac{x^3 dx}{e^x \mp 1} = \frac{\pi^2}{30} \hat{g}_i T_i^4, \quad \hat{g}_i = \begin{cases} g_i \text{ for bosons,} \\ \dfrac{7}{8}\, g_i \text{ for fermions.} \end{cases}$$

The well-known formulas are used here (see p. 155 or any relevant math reference book):

$$\int_0^\infty \frac{x^n dx}{e^x - 1} = \Gamma(n+1)\zeta(n+1), \quad \int_0^\infty \frac{x^n dx}{e^x + 1} = \Gamma(n+1)\zeta(n+1)\left(1 - \frac{1}{2^n}\right), \quad \zeta(4) = \frac{\pi^4}{90}.$$

Now, by using the equations of state $3p_i = \rho_i$ valid for ultrarelativistic particles, we obtain

$$s = \frac{4}{3}\sum_i \frac{\rho_i}{T_i} = \frac{2}{45}\pi^2 g_* T^3, \quad \text{where} \quad g_* = g_*^{\text{th}} + g_*^{\text{dec}}, \quad T = T_\gamma;$$

here we introduced the effective numbers of degrees of freedom (NDF) of particles which are in thermal equilibrium with γs (g_*^{th}) and those that are decoupled from equilibrium with photons (g_*^{dec}):

$$g_*^{\text{th}} = \sum_i \hat{g}_i \quad \text{and} \quad g_*^{\text{dec}} = \sum_i \hat{g}_i \left(\frac{T_i}{T}\right)^4.$$

i	$q\,\overline{q}$, $p, n, \ell^\pm$	ν_ℓ, $\overline{\nu}_\ell$	γ, g	$W^\pm$, Z	H
g_i	2	1	2	3	1

2. Homework: Calculate g_* for $T \gg m_t \approx 173$ GeV and for $T = 1 - 100$ MeV.

3. Freeze-out temperature. At energies $E_\nu \sim T \sim 2 - 3$ MeV, ν and $\overline{\nu}$ cannot produce particles heavier than $e^\pm$, but can scatter on each other or on $e^\pm$ and participate in the reactions $e^+e^- \leftrightarrow \nu\overline{\nu}$. The cross sections of all these processes are of the same order (see pp. 157 and 158):

$$\sigma_\nu \sim G_F^2 E_\nu^2 \sim G_F^2 T^2$$

($G_F \simeq 1.17 \times 10^{-5}$ GeV^{-2} is the Fermi constant). The mean free path (= time between collisions) is

$$\tau_\nu = \langle n \sigma_\nu v_{\text{rel}} \rangle^{-1},$$

where n is the equilibrium number density of the initial particle,

$$n = \frac{g}{2\pi^2}\int_0^\infty \frac{k^2 dk}{\exp(k/T)+1} = \frac{3}{4} g \frac{\zeta(3)}{\pi^2} T^3, \quad \zeta(3) \approx 1.202,$$

and $v_{\rm rel} \simeq 1$ is the relative velocity of the colliding particle. Therefore, $\tau_\nu \sim 1/\left(G_F^2 T^5\right)$ and the number of collisions that occurred after the time t can (very approximately) be estimated as follows

$$N_{\rm coll} = \int_t^\infty \frac{dt'}{\tau_\nu(t')} \sim \frac{t}{\tau_\nu(t)} \sim \frac{1}{H(t)\tau_\nu(t)},$$

where $H(t) = T^2/M_P$ is the Hubble "constant" ($M_P = \sqrt{\hbar c/G} \simeq 2.18 \times 10^{-5}$ g $\simeq 1.22 \times 10^{19}$ GeV is the Planck mass and $G \simeq 6.674 \times 10^{-11}$ kg^{-1}m^{3}s^{-2} is the gravitational constant).

• Neutrinos are in thermal equilibrium at $N_{\rm coll} \gg 1$ and are free streaming at $N_{\rm coll} \ll 1$. Therefore, they decouple from matter ("freeze-out") at $N_{\rm coll} \sim 1$. Thus, the freeze-out temperature is

$$T_\nu^{\text{freeze-out}} \sim \left(M_P G_F^2\right)^{-1/3} \sim 2 - 3 \text{ MeV}.$$

4. CνB temperature. Since the total entropies of γ, $e^\pm$, and $\nu/\overline{\nu}$ are separately conserved with good precision during the γs' decoupling from the matter and their heating due to e^+e^- annihilation,

$$g_*(aT)^3\big|_{\rm before} = g_*(aT)^3\big|_{\rm after}, \quad a = a(t) = (1+z)^{-1}$$

(a is the scale factor and z is the redshift). The effective NDF of γ and $e^\pm$ before and after the e^+e^- annihilation are $2 + 2 \cdot 2 \cdot (7/8) = 11/2$ and 2, respectively. Thus, neglecting a small residual reheating of neutrinos, non-equilibrium corrections, and so on, we have

$$T_\nu = (4/11)^{1/3} T_\gamma \approx 0.714\, T_\gamma$$

This relation remains the same today. Based on the present-day value from *Planck* 2018 one finds

$$T_{\rm CMB} = 2.7255 \text{ K} \quad \Longrightarrow \quad T_\nu^0 \approx 1.945 \text{ K} \approx 0.168 \text{ meV}.$$

Problem: Estimate the age of the Universe at the time of the neutrino freeze-out.

5. CνB particle density. For each neutrino mass eigenstate we get

$$n_\nu + n_{\overline{\nu}} = \frac{3}{2}\frac{\zeta(3)}{\pi^2}T_\nu^3 = \frac{6}{11}\frac{\zeta(3)}{\pi^2}T_\gamma^3 = \frac{3}{11}\,n_\gamma.$$

This relation remains the same today. Based on the present-day value from *Planck* 2018 one finds

$$n_{\text{CMB}} \simeq 410.5\ \text{cm}^{-3} \quad\Longrightarrow\quad n^0_{\nu+\overline{\nu}} \simeq 112\ \text{cm}^{-3}.$$

For a more advanced approach (relativistic Boltzmann equations), see Sect. **2.5**, p. 156.

6. Number of effective neutrino species.

The radiation after $e^\pm$ disappears consists of γs and νs. Before some of νs become nonrelativistic, the radiation density is expressed as

$$\rho_{\text{rad}} = \left[1 + N_{\text{eff}}\,\frac{7}{8}\,\left(\frac{4}{11}\right)^{4/3}\right]\rho_\gamma, \tag{1}$$

where N_{eff}, the effective number of thermally excited NDFs, is just a way to parameterize ρ_{rad}.

The "canonical" number of effective neutrino species is slightly larger than 3:

$$N_{\text{eff}} = \mathbf{3.045(1) = 3 + 0.010 + 0.035}$$

0.010 comes from plasma effects, reducing ρ_γ, and 0.035 comes from non-instant neutrino decoupling from hotter e^+e^- (providing the residual neutrino heating). Additional adjustments ($\sim 0.04 - 0.05$) come from QED radiative corrections and neutrino oscillation effects (with MSW and damping).

- More generally, the number of effective neutrino species in cosmological plasma, N_{eff}, is defined as the ratio of the energy density of **all** relativistic particles, excluding CMB γs, normalized to the energy density of one type of massless equilibrium $\nu + \overline{\nu}$.
- Recall the LEP+SLC result $N_\nu = 2.984 \pm 0.008$ obtained from $\sigma_{e^+e^-\to\text{hadrons}}$ at $E_{\text{cm}} \sim m_Z$.

2.3 Planck 2018: neutrino summary vs. earlier data.

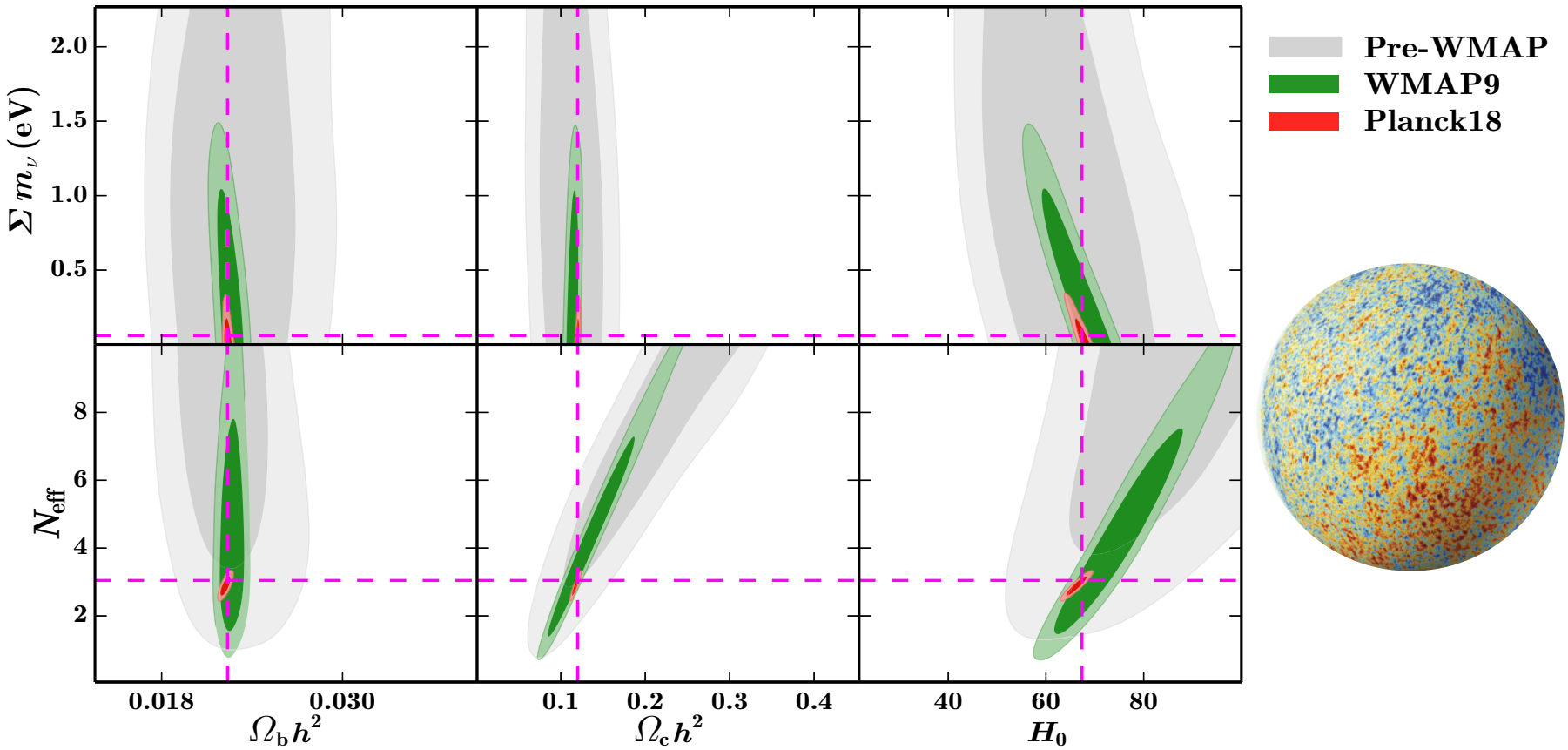

Successive reductions in the allowed parameter space for various one-parameter extensions to ΛCDM, from pre-WMAP (MAXIMA, DASI, BOOMERANG, VSA, CBI) to *Planck*. The contours display the 68 % and 95 % C.L. for the extra parameter vs. five other base-ΛCDM parameters. The dashed lines indicate the ΛCDM best-fit parameters or fixed default values of the extended parameters.

[Adapted from N. Aghanim *et al.* (*Planck* Collaboration), "Planck 2018 results. I. Overview and the cosmological legacy of *Planck*," Astron. Astrophys. **641** (2020) A1, arXiv:1807.06205 [astro-ph.CO];]

Let's repeat the final (base) *Planck* 2018 (+BAO) result on neutrino parameters:

$$\boldsymbol{\sum m_\nu < 0.12 \text{ eV}, \quad N_{\text{eff}} = 2.99 \pm 0.17, \quad \Delta N_{\text{eff}} < 0.3.}$$

Roughly speaking, the constrain on $\boldsymbol{\Delta N_{\text{eff}}}$ means that sterile neutrinos are not supported by CMB.

But (!) This constraint implies degenerate mass hierarchy (DH), $m_i = \sum m_\nu/3$, and many other model assumptions. Results for other ν mass spectra have been obtained recently ($m_0 \equiv m_{\min}$):[a]

	Base			Base+SNe		
	DH	NH	IH	DH	NH	IH
$\Lambda\text{CDM} + \sum m_\nu$						
ω_c	0.1194 ± 0.0009	0.1192 ± 0.0009	0.1191 ± 0.0009	0.1193 ± 0.0009	0.1191 ± 0.0009	0.1189 ± 0.0009
ω_b	0.02242 ± 0.00013	$0.02242^{+0.00013}_{-0.00014}$	0.02243 ± 0.00013	0.02243 ± 0.00013	0.02244 ± 0.00013	0.02244 ± 0.00013
Θ_s	1.04100 ± 0.00029	1.04100 ± 0.00029	1.04100 ± 0.00029	1.04102 ± 0.00029	1.04103 ± 0.00029	1.04103 ± 0.00029
τ	$0.0554^{+0.0068}_{-0.0076}$	$0.0569^{+0.0066}_{-0.0076}$	$0.0585^{+0.0069}_{-0.0076}$	0.0556 ± 0.0071	$0.0573^{+0.0069}_{-0.0076}$	$0.0588^{+0.0068}_{-0.0077}$
n_s	0.9666 ± 0.0036	0.9668 ± 0.0037	0.9671 ± 0.0037	0.9669 ± 0.0036	0.9673 ± 0.0036	0.9675 ± 0.0037
$\ln[10^{10} A_s]$	$3.048^{+0.014}_{-0.015}$	$3.051^{+0.014}_{-0.015}$	3.053 ± 0.015	3.046 ± 0.014	3.049 ± 0.014	$3.052^{+0.014}_{-0.015}$
m_0 (eV)	< 0.040	< 0.040	< 0.042	< 0.038	< 0.038	< 0.039
$\sum m_\nu$ (eV)	< 0.12	< 0.15	< 0.17	< 0.11	< 0.14	< 0.16
H_0 (km/s/Mpc)	$67.81^{+0.54}_{-0.46}$	$67.50^{+0.49}_{-0.44}$	67.22 ± 0.45	$67.89^{+0.52}_{-0.45}$	67.59 ± 0.44	67.33 ± 0.43
Tension with Cepheides						
σ_8	$0.814^{+0.010}_{-0.007}$	$0.806^{+0.009}_{-0.006}$	$0.799^{+0.008}_{-0.006}$	$0.815^{+0.010}_{-0.007}$	$0.806^{+0.008}_{-0.006}$	$0.799^{+0.008}_{-0.006}$
S_8	0.827 ± 0.011	0.823 ± 0.011	0.820 ± 0.011	0.826 ± 0.011	0.822 ± 0.011	0.818 ± 0.011
$\Delta\chi^2 = \chi^2 - \chi^2_{IH}$	-2.89	-0.95	0	-2.73	-1.27	0

Looking ahead, it is instructive to compare these results with the current constraints derived from the oscillation experiments: $\sum m_\nu^{\text{NH}} \gtrsim 0.056$ eV and $\sum m_\nu^{\text{IH}} \gtrsim 0.1$ eV (see p. 437 for details).

[a] Sh. R. Choudhury & S. Hannestad, "Updated results on neutrino mass and mass hierarchy from cosmology with Planck 2018 likelihoods," JCAP07(2020)037, arXiv:1907.12598 [astro-ph.CO].

2.3.1 A short summary of neutrino mass sum.

Current global fits to data from neutrino oscillation experiments obtained constraints for two different mass squared splittings (see Sect. **12.2.2**, p. 437 for more details and explanations):

$$m_2^2 - m_1^2 = 7.42^{+0.21}_{-0.20} \times 10^{-5}\ \text{eV}^2 \quad (\text{“solar” for NH and IH})$$
$$|m_3^2 - m_1^2| = \left(2.51^{+0.027}_{-0.027}\ \text{or}\ 2.49^{+0.026}_{-0.028}\right) \times 10^{-3}\ \text{eV}^2 \quad (\text{“atmospheric” for NH or IH})$$

These measurements imply that at least two of the neutrino mass eigenstates are nonzero and two scenarios are possible, related to the ordering of the masses:

$m_1 < m_2 < m_3$ for normal hierarchy (NH) or $m_3 < m_1 < m_2$ for inverted hierarchy (IH).

These data set a lower bounds on $\sum m_\nu \equiv \sum_{i=1}^{3} m_i$:

$$\sum m_\nu^{\text{NH}} > 0.0587 \pm 0.0003\ \text{eV} \quad \text{and} \quad \sum m_\nu^{\text{IH}} > 0.0983 \pm 0.0006\ \text{eV}.$$

The cosmology sets upper limit on the value

$$\Omega_\nu = \frac{\rho_\nu}{\rho_{\text{crit}}} = \frac{G}{\pi^2 H_0^2} \sum_i^{N_\nu} \int \frac{d^3 p_i E_i}{e^{E_i/T_{\nu,i}} + 1} \approx \frac{\sum m_\nu}{93.14\, h^2\ \text{eV}}.$$

The approximation on the right-hand side is good for the case of degenerate masses (very unlikely) and when all neutrinos are non-relativistic (may or may not be true today). In any case, the approximation is used in most cosmological analyses.

Here and below, the today Hubble expansion rate is parameterized as $H_0 \equiv 100h\,\text{km}\,\text{s}^{-1}\,\text{Mpc}^{-1}$ and $h = 0.674(5)$ is the normalized Hubble rate.

The critical density is

$$\rho_{\text{crit}} = \frac{3H_0^2}{8\pi G} = \frac{3H_0^2 M_{\text{Pl}}^2}{8\pi} = \begin{cases} 1.87834(4) \times 10^{-29} h^2 \text{ g/cm}^3 \approx 0.853 \times 10^{-29} \text{ g/cm}^3 \\ 1.053672(24) \times 10^{-5} h^2 \text{ GeV/cm}^3 \approx 0.479 \times 10^{-5} \text{ GeV/cm}^3 \end{cases}$$

The Standard Models of particle physics and cosmology make a robust prediction that the CνB number density is ≈ 112 cm^{-3} per species (see p. 147). Taking it into account implies that massive neutrinos constitute the following fraction of the total matter density in today's Universe:

$$\text{Mixing} \implies \boxed{3.81 \times 10^{-3} < \frac{\rho_\nu}{\rho_m} = \frac{\Omega_\nu}{\Omega_m} = \frac{\sum m_\nu}{29.34\, h^2 \text{ eV}} < 9.52 \times 10^{-3}} \impliedby \text{CMB+BAO}$$

Long before the neutrino's fraction was more essential.

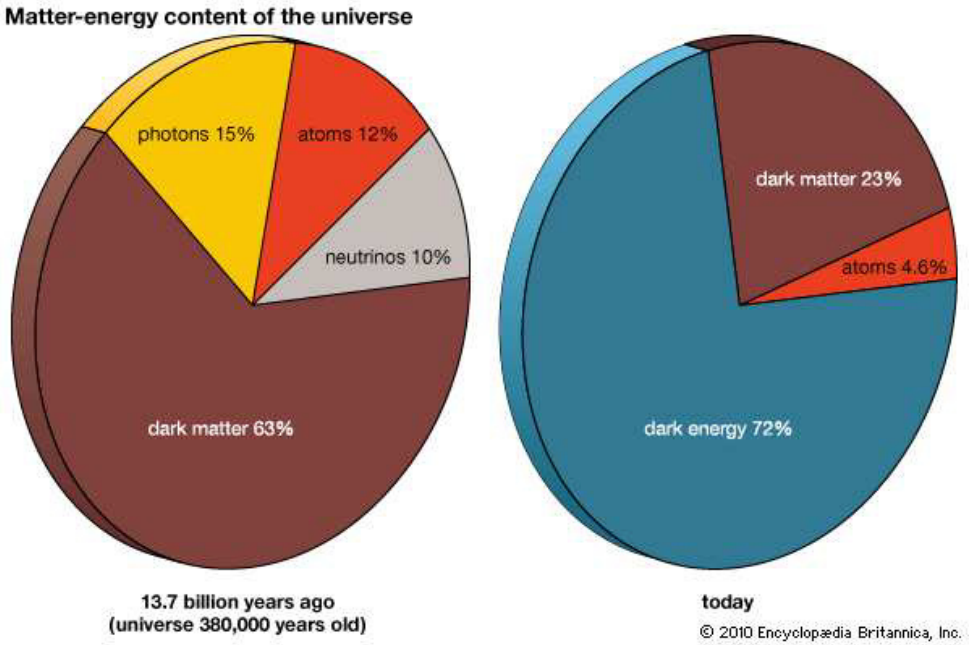

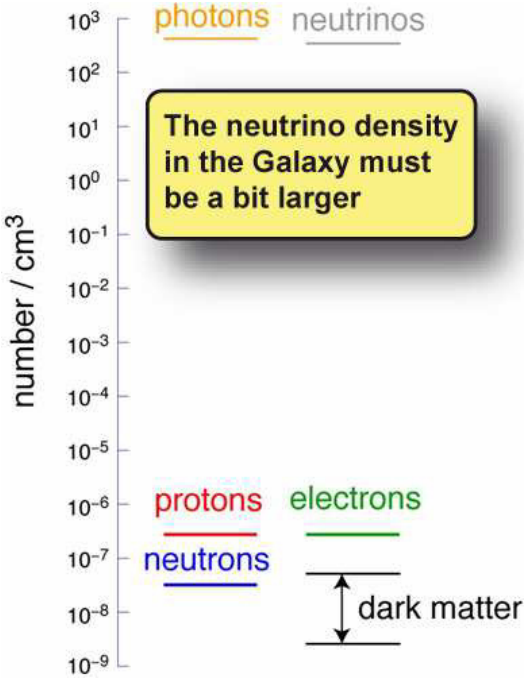

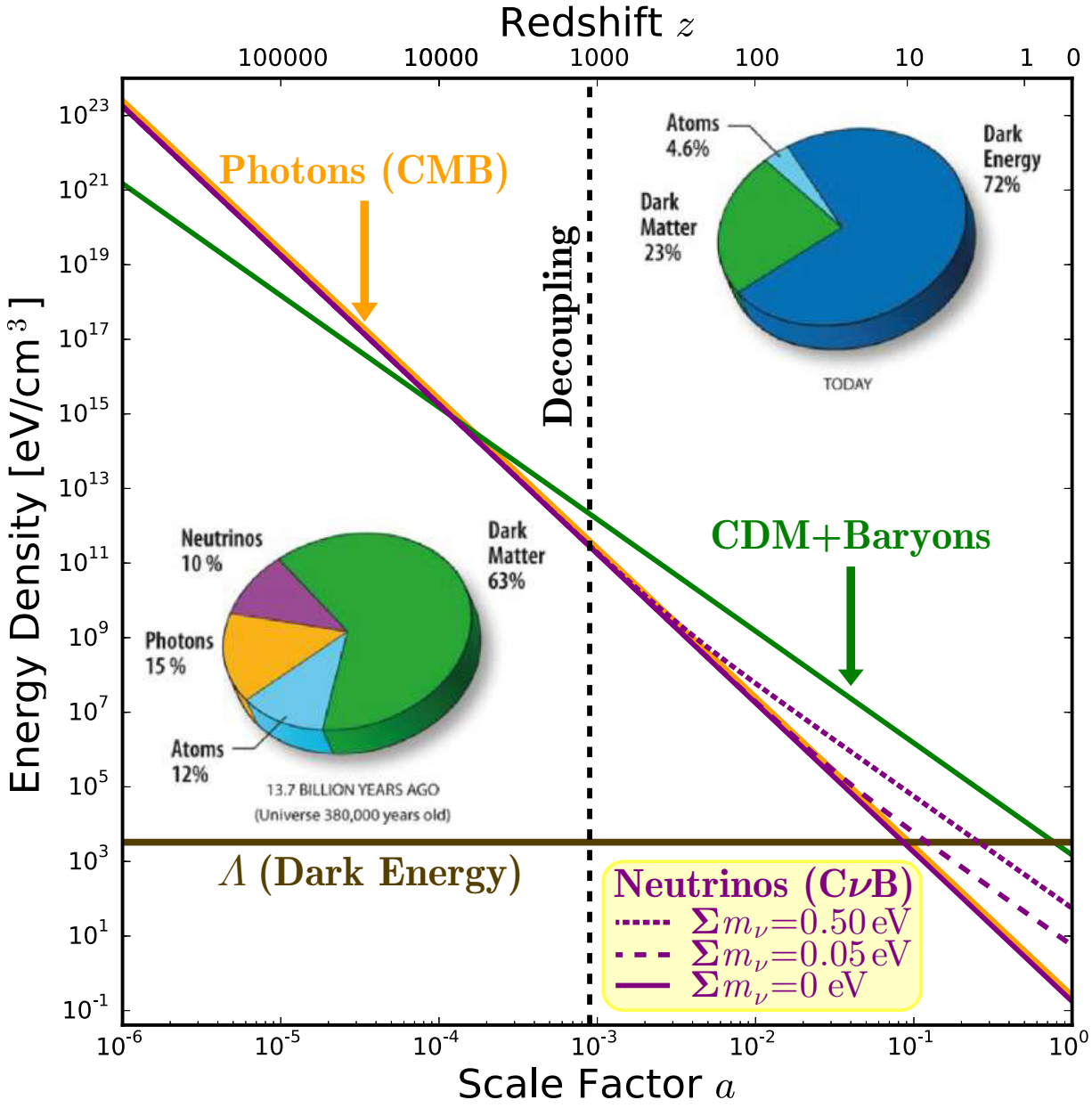

[Figure is taken from J. Carlstrom (for the CMB-S4 collaboration), "CMB Stage 4 Update," AAAC January 28, 2016.]

◁ Neutrinos were ultrarelativistic at the γ decoupling epoch ($z \sim 10^3$) and are a part of matter budget today ($z = 0$).

Reminder: The scale factor $a(t)$ is defined by

$$d(t) = a(t)d(t_0), \quad a(t_0) = 1,$$

where $d(t)$ is the proper distance at epoch t and $t_0 = 13.799 \pm 0.021\,\text{Gyr}$ is the present age of the Universe. From the geodesic equation for a light wave

$$ds^2 = \frac{a^2 dr^2}{1 - kr^2} - dt^2 = 0$$

($c = 1$) it follows that

$$1 + z = \frac{\lambda_{\text{obsv}}}{\lambda_{\text{emit}}} = \frac{a(t_0)}{a(t)}.$$

Derivation of the redshift effect.

The geodesic equation for a light wave in a Friedmann Universe reads

$$dt^2 = \frac{a^2 dr^2}{1-kr^2} \quad \text{or} \quad dt = \pm\frac{a(t)dr}{\sqrt{1-kr^2}},$$

$$\Downarrow$$

$$\int_t^{t_0} \frac{dt'}{a(t')} = +\int_0^R \frac{dr}{\sqrt{1-kr^2}} = \int_{t+\lambda(t)}^{t_0+\lambda(t_0)} \frac{dt'}{a(t')},$$

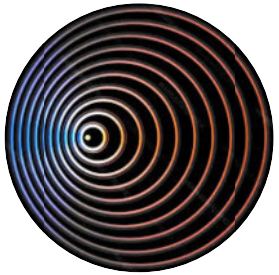

since, due to changing the metric, the wavelength of light (λ) is not the same for the two considered times t and t_0 at fixed positions of the source and detector (recall that $c = 1$). After simple manipulations we get:

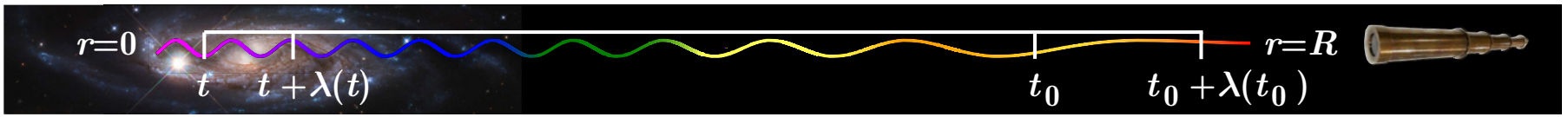

$$\int_t^{t_0} = \int_t^{t+\lambda(t)} + \int_{t+\lambda(t)}^{t_0} = \int_{t+\lambda(t)}^{t_0+\lambda(t_0)} = \int_{t+\lambda(t}^{t_0} + \int_{t_0}^{t_0+\lambda(t_0)}$$

$$\Downarrow$$

$$\int_{t_0}^{t_0+\lambda(t_0)} \frac{dt'}{a(t')} = \int_t^{t+\lambda(t)} \frac{dt'}{a(t')}.$$

For a short period of one light wave cycle, the scale factor is essentially a constant; this is true for both $a(t_0)$ and $a(t)$, that is, in a very good precision, $a(t_0+\lambda(t_0)) = a(t_0)$ and $a(t+\lambda(t)) = a(t)$. Thus

$$\lambda(t_0)/a(t_0) = \lambda(t)/a(t).$$

Then using the definition for the redshift, $z = (\lambda_{\text{obsv}} - \lambda_{\text{emit}})/\lambda_{\text{emit}} = [\lambda(t_0) - \lambda(t)]/\lambda(t)$, we obtain

$$1 + z = a(t_0)/a(t).$$

2.4 Cosmological probes of the neutrino mass (a bit obsolete).

Probe	Current $\sum m_\nu$ (eV)	Forecast $\sum m_\nu$ (eV)	Key Systematics
CMB Primordial	1.3	0.6	Recombination
CMB Primordial + Distance	0.58	0.35	Distance measurements
Lensing of CMB	∞	$0.2 - 0.05$	NG of Secondary anisotropies
Galaxy Distribution	0.6	0.1	Nonlinearities, Bias
Lensing of Galaxies	0.6	0.07	Baryons, NL, Photometr. redshifts
Lyman α (121.6 nm)	0.2	0.1	Bias, Metals, QSO continuum
21 cm	∞	$0.1 - 0.006$	Foregrounds, Astrophys. modeling
Galaxy Clusters	0.3	0.1	Mass Function, Mass Calibration
Core-Collapse SN	∞	$\theta_{13} > 0.001^*$	Emergent ν spectra

* **If the neutrinos have the normal mass hierarchy, supernovae spectra are sensitive to $\theta_{13} \sim 10^{-3}$. The inverted hierarchy produces a different signature, but one that is insensitive to θ_{13}.**

"Current" denotes published (before 2011) 95% C.L. upper bound on $\sum m_\nu$ ($\approx 12.5\Omega_\nu/\Omega_m$ eV) obtained from currently operating surveys, while "Forecast" indicates the forecasted 95% sensitivity on $\sum m_\nu$ from future observations. The numbers are derived for a minimal "vanilla+m_ν" model.[a]

[a] K. N. Abazajian *et al.*, "Cosmological and astrophysical neutrino mass measurements," Astropart. Phys. **35** (2011) 177–184, arXiv:1103.5083 [astro-ph.CO].

Parameters of the vanilla+m_ν model

- amplitude of fluctuations (A_s),
- slope of the spectral index of the primordial fluctuations (n_s),
- baryon density ($\Omega_b h^2$),
- matter density ($\Omega_m h^2$),
- epoch of reionization (τ),
- present-day Hubble expansion rate (H), and
- $\sum m_\nu$.

Main physical assumptions

- Universe starts with a hot big bang ($a = 0$).
- Universe starts almost homogeneous and isotropic.
- Universe is flat.
- Early evolution ($z > 3000$) is radiation-dominated ($a \propto t^{1/2}$).
- From $z \sim 3000$ to ~ 0.5, matter-dominated ($a \propto t^{2/3}$).
- Late evolution ($z \lesssim 0.5$), dark-energy dominated ($d^2a/dt^2 > 0$).
- Initially small fluctuations collapse and form structure.

Digression: Bose & Fermi statistics.

The ultrarelativistic Fermi-Dirac and Bose-Einstein distribution functions are given by ($c = \hbar = k_B = 1$)

$$f(p) = \frac{1}{\exp(p/T) \pm 1}, \quad (+ \text{ for FD}, \ - \text{ for BE}).$$

Let's denote

$$I^n_\pm = \int_0^\infty \frac{x^n dx}{e^x \pm 1}.$$

Then

$$I^n_- - I^n_+ = 2\int_0^\infty \frac{x^n dx}{e^{2x} - 1} = \frac{1}{2^n} I^n_- \quad \Longrightarrow \quad \boxed{\frac{I^n_+}{I^n_-} = 1 - \frac{1}{2^n}}.$$

2.5 Kinetics of neutrinos in early Universe (very briefly).

In the approximation of a weakly interacting gas or plasma, the fundamental equation governing the evolution of particle abundances in the expanding Universe is the general-relativistic Boltzmann equation (BE). [a]

$$\hat{L}f = \sum C[f]. \tag{2}$$

Here $\hat{L}$ is the Liouville operator, $f = f(p, x)$ is distribution function, C is the collision integral (CI) and sum is over all possible interactions. In the general case $\hat{L}$ is defined through Christoffel symbols,

$$\hat{L} = p^\mu \frac{\partial}{\partial x^\mu} - \Gamma^\mu_{\nu\sigma} p^\nu p^\sigma \frac{\partial}{\partial p^\mu}, \quad \Gamma^\mu_{\nu\sigma} = \frac{1}{2} g^{\mu\lambda} \left(g_{\lambda\sigma,\nu} + g_{\nu\lambda,\sigma} - g_{\nu\sigma,\lambda} \right),$$

but if all distributions are homogeneous and isotropic, that is $f = f(|\mathbf{p}|, t)$, it is drastically simplified:

$$\hat{L} = \frac{\partial}{\partial t} - \frac{\dot{a}}{a} |\mathbf{p}| \frac{\partial}{\partial |\mathbf{p}|}.$$

Here $a = a(t)$ is the cosmic (Robertson-Walker) scale factor – a key parameter of Friedmann's equations (that follow from Einstein equation for perfect fluid and cosmological principle),

$$3 \frac{\dot{a}^2 + k}{a^2} = 8\pi G\rho + \Lambda, \quad \text{(FI)} \quad 3 \frac{\ddot{a}}{a} = -4\pi G(\rho + 3p) + \Lambda, \quad \text{(FII)}$$

G and Λ are the gravitational (Newton) and cosmological constants, $\rho = \rho(t)$ and $p = p(t)$ are the density and pressure, respectively, k is the integer constant $(0, \pm 1)$ throughout a particular solution and defines the shape of the Universe, $\dot{a}/a \equiv H(t)$ is the Hubble parameter; $c = 1$ as usual.

[a] See, e.g., J. Bernstein, Kinetic theory in the expanding universe (Cambridge Monographs on Mathematical Physics, Cambridge University Press, New York, New Rochelle, Melbourne, Sydney, 1988) and Refs. at p. 158.

The CI for fermion 1 participating in a 2-particle process $12 \to 34$ can be written as

$$C[f_1] = \frac{1}{2E_1}\int\left(\prod_{i=2}^{4}\frac{d^3p_i}{(2\pi)^3 2E_i}\right)[(1-f_1)(1-f_2)f_3f_4 - f_1f_2(1-f_3)(1-f_4)]$$
$$\times\langle|M_{12\to34}|^2\rangle(2\pi)^4\delta^4(p_1+p_2-p_3-p_4),$$

$\langle\cdots\rangle$ denotes symmetrization (multiplication to $1/2$ for each pair of identical particles in initial or final states) and summation over all spin states but 1. The main reactions are shown in two Tables, where the matrix elements were calculated in the 4-fermion approximation for massless neutrinos.

Reaction	$\langle\|M_{12\to34}\|^2\rangle$
$\nu_e\overline{\nu}_e \to \nu_e\overline{\nu}_e$	$128G_F^2(p_1p_4)(p_2p_3)$
$\nu_e\overline{\nu}_{\mu,\tau} \to \nu_e\overline{\nu}_{\mu,\tau}$	$32G_F^2(p_1p_4)(p_2p_3)$
$\nu_e\overline{\nu}_e \to \nu_{\mu,\tau}\overline{\nu}_{\mu,\tau}$	$128G_F^2(p_1p_4)(p_2p_3)$
$\nu_e\nu_{e,\mu,\tau} \to \nu_e\nu_{e,\mu,\tau}$	$32G_F^2(p_1p_2)(p_3p_4)$
$\nu_e e^- \to \nu_e e^-$	$32G_F^2[(C_V+C_A)^2(p_1p_2)(p_3p_4) + (C_V-C_A)^2(p_1p_4)(p_2p_3) - (C_V^2-C_A^2)m_e^2(p_1p_3)]$
$\nu_e e^+ \to \nu_e e^+$	$32G_F^2[(C_V+C_A)^2(p_1p_4)(p_2p_3) + (C_V-C_A)^2(p_1p_3)(p_2p_4) - (C_V^2-C_A^2)m_e^2(p_1p_2)]$
$\nu_e\overline{\nu}_e \to e^-e^+$	$32G_F^2[(C_V+C_A)^2(p_1p_4)(p_2p_3) + (C_V-C_A)^2(p_1p_3)(p_2p_4) + (C_V^2-C_A^2)m_e^2(p_1p_2)]$

Reaction $(\alpha, \beta = \mu, \tau)$	$\langle\lvert M_{12\to34}\rvert^2\rangle$
$\nu_\alpha\overline{\nu}_\alpha \to \nu_\alpha\overline{\nu}_\alpha$	$128G_F^2(p_1p_4)(p_2p_3)$
$\nu_\alpha\overline{\nu}_\alpha \to \nu_e\overline{\nu}_e$	$32G_F^2(p_1p_4)(p_2p_3)$
$\nu_\alpha\overline{\nu}_\beta \to \nu_\alpha\overline{\nu}_\beta\ (\beta \neq \alpha)$	$32G_F^2(p_1p_4)(p_2p_3)$
$\nu_\alpha\overline{\nu}_\alpha \to \nu_\beta\overline{\nu}_\beta\ (\beta \neq \alpha)$	$32G_F^2(p_1p_4)(p_2p_3)$
$\nu_\alpha\overline{\nu}_e \to \nu_\alpha\overline{\nu}_e$	$32G_F^2(p_1p_4)(p_2p_3)$
$\nu_\alpha\nu_{e,\mu,\tau} \to \nu_\alpha\nu_{e,\mu,\tau}$	$32G_F^2(p_1p_2)(p_3p_4)$
$\nu_\alpha e^- \to \nu_\alpha e^-$	$32G_F^2\{(2-C_V-C_A)^2(p_1p_2)(p_3p_4)+(C_V-C_A)^2(p_1p_4)(p_2p_3)$ $-[(1-C_V)^2-(1-C_A)^2]m_e^2(p_1p_3)\}$
$\nu_\alpha e^+ \to \nu_\alpha e^+$	$32G_F^2\{(2-C_V-C_A)^2(p_1p_4)(p_2p_3)+(C_V-C_A)^2(p_1p_2)(p_3p_4)$ $-[(1-C_V)^2-(1-C_A)^2]m_e^2(p_1p_3)\}$
$\nu_\alpha\overline{\nu}_\alpha \to e^-e^+$	$32G_F^2\{(2-C_V-C_A)^2(p_1p_4)(p_2p_3)+(C_V-C_A)^2(p_1p_3)(p_2p_4)$ $-[(1-C_V)^2-(1-C_A)^2]m_e^2(p_1p_2)\}$

Here and below, $C_V = \frac{1}{2} + 2\sin^2\theta_W$ and $C_A = \frac{1}{2}$, θ_W is the Weinberg angle or weak mixing angle ($\sin^2\theta_W = 1 - m_W^2/m_Z^2 = 0.23153(4)$).

[The data in tables are borrowed from S. Hannestad & J. Madsen, "Neutrino decoupling in the early universe," Phys. Rev. D **52** (1995) 1764–1769, astro-ph/9506015 [astro-ph]. Derivation of the CI can be found in R. V. Wagoner, "The early Universe," in "Physical cosmology" (Les Houches 32, NH, 1979) (Elsevier, 1980), ed. by R. Balian, J. Audouze, and D. N. Schramm, pp. 398–442. A useful approach (though not within the framework of the general theory of relativity) is given in К. П. Гуров. «Основания кинетической теории, метод Н. Н. Боголюбова». М. «Наука». 1966.]

There exists a corresponding set of equations for the antineutrino distribution functions. In absence of an asymmetry it is not needed since neutrinos and antineutrinos follow the same evolution.

As an example, Figure ▷ shows the (normalized) effective temperatures of $\nu_{e,\mu,\tau}$, defined as

$$T_{\text{eff}} = \frac{p_\nu}{\ln\left[1/f(p_\nu) - 1\right]}$$

and evaluated after a numerical solution of the above equations.[a] Although the non-equilibrium effect is less than $\approx 0.8\%$, it is not negligible.

The most serious drawbacks of this calculation is in neglecting the neutrino masses, mixing, and coherent scattering (see p. 163).

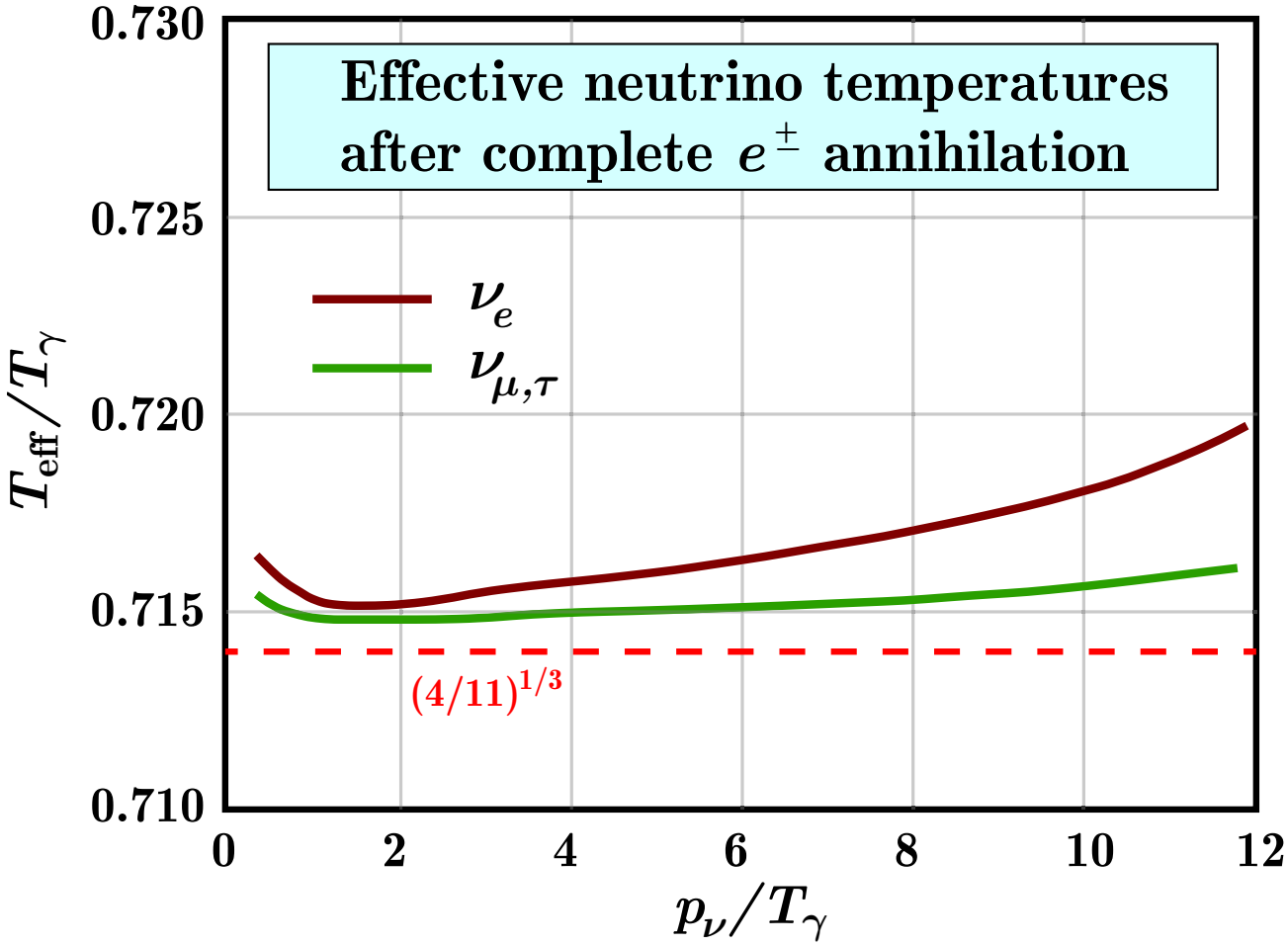

[a] S. Hannestad & J. Madsen, "Neutrino decoupling in the early universe," Phys. Rev. D **52** (1995) 1764–1769, astro-ph/9506015.

A more general form of the collision integral

The CI for particle a participating in the reactions $a + B \longleftrightarrow C$ (where B and C are generally multiparticle states) is

$$C[f_a] = \frac{1}{2E_a} \sum_{B,C} \int \left(\prod_{i \in B+C} \frac{d^3 p_i}{(2\pi)^3 2E_i} \right) (2\pi)^4 \delta^4 (p_a + p_B - p_C)$$
$$\times \left[\langle |M_{C \to aB}|^2 \rangle \prod_{i \in a+B} (1 - \zeta_i f_i) \prod_{i \in C} f_i - \langle |M_{aB \to C}|^2 \rangle \prod_{i \in C} (1 - \zeta_i f_i) \prod_{i \in a+B} f_i \right],$$

where $\zeta_i = -1$ for bosons and $+1$ for fermions. In thermal equilibrium $C[f_a] \equiv C[f_a^{\mathsf{eq}}] = 0$ and

$$f_i^{\mathsf{eq}} = f_i^{\mathsf{eq}}(E_i, \mu_i, T_i) = \frac{1}{\exp\left[(E_i - \mu_i)/T_i\right] + \zeta_i}, \quad i \in a + B + C. \tag{3}$$

The chemical potential μ_i and temperature T_i are functions of time.

Problem: Prove that $C[f_a^{\mathsf{eq}}] = 0$ assuming T invariance and conservation of the chemical potentials.

- The chemical potentials conserve only in thermal equilibrium and any system evolves to this state if the reaction rates are sufficiently high.
- In elastic scattering, the chemical potential conservation condition is met automatically. Therefore, elastic reactions bring the system to the equilibrium state, forming the canonical energy dependence of the distribution functions (3).
- For bosons, the equilibrium solution (3) is not unique (Bose condensate).
- The CI reduces to the usual Boltzmann CI for non-identical particles as $\zeta_i = 0$ (low particle density limit).

Let's very schematically explain the origin of the factors f_i and $(1 \pm f_i)$ in the integrand of CI.[a]

The probability of transition $|a + B\rangle \to |C\rangle$ during a (proper) time interval Δt in a volume ΔV is

$$|\langle C|\mathbf{S} - \mathbf{1}|a + B\rangle|^2 \propto \Delta V \Delta t \delta^4(p_a + p_B - p_C)|\langle C|\mathbf{T}|a + B\rangle|^2 \tag{4}$$

in terms of the standard QFT $\mathbf{S}$ and $\mathbf{T}$ matrices. If a_j and $a_j^\dagger$ are the annihilation and creation operators for particle j in a momentum eigenstate, then the operator $\mathbf{T}$ must be proportional to $a_{c_1}^\dagger a_{c_2}^\dagger \ldots a_a a_{b_1} a_{b_2} \ldots$, where $b_1, b_2, \ldots \in B$ and $c_1, c_2, \ldots \in C$ for such a transition.

Let's remind the standard definition for the action of the operators a_j and $a_j^\dagger$ on the Fock state vector of the particle j in the occupation number representation:

Bosons:

$$a_j \; |n_1, n_2, \ldots, n_j, \ldots\rangle = \begin{cases} \sqrt{n_j} \; |n_1, n_2, \ldots, n_j - 1, \ldots\rangle & \text{if } n_j \geq 1, \\ 0 & \text{if } n_j = 0. \end{cases}$$

$$a_j^\dagger \; |n_1, n_2, \ldots, n_j, \ldots\rangle = \sqrt{n_j + 1} \; |n_1, n_2, \ldots, n_j + 1, \ldots\rangle.$$

Fermions:

$$a_j \; |n_1, n_2, \ldots, n_j, \ldots\rangle = \begin{cases} (-1)^{n_1 + n_2 \ldots + n_{j-1}} |n_1, n_2, \ldots, n_{j-1}, 0, \ldots\rangle & \text{if } n_j = 1, \\ 0 & \text{if } n_j = 0; \end{cases}$$

$$a_j^\dagger \; |n_1, n_2, \ldots, n_j, \ldots\rangle = \begin{cases} (-1)^{n_1 + n_2 \ldots + n_{j-1}} |n_1, n_2, \ldots, n_{j-1}, 1, \ldots\rangle & \text{if } n_j = 0, \\ 0 & \text{if } n_j = 1. \end{cases}$$

The factors $\sqrt{n_j}$ and $\sqrt{n_j + 1}$ appear since each multi-particle bosonic state is properly normalized.

[a] Here we partially follow the review by R. V. Wagoner, "The early Universe," in "Physical cosmology" (Les Houches 32, NH, 1979) (Elsevier, 1980), ed. by R. Balian, J. Audouze, and D. N. Schramm, pp. 398–442.

Therefore for both cases we can write (although it is a little bit tricky):

$$a_j \; |n_1, n_2, \ldots, n_j, \ldots\rangle = (-1)^{s_j} \sqrt{n_j} \; |n_1, n_2, \ldots, n_j - 1, \ldots\rangle,$$
$$a_j^\dagger \; |n_1, n_2, \ldots, n_j, \ldots\rangle = (-1)^{s_j} \sqrt{1 - \zeta_j n_j} \; |n_1, n_2, \ldots, n_j + 1, \ldots\rangle.$$

Here $\zeta_i = -1(+1)$ for bosons (fermions), the phase integer s_j plays no role, as well as formal definitions of the unphysical "states" with negative occupation numbers or with $n_j = 2$ for fermions.

The average number of transitions $|a(p_a) + B\,(p_{b_1}, p_{b_2}, \ldots)\rangle \to |C\,(p_{c_1}, p_{c_2}, \ldots)\rangle$ from momentum elements[a] $d\Pi_a, d\Pi_{b_1}, d\Pi_{b_2}, \ldots$ to $d\Pi_{c_1}, d\Pi_{c_2}, \ldots$ occurring within the (proper) space-time volume $\Delta V \Delta t$ must be of the form (up to δ-function)

$$\propto \Delta V \Delta t \; d\Pi_a f_a d\Pi_{b_1} f_{b_1} d\Pi_{b_2} f_{b_2} \cdots d\Pi_{c_1} \left[1 - \zeta_{c_1} f_{c_1}\right] d\Pi_{c_2} \left[1 - \zeta_{c_2} f_{c_2}\right] \cdots \; |M_{a+B\to C}|^2,$$

where now $f_j = \overline{n}_j$ is the distribution function = the number of particles of type j per unit element of (normalized) phase space = the occupation number averaged over "externally statistical conditions".[b]

Similarly, the average number of transitions $|C\,(p_{c_1}, p_{c_2}, \ldots)\rangle \to |a(p_a) + B\,(p_{b_1}, p_{b_2}, \ldots)\rangle$ must be

$$\propto \Delta V \Delta t \; d\Pi_a \left[1 - \zeta_a f_a\right] d\Pi_{b_1} \left[1 - \zeta_{b1} f_{b_1}\right] d\Pi_{b_2} \left[1 - \zeta_{b2} f_{b_2}\right] \cdots d\Pi_{c_1} f_{c_1} d\Pi_{c_2} f_{c_2} \cdots \; |M_{C\to a+B}|^2.$$

This finally leads to the desired result for CI.

In contrast to classical systems, in quantum systems the probabilities of direct and reverse transitions depend not only on the averaged of the relative occupation numbers of the initial states of the colliding particles, but also on the average relative occupation numbers of final states.

[a] $d\Pi_a = \sqrt{-g} d^3 p_a / (2\pi)^3 2E_{\mathbf{p}_a}$, $g = |g_{\mu\nu}|$ and we assume almost flat space-time $\Longrightarrow g = -1$.
[b] The transition from n_j to f_j is the most difficult step of our intuitive derivation.

Including flavor oscillations (very, very briefly)

[We'll come back to this section after we have studied the MSW effect (see Sect. 22).]

To include the neutrino mixing and coherent interactions, the neutrino ensemble is described by generalizing the neutrino density functions (occupation numbers) by the 3×3 density matrix $\boldsymbol{\rho} = ||\rho_{\alpha\beta}(|\mathbf{p}|, t)||$ ($\alpha, \beta = e, \mu, \tau$).[a] The diagonal elements, $\rho_{\alpha\alpha}$, correspond to the usual density functions f_α, while the off-diagonal terms takes into account the neutrino flavor mixing.
The generalized BE for neutrino ν_α is (cf. Eq. (2))

$$\left(\frac{\partial}{\partial t} - H\,|\mathbf{p}|\,\frac{\partial}{\partial |\mathbf{p}|}\right)\boldsymbol{\rho} = -i\left[\mathbf{V}\mathbf{H}_0\mathbf{V}^\dagger + \mathbf{W}, \boldsymbol{\rho}\right] + \mathbf{C}[\boldsymbol{\rho}],$$

where $\mathbf{H}_0 = \mathrm{diag}(m_1^2, m_2^2, m_3^2)/2|\mathbf{p}|$, $\mathbf{V}$ is the vacuum mixing matrix, $\mathbf{W}$ is the matrix responsible for coherent (zero-angle) neutrino-matter interactions,

$$\mathbf{C}[\boldsymbol{\rho}] = ||C[\rho_{\alpha\beta}]||, \quad C[\rho_{\alpha\beta}] = -D\,\rho_{\alpha\beta}, \quad \alpha \neq \beta \quad (D \text{ is a so-called "damping function"}),$$

$$C[\rho_{\alpha\alpha}] = \frac{1}{2E_1}\sum_{\text{reactions}}\int\left(\prod_{i=2}^{4}\frac{d^3p_i}{(2\pi)^3 2E_i}\right)[(1-\rho_{\alpha\alpha})(1-f_2)f_3f_4 - \rho_{\alpha\alpha}f_2(1-f_3)(1-f_4)]$$
$$\times\langle|M_{12\to34}|^2\rangle(2\pi)^4\delta^4(p_1+p_2-p_3-p_4).$$

Particle 1 is ν_α and $\mathbf{p} = \mathbf{p}_1$. If the particle $i = 2$, 3 or 4 is a neutrino ν_β, one must replace f_i with the corresponding diagonal term $\rho_{\beta\beta}$.

[a] G. Sigl & G. Raffelt, "General kinetic description of relativistic mixed neutrinos," Nucl. Phys. B **406** (1993) 423–451; B. H. McKellar & M. J. Thomson, "Oscillating neutrinos in the early universe," Phys. Rev. D **49** (1994) 2710–2728; G. Mangano *et al.*, "Relic neutrino decoupling including flavour oscillations," Nucl. Phys. B **729** (2005) 221–234; P. F. de Salas & S. Pastor, "Relic neutrino decoupling with flavour oscillations revisited," JCAP07(2016)051, arXiv:1606.06986 [hep-ph].

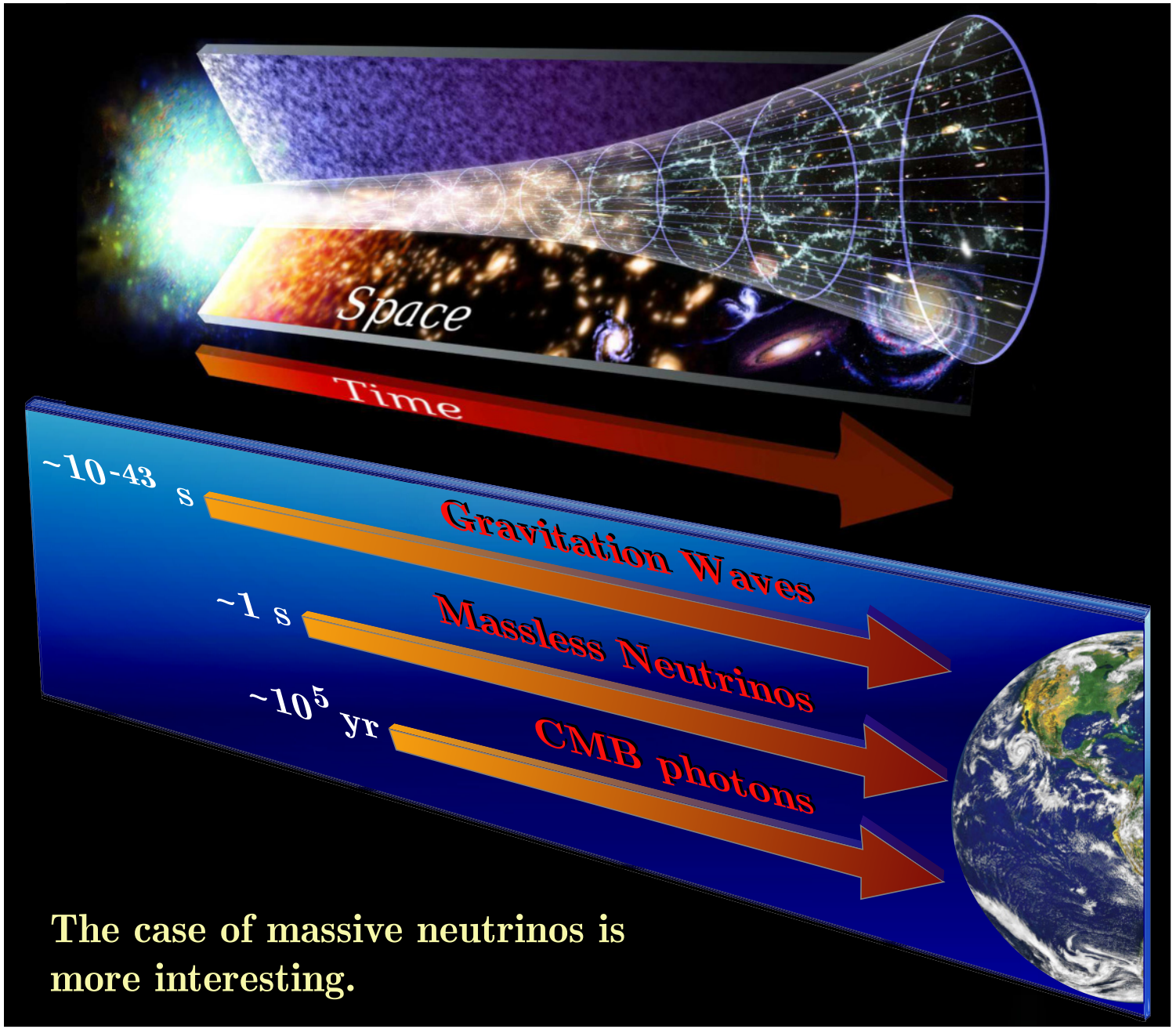
Space
Time
~10-43 s
Gravitation Waves
~1 s
Massless Neutrinos
~10^5 yr
CMB photons
The case of massive neutrinos is more interesting.

2.6 Last scattering surface of neutrinos.

The geodesic equation for neutrinos with definite mass m_ν can be written as

$$v_\nu(t)dt = \pm\frac{adr}{\sqrt{1-kr^2}},$$

where $v_\nu(t) = p_\nu(t)/E_\nu(t) = p_\nu(t)/\sqrt{p_\nu^2(t)+m_\nu^2}$ is the neutrino velocity. Massive neutrinos slow down once they become nonrelativistic, so the integral determining the distance to the last scattering surface (LSS) generalizes to[a]

$$\chi = \int_{t_i}^{t_0}\frac{v(t)dt}{a(t)} = \int_{t_i}^{t_0}\frac{dt}{a(t)}\frac{p_0/a(t)}{\sqrt{[p_0/a(t)]^2+m_\nu^2}},$$

where p_0 is the current neutrino momentum. Massive neutrinos travel more slowly than massless ones so arrive here from much closer distances. The CνB temperature today is $T_\nu = 1.95\times10^{-4}$ eV, so there will be a range of p_0's drawn from a Fermi-Dirac distribution, each of which will be associated with a different distance to the LSS.

Figures at pp. 166 and 167 show, respectively, the comoving distance traveled by a massive neutrino since decoupling as a function of m_ν for two different values of p_0 and the probability that a neutrino with mass m_ν last scatters at a given comoving distance from us (the so-called visibility function; the definition is given in the legend to the Figure).

[a] The details see in G. S. Bisnovatyi-Kogan and Z. F. Seidov, Astron. Zh. **60** (1983) 220–222 [Sov. Astron. **27** (1983) 125-126]; G. S. Bisnovatyi-Kogan and Z. F. Seidov, Astrophys. Space Sci. **102** (1984) 131–154; S. Dodelson and M. Vesterinen, "Cosmic neutrino last scattering surface," Phys. Rev. Lett. **103** (2009) 171301, arXiv:0907.2887 [astro-ph.CO]; Erratum: *ibid.* **103** (2009) 249901.

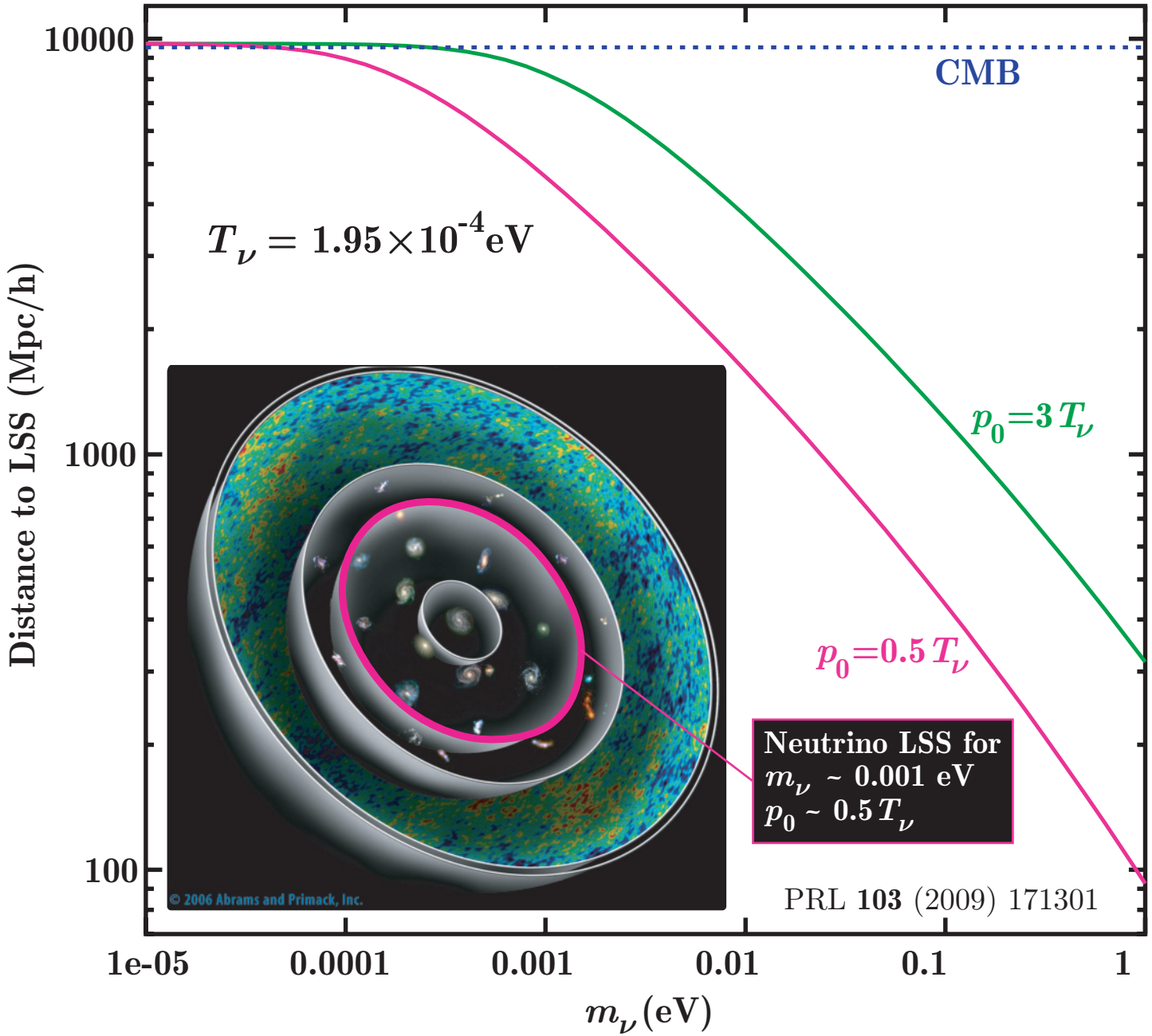
10000
1000
100
Distance to LSS (Mpc/h)
CMB
$T_\nu = 1.95\times10^{-4}$eV
p_0=3 T_ν
p_0=0.5 T_ν
Neutrino LSS for
m_ν ~ 0.001 eV
p_0 ~ 0.5 T_ν
© 2006 Abrams and Primack, Inc.
PRL 103 (2009) 171301
1e-05
0.0001
0.001
0.01
0.1
1
m_ν(eV)

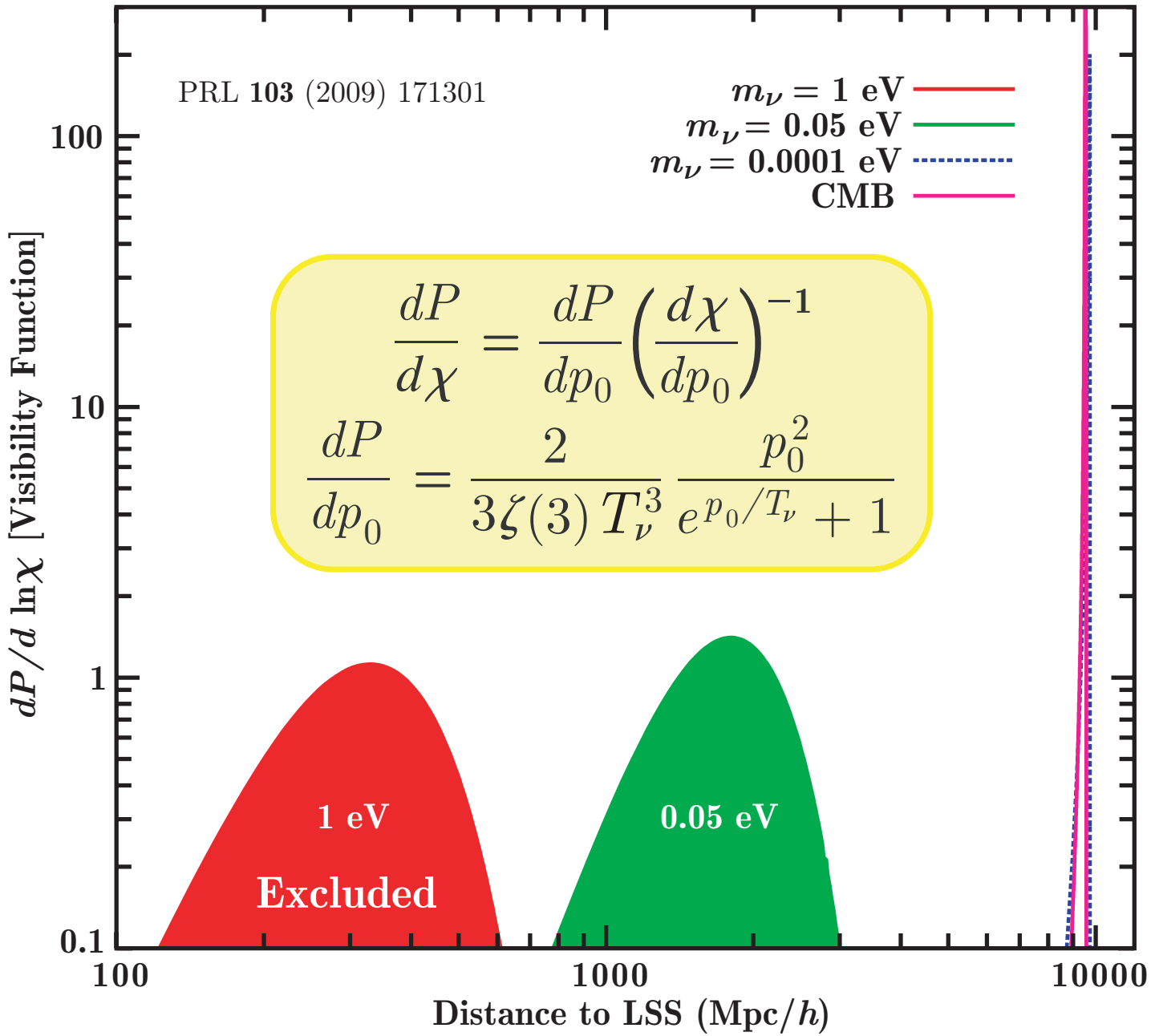
PRL 103 (2009) 171301
$m_\nu = 1$ eV
$m_\nu = 0.05$ eV
$m_\nu = 0.0001$ eV
CMB
$\frac{dP}{d\chi} = \frac{dP}{dp_0}\left(\frac{d\chi}{dp_0}\right)^{-1}$
$\frac{dP}{dp_0} = \frac{2}{3\zeta(3)\,T_\nu^3}\,\frac{p_0^2}{e^{p_0/T_\nu}+1}$
1 eV
Excluded
0.05 eV
100
10
1
0.1
100
1000
10000
$dP/d\ \ln\chi$ [Visibility Function]
Distance to LSS (Mpc/h)

2.7 Neutrino & cosmic structure formation.

Neutrinos with mass on the sub-eV scale behave as a hot component of dark matter. Neutrinos stream out of high-density regions into low-density regions, thereby damping out small-scale density perturbations.

Figure shows the slices of baryon density distribution. All slices are $200\,h^{-1}\mathrm{Mpc}$ wide and show the baryonic mass averaged over the volume of a grid cell. Each grid cell is $\sim 391\,h^{-1}\mathrm{kpc}$. The *top panel* shows a simulation without neutrinos ($\Omega_\nu = 0$). The middle and the *bottom panels* are taken from simulations with $\Omega_\nu = 0.02$ ($\Sigma m_\nu = 0.95$ eV) and $\Omega_\nu = 0.04$ ($\Sigma m_\nu = 1.90$ eV). The baryon density fields in the middle and the *bottom panels* are less evolved relative to the no-neutrino (*top panel*) case.

(The unrealistically large neutrino masses were chosen so as to make the comparison clear.)

The simulations were run with the number of CDM particles $N_{\mathsf{CDM}} = 256^3$ and number of gas particles $N_{\mathsf{gas}} = 512^3$. The density projections were made using the analysis and visualization tool YT (python-based package for analysing ENZO[a]).

[S. Agarwal & H. A. Feldman, "The effect of massive neutrinos on the matter power spectrum," Mon. Not. Roy. Astron. Soc. **410** (2011) 1647–1654.]

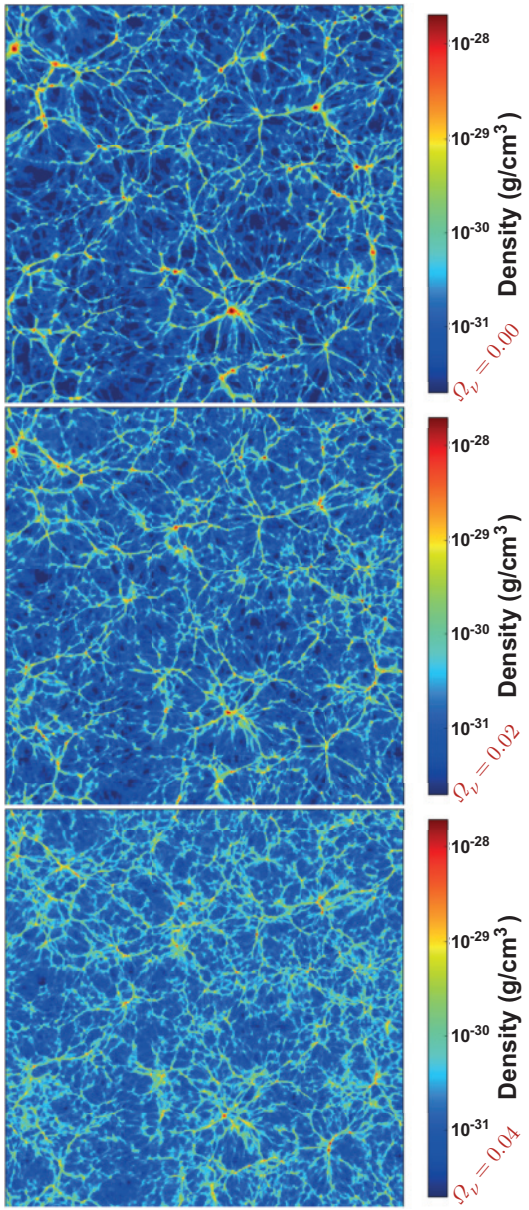

[a] ENZO 1.5 code is a publicly available adaptive mesh refinement, grid-based hybrid code (hydro + N-body) designed to simulate cosmological structure formation; see URL: ⟨ http://lca.ucsd.edu/projects/enzo ⟩.

Again: cosmic structures form by gravitational instability of primordial quantum density fluctuations in the early Universe, but adding a fraction of neutrinos or other hot dark matter may suppresses the small-scale substructures.

Figure on the right shows a simulation which adopted even *less realistic* neutrino masses than those shown in the previous slide (definitely excluded by the modern data). It however clearly shows that the hot neutrinos tend to "wash out" the small cosmological structures.

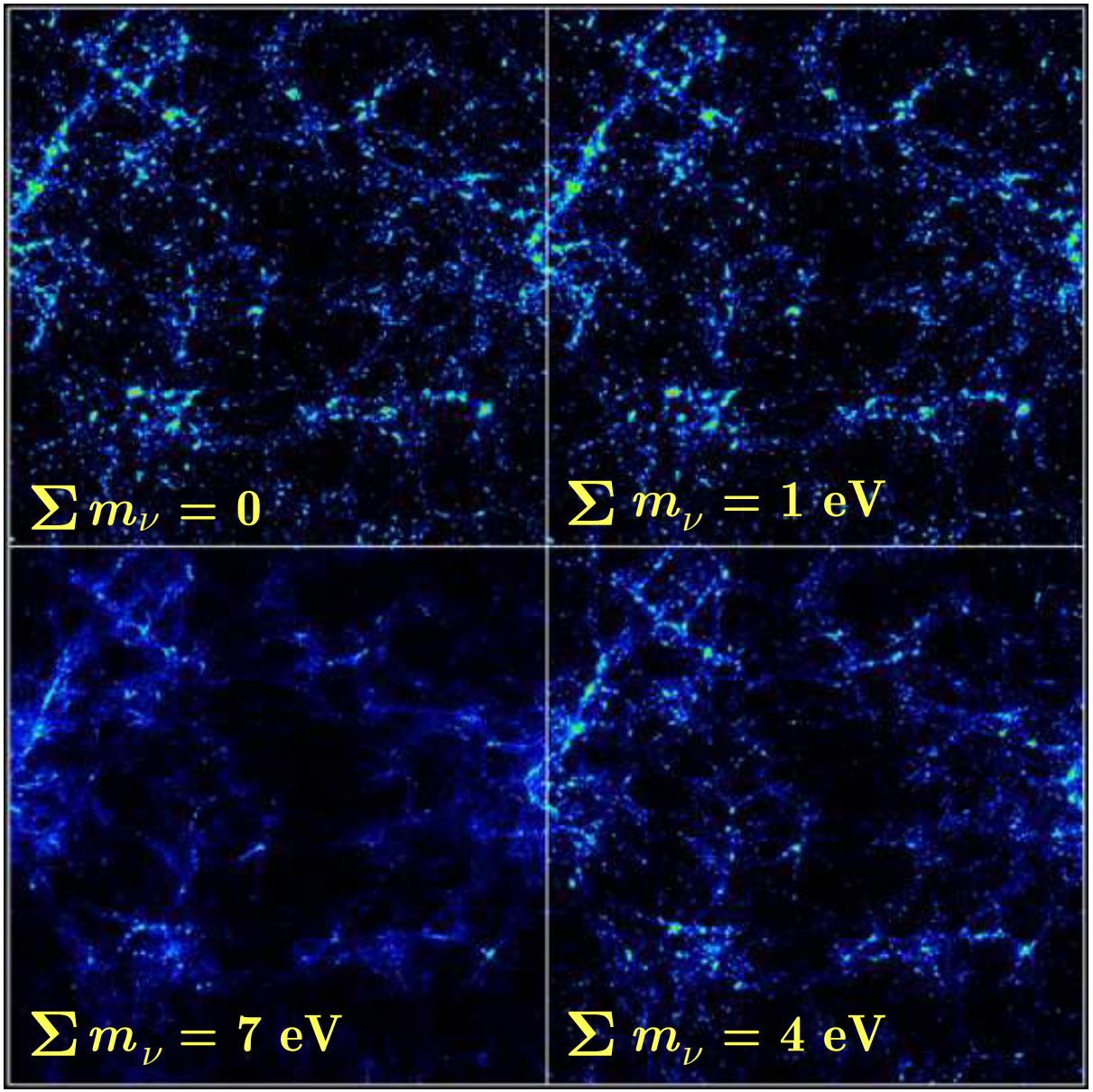

[A. Blondel, "Du soleil à la terre... Descendons-nous des neutrinos?" ⟨http://player.slideplayer.fr/4/1576394/#⟩; see also ⟨http://dpnc.unige.ch/users/blondel/talks/nuphysique-aujourdhui-2010-09-22.pdf⟩.]

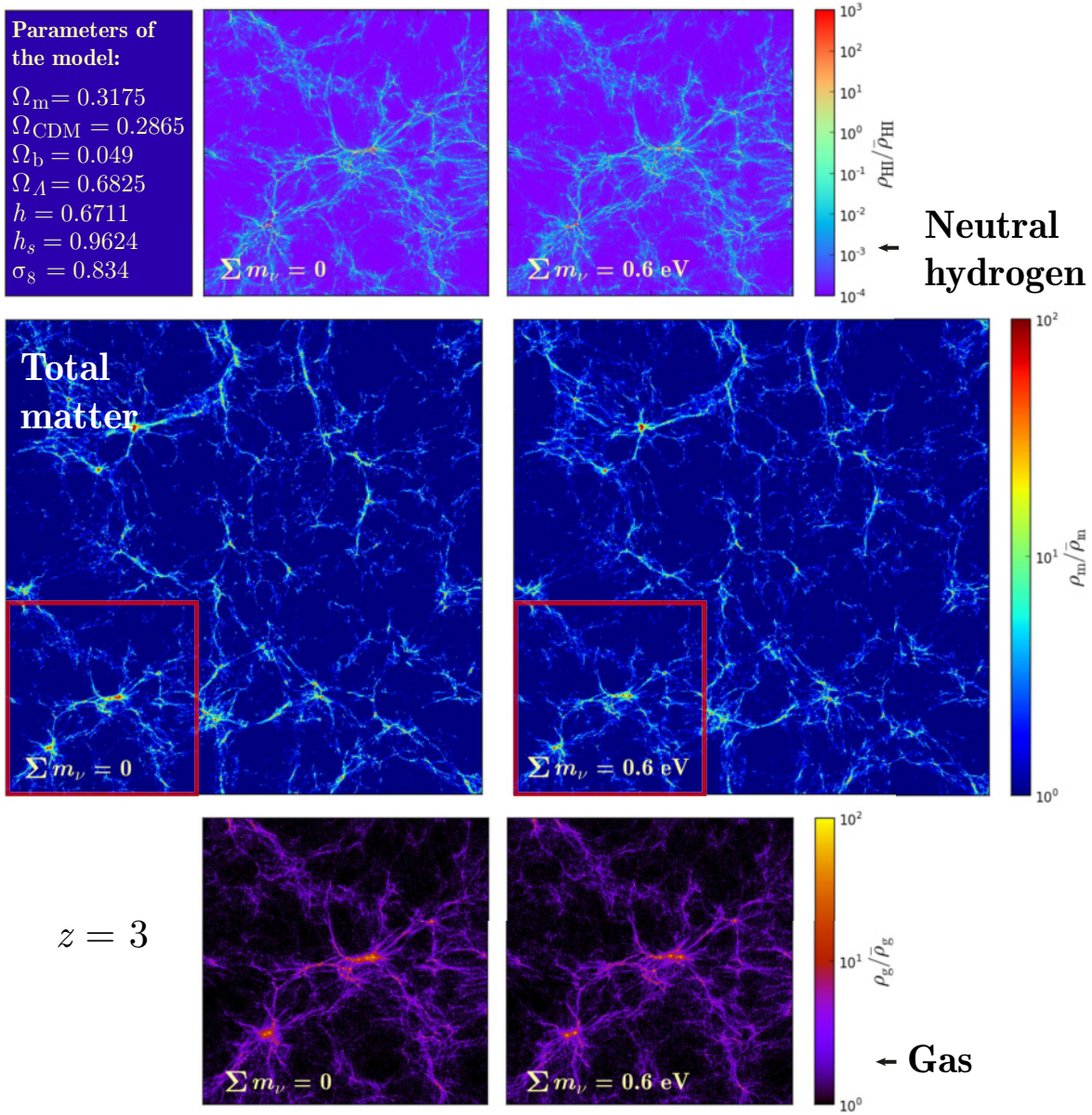

◁ Spatial distribution of neutral Hydrogen (top row), matter (middle row) and gas (bottom row) at $z = 3$ in a flat cosmology ($\Omega_\Lambda + \Omega_{\rm m} = 1$) with massless neutrinos (left) and with $\sum m_\nu = 0.6$ eV (right). The images have been created by taking a slice of $2\ h^{-1}$ Mpc width. The spatial distribution of total matter is shown over the whole box (i.e. in a slice of $50 \times 50 \times 2\ (h^{-1}\ {\rm Mpc})^3$), while the gas and HI images display a zoom over the region marked with a red square. As can be seen, the differences in the spatial distribution of matter, gas, and (in particular) neutral Hydrogen between the two models are very small.

[From F. Villaescusa-Navarro, Ph. Bull, and M. Viel, "Weighing neutrinos with cosmic neutral Hydrogen," ApJ **814** (2015) 146, arXiv:1507.05102 [astro-ph.CO].]

2.8 A cosmic view of neutrino ripples.

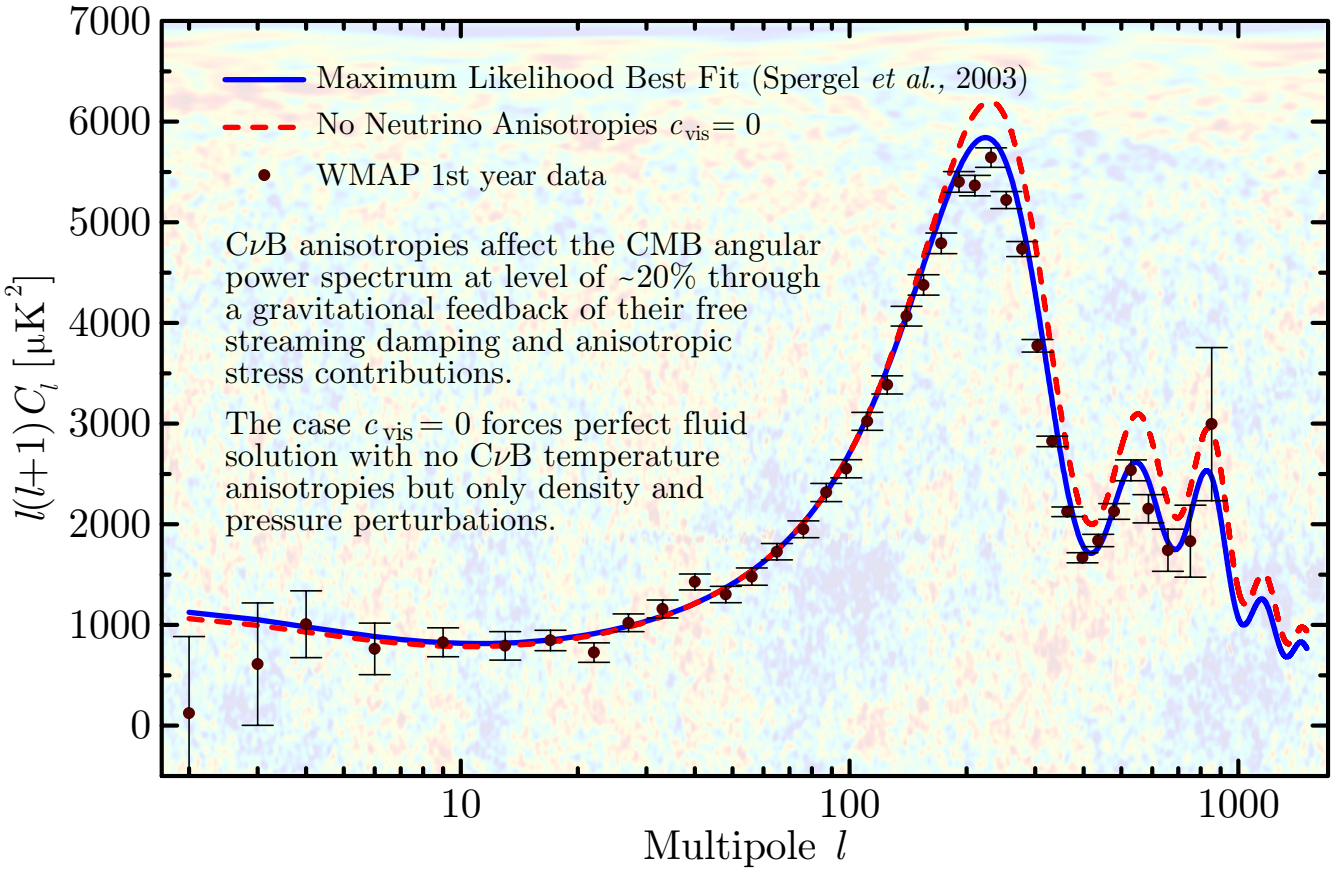

The effect of CνB anisotropies on the CMB temperature angular power spectrum. The standard model with parameters which provide the maximum likelihood best fit to WMAP is plotted against the same model but with no CνB anisotropies. The 1st year WMAP data is also plotted for comparison. [The standard expectation for the "viscosity parameter" c_{vis} is $1/\sqrt{3}$.]

[From R. Trotta and A. Melchiorri, "Indication for primordial anisotropies in the neutrino background from WMAP and SDSS," Phys. Rev. Lett. **95** (2005) 011305, astro-ph/0412066.]

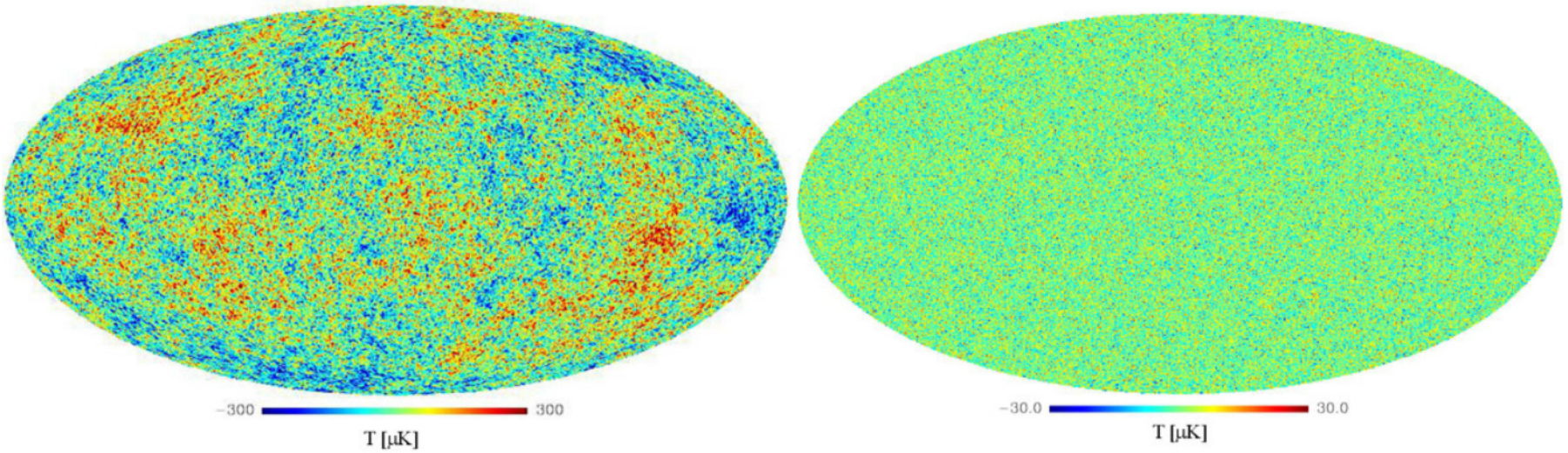

Right panel: Simulation showing the distribution on the sky of the CMB temperature fluctuations with neutrinos as predicted in the standard cosmological model (ΛCDM). *Left panel*: The net effect on the CMB of the presence of neutrino ripples, interpreted as the signature of existence of the CνB density and pressure fluctuations. [Original Source: Oxford News Release. Image credit: Roberto Trotta.]

The discovery of the ripples of primordial origin in the CνB, made by combining data produced by the NASA Wilkinson Microwave Anisotropy Probe (WMAP) satellite and clustering data from the Sloan Digital Sky Survey (SDSS), confirms the predictions of both the Big Bang paradigm and the Standard Model of particle physics.

The WMAP+SDSS data favor $c^2_{\rm vis} = 1/3$ with odds slightly larger than 2:1 (possibly plagued by systematics), irrespective of the assumptions on the CνB density, constituting positive (of course, model dependent) evidence in favor of the Standard Model value.

Current *Planck* results:[a]

The mean values of the squares of the neutrino viscosity parameter $c_{\rm vis}$ and effective sound speed $c_{\rm eff}$[b] and their 68% errors are

$$\left.\begin{aligned} c^2_{\rm eff} &= 0.312 \pm 0.011 \\ c^2_{\rm vis} &= 0.47^{+0.26}_{-0.12} \end{aligned}\right\} \quad \textit{Planck}\ \text{TT+lowP}, \tag{5a}$$

$$\left.\begin{aligned} c^2_{\rm eff} &= 0.316 \pm 0.010 \\ c^2_{\rm vis} &= 0.44^{+0.15}_{-0.10} \end{aligned}\right\} \quad \textit{Planck}\ \text{TT+lowP+BAO}, \tag{5b}$$

$$\left.\begin{aligned} c^2_{\rm eff} &= 0.3240 \pm 0.0060 \\ c^2_{\rm vis} &= 0.327 \pm 0.037 \end{aligned}\right\} \quad \textit{Planck}\ \text{TT,TE,EE+lowP}, \tag{5c}$$

$$\left.\begin{aligned} c^2_{\rm eff} &= 0.3242 \pm 0.0059 \\ c^2_{\rm vis} &= 0.331 \pm 0.037 \end{aligned}\right\} \quad \textit{Planck}\ \text{TT,TE,EE+lowP+BAO}. \tag{5d}$$

Constraints on these parameters are consistent with the conventional (adiabatic) ΛCDM values $c^2_{\rm eff} = c^2_{\rm vis} = 1/3$ to within 2% and 10% respectively. A vanishing value of $c^2_{\rm vis}$, which might imply a strong interaction between neutrinos and other species, is excluded at more than the $95\,\%$ level arising from the *Planck* temperature data. This conclusion is greatly strengthened (to about $9\,\sigma$) when *Planck* polarization data are included.

[a] P. A. R. Ade *et al.* (*Planck* Collaboration), "*Planck* 2015 results. XIII. Cosmological parameters," Astron. Astrophys. **594** (2016) A13, arXiv: 1502.01589 [astro-ph.CO]. The results below have not yet been updated in the latest published *Planck* analysis (fall 2023).

[b] $c^2_{\rm eff} = \dot{\overline{p}}/\dot{\overline{\rho}}$ in the adiabatic approximation and for ultrarelativistic particles ($3p = \rho$) $c^2_{\rm eff} = 1/3$.

3 Neutrinos from BBN.

The Big Bang Nucleosynthesis (BBN) is the creation of the light elements and isotopes thereof of primordial cosmic composition (which to a large degree is the cosmic composition) of the observable Universe. BBN produced overwhelmingly most of the modern cosmic abundances of Hydrogen, Deuterium, and Helium-3 and 4. Also it produced some significant part or maybe almost all of the cosmic abundance of Lithium-6 and Lithium-7.

BBN (cosmic time $\sim 10 - 1200$ s) occurred ~ 13.8 Gyr ago.

Figure shows a fragment of the full nuclear network of the BBN reactions that produce the lightest (and most abundant) isotopes. ▷

A more detailed BBN network is shown at p. 176.

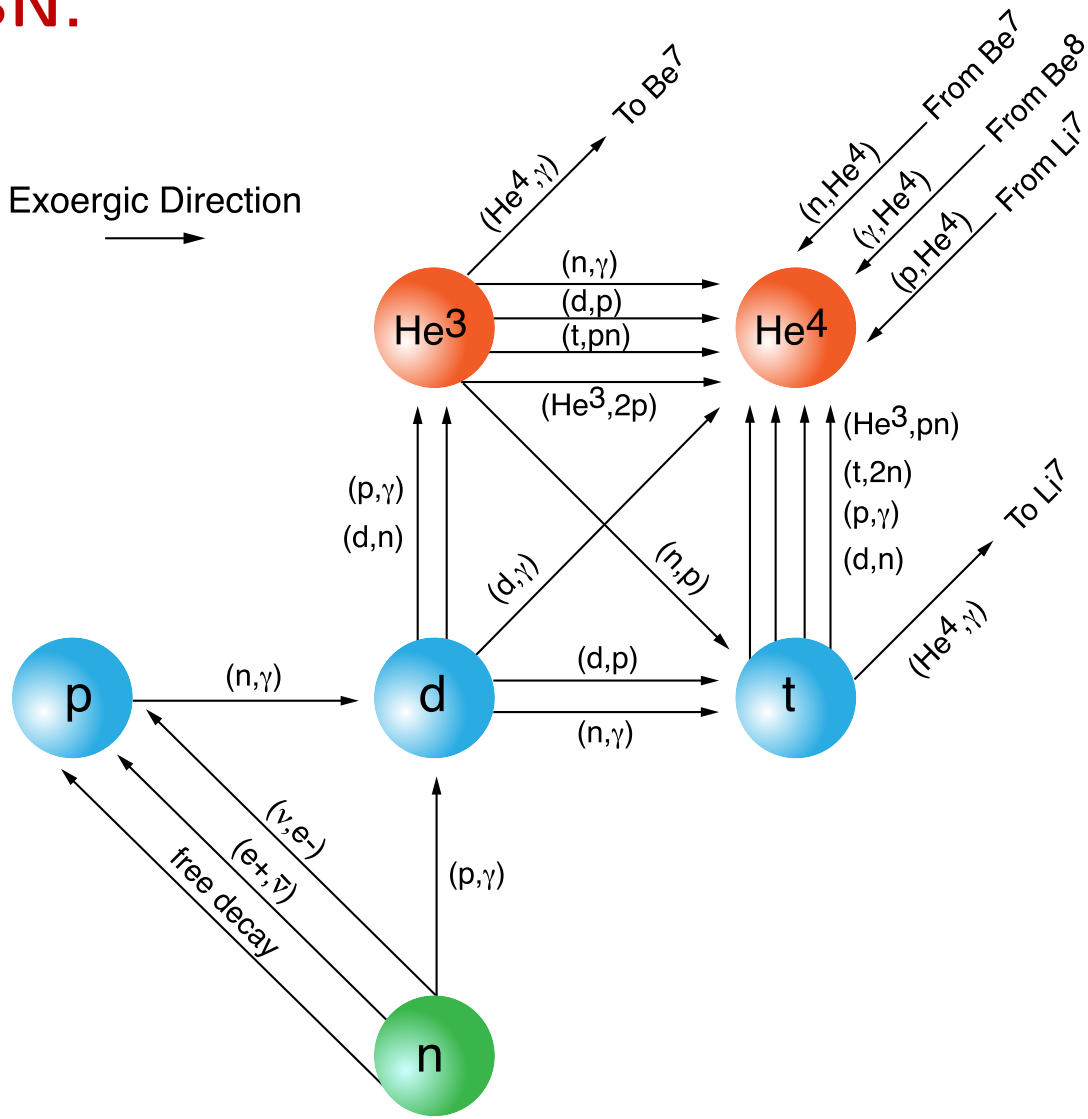

[Figure is borrowed from the Cococubed website http://cococubed.asu.edu/code_pages/net_bigbang.shtml.]

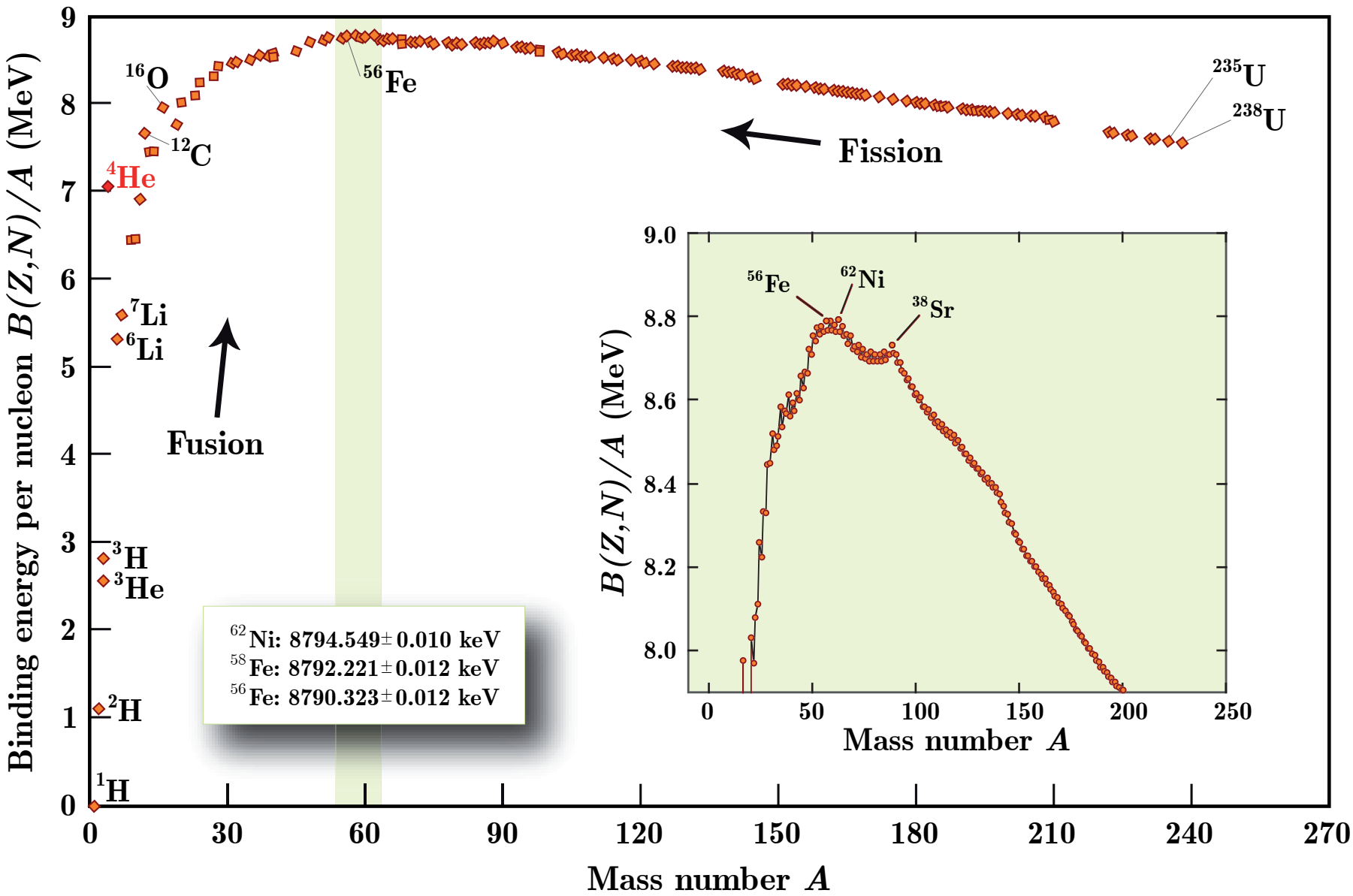
Binding energy per nucleon $B(Z,N)/A$ (MeV)
Mass number A
^{16}O
^{56}Fe
^{235}U
^{238}U
^{12}C
^{4}He
Fission
Fusion
^{7}Li
^{6}Li
^{3}H
^{3}He
^{2}H
^{1}H
^{62}Ni: 8794.549 ± 0.010 keV
^{58}Fe: 8792.221 ± 0.012 keV
^{56}Fe: 8790.323 ± 0.012 keV
^{56}Fe
^{62}Ni
^{38}Sr
$B(Z,N)/A$ (MeV)
Mass number A

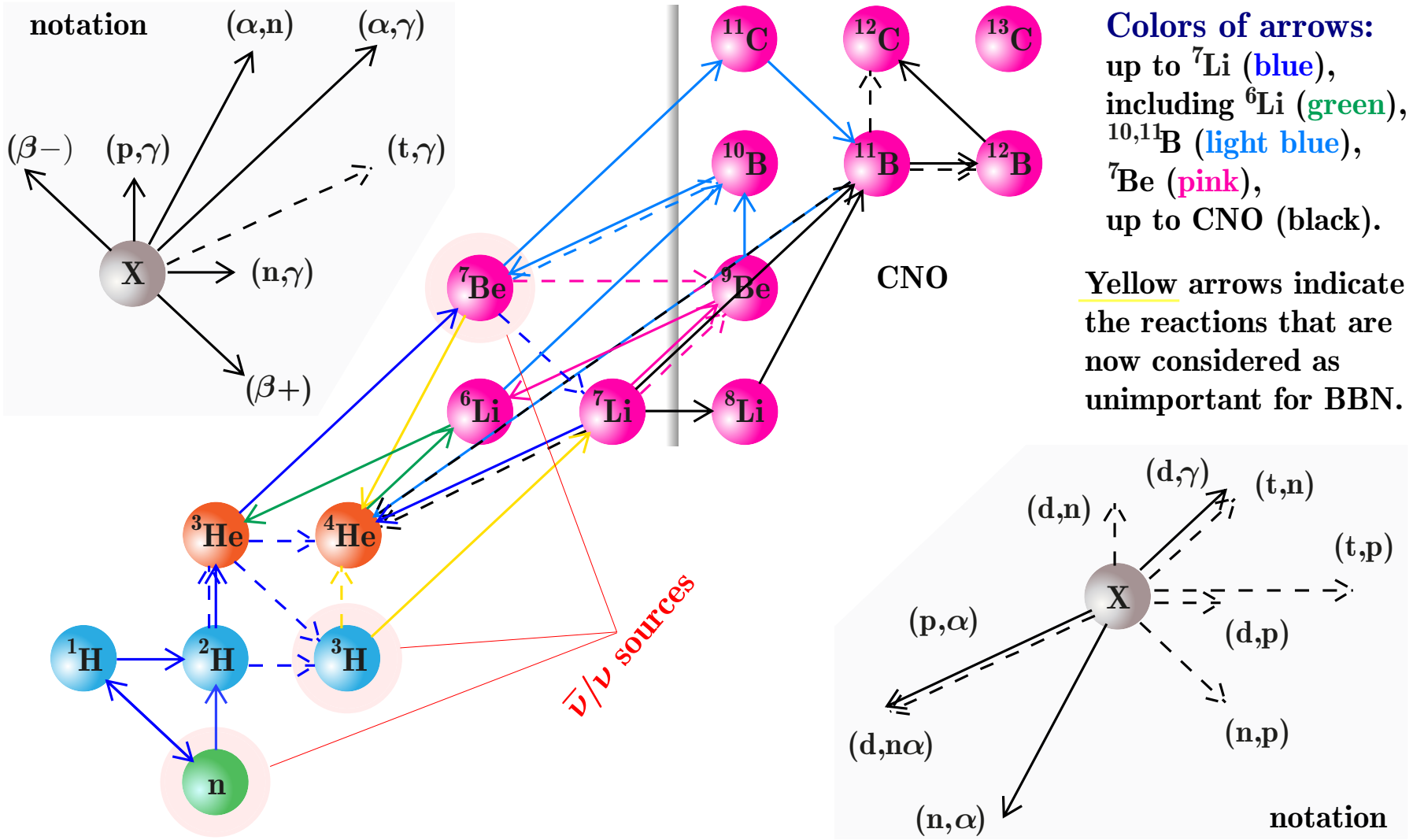

Nuclear network of the most important reactions in BBN (out of the 424) producing or destructing light isotopes up to CNO. The symbols for the arrows include their length and direction.

[Adapted from C. Pitrou *et al.*, "Precision big bang nucleosynthesis with improved Helium-4 predictions," Phys. Rept. **754** (2018) 1–66, arXiv:1801.08023 [astro-ph.CO].]

BBN – another presentation.

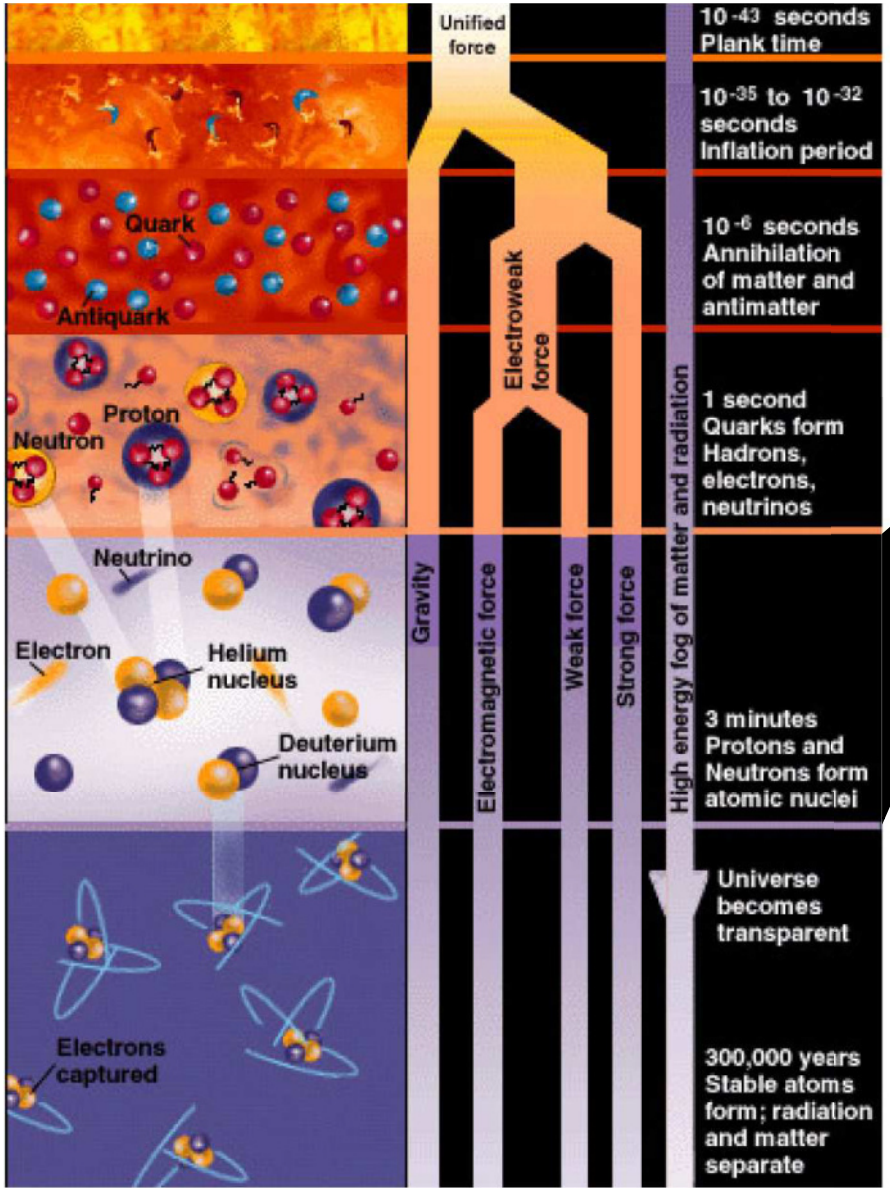

$$
\begin{aligned}
&n^0 \longrightarrow p^+ + e^- + \bar{\nu}_e && p^+ + n^0 \longrightarrow {}^2_1\mathrm{D} + \gamma \\
&{}^2_1\mathrm{D} + p^+ \longrightarrow {}^3_2\mathrm{He} + \gamma && {}^2_1\mathrm{D} + {}^2_1\mathrm{D} \longrightarrow {}^3_2\mathrm{He} + n^0 \\
&{}^2_1\mathrm{D} + {}^2_1\mathrm{D} \longrightarrow {}^3_1\mathrm{T} + p^+ && {}^3_1\mathrm{T} + {}^2_1\mathrm{D} \longrightarrow {}^4_2\mathrm{He} + n^0 \\
&{}^3_2\mathrm{He} + {}^4_2\mathrm{He} \longrightarrow {}^7_3\mathrm{Li} + \gamma && {}^3_2\mathrm{He} + n^0 \longrightarrow {}^3_1\mathrm{T} + p^+ \\
&{}^3_2\mathrm{He} + {}^2_1\mathrm{D} \longrightarrow {}^4_2\mathrm{He} + p^+ && {}^3_2\mathrm{He} + {}^4_2\mathrm{He} \longrightarrow {}^7_4\mathrm{Be} + \gamma \\
&{}^7_3\mathrm{Li} + p^+ \longrightarrow {}^4_2\mathrm{He} + {}^4_2\mathrm{He} && {}^7_4\mathrm{Be} + n^0 \longrightarrow {}^7_3\mathrm{Li} + p^+
\end{aligned}
$$

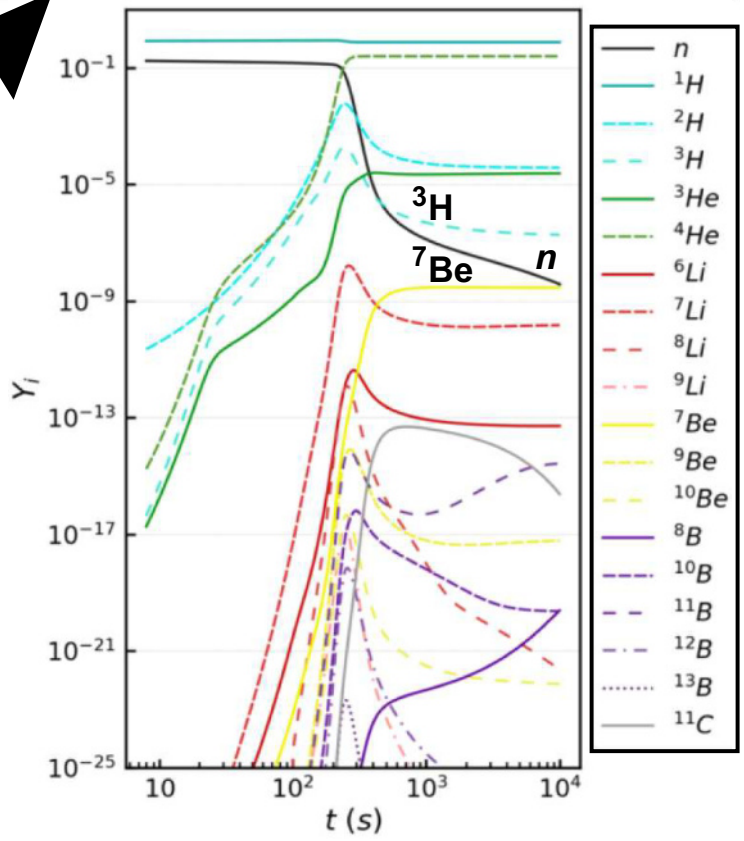

Digression: The primordial Lithium problem.

Precise knowledge of the baryon-to-photon ratio $\eta = n_b/n_\gamma$ of the Universe from observations of the CMB anisotropies has made the Standard BBN a parameter-free theory. Although, there is a good agreement over a range of nine orders of magnitude between abundances of light elements deduced from observations and calculated in BBN, there remains a yet-unexplained discrepancy of ^{7}Li abundance higher by a factor of $3-4$ when calculated theoretically. The primordial abundances depend on

- astrophysical nuclear reaction rates,
- number of light neutrino flavors (N_ν),
- neutron lifetime (τ_n), and
- baryon-to-photon ratio (η).

The discrepancy is not yet explained.

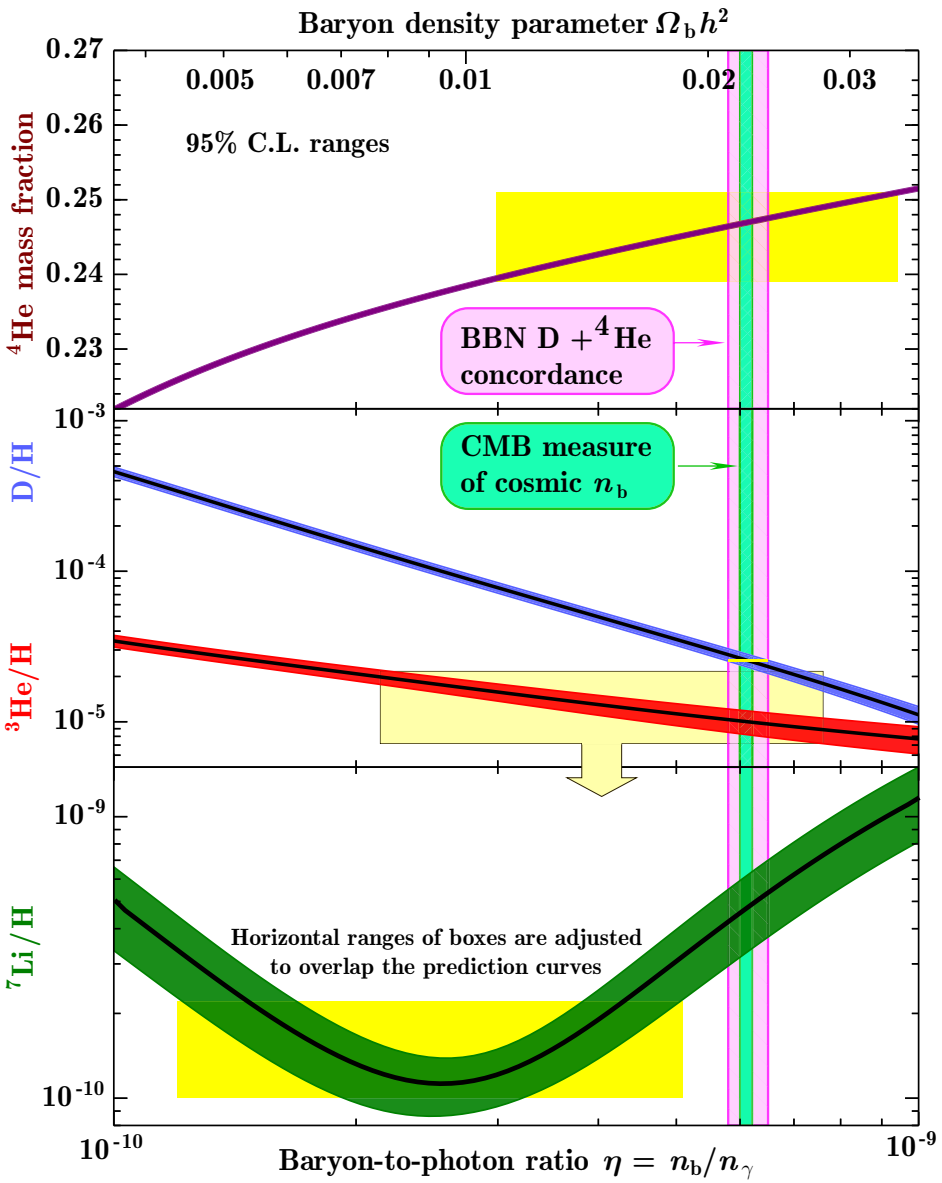

[Figure is adapted from P. A. Zyla *et al.* (Particle Data Group), "Review of Particle Physics," PTEP **2020** (2020) 083C01. Exp. limit for ^{3}He/H is added.]

So, during the first few minutes, the Universe produces observed light elements. Subsequent decays of neutrons and tritons,

$$n \to p + e^- + \overline{\nu}_e$$
$$(\text{half-life} = 611 \pm 1 \text{ s}),$$
$$^3\text{H} \to {}^3\text{He} + e^- + \overline{\nu}_e$$
$$(\text{half-life} = 12.32 \pm 0.02 \text{ yr}),$$

produce a very small $\overline{\nu}_e$ flux. Later ^{7}Be produce (even smaller) flux of ν_e of 861.8 keV (89.6%) or 384.2 keV (10.4%) through bound-electron capture,

$$^7\text{Be} + e^- \to {}^7\text{Li} + \nu_e$$
$$(\text{half-life} = 53.3 \text{ d}).$$

Figure shows evolution of light-element abundances as indicated at the lines. Colored solid lines are neutrons (n) and the unstable but longlived isotopes Tritium (T) and beryllium (^{7}Be), which produced $\overline{\nu}_e$ and ν_e but have not themselves survived to this day.

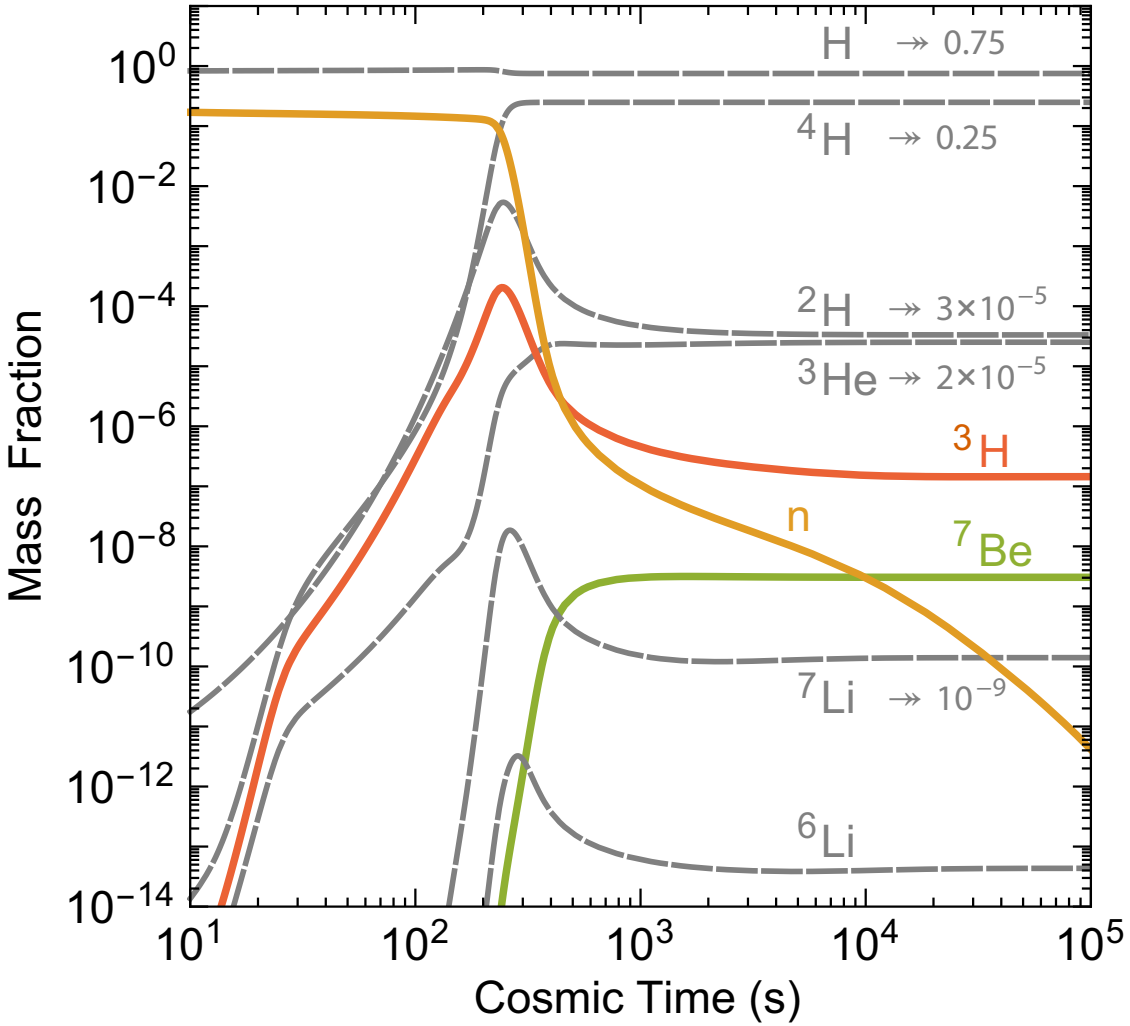

[Figure is adapted from E. Vitagliano *et al.* (2020), see Ref. at p. 75.]

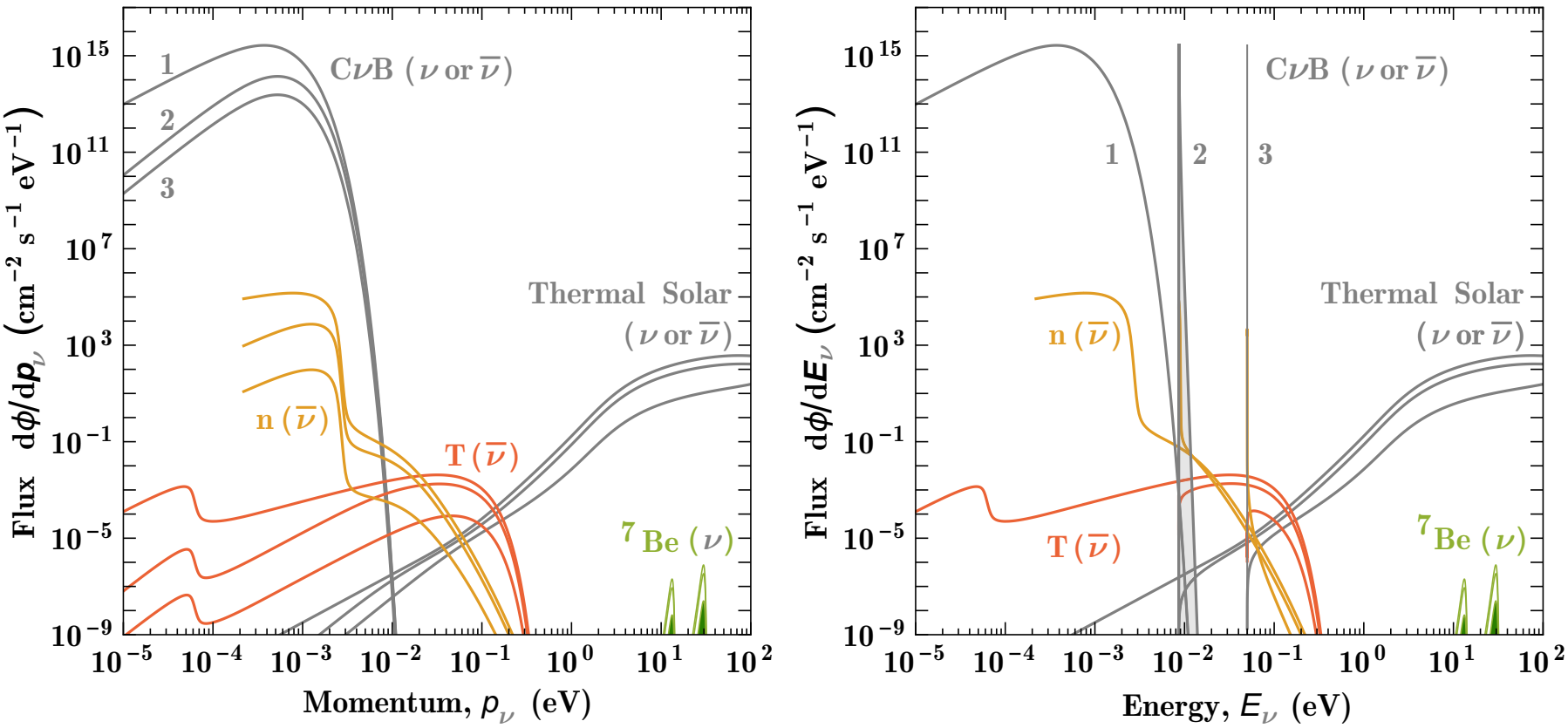

Flux densities of the lowest-energy mass eigenstates ν_i and $\overline{\nu}_i$ with $m_i = 0,\ 8.6,\ 50$ meV from several sources (CνB, BBN, Sun), calculated using the probabilities (mass-eigenstate content) listed in Table:

CνB			BBN			Sun (bremsstrahlung)		
1	2	3	1	2	3	1	2	3
1/3	1/3	1/3	0.681	0.297	0.022	0.432	0.323	0.245

[Figures are borrowed from E. Vitagliano *et al.* (2020), see Ref. at p. 75.]

Explanation of the above table.

- **CνB**: The relic νs and $\overline{\nu}$s consist essentially of an equal mixture of all flavors
  $\Longrightarrow$ the probability for finding a random flavor in any of the mass eigenstates is $1/3$.
  The flavor density matrix is essentially proportional to the unit matrix from the beginning
  $\Longrightarrow$ The flavor conversion (including MSW) don't seem to have any effect.
- **BBN**: The BBN neutrinos are produced in the electron flavor, so their flavor content will change with time. Flavor evolution in the early Universe can involve many complications. e.g., neutrinos themselves are an important background medium, leading to collective flavor evolution, However, the BBN neutrinos are largely produced after BBN is complete at $T \gtrsim 60$ MeV.
  The matter density in the post-BBN era is $\sim 10^{-5}$ g/cm^3.
  $\Longrightarrow$ matter effects and collective neutrino oscillations are not important.
  $\Longrightarrow$ Flavor evolution of MeV-range neutrinos occurs in the vacuum, and the mass content of the initial flavor states does not evolve.
  $\Longrightarrow$ One can use the best-fit probabilities of finding $\nu_e/\overline{\nu}_e$ in $\nu_i/\overline{\nu}_i$ states given in p. 436.
- **Sun**: The main processes of thermal ν and $\overline{\nu}$ production in the solar plasma, are
  - plasmon decay, $\gamma \to \overline{\nu}\nu$,
  - Compton process (photoproduction), $\gamma + e \to e + \overline{\nu}\nu$,
  - bremsstrahlung, $e + (Ze) \to (Ze) + e + \overline{\nu}\nu$ (dominates at low energies), and
  - atomic free-bound and bound-bound transitions, $(Ze)^* \to (Ze) + \overline{\nu}\nu$.

  The thermal neutrinos have energies $\lesssim$ keV, corresponding to the temperature in the solar core. Bremsstrahlung produces almost pure $\nu_e\overline{\nu}_e$ fluxes due to vector-current interaction and fluxes of any flavor equally due to axial-vector interaction. Adding the vector (28.4%) and axial-vector (71.6%) contributions gives the above numbers. Higher-energies range is more complicated.

3.1 $N_{\rm eff}^{\nu}$ from BBN (after *Planck*-2015).

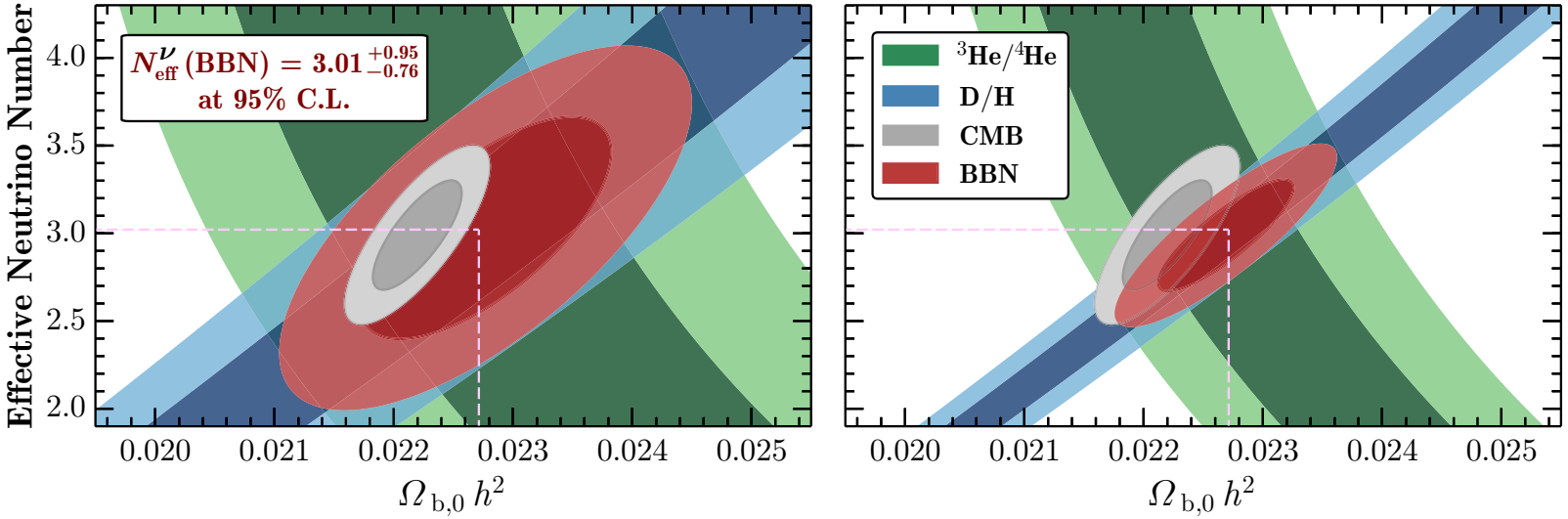

Likelihood distributions (combined confidence contours) of the baryon density $\Omega_{b,0}h^2$ and effective number of neutrino species $N_{\rm eff}^{\nu}$. The D/H and ^{3}He/^{4}He contours are displayed, where dark and light shades represent the 68% and 95% confidence contours, respectively. The measured ^{3}He/^{4}He isotope ratio is derived from solar system meteorite samples.[a] The grey contours illustrate the results from the *Planck*-2015 satellite observations of the CMB temperature fluctuations. The red contours show the combined D/H and ^{3}He/^{4}He (BBN only) confidence regions. The slight shift is insignificant.

The BBN contours in *left panel* use a 5% and 3% standard error, respectively, for the BBN calculations, due to uncertainties in the nuclear reaction rates. The *right panel* illustrates the same contours, now assuming a 1% uncertainty on the nuclear reaction rates, and the same observational measures. Note that the BBN contours in *right panel* comparable in size to the *Planck*-2015 results.

[From R. Cooke, "Big Bang nucleosynthesis and the Helium isotope ratio," ApJL **812** (2015) L12, arXiv:1510.02801 [astro-ph.CO]. See also bottom left Figure at p. 102.]

[a] Is intended to be illustrative as this determination may not reflect the primordial value.

3.2 $N_{\rm eff}^{\nu}$ from BBN (progress after *Planck*-2018).

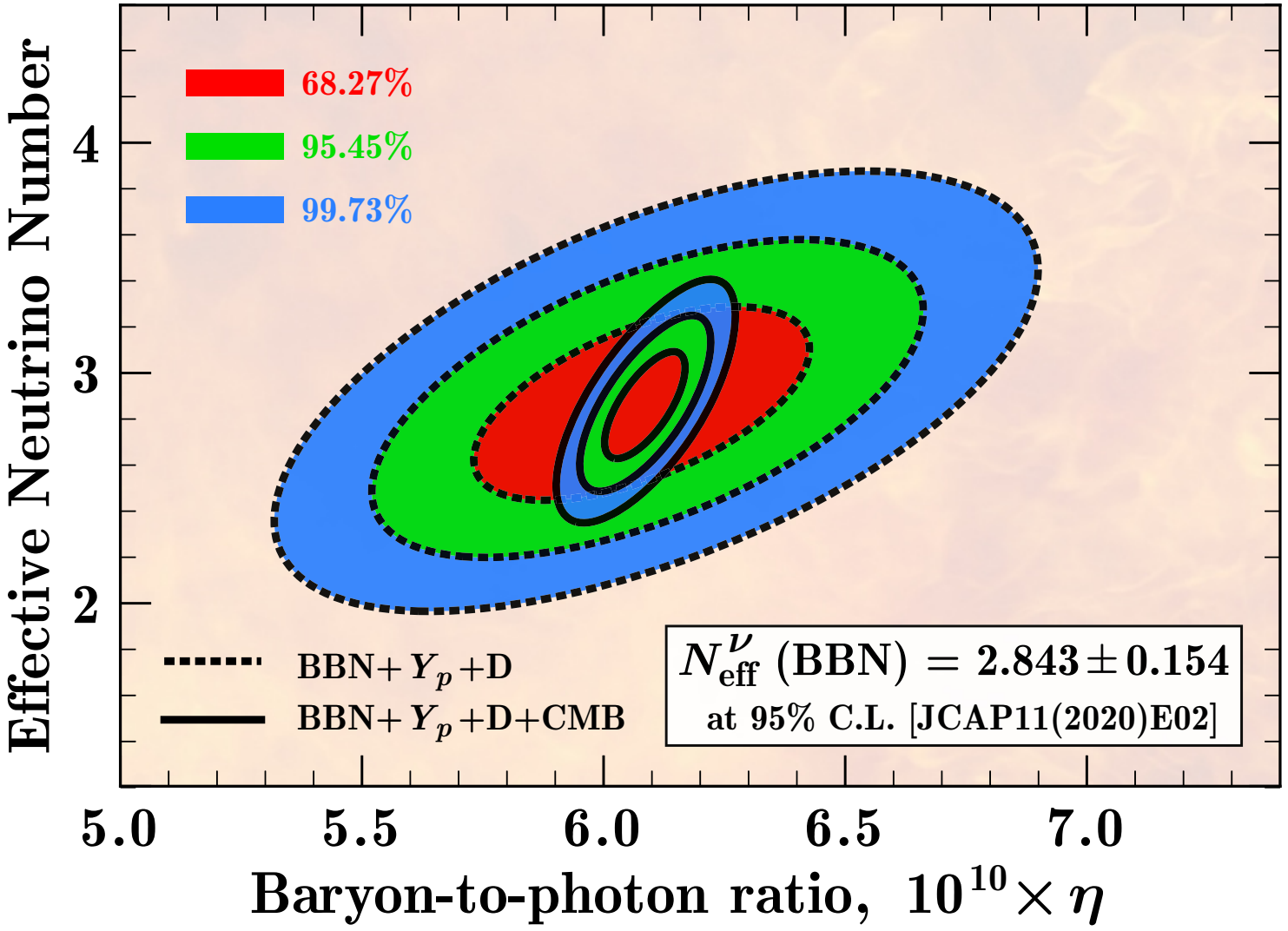

Likelihood distributions in $(N_{\rm eff}^{\nu}, \eta)$ space (here Y_p and D are the ^{4}He and D mass fractions).

[From B. D. Fields *et al.*, "Big-Bang Nucleosynthesis after Planck," JCAP03(2020)010, arXiv:1912.01132 [astro-ph.CO].]

4 Solar neutrinos (thermonuclear).

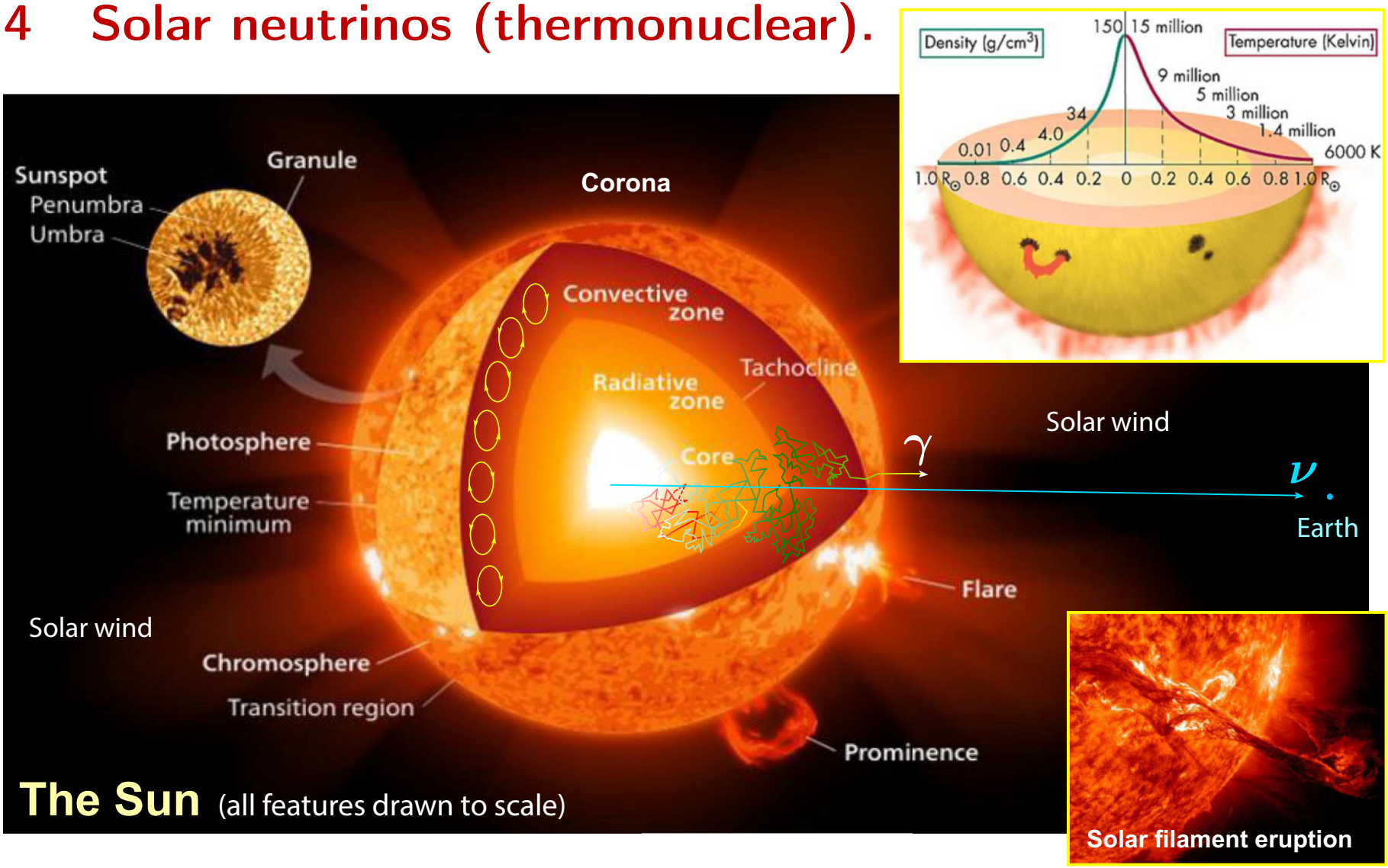

Various regions of the surface and interior of the Sun. [From ⟨https://medium.com/starts-with-a-bang/11-scientific-advances-of-the-last-100-years-gave-us-our-entire-universe-b9e17f1adcd6⟩.]

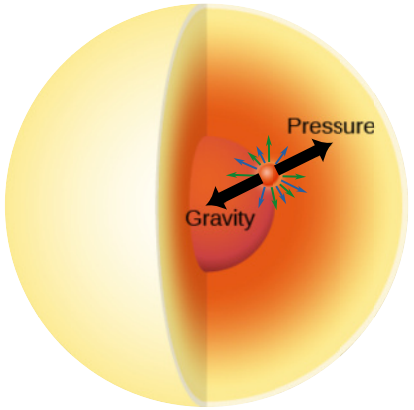

The life of any star is an unceasing struggle between gravity and pressure. Both act in all directions, but gravity tries to compress everything to the star's core and pressure decreases with increasing distance from the core, by that pushing stellar layers outward. When gravity dominates, the star contracts causing the pressure to rise and thus resisting further contraction. When the outward pressure gradient dominates, stellar layers expand, thus decreasing the pressure and terminating further expansion of the star.

Since a star shines, it loses energy from its interior. This reduces the pressure and leads to contraction of the star. Without a mechanism of restoring the energy lost, a typical star cannot live more than some tens of millions of years. It has long been known that such a mechanism is provided by the reactions of thermonuclear fusion (the formation of light nuclei from lighter ones) within the star.[a]

If the daughter nucleus is more bound than the fusing ones, the reaction releases nuclear binding energy. The latter rises steeply from zero for ^{1}H to 7.074 MeV ($\sim 10^{-12}$ J) per proton for ^{4}He and reaches a peak at about 8.79 MeV per nucleon for the iron-nickel group before decreasing for heavier isotopes (see Figure at p. 175). If a star initially consisted of pure Hydrogen, it could gain a maximum of about 8.79 MeV per nucleon by fusion to iron[b]. This is an extremely complicated and multistage process occurring at very high temperatures and densities. But most of the available nuclear binding energy ($\sim 80\%$) is already released when ^{4}He is built up in the first stage. The transmutation of four protons into one α particle is the fully dominant energy source for the present-day Sun.

[a] This source of stellar energy was independently suggested by Jean Baptiste Perrin (1919) and Arthur Stanley Eddington (1920). But the first to propose the principle of nuclear fusion was William Draper Harkins (1915).

[b] The binding energy per nucleon for the three most tightly bound isotopes are 8790.323 ± 0.012 keV (^{56}Fe), 8792.221 ± 0.012 keV (^{58}Fe), and 8794.549 ± 0.010 keV (^{62}Ni); the isotope ^{56}Fe is the end product of normal stellar fusion because it is in very close but unbridgeable proximity to the most stable isotope ^{62}Ni.

The energy production rate averaged over the solar core does not catch our fancy: it is as low as $10-15$ W/m^3 that is compatible with the power of a pocket torch. However the luminosity of the Sun is about 4×10^{26} W, equivalent to $\sim 10^{17}$ typical nuclear power plants.

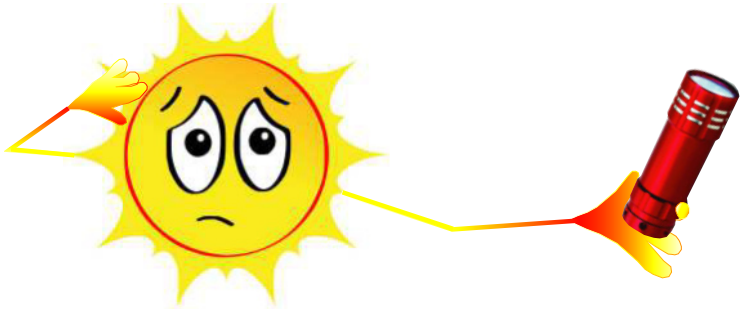

The net luminosity is so huge because the Sun converts $\sim 7\times10^8$ metric tons of Hydrogen (or about 4×10^{38} protons) to Helium per second. The Hydrogen is consumed at a lower rate than in any other evolutionary phase of the Sun and thus the central Hydrogen-burning lifetime of the Sun is much longer than that for other phases of its evolution. The Sun contains $\sim 10^{57}$ atoms (mostly Hydrogen, with a little Helium and traces of the other elements like Carbon, Nitrogen, Oxygen, Magnesium, and so on); so it has enough fuel to shine actively for more than 10^{10} years.

A conversion of a proton into a bound neutron is only possible with production of an electron neutrino through β^+ decay or electron capture. The Hydrogen-to-Helium fusion is also a rather multistage process which occurs in two key simultaneously running reaction sequences, the pp (or proton-proton) chains and the CNO (Carbon-Nitrogen-Oxygen) cycle[a] and the neutrinos are necessarily emitted as a result of some of the pp and CNO reactions.

Since the low-energy neutrinos are extremely penetrating ultrarelativistic particles, they escape the Sun in two seconds without being scattered or absorbed[b] and reach the Earth in about eight minutes from the time they were produced. By detecting these neutrinos, we may learn a lot about the "instantaneous" conditions inside the Sun and, as a surprising bonus, about the neutrinos themselves.

[a] Both sequences were worked out at the end of 1930s by Carl Friedrich von Weizsäcker and Hans Albrecht Bethe, though *without mentioning the neutrinos* (note that Bethe knew the theory of Fermi).

[b] The ν-N interaction cross section, σ_ν, at $E_\nu = 1$ MeV is about 10^{-44} cm^2. So the mean free pass $\lambda_\nu = 1/(\sigma_\nu n) \sim m_p/(\sigma_\nu \rho)$ of the 1 MeV neutrinos in the matter of density $\rho = 100$ g/cm^3 is $\sim 10^{15}$ km ~ 0.1 pc.

4.1 pp chain.

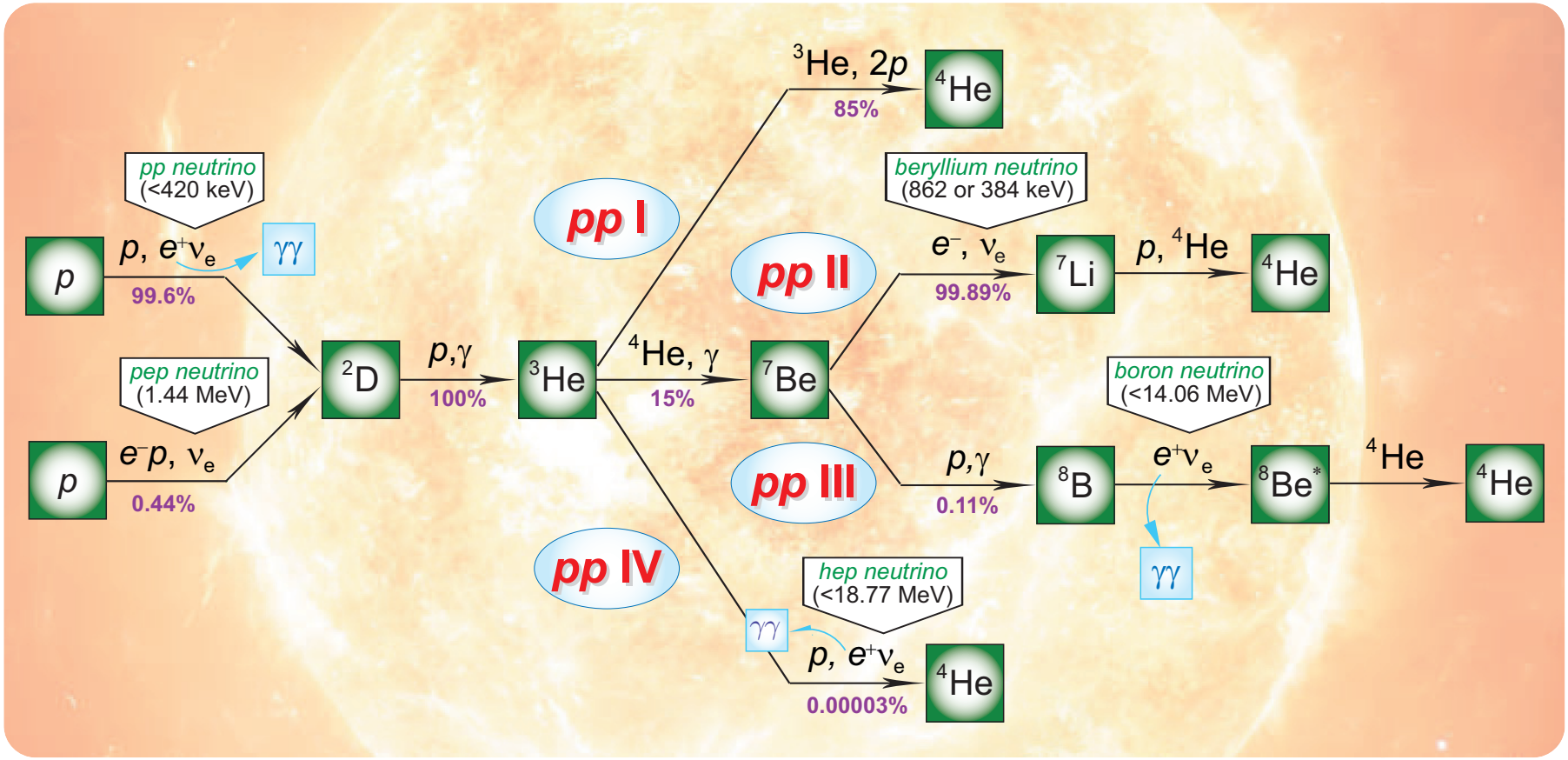

The diagram shows the full pp chain responsible for production of about 98.4% of the solar energy.
The neutrinos export 3%, 4%, and 28% of the energy in pp I, pp II, pp III, respectively.
All four pp chains are active simultaneously in a H-burning star containing significant ^{4}He.
The details depend on density, temperature and composition but in Sun the pp I dominates.

4.2 CNO bi-cycle.

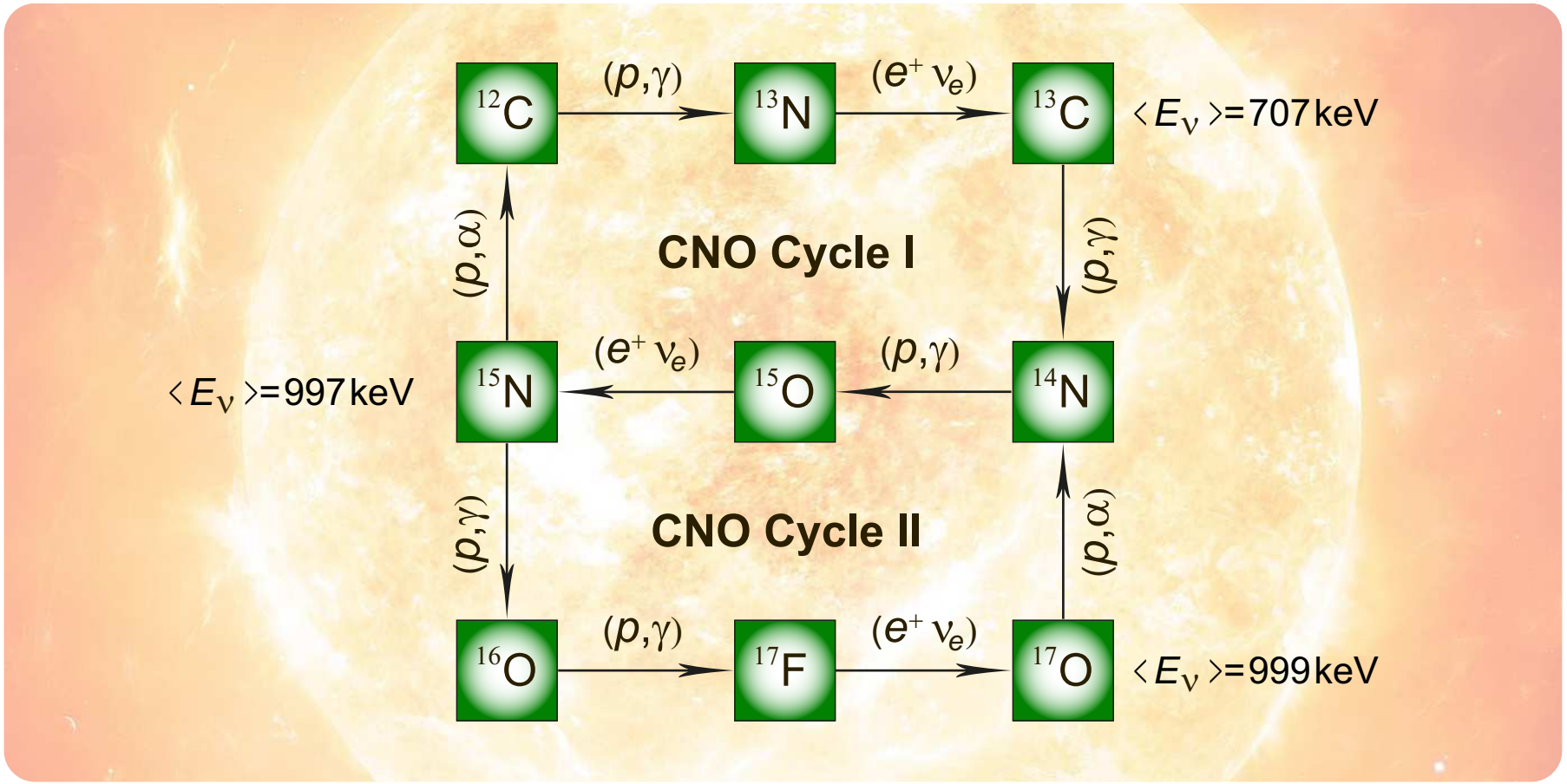

The diagram of the full CNO bi-cycle responsible for production of about 1.5–1.6% of the solar energy. The cycle I dominates in Sun but cycle II is not insignificant. The CNO cycles III and IV (not shown, will be discussed in Sect. **30.1**, p. 730) are essential for the Hydrogen burning in massive stars. The full CNO reaction net includes ^{18,19}F, ^{18}O, and ^{18,20}Ne.

4.3 Solar neutrino fluxes.

Figure shows the pp and CNO neutrino fluxes (versus energy) on Earth, calculated in the comprehensive solar model "BS05(OP)" by John N. Bahcall *et al.* ▷ Line and spectral fluxes are, respectively, in $\mathrm{cm}^{-2}\mathrm{s}^{-1}$ and in $\mathrm{cm}^{-2}\mathrm{s}^{-1}\mathrm{MeV}^{-1}$. Some minor neutrino contributions are not included. Also shown are the uncertainties of the neutrino flux calculation (on the $1\ \sigma$ level) and the threshold neutrino energies for the gallium, chlorine, and three water-Cherenkov detectors.

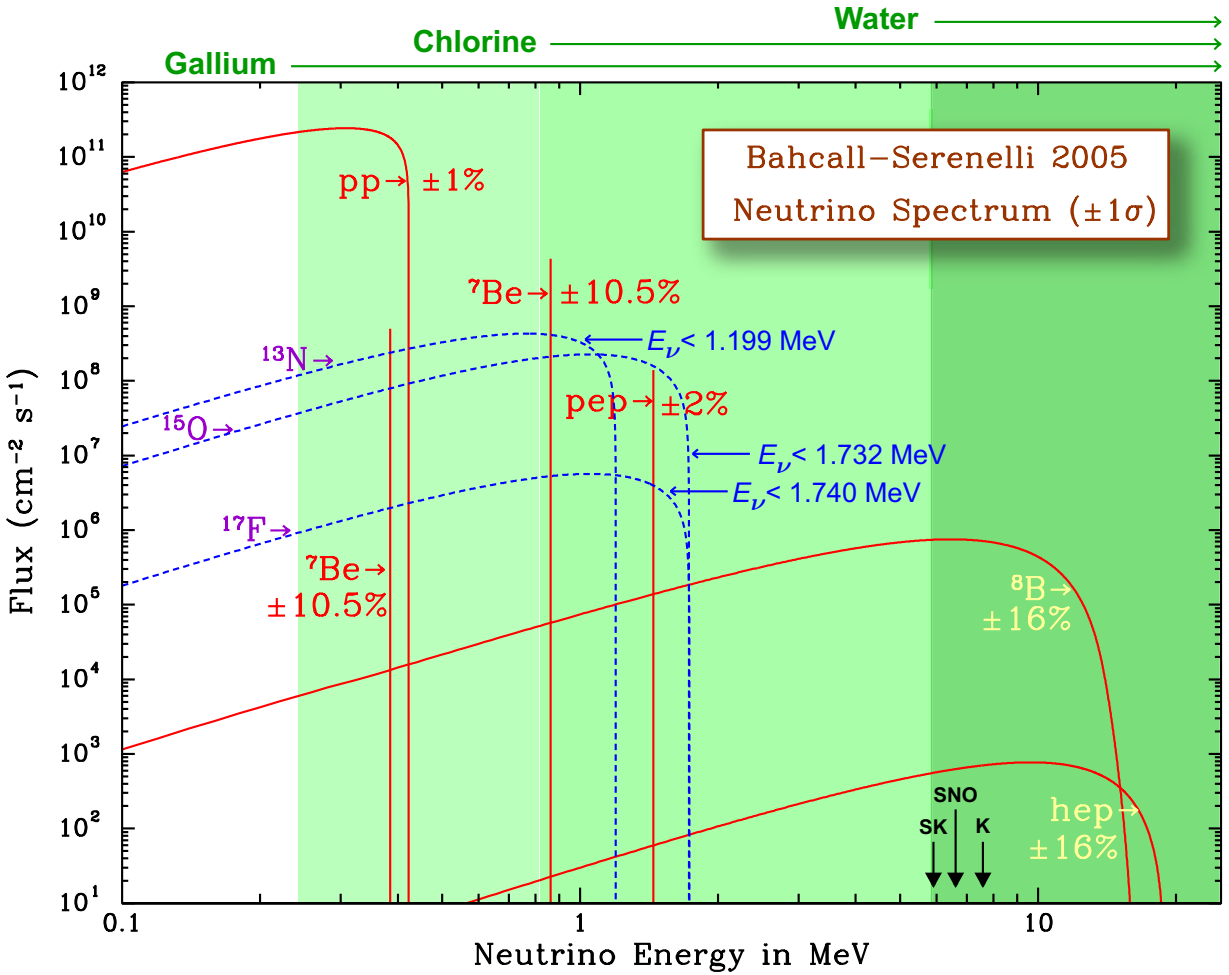

[Figure is taken from J. N. Bahcall, A. M. Serenelli & S. Basu, "New solar opacities, abundances, helioseismology, and neutrino fluxes," ApJ **621** (2005) L85–L88, astro-ph/0412440. For more detail, see p. 732.]

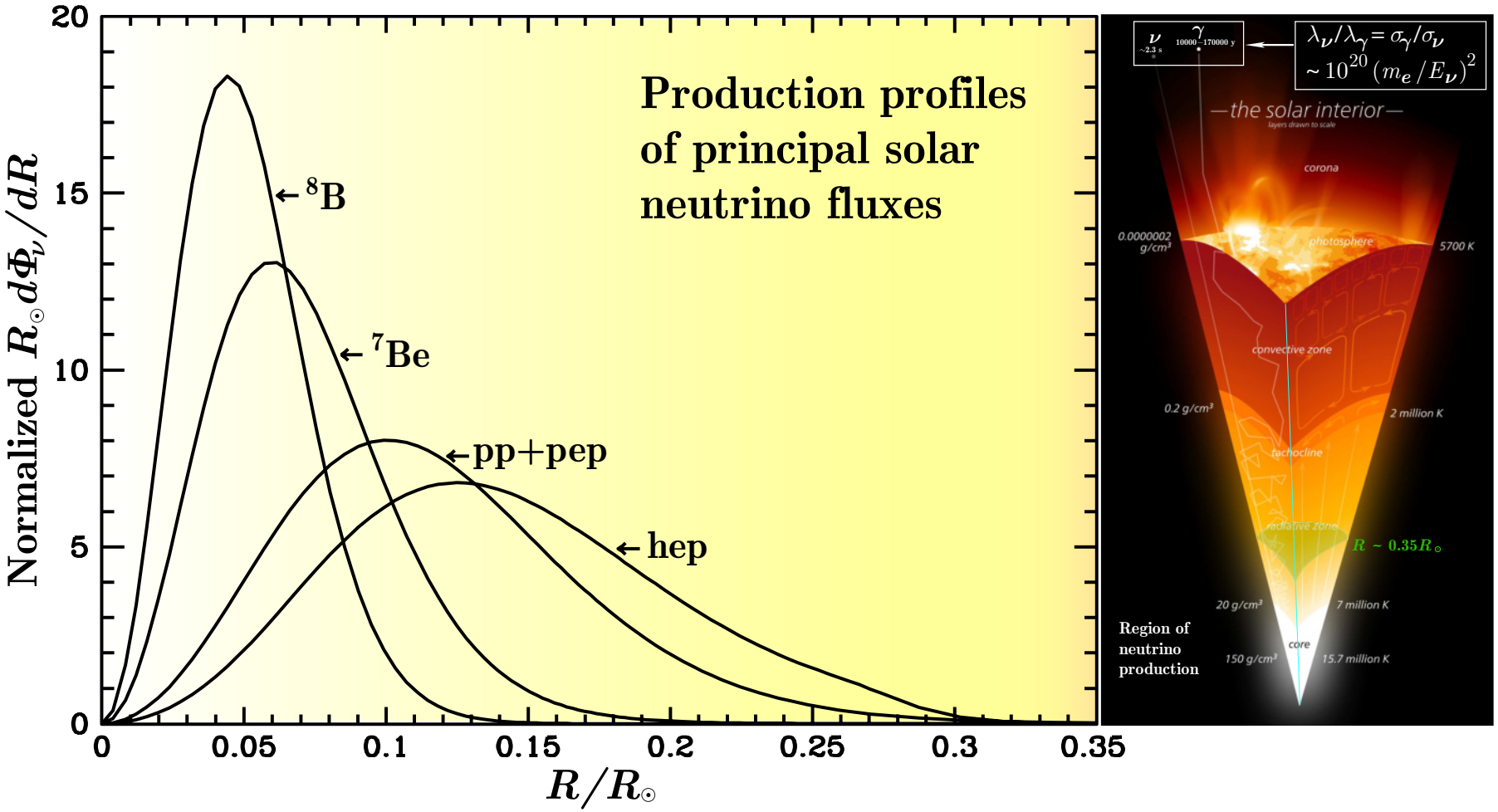

The left figure shows the normalized flows (production profiles)[a] of the pp-chain neutrinos produced within the solar core, calculated within the so-called "BS05(OP)" SSM as functions of the relative solar radius $R/R_\odot$ (see also p. 719). The right figure schematically illustrates the solar interior.

[Data for the left figure were taken from John Bahcall's homepage, URL: ⟨ http://www.sns.ias.edu/~jnb/ ⟩.]

[a] The production profiles are normalized to unity when integrated over $R/R_\odot$.

4.4 Future of the Sun.

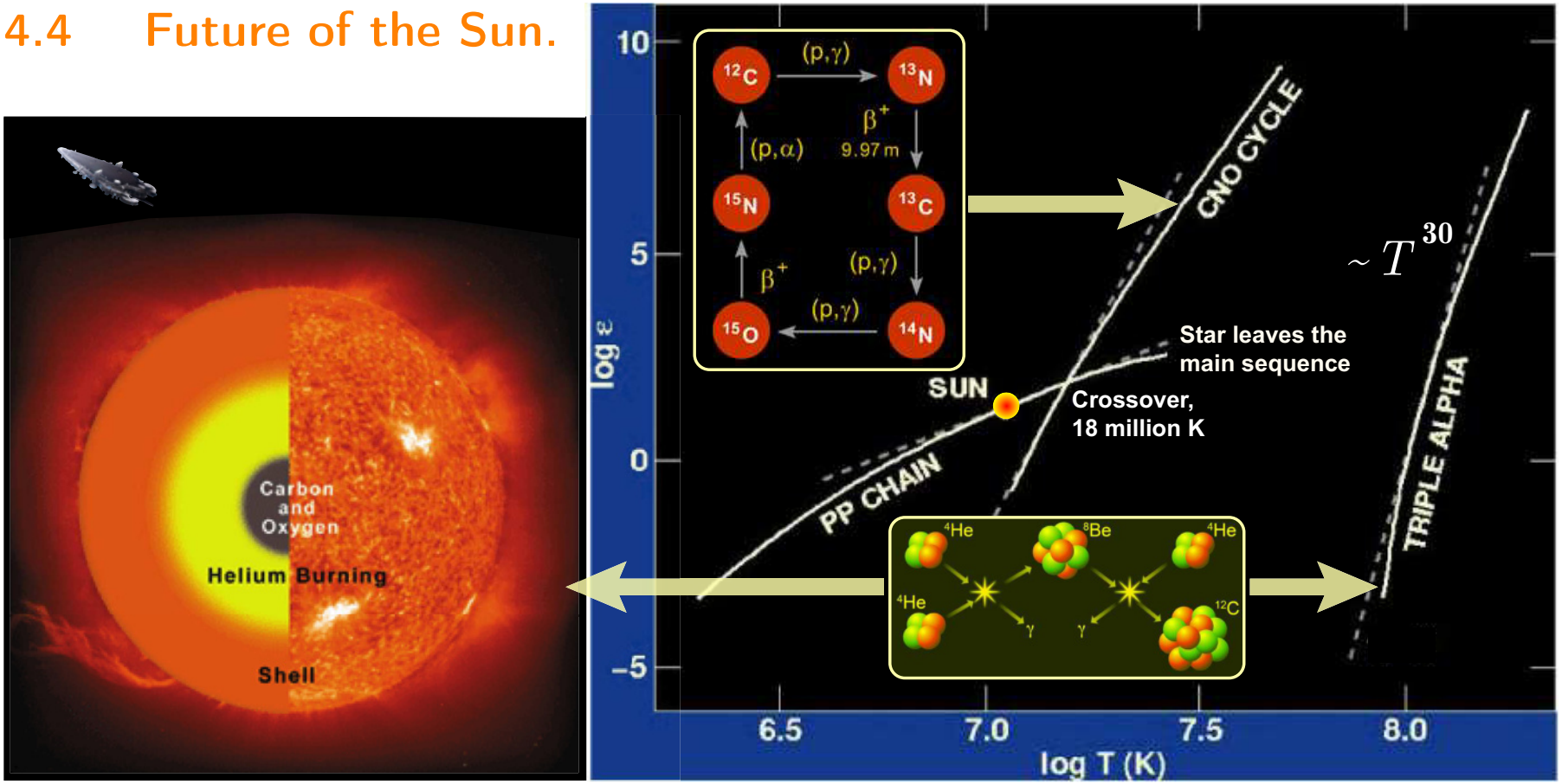

When there is no longer any Hydrogen left to burn in the central regions of a star, gravity compresses the core until the temperature reaches the point where Helium burning reactions become possible. In such reactions, two ^{4}He nuclei fuse to form a ^{8}Be nucleus, but this is very unstable to fission and rapidly decays to two ^{4}He nuclei again. Very rarely, however, a third Helium nucleus can be added to ^{8}Be before it decays, forming ^{12}C by the so-called triple-alpha reaction (energy release 7.3 MeV):

$$^4\mathrm{He} + {}^4\mathrm{He} \rightarrow {}^8\mathrm{Be}, \quad {}^8\mathrm{Be} + {}^4\mathrm{He} \rightarrow {}^{12}\mathrm{C} + \gamma.$$

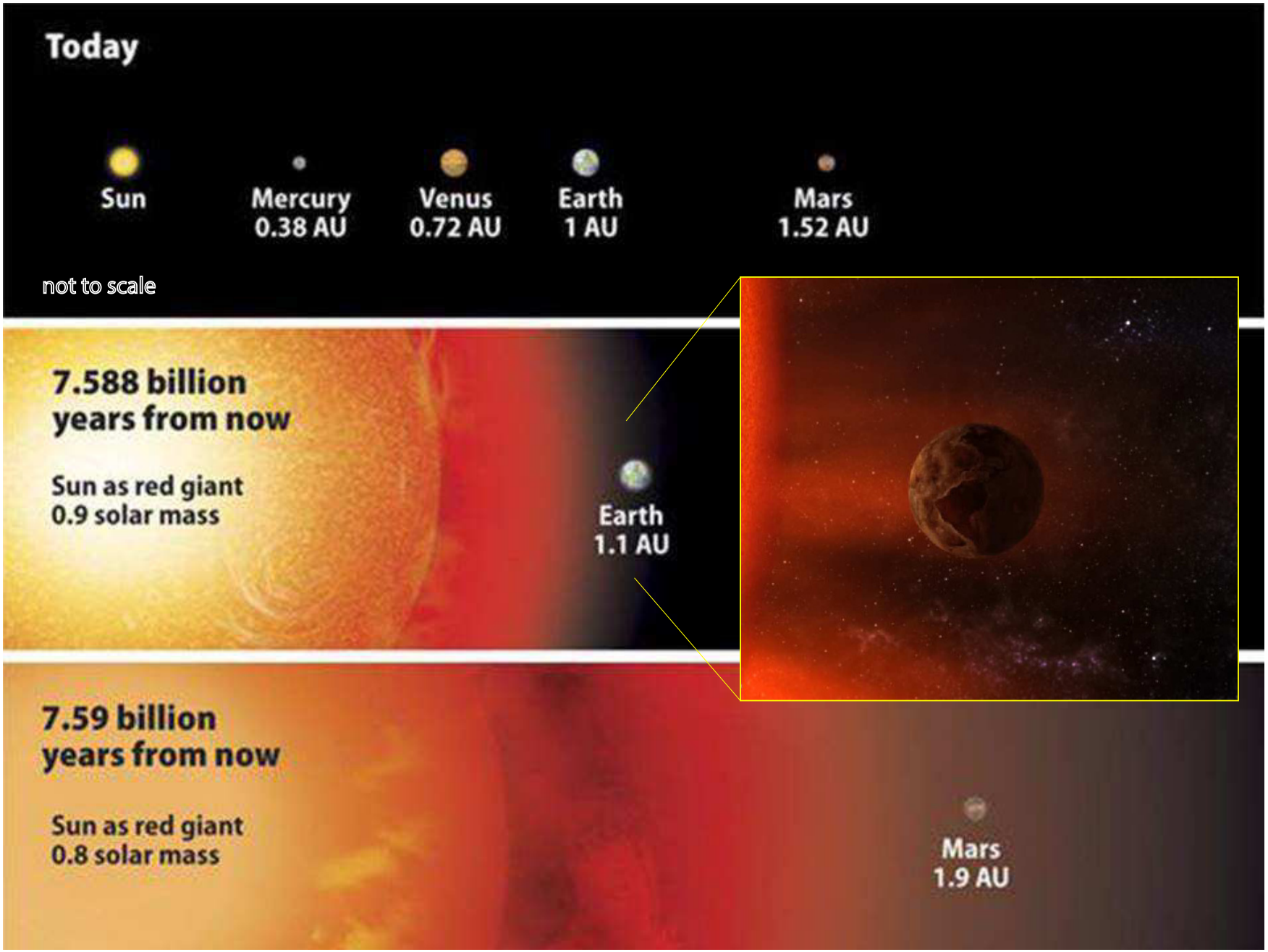
Today
Sun
Mercury
0.38 AU
Venus
0.72 AU
Earth
1 AU
Mars
1.52 AU
not to scale
7.588 billion
years from now
Sun as red giant
0.9 solar mass
Earth
1.1 AU
7.59 billion
years from now
Sun as red giant
0.8 solar mass
Mars
1.9 AU

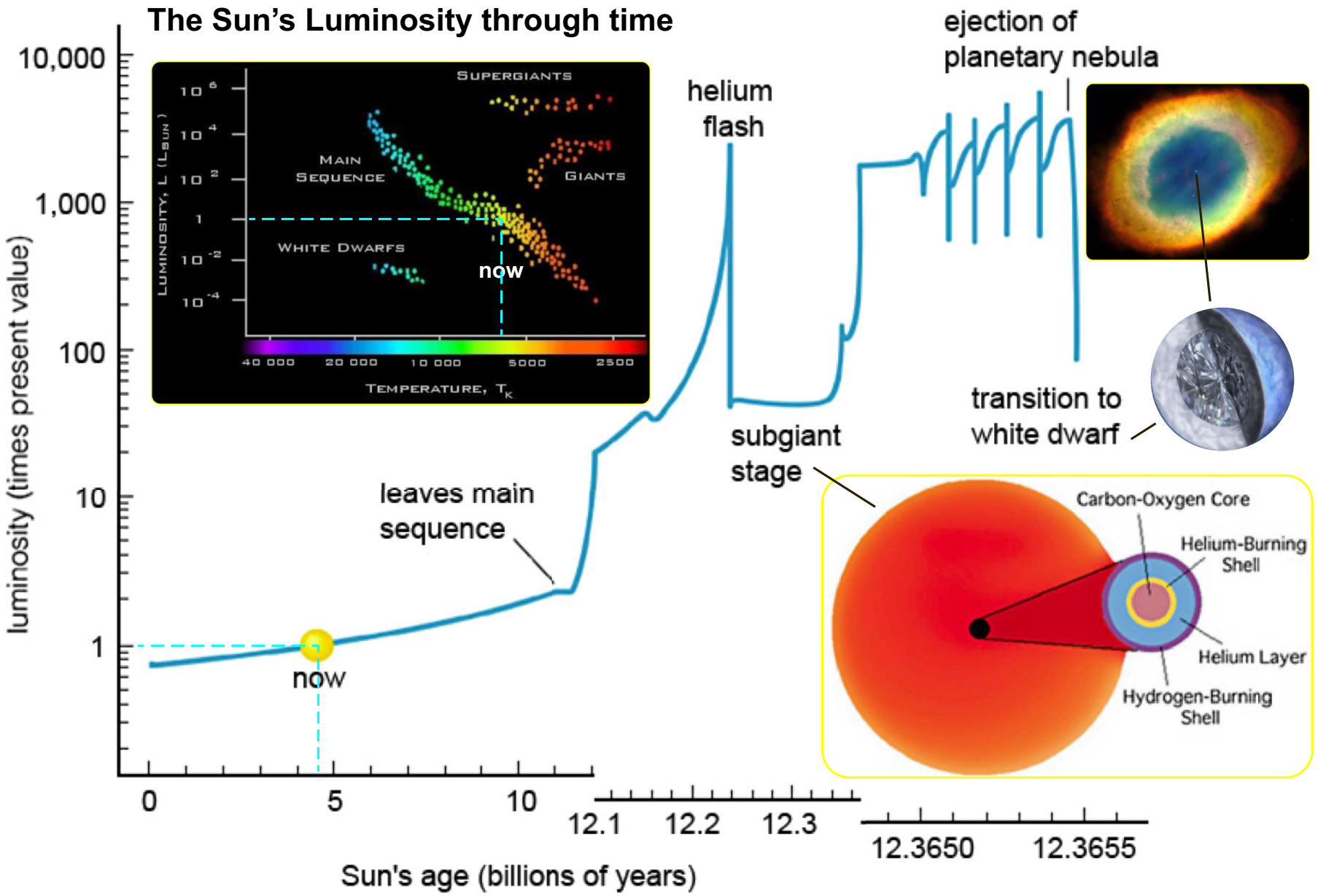
The Sun's Luminosity through time
10,000
1,000
100
10
1
luminosity (times present value)
0
5
10
12.1
12.2
12.3
12.3650
12.3655
Sun's age (billions of years)
now
leaves main sequence
helium flash
subgiant stage
ejection of planetary nebula
transition to white dwarf
Supergiants
Main Sequence
Giants
White Dwarfs
now
Luminosity, L (L sun)
Temperature, T K
40 000
20 000
10 000
5000
2500
Carbon-Oxygen Core
Helium-Burning Shell
Helium Layer
Hydrogen-Burning Shell

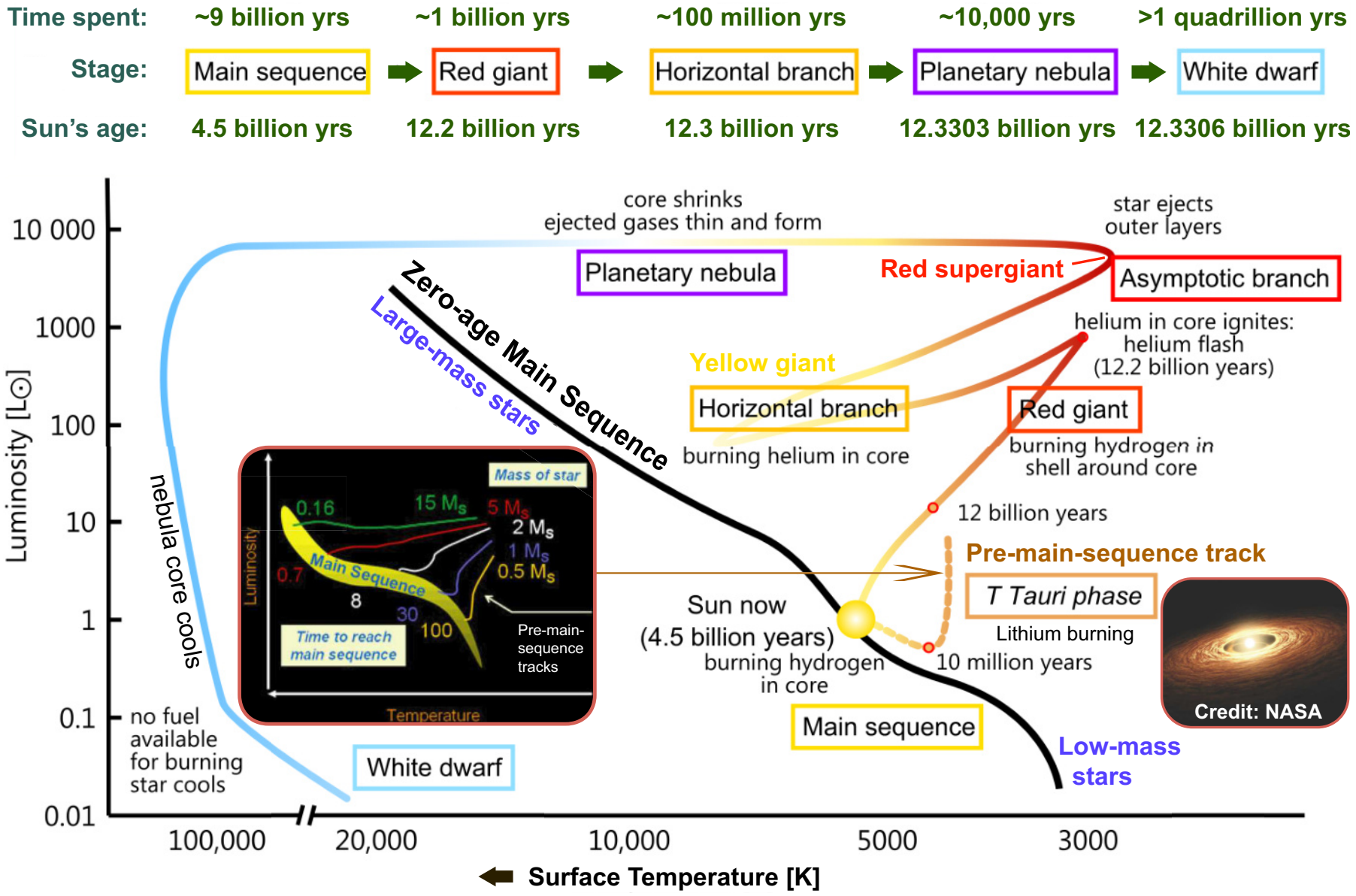

Pre- to post-main-sequence evolution for the Sun. [From https://universe-review.ca/F08-star06.htm].

4.5 Chronology of the solar neutrino experiments.

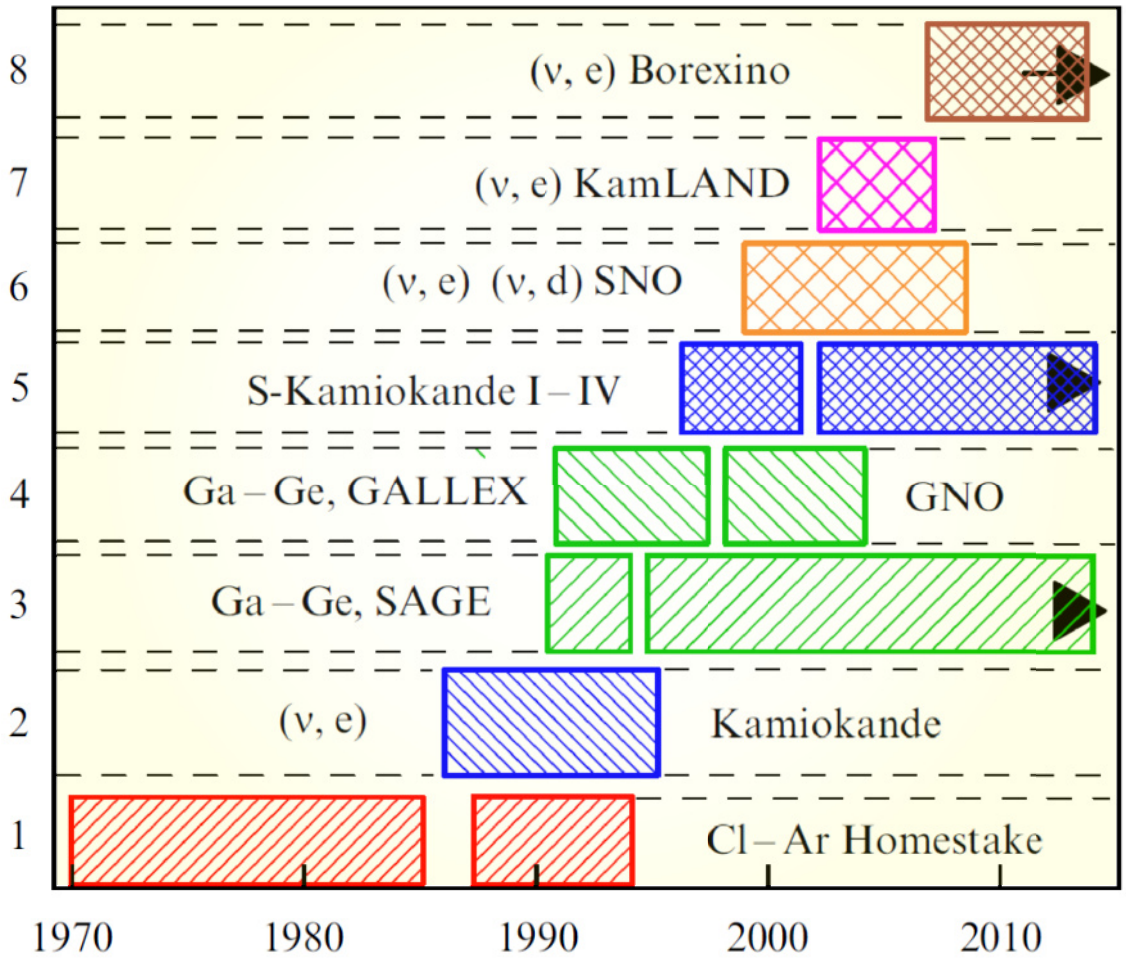

[Borrowed from the lecture by Oleg Smirnov, "Solar- and geo-neutrinos" given on the VIth International Pontecorvo Neutrino Physics School, August 27 – September 4, 2015, Horný Smokovec, Slovakia,
URL: ⟨ http://theor.jinr.ru/~neutrino15/talks/Smirnov.pdf ⟩.]

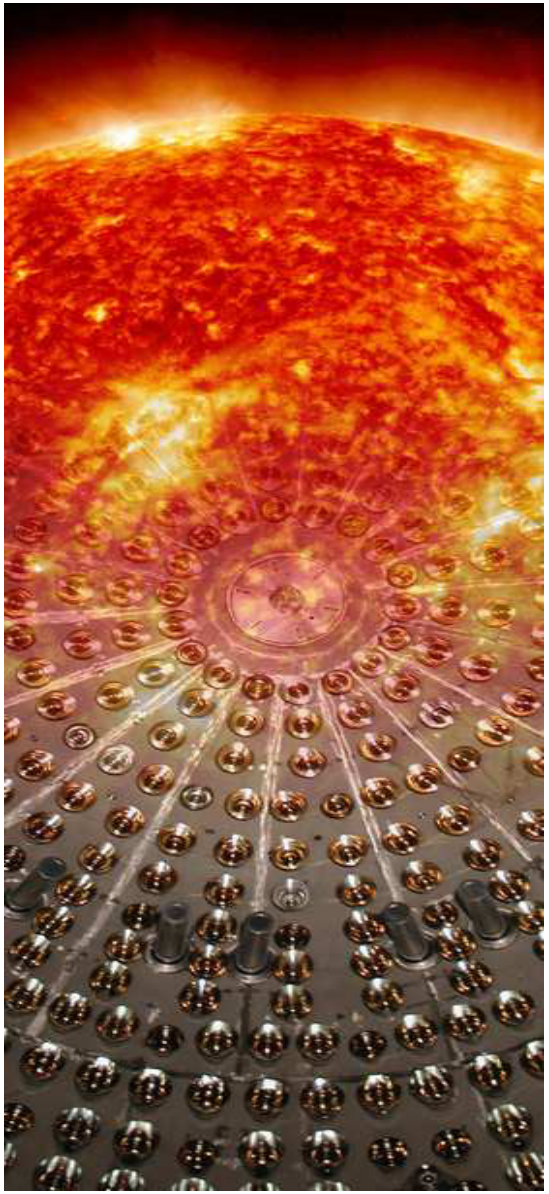

5 Geoneutrinos and interior structure of the Earth.

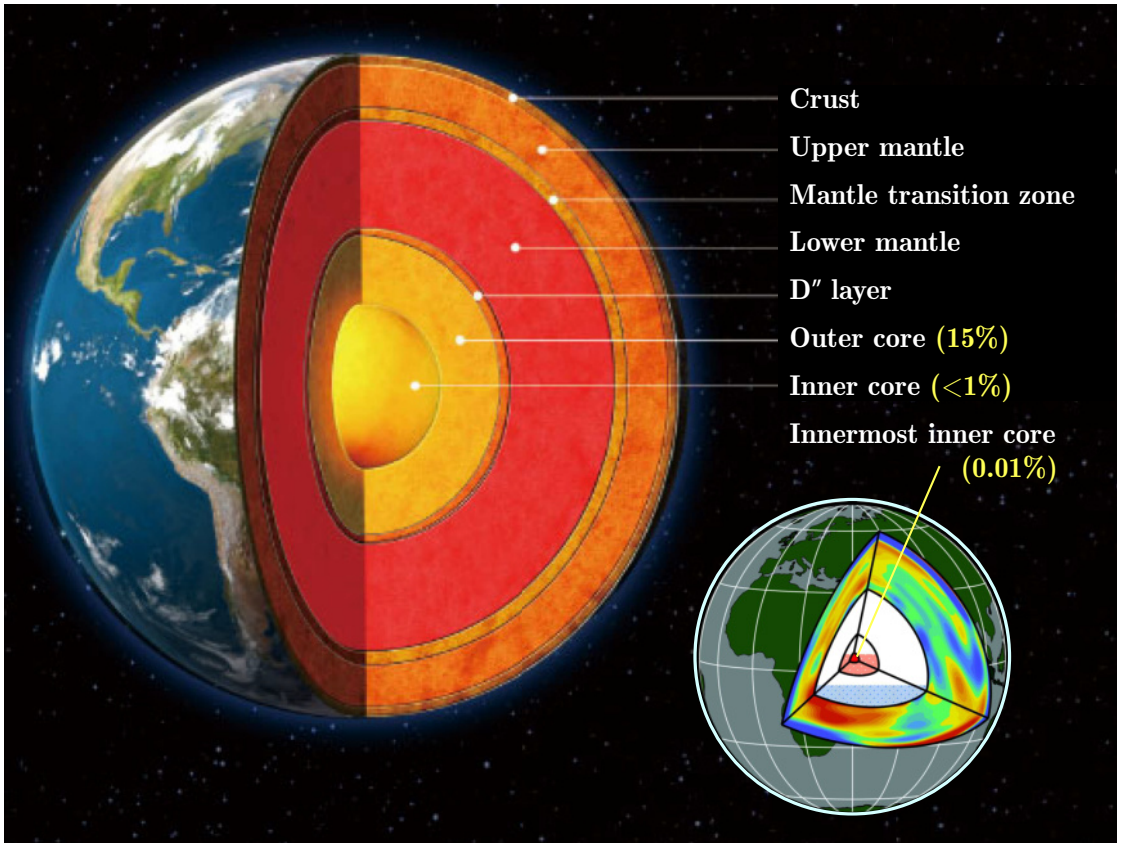

"Almost everything known or inferred about the inner core, from seismology or indirect inference, is controversial".

D. L. Anderson, "The inner core of Earth," Proc. Natl. Acad. Sci. USA **99** (2002) 13966–13968.

◁ A schematic view of Earth's interior.

The volumetric relation of the various regions of the core to the whole Earth is shown in the insert:

outer core (pale blue) occupies 15%, the inner core (pink) occupies less than 1%, and innermost inner core (red) constitutes only 0.01% of Earth's volume.

The Earth core lies beneath 3,000-km thick, heterogeneous mantle (anomalies with higher than average seismic speed are shown in blue and those with lower than average speed are shown in red) making investigations of core properties challenging.

5.1 Preliminary reference Earth model.

For the radial density distribution in the Earth, it is now conventional to use the so-called "Preliminary Reference Earth Model" (PREM).[a]

In PREM, the Earth is divided into 10 concentric layers and the density distribution, $\rho = \rho(R)$, in each layer is approximated by a cubical polynomial:

$$\rho(R) = \sum_{k=0}^{3} a_{nk} \left(R/R_\oplus\right)^k ,$$
$$R_n \le R < R_{n+1},$$
$$n = 0, 1, \ldots, 9$$
$$(R_0 = 0,\ R_{10} = R_\oplus).$$

The nonzero coefficients a_{nk} [in g/cm^3] are listed in Table.

n	R_{n+1} (km)	a_{n0}	a_{n1}	a_{n2}	a_{n3}
0	1221.5	13.0885		-8.8381	
1	3480.0	12.5815	-1.2638	-3.6426	-5.5281
2	5701.0	7.9565	-6.4761	5.5283	-3.0807
3	5771.0	5.3197	-1.4836		
4	5971.0	11.2494	-8.0298		
5	6151.0	7.1089	-3.8045		
6	6346.6	2.6910	0.6924		
7	6356.0	2.9000	← *crust* (must be replaced		
8	6368.0	2.6000	with the local values)		
9	6371.0	1.0200	← *ocean* (ditto)		

Coefficients of the polynomials for the PREM.

[a] A. M. Dziewonski and D. L. Anderson, Phys. Earth Planet. Inter. **25** (1981) 297–356; see also A. M. Dziewonski, "Earth structure, global," in Encyclopedia of solid Earth geophysics, edited by D. E. James (Van Nostrand Reinhold, New York, 1989), pp. 331–359.

The figure on the left shows the Earth layers according to PREM. The four outermost and two inner layers are shown as single ones. Radial density distribution in the Earth calculated according to PREM is shown in Figure on the right.

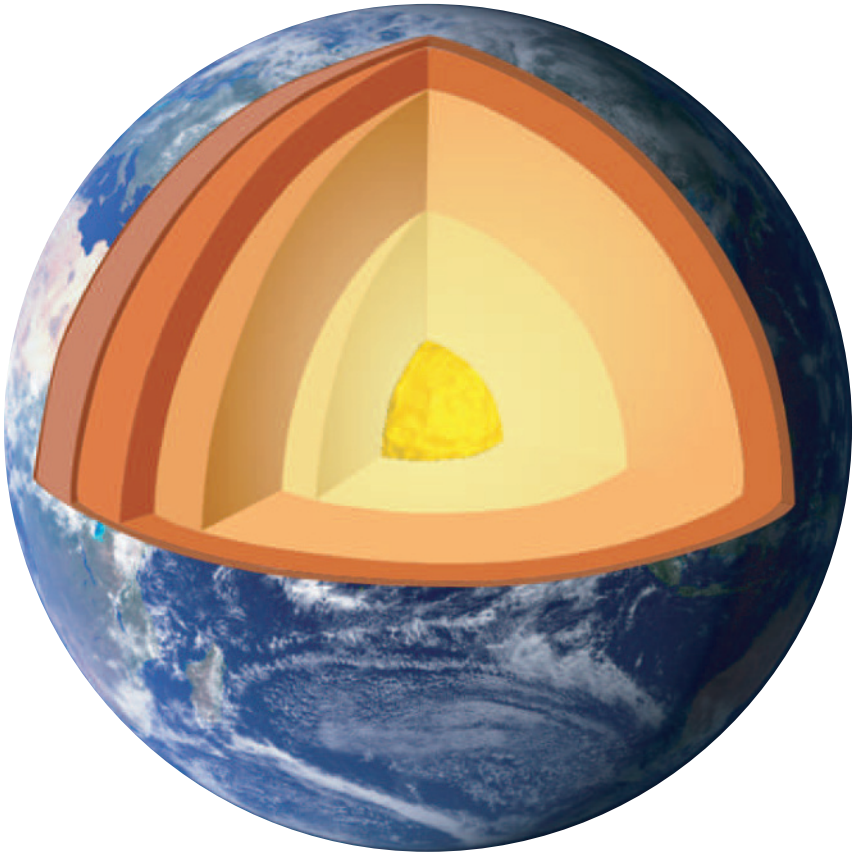

A schematic view of the Earth layers according to PREM.

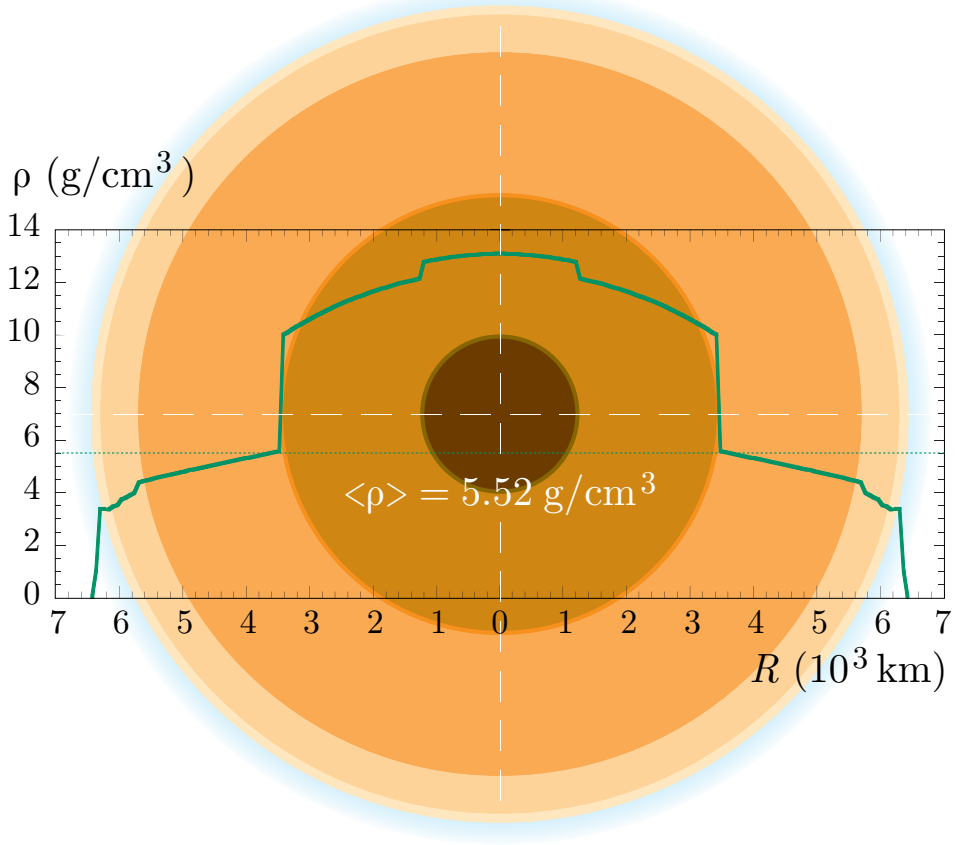

Radial density distribution in the Earth according to PREM.

5.2 Chemical composition of the Earth (where the devil dwells in?)

Measurements of the propagation of seismological waves in the Earth and studies of the properties of minerals under high pressure, have been combined to determine the chemical composition of the Earth's interior.

It is dominated by the elements **iron (Fe)**, **oxygen (O)**, **silicon (Si)**, **magnesium (Mg)**, **nickel (Ni)** and **sulfur (S)**. This is because most of the mass of the Earth occurs within the mantle which is composed largely of the ferromagnesium silicate minerals olivine and pyroxenes.

- The **crust** of the Earth mainly comprises the minerals plagioclase, quartz and hornblende and is dominated by the elements **oxygen (O)**, **silicon (Si)**, **aluminium (Al)**, **iron (Fe)**, **calcium (Ca)**, **sodium (Na)** and **potassium (K)**.
- The **core** of the Earth is largely composed of iron-nickel alloy.

Element	1980/82	1993
Magnesium (Mg)	0.0475	0.0389
Silicon (Si)	0.0326	0.0376
Calcium (Ca)	0.0184	0.0178
Sulfur (S)	0.284	0.285
Iron (Fe)	1.45	1.46
Nickel (Ni)	0.0831	0.0871

Masses ($\times 10^{27}$ g) of the six most abundant elements in the whole Earth's core as estimated by Herndon.

[For more details, see J. M. Herndon, Phys. Earth Planet. Inter. **105** (1998) 1 and references therein.]

The overall composition of the Earth is very similar to that of meteorites, and because of this, it is thought that the Earth originally formed from *planetesimals* composed largely of metallic iron and silicates.

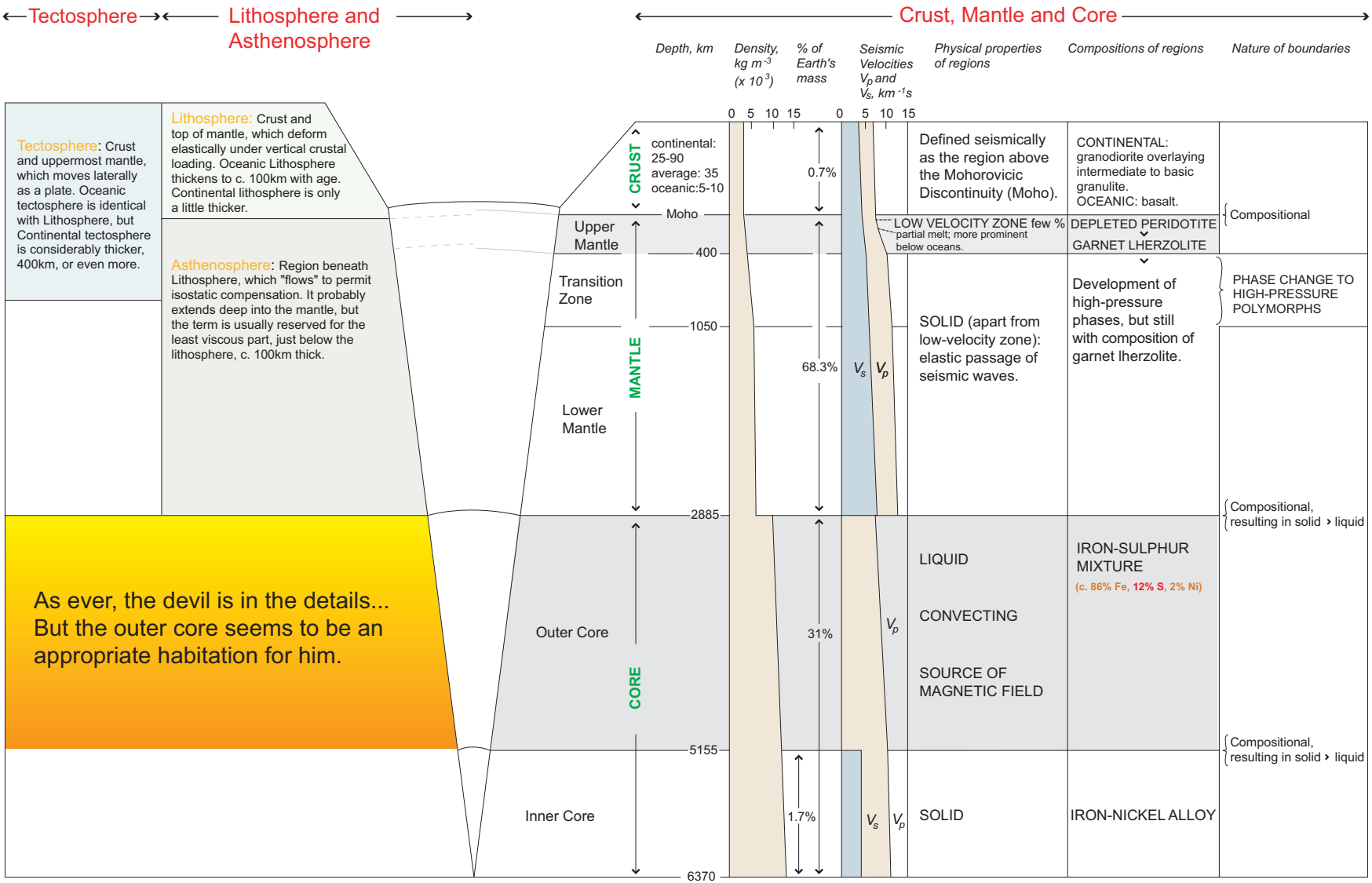

Structure and composition of the Earth according to the Australian Museum online [From URL: <http://www.amonline.net.au/>].

5.3 Charge-to-mass ratio distribution in the Earth.

The mean charge-to-mass ratio, $\langle Z/A \rangle$, has been estimated by Bahcall and Krastev.[a]

Summary:

- $\langle Z/A \rangle = 0.468$ for the core (83% Fe, 9% Ni and 8% light elements with $Z/A = 0.5$),
- $\langle Z/A \rangle = 0.497$ for the mantle (41.2% SiO_2, 52.7% MgO and 6.1% FeO).

[These data are only in qualitative agreement with those in the Figure.]

The charge composition of the Earth may also be illustrated in terms of the number densities of u and d quarks and electrons.

The composition is almost isoscalar but the deviations are not negligible.

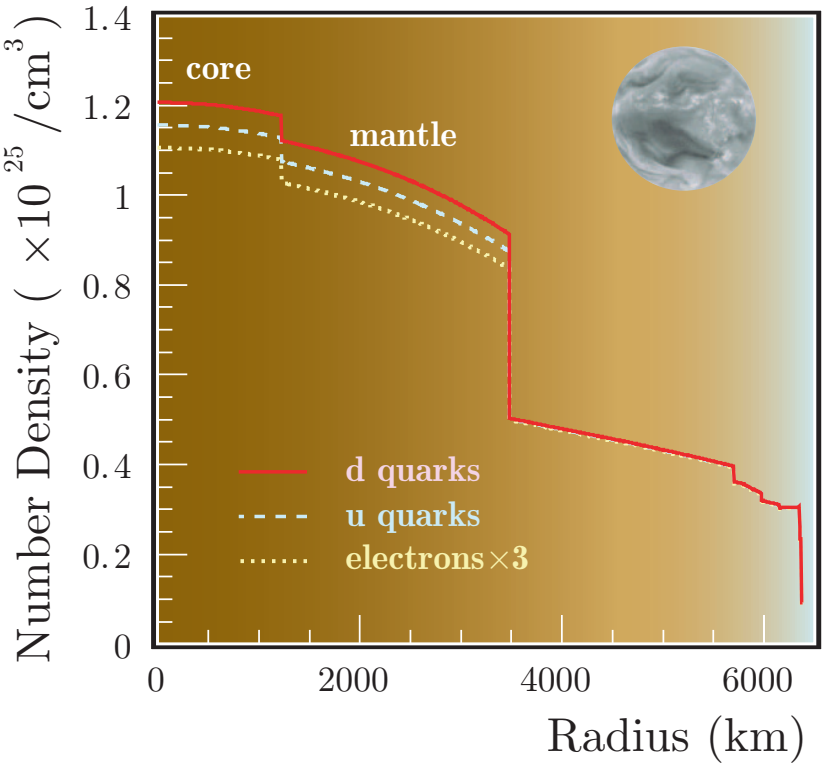

Estimated number densities of quarks and electrons vs distance from the center of the Earth. [From J. Kameda, Ph. D Thesis, University of Tokyo, September, 2002.]

[a] J. N. Bahcall and P. I. Krastev, Phys. Rev. C **56** (1997) 2839–2857. The estimations are based on the experimental data from Y. Zhao and D. L. Anderson, Phys. Earth Planet. Inter. **85** (1994) 273–292.

5.4 Earth's surface heat flow.

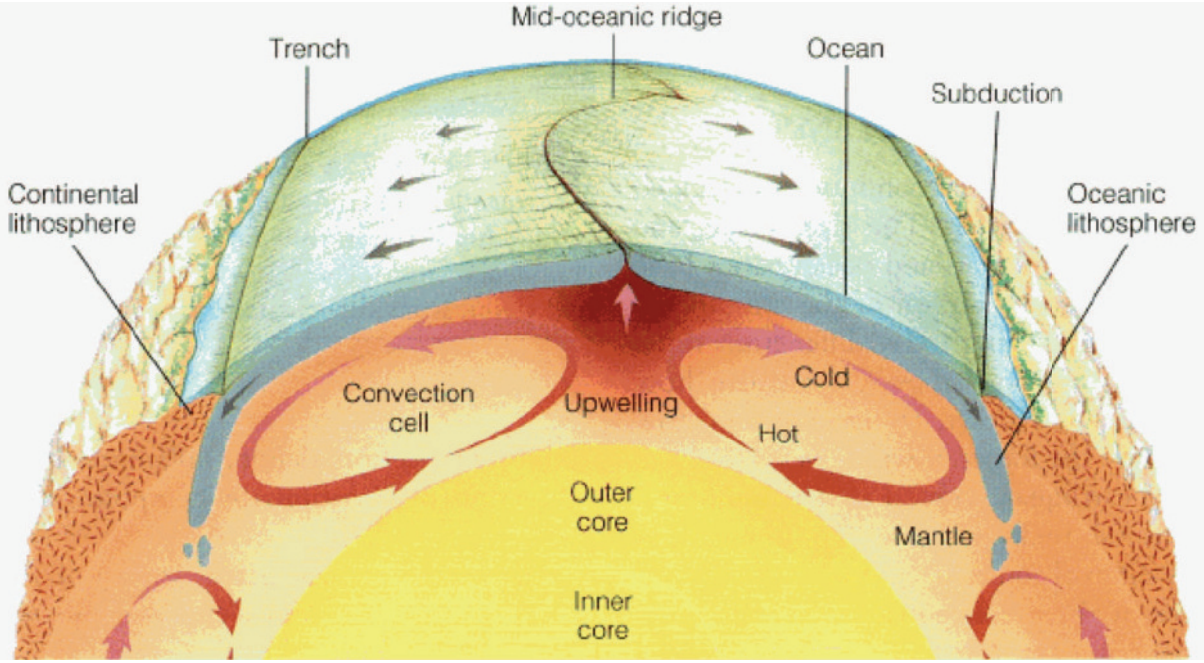

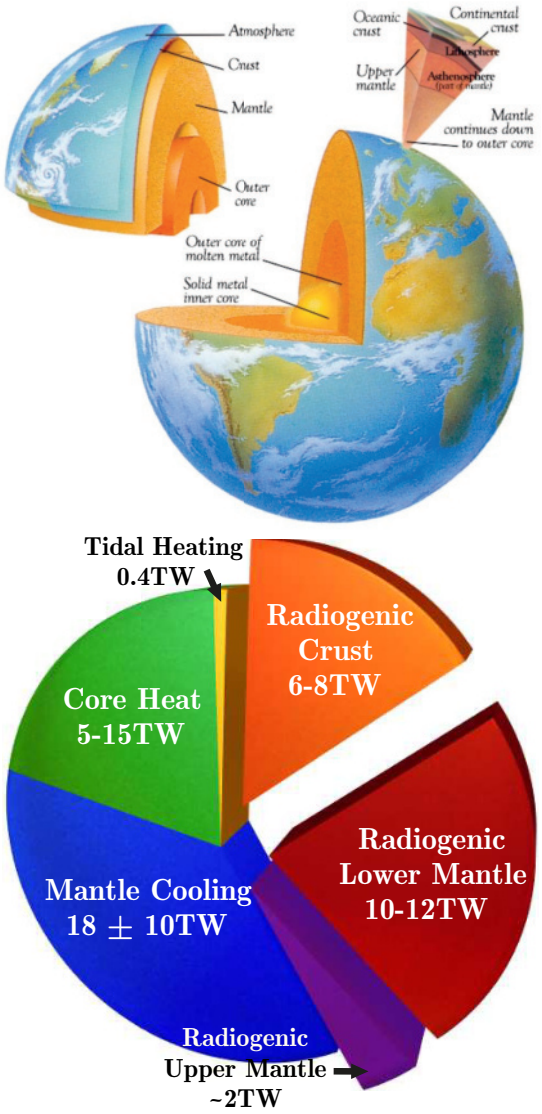

Where does the energy for convections, plate tectonics, etc. come from?

Total heat flow: 46 ± 3 TW (47 ± 2 TW).

$30 - 32$ TW measured (mainly based on bore holes), then extrapolated to account for ocean surface.

5.5 How the Earth is heating up.

The current estimate of radiogenic heat due to U, Th, and K decay is 20 ± 3 TW.

- Abundances of elements in extra-terrestrial rocks (namely, in carbonaceous chondritic meteorites) are similar to those in the solar photosphere.
- Composition of the Earth should be similar to these chondrites (which are believed to be of the same origin from which the Sun and Earth were formed)[a].
- These chondrites contain ^{238}U, ^{232}Th, and ^{40}K. Hence there should be similar concentrations of these isotopes in the Earth.
- From these meteorites, it is known that the Th/U mass ratio is about 3.9.
- Using these data, a typical "reference" model predicts:
  - Uranium and Thorium account for about 8 TW each,
  - Potassium accounts for 3–4 TW.

  ⇓

  Total radioactive power is therefore around 20 TW.

[a] Note that this is a very plausible inference, rather than a well-established fact, see, e.g., I. H. Campbell & H. St. C. O'Neill, "Evidence *against* a chondritic Earth," Nature **483** (2012) 553–558.

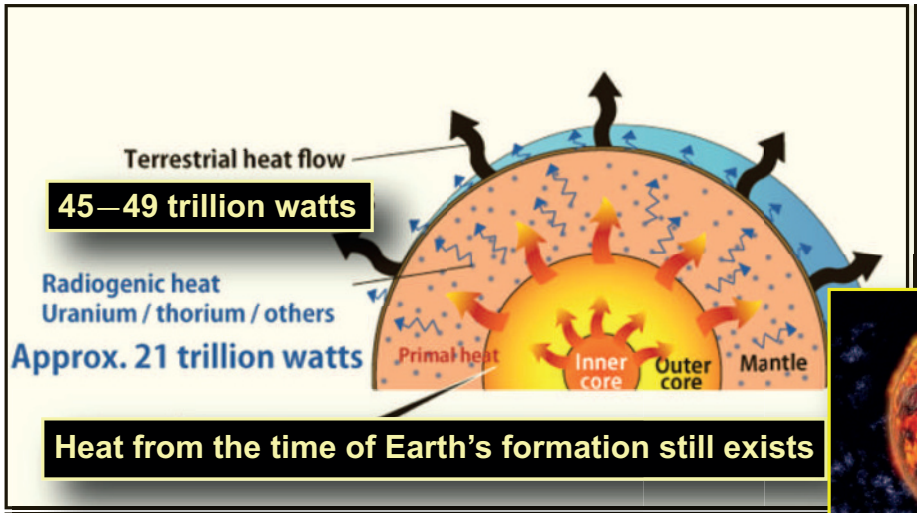
Terrestrial heat flow
45–49 trillion watts
Radiogenic heat
Uranium / thorium / others
Approx. 21 trillion watts
Primal heat
Inner core
Outer core
Mantle
Heat from the time of Earth's formation still exists

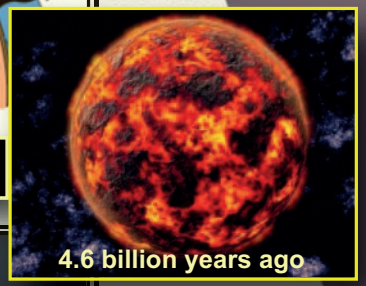
4.6 billion years ago

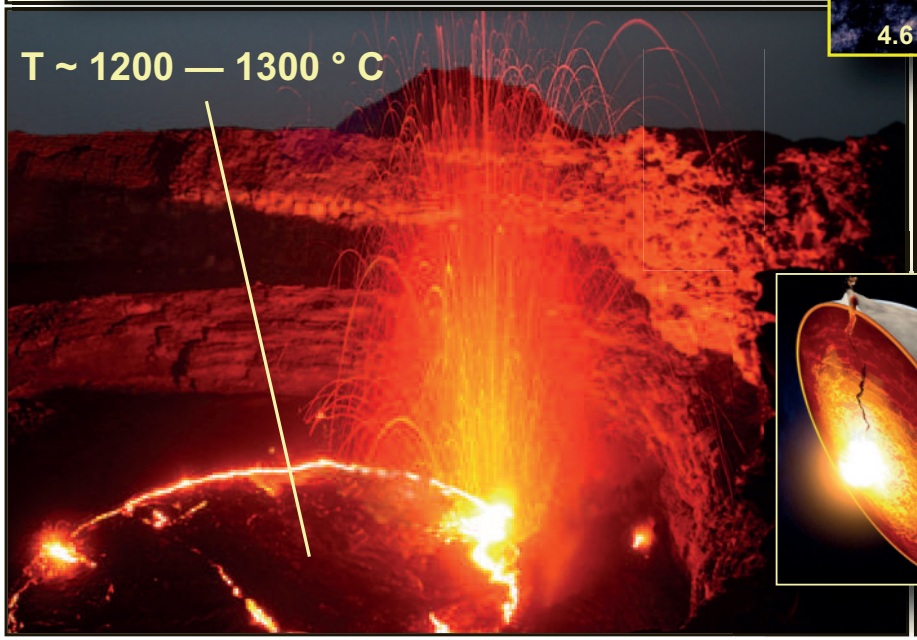
T ~ 1200 — 1300 ° C

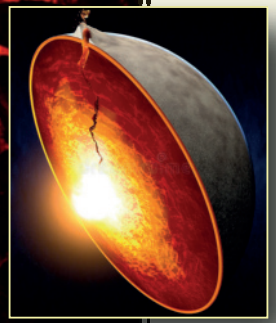

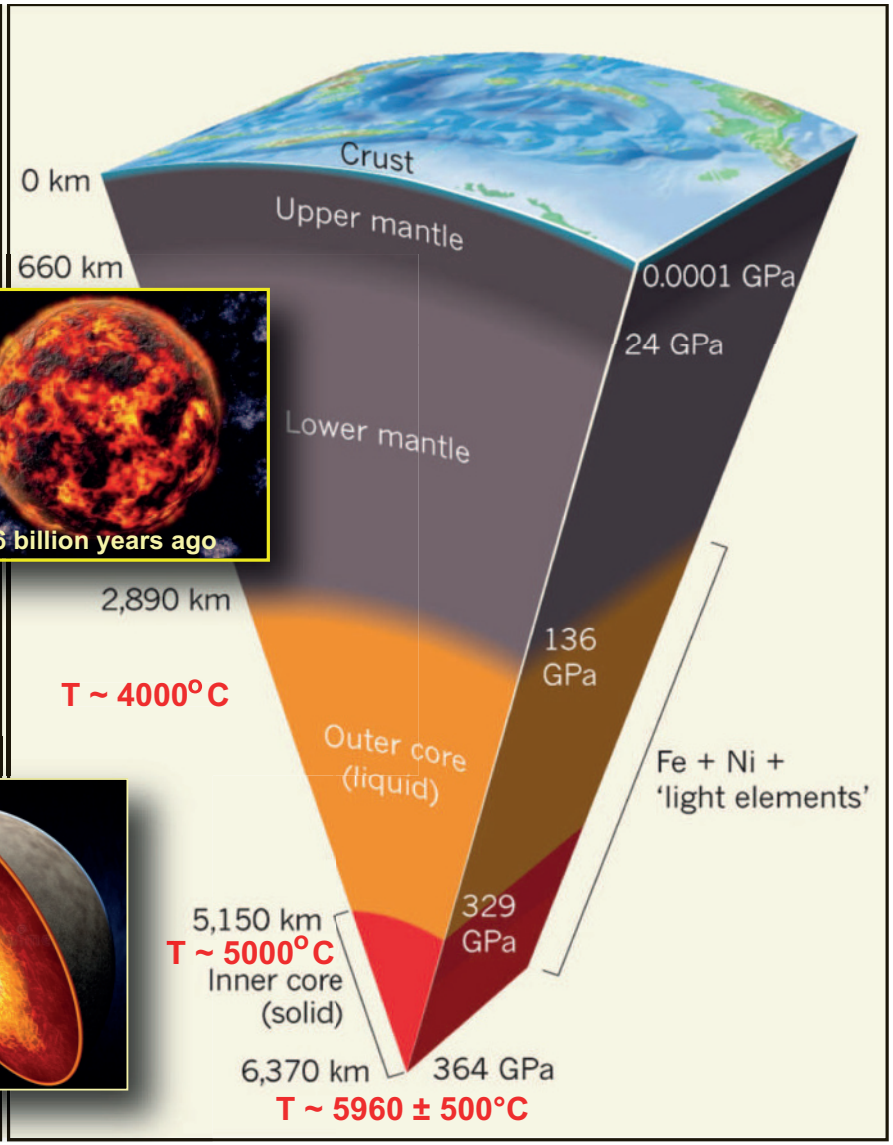
0 km
Crust
Upper mantle
660 km
0.0001 GPa
24 GPa
Lower mantle
2,890 km
136 GPa
T ~ 4000°C
Outer core (liquid)
Fe + Ni + 'light elements'
329 GPa
5,150 km
T ~ 5000°C
Inner core (solid)
6,370 km
364 GPa
T ~ 5960 ± 500°C

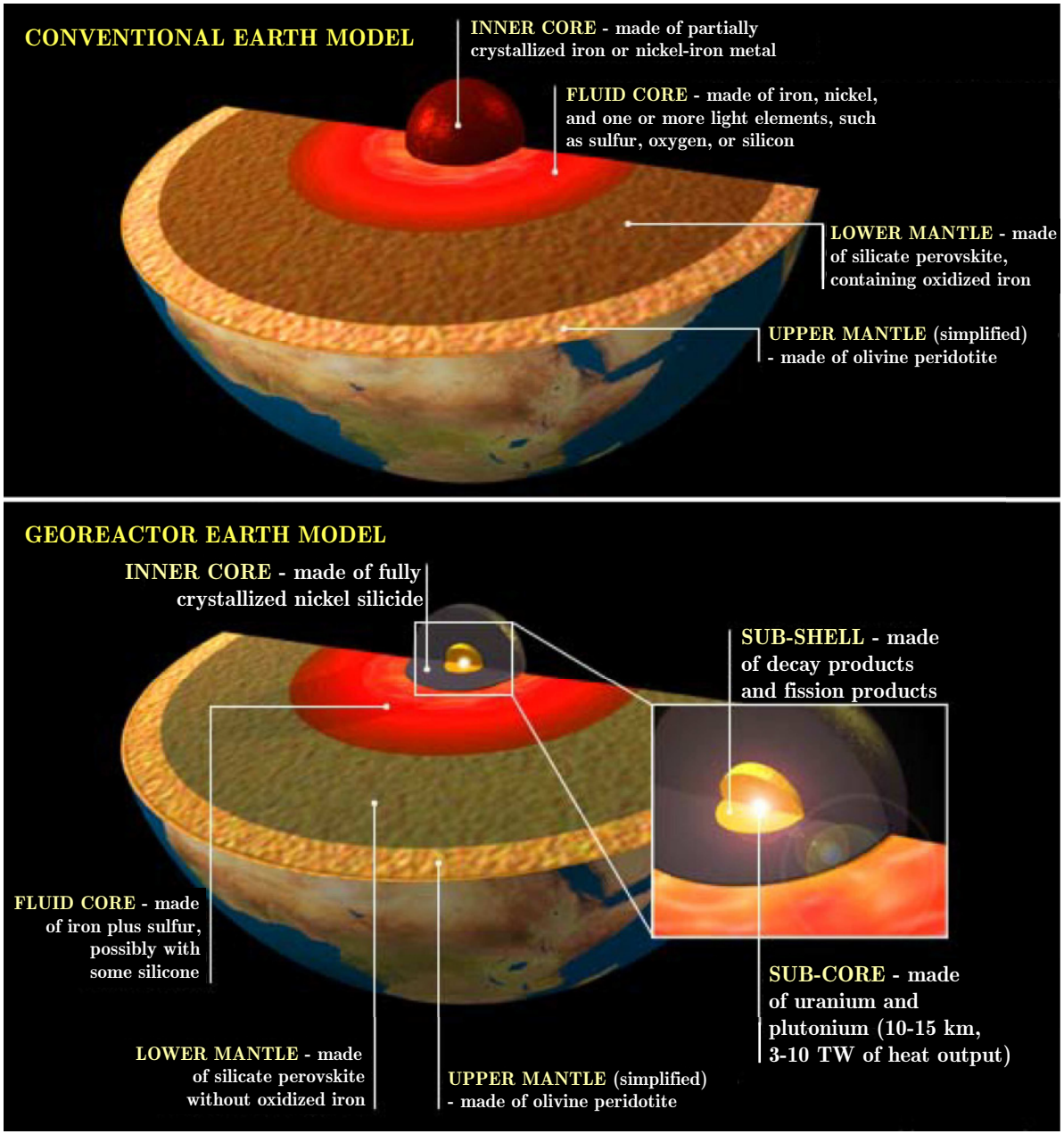

Georeactor is not a mainstream model but it is motivated by

- the observation that the $^3He/^4He$ high at some volcanic eructations,
- Oklo natural reactor 2 Gy ago (anomalous $^{235}U/^{238}U$, $^{140}Ce/^{142}Ce$, $^{147}Sm/^{149}Sm$ ratios, concentrations of Nd isotopes).

The georeactor in the center of Earth should produce $\overline{\nu}$s according to reactor spectrum.

Decay chain (natural abundance, half-life)	$E_{\max}$ [MeV]	Q [MeV]	Q_{eff} [MeV]	$\varepsilon_{\overline{\nu}}$ [1/(kg s)]	ε_H [W/kg]	$\varepsilon'_{\overline{\nu}}$ [1/(kg s)]	ε'_H [W/kg]
$^{238}\text{U} \to {}^{206}\text{Pb} + 8\,{}^4\text{He} + 6e + 6\overline{\nu}$	3.26	51.7	47.7	7.46×10^{7}	0.95×10^{-4}	7.41×10^{7}	0.94×10^{-4}
(NA $= 0.9927$, $T_{1/2} = 4.47\times10^{9}$ yr)							
$^{232}\text{Th} \to {}^{208}\text{Pb} + 6\,{}^4\text{He} + 4e + 4\overline{\nu}$	2.25	42.7	40.4	1.62×10^{7}	0.27×10^{-4}	1.62×10^{7}	0.27×10^{-4}
(NA $= 1.0000$, $T_{1/2} = 1.40\times10^{10}$ yr)							
$^{40}\text{K} \to {}^{40}\text{Ca} + e + \overline{\nu}$ (89%)	1.311	1.311	0.590	2.32×10^{8}	0.22×10^{-4}	2.71×10^{4}	2.55×10^{-9}
$^{40}\text{K} + e \to {}^{40}\text{Ar} + \nu$ (11%)	0.044	1.505	1.461	$=$	0.65×10^{-5}	$=$	0.78×10^{-9}
(NA $= 1.17\times10^{-4}$, $T_{1/2} = 1.28\times10^{9}$ yr)							
$^{235}\text{U} \to {}^{207}\text{Pb} + 7\,{}^4\text{He} + 4e + 4\overline{\nu}$	1.23	46.4	44	3.19×10^{8}	0.56×10^{-3}	2.30×10^{6}	0.40×10^{-5}
(NA $= 0.0072$, $T_{1/2} = 7.04\times10^{8}$ yr)							
$^{87}\text{Rb} \to {}^{87}\text{Sr} + e + \overline{\nu}$	0.283	0.283	0.122	3.20×10^{6}	0.61×10^{-7}	8.91×10^{5}	0.17×10^{-7}
(NA $= 0.2783$, $T_{1/2} = 4.75\times10^{10}$ yr)							

Properties of ^{238}U, ^{232}Th, ^{40}K, ^{235}U, and ^{87}Rb and of their (anti)neutrinos. For each parent nucleus the table presents the natural isotopic mass abundance (NA), half-life ($T_{1/2}$), (anti)neutrino maximal energy ($E_{\max}$), Q value, $Q_{\text{eff}} = Q - \langle E_{(\nu,\overline{\nu})} \rangle$, antineutrino and heat production rates for unit mass of the isotope ($\varepsilon_{\overline{\nu}}$, ε_H), and for unit mass at natural isotopic composition ($\varepsilon'_{\overline{\nu}}$, ε'_H). Note that antineutrinos with energy above threshold for inverse beta decay on free proton ($E_{\text{th}} = 1.806$ MeV) are produced only in the firsts two decay chains.

[From G. Fiorentini *et al.*, "Geo-neutrinos and Earth's interior," Phys. Rept. **453** (2007) 117–172, arXiv:0707.3203 [physics.geo-ph].]

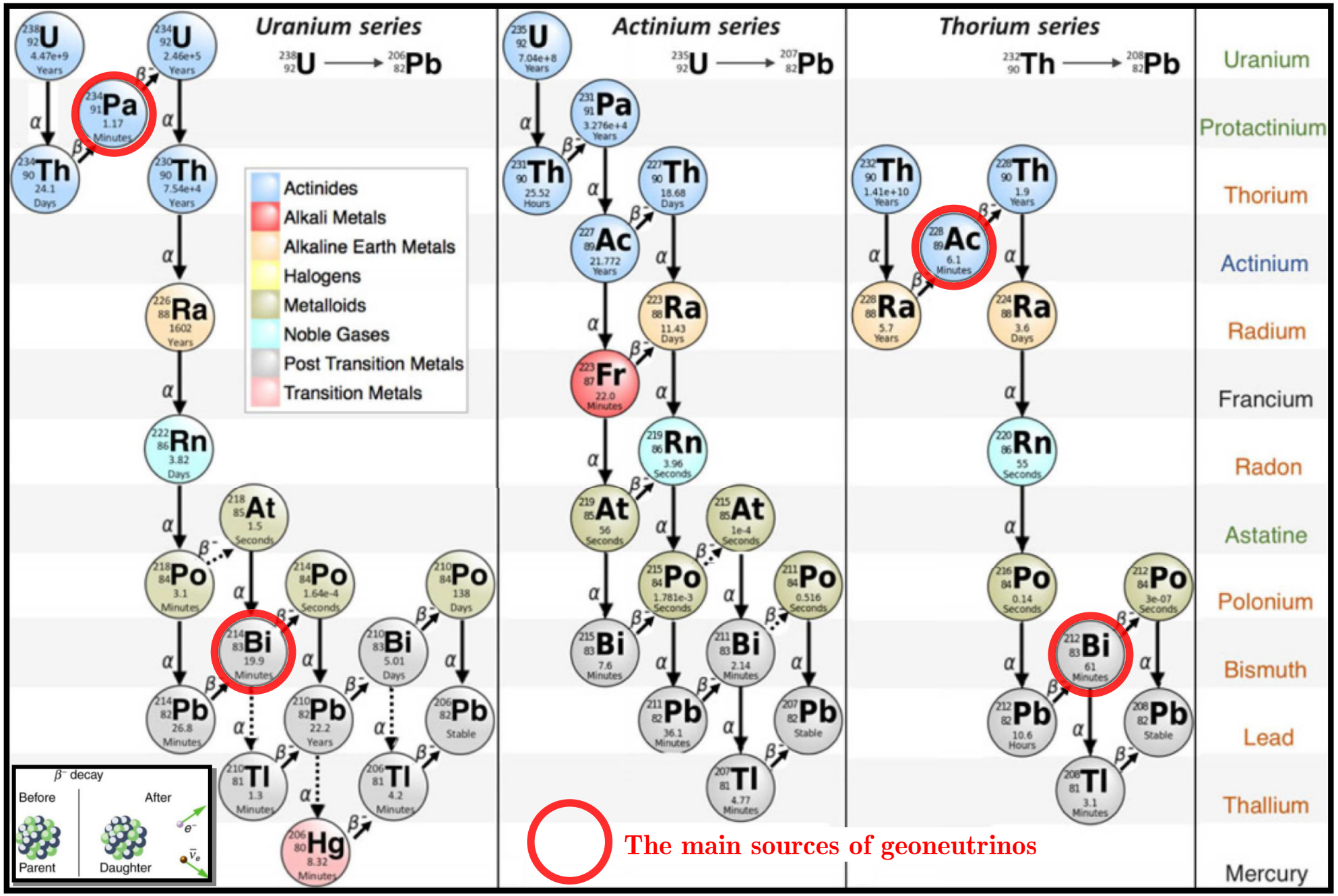
Uranium series
238 92 U → 206 82 Pb
Actinium series
235 92 U → 207 82 Pb
Thorium series
232 90 Th → 208 82 Pb
Actinides
Alkali Metals
Alkaline Earth Metals
Halogens
Metalloids
Noble Gases
Post Transition Metals
Transition Metals
β⁻ decay
Before
After
Parent
Daughter
The main sources of geoneutrinos
Uranium
Protactinium
Thorium
Actinium
Radium
Francium
Radon
Astatine
Polonium
Bismuth
Lead
Thallium
Mercury

It is difficult to detect the main part of the radiogenically produced $\overline{\nu}_e$s; e.g., the detection mechanism in LENA (projected large volume liquid scintillation detector for Low Energy Neutrino Astronomy) is the $\overline{\nu}_e$ capture on Hydrogen ($\overline{\nu}_e + p \rightarrow n + e^+$). Therefore, only some of the $\overline{\nu}$s originating in ^{238}U and ^{232}Th chains are suitable as they can reach energies above the 1.8 MeV threshold. The low-energy $\overline{\nu}$s (from potassium, etc.) are completely lost to detection.

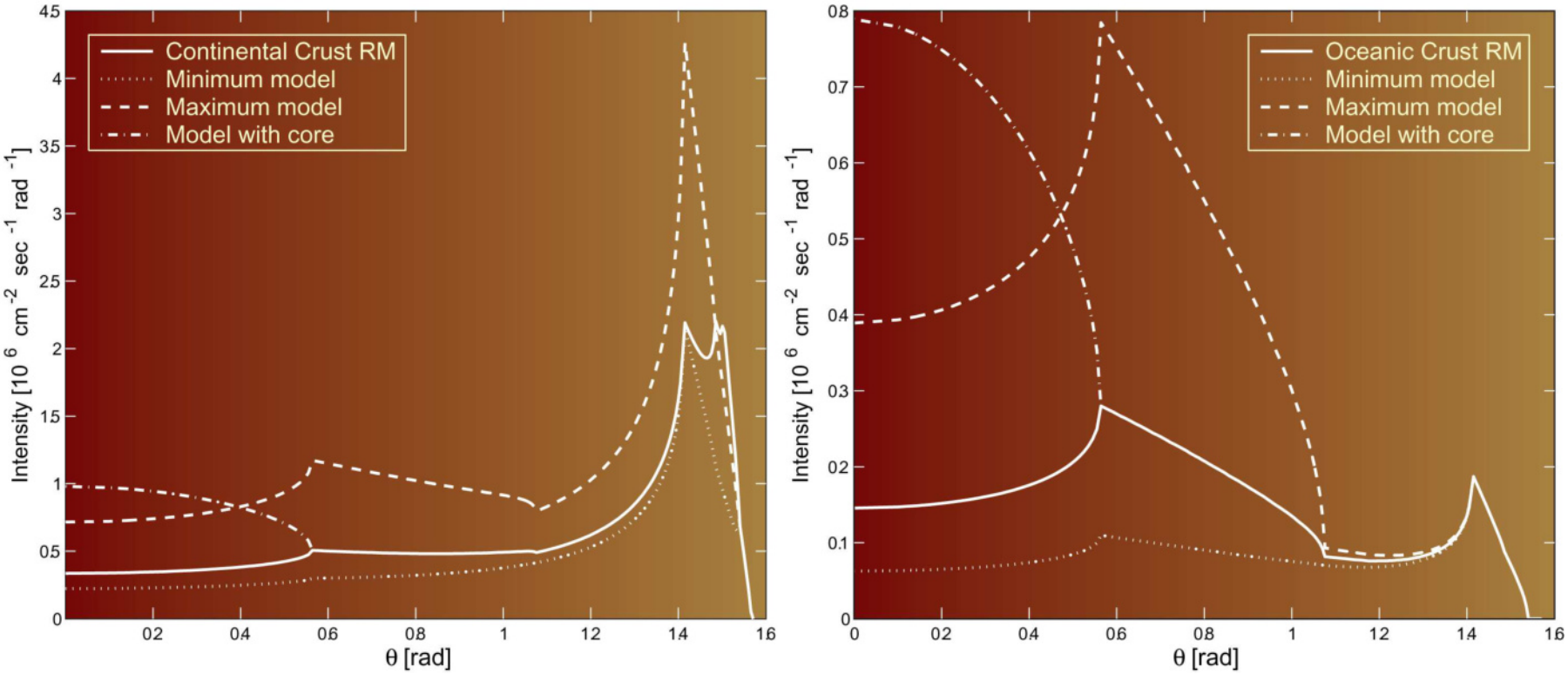

Figure shows the angular distributions of terrestrial antineutrinos as they will be seen by LENA for the continental crust (*left panel*) and oceanic crust (*right panel*) reference models. The 1.8 MeV energy threshold of the detection reaction and the $\overline{\nu}_e$ energy spectra are taken into account. Also shown the model-dependent variations of the intensity.

[Taken from K. A. Hochmuth *et al.*, "Probing the Earth's interior with a large-volume liquid scintillator detector," Astropart. Phys. **27** (2007) 21–29, hep-ph/0509136.]

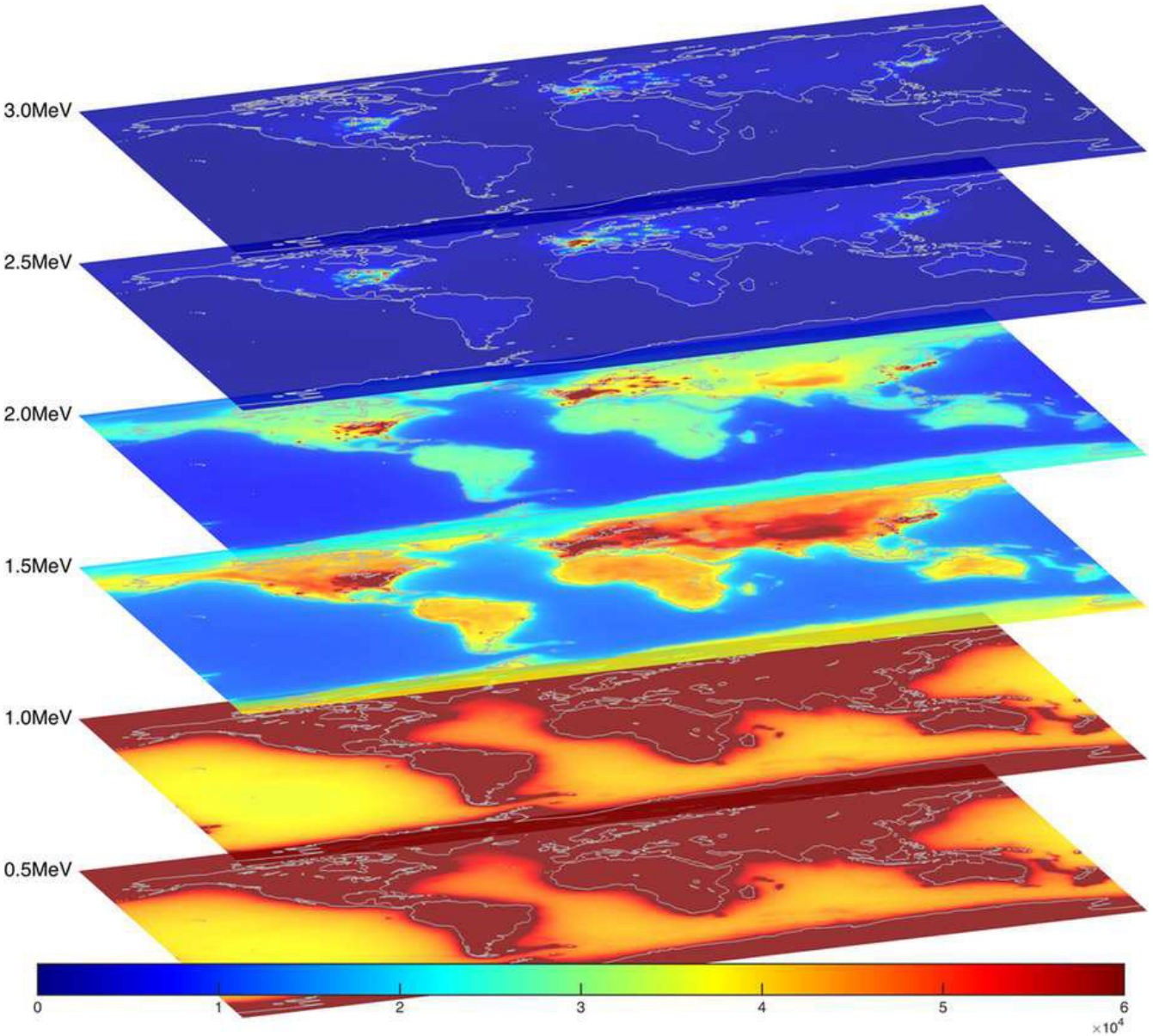

AGM2015 electron antineutrino flux (in units $\overline{\nu}_e/(\text{cm}^2\,\text{s}\,\text{keV})$) displayed at 6 select energy bins out of the 1100 total AGM2015 energy bins, which uniformly span the $0 - 11$ MeV $\overline{\nu}_e$ energy range. Each energy bin is 10 keV wide. In conjunction with 720 longitude bins and 360 latitude bins, the highest resolution AGM2015 map is a $360 \times 720 \times 1100$ 3D matrix comprising $\sim 3 \times 10^8$ elements total.

[From S. M. Usman *et al.*, "AGM2015: Antineutrino Global Map 2015," Sci. Rep. **5** (2015) 13945, arXiv:1509.03898 [physics.ins-det].]

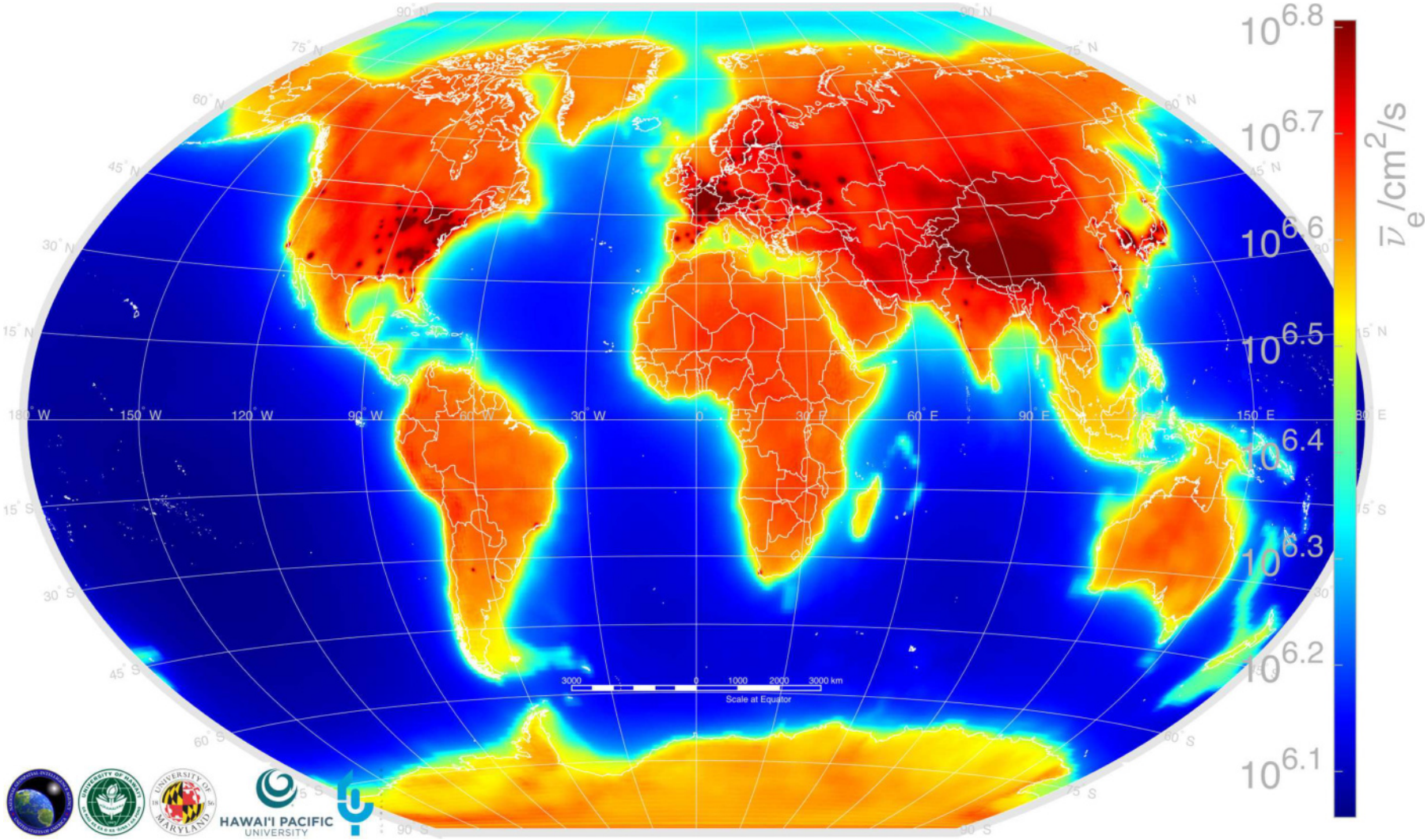

AGM2015: A worldwide $\overline{\nu}_e$ flux map combining geo-$\overline{\nu}_e$s from natural ^{238}U and ^{232}Th decay in the Earth's crust and mantle as well as $\overline{\nu}_e$s emitted by the man-made power reactors worldwide. Flux units are $\overline{\nu}_e/(\mathrm{cm}^2\mathrm{s})$ at the Earth's surface. The map includes $\overline{\nu}_e$s of all energies.

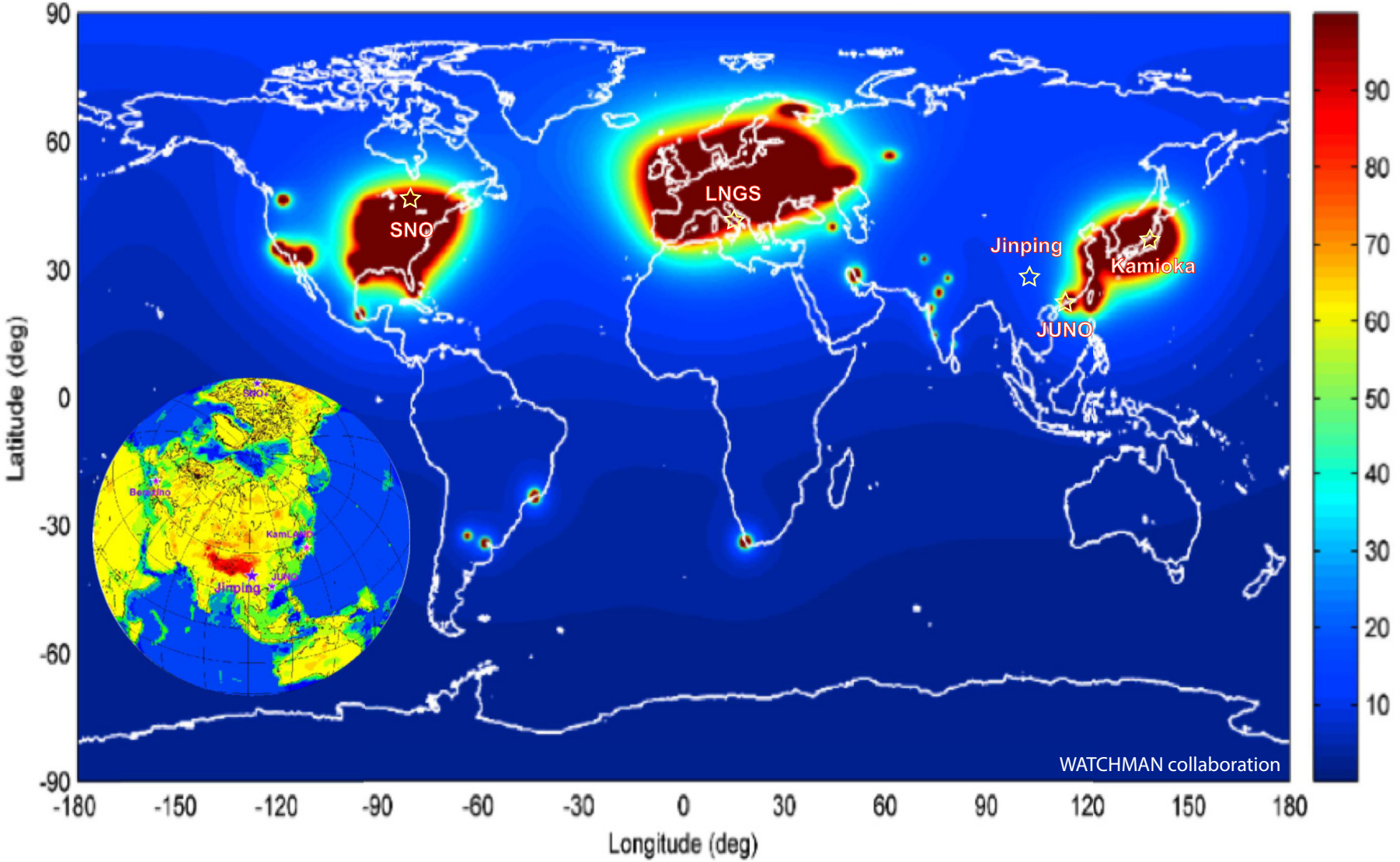

A map of the global nuclear reactor $\overline{\nu}_e$ flux, showing the three important industrialized regions that dominate the worldwide flux (by WATCHMAN simulation package).
[From URL: ⟨https://ldrd-annual.llnl.gov/ldrd-annual-2015/nuclear/water⟩.]

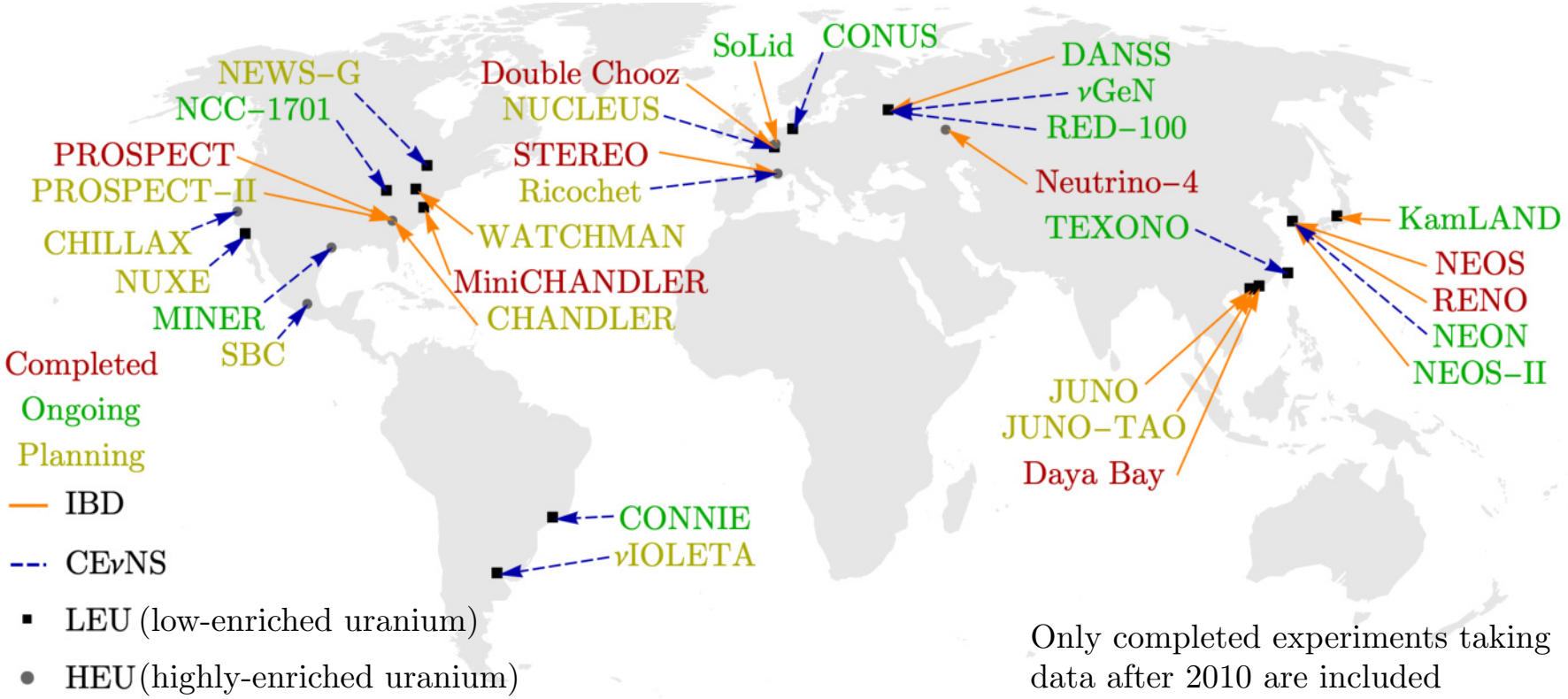

Map of planned, current, and recently completed reactor (or potentially reactor-related as, e.g., NEWS-G) antineutrino experiments relying on the inverse beta decay (IBD) or coherent elastic neutrino-nucleus scattering (CEνNS) detection channels. The text color indicates experimental status ($\sim$ Fall 2021), while the arrow color indicates the interaction channel used by the experiment.

[From O. A. Akindele *et al.*, "HEP physics opportunities using reactor antineutrinos: A Snowmass 2021 White Paper Submission," arXiv:2203.07214 [hep-ex]; see also L. Fields *et al.* (Neutrino Frontier Topical Group 09), "Report of the topical group on artificial neutrino sources for Snowmass 2021," arXiv:2209.07480 [hep-ex].]

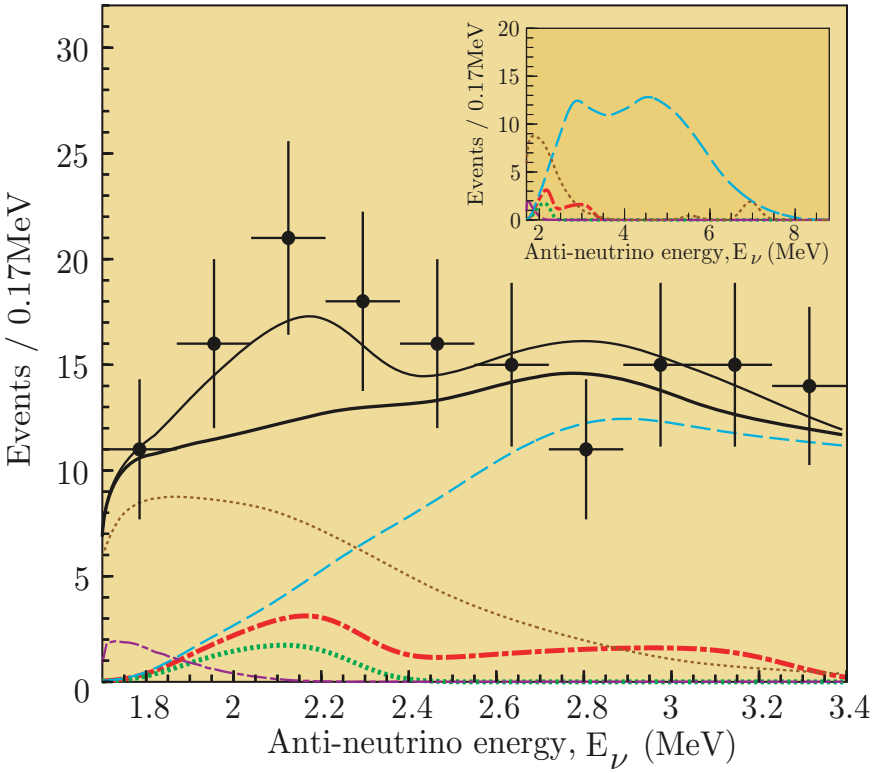

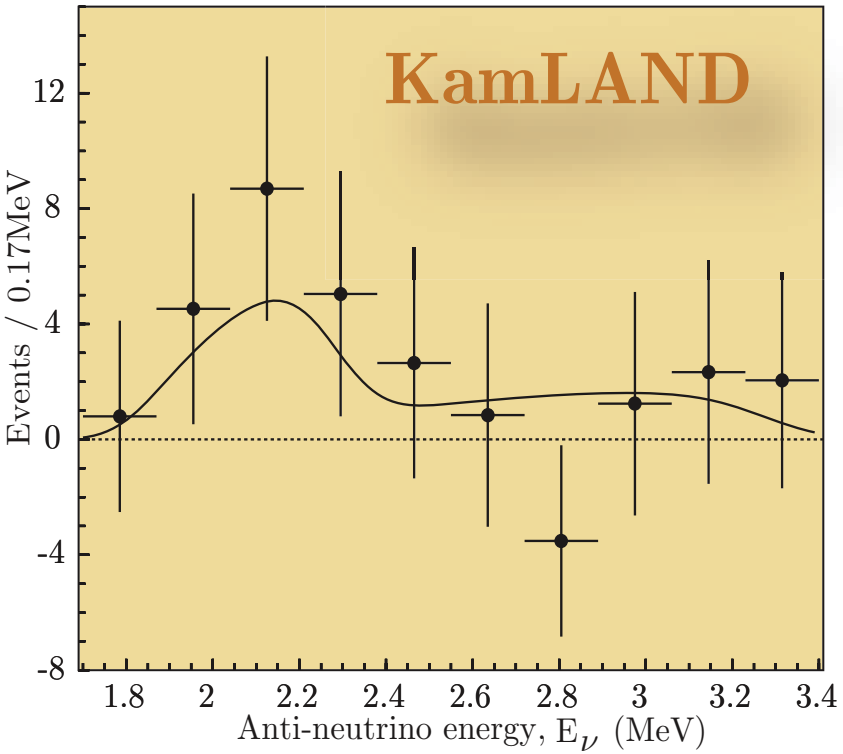

Left panel: $\overline{\nu}_e$ energy spectra of the candidate events (data), the total expectation (thin solid black line), the total background (thick solid black line), the expected ^{238}U (dot-dashed red line), the expected ^{232}Th (dotted green line), and the backgrounds due to reactor $\overline{\nu}_e$ (dash blue line), $^{13}\mathrm{C}(\alpha, n)^{16}\mathrm{O}$ reactions (dotted brown line) and random coincidences (dot-dashed violet line). The inset shows the expected signal extended to higher energies.

Right panel: $\overline{\nu}_e$ energy spectra of the candidate events substructed by the total backgrounds.

[From A. Suzuki (for the KamLAND Collaboration), "Reactor- and geo-neutrino detections from KamLAND," AIP Conf. Proc. **815** (2006) 19–28.]

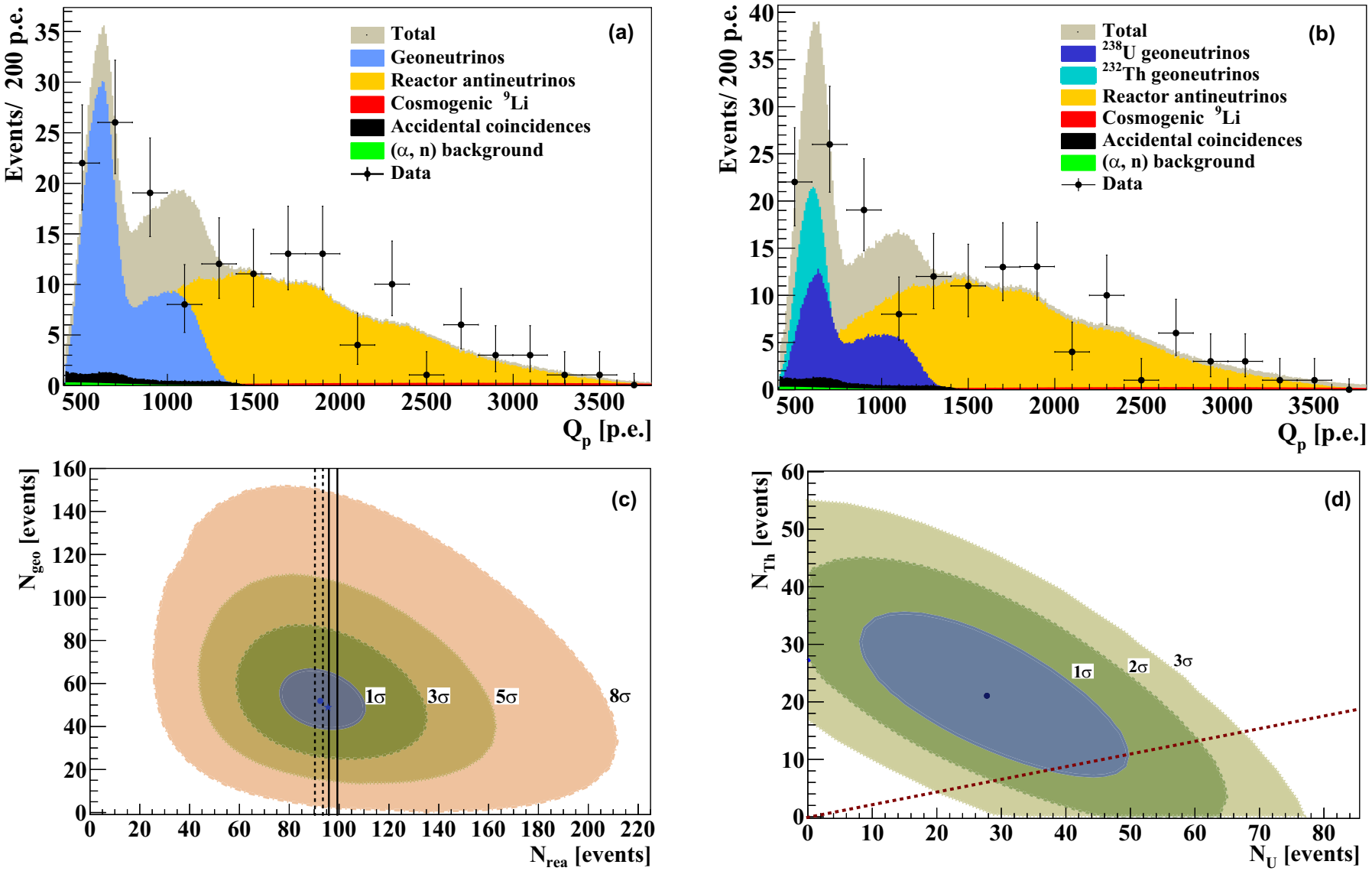

Results of the 2019 Borexino analysis of 154 golden IBD candidates (see the next slide for details).

[From M. Agostini *et al.* (Borexino Collaboration), "Comprehensive geoneutrino analysis with Borexino," Phys. Rev. D **101** (2020) 012009, arXiv:1909.02257 [hep-ex].]

Explanation to previous slide:

The current Borexino analysis is the result of 3262.74 days of data collected between December 2007 and April 2019; compare with the earlier (2015) Borexino analysis, shown at p. 858.

Panels (a) and (b) show the prompt light yield spectra, in units of photoelectrons (p.e.), of geo-$\overline{\nu}_e$ candidates versus prompt event energy Q (also in p.e.); notice the slightly different vertical scales.

(a) Spectral fit of the data (black points with Poissonian errors) assuming the chondritic Th/U ratio. The total fit function containing all signal and background components is shown in brownish-grey. Geoneutrinos (blue) and reactor antineutrinos (yellow) were kept as free fit parameters. Other nonantineutrino backgrounds were constrained in the fit.

(b) Similar fit as in (a) but with ^{238}U (dark blue) and ^{232}Th (cyan) contributions as free and independent fit components.

(c) The best fit point (blue dot) and the contours for the 2D coverage of 68%, 99.7%, $(100 - 5.7 \times 10^{-5})\%$, and $(100 - 1.2 \times 10^{-13})\%$ (corresponding to 1σ, 3σ, 5σ, and 8σ, respectively), for N_{geo} (number of geoneutrinos) versus N_{rea} (number of reactor antineutrinos) assuming Th/U chondritic ratio. The vertical lines mark the 1σ bands of the expected reactor antineutrino signal (solid – without so-called "5 MeV excess," dashed – with the "5 MeV excess"). For comparison, the blue star shows the best fit performed assuming the ^{238}U and ^{232}Th contributions as free and independent fit components.

(d) The best fit (blue dot) and the 68%, 95.5%, and 99.7% coverage contours (corresponding to 1σ, 2σ, and 3σ contours) N_{Th} versus N_U. The dashed line represents the chondritic Th/U ratio.

The existence of a hypothetical georeactor at the center of the Earth (see p. 205) having power greater than 2.4 TW is excluded at 95% C.L.

A summary of the earlier results on the geo-$\overline{\nu}_e$ measurements.

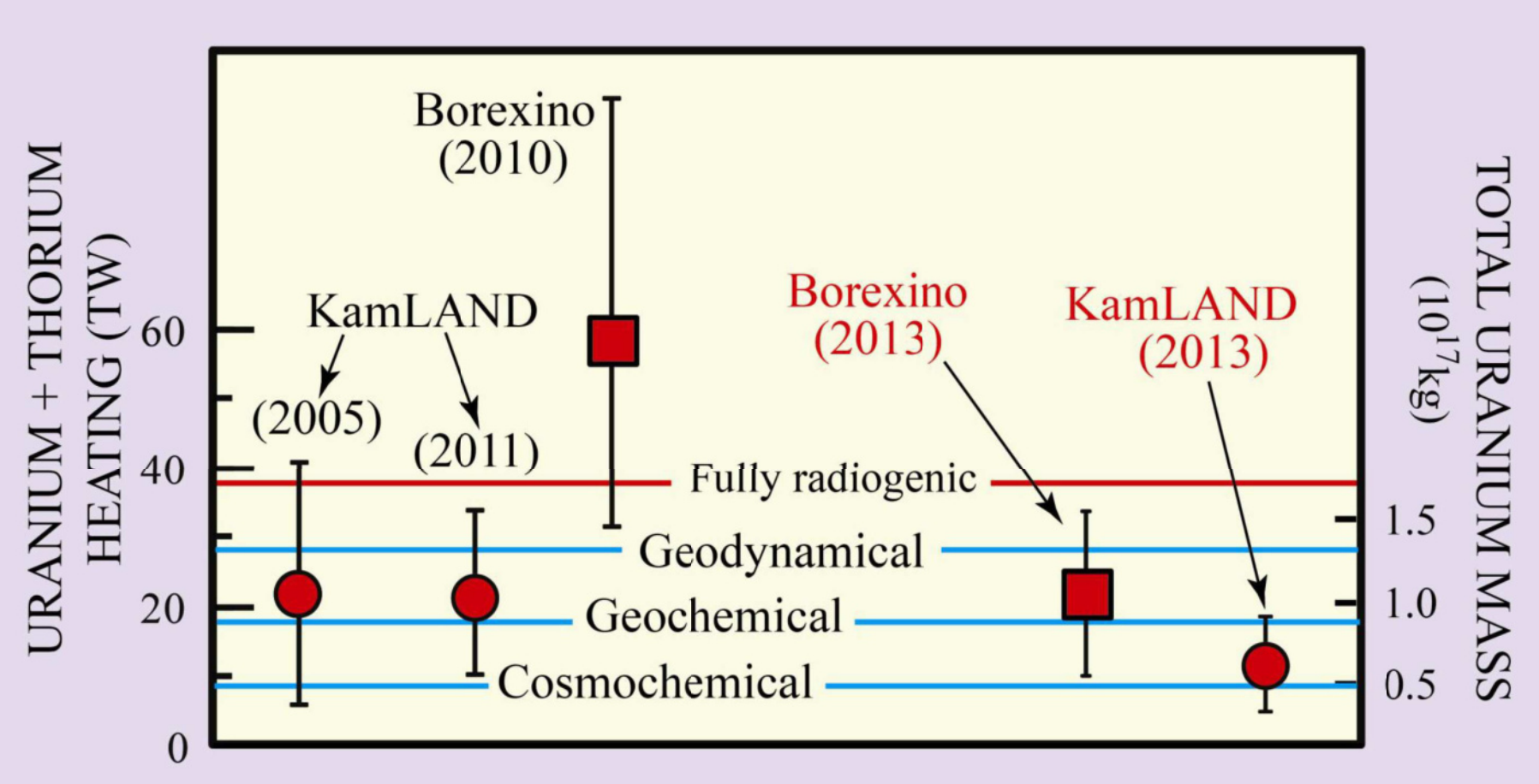

[Borrowed from the lecture by Oleg Smirnov, "Solar- and geo-neutrinos" given on the VIth International Pontecorvo Neutrino Physics School, August 27 – September 4, 2015, Horný Smokovec, Slovakia,
URL: ⟨ <http://theor.jinr.ru/~neutrino15/talks/Smirnov.pdf ⟩.]

Classes	$M_{BSE}(U)$ [10^{16} kg]	$M_{BSE}(Th)$ [10^{16} kg]	$M_{BSE}(K)$ [10^{19} kg]	$M_{BSE}(Th)/M_{BSE}(U)$	$M_{BSE}(K)/M_{BSE}(U)$ [10^4]	$H_{BSE}(U+Th)$ [TW]	$H_{BSE}(U+Th+K)$ [TW]	U_R
Poor-H	5.2 ± 0.9	19.1 ± 2.4	67.3 ± 11.5	3.7	1.3	10.1 ± 1.5	12.4 ± 1.9	$0.14^{+0.06}_{-0.05}$
Medium-H	8.2 ± 1.3	31.3 ± 4.6	98.7 ± 16.9	3.8	1.2	16.3 ± 2.5	19.7 ± 3.1	0.32 ± 0.08
Rich-H	13.3 ± 1.5	53.3 ± 5.3	133.2 ± 13.3	4.0	1.0	27.1 ± 2.9	31.7 ± 3.4	0.62 ± 0.09

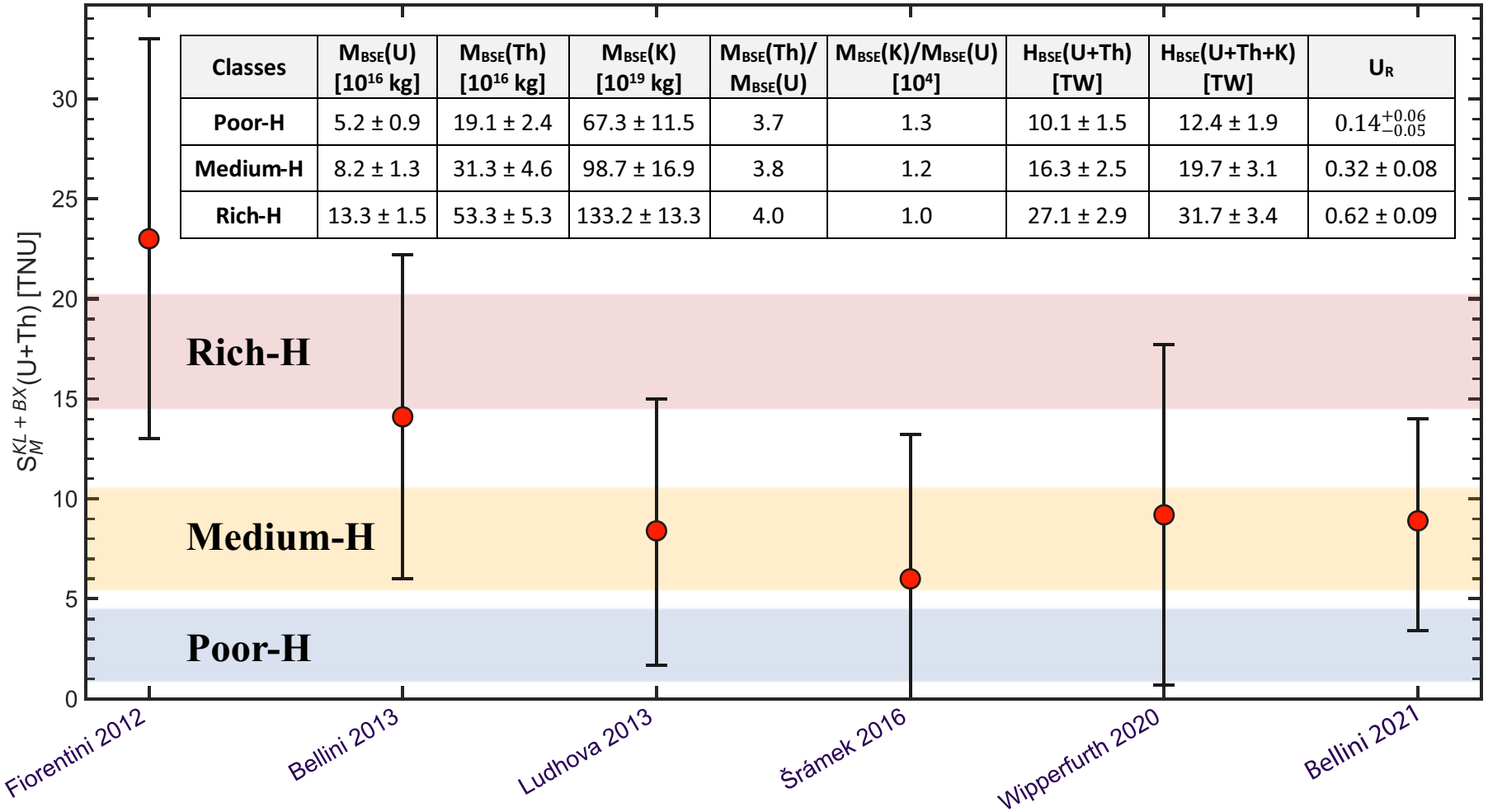

Collection of the published mantle signals obtained from the combination of Borexino and KamLAND experimental results, together with the predictions (horizontal bands) of Poor-H, Medium-H, and Rich-H models (see Table). The horizontal bands correspond to the 68% coverage interval for the mantle signal predicted by the three models, calculated by substituting predicted mantle heat.

[From G. Bellini *et al.*, "Geoneutrinos and geoscience: an intriguing joint-venture," Riv. Nuovo Cim. **45** (2022) 1–105, arXiv:2109.01482 [physics.geo-ph].]

Site	Reservoir	$\Phi(^{238}\mathrm{U})$ $(10^6\,\mathrm{cm}^{-2}\,\mathrm{s}^{-1})$	$\Phi(^{235}\mathrm{U})$ $(10^6\,\mathrm{cm}^{-2}\,\mathrm{s}^{-1})$	$\Phi(^{232}\mathrm{Th})$ $(10^6\,\mathrm{cm}^{-2}\,\mathrm{s}^{-1})$	$\Phi(^{40}\mathrm{K})$ $(10^6\,\mathrm{cm}^{-2}\,\mathrm{s}^{-1})$
Kamioka (Japan)	Crust	2.50 ± 0.65	0.08 ± 0.02	2.34 ± 0.35	10.0 ± 1.5
	Mantle	1.01 (0.71) ± 0.83	0.03 (0.02) ± 0.03	0.70 (0.63) ± 0.64	5.08 (3.56) ± 4.21
	Core	0.000 (0.300)	0.000 (0.009)	0.000 (0.066)	—
	Total	**3.51 ± 1.05**	**0.11 ± 0.03**	**3.04 ± 0.73**	**15.1 (13.6) ± 4.5**
Gran Sasso (Italy)	Crust	3.18 ± 0.79	0.10 ± 0.02	3.00 ± 0.43	12.7 ± 1.8
	Mantle	1.00 (0.70) ± 0.82	0.03 (0.02) ± 0.03	0.70 (0.63) ± 0.63	5.05 (3.54) ± 4.18
	Core	0.000 (0.301)	0.000 (0.009)	0.000 (0.066)	—
	Total	**4.19 ± 1.14**	**0.13 ± 0.04**	**3.70 ± 0.77**	**17.8 (16.3) ± 4.6**
SNOLab (Canada)	Crust	3.51 ± 0.91	0.11 ± 0.03	3.32 ± 0.48	14.4 ± 2.1
	Mantle	1.01 (0.71) ± 0.82	0.03 (0.02) ± 0.03	0.70 (0.63) ± 0.64	5.06 (3.54) ± 4.19
	Core	0.000 (0.301)	0.000 (0.009)	0.000 (0.066)	—
	Total	**4.52 ± 1.23**	**0.14 ± 0.04**	**4.02 ± 0.79**	**19.5 (18.0) ± 4.7**

Predicted fluxes of geo-$\overline{\nu}_e$s at three underground sites, potentially measurable by using the antineutrino-electron elastic scattering and low-background, direction-sensitive tracking detectors. The fluxes from uranium (U), thorium (Th) and potassium (K) decays in the crust, mantle, and core are estimated assuming a sub-crustal Earth model with a homogeneous mantle and 0 (10) p.p.b. U, Th (with no K) in the core. Values given here do not include the effect of neutrino oscillation. Uncertainties are calculated by propagating the uncertainties on the elemental abundances.

[Table and figure in next slide are taken from M. Leyton, S. Dye, & J. Monroe, "Exploring the hidden interior of the Earth with directional neutrino measurements," Nature Comm. **8** (2017) 15989, arXiv:1710.06724 [physics.geo-ph].]

6 Atmospheric neutrinos.

6.1 Importance of atmospheric neutrinos for astroparticle physics

The mechanism of neutrino production in the atmosphere is well understood: Electron and muon neutrinos and antineutrinos come into being from decay of unstable particles, generated in the collisions of primary and secondary cosmic rays with air nuclei. Fraction of tau neutrinos and antineutrinos in the atmospheric neutrino (AN) flux is very small because ν_τ and $\overline{\nu}_\tau$ arise only from the decay of heavy particles (like D_s or B mesons) whose production cross sections are small.

However the chain of processes which lead to lepton generation is rather intricate seeing that the primaries and secondaries (both stable and unstable) can repeatedly interact in the atmosphere with absorption, regeneration or overcharging, and dissipation of energy through electromagnetic interactions.

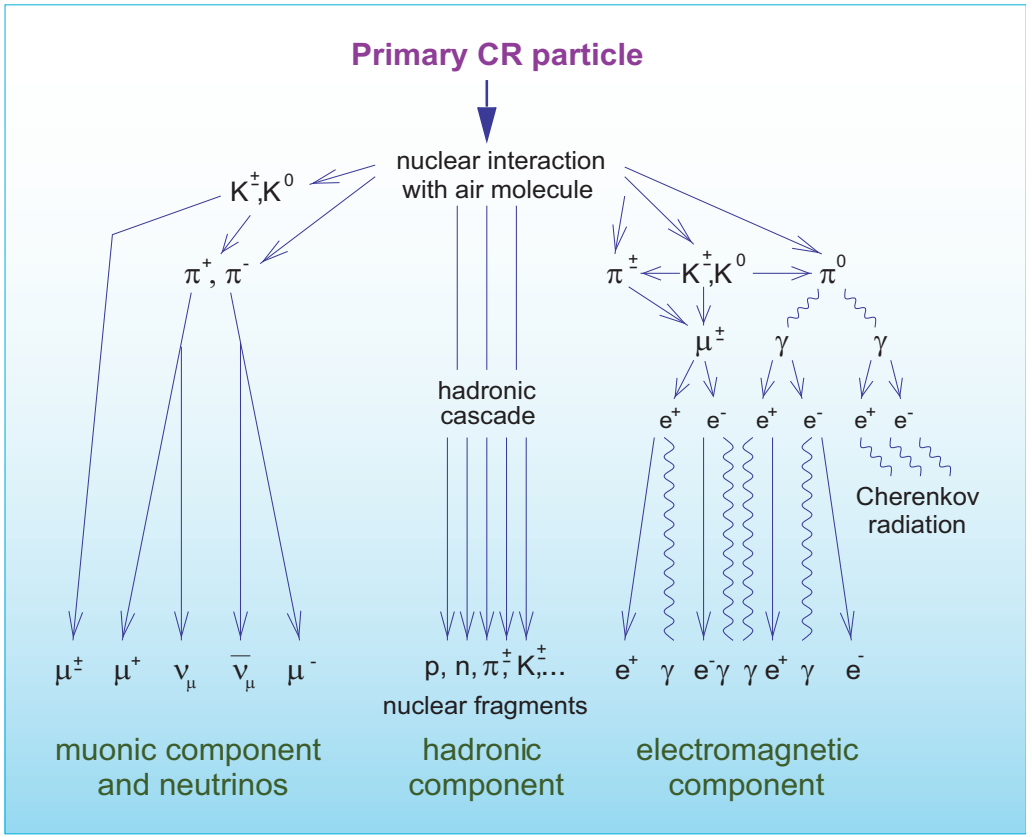

A schematic view of atmospheric cascade initiated by a primary cosmic-ray particle.

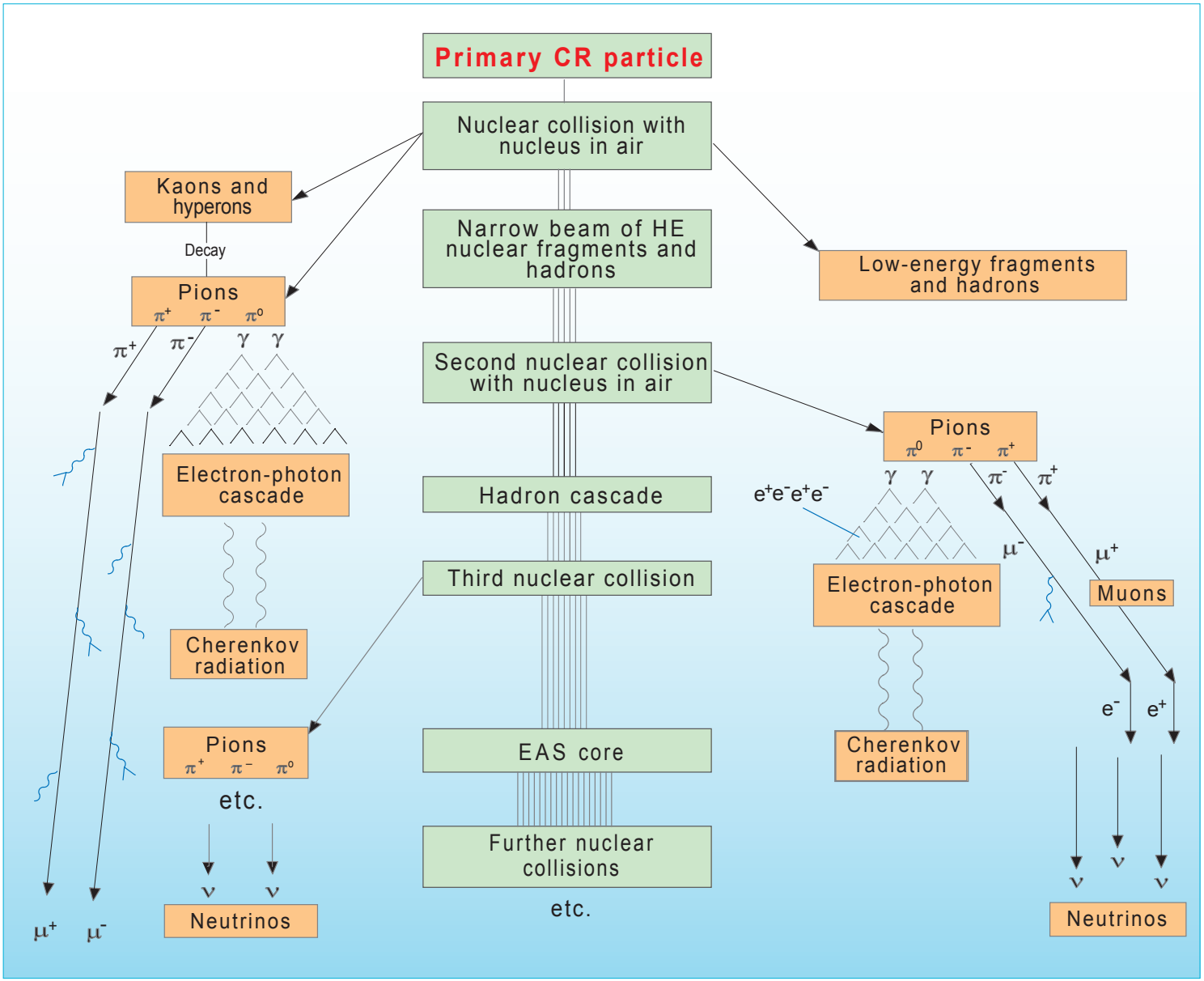

Another schematic view of the cosmic-ray initiated cascade process in the atmosphere.

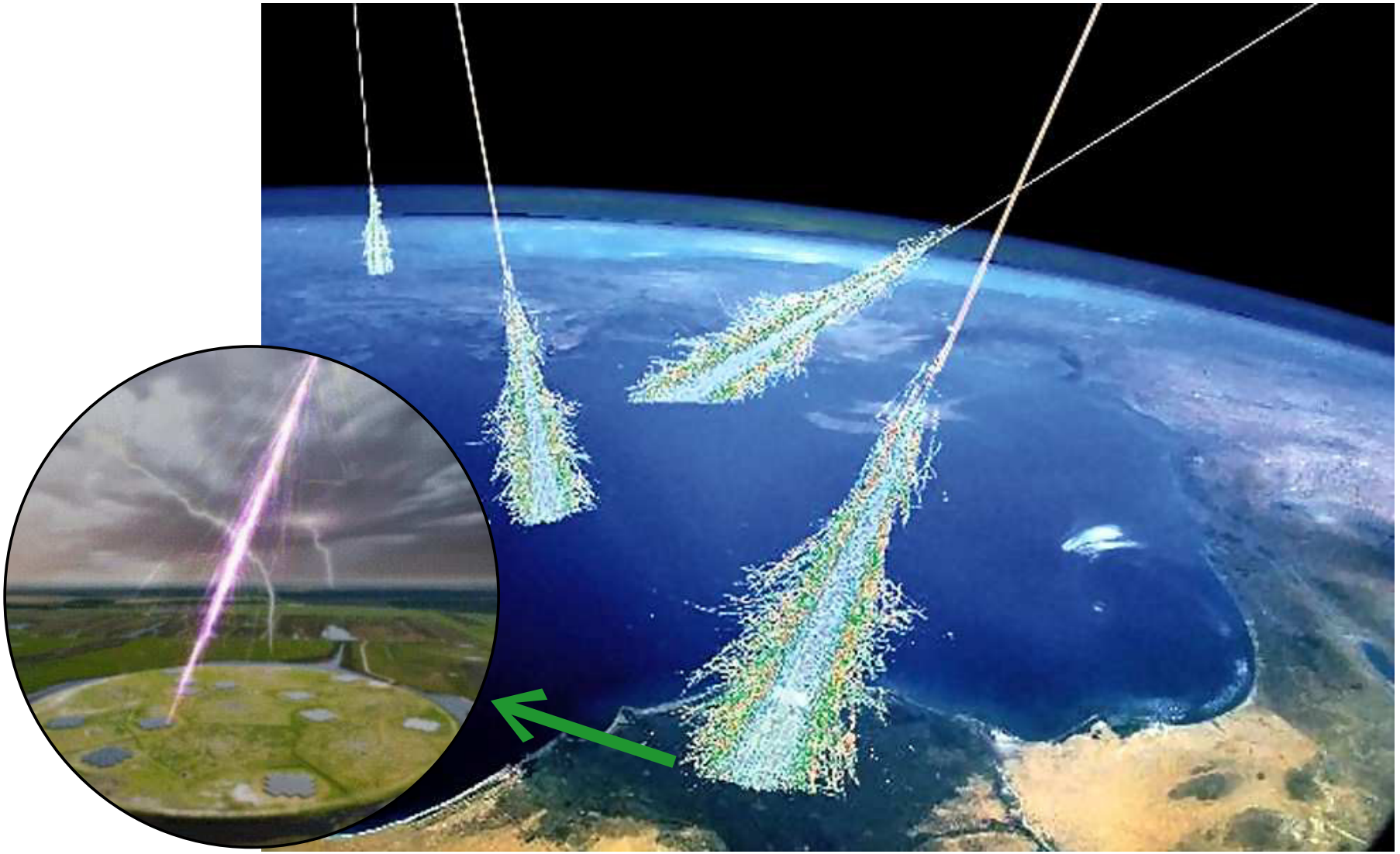

An artist's view of extensive air showers: cosmic rays, through the air showers they produce, are hypothesized to help increase the rate of cloud formation in the same process as a cloud chamber.

[From ⟨ https://www.sensorcast.org/wiki/index.php/File:CosmicRaysClouds.jpg ⟩.]

6.2 Some complicating factors.

- **Geomagnetic effects.** At low energies, the Earth's magnetic field gives rise to the spatial (longitudinal and latitudinal) and angular (zenithal and azimuthal) asymmetries in the lepton fluxes. Complicated structure of the real geomagnetic field, the Earth's penumbra, and re-entrant albedo embarrass the analysis of the geomagnetic effects.
- **Solar activity.** Quasi-periodical variations of solar activity modify the low-energy part of the primary cosmic-ray spectrum and therefore affect the muon and neutrino intensities (below some hundreds of MeV), making them time-dependent.
- **3D effects.** At very low energies ($E_{\mu,\nu} \lesssim 500$ MeV), the 3-dimensionality of nuclear reactions and decays is important.
- **Meteorological effects.** These are essential at all energies of interest.
- **Muon polarization and depolarization effects.** Muons whose decay is an important source of neutrinos up to the multi-TeV energy range, change their polarization due to energy loss and multiply scattering, affecting the neutrino spectra.
- **Branchy chains.** With increasing energy, life-times of light mesons grow and the production and decay chains become branchy: "anything produce everything".

Consequently, an accurate calculation of the muon and neutrino fluxes presents a hard multi-factor problem complicated by uncertainties in the primary cosmic-ray spectrum and composition, inclusive and total inelastic cross sections for particle interactions and by pure computational difficulties.

6.3 Ergo...

Solution to the AN problem is of prime necessity for the study of many fundamental issues of particle physics, astrophysics, and cosmology.

- **AN as annoying background.** The AN flux represents an unavoidable background for some key low-energy experiments with underground detectors, e. g.:
  - Search for proton decay ($\Delta B = 1$) and $n \to \overline{n}$ transitions in nuclei ($\Delta B = 2$).

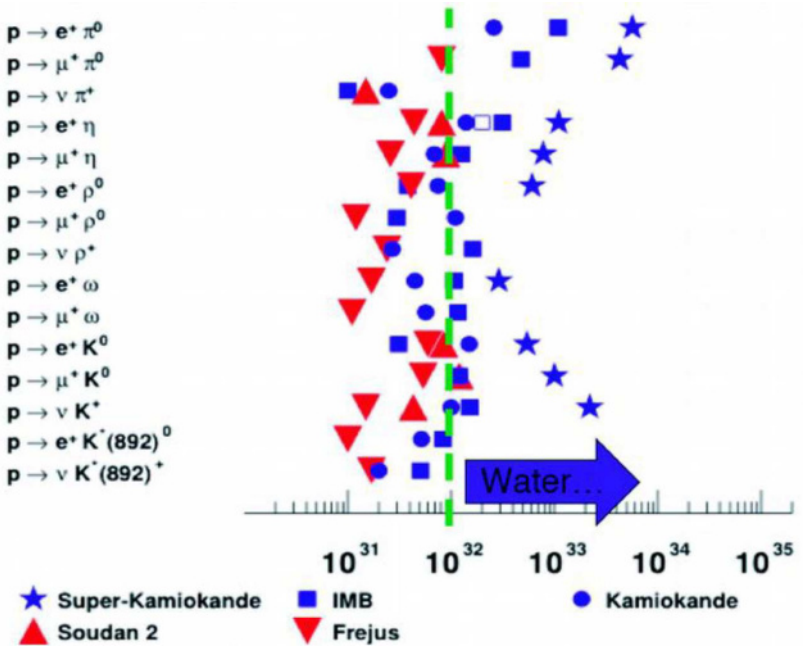

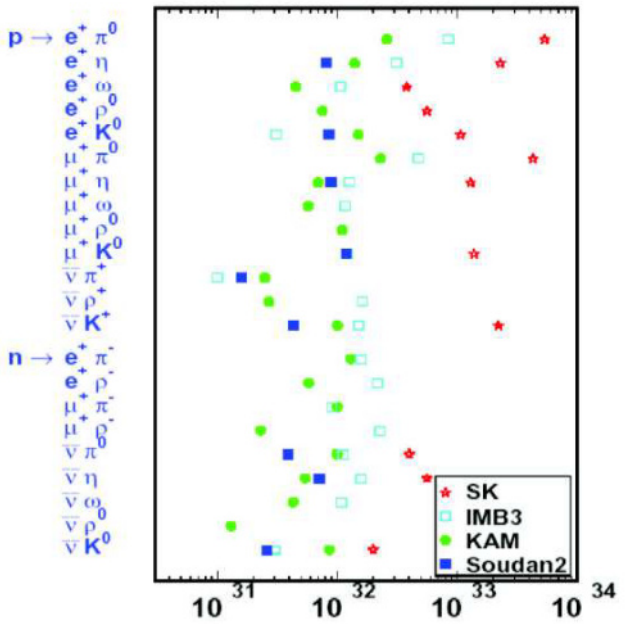

The best current lower limit on $T_{n\to\overline{n}}$ for neutrons bound in ^{16}O is 1.9×10^{32} yrs.[a]
The corresponding (theoretically estimated) lower limit for the free neutron oscillation time ($\tau_{n\to\overline{n}}$) 2.7×10^8 s (cf. the limit $\tau_{n\to\overline{n}} > 0.86 \times 10^8$ s set in the ILL/Grenoble experiment).

[a] K. Abe *et al.* (Super-Kamiokande Collaboration), "Search for $n-\overline{n}$ oscillation in Super-Kamiokande," Phys. Rev. D **91** (2015) 072006, arXiv:1109.4227 [hep-ex].

6.4 Digression: Proton decay.

GUTs generally predict the existence of new gauge bosons X (leptoquarks) which can mediate baryon number violating processes such as proton decay through diagrams such as shown in the *Right panel*:

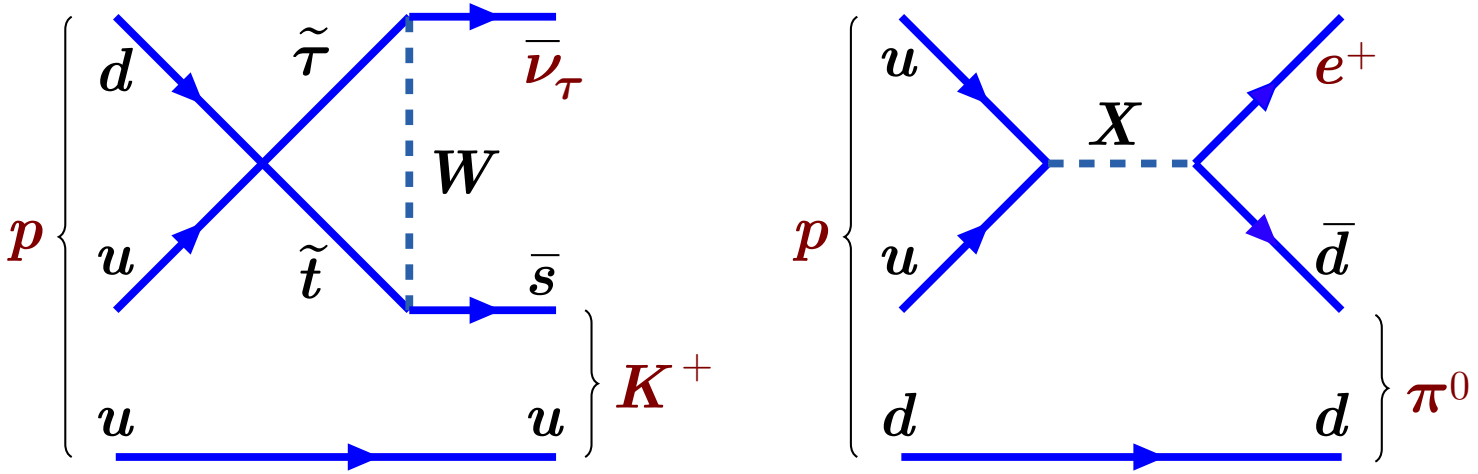

Feynman diagrams for proton decay modes from supersymmetric GUT, $p \to \overline{\nu} K^+$ (left) and gauge mediation GUT models, $p \to e^+ \pi^0$ (right).

The expected proton (and also bound neutron) lifetime τ_p in simplest gauge GUTs is of order

$$\tau_p \approx \frac{1}{\alpha_G^2} \frac{M_X^4}{m_p^5}, \quad \alpha_G \equiv \frac{g_G^2}{4\pi},$$

where g_G is a universal gauge coupling (G is a gauge group, e.g. SU(5)).

More detailed analyses encounter the three classes of diagrams but yield similar result.

Two-quark fusion

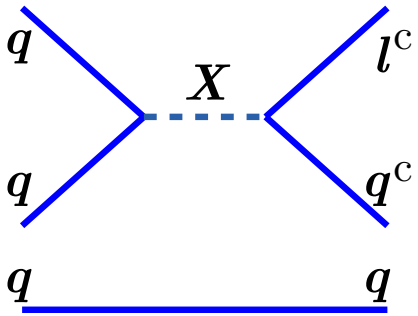

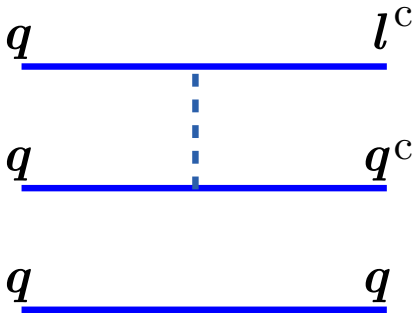

Quark decay

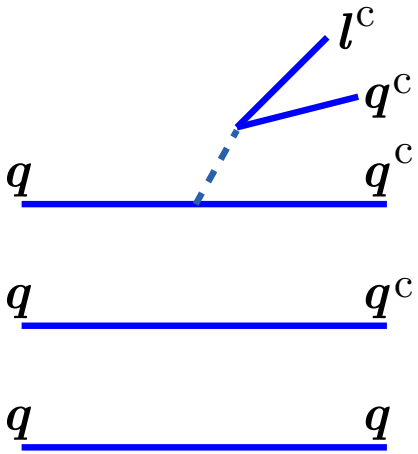

Three-Quark fusion

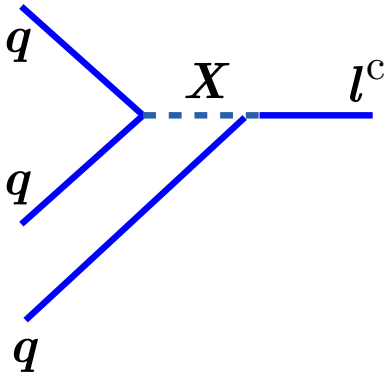

- It is usually assumed that the two-quark fusion diagrams dominate.
- The quark decay diagram is suppressed by phase space.
- The three-quark fusion diagram (with gluons radiated from the quarks absorbed by surrounding nucleons) is generally important in nuclei, although the uncertainties are large.

The existing limit

$$\frac{\tau_p}{B(p \to e^+ \pi^0)} > 8.2 \times 10^{33} \text{ yr}$$

therefore requires

$$M_X \gtrsim 10^{15} \text{ GeV}.$$

p DECAY MODES	Parton mean life (10^{30} years)	Confidence level	p (MeV/c)
Antilepton + meson			
$N \to e^+\pi$	**>2000 (n), >8200 (p)**	90%	459
$N \to \mu^+\pi$	**>1000 (n), >6600 (p)**	90%	453
$N \to \nu\pi$	>1100 (n), >390 (p)	90%	459
$p \to e^+\eta$	>4200	90%	309
$p \to \mu^+\eta$	>270 (n), >710 (p)	90%	297
$n \to \nu\eta$	>1300	90%	310
$N \to e^+\rho$	>228 (n), >160 (p)	90%	149
$N \to \mu^+\rho$	>158	90%	113
$N \to \nu\rho$	>19 (n), >162 (p)	90%	149
$p \to e^+\omega$	>320	90%	113
$p \to \mu^+\omega$	>780	90%	149
$n \to \nu\omega$	>108	90%	144
$N \to e^+K$	>17 (n), >1000 (p)	90%	339
$N \to \mu^+K$	>26 (n), >1600 (p)	90%	329
$N \to \nu K$	>86 (n), >5900 (p)	90%	339
$n \to \nu K_S^0$	>260	90%	338
$p \to e^+K^*(892)^0$	>84	90%	45
$N \to e^+K^*(892)$	>78 (n), >51 (p)	90%	45
Antilepton + mesons			
$p \to e^+\pi^+\pi^-$	>82	90%	448
$p \to e^+\pi^0\pi^0$	>147	90%	449
$n \to e^+\pi^-\pi^0$	>52	90%	449
$p \to \mu^+\pi^+\pi^-$	>133	90%	425
$p \to \mu^+\pi^0\pi^0$	>101	90%	427
$n \to \mu^+\pi^0\pi^0$	>74	90%	427
$n \to e^+K^0\pi^-$	>18	90%	319
Lepton + meson			
$n \to e^-\pi^+$	>65	90%	459
$n \to \mu^-\pi^+$	>49	90%	453
$n \to e^-\rho^+$	>62	90%	150
$n \to \mu^-\rho^+$	>7	90%	115
$n \to e^-K^+$	>32	90%	340
$n \to \mu^-K^+$	>57	90%	330
Lepton + mesons			
$p \to e^-\pi^+\pi^+$	>30	90%	448
$n \to e^-\pi^-\pi^0$	>29	90%	449
$p \to \mu^-\pi^+\pi^0$	>17	90%	425
$n \to \mu^-\pi^-\pi^0$	>34	90%	427
$p \to e^-\pi^+K^+$	>75	90%	320
$p \to \mu^-\pi^+K^+$	>245	90%	279
Antilepton + photon(s)			
$p \to e^+\gamma$	>670	90%	469
$p \to \mu^+\gamma$	>478	90%	463
$n \to \nu\gamma$	>550	90%	470
$p \to e^+\gamma\gamma$	>100	90%	469
$n \to \nu\gamma\gamma$	>219	90%	470
Antilepton + single massless			
$p \to e^+X$	>790	90%	–
$p \to \mu^+X$	>410	90%	–
Three (or more) leptons			
$p \to e^+e^+e^-$	>793	90%	469
$p \to e^+\mu^+\mu^-$	>359	90%	457
$p \to e^+\nu\nu$	>170	90%	469
$n \to e^+e^-\nu$	>257	90%	470
$n \to \mu^+e^-\nu$	>83	90%	464
$n \to \mu^+\mu^-\nu$	>79	90%	458
$p \to \mu^+e^+e^-$	>529	90%	463
$p \to \mu^+\mu^+\mu^-$	>675	90%	439
$p \to \mu^+\nu\nu$	>220	90%	463
$p \to e^-\mu^+\mu^+$	>6	90%	457
$n \to \nu\nu\nu$	$>5\times10^{-4}$	90%	470
Inclusive modes			
$N \to e^+$anything	>0.6 (n,p)	90%	–
$N \to \mu^+$anything	>12 (n,p)	90%	–
$N \to e^+\pi^0$anything	>0.6 (n,p)	90%	–
ΔB=2 dinucleon modes			
The following are lifetime limits per iron nucleus		90%	–
$pp \to \pi^+\pi^+$	>72.2	90%	–
$pn \to \pi^+\pi^0$	>170	90%	–
$nn \to \pi^+\pi^-$	>0.7	90%	–
$nn \to \pi^0\pi^0$	>404	90%	–
$pp \to K^+K^+$	>170	90%	–
$pp \to e^+e^+$	>5.8	90%	–
$pp \to e^+\mu^+$	>3.6	90%	–
$pp \to \mu^+\mu^+$	>1.7	90%	–
$pn \to e^+\overline{\nu}$	>260	90%	–
$pn \to \mu^+\overline{\nu}$	>200	90%	–
$pn \to \tau^+\overline{\nu}_\tau$	>29	90%	–
$nn \to \nu_e\overline{\nu}_e$	>1.4	90%	–
$nn \to \nu_\mu\overline{\nu}_\mu$	>1.4	90%	–
$pn \to$ invisible	$>2.1\times10^{-5}$	90%	–
$pp \to$ invisible	$>5\times10^{-5}$	90%	–

[From C. Patrignani *et al.* (Particle Data Group), "Review of particle physics," Chin. Phys. C **40** (2016) 100001.]

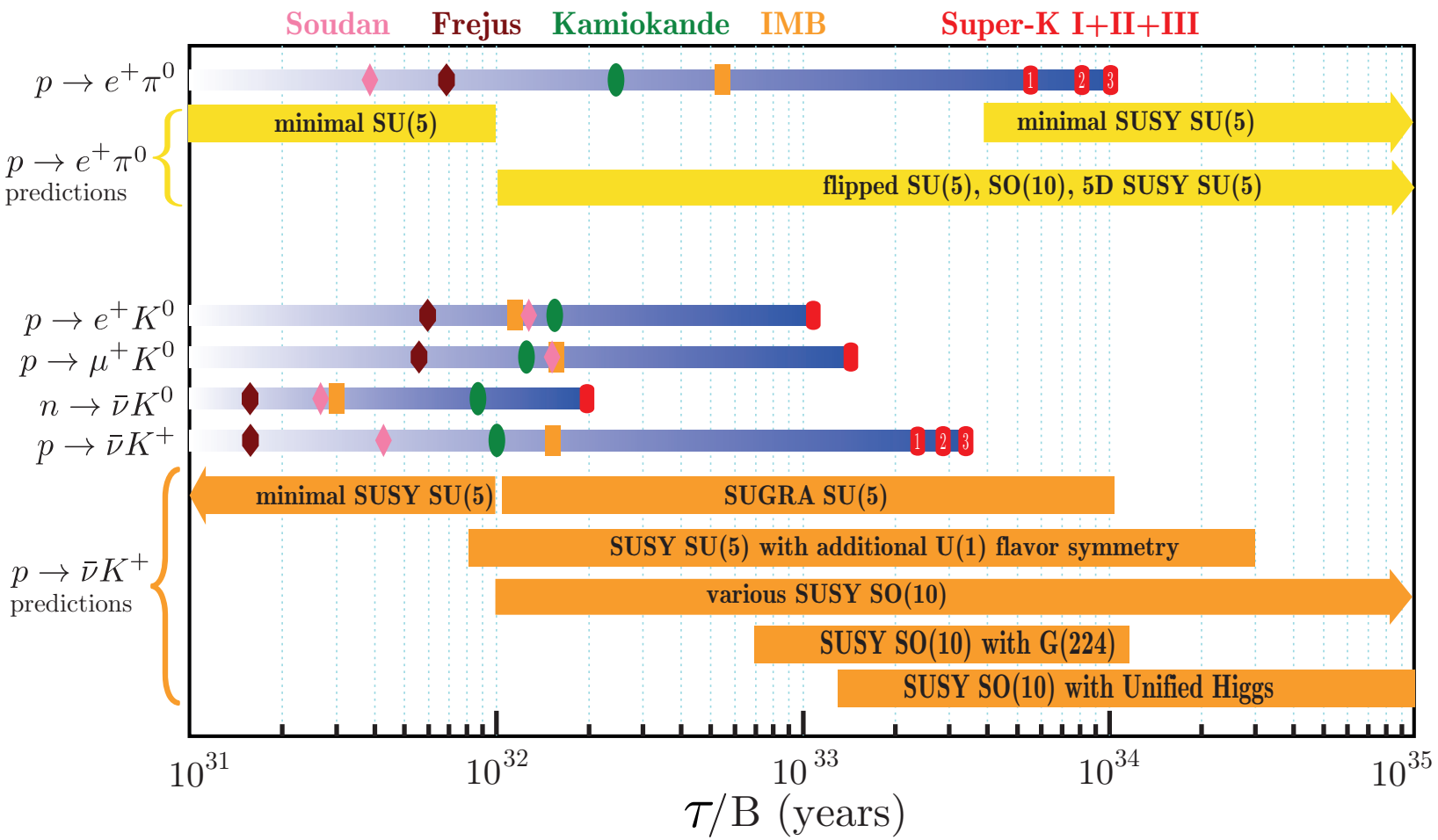

Proton decay lifetime limits (status on 2012) compared to lifetime ranges predicted by Grand Unified Theories. The upper section is for $p \to e^+\pi^0$, most commonly caused by gauge mediation. The lower section is for SUSY-motivated models, which commonly predict decay modes with kaons in the final state. The marker symbols indicate published experimental limits, as indicated by colors on top of the figure. [From "Conceptual Design Report. The Neutrino Experiment," Vol. w. LBNF-DUNE Physics (April 6, 2015).]

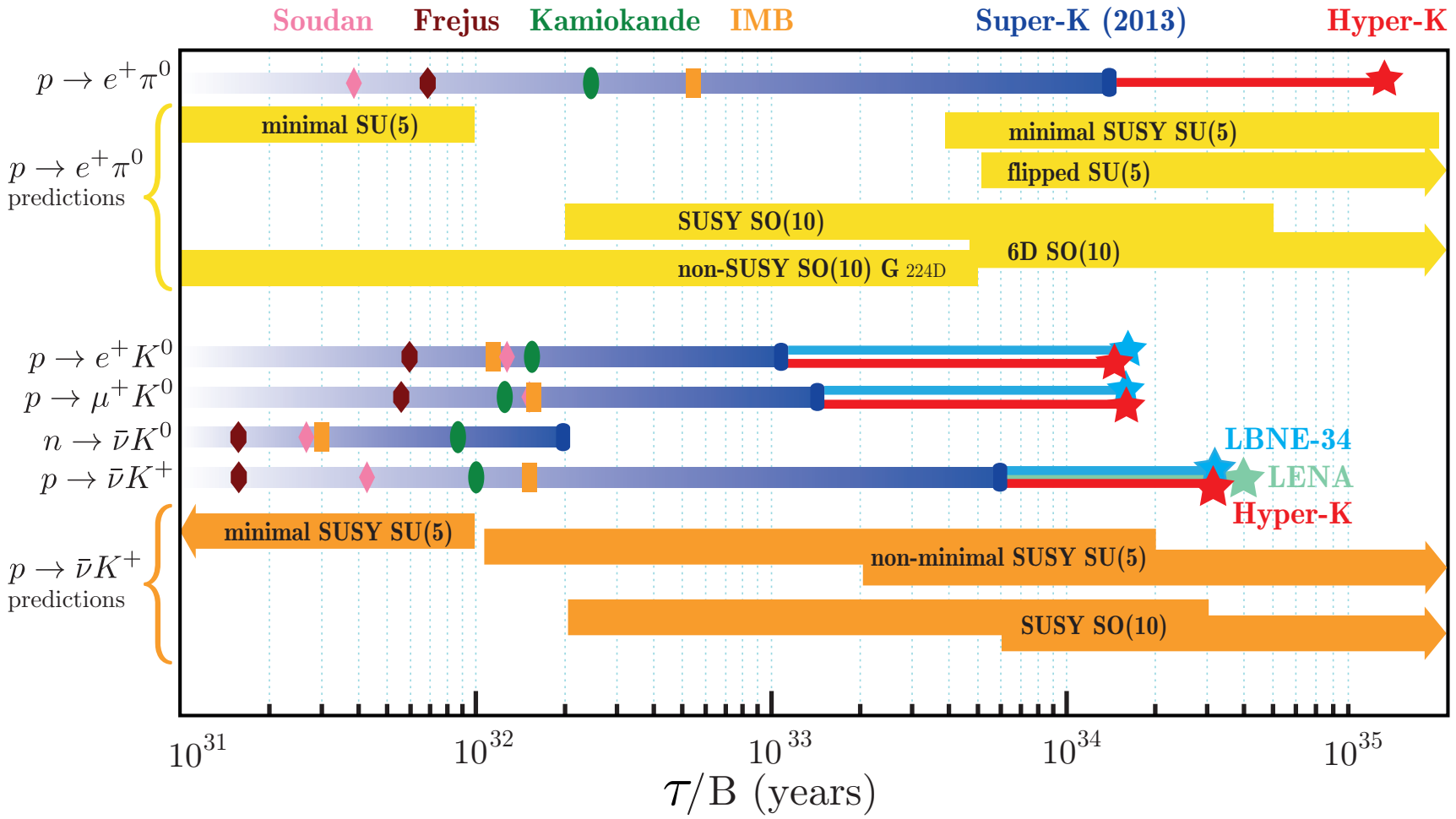

Proton decay lifetime limits that can be achieved by proposed future experiments (LBNE/DUNE 34-kt, LENA, Hyper-Kamiokande). The limits are at 90% C.L., calculated for a Poisson process including background, assuming that the detected events equal the expected background. The marker symbols are the same as in the previous slide.

[From "Conceptual Design Report. The Neutrino Experiment," Vol. w. LBNF-DUNE Physics (April 6, 2015).]

The main methods of $p \to \overline{\nu} K^+$ detection.

The K^+ is identified via its decay daughters:

1. $K \to \mu^+ \nu_\mu$, in delayed coincidence with deexcitation γ rays from the remnant nucleus from p decay within an oxygen nucleus [background-free but shows low efficiencies of 9.1% due to backgrounds around the deexcitation γ ray energy];
2. $K \to \mu^+ \nu_\mu$, monoenergetic muon search [less sensitive than the other methods due to the large AN background];
3. $K \to \pi^+ \pi^0$, search [background-free but shows low efficiencies of 10.0% due to limited resolution for reconstructed pion momentum].

Liquid scintillator (LS) detectors are expected to achieve higher detection efficiency with a lower systematic uncertainty because the scintillation light from the K^+ can be readily observed, resulting in a clear delayed coincidence signature with the signals from the K^+ decay daughters.

In addition, the kinetic energy distribution of the decay K^+ measured by scintillation will peak at ~ 105 MeV, with a spread due to nuclear effects and detector resolution, and will provide strong evidence to claim the $p \to \overline{\nu} K^+$ detection.

Current limits on the partial proton lifetime $\tau_p / B(p \to \overline{\nu} K^+)$, 90% C.L.

KamLAND: 5.4×10^{32} yr

[K. Asakura *et al.* (KamLAND Collaboration), Phys. Rev. D **92** (2015) 052006, arXiv:1505.03612 [hep-ex].]

Super-Kamiokande: 5.9×10^{33} yr

[K. Abe *et al.* (Super-Kamiokande Collaboration), Phys. Rev. D **90** (2014) 072005, arXiv:1408.1195 [hep-ex].]

This excludes SUSY SU(5) GUT with minimal assumptions predicting $\tau_p / B(p \to \overline{\nu} K^+) < 10^{32}$ yr. Extended SUSY-GUT models giving $\tau_p / B(p \to \overline{\nu} K^+) \gtrsim 10^{33}$ yr are still under question.

6.5 Ergo... (continued).

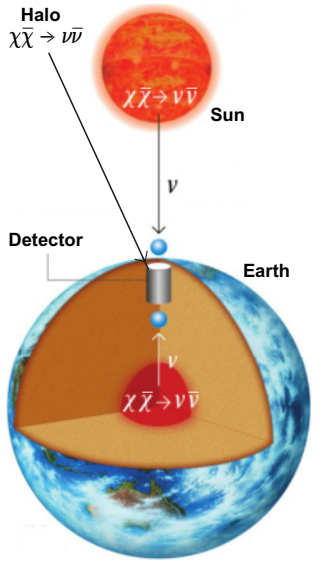

- Most of experiments on high-energy neutrino astrophysics with present-day and future large full-size underground, underwater/ice neutrino telescopes:
  - detection of neutrinos from the (quasi)diffuse neutrino backgrounds,
  - indirect detection of *non-relativistic* dark matter through νs produced in the annihilation of the DM particles captured in Earth and Sun, or
  - direct detection of *relativistic* WIMPs (weakly-interacting massive particles) of astrophysical or cosmological origin.

  These experiments will be an effect of the AN flux at energies from ~ 1 TeV to some tens of PeV. However, in the absence of a generally recognized and tried model for charm hadroproduction (see below), the current estimates of the ν_μ and (most notably) ν_e backgrounds have unacceptably wide scatter even at multi-TeV neutrino energies, which shoots up with energy. At $E_\nu \sim 100$ TeV, different estimates of the ν_μ and ν_e spectra vary within a few orders of magnitude.
- **Study of HE and UHE neutrino interactions.** Measurements of the cross sections for $\nu_\ell N$ and $\overline{\nu}_\ell N$ charged-current interactions at $\sqrt{s} \sim m_W$ ($E_\nu \sim 3.4$ TeV) provide an important test for the Standard Model. With modern accelerators, the interactions of neutrinos are studied at energies up to several hundreds of GeV whereas deep underwater experiments with AN will enable to enlarge the region of neutrino energies up to a few tens of TeV.
- **Study of Neutrino oscillations and all that.** At the same time, the AN flux is a natural instrument for studying neutrino oscillations, neutrino decay and neutrino interactions with matter at energies beyond the reach of accelerator experiments. Search for neutrino oscillations with underground detectors is the main issue of several lectures.

6.6 Digression: Cosmic rays.

See presentation “Cosmic Rays” ([**CR**] from here) and, for more details, the course “Introduction to Cosmic Rays,” available at URL: ⟨http://theor.jinr.ru/~vnaumov/Eng/JINR_Lectures/NPA.html⟩.

6.7 ANs at low & intermediate energies: Geomagnetic effects.

Due to geomagnetic effects, the low-energy AN spectra and angular distributions are quite different for different sites of the globe. Figures at p. 236 display the predictions of CORT package for ten underground neutrino laboratories listed in Table at p. 235.

The ν_e, $\overline{\nu}_e$, ν_μ, and $\overline{\nu}_\mu$ energy spectra averaged over all zenith and azimuth angles are shown in *left panel* of the Figure at p. 236. The ratios of the AN fluxes averaged over the lower and upper semispheres ("up-to-down" ratios) are shown in *right panel*. As a result of geomagnetic effects, the spectra and up-to-down ratios at energies below a few GeV are quite distinct for five groups of underground labs: 1) SOUDAN + SNO/SNOLAB + IMB, 2) HPW, NUSEX + Fréjus, 3) Gran Sasso + Baksan, 4) Kamioka and 5) KGF.

Technical note:

The exact definition of the fluxes of upward- and downward-going neutrinos is given by the following formulas:

$$F_\nu^{\mathsf{down}}(E) = \int_0^1 \langle F_\nu(E,\vartheta)\rangle_\varphi \, d\cos\vartheta, \tag{6a}$$

$$F_\nu^{\mathsf{up}}\,(E) = \int_{-1}^0 \langle F_\nu(E,\vartheta)\rangle_\varphi \, d\cos\vartheta, \tag{6b}$$

where

$$\langle F_\nu(E,\vartheta)\rangle_\varphi = \frac{1}{2\pi}\int_0^{2\pi} F_\nu\left(E,\vartheta,R_c\left(\Theta,\Phi,\vartheta,\varphi\right)\right)d\varphi, \qquad \text{for} \quad 0 \le \vartheta \le \frac{\pi}{2}, \tag{7a}$$

$$= \frac{1}{2\pi}\int_0^{2\pi} F_\nu\left(E,\vartheta^*,R_c\left(\Theta^*,\Phi^*,\vartheta^*,\varphi^*\right)\right)d\varphi, \qquad \text{for} \quad \frac{\pi}{2} \le \vartheta \le \pi, \tag{7b}$$

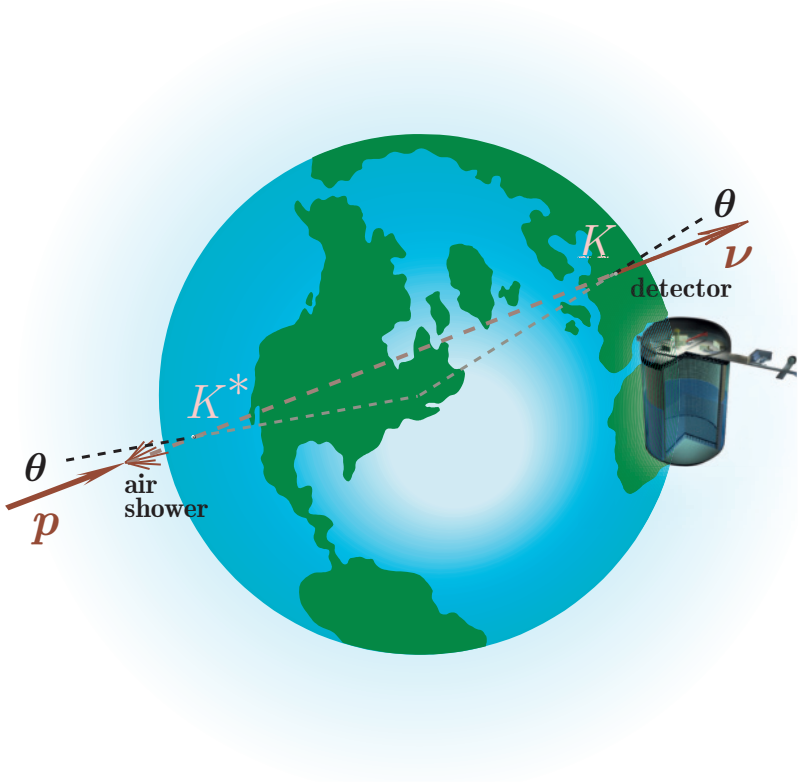

△ Neutrinos from antipodes: how the geomagnetic coordinates of two points (K and K^*) on the surface of the globe located on the same chord are related to each other.

$F_\nu\left(E,\vartheta,R_c\right)$ is the neutrino differential energy spectrum on the Earth surface with the oblique geomagnetic cutoff rigidity R_c which is a function of the geomagnetic latitude and longitude, Θ and Φ, and zenith and azimuthal angles, ϑ and φ (all are defined in the frame of the detector, K, see Figure).

The starred variables in Eq. (7b) are the corresponding angles defined in the local frame K^* associated with the neutrino entry point.

Clearly, the azimuthal dependence of the neutrino flux is only due to the geomagnetic effects. Therefore, within the framework of the 1D cascade theory, it is a function of three variables E, ϑ and R_c.

It is a useful (and not quite trivial) exercise in spherical geometry to prove that[a]

$$\begin{aligned}
\sin\Theta^* &= \sin 2\vartheta \sin\varphi \cos\Theta - \cos\vartheta \sin\Theta, \quad |\Theta^*| < \pi/2, \\
\sin\left(\Phi^* - \Phi\right) &= \sin 2\vartheta \cos\varphi / \cos\Theta^*, \\
\cos\left(\Phi^* - \Phi\right) &= -\left(\sin 2\vartheta \sin\varphi \sin\Theta + \cos 2\vartheta \cos\Theta\right) / \cos\Theta^*, \\
\vartheta^* &= \pi - \vartheta, \\
\sin\varphi^* &= \left(\sin 2\vartheta \sin\Theta + \cos 2\vartheta \sin\varphi \cos\Theta\right) / \cos\Theta^*, \\
\cos\varphi^* &= \cos\varphi \cos\Theta / \cos\Theta^*.
\end{aligned}$$

For near horizontal directions ($|\vartheta - \pi/2| \ll 1$) the above formulas yield

$$\begin{aligned}
\Theta^* &\simeq \Theta + (\pi - 2\vartheta) \sin\Phi, \\
\Phi^* &\simeq \Phi - (\pi - 2\vartheta) \cos\Phi \tan\Theta, \\
\varphi^* &\simeq \varphi + (\pi - 2\vartheta) \cos\Phi \sec\Theta.
\end{aligned}$$

Finally, the 4π averaged AN flux is

$$\langle F_\nu(E)\rangle_{4\pi} = \int_{-1}^{1} \langle F_\nu(E,\vartheta)\rangle_\varphi \, d\cos\vartheta = \frac{1}{2}\left[F_\nu^{\text{down}}(E) + F_\nu^{\text{up}}(E)\right],$$

where $F_\nu^{\text{down,up}}$ and $\langle F_\nu(E,\vartheta)\rangle_\varphi$ are given by Eqs. (6) and (7), respectively.

[a] Of course, we neglect the nonsphericity of the Earth and (somewhat more importantly) the slight asymmetry of points K and K^*, since the detector is usually located underground or underwater.

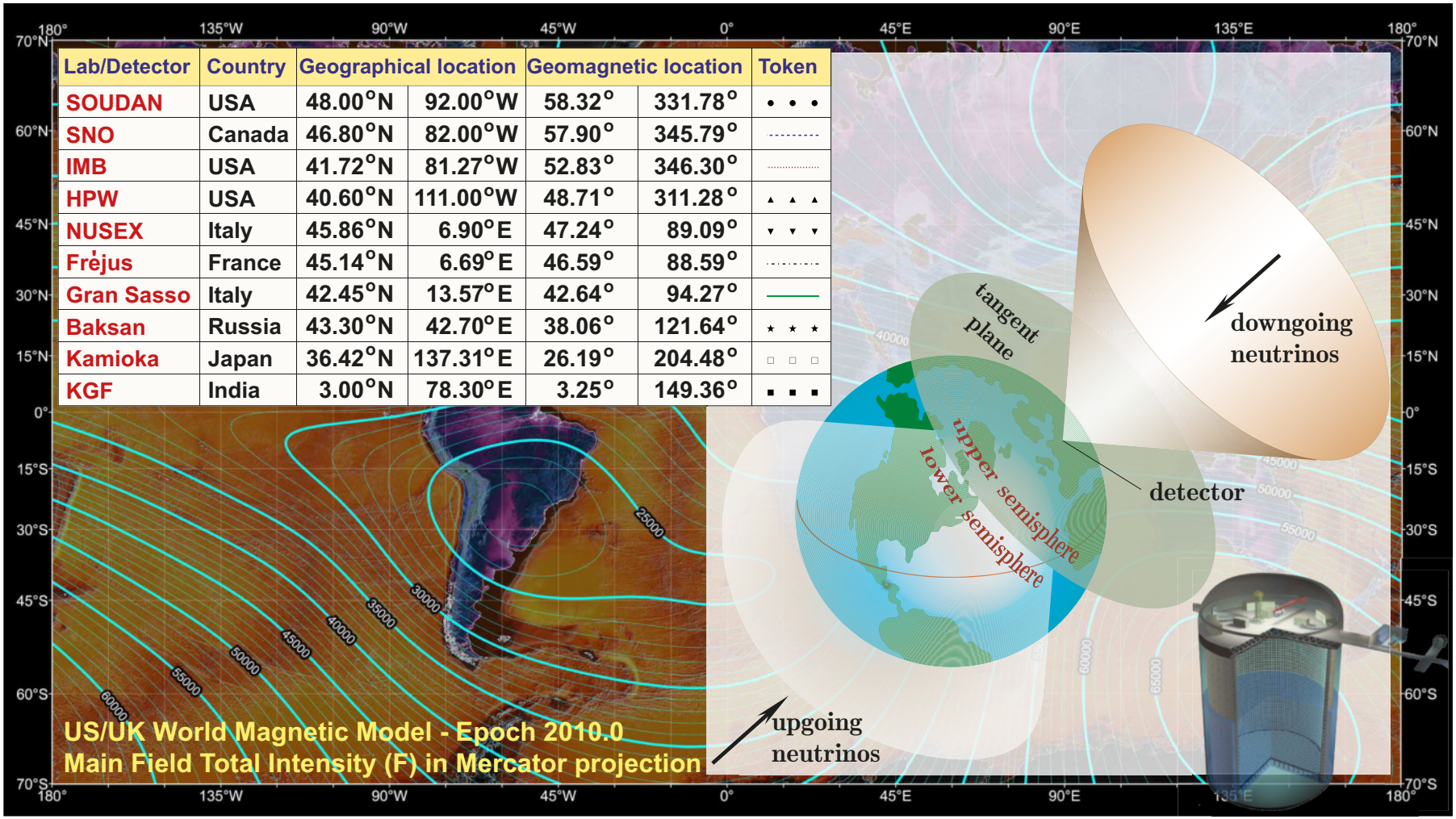

Lab/Detector	Country	Geographical location		Geomagnetic location		Token
SOUDAN	USA	48.00°N	92.00°W	58.32°	331.78°	• • •
SNO	Canada	46.80°N	82.00°W	57.90°	345.79°	----------
IMB	USA	41.72°N	81.27°W	52.83°	346.30°	··········
HPW	USA	40.60°N	111.00°W	48.71°	311.28°	▲ ▲ ▲
NUSEX	Italy	45.86°N	6.90°E	47.24°	89.09°	▾ ▾ ▾
Frėjus	France	45.14°N	6.69°E	46.59°	88.59°	-·-·-·-·-
Gran Sasso	Italy	42.45°N	13.57°E	42.64°	94.27°	———
Baksan	Russia	43.30°N	42.70°E	38.06°	121.64°	★ ★ ★
Kamioka	Japan	36.42°N	137.31°E	26.19°	204.48°	□ □ □
KGF	India	3.00°N	78.30°E	3.25°	149.36°	■ ■ ■

Table shows a list of ten past and present underground laboratories. The "tokens" in the last column are used in next slide. The figure on the right schematically illustrates averaging over the upper and lower hemispheres. The background represents a map with isolines of the geomagnetic field intensity.

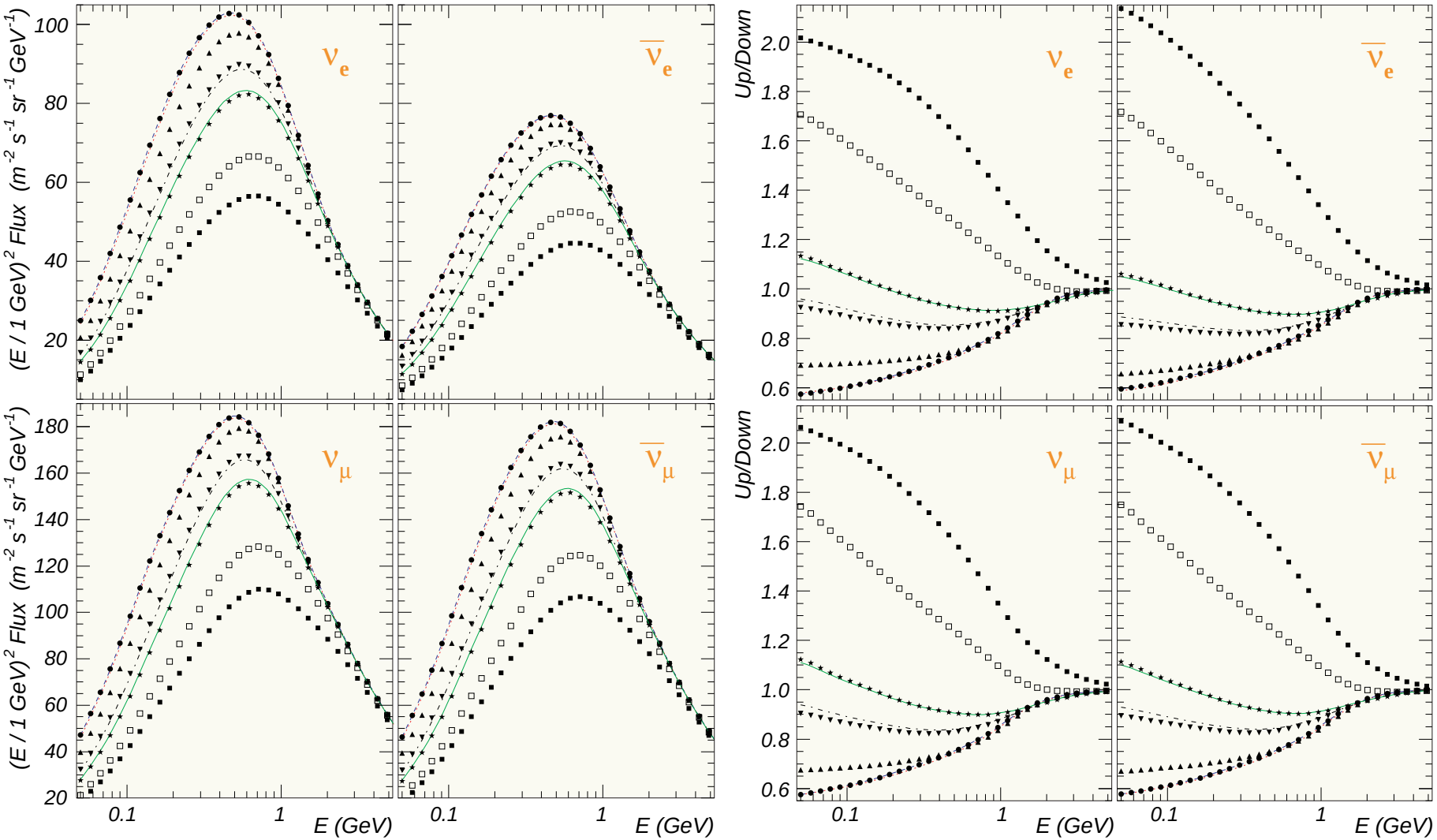

The 4π-averaged fluxes (*left panel*) and up-to-down ratios (*right panel*) of the ν_e, $\overline{\nu}_e$, ν_μ, and $\overline{\nu}_\mu$ fluxes for ten underground laboratories (see Table at p. 235 for the notation).

[From VN, "Atmospheric muons and neutrinos," in: *Proc. of the 2nd Workshop on Methodical Aspects of Underwater/Ice Neutrino Telescopes*, Hamburg, August 15–16, 2001, ed. by R. Wischnewski, pp.31–46, arXiv:hep-ph/0201310.]

6.8 ANs at low & intermediate energies: Evidence of oscillations.

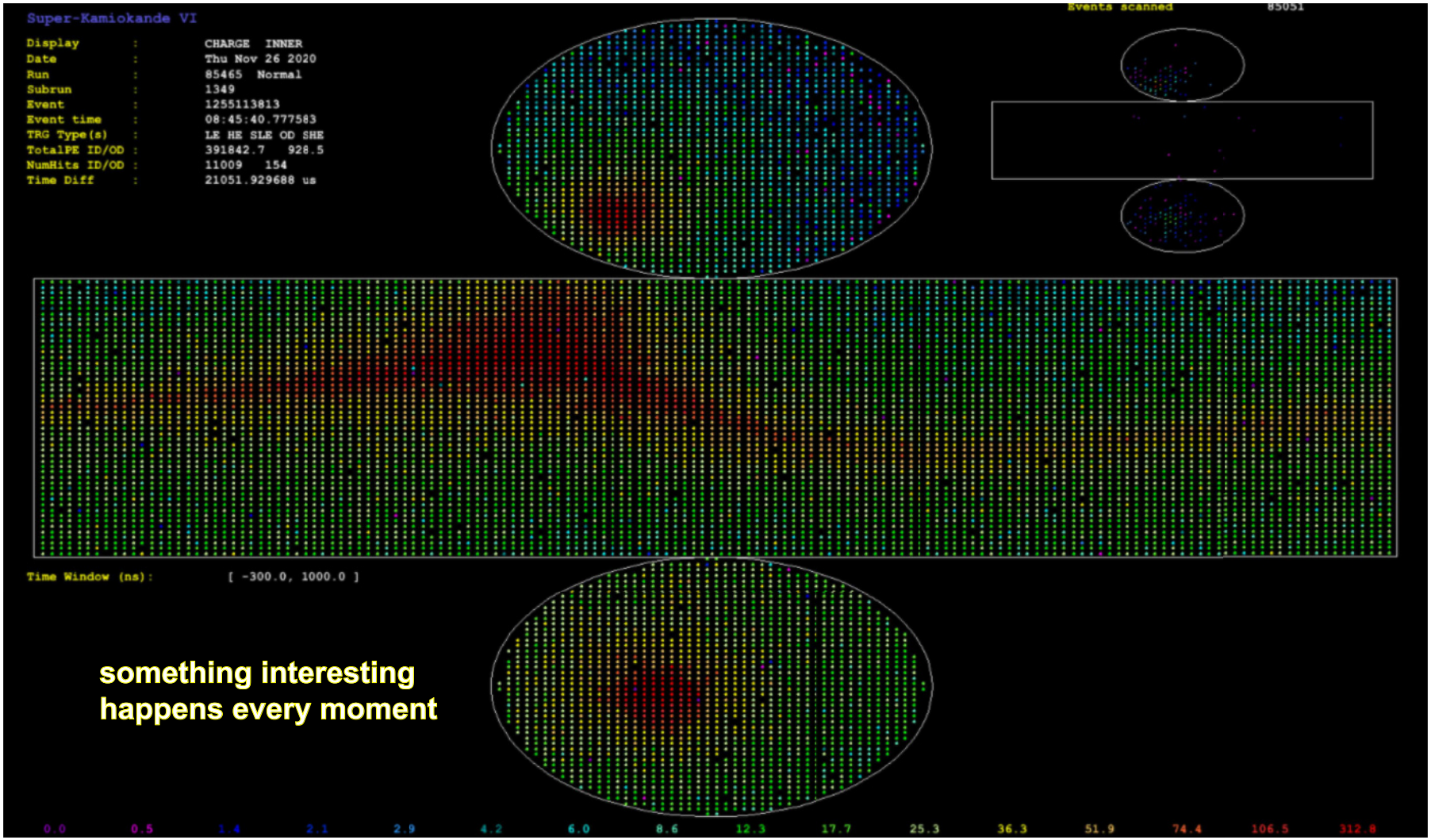

An event in the Super-Kamiokande Realtime Monitor which looks like a down-going through-going atmospheric muon. [From ⟨ http://www-sk.icrr.u-tokyo.ac.jp/realtimemonitor/ ⟩. Provided by Kamioka Observatory, ICRR, University of Tokyo]

The neutrino events and the cosmic ray muon events are distinguished by the number of photons detected by the PMTs of the outer detector. When the CR muon enters the outer detector, the Cherenkov light is emitted immediately. The muon runs into the water and continues to emit the Cherenkov light, which is detected by the inner PMTs. On the other hand, in most case of neutrino events, only the inner PMTs have hits and the outer PMTs do not. So the outer PMTs are very effective to roughly distinguish neutrino events from charged particles such as CR muons.

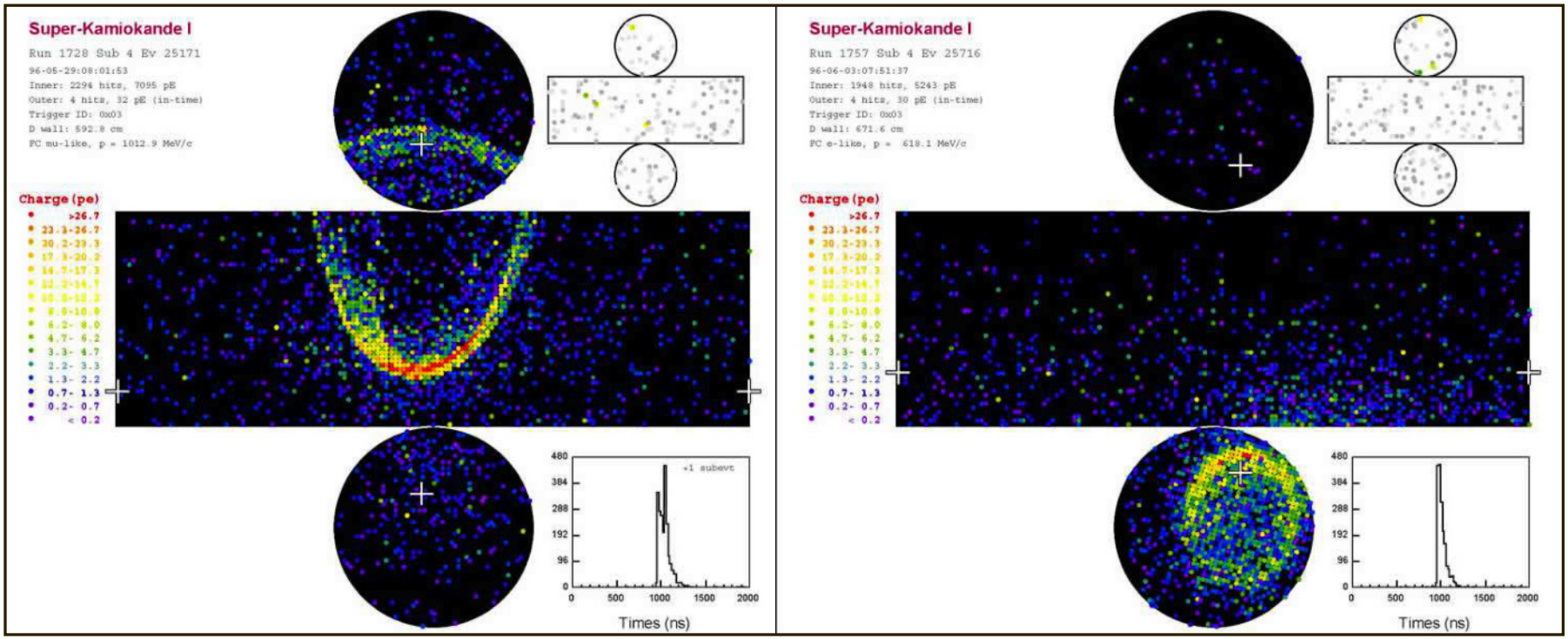

Left panel: A Cherenkov ring occurred by a muon neutrino which interacts with a nucleon in water and transforms to a muon. The outer detector has few hits in the right-upper display.

Right panel: An electron neutrino event where the neutrino interacts with an electron in water. The emitted electron generates a shower, leading to the fuzzy edge of the Cherenkov ring.

[From ⟨ http://www-sk.icrr.u-tokyo.ac.jp/sk/detector/eventdisplay-e.html ⟩.]

The high effective granularity of the Super Kamiokande detector allows the accurate measurement of the energy, position, and direction of charged particles in the few MeV – few GeV energy range, and the pattern of hit phototubes also allows electrons to be distinguished from heavier particles like muons or pions. Figure shows the hit patterns from typical muon, electron, and neutral pion events in Super-Kamiokande.

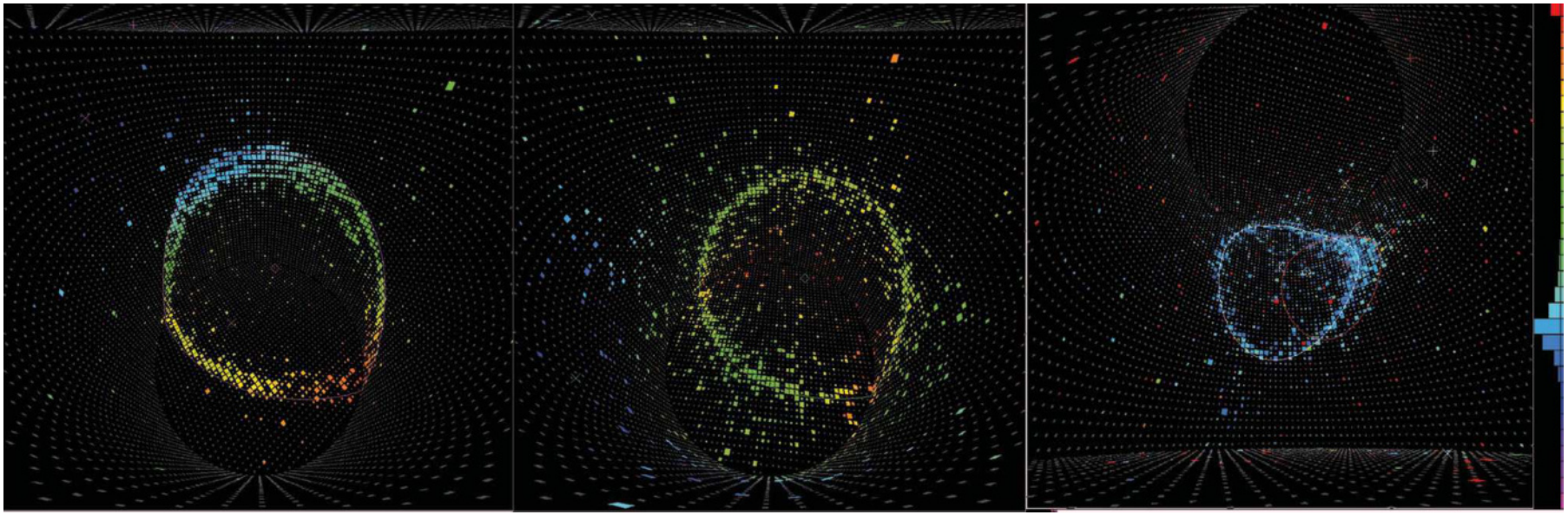

Left panel: a muon induced event, showing the clearly defined ring structure.

Middle panel: an electron induced event, showing the fuzzier ring caused by showering.

Right panel: an event from a π^0, and a 2nd ring can be seen on the right edge of the main ring.

Each colored square indicates a hit photomultiplier, with the size of the square showing the amount of charge in the phototube and the color the relative timing. The event discrimination is good enough to remove all but a handful of background events from the electron neutrino appearance sample.

[Borrowed from D. Wark, "The T2K experiment" (feature article), Nucl. Phys. News **19** (2009) 26–33.]

6.9 Comparison with data at low and medium energies.

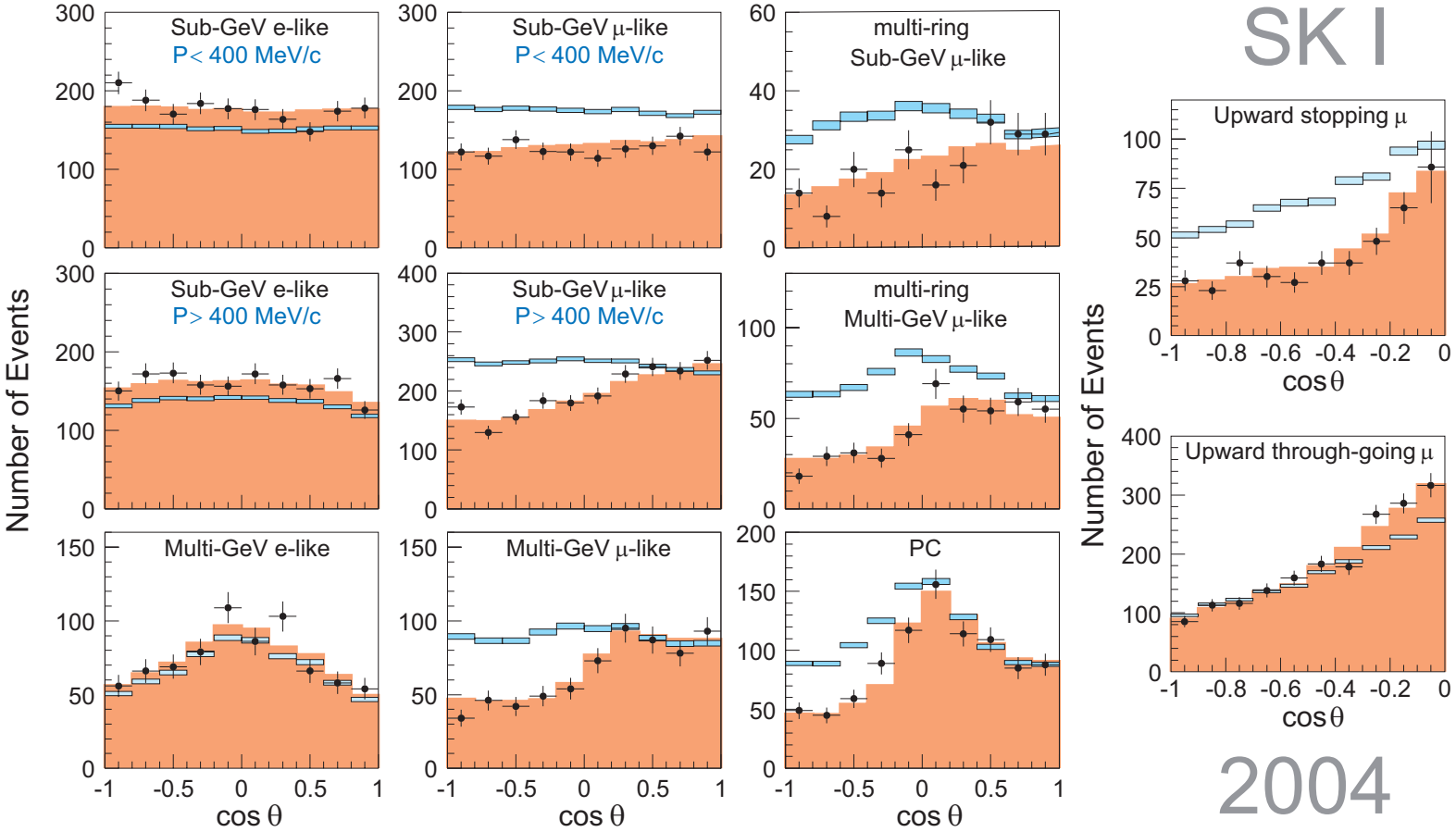

Zenith angle distributions for fully-contained 1-ring, multi-ring, partially-contained and upward events in Super-Kamiokande I (1489 day exposure). The points show the data, boxes – the non-oscillated MC events (the height of the boxes shows the statistical error) and the histograms – the best-fit expectations for $\nu_\mu \leftrightarrow \nu_\tau$ oscillations with $\theta = 45^\circ$ and $\Delta m^2 = 0.0021$ eV^2. The height of the boxes shows the statistical error of the MC.

[From Y. Ashie *et al.* (Super-Kamiokande Collaboration), Phys. Rev. D **71** (2005) 112005, hep-ex/0501064.]

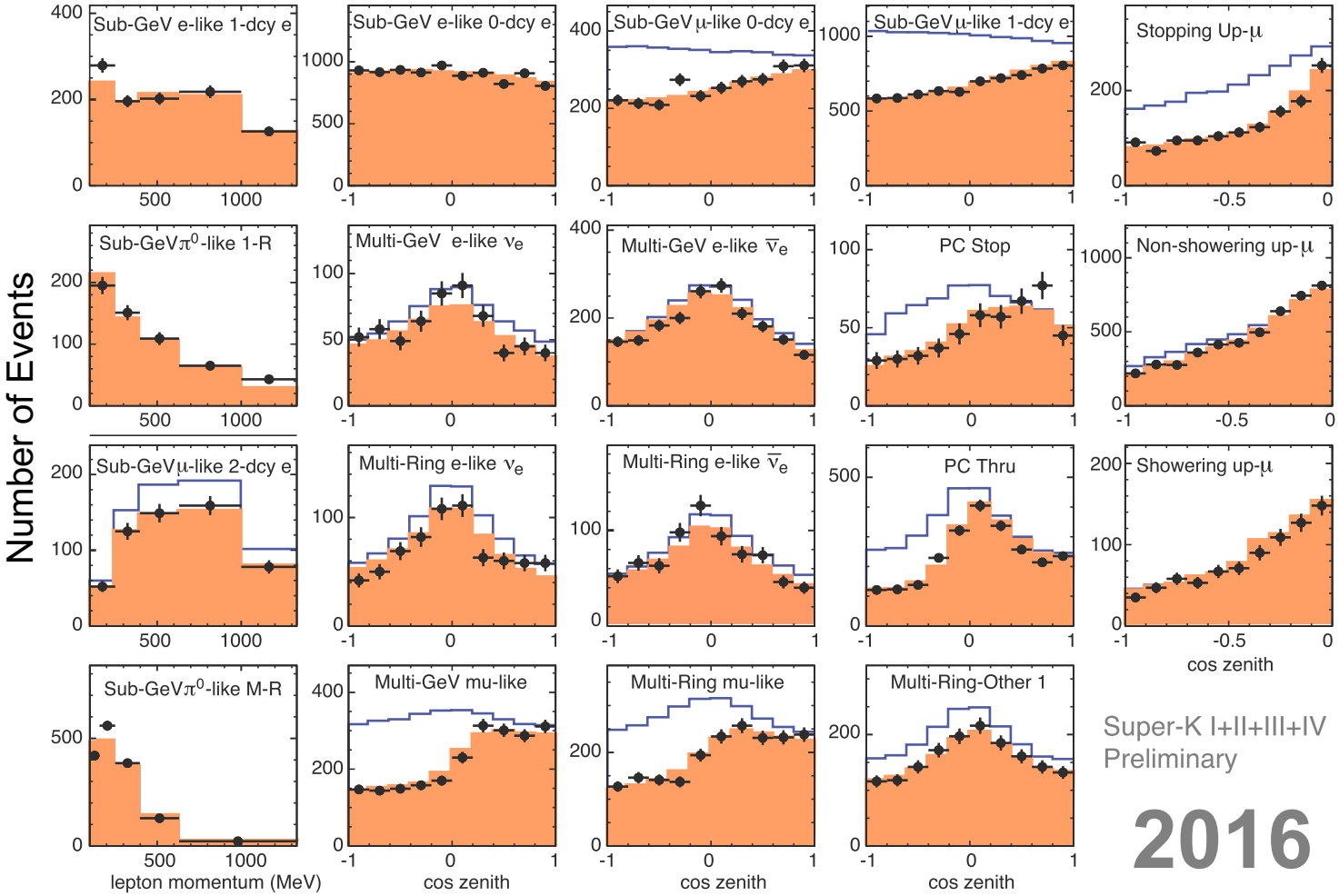

Zenith angle and momentum distributions for atmospheric neutrino subsamples used for recent analyses by Super-Kamiokande to study subleading effects, preferences for mass hierarchy and δ_{CP}, as well as searches for astrophysical neutrino sources such as dark matter annihilation.

[From T. Kajita *et al.* (for the Super-Kamiokande Collaboration), "Establishing atmospheric neutrino oscillations with Super-Kamiokande, "Nucl. Phys. B **908** (2016) 14–29.]

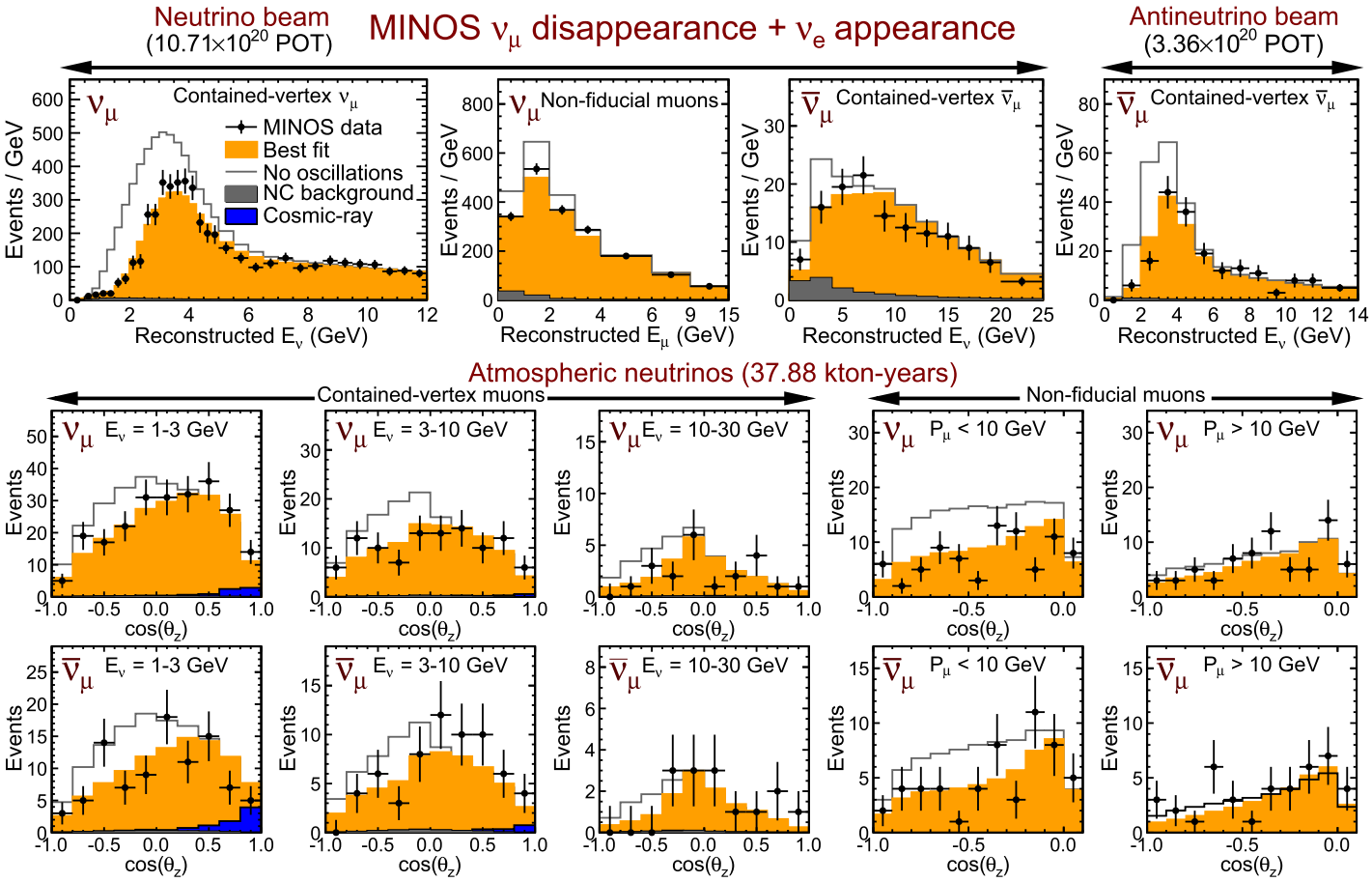

The event spectra at MINOS (see p. 936) from 10.71×10^{20} POT FHC (ν_μ-dominated) mode, 3.36×10^{20} POT RHC ($\overline{\nu}_\mu$-dominated) mode and 37.88 kt·yrs of atmospheric data. The data are shown compared to the prediction in absence of oscillations (grey lines) and to the best-fit prediction (red). The beam histograms (top) also include the NC background component (filled grey) and the atmospheric histograms (bottom) include the cosmic-ray background contribution filled blue).
[From L. H. Whitehead (for the MINOS Collaboration), "Neutrino oscillations with MINOS and MINOS+," Nucl. Phys. B **908** (2016) 130–150. (POT = Protons-on-Target, FHC = Forward Horn Current, RHC = Reverse Horn Current.)]

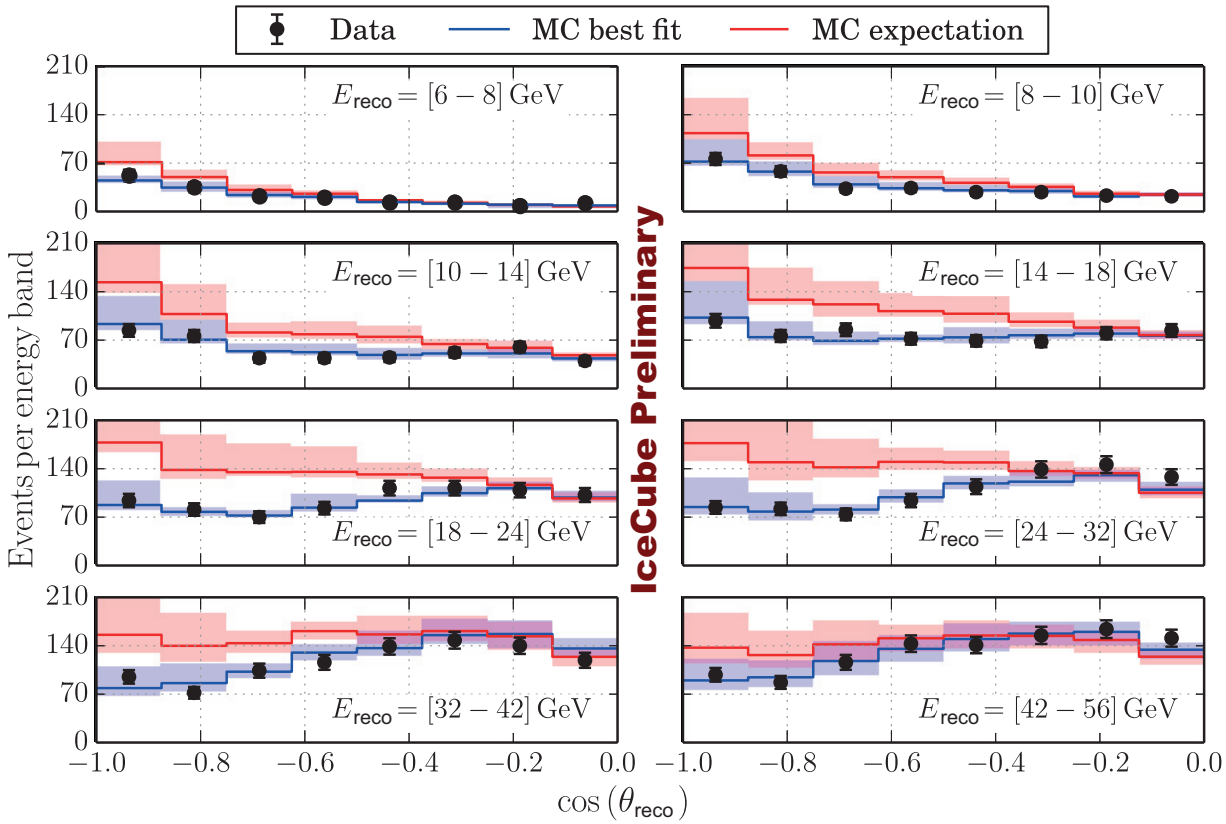

The **DeepCore** sub-array consists of 8 strings irregularly placed in the center of the IceCube detector. The string-to-string distances in this region range from 40 to 70 m. The strings are instrumented starting at a depth of 1760 m, and house PMTs with 35% higher efficiency than the standard IceCube PMTs. The separation between Digital Optical Modules (DOMs) in a string is of 7 m, with a *dusty* gap of 250 m between the DOMs 10 and 11.

△ Distribution of events in IceCube as a function of reconstructed direction and energy. Data are compared to the best fit and expectation without oscillations. Bands indicate assumed systematic uncertainties. The events of interest for the measurement are ν_μ and $\overline{\nu}_\mu$ charged current interactions in the DeepCore fiducial volume. Between May 2011 and April 2014, 953 days of good detector live-time are used. The analysis selects 5174 events with an expectation from simulation of 6980 without oscillations.

[From J. P. Yanez (for the IceCube Collaboration), "Results from atmospheric neutrino oscillations with IceCube DeepCore," AIP Conf. Proc. **1666** (2015) 100002.]

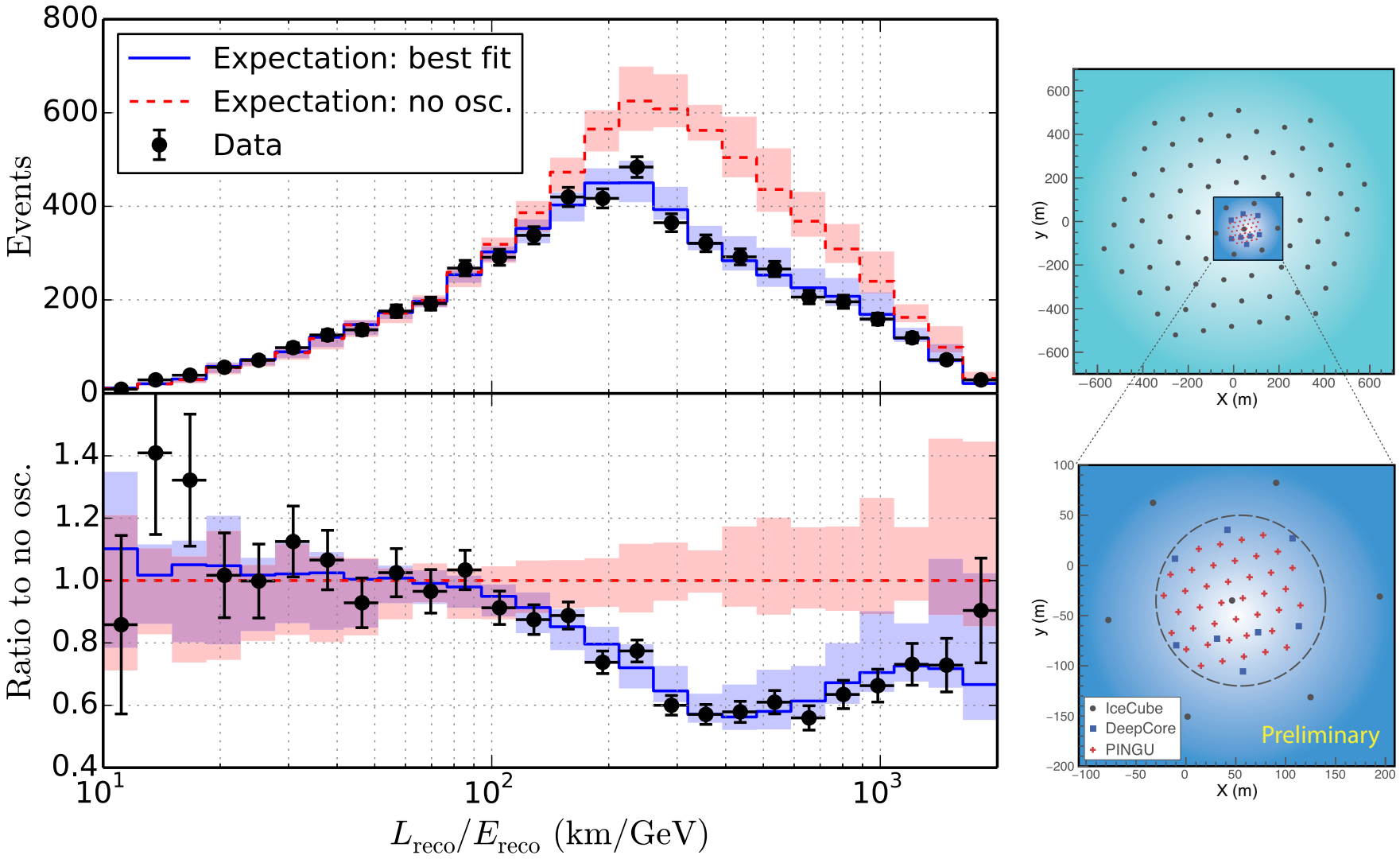

The events from 953 days of the IceCube-DeepCore data used in the analysis, plotted against L/E so that deviations arising from the oscillation can be seen. The solid line shows the best fit to the data while the dashed line illustrates the "no oscillation" scenario.

[From M. G. Aartsen *et al.*, "Neutrino oscillation studies with IceCube-DeepCore," Nucl. Phys. B **908** (2016) 161–177.]

6.10 AN fluxes at high & very high energies.

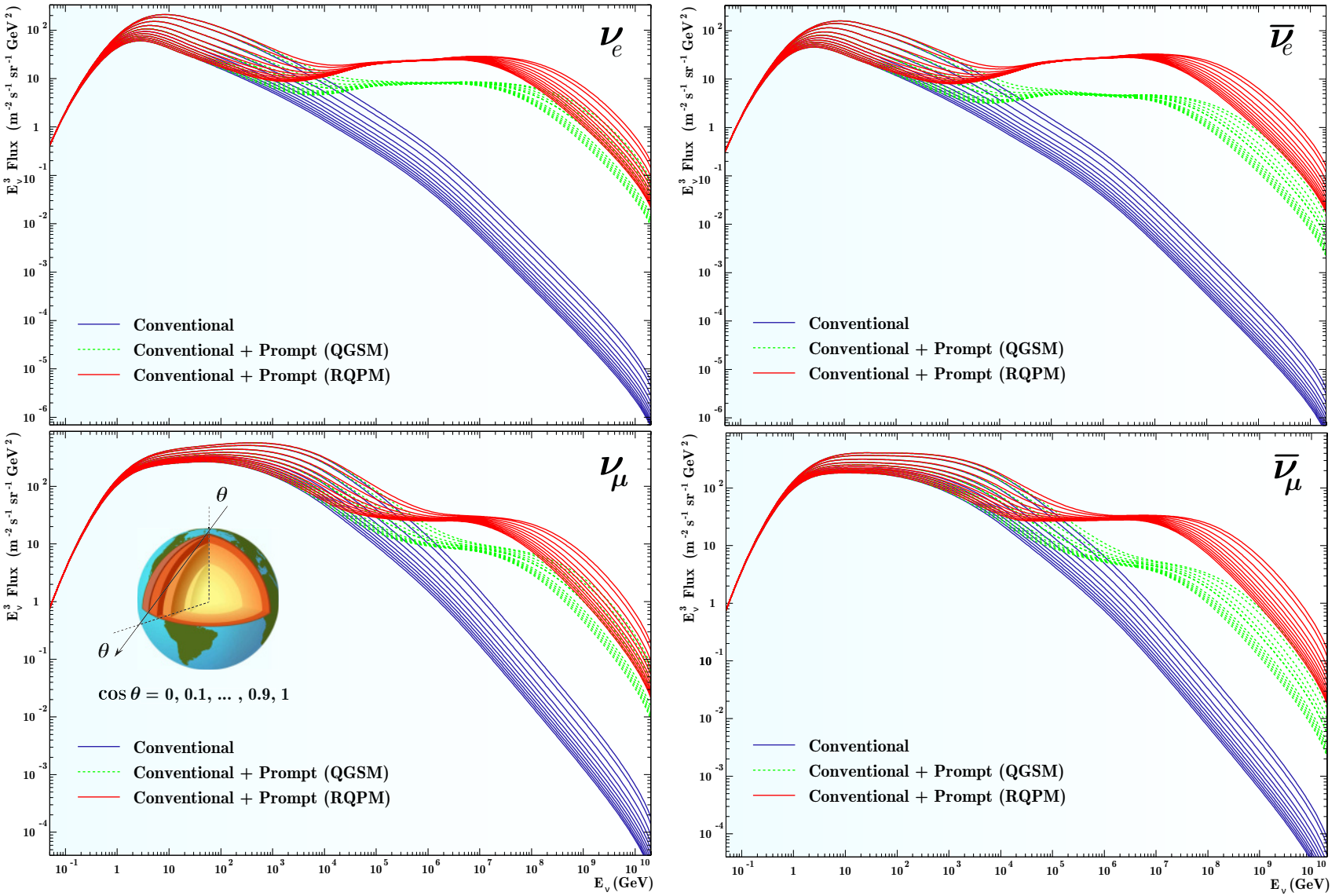

The energy spectra of downward-going ANs for 11 zenith angles with $\cos\theta$ varied from 0 to 1 with an increment of 0.1. The range below several GeVs is for Kamioka site. [See Ref. at p. 236.]

6.11 Comparison with data at high energies.

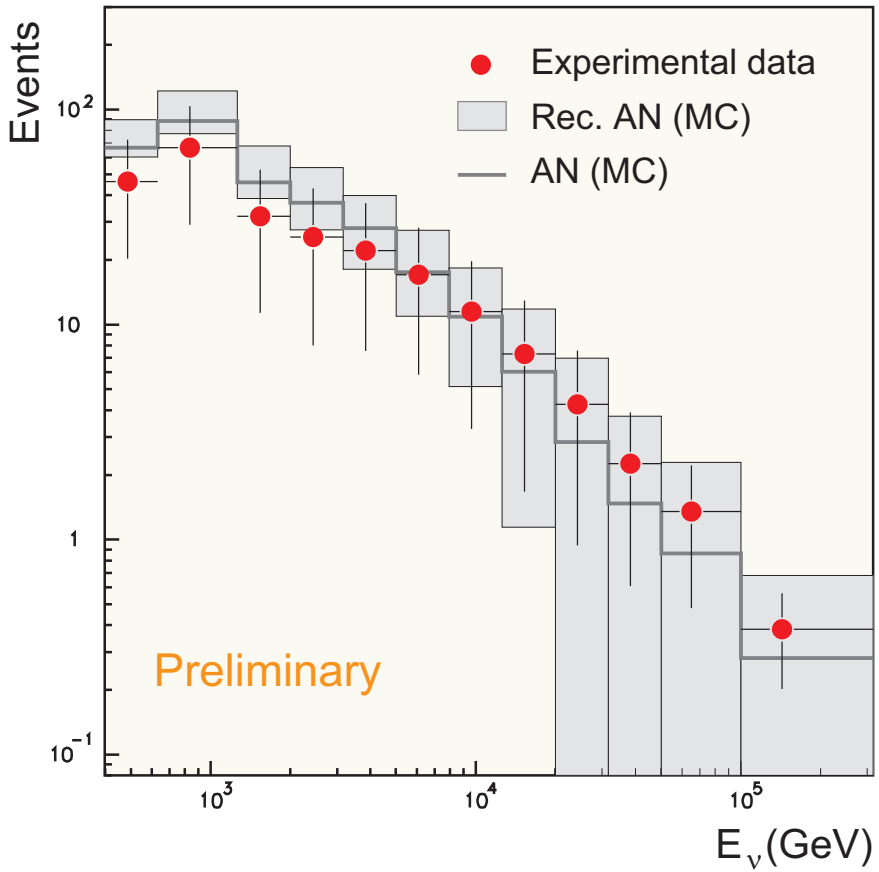

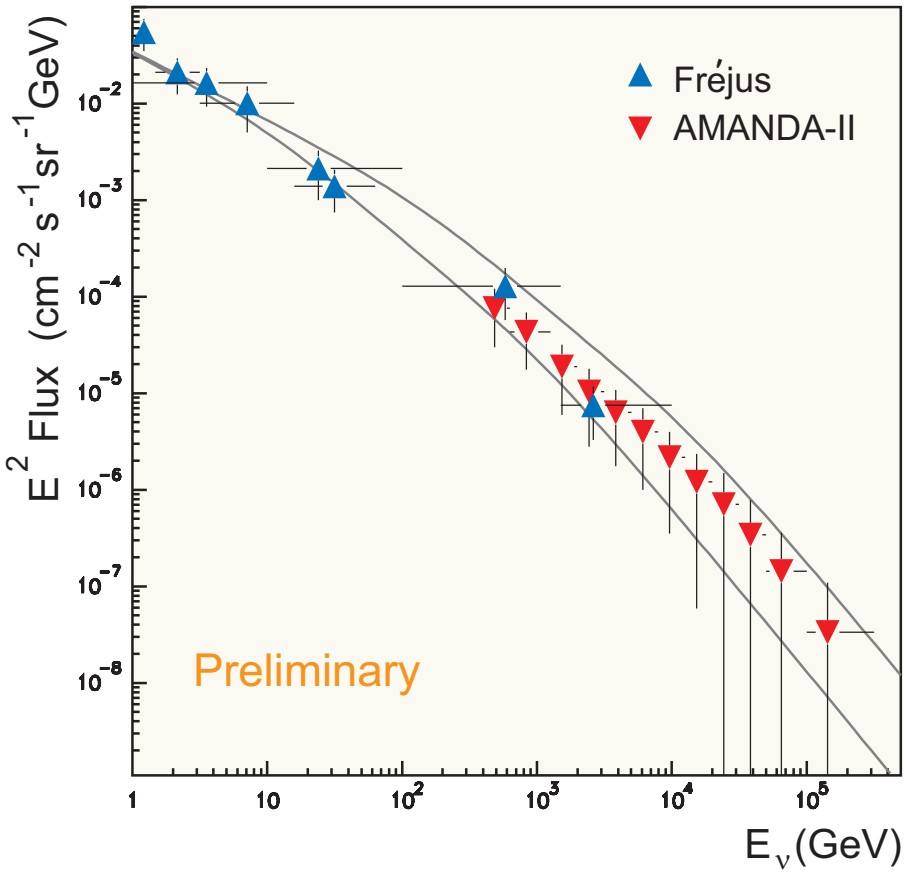

Reconstructed neutrino spectra in AMANDA-II. *Left panel*: on filter level (solid: energy distribution of atmospheric neutrino expectation, boxes: unfolded energy distribution of AN (MC), points: reconstructed data). *Right panel*: reconstructed fluxes compared to Fréjus data. The data are a little out of date and are now only of historical interest (see next slide).

[From H. Geenen (for the AMANDA Collaboration), contribution to the 28th ICRC, Tsukuda, Japan, July 31 – August 7, 2003 (see the AMANDA Berkeley Group homepage ⟨ http://area51.berkeley.edu/ ⟩).]

State of the art on September 2013.

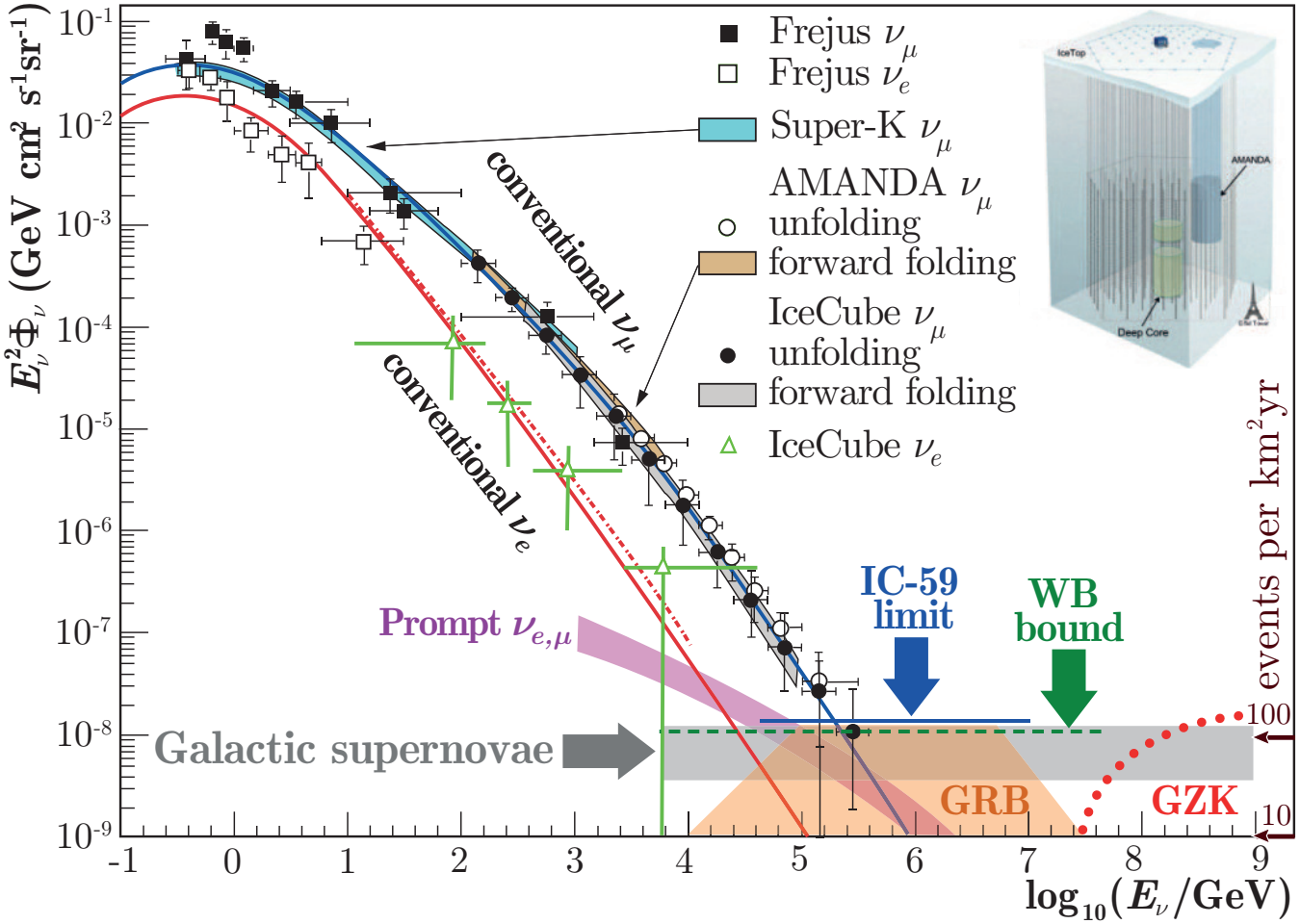

◁ The atmospheric muon and electron neutrino fluxes as measured by several experiments, together with the theoretical predictions. Also shown is a sample expectation of the cosmic-neutrino fluxes produced by SNRs, GRBs, cosmogenic (GZK) neutrino flux, Waxman-Bahcall (WB) upper bound, and the IceCube upper limit (IC-59, 59-string configuration) for cosmic muon neutrinos.

[From A. Kappes (for the IceCube Collaboration), "Neutrino astronomy with the IceCube observatory," J. Phys. Conf. Ser. **409** (2013) 012014, arXiv:1209.5855 [astro-ph.HE]; F. Halzen, "The highest energy neutrinos: first evidence for cosmic origin," in Proceedings of the 33rd International Cosmic Ray Conference (Rio de Janeiro, July 2–9, 2013), p. 1289–1299.]

7 Astrophysical neutrinos.

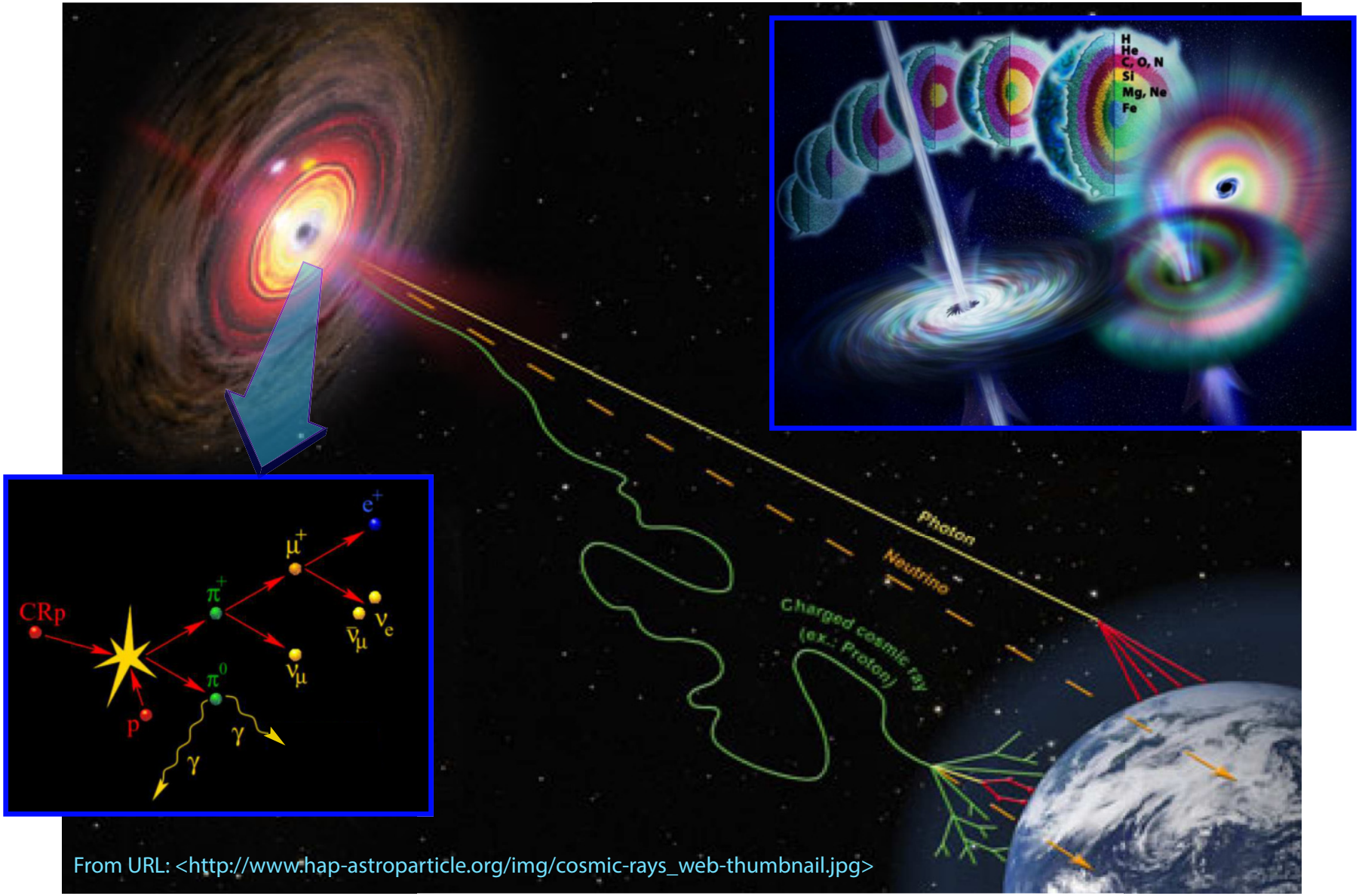

From URL: <http://www.hap-astroparticle.org/img/cosmic-rays_web-thumbnail.jpg>

7.1 Cosmic magnetic fields.

7.1.1 Pitch angle, gyroradius, etc.

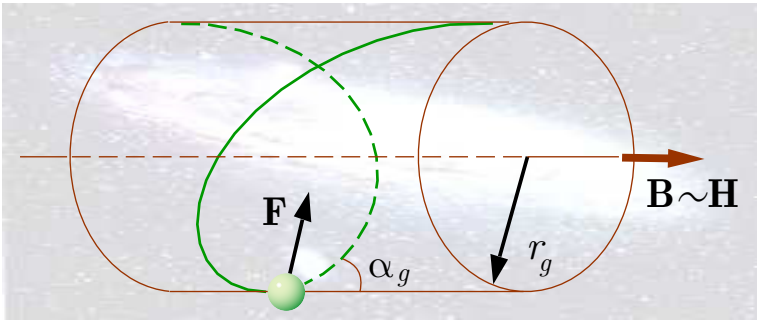

An electric charge Ze traveling with velocity $\mathbf{v}$ through a cosmic magnetic field with induction $\mathbf{B}$ experiences Lorentz force

$$\mathbf{F} = Ze(\mathbf{v} \times \mathbf{B}) \quad \text{(as usually, we put } c = 1\text{).} \quad (8)$$

According to Eq. (8), the charge spirals along the field lines without changing energy E. In a constant magnetic field, the particle describes a helical motion with constant pitch. The velocity component $v_{\parallel}$ along the direction of the field $\mathbf{B}$ is a constant of the motion and the circulate (or transverse) velocity $v_{\perp}$ about the field lines then defines the pitch angle

$$\alpha_g = \arctan\left(v_{\perp}/v_{\parallel}\right).$$

The radius r_g of the circular orbit that the particle describes transverse to the field is called gyroradius or Larmor radius. It can be obtained by setting the Lorentz force (8) equal to the centrifugal force acting on the particle. Let $p_{\perp} = v_{\perp}E$ be the transverse momentum and

$$\omega_g = v_{\perp}/r_g$$

is the gyrofrequency (or cyclotron frequency) then the centrifugal force has magnitude

$$p_{\perp}\omega_g = p_{\perp}v_{\perp}/r_g. \quad (9)$$

From Eqs. (8) and (9) we have $p_\perp v_\perp / r_g = Z|e|Bv_\perp$ (where $B = |\mathbf{B}|$) and thus

$$r_g = \frac{p_\perp}{Z|e|B} \equiv \frac{1\,\text{cm}}{300Z}\left(\frac{R}{1\,\text{Volt}}\right)\left(\frac{1\,\text{Gauss}}{B}\right), \qquad R = Br_g = \frac{p_\perp}{Z|e|}; \tag{10}$$

R is called magnetic rigidity.[a] Note that for arbitrary magnetic field $\mathbf{B} = \mathbf{B}(\mathbf{r}, \mathbf{t})$, Eqs. (10) provide *definition* of the local instantaneous gyroradius.

In most cosmic gases the magnetic permeability μ is close to 1. So for all practical purposes

$$\mathbf{B} = \mu\mathbf{H} \simeq \mathbf{H}.$$

Eq. (10) for r_g can also be rewritten in the form[b]

$$r_g \approx \frac{2.2\,\text{au}}{Z}\left(\frac{p_\perp}{10\ \text{GeV/c}}\right)\left(\frac{10^{-6}\ \text{G}}{H}\right) \qquad (1\,\text{au} \simeq 1.5 \times 10^{13}\ \text{cm}).$$

suitable for high-energy astrophysics. Since $H = 10^{-6}$ G is a typical magnitude of interstellar magnetic fields, the above equation shows that the gyroradii of high-energy cosmic rays are comparable with the size of a planetary system or even larger.

[a] $R = p/Z|e|$ (conventional definition in astrophysics) for motion strictly perpendicular to the field.
[b] $[\mathbf{B}]$ = Gauss, $[\mathbf{H}]$ = Oersted (= Ørsted), but in fact G ≡ Oe (= Ø).

7.1.2 Frozen-in flows.

Let's now estimate the typical value of the velocity of a thermal particle with a mass $m \sim 1$ GeV and charge $Z = 1$ moving in a cosmic gas cloud. Taking the gas temperature $T \sim 100$ K, we can write [a]

$$v_{\text{thermal}} \sim \sqrt{3kT/m} \simeq 5 \times 10^{-6} \simeq 1.5\,\text{km/s},$$
$$\Downarrow$$
$$r_g^{\text{thermal}} \sim 1.5 \times 10^{7}\,\text{cm} \times \left(\frac{10^{-6}\ \text{G}}{H}\right).$$

This is usually a very small value compared to the expected dimensions of the typical interstellar fields. Therefore, charged particles moving with thermal velocities characteristic of cosmic gases are effectively tied to the magnetic field lines. Some typical examples are given in the table, from which it can be seen that the gyroradii are indeed many orders of magnitude smaller than the sizes of the areas of their concentration in Cosmos.

Cosmic medium	Example	Size (cm)	H (G)	r_g (cm)
Comet ionized tail	Halley's comet	5×10^{12}	3×10^{-5}	3×10^{6}
Stellar wind	Solar wind near Earth	1×10^{13} (nominal)	3×10^{-5}	3×10^{6}
Supernova remnant	Crab nebula	5×10^{18}	3×10^{-4}	5×10^{4}
Spiral galaxy arm	Milky Way, M31	3×10^{20}	$\sim 10^{-5}$	$\sim 10^{8}$
Extragalactic medium	Metagalaxy	from $\sim 10^{28}$ to cosmic horizon	$\lesssim 10^{-9}$ (?)	$\gtrsim 10^{10}$

[a] Here $k \simeq 8.62 \times 10^{-14}$ GeV/K is the Boltzmann constant. Note that the chosen temperature of 100 K is very high, and in fact our estimates of the gyroradii of thermal particles reflect rather their upper limits.

Charged particles can move quite freely along the lines of force but have difficulty moving across them any significant distance. In other words, the thermal particles are essentially "frozen onto" the field like relic mammoths frozen onto ice or onto the Siberian permafrost.

In fact, the cosmic magnetic fields have their origins in the organized motion of charged particles. That is why one can also say that the magnetic fields are "frozen" into the interstellar medium. The motion of such gas-field or, more generally, plasma-field hybrids is called frozen-in flow.

Unlike the canned mammoths, the charged thermal particles can diffuse across the magnetic fields due to collisions with surrounding particles. If the particle collisions are frequent, they tend to destroy the magnetic fields. For this reason, frozen-in fields cannot be maintained in dense plasmas.

Another type of particle motion is their drift due to the presence of additional fields, such as gravitational and electrostatic. Drifts do not directly act to dissipate cosmic magnetic fields but, in conjunction with collisions, they affect the frozen-in flows.

Interplanetary magnetic field in the neighborhood of the Earth's bow shock.

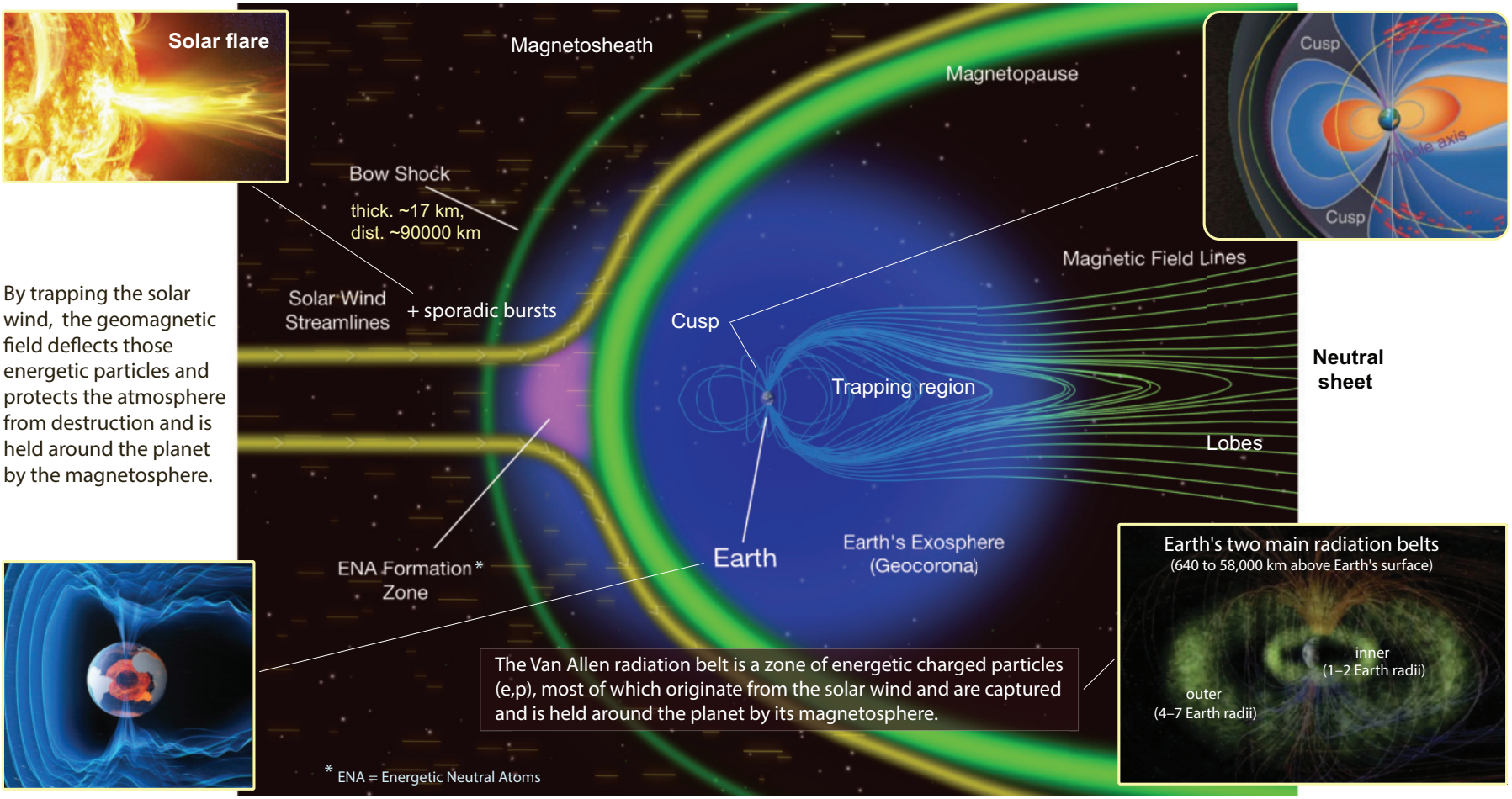

The Sun produces a hot gas that travels through space at about 10^6 miles per hour, carrying charged particles and magnetism outward past the planets. Thanks to the geomagnetic field, the solar wind is stopped and deflected around Earth so that most of it does not hit our atmosphere head on.

Changes on the Sun affect the solar wind flow; for example, solar flares, which are explosions associated with sunspots, cause strong gusts of the solar wind.

Polarized Emission from Milky Way Dust

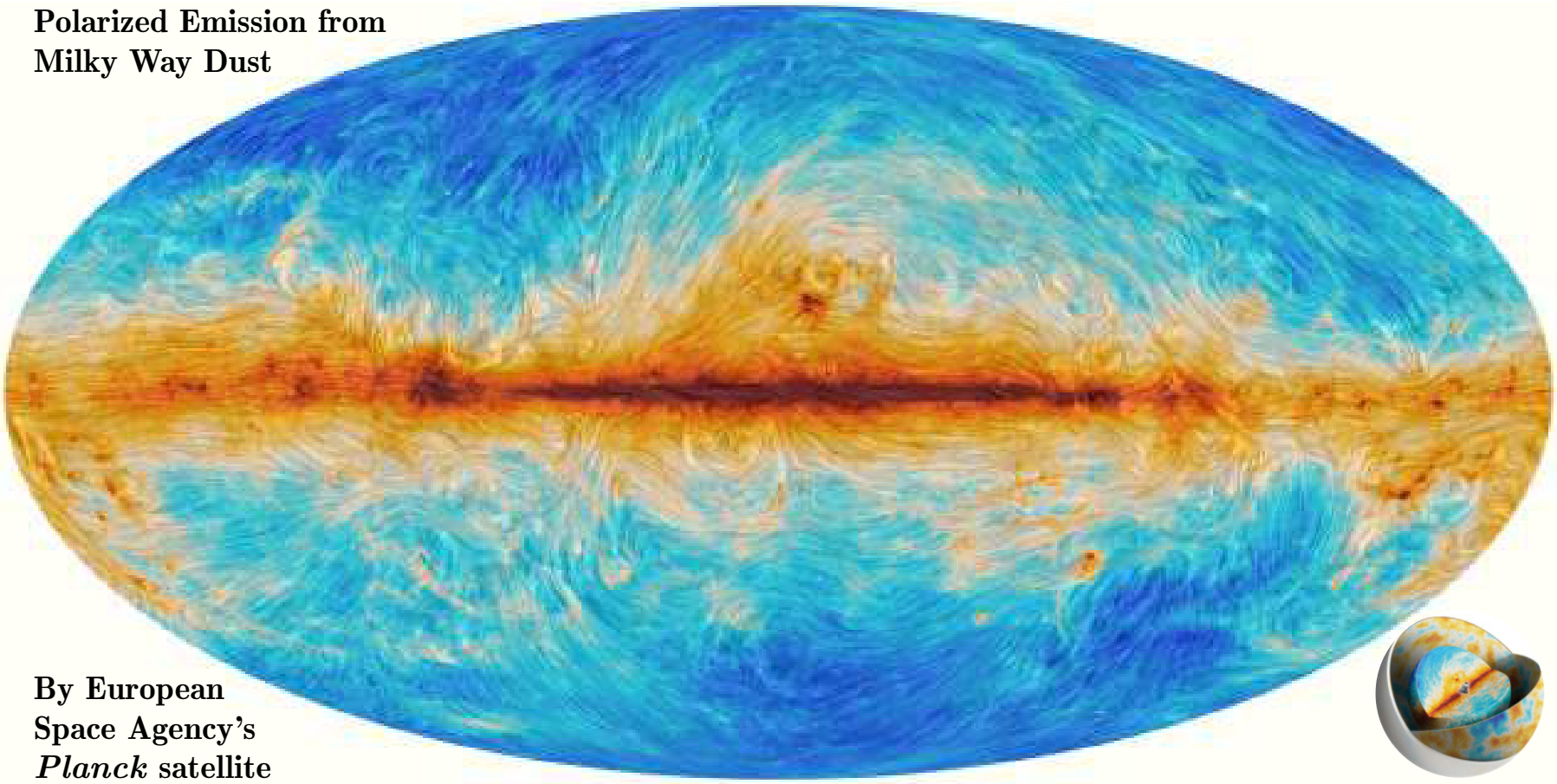

By European Space Agency's *Planck* satellite

Interstellar clouds of gas and dust are threaded by the galaxy's magnetic field, and dust grains tend to align their longest axis at right angles to the direction of the field. As a result, the light emitted by dust grains is partly polarized – it vibrates in a preferred direction – and, as such, could be caught by the polarization-sensitive detectors on *Planck*.

The polarized emission of interstellar dust allow to reconstruct the galaxy's magnetic field.
[From URL: ⟨ http://cuyastro.org/2015/02/10/tracing-the-milky-ways-magnetic-field/ ⟩.]

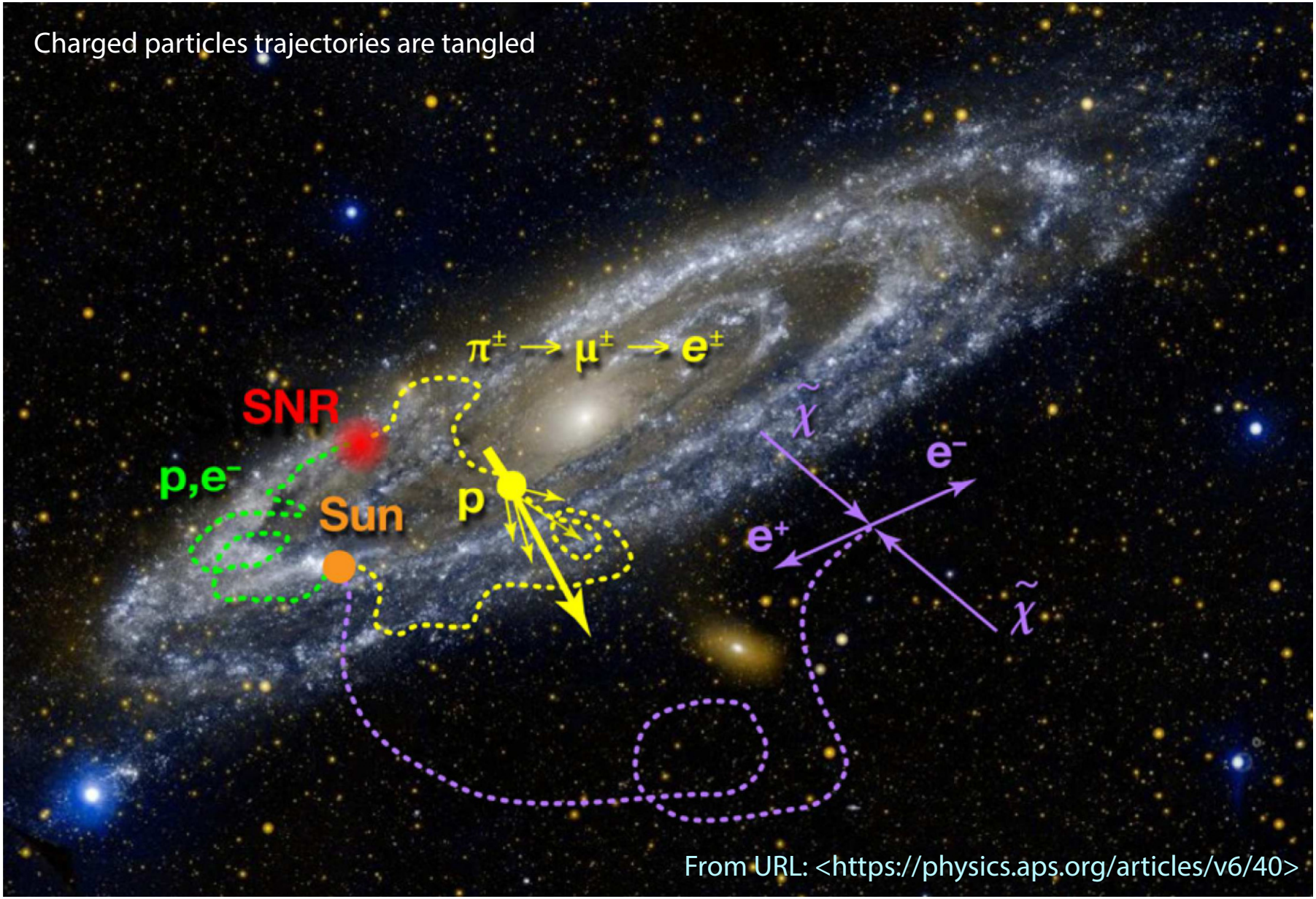
Charged particles trajectories are tangled
$\pi^{\pm} \rightarrow \mu^{\pm} \rightarrow e^{\pm}$
SNR
p,e⁻
Sun
p
$\tilde{\chi}$
e⁻
e⁺
$\tilde{\chi}$
From URL: <https://physics.aps.org/articles/v6/40>

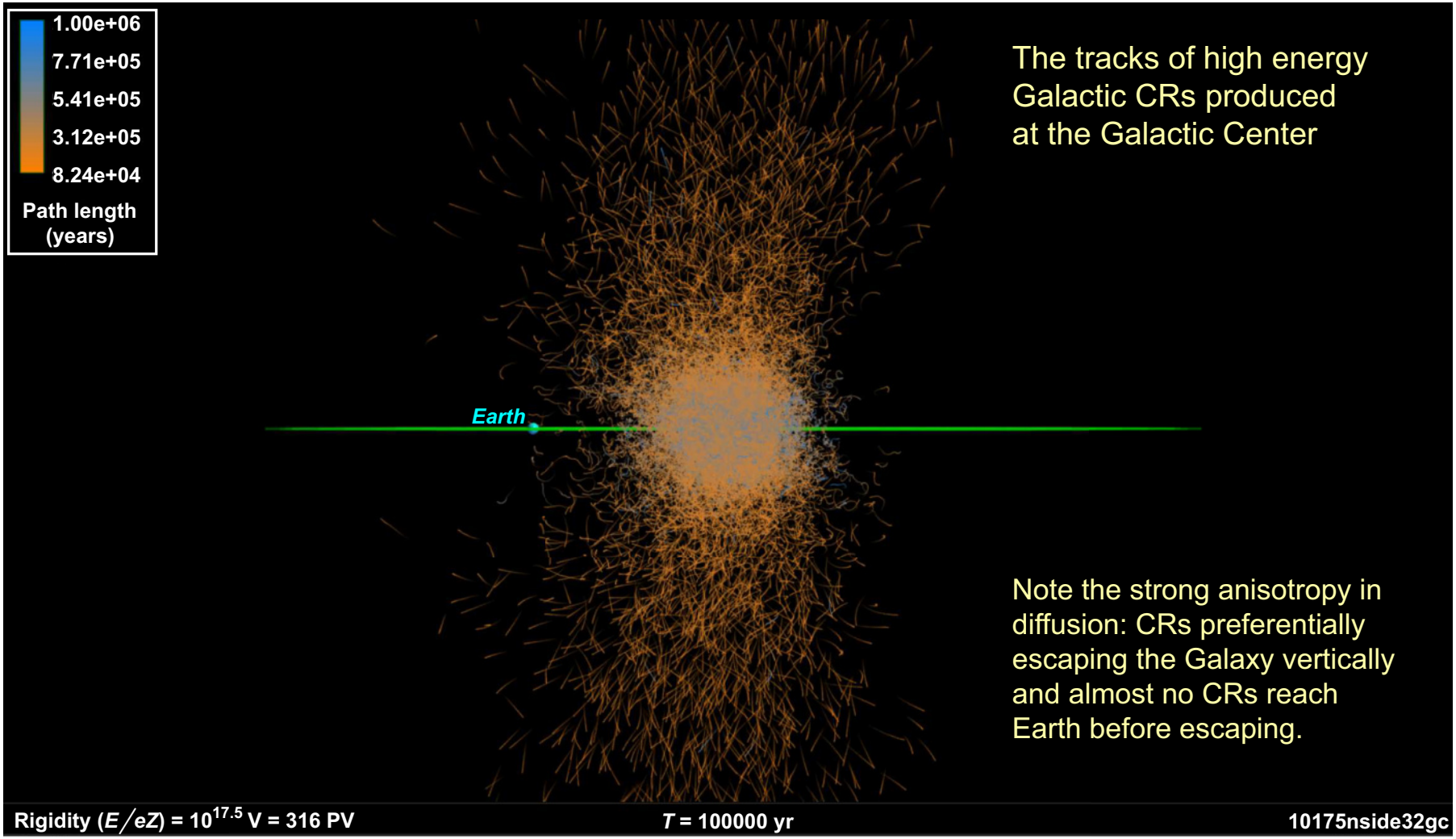

A snapshot of 0.3 EV CRs from an explosion at the Galactic Center, 100 kyr after the explosion.
[From G. R. Farrar, N. Awal, D. Khurana & M. Sutherland, "The Galactic magnetic field and UHECR optics," arXiv:1508.04530 [astro-ph.HE]; see also G. R. Farrar, "The Galactic magnetic field and its lensing of ultrahigh energy and Galactic cosmic rays," arXiv:1512.00051 [astro-ph.GA].]

7.2 Particle acceleration.

7.2.1 Mechanical (toy) model.

Let us consider an elastic collision of a relativistic particle from a moving object, say a ping-pong racket, whose mass is much larger than the total energy of the particle (ball).

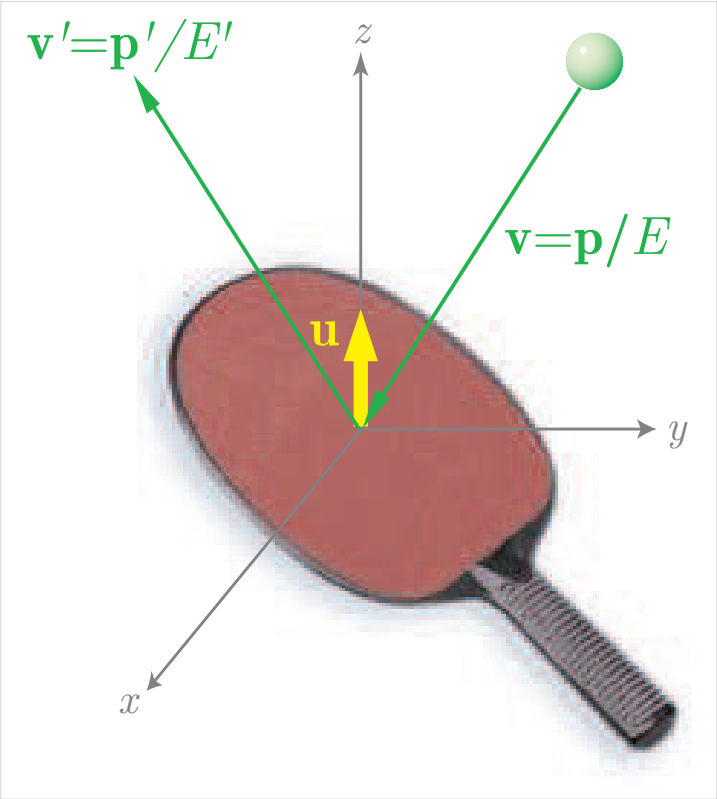

Relativistic ping-pong.

The energy and momentum of the ball viewed from the rest frame of the racket (RF) relate to that from the lab. frame (LF) through the Lorentz boost along the racket's velocity $\mathbf{u}$ (for simplicity, we assume that $\mathbf{u}$ is perpendicular to the racket's plane):

before collision	after collision
$\widetilde{E} = \Gamma\left(E - up_{\parallel}\right),$	$\widetilde{E}' = \Gamma\left(E' - up'_{\parallel}\right),$
$\widetilde{p}_{\parallel} = \Gamma\left(p_{\parallel} - uE\right),$	$\widetilde{p}'_{\parallel} = \Gamma\left(p'_{\parallel} - uE'\right),$
$\widetilde{p}_{\perp} = p_{\perp},$	$\widetilde{p}'_{\perp} = p'_{\perp}.$

Here $\Gamma = 1/\sqrt{1-u^2}$ is the Lorentz factor, $u = |\mathbf{u}|$, tilde ($\widetilde{}$) marks the values in RF, index $\parallel$ ($\perp$) marks the components of the particle's momenta $\mathbf{p}, \mathbf{p}'$ and velocities $\mathbf{v} = \mathbf{p}/E, \mathbf{v}' = \mathbf{p}'/E'$ parallel (perpendicular) to the velocity $\mathbf{u}$.

According to our assumptions,

$$\widetilde{E}' = \widetilde{E} \quad \text{and} \quad \widetilde{v}_{\parallel}' = -\widetilde{v}_{\parallel} \quad (\text{or} \quad \mathbf{u}\widetilde{\mathbf{v}}' = -\mathbf{u}\widetilde{\mathbf{v}}).$$

By applying these relations and the Lorentz transformations, we obtain

$$\left(1 - uv_{\parallel}'\right) E' = \left(1 - uv_{\parallel}\right) E, \qquad \left(v_{\parallel}' - u\right) E' = -\left(v_{\parallel} - u\right) E,$$

$$\Downarrow$$

$$\left(1 - u^2\right) E' = \left(1 - 2uv_{\parallel} + u^2\right) E,$$

$$\Downarrow$$

$$\boxed{\frac{E'}{E} = \frac{1 - 2\mathbf{uv} + u^2}{1 - u^2}, \qquad \frac{\Delta E}{E} = \frac{2\left(-\mathbf{uv} + u^2\right)}{1 - u^2}, \qquad \Delta E = E' - E.}$$

The energy change will be either positive (gain) or negative (loss), subject to the angle θ between the vectors $\mathbf{v}$ and $\mathbf{u}$ ($\cos\theta = \mathbf{vu}/uv$). Assuming $v > u$ yields the conditions:

$$\Delta E > 0 \quad \text{if} \quad -1 \leq \cos\theta < \frac{u}{v}$$

$$\Delta E \leq 0 \quad \text{if} \quad \frac{u}{v} \leq \cos\theta \leq 1.$$

The maximum energy gain is larger than the maximum energy loss:

$$\Delta E_+ - |\Delta E_-| = \frac{4u^2 E}{1 - u^2}.$$

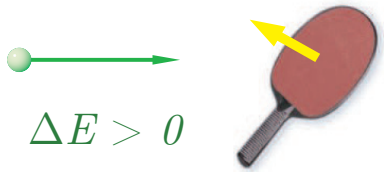

head-on collision

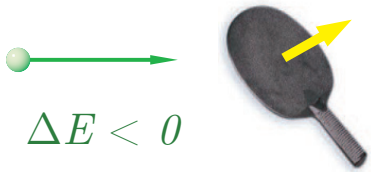

overtaking collision

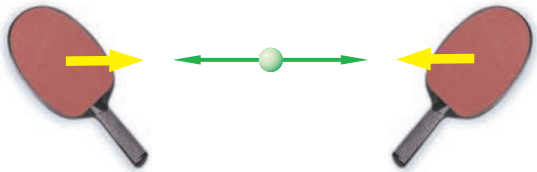

"accelerator"

In particular, for an ultrarelativistic particle and nonrelativistic racket ($u \ll v \approx 1$):

$\Delta E > 0$ for head-on collisions but

$\Delta E < 0$ for overtaking collisions.

It is intuitively clear that head-on collisions are more frequent than overtaking collisions causing, on the average, a net energy gain.

Problems:

1. Prove that $v'_{\parallel} = -v_{\parallel} + \dfrac{2u(1-v_{\parallel}^2)}{2uv_{\parallel} - (1+u^2)}$ and thus
$v'_{\parallel} \approx \mp 1 \pm (1 \mp v_{\parallel}) \left(\dfrac{1 \pm u}{1 \mp u}\right)^2$ when $v_{\parallel} \approx \pm 1$ and $u \ll 1$.
2. Study the case of a (ultra)relativistic racket.
3. Try to generalize our toy model by avoiding the assumption that $\mathbf{u}$ is perpendicular to racket's plane.

7.2.2 Second-order Fermi acceleration.

Let us now assume that many rackets are distributed uniformly in space and their velocities are all equal in magnitude and isotropically directed. Then the probability $\mathcal{P}(\mathbf{v},\mathbf{u})$ for the particle having velocity $\mathbf{v}$ (relative to the lab. frame) to collide with a racket having velocity $\mathbf{u}$ is proportional to the relative velocity $|\mathbf{v}-\mathbf{u}|$ (the flux is proportional to the velocity):

$$\mathcal{P}(\mathbf{v},\mathbf{u}) = \frac{|\mathbf{v}-\mathbf{u}|}{A}$$

and the factor A (which can only depend on v and u) can be found from the normalization condition

$$\int_{-1}^{1} \mathcal{P}(\mathbf{v},\mathbf{u})\, d\cos\theta = 1.$$

After simple integration

$$\int_{-1}^{1} |\mathbf{v}-\mathbf{u}|\, d\cos\theta = \int_{-1}^{1} \sqrt{v^2 - 2vu\cos\theta + u^2}\, d\cos\theta = \frac{(v+u)^3 - (v-u)^3}{3vu},$$

we obtain

$$A = 2v\left(1 + \frac{u^2}{3v^2}\right).$$

Finally, the probability is given by

$$\mathcal{P}\left(\mathbf{v},\mathbf{u}\right)=\frac{\left|\mathbf{v}-\mathbf{u}\right|}{2v\left(1+\dfrac{u^2}{3v^2}\right)}\qquad(v>u). \tag{11}$$

Then, taking into account that

$$\int_{-1}^{1}\mathbf{vu}\left|\mathbf{v}-\mathbf{u}\right|d\cos\theta=-\frac{2vu^2}{3}\left(1-\frac{u^2}{5v^2}\right),$$

we can calculate the average values of $\cos\theta$ and energy gain, ΔE, per collision:

$$\left\langle\cos\theta\right\rangle\equiv\int_{-1}^{1}\cos\theta\,\mathcal{P}\left(\mathbf{v},\mathbf{u}\right)\,d\cos\theta=-\frac{u}{3v}\left(\frac{1-u^2/5v^2}{1+u^2/3v^2}\right), \tag{12a}$$

$$\left\langle\Delta E\right\rangle\equiv\int_{-1}^{1}\Delta E\,\mathcal{P}\left(\mathbf{v},\mathbf{u}\right)\,d\cos\theta=\frac{8u^2E}{3(1-u^2)}\left(\frac{1+u^2/5v^2}{1+u^2/3v^2}\right). \tag{12b}$$

In the case of nonrelativistic rackets, $u^2\ll v^2$, the relative energy gain is proportional to u^2 and is independent of v:

$$\frac{\left\langle\Delta E\right\rangle}{E}\approx\frac{8}{3}u^2\equiv\varkappa. \tag{13}$$

This is a common feature of the second-order Fermi acceleration.

This mechanism is slow and inefficient but it provides the basic idea for more realistic models of cosmic-ray particle acceleration.

7.2.3 Power-law spectrum.

In the next step of our analysis we assume that many particles (balls) of the same energy E_0 were injected into the "Fermi accelerator" by some (unknown) mechanism. These particles may collide with the rackets, but we forbid them to collide with each other and exchange energy.[a] This means that their number density is assumed to be small. Some particles may be lost from the accelerator due to inelastic interactions with matter inside it or simply because they leak out from the system if it has a finite volume. We assume that the mean characteristic time of that, τ_e, is energy and time independent. It means that all particles have the same probability, dt/τ_e, of escaping in any time interval dt. Let $N(t)$ be the number of particles in the system at time t. Then

$$\frac{dN(t)}{N(t)} = -\frac{dt}{\tau_e}, \tag{14a}$$

$$\Downarrow$$

$$\frac{N(t')}{N(t)} = \exp\left[-\frac{(t'-t)}{\tau_e}\right]. \tag{14b}$$

Let τ_c be the average time between the collisions (thus the mean free path of the particles is $L_c = \tau_c v \simeq \tau_c$ if $v \simeq 1$). Putting $t' = t + \tau_c$ in Eq. (14b) then shows that $\exp(-\tau_c/\tau_e)$ is the fraction of particles survived during the time between successive collisions.

[a] The rackets may collide with each other if they wish.

If the initial energy E_0 of particles was ultrarelativistic then, according to Eq. (13), their average energy $E = E_n$ after n collisions becomes

$$E = (1+\varkappa)^n E_0 \quad \Rightarrow \quad n = \frac{\ln(E/E_0)}{\ln(1+\varkappa)}.$$

Therefore the number of particles having energies greater than E (that is the integral energy spectrum) is

$$N(>E) = K\sum_{l\geq n}\exp\left(-\frac{l\tau_c}{\tau_e}\right) = K\exp\left(-\frac{n\tau_c}{\tau_e}\right)\sum_{l\geq 0}\exp\left(-\frac{l\tau_c}{\tau_e}\right)$$

$$= \frac{K\exp\left(-\dfrac{n\tau_c}{\tau_e}\right)}{1-\exp\left(-\dfrac{\tau_c}{\tau_e}\right)} = \frac{K\left(\dfrac{E}{E_0}\right)^{-\gamma}}{1-\exp\left(-\dfrac{\tau_c}{\tau_e}\right)},$$

where K is some constant and

$$\gamma = \frac{\tau_c}{\tau_e\ln(1+\varkappa)} \approx \frac{\tau_c}{\varkappa\tau_e};$$

in the last equality we used the condition $\varkappa \propto u^2 \ll 1$. Since $N(>E_0) \equiv N(\geq E_0) = N_0$ is the number of injected particles,

$$K = \left[1-\exp\left(-\frac{\tau_c}{\tau_e}\right)\right] N_0$$

and therefore

$$N(>E) = N_0\left(\frac{E_0}{E}\right)^{\gamma}.$$

From the obtained integral energy spectrum we immediately derive the differential spectrum:

$$N(E) = -\frac{dN(>E)}{dE} = \frac{\gamma N_0}{E_0}\left(\frac{E_0}{E}\right)^{\gamma+1}.$$

So we arrive at the desired power-law spectra. Note, however, that the power law for the integral spectrum can be rewritten in the form

$$\frac{dN(>E)}{N(>E)} = -\gamma\frac{dE}{E},$$

which relates the relative loss in the number of particles to the relative gain in energy by the remaining particles. This is a very general law, which is not at all specific exclusively to the physical mechanism in question.

Moreover, and that's even more frustrating, the power-law exponent is not universal. In order to have $\gamma \sim 1$ (preferably $\gamma \approx 2.7$, see p. 281), there should be $\tau_c \sim \varkappa\tau_e \ll \tau_e$, that is the collisions should be much more frequent than the processes resulting in escape of particles from the Fermi accelerator. This condition is not very realistic.

Many other questions arise immediately: Are there some real analogs of our rackets in Cosmos? Who plays this relativistic Ping-Pong and who supplies the players with the *preaccelerated* balls?

Problem: Please, fill up the list of questions.

To answer some of these questions we have to consider some features of cosmic medium and magnetic fields.

7.2.4 Stochastic collisions with magnetic clouds.

Both interstellar medium and the magnetic fields frozen into it are highly inhomogeneous. Let us assume however that the field slowly changes in space that is the typical scale of the magnetic inhomogeneities L_H is very large compared to the particle gyroradius,

$$L_H \gg r_g.$$

Then the transverse to $\mathbf{H} = \mathbf{H}(\mathbf{r})$ component of the momentum obeys the low[a]

$$\frac{p_\perp^2}{H(\mathbf{r})} = \frac{p^2}{H_p}, \tag{15}$$

where the critical field H_p is a constant. The left part of Eq. (15) is called the first adiabatic invariant. Eq. (15) can be rewritten as

$$\sin^2 \alpha_g = \frac{H(\mathbf{r})}{H_p}, \tag{16}$$

where α_g is the pitch angle defined in Sect. **7.1.1**, p. 249. Hence, as the particle approaches a region where $H = H_p$ the pitch angle attains the maximum possible value of $\pi/2$. At this point the particle is reflected back along the same line of force and spirals backwards.

[a] This is a consequence of conservation of magnetic (dipole) moment, $\mu = mv_\perp^2/2H$, in the constant magnetic field H; the moment remains an adiabatic invariant for the charged particles in slowly varying fields.

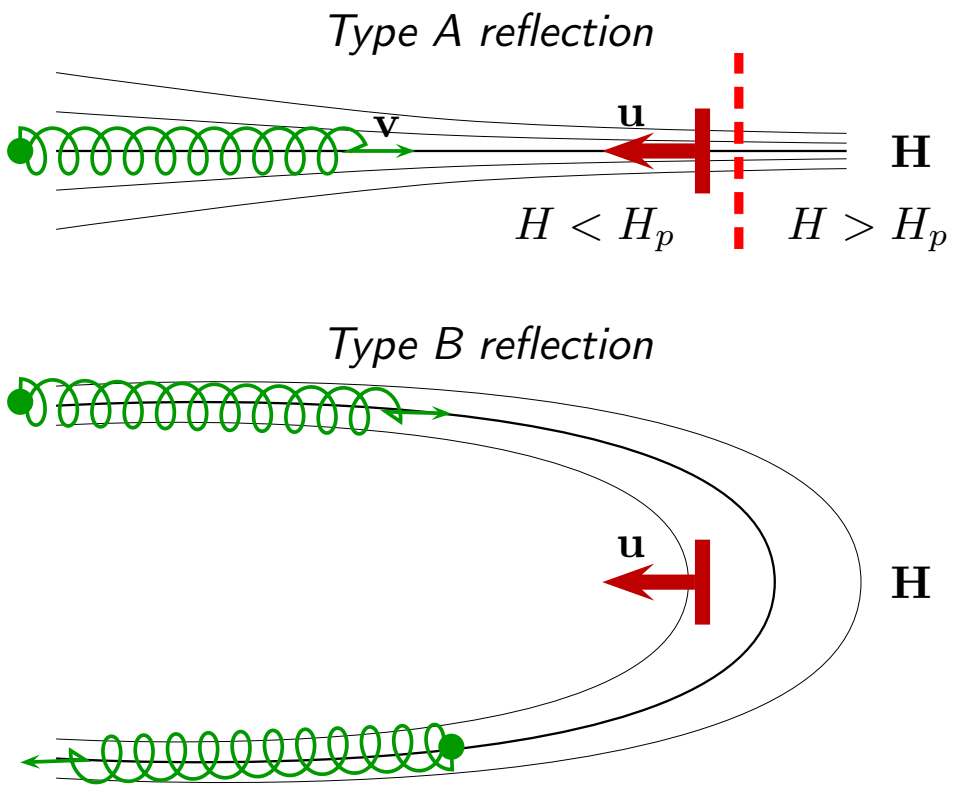

Collisions with moving magnetic irregularities leading to reflection.

This is, according to Fermi,[a] the "type A" reflection. Somewhat similar process takes place when the particle spirals around a curve of the line of force ("type B" reflection).

[a] E. Fermi, "On the origin of the cosmic radiation," Phys. Rept. **75** (1949) 1169–1174; see also E. Fermi, "Galactic magnetic field and the origin of cosmic radiation," ApJ **119** (1954) 1–6.

Figure below schematically shows an example of a "magnetic trap" or "magnetic bottle". Its action is obvious from the previous consideration. If the Helmholtz coils move toward each other, the particle is accelerated.

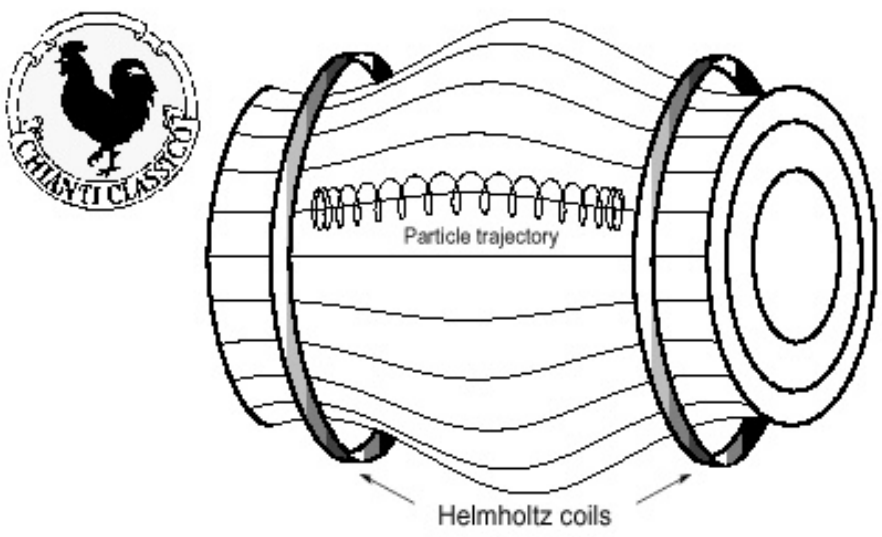

Motion of a trapped charged particle in a in a magnetic bottle produced by two single axis Helmholtz coils. An example of the coil design is shown on the right.

A well-known example of the cosmic magnetic trap is the Van Allen radiation belts, which surround the Earth. The radiation belt particles are trapped by the field because the field lines converge (i.e., the field gets stronger) at the poles. As a charged particle, spiraling about a field line enters a region of converging magnetic fields, it experiences a net displacement force in the direction of the weaker field, which causes the particle to oscillate between the poles (see next slide). The end result is that a population of energetic particles is trapped within the dipolar structure.

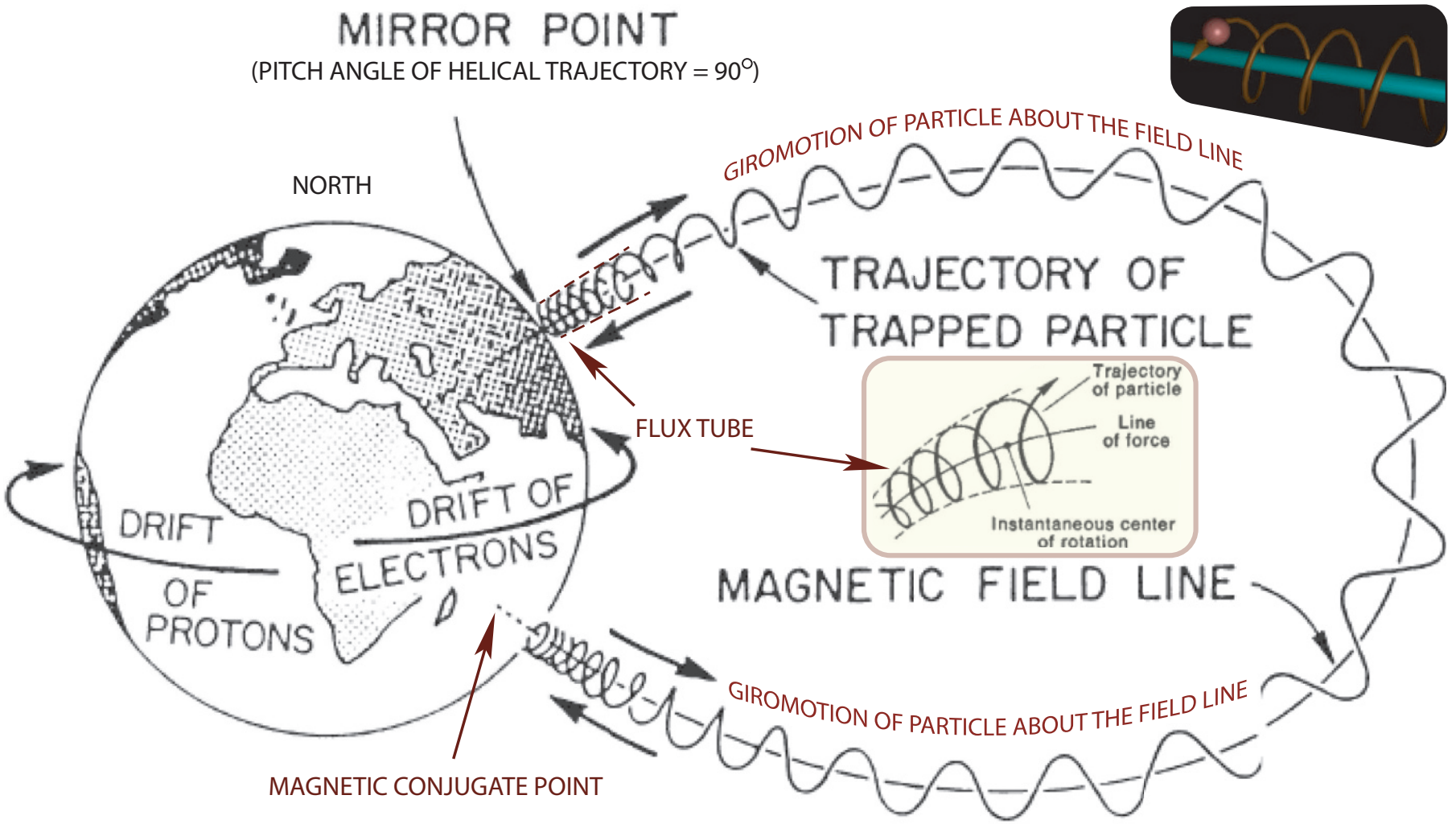

Mirroring of a trapped particle in the Earth's magnetic field. The dipole-like structure of the geomagnetic field provides the mechanism for a trapped population of energetic particles.

[From A. P. Stern & N. F. Ness, "Planetary magnetospheres," NASA technical memorandum 83841, Goddard Space Flight Center, Greenbelt, MD, 1981.]

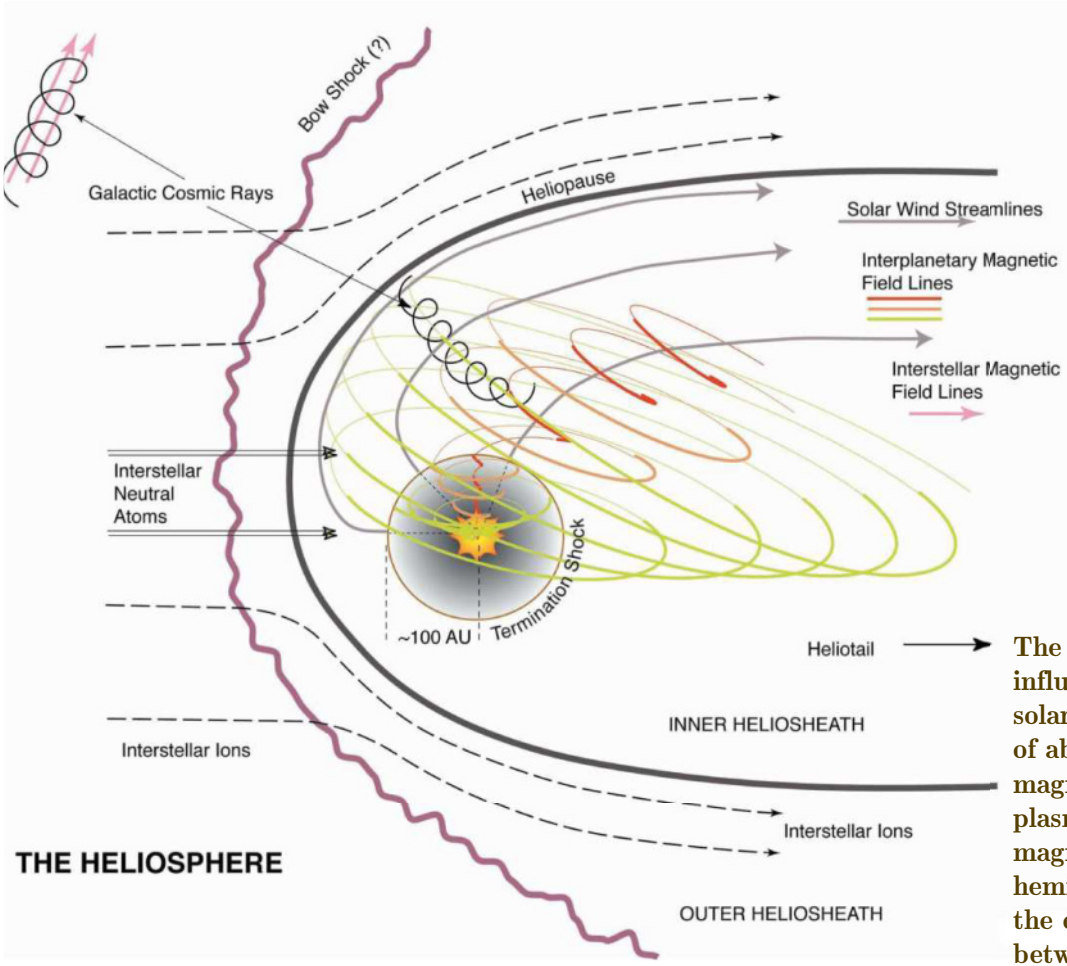

courtesy S.T.Suess

The plasma flow and with it the frozen–in magnetic field around the Earth is governed by two effects: the interstellar wind, caused by the motion of the solar system through the interstellar medium, and the solar wind, the hot coronal plasma continuously launched by the sun at supersonic speeds (up to 800 km/s closer to the poles and in quiet solar conditions) since there is no pressure equilibrium in the solar corona. The solar wind is initially radial and discontinuously slows down to subsonic speeds at a distance of ~ 80 – 90AU, the so–called "termination shock". At even larger distances, the heliopause marks the surface inside of which (inner heliosheath) the solar flow and magnetic fields dominate and outside of which (outer heliosheath), the interstellar flow and magnetic fields dominate. Past the termination shock, in the inner heliosheath, the solar wind curves from its radial form, turns over and flows towards the interstellar downstream direction, the heliotail.

The structure of the magnetic field inside the heliosphere is influenced by the magnetic field structure launched with the solar wind and by rotation: The sun is rotating with a period of about 25 days and the rotation axis is misaligned with the magnetic axis. As the magnetic field is frozen into the cosmic plasma, together with the solar wind this leads to a twist of magnetic field lines into the so-called Parker spiral. In one hemisphere, the magnetic field is directed inward and in the other hemisphere it is directed outward. The transition between both polarity regions is taking place in a surface which due to the misalignment of rotation and magnetic axis by the so–called tilt–angle takes a wavy shape: the "wavy heliospheric current sheet".

A schematic view of the interaction of the interstellar medium with the solar environment.

[From M. Ahlers & Ph. Mertsch, "Origin of small-scale anisotropies in galactic cosmic rays," Prog. Part. Nucl. Phys. **9** (2017) 184–216, arXiv:1612.01873 [astro-ph.HE].]

The magnetic inhomogeneities shown at p. 266 sometimes called "magnetic mirrors", are the real analog of our rackets which almost elastically scatter cosmic ray particles.
Since the frozen magnetic field is very stable compared to the time of collision with a fast particle and remains unchanged during the collision, the collision is mechanically similar to that of a fast lightweight ball with a slowly moving massive object (racket).
The particle would gain energy due to head-on collisions and lose it in overtaking collisions.

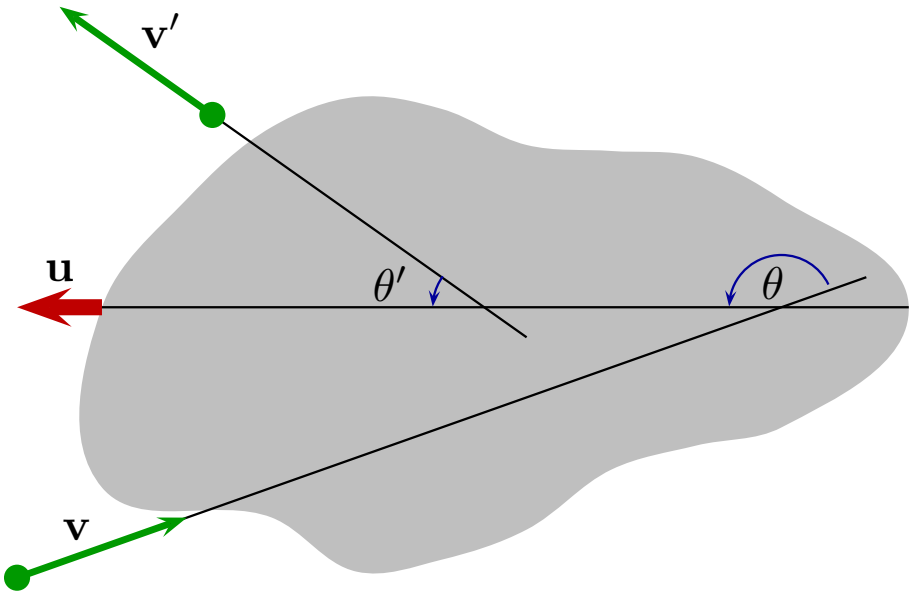

Schematic view of a charged particle collision with moving cloud. Direction of a particle is randomized by scattering on the heterogeneous magnetic field tied to the cloud.

◦ The motion of the particle scattered on the random magnetic field irregularities (turbulences) inside a magnetic cloud can be treated as a random walk.

◦ In full analogy with the mechanical model, the probability of head-on collisions is higher than that of overtaking collisions and, therefore, the particles will, on average, gain energy.

◦ We'll assume that the injected particle moves fast compared to the cloud ($v \gg u$) and can scatter only on the magnetic irregularities frozen into the cloud, but not on thermal particles. Therefore, we neglect all possible mechanisms of energy loss except the Fermi mechanism.

Using the same notation as in Sect. **7.2**, p. 257, we can write

$$\begin{aligned}\widetilde{E} &= \Gamma\left(E - up_{\parallel}\right)\\ &= \Gamma E\left(1 - uv_{\parallel}\right),\end{aligned}$$

Going back to the lab. frame, we have

$$\begin{aligned}E' &= \Gamma\left(\widetilde{E}' + up'_{\parallel}\right)\\ &= \Gamma\widetilde{E}'\left(1 + uv'_{\parallel}\right).\end{aligned}$$

The energy is conserved in the cloud's rest frame, $\widetilde{E} = \widetilde{E}'$.

Therefore

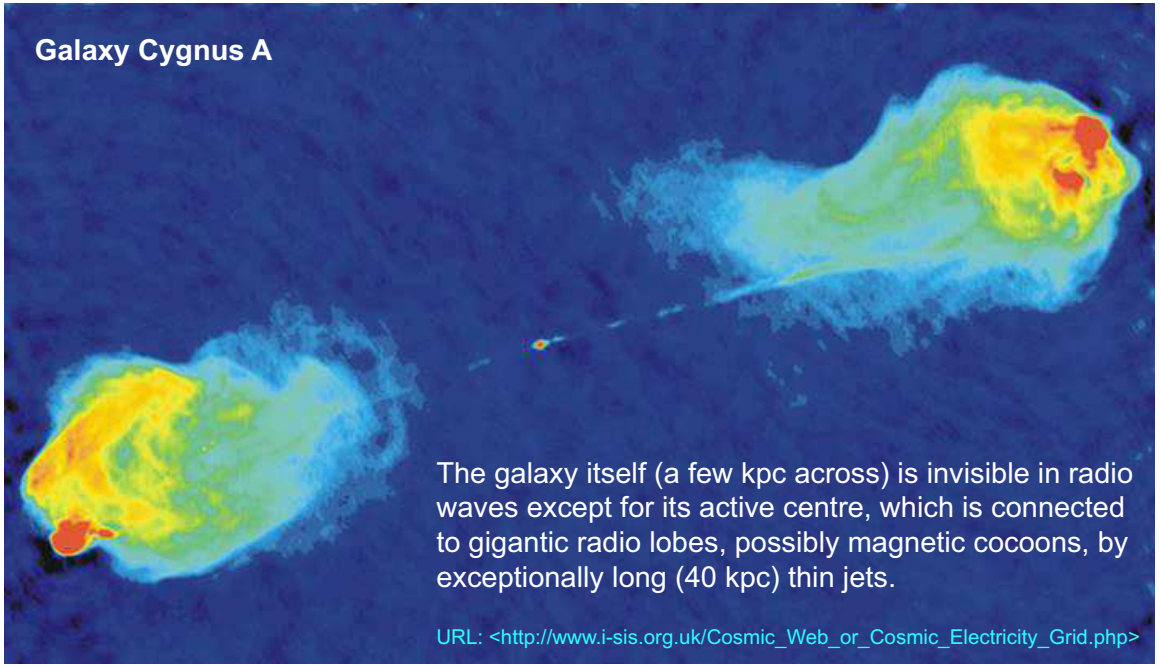

Radio image of Cygnus A dwarfed by huge double magnetized radio lobes at the ends of bipolar jets; red spots are very bright "hotspots".

$$E' = \Gamma^2 E\left(1 - uv_{\parallel}\right)\left(1 + uv'_{\parallel}\right) = \Gamma^2 E\left(1 - uv_{\parallel} + uv'_{\parallel} - u^2 v_{\parallel} v'_{\parallel}\right)$$

or, in terms of the angles defined in the figure shown in previous slide,

$$\frac{\Delta E}{E} = \Gamma^2\left(1 - uv\cos\theta + u\widetilde{v}'\cos\widetilde{\theta}' - u^2 v\widetilde{v}'\cos\theta\cos\widetilde{\theta}'\right) - 1. \tag{17}$$

Neglecting the $\mathcal{O}(u^2)$ contributions, this equation simplifies to

$$\frac{\Delta E}{E} \simeq -uv\cos\theta + u\widetilde{v}'\cos\widetilde{\theta}' \simeq uv\left(\cos\widetilde{\theta}' - \cos\theta\right).$$

A crucial step: Since the motion of particles inside the cloud is assumed to be random (or, which is actually the same thing, the distribution of the magnetic field irregularities in the cloud is random), all values of $\widetilde{\theta}'$ are equally probable, and we can safely put $\langle \cos \widetilde{\theta}' \rangle = 0$. Neglecting the $\mathcal{O}(u^2)$ contributions in Eq. (12a) (which is obviously applicable to the considered situation) then yields

$$\langle \cos \theta \rangle \simeq -\frac{u}{3v}.$$

Now, by averaging Eq. (17) and putting $v = 1$, we get the result

$$\frac{\langle \Delta E \rangle}{E} \simeq \frac{4}{3} u^2,$$

which is *within a factor of 2* the same as given by Eq. (13) (the origin of this difference is obvious).

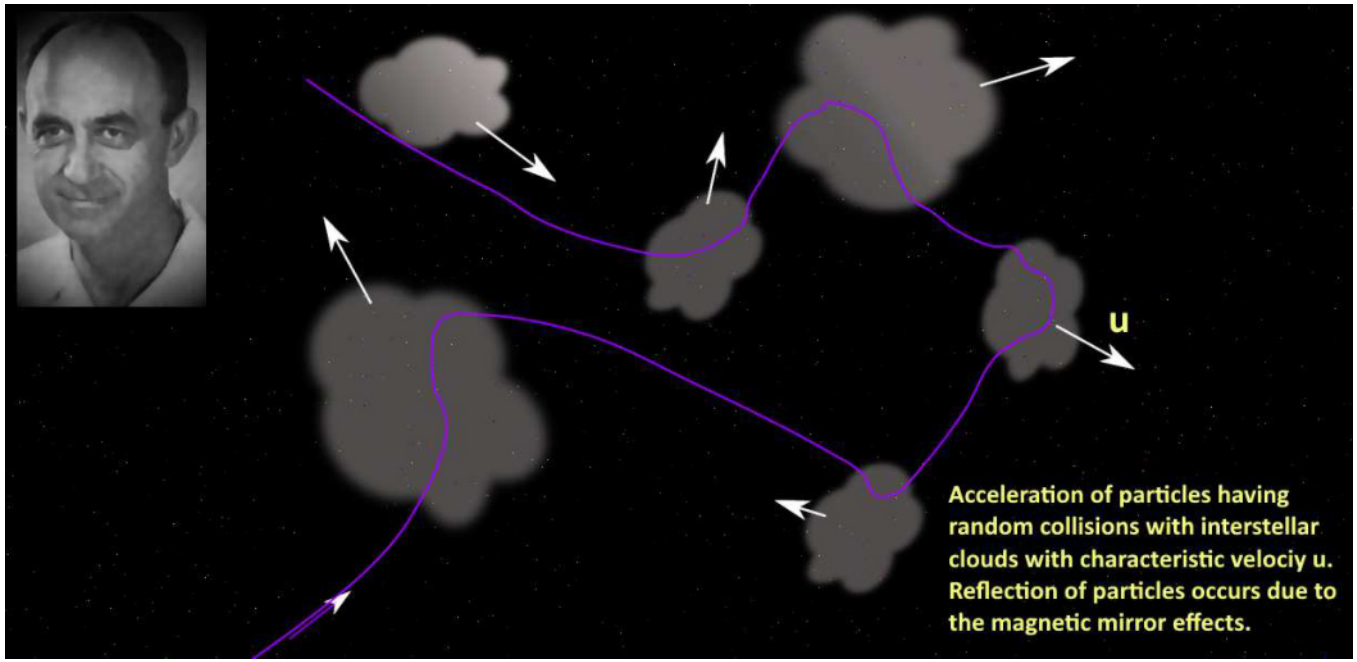

This mechanism is called second order stochastic Fermi acceleration.

7.2.5 First-order Fermi acceleration at shock fronts.

[Krymsky (1977), Axford, Leer, & Skadron (1977), Bell (1978), Blandford & Ostriker (1978).][a]

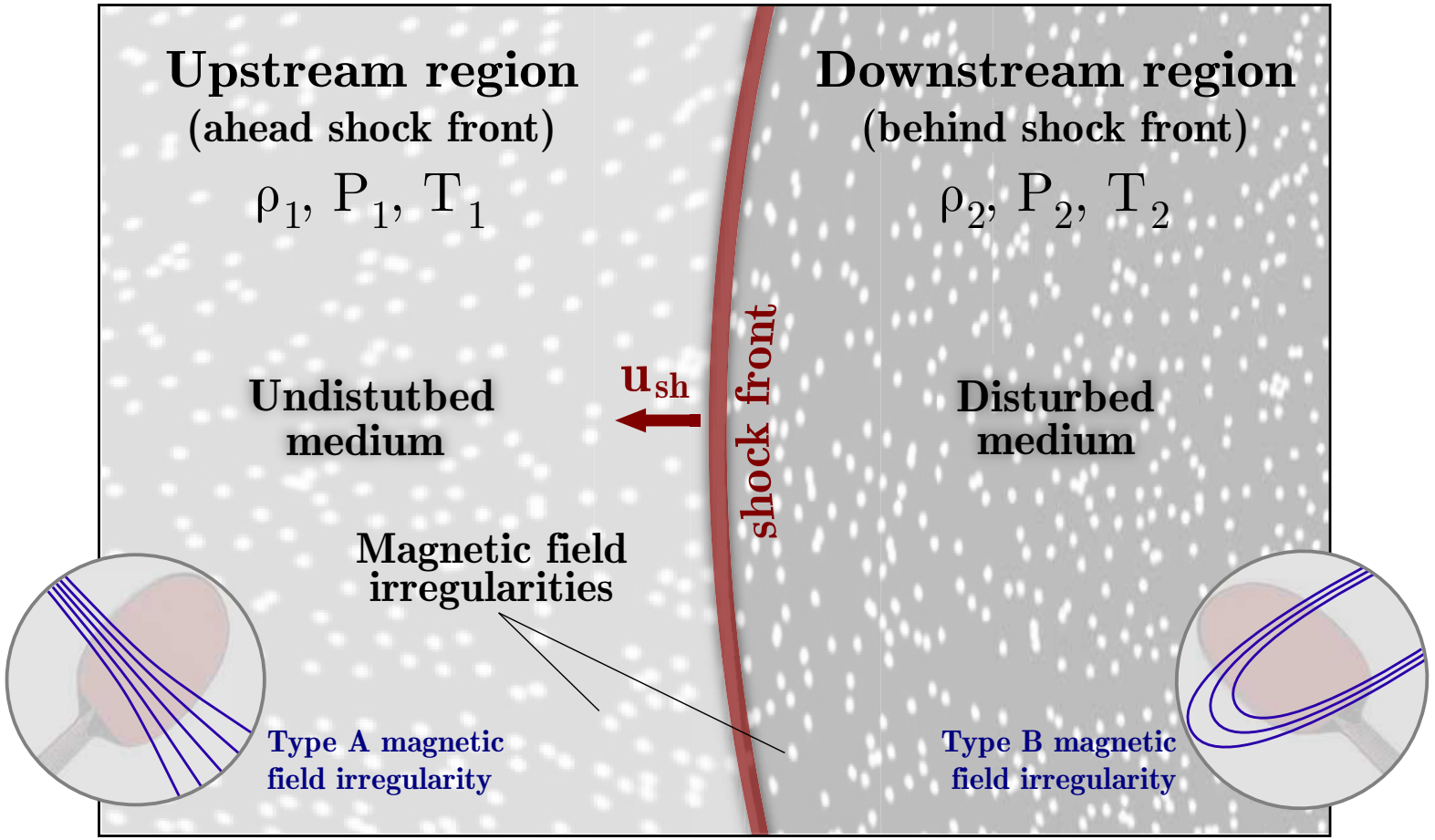

Below are a few real-life examples. They show that real life is very different from our models.

[a] The most important work is A. R. Bell, "The acceleration of cosmic rays in shock fronts – I," Mon. Not. Roy. Astron. Soc. **182** (1978) 147–156.

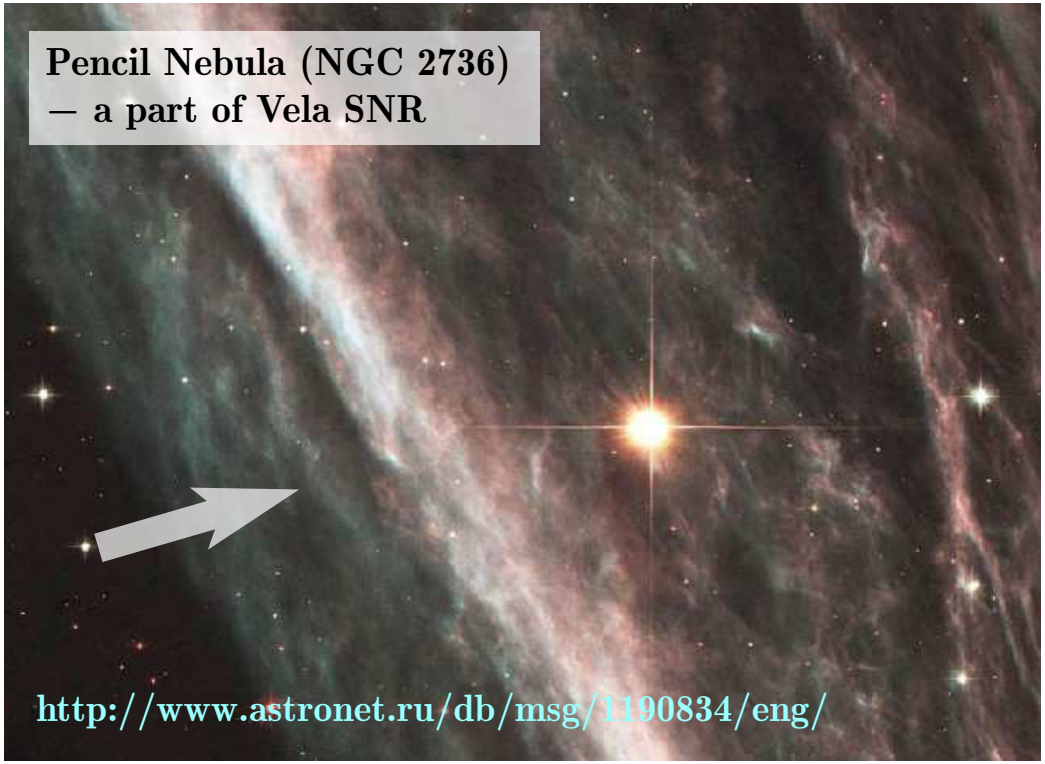

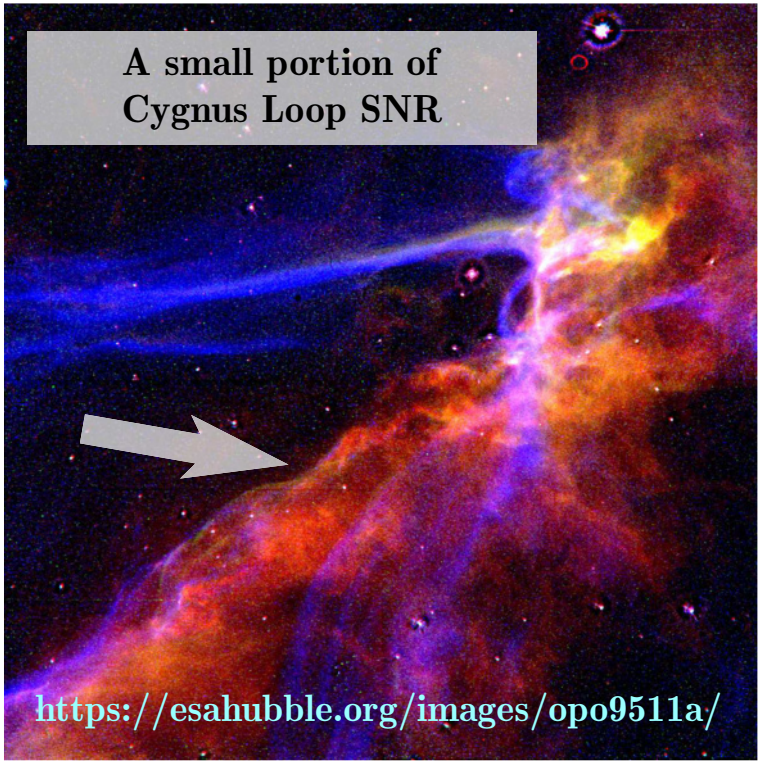

At 5×10^5 km/h, a SN shockwave NGC 2736 plows through interstellar space. This is an expanding shell of a star that exploded about 11,000 yr ago. Initially the shockwave was moving at millions of km/h, but the weight of all the gas it has swept up has slowed it down considerably.
The region shown spans nearly a ly across, a very small part of the 100+ ly span of the entire Vela SNR. The shockwave moves from left to right, as can be discerned by the lack of gas on the left.

Cygnus Loop is the expanding blastwave from a SN explosion which occurred about 15,000 yr ago. The blastwave, which is moving from left to right across the field of view, has recently hit a cloud of denser than average interstellar gas. This collision drives shock waves into the cloud that heats interstellar gas, causing it to glow. The SNR lies 2,500 ly away in the constellation Cygnus (Swan).

△ One of the two shock waves observed in the galaxy cluster Abell 3667 (located about 7.3×10^8 ly from Earth, contains more than 550 galaxies). It is the largest cosmic shock waves observed so far. The shock waves propagate at 1500 km/s and are ≈ 60 times the size of Milky Way. The shock waves are threaded by an intricate pattern of bright filaments that trace the location of giant magnetic field lines and the regions where electrons are accelerated. [Image by MeerKAT radio telescope, 2022.]

We'll consider super-simplified (but commonly used) model of parallel (or planar) diffusive shock.

Basic assumptions:

- the shock front is an infinite plane (front width is negligible);
- the ionized gas media behind and ahead the shock front are spatially infinite;
- the gas in the shock is compressed by a factor $r = u_1/u_2$, so that the downstream velocity relative to the shock front is $u_2 = u_{\rm sh}/r$;

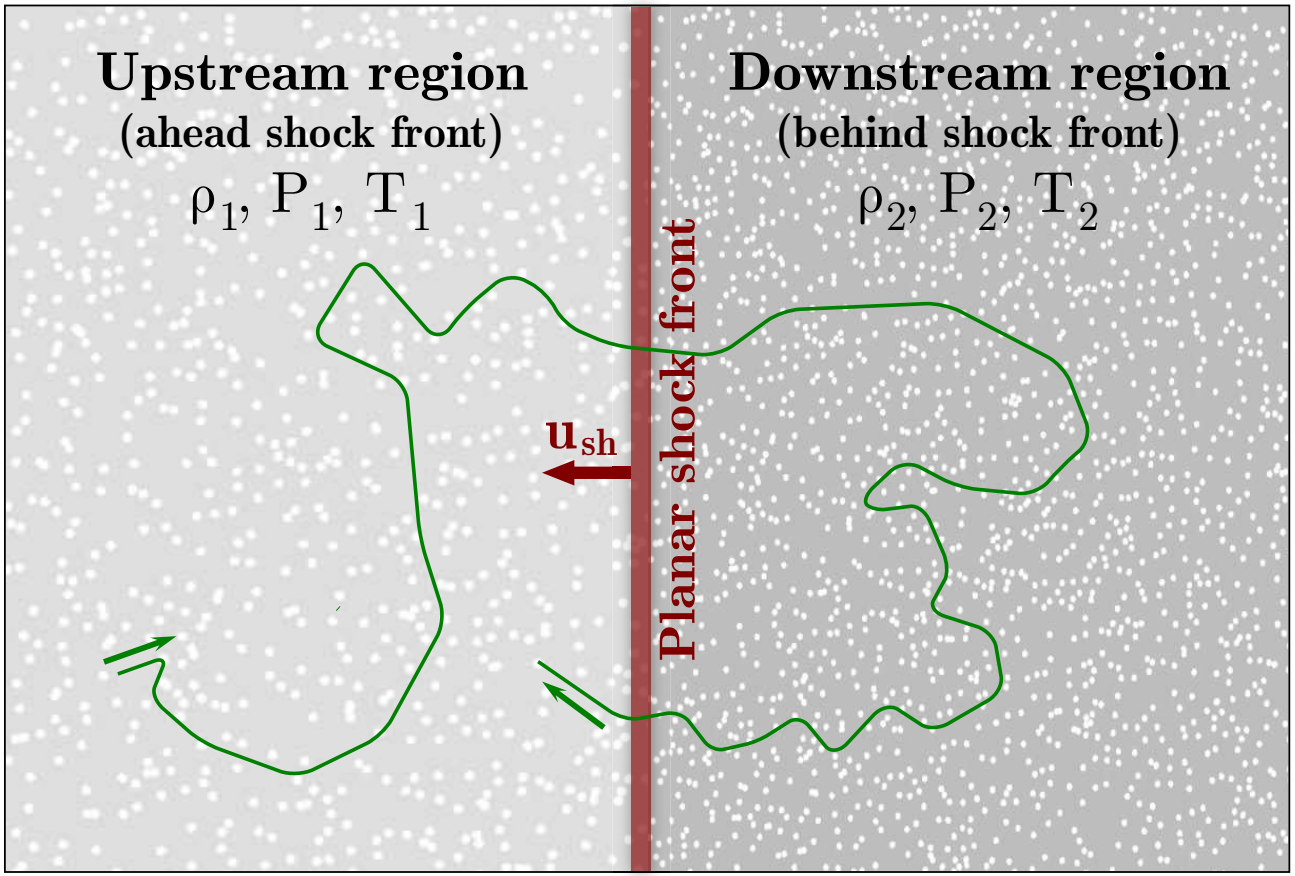

- there is no limitation in time, the relevant physical quantities are in a steady state;
- there are inhomogeneities of the magnetic field, both before and after the shock front, which isotropize the injected relativistic charged particles;
- the propagation of the particles is diffusive in both media, there are no inelastic collisions;
- the shock is nonrelativistic $u_{\rm sh} \ll 1$ while the injected particles are relativistic.

Energy gain after a cycle U → D → U[a]

$$\begin{aligned} E'_{\rm in} &= \Gamma\left(E_{\rm in} - \beta p_{\rm in}\cos\theta_{\rm in}\right) \\ &= \Gamma E_{\rm in}\left(1 - \beta v_{\rm in}\mu_{\rm in}\right), \\ E_{\rm out} &= \Gamma\left(E'_{\rm out} + \beta p'_{\rm out}\cos\theta_{\rm out}\right) \\ &= \Gamma E'_{\rm out}\left(1 + \beta v'_{\rm out}\mu'_{\rm out}\right), \end{aligned}$$

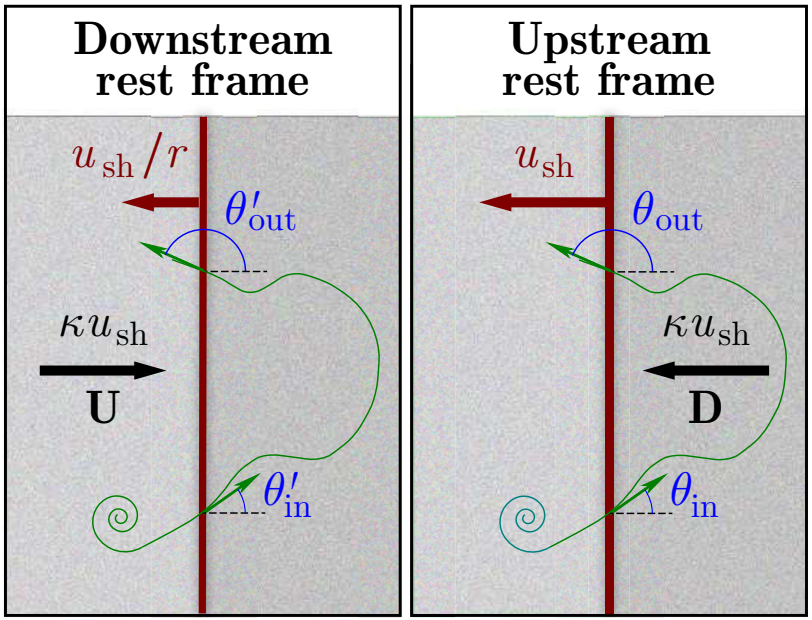

where $\Gamma = 1/\sqrt{1-\beta^2}$, $\beta = \kappa u_{\rm sh}$, $\kappa = (r-1)/r$.
Since the collisions are assumed to be elastic

$$E'_{\rm out} = E'_{\rm in}.$$

Therefore

$$E_{\rm out} = \Gamma^2 E_{\rm in}\left(1 - \beta v_{\rm in}\mu_{\rm in}\right)\left(1 + \beta v'_{\rm out}\mu'_{\rm out}\right),$$

$$\Downarrow$$

$$\begin{aligned} E_{\rm out} - E_{\rm in} &= \Gamma^2 E_{\rm in}\left[\beta\left(v'_{\rm out}\mu'_{\rm out} - v_{\rm in}\mu_{\rm in}\right) + \beta^2\left(1 - v_{\rm in}v'_{\rm out}\mu_{\rm in}\mu'_{\rm out}\right)\right] \\ &\simeq \frac{\beta}{1-\beta^2} E_{\rm in}\left[\mu'_{\rm out} - \mu_{\rm in} + \beta\left(1 - \mu_{\rm in}\mu'_{\rm out}\right)\right]. \end{aligned}$$

In obtaining the last equality, we assumed that $v_{\rm in} \simeq v'_{\rm out} \simeq 1$. Moreover, it is implicitly assumed that the motion of the shock front is nonrelativistic, or at least not ultrarelativistic, if only so that the particle moving downstream could cross the front.

[a] Below we use unprimed quantities for the upstream frame and primed quantities for the downstream frame.

A crucial step: The number of particles passing the shock front at an angle between θ and $\theta + d\theta$, through a unit surface per unit time is proportional to $\cos\theta d\Omega \propto \mu d\mu$. Therefore

$$\langle \mu_{\rm in} \rangle = \frac{\int_0^1 \mu^2 d\mu}{\int_0^1 \mu d\mu} = \frac{1/3}{1/2} = \frac{2}{3}, \quad \langle \mu'_{\rm out} \rangle = \frac{\int_{-1}^0 \mu^2 d\mu}{\int_{-1}^0 \mu d\mu} = \frac{1/3}{-1/2} = -\frac{2}{3},$$

$$\Downarrow$$

$$\left\langle \frac{\Delta E}{E} \right\rangle \simeq \frac{4\beta}{3(1-\beta^2)} \left(1 + \frac{13}{12}\beta\right) \simeq \underset{\text{assuming } \beta \ll 1}{\frac{4}{3}\beta} = \frac{4}{3}\left(\frac{r-1}{r}\right) u_{\rm sh}.$$

For a particle crossing the other way, D $\rightarrow$ U $\rightarrow$ D, the result remains the same (**check it out, please**).

$$\Downarrow$$

- The mean energy gain is always positive.
- The mean energy gain is first order in $u_{\rm sh}$ and is basically independent of any detail on how particles scatter back and forth.

• However, the calculations implicitly assumed that the scattering in the upstream (downstream) region drives the angular distribution to be isotropic in the upstream (downstream) frame.

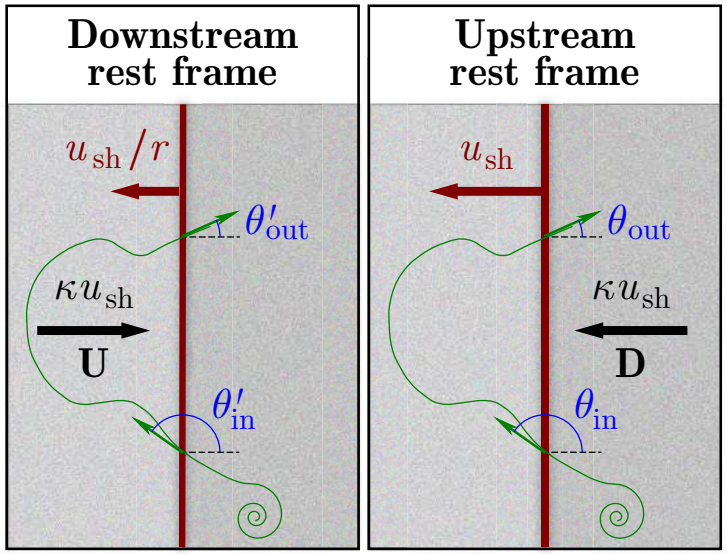

Spectrum of accelerated particles

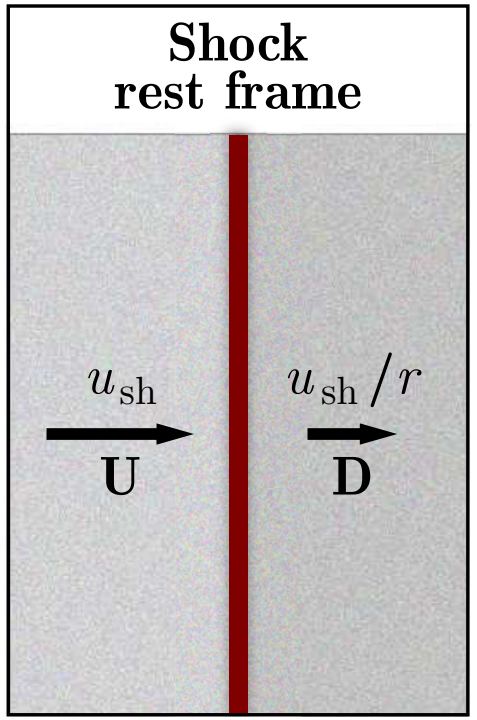

Let n_0 ($\approx$ const) be the accelerated particle density (here we use the shock rest frame). Due to the global advection of the downstream fluid away from the shock front with a velocity $v_2 = u_{\rm sh}/r$, the flux of accelerated particles passing through a unit surface very far away from the shock is $n_0 v_2 = n_0 u_{\rm sh}/r$. On the other hand the flux of particles crossing the shock from upstream to downstream is given by

$$\frac{n_0}{4\pi}\int_{0\le\mu\le 1} v\mu d\Omega = \frac{2\pi n_0 v}{4\pi}\int_0^1 \mu d\mu = \frac{n_0 v}{4} \simeq \frac{n_0}{4}.$$

The escape probability (invariant!) is then the ratio of these two fluxes:

$$\mathcal{P}_{\rm esc} = \frac{n_0 u_{\rm sh}/r}{n_0/4} = \frac{4}{r}u_{\rm sh}.$$

Let's go to the upstream frame. After one cycle, the mean energy of particles injected to upstream with the energy E_0 is $E_1 = (1+\varkappa)E_0$, where $\varkappa = 4\kappa u_{\rm sh}/3$. The mean energy after n cycles is

$$E_n = (1+\varkappa)^n E_0 \quad\Longrightarrow\quad n = \frac{\ln(E_n/E_0)}{\ln(1+\varkappa)}.$$

On the other hand, if the number of initially injected particles was N_0, then after n cycles

$$N_n = (1-\mathcal{P}_{\rm esc})^n N_0 \equiv N(>E_n)$$

particles remain. The latter identity simply means that particles with energy $> E_n$ will either break out of the cycle or continue for several more cycles, i.e., the energy cannot be $< E_n$.

Now omitting the subscript n, we obtain

$$N(>E) = N_0 \left(\frac{E_0}{E}\right)^{\gamma}, \quad \text{where} \quad \gamma = -\frac{\ln(1-\mathcal{P}_{\text{esc}})}{\ln(1+\varkappa)}.$$

Taking into account that $\mathcal{P}_{\text{esc}} \ll 1$ and $\varkappa \ll 1$ (assuming that $u_{\text{sh}} \ll 1$) we have

$$\gamma \simeq \frac{3}{r-1}, \quad \gamma+1 \simeq \frac{r+2}{r-1}.$$

The differential energy spectrum $N(E) = -dN(>E)/dE$ has the form

$$\boxed{N(E) = \frac{\gamma N_0}{E_0}\left(\frac{E_0}{E}\right)^{\gamma+1}}.$$

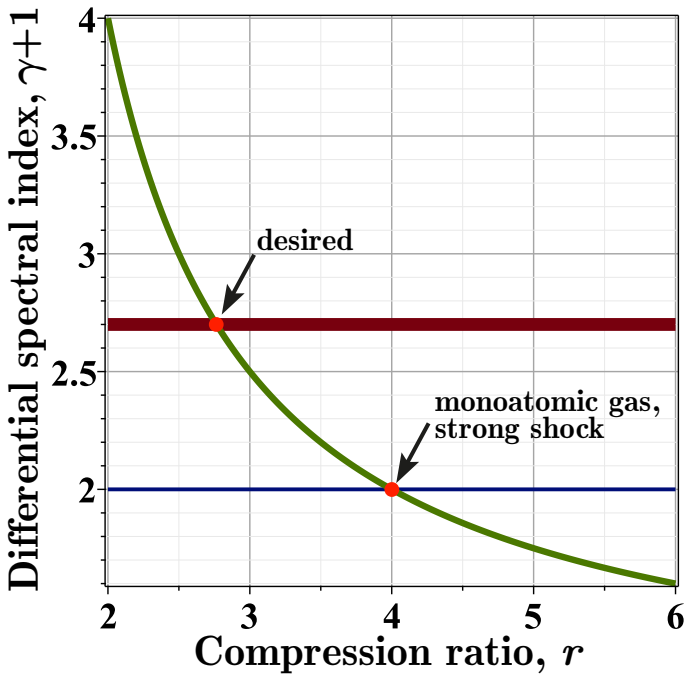

So the diffuse shock acceleration (DSA) can be considered one of the fundamental processes that can account for cosmic ray acceleration. However there are some observational evidences that question the validity of the DSA mechanism, at least in its simplest form... which is generally not surprising.[a]

[a] For a comprehensive recent review, see S. Perri, A. Bykov, H. Fahr, H. Fichtner, & J. Giacalone, "Recent developments in particle acceleration at shocks: theory and observations," Space Sci. Rev. **218** (2022) 26.

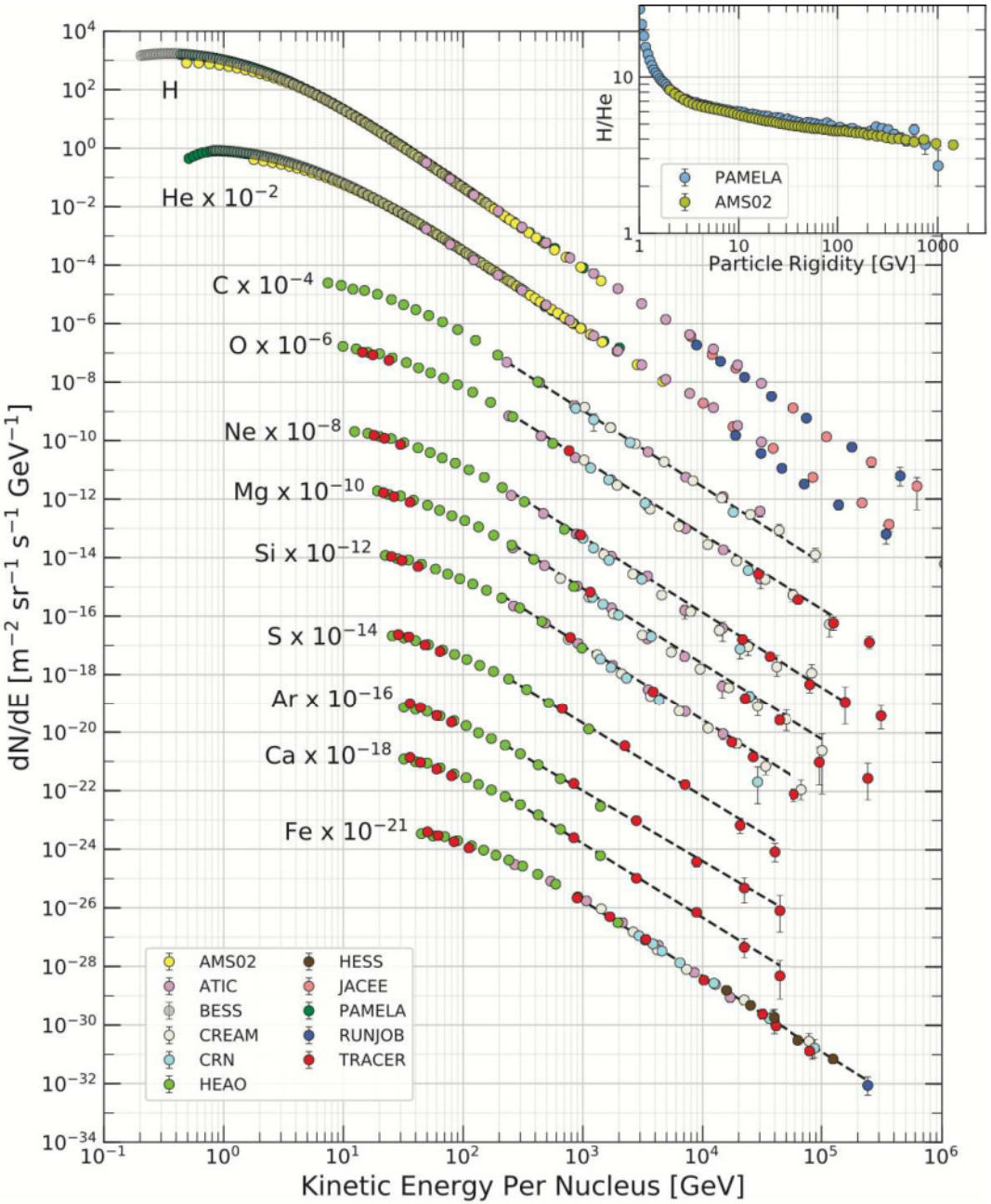

◁ Fluxes of nuclei of the primary cosmic radiation in particles per energy per nucleus are plotted vs. kinetic energy per nucleus using data from many modern direct measurements performed with particle detectors on satellites or balloons. The inset shows the H/He ratio as a function of magnetic rigidity.

The intensity of primary nucleons in the energy range from several GeV to somewhat beyond 100 TeV is given approximately by

$$1.8 \times 10^4 \left(\frac{E}{1\,\text{GeV}}\right)^{-2.7} \frac{\text{nucleon}}{\text{m}^2\,\text{s}\,\text{sr}\,\text{GeV}},$$

where E is the total energy-per-nucleon.

[From R. L. Workman *et al.* (Particle Data Group), "Review of particle physics," PTEP **2022** (2022) 083C01.]

An (incomplete) list of particle acceleration mechanisms[a]

- Diffusive shock acceleration (+ non-linear modification)
- Stochastic Fermi acceleration
- Turbulent acceleration
- Magneto-hydrodynamic turbulence
- Magnetic reconnection
- Alfvenic acceleration (magnetic pumping)
- Shear acceleration
- Shock surfing acceleration
- Shock drift acceleration
- Direct acceleration by electric fields
- Acceleration in magnetospheric eternally collapsing objects

[a] Not yet done...

7.3 Hillas Condition.

◦ In order to estimate the maximum energy to which a particle can be accelerated in a certain astrophysical environment a simple model can be employed. A particle with energy E and charge Ze in a homogeneous magnetic field B (strictly the component of $\mathbf{B}$ normal to the particle's velocity) moves with a gyroradius $r_g = E/BZe$. $\Longrightarrow$ The particle can be accelerated to a maximum energy

$$\boxed{E_{\max} \sim ZeBL}$$

in a region of size L before its gyroradius becomes too big to be confined in the magnetic field.[a] This estimation is called the Hillas condition (criterion). Using typical values and estimates for the magnetic field and the size of the acceleration region, the so-called Hillas plot is obtained.

◦ Hillas plots in the next two slides, show different astrophysical environments – candidates for the cosmic accelerators, their typical or expected sizes (x-axis) and magnetic fields (y-axis).

Note: The data borrowed from several sources may vary within orders of magnitude!

The astrophysical media with larger sizes or stronger fields than those indicated by the straight lines provide necessary (but by no means sufficient) conditions for achieving a given acceleration.

◦ If one includes a specific mechanism of acceleration (e.g., shock waves or multiple magnetic scattering centers), the maximum energy is given by [numbers in the formula are typical for SNR]

$$E_{\max} \sim \frac{uZeBL}{\eta} \approx Z \left(\frac{10}{\eta}\right) \left(\frac{u}{0.01}\right) \left(\frac{B}{3\,\mu\text{G}}\right) \left(\frac{L}{10\,\text{ps}}\right) \text{TeV},$$

where $\eta \geq 1$ parametrizes the efficiency of acceleration with $\eta = 1$ the maximum achievable efficiency (= Bohm limit) and u is the shock velocity or characteristic velocity of the scattering centers.

[a] More accurately, $L = L_c\Gamma$, where L_c is the **comoving** size of the accelerator and Γ is the Lorentz factor of its bulk motion ($\Gamma \sim 10 - 50$ in AGN jets and $\Gamma \sim 10 - 1000$ in GRBs).

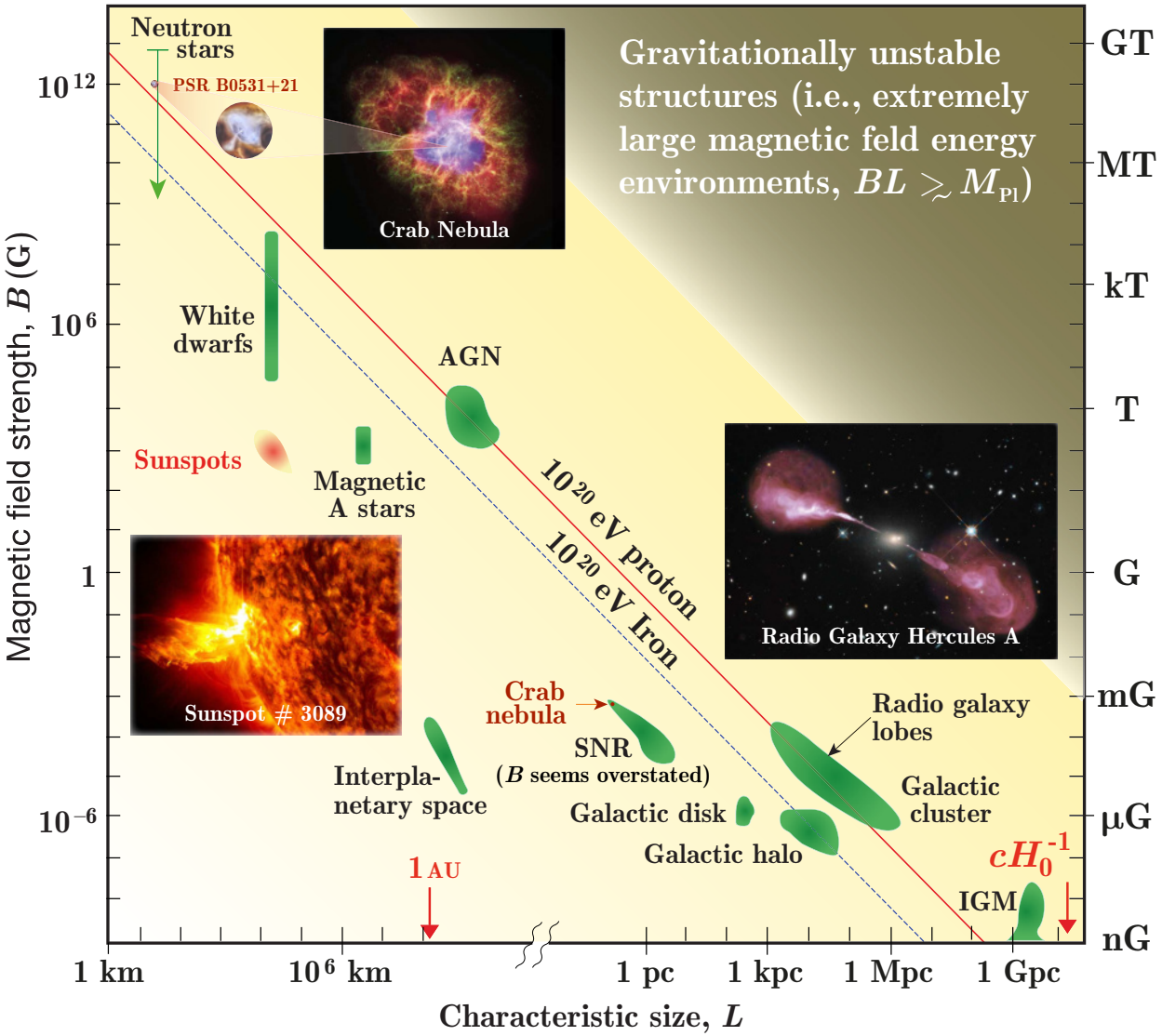

The Hillas diagram

[Figure is adapted from P. M. Bauleo, & J. Rodríguez Martino, "The dawn of the particle astronomy era in ultra-high-energy cosmic rays," Nature **458**, No. 7240 (2009) 847–851. A few issues added.]

Important: the diagram shows only the potential of the (non-exotic) sources.

An illustrative example: the maximum recorded energy of protons from large solar flares was only about 20 GeV. The prompt proton pulse has the exponential spectrum $F_p \propto \exp(E_{\rm kin}/E_0)$ (the values of E_0 do not differ much for different proton events). On the Earth's orbit the spectrum becomes of a power type $F_p \propto (E_1/E_{\rm kin})^\gamma$ with $\gamma = 4-6$ for $E_{\rm kin} = 0.5-1.0$ GeV. The theoretical maximum energy of solar-flare protons is about 40 GeV.

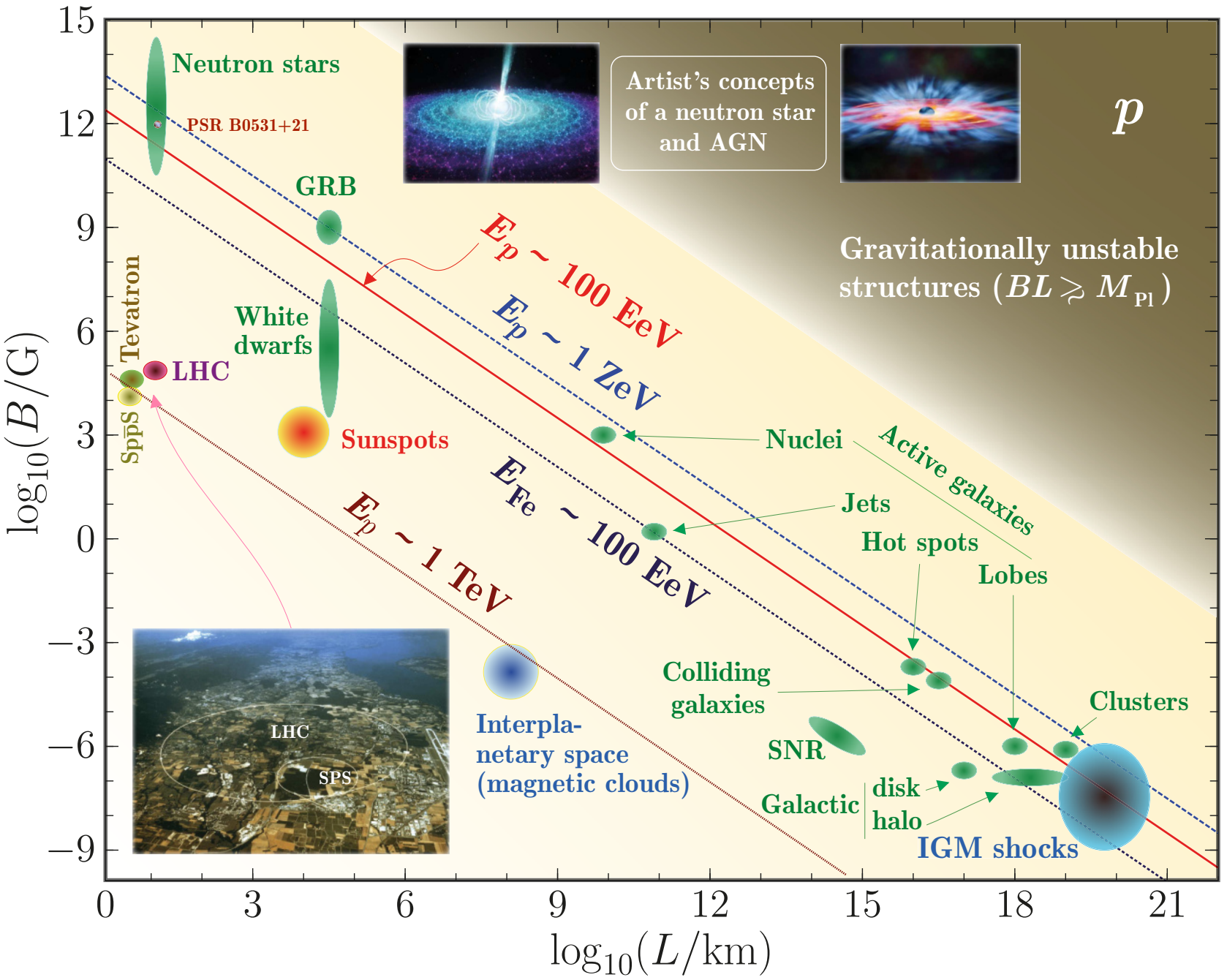
Neutron stars
PSR B0531+21
GRB
White dwarfs
Tevatron
LHC
SppS
Sunspots
Artist's concepts of a neutron star and AGN
p
Gravitationally unstable structures ($BL \gtrsim M_{\rm Pl}$)
$E_p \sim 100$ EeV
$E_p \sim 1$ ZeV
$E_{\rm Fe} \sim 100$ EeV
$E_p \sim 1$ TeV
Nuclei
Active galaxies
Jets
Hot spots
Lobes
Colliding galaxies
Clusters
SNR
Interplanetary space (magnetic clouds)
Galactic
disk
halo
IGM shocks
LHC
SPS
$\log_{10}(B/{\rm G})$
$\log_{10}(L/{\rm km})$
15
12
9
6
3
0
−3
−6
−9
0
3
6
9
12
15
18
21

7.4 Candidate neutrino sources.

Point neutrino sources

- ⋆ **Young supernova remnants**
  [due to CR acceleration by shock waves from SN explosions]
- ⋆ **Accreting neutron stars and black holes**
- ⋆ **Coalescing binary (multiple) systems**
  [pulsar + giant, pulsar + star filling its Roche lobe, white dwarf + (super)giant, etc.]
- ⋆ **The Galactic center**
  [accreting supermassive black hole (SMBH) or tidal disruption of stars by (jetting) SMBHs]
- ⋆ **Gamma-Ray Bursts (GRBs)**
  [example: γs and νs arise from decay of pions produced in shock front collisions]
- ⋆ **Hidden or latent sources**
  [young SN shell, cocooned (super)massive black hole (MBH/SMBH) in AGN, Thorne–Żytkow star (binary with a neutron star or black hole submerged into a red supergiant core), AGN with standing shock in the vicinity of a MBH/SMBH]
- ⋆ **Active Galactic Nuclei (AGNs) & SBGs**
  [Blazars (radio-loud AGNs – quasars and Lacertae or BL Lac objects), Seyfert, radio, and N galaxies; extragalactic jets from AGNs; Starburst galaxies (SBGs)]

Diffuse neutrino backgrounds

- ⋆ **Galactic neutrinos**
  [including νs from CR interactions with the spherical halo of baryonic dark matter]
- ⋆ **Quasi-diffuse background from AGNs/SMBHs**
- ⋆ **Neutrinos from intergalactic space**
  [the most important are cosmogenic (GZK) UHE νs from the CR spectrum tail (GZK cutoff)]
- ⋆ **Pregalactic neutrinos, νs from the bright phase of galaxy evolution & starburst galaxies**
- ⋆ **Neutrinos from annihilation or decay of dark-matter particles**

Speculative sources of the highest-energy νs (SUSY, SUGRA, M-theory, . . ., Sci-Fi)

- ⋆ **Topological defects**
  [ultra-heavy particle emission and acceleration by saturated superconducting cosmic strings, cusp radiation from ordinary (open) cosmic strings, vortons, branes, global monopoles, etc.]
- ⋆ **Primordial (mini) black hole evaporation**
- ⋆ **Decay of super-heavy exotic particles**
  [long-lived Big Bang relics or Planckian mass ($M_P = \sqrt{\hbar c/G} \approx 1.221 \times 10^{19}$ GeV) objects (planckeons ∼ fridmons ∼ maximons ∼ cosmions)]
- ⋆ **Byproducts of quantum gravitational collapse**
  [black hole firewalls & fuzzballs, wormholes, etc.]

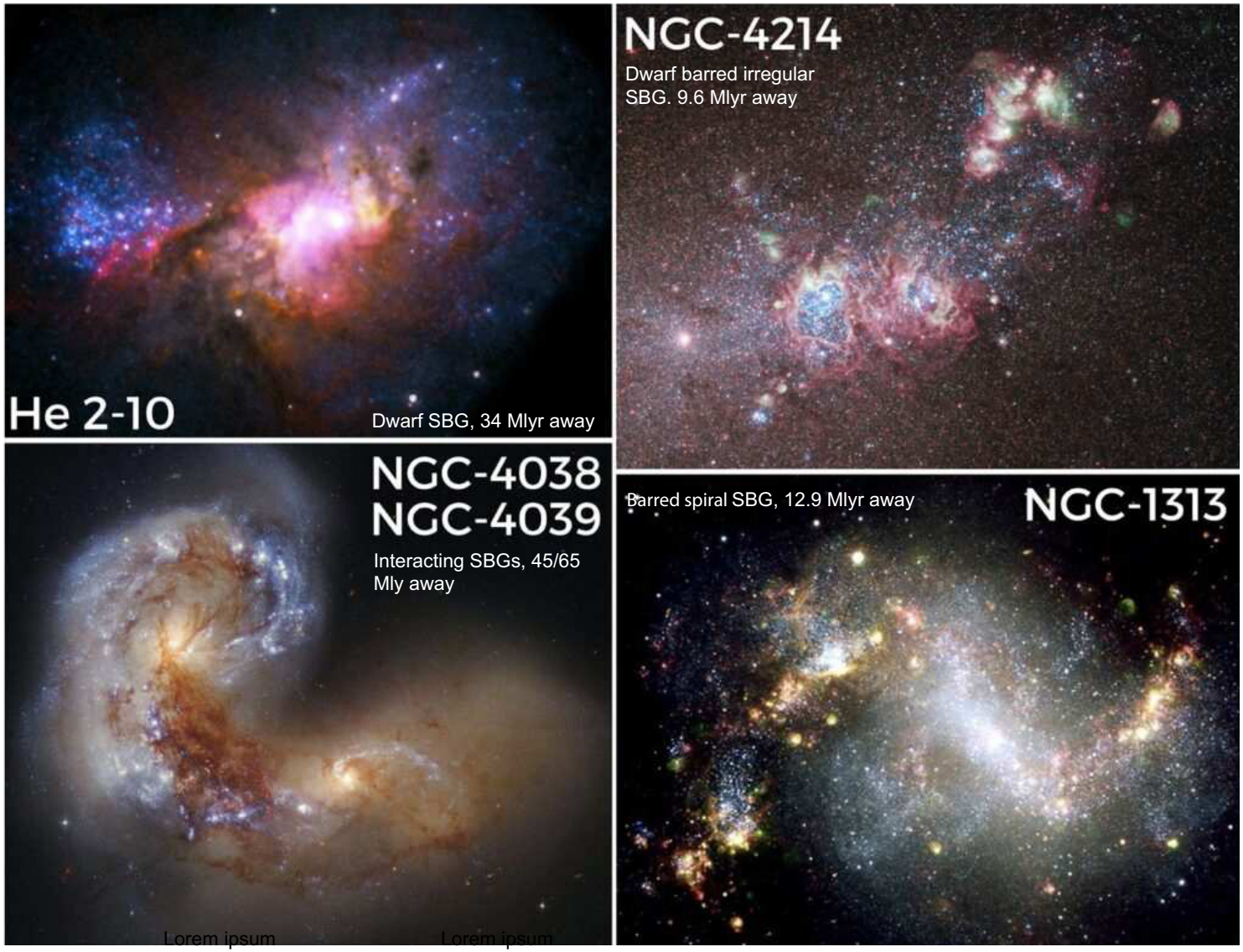

Starburst galaxies (now attracting increased interest thanks to recent hints from Auger, see [**CR**]). Note that all SBGs shown are well within the GZK sphere with a radius of 160–320 Mly.

[Images are taken from URL: ⟨ https://www.starburst.io/blog/starburst-galaxy-whats-in-a-name/ ⟩.]

7.4.1 Diffuse galactic neutrinos.

A view of the Milky Way galaxy in microwaves, captured by the European Space Agency's *Planck* satellite. ▷
The top view is a combination of the four bottom slides.
Each of the four slides shows a different element: top left is dust, top right is gas, bottom left is light created by free particles that zip past one another without quite colliding, bottom right is light created when charged particles get caught up in the Galaxy's magnetic field.

Credit: ESA/NASA/JPL-Caltech.
[From URL: ⟨ https://en.wikiversity.org/wiki/Radiation_astronomy/Microwaves ⟩.]

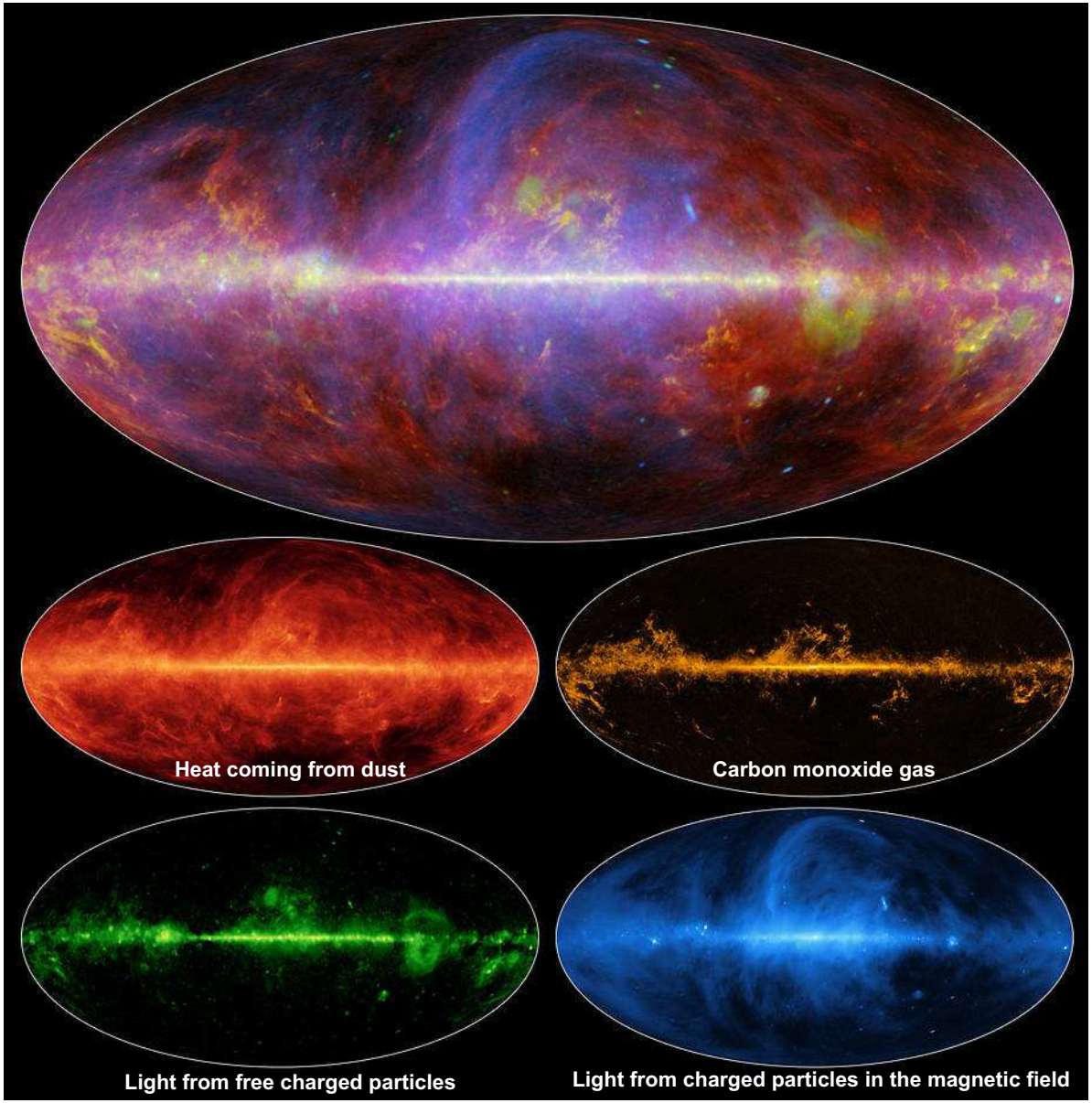

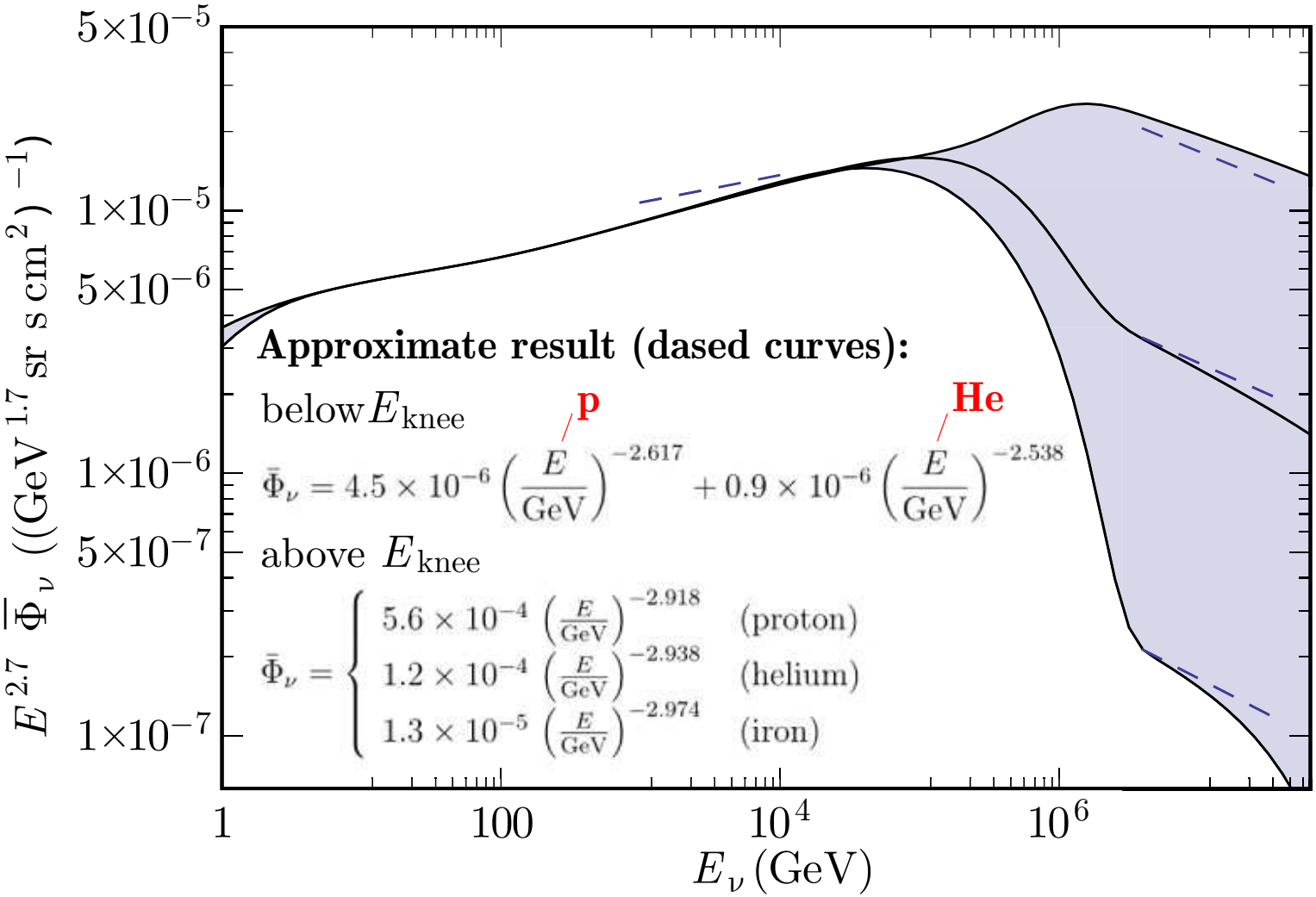

Predicted diffuse $\nu + \overline{\nu}$ flux from interactions of cosmic rays with interstellar matter in our Galaxy. Figure shows the average (over all directions) $\nu + \overline{\nu}$ flux reaching the Earth. The shaded region corresponds to three possible CR compositions (H, He or Fe) at $E_{\mathsf{CR}} > E_{\mathsf{knee}}$.

[Adapted from J. M. Carceller & M. Masip, "Diffuse flux of galactic neutrinos and gamma rays," JCAP03(2017)013, arXiv:1610.02552 [astro-ph.HE].]

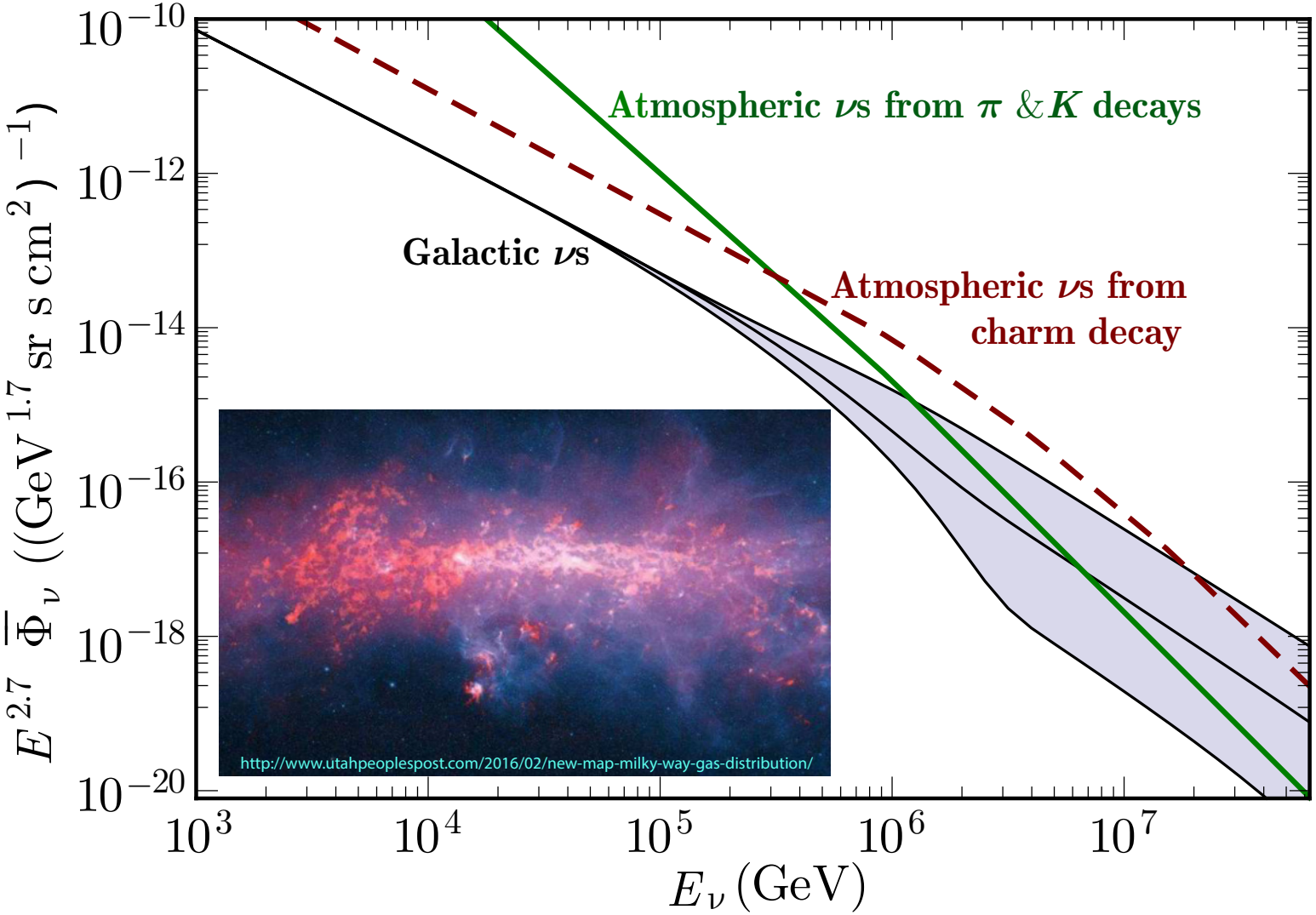

Comparison of the fluxes from previous slide with the conventional ("π, K") atmospheric neutrino fluxes (solid) and from forward charmed hadron decays (dashes). Insert shows a new map of very dense and very cold gas distributed across the Milky Way (by Apex telescope in the Atacama Desert).
[Adapted from J. M. Carceller & M. Masip, 2016; see Ref. in previous page.]

AGNs

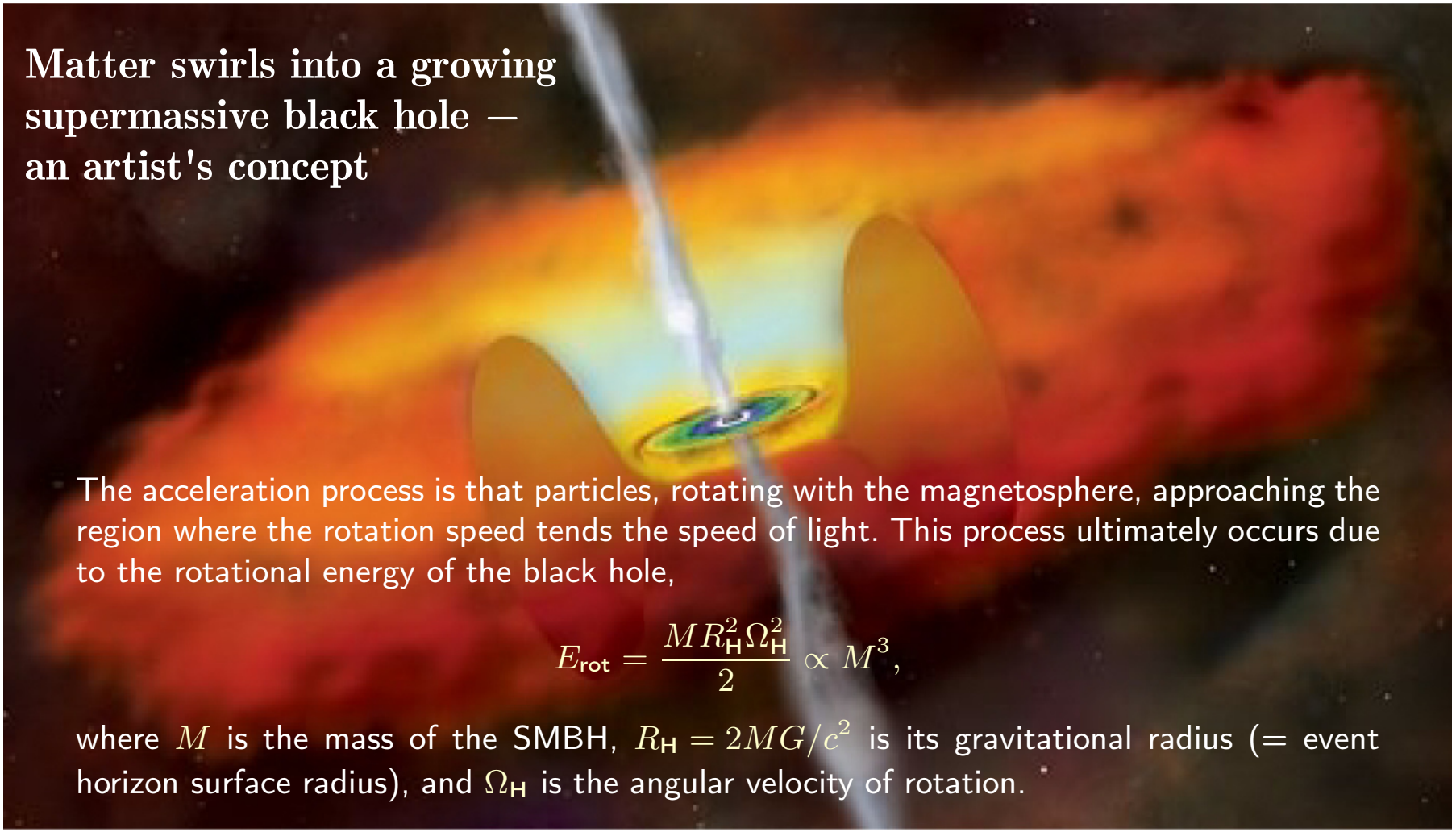

The acceleration process is that particles, rotating with the magnetosphere, approaching the region where the rotation speed tends the speed of light. This process ultimately occurs due to the rotational energy of the black hole,

$$E_{\mathsf{rot}} = \frac{M R_{\mathsf{H}}^2 \Omega_{\mathsf{H}}^2}{2} \propto M^3,$$

where M is the mass of the SMBH, $R_{\mathsf{H}} = 2MG/c^2$ is its gravitational radius (= event horizon surface radius), and Ω_{H} is the angular velocity of rotation.

[Figure is taken from URL: ⟨ http://science.nasa.gov/science-news/science-at-nasa/2007/27jul_piranha/ ⟩.]

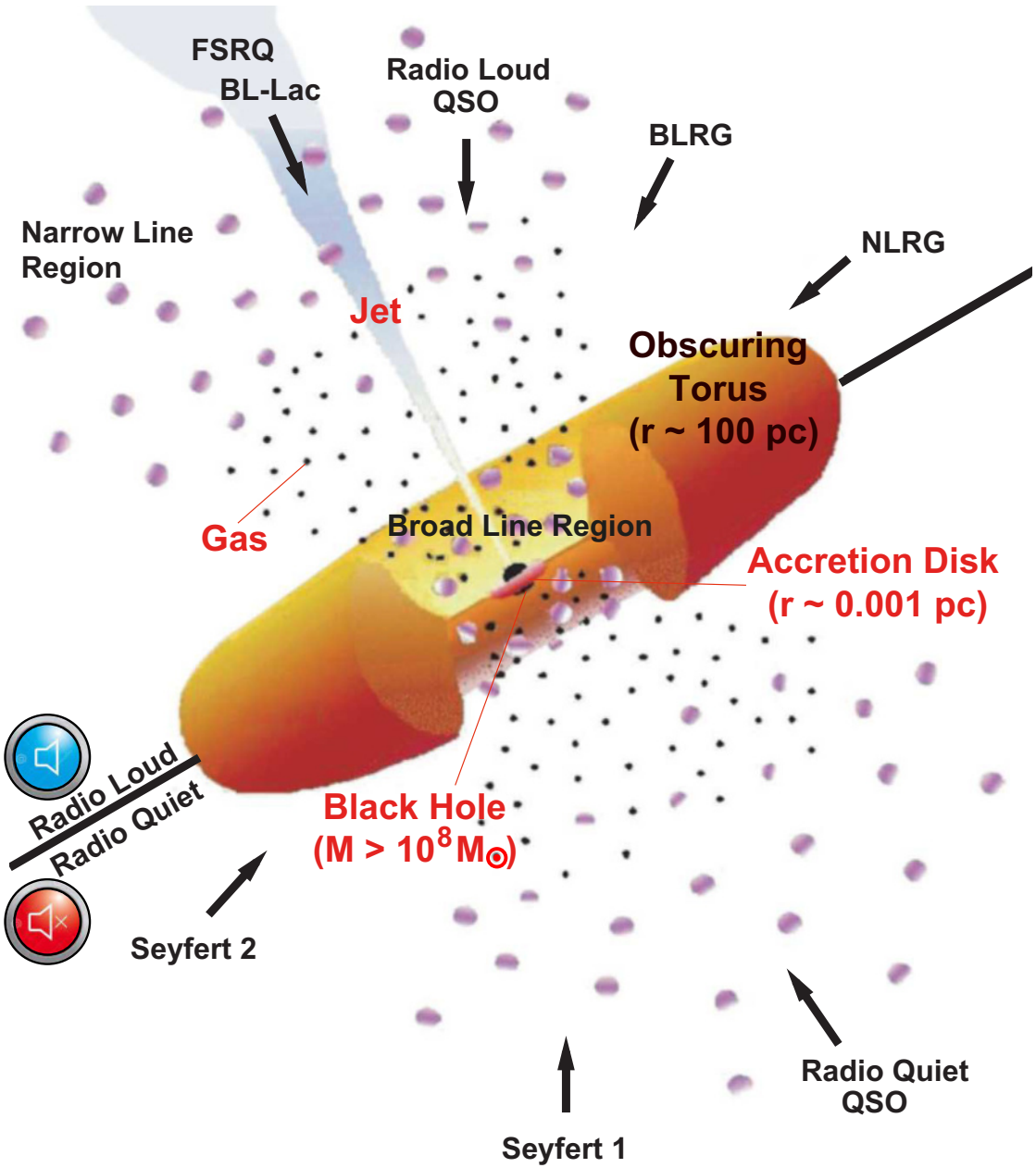

Unification model for AGN

Schematic view of the model. The upper half corresponds to a radio-loud AGN, the lower half to a radio-quiet AGN. A central black hole is surrounded by an accretion disk and a toroidal dust cloud. Perpendicular to it a relativistic jet can form. The different morphologies observed from these objects are caused by different viewing angles.

Glossary of Acronyms

BLRG: Broad-Line Radio Galaxies
FSRQ: Flat Spectrum Radio Quasars
QSO : Quasi-Stellar Object
NLRG: Narrow-Line Radio Galaxies
SSRQ: Steep Spectrum Radio Quasars

[C. M. Urry & P. Padovani, "Unified schemes for radio-loud active galactic nuclei," Publ. Astron. Soc. Pac. **107** (1995) 803–845, astro-ph/9506063.]

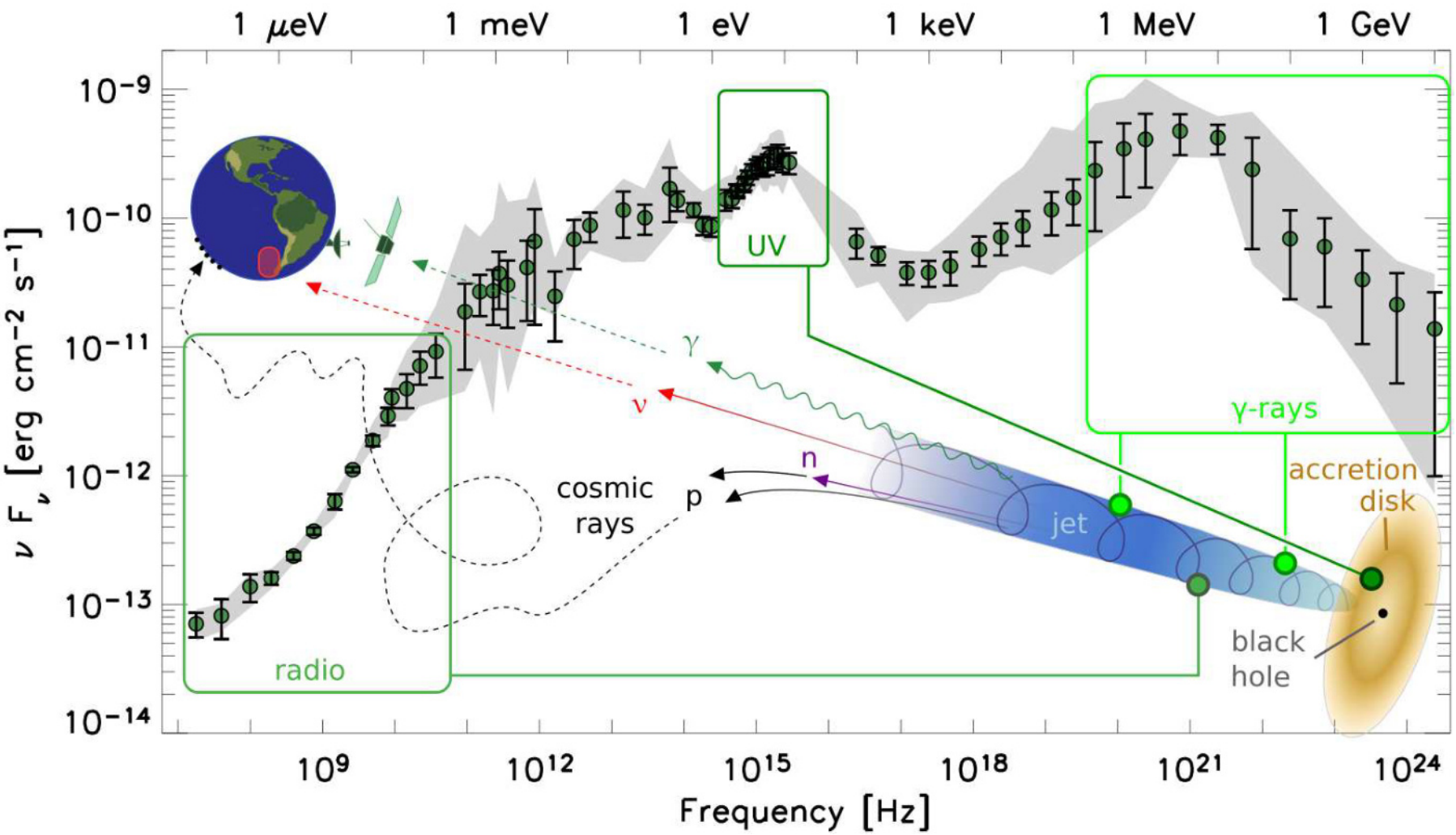

It is believed that AGN jets resulting from accretion onto the central supermassive black hole are the most powerful and long-lived particle accelerators in the Universe. Non-thermal processes operating in jets are responsible for multi-messenger emissions, such as broadband electromagnetic radiation and high-energy neutrinos. The observed broadband radiation usually follows a double humped structure. [From B. Rani, "Multi-physics of AGN jets in the multi-messenger era," arXiv:1903.04504v1 [astro-ph.HE].]

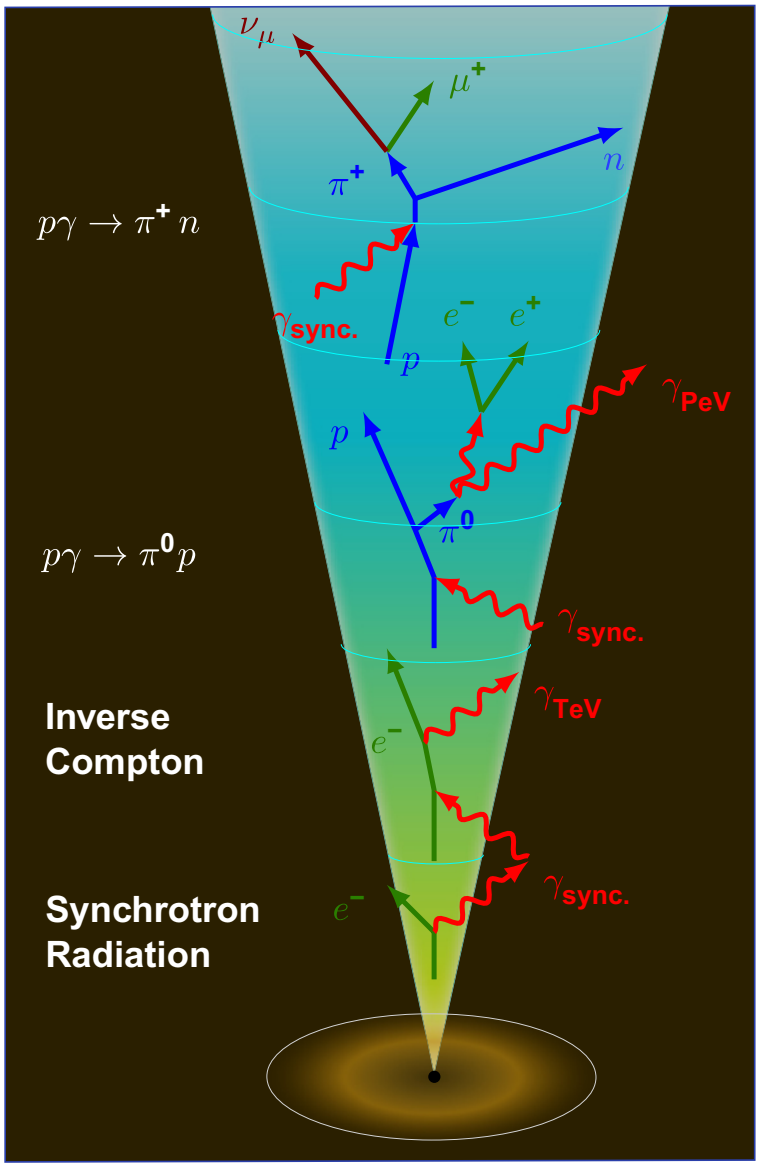

The protons from cosmic accelerators, like AGN, must also generate neutrinos, via charged pion production in collisions with the ambient matter and radiation fields. The kinematic threshold for the $p\gamma$ process is determined by the photon energies in the radiation field. For ambient γs in the UV region, as characteristic for AGNs, it is in the range of several PeV. If the γs have a broad spectrum, such as the power-law for γs generated by synchrotron radiation (SR), the threshold is "smeared" to lower energies.

◁ Figure sketches the major processes happening in a combined model where both electrons and hadrons are accelerated along the AGN jet. The SR from electrons serves as target for Inverse Compton (IC) scattering as well as for proton collisions. Electrons are cooled by synchrotron emission and may boost the SR to the $10 - 100$ TeV range but certainly not to PeV energies. So, the observation of PeV γs would be a clear proof of hadron acceleration. Unfortunately, the range of PeV photons does not exceed the size of the Galaxy, since they are absorbed by the process $\gamma_{\text{PeV}} + \gamma_{\text{CMB}} \to e^+ e^-$ (see [**CR**]).

[From U. F. Katz & Ch. Spiering, "High-energy neutrino astrophysics: Status and perspectives," Prog. Part. Nucl. Phys. **67** (2012) 651–704, 1111.0507 [astro-ph.HE].]

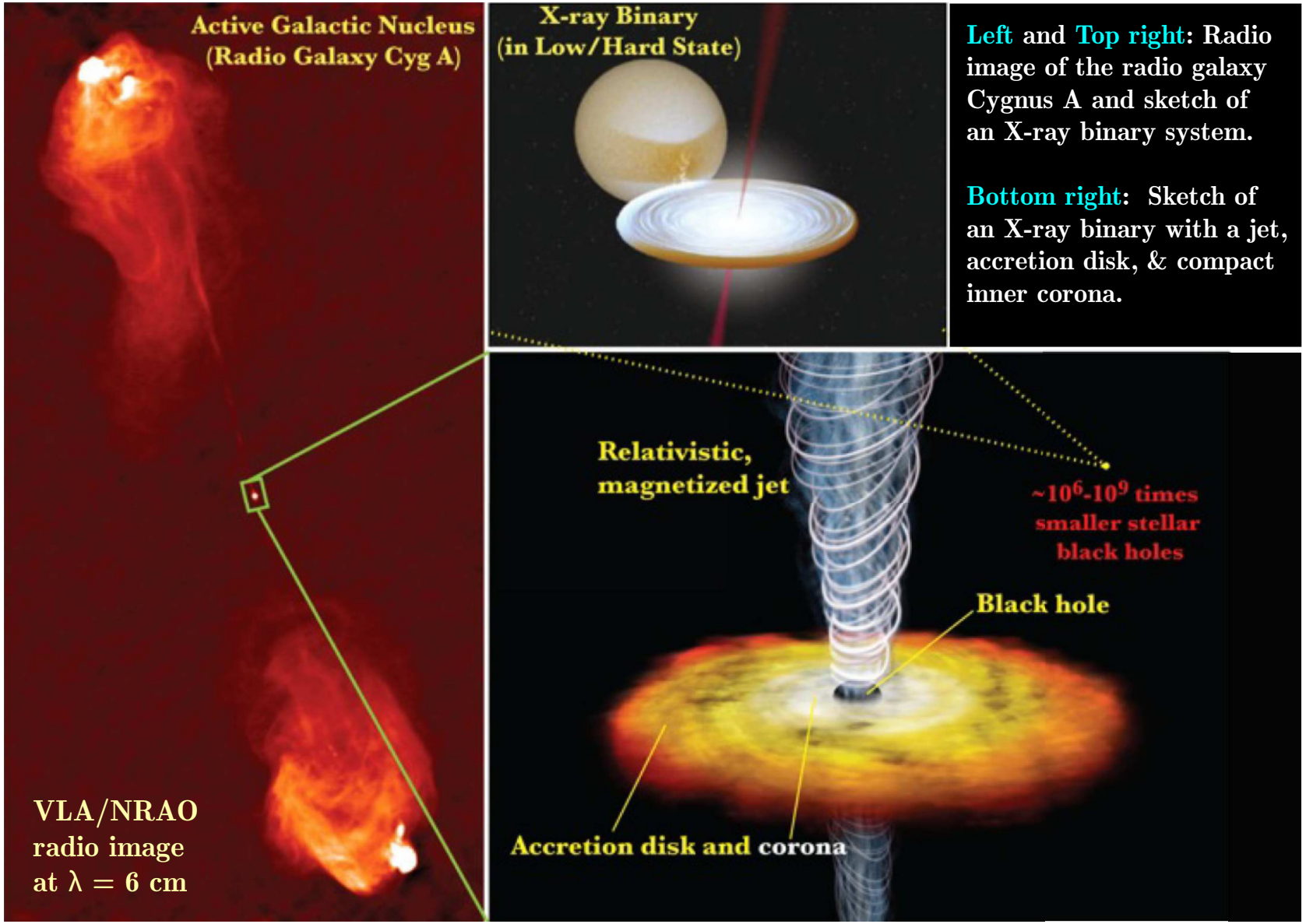

[From URL: ⟨ http://www.astro.uva.nl/research/compacts/accretion-and-jet-formation/ ⟩.]

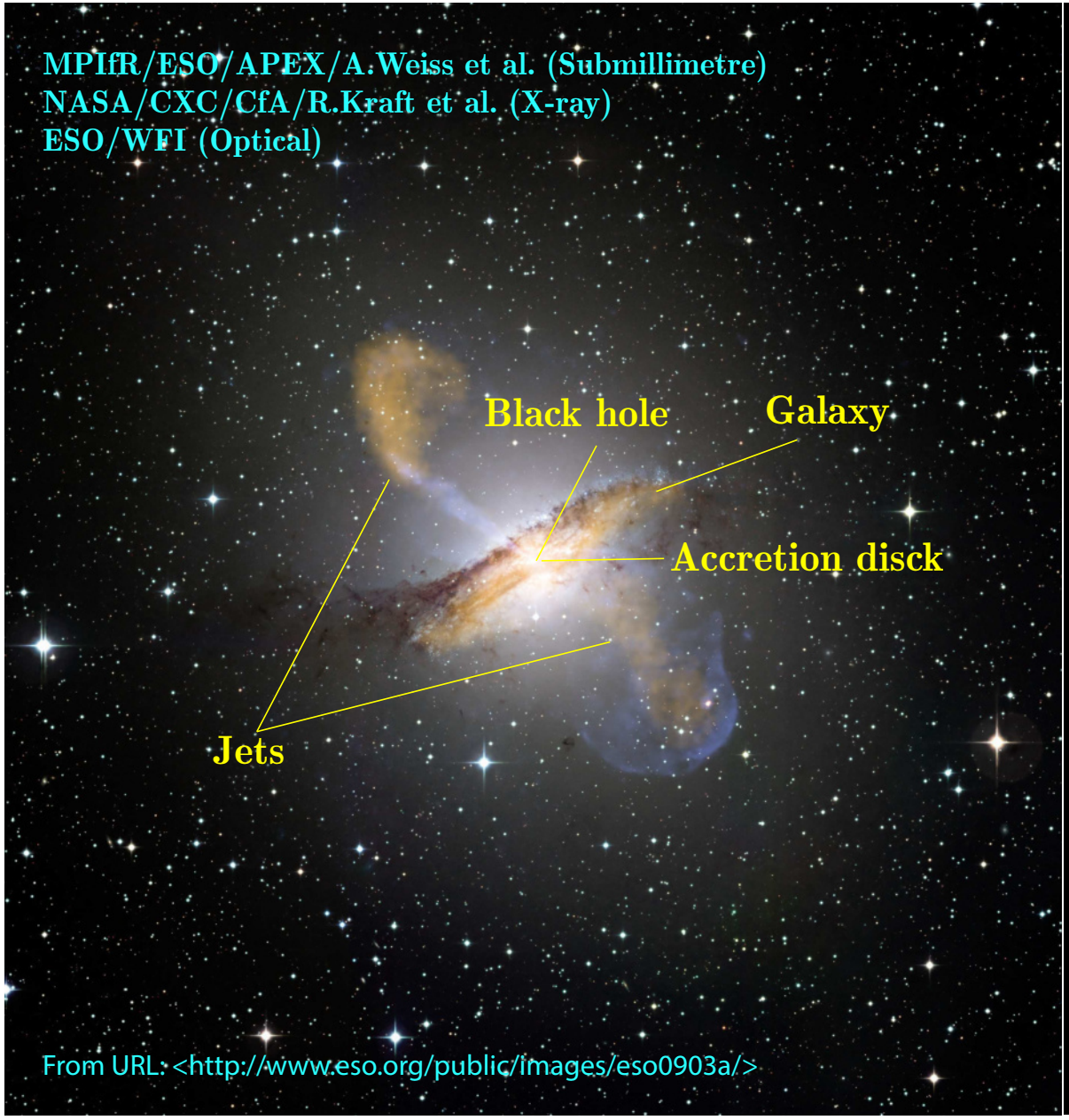

Colour composite image of Centaurus A, revealing the lobes and jets emanating from the AGN's central black hole.

This is a composite of images obtained with three instruments, operating at very different wavelengths.

The 870-micron submillimetre data, from LABOCA on APEX, are shown in orange.

X-ray data from the Chandra X-ray Observatory are shown in blue.

Visible light data from the Wide Field Imager (WFI) on the MPG/ESO 2.2 m telescope located at La Silla, Chile, show the background stars and the galaxy's characteristic dust lane in close to "true colour".

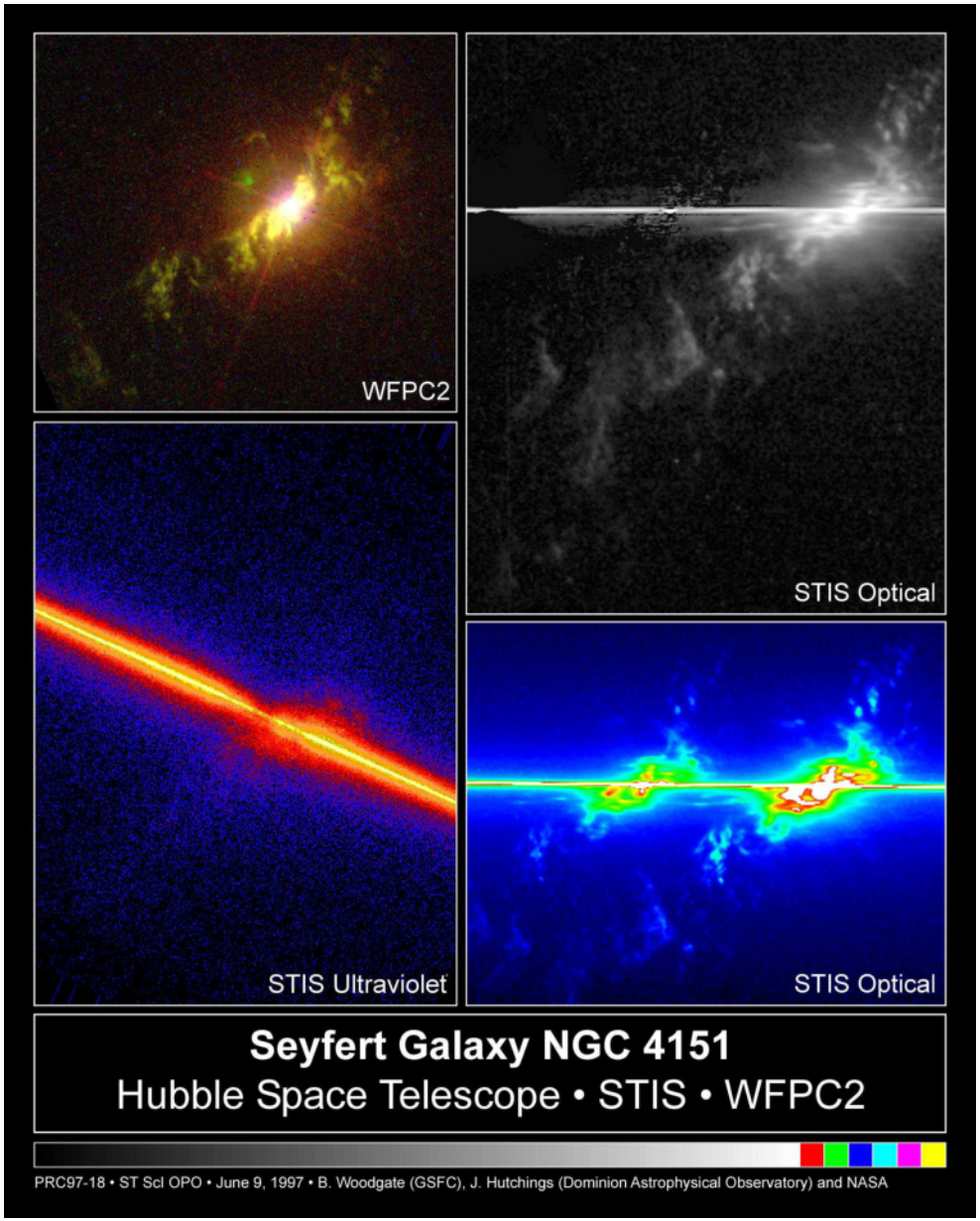

◁ The Space Telescope Imaging Spectrograph (STIS) simultaneously records, in unprecedented detail, the velocities of hundreds of gas knots streaming at a few $\times 10^5$ km/h from the nucleus of NGC 4151, thought to house a supermassive black hole (SMBH). This is the first time the velocity structure in the heart of this object, or similar objects, has been mapped so vividly this close to its central BH.

The twin cones of gas emission are powered by the energy released from the SMBH believed to reside at the heart of this Seyfert galaxy.

The STIS data clearly show that the gas knots illuminated by one of these cones is rapidly moving towards us, while the gas knots illuminated by the other cone are rapidly receding.

See details and references in the next slide.

The figures in the previous slide show:

WFPC2 (*upper left*) – A Hubble Wide Field Planetary Camera 2 image of the oxygen emission (5007 Å) from the gas at the heart of NGC 4151. Though the twin cone structure can be seen, the image does not provide any information about the motion of the oxygen gas.

STIS OPTICAL (*upper right*) – In this STIS spectral image of the oxygen gas, the velocities of the knots are determined by comparing the knots of gas in the stationary WFPC2 image to the horizontal location of the knots in the STIS image.

STIS OPTICAL (*lower right*) – In this false color image the two emission lines of oxygen gas (the weaker one at 4959 Å and the stronger one at 5007 Å) are clearly visible. The horizontal line passing through the image is from the light generated by the powerful BH at the center of NGC 4151.

STIS ULTRAVIOLET (*lower left*) – This STIS spectral image shows the velocity distribution of the carbon emission from the gas in the core of NGC 4151. It requires more energy to make the carbon gas glow (CIV at 1549Å) than it does to ionize the oxygen gas seen in the other images. This means we expect that the carbon emitting gas is closer to the heart of the energy source.

The images have been rotated to show the same orientation of NGC 4151.

Credit: John Hutchings (Dominion Astrophysical Observatory), Bruce Woodgate (GSFC/NASA), Mary Beth Kaiser (Johns Hopkins University), Steven Kraemer (Catholic University of America), and the STIS Team.

[From ⟨https://commons.wikimedia.org/wiki/File:Seyfert_galaxy_NGC4151_(GL-2002-001035).jpg⟩; for detail, see NASA Technical Reports Server, URL: ⟨http://nix.larc.nasa.gov/search.jsp?R=GL-2002-001035⟩.]

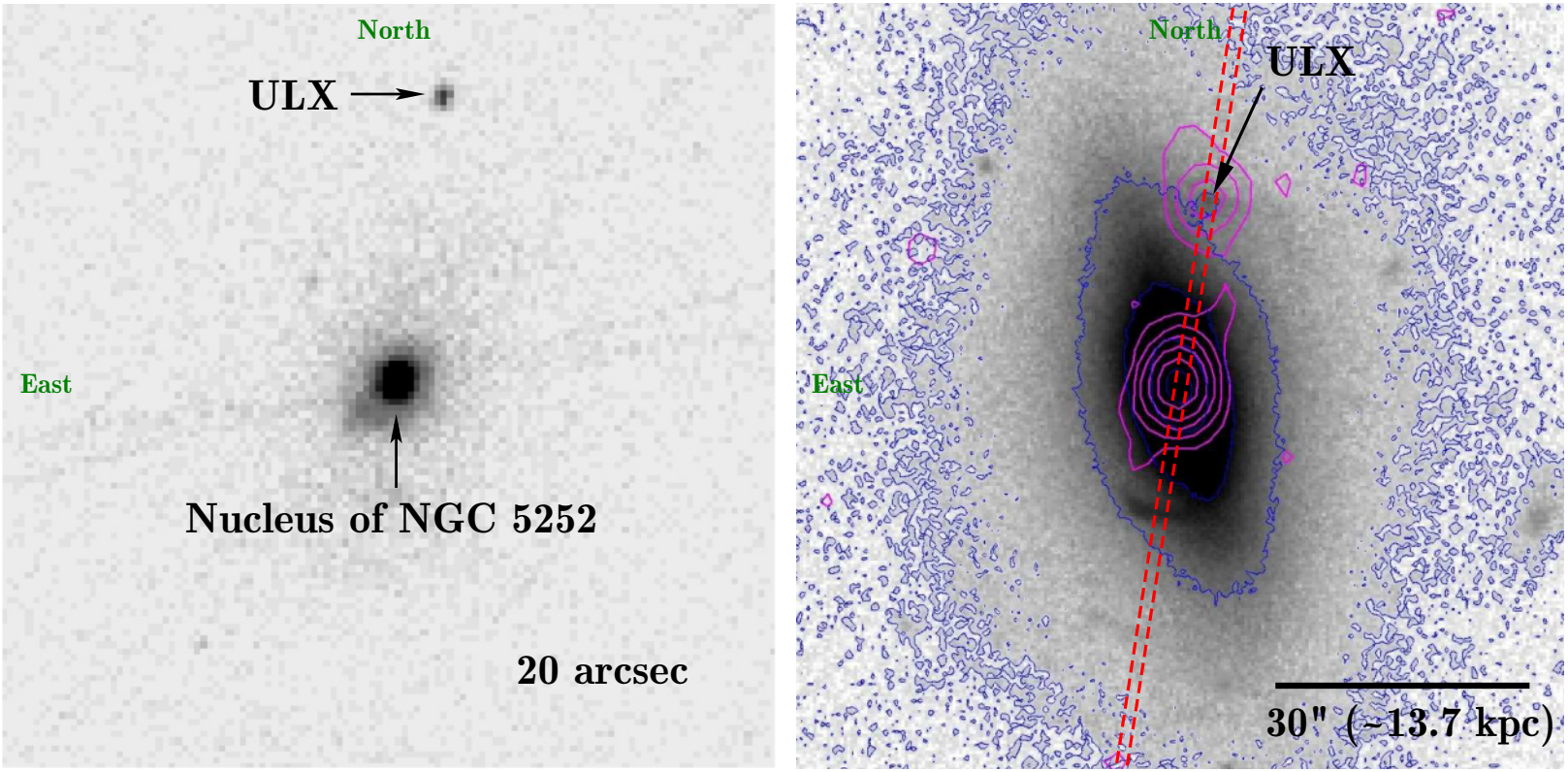

Left panel: Chandra ACIS-S image of the NGC 5252 in the 0.3–8 keV band, centered on the X-ray bright NGC 5252 active nucleus. The Ultraluminous X-ray source (ULX) is located to the north. *Right panel*: An image of NGC 5252 from Sloan Digital Sky Survey. Blue contours represent the surface brightness. Magenta contours represent radio continuum at 20 cm from the FIRST survey. The ULX appears to have optical and radio counterparts. The long-slit position is denoted by the red dashed lines. A likely explanation is an accreting black hole with a mass $M_{\rm BH} \gtrsim 10^4 \times M_\odot$, which might be a stripped remnant of a merging dwarf galaxy.

[Taken from M. Kim *et al.*, "An off-nucleus nonstellar black hole in the Seyfert galaxy NGC 5252," ApJ **814** (2015) 8, arXiv:1510.08854 [astro-ph.GA].]

7.4.2 GRBs.

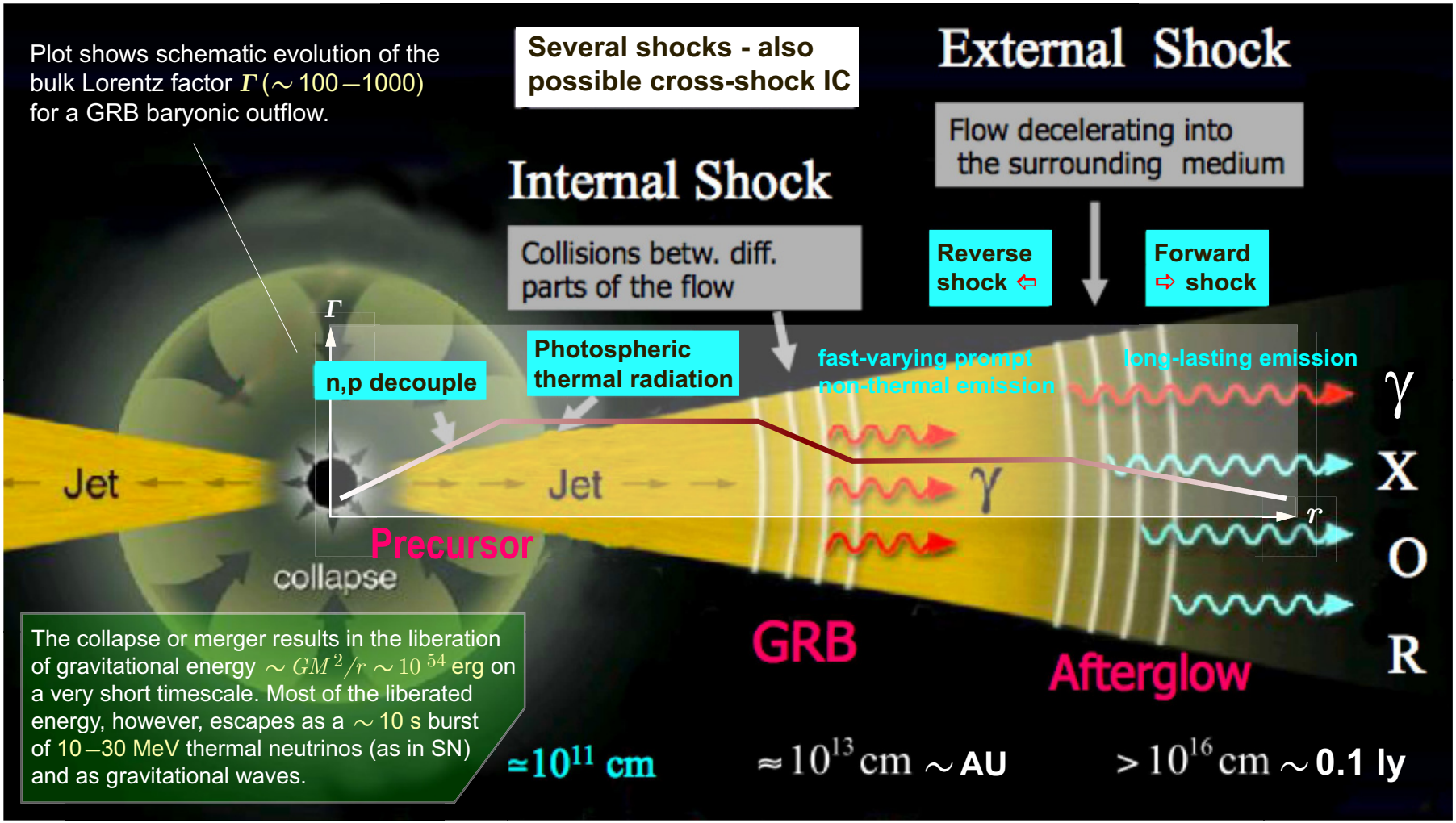

A scheme of the GRB emission zones (either or both ν & γ): subphotospheric (innermost), photospheric, internal and external shocks. The GRB jet may produce multi-GeV to PeV νs.
[From P. Meszaros, "Gamma ray bursts as neutrino sources," JCAP03(2017)013, arXiv:1511.01396v4 [astro-ph.HE].]

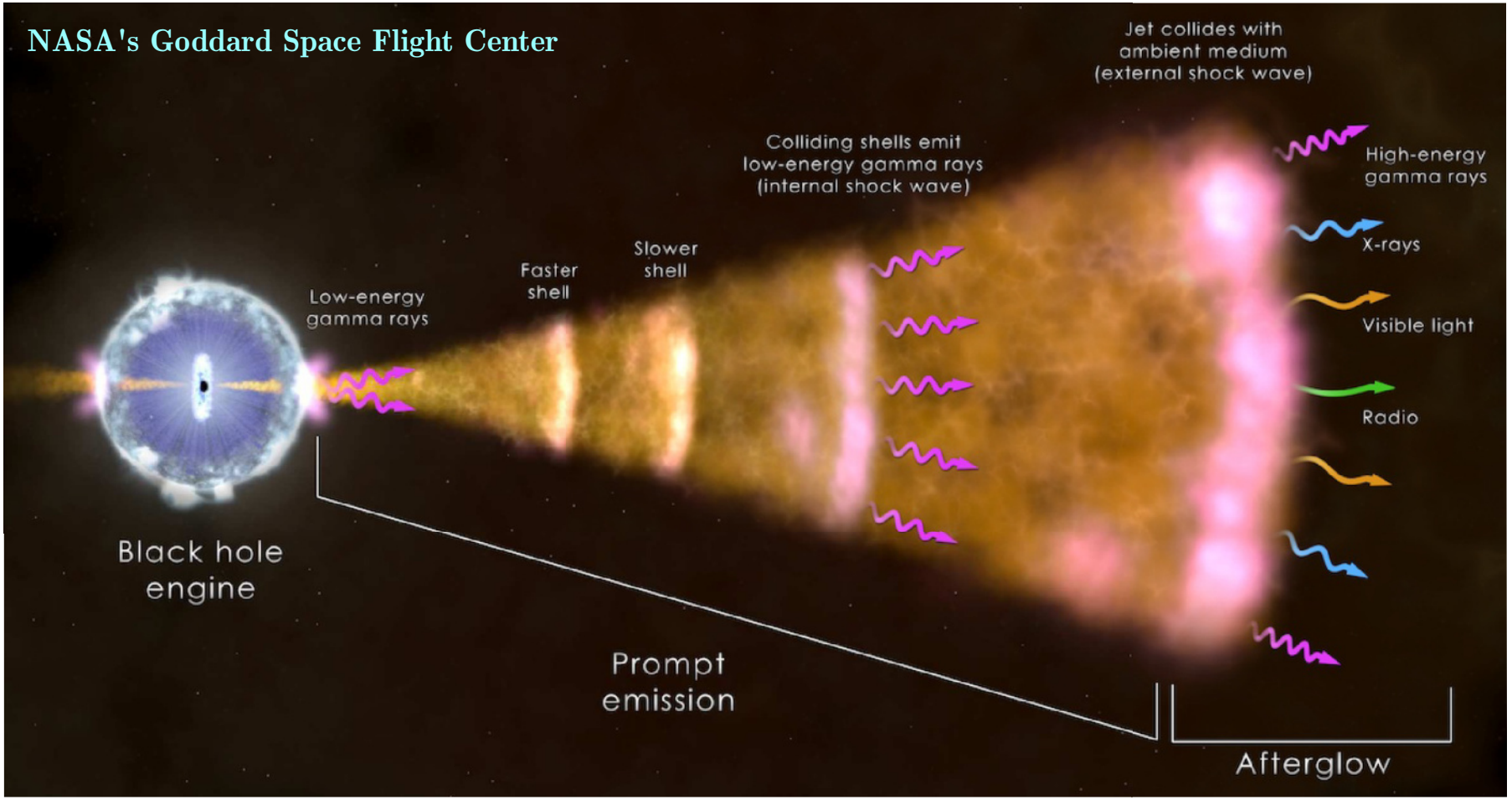

In the most common type of GRB, illustrated here, a dying massive star forms a black hole (left), which drives a particle jet into space. Light across the spectrum arises from hot gas near the progenitor star, from collisions within the jet, and through the interaction of the jet with its surroundings.

[From URL: ⟨ http://science.psu.edu/news-and-events/2015-news/Murase4-2015 ⟩.]

A Short GRB model.

The outflow of high energy particles is likely to originate from a black hole that is accreting matter. The black hole may be formed by either the merger of two neutron stars, or by the collapse of a particularly massive star. If a part of the neutron star is ripped apart in the process, it can accrete onto the black hole and can supply the matter that will be accelerated to high energies and produce neutrinos.

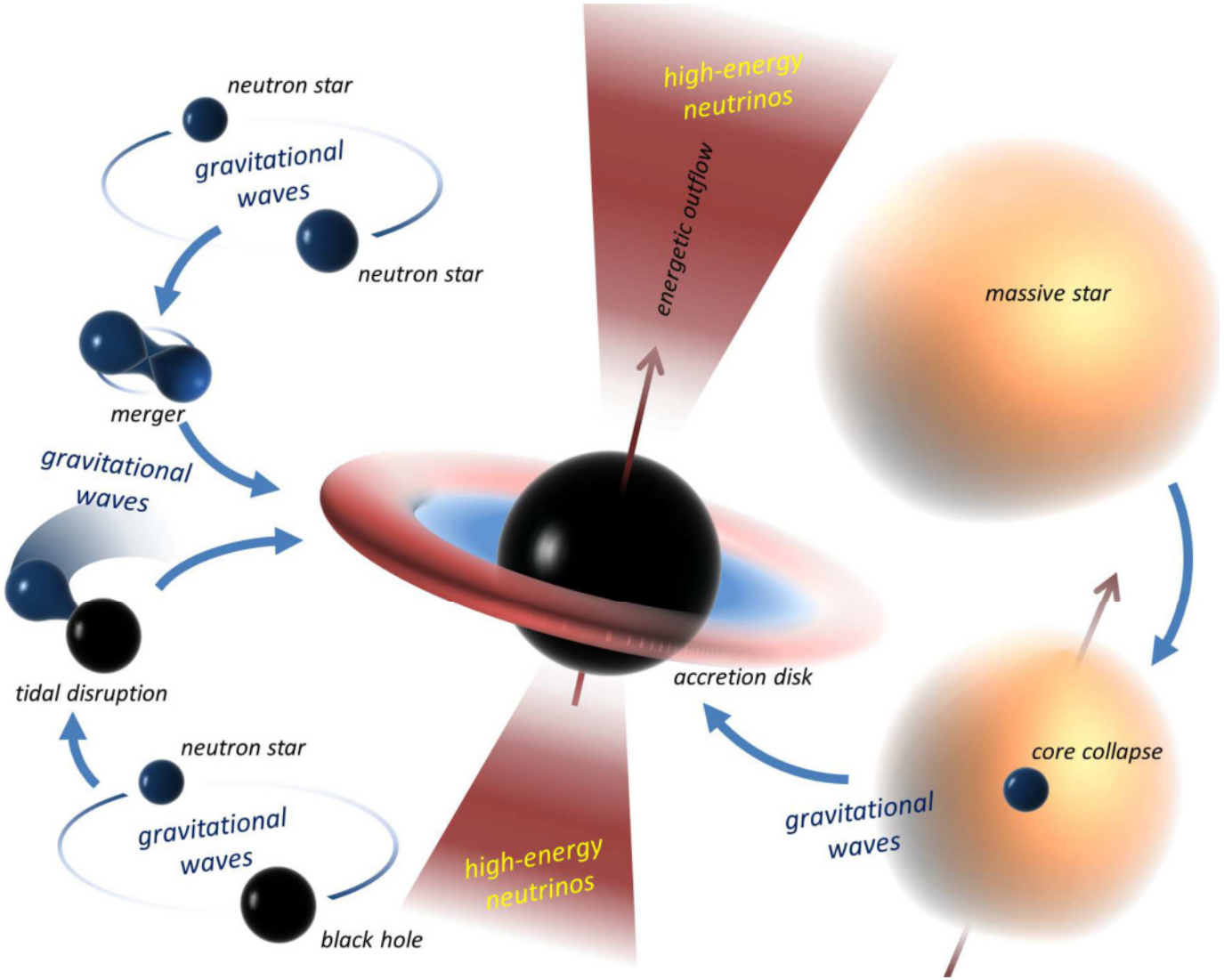

[For detais, see I. Bartos, P. Brady & S. Márka, "How gravitational-wave observations can shape the gamma-ray burst paradigm," Class. Quant. Grav. **3** (2013) 123001, arXiv:1212.2289 [astro-ph.CO]. See also pp. 109–113.]

7.5 Expected fluxes and upper limits (of historical interest only).

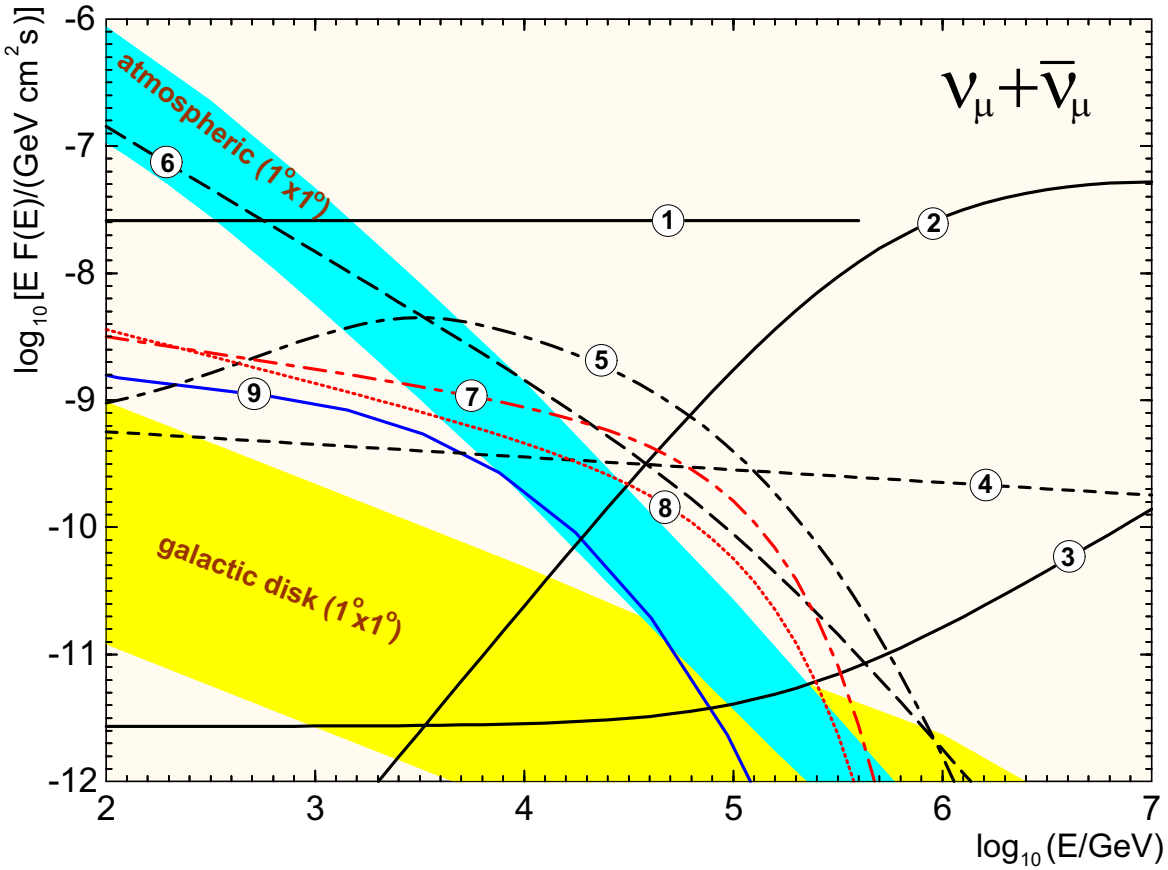

Summary of expected $\nu_\mu + \overline{\nu}_\mu$ intensities from candidate cosmic-ray accelerators ("point sources").

[Borrowed from J. G. Learned & K. Mannheim, "High-energy neutrino astrophysics," Ann. Rev. Nucl. Part. Sci. **50** (2000) 679–749, Fig. 8.]

Shaded regions

Cerulean band: background from terrestrial atmosphere including prompt neutrinos from charm production within an angular bin $1^\circ \times 1^\circ$ [Thunman *et al.* (1996)];
Yellow band: background from Galactic disk within an angular bin $1^\circ \times 1^\circ$ [Thunman *et al.* (1996)].

Numbered lines

1 – Nellen *et al.* (1993) model for the core emission from 3C273 due to pp interactions (or similarly Mrk501 during its outburst in 1997 if it emits half of its TeV gamma ray flux in neutrinos);
2 – Stecker & Salamon (1996) model for the core emission from 3C273 due to $p\gamma$ interactions;
3 – Mannheim (1993) model for the relativistic jet of 3C273 including pp and $p\gamma$ interactions;
4 – Coma cluster according to the model of Colafrancesco & Blasi (1998);
5 – Crab nebula, Model I due to Bednarek & Protheroe (1997);
6 – cosmic-ray induced neutrinos from Sun according to Ingelman & Thunman (1996);
7 – supernova remnant IC444 according to the model of Gaisser *et al.* (1998);
8 – supernova remnant γ Cygni according to Gaisser *et al.* (1998);
9 – CasA according to the model of Atoyan *et al.* (2000) (adopting $L_\nu = L_\gamma$ and $E_\nu = 0.5 E_\gamma$).

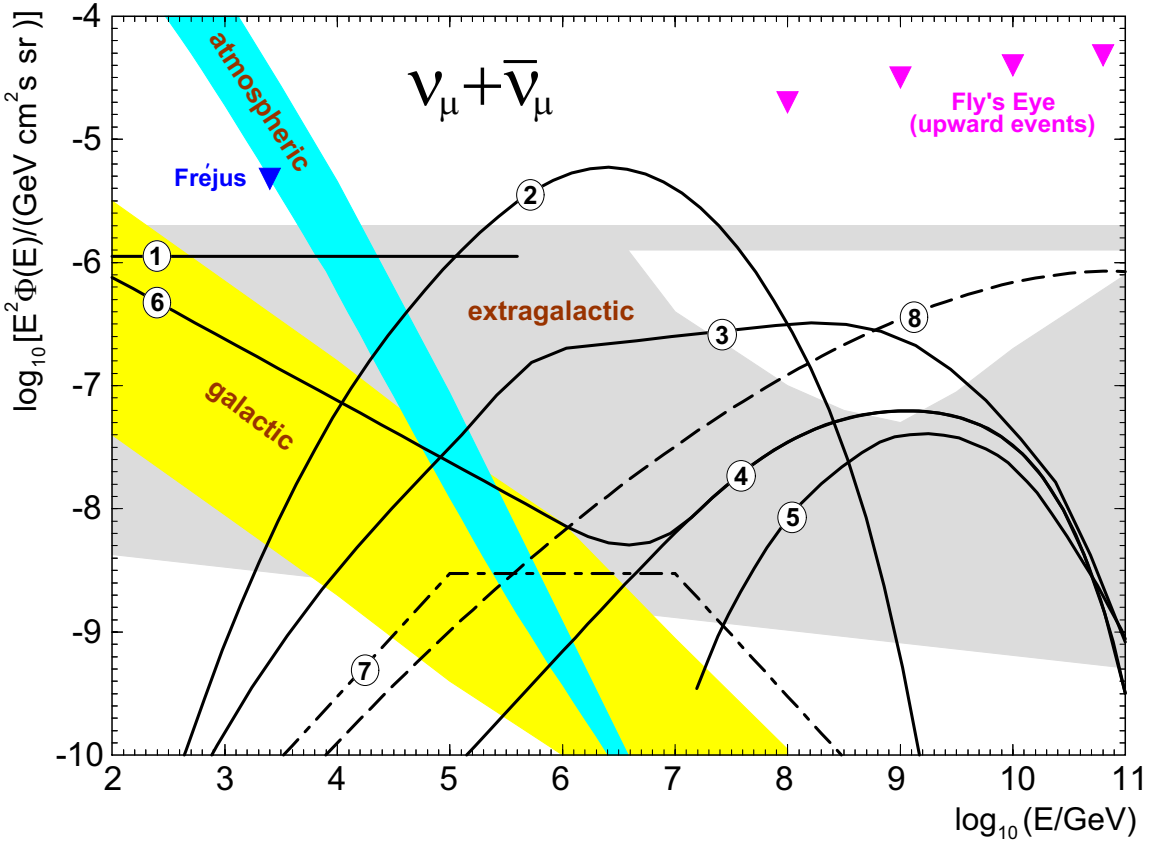

Summary of expected $\nu_\mu + \overline{\nu}_\mu$ intensities for diffuse emission from various sources. The experimental data (triangles) are from Frejús proton decay detector (limit on any excess above the atmospheric background) and Fly's Eye fluorescence air shower detector (limits on upward events).

[Borrowed from J. G. Learned & K. Mannheim, "High-energy neutrino astrophysics," Ann. Rev. Nucl. Part. Sci. **50** (2000) 679–749, Fig. 10.]

Shaded regions

Cerulean band: terrestrial atmosphere in the horizontal (upper boundary) and vertical (lower boundary) directions including prompt neutrinos from charm production [Thunman *et al.* (1996)];
Yellow band: Galactic disk towards the center (upper boundary) and the poles (lower boundary) [Thunman *et al.* (1996)];
Gray area: unresolved extragalactic sources from which gamma rays and cosmic-ray nucleons escape freely (curved upper boundary) and from which only gamma rays escape (straight upper boundary) [Mannheim *et al.* (1999)], cosmic-ray storage in galaxy clusters (lower boundary) [Colafrancesco & Blasi (1998)].

Numbered lines

1 – Nellen *et al.* (1993) model for pp interactions in the core of AGN;
2 – Stecker & Salamon (1996) model for $p\gamma$ interactions in the core of AGN (from which nucleons can not freely escape);
3 – Mannheim *et al.* (1999) maximum model for $p\gamma$ interactions in extragalactic sources;
4 – Mannheim (1995) model A for $p\gamma$ interactions in blazar jets producing UHECRs through neutron escape;
5 – $p\gamma$ interactions due to UHE cosmic rays escaping from radio galaxies and traveling through the 2.7 K background according to the model of Rachen & Biermann (1993, 1996);
6 – pp interactions in host galaxies of blazar jets as assumed in the model of Mannheim (1995);
7 – GRB model by Waxman & Bahcall (1997);
8 – decaying X, Y gauge bosons of mass 10 PeV created at topological defects as in the models of Sigl (1998) and Birkel & Sarkar (1998).

7.6 Digression: The Galaxy & coordinate systems.

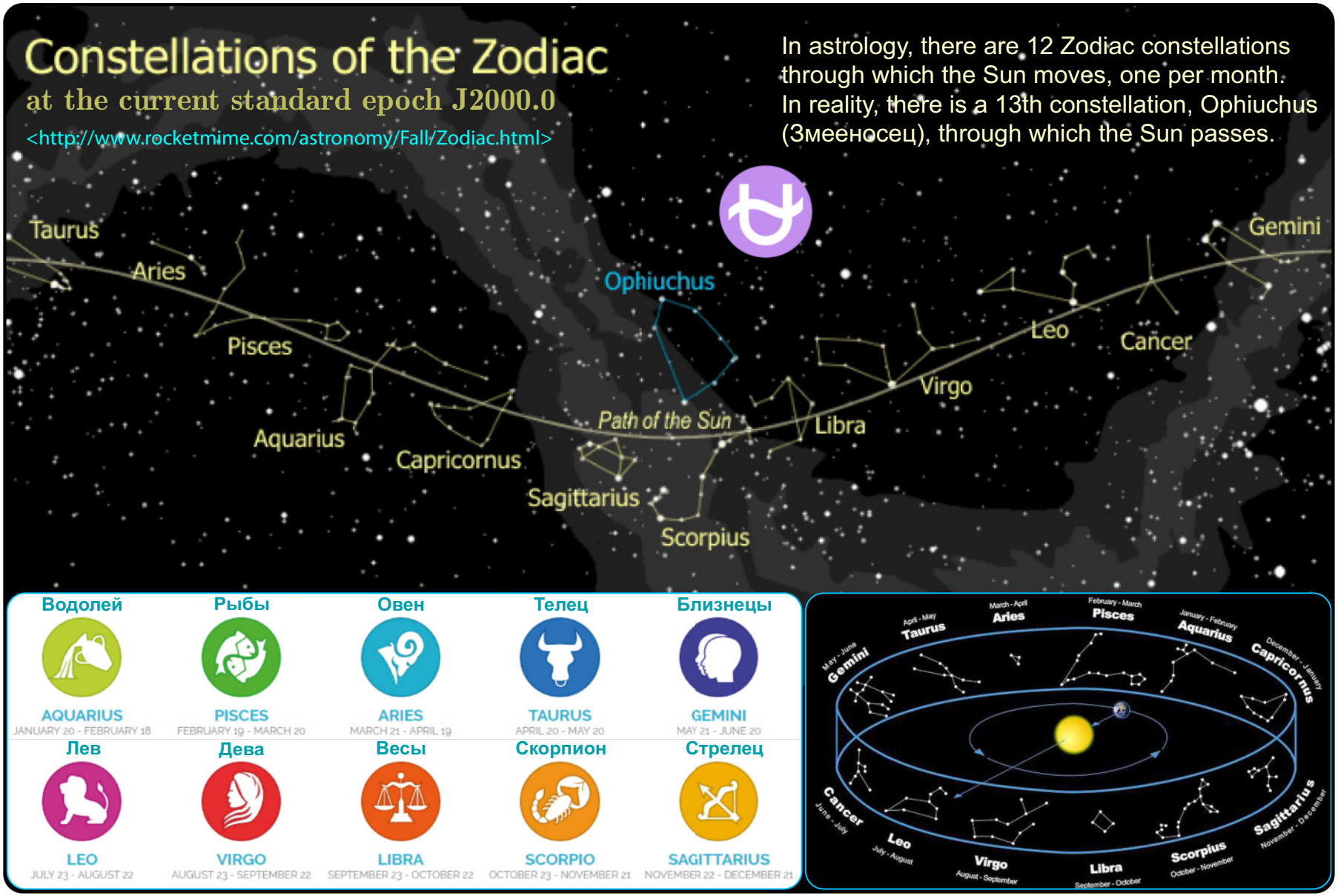

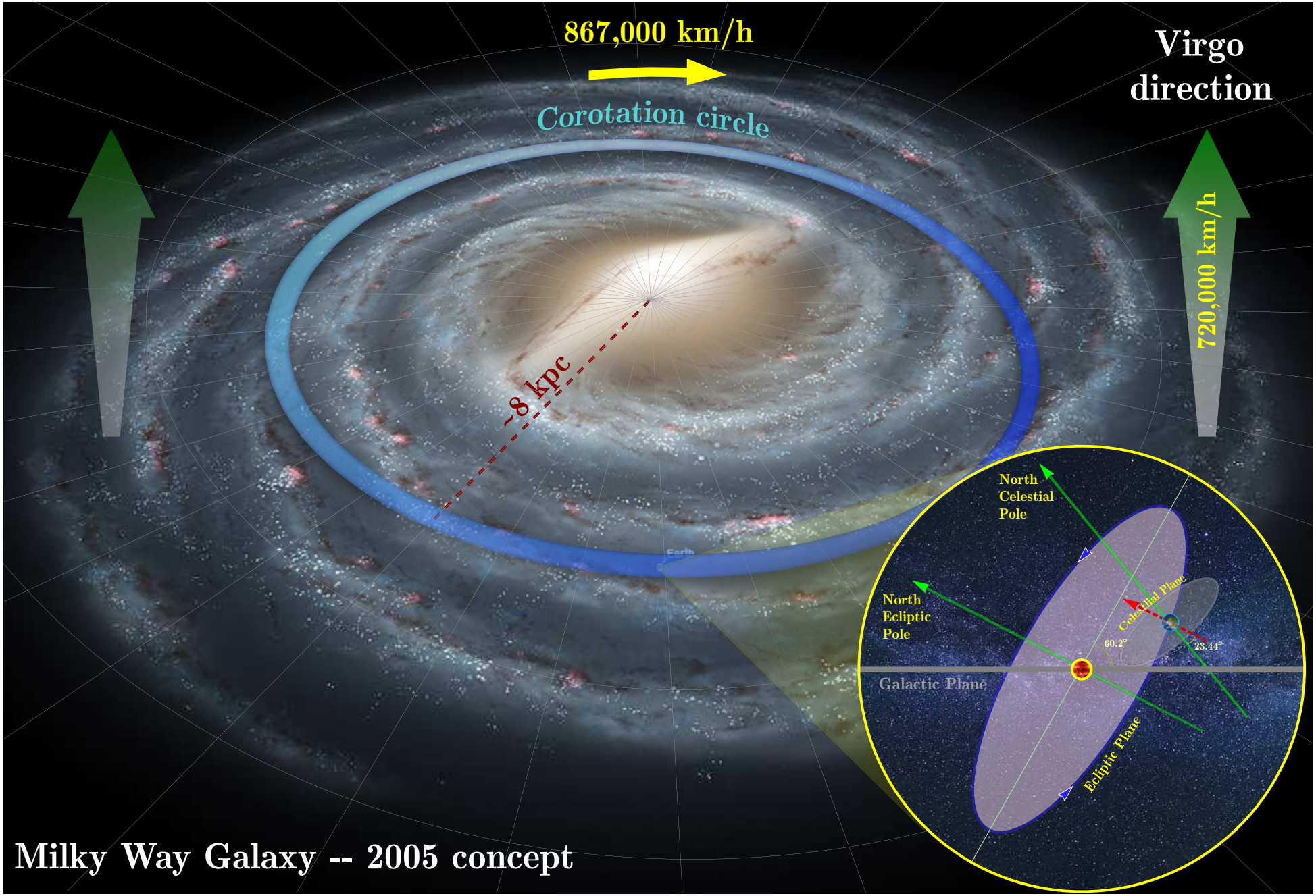
867,000 km/h
Virgo direction
Corotation circle
720,000 km/h
~8 kpc
North Celestial Pole
North Ecliptic Pole
Celestial Plane
60.2°
23.44°
Galactic Plane
Ecliptic Plane
Milky Way Galaxy -- 2005 concept

Equatorial coordinate system (ECS).

ECS is a celestial coordinate system widely used to specify the positions of celestial objects. The system may be implemented in *spherical* or *rectangular* coordinates, both defined by an origin at the center of the Earth, (so the coordinates are geocentric) a fundamental plane consisting of the projection of the Earth's equator onto the celestial sphere (forming the celestial equator), a primary direction towards the vernal equinox, and a right-handed convention.

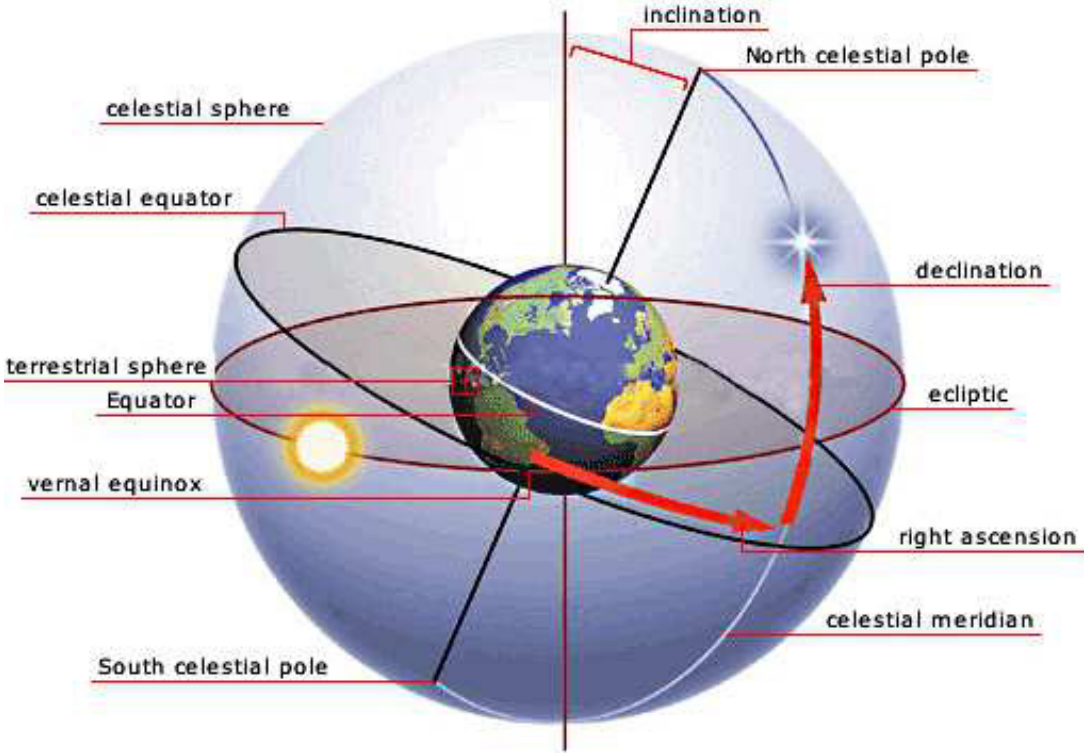

Declination (δ) of an object is an angular distance in degrees measured from the celestial equator along the meridian through the object. It is measured north and south of the celestial equator and ranges from 0° (equator) to $\pm 90^\circ$ (north/south celestial poles).
Right ascension (α) is the angle between the vernal equinox (the intersection of the ecliptic and the celestial equator) and the intersection of the meridian through a celestial object and the celestial equator. RA is usually measured from $0\,\mathrm{h}$ to $24\,\mathrm{h}$ along the celestial equator eastwards (counterclockwise) from the vernal equinox.

Galactic coordinate system (GCS).

GCS is a celestial coordinate system in spherical coordinates, with the Sun as its center, the primary direction aligned with the approximate center of the Milky Way galaxy, and the fundamental plane approximately in the galactic plane. The angular distances are usually measured in degrees ($^\circ$).

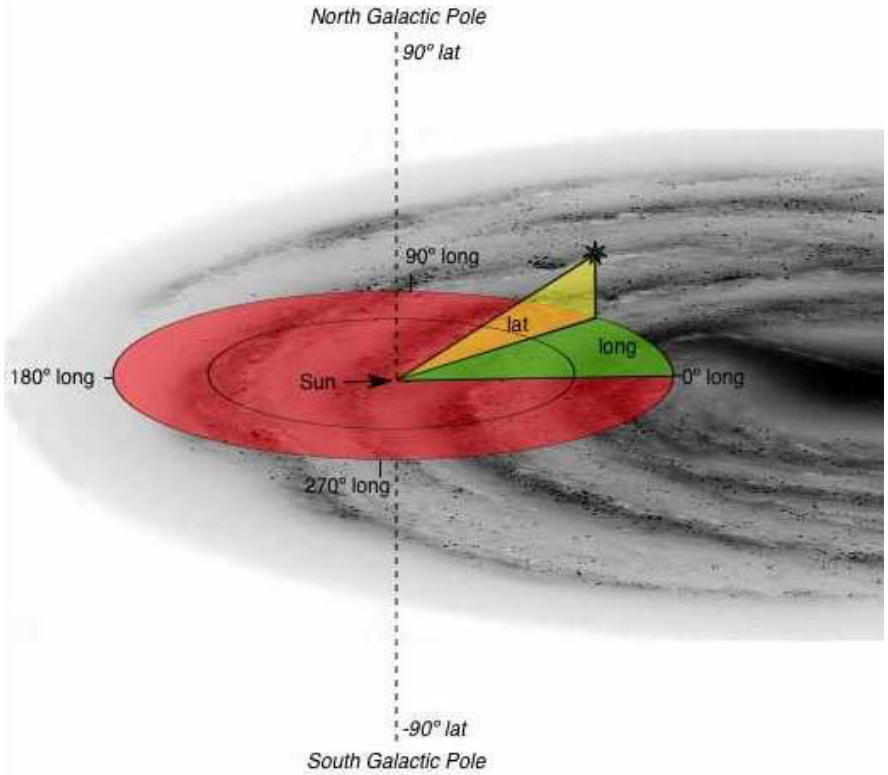

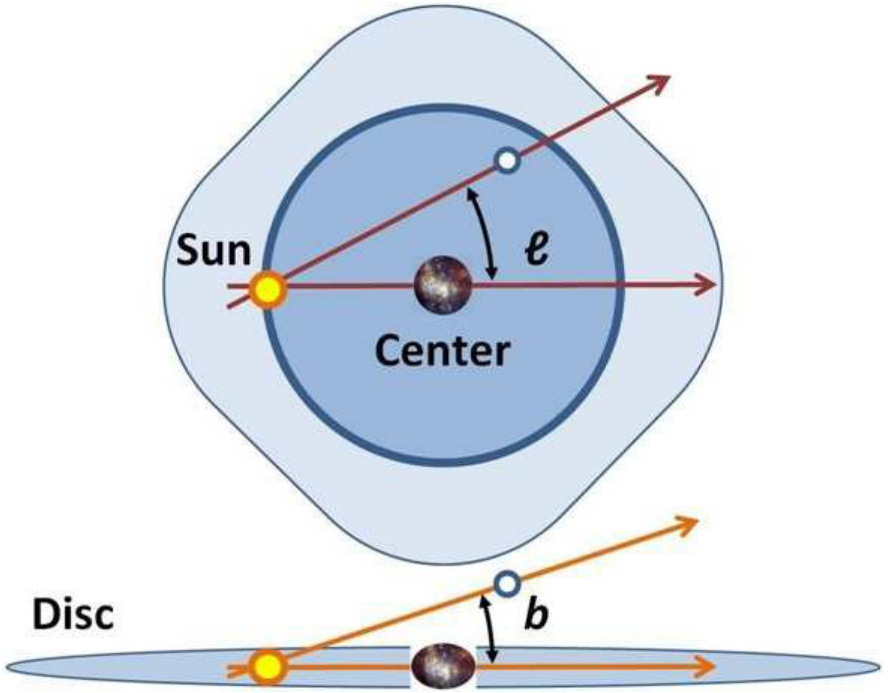

Galactic longitude (l) measures the angular distance of an object eastward along the galactic equator from the galactic center.

Galactic latitude (b) measures the angular distance of an object perpendicular to the galactic equator, positive to the north, negative to the south (e.g., *north* galactic pole has a latitude of $+90^\circ$).

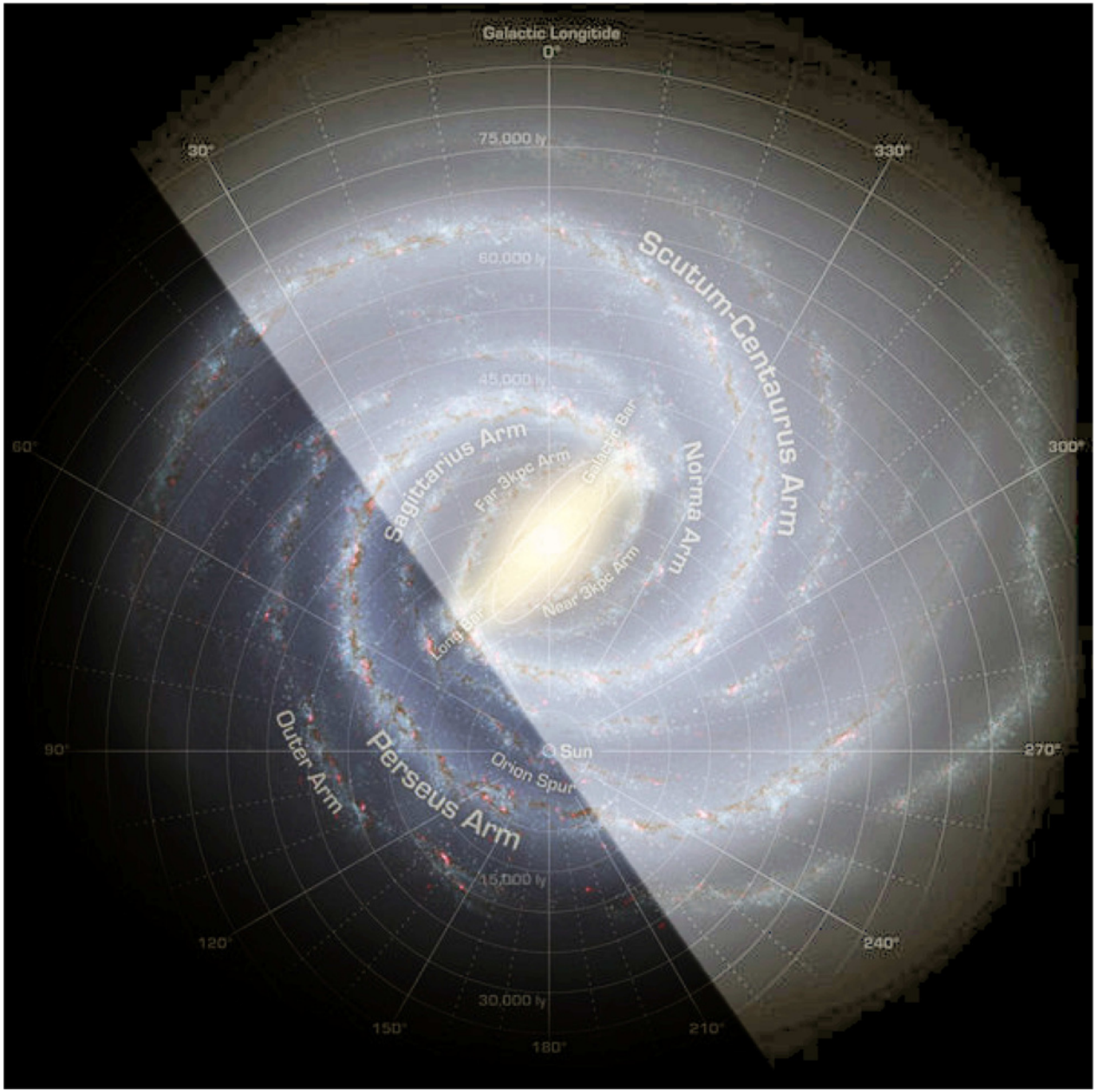

Sketch (based on optical, infrared, and radio data) of approximately how the Galaxy is likely to appear viewed face-on with Galactic coordinates overlaid and the locations of spiral arms and the Sun indicated. Also indicated the part of the Galaxy within the field of view of the IceCube analyses is from galactic longitude $40^\circ - 210^\circ$ (i.e. lower left region).

[From R. Abbasi *et al.* (IceCube Collaboration), "Searches for high-energy neutrino emission in the Galaxy with the combined IceCube-AMANDA detector," ApJ **763** (2013) 33, arXiv:1210.3273 [astro-ph.HE].]

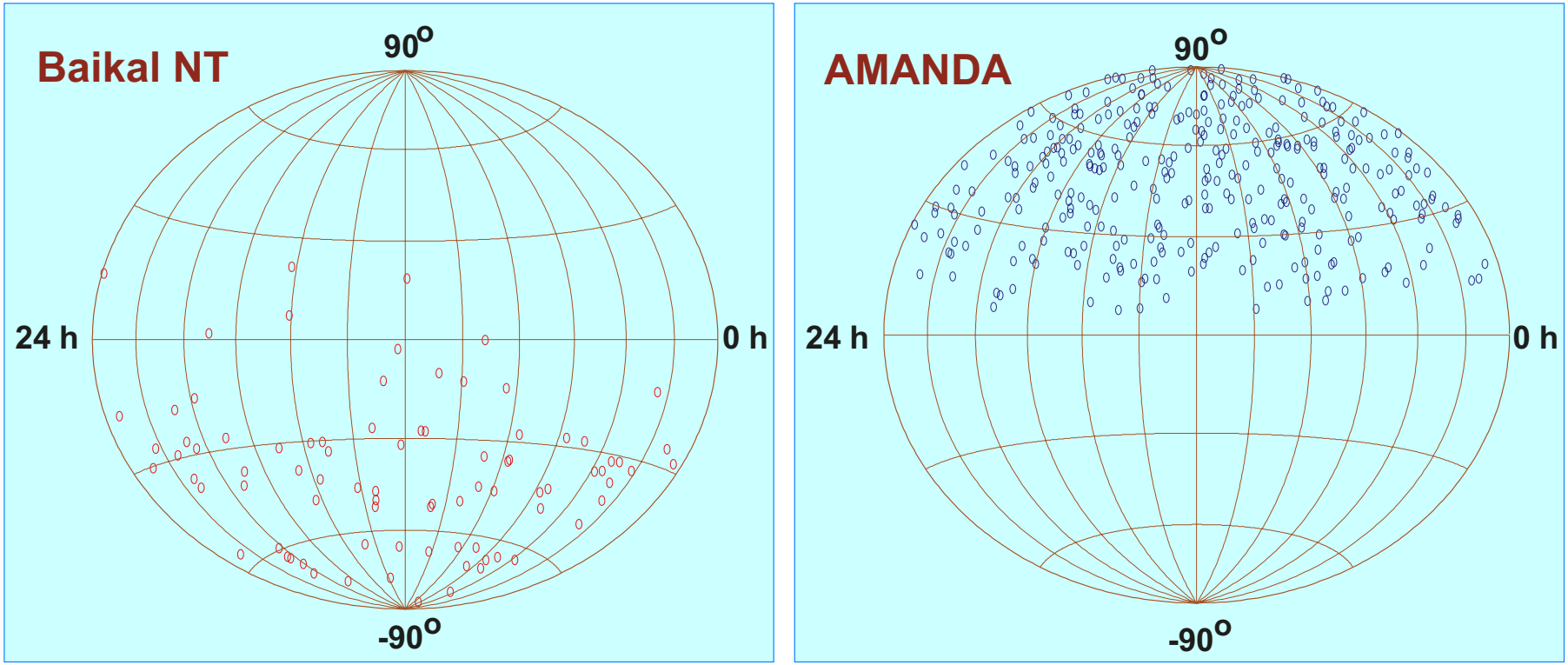

Skyplots (in equatorial coordinates) of 84 upward-going muon events recorded in the Baikal NT-200 experiment[a] *left panel* (status on 2003) and upward-going muon events as seen with AMANDA-B10 experiment in 1997[b] *right panel* (status on 2001). The background of non-neutrino events in AMANDA is estimated to be less than 10%. The plots are shown as an illustration of using the ESC.

[a] R. Wischnewski (for the Baikal Collaboration), "Results from the Baikal neutrino telescope," contribution to the 28th ICRC, Tsukuda, Japan, July 31 – August 7, 2003 (astro-ph/0305302).

[b] J. Ahrens *et al.*, "Observation of high energy atmospheric neutrinos with the Antarctic muon and neutrino detector array" Phys. Rev. D **66** (2002) 012005, astro-ph/0205109; see also G. C. Hill (for the AMANDA collaboration), "Results from AMANDA," astro-ph/0106064.

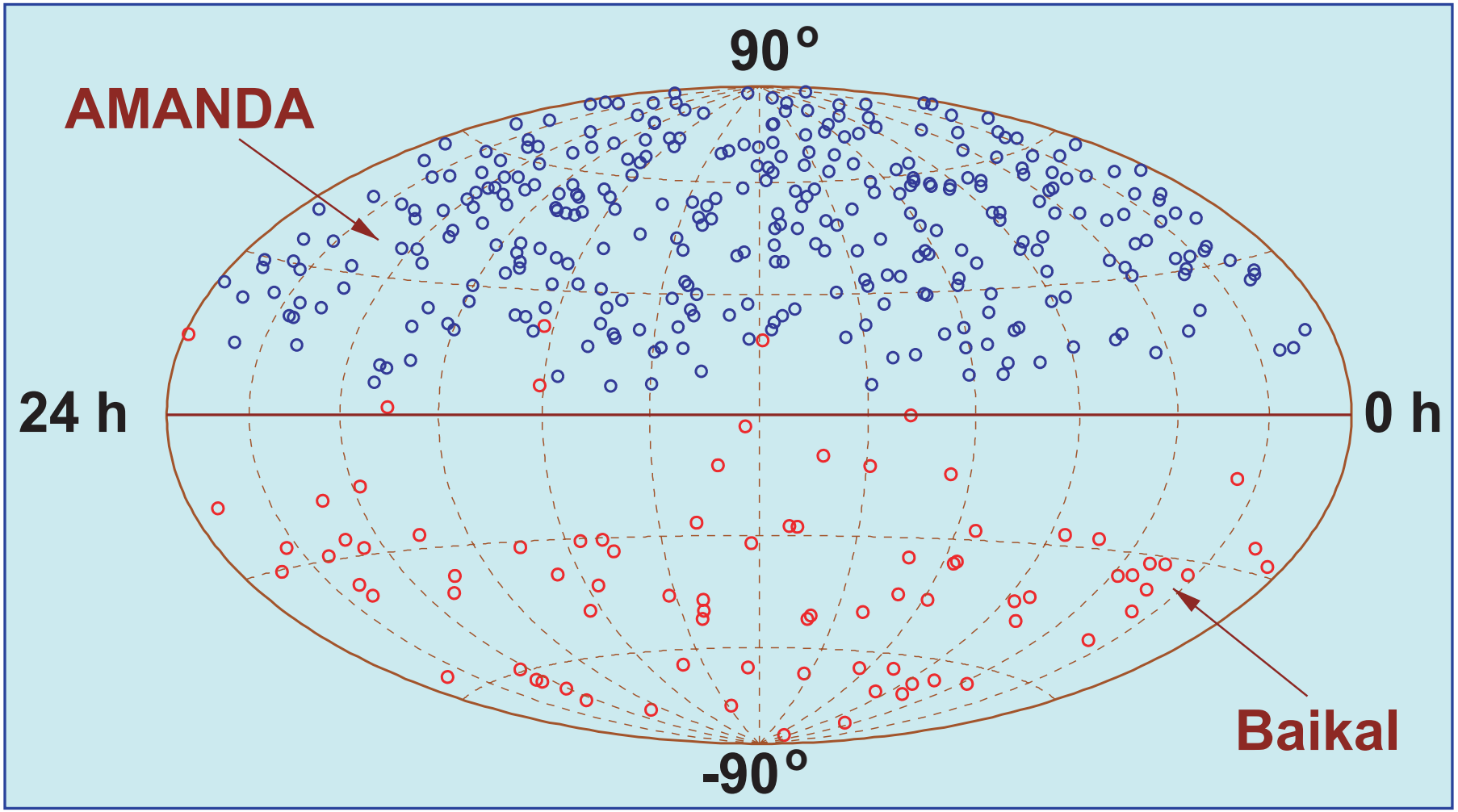

Merged skyplot of upward-going events recorded in both Baikal NT-200 and AMANDA-B10 experiments, illustrating the mutual complementarity of telescopes. The data are the same as in the previous slide.

7.7 Expected fluxes and upper limits (continued).

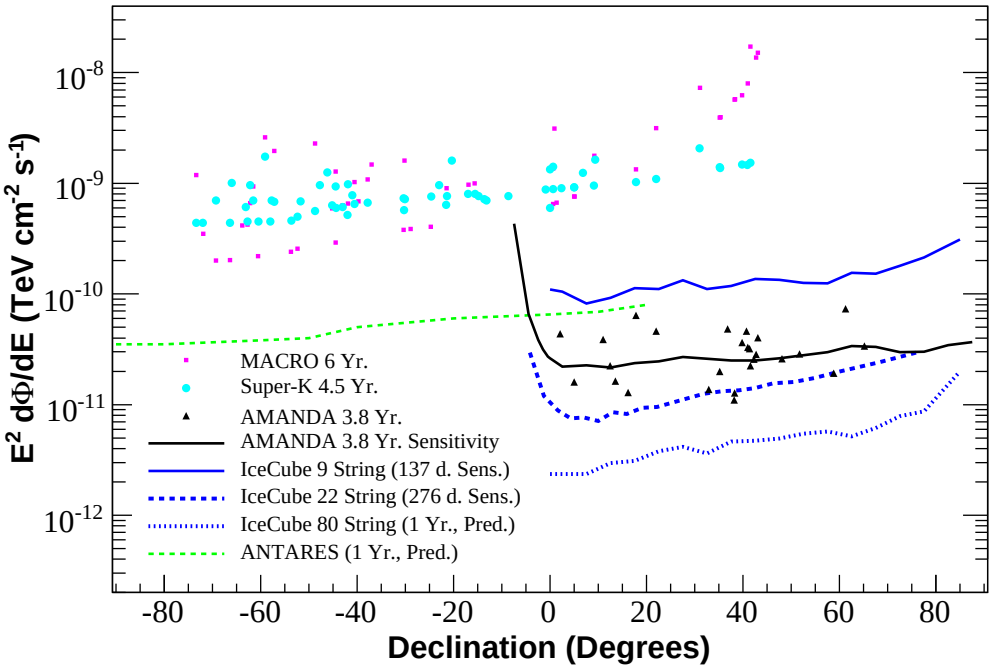

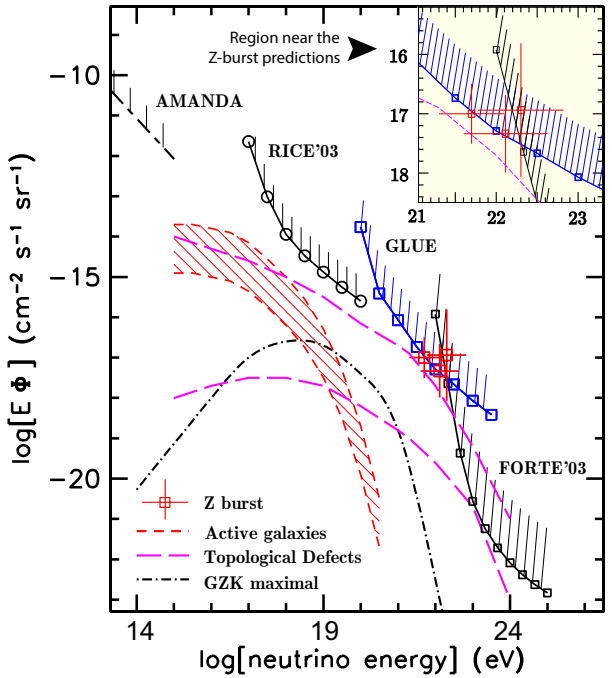

Left panel: Flux limits vs. declination (δ) for AMANDA-II, MACRO, & Super-K, $E^{-2} \times d\Phi_{\nu_\mu}/dE$ sensitivity for AMANDA-II and the IceCube 9-string analysis, and predicted sensitivity for ANTARES and IceCube. The energy range is 1.9 TeV to 2.5 PeV. The AMANDA-II $\nu_\mu + \nu_\tau$ limits are divided by 2 to compare with limits on only ν_μ. [Status on 2009; an illustration of using the ESC.]

[From R. Abbasi *et al.* (The IceCube Collaboration), "Search for point sources of high energy neutrinos with final data from AMANDA-II," Phys. Rev. D **79** (2009) 062001, arXiv:0809.1646 [astro-ph].]

Right panel: Model neutrino fluxes & upper limits from AMANDA, RICE, GLUE & FORTE. Inset expands the region near the Z-burst predictions. [Status on 2003; for details, see Sect. **7.16**, p. 348.]

[From P. W. Gorham *et al.*, "Experimental limit on the cosmic diffuse ultra-high energy neutrino flux," Phys. Rev. Lett. **93** (2004) 041101, astro-ph/0310232v3.]

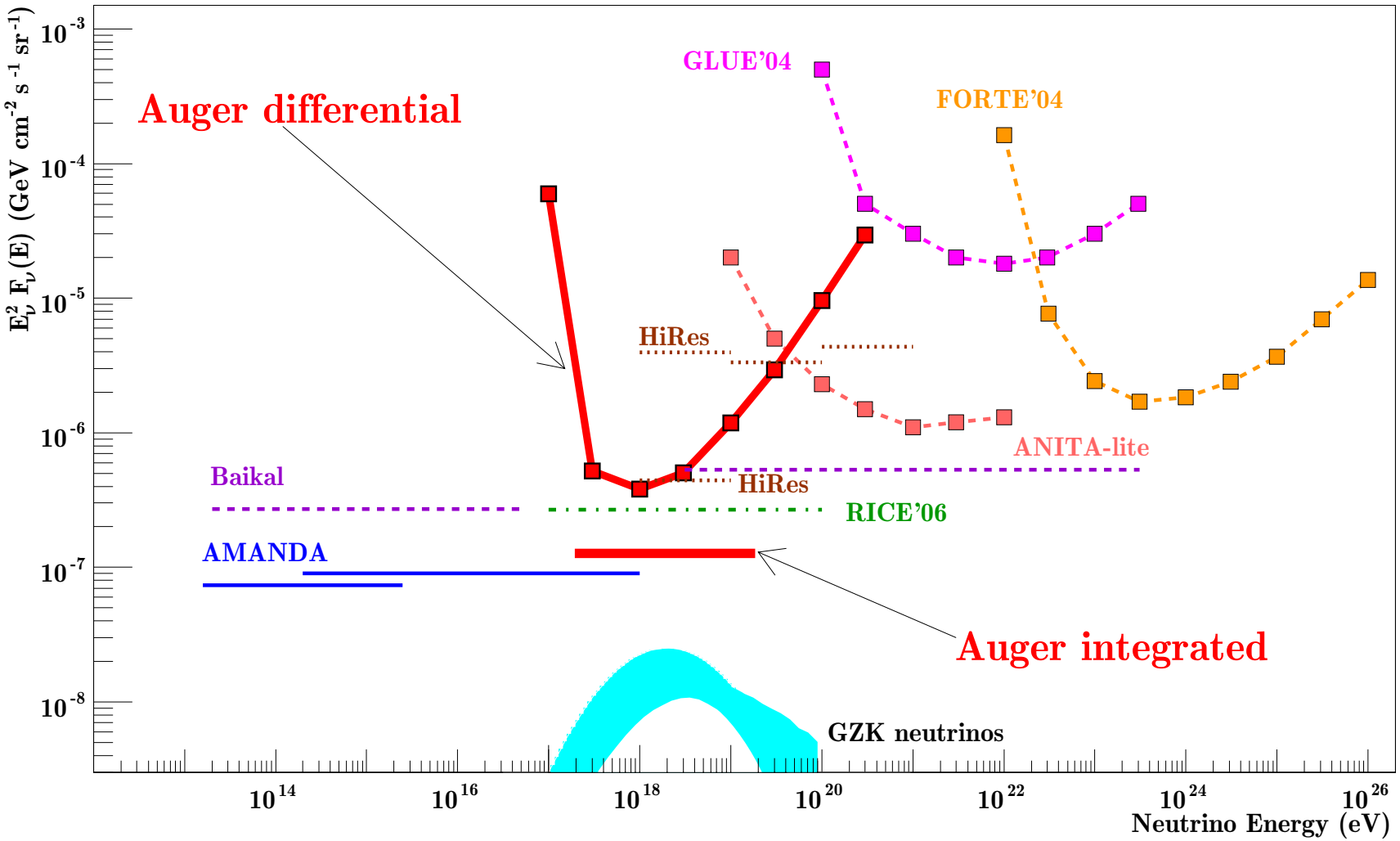

The 90% CL bounds on diffuse flux of ν_τ from Auger. Bounds from other experiments apply assuming equal proportions of the three ν flavors (horizontal lines assume E_ν^{-2} spectrum). Shaded region indicates optimistic expectations for the GZK neutrinos (see p. 348 for current predictions).

[From E. Roulet (for the Pierre Auger Collaboration), "Recent results from the Pierre Auger Observatory," J. Phys. Conf. Ser. **136** (2008) 022051, arXiv:0809.2210 [astro-ph].]

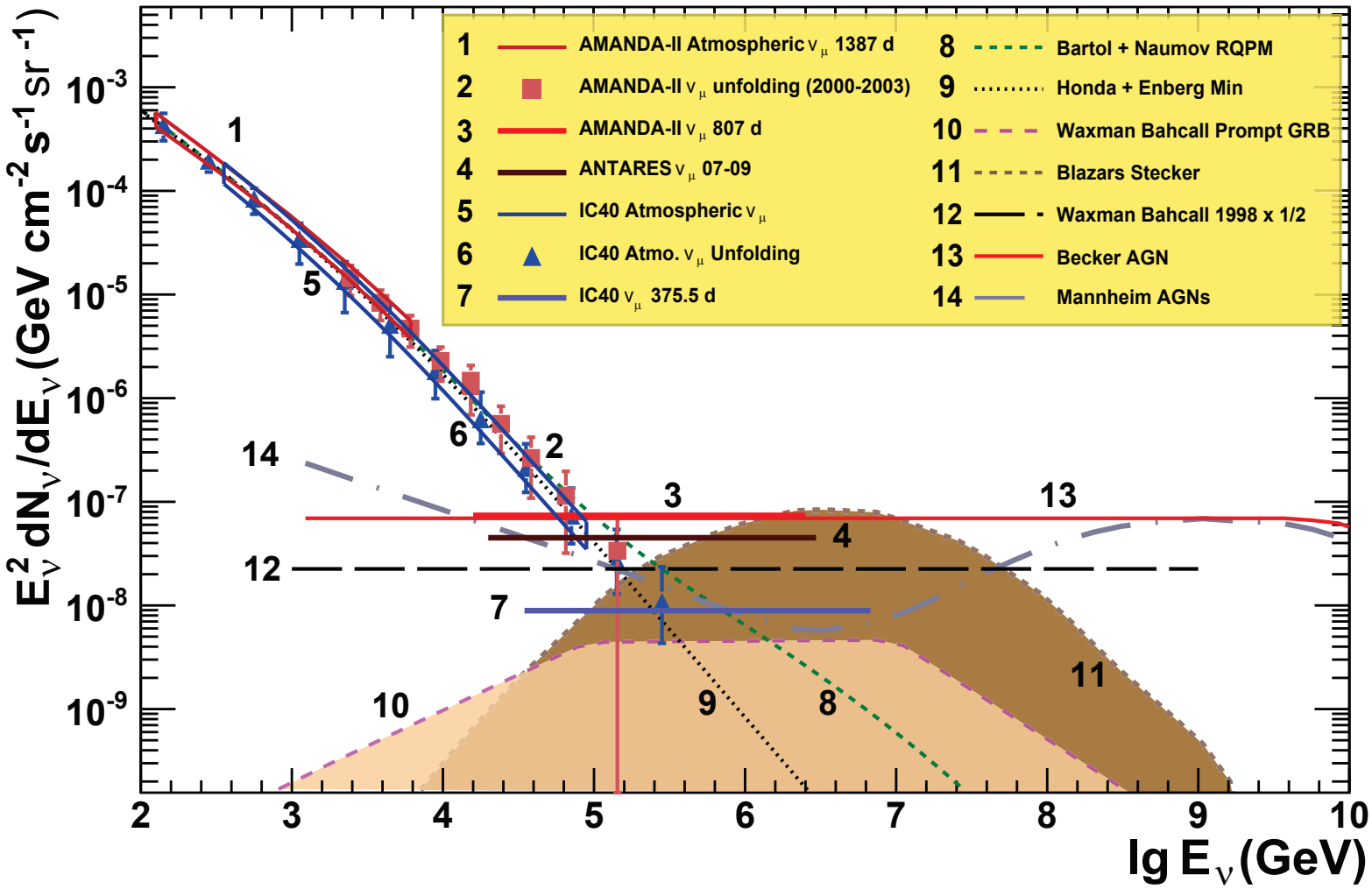

Upper limits on an astrophysical ν_μ flux with an E^2 spectrum along with several theoretical model predictions of diffuse astrophysical ν_μs from different sources. The data shown are from AMANDA-II, IceCube 40-string (IC40) unfolding measurement, and IC40 atmospheric ν_μ.

[From R. Abbasi *et al.* (IceCube Collaboration), "A search for a diffuse flux of astrophysical muon neutrinos with the IceCube 40-string detector," Phys. Rev. D **84** (2011) 082001, arXiv:1104.5187 [astro-ph.HE].]

7.8 IceCube revolution.

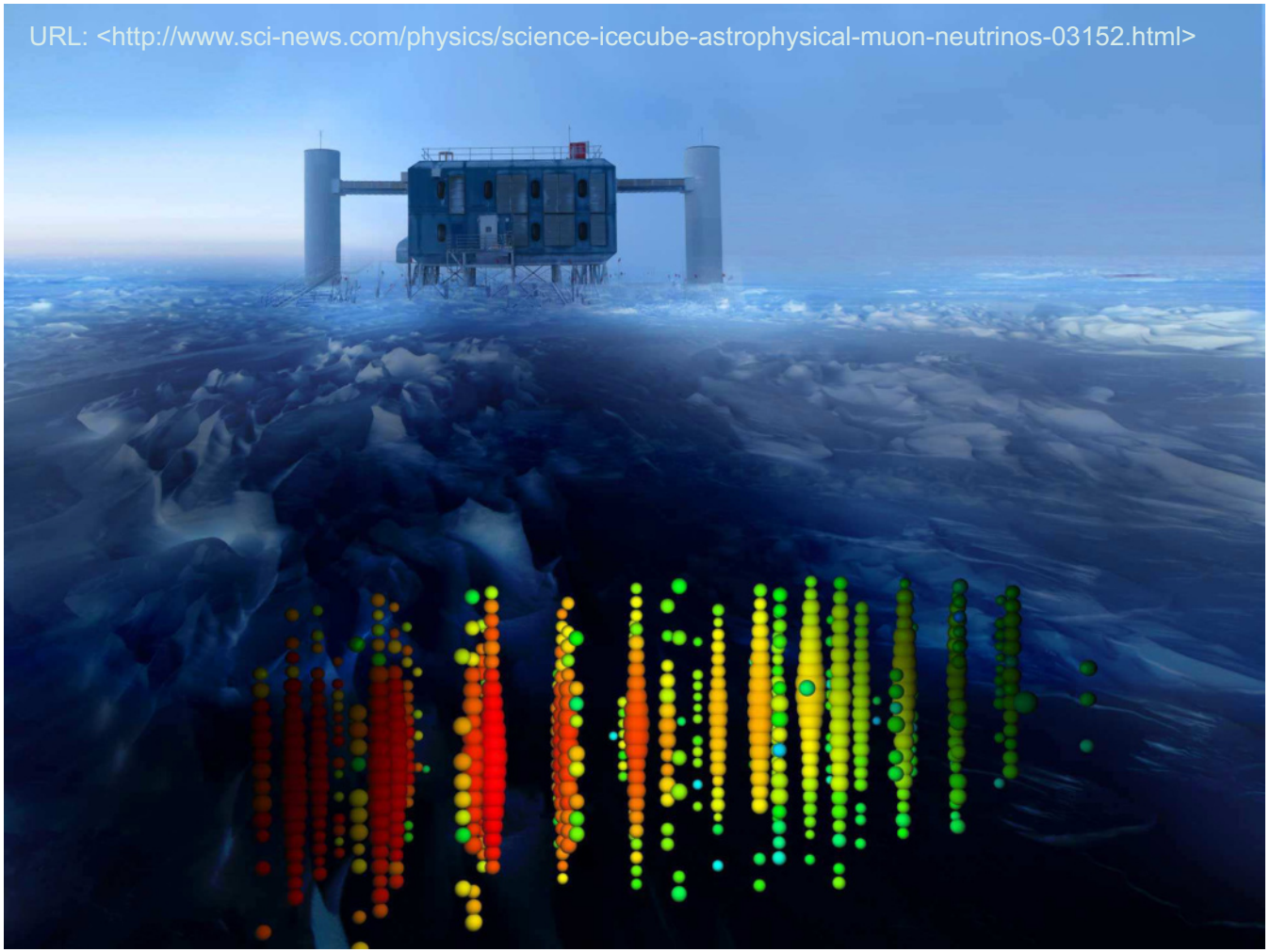

[Look first at pp. 68–70 (Part I). The data shown at pp. 316–319 are taken from M. G. Aartsen *et al.* (IceCube Collaboration), "Observation of high-energy astrophysical neutrinos in three years of IceCube data," Phys. Rev. Lett. **113** (2014) 101101, arXiv:1405.5303 [astro-ph.HE]; note that the eprint version contains very useful supplement materials.]

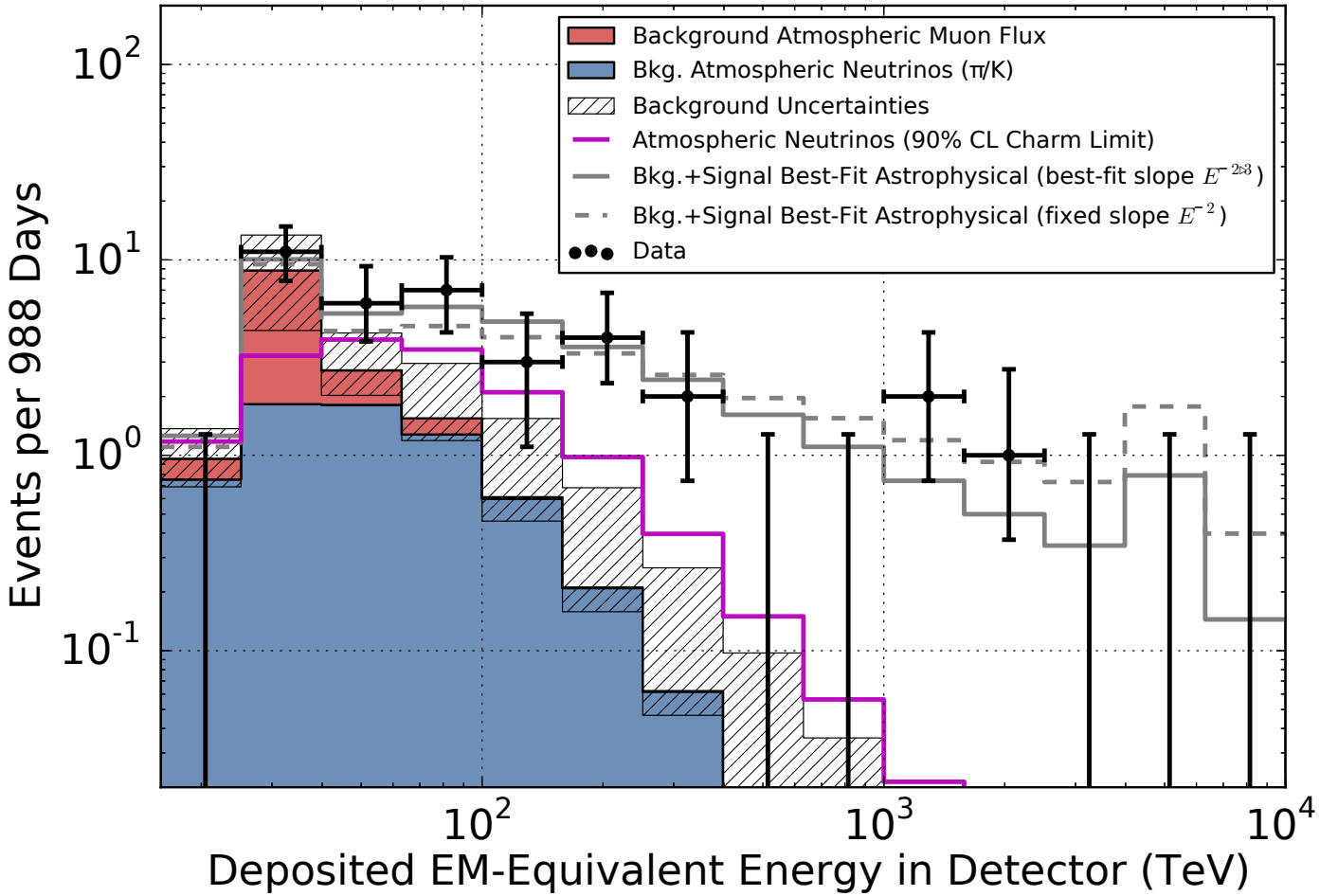

Deposited energies of observed events with predictions. The hashed region shows uncertainties on the sum of all backgrounds. Muons (red) are computed from simulation to overcome statistical limitations in the background measurement and scaled to match the total measured background rate. Atmospheric neutrinos and uncertainties thereon are derived from previous IceCube's measurements of both the π/K and charm components of the atmospheric ν_μ spectrum. A gap larger than the one between 400 and 1000 TeV appears in 43% of realizations of the best-fit continuous spectrum.

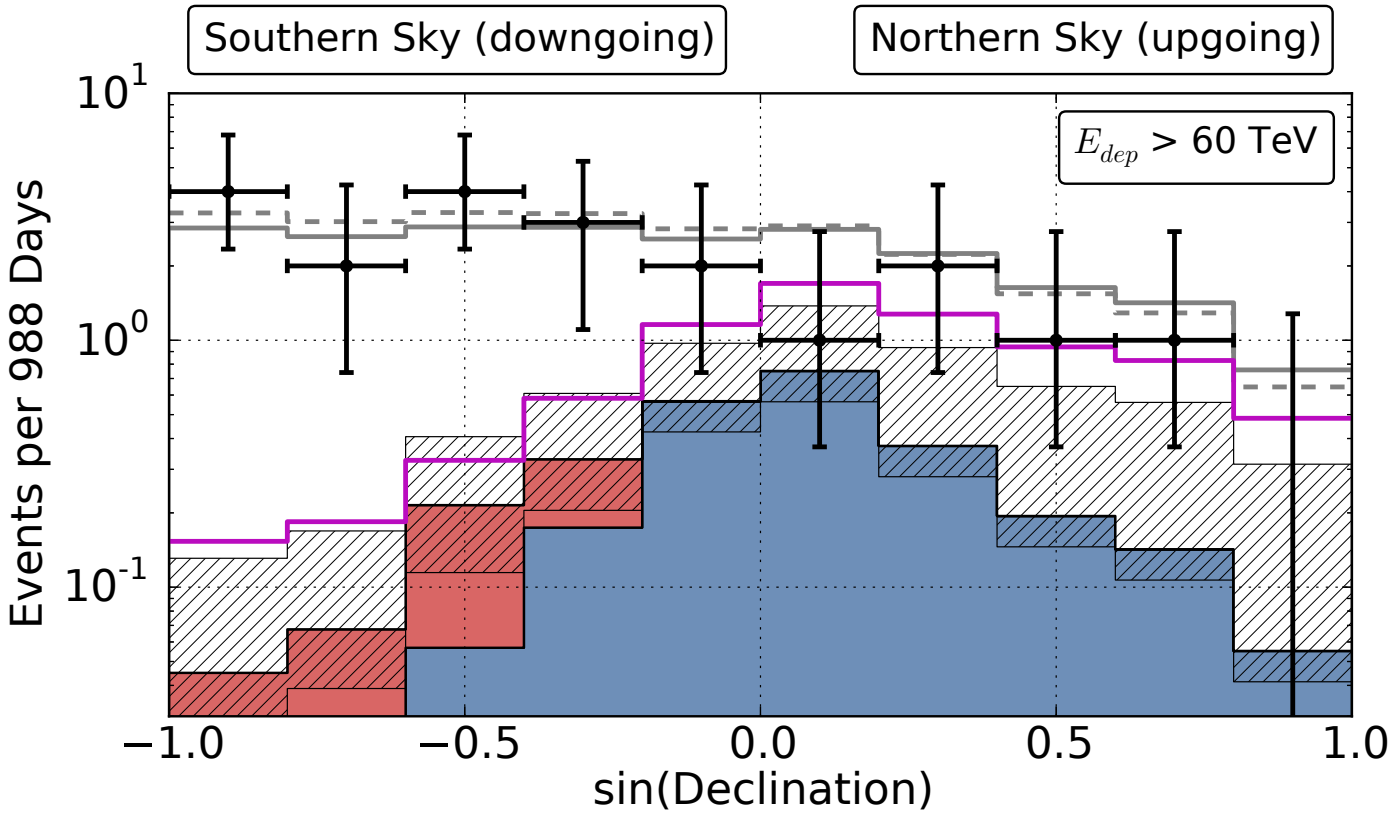

Arrival angles of events with deposited energy above 60 TeV, as used in the IceCube's fit and above the majority of the cosmic-ray muon background. The increasing opacity of the Earth to high energy neutrinos is visible at the right of the plot. Vetoing atmospheric neutrinos by muons from their parent air showers depresses the atmospheric neutrino background on the left. The data are described well by the expected backgrounds and a hard astrophysical isotropic neutrino flux (gray lines). Colors as in Figure at p. 316.

Conclusion: both the energy spectrum and arrival directions of the events are consistent with expectations for an origin in a hard isotropic 1:1:1 neutrino flux; the best-fit atmospheric-only alternative model (extreme scenario) is disfavored at 5.7σ using a likelihood ratio test.

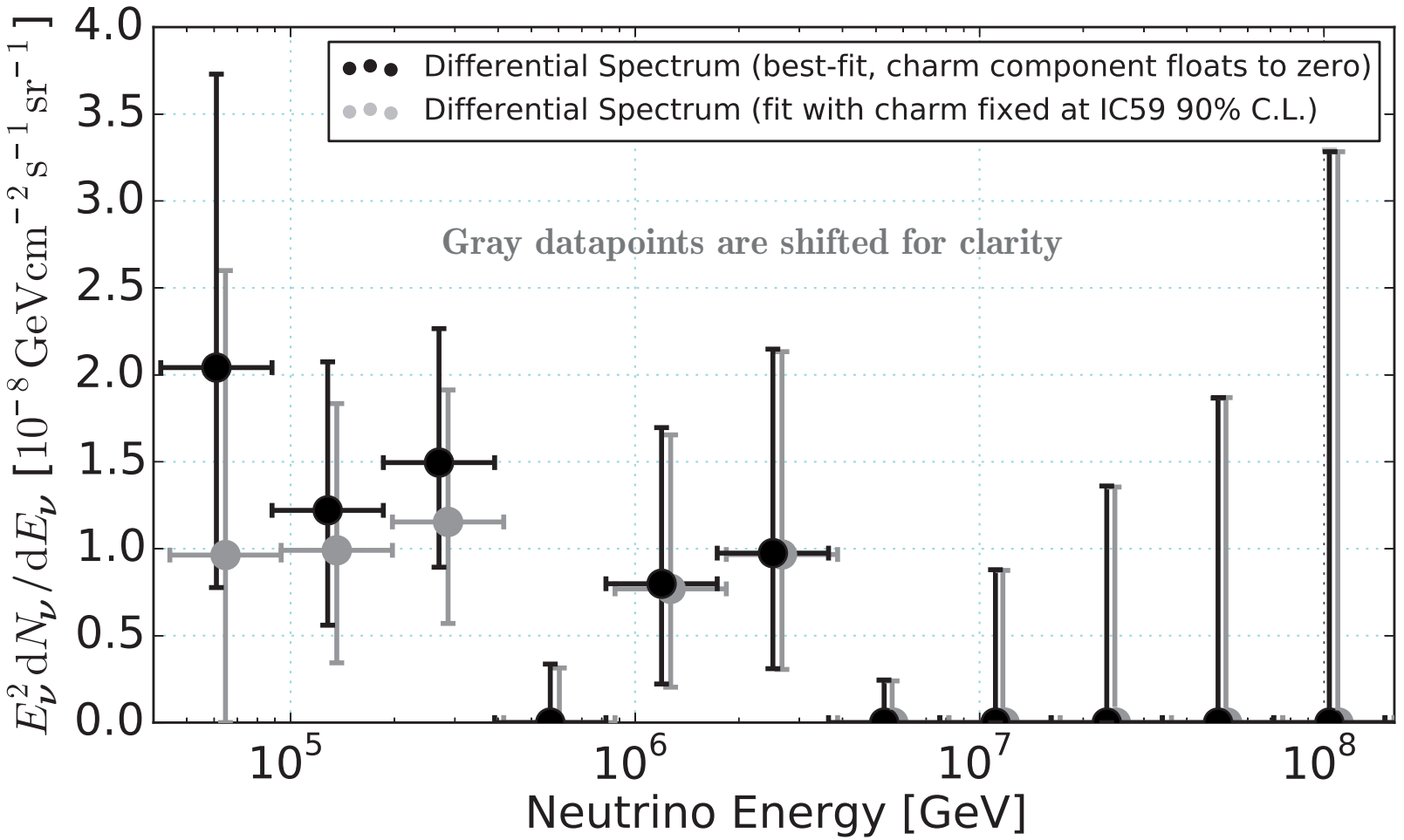

Unfolded extraterrestrial neutrino flux ($\nu + \overline{\nu}$) as a function of energy. Vertical error bars indicate the $2\Delta\mathcal{L} = \pm 1$ contours of the flux in each energy bin, holding all other values, including background normalizations, fixed. These provide approximate 68% confidence ranges. An increase in the charm atmospheric background to the level of the 90% C.L. limit from the northern hemisphere ν_μ spectrum would reduce the inferred astrophysical flux at low energies to the level shown for comparison in light gray. The best-fit power law is $E_\nu^2 \phi_\nu(E_\nu) = 1.5 \times 10^{-8} (E_\nu/100\,\mathrm{TeV})^{-0.3}\,\mathrm{GeV\,cm^{-2}s^{-1}sr^{-1}}$.

▷

Arrival directions of the events in equatorial and galactic coordinates. Shower-like events (median angular resolution $\sim 15^\circ$) are marked with $+$ and those containing muon tracks ($\lesssim 1^\circ$) with $\times$. Approximately 40% of the events (mostly tracks) are expected to originate from atmospheric backgrounds. Event IDs are time ordered. The gray line denotes the equatorial plane. Colors show the test statistic (TS) for the point source clustering test at each location.

No significant clustering was observed.

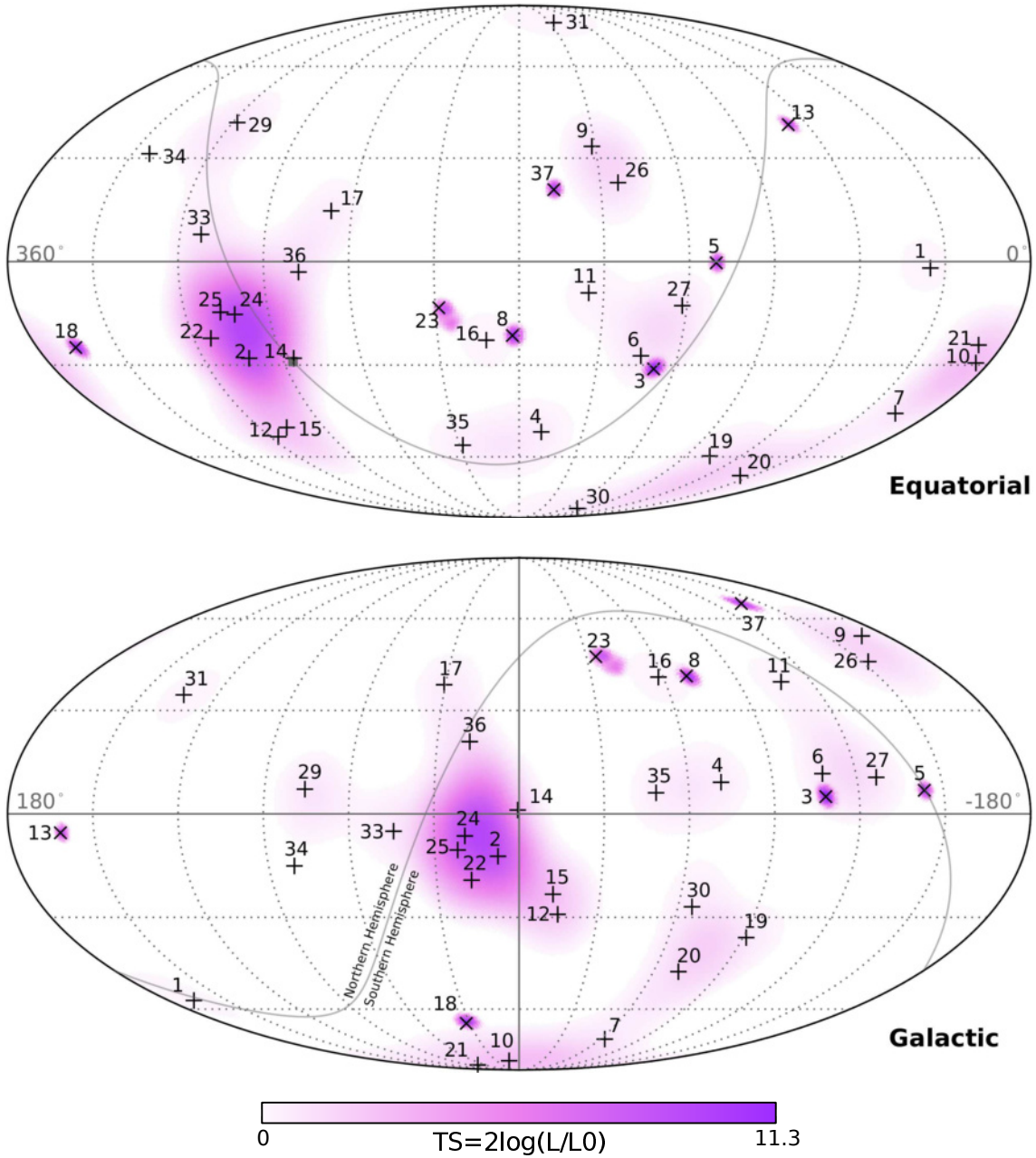

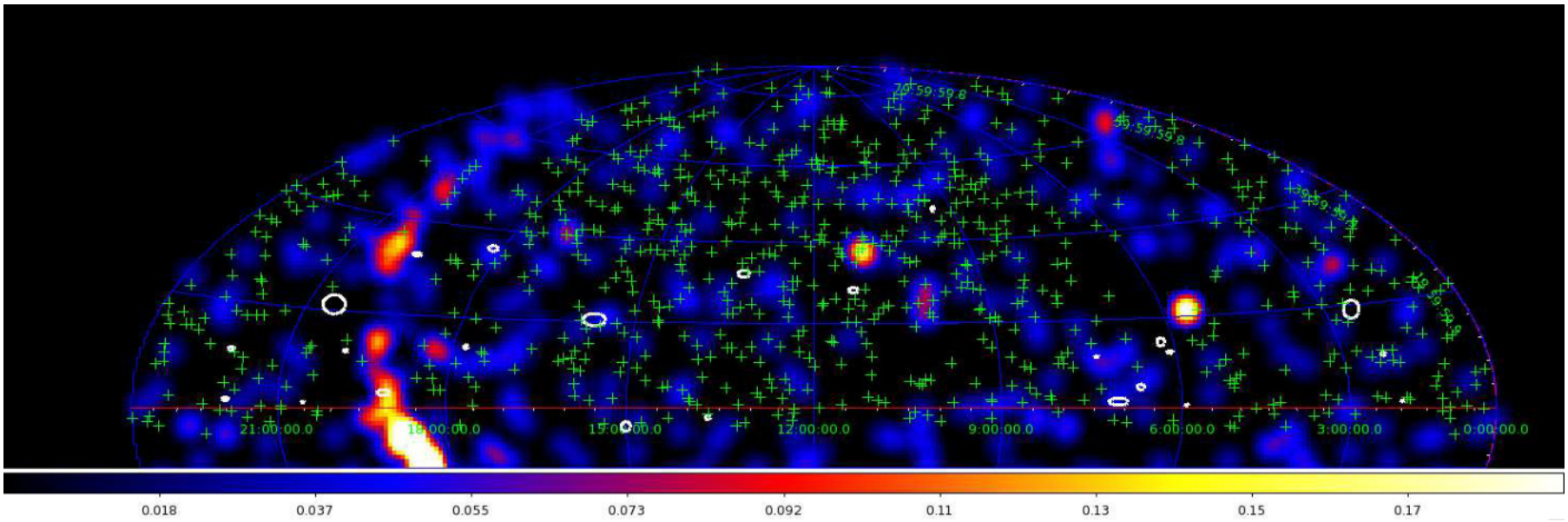

△ IceCube muon neutrino events (white ellipses) with direction uncertainty less than 4 degrees, overlaid over *Fermi*/LAT countmap of the Northern sky in the energy range above 1 TeV, smoothed with 3 degree Gaussian. Green crosses show blazars selected for the stacking analysis of the publicly available the *Fermi*/LAT data collected during the time period between August 2008 and June 2016.

Conclusion: Non-detection of neutrino flux from the stacked blazar sample rules out the proton induced cascade models in which the high-energy emission is powered by interactions of shock accelerated proton beam in the AGN jet with the ambient matter or with the radiation field of the black hole accretion disk. IceCube constraint could be avoided if the spectrum of accelerated protons is sharply peaking in the ultra-high-energy cosmic ray range, as in the models of acceleration in the magnetic reconnection regions or in the vacuum gaps of black hole magnetospheres.

[From A. Neronov, D. V. Semikoz, and K. Ptitsyna, "Strong constraint on hadronic models of blazar activity from *Fermi* and IceCube stacking analysis," Astron. Astrophys. **603** (2017) A135, arXiv:1611.06338v2 [astro-ph.HE].]

7.9 Digression: A few remarks about Schwarzschild black holes.

Schwarzschild radius:

$$R_{\mathsf{S}} = \frac{2GM}{c^2} \simeq 2.95 \text{ km } \frac{M}{M_\odot},$$

Hawking temperature:

$$T_{\mathsf{H}} = \frac{\hbar c^3}{8\pi G k M} \simeq 6.17 \times 10^{-8} \text{ K } \frac{M_\odot}{M}$$

$(kT_{\mathsf{H}} = M_{\mathsf{P}}c^2/8\pi \text{ for } M = M_{\mathsf{P}}).$

Evaporation time:

$$\tau_{\mathsf{ev}} = \frac{5120\pi G^2 M^3}{\hbar c^4} \simeq 2.10 \times 10^{67} \text{ years } \left(\frac{M}{M_\odot}\right)^3.$$

Note: Hawking photons are not born near the horizon. Why?

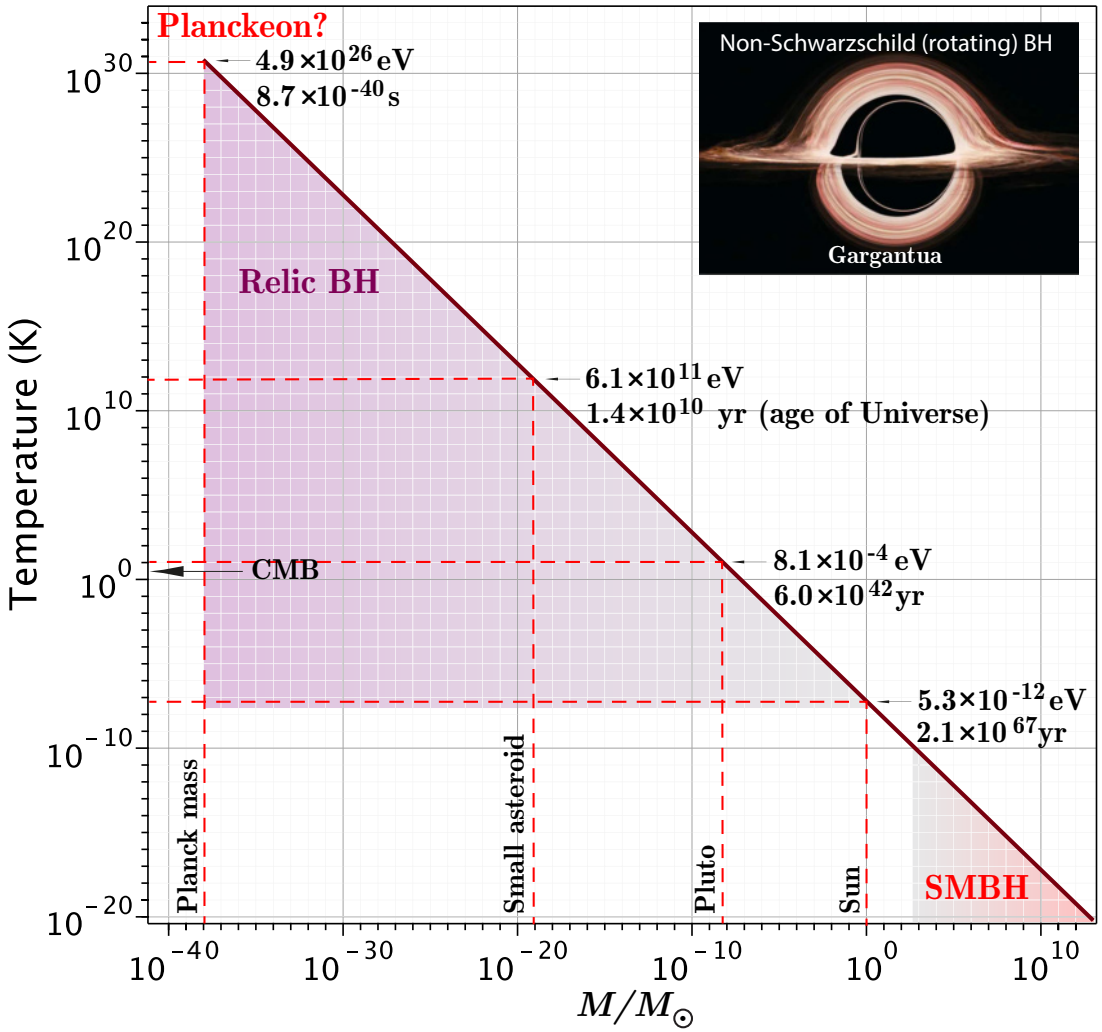

Problem: Check that the wavelength of radiation with energy $E_\gamma = kT_{\mathsf{H}}$ is $\lambda_\gamma = 8\pi^2 R_{\mathsf{S}}$.

Neutrinos from black hole firewalls (an example of a Sci-Fi scenario)

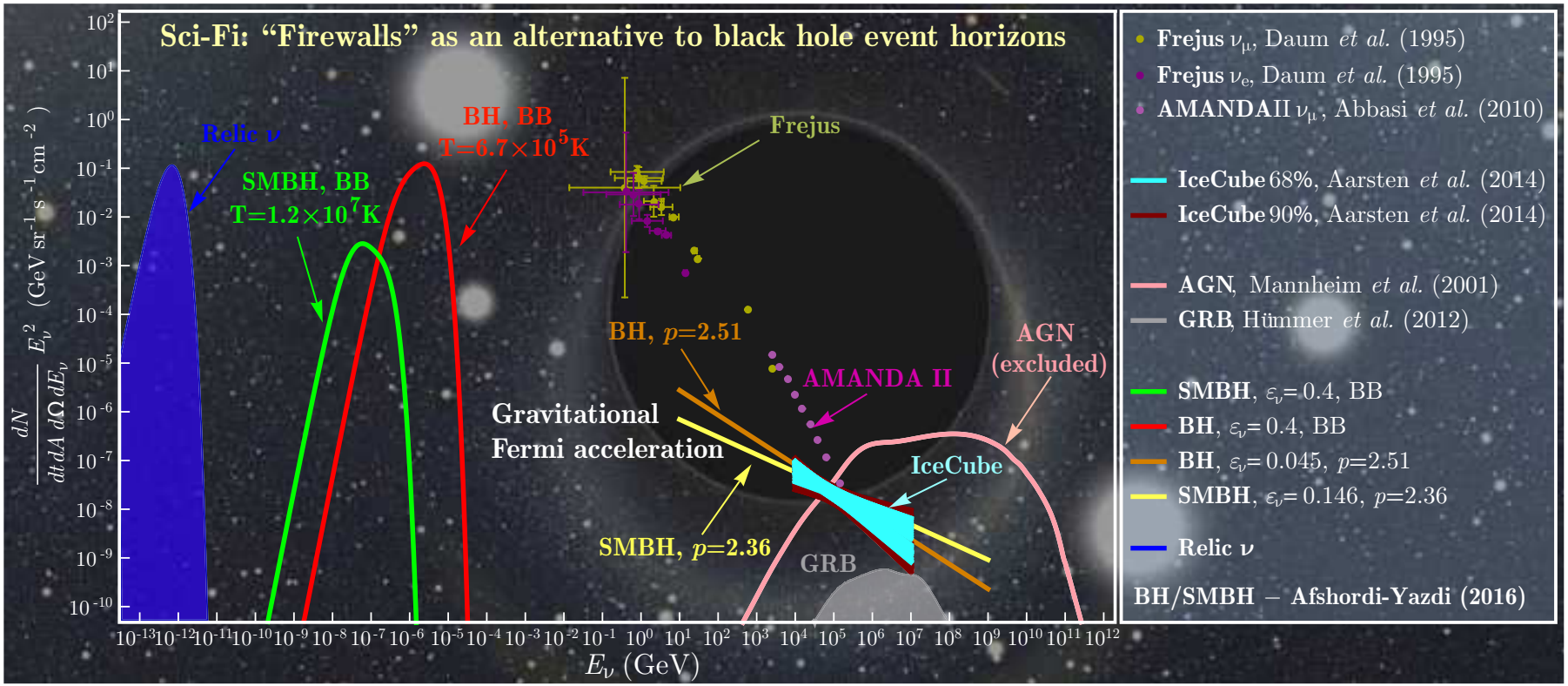

△ Figure shows the neutrino fluxes from surfaces of black holes as expected in the phenomenological BH firewall mechanisms: gravitational Fermi acceleration (neutrinos bounce back and forth between the accretion flow and the BH firewall through gravitational scattering, forming a power-law spectrum) and blackbody radiation (BHs are assumed to be in approximate steady state close to thermodynamic equilibrium). More traditional model predictions and some observational data are also shown for comparison.

[From N. Afshordi and Y. K. Yazdi, "Firewall phenomenology with astrophysical neutrinos," Class. Quant. Grav. **33** (2016) 235017, arXiv:1502.01023 [astro-ph.HE].]

7.10 Selected results from ANTARES.

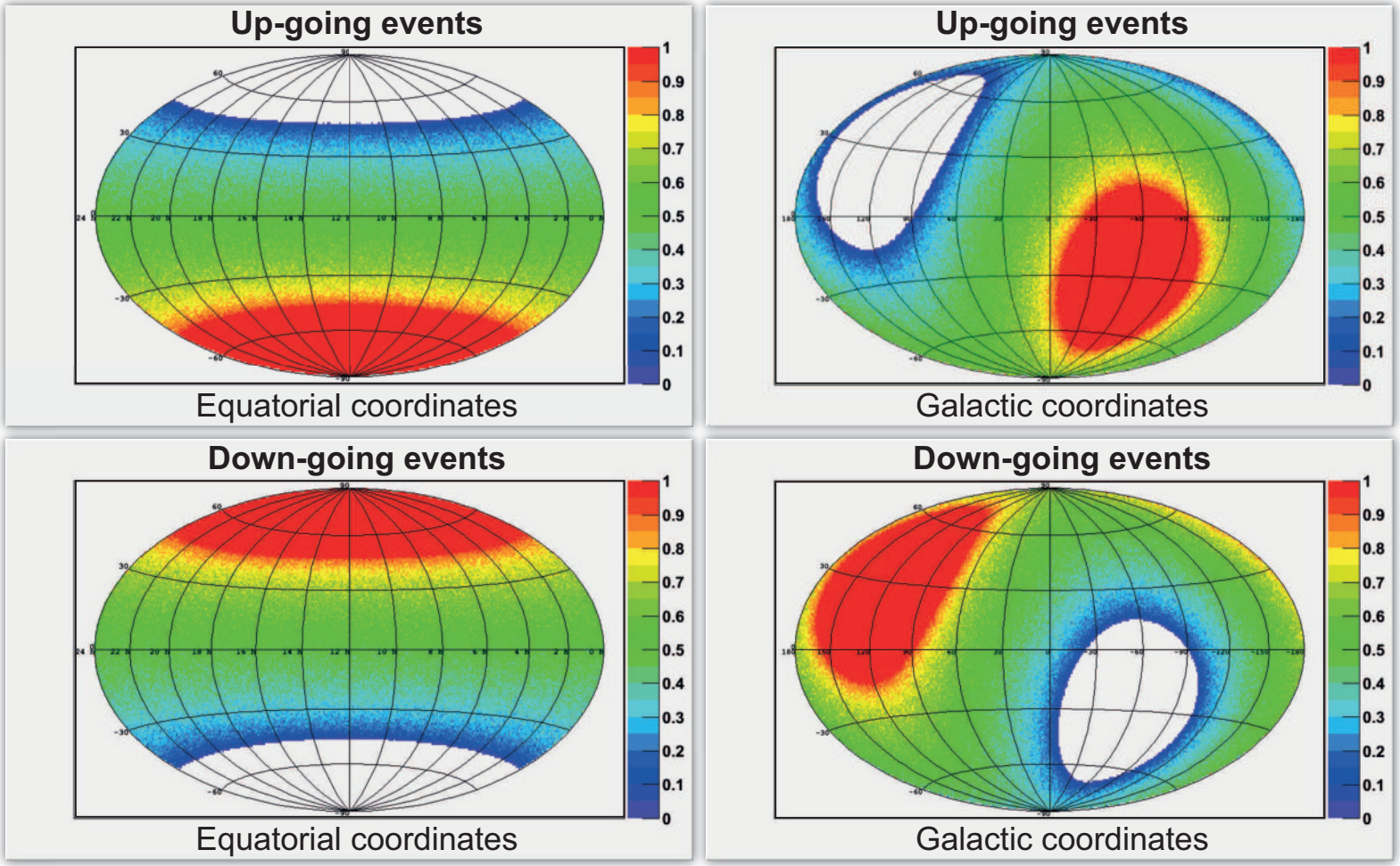

ANTARES sky visibility with up-going and down-going events in equatorial and galactic coordinates.

[From Ch. Perrina, "Search for cosmic high energy down-going neutrino fluxes from point-like sources with ANTARES," J. Phys. Conf. Ser. **689** (2016) 012013; the data are shown at p. 325.]

ANTARES upper limit (magenta line) on the neutrino flux integrated over the solid angle $\Delta\Omega = 0.145$ sr corresponding to the Galactic Plane region $|\ell| < 40°$, $|b| < 3°$. The limit is compared to theoretical expectations, assuming a CR cut-off at 5×10^7 GeV, both with (KRA_γ) and without (KRA) spectral hardening [the KRA model assumes a Kraichnan spectrum for the galactic turbulent magnetic field].

The neutrino flux (dot-dashed line) extrapolated from the *Fermi*/LAT diffuse γ-flux (purple circles) up to IceCube energies is shown. The implied flux from the 37 events from the IceCube 3 years sample is shown as dark green triangles. ▷

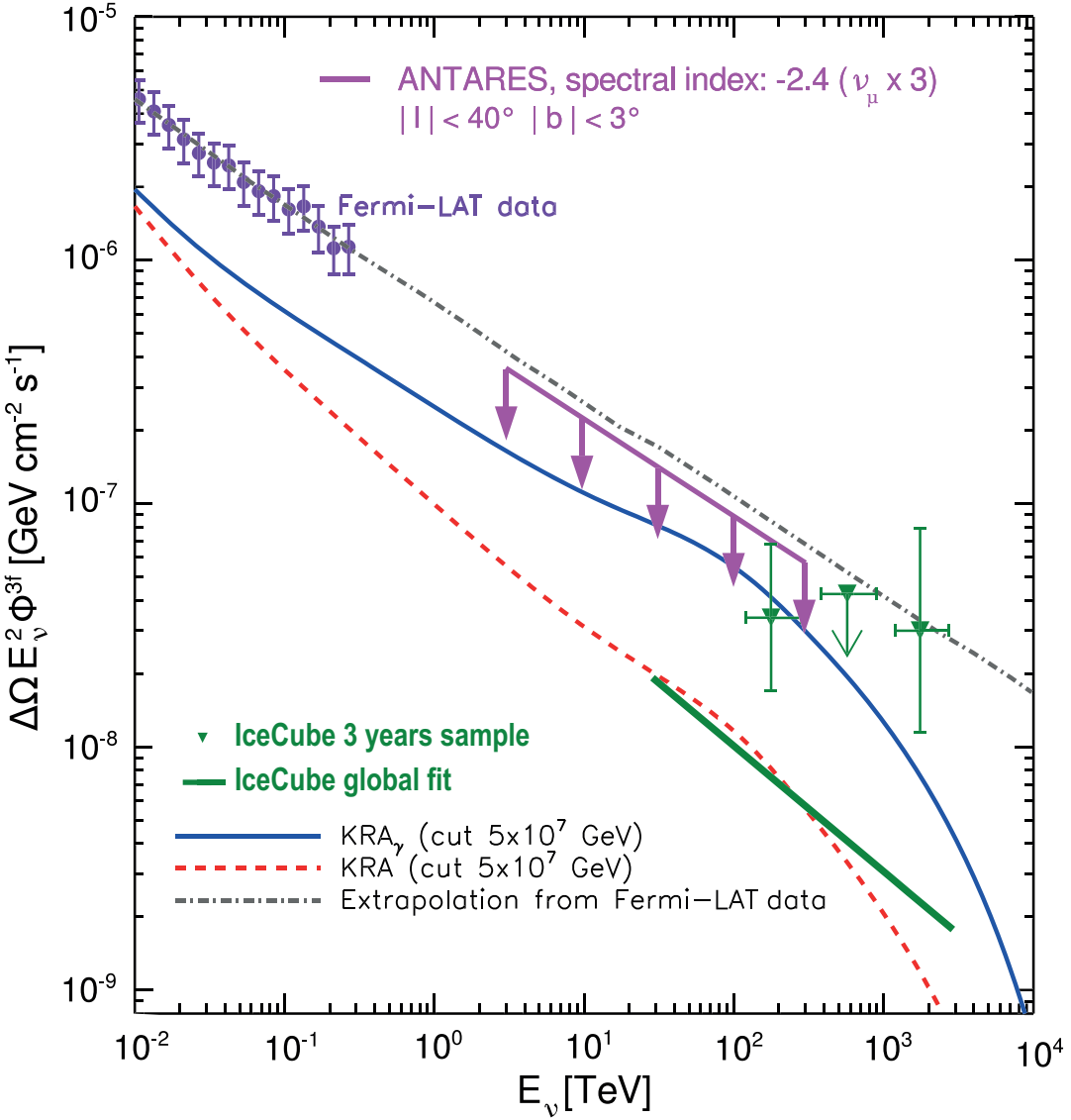

The solid dark green line shows the all-sky average neutrino intensity from the IceCube global fit analysis in the energy range 25 TeV–2.8 PeV integrated over $\Delta\Omega$. [See reference below.]

[Figure in previous slide is taken from S. Adrian-Martinez *et al.* (ANTARES Collaboration), "Constraints on the neutrino emission from the Galactic Ridge with the ANTARES telescope," Phys. Lett. B **760** (2016) 143–148, arXiv:1602.03036 [astro-ph.HE].]

As is seen from Figure at p. 323, the region of the sky where declinations are larger than $\sim 45^\circ$ is not covered by the observation of up-going events, but it becomes accessible by studying down-going ones.

The figure on the right shows 90% C.L. flux upper limits on a ν_μ flux $\propto E_\nu^{-2}$ and ANTARES sensitivity as a function of the source declination. The results of a down-going analysis are presented in azure. They provide the telescope sensitivity and upper limits on a cosmic neutrino flux originated from a list of candidate sources with $\delta > 36^\circ$. IceCube and ANTARES results, obtained through the analysis of up-going tracks, are also shown for comparison. ▷

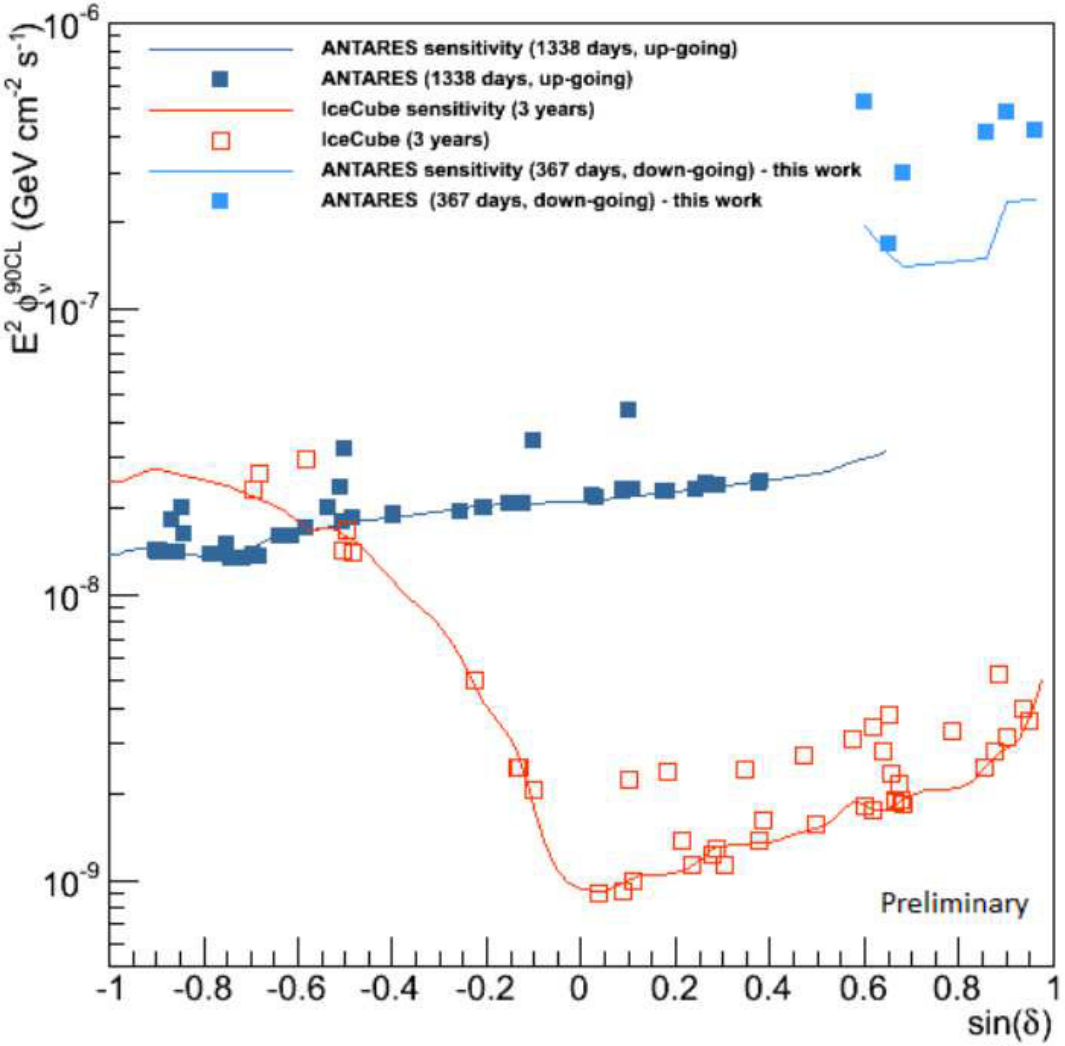

[From Ch. Perrina, "Search for cosmic high energy down-going neutrino fluxes from point-like sources with ANTARES," J. Phys. Conf. Ser. **689** (2016) 012013.]

Neutrinos from quasar outflows.

The Very Large Telescope (VLT) team of the European Southern Observatory (ESO) in Chile reported (2012) that a mass equal to about 400 suns is streaming away from the quasar SDSS J1106+1939 every year at a speed of 8000 km/s.

"We have discovered the most energetic quasar outflow known to date. The rate that energy is carried away by this huge mass of material ejected at high speed from SDSS J1106+1939 is at least equivalent to two million million times the power output of the Sun. This is about 100 times higher than the total power output of the Milky Way galaxy – it's a real monster of an outflow. This is the first time that a quasar outflow has been measured to have the sort of very high energies that are predicted by theory,"

Nahum Arav, team leader

Theoretical simulations of galaxies suggest quasar outflows could explain how the mass of a galaxy is linked to its central black hole mass, and why there are so few "large" galaxies in the Universe.

[From URL: ⟨http://metanerds.blogspot.ru/2012/11/massive-quaser-outflow.html⟩.]

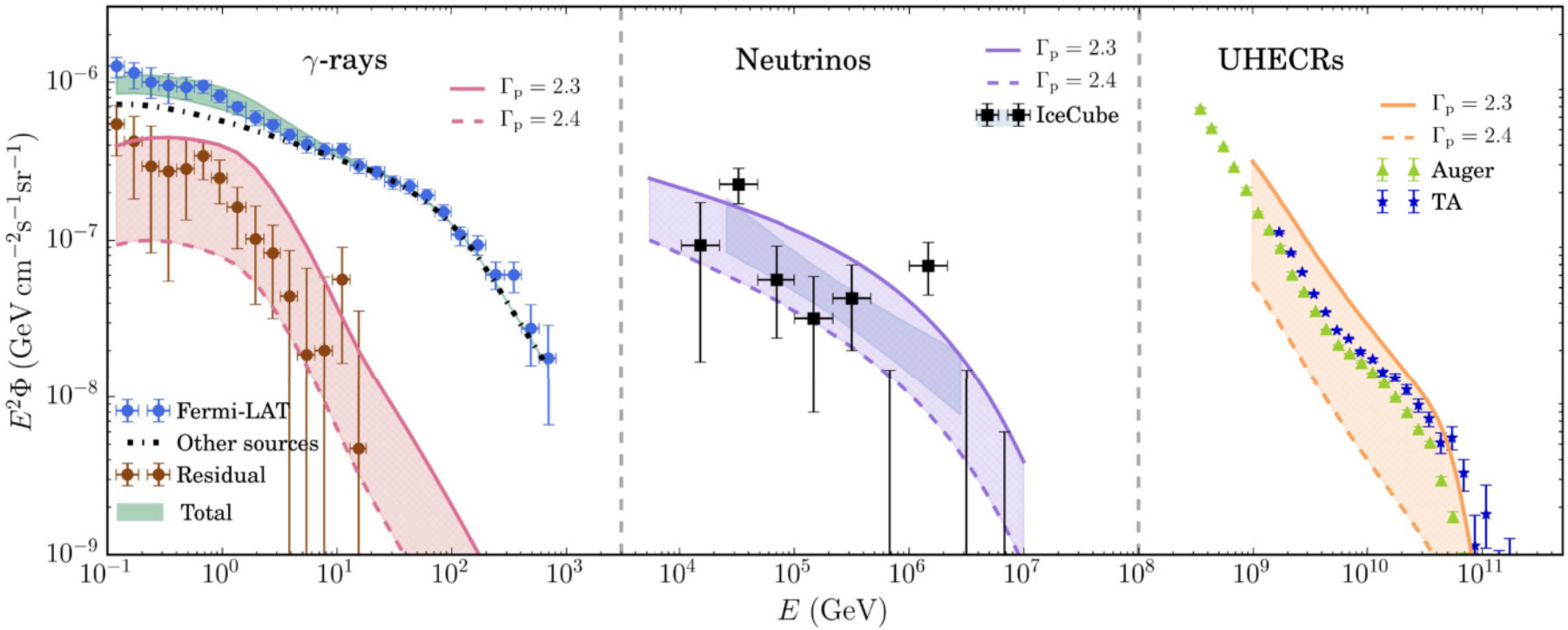

△ γ-ray, neutrinos, and UHECRs produced by quasar outflows. The fluxes for the power-law index $\Gamma_p = 2.3$ and 2.4 are shown by the hatched regions. "Other sources" include contributions to the extragalactic γ-ray background from blazars, radio galaxies and star-forming galaxies (plotted in comparison with the recent *Fermi*/LAT data); The cumulative neutrino background observed by IceCube, represented by the data points and the gray band. Right panel shows the data from Pierre Auger Observatory, Telescope Array, and derived cumulative UHECR intensity.

Conclusion: Quasar outflows can naturally explain all three messengers with parameters consistent with observations and theoretical models.

[From X. Wang and A. Loeb, "From Ultra high energy cosmic rays from non-relativistic quasar outflows," Phys. Rev. D **95** (2017) 063007, arXiv:1611.07616 [astro-ph.HE].]

7.11 Testing decay of astrophysical neutrinos.

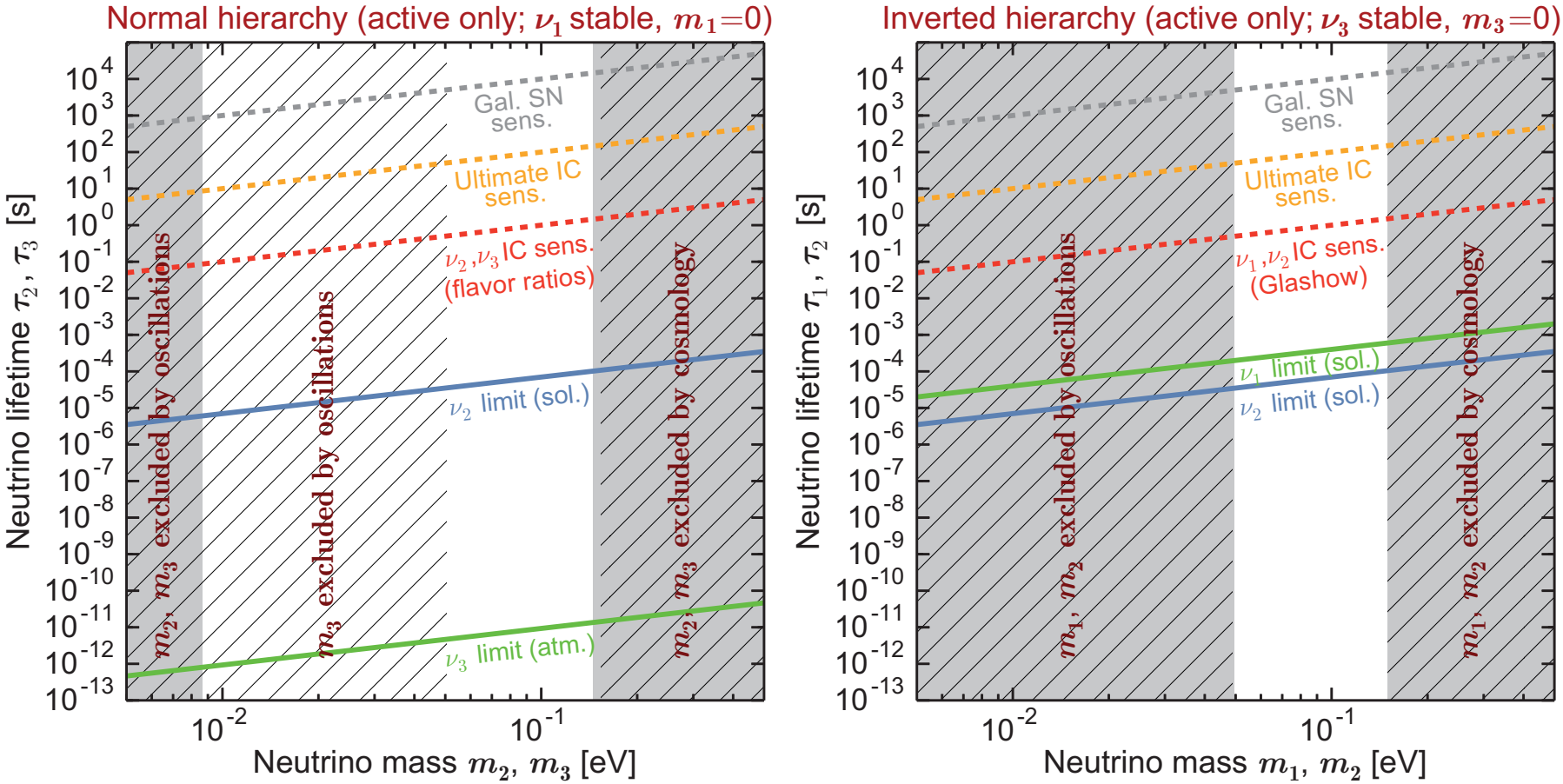

Figure shows present constraints and future sensitivities on lifetimes and masses of mass eigenstates ν_i $(i = 1, 2, 3)$, where and below, ν_i stands for $\nu_i + \overline{\nu}_i$. with hatched gray disallowed, hatched white allowed only for some eigenstates, and non-hatched white allowed for all. The thick red dashed lines indicate the estimates sensitivity. *Left panel*: Normal hierarchy. *Right panel*: Inverted hierarchy.

In the normal hierarchy (NH), ν_2 and ν_3 are unstable and heavier than ν_1, which is stable. In the inverted hierarchy (IH), ν_1 and ν_2 are unstable and heavier than ν_3, which is stable.

Short explanation of labels in the figure on previous slide:

- "Gal. SN sens," – Galactic supernova sensitivity of $\tau/m \gtrsim 10^5$ s eV^{-1} that could be reached by detecting neutrinos of 10 MeV from a supernova 10 kpc away.
- "Ultimate IC sens," – Ultimate IceCube sensitivity of $\tau/m \gtrsim 10^3$ s eV^{-1} could be reached by detecting neutrinos of 100 TeV from sources 1 Gpc away.
- "IC sens. (flavor ratio)" – Estimated IceCube sensitivity of $\tau/m \gtrsim 10$ s eV^{-1}.
- "IC sens. (Glashow)" – For $\overline{\nu}_e$ of energies around 6.3 PeV, the Glashow resonance is expected to increase the shower rate and thus the IceCube sensitivity.
- "limit (sol.)" – Limit from solar neutrino experiments.
- "limit (atm.)" – Limit from atmospheric neutrino experiments.

[From M. Bustamante *et al.*, "Testing decay of astrophysical neutrinos with incomplete information," Phys. Rev. D **D95** (2017) 063013, arXiv:1610.02096 [astro-ph.HE].]

7.12 IceCube-170922A.

Previous detections of individual astrophysical sources of neutrinos are limited to the Sun and the supernova 1987A, whereas the origins of the diffuse flux of high-energy cosmic neutrinos remain unidentified. On 22 September 2017, IceCube Collaboration detected a high-energy neutrino, IceCube-170922A, with an energy of about 290 TeV. Its arrival direction was consistent with the location of a known γ-ray blazar, TXS 0506+056, observed to be in a flaring state. An extensive multiwavelength campaign followed, ranging from radio frequencies to γ-rays. These observations characterize the variability and energetics of the blazar and include the detection of TXS 0506+056 in very-high-energy γ-rays.

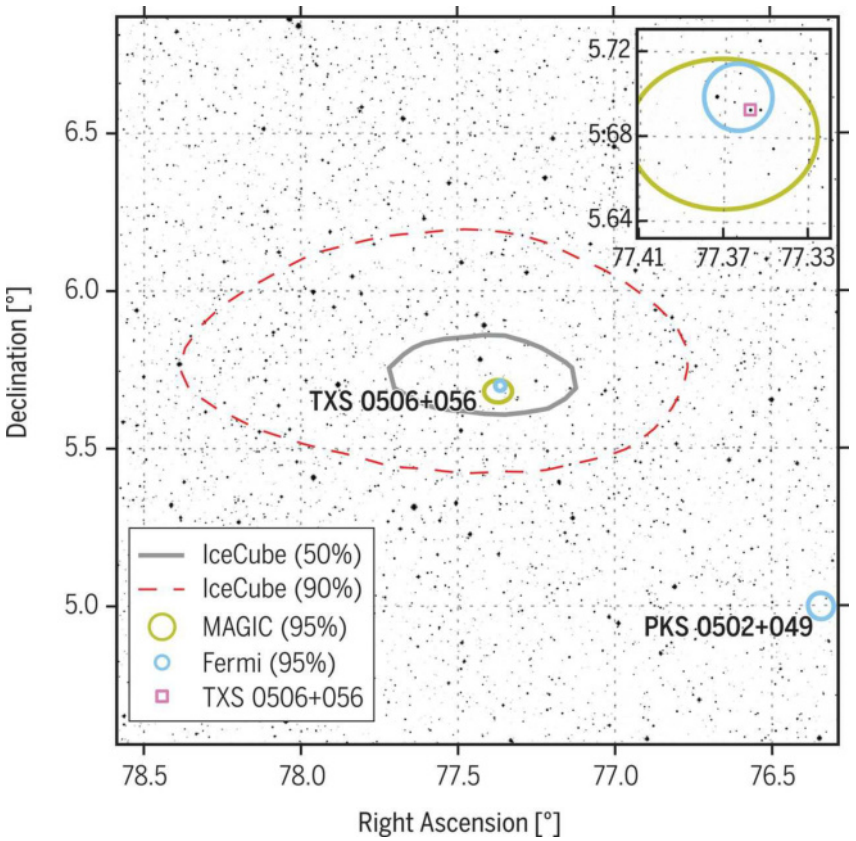

This observation of a neutrino in spatial coincidence with a γ-ray-emitting blazar during an active phase suggests that blazars may be a source of high-energy neutrinos.

[This section is based on M.G. Aartsen *et al.* (IceCube, Fermi-LAT, MAGIC, AGILE, ASAS-SN, HAWC, H.E.S.S., INTEGRAL, Kanata, Kiso, Kapteyn, Liverpool Telescope, Subaru, Swift, NuSTAR, VERITAS, and VLA/17B-403 Collaborations) "Multimessenger observations of a flaring blazar coincident with high-energy neutrino IceCube-170922A," Science **361**, Iss. 6398 (2018) eaat1378, arXiv:1807.08816 [astro-ph.HE].]

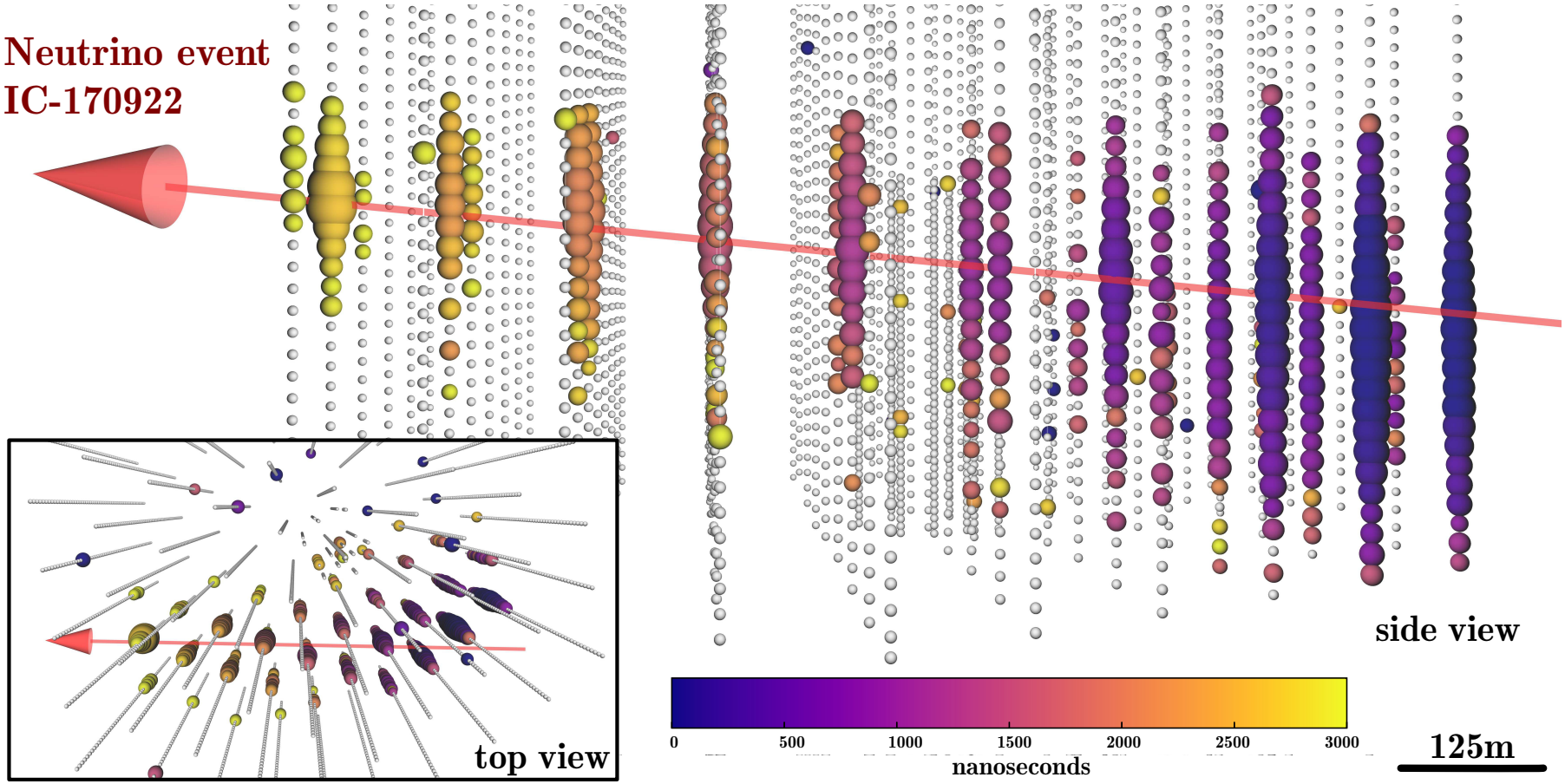

The time at which a digital optical module (DOM) observed a signal is reflected in the color of the hit. Times shown are relative to the first DOM hit according to the track reconstruction, and earlier and later times are shown with the same colors as the first and last times, respectively. The total time the event took to cross the detector is ~ 3000 ns. The size of a colored sphere is proportional to the logarithm of the amount of light observed at the DOM. The best-fitting track direction (arrow) consistent with a zenith angle $5.7^{+0.5}_{-0.3}$ degrees below the horizon.

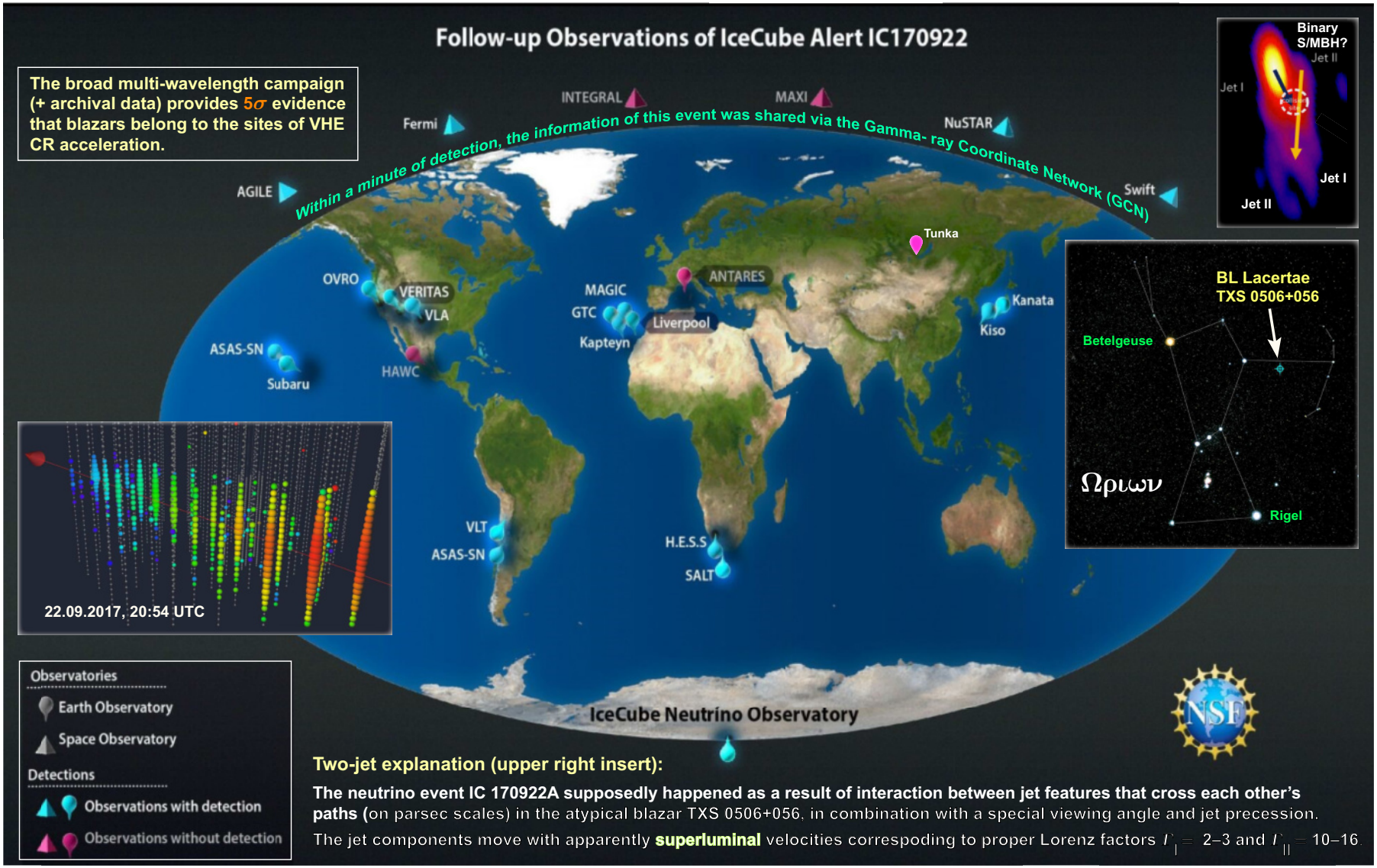

[Figure uses the data from several sources. For the two-jet interpretation of the IC-170922A event, see S. Britzen *et al.*, "A cosmic collider: Was the IceCube neutrino generated in a precessing jet-jet interaction in TXS 0506+056?" Astron. Astrophys. **630** (2019) A103, Astron. Astrophys. **632** (2019) C3 (Corrigendum).]

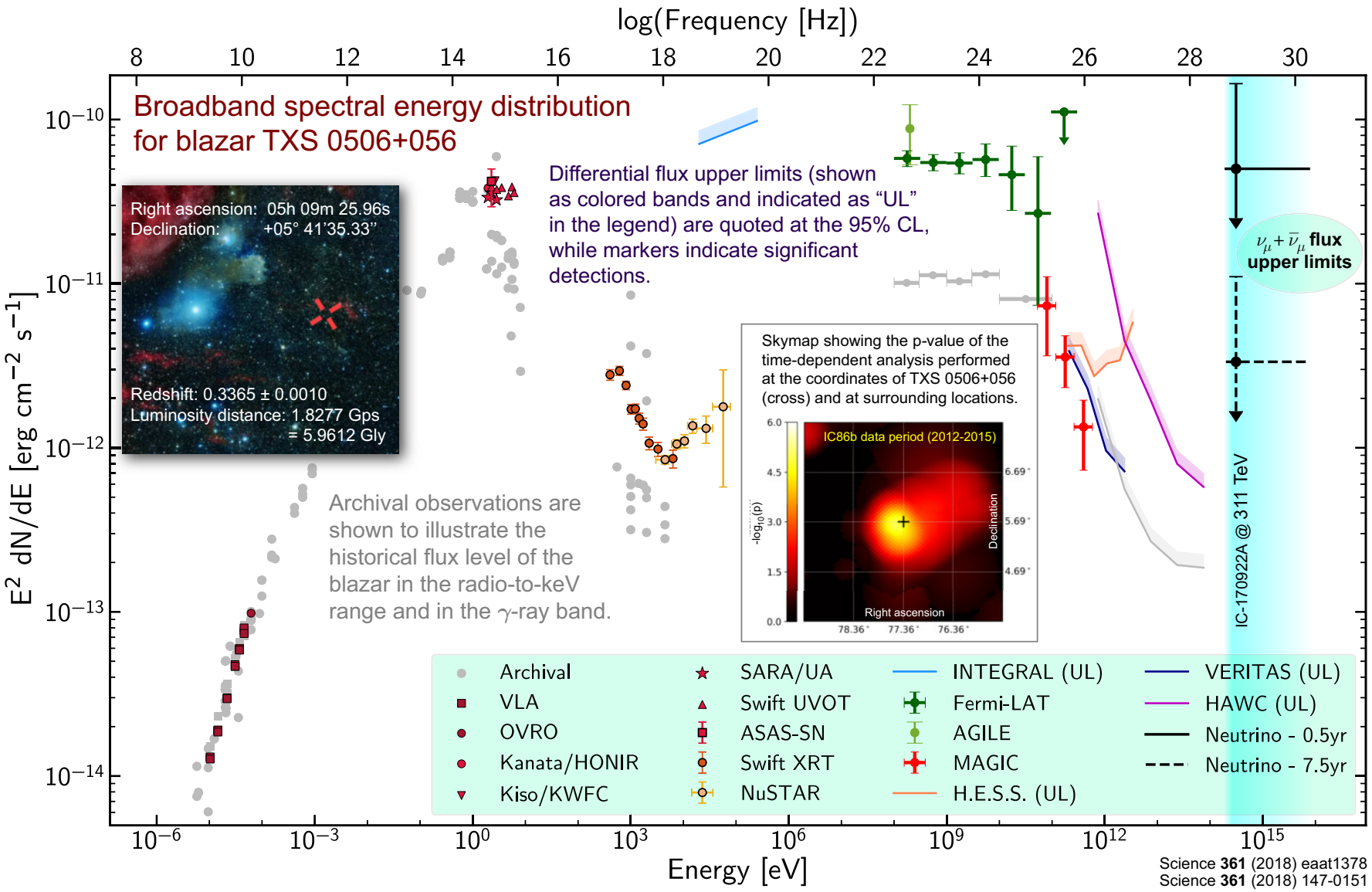

Representative $\nu_\mu + \overline{\nu}_\mu$ flux upper limits that produce on average one detection like IC-170922A over a period of 0.5 and 7.5 years are shown, assuming a spectrum of $dN/dE_\nu \propto E_\nu^2$ at the most probable (anti)neutrino energy $E_\nu^{\text{prob}} = 311$ TeV (more recent estimation yields $E_\nu^{\text{prob}} \approx 290$ TeV).

7.13 Astrophysical τ neutrinos in IceCube.

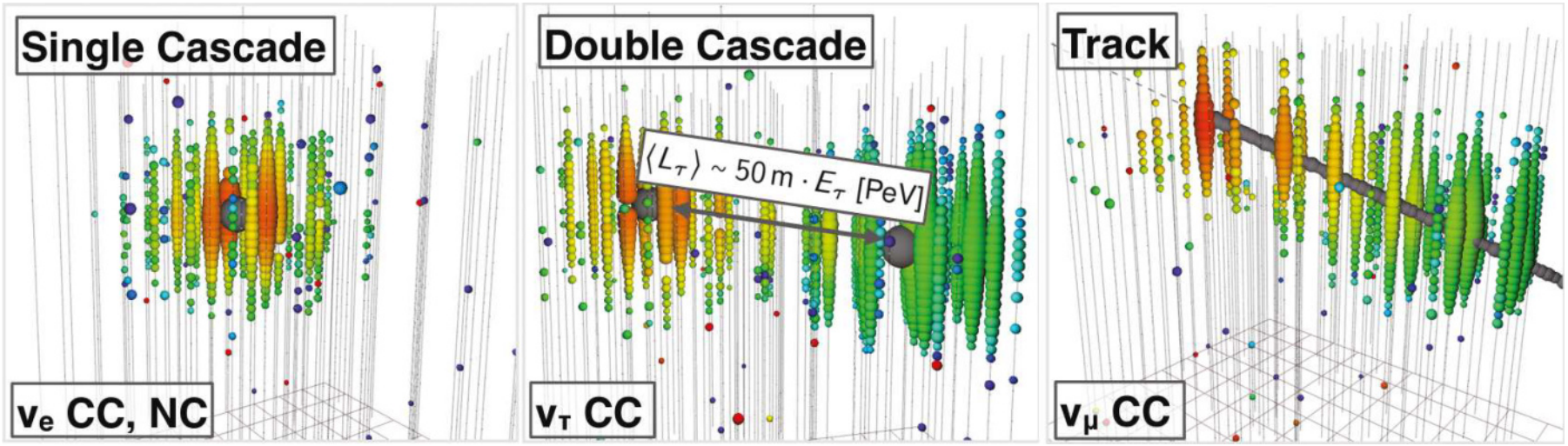

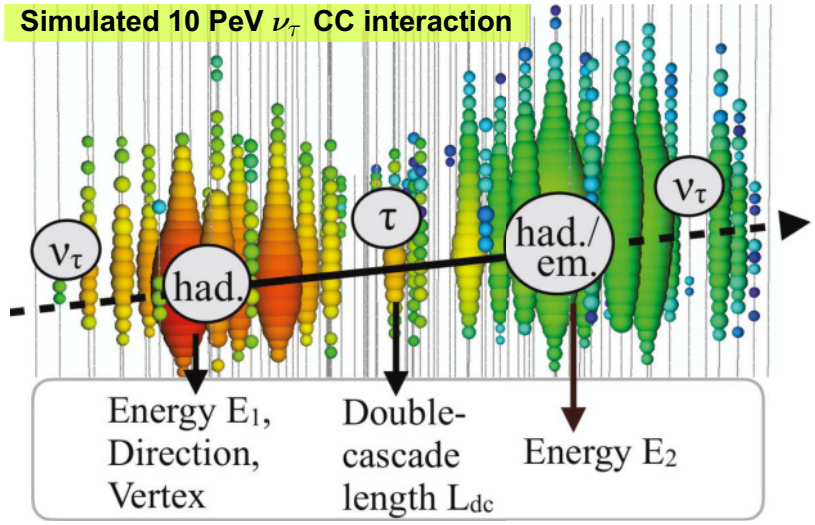

△ Simulated HE event topologies in IceCube:

- **Single cascade** – ν_e CC and all NC interactions ($\delta\theta = (15-20)^\circ$, $\delta E/E \approx 15\%$).
- **Double cascade** – ν_τ CC interaction with the subsequent τ decay producing a hadronic or electromagnetic cascade ($E_\tau \gtrsim 100$ TeV).
- **Track** – (i) ν_μ CC interaction, (ii) ν_τ CC interaction with subsequent decay of the τ into a muon, (iii) single atmospheric muon, (iv) atmospheric muon group, or (i)+(iv), etc. ($\delta\theta \lesssim 1^\circ$, $\delta E/E$ rather uncertain).

[Figures are taken from J. Stachurska, "Astrophysical tau neutrinos in IceCube," Ph.D. Thesis, Humboldt-Universität zu Berlin, April 2020.]

τ-neutrino candidates

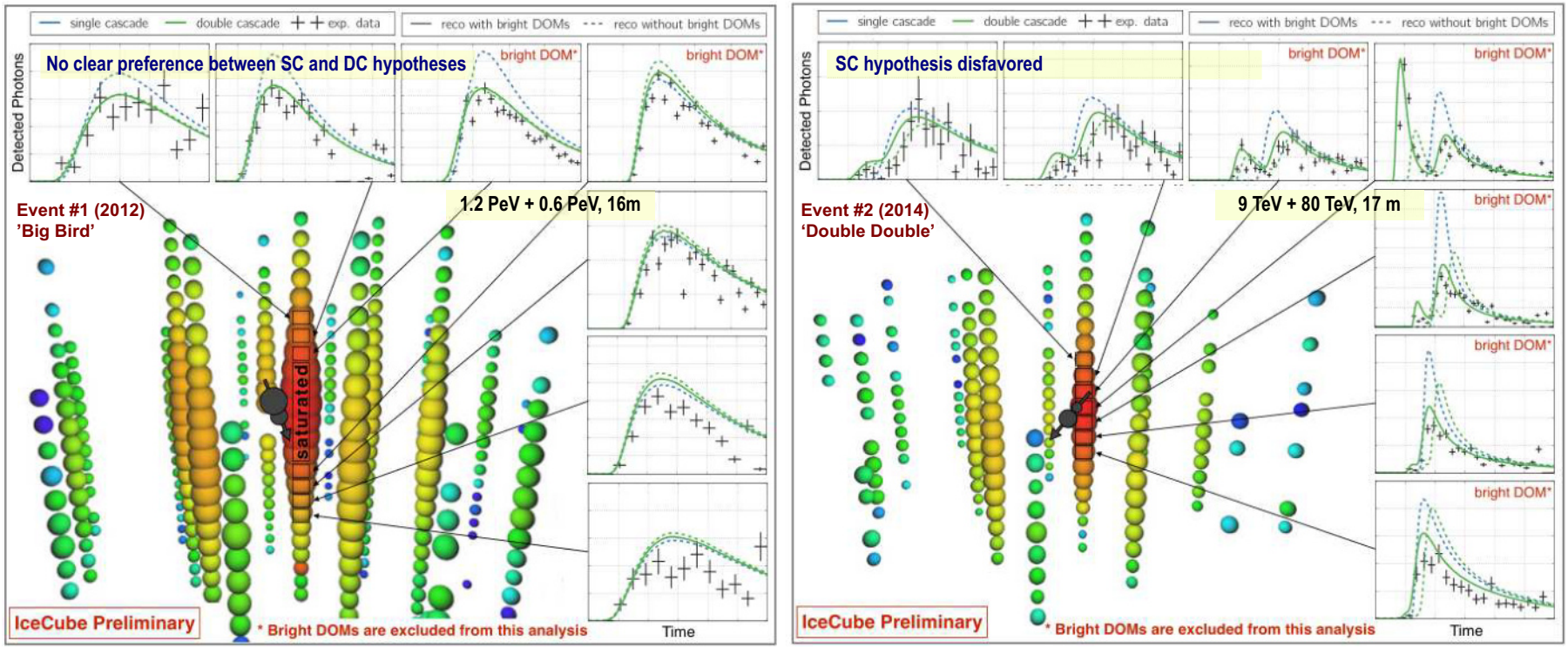

Double cascade (DC) event candidates: The reconstructed DC positions (directions) are indicated as grey circles (arrows). The size of the circles illustrates the relative deposited energy of the two cascades. For several digital optical modules (DOMs), the photon counts over time are displayed alongside with the predicted probability distribution functions (PDFs) for a single and double cascade hypothesis. Compatibility each of the cascades with a background hypothesis is not fully excluded. Note: "Bright" DOMs have collected 10 times more light than the average DOM for an event and can bias the reconstruction at the highest measured energies.

[Figure is taken from J. Stachurska (for the IceCube Collaboration) "IceCube high energy starting events at 7.5 years – new measurements of flux and flavor," Eur. Phys. J. Web. Conf. **207** (2019) 02005.]

7.14 What's next? P-ONE @ ONC, PLEνM,...

The νN cross section increases with increasing neutrino energy (see Sect. **8**), making the Earth significantly less transparent to neutrinos with energies above ≈ 50 TeV.[a] Neutrino telescopes are therefore effectively blind to very high-energy neutrinos crossing the Earth.

In order to obtain an all-sky neutrino exposure, it will therefore be essential to combine the information from the various telescopes. Each telescope is designed to send alerts to the entire astronomy community, including the other neutrino telescopes, making it possible to follow in real time the temporal evolution of a transient event emitting in the PeV energy region.

References:

- E. Resconi, "High energy neutrino astronomy: The need of a planetary scale effort," report at UK HEP Forum "Experimental physics with cosmic particles," September 24–25, 2019.
- K. Holzapfel (for the P-ONE team), "P-ONE – Pacific Ocean Neutrino Explorer," report at EPS-HEP 2019, July 10–17, 2019.
- M. Agostini *et al.*, "The Pacific Ocean Neutrino Experiment, " Nature Astron. **4** (2020) 913–915 (comment), arXiv:2005.09493 [astro-ph.HE].
- M. Agostini *et al.*, "The Pacific Ocean Neutrino Experiment: A new cabled observatory within Ocean Networks Canada," Snowmass 2021 – Letter of Interest.

Abbreviations:

P-ONE – Pacific Ocean Neutrino Explorer/Experiment
ONC – Ocean Networks Canada (northeast Pacific Ocean, Salish Sea)
PLEνM = PLEnuM – Planetary Neutrino Monitoring System (very tentative name)

[a] E.g., $\lesssim 20\%$ (5%) of the neutrinos with energy of 100 TeV (1 PeV) can cross the Earth at $\cos\theta = -0.8$.

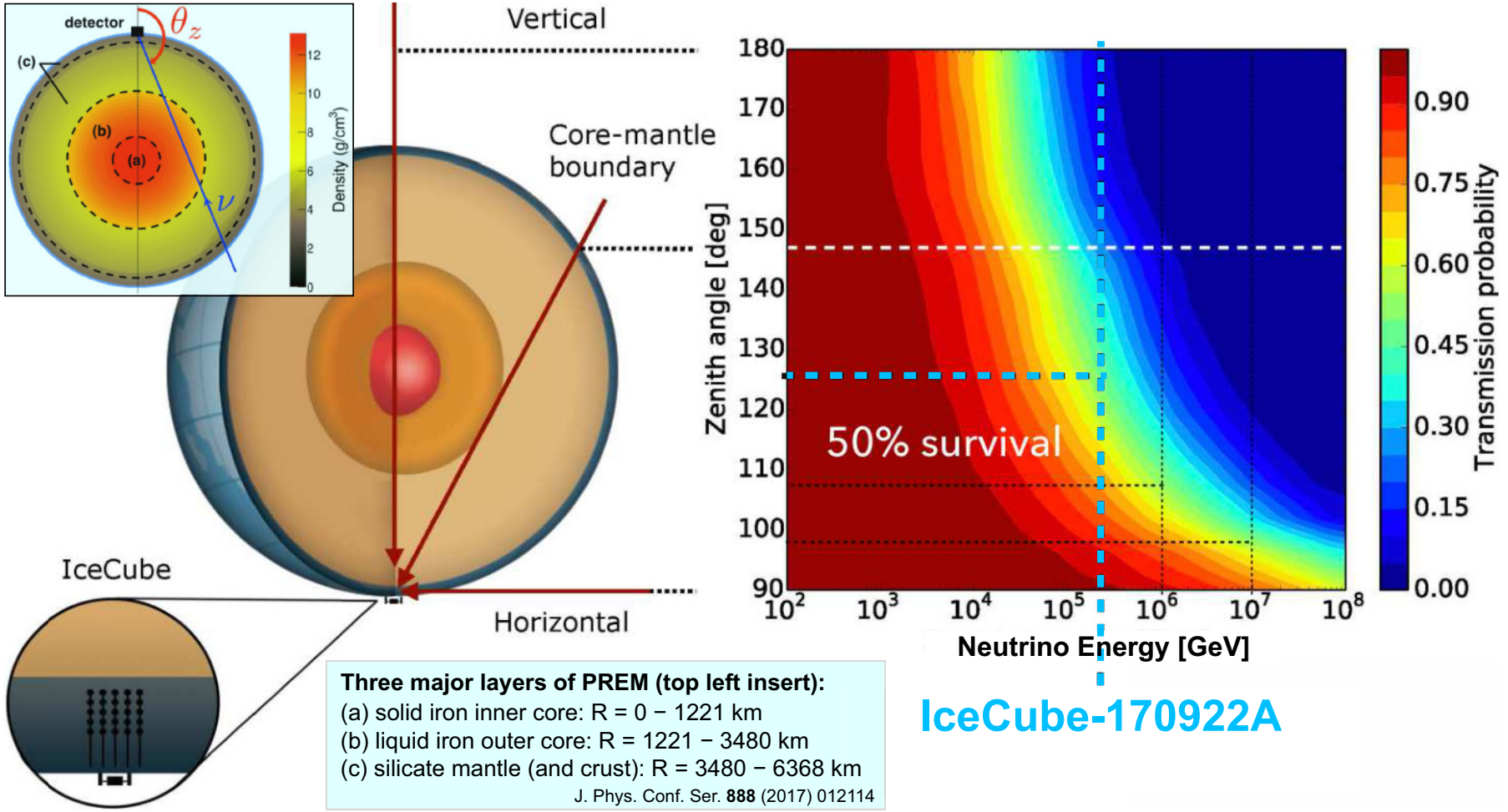

Three major layers of PREM (top left insert):
(a) solid iron inner core: R = 0 − 1221 km
(b) liquid iron outer core: R = 1221 − 3480 km
(c) silicate mantle (and crust): R = 3480 − 6368 km
J. Phys. Conf. Ser. **888** (2017) 012114

Neutrino absorption in the Earth. *Left panel*: Absorption is observed by measuring how the neutrino energy spectrum changes with the zenith angle. *Right panel*: Standard model prediction for the transmission probability of neutrinos passing through the Earth as a function of energy and zenith angle. Both CC and NC interactions are included but the latter lead to the neutrino energy loss.

[Figure is taken from M. G. Aartsen *et al.* (IceCube Collaboration), "Measurement of the multi-TeV neutrino interaction cross-section with IceCube using Earth absorption," Nature **55** (2017) 596–600, arXiv:1711.08119 [hep-ex].]

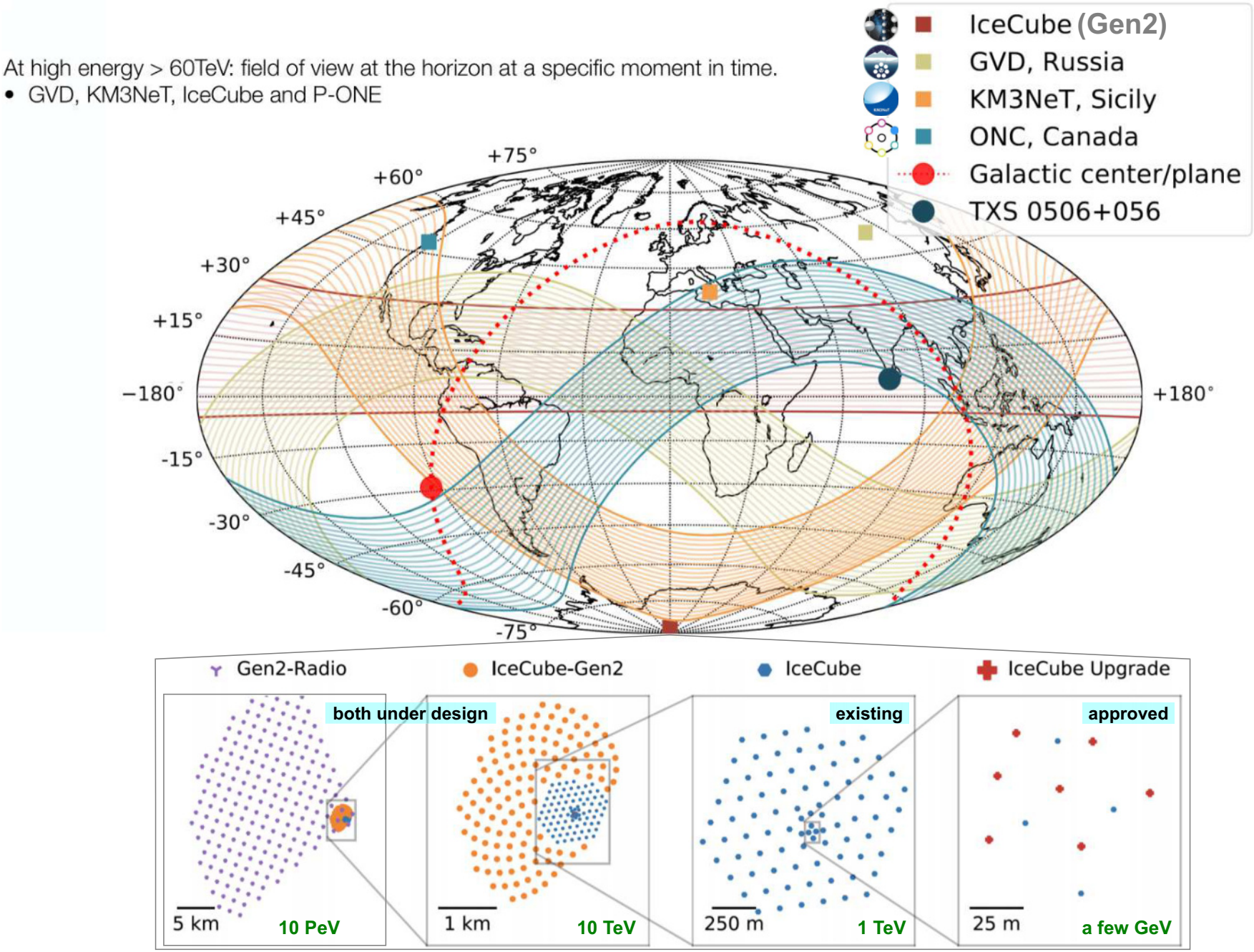
At high energy > 60TeV: field of view at the horizon at a specific moment in time.
• GVD, KM3NeT, IceCube and P-ONE
IceCube (Gen2)
GVD, Russia
KM3NeT, Sicily
ONC, Canada
Galactic center/plane
TXS 0506+056
+75°
+60°
+45°
+30°
+15°
−180°
+180°
-15°
-30°
-45°
-60°
-75°
Gen2-Radio
IceCube-Gen2
IceCube
IceCube Upgrade
both under design
existing
approved
5 km
10 PeV
1 km
10 TeV
250 m
1 TeV
25 m
a few GeV

P-ONE will be installed and operated within one of the world's largest and most advanced cabled ocean observatories, ONC. ONC is composed of many infrastructures, the largest being the North East Pacific Time-series Underwater Networked Experiment (NEPTUNE).

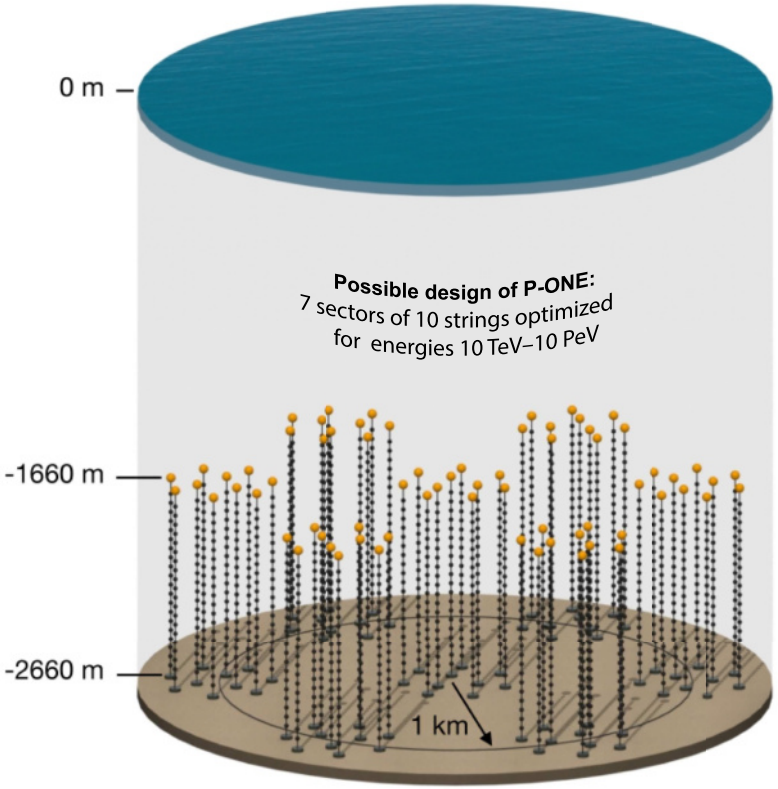

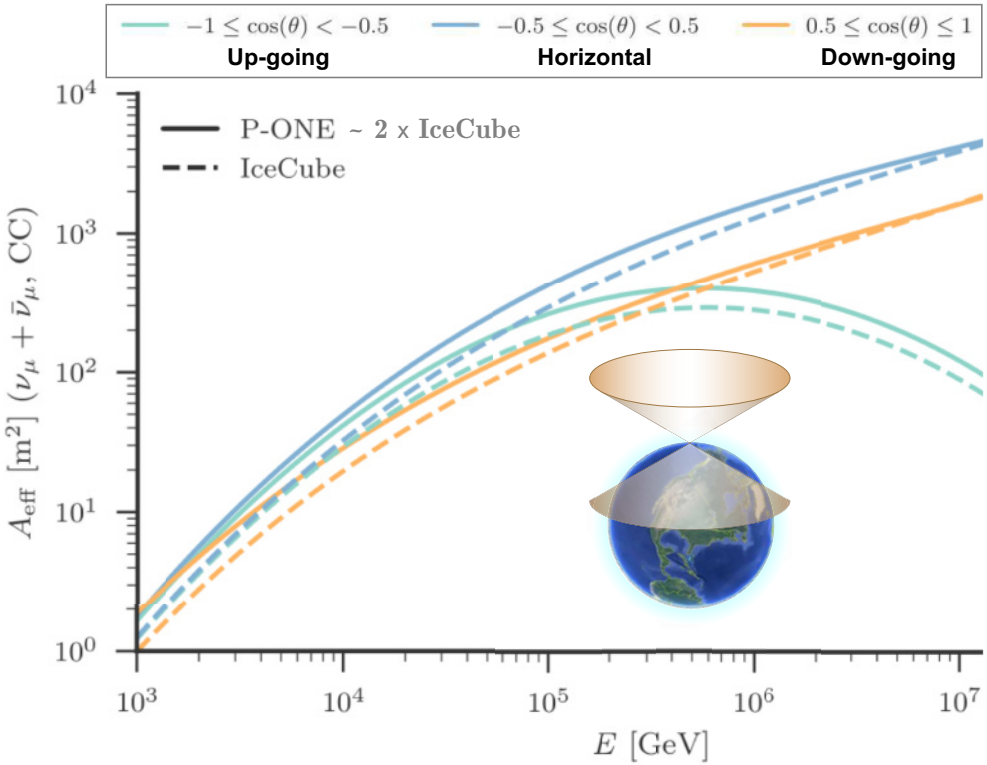

The effective area of P-ONE is calculated by requiring a minimum deposit of 100 GeV of energy, and a minimum track of 100 m in one sector. Calculations account for the absorption effect, which is more relevant for the HE neutrinos transiting deep through the Earth. Neutrinos traveling in the horizontal declination band are nearly absorption-free, even at energies above the PeV scale.

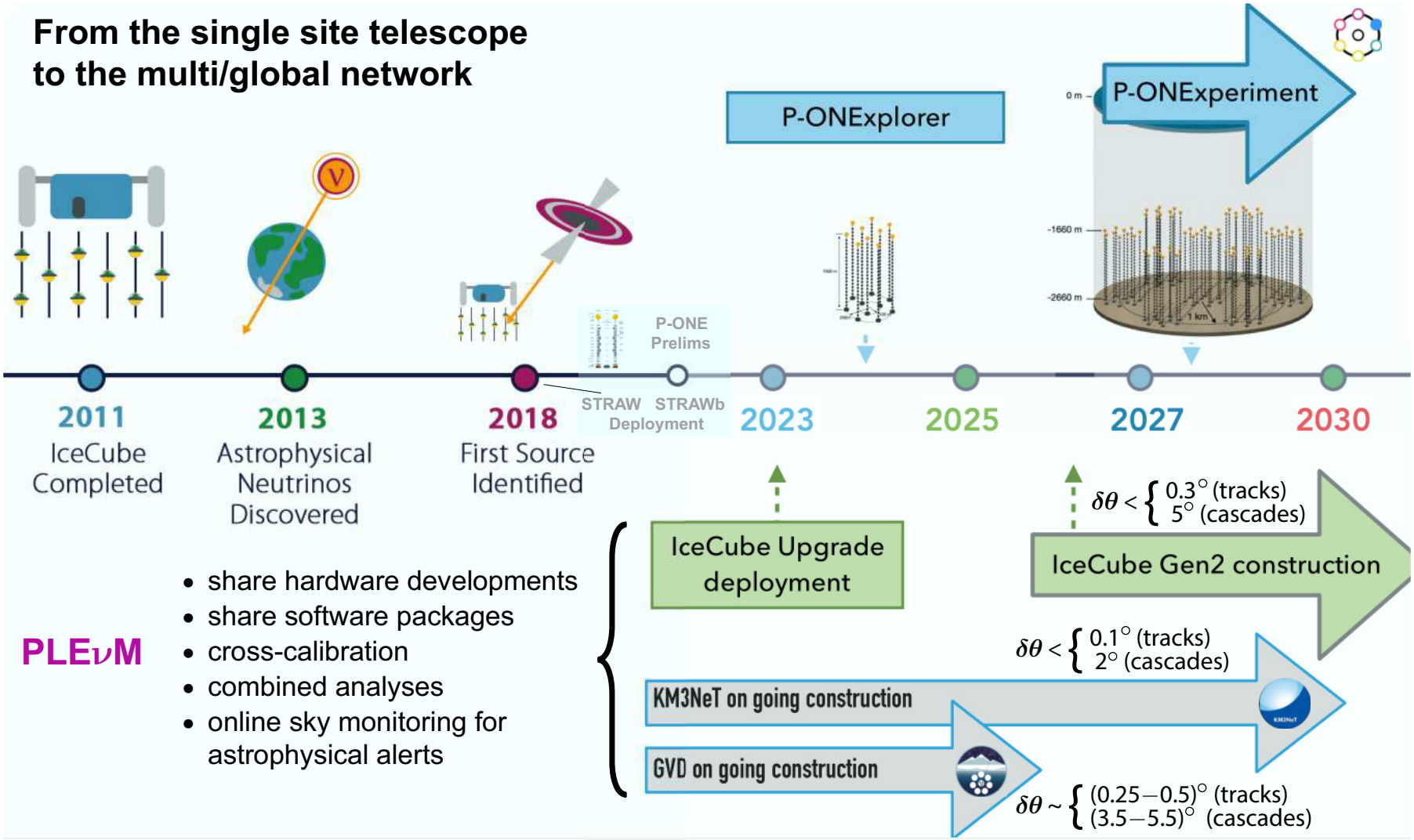

Boost of the discovery potential for cosmic accelerators up to factor 100!

For more details, see p. 957 in Appendix P.

7.15 Cosmogenic neutrino production.

During their journey from a source to an observer, UHECRs traverse cosmological distances and interact with magnetic fields and radiation fields of the astrophysical backgrounds, mainly the cosmic microwave (CMB), extragalactic light (ELB), and infrared (IRB).[a]

◦ The energy spectrum of protons[b] is affected almost only by the CMB and the processes that affect the propagation are pion photoproduction and e^+e^- pair photoproduction:

$$p+\gamma_{\text{bg}} \to p+\pi^0, \quad p+\gamma_{\text{bg}} \to n+\pi^+, \quad \text{and} \quad p+\gamma_{\text{bg}} \to p+e^++e^-.$$

Less important, but not entirely insignificant, are the multipion production processes:

$$p+\gamma_{\text{bg}} \to p+2\pi^0, \quad p+\gamma_{\text{bg}} \to p+\pi^++\pi^-, \quad p+\gamma_{\text{bg}} \to n+\pi^0+\pi^+, \quad \text{etc.}$$

◦ Propagation of nuclei is also almost negligibly affected by the ELB and IRB; the relevant interaction processes are photodisintegration/photoerosion, $(A,Z)+\gamma_{\text{bg}} \to (A',Z')+X$ (where the daughter nucleus (A',Z') can be stable or unstable and X can contain ps, ns, αs, etc., see below) and very rarely considered pair production, $(A,Z)+\gamma_{\text{bg}} \to (A,Z)+e^++e^-$, and nuclear pion photoproduction:

$$(A,Z)+\gamma_{\text{bg}} \to (A-1,Z)+p+\pi^-, \quad (A,Z)+\gamma_{\text{bg}} \to (A-1,Z)+n+\pi^0,$$
$$(A,Z)+\gamma_{\text{bg}} \to (A,Z-1)+n+\pi^+, \quad (A,Z)+\gamma_{\text{bg}} \to (A,Z-1)+p+\pi^0.$$

Some additional processes can make a minor contribution, e.g., muon pair photoproduction, $p\gamma_{\text{bg}} \to p\mu^+\mu^-$, slightly increases the cosmogenic neutrino flux and elastic scattering off the background γs, $(A,Z)+\gamma_{\text{bg}} \to (A,Z)+\gamma$, increases the cosmogenic photon flux.

[a] For some additional details, see [**CR**] (URL is given at p. 231.)

[b] The neutron mean path $\Gamma_n c\tau_n \approx 85.5\left(\Gamma_n/10^{10}\right)$ kps is much shorter than all other time scales involved.

A little more about photodisintegration.[a]

To describe the changes in abundance of the heavy nuclei as a result of the UHECR interaction with the photon background (mainly CMB), a nuclear reaction network including all interactions of interest must be used. The chosen set of nuclear species is coupled by a system of differential equations ("transport equations") corresponding to all the reactions affecting each nucleus, i.e. mainly photodisintegrations and β-decays. The equilibrium rate of change of the number density $N_{Z,A}$ of nucleus (Z,A) with charge number Z and mass number A can be written as

$$
\begin{aligned}
dN_{Z,A}/dt = {} & N_{Z+1,A}\lambda_{\beta}^{Z+1,A} + N_{Z-1,A}\lambda_{\beta}^{Z-1,A} - N_{Z,A}\lambda_{\beta}^{Z,A} \qquad \leftarrow \text{sources of } \nu_e, \overline{\nu}_e, \text{ and } e^{\pm} \\
& + N_{Z,A+1}\lambda_{\gamma,n}^{Z,A+1} + N_{Z+1,A+1}\lambda_{\gamma,p}^{Z+1,A+1} + N_{Z+2,A+4}\lambda_{\gamma,\alpha}^{Z+2,A+4} \\
& + N_{Z,A+2}\lambda_{\gamma,nn}^{Z,A+2} + N_{Z+2,A+2}\lambda_{\gamma,pp}^{Z+2,A+2} + N_{Z+4,A+8}\lambda_{\gamma,\alpha\alpha}^{Z+4,A+8} \\
& + N_{Z+1,A+2}\lambda_{\gamma,np}^{Z+1,A+2} + N_{Z+2,A+5}\lambda_{\gamma,n\alpha}^{Z+2,A+5} + N_{Z+3,A+5}\lambda_{\gamma,p\alpha}^{Z+3,A+5} \\
& - N_{Z,A}\sum_{X}\lambda_{\gamma,X}^{Z,A},
\end{aligned}
$$

where $\lambda_{\beta}^{Z,A}$ is the β-decay rate of nucleus (Z,A) and $\lambda_{\gamma,X}^{Z,A}$ – its rate of photoerosion followed by the emission of a single neutron $(X=n)$, proton $(X=p)$ or ^{4}He nuclei $(X=\alpha)$ or by the emission of multiple particles such as nn, pp, np, $n\alpha$, $p\alpha$, $\alpha\alpha$, ..., including all open channels for a given background photon energy distribution, that is, there is something else to add to the equations.

The photodisintegration effect is illustrated below for source of ^{56}Fe nuclei with energy 10^{21} eV.

[a] E. Khan, S. Goriely, D. Allard, E. Parizot, T. Suomijärvi, A. J. Koning, S. Hilaire, M. C. Duijvestijn, "Photodisintegration of ultra-high-energy cosmic rays revisited," Astropart. Phys. **23** (2005) 191–201, arXiv:astro-ph/0412109.

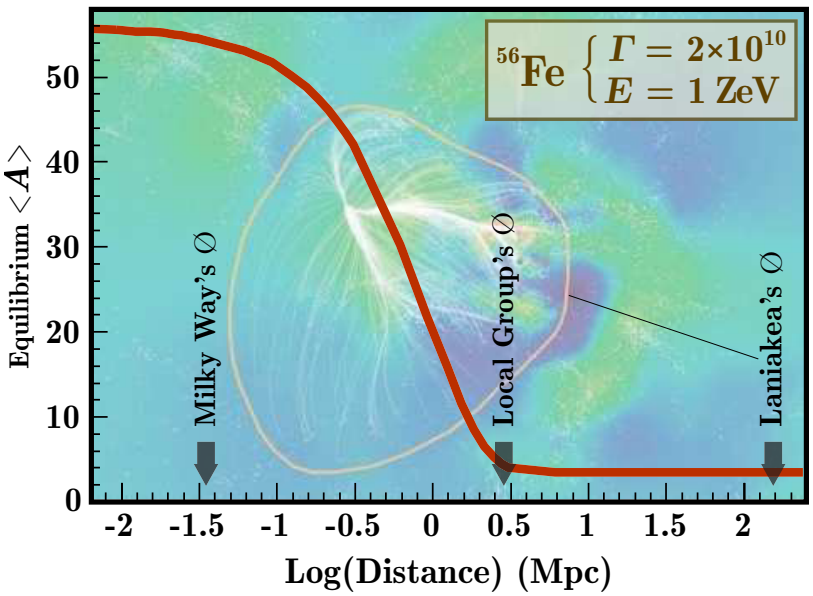

For experts: The photoreaction cross sections are estimated with the reaction code 'Talys'. The Generalized Lorentzian model is used for the $E1$-strength function.

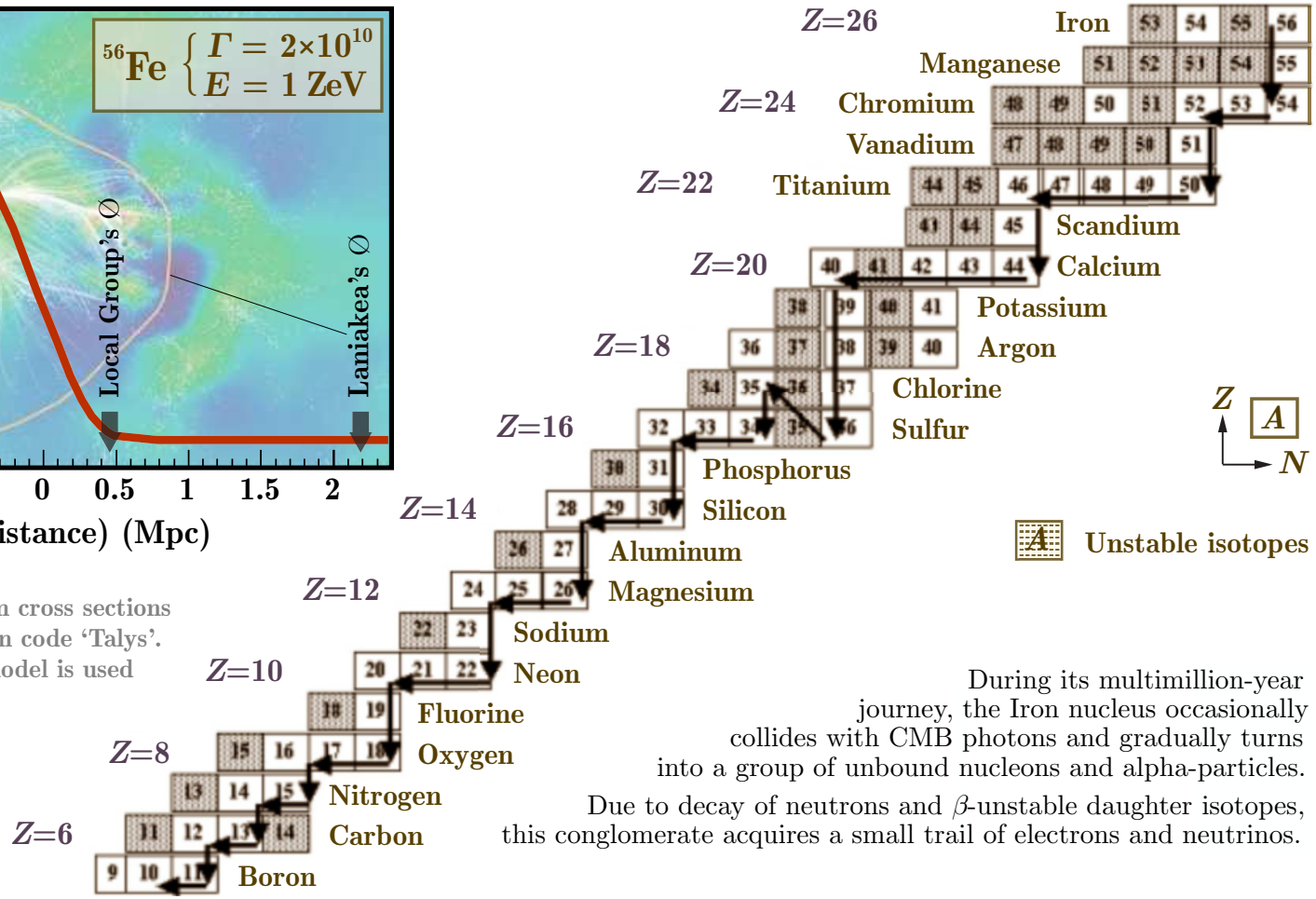

During its multimillion-year journey, the Iron nucleus occasionally collides with CMB photons and gradually turns into a group of unbound nucleons and alpha-particles.

Due to decay of neutrons and β-unstable daughter isotopes, this conglomerate acquires a small trail of electrons and neutrinos.

△ Nuclei involved in the photodisintegration process of Iron with $\Gamma = 2 \times 10^{10}$. About 85 nuclei are involved and numerous open channels can compete since the Lorentz dilation allows β-unstable nuclei with half-lives $\sim$ hour to survive over a Mpc scale, and thus have a chance to interact with a CMB photon. Insert shows evolution of the average A with respect to the distance of a ^{56}Fe source.

[Adapted from E. Khan *et al.*, "Photodisintegration of ultra-high-energy cosmic rays revisited," Astropart. Phys. **23** (2005) 191–201, arXiv:astro-ph/0412109. (Highly recommended for further study.)]

◦ **Neutrinos:** The processes of the cosmogenic neutrino and antineutrino production are

$$\pi^{\pm} \to \mu^{\pm} + \nu_{\mu}/\overline{\nu}_{\mu}, \quad \mu^{\pm} \to e^{\pm} + \nu_e/\overline{\nu}_e + \overline{\nu}_{\mu}/\nu_{\mu}, \quad n \to p + e^{+} + \nu_e, \quad n \to p + e^{+} + \nu_e + \gamma,$$

and nuclear $\beta^{\mp}$ decay of short-lived secondary nuclei:

$$(A, Z) \to (A - 1, Z) + e^{-} + \overline{\nu}_e \quad \text{and} \quad (A, Z) \to (A, Z - 1) + e^{+} + \nu_e.$$

Neutrino interactions with CνB are usually neglected, but taking into account neutrino mixing is very important, because it leads to the evolution of the flavor composition of the neutrino flux.

◦ **Photons & electrons:** The processes of the UHE cosmogenic photon production are neutral pion decay ($\pi^0 \to \gamma\gamma$) and the aforementioned decay of muons and neutrons. At energies below the photodisintegration threshold, background γs elastically scatter off CR ray nuclei,

$$(A, Z) + \gamma_{\text{bg}} \to (A, Z) + \gamma.$$

One or more photons can be emitted in the nuclear relaxation process following a radioactive decay,

$$(A, Z)^{*} \to (A, Z) + a\gamma, \quad a = 1, 2, \ldots.$$

While propagating through intergalactic space, CR γs experience (double) pair production ((D)PP):

$$\gamma + \gamma_{\text{bg}} \to e^{+} + e^{-} \quad (\textbf{PP}), \qquad \gamma + \gamma_{\text{bg}} \to e^{+} + e^{-} + e^{+} + e^{-} \quad (\textbf{DPP}),$$

whereas CR electrons and positrons experience triplet pair production (TPP) and inverse Compton scattering (ICS):

$$e + \gamma_{\text{bg}} \to e + e^{+} + e^{-} \quad (\textbf{TPP}), \qquad e + \gamma_{\text{bg}} \to e + \gamma \quad (\textbf{ICS}).$$

Electrons and positrons can also suffer significant energy losses via synchrotron radiation in the presence of magnetic fields. The secondary particles from these processes interact in turn, forming electromagnetic cascades down to GeV energies.

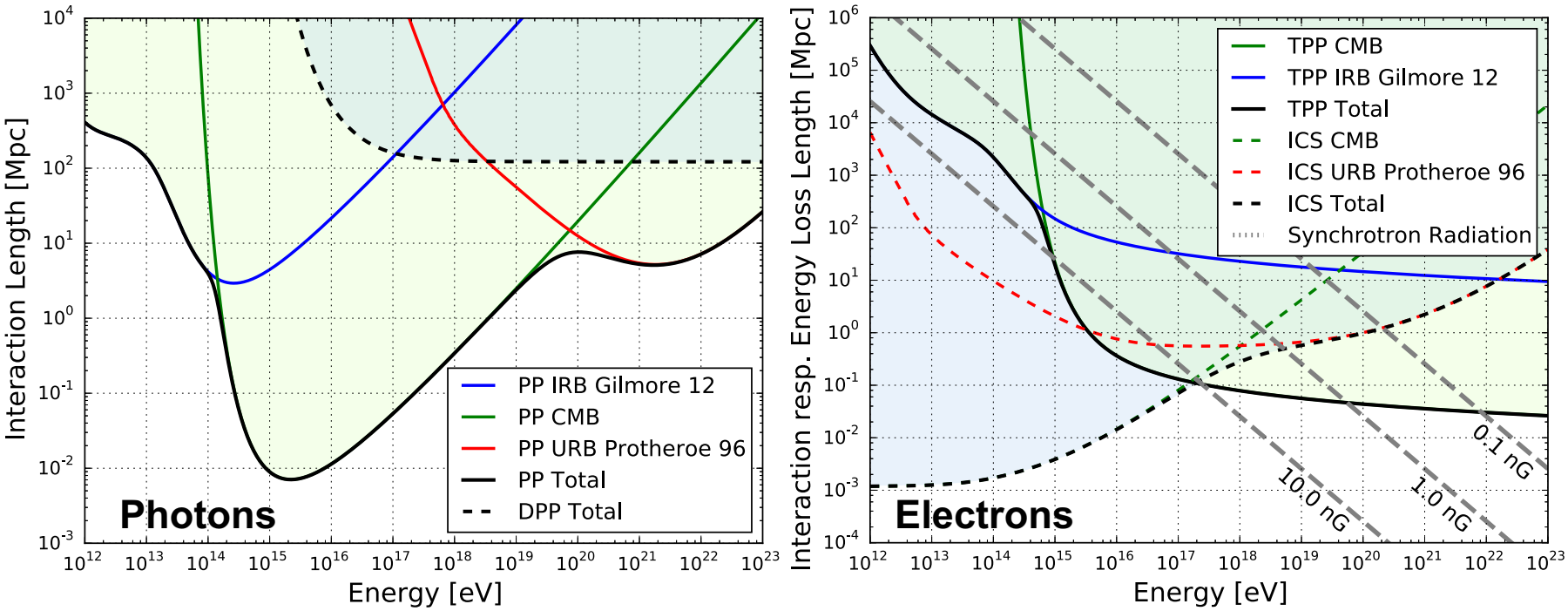

Interaction lengths for CR photons (left) and electrons (right) interacting with cosmic photon backgrounds. The relevant processes are pair production (PP) and double pair production (DPP) for photons, and triplet pair production (TPP) and inverse Compton scattering (ICS) for electrons. Colored lines show the contribution of the individual photon fields, IRB (blue), CMB (green) and radio background (red). In addition, the energy loss length of synchrotron radiation is indicated for three magnetic field strengths (gray inclined dashed straight lines). Synchrotron radiation can dominate at the highest energies depending on the intergalactic magnetic field strength, although $B_{\text{IGMF}} \lesssim 0.1\,\text{nG}$ seems more realistic than the larger values. Are Galactic fields significant?...

[Adapted from C. Heiter, D. Kuempel, D. Walz, & M. Erdmann, "Production and propagation of ultra-high energy photons using CRPropa 3," Astropart. Phys. **102** (2018) 39-50, arXiv:1710.11406 [astro-ph.IM].]

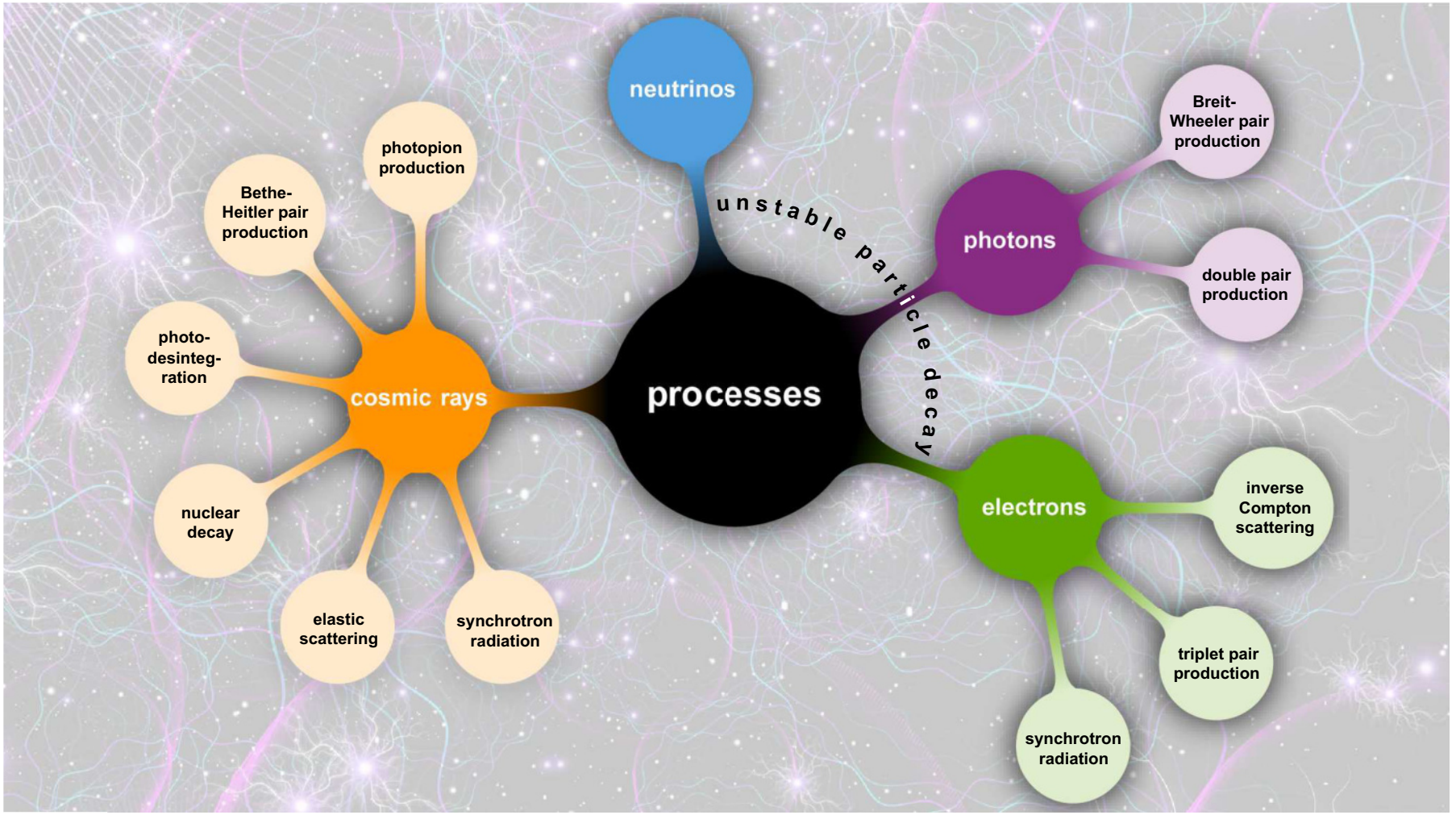

A schema of the interactions and energy-loss processes implemented in CRPropa 3.2 (a Monte Carlo code for modelling the propagation of high-energy particles in cosmos) for several types of particles.

[Adapted from R. A. Batista *et al.*, "CRPropa 3.2 – an advanced framework for high-energy particle propagation in extragalactic and galactic spaces," JCAP09(2022)35, arXiv:2208.00107 [astro-ph.HE].]

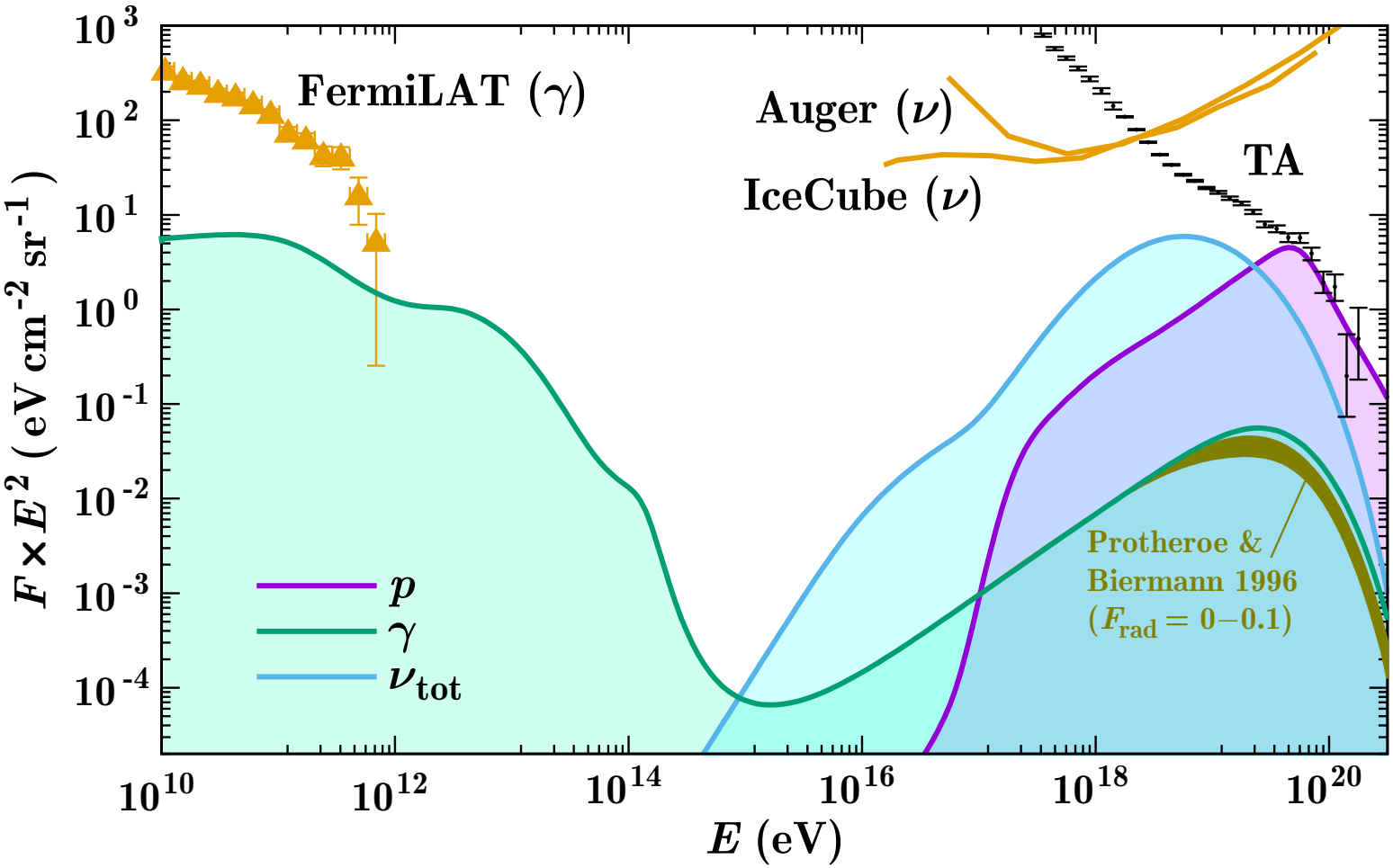

An example of the photon and all-flavor neutrino spectra produced by the the highest-energy protons, calculated according to a model normalized to the Telescope Array (TA) data. The model assumes that 100% of the UHECR TA flux above 40 EeV consists of protons and UHECR γs correspond to a 10% of the "reference" extragalactic radio background (by Clark *et al.*, 1970).

[Adapted from G. B. Gelmini, O. Kalashev, & D. Semikoz, "Upper limit on the diffuse radio background from GZK photon observation," Universe **8** (2022) 402, arXiv:2206.00408 [astro-ph.HE].]

7.16 UHE neutrino detection.

Three methods for detecting UHE neutrinos:

- ⋆ **Radio detection**
  [ANITA, ARA, ARIANNA, Ashra NTA, AURA, CODALEMA, ELVIS, FORTE, GLINT, GLUE, GMRT, GRAND, Ooty RT, HASRA, IceRay, LOFAR, LOPES, LORD, LUNASKA Parkes, POEMMA, RESUN, RICE, RNO-G, SalSA, SKA, TREND, Trinity, WSRT NuMoon,...]
- ⋆ **Sonic/acoustic detection**
  [ACoRNE, AMADEUS, AUTEC, SAUND, SPATS+HADES,...]
- ⋆ **Fluorescence detection**
  [JEM-EUSO, S-EUSO, EUNO, OWL, KOSMOTEPETL Project (KLYPVE, TUS),...]

Several representative examples of radio detectors are discussed below.

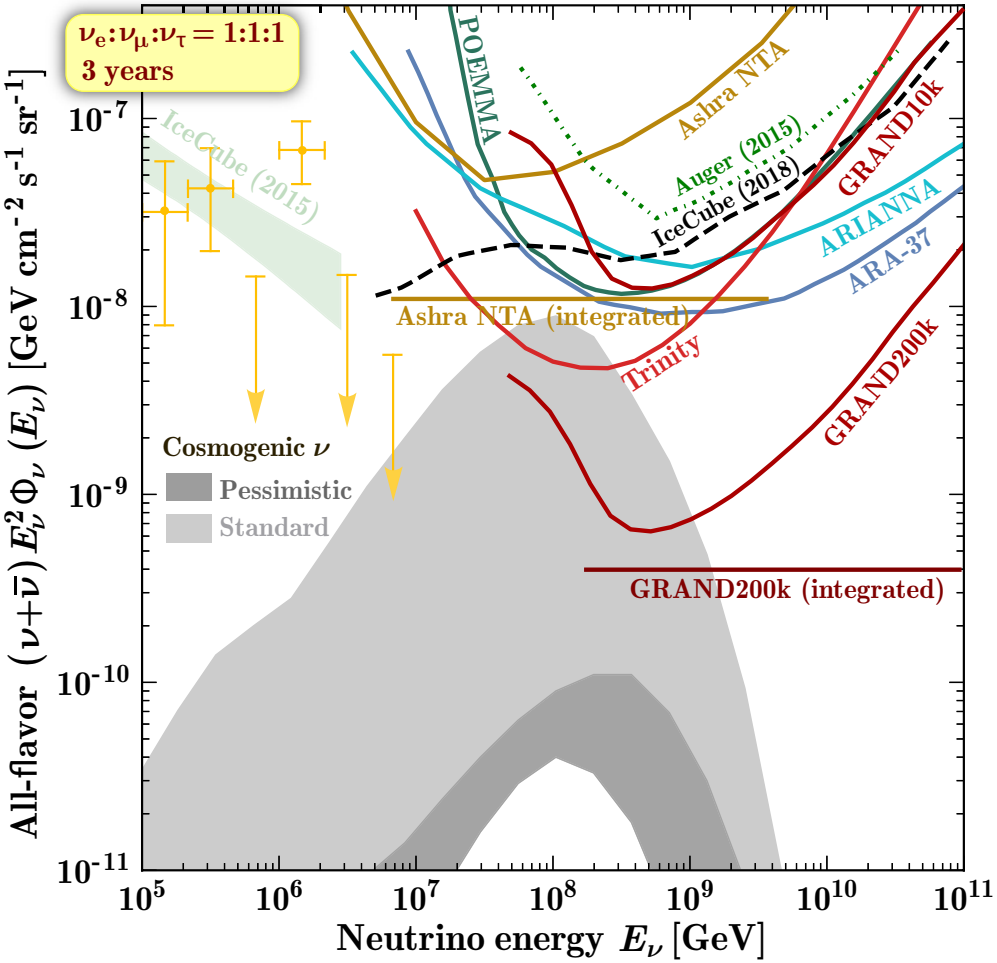

△ Sensitivity of several experiments, neutrino flux predictions, and existing flux constraints.

[From A. Nepomuk Otte, "Trinity: An air-shower imaging system for the detection of cosmogenic neutrinos," Phys. Rev. D **99** (2019) 083012, arXiv:1811.09287; for details, see Ref. at p. 352.]

7.16.1 Askaryan effect.

The Askaryan effect can be described as a variation of the net charge asymmetry of a particle shower in time, in combination with Cherenkov-like effects due to refraction in (generally heterogeneous) medium; the charge excess travels with $v > c/n$. During the development of a high-energy electromagnetic cascade in normal matter, Compton, Bhabha, and Møller scattering knocks electrons from the material into the shower. In addition e^+e^- annihilation and Bhabha scattering decelerate shower positrons. The combination of these processes should lead to a net 20–30% negative charge excess for the comoving compact body of particles that carry most of the shower energy. Askaryan noted that this effect should lead to strong coherent radio and microwave Cherenkov emission for showers propagating in a dielectric.

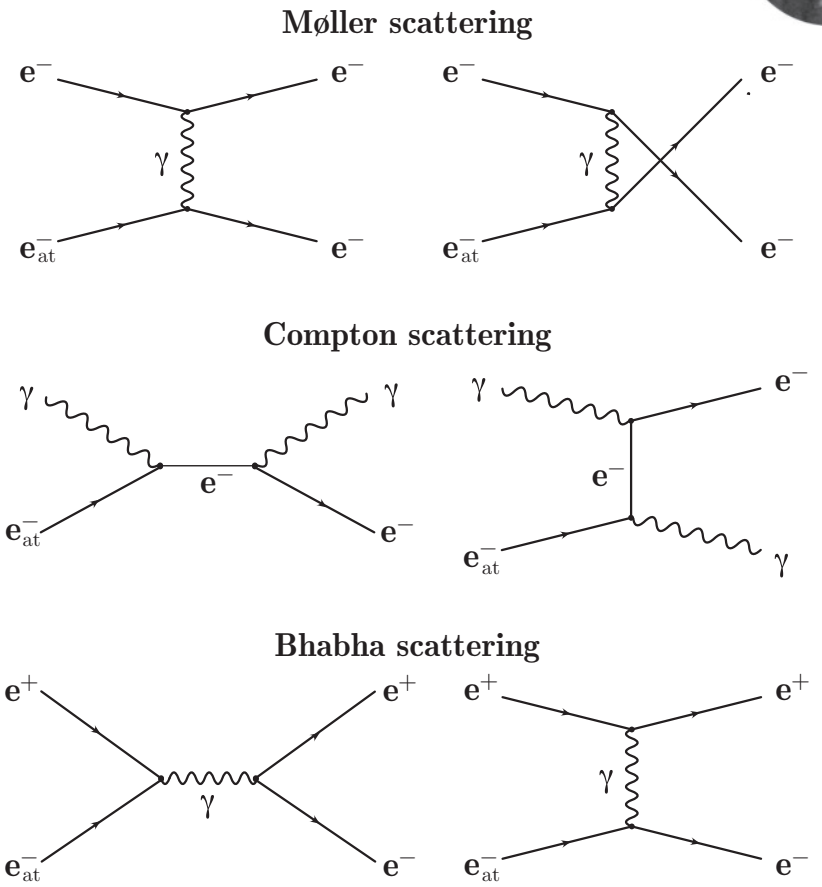

The range of wavelengths over which coherence obtains depends on the form factor of the shower bunch – wavelengths shorter than the bunch length suffer from destructive interference and coherence is lost. However, in the fully coherent regime ($\lambda > R \sim$ a few cm) the radiated energy scales quadratically with the net charge of the particle bunch, and at ultrahigh energies the resulting coherent radio emission may carry off a significant fraction of the total energy in the cascade.

7.16.2 (Geo)synchrotron emission.

The second mechanism (the main for air showers) is the (geo)magnetic effect. Here, a radio signal gets emitted by the time-variation of the transverse current in the shower. The secondary electrons and positrons are accelerated by a (geo)magnetic field. The acceleration takes place in the shower front. Following the Lorentz force the electrons and positrons get deflected in opposite directions. They are decelerated due to the interactions with air molecules. In total, this leads to a net drift of the $e^{\pm}$, moving perpendicular to the shower axis, which can be described by transverse currents.

As in the Askaryan effect, during the shower development, the number of secondaries grows until reaches its maximum and then the number starts to decrease, the shower dies out. So, the transverse currents vary in time which leads to electromagnetic radiation.

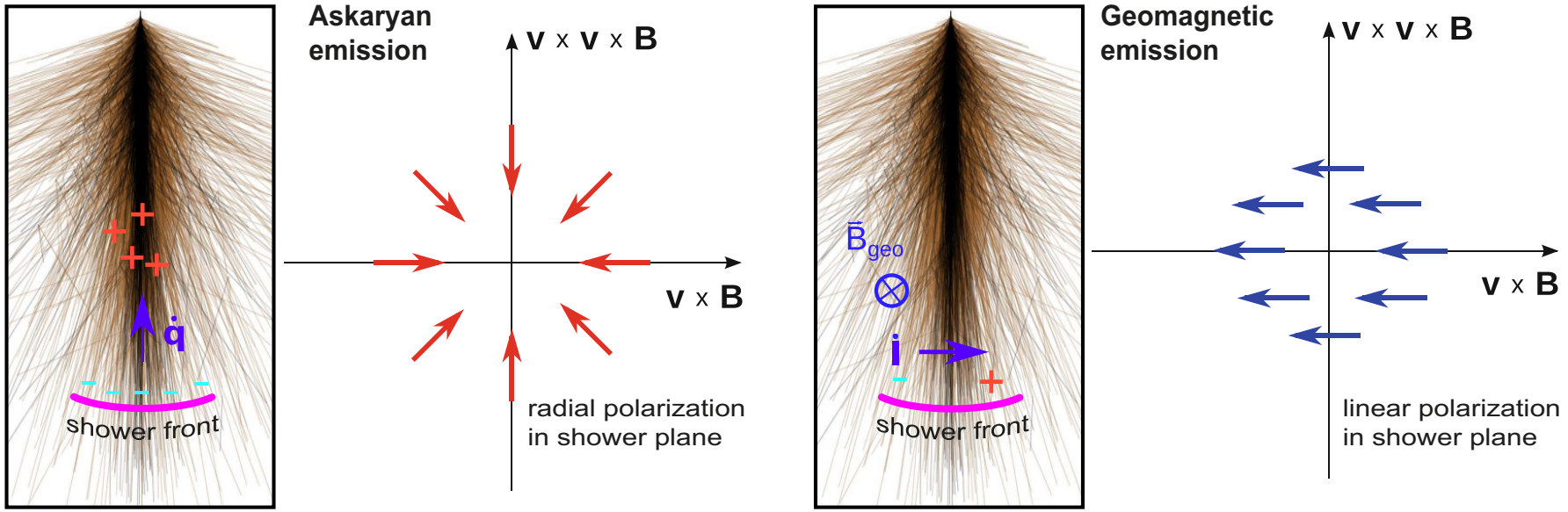

The polarization of this signal is linear with the electric field vector aligned with the Lorentz force. All charged particles in the air shower are influenced by the geomagnetic field. But since $e^{\pm}$ have the highest charge-to-mass ratio, only they can contribute significantly to the radio signal.

7.16.3 Radio detectors – a few examples.

Inverted v-shape dipole at LOPES

Butterfly at CODALEMA

LPDA at AERA

SALLA at Tunka-Rex

Various antenna types used by different radio arrays for cosmic-ray air showers. Often such simple, unsightly devices are enough to build a huge radio telescope to detect UHECRs and UHE neutrinos. [From F. G. Schroder, "Radio detection of cosmic-ray air Showers and high-energy neutrinos," Prog. Part. Nucl. Phys. **93** (2017) 1–68, arXiv:1607.08781 [astro-ph.IM]].]

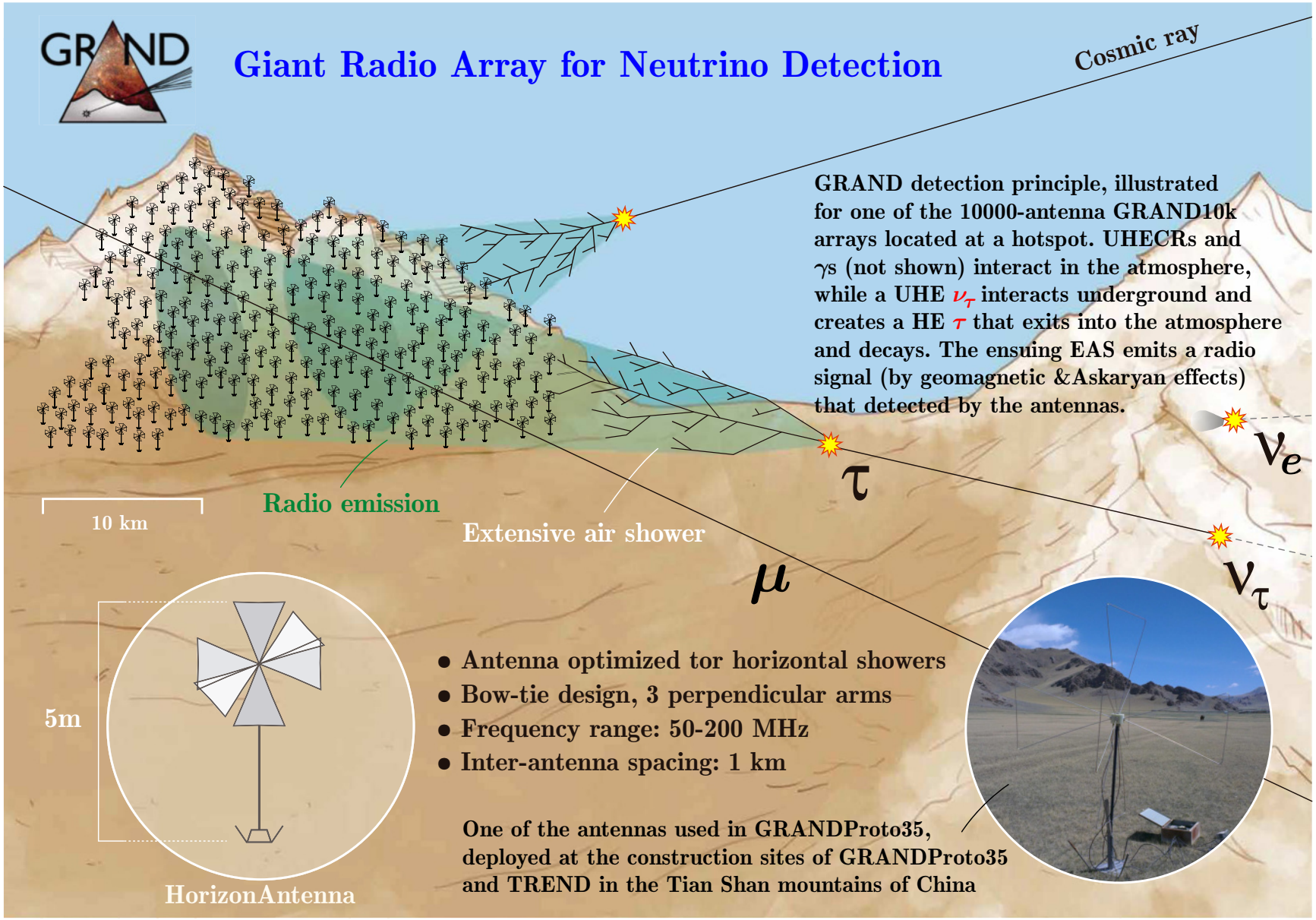

[Adapted from J. Alvarez-Muniz *et al.* (GRAND Collaboration) "The Giant Radio Array for Neutrino Detection (GRAND): Science and design," Sci. China Phys. Mech. Astron. **63** (2020) 219501, arXiv:1810.09994 [astro-ph.HE].]

ANITA has completed four flights, with the most recent being in December 2016.

ANITA ANTARCTIC IMPULSIVE TRANSIENT ANTENNA

ANITA is a balloon-borne experiment that attempts to turn Antarctica into a gigantic neutrino telescope. From its vantage point, dangling from a NASA long-duration balloon over 35 km above the ice, ANITA surveys over one million cubic kilometers of ice. ANITA is searching for the characteristic radio chirps (due to Askaryan and geosynchrotron emission) which would indicate a neutrino interacting in the ice below or emerging from the ice. The experiment is sensitive also to the UHECR interactions in the atmosphere.

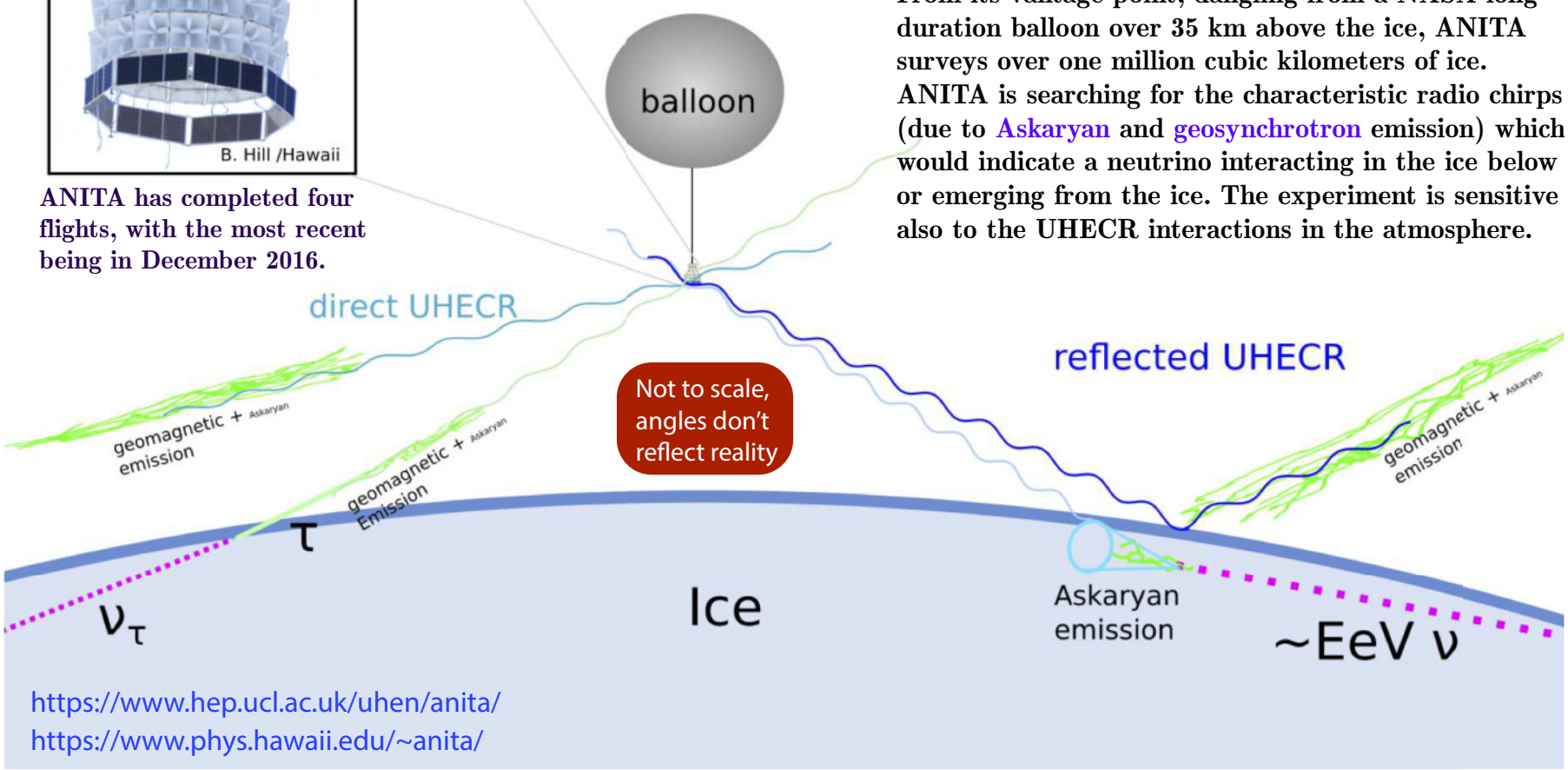

https://www.hep.ucl.ac.uk/uhen/anita/
https://www.phys.hawaii.edu/~anita/

ANITA cosmic ray events:

ANITA I (2006):
- 13 down-going
- 2 upward earth skimming
- 1 up-going

ANITA III (2014):
- 17 down-going
- 2 upward earth skimming
- 1 up-going

ANITA IV (2016):
- 1 "Askaryan event" but consistent with the background estimate

ANITA's successor, PUEO, is proposed and awaiting review

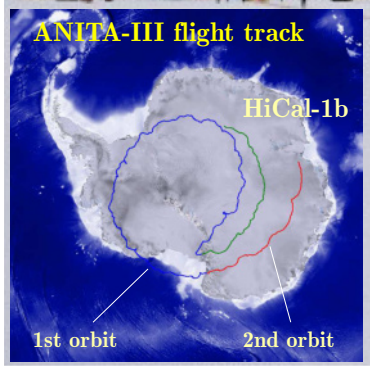

The ANITA I & III up-going events are very unexpected

IceCube sees no anomalies while its exposure is 1-60 times ANITA (depending on scenario).

"Ouch! Chute did not release after landing [of ANITA I], payload dragged ~ 1 mile. BUT: DAQ & data OK $\Longrightarrow$ success!" (Peter Gorham, a report at XXXV SLAC Summer Institute, Stanford 2007.)

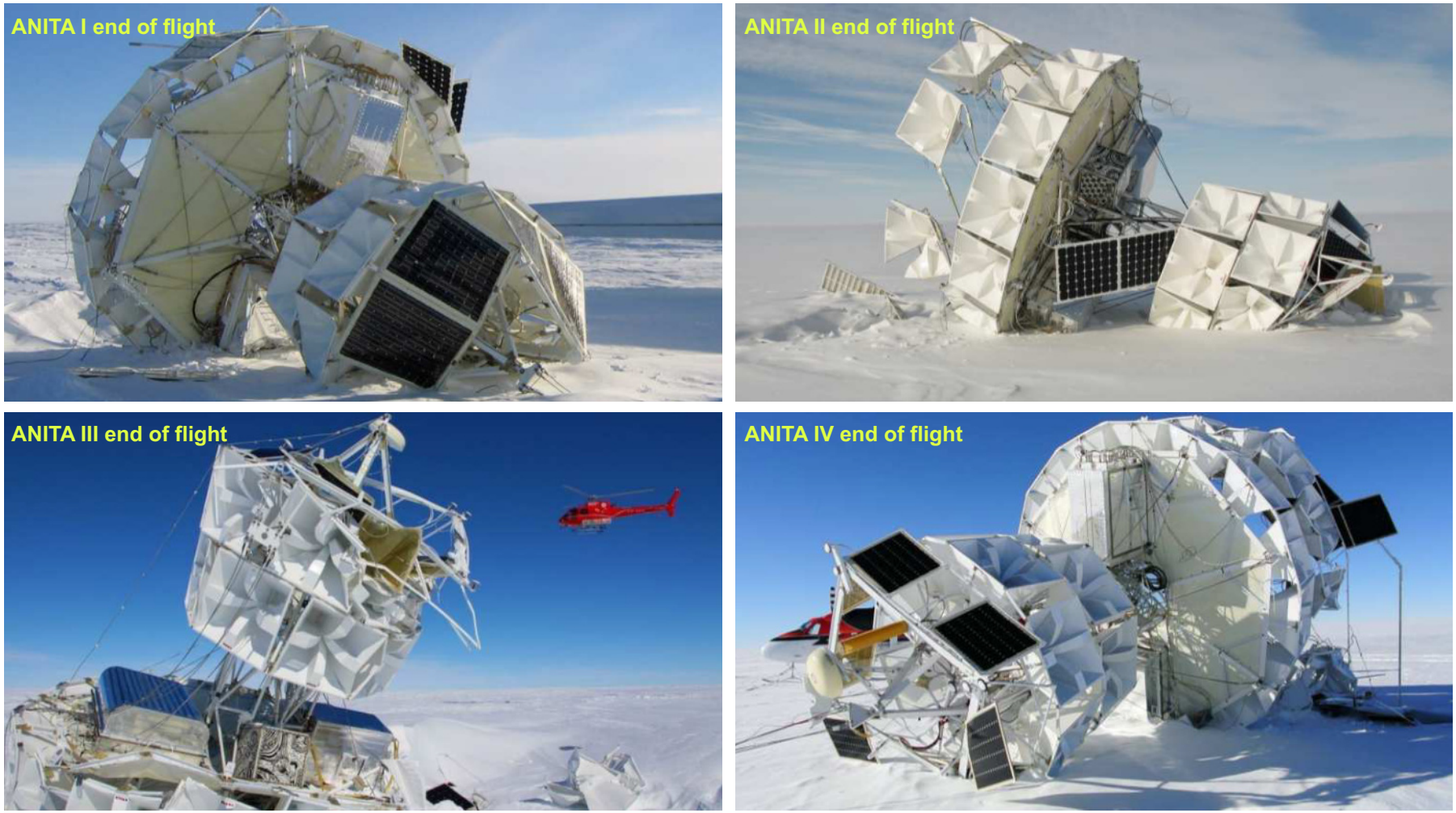

[Photos are borrowed from a report by R. Nichol, "ANITA: Hunting for neutrinos and new physics," (PSI Colloquium, November 29, 2018).]

Very rough estimation (for showers emerging at $\sim 35^\circ$ above the horizon):

	ANITA	IceCube
Effective volume	$\sim 4\ \text{km}^2 \times D$	$\sim 1\ \text{km}^3$
Exposure time	57 days	2078 days

$$\Downarrow$$

$$\frac{\#\ \text{IceCube events}}{\#\ \text{ANITA events}} \approx 3\left(\frac{D}{3.2\,\text{km}}\right)$$

- Null signal in IceCube.
- One upgoing PeV muon track event observed in IceCube could be reinterpreted as an EeV τ track but it is not quite enough to explain the puzzle.

Figure on the right is taken from Ref. [10] (see p. 991 for the list of relevant references).

The main features of the ANITA anomalous events are summarized in the table below.

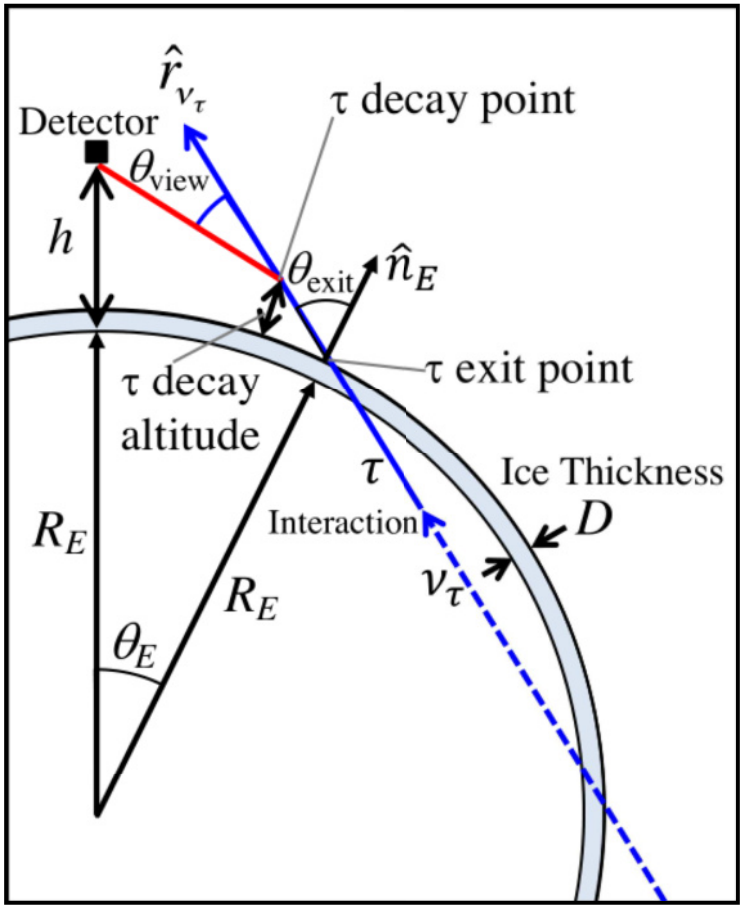

ANITA detection geometry.

Event # (flight)	3985267 (ANITA-I)	15717147 (ANITA-III)	Ref.
Date, time	2006-12-28, 00:33:20 UTC	2014-12-20, 08:33:22.5 UTC	[2]
Ground position (Lat., Lon.)	-82.6559°, $+17.2842^\circ$	-81.39856°, $+129.01626^\circ$	[2]
Arrival angles (El., Az.)	$(-27.4 \pm 0.3)^\circ$, $+159.65 \pm 0.7)^\circ$	$(-35.0 \pm 0.3)^\circ$, $(61.41 \pm 0.7)^\circ$	[2]
Zenith angle z'/z	$(117.4 \pm 0.3)^\circ/(116.8 \pm 0.3)^\circ$	$(125.0 \pm 0.3)^\circ/(124.5 \pm 0.3)^\circ$	[10]
Equatorial coord. (RA, Dec.)	$+282.14064^\circ$, $+20.33043^\circ$	$+50.78203^\circ$, $+38.65498^\circ$	[2]
Altitude	2.56 km	2.75 km	[2]
Ice depth	3.53 km	3.22 km	[2]
Shower energy[a]	0.60 ± 0.40 EeV	$0.56^{+0.30}_{-0.20}$ EeV	[2]
Earth chord length	5740 ± 60 km	7210 ± 55 km	[10]
Mean interaction length[b]	290 km	265 km	[10]
Attenuation factor	$2.5^{+0.5}_{-0.6} \times 10^{-9}$ 1.2×10^{-9}	$1.5^{+0.3}_{-0.4} \times 10^{-12}$ 1.4×10^{-13}	↲ [8]
Probability of success[c]	$\mathbf{(4.4 \pm 0.5) \times 10^{-7}}$	$\mathbf{(3.2 \pm 0.6) \times 10^{-8}}$	[10]

[a] For upward shower initiation at or near ice surface.
[b] SM estimation assuming $E_\nu = 1$ EeV (most likely neutrino energy for emergent high energy τ).
[c] Simulated by injecting a 1 EeV ν_τ to find probability of emergent τ with $E_\tau > 0.1$ EeV.

The ANITA events require an incoming 1 EeV neutrino flux of about 1.2×10^7 km^{-2}sr^{-1}yr^{-1} (SM estimation within "$\nu_\tau \to \tau$" scenario) while the Auger/IceCube limit is 6 km^{-2}sr^{-1}yr^{-1}!

A more conservative conclusion from Ref. [10]: "...a ν_τ origin of the anomalous ANITA events would imply a neutrino flux at least two orders of magnitude above current bounds."

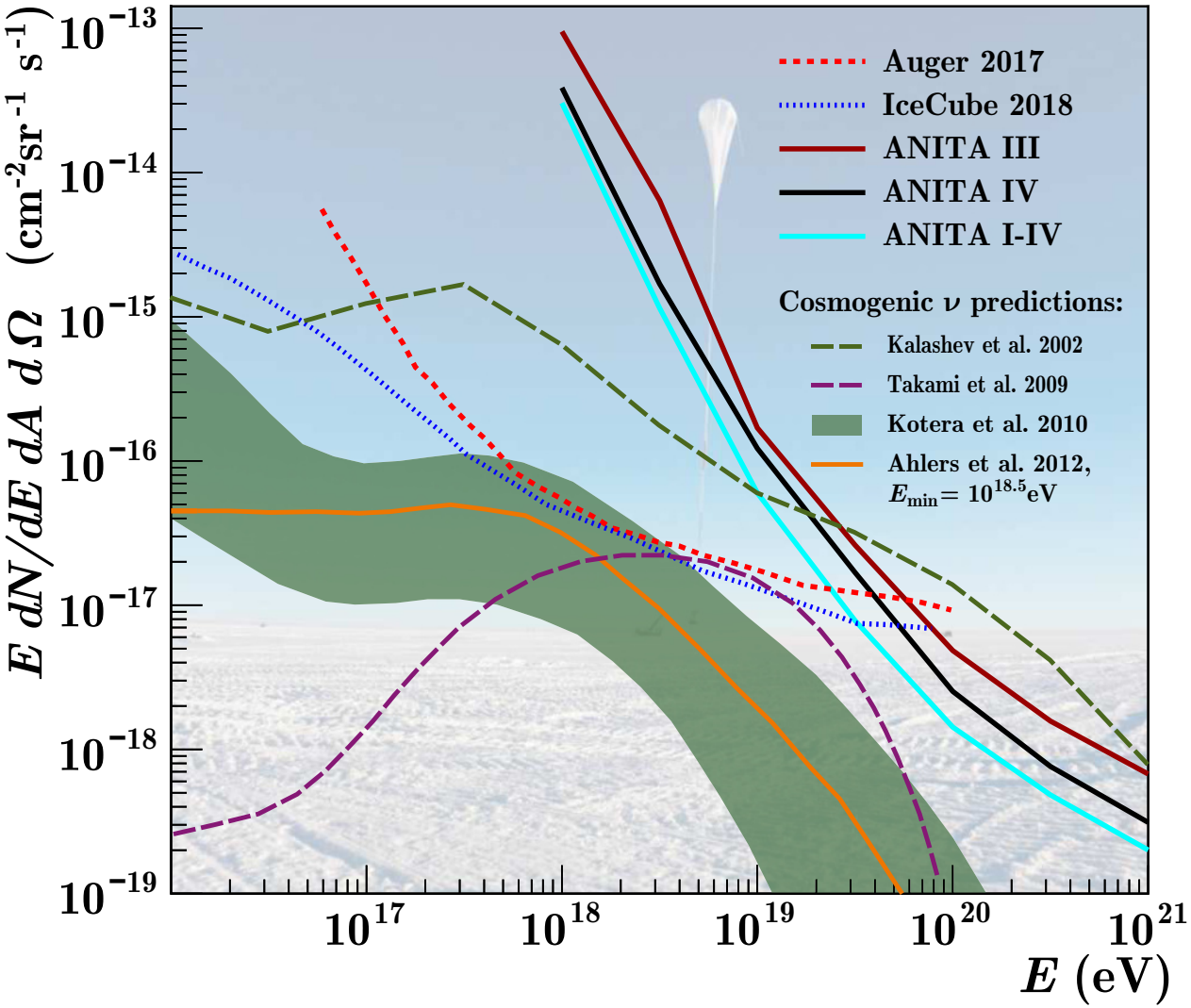

◁ ANITA IV limit on the all flavor diffuse UHE neutrino flux (using a livetime of 24.25 days) and a combined limit from ANITA I-IV. The recent UHE neutrino limits from the Auger and IceCube experiments, and four cosmogenic neutrino models are also displayed. The table below lists the ANITA IV effective area (A_{eff}) as a function of neutrino energy used to make the limit, not including analysis efficiency.

$\log_{10}(E/\text{eV})$	18	18.5	19	19.5	20	20.5	21
A_{eff} (km^2·sr)	0.0032	0.033	0.43	**3.1**	**21**	**68**	**167**

[Taken from P. W. Gorham *et al.* (ANITA Collaboration), "Constraints on the ultra-high energy cosmic neutrino flux from the fourth flight of ANITA," Phys. Rev. D **99** (2019) 122001, arXiv:1902.04005 [astro-ph.HE].]

Detection of ultrahigh-energy neutrinos in ARA

ARA (**A**skaryan **R**adio **A**rray) will be composed of a series of instruments configured firmly in the Antarctic ice beneath the South Pole.

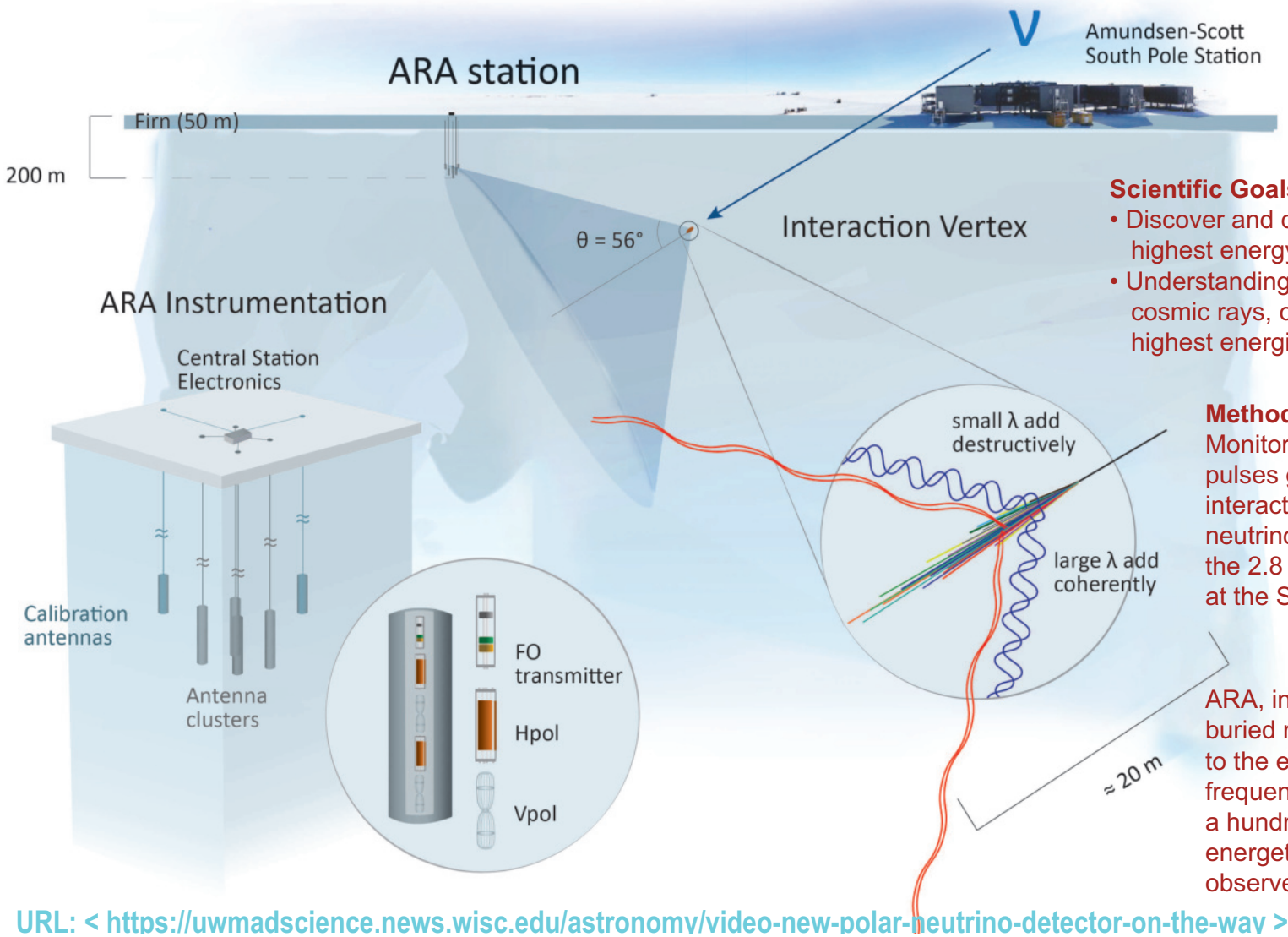

Scientific Goals:

- Discover and determine the flux of highest energy cosmic neutrinos.
- Understanding of highest energy cosmic rays, other phenomena at highest energies.

Method:

Monitor the ice for radio pulses generated by interactions of cosmic neutrinos with nuclei of the 2.8 km thick ice sheet at the South Pole.

ARA, in essence, is a large, buried radio antenna tuned to the electromagnetic frequencies of neutrinos, a hundred times more energetic than the ones observed by IceCube.

URL: < https://uwmadscience.news.wisc.edu/astronomy/video-new-polar-neutrino-detector-on-the-way >

ARIANNA (**A**ntarctic **R**oss **I**ce shelf **ANt**enna **N**eutrino **A**rray) is another experiment based on the shower radio emission. It is a surface array of radio antennas designed to detect UHE (in particular cosmogenic) neutrinos. The experiment is currently (2020) in its pilot phase.

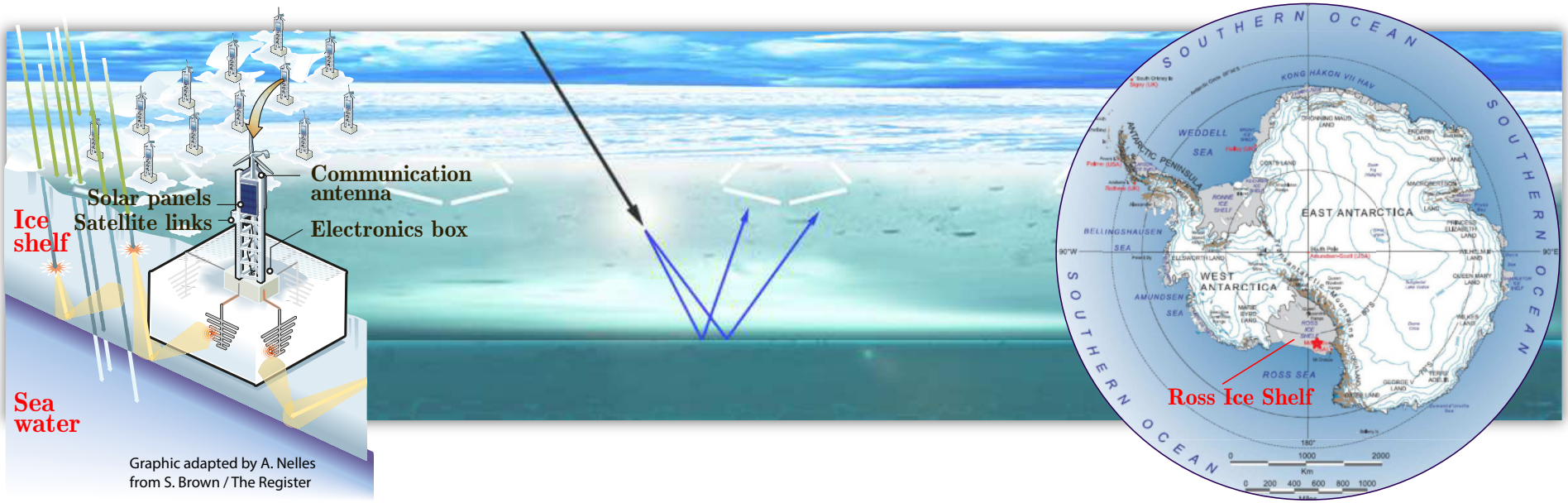

[From URL: ⟨http://newscenter.lbl.gov/2010/04/19/neutrinos-cosmic-rays/⟩.]

An energetic neutrino striking the upper atmosphere creates a shower of particles in which electrons predominate. When the shower enters the ice, it sheds Cherenkov radiation in the form of radio waves, which reflect from the interface of ice and water and are detected by antennas buried in the snow.

The Ross Ice Shelf makes an ideal component of the ARIANNA detector – not least because the interface where the ice, hundreds of meters thick, meets the liquid water below is an excellent mirror for reflecting radio waves. Signals from neutrino events overhead can be detected by looking for radio waves that have been reflected from this mirror. For neutrinos arriving horizontally, some of the radio waves will be directly detected, and some will be detected after being reflected.

For details and references, see the ARIANNA collaboration webpage ⟨https://arianna.ps.uci.edu/⟩.

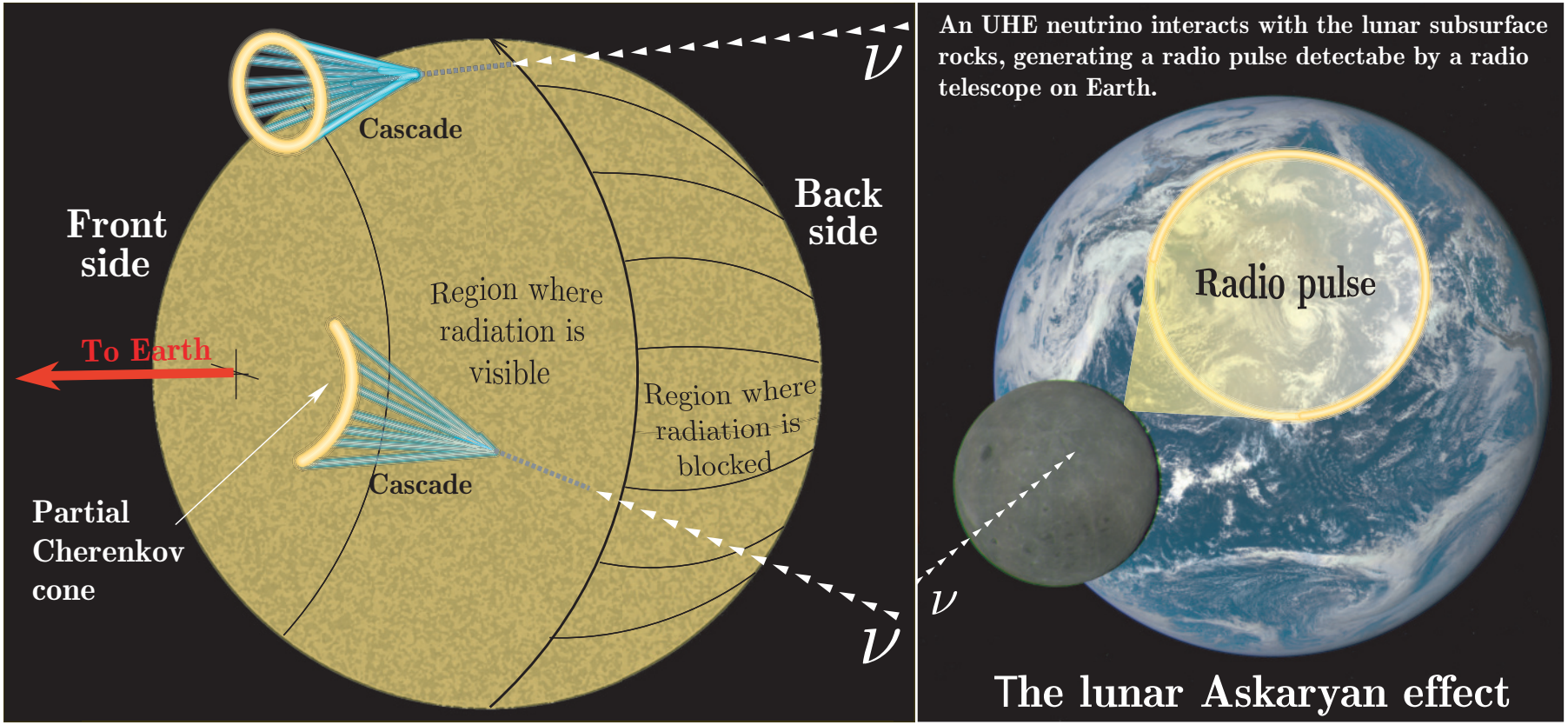

Geometry of lunar neutrino cascade event detection. At 100 EeV the interaction length of a neutrino for the dominant deep inelastic hadronic scattering interactions (averaging over the charged and neutral current processes) is about 60 km ($R_{\leftmoon} = 1740$ km). Upon interaction, a cascade ~ 10 m long forms, and Compton scattering, positron annihilation, and other processes lead to a $\sim 20\%$ negative charge excess. This cascade radiates a cone of coherent Cherenkov emission at an angle from the shower axis of $\theta_C = \cos^{-1}(1/\beta\sqrt{\epsilon}) \simeq 54^\circ$, with an angular spread of $\Delta\theta \simeq 1^\circ$ at 2 GHz.
[Adapted from P. W. Gorham *et al.*, "Experimental limit on the cosmic diffuse ultrahigh energy neutrino flux," Phys. Rev. Lett. **93** (2004) 041101, astro-ph/0310232v3.]

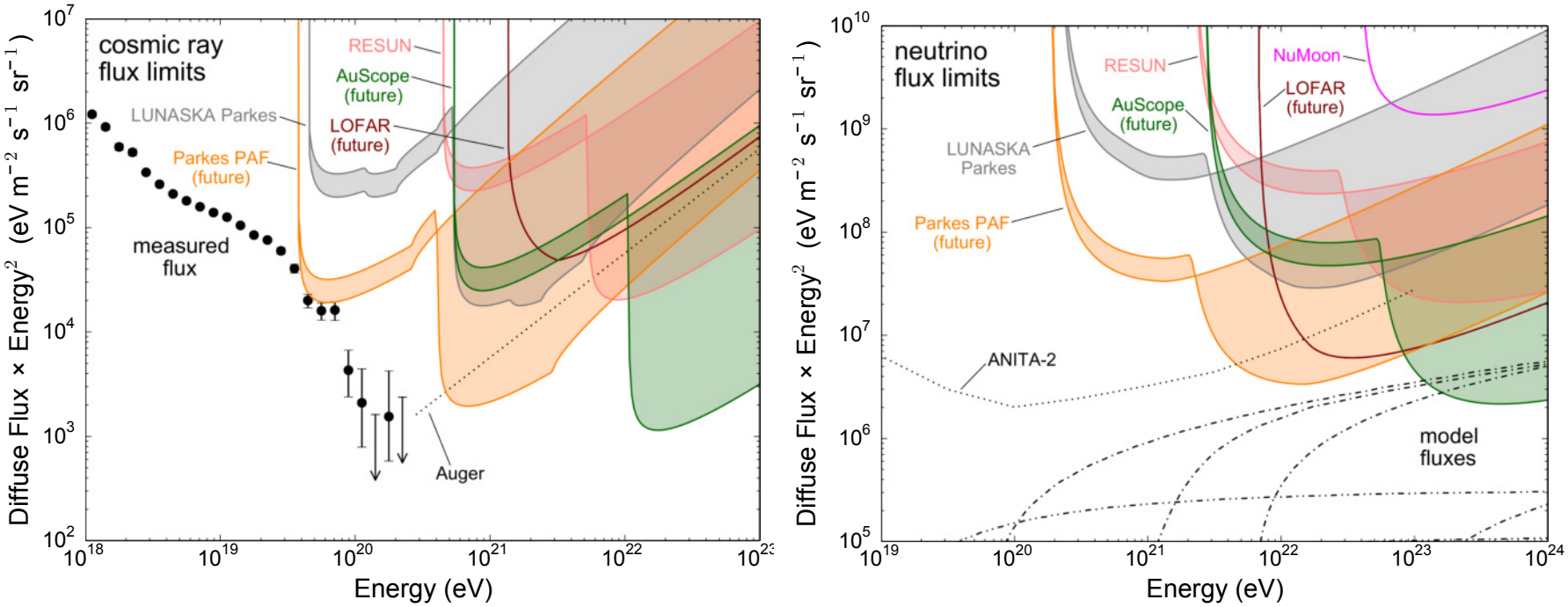

Model-independent differential limits on the fluxes of UHECRs (*left panel*) and neutrinos (*right panel*) set by the NuMoon, RESUN, & LUNASKA Parkes lunar Askaryan experiments. Also shown are potential limits that could be set by future lunar Askaryan experiments with nominal observing times of 200 h with LOFAR and a phased-array feed (PAF) on the Parkes radio telescope, or 2900 h with AuScope. Shading shows the range of uncertainty associated with models of the small-scale lunar surface roughness. Filled circles show the cosmic-ray flux measured by the Pierre Auger Observatory, dash-dotted lines show the neutrino flux from exotic-physics models, and dotted lines show the limits established by the Auger and the ANITA-2 experiment.

[From J. D. Bray, "Sensitivity of lunar particle-detection experiments," Eur. Phys. J. Web. Conf. **135** (2017) 04002, arXiv:1612.00329 [astro-ph.IM].]

Part III

Neutrino Interactions with Matter

8 Tentative representation of the cross sections.

8.1 Introductory notes.

Anticipating the kinematics section, let us look at the energy thresholds of the simplest (anti)neutrino-induced charged-current (CC) reactions.

Reaction	E_ν^{th}	Reaction	E_ν^{th}
$\nu_e + {}^{71}_{31}\text{Ga} \to {}^{71}_{32}\text{Ge} + e^-$	0.232 MeV	$\nu_e + {}^{37}_{17}\text{Cl} \to {}^{37}_{18}\text{Ar} + e^-$	0.814 MeV
$\nu_\ell + {}^{2}_{1}D \to p + n + \nu_\ell$	2.226 MeV	$\nu_e + {}^{2}_{1}D \to p + p + e^-$	1.443 MeV
$\nu_\ell + {}^{3}_{1}T \to {}^{2}_{1}D + n + \nu_\ell$	5.752 MeV	$\nu_e + {}^{3}_{1}\text{T} \to {}^{3}_{2}\text{He} + e^-$	0.465 MeV
$\nu_\ell + {}^{3}_{1}T \to p + 2n + \nu_\ell$	7.983 MeV		
$\nu_e + n \to p + e^-$	0	$\overline{\nu}_e + p \to n + e^+$	1.806 MeV
$\nu_\mu + n \to p + \mu^-$	110.162 MeV	$\overline{\nu}_\mu + p \to n + \mu^+$	113.047 MeV
$\nu_\tau + n \to p + \tau^-$	3.4538 GeV	$\overline{\nu}_\tau + p \to n + \tau^+$	3.4636 GeV
$\nu_\mu + e^- \to \mu^- + \nu_e$	10.9231 GeV		
$\nu_\tau + e^- \to \tau^- + \nu_e$	3.0899 TeV		

How well we know the neutrino interactions? Alas, not well enough! The most common behavior: rapid growth of the cross sections with energy.

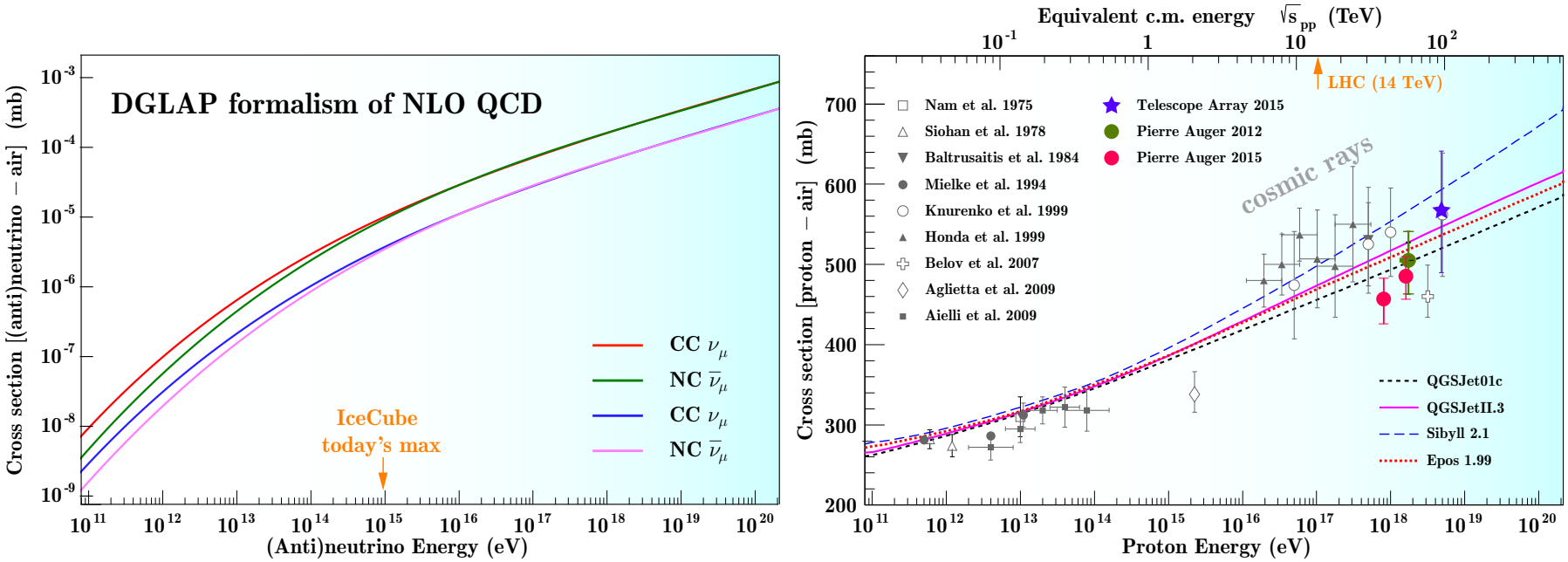

Left panel: CC and NC cross sections of ν_μ and $\overline{\nu}_\mu$ interactions with air evaluated within the Dokshitzer-Gribov-Lipatov-Altarelli-Parisi (DGLAP) formalism of NLO QCD using modern PDF fits.[a] *Right panel*: Proton-air cross section (shown for comparison).[b] The main features are quite obvious the (anti)neutrino cross section grows with energy according to a power law (close to linear at lowest energies shown, see details below) while the proton cross section grows only logarithmically. However, even at ultra-high (hardly accessible today) energies, the (anti)neutrino cross section remains many orders of magnitude less than the proton one.

[a] See A. Cooper-Sarkar, K. Road, Ph. Mertsch & S. Sarkar, "The high energy neutrino cross-section in the Standard Model and its uncertainty," JHEP08(2011)042, arXiv:1106.3723v2 [hep-ph].

[b] The data and model predictions are borrowed from R. Conceição (for the Pierre Auger Collaboration), "High-energy interactions at the Pierre Auger Observatory," PoS(EPS-HEP2015)382, arXiv:1510.06898 [astro-ph.HE] and D. Góra (for the Pierre Auger Collaboration), "Particle physics in cosmic rays," Int. J. Mod. Phys. A **36** (2021) 2141010, arXiv:2110.02685 [astro-ph.HE].

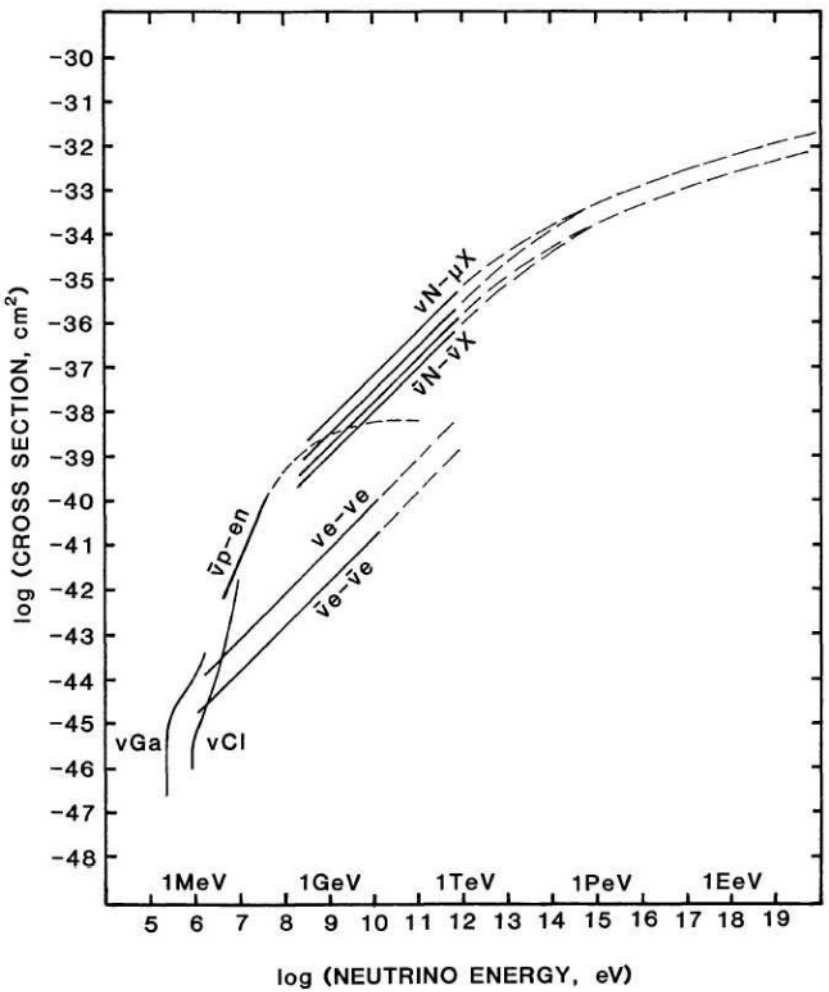

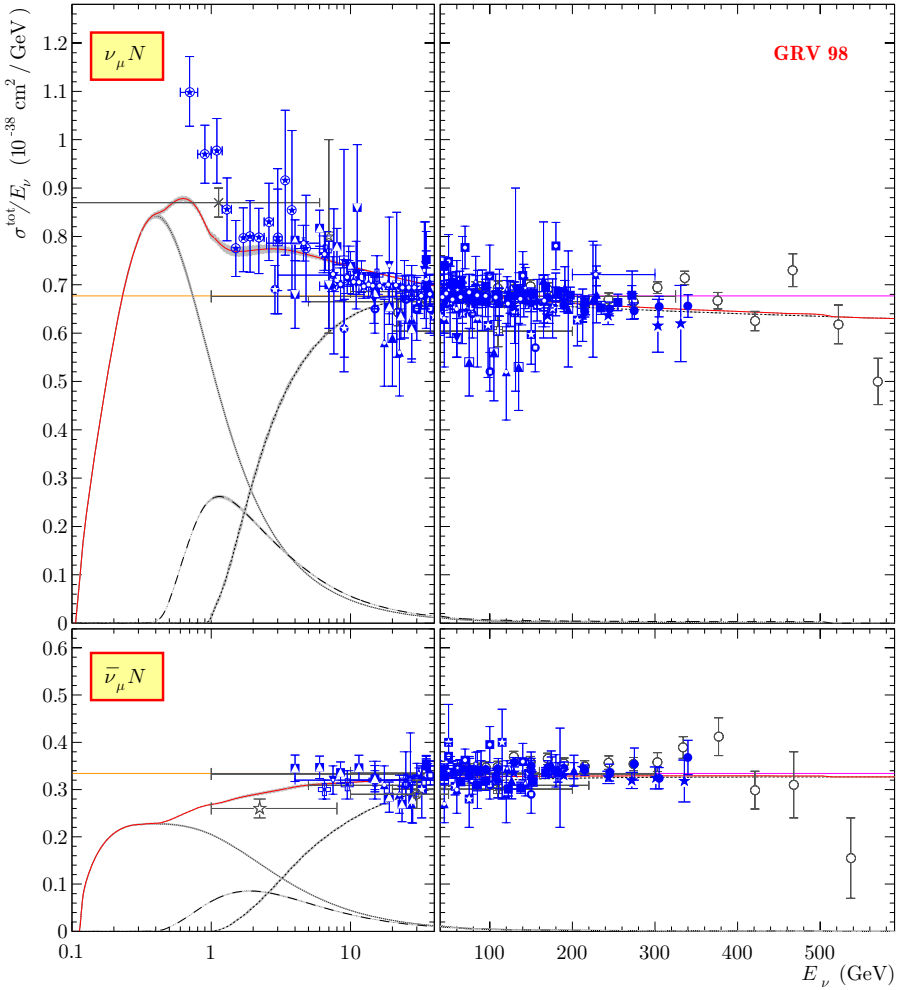

Left panel: A tentative representation of the cross sections for neutrino interactions with nuclei, nucleons and electrons. [From A. M. Bakich, "Aspects of neutrino astronomy," Space Sci. Rev. **49** (1989) 259–310.]
Right panel: Predicted and measured slopes of $\nu_\mu N$ and $\overline{\nu}_\mu N$ total cross sections. Three main contributions [QES, RES (ExRS), and DIS (GRV 98)] and their sums are shown.
[From K. S. Kuzmin *et al.*, "How to sum contributions into the total charged-current neutrino-nucleon cross section," Phys. Atom. Nucl. **69** (2005) 1857–1871, hep-ph/0511308; for a more detailed and updated plot, see p. 411.]

8.2 Cross sections for solar neutrino detection.

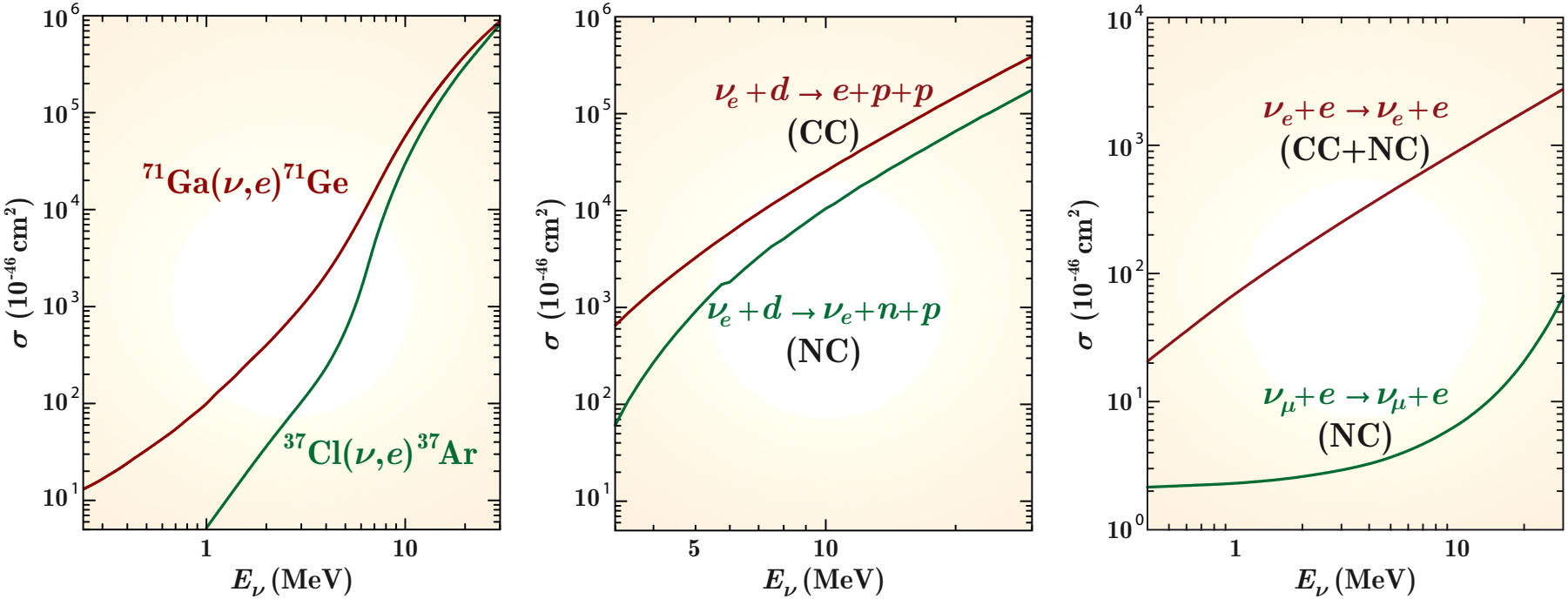

Low-energy neutrino capture cross sections for Gallium and Chlorine (*left panel*), CC and NC induced neutrino cross sections for Deuterium [used in SNO] (*middle panel*), and neutrino–electron scattering cross sections [used in SNO and Super-Kamiokande] (*right panel*) vs. neutrino energy.

[VN, "Solar neutrinos. Astrophysical aspects," Phys. Part. Nucl. Lett. **8** (2011) 683–703. The data are taken from J. N. Bahcall *et al.*, "Standard neutrino spectrum from ^{8}B decay," Phys. Rev. C **54** (1996) 411–422, J. N. Bahcall, "Gallium solar neutrino experiments: Absorption cross sections, neutrino spectra, and predicted event rates," Phys. Rev. C **56** (1997) 3391–3409, S. Ying *et al.*, "Charged- and neutra-current solar-neutrino cross sections for heavy-water Cherenkov detectors," Phys. Rev. C **45** (1992) 1982–1987, and J. N. Bahcall *et al.*, "Solar neutrinos: Radiative corrections in neutrino-electron scattering experiments," Phys. Rev. D **51** (1995) 6146–6158.]

8.3 Cross sections for supernova neutrino detection.

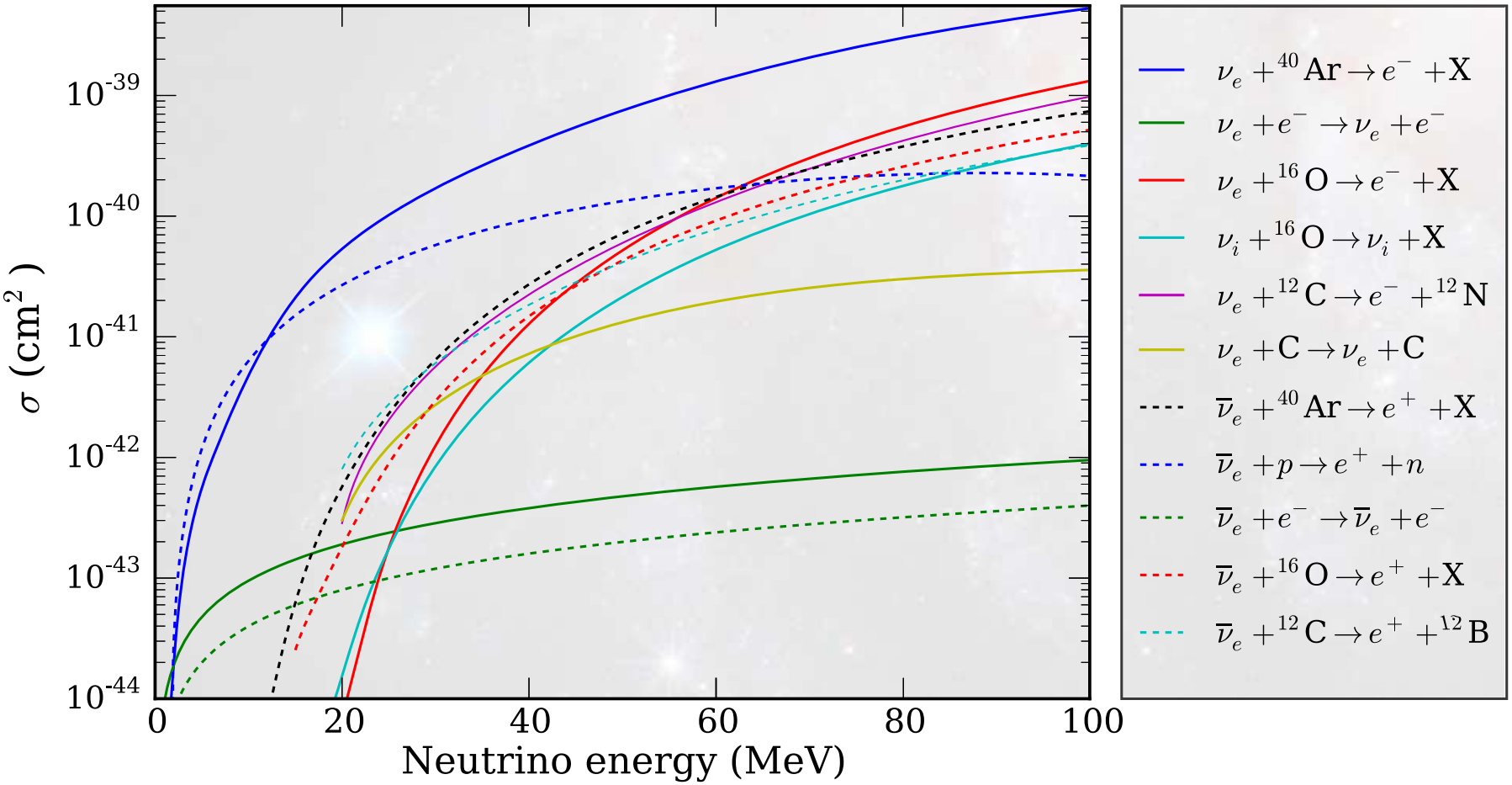

The ν_e and $\overline{\nu}_e$ matter-interaction cross sections at low energies (needed, e.g., for supernova neutrino detection). The ${}^{16}\mathrm{O}(\overline{\nu}_e, e^+)\mathrm{X}$ cross section and both the ${}^{12}\mathrm{C}$ cross sections are not plotted to zero at low energies due to a lack of tabulated data at these energy values from the sources used.

[Adapted from J. Wallace, A. Burrows, & J. C. Dolence, "Detecting the supernova breakout burst in terrestrial neutrino detectors," ApJ **817** (2016) 182, arXiv:1510.01338 [astro-ph.HE].]

8.4 Cross sections at accelerator energies.

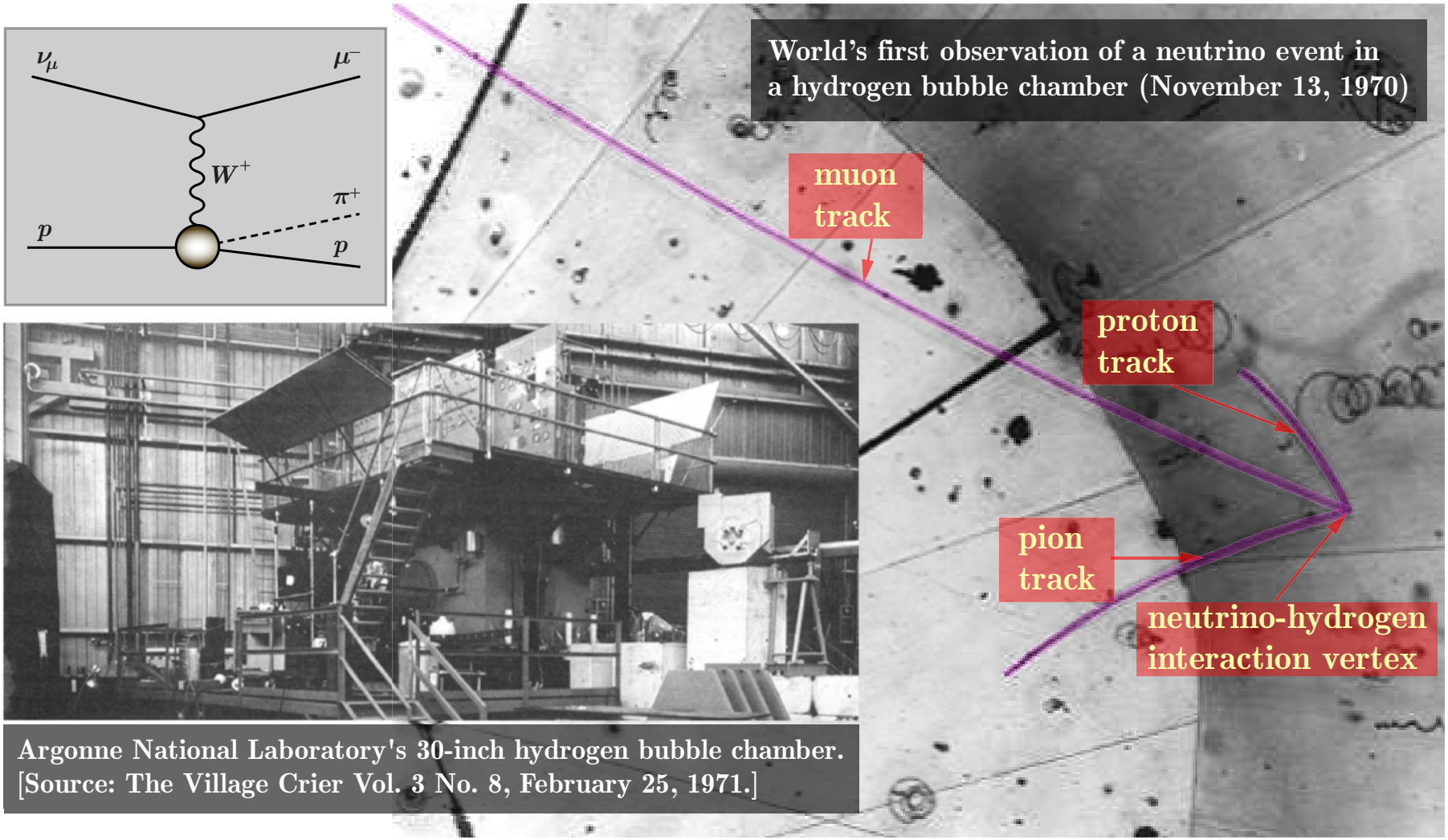

A photograph from the Zero Gradient Synchrotron's 12-foot bubble chamber at ANL. The invisible neutrino strikes a proton producing three tracks. [See URL: ⟨http://history.fnal.gov/neutrino.html⟩.]

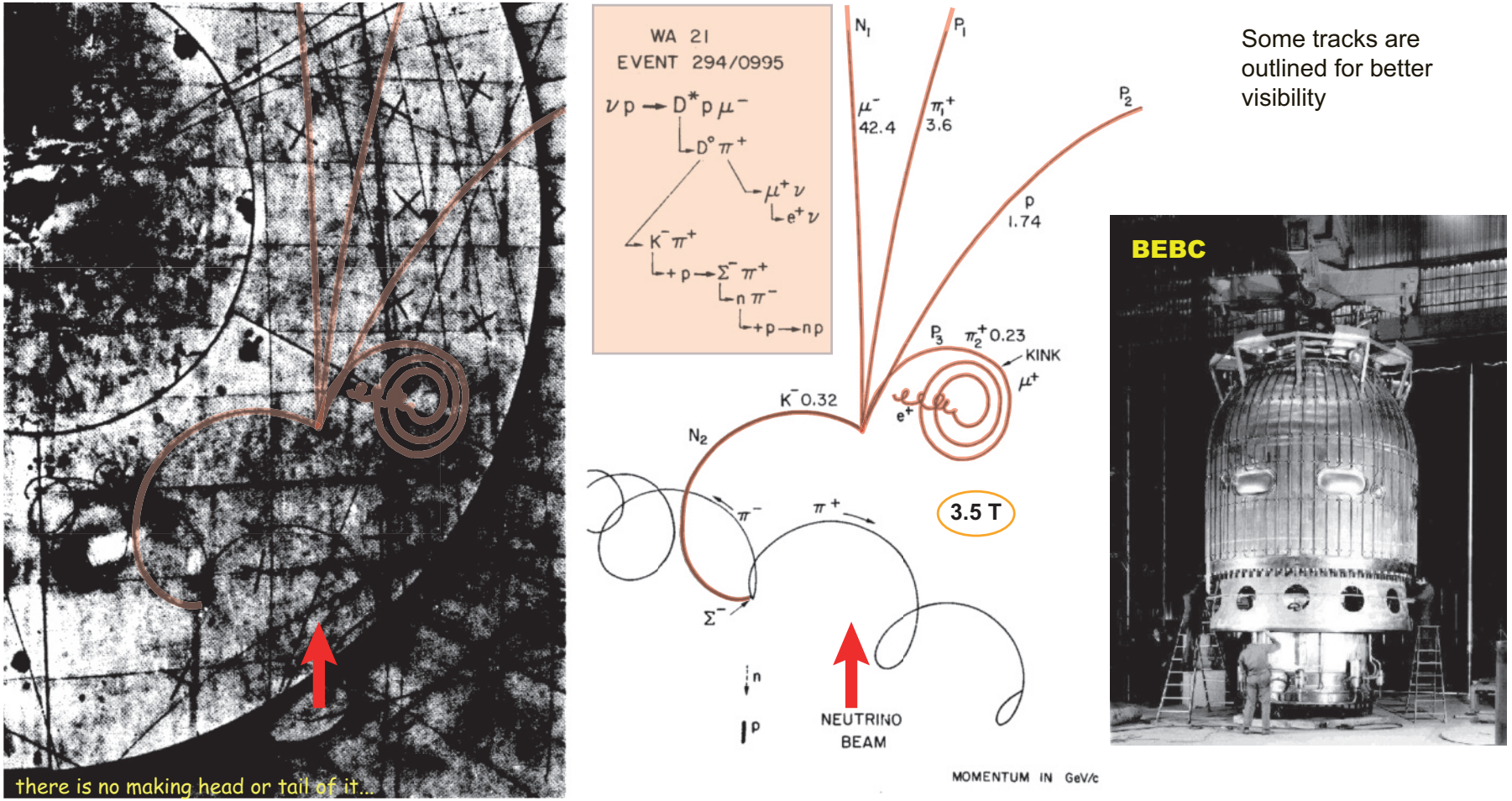

Photograph of an event with production of charmed meson D^{*+} as observed in the Hydrogen-filled bubble chamber BEBC (shown in insert at right) exposed to the CERN wide-band neutrino beam produced by 350 GeV protons from the SPS accelerator ($\langle E_\nu \rangle = 45$ GeV). Also shown a drawing of that event with labeling of tracks and list of sequence of interactions and decays.

[From J. Blietschau *et al.* (Aachen-Bonn-CERN-Munich-Oxford Collaboration), "Production of charmed mesons in neutrino interactions in Hydrogen," Phys. Lett. B **86** (1979) 108–114.]

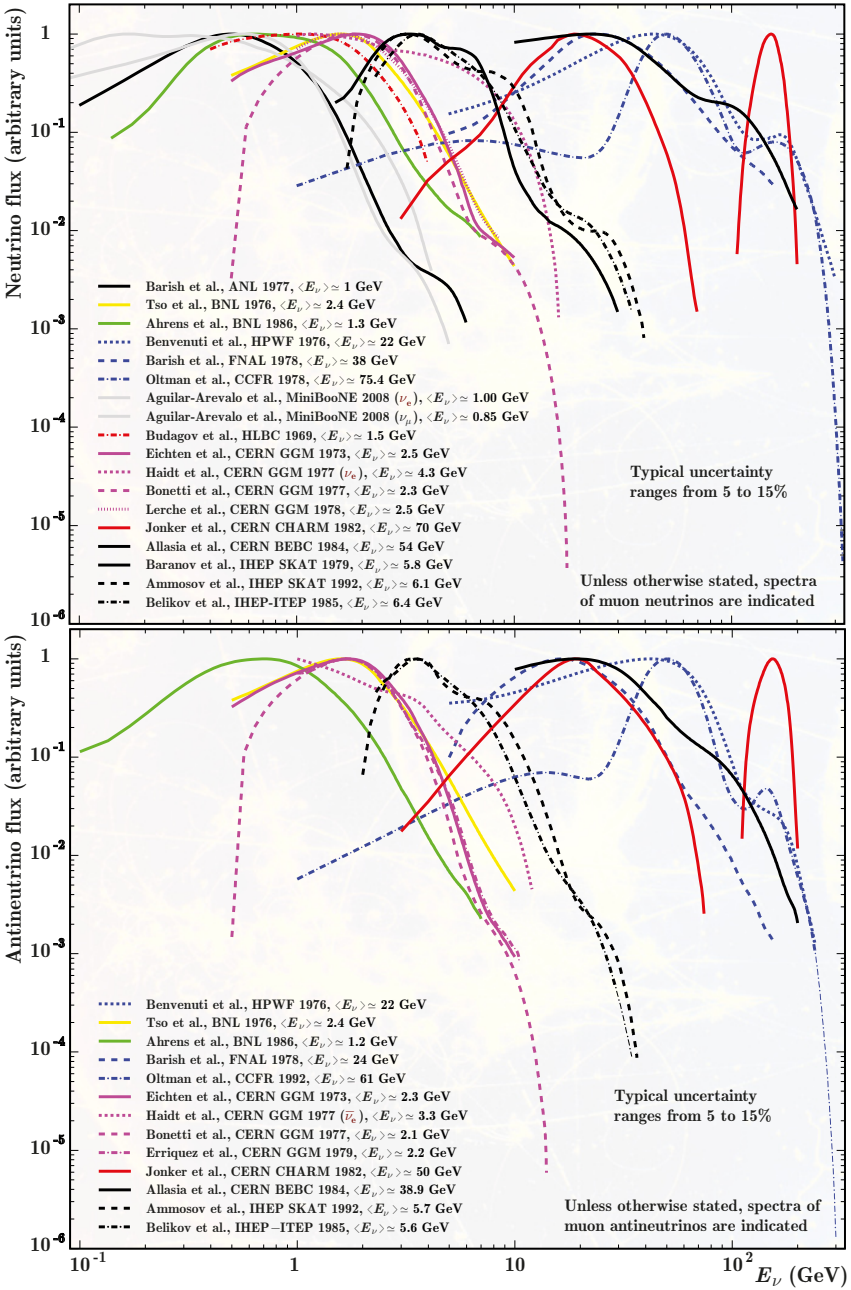

◁ Calculated muon and electron neutrino and antineutrino energy spectra in several past and ongoing accelerator experiments (a.u.).

[K. S. Kuzmin & VN (unpublished). The data are collected from many sources and parameterized.]

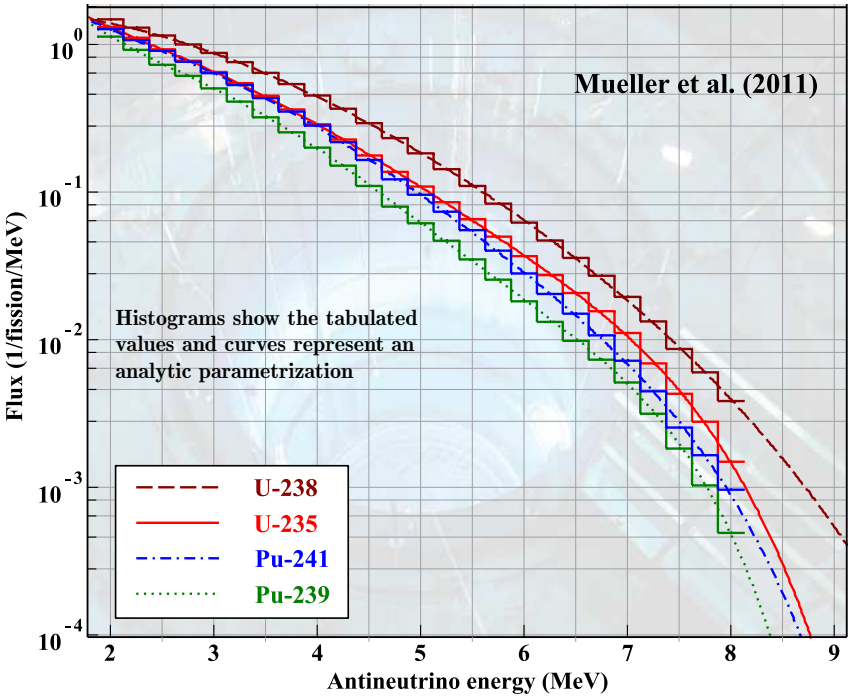

△ Antineutrino energy spectra by Th. A. Mueller *et al.* [Phys. Rev. C **83** (2011) 054615].

[For more details, see VN & D. S. Shkirmanov, "Reactor antineutrino anomaly reanalysis in context of inverse-square law violation," Universe **7** (2021) 246.]

9 Kinematics.

9.1 Elastic and quasielastic scattering.

Let us write down a list of useful kinematic formulas for the CCQE reaction $\nu + N \to \ell + N'$ ($\ell = e, \mu, \tau$) taking into account the difference between the masses of initial and final nucleons (M_i and M_f, respectively) but neglecting the neutrino masses. We use the following notation for the kinematic variables in the lab. frame:

$$k \equiv p_\nu = (E_\nu, \mathbf{p}_\nu), \quad k' \equiv p_\ell = (E_\ell, \mathbf{p}_\ell),$$
$$p \equiv p_i = (E_i, \mathbf{p}_i), \quad p' \equiv p_f = (E_f, \mathbf{p}_f).$$

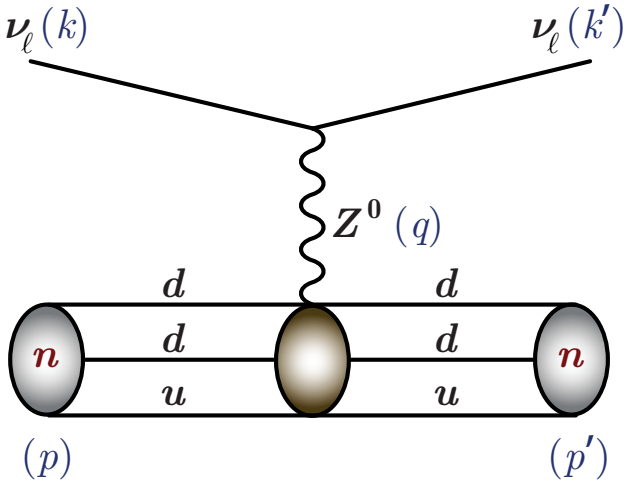

The particle energies in the center-of-mass frame (CMF) are

$$E^*_\nu = \frac{s - M_i^2}{2\sqrt{s}}, \quad E^*_\ell = \frac{s + m_\ell^2 - M_f^2}{2\sqrt{s}},$$
$$E^*_i = \frac{s + M_i^2}{2\sqrt{s}}, \quad E^*_f = \frac{s - m_\ell^2 + M_f^2}{2\sqrt{s}},$$

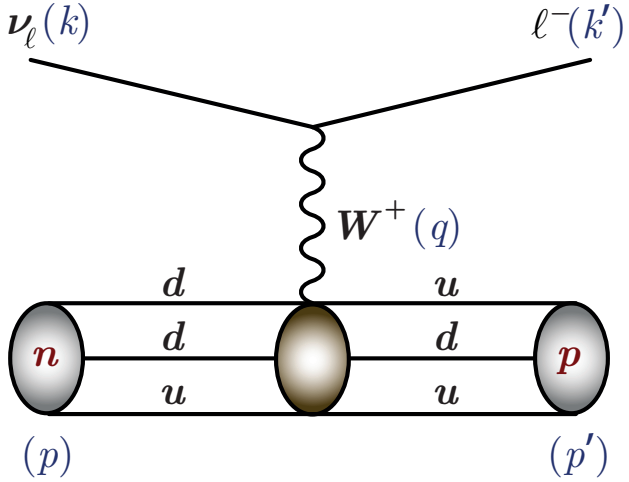

where $s = (k+p)^2 = (k'+p')^2 = M_i\,(2E_\nu + M_i)$; clearly $\sqrt{s} = E^*_\nu + E^*_\ell = E^*_i + E^*_f$ (s is one of the standard Lorentz-invariant Mandelstam variables).

For the elastic νN scattering, it is enough just to put $m_\ell = 0$ in the above formulas.

The energy–momentum conservation

$$\boxed{k + p = k' + p'}$$

provides

$$(k - k')^2 = (p - p')^2 \quad \Longrightarrow \quad E_\nu P_\ell \cos\theta = E_\ell \left(E_\nu + M_i\right) - \sqrt{s} E_\ell^*, \tag{18}$$

where θ is the scattering angle ($\mathbf{p}_\nu \mathbf{p}_\ell = E_\nu P_\ell \cos\theta$) and $P_a = |\mathbf{p}_a|$ for any particle $a = \nu, \ell, \ldots$ Let's define the dimensionless function (sine of the "branching angle", as follows from Eqs. (19)):

$$\zeta = \zeta(s) = \frac{\left(E_\nu^* + E_i^*\right) P_\ell^*}{m_\ell E_\nu} = \frac{2 M_i \sqrt{s} P_\ell^*}{m_\ell \left(s - M_i^2\right)} = \frac{M_i \sqrt{\left(s + m_\ell^2 - M_f^2\right)^2 - 4 m_\ell^2 s}}{m_\ell \left(s - M_i^2\right)}.$$

Using it, the two solutions to Eq. (18) can be written in terms of the module of the lepton momentum $P_\ell \equiv |\mathbf{p}_\ell| = P_\ell^\pm(\theta)$ or lepton energy $E_\ell = E_\ell^\pm(\theta)$ (one follows from the other):

$$P_\ell^\pm(\theta) = \frac{E_\nu^* \left(M_i E_\ell^* \cos\theta \pm m_\ell E_i^* \sqrt{\zeta^2 - \sin^2\theta}\right)}{M_i^2 + \left(E_\nu^*\right)^2 \sin^2\theta}, \tag{19a}$$

$$E_\ell^\pm(\theta) = \frac{M_i E_\ell^* E_i^* \pm m_\ell \left(E_\nu^*\right)^2 \cos\theta \sqrt{\zeta^2 - \sin^2\theta}}{M_i^2 + \left(E_\nu^*\right)^2 \sin^2\theta}. \tag{19b}$$

According to Eq. (19a),

$$P_\ell^+(\theta) P_\ell^-(\theta) = m_\ell^2 E_\nu^2 - \left(P_\ell^*\right)^2 s = m_\ell^2 E_\nu^2 \left(1 - \zeta^2\right). \tag{20}$$

Therefore for $\zeta \leq 1$ there are two solutions, $P_\ell^+(\theta)$ and $P_\ell^-(\theta)$, while for $\zeta > 1$ there is only one solution, $P_\ell^+(\theta)$ (see proof in Appendix A, p. 831).

One can prove that the parameter ζ is a *decreasing* function of s for e^- production and an *increasing* function for e^+, $\mu^\pm$, and $\tau^\pm$ productions. In the last cases

$$0 \leq \zeta < \frac{M_i}{m_\ell}.$$

Since $m_\tau > m_{p,n}$ ($m_n/m_\tau \approx 0.528740$, $m_p/m_\tau \approx 0.528012$) we conclude that for τ lepton production there are *two branches* of solutions at any neutrino energy above the reaction threshold. All this is illustrated in Figure at p. 362.

The maximum scattering angle for τ production is[a]

$$\theta_\tau^{\max} = \begin{cases} \arcsin(m_n/m_\tau) \approx 31.9203^\circ & \text{for} \quad \tau^- \\ \arcsin(m_p/m_\tau) \approx 31.8712^\circ & \text{for} \quad \tau^+. \end{cases}$$

At a fixed neutrino energy, the following conditions hold:

$$E_\ell^{\min} \leq E_\ell \leq E_\ell^{\max}, \quad P_\ell^{\min} \leq P_\ell \leq P_\ell^{\max}, \quad \text{and} \quad Q^2_{\min} \leq Q^2 \equiv -q^2 \leq Q^2_{\max}, \tag{21}$$

where

$$E_\ell^{\min,\max} = \frac{E_\ell^* \left(E_\nu + M_i\right) \mp P_\ell^* E_\nu}{\sqrt{s}}, \quad P_\ell^{\min,\max} = \frac{\left|E_\ell^* E_\nu \mp P_\ell^* \left(E_\nu + M_i\right)\right|}{\sqrt{s}}$$

and

$$Q^2_{\min,\max} = 2E_\nu^* \left(E_\ell^* \mp P_\ell^*\right) - m_\ell^2 = \frac{\left(s - M_i^2\right)\left(E_\ell^* \mp P_\ell^*\right)}{\sqrt{s}} - m_\ell^2 = m_\ell^2 \left[\frac{s - M_i^2}{\left(E_\ell^* \pm P_\ell^*\right)\sqrt{s}} - 1\right],$$

[a] For the isoscalar nucleon target with the mass of $\left(m_p + m_n\right)/2$, it is about 31.896°.

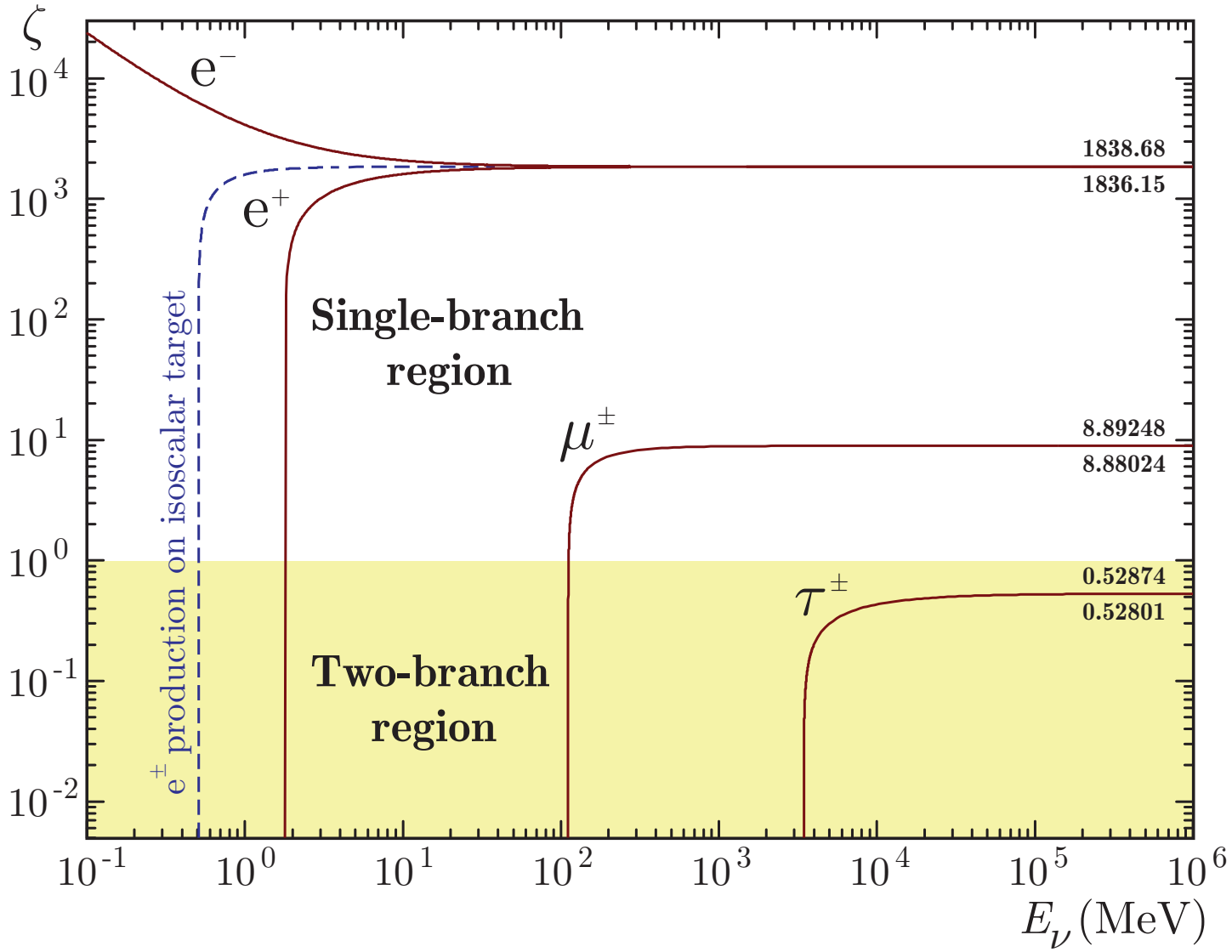

Parameter ζ as a function of (anti)neutrino energy for the quasielastic neutrinoproduction of $e^\pm$, $\mu^\pm$ and $\tau^\pm$. The differences between the curves for production of μs and τs of different charges are indistinguishable in this scale. Asymptotic values of the function $\zeta(E_\nu)$ are shown near the curves.

9.2 Pion neutrinoproduction.

As the simplest example of the inelastic exclusive reaction, consider the NC/CC induced single pion neutrinoproduction (NC1π/CC1π in common abbreviations),

$$\nu_\ell + N_i \to \ell^- + N_f + \pi \quad \text{or} \quad \overline{\nu}_\ell + N_i \to \ell^+ + N_f + \pi.$$

The neutrino and lepton energies in the center-of-mass frame of the neutrino-nucleon initial state are, respectively,

$$E^*_\nu = \frac{s - M_i^2}{2\sqrt{s}} \quad \text{and} \quad E^*_\ell \equiv E^*_\ell(W) = \frac{s + m_\ell^2 - W^2}{2\sqrt{s}},$$

while the initial (target) nucleon and the final hadronic state (resonance) energies are, respectively,

$$E^*_i = \frac{s + M_i^2}{2\sqrt{s}} \quad \text{and} \quad E^*_f \equiv E^*_f(W) = \frac{s - m_\ell^2 + W^2}{2\sqrt{s}}.$$

Here

$$\begin{aligned} W^2 &= (p' + p_\pi)^2 = (p+q)^2 \\ &= M_i^2 - Q^2 + 2M_i\,(E_\nu - E_\ell) \end{aligned} \qquad (22)$$

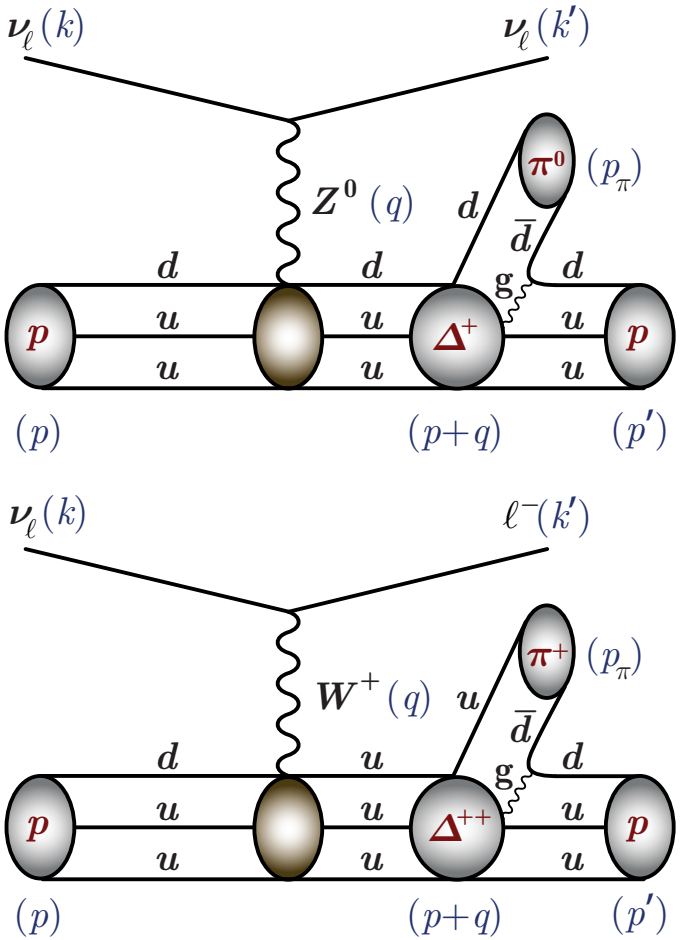

is the invariant mass squared of the final hadronic state $N_f\,(p) + \pi\,(p_\pi)$ and $q = k - k'$ is the 4-momentum transfer, and, as usually, $Q^2 = -q^2$.

Clearly

$$W_-^2 \leq W^2 \leq W_+^2,$$

where

$$W_- = M_f + m_\pi \quad \text{and} \quad W_+ = \sqrt{s} - m_\ell;$$

and the upper limit is obtained from the condition

$$E_\ell^* \geq m_\ell.$$

The reaction threshold is given by $s^{\text{th}} = (M_f + m_\ell + m_\pi)^2$ and the neutrino energy threshold is

$$E_\nu^{\text{th}} = \frac{s^{\text{th}} - M_i^2}{2M_i} = \frac{(M_f + m_\ell + m_\pi)^2 - M_i^2}{2M_i}.$$

The bounds for the variable

$$Q^2 \equiv -q^2 = 2\left(kk'\right) - m_\ell^2 = 2E_\nu\left(E_\ell - P_\ell \cos\theta\right) - m_\ell^2 \tag{23}$$

can be found in terms of variable W by rewriting Eq. (23) in the CMF,

$$Q^2 = 2E_\nu^*\left(E_\ell^* - P_\ell^* \cos\theta^*\right) - m_\ell^2,$$

and putting $\cos\theta^* = \pm 1$. In this way we have

$$Q_-^2 \leq Q^2 \leq Q_+^2, \quad \text{where} \quad Q_\pm^2 = 2E_\nu^*\left(E_\ell^* \pm P_\ell^*\right) - m_\ell^2.$$

In full analogy to the QE case, by combining Eqs. (22) and (23), we can derive the equation

$$E_\nu P_\ell \cos\theta = E_\ell\left(E_\nu + M_i\right) - \sqrt{s}E_\ell^*(W). \tag{24}$$

The formal solution to Eq. (24) is given by

$$P_\ell^\pm(\theta, W) = \frac{E_\nu^* \left(M_i E_\ell^* \cos\theta \pm m_\ell E_i^* \sqrt{\zeta^2 - \sin^2\theta} \right)}{M_i^2 + (E_\nu^*)^2 \sin^2\theta}, \tag{25a}$$

$$E_\ell^\pm(\theta, W) = \frac{M_i E_\ell^* E_i^* \pm m_\ell (E_\nu^*)^2 \cos\theta \sqrt{\zeta^2 - \sin^2\theta}}{M_i^2 + (E_\nu^*)^2 \sin^2\theta}, \tag{25b}$$

where θ is the scattering angle ($\mathbf{p}_\nu \mathbf{p}_\ell = E_\nu P_\ell \cos\theta$) and

$$\zeta \equiv \zeta(W) = \frac{2M_i\sqrt{s}P_\ell^*}{m_\ell (s - M_i^2)} = \frac{M_i \sqrt{(s + m_\ell^2 - W^2)^2 - 4m_\ell^2 s}}{m_\ell (s - M_i^2)}.$$

Since, according to Eq. (25a),

$$P_\ell^+(\theta, W) P_\ell^-(\theta, W) = m_\ell^2 E_\nu^2 \left[1 - \zeta^2(W)\right]. \tag{26}$$

Therefore, for given θ and W, there are two solutions, P_ℓ^+ and P_ℓ^-, when $\zeta(W) \leq 1$ and the only solution, P_ℓ^+, when $\zeta(W) > 1$. Finally, taking into account the conditions $\zeta(W) \geq \sin\theta$ and $\sin\theta \geq 0$ we conclude that

$$P_\ell = P_\ell^+(\theta, W), \quad E_\ell = E_\ell^+(\theta, W), \quad 0 \leq \theta \leq \pi, \qquad \text{if} \quad \zeta(W) > 1,$$
$$P_\ell = P_\ell^\pm(\theta, W), \quad E_\ell = E_\ell^\pm(\theta, W), \quad 0 \leq \theta < \arcsin\zeta(W), \qquad \text{if} \quad \zeta(W) \leq 1.$$

The asymptotic value of the limiting angle at $s \gg W^2$ is given by

$$\arcsin\zeta(W) \to \arcsin\left(\frac{M_i}{m_\ell}\right) \quad \text{if} \quad M_i \leq m_\ell.$$

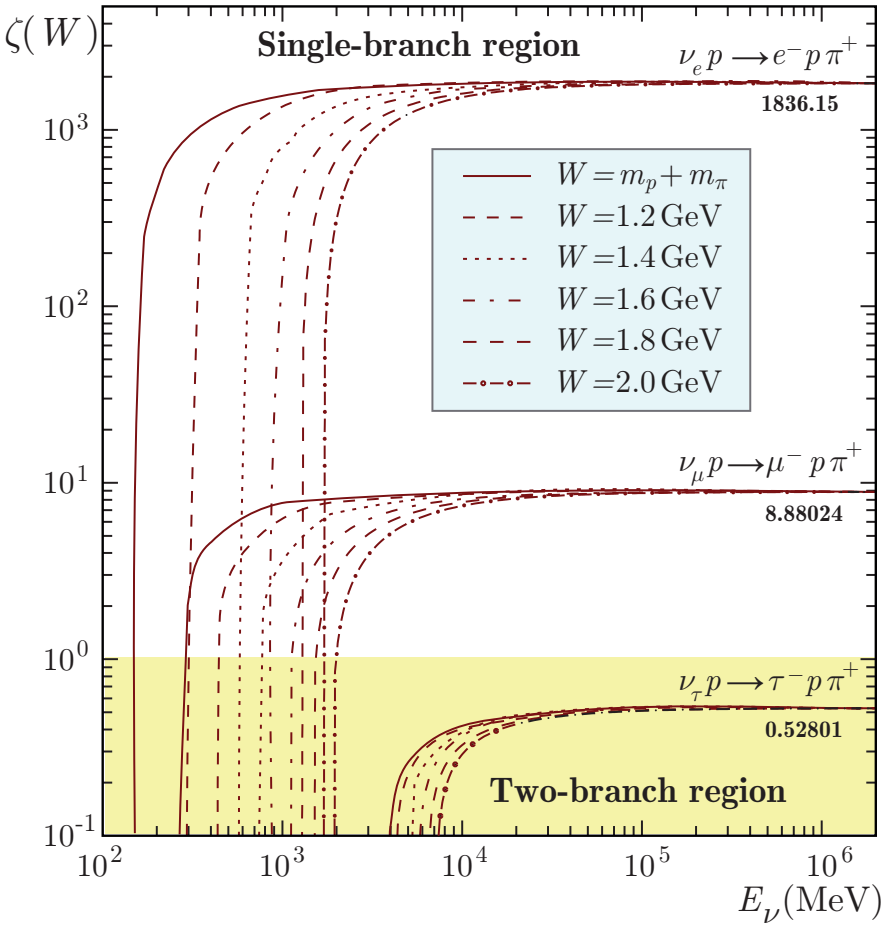

Parameter $\zeta(W)$ as a function of neutrino energy for three reactions of single pion production calculated with several values of W (cf. Figure at p. 375).

The condition $\zeta = 1$ defines the energy at which the 2nd solution, P_ℓ^-, disappears. It can be rewritten in terms of the neutrino energy as

$$\left[E_\nu - \epsilon_\nu^-(W)\right]\left[E_\nu - \epsilon_\nu^+(W)\right] = 0 \qquad (27a)$$

with

$$\epsilon_\nu^\pm(W) = \frac{W^2 - (M_i \mp m_\ell)^2}{2\,(M_i \mp m_\ell)}$$

and

$$\epsilon_\nu^+ - \epsilon_\nu^- = m_\ell \left(1 + \frac{W^2}{M_i^2 - m_\ell^2}\right).$$

In terms of variable s Eq. (27a) reads:

$$\left[s - s^-(W)\right]\left[s - s^+(W)\right] = 0, \qquad (27b)$$

where

$$s^\pm(W) = M_i\left[2\,\epsilon_\nu^\pm(W) + M_i\right] = \frac{M_i\left[W^2 - m_\ell\,(m_\ell \mp M_i)\right]}{M_i \mp m_\ell}.$$

It's easy to get that

$$s^+(W) - s^-(W) = 2M_i\left[\epsilon_\nu^+(W) - \epsilon_\nu^-(W)\right] = 2m_\ell M_i\left(1 + \frac{W^2}{M_i^2 - m_\ell^2}\right).$$

9.3 Deep inelastic scattering.

The following set of invariant variables is conventionally in use for description of the νN deep inelastic scattering (DIS):[a]

$$
\begin{aligned}
s &= (k+p)^2 = \left(k' + p_X\right)^2 = 2ME_\nu + M^2, \\
Q^2 &= -q^2 = -\left(k - k'\right)^2 = 2MxyE_\nu, \\
W^2 &= p_X^2 = (p+q)^2 = 2M(1-x)yE_\nu + M^2, \\
\nu &= \frac{(pq)}{M} = yE_\nu = E_\nu - E_\ell, \\
x &= \frac{Q^2}{2(pq)} = \frac{Q^2}{2MyE_\nu} \quad \text{(Bjorken variable)}, \\
y &= \frac{(pq)}{(pk)} = 1 - \frac{E_\ell}{E_\nu} \quad \text{(inelasticity)}.
\end{aligned}
$$

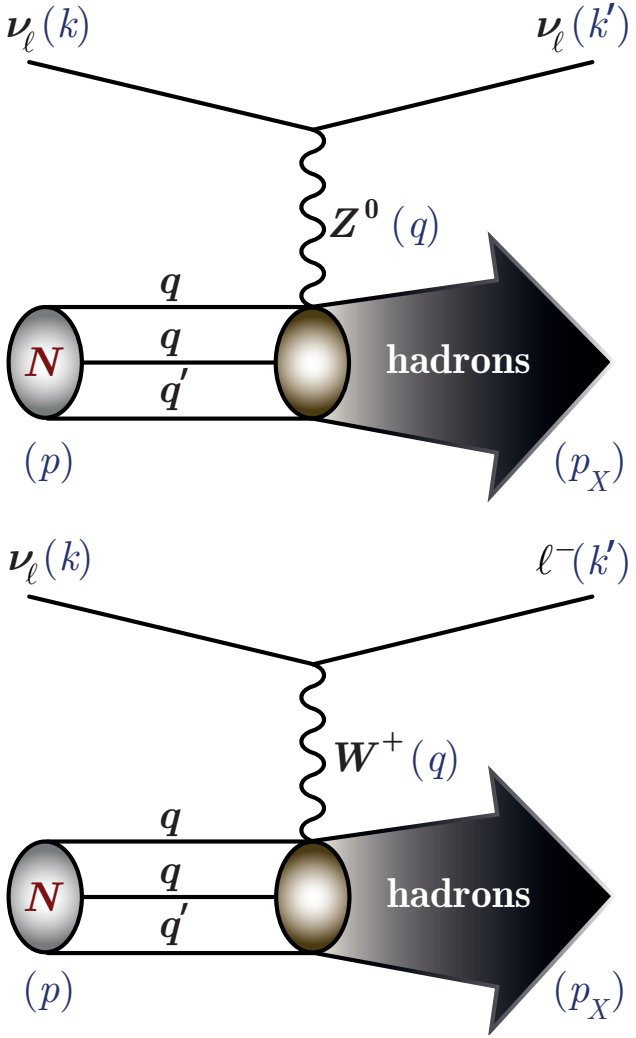

The center-of-mass neutrino and lepton energies are

$$E_\nu^* = \frac{s - M^2}{2\sqrt{s}} \quad \text{and} \quad E_\ell^* = \frac{s + m_\ell^2 - W^2}{2\sqrt{s}}.$$

[a] In this section, we use the approximation

$$M_i = M_f = M \equiv (m_p + m_n)/2.$$

For more details, see Appendix B, p. 839.

The reaction threshold energy is given by

$$E_\nu^{\text{th}} = \frac{s^{\text{th}} - M^2}{2M} = \frac{(m_\ell + W_{\text{cut}})^2 - M^2}{2M},$$

where W_{cut} is a conventional cutoff in invariant hadronic mass W necessary to avoid double counting. Clearly $W_{\text{cut}} \geq W_- = \sum_{i\in X} m_i \geq M + m_\pi$. The physical boundaries for the W are

$$W_{\text{cut}} \leq W \leq \sqrt{s} - m_\ell,$$

where, as in previous cases, the upper limit is obtained from the condition $E_\ell^* \geq m_\ell$.

Although the rest of the kinematics can easily be "guessed" from the above formulas for the CC1π case, it is useful to consider one neat and fairly general methodological trick.

9.3.1 Axial vector N and kinematic boundaries.

Let's introduce the 4-pseudovector $N_\alpha = \epsilon_{\alpha\beta\gamma\delta} p^\beta k^\gamma q^\delta = \epsilon_{\alpha\beta\gamma\delta}(p+k)^\beta p^\gamma q^\delta$ and consider it in the νN center-of-mass frame (CMF). Since $\mathbf{p}^* + \mathbf{k}^* = 0$ in CMF, we have **[prove]**

$$N^* = (0, \mathbf{N}^*), \quad \text{where} \quad \mathbf{N}^* = \sqrt{s}\left(\mathbf{k}^* \times \mathbf{k}'^*\right), \quad |\mathbf{N}^*| = \sqrt{s} E_\nu^* P_\ell^* \sin\theta^*$$

(of course $0 \leq \theta^* \leq \pi \Longrightarrow 0 \leq \sin\theta^* \leq 1$). Therefore

$$N^2 = -s\left(E_\nu^* P_\ell^* \sin\theta^*\right)^2 = -\frac{1}{16}\left(s - M^2\right)^2 \left[\left(s - W^2 + m_\ell^2\right)^2 - 4m_\ell^2 s\right] \sin^2\theta^* \leq 0. \tag{28a}$$

On the other hand

$$N^2 = p^2(qk)^2 - 2(kp)(pq)(qk) + q^2(kp)^2. \tag{28b}$$

To derive Eq. (28b) we have used the identity $g^{\alpha\alpha'}\,\epsilon_{\alpha\beta\gamma\delta}\,\epsilon_{\alpha'\beta'\gamma'\delta'} = -\begin{vmatrix} g_{\alpha\beta'} & g_{\alpha\gamma'} & g_{\alpha\delta'} \\ g_{\beta\beta'} & g_{\beta\gamma'} & g_{\beta\delta'} \\ g_{\gamma\beta'} & g_{\gamma\gamma'} & g_{\gamma\delta'} \end{vmatrix}$.

which follows from $\epsilon_{\alpha\beta\gamma\delta}\,\epsilon_{\alpha'\beta'\gamma'\delta'} = -\begin{vmatrix} g_{\alpha\alpha'} & g_{\alpha\beta'} & g_{\alpha\gamma'} & g_{\alpha\delta'} \\ g_{\beta\alpha'} & g_{\beta\beta'} & g_{\beta\gamma'} & g_{\beta\delta'} \\ g_{\gamma\alpha'} & g_{\gamma\beta'} & g_{\gamma\gamma'} & g_{\gamma\delta'} \\ g_{\delta\alpha'} & g_{\delta\beta'} & g_{\delta\gamma'} & g_{\delta\delta'} \end{vmatrix}$.

By substituting

$$(qk) = -\frac{1}{2}\left(Q^2 + m_\ell^2\right), \quad (kp) = \frac{1}{2}\left(s - M^2\right), \quad (qp) = \frac{1}{2}\left(Q^2 + W^2 - M^2\right),$$

we find[a]

$$N^2 = \frac{s}{4}\left(Q^2 - Q_-^2\right)\left(Q^2 - Q_+^2\right) \quad \text{with} \quad Q_\pm^2 = Q_\pm^2(s, W) = 2E_\nu^*\left(E_\ell^* \pm P_\ell^*\right) - m_\ell^2.$$

Taking into account that $0 \le \sin\theta^* \le 1$ and condition $N^2 \le 0$, we arrive at the inequality

$$\left(Q^2 - Q_-^2\right)\left(Q^2 - Q_+^2\right) \le 0,$$

[a] The following identities are of some utility:

$$Q_-^2 + Q_+^2 = 2\left(2E_\nu^* E_\ell^* - m_\ell^2\right), \quad Q_-^2 Q_+^2 = m_\ell^2\left[4E_\nu^*\left(E_\nu^* - E_\ell^*\right) + m_\ell^2\right].$$

which yields

$$\boxed{Q_-^2 \leq Q^2 \leq Q_+^2.} \tag{29}$$

The same formally follows from the more elementary consideration discussed in Sect. **9.2**, p. 377.

The inequalities (29) can be rewritten in terms of variables y and E_ν. Since

$$\left(Q^2 + m_\ell^2\right)^2 + 4yE_\nu^2\left(Q^2 + m_\ell^2\right) - 4Q^2E_\nu^2 \leq 0, \tag{30}$$

we have

$$Q_-^2\left(y, E_\nu\right) \leq Q^2 \leq Q_+^2\left(y, E_\nu\right), \qquad Q_\pm^2\left(y, E_\nu\right) = 2E_\nu^2\left[1 - y - \frac{m_\ell^2}{2E_\nu^2} \pm \sqrt{(1-y)^2 - \frac{m_\ell^2}{E_\nu^2}}\right].$$

It is clear that

$$Q_-^2\left(y, E_\nu\right) \geq 0$$

for $y \geq -E_\nu^2/(2m_\ell^2)$ that is in fact for any y. The same can be rewritten in terms of variables y, x, and E_ν:

$$\left(1 + \frac{Mx}{2E_\nu}\right)y^2 - \left[1 - \frac{m_\ell^2}{2E_\nu^2}\left(1 + \frac{E_\nu}{Mx}\right)\right]y + \frac{m_\ell^4}{8MxE_\nu^3} \leq 0.$$

The roots are given by

$$y^\pm\left(E_\nu, x\right) = \frac{1 - \frac{m_\ell^2}{2E_\nu^2}\left(1 + \frac{E_\nu}{Mx}\right) \pm \sqrt{\left(1 - \frac{m_\ell^2}{2MxE_\nu}\right)^2 - \frac{m_\ell^2}{E_\nu^2}}}{2\left(1 + \frac{Mx}{2E_\nu}\right)}.$$

10 Elements of Dynamics.

10.1 Generic formulas.

Consider the lepton production in the charged current (CC) neutrino and antineutrino scattering from the nonpolarized nucleon target,

$$\overset{(-)}{\nu}(k) + N(p) \to \ell^{\mp}(k') + X(p'), \quad X = N', \; N' + \pi, \text{ etc.}$$

The generic form of the differential cross section for the reaction $a + b \to n$ particles is given by[a]

$$d\sigma = \frac{(2\pi)^4 \delta\left(p_f - p_i\right) \sum |\mathcal{M}_{fi}|^2}{4(2J_a+1)(2J_b+1)\sqrt{(p_a p_b)^2 - m_a^2 m_b^2}} \prod_{j=1}^{n} \frac{d\mathbf{p}_j}{(2\pi)^3 2p_j^0}.$$

$p_i = p_a + p_b$, $p_{a,b} = (p^0_{a,b}, \mathbf{p}_{a,b})$ and $J_{a,b}$ are, respectively, the 4-momenta and spins of a and b;

$p_f = \sum_{j=1}^{n} p_j$, $p_j = (p_j^0, \mathbf{p}_j)$ are the 4-momenta of the final particles;

$\mathcal{M}_{fi}$ is the matrix element related to the S matrix, $S = 1 + i(2\pi)^4 \delta(p_f - p_i)\mathcal{M}_{fi}$, and summation is over the spins of the initial particles and over (*a part*) of the final particles.

In our particular case $p_i = k + p$, $p_f = k' + p'$, where k, p, k', $p' = p_X$ are the 4-momenta of the (anti)neutrino, target nucleon N (p or n), final lepton ℓ (e, μ or τ), and final hadronic system X, respectively.

[a] See, e.g., Л. Б. Окунь. Лептоны и кварки. 2 изд. М. Наука. 1990.

Therefore

final hadron momenta

$$d\sigma = \frac{(2\pi)^4}{8(kp)}\delta\left(k+p-k'-p'\right)\sum|\mathcal{M}|^2\frac{d\mathbf{p}_\ell}{(2\pi)^3 2E_\ell}\prod_{j=1}^{n}\frac{d\mathbf{p}_j}{(2\pi)^3 2p_j^0}.$$

The matrix element is

$$\mathcal{M} = -i\frac{G_F}{\sqrt{2}}\kappa\cdot\begin{cases} j_s^\alpha(k,k')J_\alpha(p,p') & \text{for neutrino,} \\ \bar{j}_s^\alpha(k,k')J_\alpha^*(p,p') & \text{for antineutrino,}\end{cases} \qquad \kappa = \frac{M_W^2}{M_W^2-q^2} = \frac{1}{1+Q^2/M_W^2}.$$

The factor κ arises from the W-boson propagator, M_W is the W mass, G_F is the Fermi coupling;

$$j_s^\alpha(k,k') = \langle k',s|\hat{j}_\alpha^\dagger|k\rangle = \overline{u}_s(k')\gamma^\alpha\left(\frac{1-\gamma_5}{2}\right)u(k)$$

and

$$\bar{j}_s^\alpha(k,k') = \langle k',s|\hat{j}_\alpha|k\rangle = \overline{v}(k)\gamma^\alpha\left(\frac{1-\gamma_5}{2}\right)v_s(k')$$

are the weak leptonic currents[a] and $J_\alpha(p,p') = \langle p'|\hat{J}_\alpha|p\rangle$ is the weak hadronic current.

Bad news: explicit form of this current is unknown.

Good news: we don't need to know explicit form of $J_\alpha(p,p')$ for our purposes, but the price we have to pay for it is six unknown functions... [is that really a good thing?]

Considering that $d\mathbf{k}' = P_\ell^2 dP_\ell d\Omega' = P_\ell E_\ell dE_\ell d\phi d\cos\theta$ and integrating over ϕ (yields 2π) we obtain

$$\boxed{\frac{d\sigma}{dE_\ell d\cos\theta} = \frac{1}{\pi}G_F^2\kappa^2 P_\ell\mathcal{R}, \quad \mathcal{R} \equiv \frac{1}{4ME_\nu}L_{\alpha\beta}(k,k')W^{\alpha\beta}(p,q).}$$

[a] u_s and v_s (u and v) are the standard Dirac bi-spinors for the charged leptons (neutrinos).

Here $M \equiv M_i$ is the target nucleon mass,

$$L^{\alpha\beta}(k,k') = \sum_s L_s^{\alpha\beta}(k,k'), \quad L_s^{\alpha\beta}(k,k') = \begin{cases} j_s^{\alpha}(k,k') j_s^{*\beta}(k,k') & \text{for neutrino,} \\ \bar{j}_s^{\alpha}(k,k') \bar{j}_s^{*\beta}(k,k') & \text{for antineutrino.} \end{cases}$$

is the spin-averaged leptonic tensor, and

$$W_{\alpha\beta}(p,q) = (2\pi)^3 \sum_{\text{spins}} \int J_\alpha(p,p') J_\beta^*(p,p') \delta(p'-p-q) \prod_{j=1}^{n} \frac{d\mathbf{p}_j}{(2\pi)^3 2p_j^0}$$

is the spin-averaged hadronic tensor.

Leptonic tensor. Let's recall the standard relations for Dirac bispinors:

$$u_s(k)\overline{u}_s(k) = \frac{1}{2}\left(\hat{k} + m_\ell\right)(1+\gamma_5\hat{s}), \quad \Longrightarrow \quad \sum_s u_s(k)\overline{u}_s(k) = \hat{k} + m_\ell,$$

$$v_s(k)\overline{v}_s(k) = \frac{1}{2}\left(\hat{k} - m_\ell\right)(1+\gamma_5\hat{s}), \quad \Longrightarrow \quad \sum_s v_s(k)\overline{v}_s(k) = \hat{k} - m_\ell.$$

Here s is the lepton spin (axial) 4-vector,[a] satisfying the conditions $s^2 = -1$, $(sk) = 0$. For the massless left (right) polarized neutrinos (antineutrinos)

$$u(k)\overline{u}(k) = v(k)\overline{v}(k) = \frac{1}{2}\hat{k}\,(1+\gamma_5).$$

[a] See Appendix D, p. 849 for derivation of its explicit form (not necessary for calculating the cross-section).

By applying these identities we obtain:

$$L_{\alpha\beta}(k,k') = \frac{1}{4}\mathsf{Tr}\left[\left(\hat{k}' + m_\ell\right)\gamma_\alpha\left(1 \mp \gamma_5\right)\hat{k}\gamma_\beta\left(1 \mp \gamma_5\right)\right]$$
$$= 2\left[k_\alpha k'_\beta + k'_\alpha k_\beta - g_{\alpha\beta}(kk') \mp i\epsilon_{\alpha\beta\gamma\delta}k^\gamma k'^\delta\right].$$

It is seen that

$$L_{\beta\alpha}(k,k') = L^*_{\alpha\beta}(k,k'). \tag{31}$$

Hadronic tensor. There are only 6 tensor combinations that can be built from the component of the 4-vectors p and $q = k - k' = p' - p$ and elementary tensors:[a]

$$p_\alpha p_\beta, \quad q_\alpha q_\beta, \quad p_\alpha q_\beta, \quad q_\alpha p_\beta, \quad \epsilon_{\alpha\beta\gamma\delta}p^\gamma q^\delta, \quad \text{and} \quad g_{\alpha\beta}.$$

Therefore the hadronic tensor $W(p,q)$ involves 6 independent Lorentz-invariant functions W_i (called *nucleon structure functions*). We'll use the generally accepted representation:[b]

$$W_{\alpha\beta}(p,q) = -g_{\alpha\beta}W_1 + \frac{p_\alpha p_\beta}{M^2}W_2 - i\frac{\epsilon_{\alpha\beta\gamma\delta}p^\gamma q^\delta}{2M^2}W_3$$
$$+\frac{q_\alpha q_\beta}{M^2}W_4 + \frac{p_\alpha q_\beta + q_\alpha p_\beta}{2M^2}W_5 + i\frac{p_\alpha q_\beta - q_\alpha p_\beta}{2M^2}W_6.$$

In this representation, the structure functions are dimensionless due to the appropriate mass factors. From Eq. (31) it follows that

$$W_{\beta\alpha}(p,q) = W^*_{\alpha\beta}(p,q). \tag{32}$$

[a] The term $\epsilon_{\alpha\beta\gamma\delta}p^\gamma q^\delta$ appears due to parity violation in weak interactions.

[b] C. H. Llewellyn Smith, "Neutrino reactions at accelerator energies," Phys. Rept. **3C** (1972) 261–397.

Therefore the functions W_i are real. It follows from the positive semidefinite form of $W(p,q)$ that

$$0 \le \frac{\sqrt{\nu^2 - q^2}}{2M}|W_3| \le W_1 \le \left(1 - \frac{\nu^2}{q^2}\right) W_2,$$

$$\frac{q^2}{M^2}W_4 + \frac{\nu}{M}W_5 \le W_1 - \frac{\nu^2}{q^2}W_2,$$

$$\frac{1}{4}\left(W_5^2 + W_6^2\right) \le \left[q^2 W_4 + M\nu W_5 + M^2(W_2 - W_1)\right]\frac{W_1}{\nu^2 - q^2} + W_2 W_4$$

(the proof is not quite easy). More specific properties of the structure functions are defined by the particular exclusive (like CCQE) or inclusive (DIS) subprocess.

The cross section. Finally, by using the derived formulas one can find the explicit form of the Lorentz-invariant dimensionless function $\mathcal{R}$

$$\mathcal{R} = \frac{L_{\alpha\beta}W^{\alpha\beta}}{4ME_\ell} = \left(\frac{E_\ell - P_\ell\cos\theta}{M}\right)\left(W_1 + \frac{m_\ell^2}{2M^2}W_4\right) + \left(\frac{E_\ell + P_\ell\cos\theta}{2M}\right)W_2$$
$$\pm\left[\left(\frac{E_\nu + E_\ell}{M}\right)\left(\frac{E_\ell - P_\ell\cos\theta}{2M}\right) - \frac{m_\ell^2}{2M^2}\right]W_3 - \frac{m_\ell^2}{2M^2}W_5,$$

involved into the *double differential* cross section

$$\frac{d\sigma(E_\nu, E_\ell, \theta)}{dE_\ell d\cos\theta} = \frac{G_F^2 P_\ell \mathcal{R}}{\pi\left(1 + Q^2/M_W^2\right)^2}.$$

In terms of the Bjorken scaling variables

$$x = \frac{-q^2}{2(pq)} \quad \text{and} \quad y = \frac{(pq)}{(pk')}$$

(and $E_\nu = (s - M^2)/(2M)$) the function $\mathcal{R}$ can be rewritten in the explicitly invariant form:

$$\mathcal{R} = \left(xy + \frac{m_\ell^2}{2ME_\nu} \right) W_1 + \frac{E_\nu}{M} \left\{ \left(1 - y - \frac{M}{2E_\nu} xy - \frac{m_\ell^2}{4E_\nu^2} \right) W_2 \right.$$
$$\left. \pm y \left[x \left(1 - \frac{y}{2} \right) - \frac{m_\ell^2}{4ME_\nu} \right] W_3 + \frac{m_\ell^2}{2ME_\nu} \left[\left(xy + \frac{m_\ell^2}{2ME_\nu} \right) W_4 - W_5 \right] \right\},$$

Now it is easy to find the *single differential* cross section:

$$\frac{d\sigma(E_\nu, Q^2)}{dQ^2} = 2\pi \int_{E_\ell^{\min}}^{E_\ell^{\max}} dE_\ell \left| \frac{dQ^2}{d\cos\theta} \right|^{-1} \frac{d^2\sigma(E_\nu, E_\ell, \theta)}{dE_\ell d\cos\theta} = \frac{\pi}{E_\nu} \int_{E_\ell^{\min}}^{E_\ell^{\max}} \frac{dE_\ell}{P_\ell} \frac{d^2\sigma(E_\nu, E_\ell, \theta)}{dE_\ell d\cos\theta}.$$

and the *total* cross section:

$$\sigma(E_\nu) = \int_{Q_-^2}^{Q_+^2} dQ^2 \, \frac{d\sigma(E_\nu, Q^2)}{dQ^2}.$$

Here it was taken into account that

$$\frac{dQ^2}{d\cos\theta} = -2P_\ell E_\nu \quad \text{and} \quad \cos\theta = \frac{E_\ell}{P_\ell} - \frac{Q^2 + m_\ell^2}{2P_\ell E_\nu}.$$

10.2 Simplest example: CCQE cross section.

As a (relatively) simple example, we consider the generic description of the CC-induced quasielastic neutrino scattering (CCQE) off the neutron. For simplicity, we neglect the $p-n$ mass difference.

The most common (albeit inspired by the Standard Model) form of the hadronic current $J_\alpha(p,q)$ for the CCQE νn scattering is

$$J_\alpha = \langle p(p')|J_\alpha|n(p)\rangle = V_{ud}\overline{u}_p(p')\Gamma_\alpha(p,q)u_n(p).$$

Here V_{ud} is the ud transition element from the Cabibbo-Kobayashi-Maskawa (CKM) quark-mixing matrix ($V_{ud}=\cos\theta_C$) and $\Gamma_\alpha(p,q)$ is a matrix function. As any 4×4 matrix, it can be decomposed into the complete set of the Dirac matrices $\{\Gamma_A\}=\{1,\gamma_\mu,\sigma_{\mu\nu},\gamma_\mu\gamma_5,\gamma_5\}$ (see Appendix C, p. 846). Symbolically, the vertex function is $\Gamma_\alpha(p,q)=\sum_{A=1}^{16}\bar{C}_\alpha^A(p,q)\Gamma_A$ and more explicitly:

$$\begin{aligned}
\Gamma_\alpha(p,q) &= C_\alpha(p,q)1 + C_{\alpha\beta}(p,q)\gamma^\beta + C_{\alpha\beta\lambda}(p,q)\sigma^{\beta\lambda} + C'_{\alpha\beta}(p,q)\gamma^\beta\gamma_5 + C'_\alpha(p,q)\gamma_5 \\
&= (c_{11}p_\alpha + c_{12}q_\alpha)\,1 \\
&\quad + \left(c_{21}g_{\alpha\beta} + c_{22}p_\alpha p_\beta + c_{23}p_\alpha q_\beta + c_{24}q_\alpha p_\beta + c_{25}q_\alpha q_\beta + ic_{26}\epsilon_{\alpha\beta\lambda\rho}p^\lambda q^\rho\right)\gamma^\beta \\
&\quad + [c_{31}\left(g_{\alpha\beta}p_\lambda - g_{\alpha\lambda}p_\beta\right) + c_{32}\left(g_{\alpha\beta}q_\lambda - g_{\alpha\lambda}q_\beta\right) + \left(c_{33}p_\alpha + c_{34}q_\alpha\right)\left(p_\beta q_\lambda - p_\lambda q_\beta\right) \\
&\quad + i\epsilon_{\alpha\beta\lambda\rho}\left(c_{35}p^\rho + c_{36}q^\rho\right)]\,\sigma^{\beta\lambda} \\
&\quad + \left(c_{41}g_{\alpha\beta} + c_{42}p_\alpha p_\beta + c_{43}p_\alpha q_\beta + c_{44}q_\alpha p_\beta + c_{45}q_\alpha q_\beta + ic_{46}\epsilon_{\alpha\beta\lambda\rho}p^\lambda q^\rho\right)\gamma^\beta\gamma_5 \\
&\quad + \left(c_{51}p_\alpha + c_{52}q_\alpha\right)\gamma_5.
\end{aligned}$$

Here c_{ij} are some Lorentz-invariant (hence, dependent only on Q^2) coefficient functions. Although we already accounted for the simplest symmetries, the number of these functions is still too large.

The number of the coefficient functions can be decreased by taking into account the Dirac equations

$$(\hat{p} - M)\, u_n(p) = 0 \quad \text{and} \quad \overline{u}_p(p')\left(\hat{p}' - M\right) = 0$$

and using the identities from Appendix C, p. 846 (in particular, getting rid of the convolutions of gamma-matrices with the tensor $\epsilon_{\alpha\beta\lambda\rho}$). As a result, only 6 independent complex-valued functions (called *nucleon form factors*) remain in the hadronic current J_α. In the standard representation,

$$\Gamma_\alpha(p,q) = \gamma_\alpha F_V + i\sigma_{\alpha\beta}\frac{q^\beta}{2M}F_M + \frac{q_\alpha}{M}F_S + \left(\gamma_\alpha F_A + \frac{p_\alpha + p'_\alpha}{M}F_T + \frac{q_\alpha}{M}F_P\right)\gamma_5 \tag{33}$$

$\begin{cases} F_V - \text{vector} \\ F_M - \text{magnetic} \\ F_S - \text{scalar} \\ F_T - \text{tensor} \\ F_A - \text{axial-vector} \\ F_P - \text{pseudoscalar} \end{cases}$

After routine but tedious calculations one finds:

$$W_i(Q^2) = 2M^2|V_{ud}|^2 w_i(Q^2)\delta\left(2(pq) - Q^2\right),$$

$$w_1 = |F_A|^2 + x'\left(|F_V + F_M|^2 + |F_A|^2\right),$$

$$w_2 = |F_V|^2 + |F_A|^2 + x'\left(|F_M|^2 + 4|F_T|^2\right), \quad w_3 = -2\mathrm{Re}\left[F_A^*(F_V + F_M)\right],$$

$$w_4 = \frac{x'}{4}\left(|F_M - 2F_S| + 4|F_P + F_T|^2\right) - \frac{|F_M|^2}{4} + |F_S|^2 + \mathrm{Re}\left[F_V^*\left(F_S - \frac{F_M}{2}\right) - F_A^*(F_P + F_T)\right],$$

$$w_5 = w_2 + 2\mathrm{Re}\left[F_S^*\left(F_V - x'F_M\right) - F_T^*\left(F_A - 2x'F_P\right)\right],$$

$$w_6 = 2\mathrm{Im}\left[F_S^*\left(F_V - x'F_M\right) + F_T^*\left(F_A - 2x'F_P\right)\right] \qquad \left(\text{here } x' = Q^2/(4M^2)\right).$$

From these results one can derive the so-called "ABC" formula for the single differential cross section:

$$\frac{d\sigma_{\mathrm{CCQE}}}{dQ^2} = \frac{G_F^2 M^2 |V_{ud}|^2}{8\pi(1+Q^2/M_W^2)^2 E_\nu^2}\left[A\frac{m_\ell^2+Q^2}{M^2} + B\frac{s-u}{M^2} + C\frac{(s-u)^2}{M^4}\right],$$

where

$$\begin{aligned}
A &= 2x'|F_V+F_M|^2 - (1+x')|F_V|^2 - x'(1+x')|F_M|^2 + (1+x')|F_A|^2 - 4x'(1+x')|F_T|^2 \\
&\quad -\varkappa^2\left[|F_V+F_M|^2 + |F_A+2F_P|^2 - 4(1+x')(|F_A|^2+|F_P|^2)\right], \\
B &= \mp 4x'\mathrm{Re}\left[F_A^*(F_V+F_M)\right] + 4\varkappa^2\mathrm{Re}\left[F_T^*\left(F_A - x'F_P\right) - F_S^*\left(F_V - x'F_M\right)\right], \\
C &= \frac{1}{4}\left(|F_V|^2 + x'|F_M|^2 + |F_A|^2 + 4x'|F_T|^2\right);
\end{aligned}$$

$$\begin{aligned}
s &= (k+p)^2 = 2ME_\nu + M^2, \\
u &= \left(k'-p\right)^2 = m_\ell^2 - 2ME_\ell = m_\ell^2 - 2ME_\nu + Q^2 + M^2, \\
\varkappa &= \frac{m_\ell}{2M}.
\end{aligned}$$

The above formulas can be simplified further by applying symmetry considerations and experimental data. In particular, from (approximate) isotopic invariance it follows that

$$\langle p(p)|J_\alpha|n(p')\rangle^* = \langle p(p')|J_\alpha|n(p)\rangle.$$

As a result

$$W_{\alpha\beta}[\overline{\nu}_\ell p \to \ell^+ n] = W_{\alpha\beta}[\nu_\ell n \to \ell^- p].$$

10.3 Vector form factors.

The vector and magnetic FFs can be related to the corresponding FFs for the proton and neutron electromagnetic currents,

$$\langle N(p')|J^{\mathsf{em}}_{\alpha}|N(p)\rangle = \overline{u}_N(p')\left[F^N_V(Q^2)\gamma_\alpha + iF^N_M(Q^2)\frac{\sigma_{\alpha\beta}q^\beta}{2M}\right]u_N(p), \qquad (N=p,n).$$

This yields the following important relations:[a]

$$F_V(Q^2) \equiv \frac{G_E(Q^2)+x'G_M(Q^2)}{1+x'} = F^p_V(Q^2) - F^n_V(Q^2),$$
$$F_M(Q^2) \equiv \frac{G_M(Q^2)-G_E(Q^2)}{1+x'} = F^p_M(Q^2) - F^n_M(Q^2),$$

where $G_E(Q^2)$ and $G_M(Q^2)$ are so-called Sachs electric and magnetic form factors.

Isotopic symmetry provides simple relation between $G_{E,M}(Q^2)$ and *measurable* elastic electric and magnetic form factors of proton and neutron $G^{p,n}_E(Q^2)$ and $G^{p,n}_M(Q^2)$:

$$G_M(Q^2) = G^p_M(Q^2) - G^n_M(Q^2), \quad G_E(Q^2) = G^p_E(Q^2) - G^n_E(Q^2).$$

The nucleon form factors are defined so that

$$G^p_E(0)=1, \quad G^p_M(0)=\mu_p, \quad G^n_E(0)=0, \quad G^n_M(0)=\mu_n,$$

where μ_p and μ_n are the (anomalous) magnetic moment of the proton and neutron, respectively.

[a] Detailed derivation can be found, e.g., in the excellent book by Samoil Bilenky [С. М. Биленький. Лекции по физике нейтринных и лептон-нуклонных процессов (М.: «Энергоиздат», 1981); S. M. Bilenky, "Introduction to the Physics of Electroweak Interactions," transl. by G. B. Pontecorvo (Pergamon Press, 1982)].

The magnetic moments are measured with tremendous precision; the PDG 2018 suggests:[a]

$$\mu_p = (2.7928473446 \pm 0.0000000008)\mu_N, \quad \mu_n = -(1.9130427 \pm 0000005)\mu_N,$$

where

$$\mu_N = \frac{e\hbar}{2m_p} = 3.1524512550(15) \times 10^{-14} \text{ MeV/T}$$

is the nuclear magneton ($\mu_N \approx 5.45 \times 10^{-5}\mu_B$).

Unfortunately, so good precision is not the case for the nucleon form factors. By studying elastic electron-proton scattering it is possible to derive the proton form factors G_E^p and G_M^p. Experiments on electron-deuteron scattering provide information about the neutron form factors G_E^n and G_M^n.

At low Q^2, a reasonable description of the electric and magnetic form factors is given by the very simple dipole approximation:

$$G_E^p(Q^2) \approx G_D(Q^2), \quad G_M^p(Q^2) \approx \mu_p G_D(Q^2), \quad G_E^n(Q^2) \approx 0, \quad G_M^n(Q^2) \approx \mu_n G_D(Q^2),$$

where

$$G_D(Q^2) = \left(1 + \frac{Q^2}{M_V^2}\right)^{-2}, \quad M_V = 0.84 \text{ GeV}.$$

Analyses of many earlier neutrino experiments were based on this model. Today we know these form factor a little bit better.

[a] M. Tanabashi *et al.* (Particle Data Group), "Review of Particle Physics," Phys. Rev. D **98** (2018) 030001; μ_B is the Bohr magneton, $\mu_B = e\hbar/2m_e = 5.7883818012(26) \times 10^{-14}$ MeV/T. Quark model provides a simple but a bit fraudulent explanation: $\mu_p = 4\mu_u/3 - \mu_d/3 = 2.79\mu_N$, $\mu_n = 4\mu_d/3 - \mu_u/3 = -1.86\mu_N$; here the constituent quark mass were used, whereas the current quark masses are only about 1% that of the nucleon.

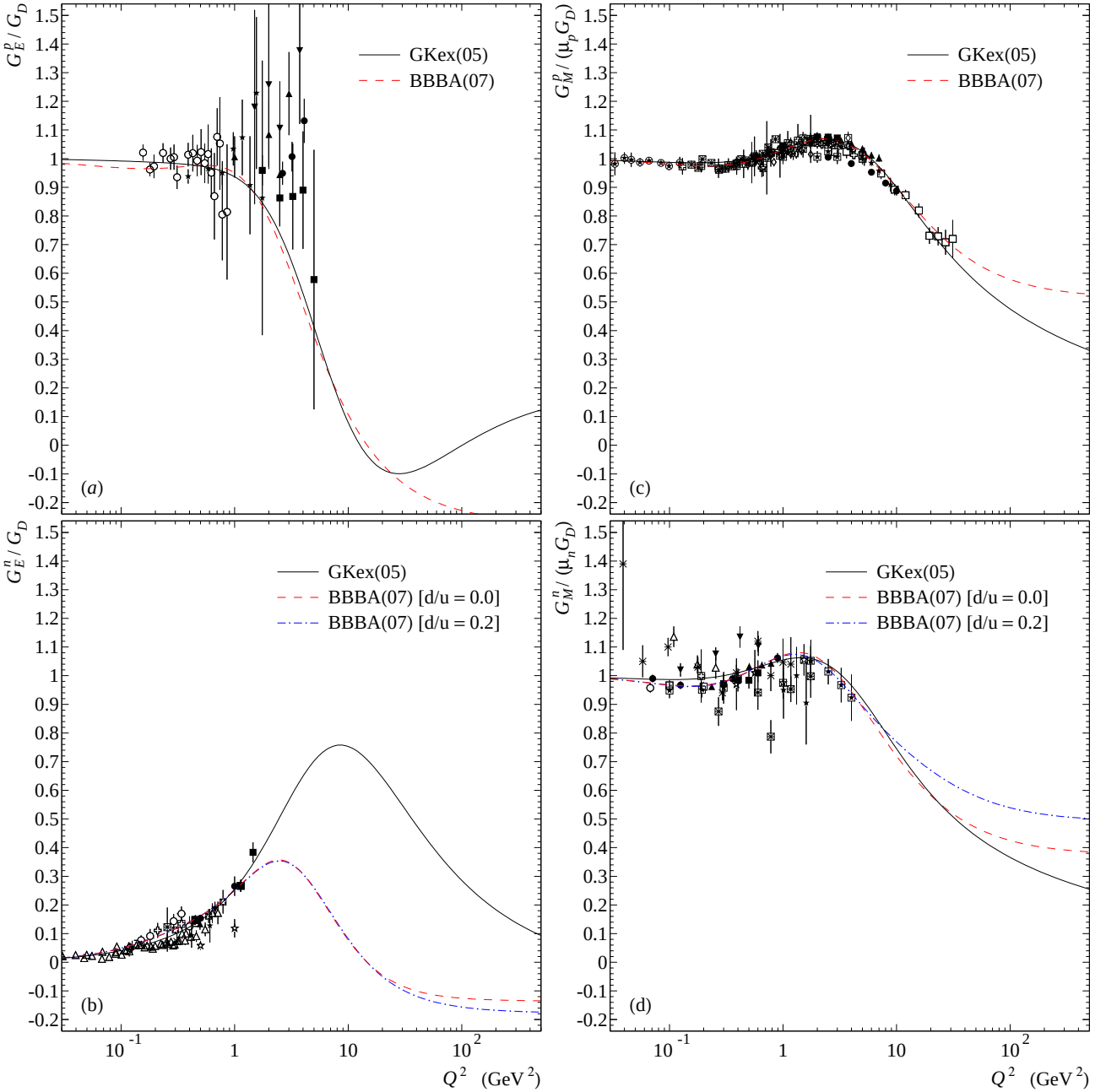

◁ Comparison of two phenomenological models for the electric and magnetic form factors of proton and neutron divided by the dipole function G_D (see previous slide) with the data from electron scattering experiments. The two versions of the so-called "BBBA(07)" parametrization are shown for the neutron form factors.

[For more details and references, see K. S. Kuzmin *et al.*, "Quasielastic axial-vector mass from experiments on neutrino-nucleus scattering," Eur. Phys. J. C **54** (2008) 517–538.]

Digression: Hypercharge & G-parity.

The hypercharge Y is defined (for hadrons only!) as the sum

$$Y = B\ [\text{Baryon number}] + \mathcal{S}\ [\text{Strangeness}] + \mathcal{C}\ [\text{Charm(ness)}] + \mathcal{B}\ [\text{Bottomness}] + \mathcal{T}\ [\text{Topness}].$$

The Gell-Mann–Nishijima formula relates Y with the third component of isospin I_3 and electric charge Q:

$$Q = \frac{1}{2}Y + I_3.$$

This formula directly follows from the definitions in terms of quark content [**prove**]:

$$B = \frac{1}{3}\sum_q \Delta n_q, \quad Q = \frac{2}{3}\sum_{q=u,c,t} \Delta n_q - \frac{1}{3}\sum_{q=d,s,b} \Delta n_q,$$
$$\mathcal{S} = -\Delta n_s, \quad \mathcal{C} = +\Delta n_c, \quad \mathcal{B} = -\Delta n_b, \quad \mathcal{T} = +\Delta n_t,$$
$$I_3 = \frac{1}{2}\left(\Delta n_u - \Delta n_d\right),$$

in which $\Delta n_q = n_q - n_{\overline{q}}$ and n_q ($n_{\overline{q}}$) is the number of valence quarks (antiquarks) in the particle.
NOTE: All quarks but u and d have $I = 0$... why?

The G-parity operator is defined as

$$G = C\exp\left(i\pi I_2\right),$$

where C is the C-parity operator [see Sect. **13**, p. 462 for more details], and I_2 is the operator associated with the 2nd component of the isospin.

Digression: Weak Hypercharge.

⋆ The weak force cares about the "handedness" or chirality of particles. Every fermion comes in left- and right-handed varieties,[a] which (quite roughly speaking) spin in opposite ways. The weak force interacts only with left-handed particles and right-handed antiparticles. For example,

$$\text{experiment always sees } n_L \to p_L + e^-_L + \overline{\nu}_{e,R} \text{ and never } n_R \to p_R + e^-_R + \overline{\nu}_{e,L}.$$

$\Longrightarrow$ Weak interactions are left–right asymmetrical = look different when viewed in a mirror.

⋆ The isospin is not conserved in weak interactions: $n(udd)|_{I_3=-1/2} \to p(uud)|_{I_3=+1/2} + e^- + \overline{\nu}_e$.
But isospin can be extended beyond quarks. Let's define $I_3(\nu_L) = 1/2$ and $I_3(e^-_L) = -1/2$, then

$$\begin{array}{rccccccc} & n_L & \to & p_L & + & e^-_L & + & \overline{\nu}_{e,R} \\ I_3: & -1/2 & = & 1/2 & - & 1/2 & - & 1/2 \end{array}$$

where we have used the rule that isospin reverses sign for antiparticles. This isospin extension is called **weak isospin**. It turns out to be fundamental concept to the theory of weak interactions. Unlike regular **approximate** isospin symmetry, weak isospin symmetry turns out to be **exact**.

	Q	I_3		Q	I_3
ν_L	0	$+\frac{1}{2}$	ν_R	0	0
e^-_L	-1	$-\frac{1}{2}$	e^-_R	-1	0
u_L	$+\frac{2}{3}$	$+\frac{1}{2}$	u_R	$+\frac{2}{3}$	0
d_L	$-\frac{1}{3}$	$-\frac{1}{2}$	d_R	$-\frac{1}{3}$	0

⋆ **Weak hypercharge**, Y, which relates the weak isospin I_3 to the charge Q via the Gell-Mann–Nishijima formula

$$Q = I_3 + Y/2,$$

is a quantity that is vital to the Standard Model.

Weak hypercharge is the generator of the $U(1)$ component of the electroweak gauge group.

[a] Spinor field ψ is the sum of $\psi_L = \frac{1}{2}(1-\gamma_5)\psi$ and $\psi_R = \frac{1}{2}(1+\gamma_5)\psi$; we'll discuss this issue in Chap. 11.

First- and second-class currents.

According to Weinberg's theorem,[a] the hypercharge conserved "$V-A$" hadronic current, $J_\alpha = V_\alpha - A_\alpha$, can be split into two parts: $J_\alpha = J_\alpha^{(I)} + J_\alpha^{(II)}$ or, in terms of the vector and axial contributions,

$$V_\alpha = V_\alpha^{(I)} + V_\alpha^{(II)} \quad \text{and} \quad A_\alpha = A_\alpha^{(I)} + A_\alpha^{(II)}.$$

Then the 1st- and 2nd-class currents are transformed as

$$\left.\begin{aligned} GV_\alpha^{(I)}G^{-1} &= +V_\alpha^{(I)} \quad (V, M) \\ GA_\alpha^{(I)}G^{-1} &= -A_\alpha^{(I)} \quad (A, P) \end{aligned}\right\} \textbf{FCC}, \qquad \left.\begin{aligned} GV_\alpha^{(II)}G^{-1} &= -V_\alpha^{(II)} \quad (S) \\ GA_\alpha^{(II)}G^{-1} &= +A_\alpha^{(II)} \quad (T) \end{aligned}\right\} \textbf{SCC}.$$

General restrictions for the form factors.

- T invariance $\Longrightarrow$ $\mathrm{Im}\,(F_V, F_M, F_A, F_P, F_S, F_T) = 0$;
- C invariance $\Longrightarrow$ $\mathrm{Im}\,(F_V, F_M, F_A, F_P) = 0$ and $\mathrm{Re}\,(F_S, F_T) = 0$;
- T invariance + C invariance $\Longrightarrow$ $F_S = F_T = 0$ $\Longrightarrow$ no SCC;
- $\partial_\alpha V^\alpha = 0$ (CVC) $\Longrightarrow$ $F_S = 0$ (hardly measurable).

[a] S. Weinberg, "Charge symmetry of weak interactions," Phys. Rept. **112** (1958) 1375–1379.

10.4 Axial-vector and induced pseudoscalar form factors.

For the axial and pseudoscalar form factors it is conventional to use the so-called dipole parametrizations[a]

$$F_A(Q^2) = F_A(0)\left(1+\frac{Q^2}{M_A^2}\right)^{-2}, \tag{34}$$

$$F_P(Q^2) = \frac{2M^2}{m_\pi^2+Q^2}F_A(Q^2), \tag{35}$$

where $F_A(0) = g_A \approx -1.267$ is the axial coupling, m_π is the charged pion mass, and M_A is the axial-vector mass treated as a free parameter. In fact, Eq. (35) is a conjecture inspired by the hypothesis of partial conservation of the axial current (PCAC), expectation that the form factor F_P is dominated by the pion pole near $Q^2 = 0$, and the "technical" condition

$$m_\pi^2 \left|\frac{1}{F_A(0)}\frac{dF_A(Q^2)}{dQ^2}\right|_{Q^2=0} = \frac{2m_\pi^2}{M_A^2} \ll 1,$$

which is obviously fulfilled for the experimental lower limit of M_A. Considering that the pseudoscalar contribution enters into the cross sections multiplied by $(m_\ell/M)^2$, the uncertainty caused by this approximation may only be significant for $\nu_\tau/\overline{\nu}_\tau$ induced reactions and it is not very important for reactions induced by $\nu_{e,\mu}/\overline{\nu}_{e,\mu}$.

[a] This is by no means the only parameterization. For example, the so-called z-expansion is now popular. The generic form of this parametrization is given by $G(t) = \sum_k c_k z^k$, $z = \left(\sqrt{t_{\text{cut}}+t}-\sqrt{t}\right) / \left(\sqrt{t_{\text{cut}}+t}+\sqrt{t}\right)$.

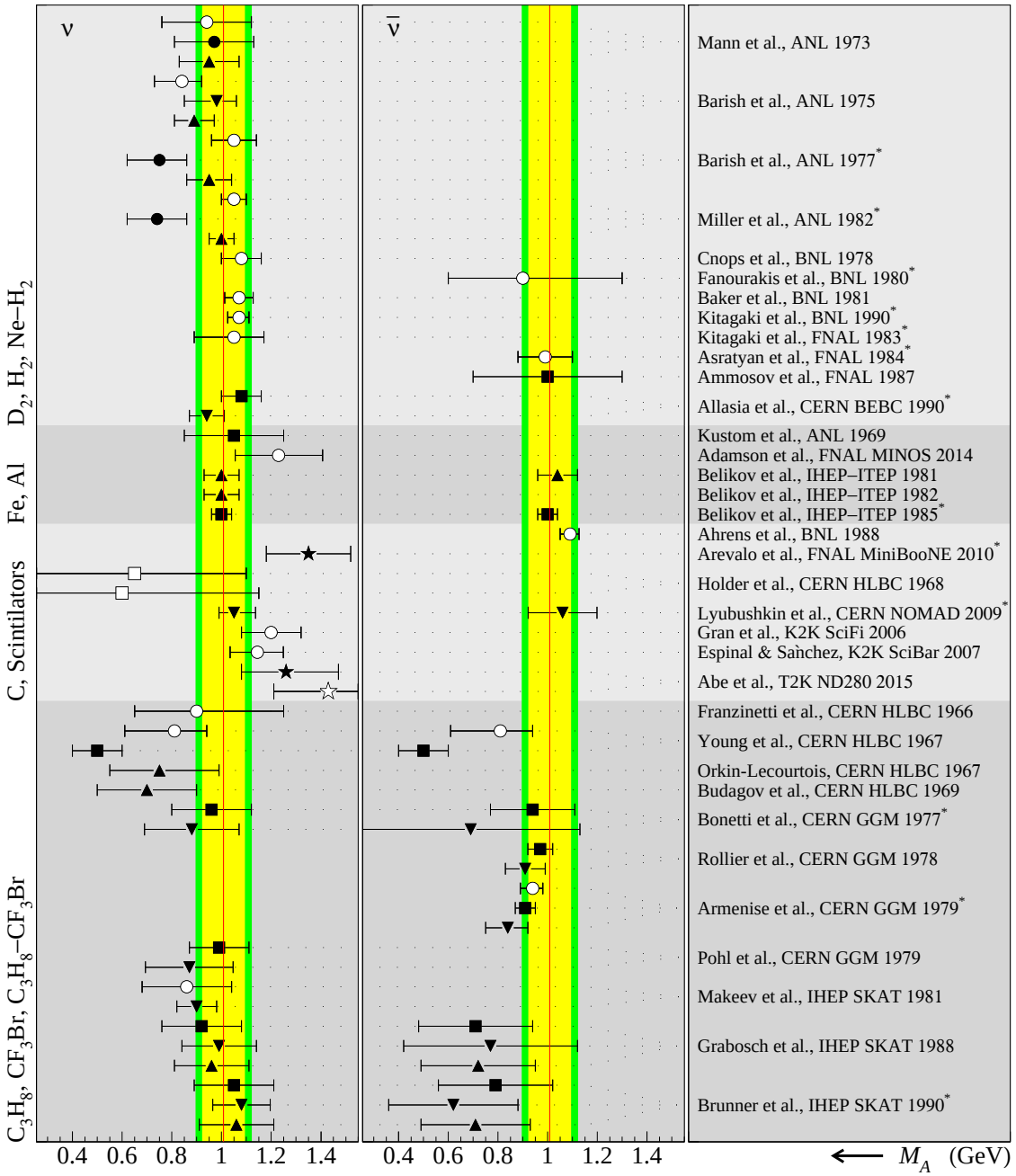

◁ Summary of the M_A values extracted in the neutrino accelerator experiments at ANL, BNL, FNAL, CENR, IHEP-ITEP, and T2K. The data were obtained using very different input models for the electromagnetic form factors and nuclear effect.

Vertical red lines show the mean values of M_A obtained in a global analysis of the Deuterium data performed within an unified model. Yellow and green bands represent 1σ and 2σ uncertainties.

[From I. D. Kakorin, K. S. Kuzmin & VN, "A unified empirical model for quasielastic interactions of neutrino and antineutrino with nuclei," Phys. Part. Nucl. Lett. **17** (2020) 265–288.]

In order to illustrate possible SCC effects one considers the following *toy* model for the nonstandard (in general complex) SCC induced scalar and tensor form factors:

$$F_S\left(q^2\right)=\xi_S e^{i\phi_S}\left(1-\frac{q^2}{M_S^2}\right)^{-2} \quad \text{and} \quad F_T\left(q^2\right)=\xi_T e^{i\phi_T} F_A(0)\left(1-\frac{q^2}{M_T^2}\right)^{-2}.$$

The model includes six free parameters, $\xi_{S,T} \geq 0$, $\phi_{S,T}$, and $M_{S,T}$.

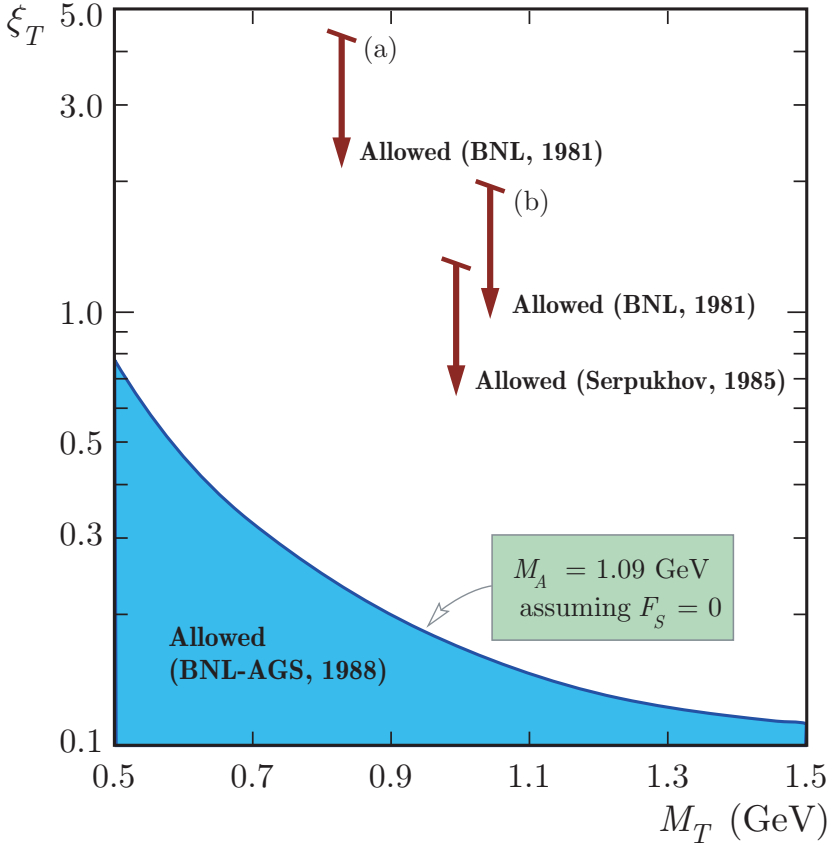

Such a parametrization has been used by the BNL Collaboration,[a] assuming CVC (that is $\xi_S = 0$). The 90% C.L. upper limit was not very restrictive: $\boxed{\xi_T < 2}$ assuming $M_A = M_T = M$ [arrow (b)]. Later on, it has been used in the experiments at Serpukhov (IHEP)[b] and Brookhaven (BNL-AGS).[c]

All these experiments *found no evidence for SCC.*

◁ The strongest (90% C.L.) upper limit on ξ_T has been obtained by the BNL-AGS as a function of the "tensor mass," M_T [blue curve]. It ranges from about 0.78 at $M_T = 0.5$ GeV to about 0.11 at $M_T = 1.5$ GeV.

[a] N. J. Baker *et al.*, Phys. Rev. D **23** (1981) 2499–2505 [ν_μ beam with $\langle E_\nu \rangle = 1.6$ GeV].

[b] S. V. Belikov *et al.*, Z. Phys. A **320** (1985) 625–633 [ν_μ and $\overline{\nu}_\mu$ beams with $E_\nu = 3 - 30$ GeV].

[c] L. A. Ahrens *et al.*, Phys. Lett. B **202** (1988) 284–288 [$\overline{\nu}_\mu$ beam with $\langle E_\nu \rangle = 1.2$ GeV].

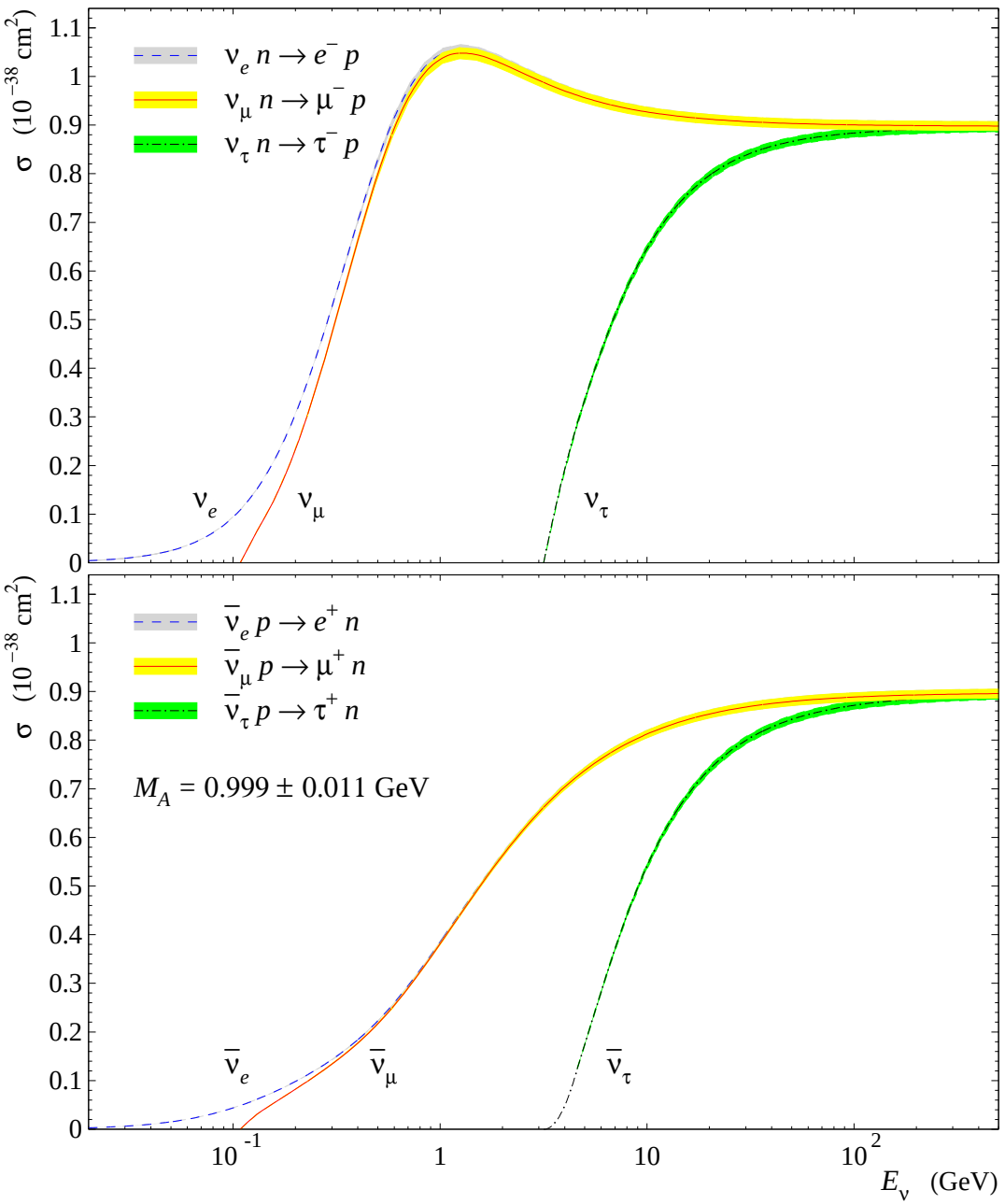

◁ Total cross sections for the electron, muon and τ neutrino and antineutrino CCQE interactions with free nucleons calculated using the dipole model of the axial-vector form factor with $M_A = 0.999 \pm 0.011$ GeV and the BBBA(07) model for the vector form factors of the nucleon with $d/u = 0$ (see p. 395). Shaded bands represent the uncertainty due to the 1σ error in determination of the parameter M_A.

Note: An updated value of M_A extracted from the Deuterium data is

$$M_A^{(D)} = 1.003^{+0.085\,(0.112)}_{-0.084\,(0.111)} \text{ GeV}$$

Inclusion of the current (2017) data from heavier nuclear (mainly carbonaceous) targets yields

$$M_A = 1.01 \pm 0.025\,(0.030) \text{ GeV}$$

with $\chi^2/\text{NDF} \approx 0.72$.

10.5 Nuclear effects.

Most current neutrino detectors use heavy materials such as scintillator, water, iron, or noble liquids. As a result, the νN phenomenology must be expanded to include the effects of interactions within a complex nucleus. This is a very difficult problem still not satisfactory solved.

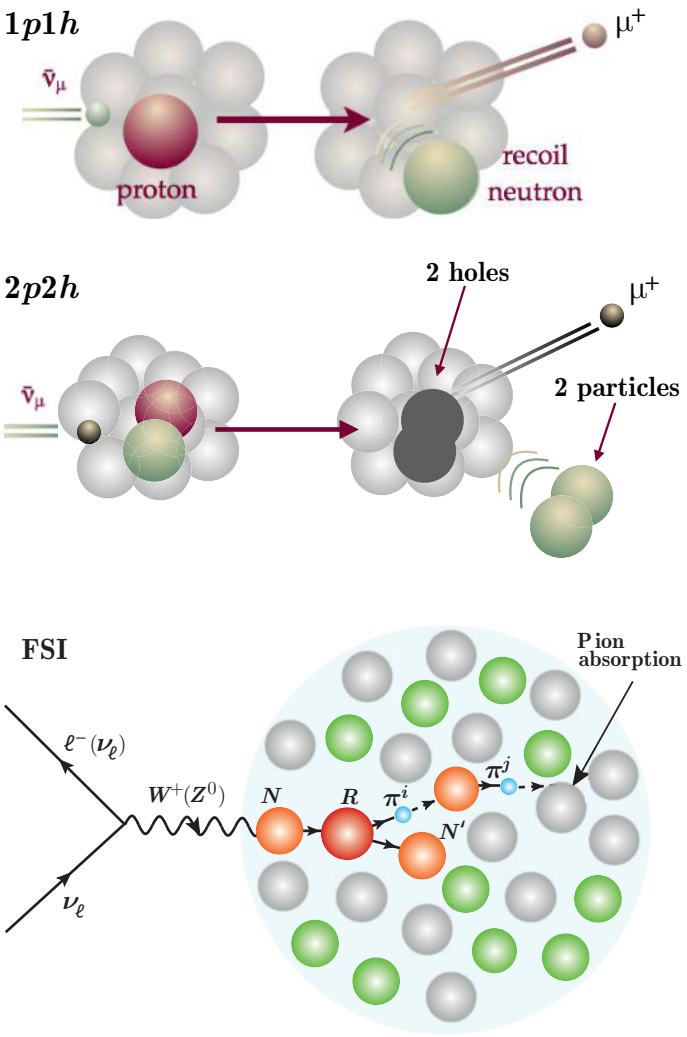

There is substantial evidence that a significant part of neutrino interactions involve scattering from correlated nucleon pairs. This process is alternately described as a $2p2h$ or MEC (Meson Exchange Current) process.

◁ Figure schematically illustrates a standard CCQE process where $\overline{\nu}$ interacts with a single proton inside a nucleus and produces a recoil neutron (top) and a $2p2h$ process where $\overline{\nu}$ interacts quasi-elastically with a np pair in the nucleus producing a two-nucleon final state (bottom).
The products of the initial scatter traverse the nuclear matter. This can lead to rescattering, production, or absorption of final-state hadrons, and results in a final state that differs from the one that would be expected from the initial νN interaction.

◁ Figure shows the case when the ν interaction causes a heavy resonance, which decays to a nucleon and pion (see diagram at p. 376), the latter being absorbed, mimicking a QE interaction signature.

[Figures are borrowed from M. Sajjad Athar *et al.*, "Status and perspectives of neutrino physics," Prog. Part. Nucl. Phys. **124** (2022) 103947, arXiv:2111.07586v1 [hep-ph].]

10.6 Polarization density matrix.

Consider shortly the *polarized* lepton production in the CC neutrino and antineutrino scattering from the *nonpolarized* nucleon target. We'll use the formalism of *polarization density matrix* (PDM). The generic form of PDM, $\boldsymbol{\rho}$ for the reaction

$$\overset{(-)}{\nu}(k) + N(p) \to \ell^{\mp}(k') + X(p')$$

is given by

$$d\boldsymbol{\Sigma} = \left\| d\sigma_{\lambda\lambda'} \right\| \equiv \boldsymbol{\rho} d\sigma, \qquad d\sigma = d\sigma_{++} + d\sigma_{--},$$

where

$$d\sigma_{\lambda\lambda'} = \frac{(2\pi)^4 \mathcal{M}_\lambda \mathcal{M}^*_{\lambda'} \delta\left(p_f - p_i\right)}{4\sqrt{\left(p_a p_b\right)^2 - m_a^2 m_b^2}} \prod_{j=1}^{n} \frac{d\mathbf{p}_j}{(2\pi)^3 2p_j^0}.$$

The matrix elements are

$$\mathcal{M}_\lambda \propto \begin{cases} j^\alpha_\lambda\left(k,k'\right) J_\alpha\left(p,p'\right) & \text{for neutrino,} \\ \overline{j}^\alpha_\lambda\left(k,k'\right) J_\alpha\left(p,p'\right) & \text{for antineutrino,} \end{cases}$$

where

$$j^\alpha_\lambda(k,k') = \langle k',\lambda|\hat{j}^\dagger_\alpha|k\rangle = \overline{u}_\lambda(k')\gamma^\alpha\left(\frac{1-\gamma_5}{2}\right)u(k)$$

and

$$\overline{j}^\alpha_\lambda(k,k') = \langle k',\lambda|\hat{j}_\alpha|k\rangle = \overline{v}(k)\gamma^\alpha\left(\frac{1-\gamma_5}{2}\right)v_\lambda(k')$$

are the weak leptonic currents with fixed chirality.

The elements of the polarization density matrix can be found as[a]

$$\frac{d^2\sigma_{++}}{dE_\ell d\cos\theta} = K\left(\frac{E_\ell \mp P_\ell}{2M}\right)\left\{(1\pm\cos\theta)\left(W_1 \pm \frac{E_\nu \mp P_\ell}{2M}W_3\right)\right.$$
$$\left. +\frac{1\mp\cos\theta}{2}\left[W_2 + \frac{E_\ell \pm P_\ell}{M}\left(\frac{E_\ell \pm P_\ell}{M}W_4 - W_5\right)\right]\right\},$$
$$\frac{d^2\sigma_{--}}{dE_\ell d\cos\theta} = K\left(\frac{E_\ell \pm P_\ell}{2M}\right)\left\{(1\mp\cos\theta)\left(W_1 \pm \frac{E_\nu \pm P_\ell}{2M}W_3\right)\right.$$
$$\left. +\frac{1\pm\cos\theta}{2}\left[W_2 + \frac{E_\ell \mp P_\ell}{M}\left(\frac{E_\ell \mp P_\ell}{M}W_4 - W_5\right)\right]\right\},$$
$$\frac{d^2\sigma_{+-}}{dE_\ell d\cos\theta} = K\left(\frac{m\sin\theta}{4M}\right)\left[\mp\left(2W_1 - W_2 - \frac{m^2}{M^2}W_4 + \frac{E_\ell}{M}W_5\right) - \frac{E_\nu}{M}W_3 + i\frac{P_\ell}{M}W_6\right],$$
$$\frac{d^2\sigma_{-+}}{dE_\ell d\cos\theta} = K\left(\frac{m\sin\theta}{4M}\right)\left[\mp\left(2W_1 - W_2 - \frac{m^2}{M^2}W_4 + \frac{E_\ell}{M}W_5\right) - \frac{E_\nu}{M}W_3 - i\frac{P_\ell}{M}W_6\right],$$

The upper (lower) signs in the above formulas are, as above, for neutrino (antineutrino) and

$$K = \frac{G_F^2 P_\ell}{\pi}\left(1 + \frac{Q^2}{M_W^2}\right)^{-2}.$$

The rest notation is the same as above.

[a] K. S. Kuzmin *et al.*, "Lepton polarization in neutrino nucleon interactions," Mod. Phys. Lett. A **19** (2004) 2815–2829, hep-ph/0312107.

10.6.1 Lepton polarization vector.

The lepton polarization vector $\boldsymbol{\mathcal{P}} = (\mathcal{P}_1, \mathcal{P}_2, \mathcal{P}_3)$ is defined through the *polarization density matrix*[a]

$$\frac{d^2\boldsymbol{\Sigma}}{dE_\ell d\cos\theta} \equiv \left|\left| \frac{d^2\sigma_{\lambda\lambda'}}{dE_\ell d\cos\theta} \right|\right| = \frac{1}{2}\left(1 + \boldsymbol{\sigma}\boldsymbol{\mathcal{P}}\right) \frac{d^2\sigma}{dE_\ell d\cos\theta}. \tag{36}$$

Here $d^2\sigma/dE_\ell d\cos\theta$ is the differential cross section for *unpolarized* lepton production in νN collisions. Both $d^2\boldsymbol{\Sigma}/dE_\ell d\cos\theta$ and $d^2\sigma/dE_\ell d\cos\theta$ are defined for each subprocess – QES, RES, DIS, or for the sum over all three subprocesses (QES+RES+DIS) – subject to circumstances. According to Eq. (36), the *perpendicular* ($\mathcal{P}_1$), *transverse* ($\mathcal{P}_2$), and *longitudinal* ($\mathcal{P}_3$) components of the polarization vector are given by

$$\begin{aligned}
\mathcal{P}_1 \equiv \mathcal{P}_P &= \quad \rho_{+-} + \rho_{-+} \quad = \quad \frac{d^2\sigma_{+-} + d^2\sigma_{-+}}{d^2\sigma}, \\
\mathcal{P}_2 \equiv \mathcal{P}_T &= i\left(\rho_{+-} - \rho_{-+}\right) = i\,\frac{d^2\sigma_{+-} - d^2\sigma_{-+}}{d^2\sigma}, \\
\mathcal{P}_3 \equiv \mathcal{P}_L &= \quad \rho_{++} - \rho_{--} \quad = \quad \frac{d^2\sigma_{++} - d^2\sigma_{--}}{d^2\sigma},
\end{aligned}$$

$$\boldsymbol{\rho} = \frac{1}{2}\left(1 + \boldsymbol{\sigma}\boldsymbol{\mathcal{P}}\right) = \begin{pmatrix} \rho_{++} & \rho_{+-} \\ \rho_{-+} & \rho_{--} \end{pmatrix} = \frac{1}{2}\begin{pmatrix} 1+\mathcal{P}_3 & \mathcal{P}_1 - i\mathcal{P}_2 \\ \mathcal{P}_1 + i\mathcal{P}_2 & 1-\mathcal{P}_3 \end{pmatrix},$$

$$d^2\sigma = d^2\sigma_{++} + d^2\sigma_{--}.$$

[a] We use notation: $\boldsymbol{\sigma} = (\sigma_1, \sigma_2, \sigma_3)$, where σ_i are the Pauli matrices (see p. 462 and Appendix C, p. 846).

Clearly $d^2\sigma_{++}/dE_\ell d\cos\theta$ ($d^2\sigma_{--}/dE_\ell d\cos\theta$) is the cross section for production of right (left) handed lepton. Since the components $\mathcal{P}_i$ (as well as the cross section for unpolarized lepton production) must be real, we have

$$\mathrm{Im}\, d^2\sigma_{++} = \mathrm{Im}\, d^2\sigma_{--} = 0, \qquad \mathrm{Re}\, d^2\sigma_{+-} = \mathrm{Re}\, d^2\sigma_{-+}, \qquad \mathrm{Im}\, d^2\sigma_{+-} = -\mathrm{Im}\, d^2\sigma_{-+}.$$

Taking account for these equations and the condition $0 \le |\boldsymbol{\mathcal{P}}| \le 1$ for the degree of polarization $|\boldsymbol{\mathcal{P}}| = \sqrt{\mathcal{P}_1^2 + \mathcal{P}_2^2 + \mathcal{P}_3^2}$ yields the following inequalities:

$$0 \le d^2\sigma_{++} d^2\sigma_{--} - \left|d^2\sigma_{+-}\right|^2 \le \frac{1}{4}\left(d^2\sigma_{++} + d^2\sigma_{--}\right)^2,$$

providing a useful numerical test.

Once again: $\mathcal{P}_L$ ($\mathcal{P}_P$) is the component of $\boldsymbol{\mathcal{P}}$ parallel (perpendicular) to $\mathbf{p}_\ell$ in the production plane, while $\mathcal{P}_T$ is perpendicular to the production plane.

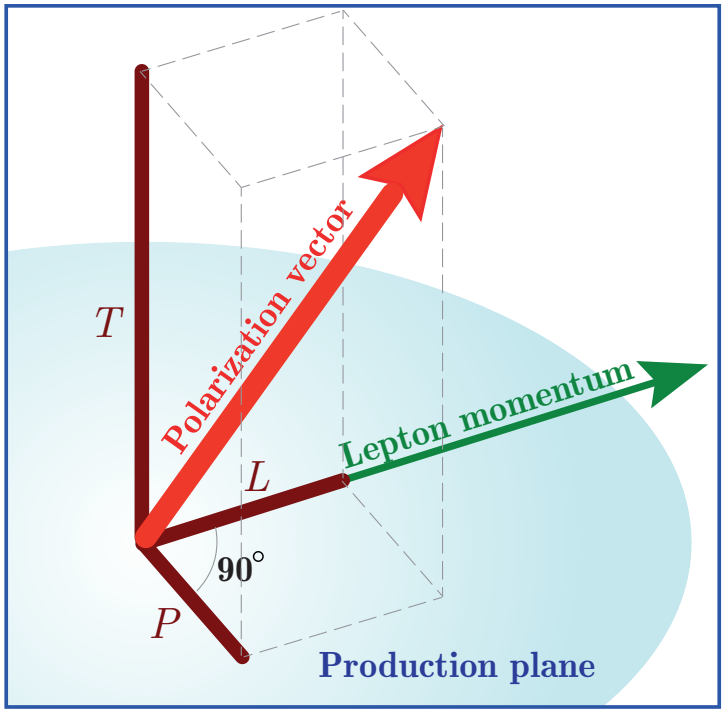

Why is this so? Let's remind ourselves that $\frac{1}{2}\sigma_i$ are the operators of the spin-$\frac{1}{2}$ projections. Hence, taking into account that

$$\mathrm{Tr}\,(\boldsymbol{\rho}) = 1, \quad \mathrm{Tr}\,(\sigma_i) = 0, \quad \text{and} \quad [\sigma_i, \sigma_j]_+ = 2\delta_{ij},$$

we obtain

$$\mathrm{Tr}\left(\boldsymbol{\rho}\frac{\sigma_i}{2}\right) = \frac{\mathcal{P}_i}{2}.$$

Therefore $\mathcal{P}_i$ are indeed the components of the lepton polarization vector (defined relative to the lepton momentum).

Note that the density matrix ρ and degree of polarization $|\mathcal{P}|$ are relativistic invariants.

By using the derived formulas we obtain the components of the polarization vector $\mathcal{P}$:

$$\mathcal{P}_P = \mp\frac{m\sin\theta}{2M\mathcal{R}}\left(2W_1 - W_2 \pm \frac{E_\nu}{M}W_3 - \frac{m^2}{M^2}W_4 + \frac{E_\ell}{M}W_5\right),$$

$$\mathcal{P}_T = -\frac{mP_\ell\sin\theta}{2M^2\mathcal{R}}\,W_6,$$

$$\mathcal{P}_L = \mp 1 \pm \frac{m^2}{M^2\mathcal{R}}\left\{\left[\left(\frac{2M}{E_\ell+P_\ell}\right)W_1 \pm \left(\frac{E_\nu - P_\ell}{E_\ell+P_\ell}\right)W_3\right]\cos^2\frac{\theta}{2}\right.$$
$$\left. + \left[\left(\frac{M}{E_\ell+P_\ell}\right)W_2 + \left(\frac{E_\ell+P_\ell}{M}\right)W_4 - W_5\right]\sin^2\frac{\theta}{2}\right\}.$$

As it should be, $\mathcal{P}_P = \mathcal{P}_T = 0$ and $\mathcal{P}_L = \mp 1$ for a massless lepton.

Another form of presentation of the longitudinal polarization,

$$\mathcal{P}_L = \mp\frac{1}{\mathcal{R}}\left\{\left(\frac{P_\ell - E_\ell\cos\theta}{M}\right)\left(W_1 - \frac{m^2}{2M^2}W_4\right) + \left(\frac{P_\ell + E_\ell\cos\theta}{2M}\right)W_2\right.$$
$$\left. \pm\left[\frac{(E_\nu + E_\ell)\,(P_\ell - E_\ell\cos\theta) + m^2\cos\theta}{2M^2}\right]W_3 - \frac{m^2\cos\theta}{2M^2}W_5\right\},$$

is a bit less transparent but more convenient for numerical calculations.

As an example, we consider numerical estimations of $\mathcal{P}_L$ and $|\mathcal{P}|$ performed in two models for the nucleon electromagnetic form factors for $\tau^\pm$ leptons produced in the CCQE reactions.[a]

[a] K. S. Kuzmin *et al.*, "Polarization of tau leptons produced in quasielastic neutrino nucleon scattering," Mod. Phys. Lett. A **19** (2004) 2919–2928, hep-ph/0403110.

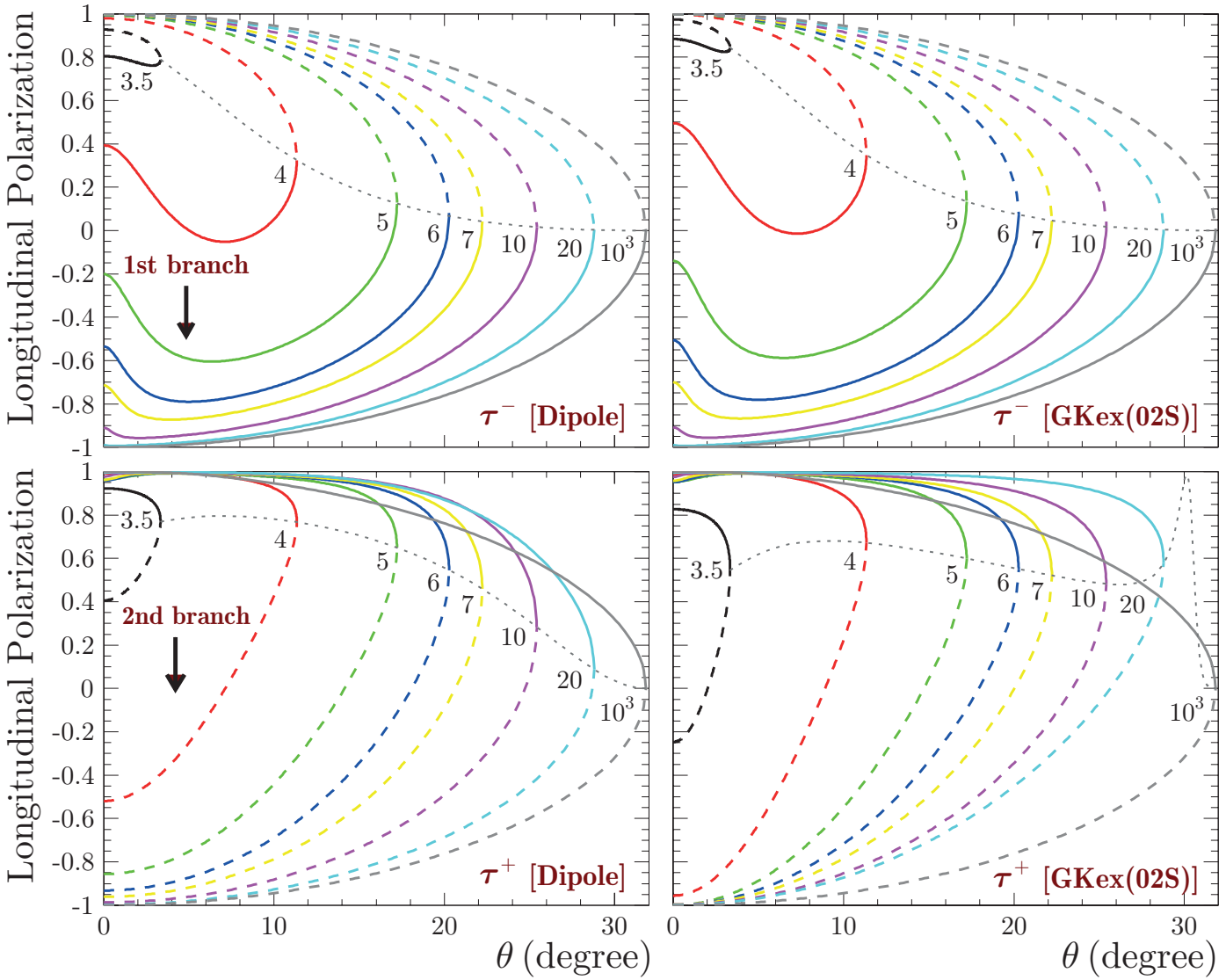

Longitudinal polarization, $\mathcal{P}_L$, evaluated in the dipole and GKex(02S) models for the nucleon electromagnetic form factors at different (anti)neutrino energies (shown near the curves in GeV). The gray dotted curves indicate the boundaries between the two kinematically allowed solutions (it is defined by the condition $\sin\theta = \zeta$). The main kinematic branches are shown by solid curves.

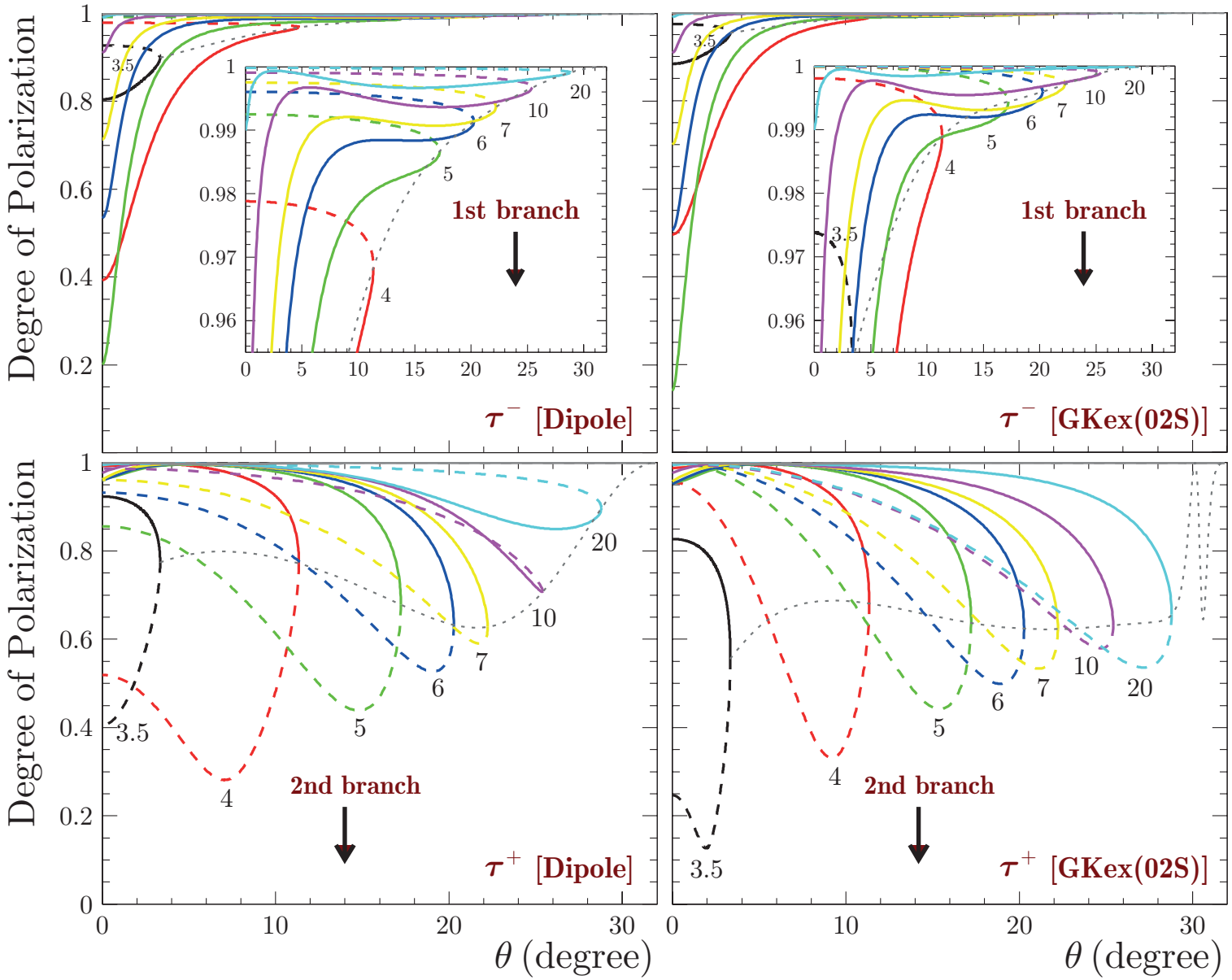

Degree of polarization, $|\mathcal{P}|$, evaluated in the two models. The notation is the same as in previous figure. The insets in the two *top panels* show a zoomed view of the graphs for $|\mathcal{P}| > 0.965$.

10.7 Comparison with experiment (a few examples).

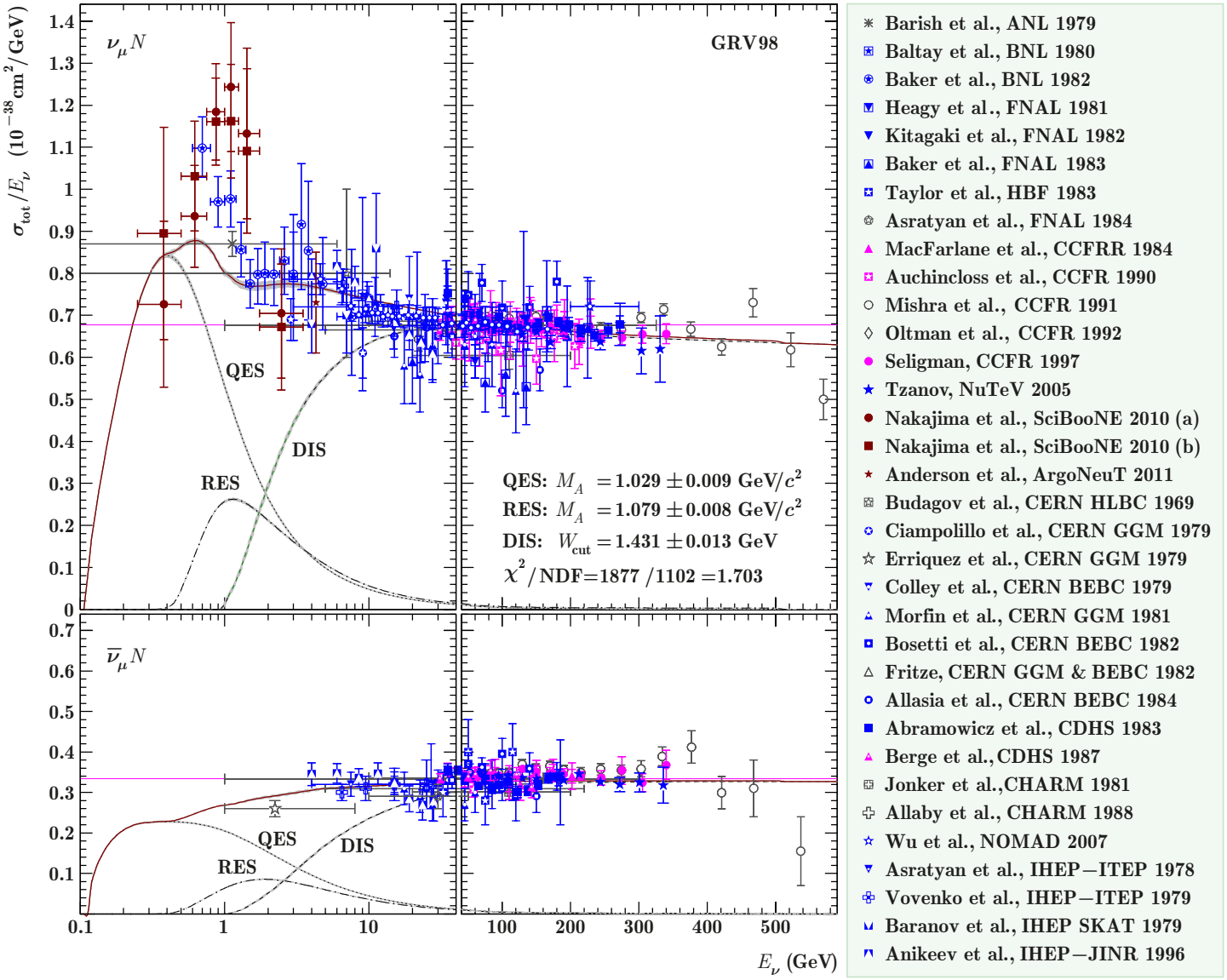

◁ A comparison of measured and predicted slopes of the $\nu_\mu N$ and $\overline{\nu}_\mu N$ total cross sections at accelerator energies for an isoscalar target.

Three main contributions are shown: QES (or CCQE), RES (or CC1π) calculated in ExRS model, and DIS calculated with GRV 98 PDFs. The best-fit parameters are shown in legend.

[From K. S. Kuzmin *et al.*, Phys. Atom. Nucl. **69** (2005) 1857–1871, hep-ph/0511308 (updated).]

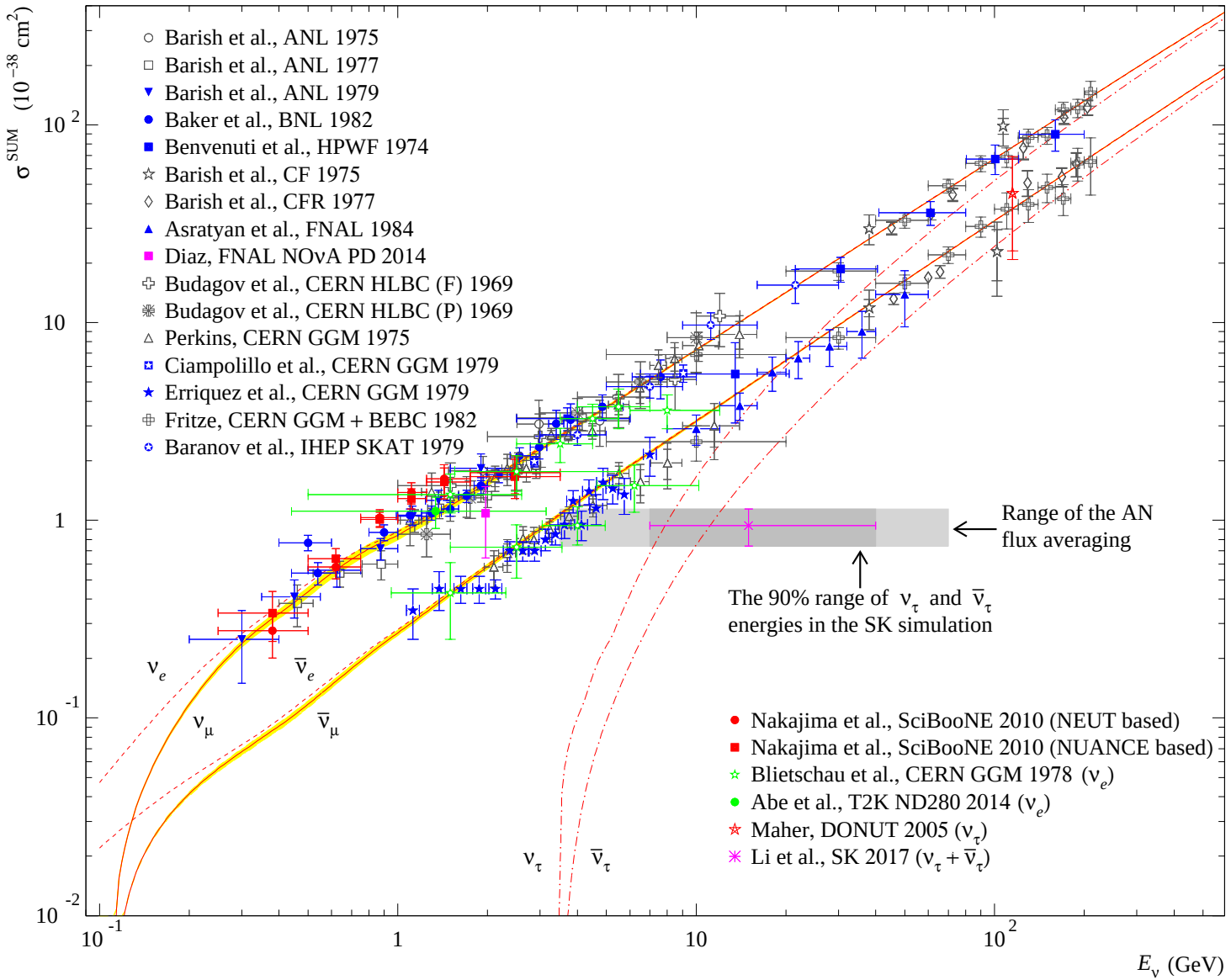

The total cross sections for $\nu_e N$, $\nu_\mu N$, $\overline{\nu}_e N$, $\overline{\nu}_\mu N$, and $\overline{\nu}_\tau N$ (N = "isoscalar nucleon").

[K. S. Kuzmin *et al.*, Phys. Atom. Nucl. **69** (2005) 1857–1871, hep-ph/0511308 (updated).]

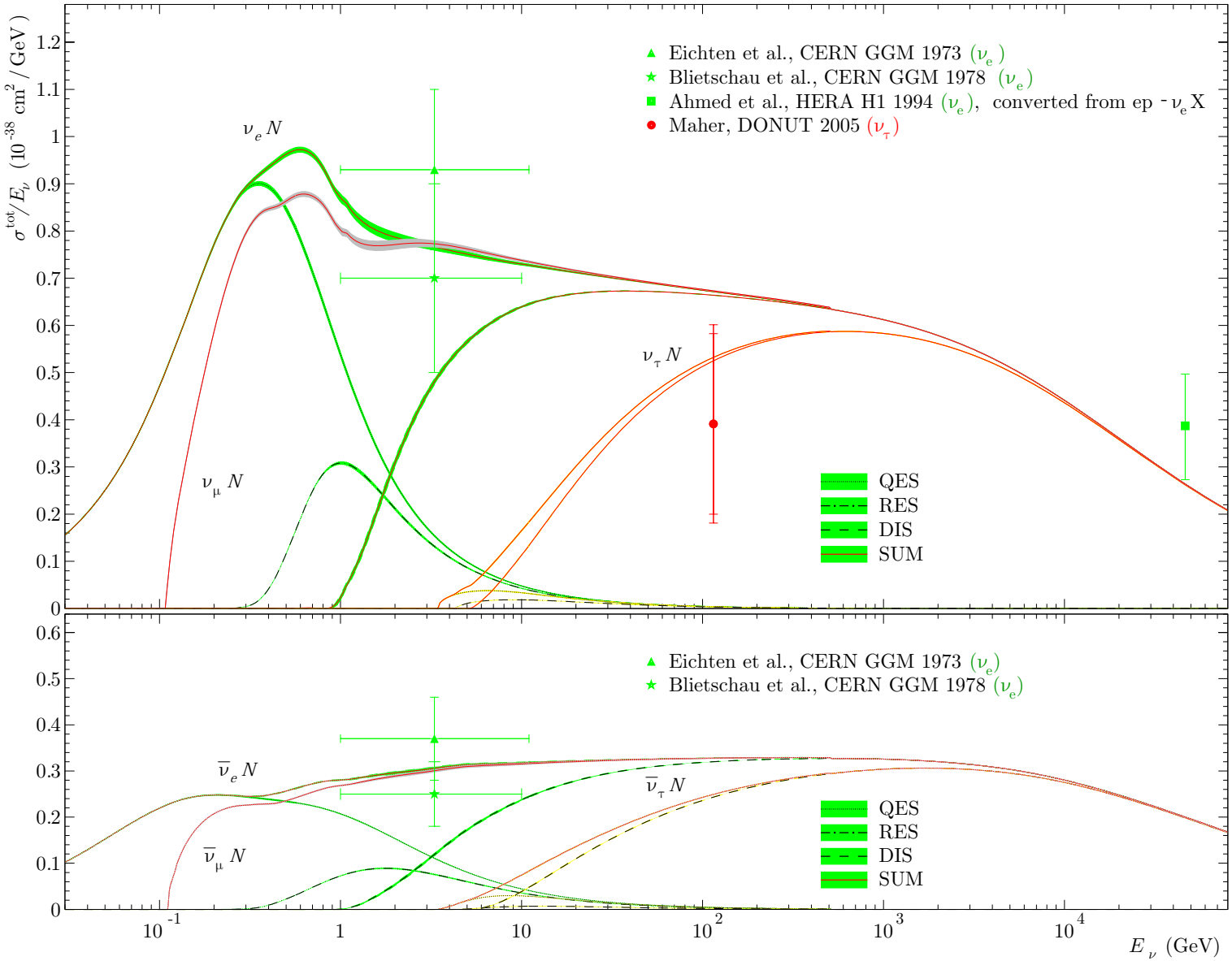

Comparison of the slopes of $\nu_{e,\mu,\tau}N$ and $\overline{\nu}_{e,\mu,\tau}N$ total cross sections; three main contributions and are shown for $\nu_{e,\tau}N$ and $\overline{\nu}_{e,\tau}N$. [K. S. Kuzmin & VN (unpublished).]

10.8 Cross sections at very high energies.

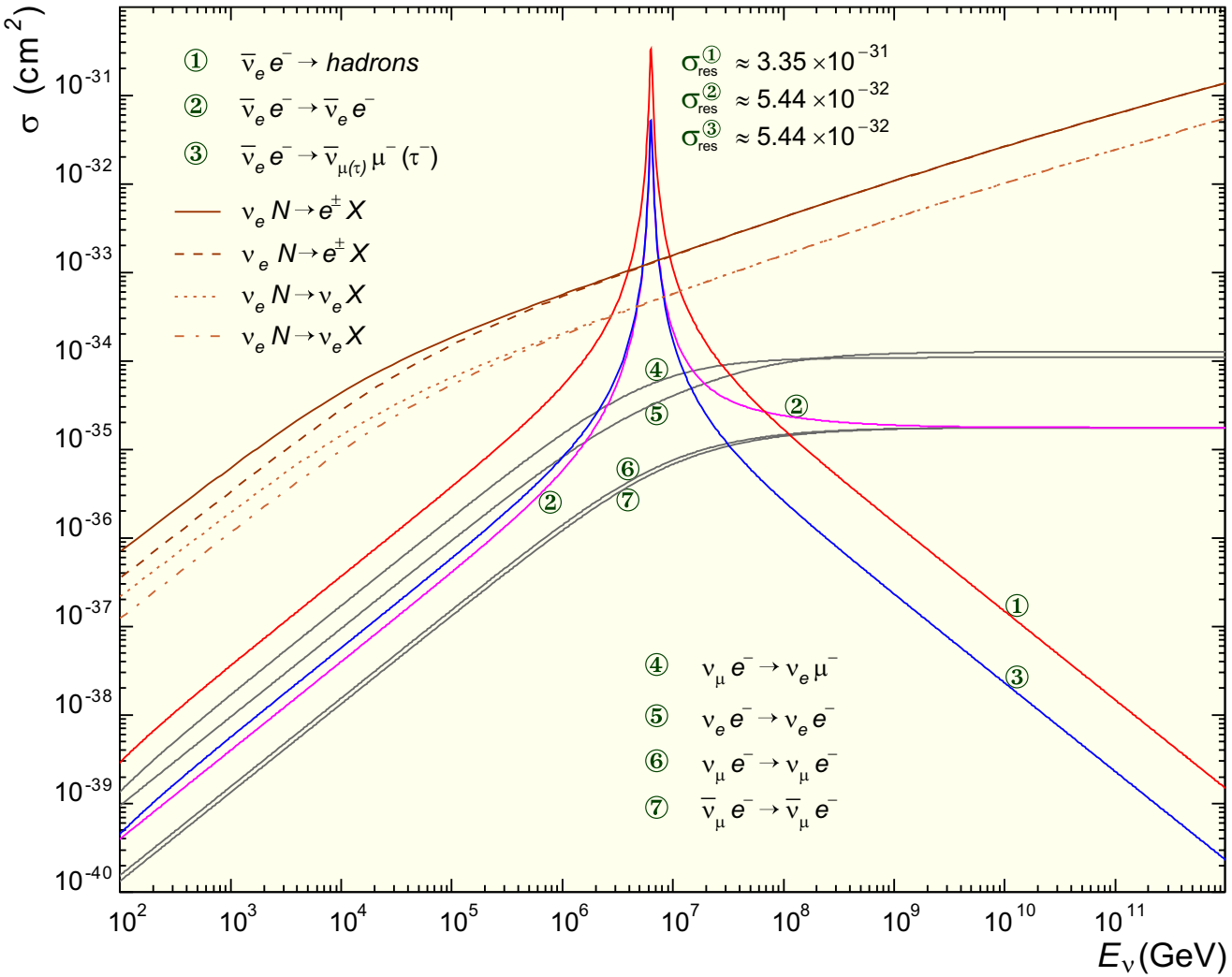

Comparison of the predicted $\nu_e(\overline{\nu}_e)$ total cross sections on electron and nucleon targets at high energies.

The picks in reactions 1–3 are due to the W boson resonance formed in the neighborhood of so-called "Glashow resonance,"

$$E_\nu^{\text{res}} = \frac{m_W^2}{2m_e} \approx 6.33\,\text{PeV}.$$

At the resonance peak,

$$\sigma^{\text{tot}}_{\overline{\nu}_e e} \approx 250\,\sigma^{\text{tot}}_{\overline{\nu}_e N}.$$

[K. S. Kuzmin *et al.* (for the ANTARES Collaboration), "Implementation of tau lepton polarization into ANTARES neutrino generator," ANTARES-Soft/2005-001.]

Integrated cross sections for neutrino-electron and neutrino-nucleon scattering at $E_\nu = m_W^2/2m_e \approx 6.331$ PeV are shown in the table:[a]

Reaction	σ (cm^2)	Reaction	σ (cm^2)
$\nu_\mu e \to \nu_\mu e$	5.86×10^{-36}	$\nu_\mu N \to \mu^- +$ anything	1.43×10^{-33}
$\overline{\nu}_\mu e \to \overline{\nu}_\mu e$	5.16×10^{-36}	$\nu_\mu N \to \nu_\mu +$ anything	6.04×10^{-34}
$\nu_\mu e \to \mu \nu_e$	5.42×10^{-35}	$\overline{\nu}_\mu N \to \mu^+ +$ anything	1.41×10^{-33}
$\nu_e e \to \nu_e e$	3.10×10^{-35}	$\overline{\nu}_\mu N \to \overline{\nu}_\mu +$ anything	5.98×10^{-34}
$\overline{\nu}_e e \to \overline{\nu}_e e$	5.215×10^{-32}		
$\overline{\nu}_e e \to \overline{\nu}_\mu \mu$	5.214×10^{-32}		
$\overline{\nu}_e e \to \overline{\nu}_\tau \tau$	5.208×10^{-32}		
$\overline{\nu}_e e \to$ hadrons	3.352×10^{-31}		
$\overline{\nu}_e e \to$ anything	4.917×10^{-31}		

Note:

The cross sections for electron targets listed in the table were calculated using the formulas given by Gandhi *et al.*, [b] but some numerical values are different since the input parameters were updated.

[a] For astrophysical applications, see, e.g., D. Biehl *et al.*, "Astrophysical neutrino production diagnostics with the Glashow resonance," JCAP01(2017)033, arXiv:1611.07983 [astro-ph.HE] and references therein.

[b] R. Gandhi, C. Quigg, M. H. Reno & I. Sarcevic, "Ultrahigh-energy neutrino interactions," Astropart. Phys. **5** (1996) 81–110, hep-ph/9512364.

Part IV

Neutrino Masses in the Standard Model

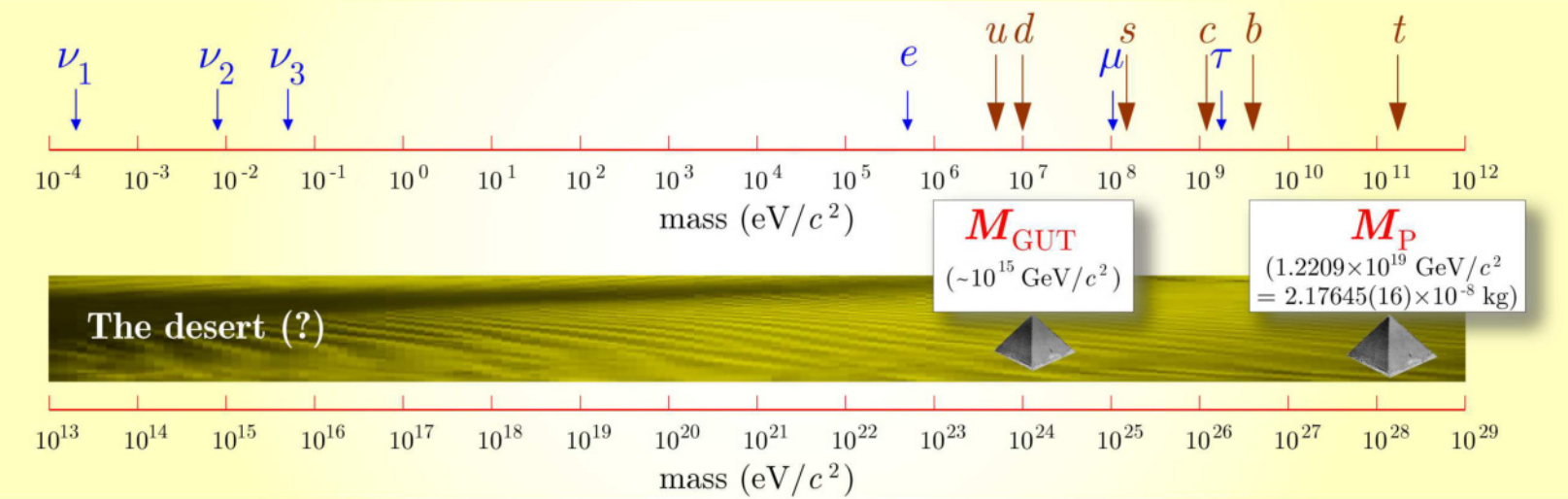

11 Interaction Lagrangian and weak currents.

In the Standard Model (SM), the charged and neutral current neutrino interactions with leptons are described by the following parts of the full Lagrangian:

$$\mathcal{L}_I^{\mathsf{CC}}(x) = -\frac{g}{2\sqrt{2}} j_\alpha^{\mathsf{CC}}(x) W^\alpha(x) + \mathsf{H.c.} \quad \text{and} \quad \mathcal{L}_I^{\mathsf{NC}}(x) = -\frac{g}{2\cos\theta_{\mathsf{W}}} j_\alpha^{\mathsf{NC}}(x) Z^\alpha(x).$$

Here g is the $SU(2)$ (electro-weak) gauge coupling constant

$$g^2 = 4\sqrt{2} m_W^2 G_F, \quad g \sin\theta_{\mathsf{W}} = |e|,$$

and θ_{W} is the weak mixing (Weinberg) angle, ($\sin^2\theta_{\mathsf{W}}(M_Z) = 0.23120$).

The leptonic charged current and neutrino neutral current are given by the expressions:

$$j_\alpha^{\mathsf{CC}}(x) = 2 \sum_{\ell=e,\mu,\tau,\ldots} \overline{\nu}_{\ell,L}(x) \gamma_\alpha \ell_L(x) \quad \text{and} \quad j_\alpha^{\mathsf{NC}}(x) = \sum_{\ell=e,\mu,\tau,\ldots} \overline{\nu}_{\ell,L}(x) \gamma_\alpha \nu_{\ell,L}(x).$$

Phenomenologically, the charged and neutral currents may include (yet unknown) heavy neutrinos and corresponding heavy charged leptons. The left- and right-handed fermion fields are defined as usually:

$$\begin{cases} \nu_{\ell,L}(x) = P_L \nu_\ell(x), \;\; \ell_L(x) = P_L \ell(x), \;\; P_L \equiv \dfrac{1}{2}(1-\gamma_5), \\ \nu_{\ell,R}(x) = P_R \nu_\ell(x), \;\; \ell_L(x) = P_R \ell(x), \;\; P_R \equiv \dfrac{1}{2}(1+\gamma_5). \end{cases}$$

Physical meaning of chiral projections for a massive Dirac fermion.

$$(\hat{p}-m)\psi=0 \quad\Longrightarrow\quad \begin{pmatrix} p_0-m & -\mathbf{p}\boldsymbol{\sigma} \\ \mathbf{p}\boldsymbol{\sigma} & -p_0-m \end{pmatrix}\begin{pmatrix}\phi\\ \chi\end{pmatrix}=0 \quad\Longrightarrow\quad \begin{cases} (\mathbf{p}\boldsymbol{\sigma})\chi=(p_0-m)\phi, \\ (\mathbf{p}\boldsymbol{\sigma})\phi=(p_0+m)\chi. \end{cases}$$

$$\psi_L=P_L\psi=\frac{1}{2}\begin{pmatrix}\phi-\chi\\ \chi-\phi\end{pmatrix}=\begin{pmatrix}\phi_-\\ -\phi_-\end{pmatrix}$$
$$\psi_R=P_R\psi=\frac{1}{2}\begin{pmatrix}\phi+\chi\\ \phi+\chi\end{pmatrix}=\begin{pmatrix}\phi_+\\ \phi_+\end{pmatrix}$$

where $\phi_\pm=\frac{1}{2}\left(1\pm\frac{\mathbf{p}\boldsymbol{\sigma}}{p_0+m}\right)\phi.$

Let $p_0\gg m$ and thus $1-|\mathbf{v}|\ll 1$, where $\mathbf{v}=\mathbf{p}/p_0$. Then, directing $\mathbf{v}$ along the z axis we obtain

$$\phi_-\simeq\frac{1-\sigma_3}{2}\,\phi=\begin{pmatrix}0&0\\0&1\end{pmatrix}\begin{pmatrix}\phi_\rightarrow\\ \phi_\leftarrow\end{pmatrix}=\begin{pmatrix}0\\ \phi_\leftarrow\end{pmatrix},\quad \phi_+\simeq\frac{1+\sigma_3}{2}\,\phi=\begin{pmatrix}1&0\\0&0\end{pmatrix}\begin{pmatrix}\phi_\rightarrow\\ \phi_\leftarrow\end{pmatrix}=\begin{pmatrix}\phi_\rightarrow\\ 0\end{pmatrix}.$$

Reminder: Pauli & Dirac matrices (for more details, see Appendix C, p. 846)

$$\sigma_0\equiv\mathbf{1}=\begin{pmatrix}1&0\\0&1\end{pmatrix},\quad \sigma_1=\begin{pmatrix}0&1\\1&0\end{pmatrix},\quad \sigma_2=\begin{pmatrix}0&-i\\i&0\end{pmatrix},\quad \sigma_3=\begin{pmatrix}1&0\\0&-1\end{pmatrix}.$$

$$\gamma^0=\gamma_0=\begin{pmatrix}\sigma_0&0\\0&-\sigma_0\end{pmatrix},\quad \gamma^k=-\gamma_k=\begin{pmatrix}0&\sigma_k\\-\sigma_k&0\end{pmatrix},\ k=1,2,3,\quad \gamma^5=\gamma_5=\begin{pmatrix}0&\sigma_0\\\sigma_0&0\end{pmatrix}.$$

Note that the kinetic term of the Lagrangian includes both L and R handed neutrinos and moreover, it can include other sterile neutrinos:

$$\mathcal{L}_0 = \frac{i}{2}\left[\overline{\boldsymbol{\nu}}(x)\gamma^\alpha\partial_\alpha\boldsymbol{\nu}(x) - \partial_\alpha\overline{\boldsymbol{\nu}}(x)\gamma^\alpha\boldsymbol{\nu}(x)\right] \equiv \frac{i}{2}\overline{\boldsymbol{\nu}}(x)\overleftrightarrow{\boldsymbol{\partial}}\boldsymbol{\nu}(x) = \frac{i}{2}\left[\overline{\boldsymbol{\nu}}_L(x)\overleftrightarrow{\boldsymbol{\partial}}\boldsymbol{\nu}_L(x) + \overline{\boldsymbol{\nu}}_R(x)\overleftrightarrow{\boldsymbol{\partial}}\boldsymbol{\nu}_R(x)\right],$$

$$\boldsymbol{\nu}(x) = \boldsymbol{\nu}_L(x) + \boldsymbol{\nu}_R(x) = \begin{pmatrix} \nu_e(x) \\ \nu_\mu(x) \\ \nu_\tau(x) \\ . \\ . \\ . \end{pmatrix}, \quad \boldsymbol{\nu}_{L/R}(x) = \begin{pmatrix} \nu_{e,L/R}(x) \\ \nu_{\mu,L/R}(x) \\ \nu_{\tau,L/R}(x) \\ . \\ . \\ . \end{pmatrix} = \frac{1 \mp \gamma_5}{2}\begin{pmatrix} \nu_e(x) \\ \nu_\mu(x) \\ \nu_\tau(x) \\ . \\ . \\ . \end{pmatrix}.$$

Neutrino chirality: $\gamma_5\nu_L = -\nu_L$ and $\gamma_5\nu_R = +\nu_R$.

The Lagrangian of the theory with massless neutrinos is invariant with respect to the global gauge transformations

$$\nu_\ell(x) \to e^{i\Lambda_\ell}\nu_\ell(x), \quad \ell(x) \to e^{i\Lambda_\ell}\ell(x) \quad \text{with} \quad \Lambda_\ell = \text{const}.$$

By Noether's theorem this leads to conservation of the individual lepton flavor numbers (more rarely called lepton flavor charges) L_ℓ. It is agreed that

$$L_\ell(\ell^-, \nu_\ell) = +1, \quad L_\ell(\ell^+, \overline{\nu}_\ell) = -1, \quad \ell^\pm = e^\pm,\ \mu^\pm,\ \tau^\pm, \text{ etc.}$$

But! **Lepton flavor conservation is not the case for massive neutrinos.**

There are two fundamentally different kinds of neutrino mass terms: Dirac and Majorana. Let's study.

12 Dirac neutrinos.

The conventional Dirac mass term for a single spinor field $\psi(x)$ is well known:

$$-m\overline{\psi}(x)\psi(x) = -m\left(\overline{\psi}_R\psi_L + \overline{\psi}_L\psi_R\right) = -m\overline{\psi}_R(x)\psi_L(x) + \text{H.c.}$$

(the identities $\overline{\psi}_L\psi_L = \overline{\psi}_R\psi_R = 0$ and $(\overline{\psi}_R\psi_L)^\dagger = \overline{\psi}_L\psi_R$ are used here).

The most general extension to the N-generation Dirac neutrino case reads:

$$\mathcal{L}_{\text{D}}(x) = -\overline{\boldsymbol{\nu}}_R(x)\mathbf{M}_{\text{D}}\boldsymbol{\nu}_L(x) + \text{H.c.},$$

where $\mathbf{M}_{\text{D}}$ is a nonsingular [to exclude massless case] complex $N \times N$ matrix.

> In general, $N \geq 3$ since the column $\boldsymbol{\nu}_L$ may include both *active* and *sterile* neutrino fields which do not enter into the standard charged and neutral currents.

Any nonsingular complex matrix can be diagonalized by means of an appropriate bi-unitary transformation

$$\mathbf{M}_{\text{D}} = \widetilde{\mathbf{V}}\mathbf{m}\mathbf{V}^\dagger, \quad \mathbf{m} = ||m_k\delta_{kl}|| = \text{diag}\,(m_1, m_2, \ldots, m_N),$$

where $\mathbf{V}$ and $\widetilde{\mathbf{V}}$ are unitary matrices and $m_k \equiv +\sqrt{m_k^2} > 0$ (see next slide). Therefore

$$\mathcal{L}_{\text{D}}(x) = -\overline{\boldsymbol{\nu}'}_R(x)\mathbf{m}\boldsymbol{\nu}'_L(x) + \text{H.c.} = -\overline{\boldsymbol{\nu}'}(x)\mathbf{m}\boldsymbol{\nu}'(x) = -\sum_{k=1}^{N} m_k\overline{\nu}_k(x)\nu_k(x),$$

where the new fields ν_k are defined by

$$\boldsymbol{\nu}'_L(x) = \mathbf{V}^\dagger\boldsymbol{\nu}_L(x), \quad \boldsymbol{\nu}'_R(x) = \widetilde{\mathbf{V}}^\dagger\boldsymbol{\nu}_R(x), \quad \boldsymbol{\nu}'(x) = (\nu_1, \nu_2, \ldots, \nu_N)^T.$$

The fields $\boldsymbol{\nu}'_R(x)$ do not enter into $\mathcal{L}_I \Longrightarrow$ the matrix $\widetilde{\mathbf{V}}$ remains out of play...

Mathematical excursus: bi-unitary diagonalization

Let's prove that any *nonsingular* matrix $\mathbf{M}$ can be diagonalized by a bi-unitary transformation.

Proof. Since $\mathbf{M}\mathbf{M}^\dagger$ is Hermitian, there exist a unitary matrix $\widetilde{\mathbf{V}}$ such that

$$\widetilde{\mathbf{V}}^\dagger \left(\mathbf{M}\mathbf{M}^\dagger\right) \widetilde{\mathbf{V}} = \mathbf{m}^2 = \mathsf{diag}\left(m_1^2, m_2^2, \ldots, m_N^2\right), \tag{37}$$

where m_i^2 are real for any i. Moreover $m_i^2 > 0$. Indeed, $\mathbf{M}^\dagger\widetilde{\mathbf{V}} = \left(\widetilde{\mathbf{V}}^\dagger\mathbf{M}\right)^\dagger$ and thus

$$m_i^2 = \sum_j \left(\widetilde{\mathbf{V}}^\dagger\mathbf{M}\right)_{ij} \left(\widetilde{\mathbf{V}}^\dagger\mathbf{M}\right)^*_{ij} = \sum_j \left| \left(\widetilde{\mathbf{V}}^\dagger\mathbf{M}\right)_{ij} \right|^2 \geq 0;$$

the equality is however excluded since $\mathbf{m}^2$ is nonsingular. However, the signs of m_k are not fixed. We'll use the convention $m_k \equiv +\sqrt{m_k^2}$, although this is a rather formal (unconstructive) solution that mathematicians are unlikely to approve.[a] Let's now define the matrix $\mathbf{V}$ as follows:

$$\mathbf{V} = \mathbf{M}^\dagger\widetilde{\mathbf{V}}\mathbf{m}^{-1}, \quad \Longleftrightarrow \quad \mathbf{V}^\dagger = \mathbf{m}^{-1}\widetilde{\mathbf{V}}^\dagger\mathbf{M},$$

$$\Downarrow$$

$$\mathbf{V}^\dagger\mathbf{V} = \mathbf{m}^{-1}\widetilde{\mathbf{V}}^\dagger\mathbf{M}\mathbf{M}^\dagger\widetilde{\mathbf{V}}\mathbf{m}^{-1} = \mathbf{m}^{-1}\mathbf{m}^2\mathbf{m}^{-1} = \mathbf{1},$$

that is the matrix $\mathbf{V}$ is unitary and, according to Eq. (37),

$$\widetilde{\mathbf{V}}^\dagger\mathbf{M}\mathbf{V} = \left(\widetilde{\mathbf{V}}^\dagger\mathbf{M}\mathbf{M}^\dagger\widetilde{\mathbf{V}}\right)\mathbf{m}^{-1} = \mathbf{m}^2\mathbf{m}^{-1} = \mathbf{m}.$$

Q.E.D.

[a] Better solution is to change the signs of the eigenfields ν_k with $m_k < 0$ (see p.479 for a telling example).

Since $\mathbf{V}\mathbf{V}^\dagger = \mathbf{V}^\dagger\mathbf{V} = \mathbf{1}$ and $\widetilde{\mathbf{V}}^\dagger\widetilde{\mathbf{V}} = \widetilde{\mathbf{V}}\widetilde{\mathbf{V}}^\dagger = \mathbf{1}$, the neutrino kinetic term in the Lagrangian is transformed to

$$\mathcal{L}_0 = \frac{i}{2}\left[\overline{\boldsymbol{\nu}}'_L(x)\overleftrightarrow{\boldsymbol{\partial}}\boldsymbol{\nu}'_L(x) + \overline{\boldsymbol{\nu}}'_R(x)\overleftrightarrow{\boldsymbol{\partial}}\boldsymbol{\nu}'_R(x)\right] = \frac{i}{2}\,\overline{\boldsymbol{\nu}'}(x)\overleftrightarrow{\boldsymbol{\partial}}\boldsymbol{\nu}'(x) = \frac{i}{2}\sum_k \overline{\nu}_k(x)\overleftrightarrow{\boldsymbol{\partial}}\nu_k(x).$$

$$\Downarrow$$

$\nu_k(x)$ is the field of a Dirac neutrino with the mass m_k and the flavor LH neutrino fields $\nu_{\ell,L}(x)$ involved into the SM weak lepton currents are linear combinations of the LH components of the fields of the neutrinos with definite masses:

$$\boldsymbol{\nu}_L = \mathbf{V}\boldsymbol{\nu}'_L \quad \text{or} \quad \nu_{\ell,L} = \sum_k V_{\ell k}\nu_{k,L}.$$

The matrix $\mathbf{V}$ is referred to as the Pontecorvo-Maki-Nakagawa-Sakata (PMNS) neutrino mixing matrix while the matrix $\widetilde{\mathbf{V}}$ is not honored with a personal name.

Quark-lepton complementarity (QLC): Of course the PMNS neutrino matrix $\mathbf{V} \equiv \mathbf{V}^{\text{PMNS}}$ it is not the same as the CKM (Cabibbo-Kobayashi-Maskawa) quark mixing matrix $\mathbf{V}' \equiv \mathbf{V}^{\text{CKM}}$. However the PMNS and CKM matrices may be, in a sense, *complementary* to each other, hinting at some hidden, possibly broken, symmetry. Looking ahead a little, let's explain what we are talking about.

The QLC means that in the generally accepted parametrization of $\mathbf{V}$ and $\mathbf{V}'$ the sums of (small) quark and (large) neutrino mixing angles are close to $\pi/4$ (within $\sim 2\sigma$ errors) for $(ij) = (12)$ and (23):

$$\theta_{12}^{\text{CKM}} + \theta_{12}^{\text{PMNS}} = \left(46.41^{+0.75}_{-0.72}\right)^\circ, \quad \theta_{23}^{\text{CKM}} + \theta_{23}^{\text{PMNS}} = \left(44.60^{+1.10}_{-0.90}\right)^\circ, \quad \text{sum} = \left(91.01^{+1.33}_{-1.15}\right)^\circ.$$

The experimental errors shown are due to errors in the PNMC mixing angles, which are much larger than the errors in the CKM mixing angles. The origin of the data (but not QLC) will be explained below.

12.1 Parametrization of mixing matrix for Dirac neutrinos.

It is well known that a complex $n \times n$ unitary matrix $\mathbf{U}$ depends on n^2 *real* parameters. [Why?]

The classical result by Francis Murnaghan[a] states that any $n \times n$ matrix from the unitary group $U(n)$ can be presented as product of the diagonal phase matrix

$$\mathbf{\Gamma} = \mathrm{diag}\left(e^{i\alpha_1}, e^{i\alpha_2}, \ldots, e^{i\alpha_n}\right),$$

containing n phases α_k, and $n(n-1)/2$ matrices $\mathbf{O}_r$ whose nontrivial building blocks have the form

$$\begin{pmatrix} \cos\theta_r & \ldots & e^{-i\phi_r}\sin\theta_r \\ \ldots\ldots & \ldots\ldots & \ldots\ldots \\ -e^{i\phi_r}\sin\theta_r & \ldots & \cos\theta_r \end{pmatrix} = \begin{pmatrix} 1 & \ldots & 0 \\ \ldots\ldots & \ldots\ldots & \ldots\ldots \\ 0 & \ldots & e^{i\phi_r} \end{pmatrix} \underbrace{\begin{pmatrix} \cos\theta_r & \ldots & \sin\theta_r \\ \ldots\ldots & \ldots\ldots & \ldots\ldots \\ -\sin\theta_r & \ldots & \cos\theta_r \end{pmatrix}}_{\text{Euler rotation}} \begin{pmatrix} 1 & \ldots & 0 \\ \ldots\ldots & \ldots\ldots & \ldots\ldots \\ 0 & \ldots & e^{-i\phi_r} \end{pmatrix};$$

the matrix $\mathbf{U}$ is a product of the matrices $\mathbf{\Gamma}$, $\mathbf{\Gamma}^\dagger$, and $\mathbf{O}_r$ whose order can be arbitrary (e.g., $\mathbf{O}_1\mathbf{\Gamma}\mathbf{O}_2\mathbf{\Gamma}^\dagger\mathbf{O}_3\cdots$). As a result, any $n \times n$ unitary matrix can be parametrized by

$n(n-1)/2$ "angles" θ_r (taking values within $[0, \pi/2]$)

and[b]

$n(n+1)/2$ "phases" α_k, ϕ_r (taking values within $[0, 2\pi)$).

The usual parametrization of both the CKM and PMNS matrices is of this type.

IMPORTANT: Murnaghan's factorization doesn't specify a sequence of the multipliers $\mathbf{\Gamma}$, $\mathbf{\Gamma}^\dagger$, and $\mathbf{O}_r$, but numerical values of the angles and phases depend on the sequence.

[a] F. D. Murnaghan, "The unitary and rotation groups (Lectures on Applied Mathematics, Volume 3)," Library of Congress Catalog Card No. 62-19096, Spartan Books, Washington, D.C. (1962).

[b] $n(n+1)/2 = n + n(n-1)/2$.

It is possible (and necessary) to reduce the number of phases by taking into account that the SM Lagrangian with the Dirac mass term is invariant with respect to the following transformation:

$$\ell \mapsto e^{ia_\ell}\ell, \quad \nu_k \mapsto e^{ib_k}\nu_k, \quad V_{\ell k} \mapsto e^{i(b_k - a_\ell)}V_{\ell k}. \tag{38}$$

This symmetry eliminates $2N-1$ phases. Why not $2N$?! This is a delicate spot.

1. The weak NC current and lepton electromagnetic current

$$j_\alpha^{\text{NC}} = \sum_\ell \overline{\nu}_{\ell,L}\gamma_\alpha\nu_{\ell,L} = \sum_k \overline{\nu}_{k,L}\gamma_\alpha\nu_{k,L} \quad \text{and} \quad j_\alpha^{\text{em}} = \sum_\ell \overline{\ell}\gamma_\alpha\ell,$$

as well as the kinetic term in the Lagrangian

$$\sum_k \left(\frac{i}{2}\overline{\nu}_k \overleftrightarrow{\partial} \nu_k - m_k\overline{\nu}_k\nu_k\right) + \sum_\ell \left(\frac{i}{2}\overline{\ell} \overleftrightarrow{\partial} \ell - m_\ell\overline{\ell}\ell\right)$$

are obviously invariant with respect to transformation (38).

2. For the weak CC current we have

$$\begin{aligned} j_\alpha^{\text{CC}} &= 2\sum_\ell \overline{\nu}_{\ell,L}\gamma_\alpha\ell_L = 2\sum_\ell\sum_k \overline{\nu}_{k,L}V_{k\ell}^*\gamma_\alpha\ell_L = 2\sum_{k\ell} \overline{\nu}_{k,L}e^{-ib_k}\left[e^{i(b_k-a_\ell)}V_{k\ell}^*\right]\gamma_\alpha e^{ia_\ell}\ell_L \\ &= 2\sum_{k\ell} \overline{\nu}_{k,L}e^{-i(b_k-b_1)}\left[e^{-i(b_k-b_1-a_\ell)}V_{k\ell}\right]^*\gamma_\alpha e^{ia_\ell}\ell_L \equiv 2\sum_{k\ell}\overline{\nu}'_{k,L}V'^*_{k\ell}\gamma_\alpha\ell'_L, \end{aligned}$$

where

$$\nu'_{k,L} = e^{i(b_k-b_1)}\nu_{k,L}, \quad \ell'_L = e^{ia_\ell}\ell_L, \quad V'_{k\ell} = e^{-i(b_k-b_1-a_\ell)}V_{k\ell} \tag{39}$$

Of course, any of the phases a_k or b_k could have been chosen here instead of b_1.

Simplest example: two-neutrino mixing

Murnaghan's factorization for a two-neutrino (ν_e, ν_μ for certainty) mixing matrix can be written as

$$\mathbf{V} = \begin{pmatrix} 1 & 0 \\ 0 & e^{+i\phi} \end{pmatrix} \begin{pmatrix} \cos\theta & \sin\theta \\ -\sin\theta & \cos\theta \end{pmatrix} \begin{pmatrix} 1 & 0 \\ 0 & e^{-i\phi} \end{pmatrix} \begin{pmatrix} e^{i\alpha_1} & 0 \\ 0 & e^{i\alpha_2} \end{pmatrix} = \begin{pmatrix} e^{-i\alpha_1}\cos\theta & e^{i(\alpha_2-\phi)}\sin\theta \\ -e^{i(\alpha_1-\phi)}\sin\theta & e^{i\alpha_2}\cos\theta \end{pmatrix}.$$

Let's prove that $\mathbf{V}'$ is just a rotation matrix. Transformation (39) can be written in matrix form:[a]

$$\mathbf{V} \longmapsto \mathbf{V}' = \left|\left| e^{-i(b_k - b_1 - a_\ell)} V_{k\ell} \right|\right| = \begin{pmatrix} e^{-i(b_1-b_1)} & 0 \\ 0 & e^{-i(b_2-b_1)} \end{pmatrix} \mathbf{V} \begin{pmatrix} e^{ia_e} & 0 \\ 0 & e^{ia_\mu} \end{pmatrix}$$

$$= \begin{pmatrix} 1 & 0 \\ 0 & e^{-i(b_2-b_1)} \end{pmatrix} \begin{pmatrix} 1 & 0 \\ 0 & e^{+i\phi} \end{pmatrix} \begin{pmatrix} \cos\theta & \sin\theta \\ -\sin\theta & \cos\theta \end{pmatrix} \begin{pmatrix} 1 & 0 \\ 0 & e^{-i\phi} \end{pmatrix} \begin{pmatrix} e^{i\alpha_1} & 0 \\ 0 & e^{i\alpha_2} \end{pmatrix} \begin{pmatrix} e^{ia_e} & 0 \\ 0 & e^{ia_\mu} \end{pmatrix}$$

$$= \begin{pmatrix} 1 & 0 \\ 0 & e^{i(\phi-b_2+b_1)} \end{pmatrix} \begin{pmatrix} \cos\theta & \sin\theta \\ -\sin\theta & \cos\theta \end{pmatrix} \begin{pmatrix} 1 & 0 \\ 0 & e^{-i\phi} \end{pmatrix} \begin{pmatrix} e^{i(\alpha_1+a_e)} & 0 \\ 0 & e^{i(\alpha_2+a_\mu)} \end{pmatrix}$$

$$= \begin{pmatrix} 1 & 0 \\ 0 & e^{i(\phi-b_2+b_1)} \end{pmatrix} \begin{pmatrix} \cos\theta & \sin\theta \\ -\sin\theta & \cos\theta \end{pmatrix} \begin{pmatrix} e^{i(\alpha_1+a_e)} & 0 \\ 0 & e^{i(\alpha_2+a_\mu-\phi)} \end{pmatrix} = \begin{pmatrix} \cos\theta & \sin\theta \\ -\sin\theta & \cos\theta \end{pmatrix},$$

where we have put $b_2 = \phi + b_1$, $a_e = -\alpha_1$, $a_\mu = \phi - \alpha_2$, and phase b_1 remained arbitrary.

[a] It is useful to note that for an arbitrary $n \times n$ matrix $\mathbf{A} = ||A_{ij}||$ the following identity holds:

$$||a_i b_j A_{ij}|| = \mathrm{diag}(a_1, \ldots, a_n)\mathbf{A}\,\mathrm{diag}(b_1, \ldots, b_n).$$

Returning to the general $N\times N$ case, we have $N-1$ arbitrary phases $b_k - b_1$ and N arbitrary phases $a_\ell - b_1$. Consequently, we can get rid of $2N-1$ unnecessary (nonphysical = unobservable) phases in the mixing matrix.[a] So, the number of physical (Dirac) phases is

$$n_{\mathsf{D}} = \frac{N(N+1)}{2} - (2N-1) = \frac{N^2-3N+2}{2} = \frac{(N-1)(N-2)}{2} \qquad (N \geq 2);$$

$$n_{\mathsf{D}}(2) = 0, \quad n_{\mathsf{D}}(3) = 1, \quad n_{\mathsf{D}}(4) = 3, \ldots$$

• The Lagrangian contains another residual symmetry: it is invariant with respect to the global phase transformation

$$\ell \mapsto e^{i\Lambda}\ell, \quad \nu_k \mapsto e^{i\Lambda}\nu_k, \quad \text{with} \quad \Lambda = \text{const}. \qquad (40)$$

This symmetry leads (thanks to Noether) to conservation of the total lepton number (charge) $L = \sum L_\ell$ that is the number common to all charged leptons and all neutrinos ν_k – analogue of the baryon charge. However, and very important,

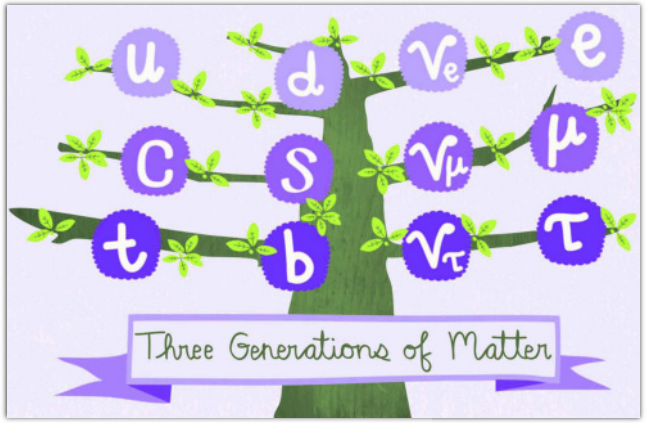

The individual lepton flavor numbers L_ℓ are no longer conserved.

• The nonzero physical phases lead to the CP (and T) violation in the neutrino sector.[b] This may have significant implications for particle physics and cosmology (leptogenesis, baryogenesis, ...).

[a] Another way to make sure that the phase count is correct is to postulate the unimodularity of the mixing matrix. This gives a linear relationship between the phases and therefore eliminates one of them.

[b] The proof can be found, e.g., in Sect. 4.6 of C. Giunti and C. W. Kim, "Fundamentals of neutrino physics and astrophysics" (Oxford University Press Inc., New York, 2007) or in Sect. 6.3 of S. M. Bilenky, "Introduction to the physics of massive and mixed neutrinos" (2nd ed.), Lect. Notes Phys. **947** (2018) 1–276. Note many differences in notation and in representation of the charge conjugation matrix C.

12.1.1 Three-neutrino case.

In the most interesting (today!) case of three lepton generations one defines the orthogonal rotation matrices in the ij-planes which depend upon the mixing angles θ_{ij}:

$$\underbrace{\mathbf{O}_{12} = \begin{pmatrix} c_{12} & s_{12} & 0 \\ -s_{12} & c_{12} & 0 \\ 0 & 0 & 1 \end{pmatrix}}_{\text{Solar matrix}}, \quad \underbrace{\mathbf{O}_{13} = \begin{pmatrix} c_{13} & 0 & s_{13} \\ 0 & 1 & 0 \\ -s_{13} & 0 & c_{13} \end{pmatrix}}_{\text{Reactor matrix}}, \quad \underbrace{\mathbf{O}_{23} = \begin{pmatrix} 1 & 0 & 0 \\ 0 & c_{23} & s_{23} \\ 0 & -s_{23} & c_{23} \end{pmatrix}}_{\text{Atmospheric matrix}},$$

(where $c_{ij} \equiv \cos\theta_{ij}$, $s_{ij} \equiv \sin\theta_{ij}$) and the diagonal matrix with the Dirac phase factor:

$$\mathbf{\Gamma}_{\mathsf{D}} = \mathsf{diag}\left(1, 1, e^{i\delta}\right).$$

The parameter δ is commonly referred to as the Dirac CP-violation/violating phase.

Finally, by applying Murnaghan's factorization, the PMNS matrix for the Dirac neutrinos can be parametrized as

$$\mathbf{V}_{(\mathsf{D})} = \mathbf{O}_{23}\mathbf{\Gamma}_{\mathsf{D}}\mathbf{O}_{13}\mathbf{\Gamma}_{\mathsf{D}}^{\dagger}\mathbf{O}_{12} = \begin{pmatrix} c_{12}c_{13} & s_{12}c_{13} & s_{13}e^{-i\delta} \\ -s_{12}c_{23} - c_{12}s_{23}s_{13}e^{i\delta} & c_{12}c_{23} - s_{12}s_{23}s_{13}e^{i\delta} & s_{23}c_{13} \\ s_{12}s_{23} - c_{12}c_{23}s_{13}e^{i\delta} & -c_{12}s_{23} - s_{12}c_{23}s_{13}e^{i\delta} & c_{23}c_{13} \end{pmatrix}.$$

- ⋆ This is the *Chau–Keung presentation* advocated by the PDG for both CKM and PMNS matrices.
- ⋆ Remember that the positioning of the factors in $\mathbf{V}_{(\mathsf{D})}$ is not fixed by the Murnaghan (or any other) algorithm and is just a subject-matter of agreement.
- ⋆ Today we believe we know a lot about the entries of this matrix.

12.1.2 Neutrino mixing parameter plot.

Status on 2010.

The regions of neutrino squared-mass splitting

$$\Delta m^2 = |\Delta m^2_{ij}| = |m^2_j - m^2_i|$$

and mixing angle favored or excluded by various experiments. Contributed to RPP-2010[a] by Hitoshi Murayama (University of California, Berkeley).

[From URL: ⟨http://hitoshi.berkeley.edu/neutrino/⟩.]

The figure shows the most rigorous results for 2010; it does not include the data of BOREXINO and neutrino telescopes (Baikal, AMANDA, IceCube). Also the data from many earlier underground experiments (BUST, NUSEX, Fréjus, IMB, Kamiokande, MACRO, SOUDAN 2) are ignored. However, all these scarcely affect the global analysis.

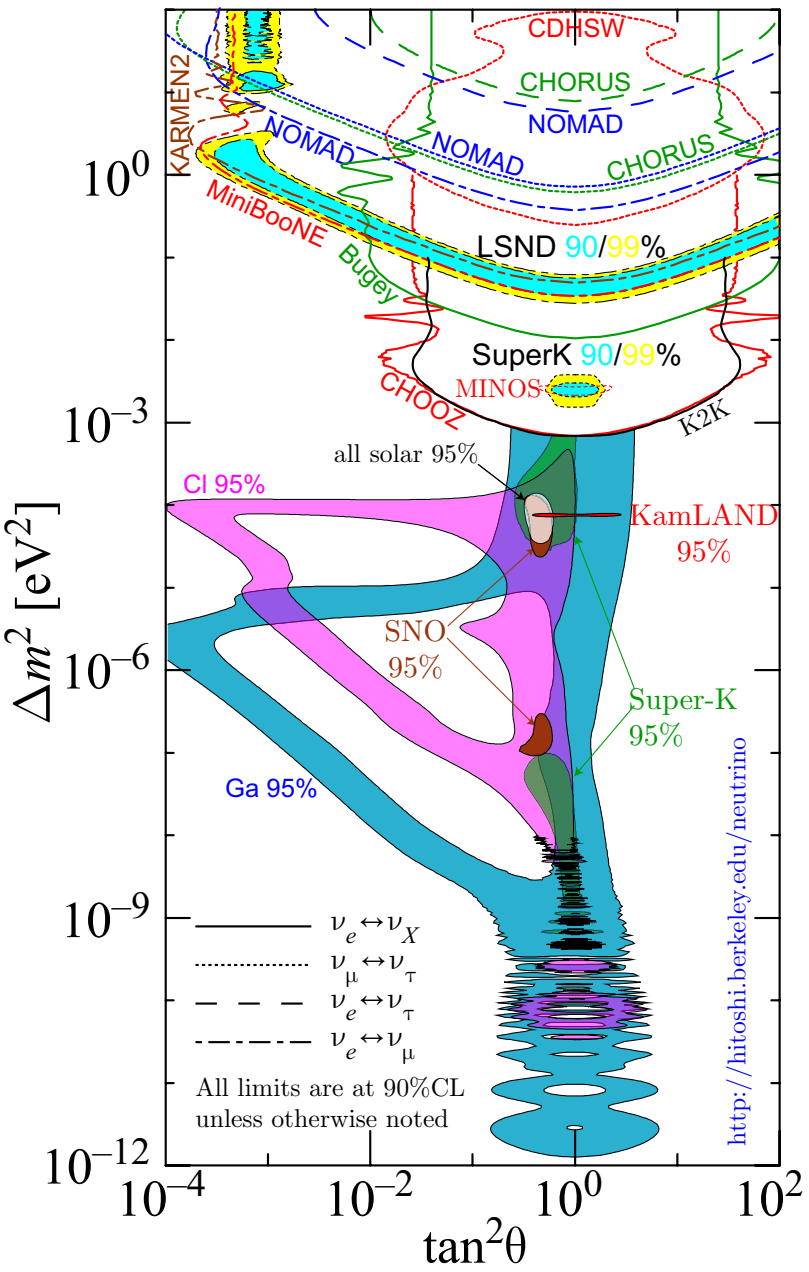

[a] K. Nakamura *et al.* (Particle Data Group), "Review of particle physics," J. Phys. G **37** (2010) 075021.

Status on 2014.

The same as in the previous slide but updated with the new data from Daya Bay, MINOS, T2K, ICARUS, & OPERA. Contributed to RPP-2014.[a]

The figure does not include the more recent data, in particular from BOREXINO, T2K, and very recent results from NOνA.

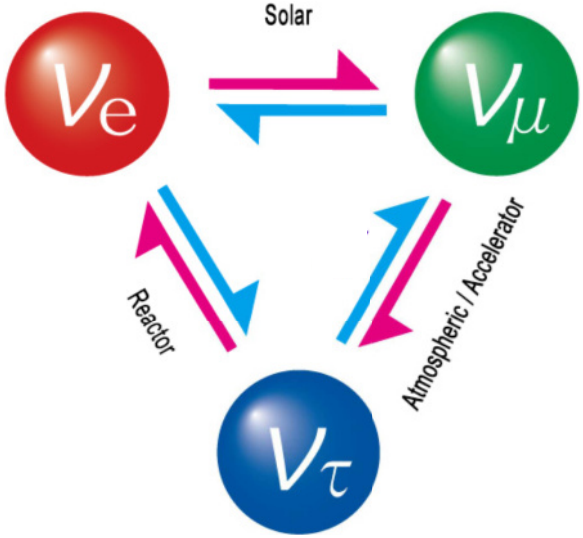

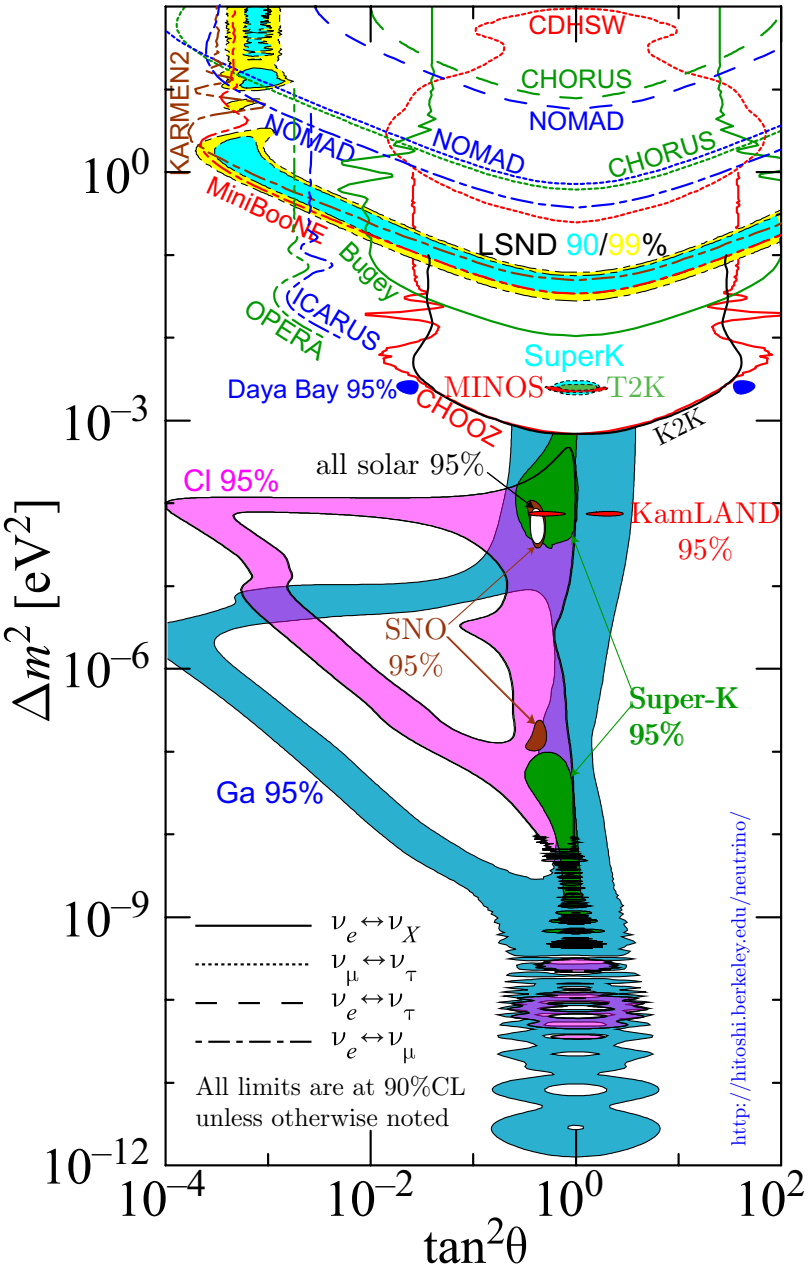

[a] K. A. Olive *et al.* (Particle Data Group), "Review of Particle Physics," Chin. Phys. C **38** (2014) 090001.

Status on 2018.

The same as in the previous slide but updated with the new data from Daya Bay, RENO, Super-K, T2K, BOREXINO, NOνA, & IceCube. Contributed to RPP-2018.[a]

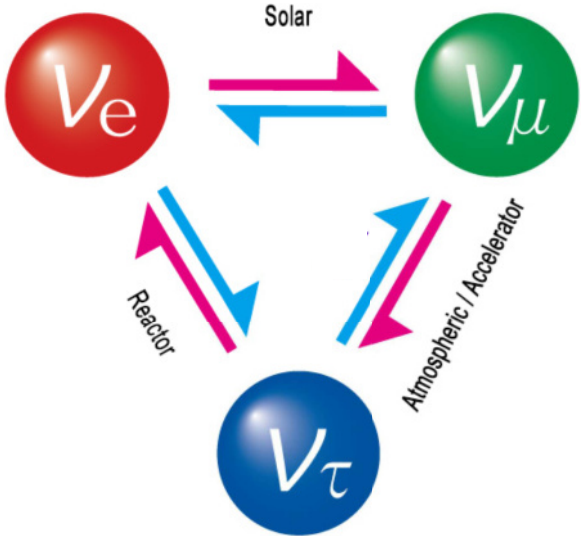

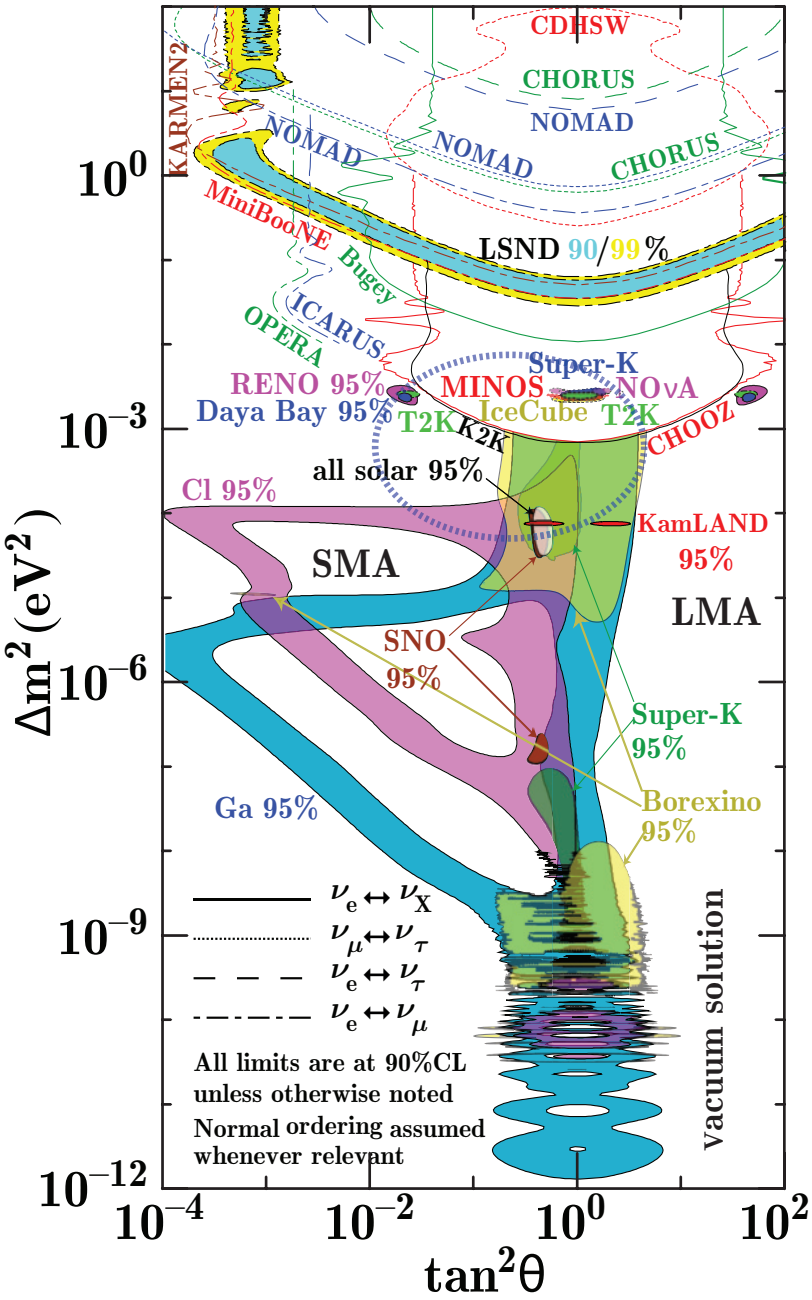

[a] M. Tanabashi *et al.* (Particle Data Group), "Review of particle physics," Phys. Rev. D **98** (2018) 030001.

12.2 Here's what we know so far (getting ahead of ourselves).

		Normal Ordering (best fit)		Inverted Ordering ($\Delta\chi^2 = 6.4$)	
		bfp $\pm 1\sigma$	3σ range	bfp $\pm 1\sigma$	3σ range
With SK atmospheric neutrino data	$\sin^2\theta_{12}$	$0.303^{+0.012}_{-0.012}$	$0.270 \to 0.341$	$0.303^{+0.012}_{-0.011}$	$0.270 \to 0.341$
	$\theta_{12}/^\circ$	$33.41^{+0.75}_{-0.72}$	$31.31 \to 35.74$	$33.41^{+0.75}_{-0.72}$	$31.31 \to 35.74$
	$\sin^2\theta_{23}$	$0.451^{+0.019}_{-0.016}$	$0.408 \to 0.603$	$0.569^{+0.016}_{-0.021}$	$0.412 \to 0.613$
	$\theta_{23}/^\circ$	$42.2^{+1.1}_{-0.9}$	$39.7 \to 51.0$	$49.0^{+1.0}_{-1.2}$	$39.9 \to 51.5$
	$\sin^2\theta_{13}$	$0.02225^{+0.00056}_{-0.00059}$	$0.02052 \to 0.02398$	$0.02223^{+0.00058}_{-0.00058}$	$0.02048 \to 0.02416$
	$\theta_{13}/^\circ$	$8.58^{+0.11}_{-0.11}$	$8.23 \to 8.91$	$8.57^{+0.11}_{-0.11}$	$8.23 \to 8.94$
	$\delta_{\rm CP}/^\circ$	232^{+36}_{-26}	$144 \to 350$	276^{+22}_{-29}	$194 \to 344$
	$\frac{\Delta m^2_{21}}{10^{-5}\ \text{eV}^2}$	$7.41^{+0.21}_{-0.20}$	$6.82 \to 8.03$	$7.41^{+0.21}_{-0.20}$	$6.82 \to 8.03$
	$\frac{\Delta m^2_{3\ell}}{10^{-3}\ \text{eV}^2}$	$+2.507^{+0.026}_{-0.027}$	$+2.427 \to +2.590$	$-2.486^{+0.025}_{-0.028}$	$-2.570 \to -2.406$

Three-flavor oscillation parameters from a recent fit to global data ("NuFIT 5.2") performed by the NuFIT team. Note that $\Delta m^2_{3\ell} \equiv \Delta m^2_{31} > 0$ for NO (NH) and $\Delta m^2_{3\ell} \equiv \Delta m^2_{32} < 0$ for IO (IH).

[See I. Esteban *et al.* (The NuFIT team), "The fate of hints: updated global analysis of three-flavor neutrino oscillations," JHEP09(2020)178, arXiv:2007.14792 [hep-ph]. Present update (November 2022) is from ⟨ http://www.nu-fit.org/ ⟩.]

List of data used in the NuFIT 5.2 analysis (November 2022).

Solar experiments:

Homestake chlorine total rate (1 dp), Gallex & GNO total rates (2 dp), SAGE total rate (1 dp), SK-I full energy and zenith spectrum (44 dp), SK-II full energy and day/night spectrum (33 dp), SK-III full energy and day/night spectrum (42 dp), SK-IV 2055-day day-night asymmetry and energy spectrum (46 dp), SNO combined analysis (7 dp), Borexino Phase-I 740.7-day low-energy data (33 dp), Borexino Phase-I 246-day high-energy data (6 dp), Borexino Phase-II 408-day low-energy data (42 dp).

Atmospheric experiments:

SK-I–IV (including SK-IV 1775-day) combined data (42 dp), IceCube/DeepCore 3-year data (64 dp).

Reactor experiments:

KamLAND combined DS1 & DS2 spectrum (17 dp), CHOOZ Fenergy spectrum (14 dp), Palo-Verde total rate (1 dp), Double-Chooz FD-I (461 days) and FD-II (212 days) spectra (54 dp), Daya-Bay 621-day spectrum (36 dp), RENO 800-day FD/ND total rates (2 dp with free normalization). SBL reactor data (including DB total flux at ND) (77 dp),

Accelerator experiments:

MINOS 10.71 PoT_{20} ν_μ-disappearance data (39 dp), MINOS 3.36 PoT_{20} $\overline{\nu}_\mu$-disappearance data (14 dp), MINOS 10.60 PoT_{20} ν_e-appearance data (5 dp), MINOS 3.30 PoT_{20} $\overline{\nu}_e$-appearance (5 dp), T2K 6.57 PoT_{20} ν_μ-disappearance data (16 dp), T2K 6.57 PoT_{20} ν_e-appearance data (5 dp, T2K 4.01 PoT_{20} $\overline{\nu}_\mu$-disappearance data (63 dp), T2K 4.01 PoT_{20} $\overline{\nu}_e$-appearance data (1 dp), NOvA 2.74 PoT_{20} ν_μ-disappearance data (18 dp), NOvA 2.74 PoT_{20} ν_e-appearance data (1 dp).

Here dp = data point(s), $\text{PoT}_{20} = 10^{20}$ PoT (Protons on Target), and EH = Experiment Hall.

Note: The dataset used in the fit has changed significantly from that used in the September 2021 analysis NuFIT 5.1. In particular, the reactor and accelerator data subsets were reduced.

NuFIT evolution.[a]

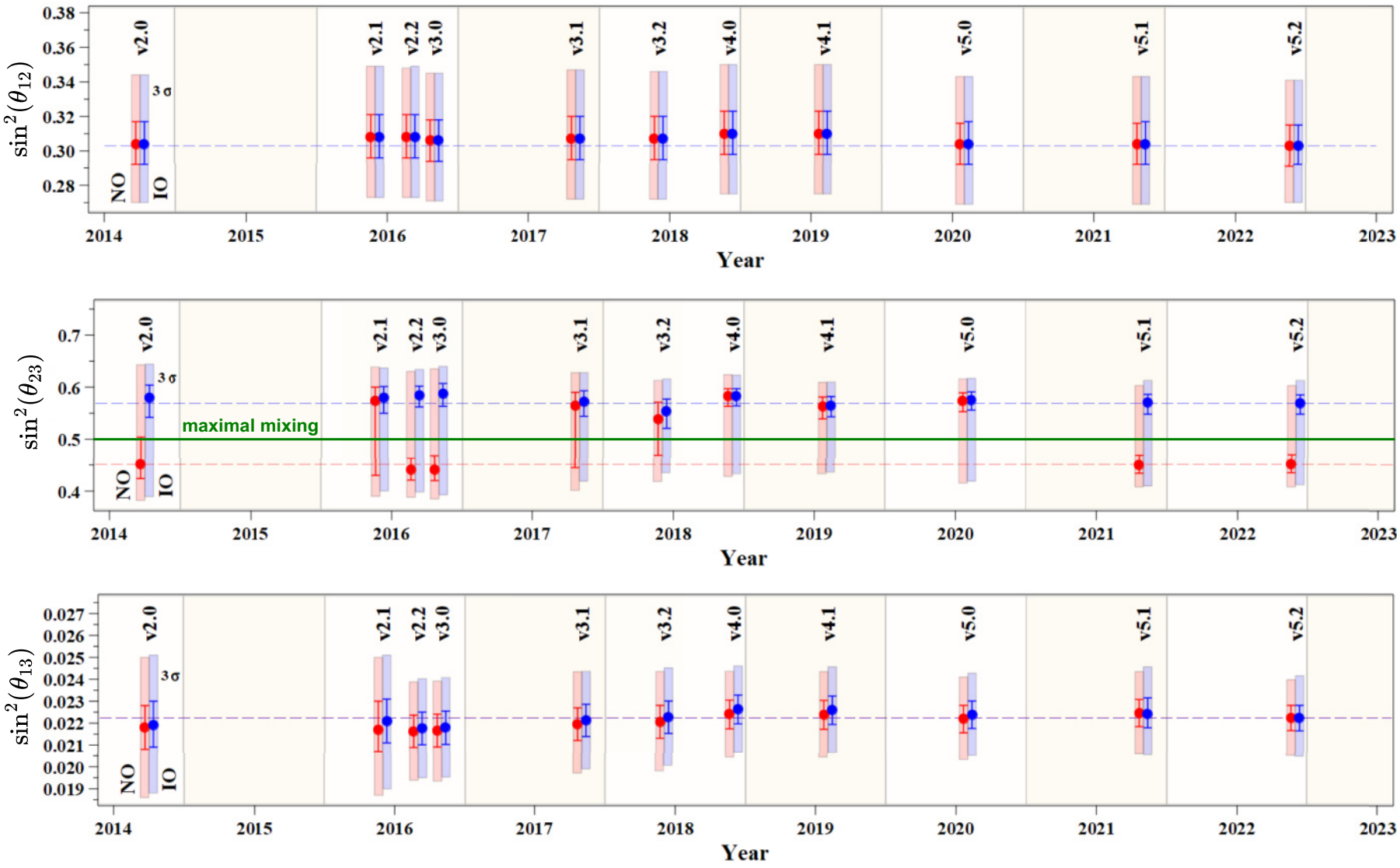

[a] For the recent review, see M. C. Gonzalez-Garcia, M. Maltoni, & Th. Schwetz, "NuFIT: Three-flavour global analyses of neutrino oscillation experiments," Universe **7** (2021) 459, arXiv:2111.03086 [hep-ph].

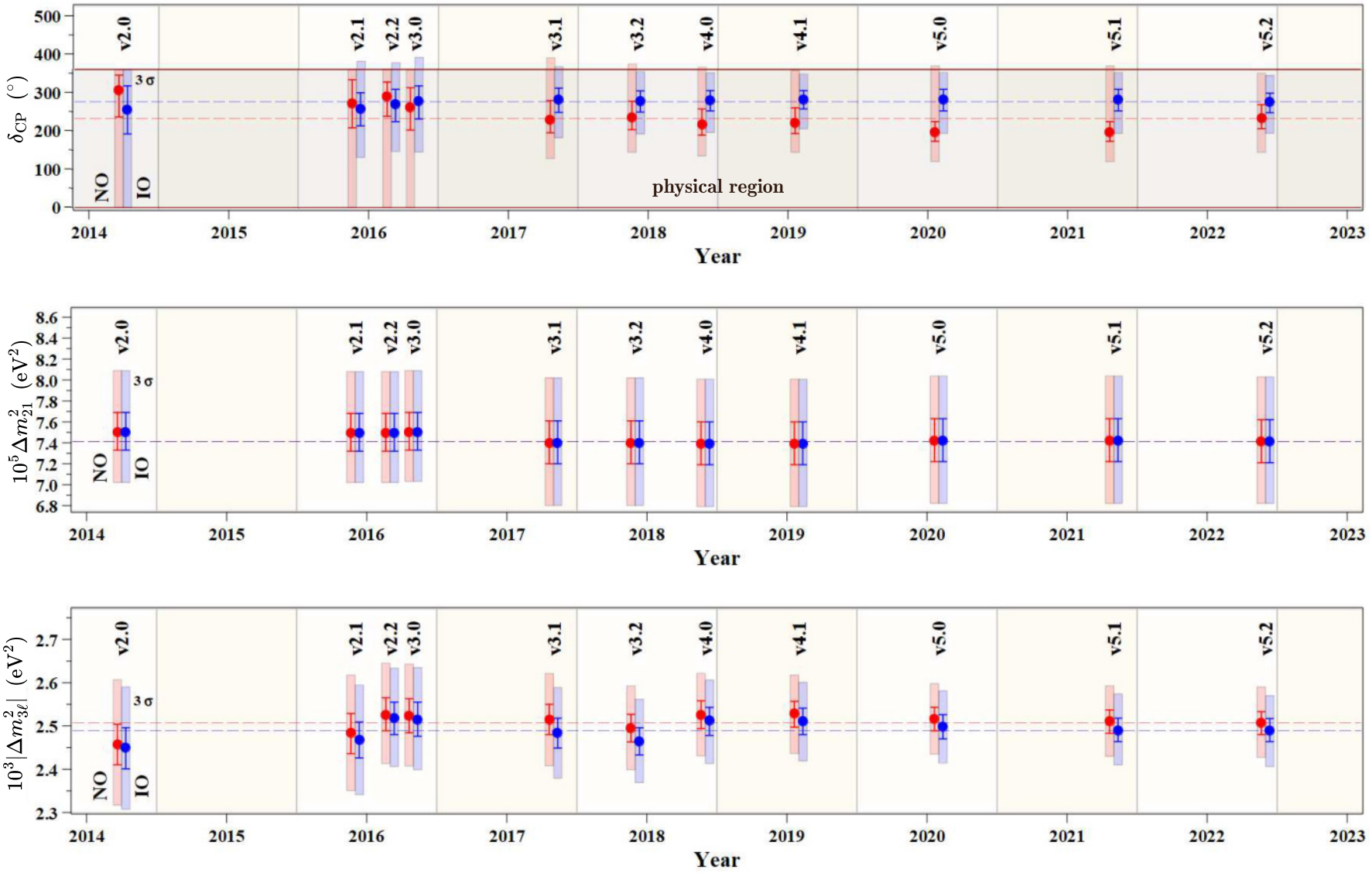

The consistency of the NuFIT team's results over the past few years makes it possible to avoid annual updates to relevant figures. Draw more physical conclusions yourself... as a homework.

In the absence of CP violation, the mixing angles may be represented as Euler angles relating the flavor and mass eigenstates. ▷

According to NuFIT 5.2 (p. 431), the best-fit mixing angles and δ for the normal mass ordering (a bit preferred today) are:

	PNMS	CKM
$\theta_{12}/^\circ$	$33.41^{+0.75}_{-0.72}$	13.00 ± 0.04
$\theta_{23}/^\circ$	$42.2^{+1.1}_{-0.9}$	$2.397^{+0.049}_{-0.042}$
$\theta_{13}/^\circ$	8.58 ± 0.11	0.201 ± 0.006
$\delta/^\circ$	197^{+42}_{-25}	65.55 ± 1.55

The CKM angles and CP phase are derived from the data given in RPP-2022.

It should be stressed that the neutrino mass spectrum is still undetermined. ▷

[Figures (slightly modified and updated) are taken from S. F. King, "Neutrino mass and mixing in the seesaw playground," Nucl. Phys. B **908** (2016) 456-466, arXiv:1511.03831 [hep-ph].]

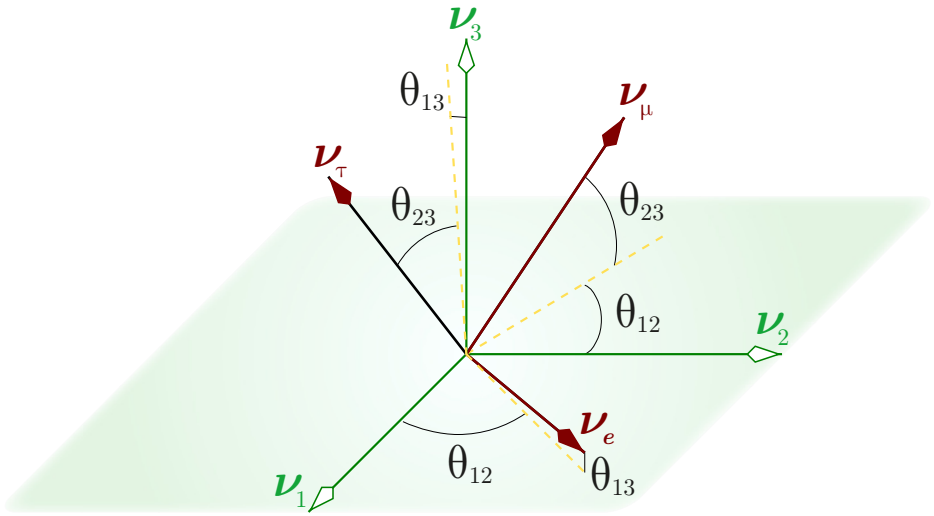

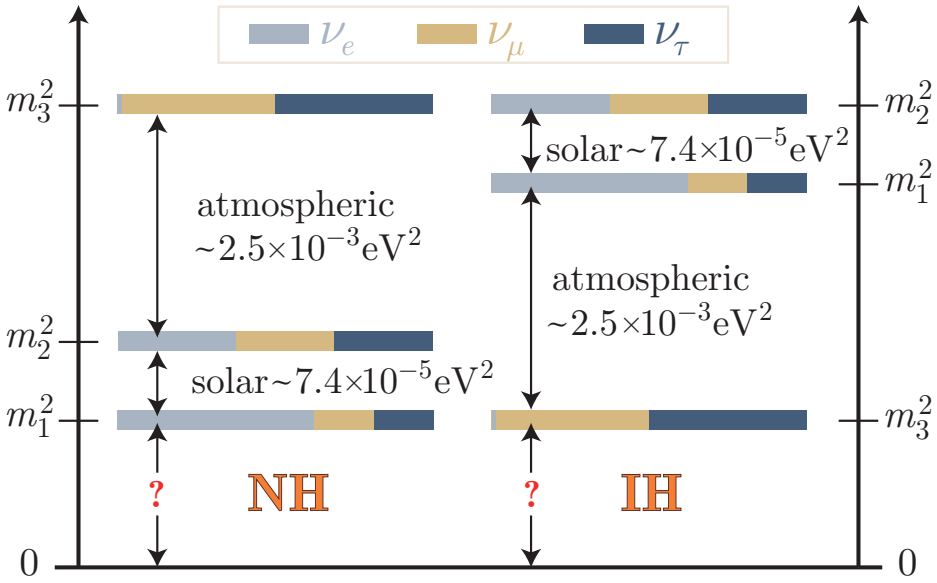

Flavor content of mass states (as well as mass content of flavor states) is the same for Dirac νs and $\overline{\nu}$s (since $\delta(\overline{\nu}) = -\delta(\nu)$) and for Majorana left/right νs (since $\left|V^{\mathsf{D}}_{\alpha i}\right| = \left|V^{\mathsf{M}}_{\alpha i}\right|$, see p. 465).

12.2.1 Flavor content of mass states and mass content of flavor states.

$$\left(|V_{\alpha i}|^2\right)_{\text{NH}} = \begin{pmatrix} 0.681 & 0.296 & 0.0223 \\ 0.131 & 0.427 & 0.441 \\ 0.187 & 0.276 & 0.537 \end{pmatrix}, \quad \left(|V_{\alpha i}|^2\right)_{\text{IH}} = \begin{pmatrix} 0.681 & 0.296 & 0.0222 \\ 0.146 & 0.297 & 0.557 \\ 0.172 & 0.407 & 0.421 \end{pmatrix}.$$

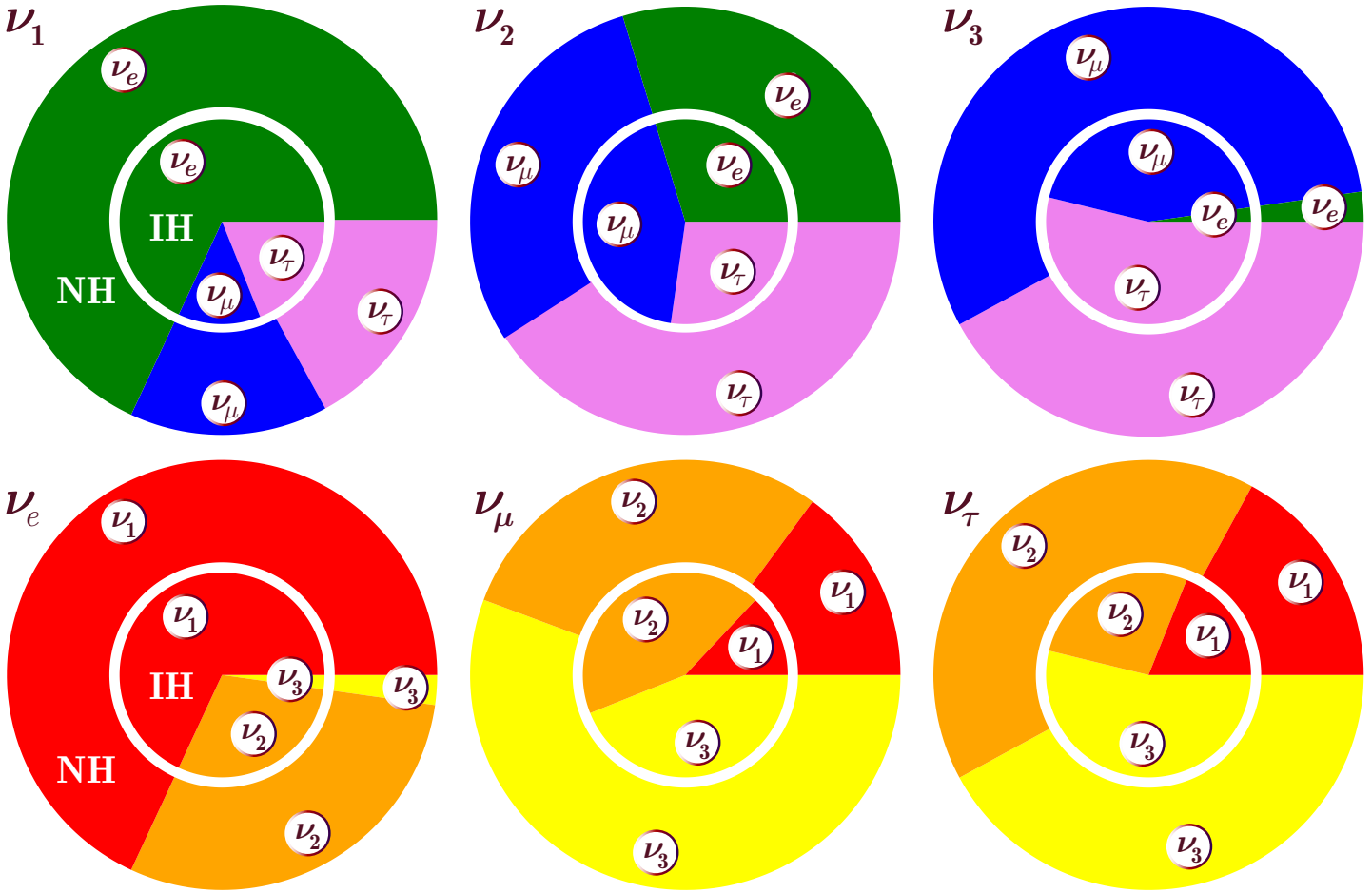

12.2.2 Current status of the neutrino masses from oscillation experiments.

So, NuFIT 5.2 provides the following constraints for the neutrino mass-squared splittings:

$$\begin{cases} \Delta m^2_{21} = m^2_2 - m^2_1 = 7.41^{+0.21}_{-0.20} \times 10^{-5}\ \text{eV}^2 & (\text{“solar” for NH and IH}), \\ \Delta m^2_{32} = m^2_3 - m^2_1 = 2.507^{+0.026}_{-0.027} \times 10^{-3}\ \text{eV}^2 & (\text{“atmospheric” for NH}), \\ \Delta m^2_{23} = m^2_2 - m^2_3 = 2.486^{+0.025}_{-0.028} \times 10^{-3}\ \text{eV}^2 & (\text{“atmospheric” for IH}), \end{cases}$$

These results imply that at least two of the neutrino eigenfields have nonzero masses and thus there are (at least) two very different possible scenarios related to the mass ordering:

$$m_1 < m_2 < m_3 \quad (\text{for NH}) \quad \text{or} \quad m_3 < m_1 < m_2 \quad (\text{for IH}).$$

Assuming that the lightest neutrino mass is very small,[a] namely $m_1 \ll m_2$ for NH, or $m_3 \ll m_1$ for IH, and using the NuFIT 5.2 results, we obtain the following estimates (below $\sum m_\nu \equiv \sum_{i=1}^{3} m_i$):[b]

$$\begin{cases} m_2 = 8.606^{+0.122}_{-0.116} \times 10^{-3}\ \text{eV}, \\ m_3 = 5.007^{+0.026}_{-0.027} \times 10^{-2}\ \text{eV}, \end{cases} \implies \sum m_\nu \geq m_2 + m_3 = 0.0587^{+0.0026}_{-0.0027}\ \text{eV} \ \ (\text{for NH})$$

$$\begin{cases} m_2 = 5.06^{+0.025}_{-0.028} \times 10^{-2}\ \text{eV}, \\ m_1 = 4.99^{+0.025}_{-0.028} \times 10^{-2}\ \text{eV}, \end{cases} \implies \sum m_\nu \geq m_1 + m_2 = 0.1005^{+0.0005}_{-0.0006}\ \text{eV} \ \ (\text{for IH})$$

Therefore, the lower bounds on $\sum m_\nu$ at 1σ C.L. for the two mass-spectrum scenarios are

$$\sum m_\nu > 0.0560\ \text{eV} \ \ (\text{for NH}) \quad \text{and} \quad \sum m_\nu > 0.0999\ \text{eV} \ \ (\text{for IH}).$$

[a] A basis for this assumption could be, e.g., the see-saw model. A more general picture is presented below.

[b] Note: the masses of the heaviest neutrinos differ by about 5.8 times for NH but by less than 1.5% for IH.

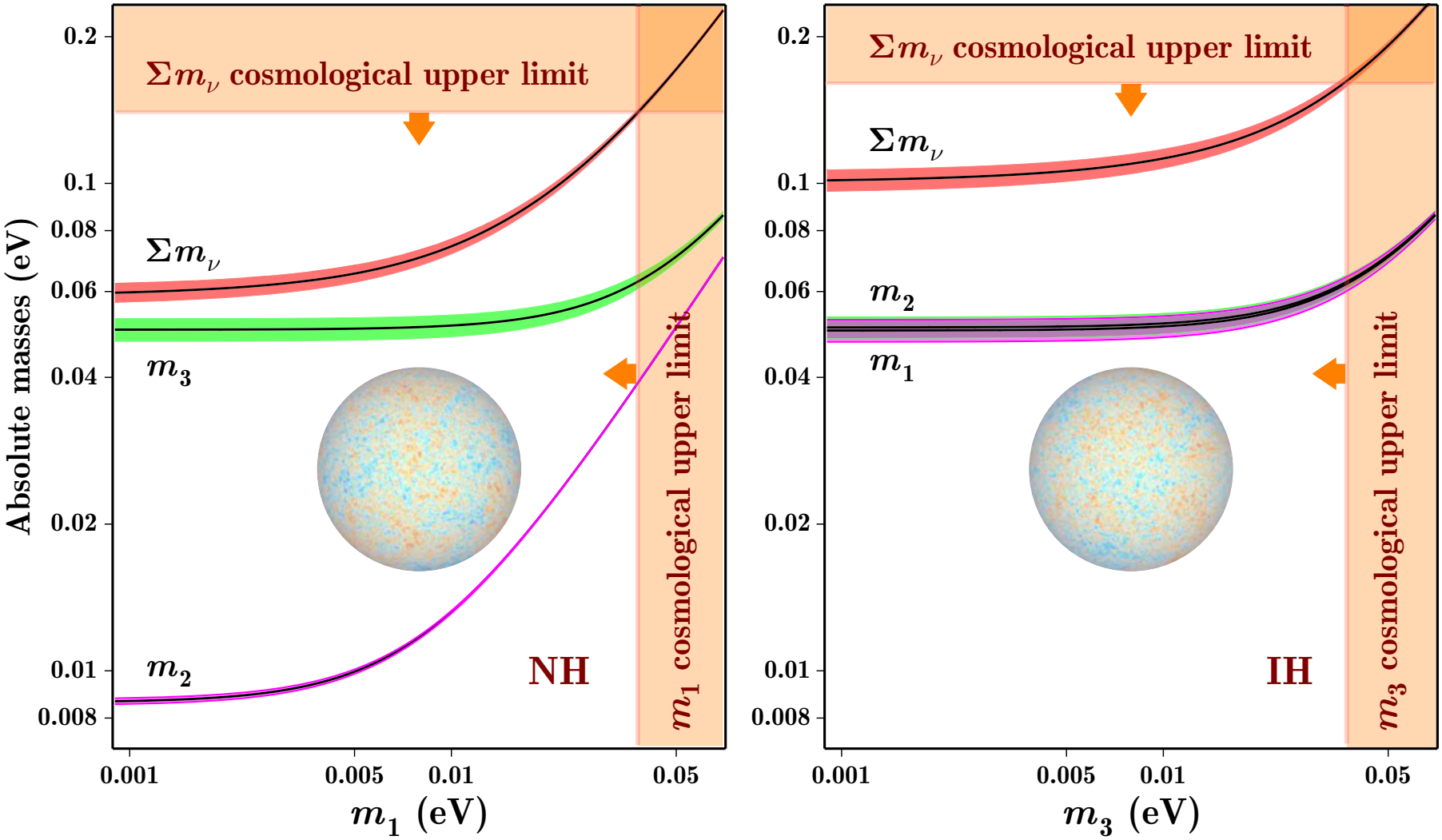

Absolute neutrino masses as functions of the lightest mass (m_1 or m_3) in the two neutrino mass spectrum scenarios. The bands are due to uncertainties in the neutrino mass-squared splittings. Cosmological ("Base+SNe") upper limits are also shown (see p. 149).

Note: Current accelerator and reactor data favor the NH scenario, but the question is not yet closed.

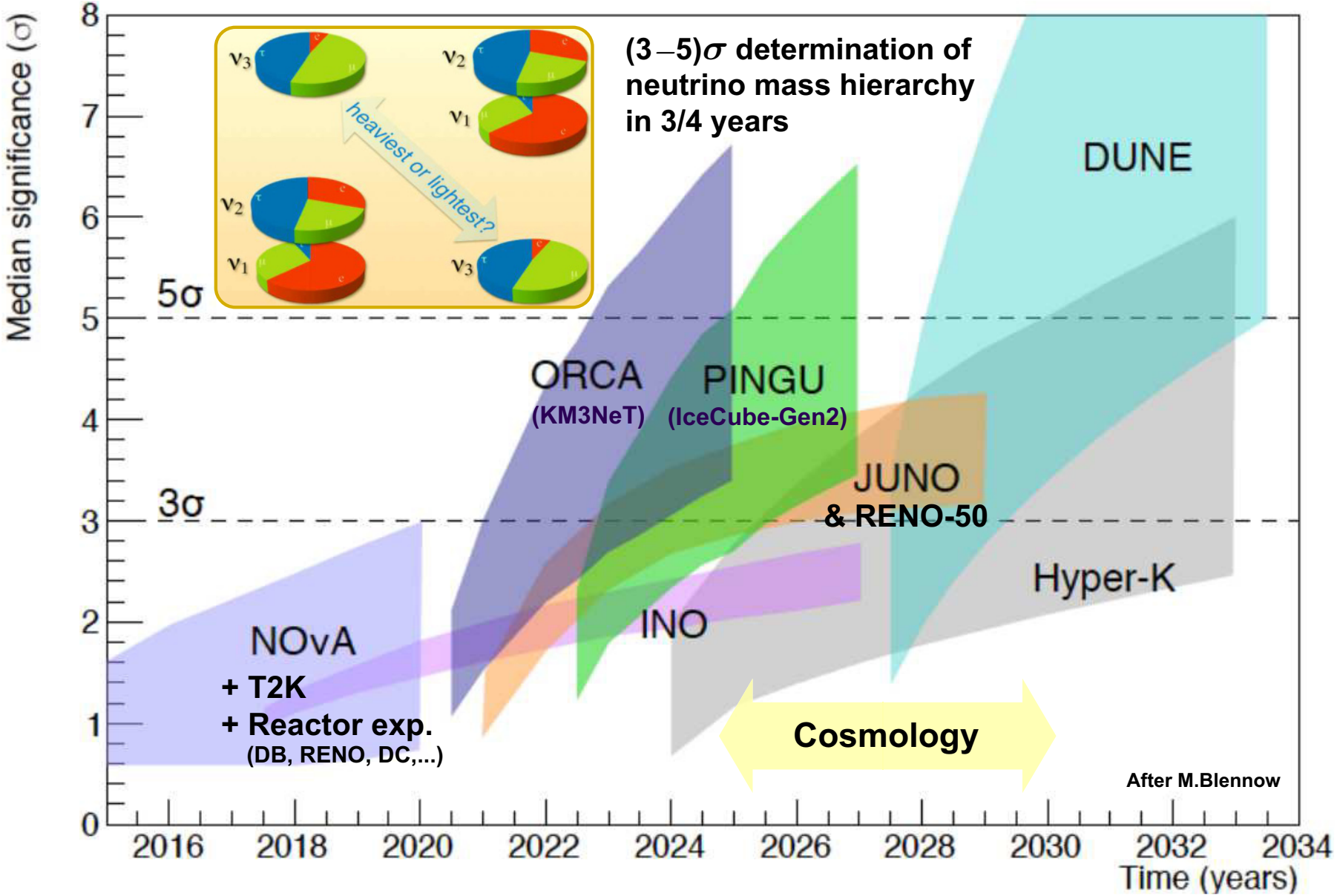

A summary of sensitivities to the neutrino mass hierarchy for various experimental approaches, with timescales, as claimed by the proponents in each case. Widths indicate main expected uncertainty.

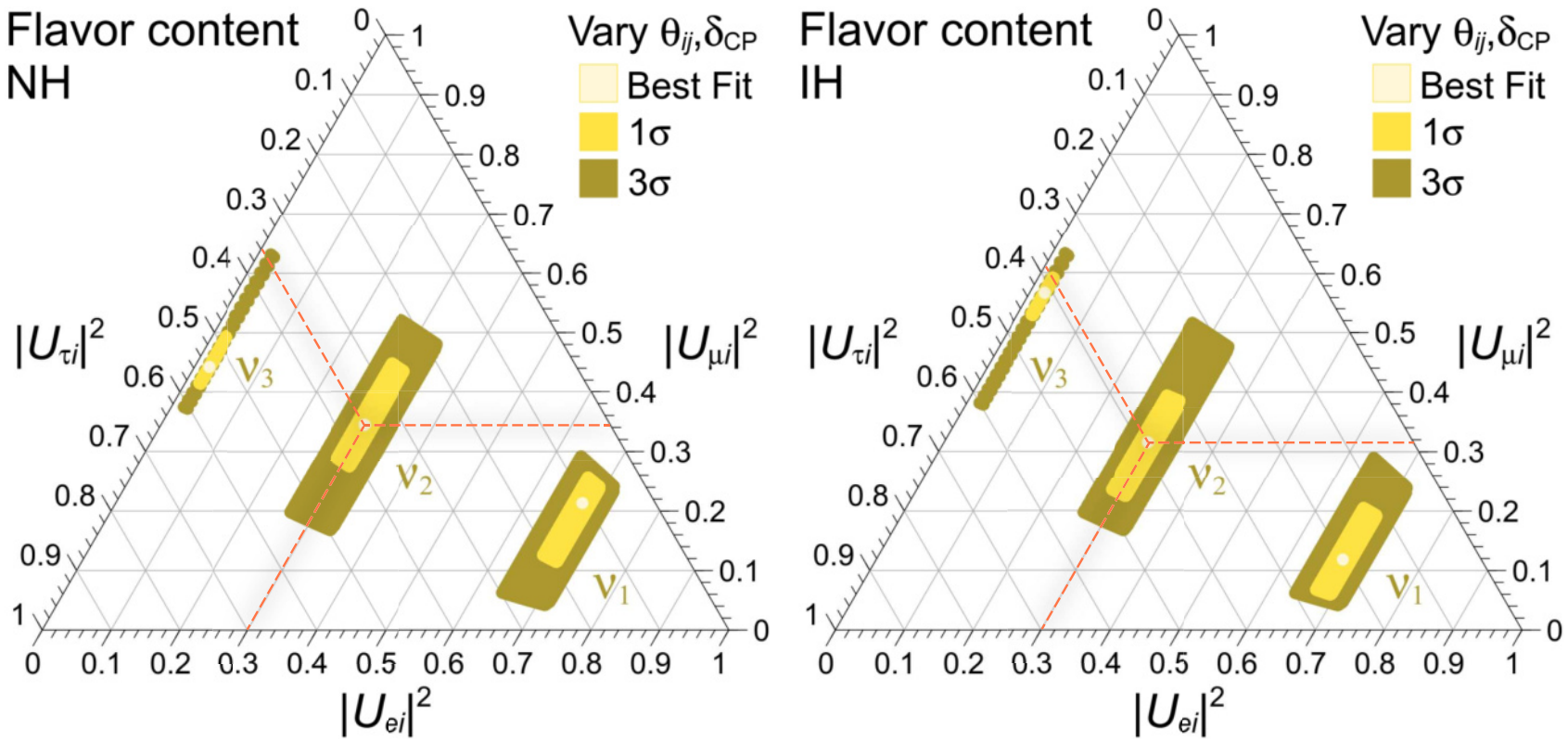

Flavor content of the three active mass eigenstates. The regions are given by the best-fit values of the mixing parameters,[a] assuming a normal and inverse mass hierarchies. The tilt of the tick marks indicates the orientation with which to read the flavor content. Here $U \equiv V$.

[M. Bustamante, J. F. Beacom, & W. Winter, "Theoretically palatable flavor combinations of astrophysical neutrinos," Phys. Rev. Lett. **115** (2015) 161302, arXiv:1506.02645 [astro-ph.HE].]

[a] The numerical values are from M. C. Gonzalez-Garcia *et al.*, "Updated fit to three neutrino mixing: status of leptonic CP violation," JHEP11(2014)052, arXiv:1409.5439 [hep-ph]. They are, of course, outdated, but that doesn't matter for our purposes – just to show another useful form of representing the mixing matrix.

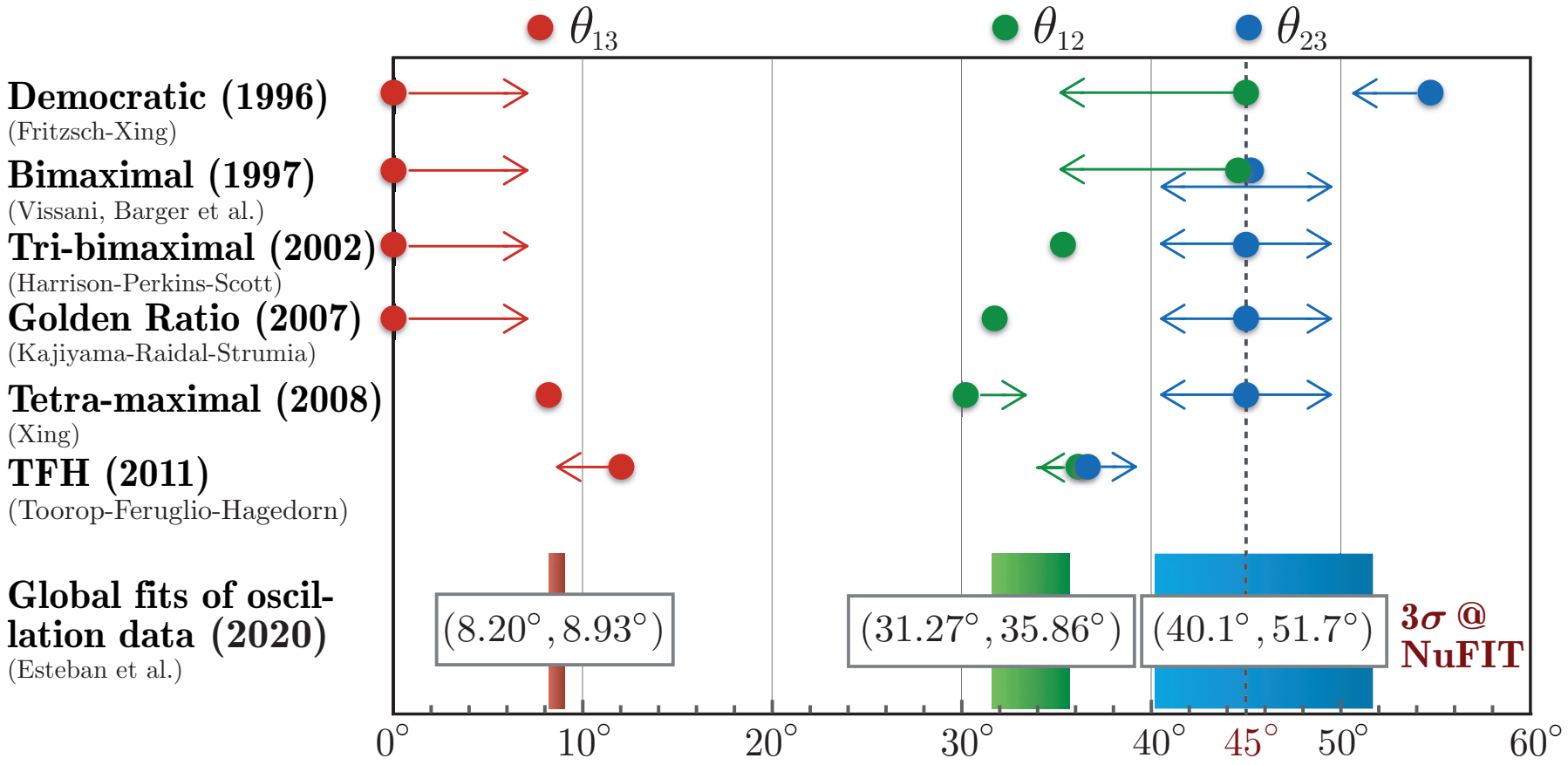

△ Figure shows the mixing angles from constant mixing patterns vs. oscillation experimental data. Several constant mixing patterns have been proposed, which invoke specific values of the angles. Many of these patterns predict a vanishing θ_{13}, and are therefore excluded by current data or require special large corrections. There is a preliminary hint (T2K, NOνA, reactors) of near-maximal CP violation with $\delta \sim 90°$ or $270°$, but the constraint in the 3σ range is too wide yet.

[Adapted from S. Pascoli & Ye-Ling Zhou, "Theoretical motivations for precision measurements of oscillation parameters," PoS(ICHEP2016)471, arXiv:1611.04817 [hep-ph]. Figure is updated after the NuFIT 5.0 (see p. 433).]

Since the Dirac mass term violates conservation of the individual lepton numbers, L_e, L_μ, L_τ, it allows many lepton family number violating processes, like

$$\mu^\pm \to e^\pm + \gamma, \quad \mu^\pm \to e^\pm + e^+ + e^-,$$
$$K^+ \to \pi^+ + \mu^\pm + e^\mp, \quad K^- \to \pi^- + \mu^\pm + e^\mp,$$
$$\mu^- + (A,Z) \to e^- + (A,Z), \quad \tau^- + (A,Z) \to \mu^- + (A,Z), \ldots$$

However the $(\beta\beta)_{0\nu}$ decay or the kaon semileptonic decays like

$$K^+ \to \pi^- + \mu^+ + e^+, \quad K^- \to \pi^+ + \mu^- + e^-,$$

etc. are still forbidden as a consequence of the total lepton charge conservation.

Current limits on the simplest lepton family number violating μ and τ decays (2022). [a]

Decay Modes	Fraction	C.L.	Decay Modes	Fraction	C.L.
$\mu^- \to e^- \nu_e \overline{\nu}_\mu$	$< 1.2\%$	90%	$\tau^- \to e^- \gamma$	$< 3.3 \times 10^{-8}$	90%
$\mu^- \to e^- \gamma$ [b]	$< 4.2 \times 10^{-13}$	90%	$\tau^- \to \mu^- \gamma$	$< 4.2 \times 10^{-8}$	90%
$\mu^- \to e^- e^+ e^-$	$< 1.0 \times 10^{-12}$	90%	$\tau^- \to e^- \pi^0$	$< 8.0 \times 10^{-8}$	90%
$\mu^- \to e^- 2\gamma$	$< 7.2 \times 10^{-11}$	90%	$\tau^- \to \mu^- \pi^0$	$< 1.1 \times 10^{-7}$	90%

These limits are not quite as impressive as might appear at first glance.

[a] From R. L. Workman *et al.* (Particle Data Group), "Review of particle physics," PTEP **2022** (2022) 083C01.

[b] The current best limit comes from the MEG experiment at the Paul Scherrer Institut (PSI), A. M. Baldini *et al.* (MEG Collaboration), "Search for the lepton flavour violating decay $\mu^+ \to e^+\gamma$ with the full dataset of the MEG experiment," Eur. Phys. J. C **76** (2016) 434, arXiv:1605.05081 [hep-ex].

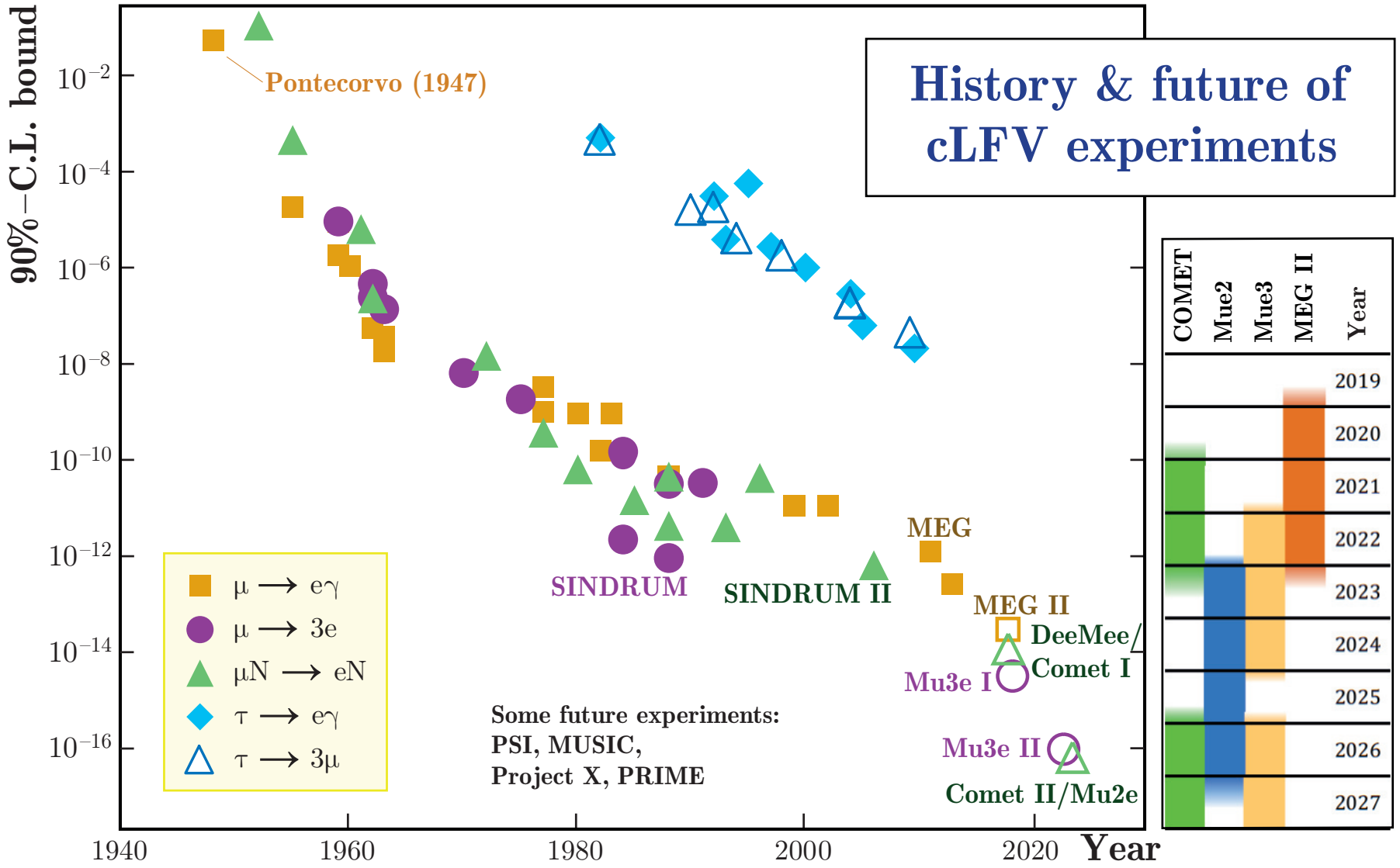

[From N. Berger, "Charged lepton flavour violation experiments," talk at the Zürich Phenomenology Workshop, January 2015 (partially updated). For more detail, see, e.g., W. J. Marciano, T. Mori & J. M. Roney, "Charged lepton flavor violation experiments," Ann. Rev. Nucl. Part. Sci. **58** (2008) 315–341; L. Calibbi & G. Signorelli, "Charged lepton flavour violation," Riv. Nuovo Cim. **41** (2018) 71–173, arXiv:1709.00294 [hep-ph].]

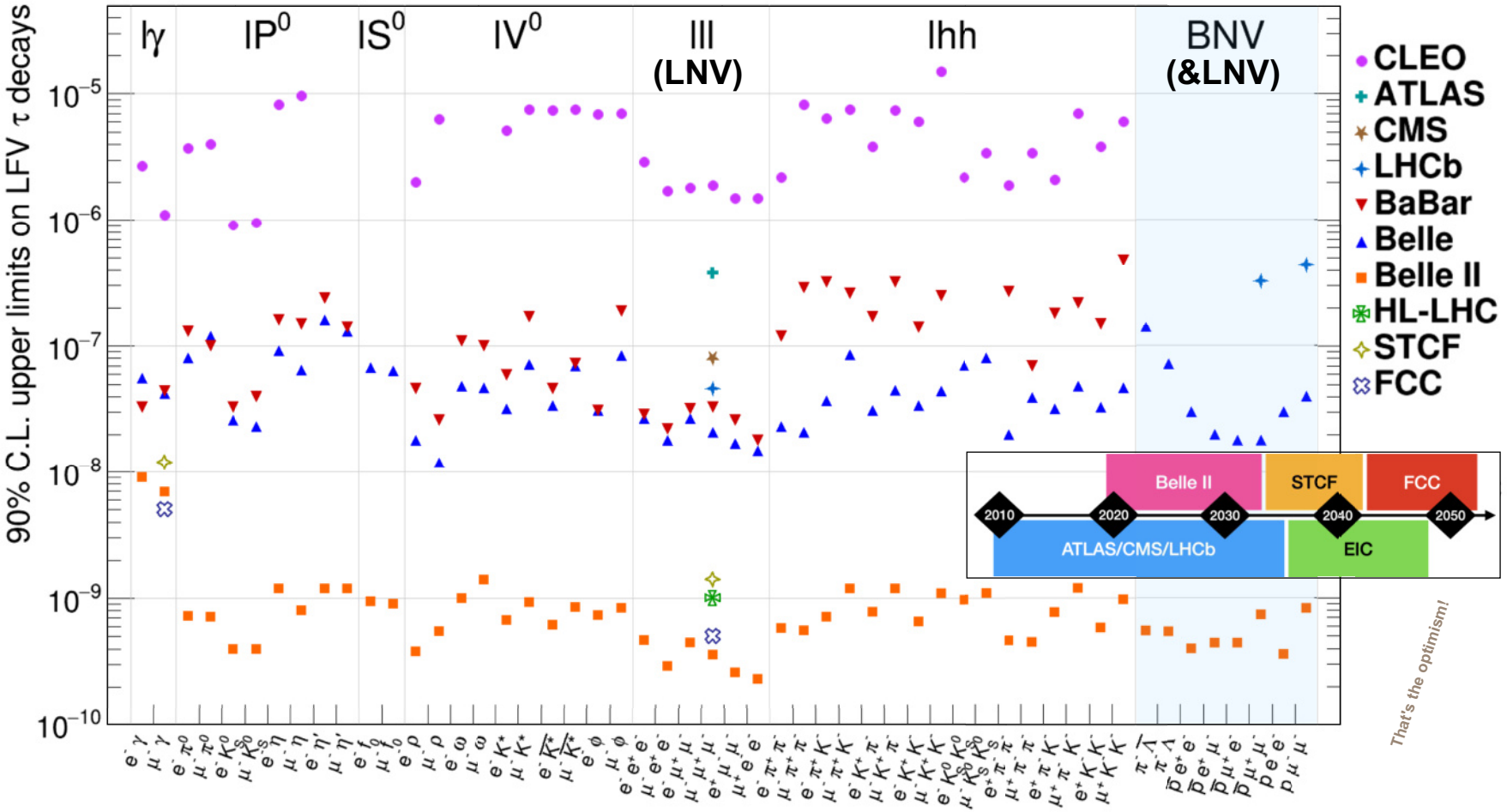

Current (Spring 2022) summary of all observed limits at past and current experiemnts, and projection of expected limits at future experiments (Belle II, SCTF, FCC, EIC) on the upper limits on LFV, LNV, and BNV in 52 benchmark τ decay channels predicted in many models beyond the Standard Model. Incert shows a tentative timeline for data-taking at the experiments probing cLFV in the τ sector.

[Adapted from S. Banerjee *et al.*, "Snowmass 2021 White Paper: Charged lepton flavor violation in the tau sector," arXiv:2203.14919v2 [hep-ph]; see also Proceedings at URL: ⟨ https://www.slac.stanford.edu/econf/C210711/ ⟩.]

12.2.3 Neutrinoless muon decay in SM.

The L_μ and L_e violating muon decay $\mu^- \to e^-\gamma$ is allowed if $V^*_{\mu k}V_{ek} \neq 0$ for $k = 1, 2$ or 3. The corresponding Feynman diagrams include W loops and thus the decay width is strongly suppressed by the neutrino to W boson mass ratios:

$$R = \frac{\Gamma\left(\mu^- \to e^-\gamma\right)}{\Gamma\left(\mu^- \to e^-\nu_\mu\overline{\nu}_e\right)} = \frac{3\alpha}{32\pi}\left|\sum_k V^*_{\mu k}V_{ek}\frac{m_k^2}{m_W^2}\right|^2.$$

Since $m_k/m_W \approx 1.244 \times 10^{-12}\,(m_k/0.1\text{ eV})$, the ratio can be estimated as

$$R \approx 5.22 \times 10^{-52}\left|\sum_k V^*_{\mu k}V_{ek}\left(\frac{m_k}{0.1\text{ eV}}\right)^2\right|^2 \lesssim 8 \times 10^{-54},$$

while the current experimental upper limit is (at least!) 40 orders of magnitude larger (see Table at p. 442):

$$R_{(\text{exp})} < 4.2 \times 10^{-13} \text{ at } 90\% \text{ C.L.} \quad (\textbf{NO GO!})$$

Some nonstandard models are much more optimistic.

We must deeply appreciate the oscillation phenomenon which makes the miserable ν mass effect measurable.

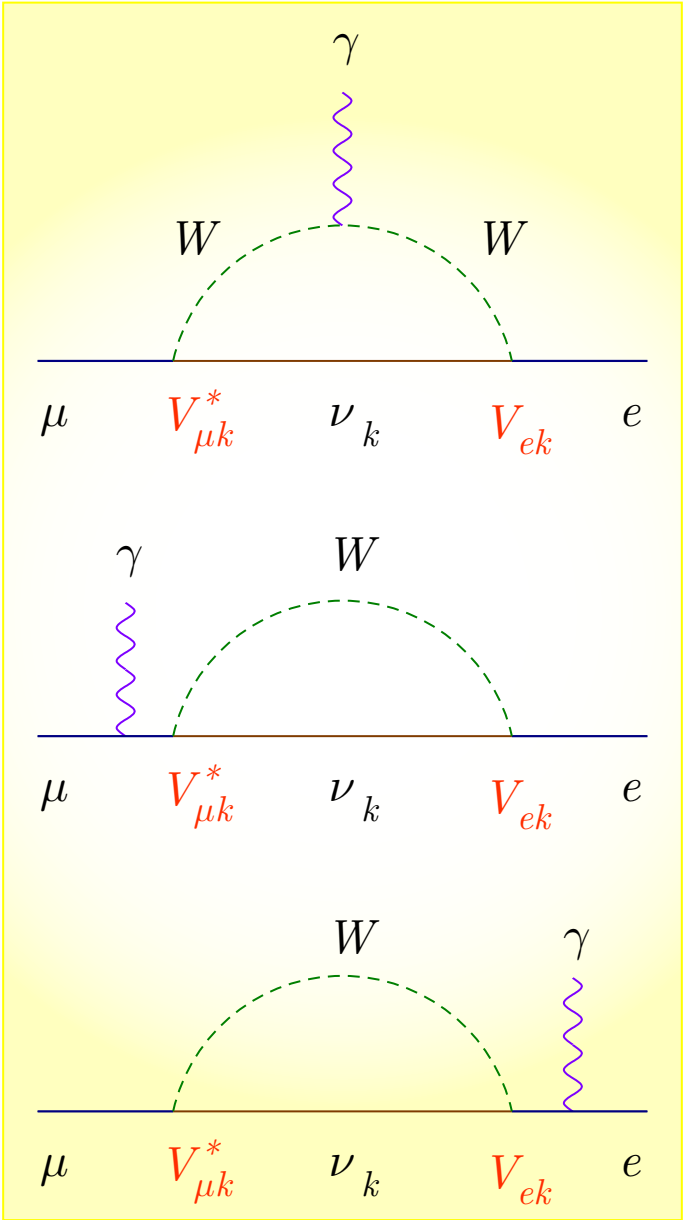

12.3 Nuclear beta decay.

The method of measurement of the (anti)neutrino mass through the investigation of the high-energy part of the β-spectrum was proposed by Perrin (1933) and Fermi (1934).
The first experiments on the measurement of the neutrino mass with this method have been done by Curran, Angus and Cockcroft (1948) and Hanna and Pontecorvo (1949).

The energy spectrum of electrons in the decay $(A, Z) \to (A, Z+1) + e^- + \overline{\nu}_e$ is[a]

$$\frac{d\Gamma}{dT} = \sum_k |V_{ek}|^2 \frac{d\Gamma_k}{dT}, \tag{41}$$

$$\frac{d\Gamma_k}{dT} = \frac{(G_F \cos\theta_C)^2}{2\pi^3} pEp_kE_k |\mathcal{M}|^2 F(T,Z)\theta(E_k - m_k). \tag{42}$$

Here G_F is the Fermi constant, θ_C is the Cabibbo angle, m_e, p, and E are the mass, magnitude of the momentum and total energy of the electron, respectively, m_k, p_k, and E_k are the mass, magnitude of the momentum and total energy of the neutrino ν_k, respectively;

$$p = \sqrt{E^2 - m_e^2}, \quad p_k = \sqrt{E_k^2 - m_k^2} = \sqrt{(Q-T)^2 - m_k^2}, \quad Q = E_k + T = E_{A,Z} - E_{A,Z+1} - m_e;$$

Q and $T = E - m_e$ are, respectively, the energy released in the decay (the endpoint of the β spectrum in case $m_k = 0$) and electron kinetic energy; $\mathcal{M}$ is the nuclear matrix element, and $F(T,Z)$ is the Fermi function, which describes the Coulomb interaction of the final-state nucleus and electron. Finally, the step function in Eq. (42) ensures that a neutrino state ν_k is only produced if its total energy is larger than its mass: $E_k = Q - T \geq m_k$.

[a] The recoil of the final nucleus and radiative corrections (luckily small) are neglected.

As it is seen from Eq. (42), the largest distortion of the β-spectrum due to neutrino masses can be observed in the region

$$Q - T \sim m_k. \tag{43}$$

However, for $\max(m_k) \simeq (0.10 - 0.15)$ eV only a very small part (about $10^{-(13-14)}$) of the decays give contribution to the region (43). It is for this reason that a relatively large part of the β-spectrum is used in the analysis.[a] Considering that $Q - T$ is k-independent, $Q - T \gg m_k$ ($\Rightarrow \theta(E_k - m_k) = 1$) and applying the unitarity condition for the mixing matrix, we can write approximately

$$\sum_k |V_{ek}|^2 p_k \approx \sum_k |V_{ek}|^2 (Q-T)\left[1 - \frac{m_k^2}{2(Q-T)^2}\right] \quad \Longleftarrow \quad 4E_k^2 \gg m_k^2$$

$$= (Q-T)\left[1 - \frac{1}{2(Q-T)^2}\sum_k |V_{ek}|^2 m_k^2\right]. \quad \Longleftarrow \quad \sum_k |V_{ek}|^2 = 1$$

$$\Longrightarrow \quad \sum_k |V_{ek}|^2 p_k \approx \sqrt{(Q-T)^2 - m_\beta^2}, \quad \text{where} \quad m_\beta^2 = \sum_k |V_{ek}|^2 m_k^2.$$

The key parameter m_β is called the effective electron neutrino mass[b] and can be written explicitly as

$$m_\beta^2 = c_{13}^2 c_{12}^2 m_1^2 + c_{13}^2 s_{12}^2 m_2^2 + s_{13}^2 m_3^2 = \begin{cases} m_1^2 + \Delta m_{21}^2 \left(1 - c_{13}^2 c_{12}^2\right) + \Delta m_{32}^2 s_{13}^2 & \text{(NH)}, \\ m_3^2 + \Delta m_{21}^2 c_{13}^2 c_{12}^2 - \Delta m_{32}^2 c_{13}^2 & \text{(IH)}. \end{cases}$$

The approximation used above is in fact valid under the condition $4(Q-T)^2 \gg \max_k\left(m_k^2\right)$.

[a] For example, in the Mainz Tritium experiment (see below) the last 70 eV of the spectrum is used.

[b] Sometimes it is referred to as $m_{\nu_e}^{\text{eff}}$ or simply m_{ν_e}.

Finally, the β-spectrum that is used for fitting the data can be presented as

$$\frac{d\Gamma}{dT} \propto p\,(T+m_e)\,|\mathcal{M}|^2\,F(T,Z)K^2(T),$$

where we have defined the *Kurie function* (sometimes called Fermi-Kurie function)

$$K(T) \propto \sqrt{\frac{d\Gamma/dT}{p\,(T+m_e)\,|\mathcal{M}|^2\,F(T,Z)}} \approx (Q-T)\left[1-\frac{m_\beta^2}{(Q-T)^2}\right]^{1/4}$$

developed by Franz Newell Devereux Kurie.

Unfortunately, the real-life situation is much more complicated.

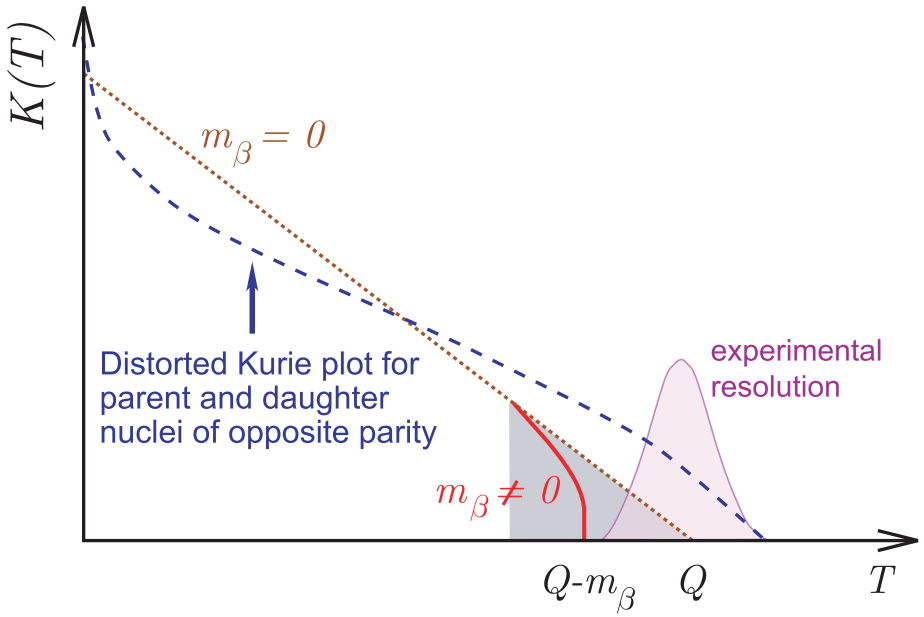

Kurie plot for allowed processes is a sensitive test of m_β, while the first order forbidden processes should have a distorted Kurie plot.

In an actual experiment, the measurable quantity is a sum of β spectra, leading each with probability $P_n = P_n(E_0 - V_n - E)$ to a final state n of excitation energy V_n:

$$\frac{d\Gamma(T,Q)}{dT} \longmapsto \sum_n P_n\,(E_0 - V_n - E)\,\frac{d\Gamma\,(T, E_0 - V_n)}{dT}.$$

Here $E_0 = Q - \mathcal{E}$ the ground-state energy and $\mathcal{E}$ is the recoil energy of the daughter nucleus.

12.3.1 Tritium beta decay.

The β decay of tritium in its molecular form,

$$\mathsf{T}_2 \to \left({}^3\mathsf{HeT}\right)^+ + e^- + \overline{\nu}_e,$$

is the basis of most sensitive experiments. Considering modern most precise direct determination of the mass difference

$$m(\mathsf{T}) - m\left({}^3\mathsf{He}\right) = (18590.1 \pm 1.7)\ \text{eV}/c^2$$

and taking into account the recoil and apparative effects (these are taken for the Mainz experiment) one derives an endpoint energy of the molecular ion $\left({}^3\mathsf{HeT}\right)^+$ ground state:

$$E_0 = (18574.3 \pm 1.7)\ \text{eV}.$$

The excitation spectrum is shown in the Figure. The first group concerns rotational and vibrational excitation of the molecule in its electronic ground state; it comprises a fraction of $P_g = 57.4\%$ of the total rate.

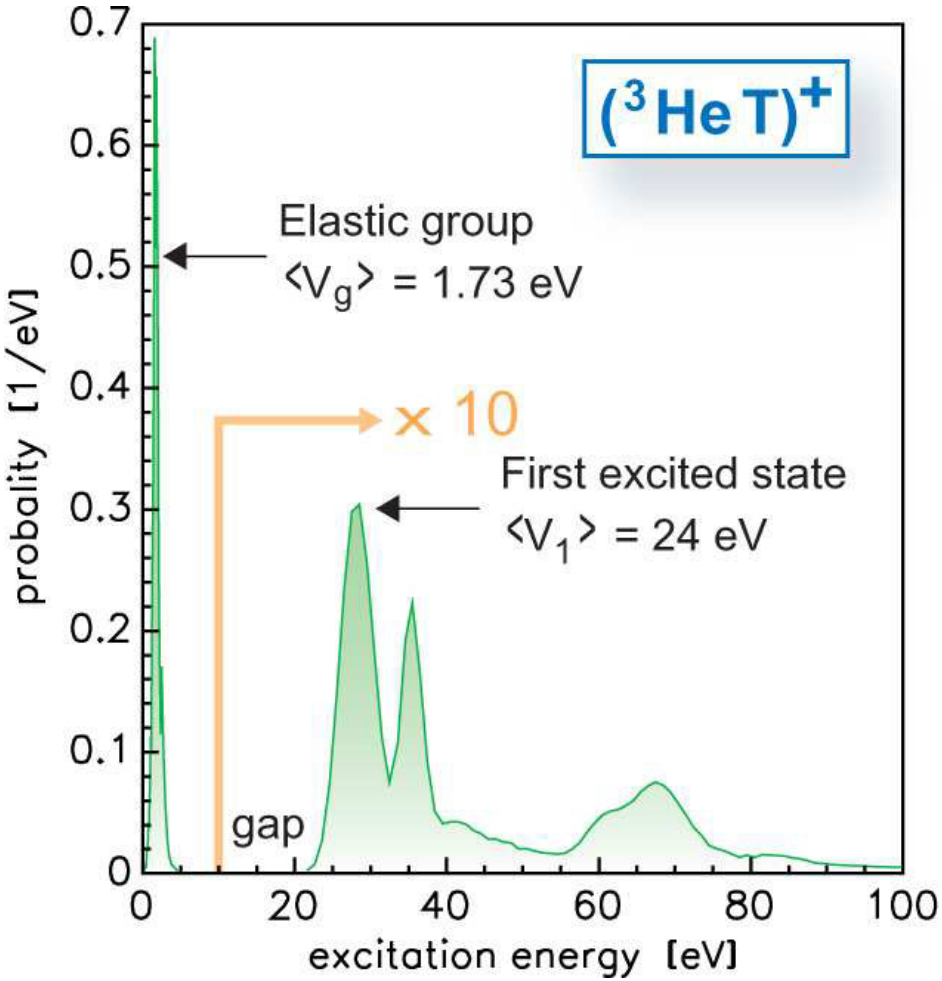

Excitation spectrum of the daughter molecular ion $\left({}^3\mathsf{HeT}\right)^+$ in β decay of molecular Tritium.

For more details, see C. Kraus *et al.*, "Final results from phase II of the Mainz neutrino mass search in Tritium β decay," Eur. Phys. J. C **40** (2005) 447–468, hep-ex/0412056.

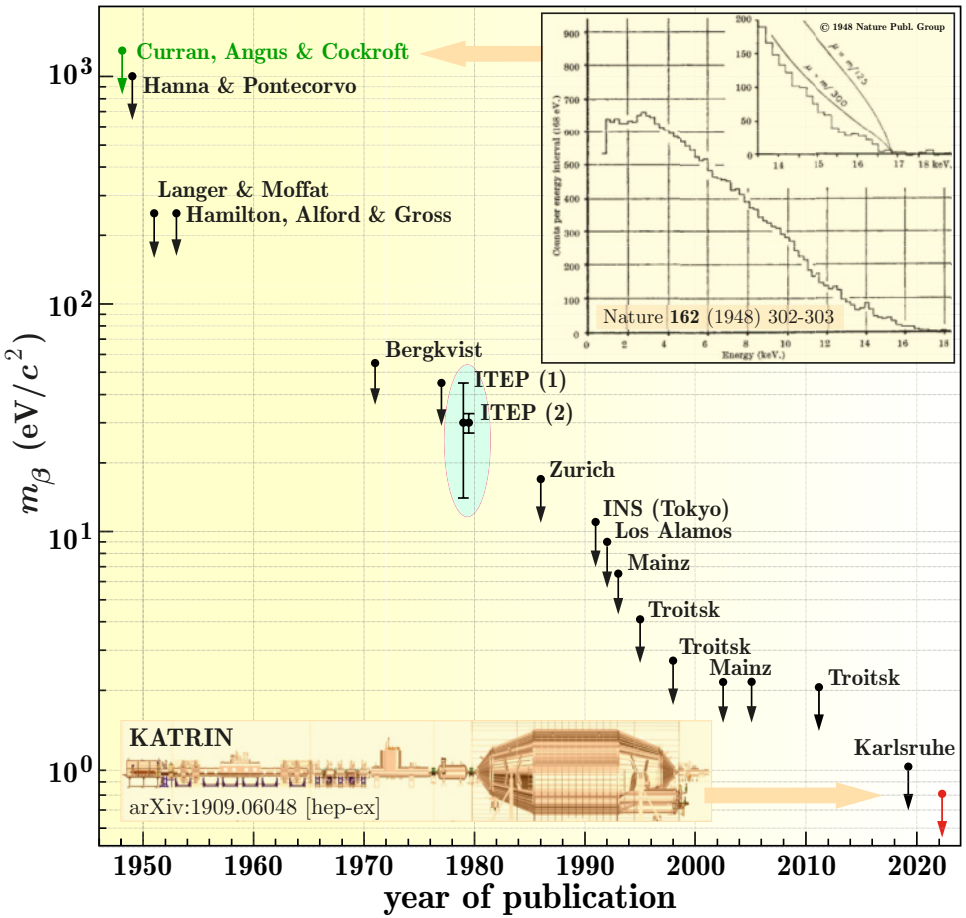

Progress of the neutrino mass measurements in Tritium β decay, including the final Mainz phase II, Troitsk, and KATRIN upper limits (see below).

[The compilation is taken from V. M. Lobashev, "Direct search for mass of neutrino," in Proceedings of the 18th International Conference on Physics in Collision ("PIC 98"), Frascati, June 17–19, 1998, pp. 179–194 and supplemented with the recent data.]

◁ The history of the search for the neutrino mass in the Tritium β decay counts more than 60 years. In 1980, the steady improvement of the upper limit was suddenly speeded up by a report of the ITEP group (Moscow) on the observation of the nonzero neutrino mass effect in the β-spectrum in the valine molecule ($C_5H_9T_2NO_2$). The reported result was[a]

$$14 \leq m_\beta \leq 46 \text{ eV}/c^2 \quad (99\% \text{ C.L.})$$

This research stimulated more than 20 experimental proposals with an intention to check this clime. Alas!... in several years the experimental groups from Zürich, Tokyo, Los Alamos, and then Livermore refuted the ITEP result.

[a] V. A. Lyubimov, E. G. Novikov, V. Z. Nozik, E. F. Tretyakov & V. S. Kosik, "An estimate of the ν_e mass from the β-spectrum of Tritium in the valine molecule," Phys. Lett. B **94** (1980) 266–268 (505 citations in InSPIRE! on December 2023).

The top figure shows the data points from the tail of the β-spectrum measured in the Los Alamos Tritium experiment compared with the expected values (the straight line) for $m_\beta = 30$ eV. The data wander from the line, ruling out the possibility of a 30-eV neutrino.
The bottom figure shows the same data points compared with the expectation for $m_\beta = 0$. While the data clearly favor a neutrino mass of zero, the best fit is actually for a slightly negative m_β. (Note that in the bottom plot, the data points lie, on average, slightly above the line, so this is not a perfect fit.)
Both plots display "residuals," which indicate how many standard deviations each data point is from a particular hypothesis.

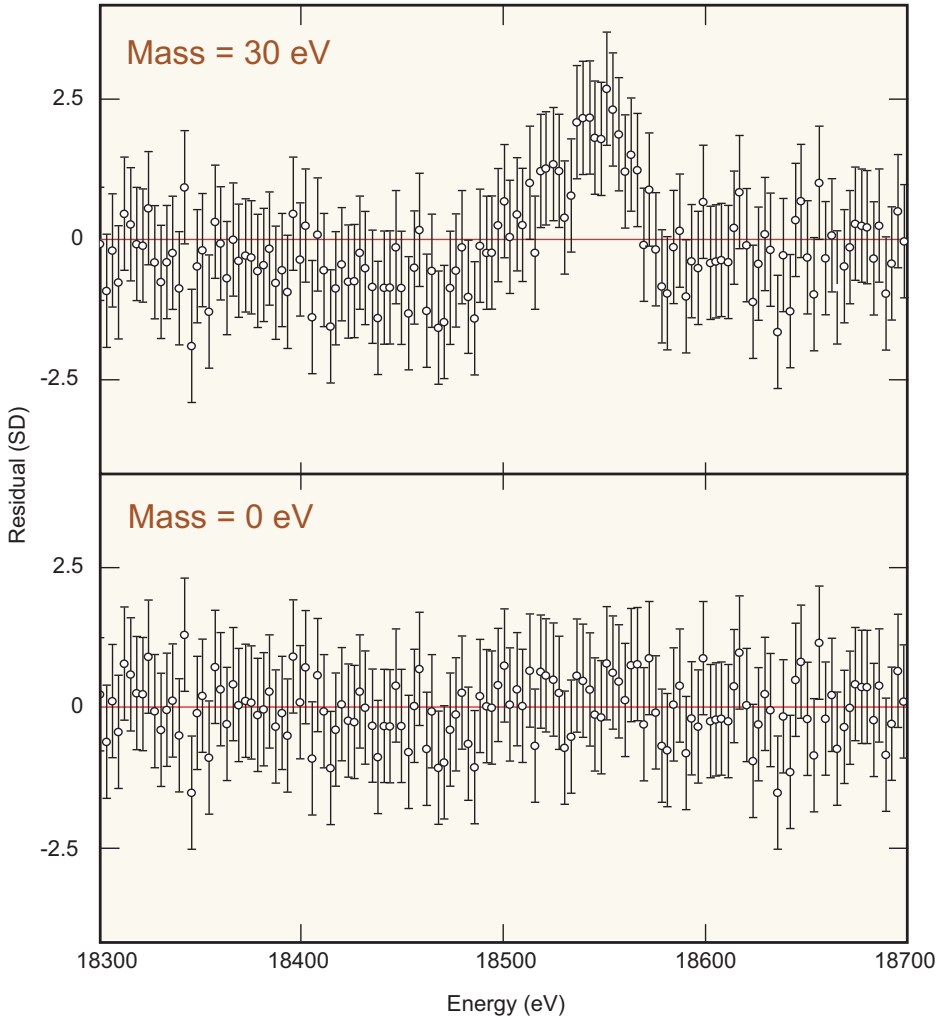

Did the neutrino weigh 30 electron volts?

[Borrowed from T. J. Bowles and R. G. H. Robertson, "Tritium beta decay and the search for neutrino mass," Los Alamos Sci. **25** (1997) 6–11.]

12.3.2 Troitsk anomaly.

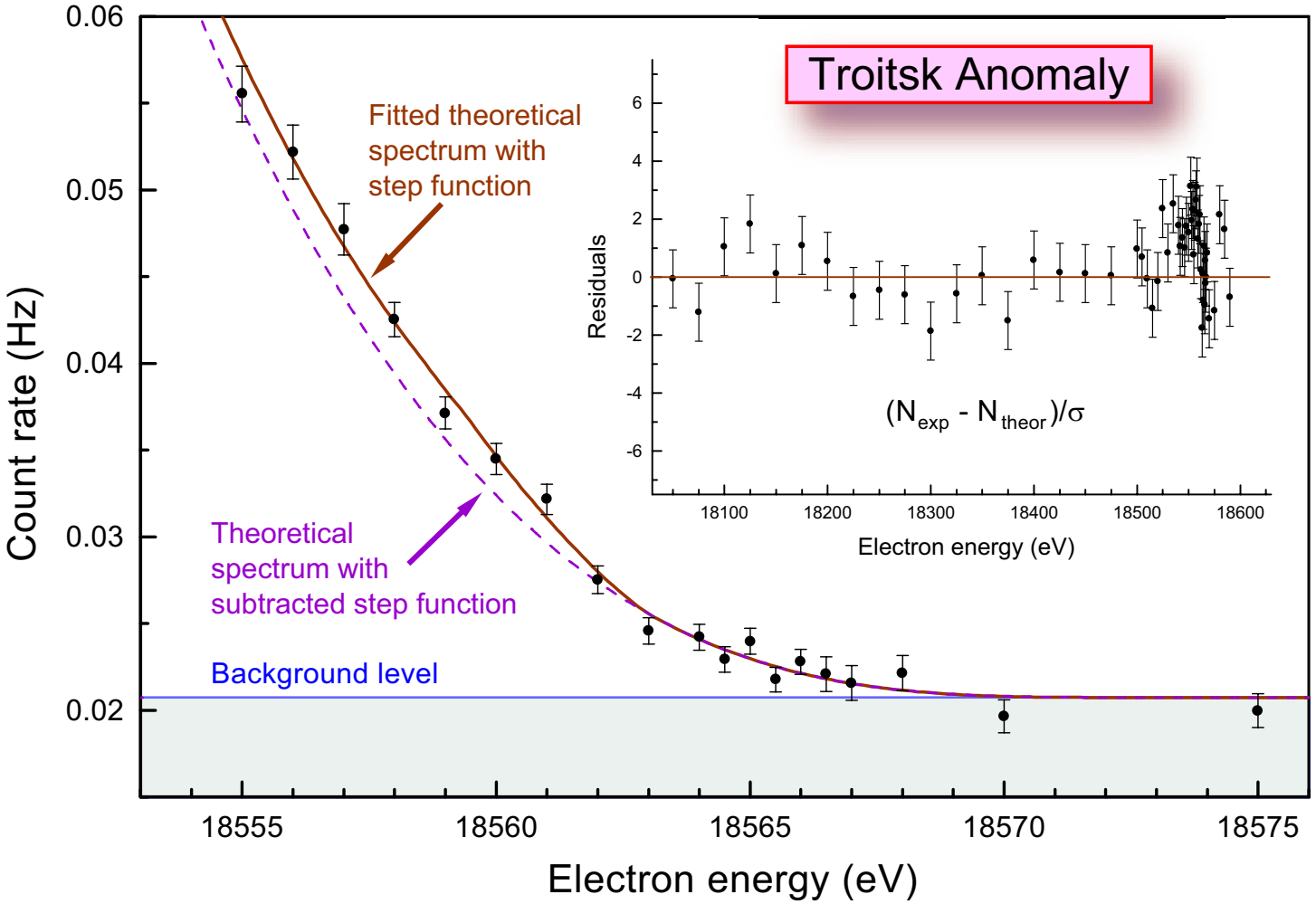

Part of experimental β-spectrum in the Troitsk ν-mass experiment near the end-point.

[V. M. Lobashev *et al.*, "Direct search for mass of neutrino and anomaly in the Tritium beta-spectrum," Phys. Lett. B **460** (1999) 227–235.]

The Troitsk group reported on a step like anomaly which appeared in their integral spectra with an amplitude of about 6×10^{-11} of the total decay rate and at variable positions in the range from 5 to 15 eV below the endpoint.

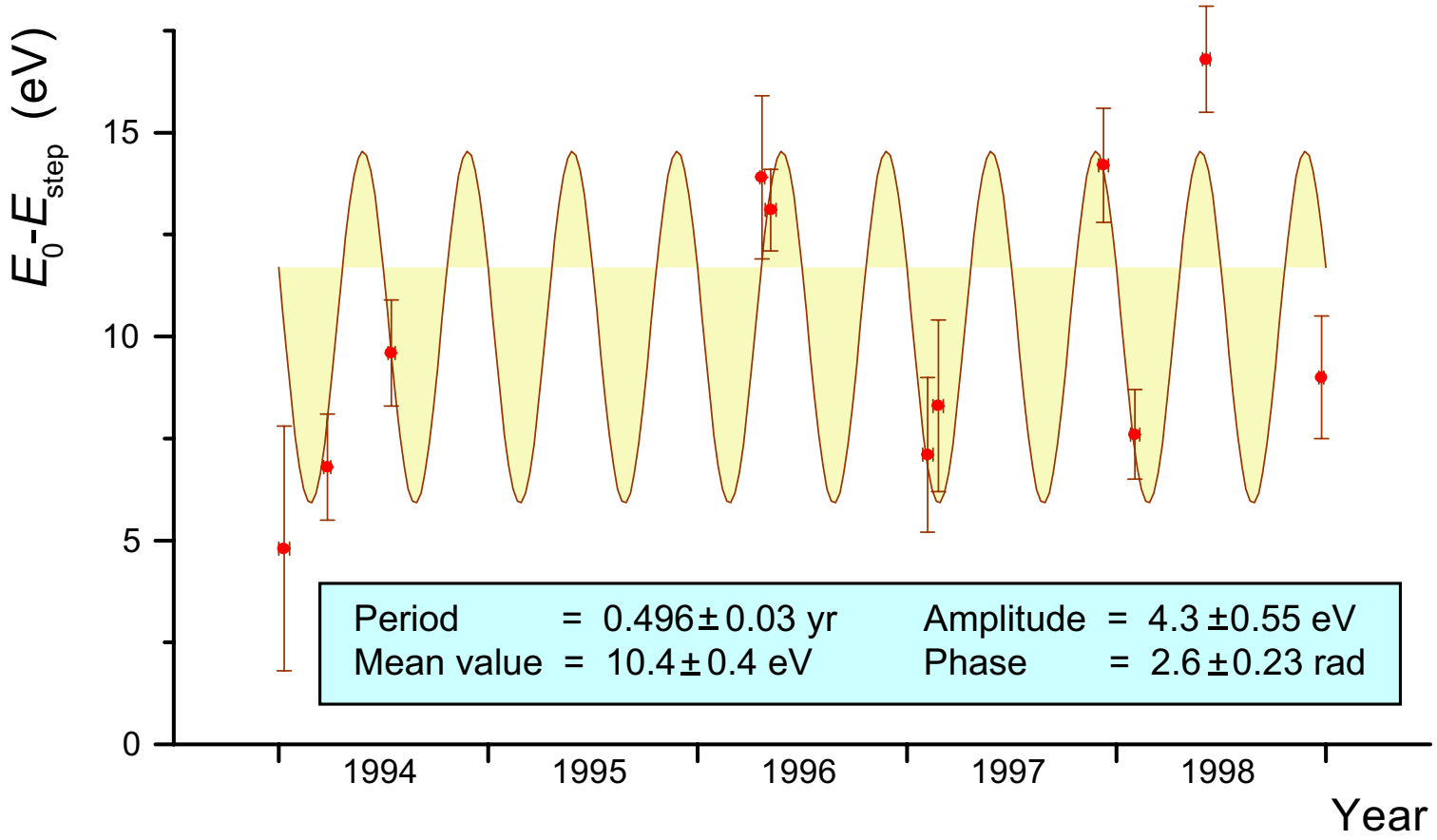

The change in time of the positions of these steps seemed to be compatible with a half year period. The phenomenology and origin of the anomaly are barely known. The authors state that "it seems to be impossible to propose any *customary* explanation of this phenomenon".

The proximity of the oscillation period of the step (bump) to *half period* of Earth circulation around the Sun allows one to remind an old speculation about an effect produced by *capture of the cosmological degenerated neutrino by Tritium atoms with emission of almost monochromatic electrons.*[a]

In order to produce the bump intensity, corresponding to 10^{-10} of total decay rate a neutrino cloud should be supposed to exist with a density as high as $0.5 \times 10^{15}\ \nu/\text{cm}^3$ that is 10^{13} times more than generally accepted average density of relic massless neutrino.

Observation of bump below the end point of β spectrum corresponds to capture of neutrino with a *negative* energy, that means assumption of binding of neutrino in the cloud. If the binding energy changes over the cloud, the Earth in its movement produces the periodical modulation of binding energy and correspondingly position of the step.

[a] G. J. Stephenson Jr. *et al.*, "Neutrino clouds," Int. J. Mod. Phys. A **13** (1998) 2765–2790, hep-ph/9603392.

Synopsis:

Stephenson *et al.* considered the possibility of a very weak coupling of neutrino to an extremely light scalar boson ϕ:

$$\mathcal{L} = \overline{\psi}\left(i\hat{\partial} - m_\nu\right)\psi + \frac{1}{2}\phi\left(\partial^2 - m_s^2\right)\phi + g\overline{\psi}\psi\phi.$$

The effective neutrino mass m_ν^* is then determined from the integral equation

$$m_\nu^* = m_\nu^0 - \frac{g^2\zeta}{2\pi^2 m_s^2}\int_0^{k_F}\frac{k^2 dk}{\sqrt{1+(k/m_\nu^*)^2}},$$

where m_ν^0 is the renormalized vacuum mass, $\zeta = 4(2)$ for Dirac (Majorana) neutrinos, k_F is the Fermi momentum.

The authors showed that for a wide range of parameters, neutrinos will tend to condense into clouds, with dimension R_{cloud} the scale of $1/m_s$. In particular,

$$R_{\text{cloud}} \sim 1\ \text{AU} \iff m_s \sim 10^{-18}\ \text{eV}.$$

The mass of such a cloud is ~ 1 ton.

An extension to more generations shows that the general conclusion remains viable.

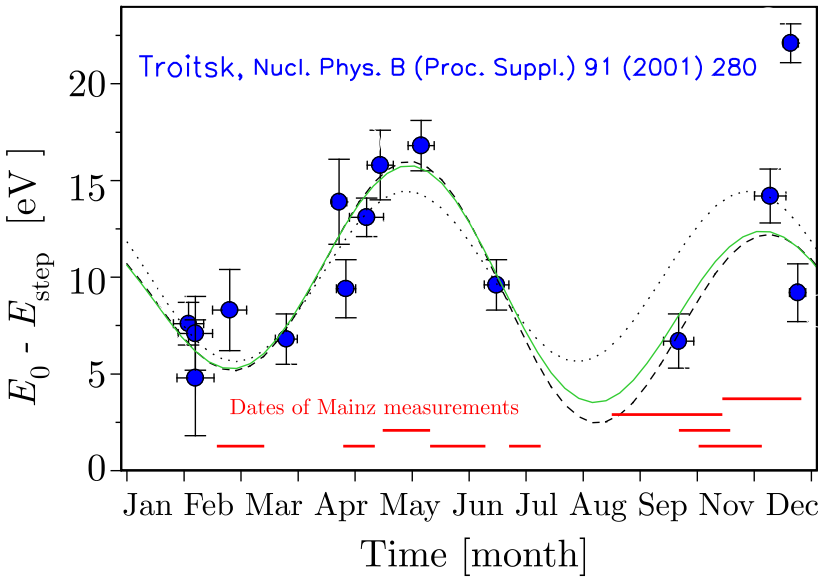

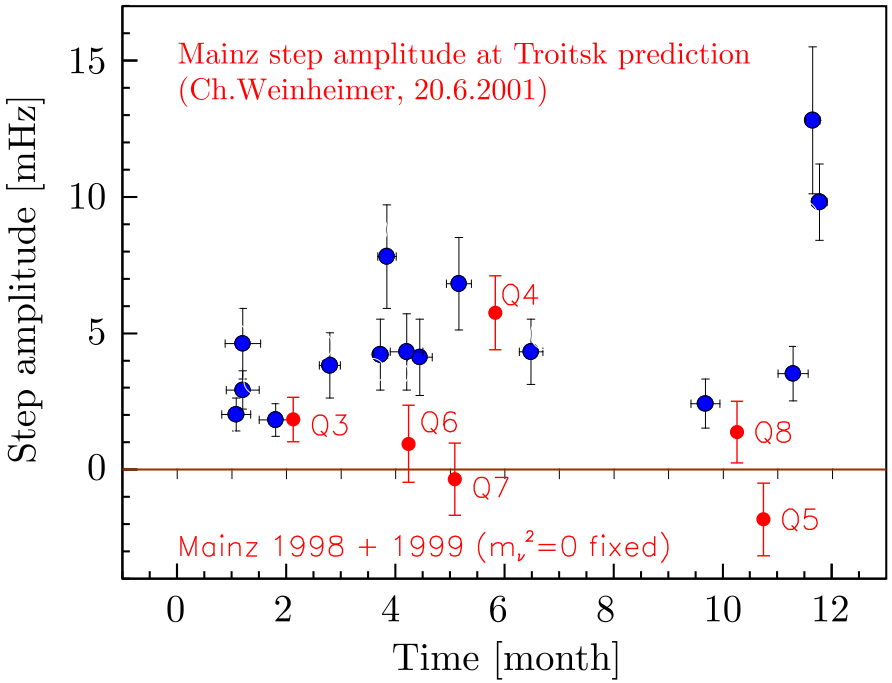

"Troitsk Anomaly" in Mainz data?

- Clear support for the "Troitsk anomaly" is only from one (Q4) out of 6 data sets. Is there something different for measurement Q4?
- But parameter space, favored by Troitsk, not fully excluded.
- Clear contradiction to 0.5 year periodicity.

A conclusion from the Mainz-2005 paper:

> *Speculations that the Troitsk anomaly might be due to a fluctuating presence of dense neutrino clouds are disproved. Rather it has to be attributed to instrumental effects...*

The Mainz experiment does not confirm the Troitsk anomaly being however in excellent agreement with the Troitsk result on m_β.

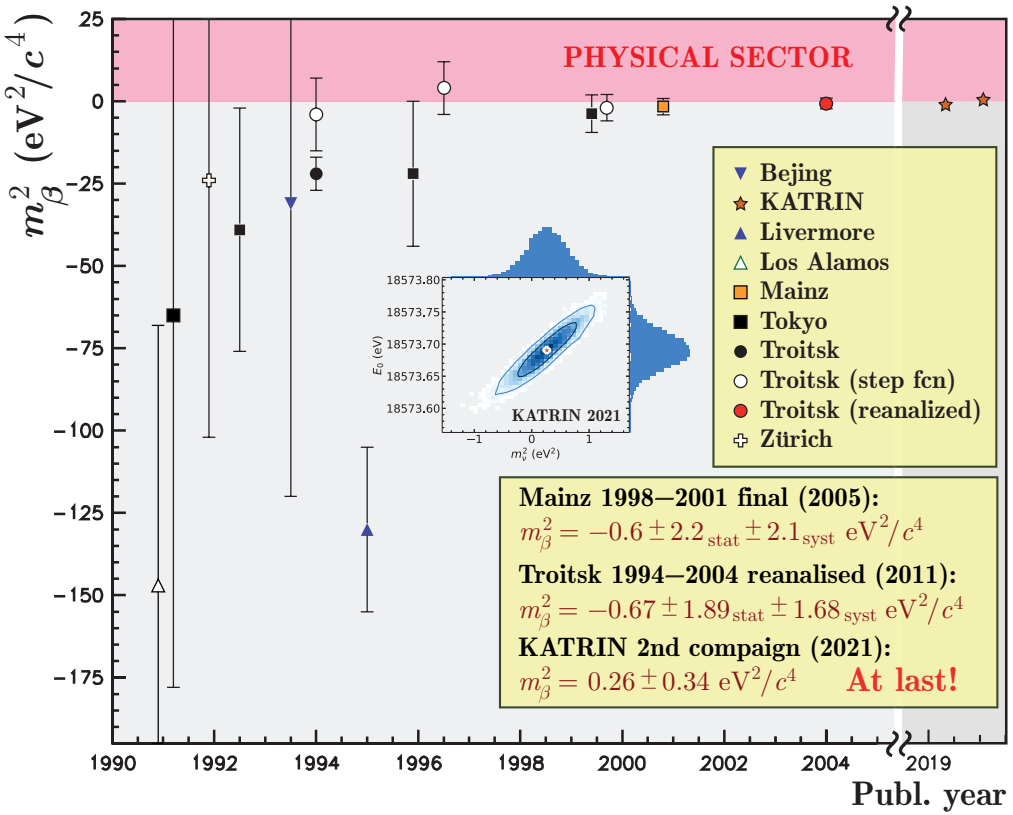

◁ The figure shows the results on the m_β^2 measurements in the Tritium β decay experiments reported after 1990.

The already finished experiments at Los Alamos, Zürich, Tokyo, Beijing and Livermore used magnetic spectrometers, while the experiments at Troitsk (ν mass), Mainz, and Karlsruhe (KATRIN) are using high-resolution electrostatic filters with magnetic adiabatic collimation.

Advancement in the observable m_β of the latest Mainz, Troitsk, and Karlsruhe results as compared to the most sensitive earlier experiments using momentum analyzing spectrometers approaches two orders of magnitude. Further progress is expected exclusively from KATRIN.

[The figure in this slide includes the data from C. Kraus *et al.*, Eur. Phys. J. C **40** (2005) 447–468, hep-ex/0412056; V. N. Aseev *et al.*, Phys. Rev. D **84** (2011) 112003, arXiv:1108.5034 [hep-ex]; M. Aker *et al.*, Phys. Rev. Lett. **123** (2019) 221802, arXiv:1909.06048 [hep-ex] M. Aker *et al.*, Nature Phys. **18** (2022) 160–166, arXiv:2105.08533 [hep-ex].]

The negative m_β^2 most probably *was* "instrumental". After KATRIN (2021), only a very small space remains for fans of heterodox models with *tachyonic* neutrino states (more generally – superpositions of *bradyon-luxon-tachyon* states), *pseudotachyonic* ($m_\nu^2 < 0$, $v = E/p$), or perhaps *superbradyonic* ($m_\nu > 0$, $v > 1$) neutrinos.

12.3.3 Summary of the Troitsk ν-mass result.

The experimental estimate for the effective neutrino mass square is[a]

$$m_\beta^2 = -0.67 \pm 2.53 \text{ eV}^2.$$

Since the final m_β^2 value is slightly negative one can derive an upper physical bound for the neutrino mass. There is no single universal way to do this, at least the Particle Data Group does not provide a recommendation. It seems that for a value which is out of the physical region the most correct way would be to calculate the so called sensitivity limit (SL). It uses errors information but not the estimate itself, i.e., it is not sensitive to how negative the estimate is.

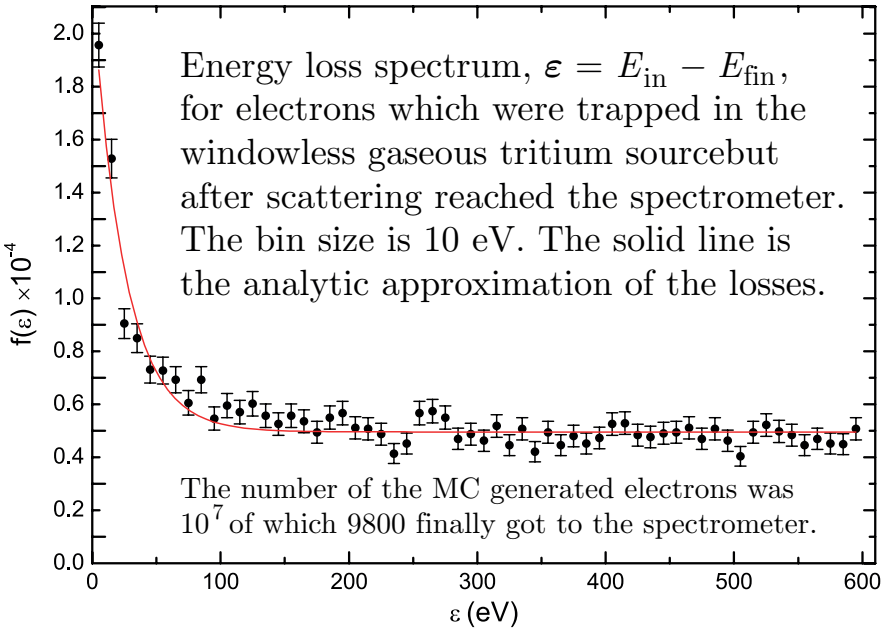

The SL is calculated as $m_\beta^2 < 2.53 \times 1.96 = 4.96$ eV^2, where 1.96 is the standard multiplier for the 95% C.L. For the SL of the effective neutrino mass it gives $m_\beta < 2.2$ eV. The Mainz group got a similar value $m_\beta < 2.4$ eV. The Bayesian and Feldman and Cousins methods provide the upper limits:

$m_\beta < 2.12$ eV at 95% C.L. (Bayesian), $m_\beta < 2.05$ eV at 95% C.L. (Feldman & Cousins).

... And no comments as to the anomaly...

[a] V. N. Aseev *et al.*, "An upper limit on electron antineutrino mass from Troitsk experiment," Phys. Rev. D **84** (2011) 112003, arXiv:1108.5034 [hep-ex].

12.3.4 Summary of the KATRIN result from the first science run (KNM1).

The best fit value of the effective neutrino mass square was found to be[a]

$$m_\beta^2 = \left(-1.0^{+0.9}_{-1.1}\right)\ \text{eV}^2.$$

This result corresponds to a 1σ statistical fluctuation to negative values of m_β^2 possessing a p-value of 0.16. The total uncertainty budget of m_β^2 is largely dominated by $\sigma\,(\text{stat})$ (0.97 eV^2) as compared to σ_{syst} (0.32 eV^2). These uncertainties are smaller by a factor of 2 and 6, respectively, compared to the final results of Troitsk and Mainz.

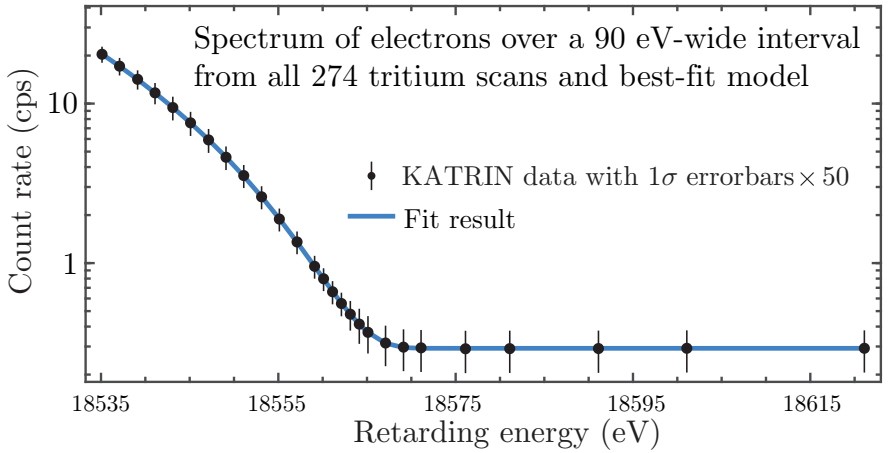

The methods of Lokhov and Tkachov (LT) and of Feldman and Cousins (FC) are then used to calculate the upper limit on the absolute mass scale of neutrino:

$$m_\beta < 1.1 \text{ eV at } 90\% \text{ C.L. (LT)}, \quad m_\beta < 0.8\ (0.9) \text{ eV at } 90\ (95)\% \text{ C.L. (FC)}.$$

The LT value (the central result of the experiment) coincides with the KATRIN sensitivity. It is based on a purely kinematic method and improves upon previous works by almost a factor of two after a measuring period of only four weeks while operating at reduced column density. After 1000 days of data taking (end of 2025) at nominal column density and further reductions of systematics the Karlsruhe Tritium Neutrino experiment KATRIN will reach a sensitivity of $0.2 - 0.3$ eV (90% C.L.).

[a] M. Aker *et al.*, "An improved upper limit on the neutrino mass from a direct kinematic method by KATRIN," Phys. Rev. Lett. **123** (2019) 221802, arXiv:1909.06048 [hep-ex].

The KATRIN spectrometer at Eggenstein-Leopoldshafen tawn, Germany, on its way to the laboratory in Karlsruhe (photo 2006).

The KATRIN experiment.

12.3.5 Summary of the KATRIN result from the second science run (KNM2).

In the 2nd physics run, the source activity was increased by a factor of 3.8 and the background was reduced by 25 % with respect to the 1st campaign.[a] A sensitivity on m_β of 0.7 eV at 90 % C.L. was reached. This is the first sub-eV sensitivity from a direct neutrino-mass experiment.

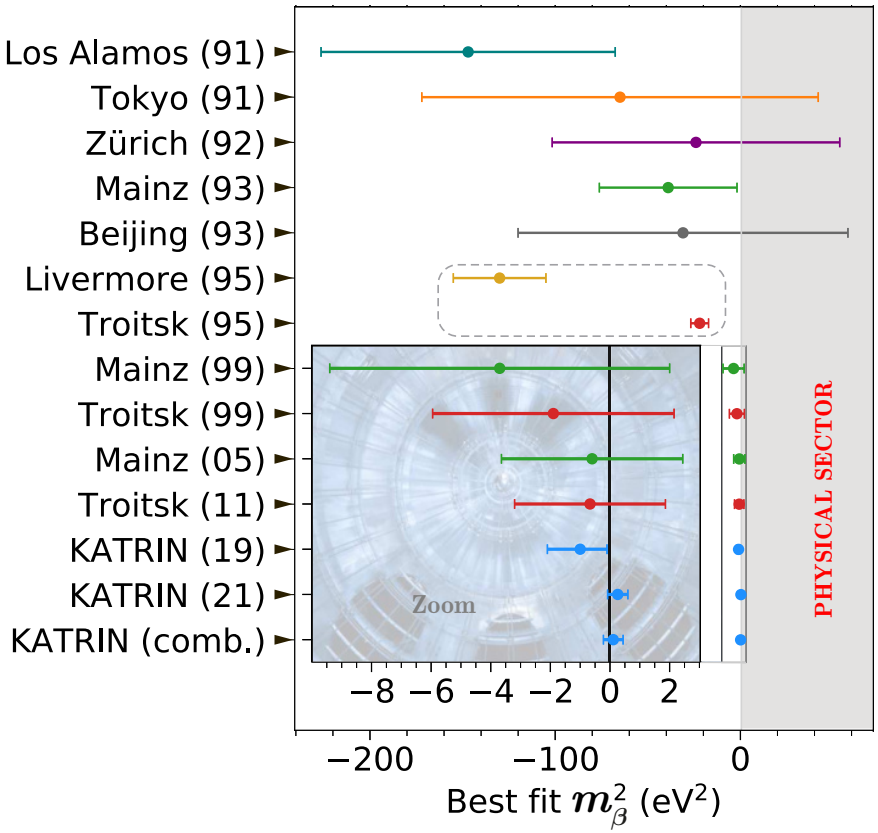

The best fit to the spectral data yields $m_\beta = 0.26 \pm 0.34$ eV, resulting in an upper limit of $m_\beta < 0.9$ eV (90 % C.L.), using the Lokhov-Tkachov method. The Feldman-Cousins technique yields the same limit. The resulting Bayesian limit at 90 % C.L. is $m_\beta < 0.85$ eV.

A simultaneous fit of both KNM1 and KNM2 data sets yields $m_\beta = 0.1 \pm 0.3$ eV, resulting an improved limit of $m_\beta < 0.8$ eV (90 % C.L.).

As both data sets are statistics-dominated, correlated systematic uncertainties between both campaigns are negligible.

◁ The figure displays the evolution of best-fit m_β results from historical ν-mass measurements (c.f. p. 456, see also p. 461).

$m_\beta < 0.9$ eV at 90 % C.L. (KNM2), $m_\beta < 0.8$ eV at 90 % C.L. (KNM1+KNM2).

[a] M. Aker *et al.*, "First direct neutrino-mass measurement with sub-eV sensitivity," Nature Phys. **18** (2022) 160–166, arXiv:2105.08533 [hep-ex]; see also J. Phys. G **49** (2022) 1100501, arXiv:2203.08059 [nucl-ex].

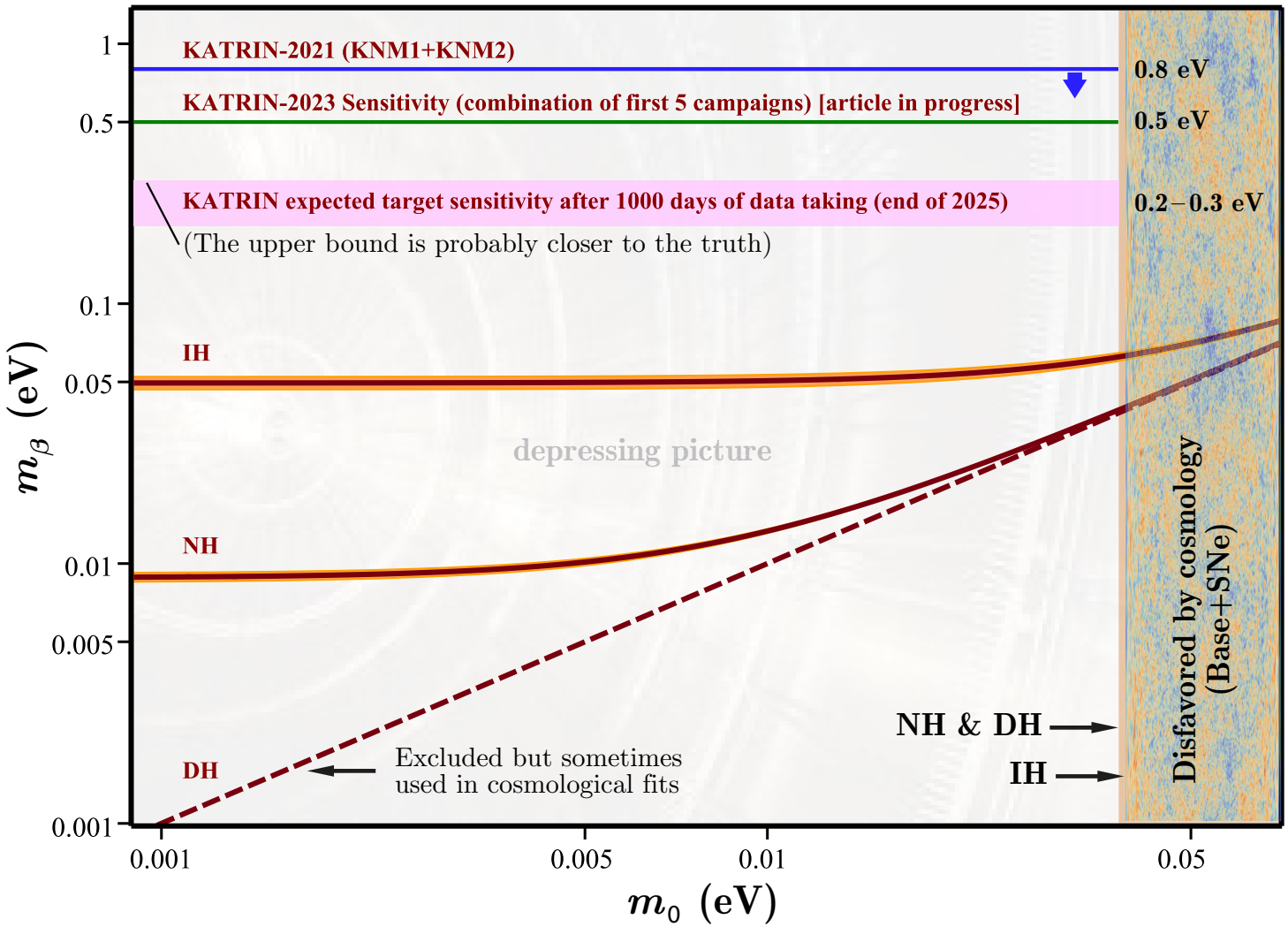

Comparison of the m_β upper limits after KATRIN with the m_β values evaluated using the NuFIT 5.2 results (as functions of the lightest neutrino mass, m_0) in the three scenarios. The bands around NH and IH curves are due to uncertainties in the neutrino mixing parameters and mass-squared splittings. Also shown are cosmological upper bounds for m_0 from *Planck* 2018 ("Base+SNe", see p. 149).

13 Majorana neutrinos.

The charge conjugated bispinor field ψ^c is defined by the transformation

$$\psi \longmapsto \psi^c = C\overline{\psi}^T, \quad \overline{\psi} \longmapsto \overline{\psi^c} = -\psi^T C,$$

where C is the charge-conjugation matrix which satisfies the conditions

$$C\gamma_\alpha^T C^\dagger = -\gamma_\alpha, \quad C\gamma_5^T C^\dagger = \gamma_5, \quad C^\dagger = C^{-1} = C, \quad C^T = -C,$$

and thus coincides (up to a phase factor) with the inversion of the axes x_0 and x_2: $C = \gamma_0\gamma_2$.

Clearly the charged fermion field ψ is different from the charge-conjugated field ψ^c but a neutral fermion field ν can coincide with the charge-conjugated one ν^c. In other words: for a neutral fermion (neutrino, neutralino) field $\nu(x)$ the following condition is not forbidden: [a]

$$\nu^c(x) = \nu(x) \quad \text{(Majorana condition)} \quad \Longleftrightarrow \quad \text{Majorana neutrino and antineutrino coincide!}$$

A few more details: In the chiral representation

$$\nu = \begin{pmatrix} \phi \\ \chi \end{pmatrix}, \quad \nu^c = C\overline{\nu}^T = \begin{pmatrix} -\sigma_2\chi^* \\ +\sigma_2\phi^* \end{pmatrix}. \quad \Longrightarrow \quad \begin{cases} \phi = -\sigma_2\chi^*, \\ \chi = +\sigma_2\phi^* \end{cases} \quad \Longrightarrow \quad \phi + \chi = \sigma_2\,(\phi - \chi)^*.$$

The Majorana neutrino is two-component, i.e., it is defined by only one chiral projection. Then (c.f. p. 418)

$$\nu_L = P_L\nu = \begin{pmatrix} \phi - \chi \\ \chi - \phi \end{pmatrix} \quad \text{and} \quad \nu_R = P_R\nu = \begin{pmatrix} \phi + \chi \\ \phi + \chi \end{pmatrix} = \nu_L^c. \quad \Longrightarrow \quad \boxed{\nu = \nu_L + \nu_R = \nu_L + \nu_L^c.}$$

[a] The simplest generalization of the Majorana condition, $\nu^c(x) = e^{i\varphi}\nu(x)$ ($\varphi = \text{const}$), is not very interesting.

The Majorana mass term in the general N-neutrino case is [Gribov & Pontecorvo (1969)]:

$$\mathcal{L}_{\mathsf{M}}(x) = -\frac{1}{2}\overline{\boldsymbol{\nu}}^{c}_{L}(x)\mathbf{M}_{\mathsf{M}}\boldsymbol{\nu}_{L}(x) + \text{H.c.},$$

Here $\mathbf{M}_{\mathsf{M}}$ is a $N \times N$ complex *nondiagonal* matrix and, in general, $N \geq 3$.

It can be proved that the $\mathbf{M}_{\mathsf{M}}$ should be symmetric, $\mathbf{M}^{T}_{\mathsf{M}} = \mathbf{M}_{\mathsf{M}}$. Assuming for simplicity that its spectrum is non-degenerated, the mass matrix can be diagonalized by means of the following transformation [Bilenky & Petcov (1987)]

$$\mathbf{M}_{\mathsf{M}} = \mathbf{V}^{*}\mathbf{m}\mathbf{V}^{\dagger}, \quad \mathbf{m} = ||m_k\delta_{kl}|| = \text{diag}\,(m_1, m_2, \ldots, m_N),$$

where $\mathbf{V}$ is a unitary matrix and $m_k \geq 0$. Therefore

$$\mathcal{L}_{\mathsf{M}}(x) = -\frac{1}{2}\left[(\overline{\boldsymbol{\nu}'}_{L})^{c}\mathbf{m}\boldsymbol{\nu}'_{L} + \overline{\boldsymbol{\nu}'}_{L}\mathbf{m}(\boldsymbol{\nu}'_{L})^{c}\right] = -\frac{1}{2}\,\overline{\boldsymbol{\nu}'}\mathbf{m}\boldsymbol{\nu}' = -\frac{1}{2}\sum_{k=1}^{N} m_k\overline{\nu}_k\nu_k,$$

$$\boldsymbol{\nu}'_{L} = \mathbf{V}^{\dagger}\boldsymbol{\nu}_{L}, \quad (\boldsymbol{\nu}'_{L})^{c} = C\left(\overline{\boldsymbol{\nu}'_{L}}\right)^{T}, \quad \boldsymbol{\nu}' = \boldsymbol{\nu}'_{L} + (\boldsymbol{\nu}'_{L})^{c}.$$

The last equality means that the fields $\nu_k(x)$ are Majorana neutrino fields. Considering that the kinetic term in the neutrino Lagrangian is transformed to[a]

$$\mathcal{L}_0 = \frac{i}{2}\,\overline{\boldsymbol{\nu}'}(x)\overleftrightarrow{\boldsymbol{\partial}}\boldsymbol{\nu}'(x) = \frac{i}{2}\sum_{k}\overline{\nu}_k(x)\overleftrightarrow{\partial}\nu_k(x),$$

one can conclude that $\nu_k(x)$ is the field with the definite mass m_k.

[a] This also explains the origin of the factor $1/2$ in the Majorana mass term.

The flavor LH neutrino fields $\nu_{\ell,L}(x)$ present in the standard weak lepton currents are linear combinations of the LH components of the fields of neutrinos with definite masses:

$$\boldsymbol{\nu}_L = \mathbf{V}\boldsymbol{\nu}'_L \quad \text{or} \quad \nu_{\ell,L} = \sum_k V_{\ell k}\nu_{k,L}.$$

Of course neutrino mixing matrix $\mathbf{V}$ is not the same as in the case of Dirac neutrinos.

There is no global gauge transformations under which the Majorana mass term (in its most general form) could be invariant. This implies that there are no conserved lepton charges that could allow us to distinguish Majorana νs and $\overline{\nu}$s. In other words,

Majorana neutrinos are truly neutral fermions.

13.1 Parametrization of mixing matrix for Majorana neutrinos.

Since the Majorana neutrinos are not rephasable, there may be a lot of extra phase factors in the mixing matrix. The Lagrangian with the Majorana mass term is invariant with respect to the transformation

$$\ell \mapsto e^{ia_\ell}\ell, \quad V_{\ell k} \mapsto e^{-ia_\ell}V_{\ell k}$$

Therefore N phases are unphysical and the number of the physical phases now is

$$\frac{N(N+1)}{2} - N = \frac{N(N-1)}{2} = \underbrace{\frac{(N-1)(N-2)}{2}}_{\text{Dirac phases}} + \underbrace{(N-1)}_{\text{Majorana phases}} = n_{\mathsf{D}} + n_{\mathsf{M}};$$

$$n_{\mathsf{M}}(2) = 1, \quad n_{\mathsf{M}}(3) = 2, \quad n_{\mathsf{M}}(4) = 3, \ldots$$

| In fact all phases are Majorana and the above notation is provisional and unorthodox.

In the case of three lepton generations one defines the diagonal matrix with the extra phase factors: $\mathbf{\Gamma}_{\mathsf{M}} = \mathrm{diag}\left(e^{i\alpha_1/2}, e^{i\alpha_2/2}, 1\right)$, where $\alpha_{1,2}$ are commonly referred to as the Majorana CP-violation phases. Then the PMNS matrix can be parametrized as

$$\mathbf{V}_{(\mathsf{M})} = \mathbf{O}_{23}\mathbf{\Gamma}_{\mathsf{D}}\mathbf{O}_{13}\mathbf{\Gamma}_{\mathsf{D}}^{\dagger}\mathbf{O}_{12}\mathbf{\Gamma}_{\mathsf{M}} = \mathbf{V}_{(\mathsf{D})}\mathbf{\Gamma}_{\mathsf{M}}$$

$$= \begin{pmatrix} c_{12}c_{13} & s_{12}c_{13} & s_{13}e^{-i\delta} \\ -s_{12}c_{23} - c_{12}s_{23}s_{13}e^{i\delta} & c_{12}c_{23} - s_{12}s_{23}s_{13}e^{i\delta} & s_{23}c_{13} \\ s_{12}s_{23} - c_{12}c_{23}s_{13}e^{i\delta} & -c_{12}s_{23} - s_{12}c_{23}s_{13}e^{i\delta} & c_{23}c_{13} \end{pmatrix} \begin{pmatrix} e^{i\alpha_1/2} & 0 & 0 \\ 0 & e^{i\alpha_2/2} & 0 \\ 0 & 0 & 1 \end{pmatrix},$$

Neither L_ℓ nor $L = \sum_\ell L_\ell$ is now conserved allowing a lot of new processes, for example, $\tau^- \to e^+(\mu^+)\pi^-\pi^-$, $\tau^- \to e^+(\mu^+)\pi^- K^-$, $\pi^- \to \mu^+\overline{\nu}_e$, $K^+ \to \pi^-\mu^+e^+$, $K^+ \to \pi^0 e^+\overline{\nu}_e$, $D^+ \to K^-\mu^+\mu^+$, $B^+ \to K^- e^+\mu^+$, $\Xi^- \to p\mu^-\mu^-$, $\Lambda_c^+ \to \Sigma^-\mu^+\mu^+$, etc.

Needless to say that no one was discovered yet [see RPP] but (may be!?) the $(\beta\beta)_{0\nu}$ decay. The following section will discuss this issue with some detail.

13.2 Neutrinoless double beta decay.

The theory with Majorana neutrinos allows the decay[a]

$$(A, Z) \to (A, Z+2) + 2e^- \quad [0\nu\beta\beta \equiv (\beta\beta)_{0\nu}]$$

with $\Delta L = 2$. The decay rate for this process is expressed as follows:

$$\left[T^{0\nu}_{1/2}\right]^{-1} = G^{0\nu}_Z \left|m_{\beta\beta}\right|^2 \left|\mathcal{M}^{0\nu}_{\mathsf{F}} - (g_A/g_V)^2 \mathcal{M}^{0\nu}_{\mathsf{GT}}\right|^2,$$

where $G^{0\nu}_Z$ is the two-body phase-space factor including coupling constant, $\mathcal{M}^{0\nu}_{\mathsf{F/GT}}$ are the Fermi/Gamow–Teller nuclear matrix elements. The constants g_V and g_A are the vector and axial-vector relative weak coupling constants, respectively. The complex parameter $m_{\beta\beta}$ is the *effective Majorana electron neutrino mass* given by

$$\begin{aligned} m_{\beta\beta} &= \sum_k V^2_{ek} m_k = \sum_k |V_{ek}|^2 e^{i\phi_k} m_k \\ &= |V_{e1}|^2 m_1 + |V_{e2}|^2 m_2 e^{i\phi_2} + |V_{e3}|^2 m_3 e^{i\phi_3}. \end{aligned}$$

Here $\phi_1 = 0$, $\phi_2 = \alpha_2 - \alpha_1$ (pure Majorana phase) and $\phi_3 = -(\alpha_2 + 2\delta)$ (mixture of Dirac and Majorana CP-violation phases). It is easy to see that $|m_{\beta\beta}| \le m_\beta$ **[prove]**.

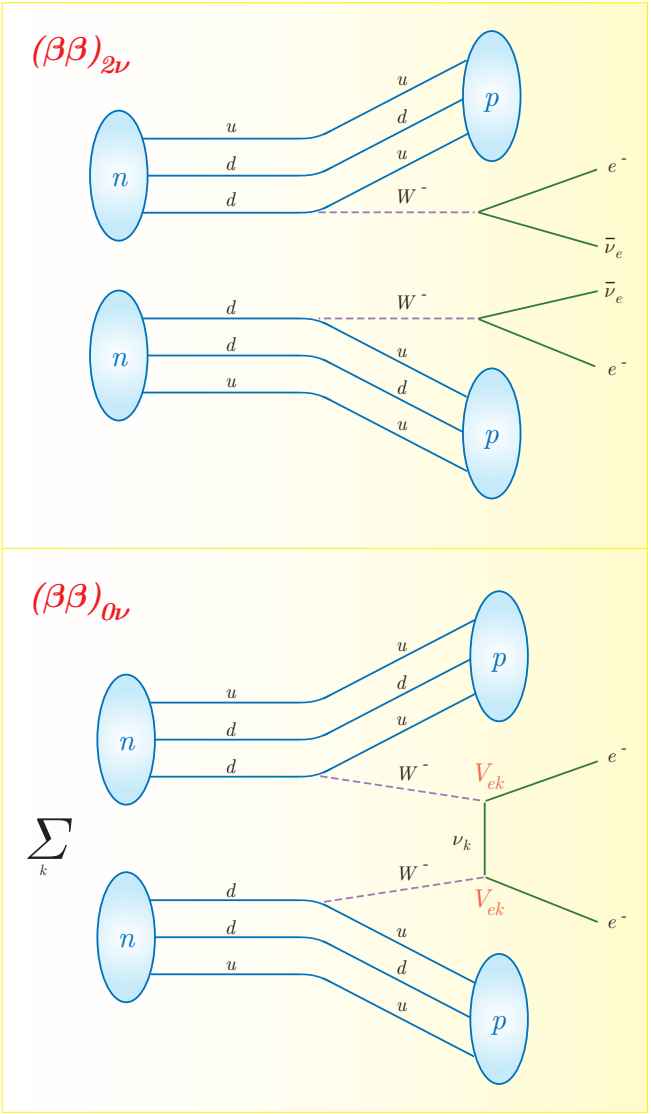

[a] The decays $2\nu\beta\beta$ and $0\nu\beta\beta$ were predicted by M. Göppert-Mayer (1935) and G. Raka (1937), respectively. Of course, they both knew nothing about quarks and W-bosons, much less about neutrino masses and mixing.

The electron sum energy spectrum of the $(\beta\beta)_{2\nu}$ mode as well as of the exotic modes with one or two majorons in final state,

$$(A, Z) \to (A, Z+2) + 2e^- + \chi,$$
$$(A, Z) \to (A, Z+2) + 2e^- + 2\chi,$$

is *continuous* because the available energy release ($Q_{\beta\beta}$) is shared between the electrons and other final state particles. In contrast, the two electrons from the $(\beta\beta)_{0\nu}$ decay carry the full available energy, and hence the electron sum energy spectrum has a sharp peak at the $Q_{\beta\beta}$ value. This feature allows one to distinguish the $(\beta\beta)_{0\nu}$ decay signal from the background.

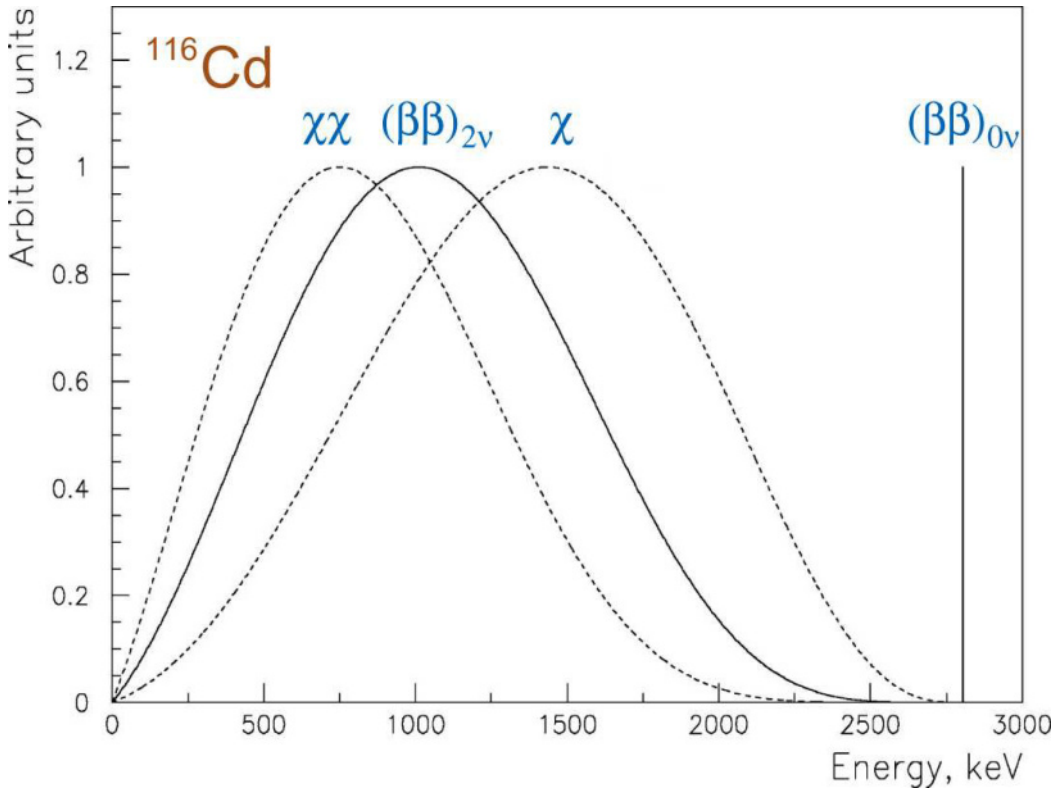

The electron sum energy spectra calculated for the different β decay modes of cadmium-116.

[From Y. Zdesenko, "Colloquium: The future of double beta decay research," Rev. Mod. Phys. **74** (2003) 663–684.]

Majoron is a Nambu-Goldstone boson, – a hypothetical neutral pseudoscalar zero-mass particle which couples to Majorana neutrinos and may be emitted in the neutrinoless β decay. It is a consequence of the spontaneous breaking of the global $B - L$ symmetry.

Best current results on $0\nu\beta\beta$ decay. The $T^{0\nu}_{1/2}$ and $\langle m_{\beta\beta}\rangle (\equiv \langle |m_{\beta\beta}| \rangle)$ limits are at 90% C.L.

Element	Isotope	$Q_{2\beta}$ (keV)	$T^{0\nu}_{1/2}$ (years)	$\langle m_{\beta\beta}\rangle$ (meV)	Experiment	Publ. year	
Calcium	^{48}Ca	4267.98	$> 2.0\times10^{22}$	$< 6000-26000$	NEMO-3	2016	⊗
			$> 5.8\times10^{22}$	$< 3500-22000$	ELEGANT-VI	2008	⊗
			$> 5.6\times10^{22}$	$< 2900-16000$	CANDLES-III	2021	
Germanium	^{76}Ge	2039.00	$> 8.3\times10^{25}$	$< 113-269$	Majorana Dem.	2023	⊗
			$> 1.8\times10^{26}$	$< 79-80$	GERDA	2020	⊗
Selenium	^{82}Se	2997.9	$> 2.5\times10^{23}$	$< 1200-1300$	NEMO-3	2018	⊗
			$> 4.6\times10^{24}$	$< 263-545$	CUPID-0	2022	⊗
Zirconium	^{96}Zr	3355.85	$> 9.2\times10^{21}$	$< 7200-19500$	NEMO-3	2010	⊗
Molybdenum	^{100}Mo	3034.40	$> 1.1\times10^{24}$	$< 330-620$	NEMO-3	2017	⊗
			$> 1.8\times10^{24}$	$< 280-490$	CUPID-Mo	2022	⊗
Cadmium	^{116}Cd	2813.50	$> 1.0\times10^{23}$	$< 1400-2500$	NEMO-3	2017	⊗
			$> 2.2\times10^{23}$	$< 1000-1700$	Aurora	2018	⊗
Tellurium	^{128}Te	866.7	$> 3.6\times10^{24}$	not evaluated	CUORE	2022	
	^{130}Te	2527.52	$> 2.8\times10^{24}$	$< 300-700$	CUORICINO	2012	⊗
			$> 2.2\times10^{25}$	$< 90-305$	CUORE	2022	
Xenon	^{136}Xe	2457.83	$> 3.5\times10^{25}$	$< 93-286$	EXO-200	2019	⊗
			$\mathbf{> 2.3\times10^{26}}$	$\mathbf{< 36-156}$	KamLAND-Zen	2023	
Neodymium	^{150}Nd	3371.38	$> 2.0\times10^{22}$	$< 1600-5300$ (?)	NEMO-3	2016	⊗

The data presented in the above table are taken from from Refs. [17–34] listed at p. 992.[a]

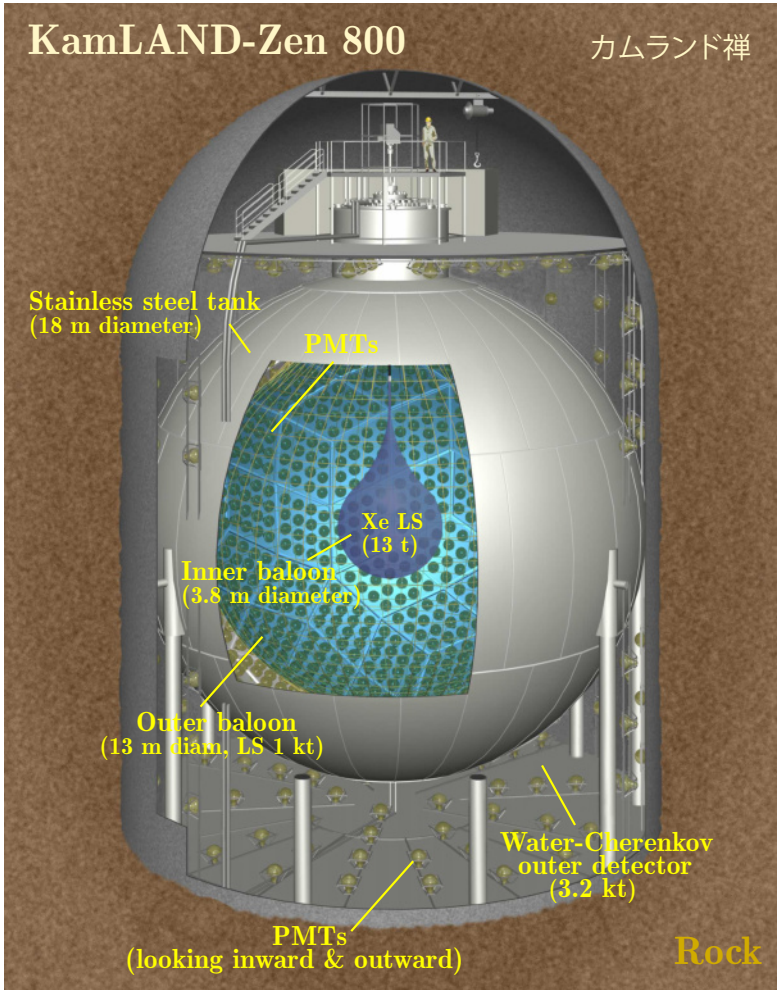

The KamLAND-Zen 800 experiment has provided stringent constraints on the $0\nu\beta\beta$ decay half-life in ^{136}Xe using a Xenon-loaded liquid scintillator [34].

The collaboration reported an improved search using an upgraded detector with almost double the amount of ^{136}Xe and an ultralow radioactivity container. Data collected between February 5, 2019, and May 8, 2021 was used with exposure of 970 kg·yr. These new data provide valuable insight into backgrounds, especially from cosmic muon spallation of Xenon, and have required the use of novel background rejection techniques. Upper limits on the effective Majorana neutrino mass turned out to be $36 - 156$ meV using commonly adopted nuclear matrix element calculations.

Note: KamLAND-Zen = **Kam**ioka **L**iquid-scintillator **A**nti**N**eutrino **D**etector (for) **Ze**ro **n**eutrino double β decay. Additionally, 'Xenon' is pronounced 'Zenon' in Japanese. There are other more subtle connotations for 'Zen'...

[a] For more information, see recent in-depth reviews: M. J. Dolinski, A. W. P. Poon, & W. Rodejohann, "Neutrinoless double-beta decay: Status and prospects," Ann. Rev. Nucl. Part. Sci. **69** (2019) 219–251, arXiv:1902.04097 [nucl-ex]; M. Agostini *et al.*, "Toward the discovery of matter creation with neutrinoless double-beta decay," Rev. Mod. Phys. **95** (2023) 025002, arXiv:2202.01787v2 [hep-ex]; A. Barabash, "Double beta decay experiments: Recent achievements and future prospects," Universe **9** (2023) 290:

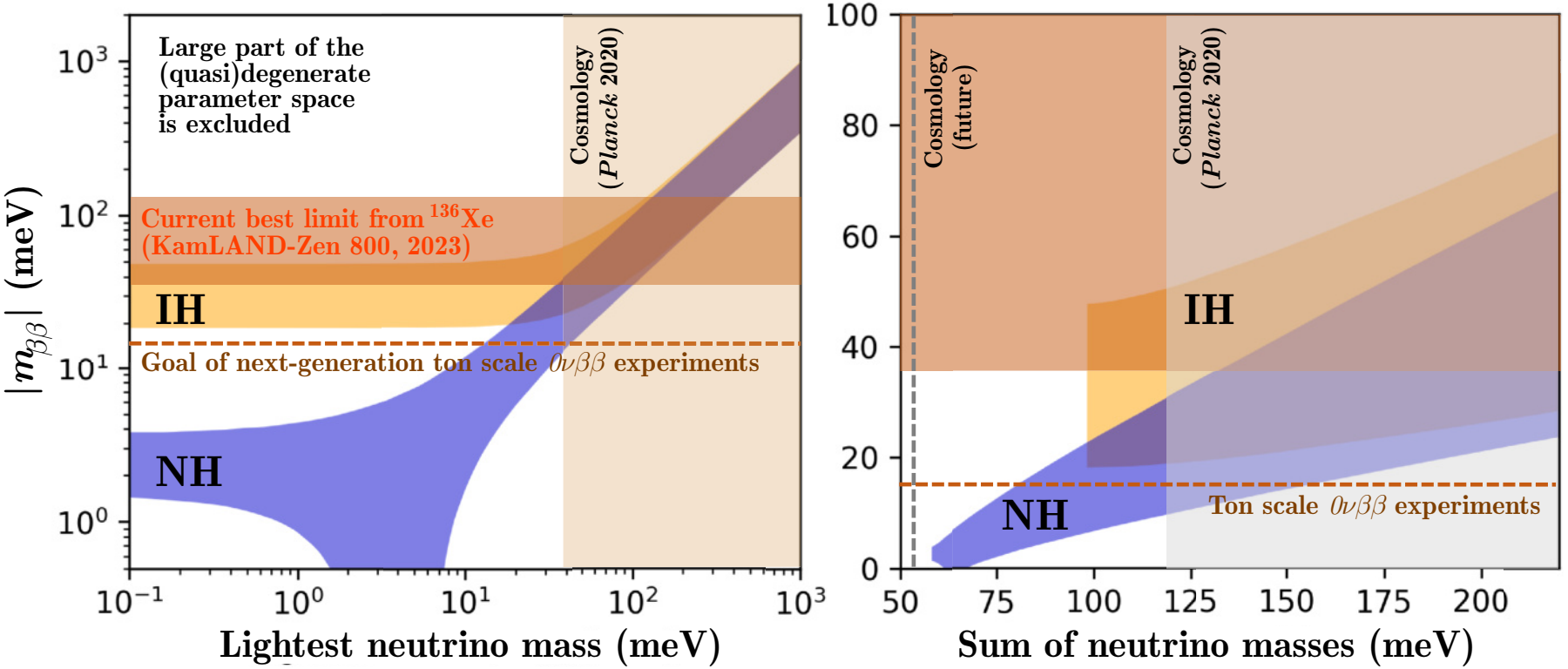

△ The 2023 status for the maximally allowed parameter space for $|m_{\beta\beta}|$ as a function of m_0 and $\sum m_\nu$, assuming the central values of the neutrino oscillation parameters based on the global fit of Zyla *et al.*, (2020) [close but not identical to NuFIT 5.2].[a] Also shown are the recent KamLAND-Zen 800 limit and the expected limit of future "ton-scale" $0\nu\beta\beta$ experiments, as well as current and expected in the near future cosmological constraints. For more details, see Appendix E, pp. 851 and 852. Alas, the data becomes outdated faster than reviews are published...

[Adapted from D. Moore, "Double beta decay review (theory & experiment)," (a review report at XVIII International Conference on Topics in Astoparticle and Underground Physics 'TAUP 2023', University of Vienna, August 29 – September 1, 2023).]

[a] Effect of the uncertainties in the oscillation parameters is not however negligible, see p. 473 below.

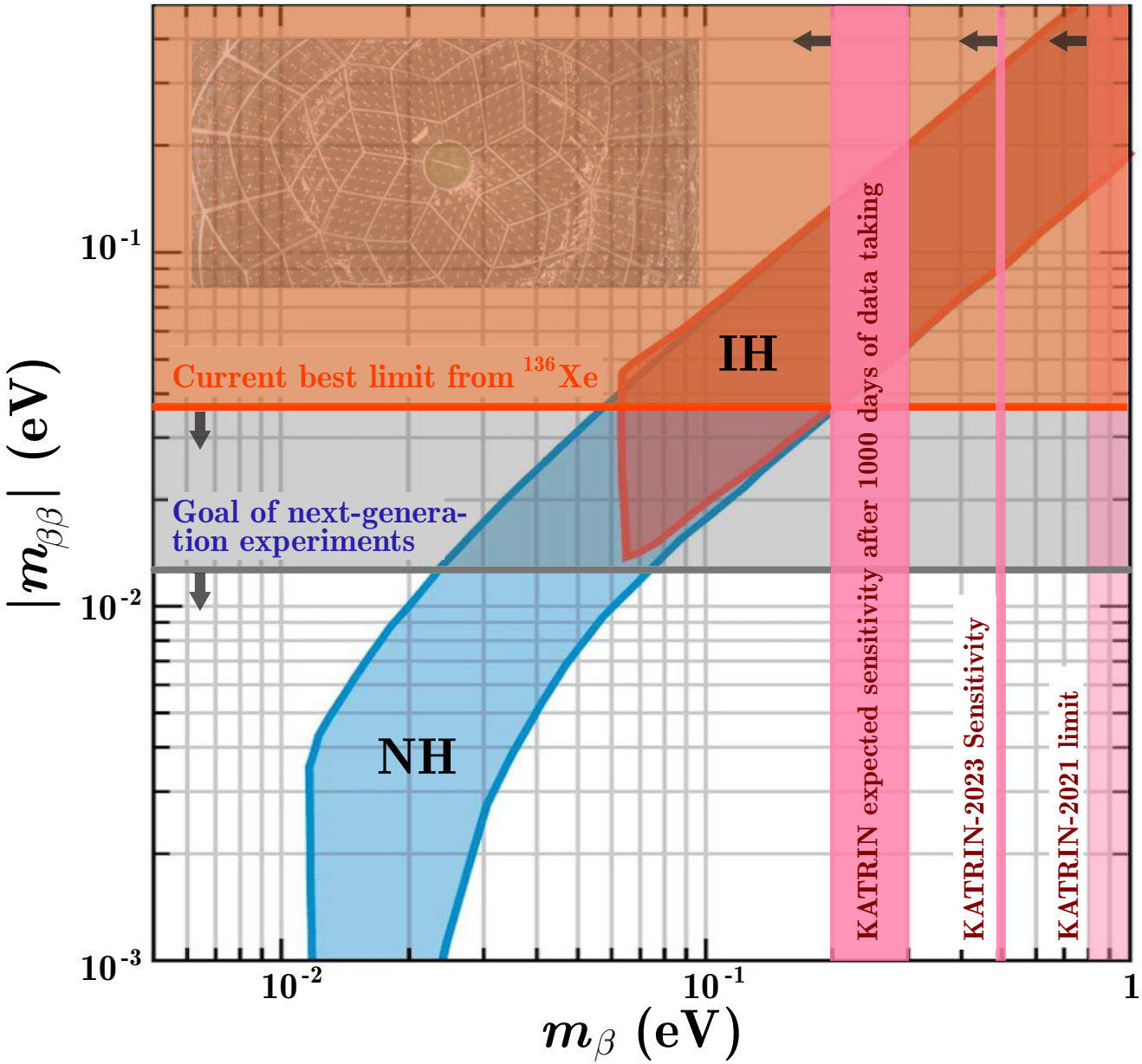

◁ Same as the previous slide, but $|m_{\beta\beta}|$ is displayed as a function of m_β. Also shown are the recent Karlsruhe limits: KATRIN-2021 (see Sect. 12.3.4, p. 458), KATRIN-2023 sensitivity limit (not published yet [December 4, 2023]), and expected sensitivity after 1000 days of data taking (end of 2025).

[Adapted from D. S. Parno, A. W. Poon, & V. Singh, "Experimental neutrino physics in a nuclear landscape," arXiv:2310.06207 [nucl-ex], submitted to Phil. Trans. Roy. Soc. Lond. A.]

How to draw allowed regions for $|m_{\beta\beta}|$ (methodological figure, the data for which are a bit outdated).

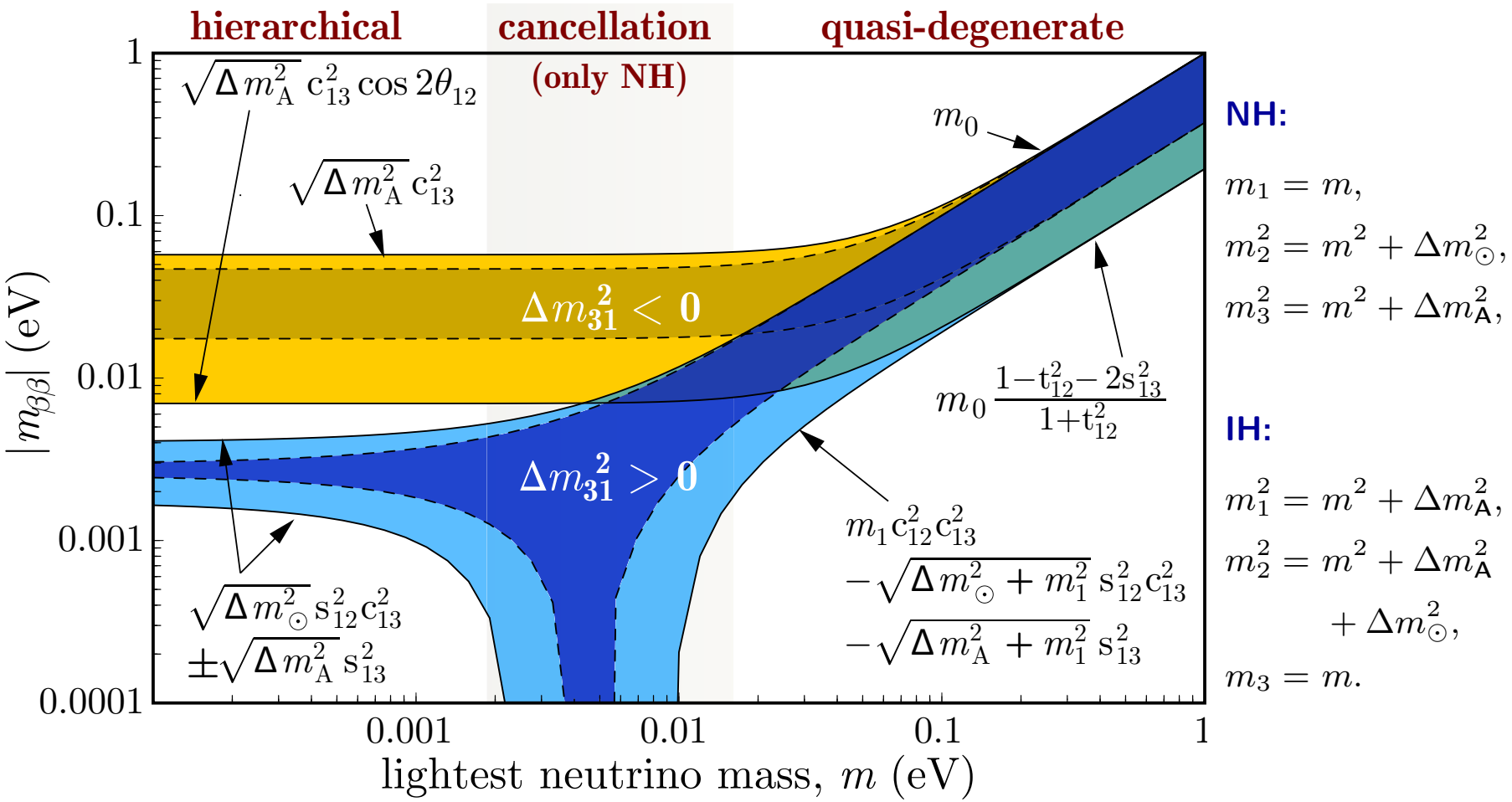

NH:

$$m_1 = m,$$
$$m_2^2 = m^2 + \Delta m^2_{\odot},$$
$$m_3^2 = m^2 + \Delta m^2_{\rm A},$$

IH:

$$m_1^2 = m^2 + \Delta m^2_{\rm A},$$
$$m_2^2 = m^2 + \Delta m^2_{\rm A} + \Delta m^2_{\odot},$$
$$m_3 = m.$$

△ The main properties of $|m_{\beta\beta}|$ vs. smallest neutrino mass (m) The value of $\sin^2 2\theta_{13} = 0.02$ was chosen, m_0 is the common mass scale (measurable in KATRIN or cosmology via $\sum_i m_i/3$) for quasi-degenerate masses $m_1 \simeq m_2 \simeq m_3 \equiv m_0 \gg \sqrt{\Delta m^2_{\rm A}}$ (corrections are small if $m \gtrsim 0.03$ eV).

[Taken from M. Lindner, A. Merle, and W. Rodejohann,"Improved limit on θ_{13} and implications for neutrino masses in neutrinoless double beta decay and cosmology," Phys. Rev. D **73** (2006) 053005, hep-ph/0512143.]

13.2.1 Schechter-Valle (black-box) theorem.

Current particle models (GUTs, R-parity[a] violating SUSY, etc.) provide mechanisms, other than neutrino mass, which can contribute to or even dominate the $0\nu\beta\beta$ process (see example below).

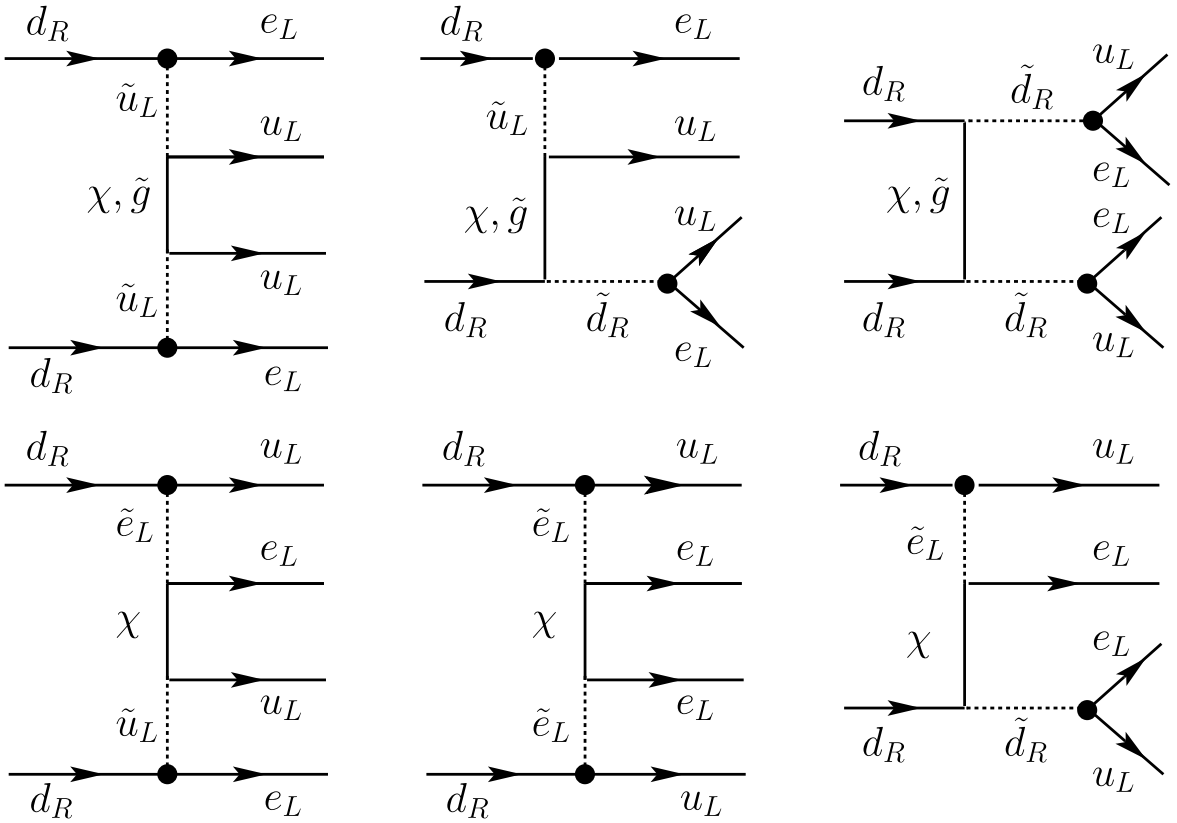

△ R-parity violating contribution to $0\nu\beta\beta$ decay mediated by sfermions and neutralinos (gluinos).
[Figure is borrowed from J. D. Vergados, H. Ejiri, and F. Simkovic, "Theory of neutrinoless double-beta decay," Rep. Prog. Phys. **75** (2012) 106301, arXiv:1205.0649 [hep-ph], where many other examples can be found.]

[a] Recall that $R = (-1)^{3B+L+2s}$, where B is baryon number, L is lepton numbers, and s is spin.

Schechter and Valle proved[a] that

for any realistic gauge theory including the usual (SM) W-gauge-field interaction with left-handed e and ν_e and with u and d quarks, if $0\nu\beta\beta$-decay takes place, regardless of the mechanism causing it, the neutrino is Majorana particle with nonzero mass.

The reason is that one can consider the $0\nu\beta\beta$ elementary interaction process $dd \to uuee$ as generated by the black box, which can include any mechanism. Then the legs of the black box can be arranged to form a diagram which generates $\overline{\nu}_e \to \nu_e$ transitions. This diagram contributes to the Majorana mass of the electron neutrino through radiative corrections at some order of perturbation theory, even if there is no tree-level Majorana neutrino mass term.

It is however clear that the black-box amplitudes are strongly suppressed (at least by a factor $\propto G_F^2$) with respect to the standard tree-level $0\nu\beta\beta$-decay amplitude. Model calculations show that the standard amplitude corresponding to a value of $|m_{\beta\beta}| = O(0.1)$ eV generates radiatively a Majorana mass $O(10^{-24})$ eV.

Generic

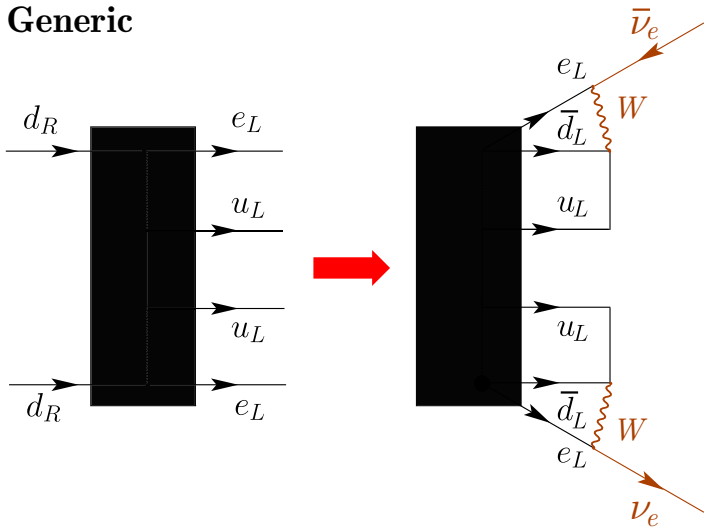

Example ($\not{R}$ SUSY)

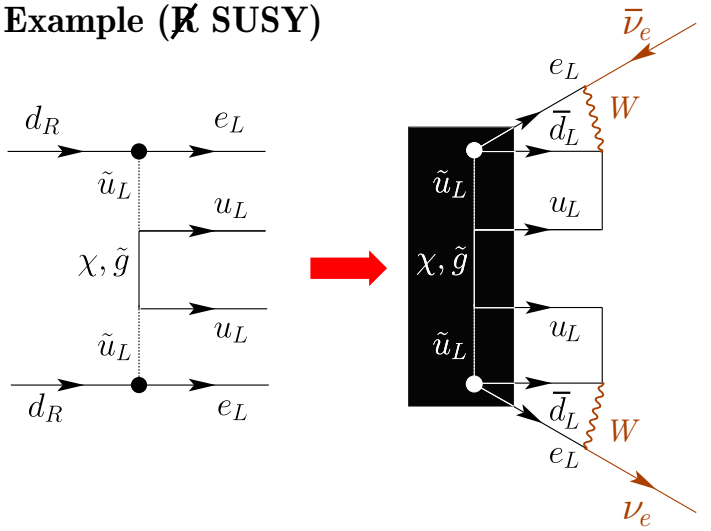

[a] J. Schechter and J. W. F. Valle, "Neutrinoless double-β decay in SU(2)×U(1) theories," Phys. Rev. D **25** (1982) 2951–2954. A generalization to 3ν (mixed) case was made by M. Hirsch, H. V. Klapdor-Kleingrothaus, and S. G. Kovalenko, "On the SUSY accompanied neutrino exchange mechanism of neutrinoless double beta decay," Phys. Lett. B **372** (1996) 181–186, Phys. Lett. B **381** (1996) 488 (erratum), hep-ph/9512237.

14 See-saw mechanism.

14.1 Dirac-Majorana mass term for one generation.

It is possible to consider mixed models in which both Majorana and Dirac mass terms are present. In order to explain in the simplest way the ideology of the see-saw mechanism, consider a toy model with one neutrino generation (flavor) but with two independent neutrino fields. ν_L and ν_R:

$$\begin{cases} \nu_L \text{ would generally represent any active neutrino (e.g., } \nu_L = \nu_{eL}), \\ \nu_R \text{ can represents a right handed field unrelated to any of these or} \\ \quad \text{it can be charge conjugate of any of the active neutrinos (e.g., } \nu_R = (\nu_{\mu L})^c). \end{cases}$$

We can write the following generic mass term between ν_L and ν_R:

$$\mathcal{L}_m = - \underbrace{m_D\, \overline{\nu}_L \nu_R}_{\text{Dirac mass term}} \underbrace{- (1/2)\left[m_L\, \overline{\nu}_L \nu_L^c + m_R\, \overline{\nu}_R^c \nu_R\right]}_{\text{Majorana mass term}} + \text{H.c.} \tag{44}$$

- ⋆ As we know, the Dirac mass term respects L while the Majorana mass term violates it.
- ⋆ The parameter m_D in Eq. (44) is in general complex; to simplify matters, we'll assume it to be real but not necessarily positive.
- ⋆ The parameters m_L, and m_R in Eq. (44) can be chosen real and (by an appropriate rephasing the fields ν_L and ν_R) non-negative, but the latter is not assumed.
- ⋆ Obviously, neither ν_L nor ν_R is a mass eigenstate.

In order to obtain the *mass basis* we can apply the useful identity

$$\overline{\nu}_L \nu_R = (\overline{\nu}_R)^c (\nu_L)^c \tag{45}$$

> The identity (45) is a particular case of the more general relation
>
> $$\overline{\psi}_1 \Gamma \psi_2 = \overline{\psi}_2^c C \Gamma^T C^{-1} \psi_1^c,$$
>
> in which $\psi_{1,2}$ are Dirac spinors and Γ represents an arbitrary combination of the Dirac γ matrices.

Relation (45) allows us to rewrite Eq. (44) as follows [**prove**]

$$\mathcal{L}_m = -\frac{1}{2} \left(\overline{\nu}_L, (\overline{\nu}_R)^c\right) \begin{pmatrix} m_L & m_D \\ m_D & m_R \end{pmatrix} \begin{pmatrix} (\nu_L)^c \\ \nu_R \end{pmatrix} + \text{H.c.} \equiv -\frac{1}{2} \overline{\boldsymbol{\nu}}_L \mathbf{M} \left(\boldsymbol{\nu}_L\right)^c + \text{H.c.}$$

If (again for simplicity) CP conservation is assumed the matrix $\mathbf{M}$ can be diagonalized by the orthogonal transformation that is rotation

$$\mathbf{V} = \begin{pmatrix} \cos\theta & \sin\theta \\ -\sin\theta & \cos\theta \end{pmatrix} \quad \text{with} \quad \theta = \frac{1}{2} \arctan\left(\frac{2m_D}{m_R - m_L}\right).$$

and we have

$$\mathbf{V}^T \mathbf{M} \mathbf{V} = \text{diag}(m_1, m_2),$$

where $m_{1,2}$ are eigenvalues of $\mathbf{M}$ given by

$$m_{1,2} = \frac{1}{2} \left(m_L + m_R \pm \sqrt{(m_L - m_R)^2 + 4m_D^2}\right).$$

Let's dwell on that a little more... It's instructive to consider a somewhat more general case:

$$\mathbf{M} = \begin{pmatrix} m_L & \mu_1 \\ \mu_2 & m_R \end{pmatrix} \quad (m_{L,R} \geq 0, \;\; \mu_{1,2} \geq 0).$$

Eigenvalues of $\mathbf{M}$ satisfy the equation $\det(\lambda - \mathbf{M}) = 0 \Longrightarrow \lambda^2 - (m_L + m_R)\,\lambda + m_L m_R - \mu_1\mu_2 = 0 \Longrightarrow$

$$\lambda_\pm = \frac{1}{2}\left[m_L + m_R \pm \sqrt{(m_L - m_R)^2 + 4\mu_1\mu_2}\right].$$

Note: λ_- can be negative if $\mu_1\mu_2 > m_L m_R$. We'll see below what to do about it.

Now we diagonalize $\mathbf{M}$ by a unitary transformation $\mathbf{V}^\dagger\mathbf{M}\mathbf{V} = \mathrm{diag}(\lambda_-, \lambda_+) \equiv \mathbf{m}$. Since the $\mathbf{M}$ is positive definite, $\mathbf{V}^\dagger = \mathbf{V}^\mathsf{T} \Longrightarrow \mathbf{V}$ is real $\Longrightarrow$ it is antisymmetric $\Longrightarrow$ it is a rotation matrix,

$$\mathbf{V} = \begin{pmatrix} \cos\theta & \sin\theta \\ -\sin\theta & \cos\theta \end{pmatrix} \Longrightarrow \mathbf{V}^\mathsf{T} = \begin{pmatrix} \cos\theta & -\sin\theta \\ \sin\theta & \cos\theta \end{pmatrix}, \quad \mathbf{V}\mathbf{V}^\mathsf{T} = \mathbf{1},$$

$$\mathbf{V}\mathbf{m}\mathbf{V}^\dagger = \mathbf{M} \Longrightarrow \begin{pmatrix} \cos^2\theta\,\lambda_- + \sin^2\theta\,\lambda_+ & \sin\theta\cos\theta\,(\lambda_+ - \lambda_-) \\ \sin\theta\cos\theta\,(\lambda_+ - \lambda_-) & \cos^2\theta\,\lambda_+ + \sin^2\theta\,\lambda_- \end{pmatrix} = \begin{pmatrix} m_L & \mu_1 \\ \mu_2 & m_R \end{pmatrix}.$$

Oh horror! We got $\sin\theta\cos\theta\,(\lambda_+ - \lambda_-) = \mu_1$ and $\sin\theta\cos\theta\,(\lambda_+ - \lambda_-) = \mu_2$. **What does that mean?!** Nothing unexpected. The Majorana mass matrix should be symmetric, otherwise the unitary transformation we need does not exist. So further we put $\mu_1 = \mu_2 = m_D$. Therefore

$$\left(\cos^2\theta - \sin^2\theta\right)(\lambda_+ - \lambda_-) = m_R - m_L \;\text{ and }\; \sin\theta\cos\theta\,(\lambda_+ - \lambda_-) = m_D.$$

Given that $\cos^2\theta - \sin^2\theta = \cos 2\theta$ and $2\sin\theta\cos\theta = \sin 2\theta$ we obtain

$$\tan 2\theta = \frac{2m_D}{m_R - m_L} \Longleftrightarrow \theta = \frac{1}{2}\arctan\left(\frac{2m_D}{m_R - m_L}\right).$$

The eigenvalues are real if (as we assume) $m_{D,L,R}$ are real, but not necessarily positive. Let us define $\zeta_k = \mathrm{sign}\, m_k$ and rewrite the mass term in the new basis:

$$\mathcal{L}_m = -\frac{1}{2}\left[\zeta_1 |m_1| \overline{\nu}_{1L} (\nu_{1L})^c + \zeta_2 |m_2| (\overline{\nu}_{2R})^c \nu_{2R}\right] + \text{H.c.}, \tag{46}$$

The new fields ν_{1L} and ν_{2R} represent chiral components of two different neutrino states with "masses" m_1 and m_2, respectively:

$$\begin{pmatrix} \nu_L \\ \nu_R^c \end{pmatrix} = \mathbf{V} \begin{pmatrix} \nu_{1L} \\ \nu_{2R}^c \end{pmatrix} \quad \Longrightarrow \quad \begin{cases} \nu_{1L} = \cos\theta\, \nu_L - \sin\theta\, \nu_R^c, \\ \nu_{2R} = \sin\theta\, \nu_L^c + \cos\theta\, \nu_R. \end{cases}$$

Now we define two 4-component fields

$$\nu_1 = \nu_{1L} + \zeta_1 (\nu_{1L})^c \quad \text{and} \quad \nu_2 = \nu_{2R} + \zeta_2 (\nu_{2R})^c.$$

Certainly, these fields are self-conjugate with respect to the C transformation:

$$\nu_k^c = \zeta_k \nu_k \quad (k = 1, 2)$$

and therefore they describe Majorana neutrinos. In terms of these fields Eq. (46) reads

$$\mathcal{L}_m = -\frac{1}{2}\left(|m_1| \overline{\nu}_1 \nu_1 + |m_2| \overline{\nu}_2 \nu_2\right). \tag{47}$$

We can conclude therefore that $\nu_k(x)$ is the Majorana neutrino field with the definite (physical) mass $|m_k|$.

There are several special cases of the Dirac-Majorana mass matrix $\mathbf{M}$ which are of considerable phenomenological importance, in particular,

(A): $\mathbf{M} = \begin{pmatrix} 0 & m \\ m & 0 \end{pmatrix} \quad \Longrightarrow \quad |m_{1,2}| = m, \quad \theta = \frac{\pi}{4}$ (maximal mixing).

Two Majorana fields are equivalent to one Dirac field.

A generalization $|m_{L,R}| \ll |m_D|$, leads to the so-called Pseudo-Dirac neutrinos.

(B): $\mathbf{M} = \begin{pmatrix} m_L & m \\ m & m_L \end{pmatrix} \quad \Longrightarrow \quad m_{1,2} = m_L \pm m_D, \quad \theta = \frac{\pi}{4}$ (maximal mixing);

(C): $\mathbf{M} = \begin{pmatrix} 0 & m \\ m & M \end{pmatrix}$ or, more generally, $|m_L| \ll |m_R|, \quad m_D > 0.$

The see-saw

The case (C) with $m \ll M$ is the simplest example of the see-saw mechanism. It leads to two masses, one very large, $m_1 \approx M$, other very small, $m_2 \approx -m^2/M \ll m$, suppressed compared to the entries in $\mathbf{M}$ [**prove**]. In particular, one can assume

$$m \sim m_\ell \text{ or } m_q \quad (0.5 \text{ MeV to } 200 \text{ GeV}) \quad \text{and} \quad M \sim M_{\text{GUT}} \sim 10^{15-16} \text{ GeV}.$$

Then $|m_2|$ can ranges from $\sim 10^{-14}$ eV to ~ 0.04 eV. The mixing between the heavy and light neutrinos is extremely small: $\theta \approx m/M \sim 10^{-20} - 10^{-13} \lll 1$.

If one eigenvalue *goes up*, the other *goes down*, and vice versa. This is the reason of the term see-saw...
a bit intricate for so simple idea...

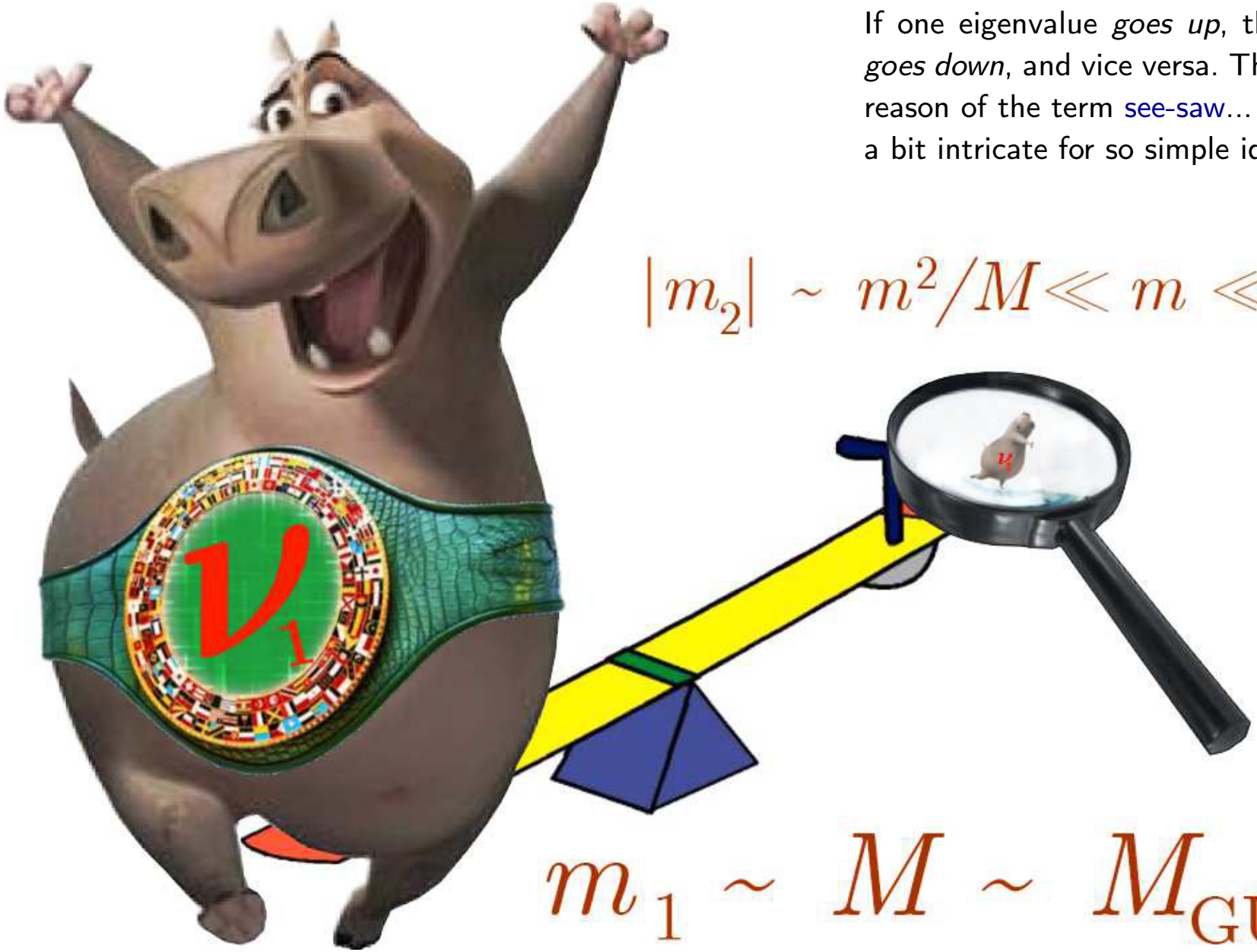

$$|m_2| \sim m^2/M \ll m \ll M$$

$$m_1 \sim M \sim M_{\rm GUT}$$

14.2 More neutral fermions.

A generalization of the above scheme to N generations is almost straightforward but technically rather cumbersome. Let's consider it schematically for the $N = 3$ case.

- If neutral fermions are added to the set of the SM fields, then the flavour neutrinos can acquire mass by mixing with them.
- The additional fermions can be
  - Gauge chiral singlets per family $\mathcal{N}$ (e.g., right-handed neutrinos) [Type I seesaw], or
  - $SU(2)_L$ scalar triplets Δ [Type II seesaw], or
  - $Y = 0$, $SU(2)_L$ triplets Σ (e.g., Wino in SUSY) [Type III seesaw], or
  - $SU(2) \times U(1)$ doublets (e.g., Higgsino in SUSY),...
- Addition of three right-handed neutrinos $\mathcal{N}_{iR}$ leads to the see-saw mechanism with the following mass terms:

$$\mathcal{L}_m = -\sum_{ij} \left[\overline{\nu}_{iL} M^D_{ij} \mathcal{N}_{jR} - \frac{1}{2} \left(\mathcal{N}_{iR}\right)^c M^R_{ij} \mathcal{N}_{jR} + \text{H.c.} \right] .$$

- The above equation leads to the following 6×6 see-saw mass matrix:

$$\mathbf{M} = \begin{pmatrix} \mathbf{0} & \mathbf{m}_D^T \\ \mathbf{m}_D & \mathbf{M}_R \end{pmatrix} .$$

  Both $\mathbf{m}_D$ and $\mathbf{M}_R$ are 3×3 matrices in the generation space.

Similar to the one-generation case we assume that the eigenvalues of $\mathbf{M}_R$ are large in comparison with the eigenvalues of $\mathbf{m}_D$. Then $\mathbf{M}$ can be approximately block-diagonalized by an unitary transformation:

$$\mathbf{U}^\dagger \mathbf{M} \mathbf{U} = \text{diag}\left(\mathbf{M}_1, \mathbf{M}_2\right) + \mathcal{O}\left(\mathbf{m}_D \mathbf{M}_R^{-1}\right),$$

where

$$\mathbf{U} = \begin{pmatrix} 1 + \frac{1}{2}\mathbf{m}_D^\dagger \left(\mathbf{M}_R \mathbf{M}_R^\dagger\right)^{-1} \mathbf{m}_D & \mathbf{m}_D^\dagger \left(\mathbf{M}_R^\dagger\right)^{-1} \\ -\mathbf{M}_R^{-1}\mathbf{m}_D & 1 + \frac{1}{2}\mathbf{M}_R^{-1}\mathbf{m}_D\mathbf{m}_D^\dagger \left(\mathbf{M}_R^\dagger\right)^{-1} \end{pmatrix},$$

$$\mathbf{M}_1 \simeq -\mathbf{m}_D^T \mathbf{M}_R^{-1} \mathbf{m}_D, \quad \text{and} \quad \mathbf{M}_2 \simeq \mathbf{M}_R.$$

The mass eigenfields are surely Majorana neutrinos.

- Quadratic see-saw: If eigenvalues of $\mathbf{M}_R$ are of the order of a large scale parameter $M \sim M_{\text{GUT}}$[a] [e.g., $\mathbf{M}_R = \mathbf{M}_1$] than the standard neutrino masses are suppressed:

$$m_i \sim \frac{m_{Di}^2}{M} \lll m_{Di},$$

  Here $m_{Di} \sim Y_i \langle H \rangle$ are the eigenvalues of $\mathbf{m}_D$. As long as these eigenvalues (or Yukawa couplings Y_i) are hierarchical, the Majorana neutrino masses display quadratic hierarchy:

$$m_1 : m_2 : m_3 \propto m_{D1}^2 : m_{D2}^2 : m_{D3}^2.$$

[a] Large M is natural in, e.g., $SO(10)$ inspired GUT models which therefore provide a nice framework to understand small neutrino masses.

- Linear see-saw: In a more special case, $\mathbf{M}_R = (M/M_D)\mathbf{M}_D$, where M_D is the generic scale of the charged fermion masses than

$$m_i \sim \frac{M_D m_{Di}}{M} \lll m_{Di}$$

but the hierarchy is now linear:

$$m_1 : m_2 : m_3 \propto m_{D1} : m_{D2} : m_{D3}.$$

The two mentioned possibilities are, in principle, experimentally distinguishable. SO, See-saw provides a mechanism potentially able to relate neutrino, lepton, and/or quark masses to the GUT scale.

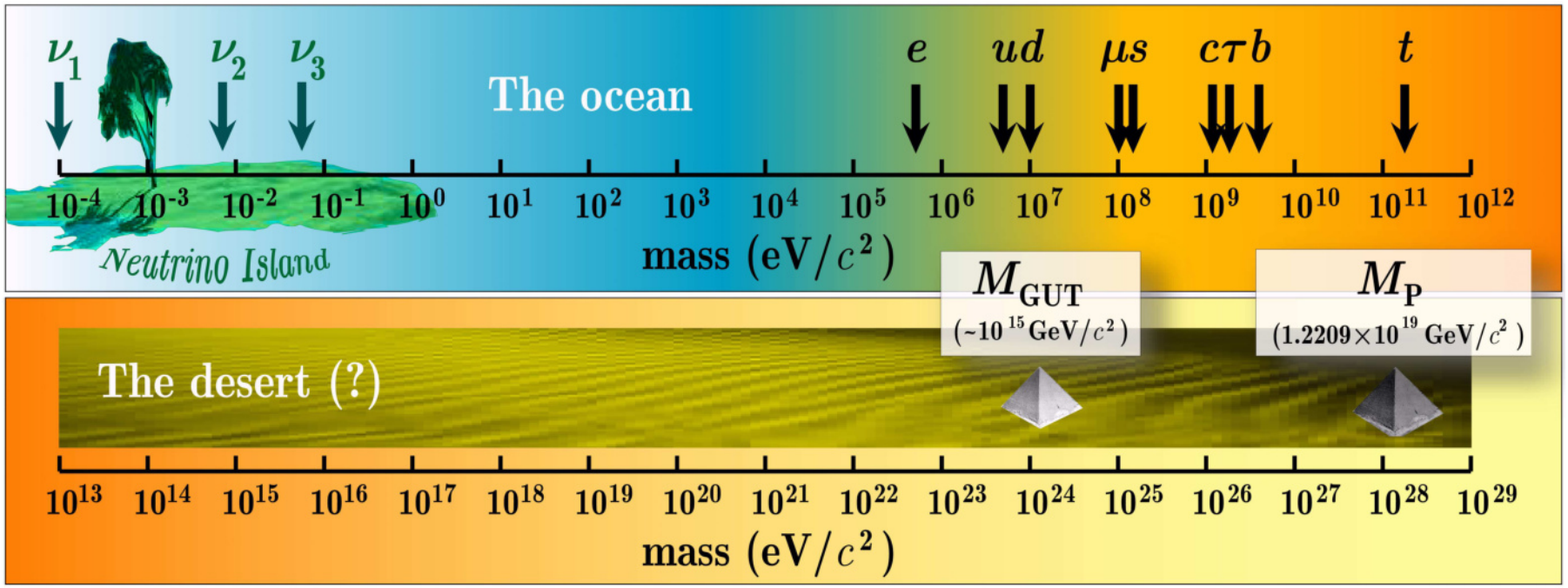

The following slides give a couple more examples for those who are interested.

14.3 Double see-saw & inverse see-saw.

The see-saw can be implemented by introducing additional neutrino singlets beyond the three RH neutrinos involved into the see-saw type I. One have to distinguish between

- RH neutrinos $\boldsymbol{\nu}_R$, which carry $B-L$ and perhaps (not necessary) form $SU(2)_R$ doublets with RH charged leptons, and
- Neutrino singlets $\boldsymbol{\nu}_S$, which have no Yukawa couplings to the LH neutrinos but may couple to $\boldsymbol{\nu}_R$.

If the singlets have nonzero Majorana masses $\mathbf{M}_{SS}$ while the RH neutrinos have a zero Majorana mass, $\mathbf{M}_{RR}=0$, the see-saw mechanism may proceed via mass couplings of the singlets to RH neutrinos, $\mathbf{M}_{RS}$. In the basis $(\boldsymbol{\nu}_L,\boldsymbol{\nu}_R,\boldsymbol{\nu}_S)$, the 9×9 mass matrix is

$$\begin{pmatrix} \mathbf{0} & \mathbf{m}_{LR} & \mathbf{0} \\ \mathbf{m}_{LR} & \mathbf{0} & \mathbf{M}_{RS} \\ \mathbf{0} & \mathbf{M}_{RS}^T & \mathbf{M}_{SS} \end{pmatrix}.$$

Assuming that the eigenvalues of $\mathbf{M}_{SS}$ are much smaller than the eigenvalues of $\mathbf{M}_{RS}$, the light physical LH Majorana neutrino masses are then doubly suppressed,

$$\mathbf{M}_1 \simeq \mathbf{m}_{LR}\mathbf{M}_{RS}^{-1}\mathbf{M}_{SS}\left(\mathbf{M}_{RS}^T\right)^{-1}\mathbf{m}_{LR}^T, \quad \mathbf{M}_2^2 \simeq \mathbf{M}_{RS}^2+\mathbf{m}_{LR}^2.$$

This scenario is usually used in string inspired models [see, e.g., R.N.Mohapatra & J.W.Valle, Phys. Rev. D **34** (1986) 1642; M.C.Gonzalez-Garcia & J.W.F.Valle, Phys. Lett. B **216** (1989) 360].

14.4 Radiative see-saw.

An alternative mechanism relies on the radiative generation of neutrino masses [H.Georgi & S.L.Glashow, Phys. Rev. D **7** (1973) 2487; P.Cheng & L.-F.Li, Phys. Rev. D **17** (1978) 2375; Phys. Rev. D **22** (1980) 2860; A.Zee, Phys. Lett. B **93** (1980) 389;. . .] In this scheme, the neutrinos are massless at the tree level, but pick up small masses due to loop corrections.

In a typical model [K.S. Babu & V.S. Mathur, Phys. Rev. D **11** (1988) 3550] the see-saw formula is modified as

$$m_\nu \sim \left(\frac{\alpha}{\pi}\right)\frac{m_l^2}{M},$$

where the prefactor $\alpha/\pi \approx 2\times 10^{-3}$ arises due to the loop structure of the neutrino mass diagram. Light neutrinos are now possible even for relatively "light" mass scale M of "new physics,"

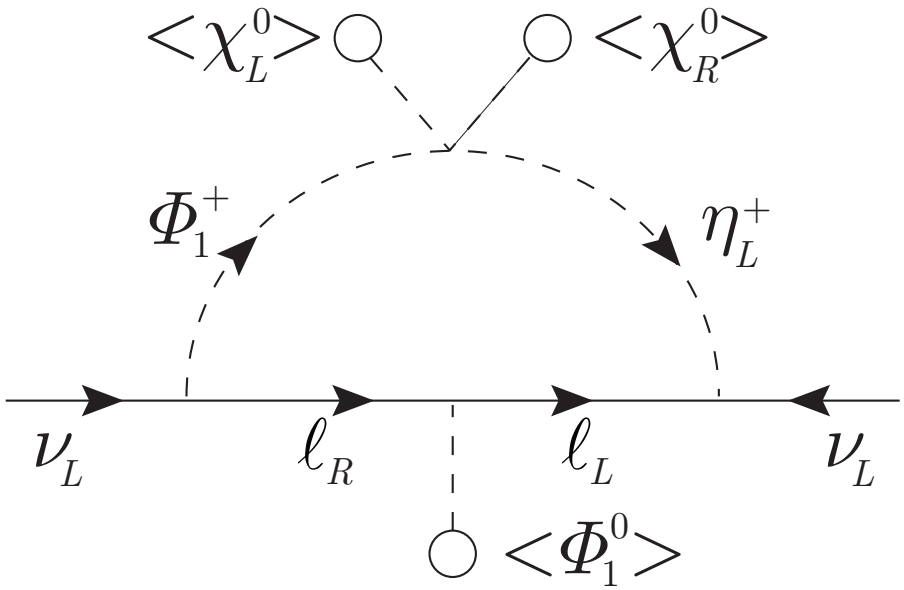

The scalar sector consists of the multiplets

$$\chi_{L,R} = \left(\chi^+, \chi^0\right)_{L,R}, \quad \Phi = \begin{pmatrix} \Phi_1^0 & \Phi_2^+ \\ \Phi_1^- & \Phi_2^0 \end{pmatrix}, \quad \eta_{L,R}^+.$$

The diagram in the figures is responsible for generation of Majorana masses for ν_L. The analogous diagram is obtained by the replacement $L \to R$ and $\Phi_1^+ \to \Phi_2^+$.

14.5 TeV-scale gauged $B-L$ symmetry with Inverse see-saw.

Consider briefly one more inverse see-saw model [S.Khalil, Phys. Rev. D **82** (2010) 077702].

The model is based on the following:

(i) The SM singlet Higgs boson, which breaks the $B-L$ gauge symmetry, has $B-L$ unit charge.

(ii) The SM singlet fermion sector includes two singlet fermions $S_{\pm}$ with $B-L$ charges ± 2 with opposite matter parity.

The Lagrangian of neutrino masses, in the flavor basis, is given by

$$\overline{\boldsymbol{\nu}}_L \mathbf{m}_D \boldsymbol{\nu}_R + \boldsymbol{\nu}_R^c \mathbf{M}_N S_- + \mu_s \overline{\boldsymbol{S}}_- \boldsymbol{S}_- .$$

In the limit $\mu_s \to 0$, which corresponds to the unbroken $(-1)^{L+S}$ symmetry, the light neutrinos remain massless. Therefore, a small nonvanishing μ_s can be considered as a slight breaking of a this global symmetry and the smallness of μ_s is natural. Small μ_s can also be generated radiatively.

In the basis $(\boldsymbol{\nu}_L, \boldsymbol{\nu}_R^c, \boldsymbol{S}_-)$, the 9×9 mass matrix is

$$\begin{pmatrix} \mathbf{0} & \mathbf{m}_D & \mathbf{0} \\ \mathbf{m}_D^T & \mathbf{0} & \mathbf{M}_N \\ \mathbf{0} & \mathbf{M}_N^T & \mu_s \end{pmatrix}.$$

So, up to the notation, it reproduces all the properties of the double see-saw.

Beyond this lecture

- SUSY & SUGRA see-saw
- TeV see-saw & Large Extra Dimensions
- See-saw & Dark Matter
- See-saw & Leptogenesis
- See-saw & Baryogenesis
- Dirac see-saw
- Top (top-bottom) see-saw
- Cascade see-saw
- ...

Conclusions [are not actually validated]

- The "mainstream" neutrino mass models, defined as see-saw models, are capable of describing the atmospheric–reactor–accelerator neutrino oscillation data, the LMA MSW solar neutrino solution, and cosmological limits.
- The Standard Model and the Minimal Supersymmetric Standard Model may naturally be extended to incorporate the see-saw mechanism.
- [A fly in the ointment] Wealth of the models ($\gg$ number of the authors of the models) greatly complicates the choice of the best one.

Afterward: Open problems in neutrino physics.

- Are neutrinos Dirac or Majorana fermions?
- What is the absolute mass scale of (known) neutrinos?
  Why neutrino masses are so small? [Does any version of see-saw work?]
  What is the neutrino mass spectrum? [sign$(\Delta m^2_{32}) \Longleftrightarrow$ NH or IH.]
  Can the lightest neutrinos be massless fermions? [Not quasiparticles in Weyl semimetals!]
- Why neutrino mixing is so different from quark mixing? Does (at least broken) QLC exist?
- What physics is responsible for the octant degeneracy (if it exists)? [sign$(\theta_{23} - 45^\circ)$.]
- What are the source and scale of CP/T violation in the neutrino sector?
  How many CP violating phases are there?
- Does CPT conserve in the neutrino sector?
- How many neutrino flavors are there?
- Whether the number of neutrinos with definite masses is equal to or greater than the number of flavor neutrinos? In other words, do sterile neutrinos exist? [a] If so,
  - What is their mass spectrum?
  - Do they mix with active neutrinos?
  - Do light (heavy) sterile neutrinos constitute hot (cold) dark matter?
- Are (all) neutrinos stable particles?

[a] Hints from LSND+MiniBooNE, Neutrino-4, SAGE+GALLEX+BEST are in tension with many other data.

Part V

Neutrino Oscillations in Vacuum

15 Quantum-mechanical treatment.

15.1 Angels vs. hippos.

According to the current theoretical understanding, the neutrino fields/states of definite flavor ($\nu_\alpha/|\nu_\alpha\rangle$, $\alpha = e, \mu, \tau$) are superpositions of the fields/states with definite, generally different masses ($\nu_i/|\nu_i\rangle$, $i = 1, 2, 3, \ldots$) [and vice versa]:

$$\nu_\alpha = \sum_i V_{\alpha i} \nu_i \qquad \text{for neutrino eigenfields,}$$

$$|\nu_\alpha\rangle = \sum_i V^*_{\alpha i} |\nu_i\rangle \qquad \text{for neutrino eigenstates.}$$

Here $V_{\alpha i}$ are the elements of the Pontecorvo-Maki-Nakagawa-Sakata (PNMS) neutrino vacuum mixing matrix $\mathbf{V}$.

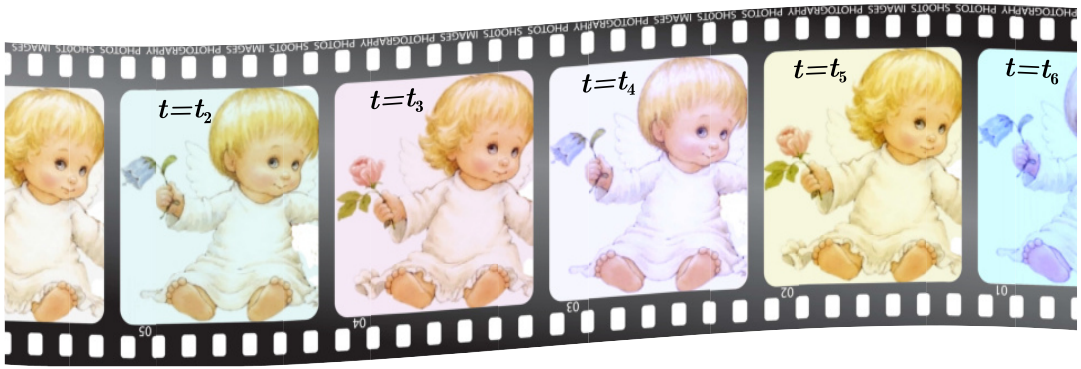

This concept leads to the possibility of transitions between the neutrinos of different flavors, $\nu_\alpha \longleftrightarrow \nu_\beta$, phenomenon known as **neutrino flavor oscillations**.

Let us introduce two types of neutrino eigenstates:

- The flavor neutrino eigenstates which can be written as a vector

$$|\boldsymbol{\nu}\rangle_f = (|\nu_e\rangle, |\nu_\mu\rangle, |\nu_\tau\rangle, \ldots)^T \equiv (|\nu_\alpha\rangle)^T$$

are defined as the states which correspond to the charge leptons $\alpha = e, \mu, \tau$. The correspondence is established through the charged current interactions of active neutrinos and charged leptons.

> Together with the standard νs, $|\boldsymbol{\nu}\rangle_f$ may include also neutrino states allied with additional heavy charged leptons, as well as the states not associated with charge leptons, like sterile neutrinos, ν_s.

In general, the flavor states have no definite masses. Therefore, they can have either definite momentum, or definite energy but not both.

- The neutrino mass eigenstates

$$|\boldsymbol{\nu}\rangle_m = (|\nu_1\rangle, |\nu_2\rangle, |\nu_3\rangle, \ldots)^T \equiv (|\nu_k\rangle)^T$$

are, by definition, the states with the definite masses m_k, $k = 1, 2, 3, \ldots$.

Since $|\nu_\alpha\rangle$ and $|\nu_k\rangle$ are not identical, they are related to each other through a unitary transformation

$$|\nu_\alpha\rangle = \sum_k \hat{V}_{\alpha k} |\nu_k\rangle \quad \text{or} \quad |\boldsymbol{\nu}\rangle_f = \hat{\mathbf{V}} |\boldsymbol{\nu}\rangle_m,$$

where $\hat{\mathbf{V}} = \| \hat{V}_{\alpha k} \|$ is a unitary (in general, $N \times N$) matrix.

To find out the correspondence between $\hat{\mathbf{V}}$ and the PMNS mixing matrix $\mathbf{V}$ we can normalize the "f" and "m" states by the following conditions

$$\langle 0|\nu_{\alpha L}(x)|\nu_{\alpha'}\rangle = \delta_{\alpha\alpha'} \quad \text{and} \quad \langle 0|\nu_{kL}(x)|\nu_{k'}\rangle = \delta_{kk'}.$$

From these conditions we obtain

$$\sum_k V_{\alpha k}\hat{V}_{\alpha' k} = \delta_{\alpha\alpha'} \quad \text{and} \quad \sum_\alpha V_{\alpha k}\hat{V}_{\alpha k'} = \delta_{kk'}.$$

Therefore

$$\hat{\mathbf{V}} \equiv \mathbf{V}^\dagger$$

and

$$\boxed{|\boldsymbol{\nu}\rangle_f = \mathbf{V}^\dagger|\boldsymbol{\nu}\rangle_m \iff |\boldsymbol{\nu}\rangle_m = \mathbf{V}|\boldsymbol{\nu}\rangle_f.} \tag{48}$$

The time evolution of a single mass eigenstate $|\nu_k\rangle$ with momentum p_ν is trivial,

$$i\frac{d}{dt}|\nu_k(t)\rangle = E_k|\nu_k(t)\rangle \implies |\nu_k(t)\rangle = e^{-iE_k(t-t_0)}|\nu_k(t_0)\rangle,$$

where $E_k = \sqrt{p_\nu^2 + m_k^2}$ is the total energy in the state $|\nu_k\rangle$. Now, assuming that all N states $|\nu_k\rangle$ have the same momentum, one can write

$$i\frac{d}{dt}|\boldsymbol{\nu}(t)\rangle_m = \mathbf{H}_0|\boldsymbol{\nu}(t)\rangle_m, \quad \text{where} \quad \mathbf{H}_0 = \text{diag}\,(E_1, E_2, E_3, \ldots). \tag{49}$$

From Eqs. (48) and (49) we have

$$i\frac{d}{dt}|\boldsymbol{\nu}(t)\rangle_f = \mathbf{V}^\dagger \mathbf{H}_0 \mathbf{V}|\boldsymbol{\nu}(t)\rangle_f. \tag{50}$$

Solution to this equation is obvious:

$$\begin{aligned}|\boldsymbol{\nu}(t)\rangle_f &= \mathbf{V}^\dagger e^{-i\mathbf{H}_0(t-t_0)}\mathbf{V}\,|\boldsymbol{\nu}(t_0)\rangle_f \\ &= \mathbf{V}^\dagger \,\mathrm{diag}\left(e^{-iE_1(t-t_0)}, e^{-iE_2(t-t_0)}, \ldots\right)\,\mathbf{V}\,|\boldsymbol{\nu}(t_0)\rangle_f.\end{aligned} \tag{51}$$

Now we can derive the survival and transition probabilities

$$\begin{aligned}P_{\alpha\beta}(t-t_0) &= P\left[\nu_\alpha(t_0)\to\nu_\beta(t)\right] = \left|\langle\nu_\beta(t)|\nu_\alpha(t_0)\rangle\right|^2 \\ &= \left|\sum_k V_{\alpha k}V^*_{\beta k}\,\exp\left[iE_k(t-t_0)\right]\right|^2 \\ &= \sum_{jk} V_{\alpha j}V_{\beta k}\left(V_{\alpha k}V_{\beta j}\right)^*\,\exp\left[i(E_j-E_k)(t-t_0)\right].\end{aligned}$$

In the ultrarelativistic limit $p_\nu^2 \gg m_k^2$, which is undoubtedly valid for all interesting circumstances (except relic neutrinos),

$$E_k = \sqrt{p_\nu^2+m_k^2} \approx p_\nu + \frac{m_k^2}{2p_\nu} \approx E_\nu + \frac{m_k^2}{2E_\nu}, \quad p_\nu \equiv E_\nu.$$

Therefore in very good approximation

$$P_{\alpha\beta}(t-t_0)=\sum_{jk}V_{\alpha j}V_{\beta k}\left(V_{\alpha k}V_{\beta j}\right)^{*}\,\exp\left[\frac{i\Delta m^2_{jk}(t-t_0)}{2E_\nu}\right].$$

As a rule, there is no way to measure t_0 and t in the same experiment.[a] But it is usually possible to measure the distance L between the source and detector. So we have to connect $t-t_0$ with L. It is easy to do in the standard ultrarelativistic approximation,

$$v_k=\frac{p_\nu}{E_k}\simeq 1-\frac{m_k^2}{2E_\nu^2}=1-0.5\times 10^{-14}\left(\frac{m_k}{0.1\text{ eV}}\right)^2\left(\frac{1\text{ MeV}}{E_\nu}\right)^2\simeq 1,$$

from which it almost evidently follows that $t-t_0\approx L$. Finally we arrive at the following formula

$$P_{\alpha\beta}(L)=\sum_{jk}V_{\alpha j}V_{\beta k}\left(V_{\alpha k}V_{\beta j}\right)^{*}\,\exp\left(\frac{2i\pi L}{L_{jk}}\right),\quad L_{jk}=\frac{4\pi E_\nu}{\Delta m^2_{jk}},\tag{52}$$

where L_{jk} (or more exactly $|L_{jk}|=|L_{kj}|$) are the so-called neutrino oscillation lengths.

It is straightforward to prove that the QM formula satisfies the probability conservation law:

$$\sum_{\alpha}P_{\alpha\beta}(L)=\sum_{\beta}P_{\alpha\beta}(L)=1.$$

The range of applicability of the standard quantum-mechanical approach is limited but enough for the interpretation of essentially all modern experiments with accelerator, reactor, atmospheric, solar, and astrophysical neutrino beams.

[a] Important exceptions will be discussed in the special section.

15.2 Energy conservation.

Although the energy of the state with definite flavor, $|\nu_\alpha(L)\rangle = |\nu_\alpha(t)\rangle$, is not defined, its mean energy, $\langle E_\alpha(t)\rangle = \langle\nu_\alpha(t)|\hat{H}|\nu_\alpha(t)\rangle$, is a well-defined and conserved quantity. Indeed,

$$\langle E_\alpha(t)\rangle = \sum_{ij} V_{\alpha i}V^*_{\alpha j}\langle\nu_i(p_\nu)|\hat{H}|\nu_j(p_\nu)\rangle = \sum_{ij} V_{\alpha i}V^*_{\alpha j}\langle\nu_i(p_\nu)|E_i|\nu_j(p_\nu)\rangle \equiv \langle E_\alpha\rangle = \text{inv.}$$

$$\langle E_\alpha\rangle = \sum_i |V_{\alpha i}|^2 E_i \simeq p_\nu + \sum_i |V_{\alpha i}|^2 \frac{m_i^2}{2p_\nu}, \quad \Longrightarrow \quad \sum_\alpha \langle E_\alpha\rangle = \sum_i E_i \simeq 3p_\nu + \sum_i \frac{m_i^2}{2p_\nu}.$$

Moreover, the mean energy of an arbitrary entangled state characterized by a certain density matrix $\boldsymbol{\rho}(t)$ is also conserved. Indeed, let the initial state have the form

$$\boldsymbol{\rho}(0) = \sum_\alpha w_\alpha |\nu_\alpha(0)\rangle\langle\nu_\alpha(0)|,$$

The mean energy of the mixed state at arbitrary time t is then written as

$$\begin{aligned}\langle E(t)\rangle &= \mathsf{Tr}\left(\hat{H}\boldsymbol{\rho}(t)\right) = \mathsf{Tr}\left(\hat{H}e^{-i\hat{H}t}\boldsymbol{\rho}(0)e^{i\hat{H}t}\right)\\ &= \sum_\alpha w_\alpha \sum_{ij} V^*_{\alpha i}V_{\alpha j}e^{-i(E_i-E_j)t}E_i\ \mathsf{Tr}|\nu_i(p_\nu)\rangle\langle\nu_j(p_\nu)|\\ &= \sum_\alpha w_\alpha \sum_i |V_{\alpha i}|^2 E_i = \text{inv}, \quad \Longrightarrow \quad \langle E(t)\rangle = \sum_\alpha w_\alpha \langle E_\alpha\rangle.\end{aligned}$$

Naturally, $\langle E(t)\rangle = \langle E_\alpha\rangle$ for the pure initial state $|\nu_\alpha(0)\rangle$ (when $\boldsymbol{\rho}(0) = |\nu_\alpha(0)\rangle\langle\nu_\alpha(0)|$).

15.3 Several examples (two- and three-flavor oscillations).

Let us now consider the simplest (toy) two-flavor model, e.g., with $i = 2, 3$ and $\alpha = \mu, \tau$ (the most favorable due to the SK and other underground experiments). The 2×2 vacuum mixing matrix can be parametrized (due to the unitarity) with a single parameter, θ $(= \theta_{23})$, the vacuum mixing angle,

$$\mathbf{V} = \begin{pmatrix} \cos\theta & \sin\theta \\ -\sin\theta & \cos\theta \end{pmatrix}, \qquad 0 \leq \theta \leq \frac{\pi}{2}.$$

In this model, Eq. (52) then becomes very simple and transparent:

$$P_{\mu\tau}(L) = P_{\tau\mu}(L) = \frac{1}{2}\sin^2 2\theta \left[1 - \cos\left(\frac{2\pi L}{L_\nu}\right)\right],$$

$$L_\nu \equiv L_{23} = \frac{4\pi E_\nu}{\Delta m^2_{23}} \approx 2R_\oplus \left(\frac{E_\nu}{10\ \text{GeV}}\right)\left(\frac{0.002\ \text{eV}^2}{\Delta m^2_{23}}\right).$$

Here $R_\oplus$ is the mean radius of Earth and 10 GeV is a typical energy in the (very wide) atmospheric neutrino spectrum. Since Earth provides variable "baseline" [from about 15 km to about 13000 km], it is surprisingly suitable for studying the atmospheric (as well as accelerator and reactor) neutrino oscillations in rather wide range of the oscillation parameters.

The next three slides show the survival and transition probabilities for the standard 3ν mixing.

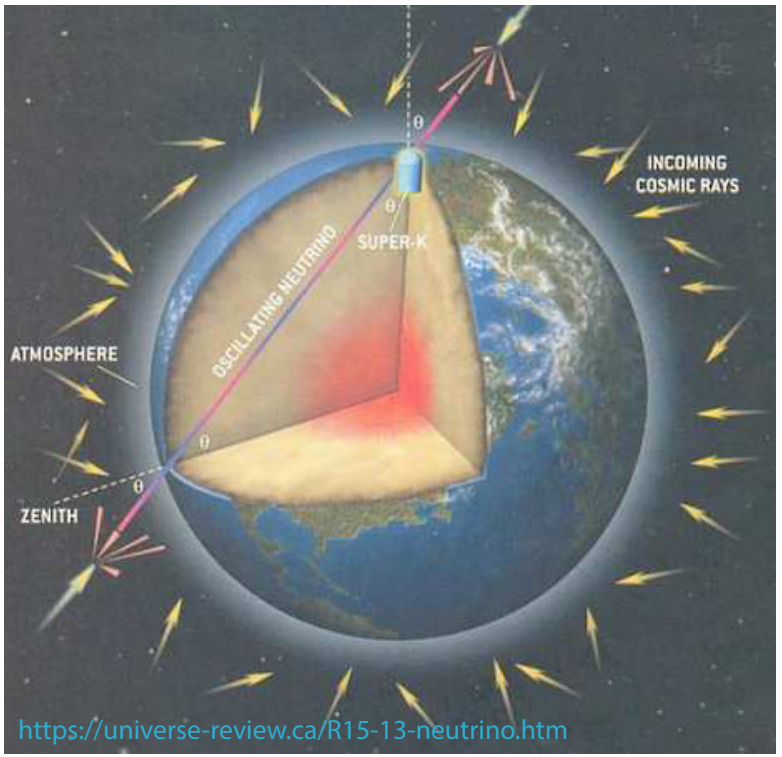

https://universe-review.ca/R15-13-neutrino.htm

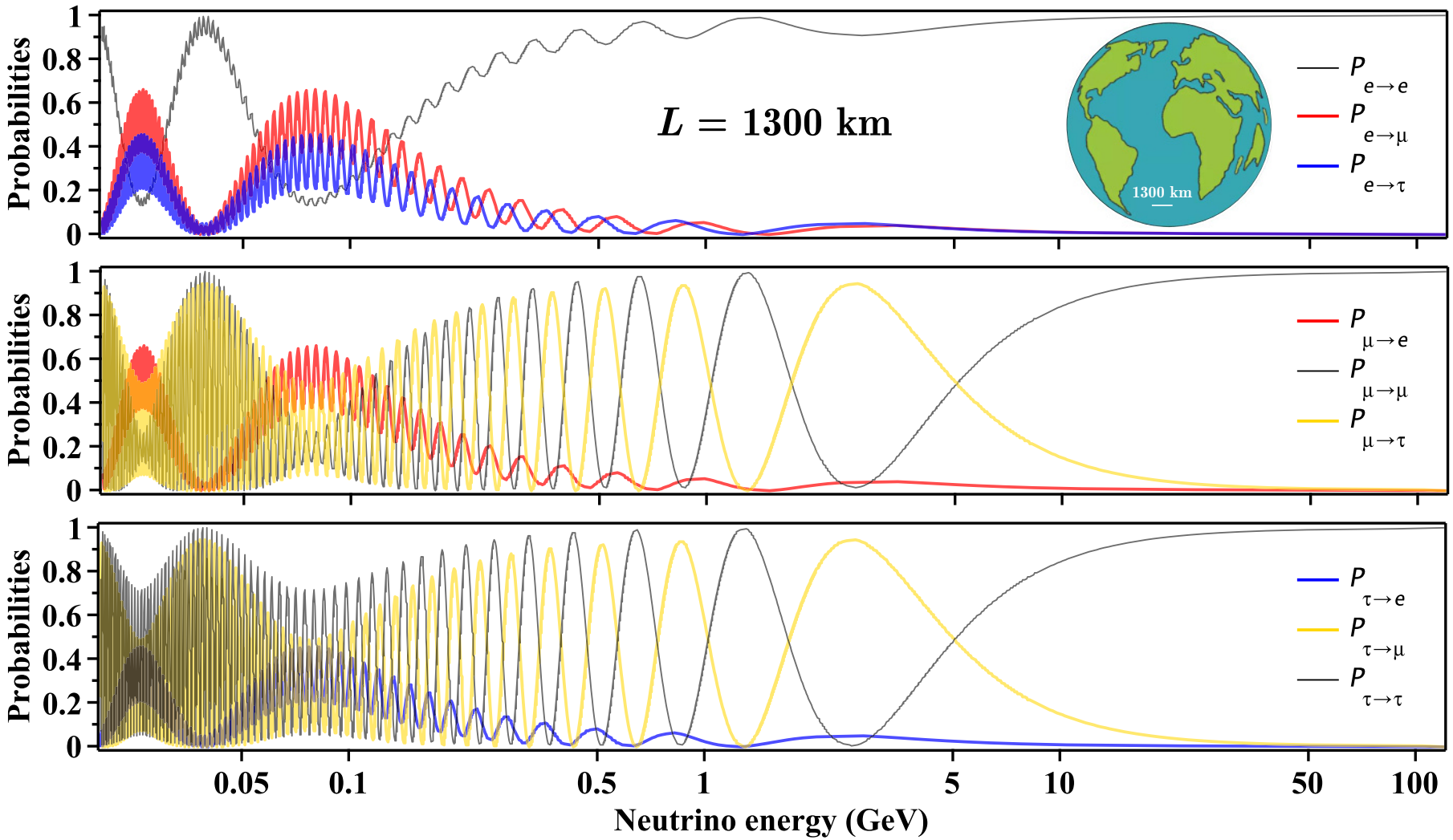

△ Example of survival and flavor transition probabilities vs. neutrino energy, E_ν, for SM neutrinos at $L = 1300\,\text{km} \approx \langle D_\oplus \rangle/10$. Here and hereafter, to compute the probabilities, the mixing parameters are fixed at their best-fit values resulting from the NuFIT 5.2 global 3ν fit to the current oscillation data, assuming normal mass hierarchy, and including Super-Kamiokande AN data (see p. 431).

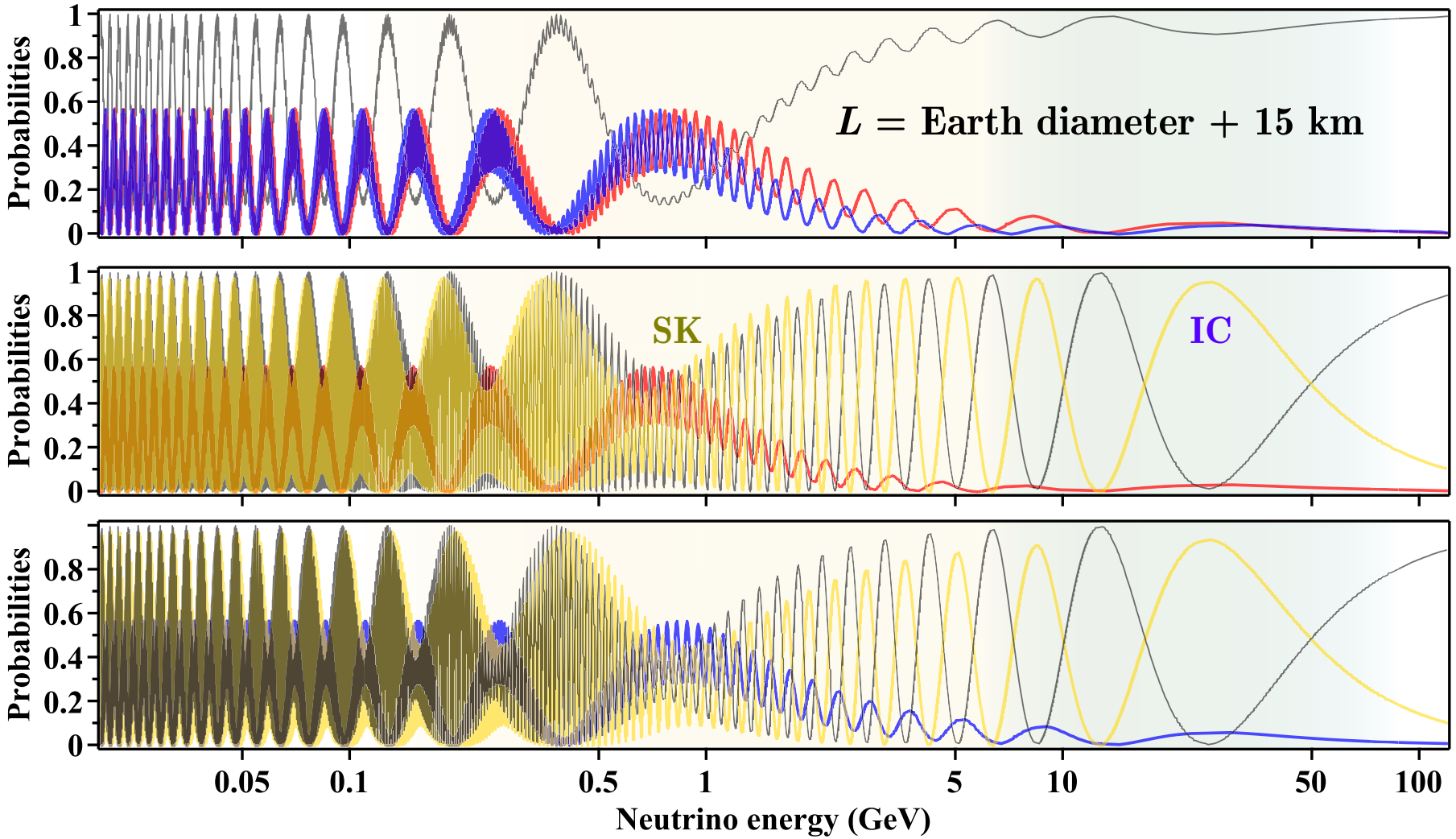

△ Same as in the previous slide (including colors), but with nearly the maximum baseline available in terrestrial experiments ($L = \langle D_\oplus \rangle + 15\,\text{km} = 12757\,\text{km}$).[a] Sensitivity ranges of SK and IC are shown. It is pertinent to note here that $P\left(\overline{\nu}_\alpha \to \overline{\nu}_\beta\right) = P\left(\nu_\alpha \to \nu_\beta\right)\big|_{\delta \mapsto -\delta} = P\left(\nu_\beta \to \nu_\alpha\right)$ **[prove]**.

[a] 15 km (above s.l.) is the typical altitude of atmospheric neutrino production in the near-vertical direction.

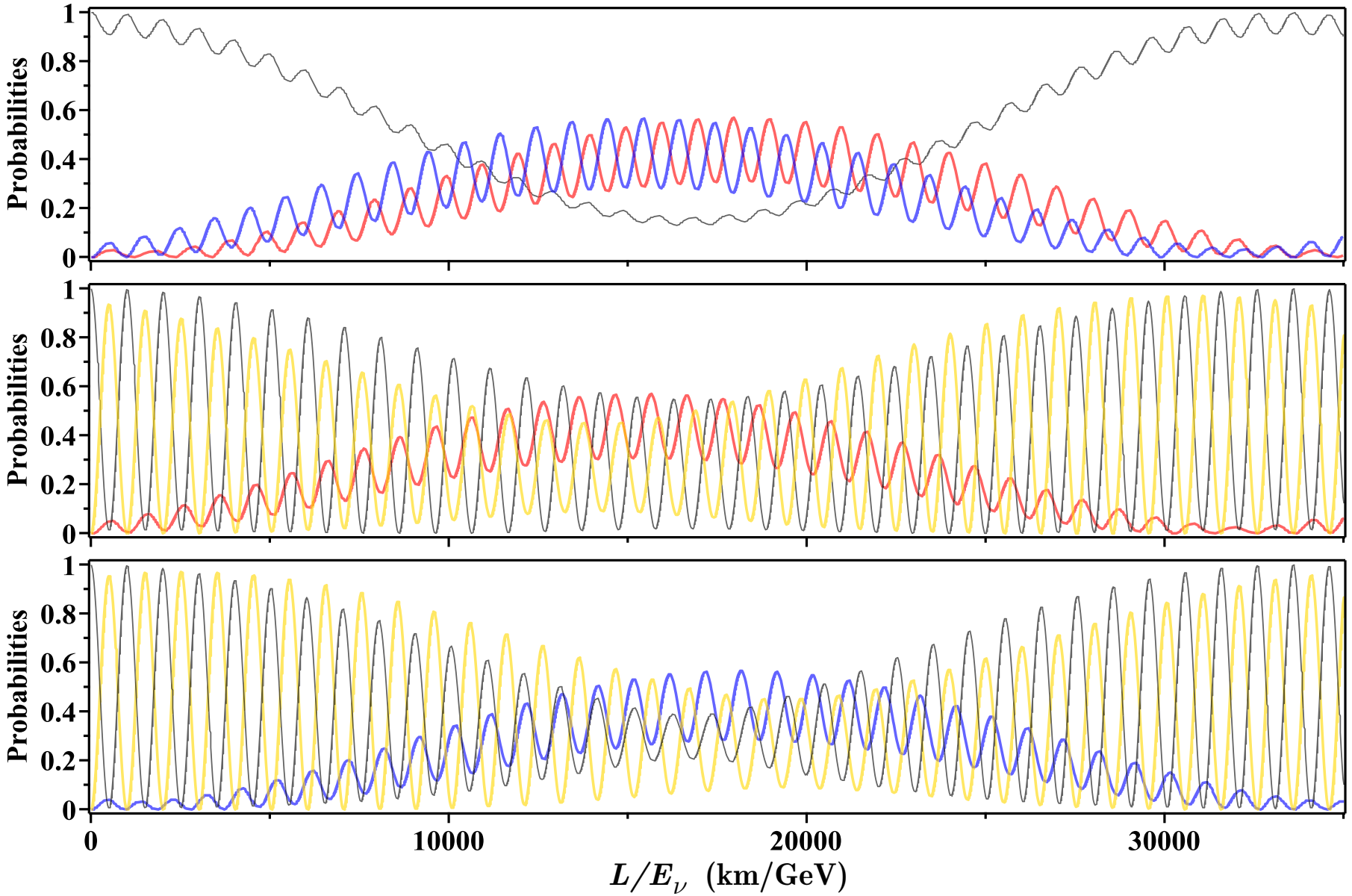

△ Survival and flavor transition probabilities vs. L/E_ν for SM neutrinos. The colors of the curves are the same as on the previous two slides. Although the picture is a bit dull, it is universal.

15.4 Summary of the standard QM theory.

The standard assumptions are intuitively transparent and (almost) commonly accepted.

[1] The neutrino flavor states $|\nu_\alpha\rangle$ associated with the charged leptons $\alpha = e, \mu, \tau$ (that is having definite lepton numbers) are not identical to the neutrino mass eigenstates $|\nu_i\rangle$ with the definite masses m_i $(i = 1, 2, 3)$.

Both sets of states are orthonormal: $\langle\nu_\beta|\nu_\alpha\rangle = \delta_{\alpha\beta}$, $\langle\nu_j|\nu_i\rangle = \delta_{ij}$.

$$\Downarrow$$

They are related to each other through a unitary transformation $\mathbf{V} = ||V_{\alpha i}||$, $\mathbf{V}\mathbf{V}^\dagger = 1$,

$$|\nu_\alpha\rangle = \sum_i V^*_{\alpha i}|\nu_i\rangle, \quad |\nu_i\rangle = \sum_\alpha V_{\alpha i}|\nu_\alpha\rangle.$$

[2] Massive neutrino states originated from any reaction or decay have the same definite momenta $\mathbf{p}_\nu$ ["equal momentum assumption" + "definite momentum assumption"].[a]

To simplify matter, we do not consider exotic processes with multiple neutrino production.

$$\Downarrow$$

The flavor states $|\nu_\alpha\rangle$ have the same momentum $\mathbf{p}_\nu$ but have no definite mass and energy.

[a] Sometimes – the same definite energies ["equal (definite) energy assumption"]. There were also completely crazy proposals in the literature, such as the assumption of equal velocities [**prove that it's excluded**].

[3] Neutrino masses are so small that in essentially all experimental circumstances (or, more precisely, in a wide class of reference frames) the neutrinos are ultrarelativistic. Hence

$$E_k = \sqrt{\mathbf{p}_\nu^2 + m_k^2} \simeq |\mathbf{p}_\nu| + \frac{m_k^2}{2|\mathbf{p}_\nu|}.$$

[4] Moreover, in the evolution equation, one can safely replace the time parameter t by the distance L between the neutrino source and detector ["light-ray approximation"].

The enumerated assumptions are sufficient to derive the nice and commonly accepted expression for the neutrino flavor transition probability [L_{jk} are the neutrino oscillation lengths]:

$$\begin{aligned} P(\nu_\alpha \to \nu_\beta; L) \equiv P_{\alpha\beta}(L) &= \sum_{jk} V_{\alpha j} V_{\beta k} \left(V_{\alpha k} V_{\beta j}\right)^* \exp\left(\frac{2i\pi L}{L_{jk}}\right) \\ &= \sum_j |V_{\alpha j}|^2 \, |V_{\beta j}|^2 + 2 \sum_{j>k} \left[\mathrm{Re}\left(V_{\alpha j}^* V_{\beta j} V_{\alpha k} V_{\beta k}^*\right) \cos\left(\frac{2\pi L}{L_{jk}}\right) \right. \\ &\quad \left. + \mathrm{Im}\left(V_{\alpha j}^* V_{\beta j} V_{\alpha k} V_{\beta k}^*\right) \sin\left(\frac{2\pi L}{L_{jk}}\right) \right], \end{aligned}$$

$$L_{jk} = \frac{4\pi E_\nu}{\Delta m_{jk}^2}, \qquad E_\nu = |\mathbf{p}_\nu|, \qquad \Delta m_{jk}^2 = m_j^2 - m_k^2.$$

Just this result is the basis for the "oscillation interpretation" of the current experiments with the natural and artificial neutrino and antineutrino beams.

15.5 Some challenges against the QM approach.

Equal-momentum assumption

Massive neutrinos ν_i have, by assumption, equal momenta: $\mathbf{p}_i = \mathbf{p}_\nu$ $(i = 1, 2, 3)$.

This key assumption seems to be unphysical being reference-frame (RF) dependent;

if it is true in a certain RF then it is false in another RF moving with the velocity $\mathbf{v}$:

$$E'_i = \Gamma_\mathbf{v} \left[E_i - (\mathbf{v}\mathbf{p}_\nu)\right], \quad \mathbf{p}'_i = \mathbf{p}_\nu + \Gamma_\mathbf{v} \left[\frac{\Gamma_\mathbf{v}(\mathbf{v}\mathbf{p}_\nu)}{\Gamma_\mathbf{v} + 1} - E_i\right] \mathbf{v},$$

$\Downarrow$ [assuming, as necessary for oscillations, that $m_i \neq m_j$] $\Downarrow$

$$\mathbf{p}'_i - \mathbf{p}'_j = \left(E'_j - E'_i\right) \mathbf{v} = \Gamma_\mathbf{v} \left(E_j - E_i\right) \mathbf{v} \neq 0.$$

Treating the Lorentz transformation as active, we conclude that the EM assumption cannot be applied to the non-monoenergetic ν beams (the case in real-life experiments).

* A similar objection exists against the alternative equal-energy assumption; in that case

$$E'_i - E'_j = \Gamma_\mathbf{v} \left(\mathbf{p}_j - \mathbf{p}_i\right) \mathbf{v} \neq 0, \quad \left|\mathbf{p}'_i - \mathbf{p}'_j\right| = \sqrt{\left|\mathbf{p}_i - \mathbf{p}_j\right|^2 + \Gamma_\mathbf{v}^2 \left[\left(\mathbf{p}_i - \mathbf{p}_j\right) \mathbf{v}\right]^2} \neq 0.$$

* Can the EM (or EE) assumption be at least a good approximation? Alas, no, it cannot.

> Let ν_μs arise from $\pi_{\mu 2}$ decays. If the pion beam has a wide momentum spectrum – from subrelativistic to ultrarelativistic (as it is, e.g., for cosmic-ray particles), the EM (or EE) condition cannot be valid even approximately within the whole spectral range of the pion neutrinos.

Light-ray approximation

The propagation time T is, by assumption, equal to the distance L traveled by the neutrino between production and detection points. But, if the massive neutrino components have the same momentum $\mathbf{p}_\nu$, their velocities are in fact different:

$$\mathbf{v}_i = \frac{\mathbf{p}_\nu}{\sqrt{\mathbf{p}_\nu^2 + m_i^2}} \quad \Longrightarrow \quad |\mathbf{v}_i - \mathbf{v}_j| \approx \frac{\Delta m^2_{ji}}{2E_\nu^2}.$$

One may naively expect that during the time T the neutrino ν_i travels the distance $L_i = |\mathbf{v}_i|T$; therefore, there must be a spread in distances of each neutrino pair

$$\delta L_{ij} = L_i - L_j \approx \frac{\Delta m^2_{ji}}{2E_\nu^2}\, L, \quad \text{where} \quad L = cT = T.$$

Δm^2_{ji}	E_ν	L	L_{ij}	$\lvert\delta L_{ij}\rvert$
Δm^2_{23}	1 GeV	$2R_\oplus$	$0.1R_\oplus$	$\sim 10^{-12}$ cm
Δm^2_{23}	1 TeV	$R_G \sim 100$ kps	$100R_\oplus$	$\sim 10^{-4}$ cm
Δm^2_{21}	1 MeV	1 AU	$0.25R_\oplus$	$\sim 10^{-3}$ cm

The values of δL_{ij} listed in the Table seem to be **fantastically** small. But

Are they sufficiently small to preserve the coherence in any circumstance?

In other words:

What is the natural scale of the distances and times?

Can light neutrinos oscillate into heavy ones or vise versa? [Can active neutrinos oscillate into sterile ones or vise versa?]

The naive QM answer is Yes. Why not? If, at least, both ν_α (light) and ν_s (heavy) are ultrarelativistic [$|\mathbf{p}_\nu| \gg \max(m_1, m_2, m_3, \ldots, M)$,] one obtains the same formula for the oscillation probability $P_{\alpha s}(L)$, since the QM formalism has no any limitation to the neutrino mass hierarchy. Moreover,

Possibility of such transitions is a basis for many speculations in astrophysics and cosmology.

But! Assume again that the neutrino source is $\pi_{\mu 2}$ decay and $M > m_\pi$. Then the transition $\nu_\alpha \to \nu_s$ in the pion rest frame is forbidden by the energy conservation. Therefore

There must be some limitations & flaws in the QM formula. What are they?

Do relic neutrinos oscillate?

Most likely, the lightest relic neutrinos are always relativistic or even ultrarelativistic, while the heavier ones are likely to become subrelativistic and then non-relativistic as the Universe expands. The naive QM approach does not know how to handle nonrelativistic neutrinos, much less how to handle a nontrivial set of mixed relativistic and nonrelativistic neutrino states.[a]

Does the motion of the neutrino source affect the transition probabilities?

To answer these and similar questions [try to add to their list]

one has to unload the UR approximation & develop a covariant formalism.

[a] Since neutrinos with different masses come from very different LSS (see **2.6**, p. 165) the problem may seem academic (it's pretty obvious that relic neutrinos don't oscillate now). But the correct theory (not intuition) should be able to work with any set of states, otherwise it turns into "Trishka's Coat" (rob Peter to pay Paul).

In the QFT approach: the effective (most probable) energies and momenta of virtual ν_is are *found to be* functions of the masses, most probable momenta and momentum spreads of all particles (wave packets) involved into the neutrino production and detection processes.
In particular, in the two limiting cases – ultrarelativistic (UR) and nonrelativistic (NR):

Ultrarelativistic case

$(|q^0_{s,d}| \sim |\mathbf{q}_{s,d}| \gg m_i)$

$$\begin{cases} E_i = E_\nu \left[1 - \mathfrak{n} r_i - \mathfrak{m} r_i^2 + \ldots\right], \\ |\mathbf{p}_i| = E_\nu \left[1 - (\mathfrak{n}+1)\, r_i - \left(\mathfrak{m} + \mathfrak{n} + \frac{1}{2}\right) r_i^2 + \ldots\right], \\ v_i = 1 - r_i - \left(2\mathfrak{n} + \frac{1}{2}\right) r_i^2 + \ldots < 1, \end{cases}$$

Nonrelativistic case

$(|q^0_{s,d}| \sim m_i \gg |\mathbf{q}_{s,d}|)$

$$\begin{cases} E_i = m_i + \dfrac{m_i v_i^2}{2}\left(1 + \dfrac{3}{4}\delta_i + \ldots\right), \\ |\mathbf{p}_i| = m_i v_i \left(1 + \dfrac{1}{2}\delta_i + \ldots\right), \\ v_i \approx \dfrac{\boldsymbol{\varrho}_i l}{1 + \varrho_i^0} \ll 1, \end{cases}$$

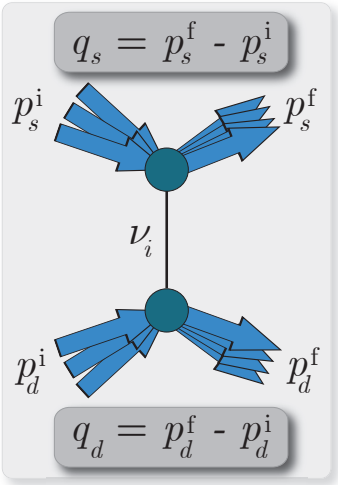

$$E_\nu \approx q_s^0 \approx -q_d^0, \quad r_i = \frac{m_i^2}{2E_\nu^2} \ll 1 \text{ (UR)},$$

$$\varrho_i^\mu = \frac{1}{m_i \mathscr{R}}\left[\widetilde{\Re}_s^{\mu 0}\left(m_i - q_s^0\right) + \widetilde{\Re}_d^{\mu 0}\left(m_i + q_d^0\right) - \widetilde{\Re}_s^{\mu k} q_s^k + \widetilde{\Re}_d^{\mu k} q_d^k\right], \quad |\varrho_i^\mu| \ll 1 \text{ (NR)}.$$

Definite momentum assumption

In the naive QM approach, the assumed definite momenta of neutrinos (both ν_α and ν_i) imply that the spatial coordinates of neutrino production ($\mathbf{X}_s$) and detection ($\mathbf{X}_d$) are fully uncertain (Heisenberg's principle).

$\Downarrow$

The distance $L = |\mathbf{X}_d - \mathbf{X}_s|$ is uncertain too, that makes the standard QM formula for the flavor transition probabilities to be strictly speaking senseless.

In the correct theory, the neutrino momentum uncertainty $\delta|\mathbf{p}_\nu|$ must be at least of the order of $\min(1/D_s, 1/D_d)$, where D_s and D_d are the characteristic dimensions of the source and detector "machines" along the neutrino beam.

$\Downarrow$

The neutrino states must be some wave packets (WP) [though having very small spreads] dependent, in general, on the quantum states of the particles [or, more exactly, also WPs] which participate in the production and detection processes.

In the QFT approach: the effective WPs of virtual UR ν_is are *found to be*

$$\psi_i^{(*)} = \exp\left\{\pm i(p_i X_{s,d}) - \frac{\widetilde{\mathfrak{D}}_i^2}{E_\nu^2}\left[(p_i X)^2 - m_i^2 X^2\right]\right\}, \qquad X = X_d - X_s,$$

where $p_i = (E_i, \mathbf{p}_i)$ and $X_{s,d}$ are the 4-vectors which characterize the space-time location of the ν production and detection processes, while $\widetilde{\mathfrak{D}}_i$ are certain (in general, complex-valued) functions of the masses, mean momenta and momentum spreads of all particles involved into these processes. [$\widetilde{\mathfrak{D}}_i/E_\nu$ and thereby ψ_i are Lorentz invariants.]

15.6 The aims and concepts of the field-theoretical approach.

The main purposes:

To define the domain of applicability of the standard quantum-mechanical (QM) theory of vacuum neutrino oscillations and obtain the QFT corrections to it.

The basic concepts:

- The "ν-oscillation" phenomenon in QFT is nothing else than a result of interference of the macroscopic Feynman diagrams perturbatively describing the lepton number violating processes with the massive neutrino fields as internal lines (propagators).
- The external lines of the macrodiagrams are wave packets rather than plane waves (therefore the standard S matrix approach should be revised).
- The external wave packet states are the covariant superpositions of the standard one-particle Fock states, satisfying a correspondence principle.

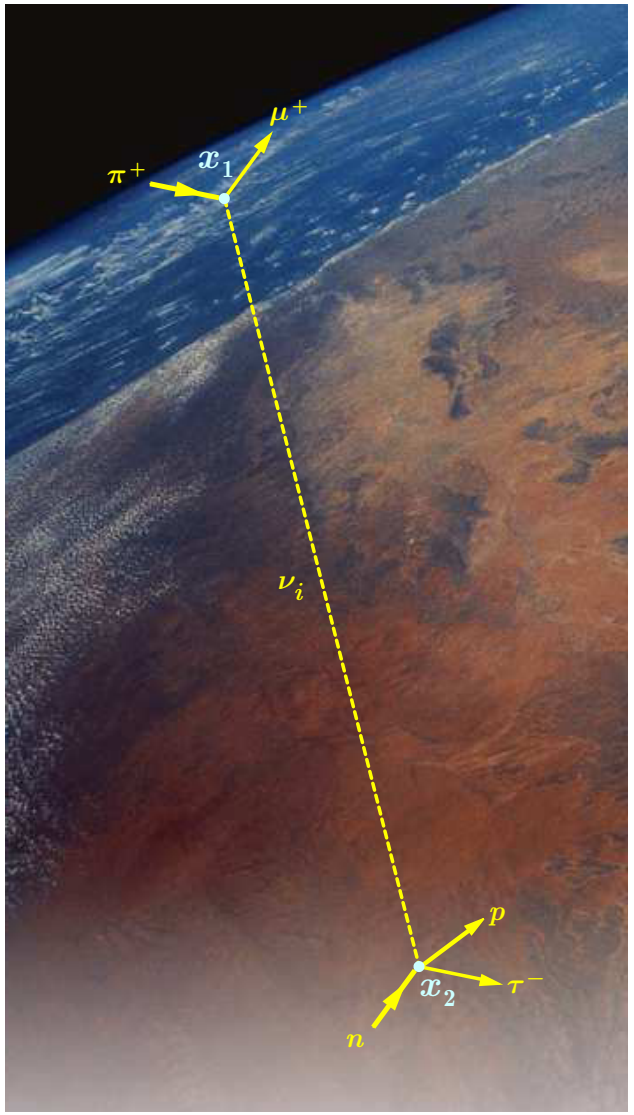

References: D. V. Naumov & VN, J. Phys. G **37** (2010) 105014, arXiv:1008.0306 [hep-ph]; Russ. Phys. J. **53** (2010) 549–574; arXiv:1110.0989 [hep-ph]; ЭЧАЯ **51** (2020) 1–209 [Phys. Part. Nucl. **51** (2020) 1–106].

15.7 A sketch of the approach.

Let us first consider the basics of the QFT approach using the simplest example.

15.7.1 QFT approach by the example of the reaction $\pi \oplus n \to \mu \oplus \tau p$.

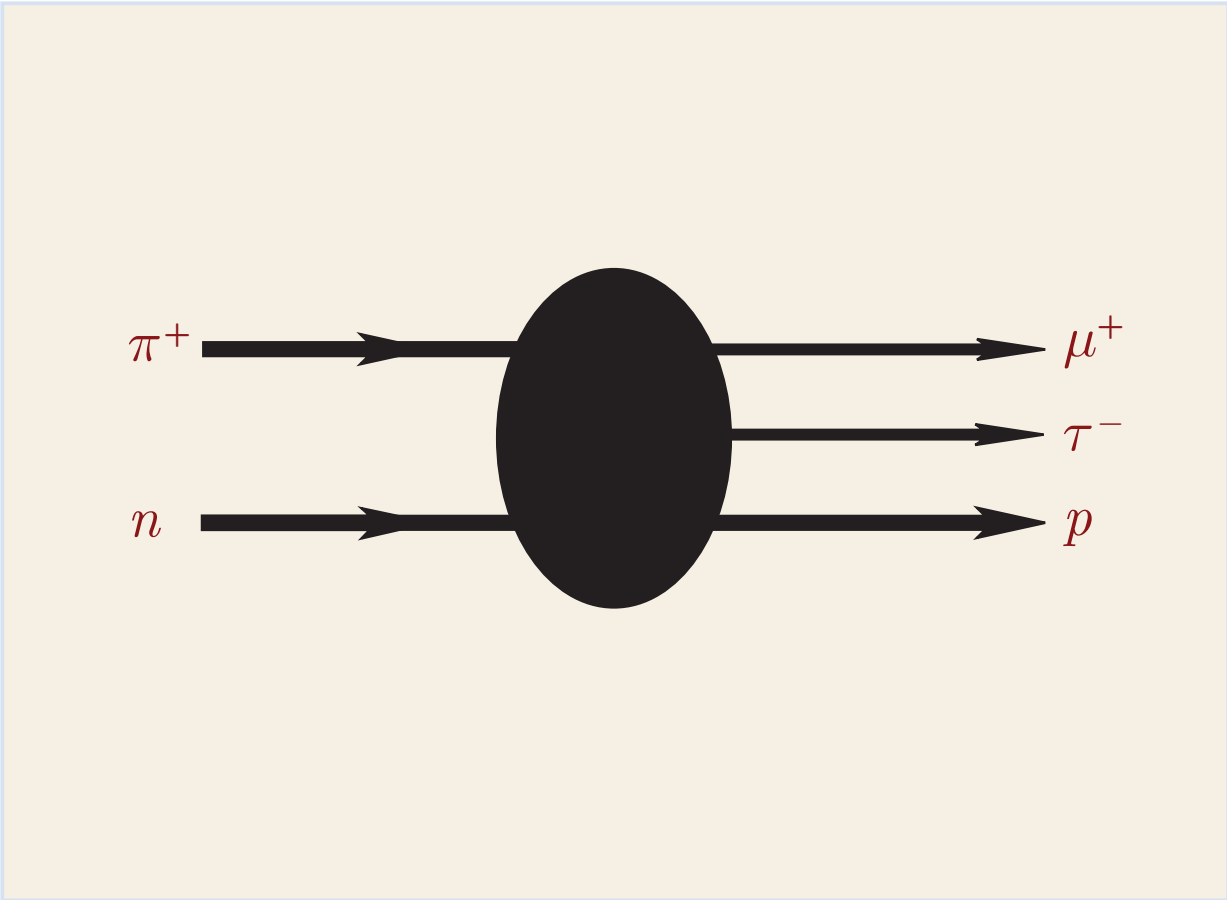

The rare reactions $\pi^+ \oplus n \to \mu^+ \oplus \tau^- p + \ldots$ were (indirectly) detected by several underground experiments (Kamiokande, IMB, Super-Kamiokande) with atmospheric neutrinos. In 2010, OPERA experiment (INFN, LNGS) with the CNGS neutrino beam announced the direct observation of the first τ^- candidate event; six candidates were recorded in several years of the detector operation.

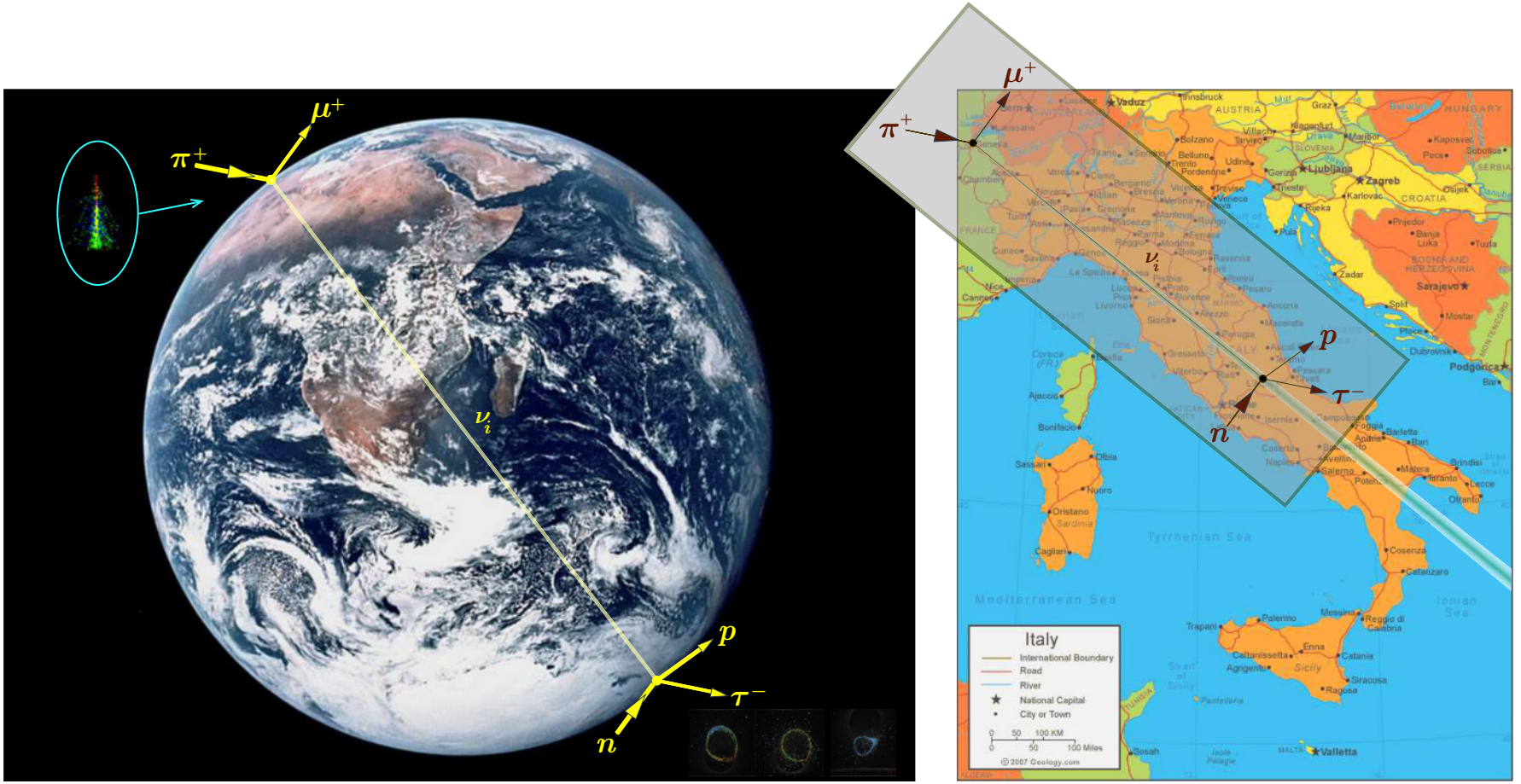

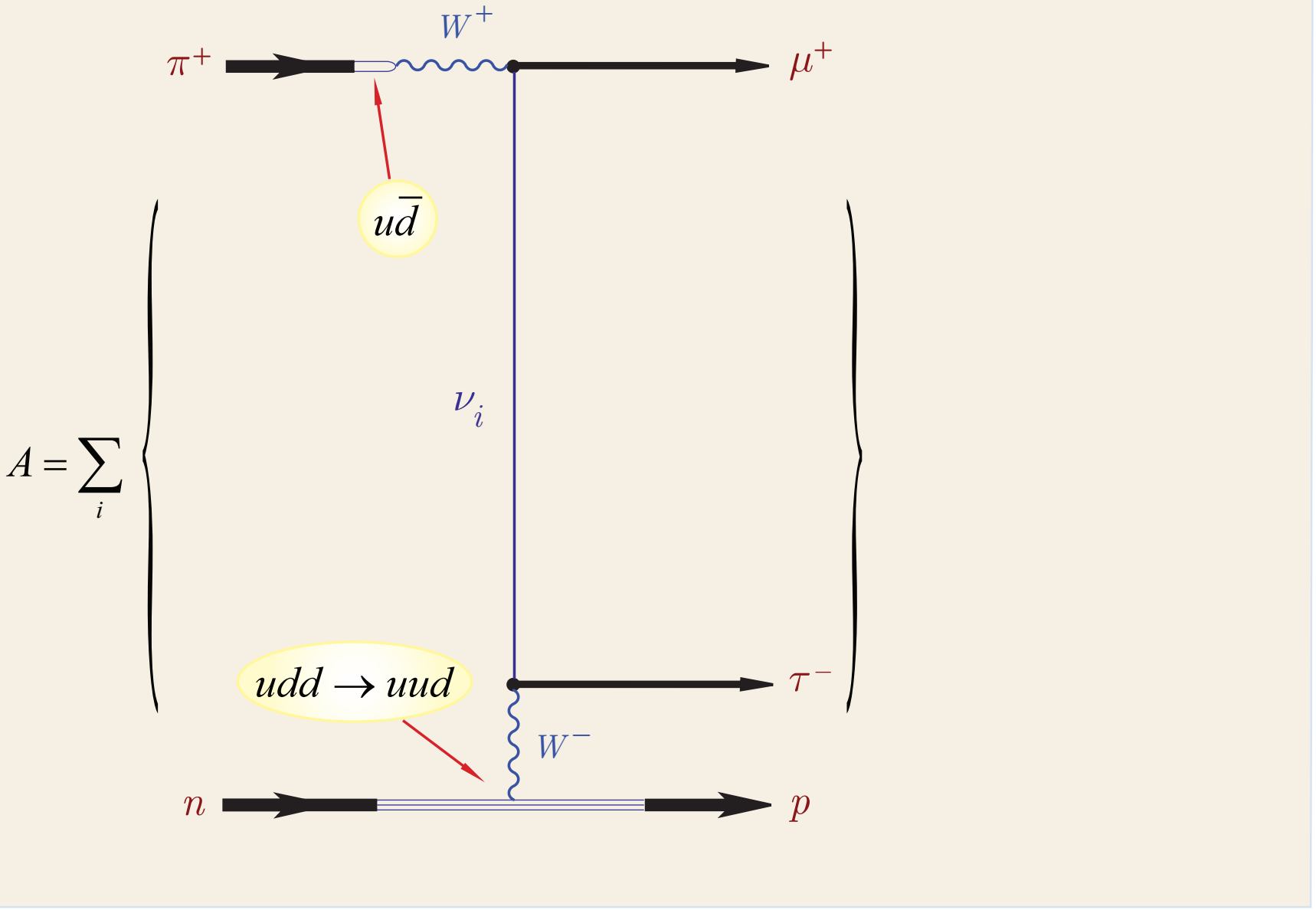
W^+
π^+
μ^+
$u\bar{d}$
$A = \sum_i$
ν_i
$udd \to uud$
τ^-
W^-
n
p

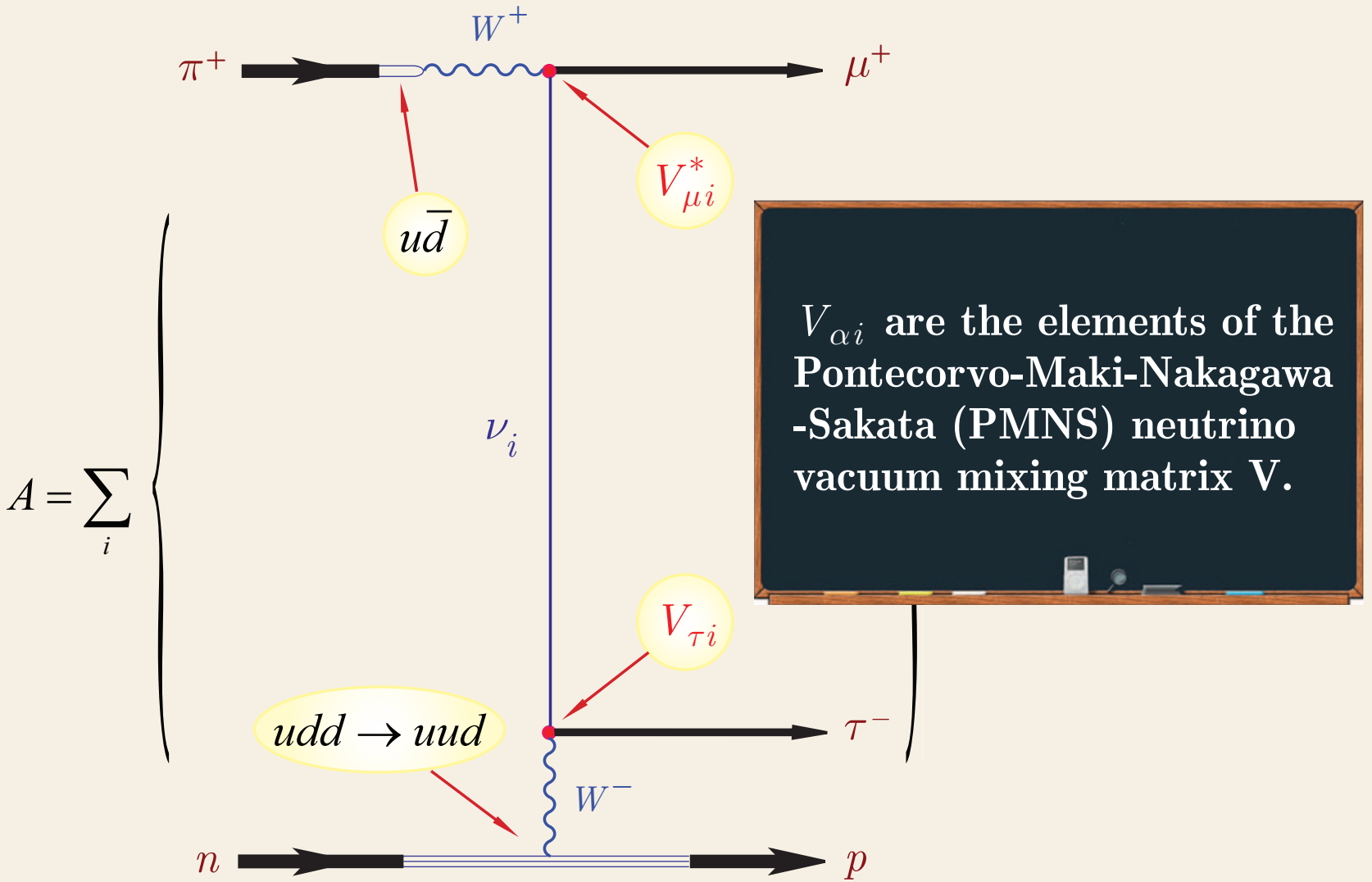

$V_{\alpha i}$ are the elements of the Pontecorvo-Maki-Nakagawa-Sakata (PMNS) neutrino vacuum mixing matrix V.

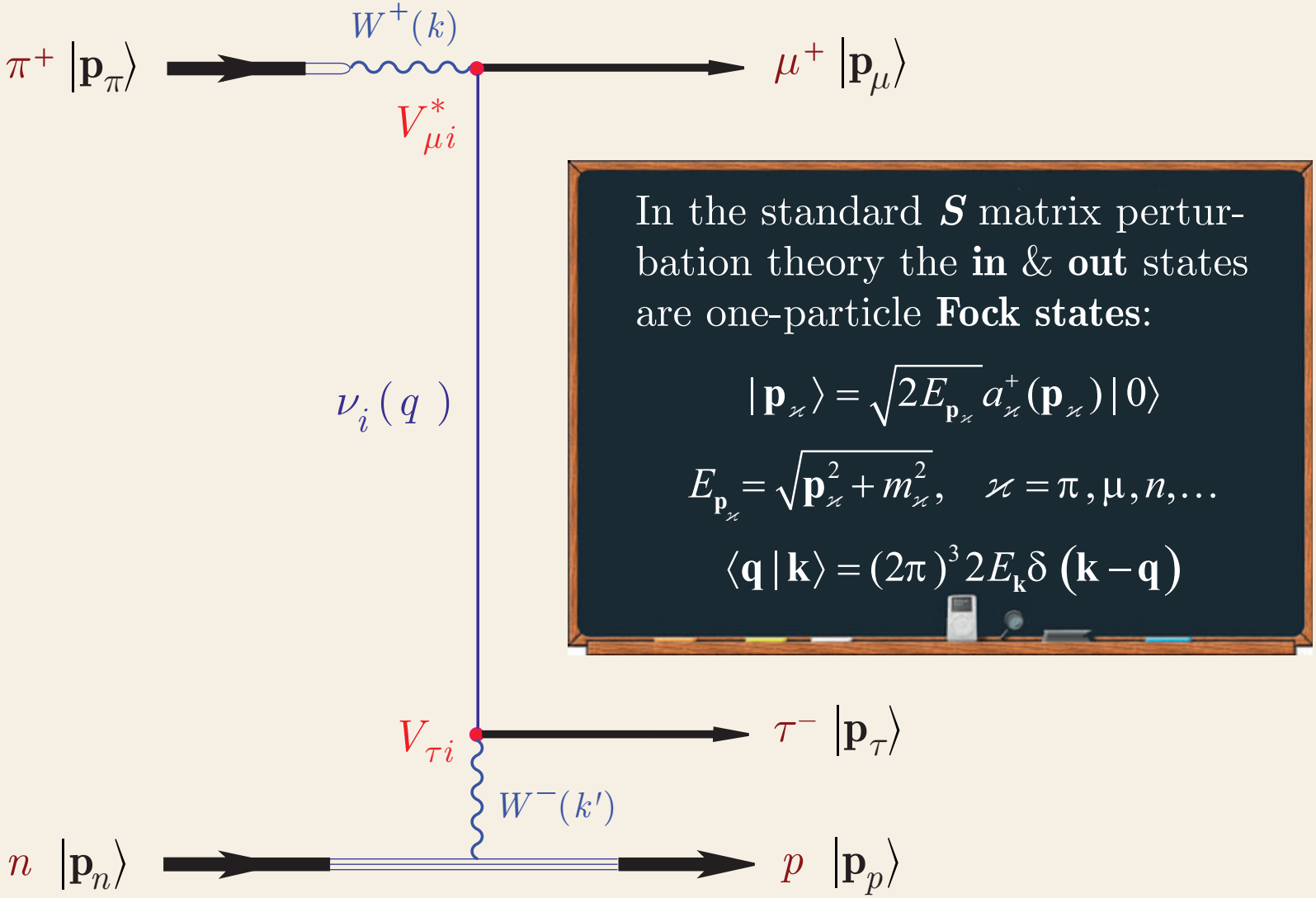

In the standard $\boldsymbol{S}$ matrix perturbation theory the **in** & **out** states are one-particle **Fock states**:

$$|\mathbf{p}_\varkappa\rangle = \sqrt{2E_{\mathbf{p}_\varkappa}}\, a^+_\varkappa(\mathbf{p}_\varkappa)\,|0\rangle$$

$$E_{\mathbf{p}_\varkappa} = \sqrt{\mathbf{p}^2_\varkappa + m^2_\varkappa}, \quad \varkappa = \pi, \mu, n, \ldots$$

$$\langle \mathbf{q}\,|\,\mathbf{k}\rangle = (2\pi)^3 2E_{\mathbf{k}}\,\delta\left(\mathbf{k}-\mathbf{q}\right)$$

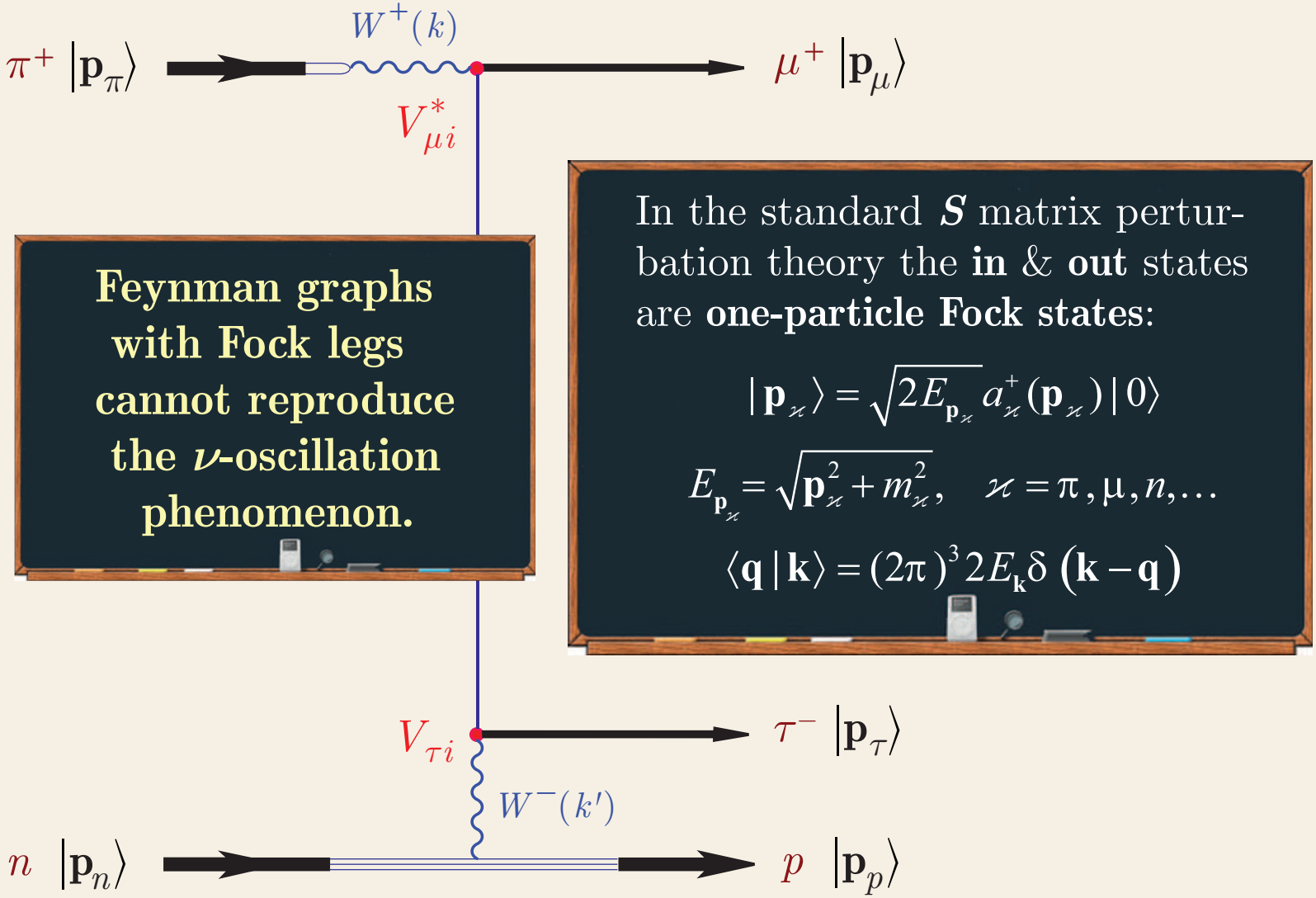
$\pi^+ \,|\mathbf{p}_\pi\rangle$
$W^+(k)$
$\mu^+ \,|\mathbf{p}_\mu\rangle$
$V^*_{\mu i}$
Feynman graphs with Fock legs cannot reproduce the ν-oscillation phenomenon.
In the standard $\boldsymbol{S}$ matrix perturbation theory the **in** & **out** states are **one-particle Fock states**:
$|\mathbf{p}_\varkappa\rangle = \sqrt{2E_{\mathbf{p}_\varkappa}}\, a^+_\varkappa(\mathbf{p}_\varkappa)\,|0\rangle$
$E_{\mathbf{p}_\varkappa} = \sqrt{\mathbf{p}^2_\varkappa + m^2_\varkappa}, \quad \varkappa = \pi, \mu, n, \ldots$
$\langle \mathbf{q}\,|\,\mathbf{k}\rangle = (2\pi)^3 2E_{\mathbf{k}}\delta\,(\mathbf{k}-\mathbf{q})$
$V_{\tau i}$
$\tau^- \,|\mathbf{p}_\tau\rangle$
$W^-(k')$
$n \,|\mathbf{p}_n\rangle$
$p \,|\mathbf{p}_p\rangle$

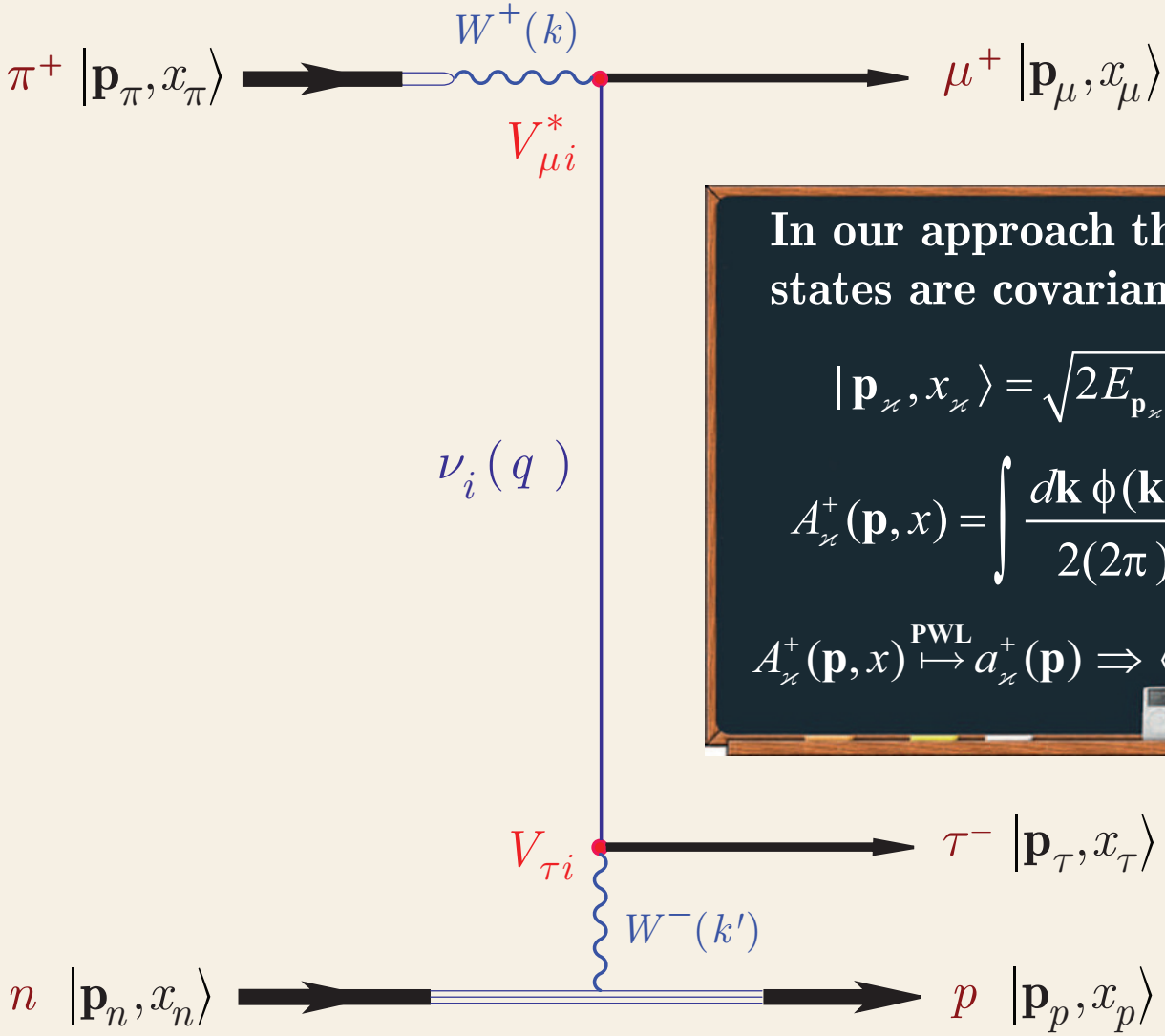

In our approach the in and out states are covariant wave packets:

$$|\mathbf{p}_\varkappa, x_\varkappa\rangle = \sqrt{2E_{\mathbf{p}_\varkappa}}\, A^+_\varkappa(\mathbf{p}_\varkappa, x_\varkappa)\,|0\rangle$$

$$A^+_\varkappa(\mathbf{p}, x) = \int \frac{d\mathbf{k}\,\phi(\mathbf{k},\mathbf{p})e^{i(k-p)x}}{2(2\pi)^3\sqrt{E_\mathbf{k}E_\mathbf{p}}}\, a^+_\varkappa(\mathbf{k})$$

$$A^+_\varkappa(\mathbf{p}, x) \overset{\text{PWL}}{\mapsto} a^+_\varkappa(\mathbf{p}) \Rightarrow \langle \mathbf{p}, x\,|\,\mathbf{p}, x\rangle = 2m\mathrm{V}_\star$$

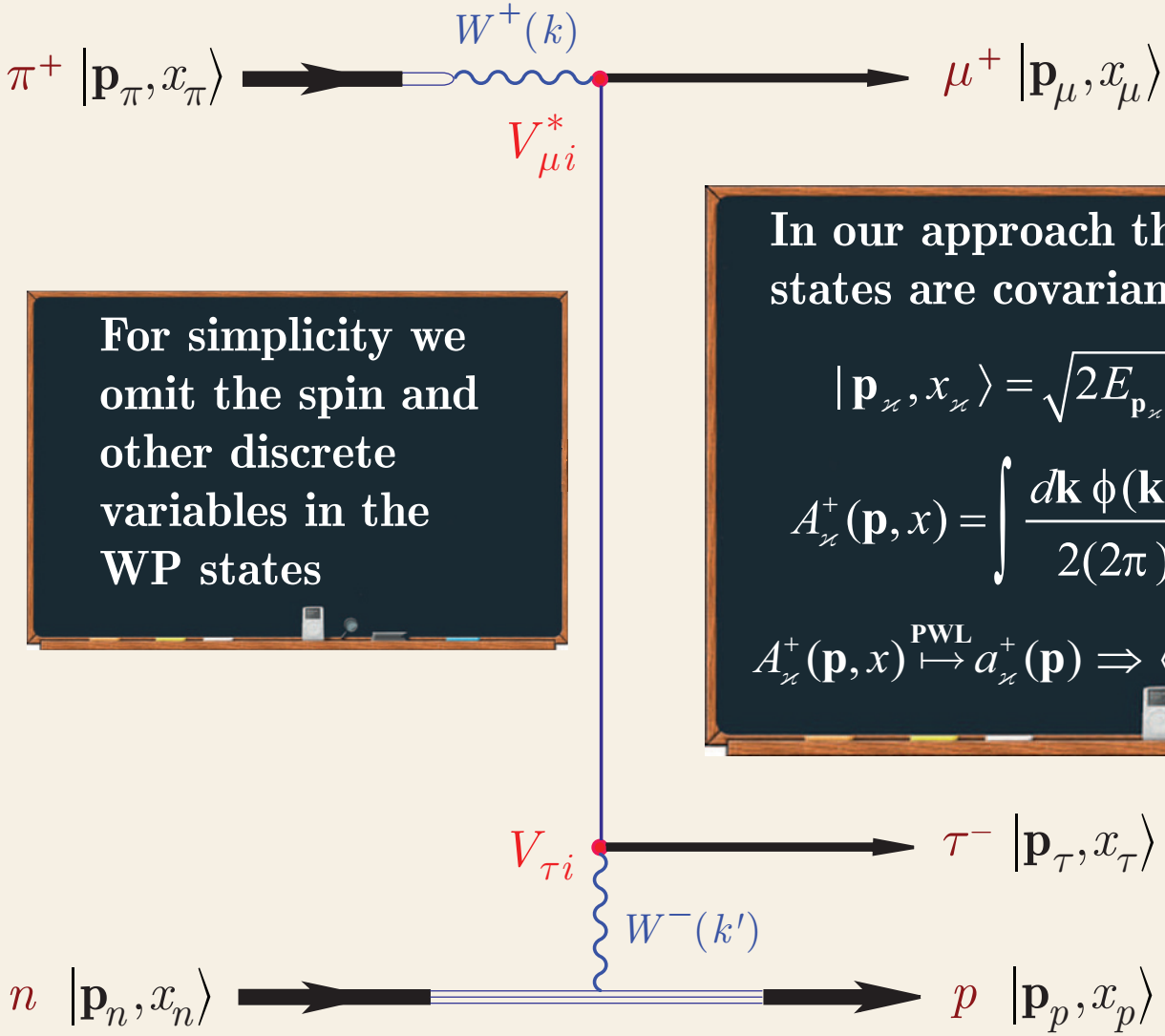

For simplicity we omit the spin and other discrete variables in the WP states

In our approach the in and out states are covariant wave packets:

$$|\mathbf{p}_\varkappa, x_\varkappa\rangle = \sqrt{2E_{\mathbf{p}_\varkappa}}\, A^+_\varkappa(\mathbf{p}_\varkappa, x_\varkappa)\,|0\rangle$$

$$A^+_\varkappa(\mathbf{p}, x) = \int \frac{d\mathbf{k}\,\phi(\mathbf{k},\mathbf{p})e^{i(k-p)x}}{2(2\pi)^3\sqrt{E_\mathbf{k}E_\mathbf{p}}}\, a^+_\varkappa(\mathbf{k})$$

$$A^+_\varkappa(\mathbf{p}, x) \overset{\text{PWL}}{\mapsto} a^+_\varkappa(\mathbf{p}) \Rightarrow \langle \mathbf{p}, x\,|\,\mathbf{p}, x\rangle = 2m\mathrm{V}_\star$$

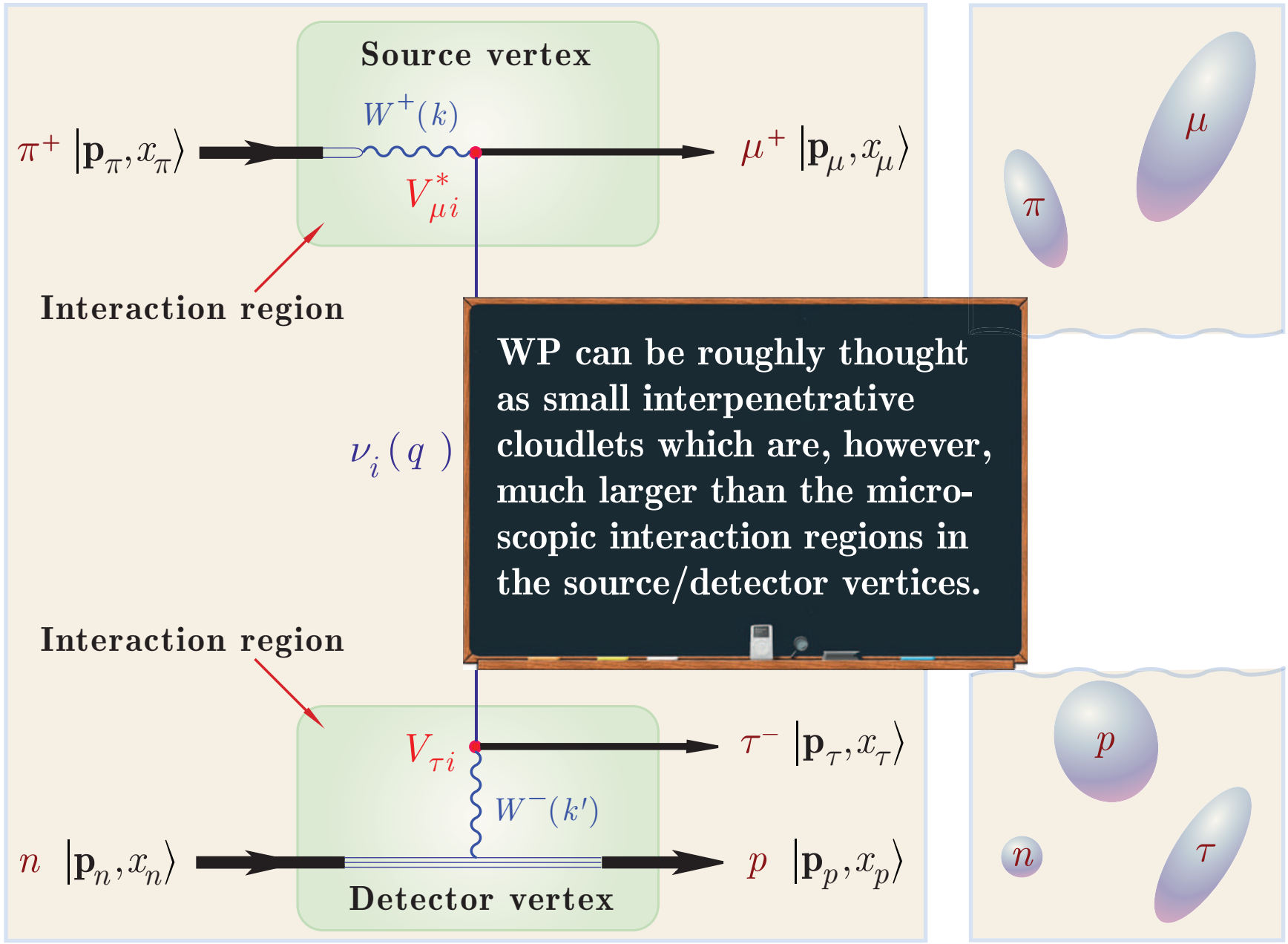
Source vertex
$W^+(k)$
$\pi^+ \ |\mathbf{p}_\pi, x_\pi\rangle$
$\mu^+ \ |\mathbf{p}_\mu, x_\mu\rangle$
$V^*_{\mu i}$
Interaction region
$\nu_i(q)$
WP can be roughly thought as small interpenetrative cloudlets which are, however, much larger than the microscopic interaction regions in the source/detector vertices.
Interaction region
$V_{\tau i}$
$\tau^- \ |\mathbf{p}_\tau, x_\tau\rangle$
$W^-(k')$
$n \ |\mathbf{p}_n, x_n\rangle$
$p \ |\mathbf{p}_p, x_p\rangle$
Detector vertex
μ
π
p
n
τ

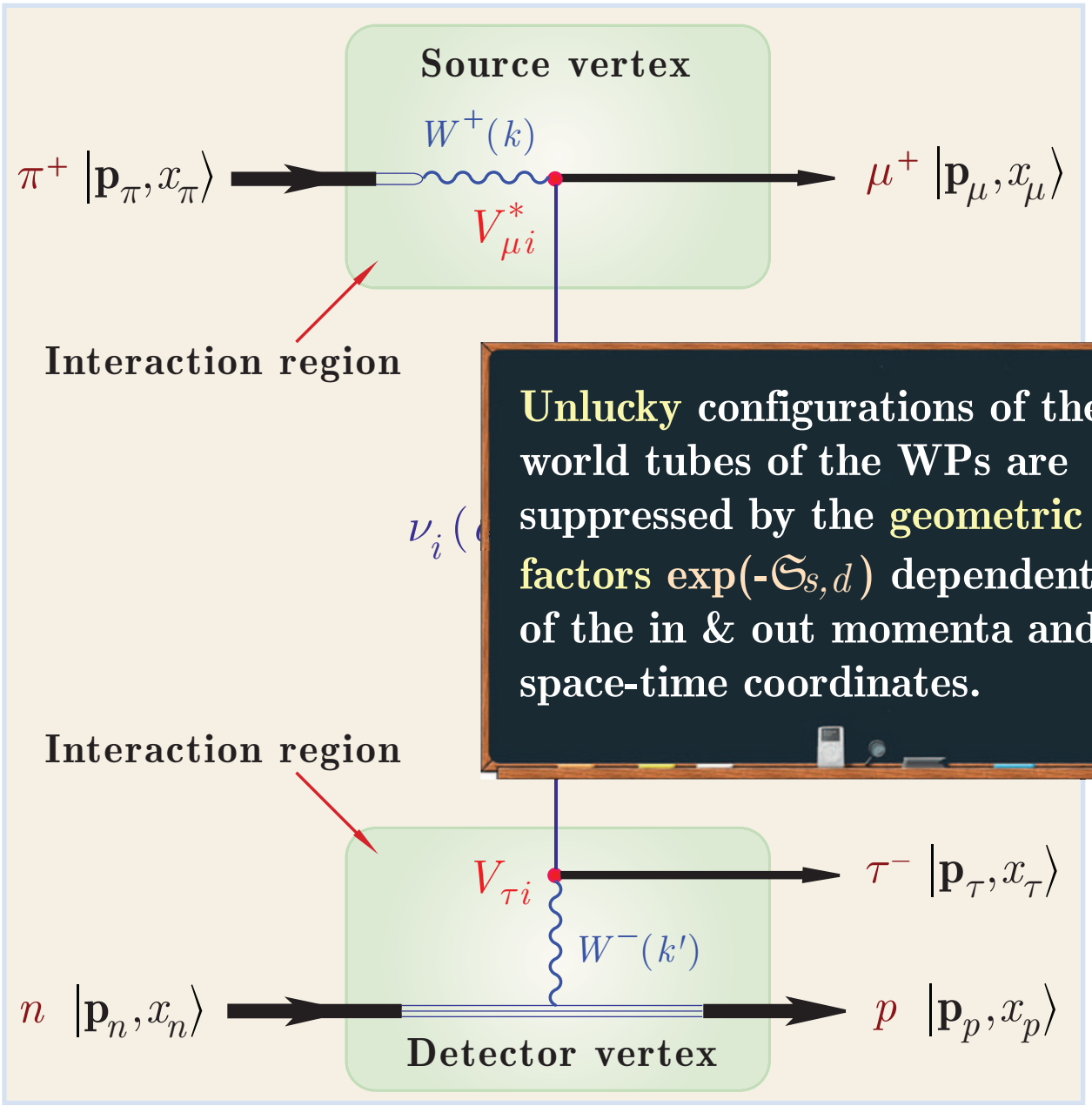
Source vertex
$W^+(k)$
$\pi^+ \ |\mathbf{p}_\pi, x_\pi\rangle$
$\mu^+ \ |\mathbf{p}_\mu, x_\mu\rangle$
$V^*_{\mu i}$
Interaction region
ν_i (
Unlucky configurations of the world tubes of the WPs are suppressed by the geometric factors exp(-$\mathfrak{S}_{s,d}$) dependent of the in & out momenta and space-time coordinates.
Interaction region
$V_{\tau i}$
$\tau^- \ |\mathbf{p}_\tau, x_\tau\rangle$
$W^-(k')$
$n \ |\mathbf{p}_n, x_n\rangle$
$p \ |\mathbf{p}_p, x_p\rangle$
Detector vertex

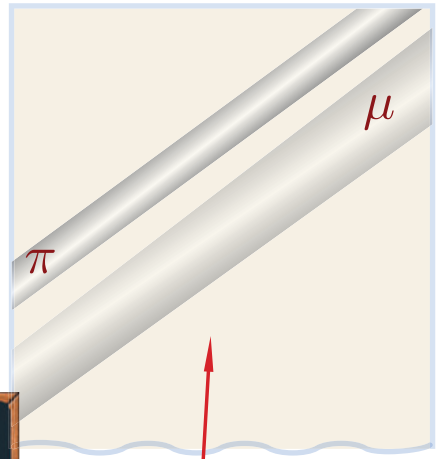
μ
π
$\propto \exp(-\mathfrak{S}_s) \ll 1$

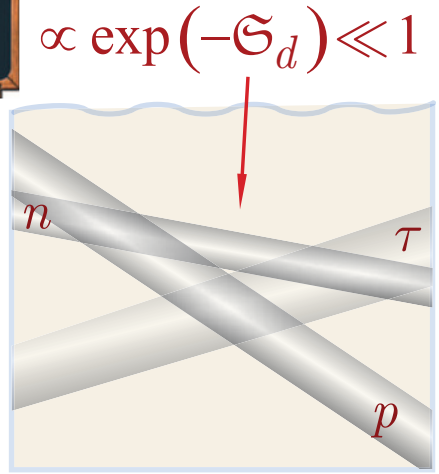
$\propto \exp(-\mathfrak{S}_d) \ll 1$
n
τ
p

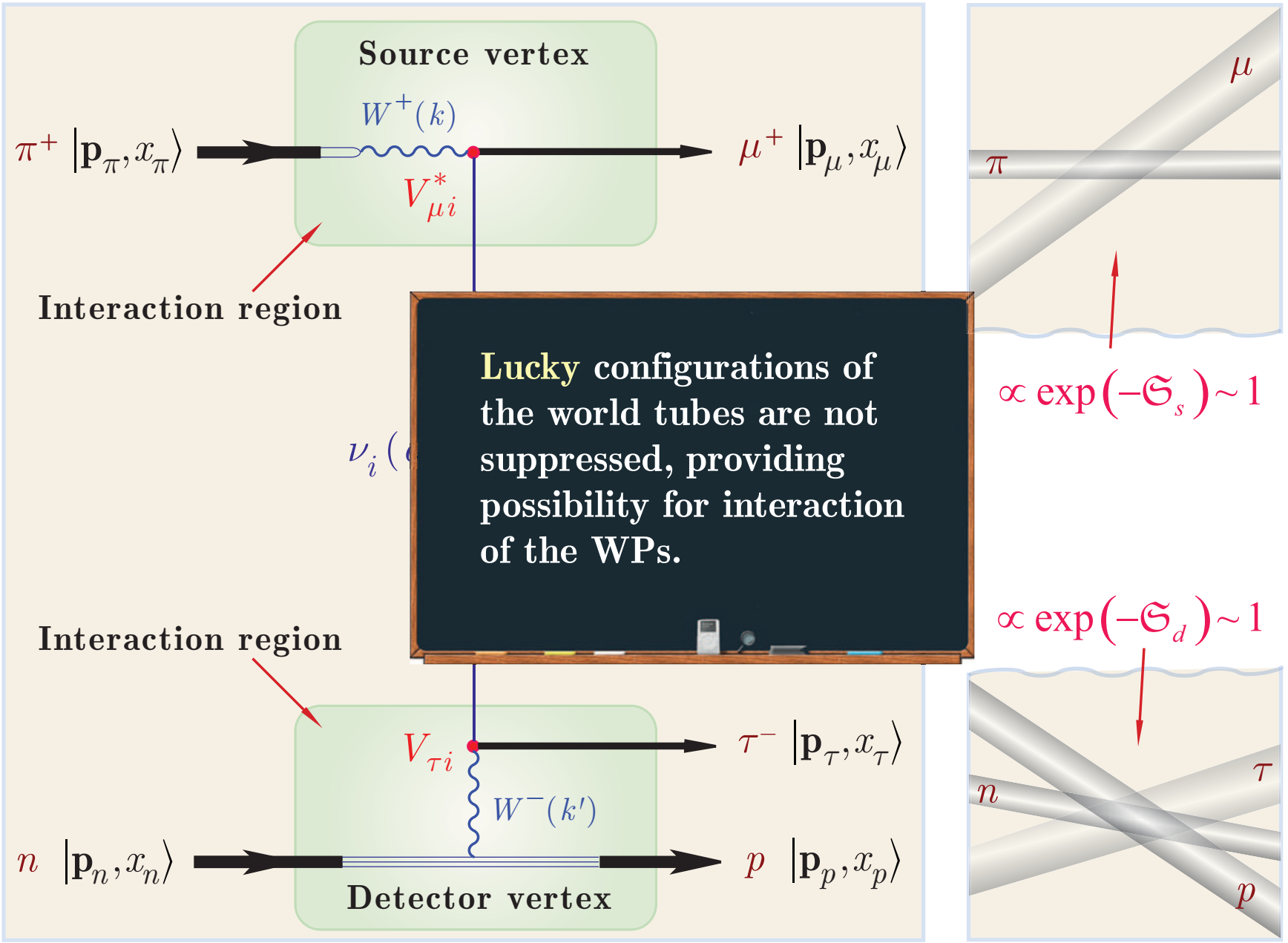
Source vertex
$W^+(k)$
$\pi^+ \ |\mathbf{p}_\pi, x_\pi\rangle$
$\mu^+ \ |\mathbf{p}_\mu, x_\mu\rangle$
$V^*_{\mu i}$
Interaction region
Lucky configurations of the world tubes are not suppressed, providing possibility for interaction of the WPs.
ν_i
Interaction region
$V_{\tau i}$
$\tau^- \ |\mathbf{p}_\tau, x_\tau\rangle$
$W^-(k')$
$n \ |\mathbf{p}_n, x_n\rangle$
$p \ |\mathbf{p}_p, x_p\rangle$
Detector vertex
μ
π
$\propto \exp(-\mathfrak{S}_s) \sim 1$
$\propto \exp(-\mathfrak{S}_d) \sim 1$
τ
n
p

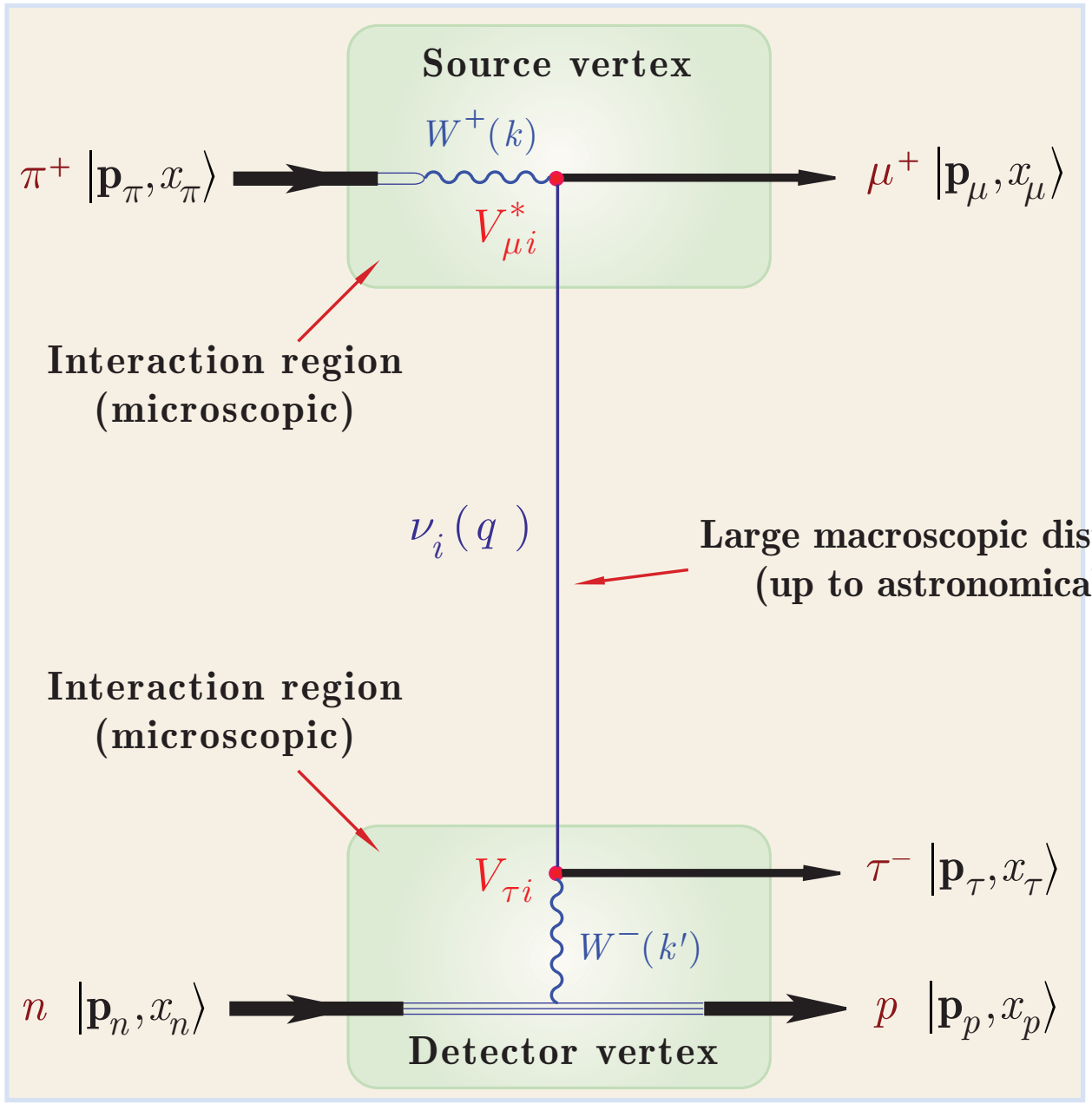
Source vertex
$W^+(k)$
$\pi^+ \ |\mathbf{p}_\pi, x_\pi\rangle$
$\mu^+ \ |\mathbf{p}_\mu, x_\mu\rangle$
$V^*_{\mu i}$
Interaction region
(microscopic)
$\nu_i\,(q\ )$
Large macroscopic distance
(up to astronomical)
Interaction region
(microscopic)
$V_{\tau i}$
$\tau^- \ |\mathbf{p}_\tau, x_\tau\rangle$
$W^-(k')$
$n \ |\mathbf{p}_n, x_n\rangle$
$p \ |\mathbf{p}_p, x_p\rangle$
Detector vertex

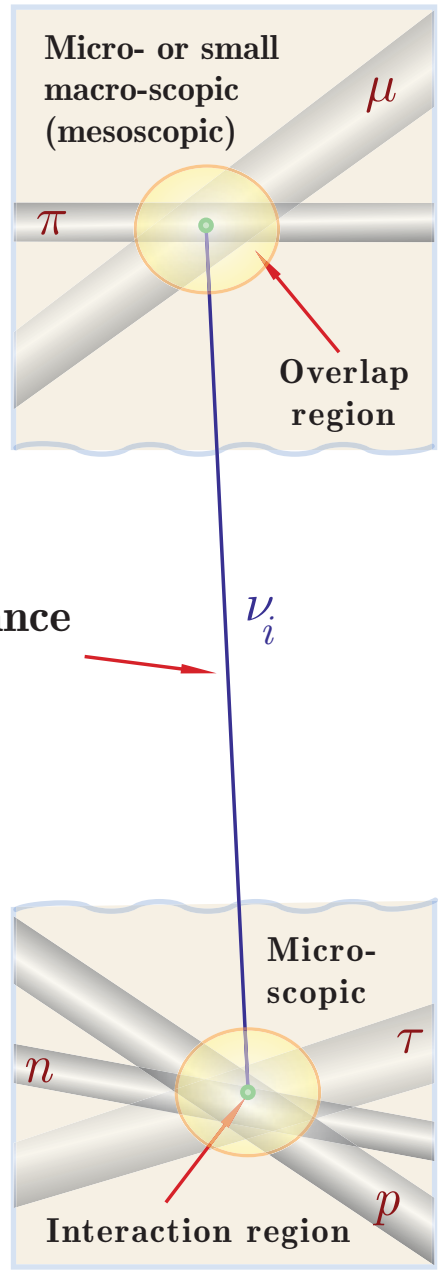
Micro- or small
macro-scopic
(mesoscopic)
μ
π
Overlap
region
ν_i
Micro-
scopic
τ
n
p
Interaction region

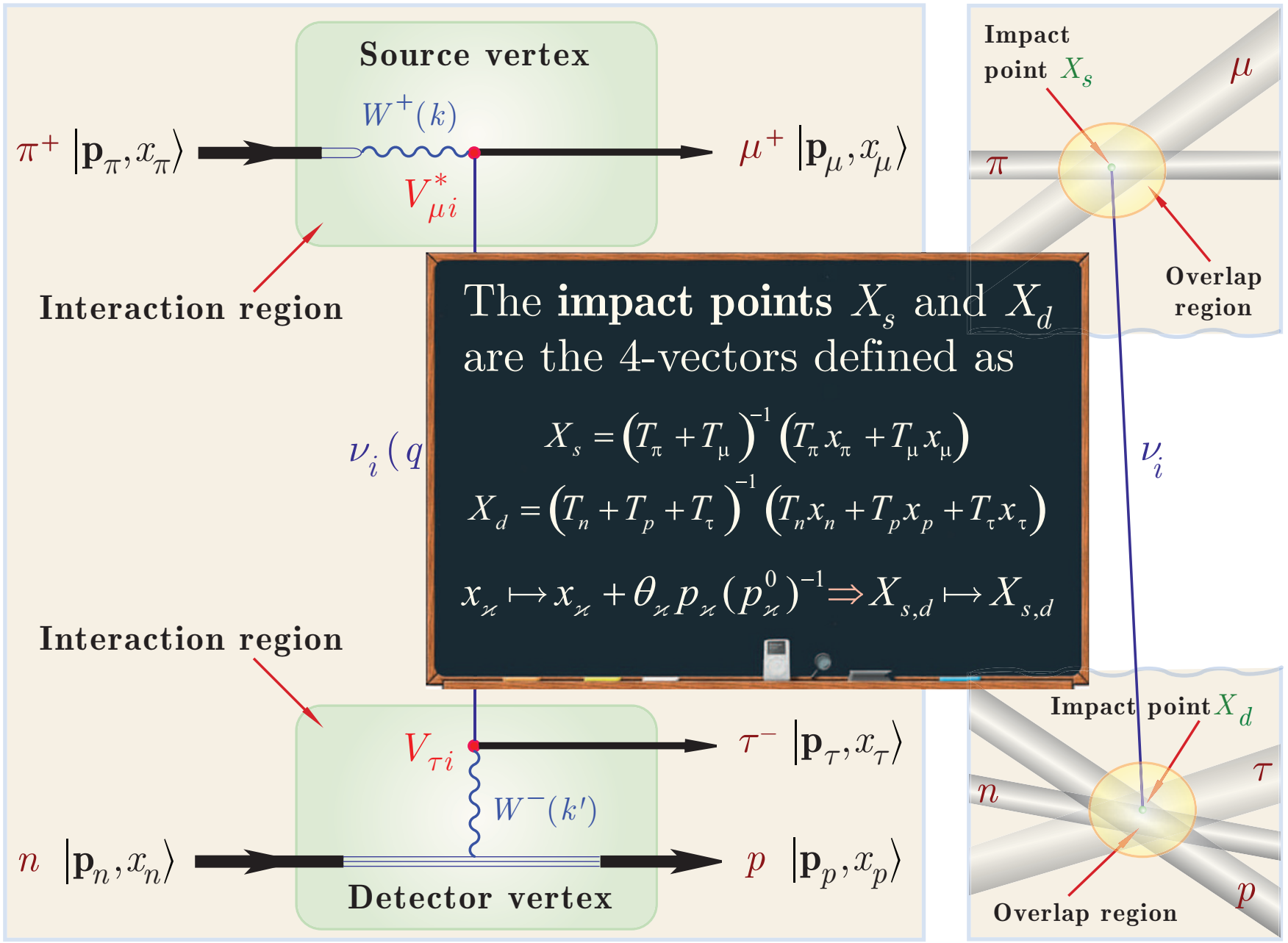
Source vertex
$W^+(k)$
$\pi^+ \ |\mathbf{p}_\pi, x_\pi\rangle$
$\mu^+ \ |\mathbf{p}_\mu, x_\mu\rangle$
$V^*_{\mu i}$
Interaction region
$\nu_i\,(q$
The impact points X_s and X_d are the 4-vectors defined as
$X_s = \left(T_\pi + T_\mu\right)^{-1}\left(T_\pi x_\pi + T_\mu x_\mu\right)$
$X_d = \left(T_n + T_p + T_\tau\right)^{-1}\left(T_n x_n + T_p x_p + T_\tau x_\tau\right)$
$x_\varkappa \mapsto x_\varkappa + \theta_\varkappa p_\varkappa (p^0_\varkappa)^{-1} \Rightarrow X_{s,d} \mapsto X_{s,d}$
Interaction region
$V_{\tau i}$
$\tau^- \ |\mathbf{p}_\tau, x_\tau\rangle$
$W^-(k')$
$n \ |\mathbf{p}_n, x_n\rangle$
$p \ |\mathbf{p}_p, x_p\rangle$
Detector vertex
Impact point X_s
μ
π
Overlap region
ν_i
Impact point X_d
τ
n
p
Overlap region

15.7.2 Space-time scales.

In the covariant WP approach there are several space-time scales:

- $T_I^{s,d}$ and $R_I^{s,d}$ – microscopic interaction time and radius defined by the Lagrangian.
- $T_O^{s,d}$ and $R_O^{s,d}$ – microscopic or small macroscopic dimensions of the overlap space-time regions of the interacting **in** and **out** packets in the source and detector vertices, defined by the effective dimensions of the packets.

  > The suppression of the "unlucky" configurations of world tubes of the external packets is governed by the geometric factor in the amplitude:
  >
  > $$\exp\left[-\left(\mathfrak{S}_s+\mathfrak{S}_d\right)\right],$$
  >
  > where $\mathfrak{S}_{s,d}$ are the positive Lorentz and translation invariant functions of $\{\mathbf{p}_\varkappa\}$ and $\{x_\varkappa\}$. In the simplest one-parameter model of WP (relativistic Gaussian packet)
  >
  > $$\mathfrak{S}_{s,d}=\sum\sigma_\varkappa^2\left|\boldsymbol{b}_\varkappa^\star\right|^2,\quad \varkappa\in S,D,$$
  >
  > where $\sigma_\varkappa$ are the momentum speeds of the packet $\varkappa$ and $\boldsymbol{b}_\varkappa^\star$ is the classical impact vector in the proper frame of the packet $\varkappa$ relative to the corresponding impact point.

- $T=X_d^0-X_s^0$ and $L=|\mathbf{X}_d-\mathbf{X}_s|$ – large macroscopic neutrino time of flight and way between the impact points X_s and X_d.
  For light neutrinos, the impact points lie very close to the light cone $T^2=L^2$.
- In usual circumstance (terrestrial experiments) $T_I^{s,d}\ll T_O^{s,d}\ll T$ and $R_I^{s,d}\ll R_O^{s,d}\ll L$.

15.7.3 Examples of macroscopic diagrams.

- The pp fusion.

The first reaction of the pp I branch

$$^1\mathrm{H} + {}^1\mathrm{H} \to {}^2\mathrm{D} + e^+ + \nu_e \quad (E_\nu < 420 \text{ keV})$$

lights the Sun (see Sect. **28.1**, p. 711) and can be detected in the Ga-Ge detectors like SAGE (Sect. **34**) and GALLEX (Sect. **35**).

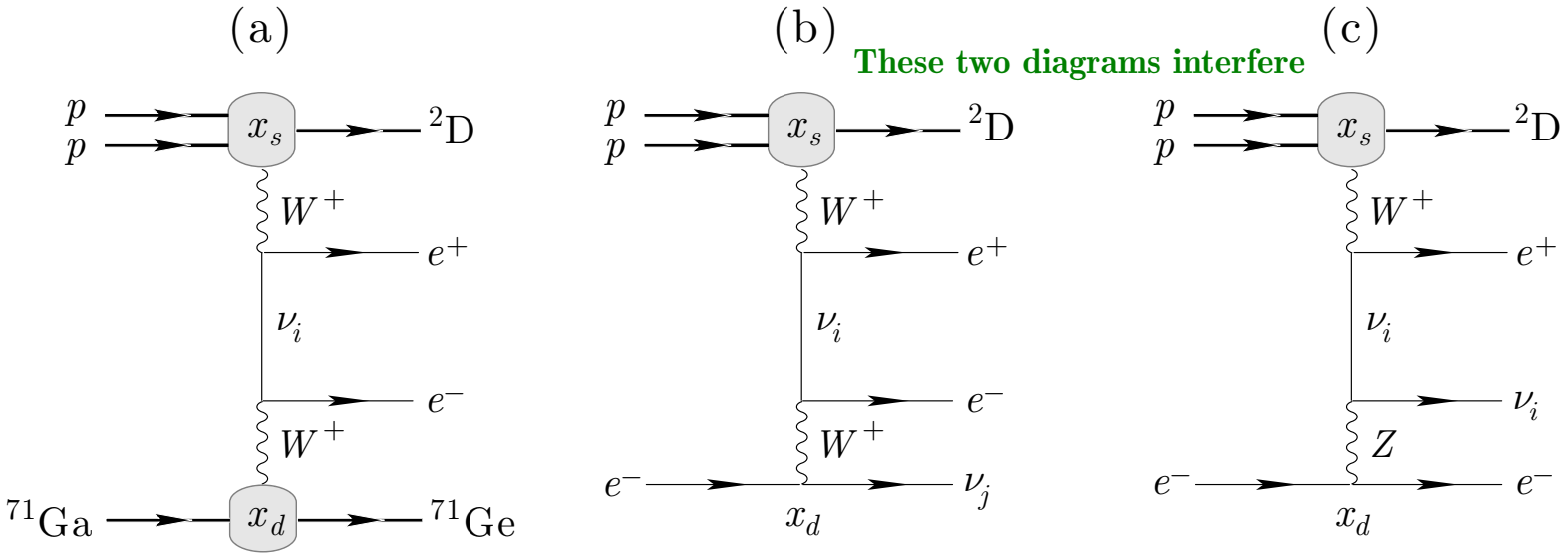

The Figure illustrates the detection of pp neutrinos with gallium (a) and electron (b,c) targets. Unfortunately, the final electron energies in the reactions (b,c) are too low to be detected by Cherenkov method (see Sect. **36.1**, p. 771).

- The *pep* fusion.

The reaction

$$^1\mathrm{H} + {}^1\mathrm{H} + e^- \to {}^2\mathrm{D} + \nu_e \quad (E_\nu = 1.44 \text{ MeV})$$

accounts for about 0.25% of the Deuterium created in the Sun in the *pp* chain (see Sect. **28.2**, p. 713). It has a characteristic time scale $\sim 10^{12}$ yr that is larger than the age of the Universe. So it is *insignificant* in the Sun as far as energy generation is concerned. Enough *pep* fusions happen to produce a detectable number of neutrinos in Ga-Ge detectors. Hence the reaction must be accounted for by those interested in the *solar neutrino problem*.

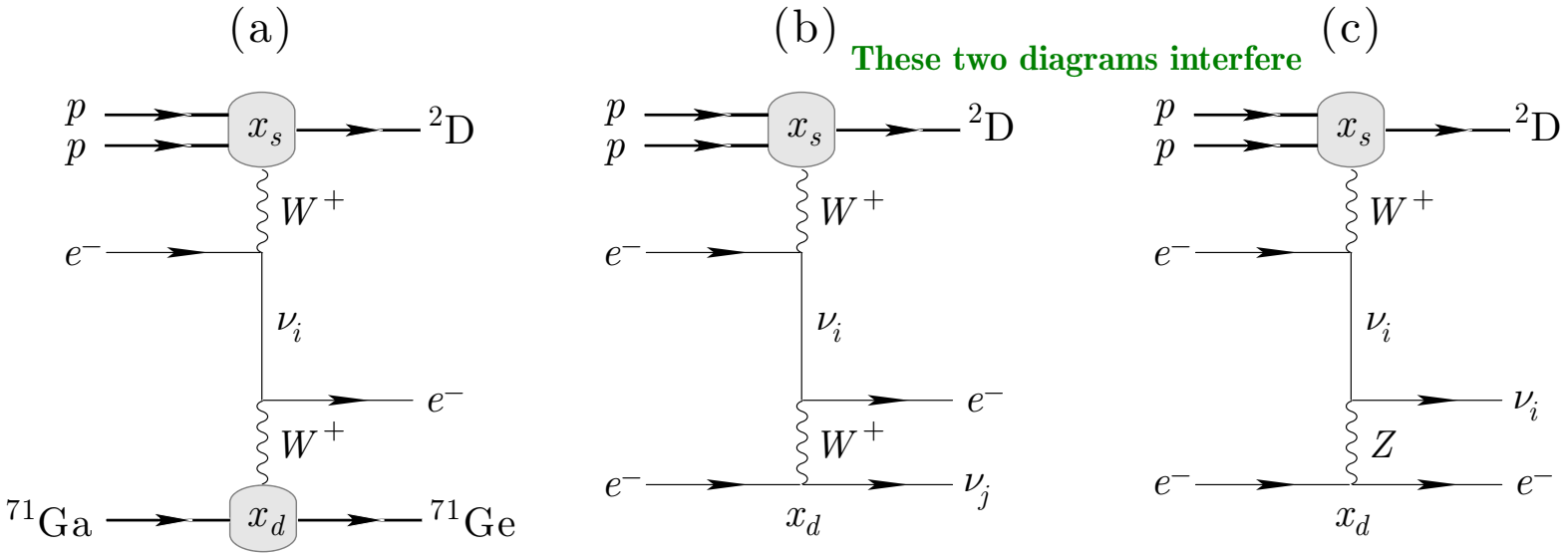

The Figure illustrates the detection of *pep* neutrinos with gallium (a) and electron (b,c) targets. Similar to the *pp* neutrino case, the diagram sets (c) and (d) interfere. While the final electron in the detector vertices of the diagrams (b,c) may have a momentum above the Cherenkov threshold, the current water-Cherenkov detectors SK and SNO+ are insensitive to the *pep* neutrinos.

- The μ_{e3} decay

$$\mu^- \to e^- + \overline{\nu}_e + \nu_\mu$$

in the source can be detected through quasielastic scattering with production of $e^\pm$, $\mu^\pm$, or $\tau^\pm$; of course, only $\mu^\pm$ production is permitted in SM. The diagrams (a) and (b) are for both Dirac and Majorana (anti)neutrinos, while diagrams (c) and (d) are only for Majorana neutrinos.

In the Majorana case, the diagrams (a), (d) and (b), (c) interfere. Potentially this provides a way for distinguishing between the Dirac and Majorana cases. Unfortunately, the diagrams (c) and (d) are suppressed by a factor $\propto m_i/E_\nu$.

Dirac or Majorana

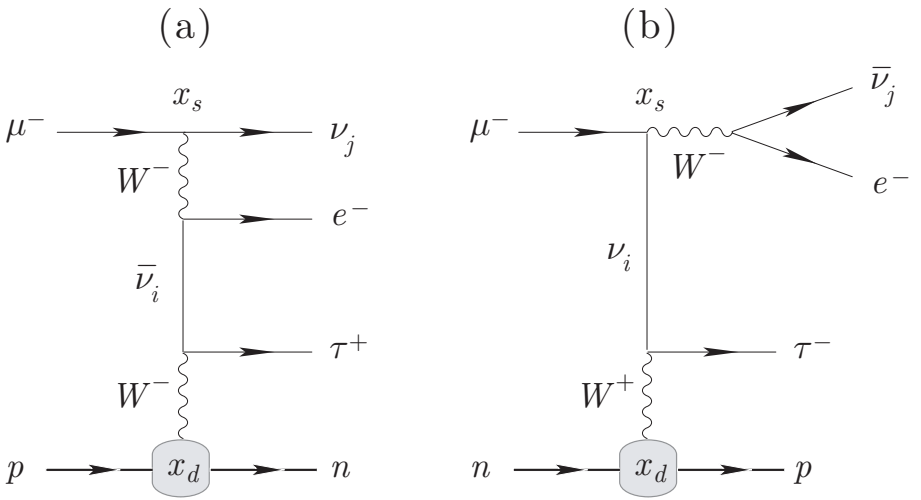

Majorana

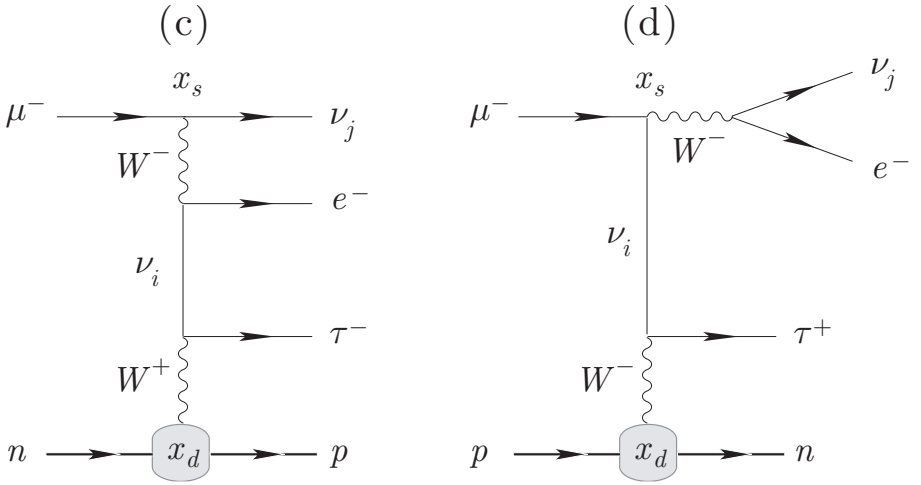

Similar diagrams can be drawn for τ_{e3} and $\tau_{\mu 3}$ decays.

16 Wave packets in quantum mechanics.

Let $|\mathbf{k}\rangle$ be the eigenstate of the on-shell (with mass m) 4-momentum operator $\hat{P} = (\hat{P}_0, \hat{\mathbf{P}})$:

$$\hat{P}_\mu |\mathbf{k}\rangle = k_\mu |\mathbf{k}\rangle \quad (\mu = 0, 1, 2, 3).$$

$$k^2 = k_0^2 - \mathbf{k}^2 = m^2 \quad \Longrightarrow \quad \hat{P}^2 |\mathbf{k}\rangle = m^2 |\mathbf{k}\rangle.$$

So the proper Lorentz transformation $k \longmapsto k' = \Lambda k$ transforms the state $|\mathbf{k}\rangle$ into $|\mathbf{k}'\rangle$:

$$|\mathbf{k}\rangle \overset{\Lambda}{\longmapsto} |\mathbf{k}'\rangle.$$

Notation : $k_0 = E_\mathbf{k} = \sqrt{\mathbf{k}^2 + m^2}$,

Normalization : $\langle \mathbf{q} | \mathbf{k} \rangle = (2\pi)^3 2E_\mathbf{k} \delta(\mathbf{q} - \mathbf{k})$,

$$\Longrightarrow \quad \int \frac{d\mathbf{k}}{(2\pi)^3 2E_\mathbf{k}} |\mathbf{k}\rangle\langle\mathbf{k}| = 1.$$

Let now $|a\rangle$ be an arbitrary «one-particle» spinless state. It can be decomposed into the full set $\{|\mathbf{k}\rangle\}$ that is represented as a wave packet:

$$|a\rangle = \int \frac{d\mathbf{k}}{(2\pi)^3 \sqrt{2E_\mathbf{k}}} \psi_\mathbf{k} |\mathbf{k}\rangle, \quad \psi_\mathbf{k} = \frac{\langle \mathbf{k} | a \rangle}{\sqrt{2E_\mathbf{k}}}.$$

But $|a\rangle$ can be decomposed in the eigenvectors of any other self-adjoint operator, e.g. – the position operator $\hat{\mathbf{X}} = (\hat{X}_1, \hat{X}_2, \hat{X}_3)$:

$$\hat{X}_i|\mathbf{x}\rangle = x_i|\mathbf{x}\rangle, \quad (i = 1, 2, 3); \qquad \langle \mathbf{y}|\mathbf{x}\rangle = \delta(\mathbf{y} - \mathbf{x}) \implies \int d\mathbf{x}|\mathbf{x}\rangle\langle\mathbf{x}| = 1.$$

Therefore

$$|a\rangle = \int d\mathbf{x}\psi_{\mathbf{x}}|\mathbf{x}\rangle, \quad \psi_{\mathbf{x}} = \langle\mathbf{x}|a\rangle.$$

Since the operator $\hat{\mathbf{P}}$ in x representation is $-i\boldsymbol{\nabla}_{\mathbf{x}}$ then

$$\mathbf{k}\langle\mathbf{k}|\mathbf{x}\rangle = \langle\mathbf{k}|\hat{\mathbf{P}}|\mathbf{x}\rangle = \langle\mathbf{k}|(-i\boldsymbol{\nabla}_{\mathbf{x}})|\mathbf{x}\rangle = -i\boldsymbol{\nabla}_{\mathbf{x}}\langle\mathbf{k}|\mathbf{x}\rangle, \implies \langle\mathbf{k}|\mathbf{x}\rangle = \sqrt{2E_{\mathbf{k}}}e^{i\mathbf{k}\mathbf{x}},$$

$$|\mathbf{x}\rangle = \int \frac{d\mathbf{k}e^{i\mathbf{k}\mathbf{x}}}{(2\pi)^3\sqrt{2E_{\mathbf{k}}}}|\mathbf{k}\rangle, \quad |\mathbf{k}\rangle = \sqrt{2E_{\mathbf{k}}}\int d\mathbf{x}e^{-i\mathbf{k}\mathbf{x}}|\mathbf{x}\rangle.$$

Therefore the wavefunctions $\psi_{\mathbf{k}}$ and $\psi_{\mathbf{x}}$ are Fourier transforms of each other:

$$\psi_{\mathbf{x}} = \int \frac{d\mathbf{k}}{(2\pi)^3}e^{-i\mathbf{k}\mathbf{x}}\psi_{\mathbf{k}}, \qquad \psi_{\mathbf{k}} = \int d\mathbf{x}e^{i\mathbf{k}\mathbf{x}}\psi_{\mathbf{x}}.$$

The norm of the state $|a\rangle$ is

$$\langle a|a\rangle = \int \frac{d\mathbf{k}}{(2\pi)^3}|\psi_{\mathbf{k}}|^2 = \int d\mathbf{x}|\psi_{\mathbf{x}}|^2.$$

16.1 Space-time localization (local limit).

- If the state $|a\rangle$ is localized in the point $\mathbf{x}_a$ that is $|a\rangle = \text{const}\,|\mathbf{x}_a\rangle$, then

$$\psi_{\mathbf{x}} = \text{const}\,\delta(\mathbf{x}-\mathbf{x}_a) \quad \Longleftrightarrow \quad \psi_{\mathbf{k}} = \text{const}\,e^{i\mathbf{k}\mathbf{x}_a}.$$

  Of course, such a state cannot be the state of a real physical particle, since its momentum is absolutely uncertain. Moreover, particle cannot be localized in a region smaller than its Compton length $\sim 1/m$. It is however important that in this mathematical limit, wavefunctions $\psi_{\mathbf{x}}$ and $\psi_{\mathbf{k}}$ depend explicitly on the spatial coordinate $\mathbf{x}_a$.

- In Real World, any physical ("particle-like") state $|a\rangle$ is localized within a finite space region S. **More formally**: the probability density $|\psi_{\mathbf{x}}|^2$ vanishes well beyond S.

In general S can be described by some equations, inequalities, or by a set of coordinates. Let's limit ourselves to the simplest case when it can be characterized by a single 3-vector $\mathbf{x}_a$ (the simples example is a sphere with the center in $\mathbf{x}_a$). Then

$\psi_{\mathbf{x}}$ must be a function of $\mathbf{x}_a$ $\Longleftrightarrow$ $\psi_{\mathbf{k}}$ must be a function of $\mathbf{x}_a$

- Similarly, if the state $|a\rangle$ has a finite lifetime, $\psi_{\mathbf{x}}$ and $\psi_{\mathbf{k}}$ must be functions of x_a^0.
- In a more general case of a space-time localization the wavefunctions depend on $\mathbf{x}_a$ & x_a^0.
- Since any Lorentz boost entangles the space-time variables, the wavefunctions $\psi_{\mathbf{x}}$ and $\psi_{\mathbf{k}}$ must depend on a 4-vector $x_a = (x_a^0, \mathbf{x}_a)$, which describes the evolution of the state in the configuration space.

16.2 Momentum localization (plane wave limit).

- Let's assume that the state $|a\rangle$ has a definite 3-momentum $\mathbf{p}_a$: $|a\rangle = \text{const}\,|\mathbf{p}_a\rangle$. Then

$$\psi_{\mathbf{k}} = \text{const}\,(2\pi)^3\sqrt{2E_{\mathbf{k}}}\,\delta(\mathbf{k}-\mathbf{p}_a) \quad \Longleftrightarrow \quad \psi_{\mathbf{x}} = \text{const}\,\sqrt{2p_a^0}\,e^{-i\mathbf{p}_a\mathbf{x}}.$$

  This state is also unphysical since it is fully delocalized in space.

  However, just such kind of states are used for description of the asymptotically free particles in the quantum scattering theory. Sometimes the plane waves are astonishingly associated with point particles... Fortunately such "interpretation" does not (usually) affect the calculations of the microscopic scattering amplitudes.

- In Real World, any physical ("particle-like") state $|a\rangle$ is localized in some finite region of the momentum space. Considerations similar to the above ones allow us to conclude that

$$\boxed{\psi_{\mathbf{k}} \text{ must be a function of } \mathbf{p}_a} \Longleftrightarrow \boxed{\psi_{\mathbf{x}} \text{ must be a function of } \mathbf{p}_a}$$

  Note: the energy variable p_a^0 (in contrast with the time variable x_a^0) is not independent since in the PW limit it becomes $\sqrt{\mathbf{p}_a^2 + m^2}$.

Finally we may conclude that the simplest wave packet $|a\rangle$ suitable for description of the particle states localized in both the configuration space and momentum space must depend on the space-time variable x_a and momentum variable $\mathbf{p}_a$:

$$\boxed{\psi_{\mathbf{k}} = \psi_{\mathbf{k}}(\mathbf{p}_a, x_a) \quad \text{and} \quad \psi_{\mathbf{x}} = \psi_{\mathbf{x}}(\mathbf{p}_a, x_a).}$$

16.3 Quasistable wave packets.

The foregoing qualitative considerations do not provide us with the exact physical meaning of variables x_a and $\mathbf{p}_a$. Let us precisely specify the latter for the special class of the states.

Definition: The quasistable packet (QSP) is the state whose norm does not depend on x_a in any inertial reference frame.

- For QSP, the 4-vector x_a can enter the function $\psi_{\mathbf{k}}$ only through a phase factor $\exp[if(x_a)]$, where $f(x_a)$ is a real function.
- Since $f(x_a)$ is dimensionless and (by assumption) does not depend on any dimension parameters, it can only depend on the dimensionless combinations of the components of the 4-vectors k, p_a ($k^2 = p_a^2 = m^2$) and x_a.
- Due to Lorentz invariance of the norm $\langle a|a\rangle$, the function $f(x_a)$ is also a Lorentz invariant. Therefore it is a function of the scalar products (kx_a), $(p_a x_a)$, and $m^2 x_a^2$ only.
- The function $f(x_a)$ must satisfy the aforementioned limiting cases, namely, it must contain the term $\mathbf{kx}_a$ in the local limit ($|a\rangle \to \text{const}\,|\mathbf{x}_a\rangle$) and does not depend on x_a in the plane wave limit ($|a\rangle \to \text{const}\,|\mathbf{p}_a\rangle$).

It is easy to see that the simplest choice of the function $f(x_a)$, which satisfies the above requirements is

$$f(x_a) = (p_a - k)x_a.$$

If we wish to describe the states which are sufficiently well localized in both the momentum space and configuration space, than this form is intrinsically unique.

Therefore our quasistable state is of the form

$$\boxed{|a\rangle \equiv |\mathbf{p}_a, x_a\rangle = \int \frac{d\mathbf{k}}{(2\pi)^3 2E_{\mathbf{k}}} e^{i(p_a - k)x_a} \phi(\mathbf{k}, \mathbf{p}_a)|\mathbf{k}\rangle,}$$

where the "form factor" $\phi(\mathbf{k}, \mathbf{p}_a)$ does not depend on x_a and the extra factor in the denominator is added to simplify at most the form factor's properties.[a] From above we find:

$$\langle \mathbf{p}_a, x_a | \mathbf{p}_a, x_a\rangle = \int \frac{d\mathbf{k}}{(2\pi)^3 2E_{\mathbf{k}}} |\phi(\mathbf{k}, \mathbf{p}_a)|^2.$$

Therefore $|\phi(\mathbf{k}, \mathbf{p}_a)|^2$ is a Lorentz scalar. Without loss of generality, we require that

$$\phi(\mathbf{k}', \mathbf{p}'_a) = \phi(\mathbf{k}, \mathbf{p}_a) \quad (k' = \Lambda k, \;\; p'_a = \Lambda p_a).$$

$$\Updownarrow$$

$$|\mathbf{p}_a, x_a\rangle \overset{\Lambda}{\longmapsto} |\mathbf{p}'_a, x'_a\rangle \quad (p'_a = \Lambda p_a, \;\; x'_a = \Lambda x_a),$$

Clearly, the wavefunctions $\psi_{\mathbf{x}}(\mathbf{p}_a, x_a)$ and $\psi_{\mathbf{k}}(\mathbf{p}_a, x_a)$ are not Lorentz scalars:

$$\psi_{\mathbf{k}}(\mathbf{p}_a, x_a) = \frac{1}{\sqrt{2E_{\mathbf{k}}}} e^{i(p_a - k)x_a} \phi(\mathbf{k}, \mathbf{p}_a),$$

$$\psi_{\mathbf{x}}(\mathbf{p}_a, x_a) = e^{ip_a x_a} \int \frac{d\mathbf{k}}{(2\pi)^3 \sqrt{2E_{\mathbf{k}}}} e^{-i\left[\mathbf{k}(\mathbf{x} - \mathbf{x}_a) + k^0 x_a^0\right]} \phi(\mathbf{k}, \mathbf{p}_a).$$

[a] And also for a better accommodation to the QFT case.

16.3.1 Further properties of QSP.

Particular case of the Lorentz invariance is the invariance of $\phi(\mathbf{k}, \mathbf{p}_a)$ relative to rotations

$$\mathbf{k} \longmapsto \mathbf{k}' = \mathbf{O}\mathbf{k}, \quad \mathbf{p}_a \longmapsto \mathbf{p}'_a = \mathbf{O}\mathbf{p}_a.$$

$$\Downarrow$$

- $\psi_{\mathbf{k}}(\mathbf{p}_a, x_a)$ and $\psi_{\mathbf{x}}(\mathbf{p}_a, x_a)$ are rotation invariants:

  $$\psi_{\mathbf{k}'}(\mathbf{p}'_a, x'_a) = \psi_{\mathbf{k}}(\mathbf{p}_a, x_a), \;\; \psi_{\mathbf{x}'}(\mathbf{p}'_a, x'_a) = \psi_{\mathbf{x}}(\mathbf{p}_a, x_a) \quad (\mathbf{x}' = \mathbf{O}\mathbf{x}, \;\; x'_a = (\mathbf{O}\mathbf{x}_a, x^0_a)).$$

  Since $|\psi_{\mathbf{x}_a}(\mathbf{p}_a, x_a)|$ does not depend on $\mathbf{x}_a$, the latter can be identified with the center of symmetry of the packet; we'll call it the center of the packet.
- $|\psi_{\mathbf{x}}(\mathbf{p}_a, x_a)|$ is invariant relative to spatial translations is space but not in time.
- $|\psi_{\mathbf{x}}(\mathbf{p}_a, x_a)| \to 0$ as $|x^0_a| \to \infty$ (the packet spreads with time in the configuration space).
- The form factor $\phi(\mathbf{k}, \mathbf{p})$ can be function of the only Lorentz invariant quantity

  $$(k-p)^2 = 2[m^2 - (kp)] = (E_{\mathbf{k}} - E_{\mathbf{p}})^2 - (\mathbf{k}-\mathbf{p})^2.$$

  $\Longrightarrow$
  - $\phi(\mathbf{k}, \mathbf{p}) = \phi(\mathbf{p}, \mathbf{k})$, $\phi(\mathbf{p}, \mathbf{p}) \equiv \phi_0$ does not depend on $\mathbf{p}$;
  - $\phi(\mathbf{k}, \mathbf{0}) = \phi(\mathbf{0}, \mathbf{k}) = \widetilde{\phi}(k_0)$ is a rotation-invariant function of $k_0 = E_{\mathbf{k}}$;
  - the norm $\langle \mathbf{p}_a, x_a | \mathbf{p}_a, x_a \rangle$ does not depend on $\mathbf{x}_a$ and $\mathbf{p}_a$.
- The states $|\mathbf{p}_a, x_a\rangle$ form a complete vector set:

  $$|\mathbf{p}_a\rangle = \frac{2p^0_a}{\phi_0} \int d\mathbf{x}_a |p_a, x_a\rangle \quad \Longrightarrow \quad \int d\mathbf{p} d\mathbf{x} d\mathbf{y} \frac{E_{\mathbf{p}}}{4\pi^3 |\phi_0|^2} |\mathbf{p}, x\rangle\langle \mathbf{p}, y| = 1.$$

16.3.2 Physical meaning of the vector $\mathbf{p}_a$.

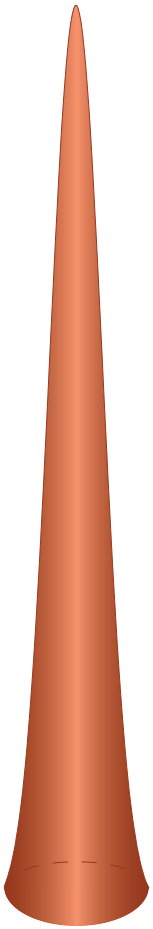

From the definition of the QSP $|\mathbf{p}_a, x_a\rangle$ it follows that

$$|\langle \mathbf{k}|\mathbf{p}_a, x_a\rangle|^2 = |\phi(\mathbf{k}, \mathbf{p}_a)|^2.$$

So $|\phi(\mathbf{k}, \mathbf{p}_a)|^2$ defines the weight with which the state $|\mathbf{k}\rangle$ enters into the wave packet state $|\mathbf{p}_a, x_a\rangle$.

It is natural to adopt that the function $|\phi(\mathbf{k}, \mathbf{p})|$ has the only maximum in the point $\mathbf{k} = \mathbf{p}$ (at that $|\phi|_{\max} = |\phi_0| > 0$) and drops rapidly as $|\mathbf{k} - \mathbf{p}| \to \infty$.

$$\Downarrow$$

$$[\nabla_{\mathbf{k}}|\phi(\mathbf{k}, \mathbf{p})|]_{\mathbf{k}=\mathbf{p}} = [\nabla_{\mathbf{p}}|\phi(\mathbf{k}, \mathbf{p})|]_{\mathbf{p}=\mathbf{k}} = 0.$$

For the form factors $\phi(\mathbf{k}, \mathbf{p}_a)$ of such class, the physical meaning of the vector $\mathbf{p}_a$ is clear:

The vector $\mathbf{p}_a$ is the most probable 3-momentum of the state $\|\mathbf{p}_a, x_a\rangle$.

Note: After this, the transition to the local limit becomes impossible and we can forget about this "strut" (which is in any case absent in QFT).

16.3.3 Mean 4-momentum and mass of QSP.

- The mean 4-momentum $\overline{P} = \left(\overline{P}_0, \overline{\mathbf{P}}\right)$ of the packet is defined by the standard QM rule:

$$\overline{P}_\mu = \overline{P}_\mu(\mathbf{p}) = \frac{\langle \mathbf{p}, x|\hat{P}_\mu|\mathbf{p}, x\rangle}{\langle \mathbf{p}, x|\mathbf{p}, x\rangle} = \frac{1}{2m\mathrm{V}_\star}\int \frac{d\mathbf{k} k_\mu |\phi(\mathbf{k}, \mathbf{p})|^2}{(2\pi)^3 2E_{\mathbf{k}}}.$$

Here and below the index a is dropped for short; the positive constant

$$\mathrm{V}_\star = \frac{\langle \mathbf{p}, x|\mathbf{p}, x\rangle}{2m} = \frac{1}{2m}\int \frac{d\mathbf{k}\,|\phi(\mathbf{k}, \mathbf{p})|^2}{(2\pi)^3 2E_{\mathbf{k}}} = \frac{1}{8\pi^2 m}\int_m^\infty dk_0 \sqrt{k_0^2 - m^2}\,|\widetilde{\phi}(k_0)|^2$$

has dimension of volume. The mean 4-momentum is the integral of motion.

- $\overline{\mathbf{P}}(\mathbf{0}) = \mathbf{0}$ due to the evenness of the function $\phi(\mathbf{k}, \mathbf{0})$. Therefore the mean (effective) mass of the packet, $\overline{m}$, is the mean energy $\overline{P}_0$ in the proper reference frame (PRF) where $\mathbf{p} = 0$:

$$\overline{m} = \overline{P}_0(\mathbf{0}) = \int \frac{d\mathbf{k}|\phi(\mathbf{k}, \mathbf{0})|^2}{4(2\pi)^3 m\mathrm{V}_\star} = \frac{1}{8\pi^2 m\mathrm{V}_\star}\int_m^\infty dk_0 k_0 \sqrt{k_0^2 - m^2}\,|\widetilde{\phi}(k_0)|^2,$$

$$\Longrightarrow \quad \frac{\overline{m}}{m} = \int_m^\infty dk_0 k_0 \sqrt{k_0^2 - m^2}\,|\widetilde{\phi}(k_0)|^2 \left[\int_m^\infty dk_0 m\sqrt{k_0^2 - m^2}\,|\widetilde{\phi}(k_0)|^2\right]^{-1} \geq 1;$$

the equality $\overline{m} = m$ only holds in the PW limit.

The QSP is heavier than its plane-wave constituents.

This very general effect is a manifestation of the nonadditivity of the relativistic mass.

In our case: the transversal to $\mathbf{p}$ components of the momenta of the states $|\mathbf{k}\rangle$ do not contribute to the mean momentum ($\mathbf{p} \times \overline{\mathbf{P}} = 0$), but do contribute to the mean energy.

Some analogy:

The mass of a gas in a bulb increases under (uniform) heating: the bulb does not get an extra momentum, but internal energy of the gas grows.

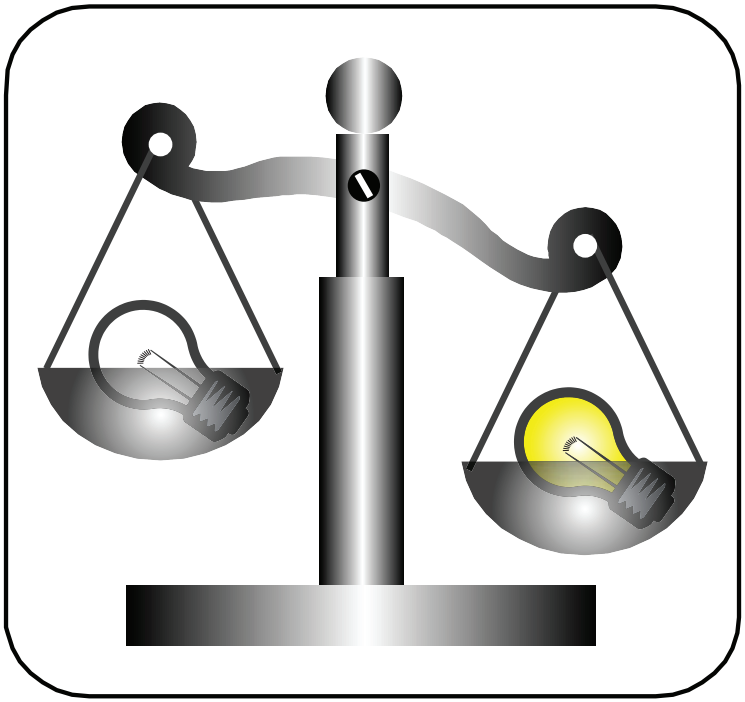

Proposal of an experiment.

Note that the mean value of the squared mass $\overline{P^2}$ is equal to m^2 and thus

$$\overline{P}^2 \geq \overline{P^2} = m^2.$$

One can prove that $\overline{P}_0 = (\overline{m}/m)E_{\mathbf{p}}$, $\overline{\mathbf{P}} = (\overline{m}/m)\mathbf{p}$. So, in the mean, QSP is on-shell:

$$\overline{P}^2 = \overline{P}_\mu \overline{P}^\mu = \overline{m}^2.$$

The mean velocity $\overline{\mathbf{P}}/\overline{P}_0$ coincides with most probable velocity $\mathbf{v}_{\mathbf{p}} = \mathbf{p}/E_{\mathbf{p}}$.

16.4 Mean position of QSP. Meaning of the space-time parameter.

Let us inquire the exact physical meaning of the space-time dependence of the state $|\mathbf{p}, x\rangle$. Consider the mean value of the position operator $\hat{\mathbf{X}}$:

$$\overline{\mathbf{x}} = \overline{\mathbf{x}}(\mathbf{p}, x) = \frac{\langle \mathbf{p}, x|\hat{\mathbf{X}}|\mathbf{p}, x\rangle}{\langle \mathbf{p}, x|\mathbf{p}, x\rangle} = \frac{1}{2m\mathrm{V}_\star}\int d\mathbf{y}\mathbf{y}|\psi_{\mathbf{y}}(\mathbf{p}, x)|^2$$

$$= \frac{1}{4m\mathrm{V}_\star}\int d\mathbf{y}\mathbf{y}\int \frac{d\mathbf{k}d\mathbf{q}}{(2\pi)^6\sqrt{E_{\mathbf{k}}E_{\mathbf{q}}}}e^{i[(\mathbf{q}-\mathbf{k})(\mathbf{y}-\mathbf{x})+(q_0-k_0)x_0]}\phi(\mathbf{k}, \mathbf{p})\phi^*(\mathbf{q}, \mathbf{p})$$

$$= \frac{1}{4m\mathrm{V}_\star}\int d\mathbf{y}(\mathbf{y}+\mathbf{x})\int \frac{d\mathbf{k}d\mathbf{q}}{(2\pi)^6\sqrt{E_{\mathbf{k}}E_{\mathbf{q}}}}e^{i[(\mathbf{q}-\mathbf{k})\mathbf{y}+(q_0-k_0)x_0]}\phi(\mathbf{k}, \mathbf{p})\phi^*(\mathbf{q}, \mathbf{p}).$$

$$\Downarrow$$

$$\overline{\mathbf{x}} = \boldsymbol{\xi}(\mathbf{p}, x_0) + \mathbf{x}, \text{ where } \boldsymbol{\xi}(\mathbf{p}, x_0) = \frac{1}{2m\mathrm{V}_\star}\int d\mathbf{y}\mathbf{y}\,|\chi_{\mathbf{y}}(\mathbf{p}, x_0)|^2 \text{ and } \chi_{\mathbf{y}}(\mathbf{p}, x_0) \equiv \psi_{\mathbf{y}}(\mathbf{p}, x)|_{\mathbf{x}=\mathbf{0}}.$$

Due to the rotation invariance of $\psi_{\mathbf{y}}(\mathbf{p}, x)$, the function $\chi_{\mathbf{y}}(\mathbf{0}, x_0)$ is even function of $\mathbf{y}$. Thus

$$\boldsymbol{\xi}(\mathbf{0}, x_0) = \mathbf{0}.$$

Since $\boldsymbol{\xi}$ is a 3-vector, and the last equality is valid for any x_0, it is equivalent to the following:

$$\boldsymbol{\xi}_\star = \mathbf{0}.$$

Here and below, the star symbol ($\star$) is used to denote the rest-frame quantities.

Let ξ_0 be the 0-component of the 4-vector $\xi = (\xi_0, \boldsymbol{\xi})$. The Lorentz boost connecting PRF with lab. frame (LF) can be written as

$$\boldsymbol{\xi}_\star = \boldsymbol{\xi} + \Gamma_{\mathbf{p}} \left[\frac{\Gamma_{\mathbf{p}}(\mathbf{v}_{\mathbf{p}}\boldsymbol{\xi})}{\Gamma_{\mathbf{p}} + 1} - \xi_0 \right] \mathbf{v}_{\mathbf{p}},$$

where

$$\mathbf{v}_{\mathbf{p}} = \mathbf{p}/E_{\mathbf{p}}, \quad \Gamma_{\mathbf{p}} = E_{\mathbf{p}}/m, \quad \text{and} \quad \boldsymbol{\xi} = \boldsymbol{\xi}(\mathbf{p}, x_0).$$

So we obtain the equation

$$\boldsymbol{\xi} = \frac{E_{\mathbf{p}}}{m} \left[\xi_0 - \frac{E_{\mathbf{p}}(\mathbf{v}_{\mathbf{p}}\boldsymbol{\xi})}{E_{\mathbf{p}} + m} \right] \mathbf{v}_{\mathbf{p}},$$

which has the only solution

$$\boldsymbol{\xi}(\mathbf{p}, x_0) = \mathbf{v}_{\mathbf{p}} \xi_0.$$

Next, it is easy to prove that $|\chi_{\mathbf{y}}(\mathbf{p}, 0)|$ is even function of $\mathbf{y}$. Hence $\boldsymbol{\xi}(\mathbf{p}, 0) = \mathbf{0}$ that is

$$\xi_0 = 0 \quad \text{as} \quad x_0 = 0.$$

Therefore ξ_0 must be identified with x_0 and we have

$$\boxed{\overline{\mathbf{x}}(\mathbf{p}, x) = \mathbf{x} + \mathbf{v}_{\mathbf{p}} x_0.}$$

Conclusions:

- In the mean, QSP follows the classical trajectory, with the most probable velocity $\mathbf{v}_{\mathbf{p}}$.
- In PRF, the mean position of the packet is just its center, $\mathbf{x}$.
- The parameter x_0 is the time counted from the moment when the mean position of the packet has been coincided with its center $\mathbf{x}$ in LF.

16.5 Effective volume of QSP.

Which is the area of localization of a wave packet in the configuration space?

> Making the perfect definition of the size or volume of a wave packet (an infinite quantum object) is an almost as thankless job as defining the size of a cloud. Nevertheless, we have to have a quantitative characteristic of the degree of localization of the packet, allowing to compare the effective sizes of different packets.

Clouds over Sochi city (April 1, 2011)

Simple example: Let $\rho(\mathbf{x})$ be the spherically symmetric density distribution of some quantity, say mass, with the center in the point $\mathbf{x} = \mathbf{0}$. Let both the full mass

$$\int d\mathbf{x}\rho(\mathbf{x}) = M$$

and the central density $\rho_0 = \rho(\mathbf{0})$ are finite. We may define the effective spatial volume V as the volume of a uniform ball of mass M with density ρ_0:

$$\mathrm{V} = M/\rho_0.$$

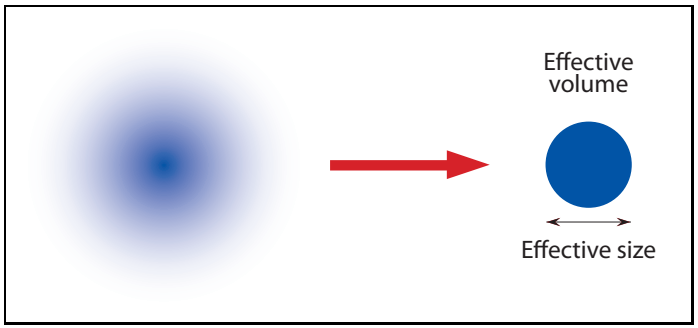

This definition, being no better and no worse than any other, is the most appropriate since it can easily be translated to the covariant quantum language.

By following the above example, we define the effective spatial volume of QSP in PRF as

$$\mathrm{V}(\mathbf{0}) = \frac{1}{\rho_\star}\int d\mathbf{y}\,|\psi_{\mathbf{y}}(\mathbf{0},x)|^2.$$

Here, the analog of the central density is the central value of the function $|\psi_{\mathbf{y}}(\mathbf{0},x)|^2$ (proportional to the probability density in PRF), $\rho_\star$, taken at the moment $x_0 = 0$:

$$\rho_\star \equiv |\psi_{\mathbf{x}}(\mathbf{0},x)|^2\big|_{x_0=0} = \left|\int \frac{d\mathbf{k}\,\widetilde{\phi}(k_0)}{(2\pi)^3\sqrt{2k_0}}\right|^2 = \frac{1}{8\pi^2}\left|\int_m^\infty dk_0\sqrt{k_0(k_0^2-m^2)}\,\widetilde{\phi}(k_0)\right|^2.$$

This is just a constant. It's easy to see that

$$\boldsymbol{\nabla}_{\mathbf{y}}|\psi_{\mathbf{y}}(\mathbf{0},x)|^2\big|_{\mathbf{y}=\mathbf{x},\,x_0=0} = \mathbf{0}.$$

Hence $\rho_\star$ is the extremum of the density function

$$|\psi_{\mathbf{y}}(\mathbf{0},x)|^2 = \int \frac{d\mathbf{k}d\mathbf{q}}{2(2\pi)^6\sqrt{k_0q_0}}e^{i[(\mathbf{q}-\mathbf{k})(\mathbf{y}-\mathbf{x})+(q_0-k_0)x_0]}\widetilde{\phi}(k_0)\widetilde{\phi}^*(q_0).$$

One more (the last) restriction: $\widetilde{\phi}(k_0) > 0$ or, equivalently, $\arg[\phi(\mathbf{k},\mathbf{p})] = 0$.

This condition, unclaimed till now, is connected with the same PW limit, in which the phase of the function $\phi(\mathbf{k},\mathbf{p})$ is zero. So it is sufficient to put $\arg[\phi(\mathbf{k},\mathbf{p})] = 0$.

In this case, it is obvious that $\rho_\star$ is the absolute maximum of $|\psi_{\mathbf{y}}(\mathbf{0},x)|^2$.

By using the definition of the norm $\langle \mathbf{p}, x | \mathbf{p}, x \rangle = 2m\mathrm{V}_\star$ we obtain

$$\mathrm{V}(\mathbf{0}) = 2m\mathrm{V}_\star/\rho_\star.$$

Taking into account the Lorentz transformation law for the volume, we find the effective volume of the packet in LF:

$$\boxed{\mathrm{V}(\mathbf{p}) = \frac{\mathrm{V}(\mathbf{0})}{\Gamma_{\mathbf{p}}} = \frac{1}{\Gamma_{\mathbf{p}}\rho_\star}\int d\mathbf{y}\,|\psi_{\mathbf{y}}(\mathbf{p}, x)|^2.}$$

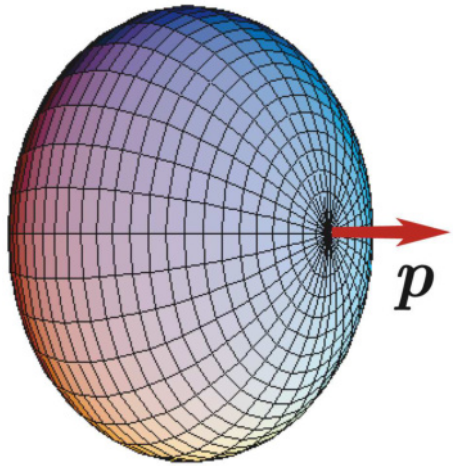

In the PW limit:

$$\phi(\mathbf{k}, \mathbf{0}) \to 16\pi^3 m\delta(\mathbf{k}) \quad \Longrightarrow \quad \rho_\star \to 2m \quad \Longrightarrow \quad \mathrm{V}(\mathbf{0}) \to \mathrm{V}_\star \to \infty.$$

Thus, for the packets well localized in the momentum space, one can put approximately

$$\mathrm{V}(\mathbf{0}) = \mathrm{V}_\star, \quad \mathrm{V}(\mathbf{p}) = \mathrm{V}_\star/\Gamma_{\mathbf{p}}.$$

The above definition of $\mathrm{V}(\mathbf{p})$ is formally applicable to any form factor. It is therefore instructive to check its self-consistency also in the local limit. While in this (unphysical) case, the integrals defining the constants $\mathrm{V}_\star$, $\rho_\star$ diverge at the upper limit of integration in k_0, their ratio vanishes $\Longrightarrow \mathrm{V}(\mathbf{p}) \to 0$ *as it should be*. Formally this fact can be proved by the standard regularization of the integrals in k_0:

$$\frac{\mathrm{V}_\star}{\rho_\star} \propto \lim_{M\to\infty} \frac{\int_m^M dk_0 \sqrt{k_0^2 - m^2}\,|\widetilde{\phi}(k_0)|^2}{\left|\int_m^M dk_0 \sqrt{k_0(k_0^2 - m^2)}\,\widetilde{\phi}(k_0)\right|^2} = \lim_{M\to\infty}\left(\int_m^M dk_0 k_0 \sqrt{k_0^2 - m^2}\right)^{-1} = \lim_{M\to\infty}\frac{3}{M^3}.$$

The effective size of QSP in PRF is naturally defined as the diameter of a ball of volume $\mathrm{V}(\mathbf{0})$.

17 Wave packets in quantum field theory.

17.1 One-particle Fock states.

The S-matrix formalism of QFT usually deals with the one-particle Fock states (FS) as the asymptotically-free states of the spin-s fields. The FS are constructed from the vacuum state:

$$|\mathbf{k},s\rangle = \sqrt{2E_{\mathbf{k}}}\, a^{\dagger}_{\mathbf{k}s}|0\rangle, \qquad a_{\mathbf{k}s}|0\rangle = 0, \qquad (E_{\mathbf{k}} = k_0 = \sqrt{\mathbf{k}^2 + m^2}),$$

and provide the QFT realization of the abstract QM states $|\mathbf{k}\rangle$ with the fixed 3-momentum.

- The conventional (anti)commutation relations for the creation/annihilation operators hold:

$$\{a_{\mathbf{q}r}, a_{\mathbf{k}s}\} = \{a^{\dagger}_{\mathbf{q}r}, a^{\dagger}_{\mathbf{k}s}\} = 0, \qquad \{a_{\mathbf{q}r}, a^{\dagger}_{\mathbf{k}s}\} = (2\pi)^3 \delta_{sr}\delta\left(\mathbf{k}-\mathbf{q}\right).$$

- The Lorentz-invariant normalization of FS is therefore singular since

$$\langle \mathbf{q},r|\mathbf{k},s\rangle = (2\pi)^3 2E_{\mathbf{k}}\delta_{sr}\delta\left(\mathbf{k}-\mathbf{q}\right).$$

- The proper Lorentz transformation induces the unitary transformation of FS:

$$k \longmapsto k' = \Lambda k \quad \Longrightarrow \quad |\mathbf{k},s\rangle \longmapsto U_{\Lambda}|\mathbf{k},s\rangle = |\mathbf{k}',s\rangle,$$

  assuming that the axis of spin quantization is oriented along the boost or rotation axis.

- This is equivalent to the following unitary transformation of the operators $a^{\dagger}_{\mathbf{k}s}$ and $a_{\mathbf{k}s}$:

$$a^{\dagger}_{\mathbf{k}s} \longmapsto U_{\Lambda} a^{\dagger}_{\mathbf{k}s} U^{-1}_{\Lambda} = \sqrt{E_{\mathbf{k}'}/E_{\mathbf{k}}}\; a^{\dagger}_{\mathbf{k}'s},$$
$$a_{\mathbf{k}s} \longmapsto U_{\Lambda} a_{\mathbf{k}s} U^{-1}_{\Lambda} = \sqrt{E_{\mathbf{k}'}/E_{\mathbf{k}}}\; a_{\mathbf{k}'s}.$$

17.2 Wave-packet states.

By the same, as above (QM), arguments referring to the localization of the state in the configuration space and momentum space, we can build the QFT wave-packet (WP) as a linear combination of the Fock states. The most general construction is

$$|\mathbf{p}, s, x\rangle = \int \frac{d\mathbf{k}}{(2\pi)^3 2E_{\mathbf{k}}} \sum_{s'} \Phi_{ss'}\left(\mathbf{k}, \mathbf{p}, x; \boldsymbol{\sigma}\right) |\mathbf{k}, s'\rangle,$$

In general, the function $\Phi_{ss'}(\mathbf{k}, \mathbf{p}, x; \boldsymbol{\sigma})$ depends not only on the momentum, space-time, and spin variables, but also on a (finite or infinite) set of parameters (constants)

$$\boldsymbol{\sigma} = \{\sigma_1, \sigma_2, \ldots\},$$

governing the shape of WP. All momenta are, by definition, on-shell [can be avoided in future].

Correspondence principle:

The wave packet state passes into the Fock state in the plane-wave limit:

$$|\mathbf{p}, s, x\rangle \overset{\text{PW}}{\longmapsto} |\mathbf{p}, s\rangle.$$

Since the parameters σ_i can always be defined in such a way to approach the PW limit as $\sigma_i \to 0$ $(\forall i)$, we can formulate the correspondence principle in the following way:

$$\lim_{\boldsymbol{\sigma}\to 0} \Phi_{ss'}\left(\mathbf{k}, \mathbf{p}, x; \boldsymbol{\sigma}\right) = (2\pi)^3 2E_{\mathbf{p}} \delta_{ss'} \delta(\mathbf{k} - \mathbf{p}).$$

Below, we'll only interested in the quasistable WP very close to FS that is very narrow in the momentum space ($\Longleftrightarrow$ all σ_i are small). Then the correspondence principle suggests that

- functions $\Phi_{ss'}$ must be Lorentz invariants (scalars),
- the x dependence of $|\Phi_{ss'}|$ can be neglected,
- $|\Phi_{ss'}| \ll |\Phi_{ss}|$ for $s' \neq s$.

These requirements can be accumulated in the following simple ansatz:

$$\Phi_{ss'}\left(\mathbf{k},\mathbf{p},x;\boldsymbol{\sigma}\right) = \delta_{ss'} e^{i\varsigma(k-p)x}\phi(\mathbf{k},\mathbf{p};\boldsymbol{\sigma}),$$

in which $\phi(\mathbf{k},\mathbf{p};\boldsymbol{\sigma})$ is a spin- and coordinate-independent Lorentz-invariant function, such that

$$\lim_{\boldsymbol{\sigma}\to 0}\phi(\mathbf{k},\mathbf{p};\boldsymbol{\sigma}) = (2\pi)^3 2E_{\mathbf{p}}\delta(\mathbf{k}-\mathbf{p})$$

(so $\phi(\mathbf{k},\mathbf{p};\boldsymbol{\sigma})$ is a "smeared" δ-function), and ς is the sign which will be fixed in a short while. Finally, the quasistable QFT wave packet [abbreviated as above by QSP] can be written as

$$\boxed{|\mathbf{p},s,x\rangle = \int \frac{d\mathbf{k}\, e^{i\varsigma(k-p)x}}{(2\pi)^3 2E_{\mathbf{k}}}\phi(\mathbf{k},\mathbf{p})|\mathbf{k},s\rangle,} \tag{53}$$

[Here and below the argument $\boldsymbol{\sigma}$ is dropped for short, but is implied.]

From (53) it is in particular follows the (expected) transformation rule:

$$|\mathbf{p},s,x\rangle \overset{\Lambda}{\longmapsto} |\mathbf{p}',s,x'\rangle \quad (p'=\Lambda p,\ \ x'=\Lambda x),$$

where again the axis of spin quantization is oriented along the boost or rotation axis.

17.2.1 The most general properties of QSP.

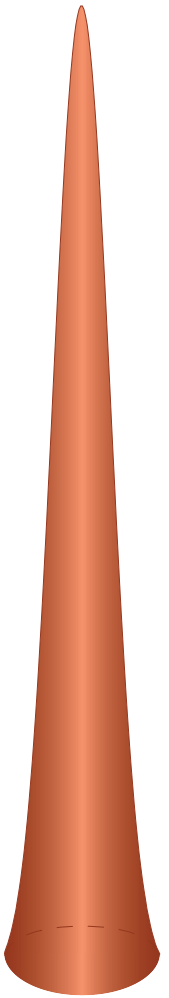

The function $\phi(\mathbf{k},\mathbf{p})$ has exactly the same properties as its QM analog.
Thus, the major properties of QSP can be summarized without derivation:

- the form factor $\phi(\mathbf{k},\mathbf{p})$ can be function of the only quantity $(k-p)^2$;
- $\phi(\mathbf{k},\mathbf{p}) = \phi(\mathbf{p},\mathbf{k})$;
- $\phi(\mathbf{p},\mathbf{p}) \equiv \phi_0$ does not depend on $\mathbf{p}$;
- $\phi(\mathbf{k},\mathbf{0}) = \phi(\mathbf{0},\mathbf{k}) = \widetilde{\phi}(k_0)$ is a rotation-invariant function of $k_0 = E_{\mathbf{k}}$;
- the norm $\langle \mathbf{p},s,x|\mathbf{p},s,x\rangle = 2m\mathrm{V}_\star$ is a constant and, moreover, the inner product $\langle \mathbf{q},r,y|\mathbf{p},s,x\rangle = \delta_{sr}e^{i(qy-px)}\mathcal{D}(\mathbf{p},\mathbf{q};x-y)$ is defined by the nonsingular and relativistic-invariant function

$$\mathcal{D}(\mathbf{p},\mathbf{q};x) = \int \frac{d\mathbf{k}}{(2\pi)^3 2E_{\mathbf{k}}}\, e^{ikx}\phi(\mathbf{k},\mathbf{p})\phi^*(\mathbf{k},\mathbf{q}) \quad [\text{for } \varsigma = +1].$$

- As in the QM case, we require that the function $\phi(\mathbf{k},\mathbf{p})$ is positive definite, has the only maximum at $\mathbf{k}=\mathbf{p}$, and drops rapidly as $|\mathbf{k}-\mathbf{p}| \to \infty$. Hence

> The vector $\mathbf{p}$ is the most probable 3-momentum of the state $|\mathbf{p},s,x\rangle$.

Technical condition [ensues from the correspondence principle; not necessary but practical.]

$$\int \frac{d\mathbf{k}}{(2\pi)^3 2E_{\mathbf{k}}}\, \phi(\mathbf{k},\mathbf{0}) = 1.$$

- The mean 4-momentum, $\overline{P}$, of QSP is the integral of motion.
- In the mean, the QSP is on-shell: $\overline{P}^2 = \overline{m}^2$, but $\overline{P^2} = m^2$.
- The QSP is heavier than its Fock constituents: $\overline{m} > m$.

The relevant formulas remain formally the same as in the QM case.

17.2.2 A nuisance (metaphysical notes).

Treating the QSP as a physical quantum state, created in collisions or decays of other particles $\varkappa$, one may expect that the function $\phi(\mathbf{k}, \mathbf{p})$ depends parametrically (through the set $\boldsymbol{\sigma}$) on the 4-momenta $Q_\varkappa$ of both primary and secondary particles participated in the creation process.

Moreover, in the most general case the set of the progenitor and accompanying particles may include ones from the whole net of the reactions which led to the production of the packet.

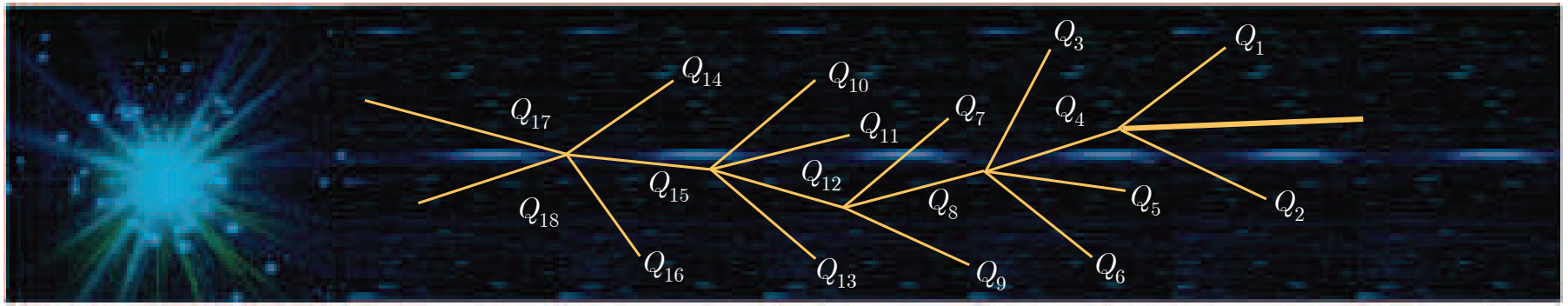

The 4-momenta $Q_\varkappa$ can enter the scalar function $\phi(\mathbf{k}, \mathbf{p})$ only through the scalar products

$$(Q_\varkappa k), \quad (Q_\varkappa p), \quad \text{and} \quad (Q_\varkappa Q_{\varkappa'}).$$

Owing to the required properties of $\phi(\mathbf{k},\mathbf{p})$, it satisfies the conditions

$$\left[\frac{\partial\phi(\mathbf{k},\mathbf{p})}{\partial k_l}\right]_{\mathbf{k}=\mathbf{p}} = \left[\frac{\partial(k-p)^2}{\partial k_l}\,\frac{\partial\phi(\mathbf{k},\mathbf{p})}{\partial(k-p)^2}\right]_{\mathbf{k}=\mathbf{p}} + \sum_{\varkappa}\left[\frac{\partial(Q_\varkappa k)}{\partial k_l}\,\frac{\partial\phi(\mathbf{k},\mathbf{p})}{\partial(Q_\varkappa k)}\right]_{\mathbf{k}=\mathbf{p}} = 0.$$

$$\Downarrow$$

$$\sum_{\varkappa} Q^0_\varkappa\left(\frac{p_l}{p^0}-\frac{Q_{\varkappa l}}{Q^0_\varkappa}\right)\left[\frac{\partial\phi(\mathbf{k},\mathbf{p})}{\partial(Q_\varkappa k)}\right]_{\mathbf{k}=\mathbf{p}} = 0 \qquad (l=1,2,3).$$

The last equations are satisfied identically (for any $\phi(\mathbf{k},\mathbf{p})$) only in the unphysical case, when the velocities of all WPs ("network relatives") $\varkappa$, are equal to each other,

$$\mathbf{v}_\varkappa = \mathbf{Q}_\varkappa/Q^0_\varkappa = \mathbf{p}/E_\mathbf{p}.$$

Thus, from the arbitrariness of the 4-momentum configurations $\{Q_\varkappa\}$, we conclude that

$$[\partial\phi(\mathbf{k},\mathbf{p})/\partial(Q_\varkappa k)]_{\mathbf{k}=\mathbf{p}} = 0 \quad \text{and (with similar arguments)} \quad [\partial\phi(\mathbf{k},\mathbf{p})/\partial(Q_\varkappa p)]_{\mathbf{p}=\mathbf{k}} = 0.$$

◦ Hence the dependence of $\phi(\mathbf{k},\mathbf{p})$ upon $(Q_\varkappa k)$ and $(Q_\varkappa p)$ must vanish, at least in the vicinity of the maximum of $\phi(\mathbf{k},\mathbf{p})$. Since only this vicinity is really important for the smeared δ-function, it is safe to neglect this dependence for QSP everywhere.

◦ The remaining scalar products $(Q_\varkappa Q_{\varkappa'})$ can be "absorbed" into the definition of the parameters σ_i. In other words, σ_i can be, in general, the scalar functions of the 4-momenta of all network relatives $\varkappa$ rather than constants. As a result, the WPs composed by identical one-particle Fock states but produced in different reactions (or reaction chains) are not, generally speaking, identical.

◦ To avoid this serious complication we will be forced to sacrifice the generality in some stages of our study, assuming voluntary that σ_i are still constants.

A note in excuse: this problem is not *by no means* specific to the covariant approach...

17.3 Wave packet in the configuration space.

Consider, as a representative example, a spin-$\frac{1}{2}$ free-field operator

$$\Psi(x) = \int \frac{d\mathbf{k}}{(2\pi)^3\sqrt{2E_{\mathbf{k}}}} \sum_s \left[a_{\mathbf{k}s}u_s(\mathbf{k})e^{-ikx} + b^\dagger_{\mathbf{k}s}v_s(\mathbf{k})e^{ikx}\right].$$

The coordinate representation of FS is a plane wave uniformly distributed over the space-time:

$$\langle 0|\Psi(x)|\mathbf{p},s\rangle = u_s(\mathbf{p})e^{-ipx},$$

So, the QFT analog of the QM wavefunction $\psi_y(\mathbf{p},x)$ in x representation is the spinor function

$$\psi_y(\mathbf{p},s,x) = \langle 0|\Psi(y)|\mathbf{p},s,x\rangle = \int \frac{d\mathbf{k}}{(2\pi)^3 2E_{\mathbf{k}}} u_s(\mathbf{k})e^{-i[ky+\varsigma(p-k)x]}\phi(\mathbf{k},\mathbf{p}). \tag{54}$$

Moreover, in the S-matrix perturbation theory, just this factor will provide the modified Feynman-rule factor for any Feynman diagram with the corresponding incoming fermion leg.

It is natural to demand that $|\psi_x(\mathbf{p},s,x)|$ does not depend on $\mathbf{x}$ in PRF because, in this case (and only in this case), the point $\mathbf{x}$ can be identified with the symmetry center of the packet.

$$\psi_x(\mathbf{p},s,x) = \langle 0|\Psi(x)|\mathbf{p},s,x\rangle = e^{-i\varsigma(px)} \int \frac{d\mathbf{k}}{(2\pi)^3 2E_{\mathbf{k}}} u_s(\mathbf{k})e^{i(\varsigma-1)(kx)}\phi(\mathbf{k},\mathbf{p}).$$

$$\Downarrow$$

The requirement is fulfilled for any form factor $\phi(\mathbf{k},\mathbf{p})$ only if $\varsigma = 1$.

So instead of Eqs. (53) and (54) we finally obtain

$$\boxed{|\mathbf{p},s,x\rangle = \int \frac{d\mathbf{k}\,\phi(\mathbf{k},\mathbf{p})e^{i(k-p)x}}{(2\pi)^3 2E_{\mathbf{k}}}|\mathbf{k},s\rangle,} \tag{55}$$

$$\Downarrow$$

$$\boxed{\psi_y(\mathbf{p},s,x) = e^{-ipx}\int \frac{d\mathbf{k}}{(2\pi)^3 2E_{\mathbf{k}}} u_s(\mathbf{k})\phi(\mathbf{k},\mathbf{p})e^{ik(x-y)}.} \tag{56}$$

The opposed (in comparison with the QM WP) sign in the exponent in Eq. (55) is caused by the identification of the function $\psi_y(\mathbf{p},s,x)$ with the matrix element $\langle 0|\Psi(y)|\mathbf{p},s,x\rangle$ what is with the incoming (or in-leg) WP rather than with its complex conjugate. Indeed, quite similarly it can be constructed the wave function for the outgoing (out-leg) WP:

$$\overline{\psi}_y(\mathbf{p},s,x) = \langle \mathbf{p},s,x|\overline{\Psi}(y)|0\rangle = e^{ipx}\int \frac{d\mathbf{k}}{(2\pi)^3 2E_{\mathbf{k}}} \overline{u}_s(\mathbf{k})\phi^*(\mathbf{k},\mathbf{p})e^{ik(y-x)}. \tag{57}$$

Obviously,

$$\overline{\psi}_y(\mathbf{p},s,x) = \psi_y^\dagger(\mathbf{p},s,x)\gamma_0,$$

and hence, for definiteness, below we will only discuss the incoming wave packets.

Clearly, the same constructions can be released for the free fields of arbitrary tensor structure.

This finalizes the construction of QSP. However we'll need to do some simplifications.

17.4 Narrow QSP approximation.

From this point we'll consider only very narrow (in the momentum space) packets, for which the function $\phi(\mathbf{k},\mathbf{p})$ is strongly peaked at the point $\mathbf{k}=\mathbf{p}$. In this case, considering that the Dirac spinor $u_s(\mathbf{k})$ is a smooth function of $\mathbf{k}$, we can write

$$\psi_y(\mathbf{p},s,x)=\langle 0|\Psi(y)|\mathbf{p},s,x\rangle \approx e^{-ipx}u_s(\mathbf{p})\psi(\mathbf{p},x-y), \tag{58}$$

where we have introduced the Lorentz-invariant function

$$\boxed{\psi(\mathbf{p},x)=\int \frac{d\mathbf{k}}{(2\pi)^3 2E_{\mathbf{k}}}\, e^{ikx}\phi(\mathbf{k},\mathbf{p})=\psi(\mathbf{0},x_\star).}$$

satisfying the Klein-Gordon equation:

$$(\Box_x - m^2)\psi(\mathbf{p},x)=0.$$

[Therefore it is a relativistic wave packet in terms of conventional scattering theory.]

The approximation (58) is valid under the condition

$$|i\nabla_{\mathbf{y}}\ln\psi(\mathbf{p},x-y)+\mathbf{p}|\ll 2E_{\mathbf{p}}, \tag{59}$$

which is fully consistent with other approximations in the subsequent analysis.

The relations analogous to (58) can be obtained for the free fields of any spin, providing us with the modified Feynman-rule factors for the external legs of any diagram. In particular, it is pertinent to note that the equality

$$\langle 0|\Phi(y)|\mathbf{p},s=0,x\rangle = e^{-ipx}\psi(\mathbf{p},x-y)$$

is exact for the scalar and pseudoscalar fields $\Phi(x)$.

From definition of $\psi(p,x)$ and the correspondence principle it follows that

$$\lim_{\sigma\to 0}\psi(\mathbf{p},x)=e^{ipx} \quad \text{and} \quad \lim_{\sigma\to 0}\psi_y(\mathbf{p},s,x)=e^{-ipy}u_s(\mathbf{p})=\langle 0|\Psi(y)|\mathbf{p},s\rangle.$$

$$\Downarrow$$

An infinitely narrow wave packet in the momentum space corresponds to a plane wave in the configuration space and vice versa.

- The effective spatial volume can be defined in the full analogy with the QM case:

$$\mathrm{V}(\mathbf{p})\stackrel{\text{def}}{=}\int d\mathbf{y}\,\frac{\psi_y^\dagger(\mathbf{p},s,x)\psi_y(\mathbf{p},s,x)}{\psi_x^\dagger(\mathbf{p},s,x)\psi_x(\mathbf{p},s,x)}=\int d\mathbf{x}|\psi(\mathbf{p},x)|^2=\int\frac{d\mathbf{k}}{(2\pi)^3}\frac{|\phi(\mathbf{k},\mathbf{p})|^2}{(2E_\mathbf{k})^2}=\frac{\mathrm{V}(\mathbf{0})}{\Gamma_\mathbf{p}}.$$

- In a similar way, we can define the mean position of the packet:

$$\overline{\mathbf{x}}\stackrel{\text{def}}{=}\frac{\int d\mathbf{y}\,\psi_y^\dagger(\mathbf{p},s,x)\,\mathbf{y}\,\psi_y(\mathbf{p},s,x)}{\int d\mathbf{y}\,\psi_y^\dagger(\mathbf{p},s,x)\psi_y(\mathbf{p},s,x)}=\frac{1}{\mathrm{V}(\mathbf{p})}\int d\mathbf{y}\,\mathbf{y}|\psi(\mathbf{p},x-y)|^2.$$

By using the properties of the function $\psi(\mathbf{p},x)$, it can be proved that

$$\overline{\mathbf{x}}=\mathbf{x}+\mathbf{v}_\mathbf{p}(y_0-x_0).$$

So, in the mean, the packet follows the classical trajectory, with the most probable velocity $\mathbf{v}_\mathbf{p}$.

17.5 Commutation function.

It is useful to introduce the auxiliary operator (wave-packet creation operator)

$$A^{\dagger}_{\mathbf{p}s}(x) = \int \frac{d\mathbf{k}\,\phi(\mathbf{k},\mathbf{p})e^{i(k-p)x}}{2(2\pi)^3\sqrt{E_{\mathbf{k}}E_{\mathbf{p}}}} a^{\dagger}_{\mathbf{k}r}. \tag{60}$$

Then the state $|\mathbf{p},s,x\rangle$ can be written in the form similar to the Fock state:

$$|\mathbf{p},s,x\rangle = \sqrt{2E_{\mathbf{p}}}A^{\dagger}_{\mathbf{p}s}(x)\,|0\rangle.$$

Clearly $A^{\dagger}_{\mathbf{p}s}(x)$ passes into $a^{\dagger}_{\mathbf{p}s}$ in the limit $\boldsymbol{\sigma} \to 0$. It can be easily proved that under the Lorentz transformation,

$$p \longmapsto p' = \Lambda p \quad \text{and} \quad x \longmapsto x' = \Lambda x,$$

the operator (60) is transformed as

$$A^{\dagger}_{\mathbf{p}s}(x) \longmapsto U_{\Lambda}A^{\dagger}_{\mathbf{p}s}(x)U^{-1}_{\Lambda} = \sqrt{E_{\mathbf{p}'}/E_{\mathbf{p}}}\,A^{\dagger}_{\mathbf{p}'s}(x').$$

The following (anti)commutation relations can be derived:

$$\left\{a_{\mathbf{q}r}, A^{\dagger}_{\mathbf{p}s}(x)\right\} = \delta_{sr}\,(4E_{\mathbf{q}}E_{\mathbf{p}})^{-1/2}\,e^{i(q-p)x}\phi(\mathbf{q},\mathbf{p}), \tag{61a}$$

$$\{A_{\mathbf{q}r}(y), A_{\mathbf{p}s}(x)\} = \left\{A^{\dagger}_{\mathbf{q}r}(y), A^{\dagger}_{\mathbf{p}s}(x)\right\} = 0, \tag{61b}$$

$$\left\{A_{\mathbf{q}r}(y), A^{\dagger}_{\mathbf{p}s}(x)\right\} = \delta_{sr}\,(4E_{\mathbf{q}}E_{\mathbf{p}})^{-1/2}\,e^{i(qy-px)}\mathcal{D}(\mathbf{p},\mathbf{q};x-y). \tag{61c}$$

Here we have defined the Lorentz- and translation-invariant commutation function

$$\mathcal{D}(\mathbf{p},\mathbf{q};x-y)=\int\frac{d\mathbf{k}}{(2\pi)^3 2E_{\mathbf{k}}}\,\phi(\mathbf{k},\mathbf{p})\phi^*(\mathbf{k},\mathbf{q})e^{ik(x-y)}.$$

From the last (anti)commutation relation it follows that

$$\langle\mathbf{q},r,y|\mathbf{p},s,x\rangle=\delta_{sr}e^{i(qy-px)}\mathcal{D}(\mathbf{p},\mathbf{q};x-y).$$

It provides, in particular, the invariant and non-singular (assuming $\boldsymbol{\sigma}\neq 0$) normalization of the wave-packet states:

$$\langle\mathbf{p},s,x|\mathbf{p},s,x\rangle=\mathcal{D}(\mathbf{p},\mathbf{p};0)=2m\mathrm{V}_\star\approx 2E_{\mathbf{p}}\mathrm{V}(\mathbf{p}). \tag{62}$$

17.5.1 Plane-wave limit.

In virtue of the correspondence principle, we have for arbitrary (smooth) function $F(\mathbf{p})$:

$$\lim_{\boldsymbol{\sigma}\to 0}\int\frac{d\mathbf{p}\,\mathcal{D}(\mathbf{p},\mathbf{q};x-y)}{(2\pi)^3 2E_{\mathbf{p}}}F(\mathbf{p})=\lim_{\boldsymbol{\sigma}\to 0}\int\frac{d\mathbf{k}\,\phi^*(\mathbf{k},\mathbf{q})}{(2\pi)^3 2E_{\mathbf{k}}}e^{ik(x-y)}F(\mathbf{k})=e^{iq(x-y)}F(\mathbf{q}),$$

$$\Downarrow$$

$$\lim_{\boldsymbol{\sigma}\to 0}\mathcal{D}(\mathbf{p},\mathbf{q};x-y)=(2\pi)^3 2E_{\mathbf{p}}\delta(\mathbf{p}-\mathbf{q})e^{ip(x-y)},$$

$$\Downarrow$$

$$\lim_{\boldsymbol{\sigma}\to 0}\left\{A_{\mathbf{q}r}(y),A^\dagger_{\mathbf{p}s}(x)\right\}=(2\pi)^3\delta_{sr}\delta\left(\mathbf{p}-\mathbf{q}\right),\quad\lim_{\boldsymbol{\sigma}\to 0}\langle\mathbf{q},r,y|\mathbf{p},s,x\rangle=(2\pi)^3\delta_{sr}2E_{\mathbf{p}}\delta\left(\mathbf{p}-\mathbf{q}\right).$$

17.5.2 Behavior of the commutation function in the center-of-inertia frame.

Certain properties of the commutation function become especially transparent in the center-of-inertia frame (CIF) of the two packets ($\mathbf{p}_* + \mathbf{q}_* = 0$) in which

$$\mathcal{D}(\mathbf{p}_*, -\mathbf{p}_*; x_* - y_*) = \int \frac{d\mathbf{k}}{(2\pi)^3 2E_{\mathbf{k}}} \phi(\mathbf{k}, \mathbf{p}_*)\phi^*(\mathbf{k}, -\mathbf{p}_*)e^{ik(x_* - y_*)}.$$

- Due to the assumed behaviour of $\phi(\mathbf{k}, \mathbf{p})$ in the vicinity of the point $\mathbf{k} = \mathbf{p}$, one may expect that $|\mathcal{D}(\mathbf{p}_*, -\mathbf{p}_*; x_* - y_*)|$ has a sharp maximum at $\mathbf{p}_* = 0$.
- On the contrary, the function $|\mathcal{D}(\mathbf{p}_*, -\mathbf{p}_*; x_* - y_*)|$ vanishes at large $|\mathbf{p}_*|$, since the maxima of the factors $|\phi(\mathbf{k}, \mathbf{p}_*)|$ and $|\phi(\mathbf{k}, -\mathbf{p}_*)|$ in the integrand are widely separated in this case and thus $|\phi(\mathbf{k}, \mathbf{p}_*)\phi^*(\mathbf{k}, -\mathbf{p}_*)| \ll 1$ for any $\mathbf{k}$.

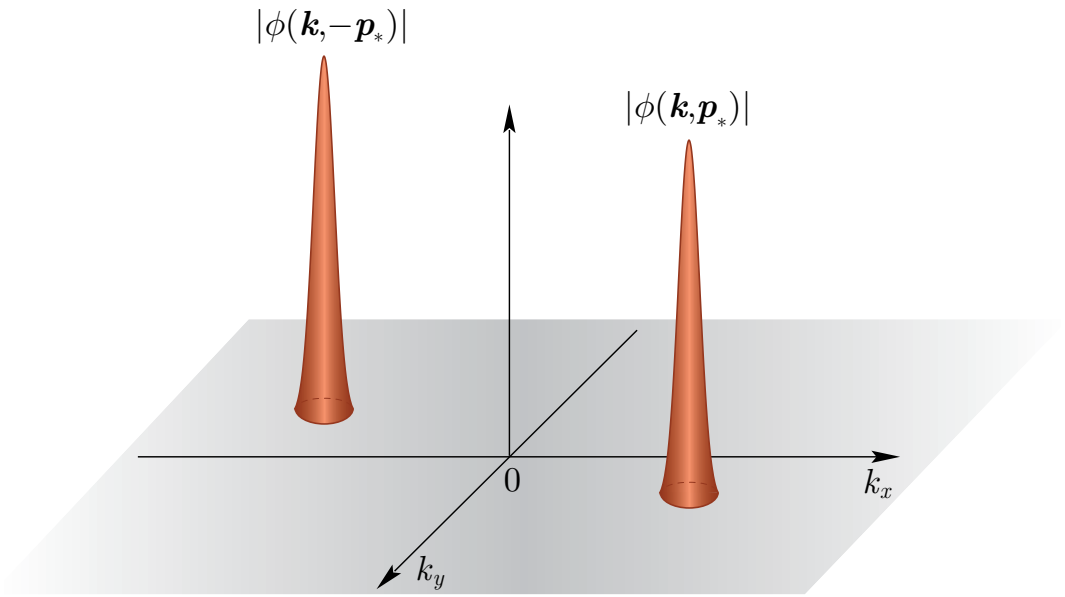

- Function $\mathcal{D}(\mathbf{p}_*, -\mathbf{p}_*; x_* - y_*)$ vanishes at any $|\boldsymbol{p}_*|$ if the points x_* and y_* are widely separated in space (that is the value of $|\mathbf{x}_* - \mathbf{y}_*|$ is large) because the phase factor $e^{-i\mathbf{k}(\mathbf{x}_* - \mathbf{y}_*)}$ in the integrand rapidly oscillates in this case.

17.5.3 Summary of kinematic relations.

To come back into the laboratory (or any other) frame we have to express the asterisked variables in terms of the non-asterisked ones.

- The Lorentz-transformation rules:

$$x^0_* = \Gamma\left(x^0 - \mathbf{vx}\right), \quad \mathbf{x}_* = \mathbf{x} + \Gamma\left[\frac{\Gamma}{\Gamma+1}(\mathbf{vx}) - x^0\right]\mathbf{v},$$

- The velocity and Lorentz factor of CIF in the lab. frame:

$$\mathbf{v} = \frac{\mathbf{p}+\mathbf{q}}{E_\mathbf{p} + E_\mathbf{q}}, \quad \Gamma = \frac{1}{\sqrt{1-\mathbf{v}^2}} = \frac{E_\mathbf{p} + E_\mathbf{q}}{E_{\mathbf{p}_*} + E_{\mathbf{q}_*}}$$

- The energies and momenta in CIF:

$$E_{\mathbf{p}_*} = E_{\mathbf{q}_*} = \frac{1}{2}\sqrt{(p+q)^2} \equiv E_*, \quad |\mathbf{p}_*| = |\mathbf{q}_*| = \frac{1}{2}\sqrt{-(p-q)^2} \equiv P_*.$$

  It is seen from the last relation that P_* vanishes as $\mathbf{p} \to \mathbf{q}$ and grows with increasing $|\mathbf{p}-\mathbf{q}|$. [Hence from the above consideration it follows that the function $|\mathcal{D}(\mathbf{p},\mathbf{q};x-y)|$ reaches its maximum at $\mathbf{p}=\mathbf{q}$ and vanishes at large values of $|\mathbf{p}-\mathbf{q}|$.]

- Useful identities:

$$2E_*x^0_* = (p+q)x, \quad 2\mathbf{p}_*\mathbf{x}_* = (q-p)x, \quad \mathbf{vx}_* = \Gamma\left(\mathbf{vx} - \mathbf{v}^2x^0\right),$$

$$\mathbf{x}^2_* = \frac{[(p+q)x]^2}{(p+q)^2} - x^2 = \Gamma^2\left(\left|\mathbf{x} - \mathbf{v}x^0\right|^2 - |\mathbf{v}\times\mathbf{x}|^2\right), \quad \mathbf{x}_* = 0 \Longleftrightarrow \mathbf{x} = \mathbf{v}x^0.$$

17.6 Multi-packet states.

[This item is important as a "prearrangement" for an extension of the formalism to include the effects of coherent forward neutrino scattering from the matter background particles.]

Let's define the ket-state (and consequently bra-states) of n identical wave packets by

$$\begin{aligned}
|\,\{\mathbf{p},s,x\}_n\rangle &\equiv |\,\mathbf{p}_1,s_1,x_1;\mathbf{p}_2,s_2,x_2;\ldots;\mathbf{p}_n,s_n,x_n\rangle \\
&= \widetilde{A}^\dagger_{\mathbf{p}_1 s_1}(x_1)\widetilde{A}^\dagger_{\mathbf{p}_2 s_2}(x_2)\cdots\widetilde{A}^\dagger_{\mathbf{p}_n s_n}(x_n)|0\rangle \\
&= (\pm 1)^{n(n-1)/2}\,\widetilde{A}^\dagger_{\mathbf{p}_n s_n}(x_n)\cdots\widetilde{A}^\dagger_{\mathbf{p}_2 s_2}(x_2)\widetilde{A}^\dagger_{\mathbf{p}_1 s_1}(x_1)|0\rangle, \\
\langle\{\mathbf{p},s,x\}_n\,| &\equiv \langle\mathbf{p}_1,s_1,x_1;\mathbf{p}_2,s_2,x_2;\ldots;\mathbf{p}_n,s_n,x_n\,| \\
&= \langle 0|\widetilde{A}_{\mathbf{p}_n s_n}(x_n)\cdots\widetilde{A}_{\mathbf{p}_2 s_2}(x_2)\widetilde{A}_{\mathbf{p}_1 s_1}(x_1) \\
&= (\pm 1)^{n(n-1)/2}\langle 0|\widetilde{A}_{\mathbf{p}_1 s_1}(x_1)\widetilde{A}_{\mathbf{p}_2 s_2}(x_2)\cdots\widetilde{A}_{\mathbf{p}_n s_n}(x_n),
\end{aligned}$$

where the sign "$+$" ("$-$") is for bosons (fermions) and

$$\widetilde{A}^\dagger_{\mathbf{p}s}(x) = \sqrt{2E_{\mathbf{p}}}\,A^\dagger_{\mathbf{p}s}(x), \quad \widetilde{A}_{\mathbf{p}s}(x) = \sqrt{2E_{\mathbf{p}}}\,A_{\mathbf{p}s}(x).$$

It is easy to see that this state is fully (anti)symmetric relative to permutation

$$(\mathbf{p}_i,s_i,x_i) \longleftrightarrow (\mathbf{p}_j,s_j,x_j) \text{ for any } 1\le i,j\le n \ (i\ne j).$$

To determine the normalization of the multi-packet states we define the $n\times n$ matrix

$$\mathbb{D}_n = \mathbb{D}\left(\{\mathbf{q},r,y\}_n,\{\mathbf{p},s,x\}_n\right) = \left|\left|\delta_{s_i r_j}(\mp 1)^{i+j}\mathcal{D}(\mathbf{p}_i,\mathbf{q}_j;x_i-y_j)\right|\right|.$$

It can be proved by induction (not so easy, see Appendix F, p. 859 ☕) that

$$\boxed{\langle\{\mathbf{q},r,y\}_n\,|\,\{\mathbf{p},s,x\}_n\rangle = \exp\left[i\sum_{i=1}^{n}(q_i y_i - p_i x_i)\right]\det\left(\mathbb{D}_n\right).} \tag{63}$$

$$\mathcal{D}(\mathbf{p},\mathbf{q};x-y) = \mathcal{D}^*(\mathbf{q},\mathbf{p};y-x) \Longrightarrow \begin{cases}\mathbb{D}\left(\{\mathbf{p},s,x\}_n,\{\mathbf{p},s,x\}_n\right) \text{ is Hermitian,}\\ \langle\{\mathbf{p},s,x\}_n\,|\,\{\mathbf{p},s,x\}_n\rangle \text{ is real.}\end{cases}$$

Examples

$$\langle\{\mathbf{p},s,x\}_1\,|\,\{\mathbf{p},s,x\}_1\rangle = 2m\mathrm{V}_\star,$$

$$\langle\{\mathbf{p},s,x\}_2\,|\,\{\mathbf{p},s,x\}_2\rangle = (2m\mathrm{V}_\star)^2 \pm \delta_{s_1 s_2}|\mathcal{D}(\mathbf{p}_1,\mathbf{p}_2;x_1-x_2)|^2,$$

$$\langle\{\mathbf{p},s,x\}_3\,|\,\{\mathbf{p},s,x\}_3\rangle = (2m\mathrm{V}_\star)^3 \pm 2m\mathrm{V}_\star\sum_{1\le i<j\le 3}\delta_{s_i s_j}|\mathcal{D}(\mathbf{p}_i,\mathbf{p}_j;x_i-x_j)|^2$$
$$+2\mathrm{Re}\prod_{1\le i<j\le 3}\left[\delta_{s_i s_j}\mathcal{D}(\mathbf{p}_i,\mathbf{p}_j;x_i-x_j)\right].$$

Simplest repercussions

Non-overlapping regime: If the space-time points $x_1, x_2, \ldots, x_n$ ($n \geq 2$) are well separated and/or the 3-momenta $\mathbf{p}_1, \mathbf{p}_2, \ldots, \mathbf{p}_n$ essentially differ from each other, the n-packet matrix element is approximately equal to $(2m\mathrm{V}_\star)^n$.

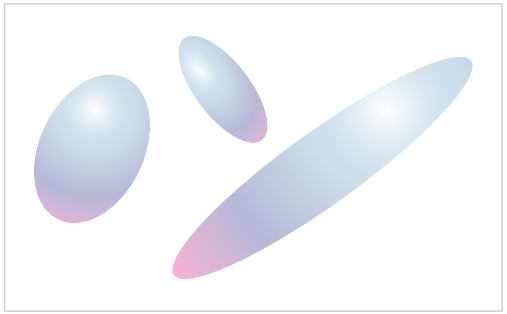

Overlapping regime: If the wave packets having the same spin projections strongly overlap in both the momentum and the configuration spaces, the n-boson matrix element tends to $n!(2m\mathrm{V}_\star)^n$, while the n-fermion matrix element vanishes.

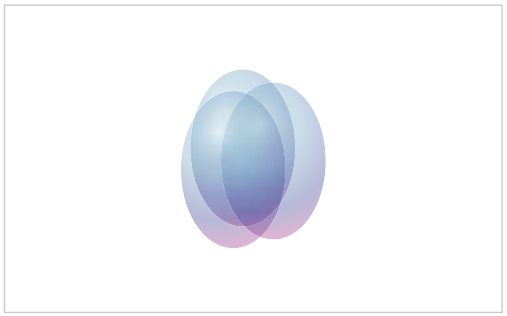

The behaviour of the n-particle matrix element in the overlapping regime is merely a manifestation of the effects of Bose attraction and Pauli blocking for identical bosons and fermions, respectively.

It is less trivial that the wave-packet formalism reproduces another intuitively evident result that the identical non-interacting bosons (fermions) with the same momenta and the same spin projections do not condense (may well coexist) if they are separated by a sufficiently large space-time interval. This result cannot be understood within the framework of the plane-wave approach.

We will return to this conceptually important issue in order to clarify the exact meaning of the words "sufficiently large space-time interval".

17.7 Relativistic Gaussian packets (RGP).

In further consideration we will use a simple model of the QFT WP state – relativistic Gaussian packet (RGP), in which the form-factor function $\phi(\mathbf{k},\mathbf{p})$ is of the form

$$\boxed{\phi(\mathbf{k},\mathbf{p}) = \frac{2\pi^2}{\sigma^2 K_1(m^2/2\sigma^2)} \exp\left(-\frac{E_{\mathbf{k}}E_{\mathbf{p}} - \mathbf{kp}}{2\sigma^2}\right) \stackrel{\text{def}}{=} \phi_G(\mathbf{k},\mathbf{p}),} \tag{64}$$

where K_1 is the modified Bessel function of the 3rd kind of order 1.

$$K_1(z) = z\int_1^\infty dt e^{-zt}\sqrt{t^2-1} \qquad \left(|\arg z| < \frac{\pi}{2}\right).$$

One can check that the function (64) has the correct plane-wave limit and satisfies the normalization conditions.

In what follows we assume $\boxed{\sigma^2 \ll m^2.}$ Then the function (64) can be rewritten as an asymptotic expansion:

$$\phi_G(\mathbf{k},\mathbf{p}) = \frac{2\pi^{3/2}}{\sigma^2}\frac{m}{\sigma}\exp\left[\frac{(k-p)^2}{4\sigma^2}\right]\left[1+\frac{3\sigma^2}{4m^2}+\mathcal{O}\left(\frac{\sigma^4}{m^4}\right)\right].$$

In the nonrelativistic case, $(|\mathbf{k}|+|\mathbf{p}|)^2 \ll 4m^2$, and only in this case this form factor coincides, up to a normalization factor, with the usual (noncovariant) Gaussian distribution:

$$\varphi_G(\mathbf{k}-\mathbf{p}) \propto \exp\left[-\frac{(\mathbf{k}-\mathbf{p})^2}{4\sigma^2}\right].$$

But it is not the case at relativistic and especially ultrarelativistic momenta, when the functions ϕ_G and φ_G significantly differ from each other.

17.7.1 Example: ultrarelativistic case.

In the UR limit ($\mathbf{p}^2 \gg m^2$, $\mathbf{k}^2 \gg m^2$) the function $\phi_G(\mathbf{k},\mathbf{p})$ behaves as

$$\phi_G(\mathbf{k},\mathbf{p}) \approx \frac{2\pi^{3/2}}{\sigma^2}\frac{m}{\sigma}\exp\left[-\frac{m^2\left(|\mathbf{k}|-|\mathbf{p}|\right)^2}{4\sigma^2|\mathbf{k}||\mathbf{p}|}-\frac{(1-\cos\theta)\,|\mathbf{k}||\mathbf{p}|}{2\sigma^2}\right] \equiv \phi_G^{\mathsf{UR}}(\mathbf{k},\mathbf{p}),$$

where θ is the angle between the vectors $\mathbf{k}$ and $\mathbf{p}$.

In particular, for $\theta = 0$ and $\pi/2$ we have

$$\phi_G^{\mathsf{UR}}\big|_{\theta=0} \propto \exp\left[-\frac{(\mathbf{k}-\mathbf{p})^2}{4\sigma^2\Gamma_{\mathbf{k}}\Gamma_{\mathbf{p}}}\right] \quad \text{and} \quad \phi_G^{\mathsf{UR}}\big|_{\theta=\pi/2} \propto \exp\left[-\frac{|\mathbf{k}||\mathbf{p}|}{2\sigma^2}\right].$$

In the first case, the relativistic effect consists in a widening of the packet (in comparison with the NR case) in the momentum space ("renormalization" of the WP width):

$$\sigma \longmapsto \sigma\sqrt{\Gamma_{\mathbf{k}}\Gamma_{\mathbf{p}}}.$$

This effect is essential for the neutrino production and absorption processes involving relativistic particles.

17.7.2 Plane-wave limit.

To illustrate the importance of the correct normalization it is useful to verify that the limit of $\phi_G(\mathbf{k},\mathbf{p})$ as $\sigma \to 0$ is indeed $\propto \delta(\mathbf{k}-\mathbf{p})$. To do this it is sufficient to prove that for any smooth function $F(\mathbf{k})$

$$\lim_{\sigma\to 0}\int \frac{d\mathbf{k}\,\phi_G(\mathbf{k},\mathbf{0})}{(2\pi)^3 2E_{\mathbf{k}}}\,F(\mathbf{k}) = F(\mathbf{0}). \tag{65}$$

The left part of the latter equality can be transformed to the following form

$$\lim_{\sigma\to 0}\frac{m}{(4\pi)^{3/2}\sigma^3}\int d\Omega_{\mathbf{k}}\int_0^\infty d|\mathbf{k}|\,\frac{\mathbf{k}^2}{E_{\mathbf{k}}}\exp\left[-\frac{m^2}{2\sigma^2}\left(\frac{E_{\mathbf{k}}}{m}-1\right)\right]F(\mathbf{k})$$

$$= \lim_{\sigma\to 0}\left(\frac{m^2}{4\pi\sigma^2}\right)^{3/2}\int d\mathbf{n}\int_0^\infty dt\exp\left(-\frac{m^2 t}{2\sigma^2}\right)\sqrt{t(t+2)}\,F\left(m\sqrt{t(t+2)}\,\mathbf{n}\right),$$

where $\mathbf{n}=\mathbf{k}/|\mathbf{k}|$. In order to estimate the integral in t one can use the famous formula[a]

$$\int_0^\infty dt t^{a-1}e^{-\nu t}f(t) \sim \nu^{-a}\Gamma(a)f(0)\,[1+o(1)] \qquad (a>0,\ \nu\to\infty), \tag{66}$$

which is valid for arbitrary continuous function $f(t)$, $t\in[0,\infty)$. Since in our case

$$a=\frac{3}{2},\quad \nu=\frac{m^2}{2\sigma^2} \quad \text{and} \quad f(t)=\sqrt{t+2}\,F\left(m\sqrt{t(t+2)}\,\mathbf{n}\right),$$

the identity (65) becomes evident.

As a result we see that the function $\phi_G(\mathbf{k},\mathbf{p})$ actually represents the simplest model of the form factor satisfying all the conditions imposed to the generic function $\phi(\mathbf{k},\mathbf{p})$.

[a] See, e.g., М. В. Федорюк. Метод перевала. М.: Наука. 1977.

17.7.3 Function $\psi_G(\mathbf{p}, x)$.

The function $\psi(\mathbf{p}, x)$ in the RGP model is

$$\psi(\mathbf{p}, x) = \frac{K_1(\zeta m^2/2\sigma^2)}{\zeta K_1(m^2/2\sigma^2)} \stackrel{\text{def}}{=} \psi_G(\mathbf{p}, x).$$

Here we have defined the dimensionless Lorentz-invariant complex variable

$$\zeta = \sqrt{1 - \frac{4\sigma^2}{m^2}\,[\sigma^2 x^2 + i(px)]};$$

$$|\zeta|^4 = \left[1 - \frac{4\sigma^4 x^2}{m^2}\right]^2 + \frac{16\sigma^4 (px)^2}{m^4},$$

$$\varphi = \arg\zeta = -\frac{1}{2}\arcsin\left[\frac{4\sigma^2(px)}{m^2|\zeta|^2}\right].$$

It can be proved that for any $\mathbf{p}$ and x

$$|\zeta| \geq 1 \quad \text{and} \quad |\varphi| < \pi/2.$$

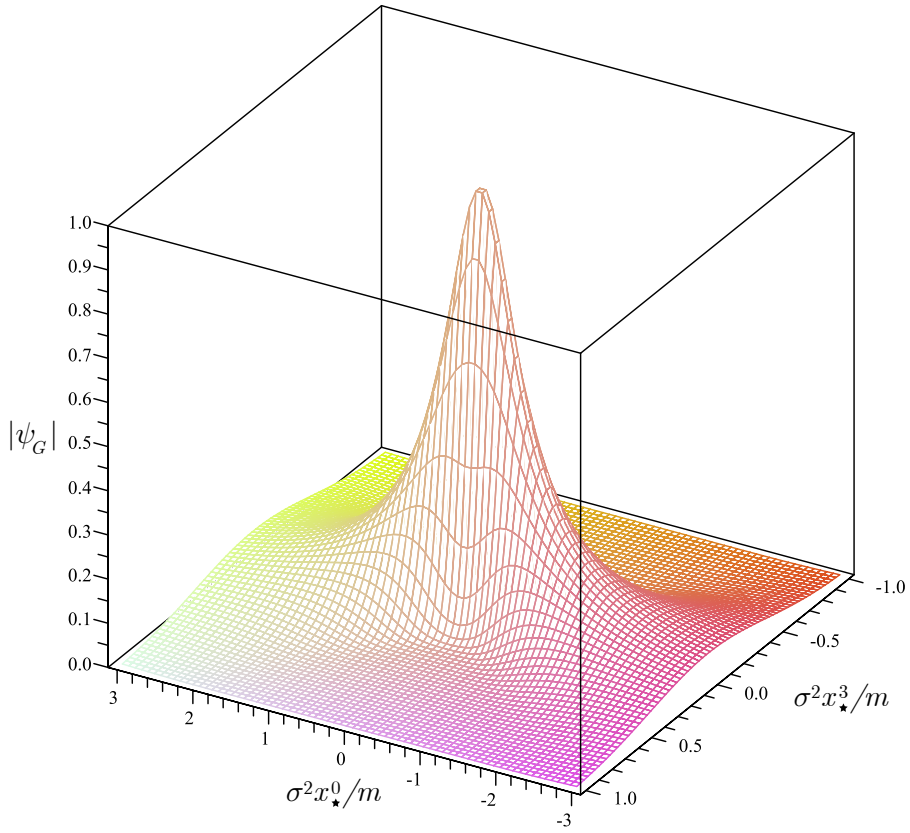

△ A 3D plot of $|\psi_G(\mathbf{0}, x_\star)|$ as a function of $\sigma^2 x^0_\star/m$ and $\sigma^2 x^3_\star/m$ [assuming that $\mathbf{x}_\star = (0, 0, x^3_\star)$]. The calculations are done for $\sigma/m = 0.1$.

Note: The unrealistically large σ/m ratio was chosen only because at more realistic $\sigma/m \ll 1$ ratios, the shape of $|\psi_G(\mathbf{0}, x_\star)|$ flattens along the spatial axis so much that pattern recognition becomes impossible.

Training

It is useful to ascertain that the function ψ_G satisfies the Klein-Gordon equation. Taking into account that

$$K_0'(z) = -K_1(z) \quad \text{and} \quad K_1'(z) = -K_0(z) - K_1(z)/z,$$

we find

$$\partial_\mu \left[\frac{K_1(z)}{z}\right] = -\left[K_0(z) + \frac{2}{z}K_1(z)\right]\frac{\partial_\mu z}{z}, \quad \text{where} \quad z = \frac{m^2\zeta}{2\sigma^2},$$

$$\Downarrow$$

$$\Box\left[\frac{K_1(z)}{z}\right] = -\left[K_0(z) + \frac{2}{z}K_1(z)\right]\frac{\Box z}{z} - \left[\frac{3}{z}K_0(z) + \left(1 + \frac{6}{z^2}\right)K_1(z)\right]\frac{(\partial_\mu z)(\partial^\mu z)}{z}. \qquad (67)$$

Next step:

$$\partial_\mu z = -\frac{m^2}{\sigma^2 z}\left(\sigma^2 x_\mu + \frac{i}{2}p_\mu\right)$$

$$\Downarrow$$

$$\Box z = -\partial_\mu\partial^\mu z = \frac{3m^2}{z} \quad \text{and} \quad (\partial_\mu z)(\partial^\mu z) = -m^2.$$

Substituting these identities into Eq. (67) and taking into account the explicit form of ψ_G we see that

$$(\Box - m^2)\psi_G = 0.$$

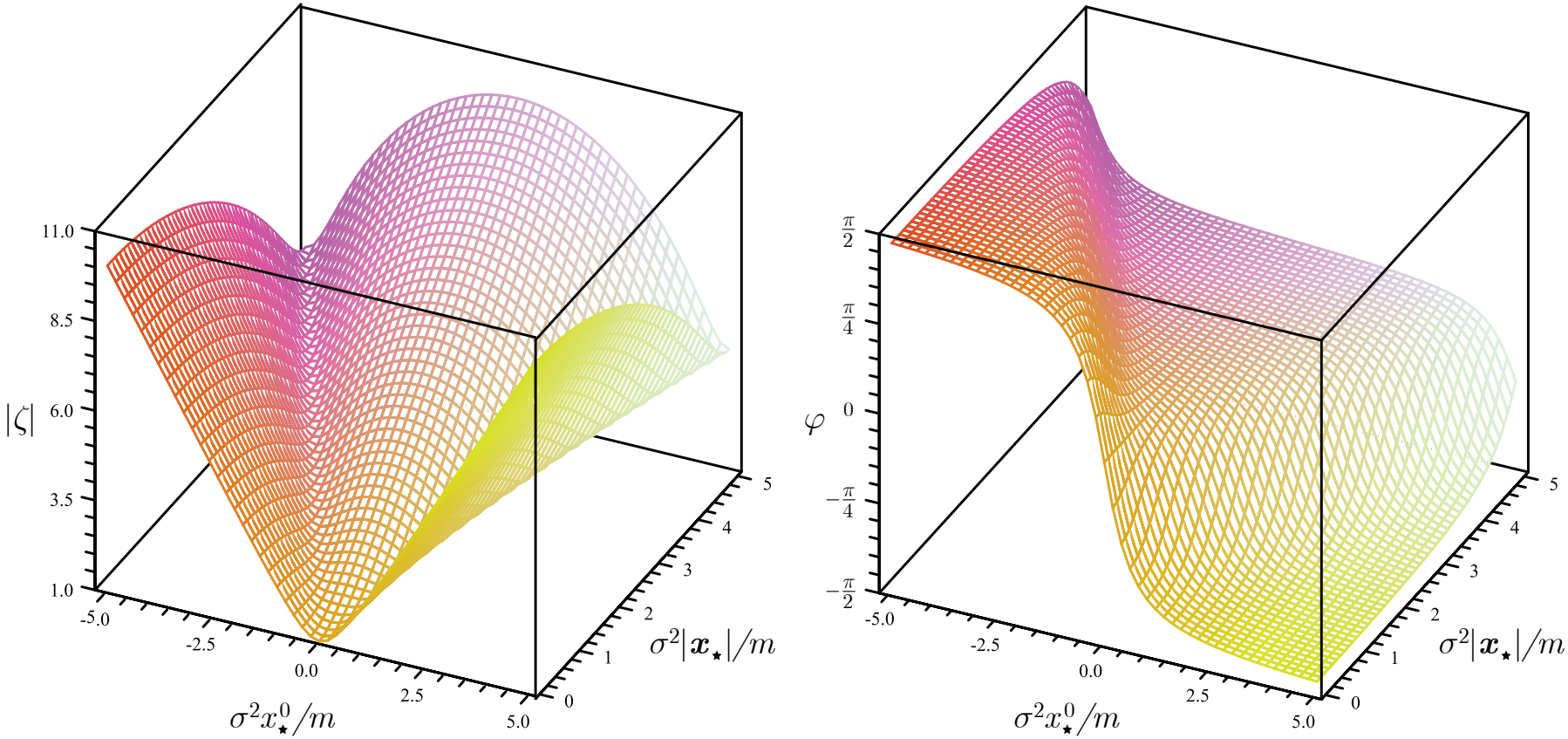

3D plots of $|\zeta|$ and $\varphi = \arg\zeta$ as functions of $\sigma^2 x^0_\star/m$ and $\sigma^2 x^3_\star/m$ [assuming that $\mathbf{x}_\star = (0, 0, x^3_\star)$]. As above, the calculations are performed for the (unrealistically large) ratio $\sigma/m = 0.1$ (see p. 561).

As we see, in spite of the simplicity of the RGP in the momentum space, its evolution in space and time is rather complicated. In what follows, we will use only a very limited space-time region around the center of the packet, in which its shape is very simple.

17.7.4 Nondiffluent regime. Contracted RGP (CRGP).

An analysis of the asymptotic expansion of $\ln\left[\psi_G(\mathbf{0},x_\star)\right]$ in powers of $\sigma^2/(m^2\zeta)$ provides the necessary and sufficient conditions of the nondiffluent behavior.

Due to the inequalities

$$|\zeta|\geq 1,\quad |\varphi|<\pi/2,\quad \text{and}\quad \sigma^2\ll m^2,$$

one can use the asymptotic expansion

$$K_1(z)\sim\sqrt{\frac{\pi}{2z}}\,e^{-z}\left[1+\frac{3}{8z}+\frac{15}{2(8z)^2}+\mathcal{O}\left(\frac{1}{z^3}\right)\right]\qquad\left(|\arg z|<\frac{3\pi}{2}\right),\tag{68}$$

which gives

$$\psi_G(\mathbf{p},x)=\frac{1}{\zeta^{3/2}}\exp\left[\frac{m^2(1-\zeta)}{2\sigma^2}\right]\left[1-\frac{3\sigma^2}{4m^2}\left(1-\frac{1}{\zeta}\right)+\frac{3\sigma^4}{32m^4}\left(1-\frac{1}{\zeta}\right)\left(11+\frac{5}{\zeta}\right)+\mathcal{O}\left(\frac{\sigma^6}{m^6}\right)\right].$$

This formula is valid for any $\mathbf{p}$ and x, but it is still too involved for our aims. Under additional restrictions the above expression can be essentially simplified by using an expansion of the variable ζ in powers of the small parameter σ^2/m^2. In the proper frame of the packet we obtain

$$\begin{aligned}\ln\left[\psi_G(\mathbf{0},x_\star)\right]=imx_\star^0&\left[1+\frac{3\sigma^2}{m^2}-\frac{\sigma^4}{m^4}\left(2m^2\mathbf{x}_\star^2-\frac{3}{2}\right)\right]\\&-\sigma^2\mathbf{x}_\star^2-\frac{3\sigma^4}{m^2}\left[(x_\star^0)^2+\mathbf{x}_\star^2\right]+\mathcal{O}\left(\frac{\sigma^6}{m^6}\right).\end{aligned}\tag{69}$$

We see that $|\psi_G(\mathbf{0},x_\star)|$ depends on time only in the $\mathcal{O}\left(\sigma^4/m^4\right)$ order.

An elementary analysis suggests that the asymptotic series (69) can be truncated by neglecting the $\mathcal{O}\left(\sigma^4/m^4\right)$ terms under the following (necessary and sufficient) conditions:

$$\sigma^2(x_\star^0)^2 \ll m^2/\sigma^2, \qquad \sigma^2|\mathbf{x}_\star|^2 \ll m^2/\sigma^2. \tag{70a}$$

They can be rewritten in the equivalent but explicitly Lorentz-invariant form:

$$(px)^2 \ll m^4/\sigma^4, \qquad (px)^2 - m^2x^2 \ll m^4/\sigma^4. \tag{70b}$$

Under these conditions, the function $\psi_G(\mathbf{p},x)$ has a very simple and transparent form:

$$\psi_G(\mathbf{p},x) = \exp\left\{i(px) - (\sigma/m)^2\left[(px)^2 - m^2x^2\right]\right\} \quad \text{[inv]} \tag{71a}$$

$$= \exp\left\{iE_{\mathbf{p}}\left(x_0 - \mathbf{v}_{\mathbf{p}}\mathbf{x}\right) - \sigma^2\Gamma_{\mathbf{p}}^2\left[\left(\mathbf{x} - \mathbf{v}_{\mathbf{p}}x_0\right)^2 - \left(\mathbf{v}_{\mathbf{p}} \times \mathbf{x}\right)^2\right]\right\} \quad \text{[LF]} \tag{71b}$$

$$= \exp\left[iE_{\mathbf{p}}\left(x_0 - \mathbf{v}_{\mathbf{p}}\mathbf{x}\right) - \sigma^2\Gamma_{\mathbf{p}}^2\left(\mathbf{x}_\parallel - \mathbf{v}_{\mathbf{p}}x_0\right)^2 - \sigma^2\mathbf{x}_\perp^2\right] \quad \text{[LF]} \tag{71c}$$

$$= \exp\left(imx_\star^0 - \sigma^2\mathbf{x}_\star^2\right). \quad \text{[PRF]} \tag{71d}$$

Let's now list the most important properties of this approximation, which we'll call the contracted relativistic Gaussian packet (CRGP).

Some properties of CRGP:

1. Near its center, the CRGP behaves (and therefore interacts!) like a plane wave.
2. The mean coordinate of the packet follows the classical trajectory (CT) $\mathbf{x} = \mathbf{v}_{\mathbf{p}}x_0$.
3. $|\psi_G(\mathbf{p},x)| = 1$ along the CT and $|\psi_G(\mathbf{p},x)| < 1$ at any deviation from it.
4. $|\psi_G(\mathbf{p},x)|$ is invariant under the transformations $\{x_0 \longmapsto x_0 + \tau,\ \mathbf{x} \longmapsto \mathbf{x} + \mathbf{v}_{\mathbf{p}}\tau\}$.
5. In the nonrelativistic limit, $\psi_G(\mathbf{p},x)$ behaves as $\exp\left[im\left(x_0 - \mathbf{v}_{\mathbf{p}}\mathbf{x}\right) - \sigma^2\left|\mathbf{x} - \mathbf{v}_{\mathbf{p}}x_0\right|^2\right]$.

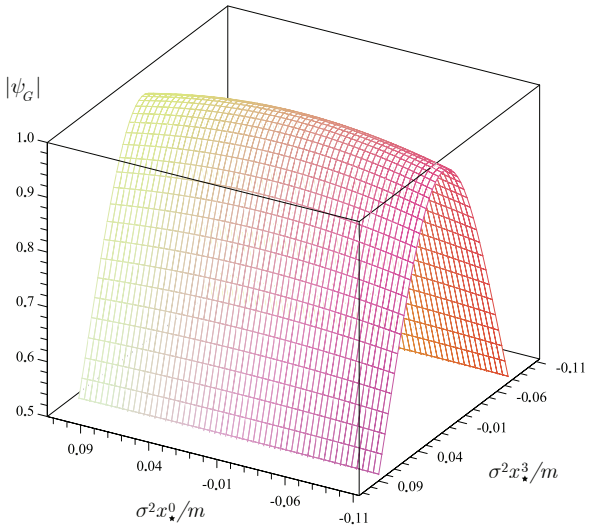

△ A 3D plot of $|\psi_G(\mathbf{0}, x_\star)|$ in the small vicinity of the maximum as a function of $\sigma^2 x^0_\star/m$ and $\sigma^2 x^3_\star/m$ [assuming that $\mathbf{x}_\star = (0, 0, x^3_\star)$]. The calculations are done for $\sigma/m = 0.1$.

The CRGP model permits to check the validity of the condition (59) necessary for the applicability of the factorization formula (58) – an essential element of the formalism. As is follows from the explicit form of $\psi_G(\mathbf{p}, x)$ in the CRGP approximation,

$$i\nabla_{\mathbf{x}} \ln \psi_G(\mathbf{p}, x) = \mathbf{p} + 2i\frac{\sigma^2}{m^2}\left[(px)\mathbf{p} - m^2\mathbf{x}\right].$$

Therefore the condition (59) can be written in the form

$$\left|(pX)\mathbf{p} - m^2\mathbf{X}\right| \ll \left(m^2/\sigma^2\right) E_{\mathbf{p}}, \qquad (72)$$

where $X = (X_0, \mathbf{X}) = (y_0 - x_0, \mathbf{y} - \mathbf{x})$. Then the elementary algebra yields

$$\begin{aligned}\left|(pX)\mathbf{p} - m^2\mathbf{X}\right|^2 &= (pX)^2\mathbf{p}^2 - 2m^2(pX)(\mathbf{pX}) + m^4\mathbf{X}^2 \\ &= (pX)^2 E_{\mathbf{p}}^2 + m^2\left[(\mathbf{pX})^2 + m^2\mathbf{X}^2 - E_{\mathbf{p}}^2 X_0^2\right] \\ &\le (pX)^2 E_{\mathbf{p}}^2 + m^2\left(\mathbf{p}^2\mathbf{X}^2 + m^2\mathbf{X}^2 - E_{\mathbf{p}}^2 X_0^2\right).\end{aligned}$$

As a result we have proved that

$$\left|(pX)\mathbf{p} - m^2\mathbf{X}\right| \le E_{\mathbf{p}}\sqrt{(pX)^2 - m^2X^2}.$$

Therefore the inequality (72) is not an independent condition but is satisfied automatically in the CRGP approximation.

It can be also proved that the quantum correction to the classical momentum vanishes on the classical trajectory $\mathbf{X} = \mathbf{v}_{\mathbf{p}} X_0$ and thus remains small on quasiclassical trajectories.

17.8 Compendium.

Exact wavefunction $\psi(\mathbf{p},x)$ for RGP:

$$\psi(\mathbf{p},x)=\frac{K_1(\zeta m^2/2\sigma^2)}{\zeta K_1(m^2/2\sigma^2)}\stackrel{\text{def}}{=}\psi_G(\mathbf{p},x),$$

$$\zeta=\sqrt{1-\frac{4\sigma^2}{m^2}\left[\sigma^2x^2+i(px)\right]}.$$

Nondiffluent regime, contracted RGP:

Under the following N&S conditions

$$\sigma^2(x^0_\star)^2\ll m^2/\sigma^2,\quad \sigma^2|\mathbf{x}_\star|^2\ll m^2/\sigma^2,$$
$$(px)^2\ll m^4/\sigma^4,\quad (px)^2-m^2x^2\ll m^4/\sigma^4.$$

Two pairs of the inequalities are equivalent.
RGP is stable in its proper frame ($\mathbf{p}^\star=0$):

$$\psi_G(\mathbf{0},x^\star)=\exp\left(imx^0_\star-\sigma^2\mathbf{x}^2_\star\right).$$

In the lab. frame it has the following form:

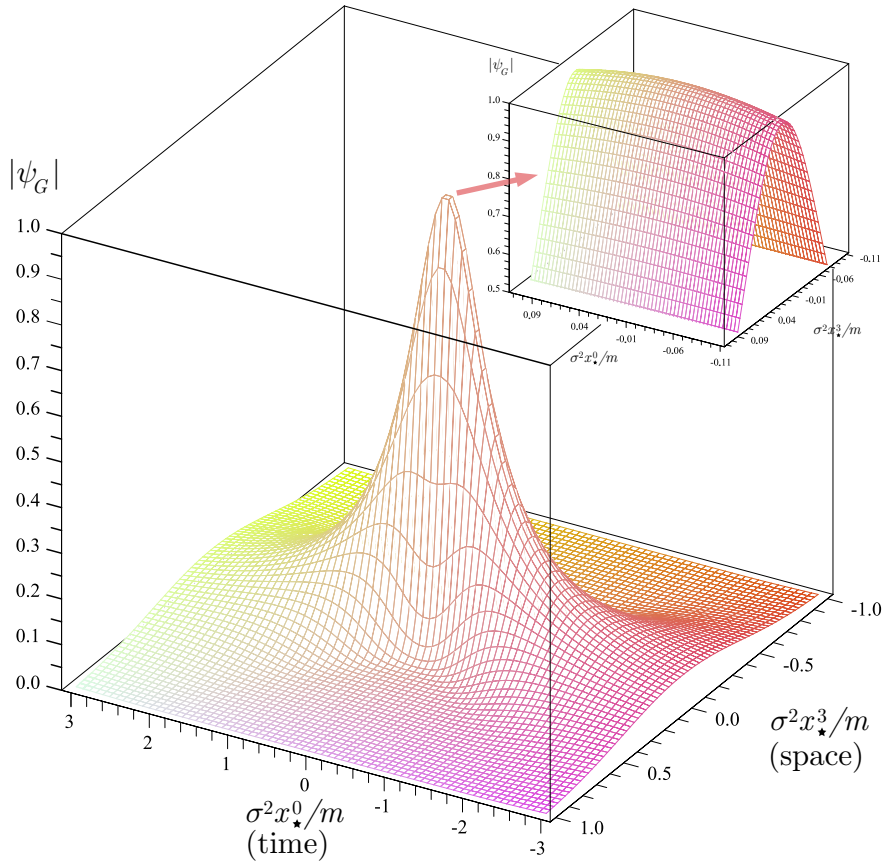

△ 3D plot of $|\psi_G(\mathbf{0},x_\star)|$ vs. $\sigma^2x^0_\star/m$ and $\sigma^2x^3_\star/m$, assuming $\mathbf{x}_\star=(0,0,x^3_\star)$ and $\sigma=0.1m$.

$$\psi_G(\mathbf{p},x)=\exp\left\{i(px)-(\sigma/m)^2\left[(px)^2-m^2x^2\right]\right\}.$$

17.9 Function $\mathcal{D}_G(\mathbf{p},\mathbf{q};x)$.

One can derive the explicit formula for the commutation function:

$$\mathcal{D}(\mathbf{p},\mathbf{q};x) = 2m\mathrm{V}_\star \frac{K_1(zm^2/\sigma^2)}{zK_1(m^2/\sigma^2)} \stackrel{\text{def}}{=} \mathcal{D}_G(\mathbf{p},\mathbf{q};x),$$

$$z = \frac{E_*}{m}\sqrt{1-\frac{\sigma^2}{E_*^2}\left[\sigma^2 x_*^2 + 2iE_* x_*^0\right]} = \frac{1}{2m}\sqrt{(p+q)^2 - 4\sigma^2\left[\sigma^2 x^2 + i(p+q)x\right]}.$$

The module and phase of z are determined by

$$|z|^4 = \frac{1}{4}\left(1+\frac{pq-2\sigma^4x^2}{m^2}\right)^2 + \left[\frac{\sigma^2(p+q)x}{m^2}\right]^2, \quad \arg\, z = -\frac{1}{2}\arcsin\left[\frac{\sigma^2(p+q)x}{m^2|z|^2}\right].$$

From these relations it can be proved that

$$|z| \geq E_*/m \geq 1 \quad \text{and} \quad |\arg\, z| < \pi/2.$$

Owing to these inequalities and condition $\sigma^2 \ll m^2$, we can write the asymptotic expansion:

$$\mathcal{D}_G(\mathbf{p},\mathbf{q};x) = \frac{2m\mathrm{V}_\star}{z^{3/2}}\exp\left[\frac{m^2(1-z)}{\sigma^2}\right]\left[1-\frac{3\sigma^2}{8m^2}\left(1-\frac{1}{z}\right)\right.$$
$$\left.+\frac{3\sigma^4}{128m^4}\left(1-\frac{1}{z}\right)\left(11+\frac{5}{z}\right)+\mathcal{O}\left(\frac{\sigma^6}{m^6}\right)\right].$$

The self-consistency demands to write down the approximation of this formula which would be accordant with the CRGP approximation for the function $\psi_G(\mathbf{p}, x)$.

$$z = \frac{E_*}{m}\left(1 + \frac{\sigma^4 \mathbf{x}_*^2}{2E_*^2}\right) - i\frac{\sigma^2 x_*^0}{m}\left(1 - \frac{\sigma^4 \mathbf{x}_*^2}{2E_*^2}\right) + \mathcal{O}\left(\frac{\sigma^8}{m^8}\right).$$

$$\Downarrow$$

$$\begin{aligned}\ln\left[\frac{\mathcal{D}_G(\mathbf{p}_*, -\mathbf{p}_*; x_*)}{2m\mathrm{V}_\star}\right] = {} & \frac{3}{2}\ln\left(\frac{m}{E_*}\right) - \frac{m(E_* - m)}{\sigma^2} - \frac{m\sigma^2 \mathbf{x}_*^2}{2E_*} + \frac{3\sigma^2(E_* - m)}{8mE_*} \\ & + imx_*^0\left\{1 + \frac{3\sigma^2}{2mE_*}\left[1 + \frac{\sigma^2}{4mE_*}\left(1 - \frac{4}{3}m^2\mathbf{x}_*^2\right)\right]\right\} \\ & - \frac{3\sigma^4}{4m^2E_*^2}\left\{m^2\left[(x_*^0)^2 + \mathbf{x}_*^2\right] - \frac{P_*^2}{4m^2}\right\} + \mathcal{O}\left(\frac{\sigma^6}{m^6}\right).\end{aligned}$$

It is now seen that, under the conditions [equivalent to those for the function $\psi_G(\mathbf{p}, x)$]

$$\boxed{\sigma^2(x_*^0)^2 \ll \frac{E_*^2}{\sigma^2} \quad \text{and} \quad \sigma^2\mathbf{x}_*^2 \ll \frac{E_*^2}{\sigma^2},} \tag{73}$$

one can retain only the four leading terms in powers of σ^2/m^2, finally obtaining:

$$\boxed{\mathcal{D}_G(\mathbf{p}_*, -\mathbf{p}_*; x_*) = \frac{2m\mathrm{V}_\star}{\Gamma_*^{3/2}}\exp\left[imx_*^0 - \frac{m^2(\Gamma_* - 1)}{\sigma^2} - \frac{\sigma^2\mathbf{x}_*^2}{2\Gamma_*}\right],} \tag{74}$$

where $\Gamma_* = E_*/m$ (Lorentz factor of CIF) and $\mathrm{V}_\star = [\pi/(2\sigma^2)]^{3/2}$ (effective volume).

Hence, as expected, $\mathcal{D}_G(\mathbf{p}_*, -\mathbf{p}_*; x_*)$ quickly vanishes when either $|\mathbf{p}_*|$ or $|\mathbf{x}_*|$ (or both) are sufficiently large.[a]

Some scarcely foreseeable features:

- The dependence of $|\mathcal{D}_G|$ on variables x_0 and $\mathbf{x}$ disappears for the classical trajectories $\mathbf{x} = \mathbf{v_p} x_0$;
- $|\mathcal{D}_G|/(2m\mathrm{V}_\star)$ exponentially vanishes at sub-relativistic energies ($\Gamma_* - 1 \sim 1$) and is nearly independent of $\mathbf{x}_*$ at ultrarelativistic energies ($\Gamma_* - 1 \gg 1$).
- For the nonrelativistic energies one gets (after transforming into the lab. frame)

$$\mathcal{D}_G(\mathbf{p}, \mathbf{q}; x) \approx 2m\mathrm{V}_\star \exp\left[im\,(x_0 - \mathbf{v}\mathbf{x}) - \frac{m^2}{8\sigma^2}\,|\mathbf{v_p} - \mathbf{v_q}|^2 - \frac{\sigma^2}{2}\,|\mathbf{x} - \mathbf{v}x_0|^2\right],$$

$$\left[\mathbf{v_p} = \mathbf{p}/m, \quad \mathbf{v_q} = \mathbf{q}/m, \quad \mathbf{v} = \tfrac{1}{2}\,(\mathbf{v_p} + \mathbf{v_q}), \qquad |\mathbf{v_p}| \ll 1, \;\; |\mathbf{v_q}| \ll 1\right]$$

  The term $\propto (m^2/\sigma^2)$ yet can be large (if $\mathbf{v_p} \neq \mathbf{v_q}$ and σ is small enough).

The correspondence principle:

All these nice features fade away in the plane-wave limit since (as it can be proved),

$$\lim_{\sigma \to 0} \mathcal{D}_G(\mathbf{p}, \mathbf{q}; x) = (2\pi)^3 2E_{\mathbf{p}} \delta(\mathbf{p} - \mathbf{q}) e^{ipx}.$$

[a] The formal conditions are evident from Eq. (74).

17.10 Multi-packet matrix elements (examples).

Consider the ME $\langle \{\mathbf{p}, s, x\}_n \,|\, \{\mathbf{p}, s, x\}_n \rangle$ with equal momenta ($\mathbf{p}_i = \mathbf{p}$, $\forall i$) for $n = 2$ and 3.
In the CIF, which coincides now with the proper frame (the same for all 1-packet "sub-states")

$$\langle \{\mathbf{p}, s, x\}_2 \,|\, \{\mathbf{p}, s, x\}_2 \rangle = (2m\mathrm{V}_\star)^2 \left[1 \pm \delta_{s_1 s_2} \exp\left(-\sigma^2 |\mathbf{x}_1^\star - \mathbf{x}_2^\star|^2\right)\right],$$

$$\langle \{\mathbf{p}, s, x\}_3 \,|\, \{\mathbf{p}, s, x\}_3 \rangle = (2m\mathrm{V}_\star)^3 \left[1 \pm \sum_{i<j} \delta_{s_i s_j} \exp\left(-\sigma^2 |\mathbf{x}_i^\star - \mathbf{x}_j^\star|^2\right) \right.$$
$$\left. + 2\delta_{s_1 s_2}\delta_{s_2 s_3}\delta_{s_3 s_1} \exp\left(-\frac{\sigma^2}{2} \sum_{i<j} |\mathbf{x}_i^\star - \mathbf{x}_j^\star|^2\right)\right].$$

So the effects of Bose-Einstein attraction and Pauli repulsion, appearing when $s_i = s_j$ for any pair (i, j), are only essential at short distances satisfying

$$\sigma^2 |\mathbf{x}_i^\star - \mathbf{x}_j^\star|^2 \lesssim 1.$$

In other words, both effects are essential when the spatial distance between the identical one-packet states (measured in their common p frame) is comparable with or shorter than the packet's dimension.

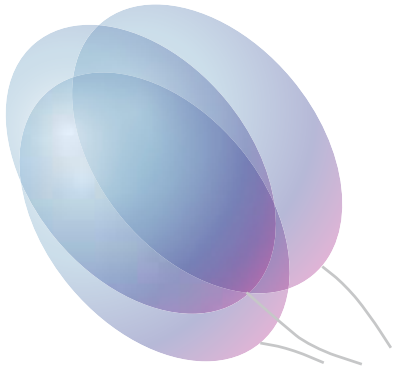

In the lab. frame the "attraction/repulsion regions" is restricted by the following condition:

$$\left|\mathbf{x}_i - \mathbf{x}_j - \mathbf{v}\left(x_i^0 - x_j^0\right)\right|^2 - |\mathbf{v} \times (\mathbf{x}_i - \mathbf{x}_j)|^2 \lesssim \mathrm{V}^{2/3}(\mathbf{p}) \qquad (\mathbf{v} = \mathbf{p}/E_\mathbf{p}).$$

17.11 Effective dimensions and momentum uncertainty of CRGP.

In the CRGP approximation, the effective volume is explicitly calculated to be

$$\mathrm{V}(\mathbf{0}) \approx \mathrm{V}_\star = \frac{2\pi^2 m K_1(m^2/\sigma^2)}{\sigma^2 \left[K_1(m^2/2\sigma^2)\right]^2} \approx \left(\frac{\pi}{2\sigma^2}\right)^{3/2}.$$

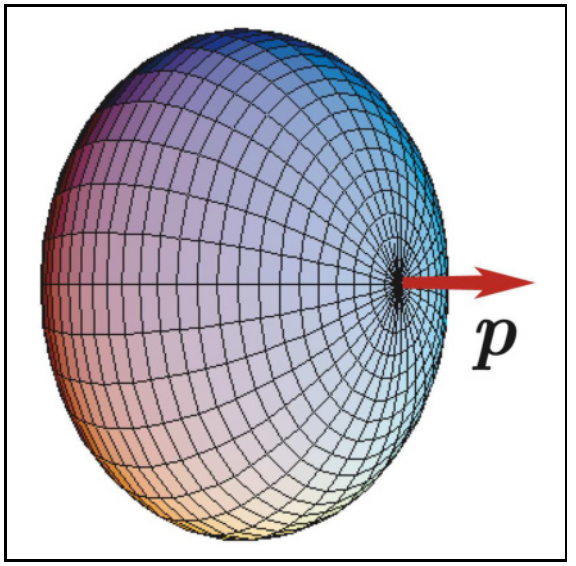

In the packet PRF, one can define its effective size as the diameter $d_\star$ of a ball of volume $\mathrm{V}_\star$,

$$d_\star = \left(\frac{6\mathrm{V}_\star}{\pi}\right)^{1/3} \approx \left(\frac{9\pi}{2}\right)^{1/6} \frac{1}{\sigma} \approx \frac{1.555}{\sigma}.$$

Then, in the lab. frame, the effective size of the packet along its momentum $\mathbf{p}$ is $d_\star/\Gamma_{\mathbf{p}}$. The pictorial model of the packet is therefore an oblate spheroid with the transversal diameter of about $1.555/\sigma$ and eccentricity of $1/\Gamma_{\mathbf{p}}$.

The volume density difference between the center and effective edge of any wave packet does not depend on mass and spread and is $\exp[(\sigma d_\star)^2/2] = \exp[(9\pi/16)^{1/3}] \approx 3.350$.

The momentum uncertainty can be evaluated as follows:

$$\begin{cases} |\delta\mathbf{p}_T|^2 = \dfrac{2}{3}\,|\delta\mathbf{p}_\star|^2 \approx 4\ln 2\,\sigma^2, \\ |\delta\mathbf{p}_L|^2 = \dfrac{1}{3}\,|\delta\mathbf{p}_\star|^2 \Gamma_{\mathbf{p}}^2 \approx 2\ln 2\,\sigma^2 \Gamma_{\mathbf{p}}^2, \end{cases} \quad \Longrightarrow \quad \boxed{|\delta\mathbf{p}| \approx \sqrt{2\ln 2\,(\Gamma_{\mathbf{p}}^2 + 2)}\,\sigma.}$$

17.12 The range of applicability of CRGP.

The inherent (probably inaccessible in reality) "upper limit" for the packet dimension, $d_\star^{\max}$, for an unstable particle is of the order of its decay length $c\tau$ (which is macroscopic for long-lived particles), while the "lower limit", $d_\star^{\min}$, is just the size of the particles composing the packet: ~ 1 fm for hadrons and $\sim 1/m$ (the Compton wavelength) for the structureless particles (leptons, gauge bosons). Any rate, due to the general restriction $\sigma^2 \ll m^2$, the permissible in the formalism dimension of the packet must be much larger than $d_\star^{\min}$.

But, for unstable particles, the conditions of applicability of the CRGP approximation (70) impose an additional and rather strong restriction to the maximum permissible value of the parameter σ. These condition should be valid during at least the life of the particle that is for

$$0 \leq |x_\star^0| \lesssim \tau = 1/\Gamma.$$

Therefore the following condition is necessary: $\sigma^4\tau^2 \ll m^2$. So $\sigma_{\max} = \sqrt{m/\tau} = \sqrt{m\Gamma}$ is the absolute upper limit for the permissible in CRGP values of σ. Correspondingly, the value

$$d_\star^{\min} = \left(\frac{9\pi}{2}\right)^{1/6} \frac{1}{\sigma_{\max}} = \left(\frac{9\pi}{2}\right)^{1/6} \left(\frac{\tau}{m}\right)^{1/2}$$

is the lower limit for the spatial dimension of the packet. Next, since we consider just the quasistable packets, σ must be much larger than Γ (or, more precisely, $\sigma^2 \gg \Gamma^2$).
Finally the combined range of applicability is given by

$$\boxed{\Gamma^2 \ll \sigma^2 \ll m\Gamma \ll m^2.}$$

Maximum permissible values of σ ($\sigma_{\max} = \sqrt{m\Gamma}$), the ratio $\Gamma/\sigma_{\max} = \sqrt{\Gamma/m}$, and minimum permissible effective dimensions $d_\star^{\min} \approx 1.55/\sqrt{m\Gamma}$ in the CRGP approximation for some longlived particles.

Particle	$\sigma_{\max}$ (eV)	$\Gamma/\sigma_{\max}$	$d_\star^{\min}$ (cm)
$\mu^\pm$	1.78×10^{-1}	1.68×10^{-9}	1.72×10^{-4}
$\tau^\pm$	2.01×10^{3}	1.13×10^{-6}	1.53×10^{-8}
$\pi^\pm$	1.88	1.35×10^{-8}	1.63×10^{-5}
π^0	3.25×10^{4}	2.41×10^{-4}	0.94×10^{-9}
$K^\pm$	5.12	1.04×10^{-8}	5.99×10^{-6}
K_S^0	6.05×10^{1}	1.22×10^{-7}	5.07×10^{-7}
K_L^0	2.53	5.08×10^{-9}	1.21×10^{-5}
$D^\pm$	1.09×10^{3}	5.82×10^{-7}	2.82×10^{-8}
D^0	1.73×10^{3}	9.28×10^{-7}	1.77×10^{-8}
$D_s^\pm$	1.61×10^{3}	8.18×10^{-7}	1.91×10^{-8}
$B^\pm$	1.46×10^{3}	2.76×10^{-7}	2.11×10^{-8}
B^0	1.51×10^{3}	2.86×10^{-7}	2.03×10^{-8}
B_s^0	1.55×10^{3}	2.89×10^{-7}	1.98×10^{-8}
n	2.64×10^{-5}	2.81×10^{-14}	1.16
Λ	5.28×10^{1}	4.74×10^{-7}	5.81×10^{-7}
$\Lambda_c^\pm$	2.74×10^{3}	1.87×10^{-6}	1.12×10^{-8}

The maximum permissible deviation of the mean mass of CRGP from the field mass, $\delta m = \overline{m} - m$, is equal to

$$\delta m_{\max} \approx \frac{3\sigma_{\max}^2}{2m} = 1.5\Gamma,$$

So, the correction to the field mass of the short-lived resonances can be essential, but for the long-lived particles we can (and we must) to neglect the weighting effect.

17.13 Feynman rules and overlap integrals.

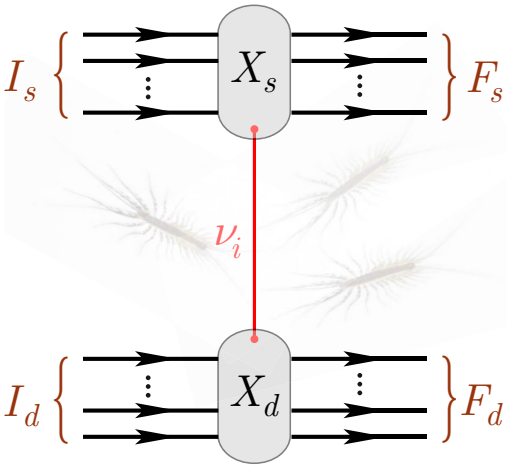

The QFT-based neutrino oscillation theory deals with generic Feynman's macrodiagrams ("myriapods"). ▷
The external legs correspond to asymptotically free incoming ("in") and outgoing ("out") wave packets (WP) in the coordinate representation. Here and below: I_s (F_s) is the set of in (out) WPs in X_s ("source"), I_d (F_d) is the set of in (out) WPs in X_d ("detector").

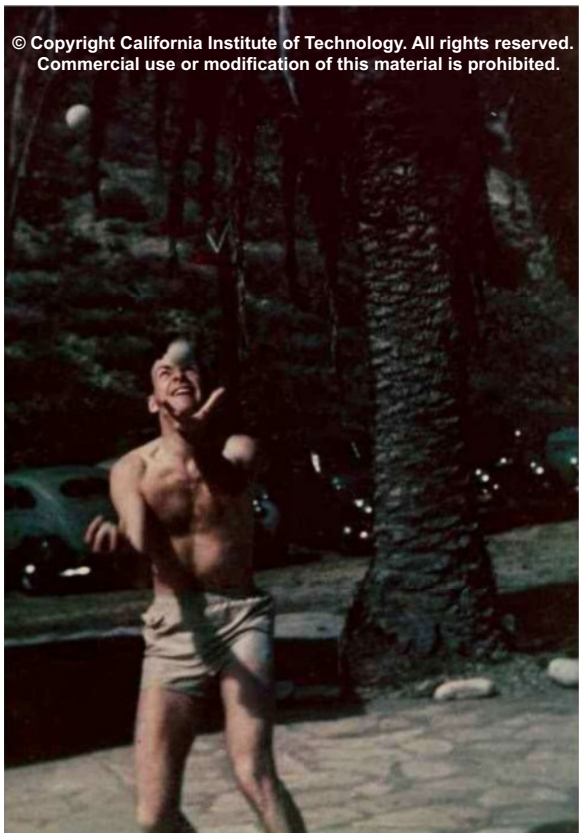

The internal line denotes the causal Green's function of the neutrino mass eigenfield ν_i ($i = 1, 2, 3, \ldots$). The blocks (vertices) X_s and X_d must be macroscopically separated in space-time. This explains the term "macroscopic Feynman diagram".

For narrow WPs, the Feynman rules in the formalism are to be modified[a] in a rather trivial way: for each external line, the *standard* (plain-wave) factor must be multiplied by

$$\begin{cases} e^{-ip_a(x_a - x)}\psi_a\left(\mathbf{p}_a, x_a - x\right) & \text{for } a \in I_s \oplus I_d, \\ e^{+ip_b(x_b - x)}\psi_b^*\left(\mathbf{p}_b, x_b - x\right) & \text{for } b \in F_s \oplus F_d, \end{cases} \tag{75}$$

where each function $\psi_\varkappa\left(\mathbf{p}_\varkappa, x\right)$ ($\varkappa = a, b$) is specified by the mass $m_\varkappa$ and momentum spread $\sigma_\varkappa$. The lines inside X_s and X_d (including possible loops) and vertex factors remain unchanged.

[a] For non-commercial purposes.

The additional factors (75) provide the following two common multipliers in the integrand of the scattering amplitude [we will call these the overlap integrals]:

$$\begin{aligned}
\mathbb{V}_s(q) &= \int dx e^{+iqx} \Big[\prod_{a\in I_s} e^{-ip_a x_a} \psi_a\left(\mathbf{p}_a, x_a - x\right) \Big] \Big[\prod_{b\in F_s} e^{ip_b x_b} \psi_b^*\left(\mathbf{p}_b, x_b - x\right) \Big], \\
\mathbb{V}_d(q) &= \int dx e^{-iqx} \Big[\prod_{a\in I_d} e^{-ip_a x_a} \psi_a\left(\mathbf{p}_a, x_a - x\right) \Big] \Big[\prod_{b\in F_d} e^{ip_b x_b} \psi_b^*\left(\mathbf{p}_b, x_b - x\right) \Big].
\end{aligned} \tag{76}$$

The function $\mathbb{V}_s$ ($\mathbb{V}_d$) characterizes the 4D overlap of the "in" and "out" wave-packet states in the source (detector) vertex, integrated over the infinite space-time volume.

In the plane-wave limit ($\sigma_\varkappa \to 0$, $\forall \varkappa$)

$$\mathbb{V}_s(q) \to (2\pi)^4 \delta\left(q - q_s\right) \quad \text{and} \quad \mathbb{V}_d(q) \to (2\pi)^4 \delta\left(q + q_d\right),$$

where q_s and q_d are the 4-momentum transfers defined by

$$q_s = \sum_{a\in I_s} p_a - \sum_{b\in F_s} p_b \quad \text{and} \quad q_d = \sum_{a\in I_d} p_a - \sum_{b\in F_d} p_b.$$

The δ functions provide the energy-momentum conservation in the vertices s and d (that is in the "subprocesses" $I_s \to F_s + \nu_i^*$ and $\nu_i^* + I_d \to F_d$) and, as a result, – in the whole process:

$$I_s \oplus I_d \to F_s \oplus F_d: \qquad \sum_{a\in I_s\oplus I_d} p_a = \sum_{b\in F_s\oplus F_d} p_b.$$

Information about the space-time coordinates of the interacting packets is completely lost.

In the general case when $\sigma_\varkappa > 0$, we may expect no more than an approximate energy-momentum conservation and lack of any singularities. To quantify this expectation, we apply the CRGP model.

$$T_\varkappa^{\mu\nu} \overset{\text{def}}{=} \sigma_\varkappa^2 \left(u_\varkappa^\mu u_\varkappa^\nu - g^{\mu\nu}\right), \qquad \left[u_\varkappa = p_\varkappa/m_\varkappa = \Gamma_\varkappa(1, \mathbf{v}_\varkappa) \text{ is the 4-velocity, } u_\varkappa^2 = 1\right]$$

$$\Downarrow$$

see Eq. (71a) →

$$\mathbb{V}_{s,d}(q) = \int dx \exp\left[i\left(\pm qx - q_{s,d}x\right) - \sum_{\varkappa\in S,D} T_\varkappa^{\mu\nu} \left(x_\varkappa - x\right)_\mu \left(x_\varkappa - x\right)_\nu\right],$$

where $S = I_s \oplus F_s$ and $D = I_d \oplus F_d$. It is useful to define the the so-called overlap tensors

$$\boxed{\mathfrak{R}_s^{\mu\nu} = \sum_{\varkappa\in S} T_\varkappa^{\mu\nu} \quad \text{and} \quad \mathfrak{R}_d^{\mu\nu} = \sum_{\varkappa\in D} T_\varkappa^{\mu\nu}.}$$

A crucial property:

$$T_\varkappa^{\mu\nu} x_\mu x_\nu = \sigma_\varkappa^2 \left[(u_\varkappa x)^2 - x^2\right] = \sigma_\varkappa^2 \mathbf{x}_{(\varkappa)}^2 \geq 0 \quad \Longrightarrow \quad \mathfrak{R}_{s,d}^{\mu\nu} x_\mu x_\nu \geq 0.$$

Consequently, there exist the positive-definite inverse overlap tensors $\widetilde{\mathfrak{R}}_s^{\mu\nu}$ and $\widetilde{\mathfrak{R}}_d^{\mu\nu}$ such that

$$\widetilde{\mathfrak{R}}_s^{\mu\lambda} \left(\mathfrak{R}_s\right)_{\lambda\nu} = \delta_\nu^\mu \quad \text{and} \quad \widetilde{\mathfrak{R}}_d^{\mu\lambda} \left(\mathfrak{R}_d\right)_{\lambda\nu} = \delta_\nu^\mu; \quad \Longleftrightarrow \quad \widetilde{\mathfrak{R}}_{s,d}^{\mu\nu} = \left(\mathfrak{R}_{s,d}^{-1}\right)_{\mu\nu},$$

or, in matrix form,

$$\widetilde{\mathfrak{R}}_{s,d} = ||\widetilde{\mathfrak{R}}_{s,d}^{\mu\nu}|| = g\, \mathfrak{R}_{s,d}^{-1}\, g, \quad \mathfrak{R}_{s,d} = ||\mathfrak{R}_{s,d}^{\mu\nu}||; \quad \Longrightarrow \quad \widetilde{\mathfrak{R}}_{s,d}^{\mu\nu} \overset{\Lambda}{\longmapsto} \Lambda_{\mu'}^\mu \Lambda_{\nu'}^\nu \widetilde{\mathfrak{R}}_{s,d}^{\mu'\nu'}.$$

The explicit form and properties of the inverse overlap tensors $\widetilde{\mathfrak{R}}_{s,d}$ and relevant convolutions are established. Important special cases, $1 \to 2$, $1 \to 3$, and $2 \to 2$, are discussed in Appendix I, p. 880.

It is proved [a] that for arbitrary process $I_s \oplus I_d \to F_s \oplus F_d$, the components of the inverse overlap tensors can be written as

$$\widetilde{\Re}^{\mu\nu}_{s,d} = \frac{1}{|\Re_{s,d}|} \sum_{a,b,c \in \mathcal{S},\mathcal{D}} \sigma_a^2 \sigma_b^2 \sigma_c^2 \mathfrak{I}^{abc\,\mu\nu}_{s,d},$$

where

Transformation properties were tested with **Maple®**

$$\mathfrak{I}^{abc\,00}_{s,d} = \left[\Gamma_a\Gamma_b - \frac{1}{3}(u_a u_b)\right](u_b u_c)(u_c u_a) + \frac{1}{2}\Gamma_a^2\left[1-(u_b u_c)^2\right] + \frac{1}{3},$$

$$\mathfrak{I}^{abc\,0i}_{s,d} = \frac{1}{2}\Gamma_c\left[(u_a u_b)^2 u_{ci} - u_{ci} - 2(u_a u_b)(u_b u_c)u_{ai} + 2(u_a u_c)u_{ai}\right] - \Gamma_b(u_a u_b)u_{ai},$$

$$\mathfrak{I}^{abc\,ij}_{s,d} = \Gamma_a\Gamma_b\left[(u_c u_a)(u_c u_b) - (u_a u_b)\right]\delta_{ij} + \frac{1}{2}\left(\Gamma_c^2 - 1\right)\left[1-(u_a u_b)^2\right]\delta_{ij} + \Gamma_b\left[\Gamma_b - \Gamma_a(u_a u_b)\right]u_{ci}u_{cj},$$
$$+\left\{\Gamma_c\left[\Gamma_a(u_b u_c) + \Gamma_b(u_c u_a) - \Gamma_c(u_a u_b)\right] - \Gamma_a\Gamma_b + (u_a u_b)\right\}u_{ai}u_{bj} \quad (i,j=1,2,3);$$

$$|\Re_{s,d}| = \sum_{a,b,c,d \in \mathcal{S},\mathcal{D}} \sigma_a^2\sigma_b^2\sigma_c^2\sigma_d^2 \left\{\frac{1}{3}\left[(u_a u_b)(u_b u_c)(u_c u_a) - 1\right] - \frac{1}{2}\Gamma_a\Gamma_b(u_a u_b)\left[(u_c u_d)^2 - 1\right]\right.$$
$$\left. + \Gamma_a\Gamma_b(u_c u_a)\left[(u_c u_d)(u_d u_b) - (u_b u_c)\right] + \frac{1}{6}\Gamma_d^2\left[3(u_b u_c)^2 - 2(u_a u_b)(u_b u_c)(u_c u_a) - 1\right]\right\} = \text{inv}.$$

In deriving, energy-momentum conservation is not assumed.

Simplest example: for the two-particle decay $a \to \ell + \nu^*$ in the source, where a is a meson (e.g., $a = \pi^\pm$), ℓ is a charged lepton and ν^* is a virtual (anti)neutrino with definite mass, we obtain:

$$\widetilde{\Re}^{\mu\nu}_{s} = \frac{\sigma_a^4 u_a^\mu u_a^\nu + \sigma_\ell^4 u_\ell^\mu u_\ell^\nu - \sigma_a^2\sigma_\ell^2\left\{g^{\mu\nu}\left[(u_a u_\ell)^2 - 1\right] - (u_a u_\ell)(u_a^\mu u_\ell^\nu + u_\ell^\mu u_a^\nu)\right\}}{\sigma_a^2\sigma_\ell^2\left(\sigma_a^2 + \sigma_\ell^2\right)\left[(u_a u_\ell)^2 - 1\right]}.$$

[a] VN & D. S. Shkirmanov, "Extended Grimus-Stockinger theorem and inverse square law violation in quantum field theory," Eur. Phys. J. C **73** (2013) 2627, arXiv:1309.1011 [hep-ph]. These formulas are not used below.

The overlap integrals in CRGP are the 4D Gaussian integrals in Minkowski space.

$$\mathbb{V}_{s,d}(q) = (2\pi)^4 \widetilde{\delta}_{s,d}\,(q \mp q_{s,d}) \exp\left[-\mathfrak{S}_{s,d} \pm i\,(q \mp q_{s,d})\cdot X_{s,d}\right],$$

$$\widetilde{\delta}_{s,d}(K) = (4\pi)^{-2} |\Re_{s,d}|^{-1/2} \exp\left(-\frac{1}{4}\widetilde{\Re}^{\mu\nu}_{s,d} K_\mu K_\nu\right),$$

$$\mathfrak{S}_{s,d} = \sum_{\varkappa,\varkappa'} \left(\delta_{\varkappa\varkappa'} T^{\mu\nu}_{\varkappa} - T^{\mu}_{\varkappa\mu'}\, \widetilde{\Re}^{\mu'\nu'}_{s,d}\, T^{\nu}_{\varkappa'\nu'}\right) x_{\varkappa\mu} x_{\varkappa'\nu},$$

$$X^{\mu}_{s,d} = \widetilde{\Re}^{\mu\nu}_{s,d} \sum_{\varkappa} T^{\lambda}_{\varkappa\nu} x_{\varkappa\lambda}.$$

Physical meaning of $\widetilde{\delta}_{s,d}$, $\mathfrak{S}_{s,d}$, and $X_{s,d}$.

- From the integral representation (where K is arbitrary 4-vector)

$$\widetilde{\delta}_{s,d}(K) = \int \frac{dx}{(2\pi)^4} \exp\left(iKx - \Re^{\mu\nu}_{s,d} x_\mu x_\nu\right)$$

it follows that $\widetilde{\delta}_{s,d}(K) \to \delta(K)$ and $\mathbb{V}_{s,d}(q) \to (2\pi)^4 \delta\,(q \mp q_{s,d})$ in the plane-wave limit[a].

$$\Downarrow$$

The Lorenz-invariant factors $\widetilde{\delta}_s\,(q - q_s)$ and $\widetilde{\delta}_d\,(q + q_d)$ are therefore responsible for the approximate energy–momentum conservation (with the accuracy governed by the momentum spreads of the interacting wave packets) in the neutrino production and detection regions.

[a] $\sigma_\varkappa \to 0,\ \forall \varkappa \Longrightarrow \Re^{\mu\nu}_{s,d} \to 0,\ \mathfrak{S}_{s,d} \to 0;\ X^{\mu}_{s,d}$ remain finite.

- The functions $\exp\left(-\mathfrak{S}_s\right)$ and $\exp\left(-\mathfrak{S}_d\right)$ are the geometric suppression factors conditioned by a partial overlap of the in and out WPs in the space-time regions of their interaction in the source and detector. This can be seen after converting $\mathfrak{S}_{s,d}$ to the form[a]

$$\mathfrak{S}_{s,d} = \sum_{\varkappa} T_{\varkappa}^{\mu\nu} \left(x_{\varkappa} - X_{s,d}\right)_{\mu} \left(x_{\varkappa} - X_{s,d}\right)_{\nu} \geq 0 \tag{77}$$

and taking into account that both $\mathfrak{S}_{s,d}$ and $X_{s,d}$ are invariants under the group of uniform rectilinear motions (here, $\tau_{\varkappa}$ are arbitrary real time parameters)

$$\left\{x_{\varkappa}^0 \longmapsto \tilde{x}_{\varkappa}^0 = x_{\varkappa}^0 + \tau_{\varkappa},\ \mathbf{x}_{\varkappa} \longmapsto \tilde{\mathbf{x}}_{\varkappa} = \mathbf{x}_{\varkappa} + \mathbf{v}_{\varkappa}\tau_{\varkappa}\right\}.$$

Due to this symmetry, Eq. (77) can be rewritten as

$$\boxed{\mathfrak{S}_{s,d} = \sum_{\varkappa} \sigma_{\varkappa}^2 \left[\left(\Gamma_{\varkappa}^2 - 1\right)\left(b_{\varkappa}^0\right)^2 + \mathbf{b}_{\varkappa}^2\right] = \sum_{\varkappa} \sigma_{\varkappa}^2 |\mathbf{b}_{\varkappa}^{(\varkappa)}|^2,}$$

$$\begin{aligned} b_{\varkappa}^0 &= \left(x_{\varkappa}^0 - X_{s,d}^0\right) - |\mathbf{v}_{\varkappa}|^{-1} \mathbf{n}_{\varkappa} \cdot \left(\mathbf{x}_{\varkappa} - \mathbf{X}_{s,d}\right), \\ \mathbf{b}_{\varkappa} &= \left(\mathbf{x}_{\varkappa} - \mathbf{X}_{s,d}\right) - \left[\mathbf{n}_{\varkappa} \cdot \left(\mathbf{x}_{\varkappa} - \mathbf{X}_{s,d}\right)\right] \mathbf{n}_{\varkappa}, \end{aligned} \qquad \left[\mathbf{n}_{\varkappa} = \begin{cases} \mathbf{v}_{\varkappa}/|\mathbf{v}_{\varkappa}|, & \text{for } \mathbf{v}_{\varkappa} \neq 0, \\ 0, & \text{for } \mathbf{v}_{\varkappa} = 0. \end{cases}\right]$$

So the 4-vector $b_{\varkappa} = (b_{\varkappa}^0, \mathbf{b}_{\varkappa})$ is the relativistic generalization of the usual impact vector, it is therefore natural to call it the impact 4-vector. The impact parameter $|\mathbf{b}_{\varkappa}|$ can also be rewritten in a more familiar form:

$$|\mathbf{b}_{\varkappa}| = |\mathbf{n}_{\varkappa} \times \left(\mathbf{x}_{\varkappa} - \mathbf{X}_{s,d}\right)| \quad \text{for} \quad \mathbf{v}_{\varkappa} \neq 0.$$

- According to the presented analysis, it is natural to call 4-vectors $X_{s,d}$ impact points.

[a] In this derivation we have used the translation invariance of the functions $\mathfrak{S}_{s,d}$.

17.13.1 Derivation of Eq. (77) for geometric suppression factors.

Let us rewrite the quadratic forms $\mathfrak{S}_s$ and $\mathfrak{S}_d$ as[a]

$$\begin{aligned}\mathfrak{S}_{s,d} &= \sum_{\varkappa,\varkappa'} T_{\varkappa}^{\mu\mu'} (\widetilde{\mathfrak{R}}_{s,d})_{\mu'\nu'} T_{\varkappa'}^{\nu'\nu} x_{\varkappa\mu} \left(x_{\varkappa} - x_{\varkappa'}\right)_{\nu} \\ &= \sum_{\varkappa} T_{\varkappa}^{\mu\nu} x_{\varkappa\mu} x_{\varkappa\nu} - \sum_{\varkappa,\varkappa'} T_{\varkappa}^{\mu\mu'} (\widetilde{\mathfrak{R}}_{s,d})_{\mu'\nu'} T_{\varkappa'}^{\nu'\nu} x_{\varkappa\mu} x_{\varkappa'\nu}.\end{aligned}$$

Inserting the unit matrix into the last term and considering definitions of $\mathfrak{S}_{s,d}$ and $X_{s,d}^{\mu}$ we find

$$\begin{aligned}\mathfrak{S}_{s,d} &= \sum_{\varkappa} T_{\varkappa}^{\mu\nu} x_{\varkappa\mu} x_{\varkappa\nu} - \left(\sum_{\varkappa} T_{\varkappa\mu'}^{\mu} x_{\varkappa\mu}\right) \widetilde{\mathfrak{R}}_{s,d}^{\mu'\lambda} (\mathfrak{R}_{s,d})_{\lambda\rho} \widetilde{\mathfrak{R}}_{s,d}^{\rho\nu'} \left(\sum_{\varkappa'} T_{\varkappa'\nu'}^{\nu} x_{\varkappa'\nu}\right) \\ &= \sum_{\varkappa} T_{\varkappa}^{\mu\nu} x_{\varkappa\mu} x_{\varkappa\nu} - (\mathfrak{R}_{s,d})_{\mu\nu} X_{s,d}^{\mu} X_{s,d}^{\nu},\end{aligned}$$

$$\Downarrow$$

$$\mathfrak{S}_{s,d} = \sum_{\varkappa} T_{\varkappa\mu\nu} \left(x_{\varkappa}^{\mu} x_{\varkappa}^{\nu} - X_{s,d}^{\mu} X_{s,d}^{\nu}\right). \tag{78}$$

The resulting expression is the weighted average (over all the external packets at the corresponding vertex of the diagram) of the quadratic deviations of the components of the 4-vectors $x_{\varkappa}$ ($\varkappa \in S, D$) from the corresponding components of the space-time points $X_{s,d}$ (impact points), with the tensor components $T_{\varkappa}^{\mu\nu}$ playing the role of "weights".

[a] Throughout this section $\varkappa, \varkappa' \in S, D$, where $S = I_s \oplus F_s$ and $D = I_d \oplus F_d$.

From definition of the 4-vectors $X_{s,d}$ and tensors $\Re_{s,d}$ follow that

$$\sum_{\varkappa} T^{\mu}_{\varkappa\nu} X^{\nu}_{s,d} = (\Re_{s,d})^{\mu}_{\nu} X^{\nu}_{s,d} = (\Re_{s,d})^{\mu}_{\nu} \widetilde{\Re}^{\nu\nu'}_{s,d} \sum_{\varkappa} T^{\lambda}_{\varkappa\nu'} x_{\varkappa\lambda} = \sum_{\varkappa} T^{\mu\nu}_{\varkappa} x_{\varkappa\nu}.$$

$$\Downarrow$$

$$\boxed{\sum_{\varkappa} T^{\mu\nu}_{\varkappa} \left(x_{\varkappa} - X_{s,d}\right)_{\nu} = 0 \quad \Longleftrightarrow \quad X^{\mu}_{s,d} = \widetilde{\Re}^{\mu\nu}_{s,d} \sum_{\varkappa} T_{\varkappa\,\nu\lambda} x^{\lambda}_{\varkappa}.} \tag{79}$$

These identities show that the impact points $X_{s,d}$ represent the weighted-mean space-time coordinates of the external wave packets. Thus, these points are the centers of the space-time regions in which the interaction of the packets in the source and detector takes place.

To fully clarify the physical and geometrical meaning of these result, it is useful to study in detail the symmetry properties of the quantities $X_{s,d}$ and $\mathfrak{S}_{s,d}$.

Translation group.

It is easy to prove that the quadratic forms $\mathfrak{S}_s$ and $\mathfrak{S}_d$ are invariant with respect to the translations of all coordinates $x_{\varkappa}$ on the same arbitrary 4-vector y,

$$x_{\varkappa} \longmapsto x'_{\varkappa} = x_{\varkappa} + y. \tag{80}$$

Indeed, with this transformation

$$X^{\mu}_{s,d} \;\longmapsto\; X'^{\mu}_{s,d} = \widetilde{\Re}^{\mu\nu}_{s,d} \sum_{\varkappa} T^{\lambda}_{\varkappa\nu} \left(x_{\varkappa} + y\right)_{\lambda} = X^{\mu}_{s,d} + \left(\widetilde{\Re}^{\mu\nu}_{s,d} \sum_{\varkappa} T^{\lambda}_{\varkappa\nu}\right) y_{\lambda} = X^{\mu}_{s,d} + y^{\mu}.$$

and therefore $X_{s,d} \longmapsto X'_{s,d} = X_{s,d} + y$. Using this property and identitities (79), we obtain

$$\mathfrak{S}_{s,d} \longmapsto \mathfrak{S}'_{s,d} = \mathfrak{S}_{s,d} + \sum_{\varkappa} T_{\varkappa\mu\nu} \left(y^\mu x^\nu_\varkappa + x^\mu_\varkappa y^\nu - y^\mu X^\nu_{s,d} - X^\mu_{s,d} y^\nu \right)$$

$$= \mathfrak{S}_{s,d} + 2y_\mu \sum_{\varkappa} T^\mu_{\varkappa\nu} \left(x^\nu_\varkappa - X^\nu_{s,d} \right) = \mathfrak{S}_{s,d}.$$

It should be noted that the quadratic forms $\mathfrak{S}_s$ and $\mathfrak{S}_d$ are also invariant with respect to the inversion of space-time coordinates, $x_\varkappa \longmapsto -x_\varkappa$. Thus, $\mathfrak{S}_{s,d}$ are Poincaré invariants.

Note now that the transformation (80) with $y = -X_{s,d}$ gives

$$x^\mu_\varkappa x^\nu_\varkappa - X^\mu_{s,d} X^\nu_{s,d} \longmapsto (x^\mu_\varkappa - X_{s,d})^\mu \, (x^\mu_\varkappa - X_{s,d})^\nu$$

Substituting this into Eq. (78) we finally arrive at representation (77) for the functions $\mathfrak{S}_{s,d}$, from which it follows that the quadratic forms $\mathfrak{S}_s$ and $\mathfrak{S}_d$ are *nonnegative* and hence the factors $\exp(-\mathfrak{S}_s)$ and $\exp(-\mathfrak{S}_d)$ suppress the amplitude at certain ("failed" or "unlucky") configurations of the momenta and space-time coordinates of the in and out WPs.

Using definition of the tensors $T_\varkappa$ (recall that $T^{\mu\nu}_\varkappa = \sigma^2_\varkappa (u^\mu_\varkappa u^\nu_\varkappa - g^{\mu\nu})$), we can rewrite Eq. (77) as

$$\mathfrak{S}_{s,d} = \sum_{\varkappa} \sigma^2_\varkappa \left\{ [u_\varkappa (x_\varkappa - X_{s,d})]^2 - (x_\varkappa - X_{s,d})^2 \right\} \tag{81a}$$

$$= \sum_{\varkappa} \sigma^2_\varkappa \left| \mathbf{x}^{(\varkappa)}_\varkappa - \mathbf{X}^{(\varkappa)}_{s,d} \right|^2. \tag{81b}$$

Here (as always) index "$(\varkappa)$" denotes that the corresponding vector is written in PRF of the packet $\varkappa$. It follows from Eq. (81b) that the suppression is small (i.e. $\mathfrak{S}_{s,d} \ll 1$) at such coordinate and momentum configurations for which the magnitudes $\sigma^2_\varkappa \left| \mathbf{x}^{(\varkappa)}_\varkappa - \mathbf{X}^{(\varkappa)}_{s,d} \right|^2$ are small at all $\varkappa \in S, D$.

Group of uniform rectilinear motions.

As is evident from Eq. (81b), $\mathfrak{S}_{s,d} = 0$ when all 4-vectors $x_\varkappa$ coincide with each other (thus, from the equality $x_\varkappa = x_{s,d}$, $\forall \varkappa \in S, D$ follows that $X_{s,d} = x_{s,d}$). But is this condition *necessary* for the functions $\mathfrak{S}_{s,d}$ to become zero? Fortunately, the answer to this question is negative.[a] To see this, note that the 4-vectors $X_\varkappa = (u_\varkappa x_\varkappa)u_\varkappa - x_\varkappa$ (and therefore their squares $X_\varkappa^2 = x_\varkappa^2 - (u_\varkappa x_\varkappa)^2$) are invariant with respect to the transformation

$$x_\varkappa^0 \longmapsto \tilde{x}_\varkappa^0 = x_\varkappa^0 + \theta_\varkappa, \quad \mathbf{x}_\varkappa \longmapsto \tilde{\mathbf{x}}_\varkappa = \mathbf{x}_\varkappa + \mathbf{v}_\varkappa \theta_\varkappa, \tag{82}$$

where $\theta_\varkappa$ is an arbitrary real parameter of dimension of time.

- Hence, the 4-vectors $X_{s,d}$ and, as can be easily seen from the representation (78), the quadratic forms $\mathfrak{S}_{s,d}$ are invariant with respect to $N_{s,d}$ parametric set of transformations (82), where $N_{s,d}$ is the number of the single-packet states contained in the initial and final states $I_{s,d}$ and $F_{s,d}$ in the source or detector vertices of the macrodiagram.
- The set of all transformations (82) forms a group describing uniform rectilinear motions of wave packets, i.e., shifts along the classical world lines of the packet's centers.
- Therefore, both $X_{s,d}$ and $\mathfrak{S}_{s,d}$ are uniquely defined by fixing the velocities $\mathbf{v}_\varkappa$ and *arbitrary* space-time points $\tilde{x}_\varkappa$ on these world lines.
- If, in particular, the classical trajectories of all in and out WPs intersect at the impact point, then $\mathfrak{S}_{s,d} = 0$ at any point of each of these trajectories.

[a] "Fortunately", because otherwise there could be no talk of asymptotically free external WPs, without which it would be impossible to use (and even to formulate) perturbation theory. It's worth recalling that the 4-vectors $x_\varkappa$ are the initial or final coordinates of the in (for $\varkappa \in I_{s,d}$ or out (for $\varkappa \in F_{s,d}$ WPs, not the coordinates of the interaction points of these packets.

◦ Thus, the packets can be macroscopically separated in space-time before and after the interaction and be considered asymptotically free, but if the velocity vectors $\mathbf{v}_a$ of in packets and the vectors $-\mathbf{v}_b$ opposite to the velocities of the asymptotically free out packets are all "targeted" to the point X_s (in the source) or X_d (in the detector), then $\mathfrak{S}_s$ or $\mathfrak{S}_d$ are zero.

◦ It is on the basis of this property that it is natural to call 4-vectors X_s and X_d as the impact points of incoming and outgoing packets in the source and detector, respectively.

◦ To make the picture of the WP interaction more visual, it is instructive to introduce the concept of the world tube, defined as a space-time cylindrical volume, spotted by a flattened spheroid, which represent the WP patterns and whose center moves along a classical trajectory.[a] In this picture, the suppression of the overlap integral (and amplitude) by the factor $\exp(-\mathfrak{S}_s)$ $(\exp(-\mathfrak{S}_d))$ is small if *all* world tubes in the source (detector) vertex intersect a certain the region surrounding the impact point.

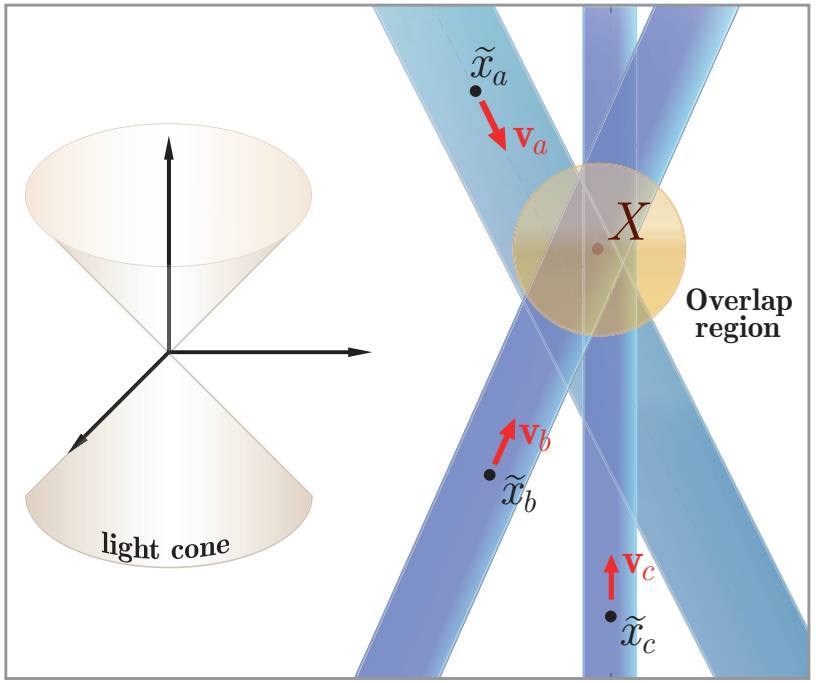

Artistic view of the "classical world tubes" of colliding wave packets (which can be represented as interpenetrating ellipsoidal "cloudlets"). The impact point X is uniquely defined by the velocities, $\mathbf{v}_{\varkappa}$, of the packets and by the space-time points $\tilde{x}_{\varkappa} = \tilde{x}_{\varkappa}(\tau_{\varkappa})$ arbitrarily chosen on the axis (thin dashed lines) of the tubes. Note that the axes do not necessarily intersect the point X.

[a] Recall that the diameter of the ellipsoid, perpendicular to the most probable WP momentum $\mathbf{p}$ (and hence the diameter of the world tube) is $d_\star \propto 1/\sigma$ (see Sect. **17.11**, p. 572), while the diameter parallel to $\mathbf{p}$ is compressed by the factor $\mathit{\Gamma}_{\mathbf{p}}$ resulting from the Lorentz contraction.

◦ **WARNING:** One should by no means take the above picture of the intersection of the world tubes as a description of the real interaction of wave packets. It illustrates the exact mathematical conditions of minimization of the geometrical suppression and refers to the exactly defined, but purely mathematical objects – the world tubes existing in the whole space-time. The physical wave packets themselves exist, generally speaking, for a finite time: in-packets a_i are annihilated (disappear) and out-packets b_i are created (arise) in the space-time domain of their interaction.
The figure attempts to depict the interaction of the WPs whose world tubes were correctly oriented. ▷

◦ As mentioned above, in a certain sense WPs behave like interpenetrating cloudlets. To illustrate this image, let's present the functions $\mathfrak{S}_s$ and $\mathfrak{S}_d$ as ratios of the overlapping integrals of special form:

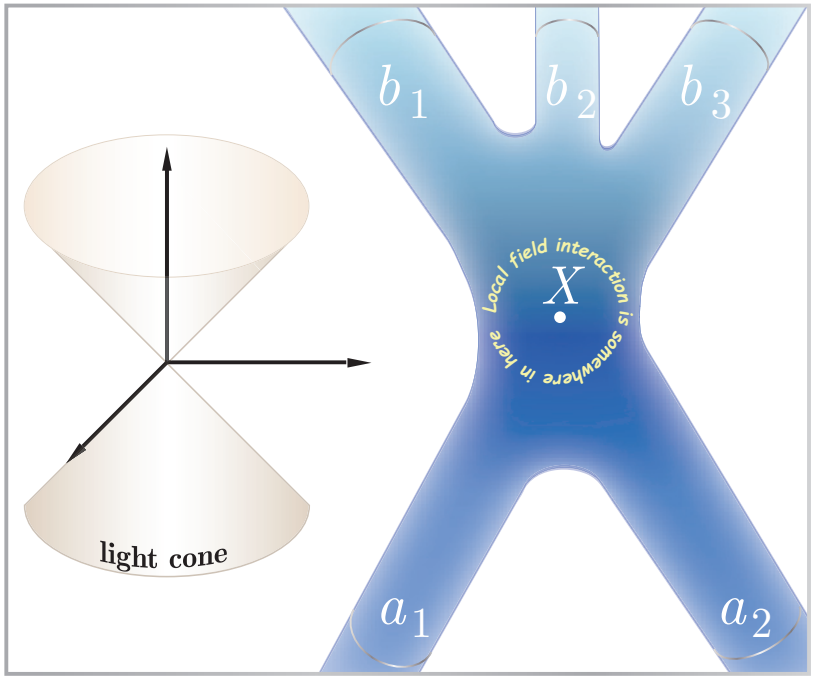

A somewhat more realistic, but still "artistic" picture of the interaction of "properly targeted" incoming (a_i) and outgoing (b_i) wave packets. Analogy with string-theory diagrams is misplaced.

$$\exp\left(-\mathfrak{S}_{s,d}\right) = \int dx \prod_{\varkappa\in S,D} |\psi_\varkappa(\mathbf{p}_\varkappa, x_\varkappa - x)| \Big/ \int dx \prod_{\varkappa\in S,D} |\psi_\varkappa(\mathbf{p}_\varkappa, x)|. \tag{83}$$

Due to the invariance of the functions $|\psi_\varkappa(\mathbf{p}_\varkappa, x_\varkappa - x)|$ under transformations (82), we can replace the coordinates $x_\varkappa$ in Eq. (83) by $y_\varkappa = (y^0_\varkappa, \mathbf{y}_\varkappa)$, where

$$y^0_\varkappa = X^0_{s,d}, \quad \mathbf{y}_\varkappa = \mathbf{x}_\varkappa + \left(X^0_{s,d} - x^0_\varkappa\right)\mathbf{v}_\varkappa, \quad \varkappa \in S \text{ or } D$$

and then rewrite Eq. (83) in the more appropriate form:

$$\exp\left(-\mathfrak{S}_{s,d}\right) = \int dx \prod_{\varkappa\in S,D} |\psi_\varkappa(\mathbf{p}_\varkappa, y_\varkappa - x)| \Big/ \int dx \prod_{\varkappa\in S,D} |\psi_\varkappa(\mathbf{p}_\varkappa, x)|. \tag{84}$$

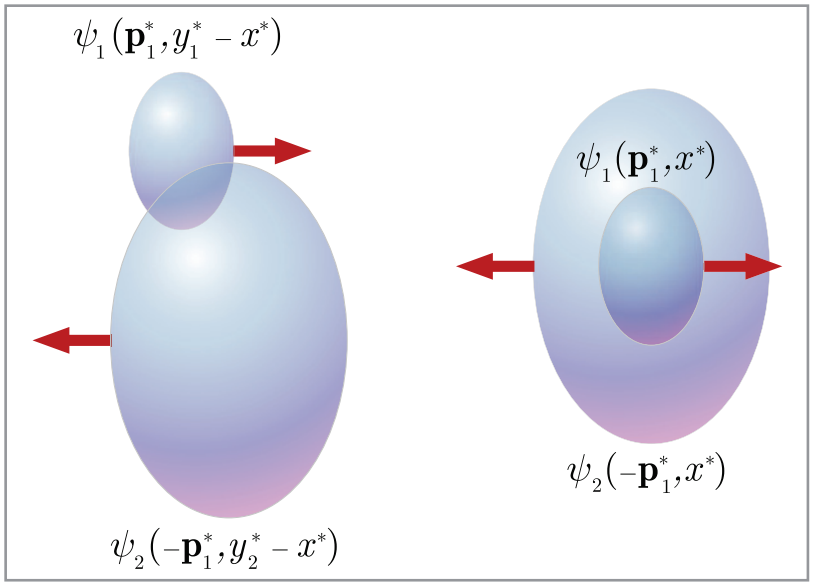

Schematic illustration of two configurations of a pair of overlapping wave packets in their CIF. The left configuration corresponds to the factor $|\psi_1(\mathbf{p}_1, y_1 - x)\psi_2(\mathbf{p}_2, y_2 - x)| = \left|\psi_1(\mathbf{p}_1^*, y_1^* - x^*)\psi_2(-\mathbf{p}_1^*, y_2^* - x^*)\right|$ in the integrand of the numerator in Eq. (84), and the right one – to the factor $|\psi_1(\mathbf{p}_1, x)\psi_2(\mathbf{p}_2, x)| = \left|\psi_1(\mathbf{p}_1^*, x^*)\psi_2(-\mathbf{p}_1^*, x^*)\right|$ in the integrand of the denominator in Eq. (84). The arrows show the momenta $\pm\mathbf{p}_1^*$. Keep in mind the warning above.

Then it becomes obvious from geometric considerations that $\exp\left(-\mathfrak{S}_{s,d}\right) < 1$ when any pair of coordinates $\mathbf{y}_\varkappa$ and $\mathbf{y}_{\varkappa'}$ do not match at the same ("impact") time, because the integrand in the numerator of the ratio (84) does not exceed that in the denominator.

◁ This statement is illustrated schematically by the example of a pair of overlapping packets 1 and 2. The packets are shown in the center-of-inertia system (CIF), where $\mathbf{p}_1^* + \mathbf{p}_2^* = 0$, and where they look like ellipsoids with effective volumes $(\pi/2)^{3/2}/(\Gamma_*\sigma_{1,2}^3)$ oblate along $\mathbf{p}_1^*$. It is seen that for any x^* (and hence for any values of the integration variable in Eq. (84)), the inequality

$$|\psi_1(\mathbf{p}_1^*, y_1^* - x^*)\psi_2(\mathbf{p}_2^*, y_2^* - x^*)| < |\psi_1(\mathbf{p}_1^*, x^*)\psi_2(\mathbf{p}_2^*, x^*)|$$

holds when $y_1^* \neq y_2^*$. Clearly the ratio (84) is small if the 4-coordinates $y_\varkappa^*$ and $y_{\varkappa'}^*$ for *any* pair of the packets $\varkappa$ and $\varkappa'$ are significantly different from each other.

17.13.2 Asymptotic conditions.

Now we can elaborate the physical conditions at which the in and out packets can be considered as free. If the geometric suppression factors are not too small (only such configurations of the momenta and coordinates contribute to the observables) then the condition of macroscopic separation of the interaction regions in S and D is equivalent to the macroscopic separation of the impact points $X_{s,d}$. We'll hold that the intervals $X^0_d - X^0_s$ and $|\mathbf{X}_d - \mathbf{X}_s|$ are large in comparison with $|x^0_\varkappa - x^0_{\varkappa'}|$ and $|\mathbf{x}_\varkappa - \mathbf{x}_{\varkappa'}|$ for $\varkappa, \varkappa' \in S$ and $\varkappa, \varkappa' \in D$.
Under such assumptions the packets certainly do not overlap $\Longrightarrow$ the sought conditions for the packets in S and D must be independent.

> We assume that the dimensions of the packets are large in comparison with the interaction radius in the corresponding vertex of the diagram. Therefore our analysis will be based *exclusively* on the properties of the geometric suppression factors $\exp\left(-\mathfrak{S}_{s,d}\right)$ which do not depend on the dynamics and do not appellate to the energy-momentum conservation.

1. First of all it is necessary to demand that the time intervals $X^0_{s,d} - x^0_a$ ($a \in I_{s,d}$) and $x^0_b - X^0_{s,d}$ ($b \in F_{s,d}$) are sufficiently large. They however cannot be arbitrarily large since the packets $\varkappa$ remain stable (do not spread) during the time $\left|X^0_{s,d} - x^0_\varkappa\right|$ only under the condition

$$\left|X^{0(\varkappa)}_{s,d} - x^{0(\varkappa)}_\varkappa\right|^2 \ll m^2_\varkappa/\sigma^4_\varkappa, \quad \forall \varkappa \in S, D. \tag{85}$$

Since $\mathfrak{S}_s$ and $\mathfrak{S}_d$ do not depend from $X^{0(\varkappa)}_{s,d}$ and $x^{0(\varkappa)}_\varkappa$ it is permissible to demand that the left part of Eq. (85) is large in comparison with the squared effective size of the packet that is

$$\left|X^{0(\varkappa)}_{s,d} - x^{0(\varkappa)}_\varkappa\right|^2 \gg 1/\sigma^2_\varkappa. \tag{86}$$

Inequalities (86) do not contradict the stationarity condition since $\sigma^2_\varkappa \ll m^2_\varkappa$.

If, in addition, $\varkappa$ is an unstable particle then one can expect that

$$\left|X_{s,d}^{0(\varkappa)} - x_{\varkappa}^{0(\varkappa)}\right| \sim \tau_{\varkappa} = 1/\Gamma_{\varkappa}. \tag{87}$$

The conditions (86) and (87) do not contradict to each other if $\sigma_{\varkappa}^2\tau_{\varkappa}^2 \gg 1$; the latter is one of the conditions of applicability of the CRGP approximation, the *full set of which* is

$$1/\tau_{\varkappa}^2 \ll \sigma_{\varkappa}^2 \ll m_{\varkappa}/\tau_{\varkappa} \ll m_{\varkappa}^2. \tag{88}$$

Since for all known long-lived elementary particles $m_{\varkappa}\tau_{\varkappa} \ggg 1$, the allowed values of the parameters $\sigma_{\varkappa}$ can vary in rather wide limits.

Thus the relativistic-invariant conditions for the time parameters $x_{\varkappa}^0$ is fully consistent with the range of applicability of the CRGP approximation (88), has the form (86) and the correct time sequence in LF is given by

$$x_a^0 < X_{s,d}^0 < x_b^0 \quad (a \in I_{s,d},\ \ b \in F_{s,d}). \tag{89}$$

These inequalities are Lorentz invariant if the points $x_{a,b}$ and $X_{s,d}$ are separated by the time-like intervals. If otherwise for some $\varkappa$ the intervals $(x_{\varkappa} - X_{s,d})^2$ are space-like the inequalities (89) have sense only in LF.

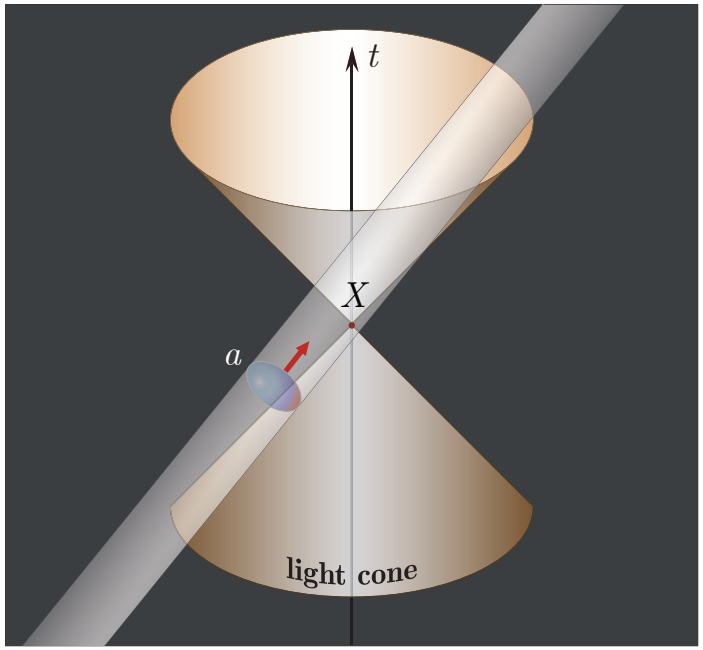

This instance must be taken into account since the packet (e.g., $a \in I_s$) can participate in the interaction even if $(x_a - X_s)^2 < 0$, but under the condition that the points inside a part of its effective volume are separated with the impact point by a time-like interval because the latter can come to be inside the classical world tube of the packet a.

From geometric considerations it can be proved that for such events $0 < |\mathbf{b}_a^\star| < d_a^\star/2$. Therefore

$$\sigma_a^2 |\mathbf{b}_a^\star|^2 < 0.605 \quad \text{and} \quad \exp\left(-\sigma_a^2 |\mathbf{b}_a^\star|^2\right) \gtrsim 0.546.$$

Clearly there the micro-causality is not violated here since all "signals" propagate strictly inside the light cones. However, in principle, the interactions of such kind would lead to observable effect which imitate the causality violation.

2. The conditions of spatial remoteness of the packets from the impact points are not in general necessary. Indeed, some packets (e.g., decaying meson or secondary charged lepton in the source, a target nucleus in the detector, etc.) can be at rest in LF before or after interaction. In this case they must be spatially close to the corresponding impact points; otherwise the amplitude will be small due to the smallness of the factors $\exp\left(-\mathfrak{S}_{s,d}\right)$.

However, all the packets must be spatially separated from each other, that is the differences of the spatial coordinates for each pair of the packets $\varkappa, \varkappa'$ must be large in comparison with the dimensions of these packets. The simplest reference frame to formulate this condition is the CIF of the pair.

Since the packet momenta in CIF are collinear ($\mathbf{p}_\varkappa^* = -\mathbf{p}_{\varkappa'}^* = \mathbf{n}_* |\mathbf{p}_\varkappa^*|$) and the only case is interesting when the classical impact parameter $\left|\mathbf{n}_* \times \left(\mathbf{x}_\varkappa^* - \mathbf{x}_{\varkappa'}^*\right)\right|$ is not larger than the transversal sizes of the packets, the distance between the packets must be large in comparison with these dimensions.

$$\left|\mathbf{x}_\varkappa^* - \mathbf{x}_{\varkappa'}^*\right|^2 \gg \frac{1}{\left(\sigma_\varkappa \Gamma_\varkappa^*\right)^2} + \frac{1}{\left(\sigma_{\varkappa'} \Gamma_{\varkappa'}^*\right)^2}. \tag{90}$$

It is not a simple matter to prove that these conditions do not contradict the conditions

$$\left|\mathbf{X}_{s,d}^{(\varkappa)} - \mathbf{x}_\varkappa^{(\varkappa)}\right|^2 \ll m_\varkappa^2/\sigma_\varkappa^4. \tag{91}$$

3. If, in particular, packets $\varkappa$ and $\varkappa'$ are states of identical particles with equal momenta (so that $\Gamma^*_{\varkappa} = \Gamma^*_{\varkappa'} = 1$) and spin projections, the condition (86) coincides with the condition of vanishing of quantum correlations at long distances between the packets of identical bosons or fermions (see Sect. 17.10). The impact parameters of such packets can be arbitrarily small, as long as one of them is in- and the other is out-state, i.e., the pair of packets describes, in fact, a state of one spectator particle. If both identical packets belong to the in- or out-state of one of the vertices of the diagram, the corresponding amplitude will be suppressed because the distance between them does not change with time[a] and, therefore, they are always far from the impact point.

It follows from Eq. (90) that ultrarelativistic (in CIF) packets forming a pair do not interact with each other even at relatively short distances. Such packets, even if they describe states of identical particles with different momenta, can have not too large impact parameters in CIF and, consequently, participate in interaction. Therefore, ultrarelativistic particles can fly in a relatively dense beam while remaining (approximately) free. Conditions (86) and (90) are not necessarily independent of one another; it is only important that they are not mutually exclusive. The inequalities (90) must be consistent with the non-spreading conditions (85) and (91). Generally speaking, these conditions can lead to additional restrictions (give lower bounds) on the admissible values of $\sigma_{\varkappa}$, which are rather difficult to analyze for the generic processes $I_s \oplus I_d \to F_s \oplus F_d$ without using the assumption that there is no geometric suppression, but such an analysis can certainly be performed for any particular process when modeling and processing data from real experiments.

[a] This suppression has nothing to do with the Pauli exclusion principle: if any two packets (not necessarily describing states of identical fermions) have the same velocities and are distant from each other at some point in time, then their classical world tubes do not intersect. To this it is necessary to add that the parameters $\sigma_{\varkappa}$ and $\sigma_{\varkappa'}$ for packets of identical particles are not fundamental characteristics of the corresponding quantum field and may, in general not coincide with each other.

If (as assumed)

$$\left|\mathbf{n}_* \times \left(\mathbf{x}^*_{\varkappa} - \mathbf{x}^*_{\varkappa'}\right)\right|^2 \lesssim 1/\sigma^2_{\varkappa} + 1/\sigma^2_{\varkappa'}$$

for *each* pair $\varkappa, \varkappa'$ from S or D, then in CIF of *every* such pair the impact point $\mathbf{X}^*_{s,d}$ is located between $\varkappa'$ and $\varkappa'$ at a small distance from their world tubes[a]. Therefore, with (86), we have

$$|\mathbf{x}^*_{\varkappa} - \mathbf{x}^*_{\varkappa'}| = \left|\left(\mathbf{x}^*_{\varkappa} - \mathbf{X}^*_{s,d}\right) + \left(\mathbf{X}^*_{s,d} - \mathbf{x}^*_{\varkappa'}\right)\right| \simeq \left|\mathbf{x}^*_{\varkappa} - \mathbf{X}^*_{s,d}\right| + \left|\mathbf{x}^*_{\varkappa'} - \mathbf{X}^*_{s,d}\right|$$

$$= \Gamma^*_{\varkappa}\sqrt{\left[\mathbf{x}^{(\varkappa)}_{\varkappa} - \mathbf{X}^{(\varkappa)}_{s,d} + \mathbf{v}^*_{\varkappa}\left(x^{0(\varkappa)}_{\varkappa} - X^{0(\varkappa)}_{s,d}\right)\right]^2 - \left[\mathbf{v}^*_{\varkappa} \times \left(\mathbf{x}^{(\varkappa)}_{\varkappa} - \mathbf{X}^{(\varkappa)}_{s,d}\right)\right]^2} + (\varkappa \mapsto \varkappa'),$$

where $\mathbf{v}^*_{\varkappa} = \mathbf{p}^*_{\varkappa}/E^*_{\varkappa}$ and $\mathbf{v}^*_{\varkappa'} = \mathbf{p}^*_{\varkappa'}/E^*_{\varkappa'}$ are the velocities of $\varkappa$ and $\varkappa'$ in CIF. Since, as follows from the Lorentz transformation, $\mathbf{v}^*_{\varkappa} \times \left(\mathbf{x}^*_{\varkappa} - \mathbf{X}^*_{s,d}\right) = \mathbf{v}^*_{\varkappa} \times \left(\mathbf{x}^{(\varkappa)}_{\varkappa} - \mathbf{X}^{(\varkappa)}_{s,d}\right)$ (and similarly for $\varkappa'$), then the following approximate inequality holds:

$$|\mathbf{x}^*_{\varkappa} - \mathbf{x}^*_{\varkappa'}| \lesssim \Gamma^*_{\varkappa}\left(\left|\mathbf{x}^{(\varkappa)}_{\varkappa} - \mathbf{X}^{(\varkappa)}_{s,d}\right| + |\mathbf{v}^*_{\varkappa}|\left|x^{0(\varkappa)}_{\varkappa} - X^{0(\varkappa)}_{s,d}\right|\right) + (\varkappa \mapsto \varkappa'),$$

in which the mutual orientations of spatial vectors and velocities in different reference systems are taken into account.

Thus, given the conditions (85) and (91), it can be stated that for any velocities $\mathbf{v}^*_{\varkappa,\varkappa'}$

$$|\mathbf{x}^*_{\varkappa} - \mathbf{x}^*_{\varkappa'}|^2 \ll 4\left(E^*_{\varkappa}/\sigma^2_{\varkappa} + E^*_{\varkappa'}/\sigma^2_{\varkappa'}\right)^2. \tag{92}$$

Comparing (92) with (90), we conclude that the conditions for the applicability of the CRGP approximation (85) and (91) do not contradict the requirement of spatial separation of packets, i.e., no additional restrictions on parameters of $\sigma_{\varkappa,\varkappa'}$ does not occur.

[a] More precisely, the distance from $\mathbf{X}^*_{s,d}$ to the classical world lines of the centers of $\varkappa'$ and $\varkappa'$ in CIF is much shorter than the distance between these centers.

18 Macroscopic amplitude.

As a practically important example, we consider the charged-current induced production of charged leptons ℓ^+_α and ℓ^-_β ($\ell_{\alpha,\beta} = e, \mu, \tau$) in the process

$$I_s \oplus I_d \to F'_s + \ell^+_\alpha \oplus F'_d + \ell^-_\beta , \qquad (93)$$

In the lowest (fourth) nonvanishing order in electroweak interactions, the process (93) is described by the sum (over $j = 1, 2, 3 \ldots$) of the macrodiagrams shown in the figure. ▷

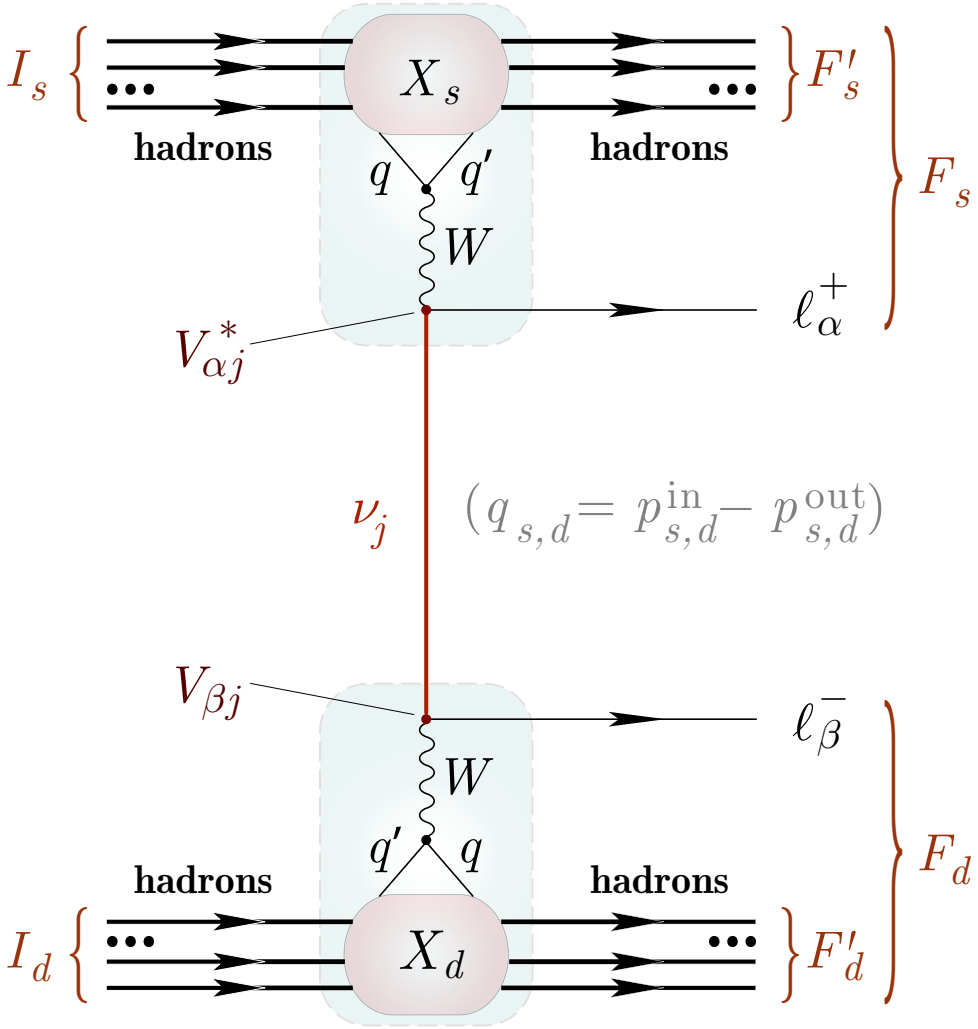

◦ We assume for definiteness that all the external substates I_s, I_d, F'_s, and F'_d consist exclusively of (asymptotically free) hadronic WPs.

◦ Consequently, if $\alpha \neq \beta$, the process (93) violates the lepton numbers L_α and L_β that is only possible via exchange of massive neutrinos (whether they are Dirac or Majorana particles).

◦ The impact points X_s and X_d in the figure are macroscopically separated and it is assumed that the asymptotic conditions discussed in Sect. 17.13.2 are satisfied.

We use the Standard Model (SM) phenomenologically (minimally) extended by inclusion of a Dirac or Majorana neutrino mass term (see Chapter 11). The quark-lepton blocks of the diagram in the lowest nonvanishing order are described by the Lagrangian (see p. 417)

$$\mathcal{L}_W(x) = -\frac{g}{2\sqrt{2}}\,[j_\ell(x)W(x) + j_q(x)W(x) + \text{H.c.}],$$

where g is the $SU(2)$ coupling, $j_{\ell,q}(x) \equiv j^{\mathsf{CC}}_{\ell,q}(x)$ are the lepton and quark weak charged currents:

$$j^\mu_\ell(x) = \sum_{\alpha i} V^*_{\alpha i}\,\overline{\nu}_i(x)O^\mu\ell_\alpha(x), \qquad j^\mu_q(x) = \sum_{qq'} V^{'*}_{qq'}\,\overline{q}(x)O^\mu q'(x) \qquad [O^\mu = \gamma^\mu(1-\gamma_5)]\,;$$

$V_{\alpha i}$ ($\alpha = e,\mu,\tau$; $i = 1,2,3$) and $V'_{qq'}$ ($q = u,c,t$; $q' = d,s,b$) are the elements of the neutrino and quark mixing matrices ($\mathbf{V}$ and $\mathbf{V}'$, respectively).

The normalized amplitude is given by the 4th order of the perturbation theory in g:

$$\mathcal{A}_{\beta\alpha} = \frac{\langle \mathbf{out}|\mathbb{S}|\mathbf{in}\rangle}{\sqrt{\langle \mathbf{in}|\mathbf{in}\rangle\langle \mathbf{out}|\mathbf{out}\rangle}} = \frac{1}{\mathcal{N}}\langle F_s \oplus F_d|\mathbb{S}_{q\ell}\mathbb{S}_h|I_s\oplus I_d\rangle. \tag{94}$$

Here

$$\mathbb{S}_{q\ell} = \left(\frac{-ig}{2\sqrt{2}}\right)^4 T\int dxdx'dydy' : j_\ell(x)W(x) :: j_q(x')W^\dagger(x') :: j^\dagger_\ell(y)W^\dagger(y) :: j^\dagger_q(y')W(y') :$$

describes the quark-lepton (perturbative) block and

$$\mathbb{S}_h = T\exp\left[i\int dz\mathcal{L}_{\mathsf{h}}(z)\right]$$

describes the hadronic (non-perturbative) block; $\mathcal{L}_{\mathsf{h}}(z)$ is the Lagrangian of the strong and (possibly) electromagnetic interactions responsible for the fragmentation and hadronization processes.

T and $:\ldots:$ are the standard symbols for the chronological and normal ordering of local operators. Since it is assumed that all necessary asymptotic conditions are fulfilled (see Sect. 17.13.2), the initial and final states can be represented as direct products of free single-packet states and use the normalization

$$\langle \text{in}|\text{in}\rangle = \prod_{a\in I_s\oplus I_d} 2E_a \mathrm{V}_a(\mathbf{p}_a), \qquad \langle \text{out}|\text{out}\rangle = \prod_{b\in F_s\oplus F_d} 2E_b \mathrm{V}_b(\mathbf{p}_b), \tag{95}$$

where $E_\varkappa \equiv \overline{E}_{\mathbf{p}_\varkappa} \approx E_{\mathbf{p}_\varkappa}$ and $\mathrm{V}_\varkappa = \mathrm{V}_\varkappa(\mathbf{p}_\varkappa)$ are, respectively, the mean energy and effective volume of the packet $\varkappa$; here and hereafter, the index $\varkappa$ is used to denote both initial (a) and final (b) WPs. Then the normalization factor $\mathcal{N}$ in Eq. (94) (in the CRGP approximation) is given by

$$\mathcal{N}^2 = \langle \mathbf{in}|\mathbf{in}\rangle\langle \mathbf{out}|\mathbf{out}\rangle = \prod_{\varkappa\in I_s\oplus I_d\oplus F_s\oplus F_d} 2E_\varkappa \mathrm{V}_\varkappa(\mathbf{p}_\varkappa).$$

Let's consider the hadronic matrix element

$$\langle F'_s\oplus F'_d|T\left[:j_q^\mu(x)::j_q^{\dagger\nu}(y):\mathbb{S}_h\right]|I_s\oplus I_d\rangle = \int\left[\prod_a \frac{d\mathbf{k}_a\phi_a(\mathbf{k}_a,\mathbf{p}_a)e^{ik_ax_a}}{(2\pi)^3 2E_{\mathbf{k}_a}}\right]$$
$$\times\int\left[\prod_b \frac{d\mathbf{k}_b\phi_b^*(\mathbf{k}_b,\mathbf{p}_b)e^{-ik_bx_b}}{(2\pi)^3 2E_{\mathbf{k}_b}}\right]\langle\{k_b\}|T\left[:j_q^\mu(x)::j_q^{\dagger\nu}(y):\mathbb{S}_h\right]|\{k_a\}\rangle. \tag{96}$$

Here we have used the definition of the WP state

$$|\mathbf{p}_\varkappa,s_\varkappa,x_\varkappa\rangle_\varkappa = \sqrt{2E_{\mathbf{p}_\varkappa}}A^\dagger_{\mathbf{p}_\varkappa,s_\varkappa}(x_\varkappa)|0\rangle = \int\frac{d\mathbf{k}\,\phi_\varkappa(\mathbf{k},\mathbf{p}_\varkappa)\,e^{i(k-p_\varkappa)x_\varkappa}}{(2\pi)^3 2E_{\mathbf{k}}}|\mathbf{k},s_\varkappa\rangle_\varkappa \tag{97}$$

and introduced an abbreviated notation for multiparticle Fock states:

$$|\ldots,\mathbf{k}_a,s_a,\ldots;a{\in}I_s{\oplus}I_d\rangle=|\{k_a\}\rangle,\quad |\ldots,\mathbf{k}_b,s_b,\ldots;b{\in}F'_s{\oplus}F'_d\rangle=|\{k_b\}\rangle.$$

◦ For stable with respect to the strong and electromagnetic interactions initial and final hadrons macroscopically separated in space and time, the matrix element (96) is reduced to the form

$$\begin{aligned}\langle F'_s{\oplus}F'_d|T\left[:j_q^{\mu}(x)::j_q^{\dagger\nu}(y):\mathbb{S}_h\right]|I_s{\oplus}I_d\rangle&=\Pi'\left(x,y;\{\mathbf{p}_{\varkappa},x_{\varkappa}\}\right)\\&\times\mathcal{J}_s^{\mu}\left(\{p_a,s_a,p_b,s_b\}\right)\mathcal{J}_d^{\nu *}\left(\{p_a,s_a,p_b,s_b\}\right),\end{aligned}\tag{98}$$

$$\begin{aligned}\Pi'\left(x,y;\{\mathbf{p}_{\varkappa},x_{\varkappa}\}\right)&=\Big[\prod_{a\in I_s}e^{-ip_ax_a}\psi_a(\mathbf{p}_a,x_a-x)\Big]\Big[\prod_{b\in F'_s}e^{ip_bx_b}\psi_b^*(\mathbf{p}_b,x_b-x)\Big]\\&\times\Big[\prod_{a\in I_d}e^{-ip_ax_a}\psi_a(\mathbf{p}_a,x_a-y)\Big]\Big[\prod_{b\in F'_d}e^{ip_bx_b}\psi_b^*(\mathbf{p}_b,x_b-y)\Big],\end{aligned}\tag{99}$$

$\mathcal{J}_s$ and $\mathcal{J}_d$ are the corresponding c-number hadronic currents in the source and detector vertices.[a] Fortunately, an explicit form of the hadronic currents will not be needed for our purposes.

◦ Let's now introduce causal Green's functions for the neutrino and W-boson:

$$\begin{aligned}G^j(x-y)&=\langle T\left[\nu_j(x)\overline{\nu}_j(y)\right]\rangle_0=\int\frac{dq}{(2\pi)^4}\,\Delta^j(q)e^{-iq(x-y)},\\G^W_{\mu\nu}(x-y)&=\langle T\left[W_{\mu}(x)W^{\dagger}_{\nu}(y)\right]\rangle_0=\int\frac{dk}{(2\pi)^4}\,\Delta_{\mu\nu}(k)\,e^{-ik(x-y)}.\end{aligned}\tag{100}$$

[a] Proof of this "factorization theorem" is done in D. V. Naumov & VN, ЭЧАЯ **51** (2020) 1–209 [Phys. Part. Nucl. **51** (2020) 1–106]. It is based on the assumed narrowness of the WP in the momentum space, the macroscopic remoteness of the interaction regions around the source and detector, and translational invariance.

Here

$$\Delta^j(q) = \frac{i}{\hat{q} - m_j + i0} = \frac{i(\hat{q} + m_j)}{q^2 - m_j^2 + i0} \qquad (\hat{q} = q^\mu \gamma_\mu) \tag{101}$$

and

$$\Delta_{\mu\nu}(k) = -i\,\frac{g_{\mu\nu} - k_\mu k_\nu / m_W^2}{k^2 - m_W^2 + i0} \tag{102}$$

are the bare propagators of the jth neutrino (with mass m_j) and W-boson (with mass m_W), respectively, and the latter is written in unitary gauge.

Now, after standard transformations, we arrive at the following expression for the amplitude:

$$\begin{aligned}\mathcal{A}_{\beta\alpha} = \frac{g^4}{64\,\mathcal{N}} \sum_j V_{\alpha j}^* V_{\beta j} \int dx dx' dy dy' \psi_\alpha^*(\mathbf{p}_\alpha, x' - x_\alpha)\psi_\beta^*(\mathbf{p}_\beta, y' - x_\beta)\Pi'\left(x, y; \{\mathbf{p}_\varkappa, x_\varkappa\}\right) \\ \times \mathcal{J}_d^{\nu *} G^W_{\nu\nu'}(y - y')\overline{u}(\mathbf{p}_\beta) O^{\nu'} G^j(y' - x') O^{\mu'} G^W_{\mu'\mu}(x' - x) v(\mathbf{p}_\alpha)\mathcal{J}_s^\mu .\end{aligned} \tag{103}$$

Here ψ_α and ψ_β are the wave functions of outgoing leptons ℓ_α^+ and ℓ_β^-, respectively; spin indices and momentum variables of the functions $\mathcal{J}_s$ and $\mathcal{J}_d$ are not written out for brevity (see Eq. (98)).

◦ Integration over the variable y' in Eq. (103), applying our standard definitions, yields the factor

$$\begin{aligned}&\int dy'\, \psi_\beta^*(\mathbf{p}_\beta, y' - x_\beta) G^W_{\nu\nu'}(y - y') G^j(y' - x') \\ &\quad = \int \frac{d\mathbf{p}\, e^{-ipx_\beta}\phi_\beta^*(\mathbf{p}, \mathbf{p}_\beta)}{(2\pi)^3 2E_{\mathbf{p}}} \int \frac{dk\, e^{-iky}\Delta_{\nu\nu'}(k)}{(2\pi)^4} \int \frac{dq\, e^{iqx'}\Delta^j(q)}{(2\pi)^4} \int dy' e^{i(k-q+p)y'} \\ &\quad = \int \frac{d\mathbf{p}}{(2\pi)^3 2E_{\mathbf{p}}} \phi_\beta^*(\mathbf{p}, \mathbf{p}_\beta) e^{-ip(x_\beta - y)} \int \frac{dq}{(2\pi)^4}\, \Delta_{\nu\nu'}(q - p)\Delta^j(q) e^{iq(x' - y)} .\end{aligned}$$

We can rewrite the latter in the form:

$$\psi^*_\beta(\mathbf{p}_\beta, y - x_\beta) \int \frac{dq}{(2\pi)^4} \Delta_{\nu\nu'}(q - p_\beta)\Delta^j(q)e^{iq(x'-y)}.$$

◦ Integration over the variable x' can be done in exactly the same way, resulting in the factor

$$\psi^*_\beta(\mathbf{p}_\beta, y - x_\beta)\psi^*_\alpha(\mathbf{p}_\alpha, x - x_\alpha) \int \frac{dq}{(2\pi)^4} \Delta_{\nu\nu'}(q - p_\beta)\Delta^j(q)\Delta_{\mu'\mu}(q + p_\alpha)e^{iq(x-y)}$$

in the integrand of the amplitude (103).

◦ Now, putting all the factors together, given the definitions (76) for the overlap integrals $\mathbb{V}_{s,d}$ and (99) for the factor Π', and introducing the tensor function

$$\mathbb{G}^j_{\nu\nu'\mu'\mu}\left(\{\mathbf{p}_\varkappa, x_\varkappa\}\right) = \int \frac{dq}{(2\pi)^4} \mathbb{V}_d(q)\Delta_{\nu\nu'}(q - p_\beta)\Delta^j(q)\Delta_{\mu'\mu}(q + p_\alpha)\mathbb{V}_s(q), \tag{104}$$

we arrive at the following expression for the amplitude (103):

$$\boxed{\mathcal{A}_{\beta\alpha} = \frac{g^4}{64\mathcal{N}} \sum_j V_{\beta j}\mathcal{J}_d^{\nu *}\overline{u}(\mathbf{p}_\beta)O^{\nu'}\mathbb{G}^j_{\nu\nu'\mu'\mu}\left(\{\mathbf{p}_\varkappa, x_\varkappa\}\right)O^{\mu'}v(\mathbf{p}_\alpha)\mathcal{J}_s^\mu V^*_{\alpha j}.} \tag{105}$$

This expression seems quite natural when we compare it to the original macrodiagram (see p. 593). The formula is formally valid for any spacing between the vertices of the diagram[a]. But in its most general form it is not easy to apply to the real neutrino oscillation experiments.

◦ Below we consider the long-distance ($L = |\mathbf{X}_d - \mathbf{X}_s| \to \infty$) asymptotics of the amplitude (105) interesting for the current experiments.

[a] Except for the relatively weak restrictions imposed by the proof of the factorization theorem (98).

18.1 Long baseline asymptotics.

At large spatial distances between the impact points $\mathbf{X}_s$ and $\mathbf{X}_d$, the integral (104) can be evaluated by means of the Grimus-Stockinger (GS) theorem.[a]

> Let $\Phi(\boldsymbol{q})$ be a thrice continuously differentiable function such that Φ itself and its 1st and 2nd derivatives decrease not slowly than $|\boldsymbol{q}|^{-2}$ as $|\boldsymbol{q}| \to \infty$. Then in the asymptotic limit of $L = |\boldsymbol{L}| \to \infty$,
>
> $$\int \frac{d\mathbf{q}}{(2\pi)^3} \frac{\Phi(\mathbf{q}) e^{i\mathbf{q}\mathbf{L}}}{s - \mathbf{q}^2 + i0} \sim \begin{cases} -\dfrac{\Phi\left(\sqrt{s}\,\mathbf{L}/L\right)}{4\pi L} \exp\left(-i\sqrt{s}L\right) + \mathcal{O}\left(L^{-3/2}\right) & \text{for } s > 0, \\ \mathcal{O}\left(L^{-2}\right) & \text{for } s < 0. \end{cases}$$

Taking into account the definition (104), implicit form of the overlap integrals and neutrino propagator (101) we see that in our case

$$\mathbf{L} = \mathbf{X}_d - \mathbf{X}_s, \quad T = X_d^0 - X_s^0, \quad s = q_0^2 - m_j^2.$$

We'll show that the integrand in (104) satisfies the requirements of the GS theorem.

[a] W. Grimus & P. Stockinger, "Real oscillations of virtual neutrinos," Phys. Rev. D **54** (1996) 3414–3419, arXiv:hep-ph/9603430. Finite-L corrections to the GS asymptotics (can be important for short baseline neutrino experiments) have been found [VN & D. S. Shkirmanov, "The extended Grimus-Stockinger theorem and the violation of the inverse square law in quantum field theory," Eur. Phys. J. C **73** (2013) 2627, arXiv:1309.1011 [hep-ph]]. Among other things, it was shown that the residual term at $s > 0$ is actually of order $\mathcal{O}\left(L^{-2}\right)$ rather than $\mathcal{O}\left(L^{-3/2}\right)$, which, however, is insignificant for the later. For further development see S. E. Korenblit & D. V. Taychenachev, "Extension of Grimus–Stockinger formula from operator expansion of free Green function," Mod. Phys. Lett. A **30** (2015) 1550074, arXiv:1401.4031 [math-ph]. For a summary, see Sect. **21**, p. 648.

The function corresponding the function $\Phi(\mathbf{q})$ in the GS theorem is, up to an inessential (q independent) multiplier,[a]

$$\widetilde{\delta}_s\left(q-q_s\right)\widetilde{\delta}_d\left(q+q_d\right)\Delta_{\nu\nu'}(q-p_\beta)(\hat{q}+m_j)\Delta_{\mu'\mu}(q+p_\alpha). \tag{106}$$

The first requirement of the theorem can be formally violated by the poles in the bare W propagators (102). In order to exclude this small trouble, we will use instead of (102) the renormalized propagator which has no singularity in the resonance region.

> The simplest recipe consists in the standard substitution $m_W^2 \longmapsto m_W^2 - im_W\Gamma_W$, in the denominator of the bare propagator (102); Γ_W is the full width of the W boson.

Since the functions $\widetilde{\delta}_s\left(q-q_s\right)$ and $\widetilde{\delta}_d\left(q+q_d\right)$ decay faster that any power of $|\mathbf{q}|^{-1}$ as $|\mathbf{q}|\to\infty$, we conclude that the function (106) satisfies the conditions of the GS theorem. As a result, in the leading order in $1/L$ the function (104) behaves as

$$\begin{aligned}\mathbb{G}^j_{\nu\nu'\mu'\mu}\left(\{\mathbf{p}_\varkappa, x_\varkappa\}\right) = \frac{e^{-\mathfrak{S}-i\Theta}}{8\pi^2 L}\int_{-\infty}^{\infty} dq_0 e^{-i\left(q_0T-|\mathbf{q}_j|\,L\right)}\widetilde{\delta}_s\left(q_j-q_s\right)\widetilde{\delta}_d\left(q_j+q_d\right)\\ \times\Delta_{\nu\nu'}(q_j-p_\beta)\left(\hat{q}_j+m_j\right)\Delta_{\mu'\mu}(q_j+p_\alpha),\end{aligned} \tag{107}$$

where

$$q_j=(q_0,\mathbf{q}_j),\quad \mathbf{q}_j=\sqrt{q_0^2-m_j^2}\,\mathbf{l},\quad \mathbf{l}=\mathbf{L}/L,\quad \mathfrak{S}=\mathfrak{S}_s+\mathfrak{S}_d,\quad \text{and}\quad \Theta=X_sq_s+X_dq_d.$$

[a] We have to note that the term in Eq. (106) proportional to the neutrino mass m_j does not contribute to the amplitude due to the matrix multipliers $O^{\mu'}$ and $O^{\nu'}$.

18.1.1 Integration in q_0.

Since the factors $\widetilde{\delta}_s\left(q_j - q_s\right)$ and $\widetilde{\delta}_d\left(q_j + q_d\right)$ under the integral sign in the right-hand part of Eq. (107) have, as the functions of q_0, very sharp maxima close to each other, the integral is saturated by the narrow vicinity of these maxima. So it can be estimated by the standard saddle point method. All calculations will be performed within the CRGP model.

According to the definition of the "smeared" δ functions (see p. 579),

$$\widetilde{\delta}_s\left(q_j - q_s\right)\widetilde{\delta}_d\left(q_j + q_d\right) = \frac{1}{(4\pi)^4\sqrt{|\Re_s||\Re_d|}}\exp\left[-\frac{1}{4}F_j(q_0)\right],$$
$$F_j(q_0) = \widetilde{\Re}_s^{\mu\nu}\left(q_j - q_s\right)_\mu\left(q_j - q_s\right)_\nu + \widetilde{\Re}_d^{\mu\nu}\left(q_j + q_d\right)_\mu\left(q_j + q_d\right)_\nu.$$

We denote

$$\begin{aligned} F_0 &= \widetilde{\Re}_s^{\mu\nu}q_{s\mu}q_{s\nu} + \widetilde{\Re}_d^{\mu\nu}q_{d\mu}q_{d\nu}, \\ Y^\mu &= \widetilde{\Re}_s^{\mu\nu}q_{s\nu} - \widetilde{\Re}_d^{\mu\nu}q_{d\nu}, \\ R^{\mu\nu} &\equiv \widetilde{\Re}^{\mu\nu} = \widetilde{\Re}_s^{\mu\nu} + \widetilde{\Re}_d^{\mu\nu}, \end{aligned} \tag{108}$$

and rewrite $F_j(q_0)$ in the following form:

$$F_j(q_0) = F_0 - 2Y_\mu q_j^\mu + R_{\mu\nu}q_j^\mu q_j^\nu. \tag{109}$$

The extremum of this function is given by

$$\frac{dF_j(q_0)}{dq_0} = \frac{2}{|\mathbf{q}_j|}\left[Rq_0|\mathbf{q}_j| - (\mathbf{Rl})\left(q_0 - |\mathbf{q}_j|\right)^2 - Y_0|\mathbf{q}_j| + (\mathbf{Yl})q_0\right] = 0, \tag{110}$$

where

$$\begin{gathered} R = R^{\mu\nu} l_\mu l_\nu = R_{00} - 2(\mathbf{Rl}) + \mathscr{R}, \\ \mathscr{R} = R_{kn} l_k l_n, \\ \mathbf{R} = (R_{01}, R_{02}, R_{03}), \\ \mathbf{Y} = (Y_1, Y_2, Y_3), \end{gathered} \tag{111}$$

and $l = (1, \mathbf{l})$. Here and below we suppose conventional summation on repeating Latin indices ($k, n = 1, 2, 3$). The root of Eq. (110), $q_0 = E_j$, will be the saddle point, if the 2nd derivative

$$\frac{d^2 F_j(q_0)}{dq_0^2} = 2R + \frac{2\,(q_0 - |\mathbf{q}_j|)}{|\mathbf{q}_j|^3} \left[(\mathbf{Rl})\,(q_0 + 2|\mathbf{q}_j|)\,(q_0 - |\mathbf{q}_j|) - (\mathbf{Yl})\,(q_0 + |\mathbf{q}_j|) \right] \tag{112a}$$

$$= 2R + \frac{2}{v_j^3} \left[(\mathbf{Rl})\,(1 + 2v_j)\,(1 - v_j)^2 - \frac{(\mathbf{Yl})}{m_j \Gamma_j^3} \right] \tag{112b}$$

(where $v_j = |\mathbf{q}_j|/q_0$ and $\Gamma_j = q_0/m_j$) is positive in this point. The straightforward method of the exact solution of Eq. (110) in the general case is described in Appendix H, p. 864. However, it is very cumbersome and therefore not very useful for practical use. Moreover, the method described in the Appendix gives an algorithm for the solution, not a formula (even if very complicated). For this reason, on pp. 870 and 876 of Appendix H we consider two most interesting particular cases- - ultrarelativistic ($v \sim 1$) and nonrelativistic ($1 - v \ll 1$), for which one can obtain comparatively simple and practically useful approximate solutions.[a] These particular solutions can also serve an additional criterion of uniqueness of the exact solution, since the latter must smoothly merge with both asymptotics.

Below we give a summary for the ultrarelativistic case, the most important for further study.

[a] In the same Appendix a strict definition of the nonrelativistic and ultrarelativistic motion of the virtual neutrino is given.

Summary (ultrarelativistic case).

In the ultrarelativistic approximation ($q_s^0 \approx -q_d^0 \gg m_j$) the stationary saddle point $q_0 = E_j$ – solution to Eq. (110) – can be found as a series in powers of the small parameter $r_j = m_j^2/(2E_\nu^2)$:

$$\begin{aligned} q_0 \equiv E_j &= E_\nu \left\{1 - \mathfrak{n} r_j - \left[\mathfrak{n}\left(2\mathfrak{n} + \frac{3}{2}\right) - \mathfrak{m}\right] r_j^2 + \mathcal{O}\left(r_j^3\right)\right\}, \\ |\mathbf{q}_j|_{q_0=E_j} \equiv P_j &= E_\nu \left\{1 - (\mathfrak{n}+1) r_j - \left[(\mathfrak{n}+1)\left(2\mathfrak{n} + \frac{1}{2}\right) - \mathfrak{m}\right] r_j^2 + \mathcal{O}\left(r_j^3\right)\right\}, \\ \frac{P_i}{E_j} \equiv v_j &= 1 - r_j - \left(2\mathfrak{n} + \frac{1}{2}\right) r_j^2 + \mathcal{O}\left(r_j^3\right), \quad E_j^2 - P_j^2 = m_j^2; \end{aligned}$$

$$\mathfrak{n} = \frac{\mathbf{Yl}}{Yl}, \quad \mathfrak{m} = \frac{\mathbf{Rl}}{R}, \quad \mathbf{R} = (R_{01}, R_{02}, R_{03}), \quad R^{\mu\nu} = \widetilde{\Re}_s^{\mu\nu} + \widetilde{\Re}_d^{\mu\nu},$$

$$R = R^{\mu\nu} l_\mu l_\nu = \mathfrak{F} E_\nu^{-2}, \quad \mathfrak{F} = \left[R^{\mu\nu} q_\mu q_\nu\right]_{q=E_\nu l} > 0,$$

$$Y^\mu = \widetilde{\Re}_s^{\mu\nu} q_{s\nu} - \widetilde{\Re}_d^{\mu\nu} q_{d\nu}, \quad E_\nu = \frac{Yl}{R}, \quad l = (1, \mathbf{l}), \quad \mathbf{l} = \frac{\mathbf{L}}{L}, \quad \mathbf{L} = \mathbf{X}_d - \mathbf{X}_s.$$

The second derivative (112b) at the point $q_0 = E_j$ is positive $\Longrightarrow$ the function $F_j(q_0)$ has at this point *absolute minimum* $\Longrightarrow$ the quantities E_j, $\mathbf{P}_j = P_j \mathbf{l}$ and $\mathbf{v}_j = v_j \mathbf{l}$ can naturally be treated as, respectively, the effective energy, momentum and velocity of the virtual neutrino ν_j.

The ultrarelativistic approximation is, of course, reference-frame dependent.
That is why the obtained result is not explicitly Lorentz-invariant.

18.2 The amplitude.

Since, as it has been proved, in both ultrarelativistic and nonrelativistic cases the function $F_j(q_0)$ has *absolute minimum* at $q_0 = E_j$, then, following the saddle-point method, in the vicinity of the minimum it can be approximated by a parabola:

$$F_j(q_0) \simeq F_j(E_j) + \frac{(q_0 - E_j)^2}{2\mathfrak{D}_j^2}. \tag{113}$$

Here we introduce a positive definite function[a]

$$\mathfrak{D}_j = \left\{ \left[d^2 F_j(q_0)/dq_0^2 \right]_{q_0 = E_j} \right\}^{-1/2}. \tag{114}$$

In the ultra-relativistic case, which we will limit our discussion to,

$$\mathfrak{D}_j \simeq \frac{E_\nu}{E_j\sqrt{2R}} \simeq \frac{E_\nu}{\sqrt{2\mathfrak{F}}} \equiv \mathfrak{D}. \tag{115}$$

Within the approximations we have made, this quantity is independent of index j (i.e., is universal for all massive neutrinos) and is small compared with the representative neutrino energy ($\mathfrak{D} \ll E_\nu$). Consider now that in the neighborhood of the stationary point E_j all multipliers of the integrand in the right-hand side of Eq. (107), except for the exponent

$$\exp\left[-\frac{1}{4} F_j(q_0) - i\left(q_0 T - \sqrt{q_0^2 - m_j^2}\, L \right) \right],$$

are weakly varying functions of the variable of integration q_0 and can therefore be taken out from the integral at the point $q_0 = E_j$.

[a] Which, as will be seen, can be interpreted as the uncertainty of the effective energy of the virtual neutrino.

Using Eq. (113) and expansion

$$\sqrt{q_0^2 - m_j^2} = P_j + \frac{1}{v_j}(q_0 - E_j) - \frac{m_j^2}{2P_j^3}(q_0 - E_j)^2 + \ldots$$

we arrive at the following simple integral:

$$I_j = \int_{-\infty}^{\infty} dq_0 \exp\left[-i\left(E_j T - P_j L\right) + i\left(\frac{L}{v_j} - T\right)(q_0 - E_j) - \frac{1}{4}F_j(E_j) - \left(\frac{1}{8\mathfrak{D}_j^2} + \frac{i m_j^2 L}{2P_j^3}\right)(q_0 - E_j)^2\right].$$

Introducing a complex-valued phase function

$$\Omega_j(T, L) = i\left(E_j T - P_j L\right) + 2\widetilde{\mathfrak{D}}_j^2\left(\frac{L}{v_j} - T\right)^2, \tag{116}$$

in which

$$\widetilde{\mathfrak{D}}_j^2 = \frac{\mathfrak{D}_j^2}{1 + i\mathfrak{r}_j} \simeq \frac{\mathfrak{D}^2}{1 + i\mathfrak{r}_j}, \quad \mathfrak{r}_j = \frac{4m_j^2\mathfrak{D}_j^2 L}{P_j^3} \simeq \frac{4m_j^2\mathfrak{D}^2 L}{E_\nu^3}, \tag{117}$$

we obtain:

$$I_j = 2\sqrt{2\pi}\widetilde{\mathfrak{D}}_j \exp\left[-\frac{1}{4}F_j(E_j) - \Omega_j(T, L)\right].$$

The complex "dispersion" $\widetilde{\mathfrak{D}}_j$ depends on the effective neutrino energy, E_ν, and the spatial distance, L, between the impact points in the source and detector.
The module and argument of the function $\widetilde{\mathfrak{D}}_j$ are given by the following formulas:

$$|\widetilde{\mathfrak{D}}_j| \simeq \mathfrak{D}\left(1 + \mathfrak{r}_j^2\right)^{-1/4}, \quad \arg(\widetilde{\mathfrak{D}}_j) \simeq \frac{1}{2}\arctan\left(\mathfrak{r}_j\right).$$

By collecting all the multipliers, we obtain the following final expression for the function (107):

$$\mathbb{G}^{j}_{\nu\nu'\mu'\mu}\left(\{\mathbf{p}_{\varkappa}, x_{\varkappa}\}\right) = \Delta_{\nu\nu'}(p_j - p_\beta)\hat{p}_j\Delta_{\mu'\mu}(p_j + p_\alpha)|\mathbb{V}_d(p_j)\mathbb{V}_s(p_j)|\frac{\widetilde{\mathfrak{D}}_j e^{-\Omega_j - i\Theta}}{i(2\pi)^{3/2}L}. \tag{118}$$

Here the 4-vector $p_j = (E_j, P_j\mathbf{l})$ is introduced and the contribution proportional to m_j is omitted. The phase factor $-ie^{-i\Theta}$ in Eq. (118) is insignificant in the squared modulus of the amplitude.

Because of the presence of smeared δ-functions $\widetilde{\delta}_s\left(p_j - q_s\right)$ and $\widetilde{\delta}_d\left(p_j + q_d\right)$ in the expressions for the overlap integrals $\mathbb{V}_s(p_j)$ and $\mathbb{V}_d(p_j)$ and responsible for the approximate energy–momentum conservation ($p_j \approx q_s \approx -q_d$), and for the assumed smallness of the neutrino masses compared to the representative energy E_ν, we can put $m_j = 0$ in the entire pre-exponential multiplier in the right-hand side of Eq. (118) (except for the term $\mathfrak{r}_j$ in the dispersion function $\widetilde{\mathfrak{D}}_j$[a]).

A crucial point: Now let's apply the identity

$$P_-\hat{p}_\nu P_+ = P_- u_-(\mathbf{p}_\nu)\overline{u}_-(\mathbf{p}_\nu)P_+$$

(in which $P_\pm \equiv P_{L,R} = \frac{1}{2}(1 \pm \gamma_5)$, $\mathbf{p}_\nu = E_\nu\mathbf{l}$, and $u_-(\mathbf{p}_\nu)$ is the usual Dirac bispinor for a free massless left-handed neutrino ν) and use it to define the matrix elements

$$\begin{aligned} M_s &= \frac{g^2}{8}\overline{u}_-(\mathbf{p}_\nu)\mathcal{J}_s^\mu\Delta_{\mu\mu'}(p_\nu + p_\alpha)O^{\mu'}u(\mathbf{p}_\alpha), \\ M_d^* &= \frac{g^2}{8}\overline{v}(\mathbf{p}_\beta)O^{\mu'}\Delta_{\mu'\mu}(p_\nu - p_\beta)\mathcal{J}_d^{*\mu}u_-(\mathbf{p}_\nu). \end{aligned} \tag{119}$$

[a] Since $\mathfrak{r}_j \propto L$, this term can be arbitrarily large if the distance L is large enough.

Obviously, these quantities describe the creation and absorption of the *real* massless neutrino in the reactions $I_s \to F'_s \ell^+_\alpha \nu$ and $\nu I_d \to F'_d \ell^-_\beta$, respectively.

Under additional conditions $|(p_\nu + p_\alpha)^2| \ll m_W^2$ and $|(p_\nu - p_\beta)^2| \ll m_W^2$, the W-boson propagator can be approximately written as $-ig_{\mu\nu}/m_W^2$, which corresponds to the four-fermion theory of weak interaction. Then, using the well-known SM identity $g^2/8 = G_F m_W^2/\sqrt{2}$, we can rewrite the matrix elements (119) as

$$M_s \approx -i(G_F/\sqrt{2})\overline{u}_-(\mathbf{p}_\nu)\mathcal{J}_s^\mu O_\mu v(\mathbf{p}_\alpha), \quad M_d^* \approx -i(G_F/\sqrt{2})\overline{u}(\mathbf{p}_\beta)\mathcal{J}_d^{*\mu} O_\mu u_-(\mathbf{p}_\nu).$$

However, this somewhat restrictive simplification (not applicable, in particular, at ultrahigh energies) is not necessary and will not be used in the following analysis.

Given the above results, we obtain an almost final expression for the amplitude (105):

$$\mathcal{A}_{\beta\alpha} = \sum_j \frac{|\mathbb{V}_s(p_j)\mathbb{V}_d(p_j)| M_s M_d^*}{i(2\pi)^{3/2}\mathcal{N}L} V^*_{\alpha j} \widetilde{\mathfrak{D}}_j V_{\beta j}\, e^{-\Omega_j - i\Theta}. \tag{120}$$

It is useful to isolate in this formula the general (j independent) multiplier responsible for the approximate conservation of energy-momentum in the vertices. For this purpose, using the explicit form of the smeared δ-functions, we write

$$\widetilde{\delta}_s(p_j - q_s)\widetilde{\delta}_d(p_j + q_d) = \widetilde{\delta}_s(p_\nu - q_s)\widetilde{\delta}_d(p_\nu + q_d)e^{-\Theta_j},$$

$$\begin{aligned}
\Theta_j &= \frac{1}{4}\left[2\left(Y_\mu - R_{\mu\mu'}p_\nu^{\mu'}\right) + R_{\mu\mu'}\left(p_\nu - p_j\right)^{\mu'}\right]\left(p_\nu - p_j\right)^\mu \\
&= \frac{1}{2}\left\{E_\nu\left[(\mathbf{Rl}) - R_{00}\right] + Y_0\right\}\left(E_\nu - E_j\right) + \frac{1}{2}\left\{E_\nu\left[(\mathbf{Rl}) - \mathscr{R}\right] - (\mathbf{Yl})\right\}\left(E_\nu - P_j\right) \\
&\quad + \frac{1}{4}\left[R_{00}\left(E_\nu - E_j\right)^2 - 2(\mathbf{Rl})\left(E_\nu - E_j\right)\left(E_\nu - P_j\right) + \mathscr{R}\left(E_\nu - P_j\right)^2\right].
\end{aligned}$$

Then the amplitude (120) can be represented in the following form:

$$\boxed{\mathcal{A}_{\beta\alpha} = \frac{|\mathbb{V}_s(p_\nu)\mathbb{V}_d(p_\nu)|M_s M_d^*}{i(2\pi)^{3/2}\mathcal{N}L}\sum_j V_{\alpha j}^* \widetilde{\mathfrak{D}}_j V_{\beta j}\, e^{-\Omega_j - \Theta_j - i\Theta}.} \tag{121}$$

Using Eq. (199), one can represent the function Θ_j as a r_j expansion:

$$\Theta_j = m_j^2 R\left[(\mathfrak{n}_0 - \mathfrak{n}) + \frac{1}{2}\left(\mathfrak{m} - \mathfrak{n} - \mathfrak{n}^2\right) r_j + \left(\mathfrak{n} + \frac{1}{2}\right)\left(\mathfrak{m} - \mathfrak{n} - \mathfrak{n}^2\right) r_j^2 + \mathcal{O}(r_j^3)\right].$$

Recall that the function $\mathfrak{n}_0$ is defined according to Eq. (207) and coincides with $\mathfrak{n}$ in the case exact conservation of energy-momentum in the vertices (see p. 870 in Appendix). Under the conditions we have taken, Eq. (205) can be written approximately:

$$\Theta_j \approx m_j^2 R\left[(\mathfrak{n}_0 - \mathfrak{n}) + \frac{1}{2}\left(\mathfrak{m} - \mathfrak{n} - \mathfrak{n}^2\right) r_j\right],$$

and in the neighborhood of the maximum of the product $\widetilde{\delta}_s(p_\nu - q_s)\widetilde{\delta}_d(p_\nu + q_d)$ (i.e. at $q_s \approx -q_d \approx p_\nu$) the difference $\mathfrak{n}_0 - \mathfrak{n}$ (whose sign is not definite) can be neglected. Then

$$\Theta_j \approx \frac{m_j^4 R\left(\mathfrak{m} - \mathfrak{n}_0 - \mathfrak{n}_0^2\right)}{4E_\nu^2} = \frac{m_j^4\left[R_{00}\mathscr{R} - (\mathbf{Rl})^2\right]}{4RE_\nu^2}. \tag{122}$$

It can be proved that this value is positive.

From the derivation of Eq. (121) and its structure, we see that it is valid not only for the class of processes considered, but, with an appropriate redefinition of the matrix elements (119), for any processes occurring due to virtual neutrino exchange between the vertices of a macrodiagram.
It is trivial to extend Eq. (120) to the diagrams with exchange of antineutrinos, for which it is only necessary to replace $V_{\alpha j}^* \longmapsto V_{\alpha j}$ and $V_{\beta j} \longmapsto V_{\beta j}^*$ and properly modify the matrix elements (119).

18.2.1 Effective neutrino wave packet.

The phase function (116) can be rewritten in the approximate Lorentz-invariant form[a]:

$$\Omega_j(T,L) = i(p_j X) + \frac{2\widetilde{\mathfrak{D}}_j^2}{E_\nu^2}\left[(p_j X)^2 - m_j^2 X^2\right], \tag{123}$$

where $X = X_d - X_s$. Consider the following factor in the amplitude (118):

$$\overline{u}_-(\mathbf{p}_\nu)\frac{1}{L}e^{-\Omega_j(T,L)}u_-(\mathbf{p}_\nu) \approx \overline{u}_-(\mathbf{p}_j)\frac{1}{L}e^{-\Omega_j(T,L)}u_-(\mathbf{p}_j)$$

Neglecting the imaginary part of the function $\widetilde{\mathfrak{D}}_j^2$, this factor can be written as the product

$$\frac{1}{|\mathbf{X}_d - \mathbf{X}_s|}\overline{\psi}^j_{X_s}(\mathbf{p}_j, X_d - X_s)\psi^j_{X_d}(\mathbf{p}_j, X_s - X_d), \tag{124}$$

in which

$$\psi^j_y(\mathbf{p}_j, x) = \exp\left\{-i(p_j y) - \frac{\mathfrak{D}_j^2}{E_\nu^2}\left[(p_j x)^2 - m_j^2 x^2\right]\right\}u_-(\mathbf{p}_j)$$

and

$$\overline{\psi}^j_y(\mathbf{p}_j, x) = \left[\psi^j_y(\mathbf{p}_j, x)\right]^\dagger \gamma_0 = \overline{u}_-(\mathbf{p}_j)\exp\left\{i(p_j y) - \frac{\mathfrak{D}_j^2}{E_\nu^2}\left[(p_j x)^2 - m_j^2 x^2\right]\right\}.$$

[a] The function $\widetilde{\mathfrak{D}}_j/E_\nu$ is invariant, to an accuracy of $\mathcal{O}(\mathfrak{r}_j^2)$.

Comparing the spinor function $\psi_y(\mathbf{p}_j, x)$ with the wave function of the generic fermion wave packet in the CRGP approximation

$$\psi_y(\mathbf{p}, s, x) = e^{-ipx} u_s(\mathbf{p}) \psi(\mathbf{p}, x-y) = u_s(\mathbf{p}) \exp\left\{-i(py) - \frac{\sigma^2}{m^2}\left[(px)^2 - m^2 x^2\right]\right\},$$

we see that the spinor function $\psi^j_{X_d}(\mathbf{p}_j, X_s - X_d)$ can be interpreted as the wave function in the x-representation describing the *incoming* wave packet of the *real* massive neutrino ν_j, the role of the parameter σ in which the value $\sigma_j = \mathfrak{D}_j/\Gamma_j$, where $\Gamma_j = E_j/m_j \simeq E_\nu/m_j$. The Dirac conjugate spinor multiplier in (124), $\overline{\psi}^j_{X_s}(\mathbf{p}_j, X_d - X_s)/|\mathbf{X}_d - \mathbf{X}_s|$, naturally interpret as *outgoing* spherical neutrino wave at a distance $|\mathbf{X}_d - \mathbf{X}_s|$ from the point of its origin $\mathbf{X}_s$.

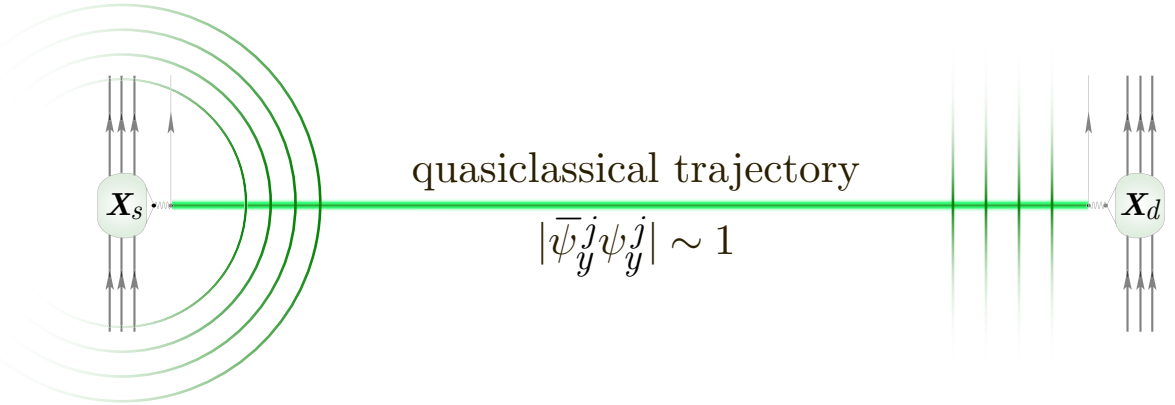

It is clear that $|\overline{\psi}^j_y \psi^j_y| \ll 1$ everywhere except in the narrow neighborhood of the classical trajectory.

Although the picture described is incomplete in many respects, the main lesson is the duality between the description of neutrino propagation by the causal propagator and the wave packet. In other words, at large distances, the virtual neutrino behaves like a wave packet[a].

[a] For more details, see also S. E. Korenblit, D. V. Taychenachev & M. V. Petropavlova, "Interpolating wave packets and composite wave functions in QFT and neutrino oscillation problem," arXiV:1712.06641 [hep-th].

Very long distances.

Since $\widetilde{\mathfrak{D}}_j$ is a complex-valued function, factorization of the form (124) generally becomes impossible. The corresponding correction, which is of obvious interest for neutrino astrophysics, can be treated as the result of a peculiar interference of the spreading neutrino in- and out-packets. The correction becomes significant at very large distances L and leads to an overall suppression of the amplitude (105) and a modification of the "oscillation" factors $\propto \exp\left[i\mathrm{Im}\Omega_j(T,L)\right]$.

A detailed study of these effects is possible only by analyzing the observed values (such as the count rate of events of a given sort in a detector), which are obtained after proper averaging of the squared modulus of the amplitude over all unmeasured variables involved in the amplitude (105). Such averaging depends on the statistical distributions (in the more general case, the kinetics) of the in-packet ensembles and the detection procedure. For the moment we will restrict ourselves to the case where these effects can be neglected. Then, using (115) and (117) we write:

$$\mathfrak{r}_j \simeq 10^{-4}\left(\frac{10^7}{\mathfrak{F}}\right)\left(\frac{m_j}{0.1\text{ eV}}\right)^2\left(\frac{1\text{ GeV}}{E_\nu}\right)\left(\frac{L}{10^4\text{ km}}\right). \tag{125}$$

From this we see that $\mathfrak{r}_j \ll 1$ for all current terrestrial (anti)neutrino experiments with

- reactor ($E_\nu \gtrsim 1$ MeV, $L \lesssim$ a few $\times\, 10^2$ km),
- accelerator ($E_\nu \gtrsim 100$ MeV, $L \lesssim$ a few $\times\, 10^3$ km, e.g., 2595 km for P2O), and
- atmospheric ($E_\nu \gtrsim 100$ MeV, $L \lesssim 1.3 \times 10^4$ km),

under the condition that $m_j \lesssim 0.1$ eV and $\mathfrak{F} \gg 10^7$.

It can be seen from typical examples that, if the conditions for the applicability of the CRGP model are met, the last condition is satisfied "with a large safety margin".

Thus $\widetilde{\mathfrak{D}}_j^2 \simeq \mathfrak{D}_j^2 \simeq \mathfrak{D}^2$ and hence

$$\frac{\sigma_j^2}{m_j^2} \simeq \frac{\mathfrak{D}^2}{E_\nu^2} = \frac{1}{2E_\nu^2 R} \simeq \frac{1}{2\mathfrak{F}}. \tag{126}$$

Taking into account the accepted conditions of narrowness of external packets in the momentum space, $\sigma_\varkappa^2 \ll m_\varkappa^2$, it automatically follows that

$$\sigma_j^2/m_i^2 \ll 10^{-7} \quad \text{and} \quad \sigma_j^2 L^2 \ll m_i^2/\sigma_j^2,$$

the last condition is a general condition of (quasi-)stability of any wave packet.

Uncertainties of neutrino energy and momentum.

The uncertainties of the energy and momentum components of the ultrarelativistic WP in the CRGP approximation are [$\delta\mathbf{p}_\parallel \times \mathbf{p} = 0$, $\delta\mathbf{p}_\perp \cdot \mathbf{p} = 0$]

$$\delta E_\mathbf{p} \approx |\delta\mathbf{p}| \approx |\delta\mathbf{p}_\parallel| \approx \sqrt{2\ln 2}\Gamma_\mathbf{p}\sigma, \quad |\delta\mathbf{p}_\perp| \approx 2\sqrt{\ln 2}\,\sigma,$$

so that the corresponding uncertainties for the ultrarelativistic neutrino WP are

$$\delta E_j \approx |\delta\mathbf{p}_j| \approx |\delta\mathbf{p}_{j\parallel}| \approx 2\sqrt{\ln 2}\mathfrak{D}, \quad |\delta\mathbf{p}_{j\perp}| \approx 2\sqrt{2\ln 2}\,\mathfrak{D}/\Gamma_j \ll |\delta\mathbf{p}_{j\parallel}|.$$

Thus, the function $\mathfrak{D}$, which depends on the masses, momenta, and momentum spreads of the external in- and out-packets, characterizes the the neutrino energy uncertainty, and $1/\mathfrak{D}$ determines (to a numerical multiplier ~ 1) effective size of the neutrino wave packet transverse to $\mathbf{p}_j$.

A pictorial model of the wave packet of an ultrarelativistic neutrino is an extremely thin disk with the ratio of transverse to longitudinal dimensions of $\Gamma_j \gg 1$.

Note: It should be emphasized that the transverse size of the neutrino WP is not included in the expression (118) for the function (107), and hence also in the amplitude (105), so the above mentioned pictorial model is not very useful for understanding the mechanism of interference of the macrodiagrams.

Much more important is the fact that the relative uncertainty of neutrino energy and momentum

$$\delta E_j/E_j \simeq \delta P_j/P_j \sim \mathfrak{D}/E_\nu \sim 1/\sqrt{\mathfrak{F}}$$

is always very small and does not depend on the neutrino energy and mass. It is in this sense that the standard quantum-mechanical assumption that neutrino states with definite masses $|\nu_j\rangle$ (and hence states with definite flavors $|\nu_\alpha\rangle$) have definite momenta.

Like any CRGP, the neutrino WP, on average, moves along a "classical trajectory" $\overline{\mathbf{L}}_j = \mathbf{v}_j T$, quantum deviations from which, $\delta\mathbf{L}_j$, are suppressed by the factor

$$\exp\left\{-2\mathfrak{D}^2\left[(\delta\mathbf{L}_j)^2/\Gamma_j^2 + (\mathbf{L}\delta\mathbf{L}_j)^2/L^2\right]\right\}.$$

Since $\mathfrak{D}^2/\Gamma_j^2 \sim m_j^2/\mathfrak{F} \lll 1$ the transverse deviations can be macroscopically large (even infinitely large in the case of a massless neutrino), but this fact has no any effect on the magnitude of the amplitude, which depends only on small longitudinal dimensions of the neutrino WP.

Thus, we have seen that the effective WP of ultrarelativistic neutrino reproduces all properties of the generic CRGP, with the only essential caveat that the parameter σ_j depends, generally speaking, on the momenta, masses, and momentum spreads of all external packets.

Note: This dependence is by no means specific for the neutrino or for the covariant formalism, since the WP of any massive particle must depend on the momenta of the WPs involved both in its formation and, generally speaking, absorption, and our convention $\sigma_\varkappa = \text{const}$ is nothing more than an approximation adopted to simplify the theory.

18.2.2 Overlap volumes.

When analyzing measurable characteristics (such as, e.g., the count rate of neutrino events in a detector) it is helpful to use the representation for the quantities $|\mathbb{V}_s(q)|^2$ and $|\mathbb{V}_d(q)|^2$, slightly different from that which can be obtained by direct application of the the explicit formula for the overlapping integrals.

The results of this section are particularly important in that they provide a rigorous calculation of the squares of δ functions that does not use artificial constructions such as

$$\delta(p_f - p_i) = \text{Time} \times \text{Volume}.$$

Therefore, the derived formulas can be useful not only in the theory of neutrino oscillations.

It is convenient to return to the definition of these integrals and write $|\mathbb{V}_{s,d}(q)|^2$ in the following form:

$$|\mathbb{V}_{s,d}(q)|^2 = \int dx \int dy \, \exp\left[i\left(q_{s,d} \pm q\right)(x-y) - \Upsilon_{s,d}(x) - \Upsilon_{s,d}(y)\right],$$

where

$$\Upsilon_{s,d}(x) = \sum_{\varkappa \in S,D} T_{\varkappa}^{\mu\nu} \left(x_\varkappa - x\right)_\mu \left(x_\varkappa - x\right)_\nu, \quad S = I_s \oplus F_s, \quad D = I_d \oplus F_d.$$

After replacing the integration variables

$$x = x' + y'/2 \quad \text{and} \quad y = x' - y'/2$$

(with unit Jacobian) the last integral can be rewritten as

$$|\mathbb{V}_{s,d}(q)|^2 = \int dy' \exp\left[i\left(q_{s,d} \pm q\right)y' - \frac{1}{2}\Re_{s,d}^{\mu\nu} y'_\mu y'_\nu\right] \int dx' \exp\left[-2\Upsilon_{s,d}(x')\right]. \qquad (127)$$

By entering the notation

$$\delta_{s,d}(K) = \int \frac{dx}{(2\pi)^4} \exp\left(iKx - \frac{1}{2}\Re^{\mu\nu}_{s,d} x_\mu x_\nu\right) = \frac{\exp\left(-\frac{1}{2}\widetilde{\Re}^{\mu\nu}_{s,d} K_\mu K_\nu\right)}{(2\pi)^2\sqrt{|\Re_{s,d}|}} \tag{128}$$

and

$$\mathrm{V}_{s,d} = \int dx \prod_{\varkappa\in S,D} |\psi_\varkappa(\mathbf{p}_\varkappa, x_\varkappa - x)|^2 = \frac{\pi^2 \exp(-2\mathfrak{S}_{s,d})}{4\sqrt{|\Re_{s,d}|}}, \tag{129}$$

represent (127) in the following compact form:

$$\boxed{|\mathbb{V}_{s,d}(q)|^2 = (2\pi)^4 \delta_{s,d}(q \mp q_{s,d})\,\mathrm{V}_{s,d}.} \tag{130}$$

The functions $\delta_s(K)$ and $\delta_d(K)$ are of course not the same as the previously used functions $\widetilde{\delta}_s(K)$ and $\widetilde{\delta}_d(K)$, but have the same plane-wave limit (i.e., $\delta_{s,d}(K) \to \delta(K)$) and similar properties.[a]

The physical meaning and symmetry properties of the functions (129) are obvious from of the previous consideration, and their integral representation suggests that the quantities V_s and V_d can be treated as 4-dimensional overlap volumes of in- and out-packets in the source and detector. It follows from the explicit form of these functions that they take maximum values,

$$\max[\mathrm{V}_{s,d}] = \mathrm{V}^0_{s,d} = \frac{\pi^2}{4\sqrt{|\Re_{s,d}|}},$$

when the classical world lines of the packets intersect at the impact points, which corresponds to the aforementioned visual picture of colliding (in) or flying apart (out) interpenetrating cloudlets.

[a] From definitions of the functions $\widetilde{\delta}_{s,d}$ and $\delta_{s,d}$ follows the identity $\left[8\pi\widetilde{\delta}_{s,d}(K)\right]^2 = \delta_{s,d}(K)/\sqrt{|\Re_{s,d}|}$.

19 Microscopic probability.

Now, using Eq. (120) and formulas for the 4-dimensional overlapping volumes $\mathrm{V}_{s,d}$ we obtain the following expression for the microscopic probability of the process (93):

$$|\mathcal{A}_{\beta\alpha}|^2 = \frac{(2\pi)^4\delta_s(p_\nu - q_s)\mathrm{V}_s|M_s|^2}{\prod\limits_{\varkappa\in S} 2E_\varkappa \mathrm{V}_\varkappa}\ \frac{(2\pi)^4\delta_d(p_\nu + q_d)\mathrm{V}_d|M_d|^2}{\prod\limits_{\varkappa\in D} 2E_\varkappa \mathrm{V}_\varkappa}$$
$$\times \frac{\mathfrak{D}^2}{(2\pi)^3 L^2}\left|\sum_j V^*_{\alpha j} V_{\beta j}\, e^{-\Omega_j - \Theta_j}\right|^2, \qquad (131)$$

This expression depends on the coordinates $x_\varkappa$ and most probable momenta $\mathbf{p}_\varkappa$ of all WPs involved in the reaction, as well as on the parameters $\sigma_\varkappa$.

The probability (131) is vanishingly small if the product of overlap volumes V_s and V_d,

$$\mathrm{V}_s\mathrm{V}_d = \left(\frac{\pi}{2}\right)^4 |\Re_s\Re_d|^{-1/2} \exp\left[-2\left(\mathfrak{S}_s + \mathfrak{S}_d\right)\right],$$

is small, i.e., if the in- and out-packets in the source and detector vertices do not overlap in the space-time regions surrounding the impact points X_s and X_d.

Note that the 4-vector p_ν also is a function of $p_\varkappa$ and $\sigma_\varkappa$, and $p_\nu = q_s = -q_d$ in the limit $\sigma_\varkappa = 0$, $\forall\varkappa$. Therefore, at sufficiently small $\sigma_\varkappa$

$$\delta_s(p_\nu - q_s)\delta_d(p_\nu + q_d) \approx \delta_s(0)\delta_d(0) = (2\pi)^{-4}|\Re_s\Re_d|^{-1/2}.$$

Well, but what is the cause for the approximate equality of q_s and $-q_d$?

To answer the above question, let's transform the expression (131) in the way suggested by Cardall[a]. Using the explicit form of the functions $\delta_{s,d}$ and $\mathfrak{D}$, it is easy to derive the approximate relation:

$$2\sqrt{\pi}\mathfrak{D}\delta_s\left(p_\nu - q_s\right)\delta_d\left(p_\nu + q_d\right)F(p_\nu) = \int dE'_\nu \delta_s\left(p'_\nu - q_s\right)\delta_d\left(p'_\nu + q_d\right)F(p'_\nu), \tag{132}$$

in which $F(p_\nu)$ is an arbitrary slowly varying function of p_ν, and $p'_\nu = (E'_\nu, \mathbf{p}'_\nu) = E'_\nu l$ ($l = (1, \mathbf{l})$). The relation (132) is valid with the same accuracy as formula (120) for the amplitude, namely, – with the accuracy of the saddle-point method used in the derivation. With Eqs. (131) and (132) we get

$$\begin{aligned}|\mathcal{A}_{\beta\alpha}|^2 = \int dE_\nu \frac{(2\pi)^4\delta_s(p_\nu - q_s)\mathrm{V}_s|M_s|^2}{\prod\limits_{\varkappa\in S} 2E_\varkappa \mathrm{V}_\varkappa} \frac{(2\pi)^4\delta_d(p_\nu + q_d)\mathrm{V}_d|M_d|^2}{\prod\limits_{\varkappa\in D} 2E_\varkappa \mathrm{V}_\varkappa} \\ \times \frac{\mathfrak{D}}{2\sqrt{\pi}(2\pi)^3 L^2}\left|\sum_j V^*_{\alpha j} V_{\beta j}\, e^{-\Omega_j - \Theta_j}\right|^2,\end{aligned} \tag{133}$$

where the dummy integration variable E'_ν is replaced by E_ν, but now it (like the vector $\mathbf{p}_\nu = E_\nu \mathbf{l}$ and 4-vector $p_\nu = E_\nu l$, $p_\nu^2 = 0$) is no longer related to the parameters of external packets.

Within the approximations made, the formulas (131) and (133) are formally equivalent, but from Eq. (133) we see that the energy-momentum conservation is now governed by the factors $\delta_s(p_\nu - q_s)$ and $\delta_d(p_\nu + q_d)$ in the integrand, which, for sufficiently small $\sigma_\varkappa$ can be replaced by the regular δ-functions... **Not now!**

The probability (133) is the most general result. However, it is too general to be directly applied to the contemporary neutrino oscillation experiments.

[a] C. Y. Cardall, "Coherence of neutrino flavor mixing in quantum field theory," Phys. Rev. D **61** (2000) 073006, arXiv:hep-ph/9909332. We call approximation (132) the "Cardall's trick,"

19.1 Macroscopic averaging.

To obtain the observable quantities, the probability must be averaged/integrated over all the unmeasurable or unused variables of incoming/outgoing WP states.

> Such a procedure can only be realized by taking into account the conditions of a real experimental environment. For these reasons and in this sense, further analysis is model-dependent.

A thought experiment:

Assume that the statistical distributions of the incoming WPs $a \in I_{s,d}$ over the mean momenta, spin projections, and space-time coordinates in the source and detector "devices" can be described by the one-particle distribution functions $f_a(\mathbf{p}_a, s_a, x_a)$. It is convenient to normalize each function f_a to the total number, $N_a(x_a^0)$, of the packets a at a time x_a^0:

$$\sum_{s_a} \int \frac{d\mathbf{x}_a d\mathbf{p}_a}{(2\pi)^3} f_a(\mathbf{p}_a, s_a, x_a) = N_a(x_a^0) \qquad (a \in I_{s,d}).$$

For clarity purposes, we (re)define the terms "source" and "detector":

$$\mathcal{S} = \mathrm{supp}_{\{x_a;\ a \in I_s\}} \prod_a f_a(\mathbf{p}_a, s_a, x_a), \quad \mathcal{D} = \mathrm{supp}_{\{x_a;\ a \in I_d\}} \prod_a f_a(\mathbf{p}_a, s_a, x_a).$$

We'll use the same terms and notation $\mathcal{S}$ and $\mathcal{D}$ also for the corresponding devices.

Suppositions:

[1] $\mathcal{S}$ and $\mathcal{D}$ are finite and mutually disjoint within the space domain.

[2] Effective spatial dimensions of $\mathcal{S}$ and $\mathcal{D}$ are small compared to the mean distance between them but very large compared to the effective dimensions ($\sim \sigma_{\varkappa}^{-1}$) of all WPs in $\mathcal{S}$ and $\mathcal{D}$.

[3] The experiment measures only the momenta of the secondaries in $\mathcal{D}$ and (due to [2]) the background events caused by the secondaries falling into $\mathcal{D}$ from $\mathcal{S}$ can be neglected.

[4] The detection efficiency in $\mathcal{D}$ is 100%.

With these assumptions, the macroscopically averaged squared amplitude (133) represents the total number, $dN_{\alpha\beta}$, of the events recorded in $\mathcal{D}$ and consisted of the secondaries $b{\in}F_d$ having the mean momenta between $\mathbf{p}_b$ and $\mathbf{p}_b + d\mathbf{p}_b$:

$$\begin{aligned}\langle\!\langle |\mathcal{A}_{\beta\alpha}|^2 \rangle\!\rangle \equiv dN_{\alpha\beta} = &\sum_{\text{spins}} \int \prod_{a\in I_s} \frac{d\mathbf{x}_a d\mathbf{p}_a f_a(\mathbf{p}_a, s_a, x_a)}{(2\pi)^3 2E_a \mathrm{V}_a} \int \left[\prod_{b\in F_s} \frac{d\mathbf{x}_b d\mathbf{p}_b}{(2\pi)^3 2E_b \mathrm{V}_b}\right] \mathrm{V}_s \\ &\times \int \prod_{a\in I_d} \frac{d\mathbf{x}_a d\mathbf{p}_a f_a(\mathbf{p}_a, s_a, x_a)}{(2\pi)^3 2E_a \mathrm{V}_a} \int \left[\prod_{b\in F_d} \frac{d\mathbf{x}_b [d\mathbf{p}_b]}{(2\pi)^3 2E_b \mathrm{V}_b}\right] \mathrm{V}_d \\ &\times \int dE_\nu (2\pi)^4 \delta_s(p_\nu - q_s) |M_s|^2 (2\pi)^4 \delta_d(p_\nu + q_d) |M_d|^2 \\ &\times \frac{\mathfrak{D}}{2\sqrt{\pi}(2\pi)^3 L^2} \left| \sum_j V_{\alpha j}^* V_{\beta j}\, e^{-\Omega_j(T,L) - \Theta_j} \right|^2 .\end{aligned} \tag{134}$$

- ▷ $\sum_{\text{spins}}$ denotes the averaging/summation over the spin projections of the in/out states.
- ▷ Symbol $[d\mathbf{p}_b]$ indicates that integration in variable $\mathbf{p}_b$ is not performed, i.e., $\int [d\mathbf{p}_b] = d\mathbf{p}_b$.

Under additional assumptions, the unwieldy expression (134) can be simplified in a few steps.

Step 1: Multidimensional integration in WP positions.

Supposition 5: The distribution functions $f_a(\mathbf{p}_a, s_a, x_a)$, as well as the factors $e^{-\Omega_j - \Omega_i^*}/L^2$ vary at large (macroscopic) scales.

> The integrand $\prod_\varkappa |\psi_\varkappa(\mathbf{p}_\varkappa, x_\varkappa - x)|^2$ in the integral representation of the overlap volumes $\mathrm{V}_{s,d}$ defined by Eq. (129) is essentially different from zero only if the classical word lines of all packets $\varkappa$ pass through a small (though not necessarily microscopic) vicinity of the integration variable (see p. 623).

Supposition 6: The edge effects can be neglected (a harmless extension of supposition [2]).

As a result, expression (134) is reduced to the following:

$$dN_{\alpha\beta} = \sum_{\text{spins}} \int dx \int dy \int d\mathfrak{P}_s \int d\mathfrak{P}_d \int dE_\nu \frac{\mathfrak{D} \left| \sum_j V_{\alpha j}^* V_{\beta j}\, e^{-\Omega_j(T,L) - \Theta_j} \right|^2}{16\pi^{7/2} |\mathbf{y} - \mathbf{x}|^2}, \tag{135}$$

where $T = y_0 - x_0$, $L = |\mathbf{y} - \mathbf{x}|$, $dx = dx_0 d\mathbf{x}$, $dy = dy_0 d\mathbf{y}$, and we defined the differential forms

$$d\mathfrak{P}_s = \prod_{a \in I_s} \frac{d\mathbf{p}_a f_a(\mathbf{p}_a, s_a, x)}{(2\pi)^3 2E_a} \prod_{b \in F_s} \frac{d\mathbf{p}_b}{(2\pi)^3 2E_b} (2\pi)^4 \delta_s(p_\nu - q_s) |M_s|^2, \tag{136a}$$

$$d\mathfrak{P}_d = \prod_{a \in I_d} \frac{d\mathbf{p}_a f_a(\mathbf{p}_a, s_a, y)}{(2\pi)^3 2E_a} \prod_{b \in F_d} \frac{[d\mathbf{p}_b]}{(2\pi)^3 2E_b} (2\pi)^4 \delta_d(p_\nu + q_d) |M_d|^2. \tag{136b}$$

Step 2: Integration in time variables.

Supposition 7: During the experiment, the distribution functions f_a in $\mathcal{S}$ and $\mathcal{D}$ vary slowly enough with time so that they can be modelled by the "rectangular ledges"

$$\begin{aligned} f_a(\mathbf{p}_a, s_a; x) &= \theta\left(x^0 - x_1^0\right)\theta\left(x_2^0 - x^0\right)\overline{f}_a(\mathbf{p}_a, s_a; \mathbf{x}) \ \text{ for } \ a\in I_s, \\ f_a(\mathbf{p}_a, s_a; y) &= \theta\left(y^0 - y_1^0\right)\theta\left(y_2^0 - y^0\right)\overline{f}_a(\mathbf{p}_a, s_a; \mathbf{y}) \ \text{ for } \ a\in I_d. \end{aligned} \tag{137}$$

Supposition 8: The time intervals needed to switch on and switch off the source and detector are negligibly small in comparison with periods of stationarity $\tau_s = x_2^0 - x_1^0$ and $\tau_d = y_2^0 - y_1^0$.

> In case of detector, the step functions in (137) can be thought as the "hardware" or "software" trigger conditions. The periods of stationarity τ_s and τ_d can be astronomically long, as it is for the solar and atmospheric neutrino experiments ($\tau_s \ggg \tau_d$ in these cases), or very short, like in the experiments with short-pulsed accelerator beams (when usually $\tau_s \lesssim \tau_d$).

Within the model (137), the only time-dependent factor in the integrand of (135) is $e^{-\Omega_j - \Omega_i^*}$. So the problem is reduced to the (comparatively) simple integral

$$\int_{y_1^0}^{y_2^0} dy^0 \int_{x_1^0}^{x_2^0} dx^0 \; e^{-\Omega_j(y^0-x^0,L)-\Omega_i^*(y^0-x^0,L)} = \frac{\sqrt{\pi}}{2\mathfrak{D}}\tau_d \exp\left(i\varphi_{ij} - \mathscr{A}_{ij}^2\right) S_{ij}. \tag{138}$$

In relation (138) we have adopted the following notation:

$$S_{ij} = \frac{\exp\left(-\mathscr{B}_{ij}^2\right)}{4\tau_d \mathfrak{D}} \sum_{l,l'=1}^{2} (-1)^{l+l'+1} \mathsf{Ierf}\left[2\mathfrak{D}\left(x_l^0 - y_{l'}^0 + \frac{L}{v_{ij}}\right) - i\mathscr{B}_{ij}\right], \tag{139}$$

$$\mathscr{A}_{ij} = (v_j - v_i)\mathfrak{D}L = \frac{2\pi\mathfrak{D}L}{E_\nu L_{ij}}, \qquad \mathscr{B}_{ij} = \frac{\Delta E_{ji}}{4\mathfrak{D}} = \frac{\pi\mathfrak{n}}{2\mathfrak{D}L_{ij}}, \tag{140}$$

$$\varphi_{ij} = \frac{2\pi L}{L_{ij}}, \qquad L_{ij} = \frac{4\pi E_\nu}{\Delta m_{ij}^2}, \qquad \frac{1}{v_{ij}} = \frac{1}{2}\left(\frac{1}{v_i} + \frac{1}{v_j}\right),$$

$$\Delta m_{ij}^2 = m_i^2 - m_j^2, \qquad \Delta E_{ij} = E_i - E_j,$$

$$\mathsf{Ierf}(z) = \int_0^z dz' \mathsf{erf}(z') + \frac{1}{\sqrt{\pi}} = z\,\mathsf{erf}(z) + \frac{1}{\sqrt{\pi}} e^{-z^2},$$

and $\mathsf{erf}(z)$ is the Gauss error function (see Appendix L, p. 922).

For a more realistic description of the beam pulse experiments, the model (137) could be readily extended by inclusion of a series of rectangular ledges followed by pauses during which $f_a = 0$.

Then substituting (138) into (135) we obtain:

$$dN_{\alpha\beta} = \tau_d \sum_{\text{spins}} \int d\mathbf{x} \int d\mathbf{y} \int d\mathfrak{P}_s \int d\mathfrak{P}_d \int dE_\nu \frac{\mathcal{P}_{\alpha\beta}(E_\nu, |\mathbf{y}-\mathbf{x}|)}{4(2\pi)^3 |\mathbf{y}-\mathbf{x}|^2}, \tag{141a}$$

$$\equiv \frac{\tau_d}{V_\mathcal{D} V_\mathcal{S}} \int d\mathbf{x} \int d\mathbf{y} \int d\Phi_\nu \int d\sigma_{\nu\mathcal{D}} \mathcal{P}_{\alpha\beta}(E_\nu, |\mathbf{y}-\mathbf{x}|). \tag{141b}$$

The differential forms $d\mathfrak{P}_{s,d}$ in (141a) are are given by Eq. (136) after substitution $f_a \longmapsto \overline{f}_a$.

Important formulas used above.

• Let $F(x)$ (where $x=(x_0,\mathbf{x})$) be a function that slowly evolves in the volume of the source or detector array during its operation. Then

$$\int\left(\prod_{\varkappa'\in S,D}\frac{d\mathbf{x}_{\varkappa'}}{\mathrm{V}_{\varkappa'}\left(\mathbf{p}_{\varkappa'}\right)}\right)\mathrm{V}_{s,d}\left(\{\mathbf{p}_{\varkappa},x_{\varkappa}\}\right)F\left(X_{s,d}\left(\{\mathbf{p}_{\varkappa'},x_{\varkappa'}\}\right)\right)$$

$$=\int\left(\prod_{\varkappa'\in S,D}\frac{d\mathbf{x}_{\varkappa'}}{\mathrm{V}_{\varkappa'}\left(\mathbf{p}_{\varkappa'}\right)}\right)\int dx\prod_{\varkappa\in S,D}\left|\psi_{\varkappa}\left(\mathbf{p}_{\varkappa},x_{\varkappa}-x\right)\right|^2F\left(X_{s,d}\left(\{\mathbf{p}_{\varkappa'},x_{\varkappa'}\}\right)\right)$$

$$\simeq\int dxF\left(x\right)\int\left(\prod_{\varkappa'\in S,D}\frac{d\mathbf{x}_{\varkappa'}}{\mathrm{V}_{\varkappa'}\left(\mathbf{p}_{\varkappa'}\right)}\right)\prod_{\varkappa\in S,D}\left|\psi_{\varkappa}\left(\mathbf{p}_{\varkappa},x_{\varkappa}-x\right)\right|^2$$

$$=\int dxF\left(x\right)\prod_{\varkappa\in S,D}\frac{1}{\mathrm{V}_{\varkappa}\left(\mathbf{p}_{\varkappa}\right)}\int d\mathbf{x}_{\varkappa}\left|\psi_{\varkappa}\left(\mathbf{p}_{\varkappa},x_{\varkappa}-x\right)\right|^2=\int dxF\left(x\right).$$

Here we used the definitions of the volumes $\mathrm{V}_{\varkappa}\left(\mathbf{p}_{\varkappa}\right)$ and $\mathrm{V}_{s,d}\left(\{\mathbf{p}_{\varkappa},x_{\varkappa}\}\right)$, and the invariance of the impact points $X_{s,d}=X_{s,d}\left(\{\mathbf{p}_{\varkappa},x_{\varkappa}\}\right)$ with respect to the group of uniform rectilinear motions.

• Generic formula for the double Gaussian integral:

$$\int_{x_1^0}^{x_2^0}dx_0\int_{y_1^0}^{y_2^0}dy_0\exp\left[-a^2\left(y_0-x_0\right)^2-b\left(y_0-x_0\right)\right]=\frac{\sqrt{\pi}}{2a^2}\exp\left(\frac{b^2}{4a^2}\right)\sum_{l,l'=1}^{2}\left(-1\right)^{l+l'+1}$$
$$\times\mathsf{Ierf}\left[a\left(x_l^0-y_{l'}^0\right)-\frac{b}{2a}\right].$$

Explanation of the factors in Eq. (141b).

- $V_{\mathcal{S}}$ and $V_{\mathcal{D}}$ are the spatial volumes of the source and detector, respectively.
- The differential form $d\Phi_\nu$ is defined in such a way that the integral

$$\frac{d\mathbf{x}}{V_{\mathcal{S}}} \int \frac{d\Phi_\nu}{dE_\nu} = d\mathbf{x} \sum_{\text{spins} \in S} \int \frac{d\mathfrak{P}_s E_\nu}{2(2\pi)^3 |\mathbf{y}-\mathbf{x}|^2} \tag{142}$$

is the flux density of neutrinos in $\mathcal{D}$, produced through the processes $I_s \to F'_s \ell^+_\alpha \nu$ in $\mathcal{S}$.

> More precisely, it is the number of neutrinos appearing per unit time and unit neutrino energy in an elementary volume $d\mathbf{x}$ around the point $\mathbf{x} \in \mathcal{S}$, travelling within the solid angle $d\boldsymbol{\Omega}_\nu$ about the flow direction $\mathbf{l} = (\mathbf{y}-\mathbf{x})/|\mathbf{y}-\mathbf{x}|$ and crossing a unit area, placed around the point $\mathbf{y} \in \mathcal{D}$ and normal to $\mathbf{l}$.

- The differential form $d\sigma_{\nu\mathcal{D}}$ is defined in such a way that

$$\frac{1}{V_{\mathcal{D}}} \int d\mathbf{y} d\sigma_{\nu\mathcal{D}} = \sum_{\text{spins} \in D} \int \frac{d\mathbf{y} d\mathfrak{P}_d}{2E_\nu} \tag{143}$$

represents the differential cross section of the neutrino scattering off the detector as a whole.

> In the particular (and the most basically important) case of neutrino scattering in the reaction $\nu a \to F'_d \ell^-_\beta$, provided that the momentum distribution of the target scatterers a is sufficiently narrow, the differential form $d\sigma_{\nu\mathcal{D}}$ becomes exactly the elementary differential cross section of this reaction multiplied by the total number of the particles a in $\mathcal{D}$.

▷ Now let us address the last sub-integral multiplier of (141b), given by

$$\mathcal{P}_{\alpha\beta}(E_\nu, L) = \sum_{ij} V^*_{\alpha i} V_{\alpha j} V_{\beta i} V^*_{\beta j} S_{ij} \exp\left(i\varphi_{ij} - \mathscr{A}^2_{ij} - \Theta_{ij}\right), \tag{144}$$

$$\Theta_{ij} = \Theta_i + \Theta_j, \tag{145}$$

$$\Theta_j = \frac{m_j^2}{2\mathfrak{D}^2}\left[(\mathfrak{n}_0 - \mathfrak{n}) + \frac{1}{2}\left(\mathfrak{m} - \mathfrak{n} - \mathfrak{n}^2\right) r_j + \left(\mathfrak{n} + \frac{1}{2}\right)\left(\mathfrak{m} - \mathfrak{n} - \mathfrak{n}^2\right) r_j^2 + \mathcal{O}(r_j^3)\right]. \tag{146}$$

Let's remind that the function $\mathfrak{n}_0$ coincides with $\mathfrak{n}$ in the case of exact energy-momentum conservation in the vertices of our diagram. Therefore in the vicinity of the maximum of the product $\widetilde{\delta}_s(p_\nu - q_s)\widetilde{\delta}_d(p_\nu + q_d)$ (that is at $q_s \approx -q_d \approx p_\nu$), which gives the main contribution into the event rate, one can neglect the alternating quantity $\mathfrak{n}_0 - \mathfrak{n}$ in (146). Taking into account the properties of the function $\mathfrak{n}$ one can also neglect the $\mathcal{O}(r_j^2)$ contributions in (146). In this approximation

$$\Theta_j \approx \frac{m_j^4 R\left(\mathfrak{m} - \mathfrak{n} - \mathfrak{n}^2\right)}{4E_\nu^2} \approx \frac{m_j^4 R\left(\mathfrak{m} - \mathfrak{n}_0 - \mathfrak{n}_0^2\right)}{4E_\nu^2} = \frac{m_j^4\left[R_{00}\mathscr{R} - (\mathbf{Rl})^2\right]}{4RE_\nu^2} \geq 0.$$

• The factor (144) coincides with the QM expression for the neutrino flavor transition probability,

$$\mathcal{P}^{(\mathsf{QM})}_{\alpha\beta}(E_\nu, L) = \sum_{ij} V_{\alpha i} V_{\beta j} V^*_{\alpha j} V^*_{\beta i} \exp\left(i\varphi_{ij}\right). \tag{147}$$

provided that $S_{ij} = 1$, $\Theta_{ij} = 0$, and $\mathscr{A}_{ij} = 0$. So it can be considered as a QFT refinement of the QM result.

BUT!

• A probabilistic interpretation of the function $\mathcal{P}_{\alpha\beta}$ can be only provisionally true, because the factors S_{ij} and $\mathscr{A}_{ij}$ involve the functions $\mathfrak{D}$, $\mathfrak{n}$, and $\mathfrak{m}$ strongly dependent on the neutrino energy E_ν and external momenta $\mathbf{p}_\varkappa$; all these (except for the momenta of secondaries in $\mathcal{D}$) are variables of integration in (141b).

As a result, the factor $\mathcal{P}_{\alpha\beta}$, as function of α and β, does not satisfy the unitarity relations

$$\sum_\alpha \mathcal{P}^{(\mathsf{QM})}_{\alpha\beta} = \sum_\beta \mathcal{P}^{(\mathsf{QM})}_{\alpha\beta} = 1,$$

which are a commonplace in the QM theory of neutrino oscillations.

The point is that the domains and shapes of the functions $\mathfrak{D}$, $\mathfrak{n}$, and $\mathfrak{m}$ are essentially different for each of the nine leptonic pairs $(\ell_\alpha, \ell_\beta)$. These differences are governed by kinematics of the subprocesses in $\mathcal{S}$ and $\mathcal{D}$ (in particular, their thresholds), that is, eventually, by the leptonic masses (m_e, m_μ, m_τ) and by the momentum spreads (σ_e, σ_μ, σ_τ) of the leptonic WPs, which are not necessarily equal to each other, perhaps even within an order of magnitude.

Thus $\mathcal{P}_{\alpha\beta}(E_\nu, L)$ is not the flavor transition probability!

Not surprising, since there is really no transition of ν_α to ν_β. So what is this?

The function $\mathcal{P}_{\alpha\beta}(E_\nu, L)$ is a quantity characterizing the probability of producing lepton ℓ_β in the detector, provided the lepton ℓ_α is produced in the source.

With this definition (albeit not mathematically rigorous) in mind, we'll call it the "probability factor", and, in addition, we'll use the term "flavor transition probability" with an idea of what is really meant.

Two more drawbacks.

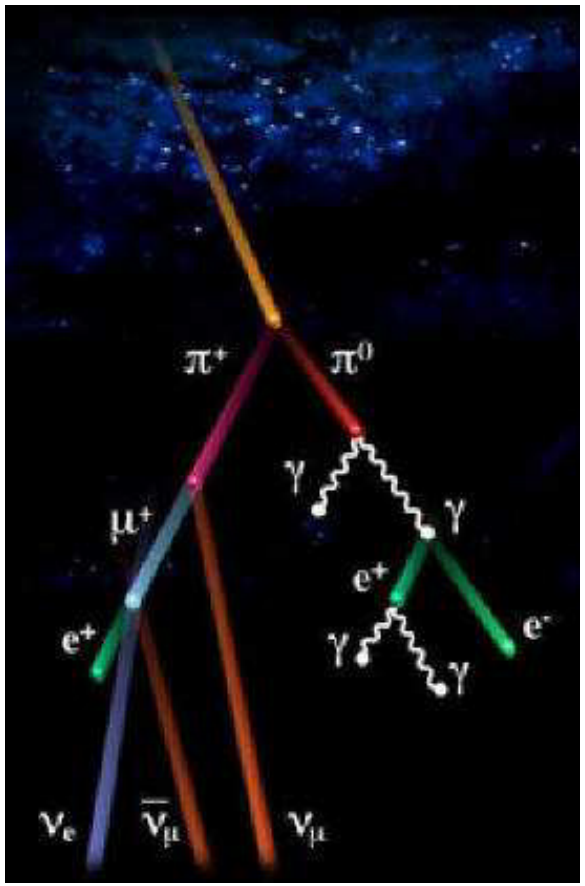

- The probabilistic treatment of $\mathcal{P}_{\alpha\beta}$ is even more problematic in real-life experiments, because the detector event rate (with ℓ_β appearance in our case) is defined by many subprocesses of different types in the source and detector.

  E.g., in the astrophysical, atmospheric and accelerator neutrino experiments, the major processes of neutrino production are in-flight decays of light mesons ($\pi_{\mu 2}$, $K_{\mu 2}$, $K_{\mu 3}$, K_{e3}, etc.) and muons, and neutrino interactions with a detector medium consist of an incoherent superposition of exclusive reactions of many types, – from (quasi)elastic to deep-inelastic.

- A "technical" difficulty is the dependence of the function S_{ij} (which will be referred to as decoherence or sometimes instrumental function) on the four "instrumental" or "experimental" time parameters x_1^0, x_2^0, y_1^0, y_2^0.

So far we have made no assumption concerning a "synchronization" of the time windows (x_1^0, x_2^0) and (y_1^0, y_2^0). Thus, it is no wonder that the decoherence factor turns to be vanishingly small in magnitude if these windows are not adjusted to account that the representative time of ultrarelativistic neutrino propagation from $\mathcal{S}$ to $\mathcal{D}$ is equal to the mean distance, $\overline{L}$, between $\mathcal{S}$ and $\mathcal{D}$.

Before discussing the role of the decoherence (instrumental) function, we perform one more, and the last, simplification of the formula for $dN_{\alpha\beta}$.

Step 3: Spatial averaging.

We'll use again the requirement that the characteristic dimensions of $\mathcal{S}$ and $\mathcal{D}$ are small compared to $\overline{L}$. Under certain conditions, this allows us to replace approximately

$$|\mathbf{y}-\mathbf{x}| \longmapsto \overline{L} = \frac{1}{2\Omega_s}\int_{\Omega_s} d\mathbf{\Omega}\left(L^F_{\mathbf{\Omega}} + L^N_{\mathbf{\Omega}}\right),$$

$$d\Phi_\nu \longmapsto d\overline{\Phi}_\nu,$$

$$d\sigma_{\nu\mathcal{D}} \longmapsto d\overline{\sigma}_{\nu\mathcal{D}}.$$

The range of applicability of this approximation is in general much more limited than that of (141b), as a consequence of additional restrictions implicitly imposed on the distribution functions $\overline{f}_a$, absolute dimensions and geometry of $\mathcal{S}$ and $\mathcal{D}$. These issues are bit more complicated then the considered above and must be the subject of special attention in the neutrino oscillation experiments.

Finally, we arrive at the very simple but rather rough expression:

$$dN_{\alpha\beta} = \tau_d \int d\overline{\Phi}_\nu \int d\overline{\sigma}_{\nu\mathcal{D}}\mathcal{P}_{\alpha\beta}(E_\nu, \overline{L}).$$

In particular, it is not applicable to the very short base-line experiments.

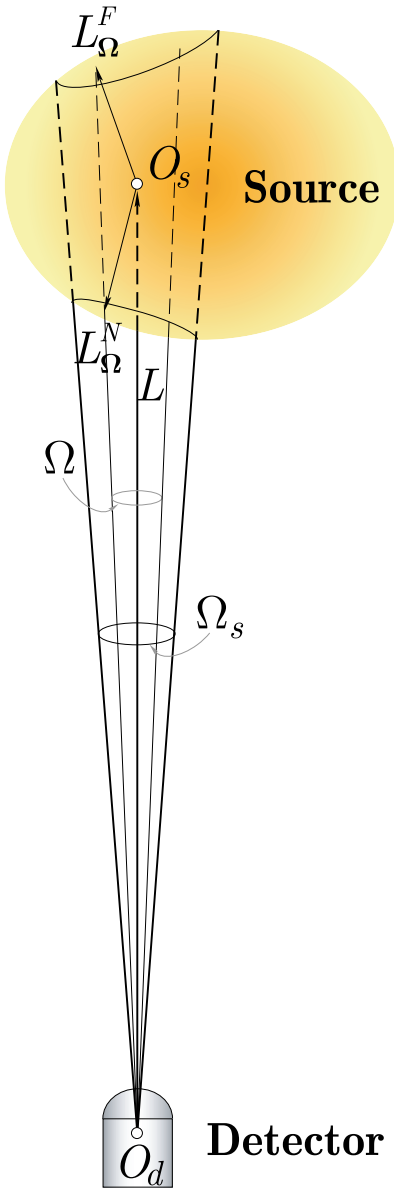

19.2 Synchronized measurements.

Let us now return to the decoherence factor, limiting ourselves to a consideration of "synchronized" measurements, in which

$$x^0_{1,2} = \mp\frac{\tau_s}{2}, \quad y^0_{1,2} = \overline{L} \mp \frac{\tau_d}{2}.$$

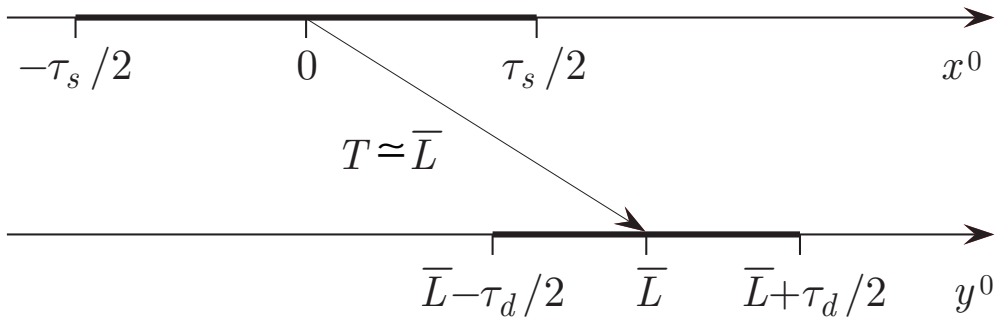

With certain technical simplifications, the factor (139) can be expressed through a real-valued function $S(t,t',b)$ of three dimensionless variables, namely:

$$S_{ij} = S\left(\mathfrak{D}\tau_s, \mathfrak{D}\tau_d, \mathscr{B}_{ij}\right),$$

$$2t'\,S(t,t',b) = \exp\left(-b^2\right)\mathrm{Re}\left[\mathsf{lerf}\left(t+t'+ib\right) - \mathsf{lerf}\left(t-t'+ib\right)\right].$$

19.2.1 Diagonal decoherence function.

$$S(t,t',0) = \frac{1}{2t'}\left[\mathsf{lerf}\left(t+t'\right) - \mathsf{lerf}\left(t-t'\right)\right] \equiv S_0(t,t'), \tag{148}$$

This function corresponds to the noninterference (neutrino mass independent) decoherence factors S_{ii}. The following inequalities can be proved:

$$0 < S_0(t,t') < 1, \quad S_0(t,t') < t/t' \ \text{ for } \ t' \geq t, \quad S_0(t+\delta t, t) > \mathsf{erf}(\delta t) \ \text{ for } \ \delta t > 0.$$

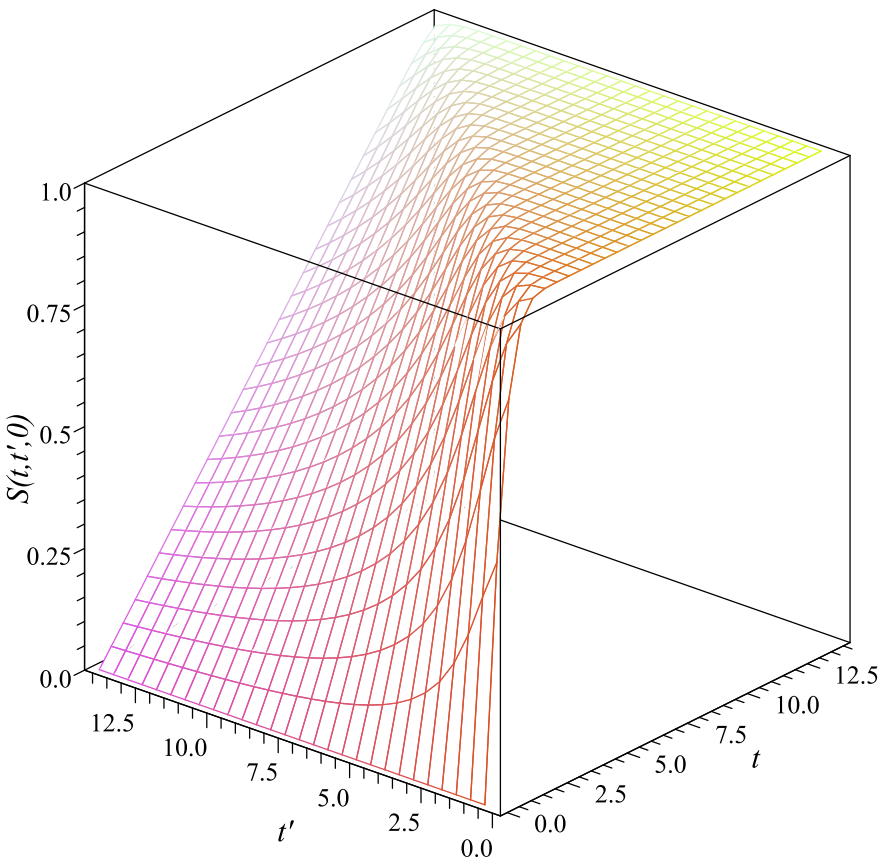

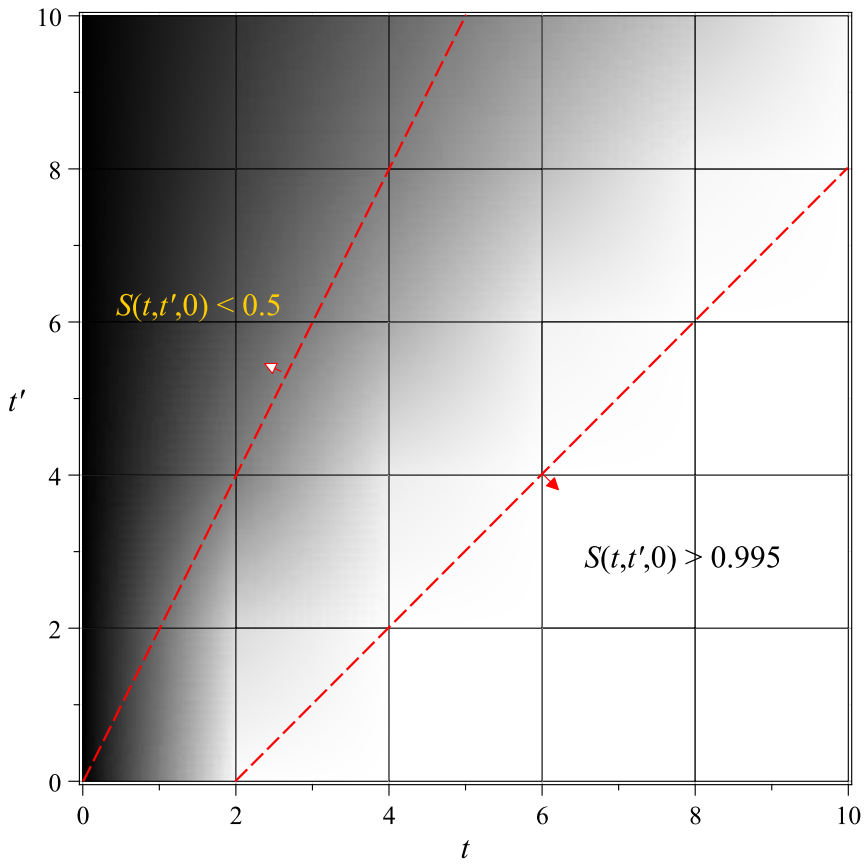

The strong dependence of the common "diagonal" (independent of i and j) suppression factor $S_0(t,t')$ on its arguments t and t' at $t \lesssim t'$ provides a potential possibility of an experimental estimation of the function $\mathfrak{D}$ (or, rather, of its mean values within the phase spaces), based on the measuring the count rate $dR_{\alpha\beta} = dN_{\alpha\beta}/\tau_d$ as a function of the detector exposure time τ_d and the source operating time τ_s (at fixed $\overline{L}$) and comparing the data with the results of a numerical (e.g., Monte-Carlo) simulation.

The optimal strategy of such an experiment should be a subject of a dedicated analysis.

For the important special case, $t' = t$ (representative, in particular, for the experiments with accelerator neutrino beams), we find

$$S_0(t,t) = \mathrm{erf}(2t) - \frac{1-e^{-4t^2}}{2\sqrt{\pi}t} \approx \begin{cases} \dfrac{2t}{\sqrt{\pi}}\left(1 - \dfrac{2t^2}{3} + \dfrac{8t^4}{15}\right) & \text{for } t \ll 1, \\ 1 - \dfrac{1}{2\sqrt{\pi}t} & \text{for } t \gg 1. \end{cases} \tag{149}$$

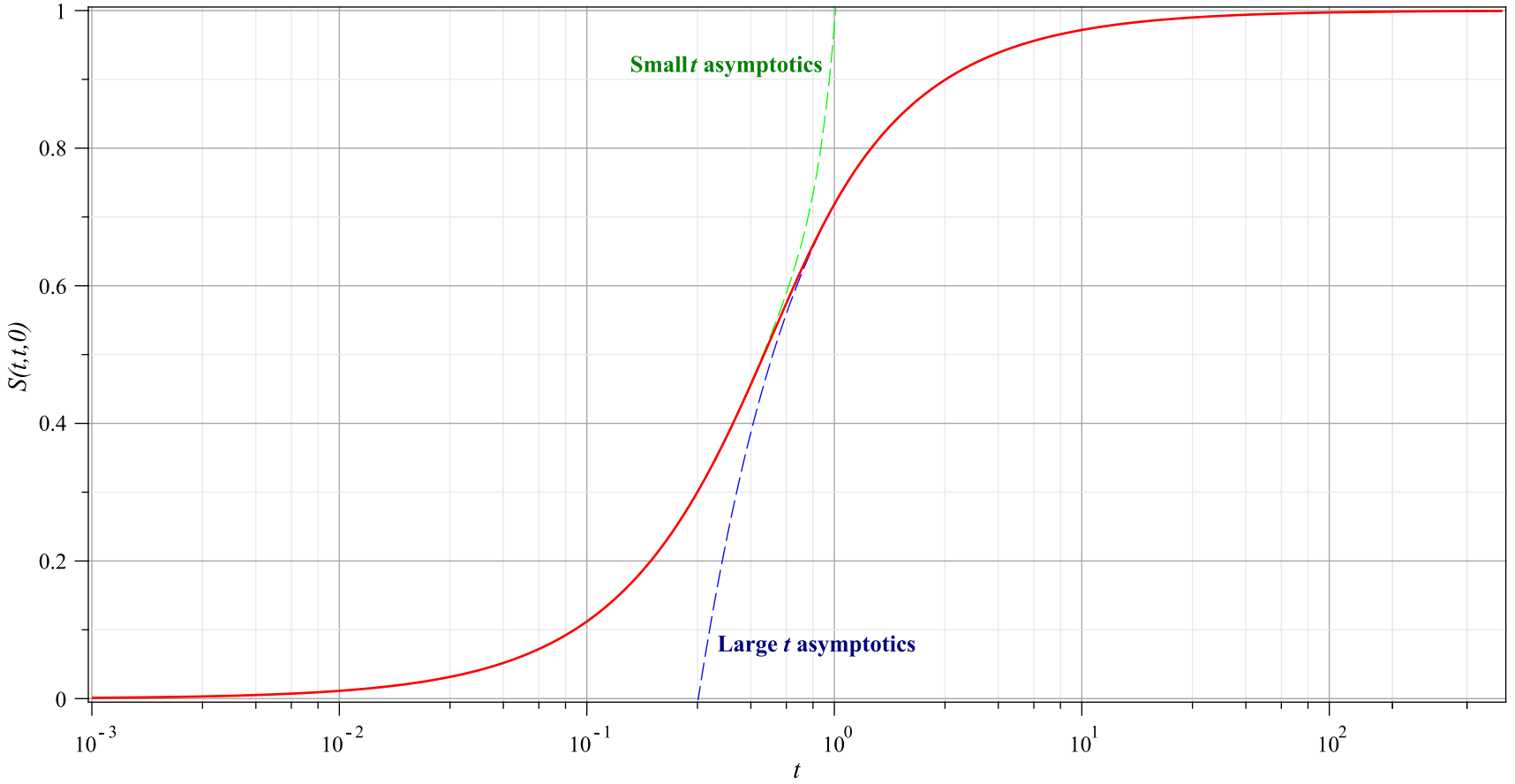

19.2.2 Nondiagonal decoherence function.

The decoherence function $S(t,t',b)$ at $b \neq 0$ is much more involved.

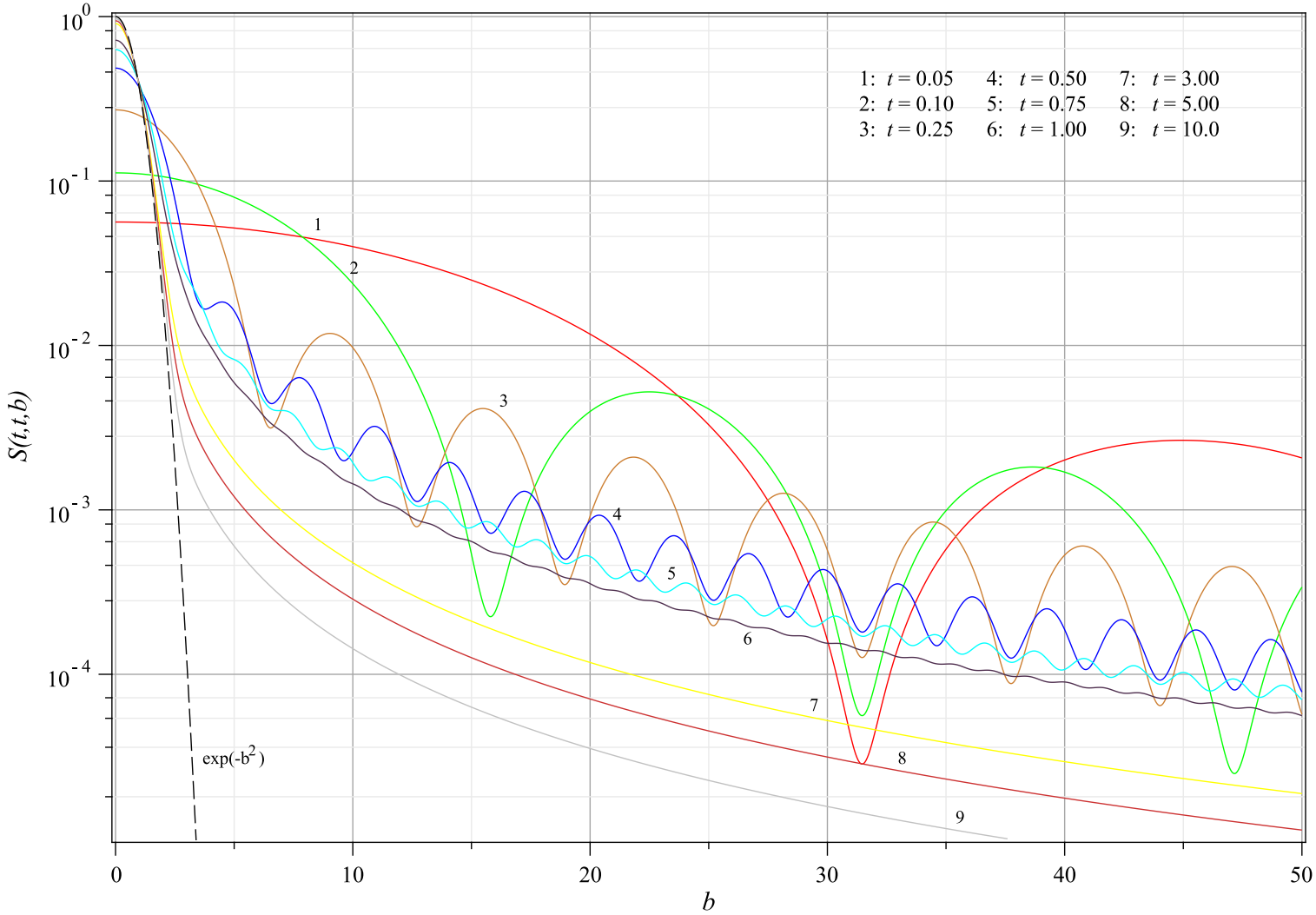

At very large t, the function $S(t,t,b)$ becomes nearly independent on t, slowly approaching the asymptotic behavior $S(t,t,b) \sim \exp(-b^2)$ $(t,t' \to \infty)$.

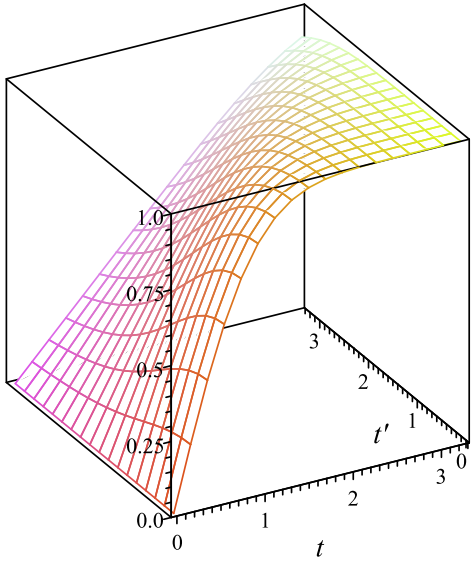

$S(t, t', 0.1)$.

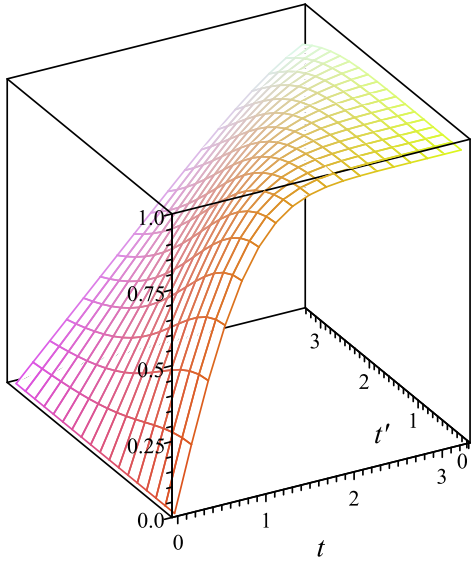

$S(t, t', 0.2)$.

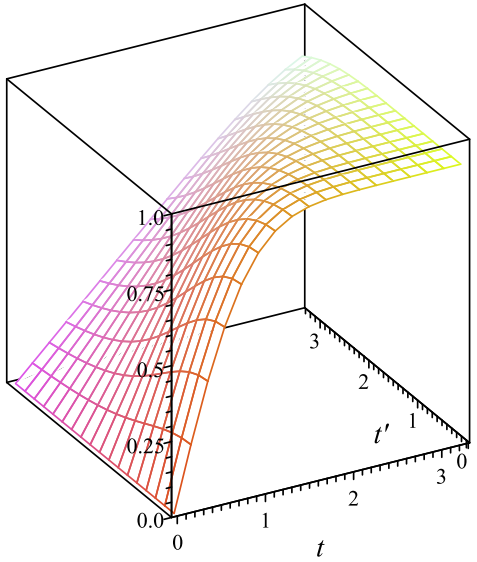

$S(t, t', 0.3)$.

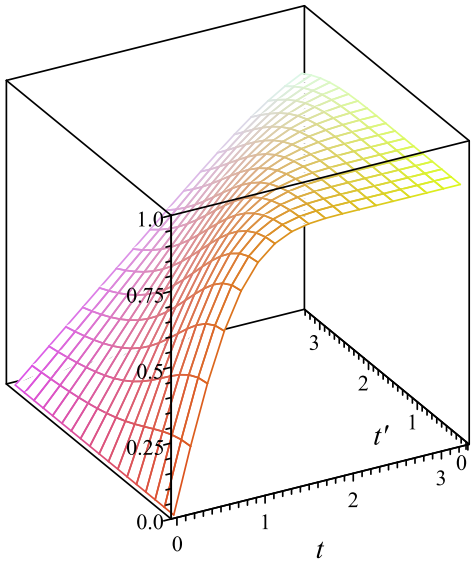

$S(t, t', 0.4)$.

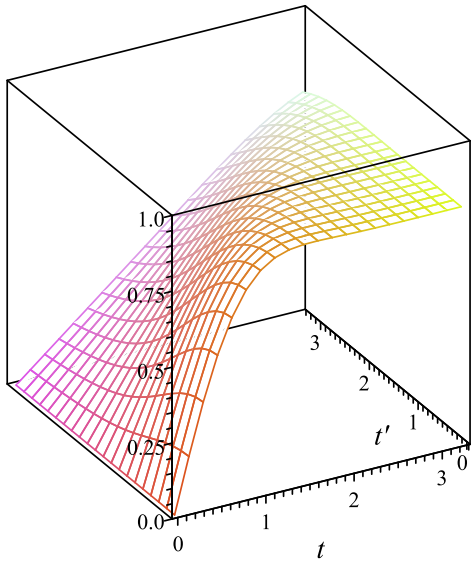

$S(t, t', 0.5)$.

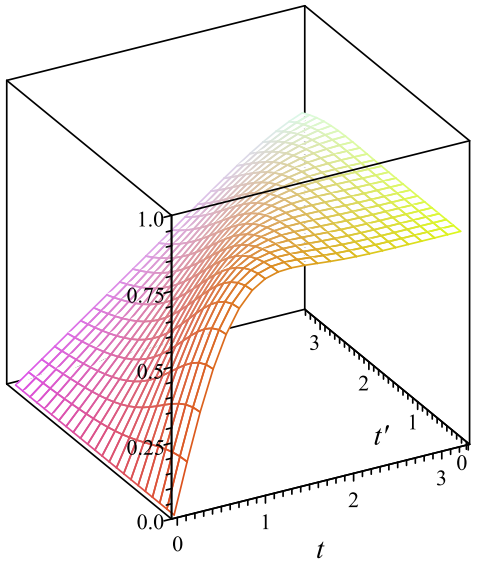

$S(t, t', 0.6)$.

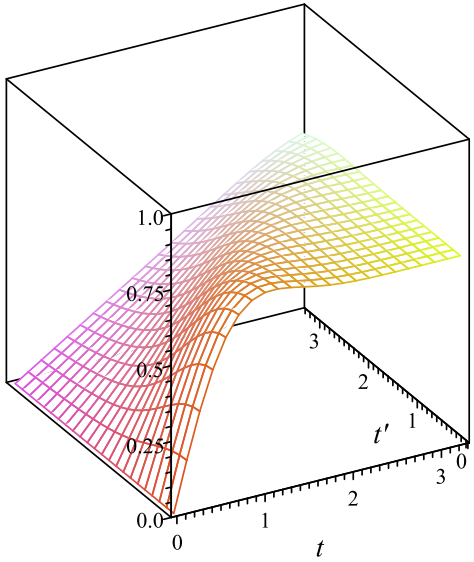

$S(t, t', 0.7)$.

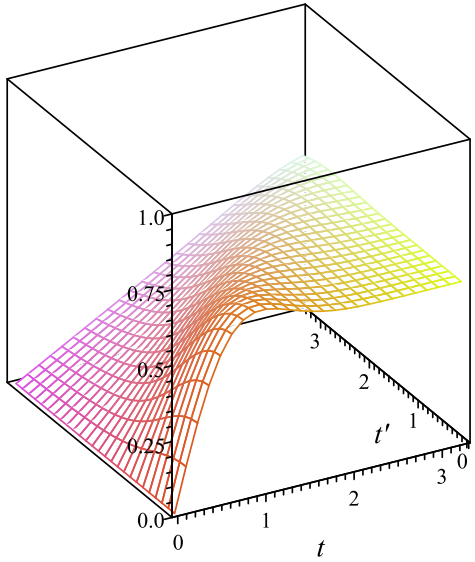

$S(t, t', 0.8)$.

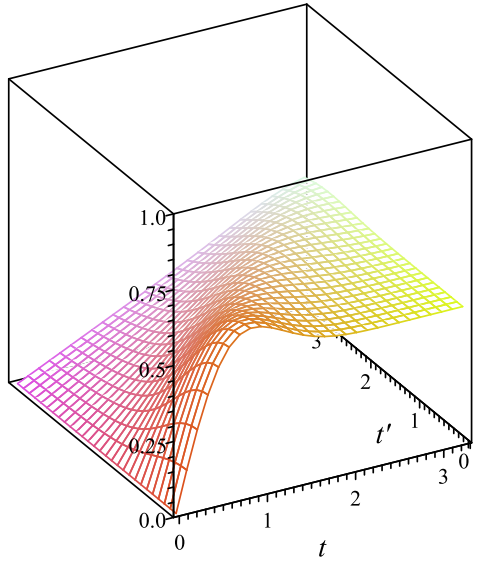

$S(t, t', 0.9)$.

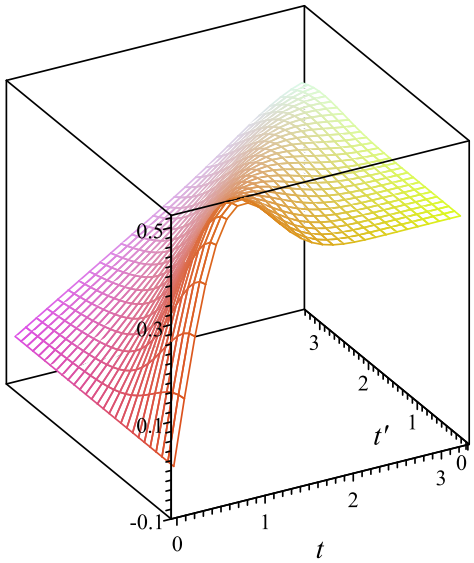

$S(t, t', 1.0)$.

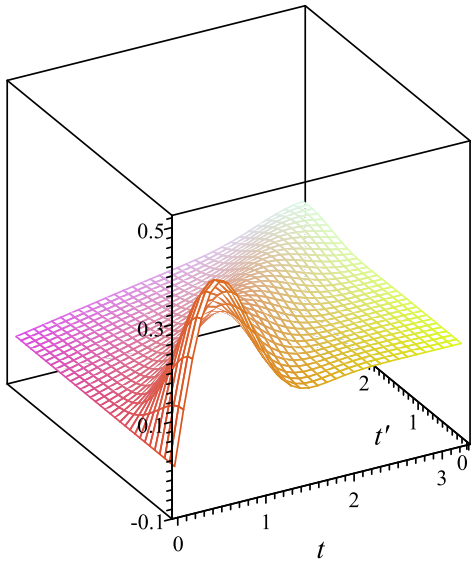

$S(t, t', 1.5)$.

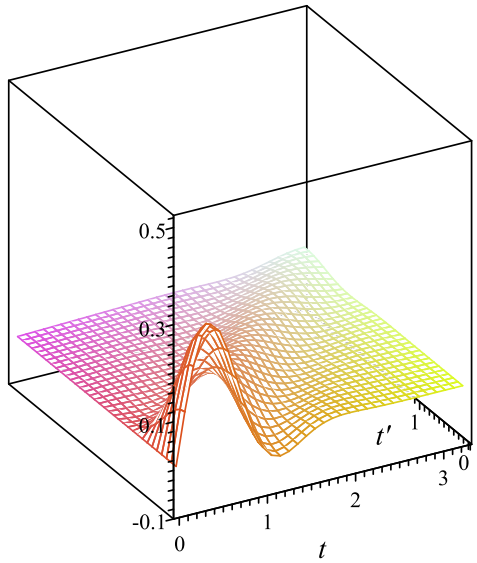

$S(t, t', 2.0)$.

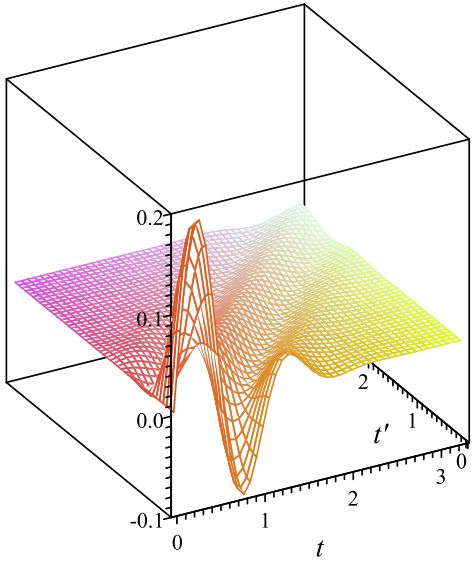

$S(t, t', 3.0)$.

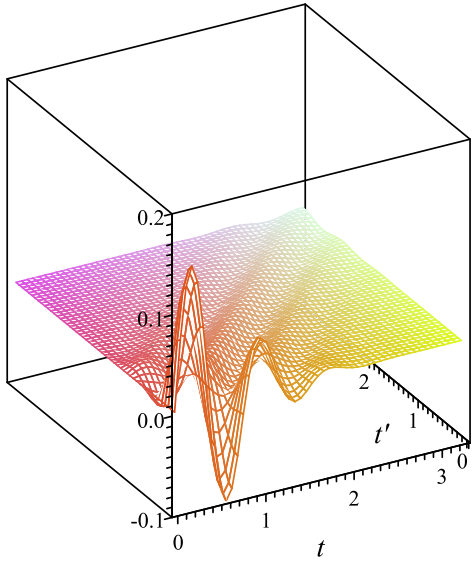

$S(t, t', 4.0)$.

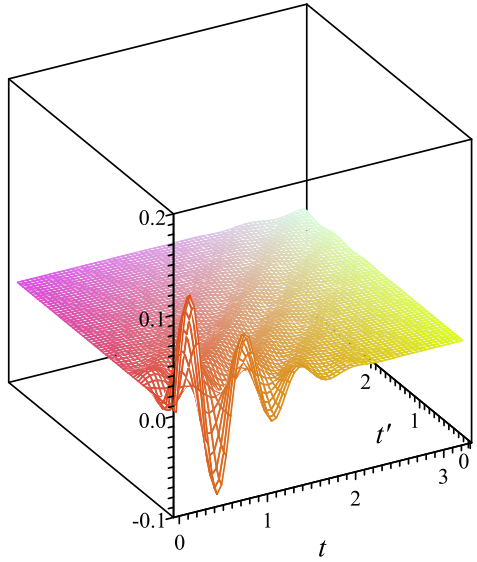

$S(t, t', 5.0)$.

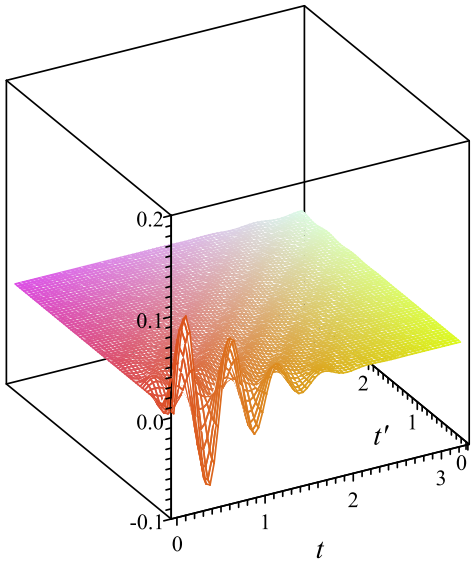

$S(t, t', 6.0)$.

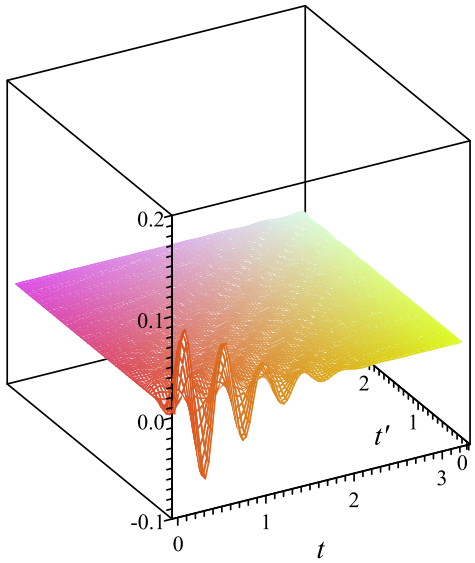

$S(t, t', 7.0)$.

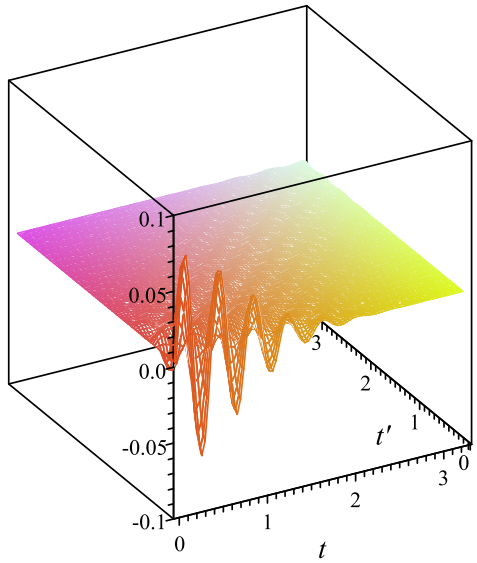

$S(t, t', 8.0)$.

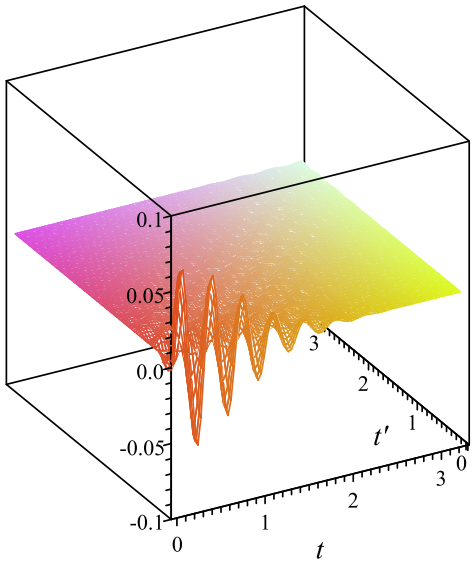

$S(t, t', 9.0)$.

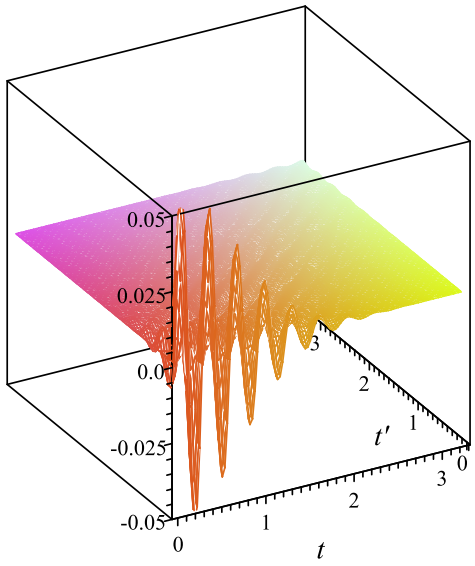

$S(t, t', 10.0)$.

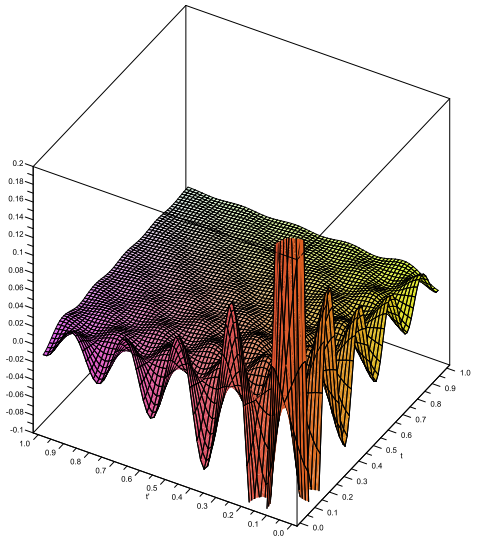

$S(t, t', 15.0)/S_0(t, t')$.

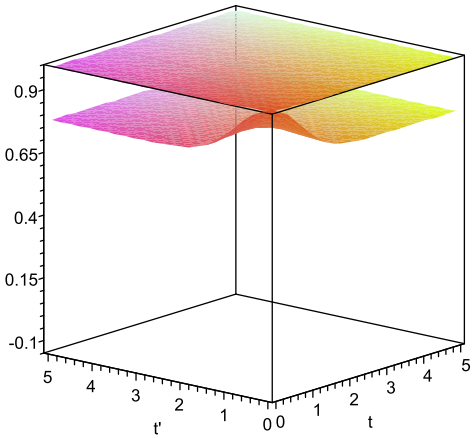

$S(t, t', 0.10)/S_0(t, t')$,
$S(t, t', 0.50)/S_0(t, t')$.

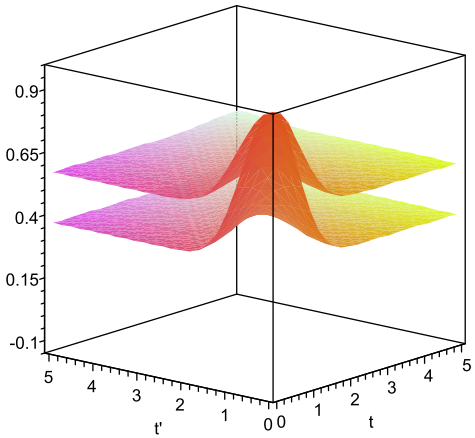

$S(t, t', 0.75)/S_0(t, t')$,
$S(t, t', 1.00)/S_0(t, t')$.

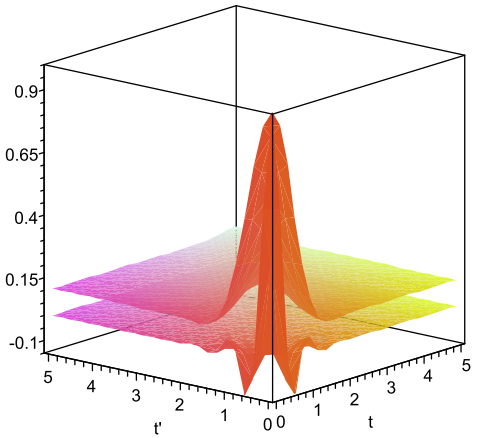

$S(t, t', 1.50)/S_0(t, t')$,
$S(t, t', 4.00)/S_0(t, t')$.

19.2.3 Flavor transitions in the asymptotic regime.

In the asymptotic regime,

$$S(t,t',b) \sim \exp(-b^2) \quad (t,t' \to \infty).$$

the probability factor (144) takes on the form already known from the literature,[a]

$$\boxed{\mathcal{P}_{\alpha\beta}(E_\nu,\overline{L}) = \sum_{ij} V^*_{\alpha i} V_{\alpha j} V_{\beta i} V^*_{\beta j} \exp\left(i\varphi_{ij} - \mathscr{A}^2_{ij} - \mathscr{B}^2_{ij} - \Theta_{ij}\right),} \tag{150}$$

but with the essential difference that the factors $\mathscr{A}_{ij}$, $\mathscr{B}_{ij}$ and Θ_{ij} do depend (through the functions $\mathfrak{D}$, $\mathfrak{n}$, and $\mathfrak{m}$) on the neutrino energy and momenta of the external WPs.

This dependence drastically affects the magnitude and shape of these factors if at least some of the WPs have relativistic momenta (that is always the case in the contemporary neutrino oscillation experiments). For sufficiently small and/or hierarchically different momentum spreads $\sigma_{\varkappa}$, the functions $\mathscr{A}_{ij}$ and $\mathscr{B}_{ij}$ may vary in many orders of magnitude through their multidimensional domain.

[a] See, e.g., C. Giunti & C. W. Kim, "Fundamentals of Neutrino Physics and Astrophysics" (Oxford University Press Inc., New York, 2007); M. Beuthe, "Oscillations of neutrinos and mesons in quantum field theory," Phys. Rept. **375** (2003) 105–218, hep-ph/0109119; M. Beuthe, "Towards a unique formula for neutrino oscillations in vacuum," Phys. Rev. D **66** (2002) 013003, hep-ph/0202068.

19.2.4 Major properties of the transition "probability".

- The factors $\exp\left(-\mathscr{A}_{ij}^2\right)$ (with $i{\neq}j$) suppress the interference terms at the distances exceeding the "coherence length"

$$L_{ij}^{\rm coh} = \frac{1}{\Delta v_{ij}\mathfrak{D}} \gg |L_{ij}| \qquad (\Delta v_{ij} = |v_j - v_i|),$$

  when the νWPs $\psi_{X_d}^i(\mathbf{p}_i, X_s - X_d)$ and $\psi_{X_d}^j(\mathbf{p}_j, X_s - X_d)$ are strongly separated in space and do not interfere anymore. Clearly $L_{ij}^{\rm coh} \to \infty$ in the plane-wave limit.

- The suppression factors $\exp\left(-\mathscr{B}_{ij}^2\right)$ ($i{\neq}j$) work in the opposite situation, when the external packets in $\mathcal{S}$ or $\mathcal{D}$ (or in both $\mathcal{S}$ and $\mathcal{D}$) are strongly delocalized
  The gross dimension of the neutrino production and absorption regions in $\mathcal{S}$ and $\mathcal{D}$ is of the order of $1/\mathfrak{D}$. The interference terms vanish if this scale is large compared to the "interference length"

$$L_{ij}^{\rm int} = \frac{1}{4\Delta E_{ij}} = \frac{2L_{ij}}{\pi\mathfrak{n}}.$$

In other words, the QFT approach predicts vanishing of neutrino oscillations in the plane-wave limit. In this limit, the flavor transition probability does not depend on $\overline{L}$, E_ν, and neutrino masses m_i and becomes

$$\mathcal{P}_{\alpha\beta}^{\rm PWL} = \sum_i |V_{\alpha i}|^2 |V_{\beta i}|^2 \leq 1.$$

Thereby, a nontrivial interference of the diagrams with the intermediate neutrinos of different masses is only possible if $\mathfrak{D} \neq 0$.

Let's try to get an idea of the scale of the factors responsible for decoherence effects.

Consider the function $f(x) = a^2x^2 + b^2/x^2$. It has the only minimum $f_{\min} = f(x_0) = 2ab$, where $x_0 = \sqrt{a/b}$ (assume $a > 0$, $b > 0$). Therefore the function $\mathscr{A}_{ij}^2 + \mathscr{B}_{ij}^2 \equiv \mathscr{D}_{ij}^2$ has the only minimum

$$\mathscr{D}_{ij}^2\Big|_{\min} = \frac{\pi^2|\mathfrak{n}|L}{E_\nu L_{ij}^2} = \frac{|\mathfrak{n}|\left(\Delta m_{ij}^2\right)^2 L}{16E_\nu^3}$$

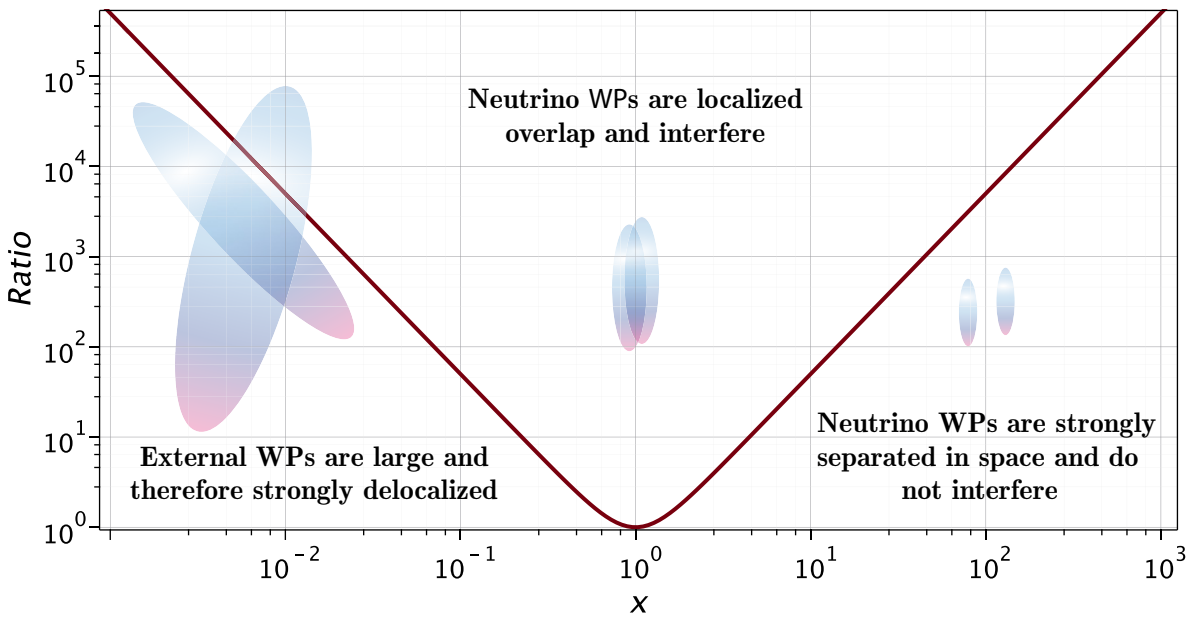

which is realized when

$$\mathfrak{D} = \frac{1}{2}\sqrt{\frac{|\mathfrak{n}|E_\nu}{L}} \equiv \mathfrak{D}_0.$$

The function $\mathfrak{D}_0$, as we see, does not depend on the neutrino mass. The ratio

$$\frac{\mathscr{D}_{ij}^2}{\mathscr{D}_{ij}^2\Big|_{\min}} = \frac{1}{2}\left(\frac{\mathfrak{D}^2}{\mathfrak{D}_0^2} + \frac{\mathfrak{D}_0^2}{\mathfrak{D}^2}\right)$$

is shown on the left as a function of $x = \mathfrak{D}/\mathfrak{D}_0$.

Both the ratio and the variable x are universal, i.e., neutrino mass-independent functions.

Two examples:

$$\mathscr{D}_{21}^2\Big|_{\min} \approx 2.0\times10^{-21}\left(\frac{\Delta m_{21}^2}{2.5\times10^{-3}\text{eV}^2}\right)^2\left(\frac{L}{10^3\text{km}}\right)\left(\frac{E_\nu}{1\,\text{GeV}}\right)^{-3}|\mathfrak{n}|, \quad \frac{\mathfrak{D}_0^2}{|\mathfrak{n}|} \approx 1.0\times10^{-9}\text{eV}^2\left(\frac{10^3E_\nu\,\text{km}}{L\,\text{GeV}}\right);$$

$$\mathscr{D}_{31}^2\Big|_{\min} \approx 2.6\times10^{-10}\left(\frac{\Delta m_{31}^2}{7.4\times10^{-5}\text{eV}^2}\right)^2\left(\frac{L}{1\,\text{a.u.}}\right)\left(\frac{E_\nu}{1\,\text{MeV}}\right)^{-3}|\mathfrak{n}|, \quad \frac{\mathfrak{D}_0^2}{|\mathfrak{n}|} \approx 6.7\times10^{-18}\text{eV}^2\left(\frac{E_\nu\,\text{a.u.}}{L\,\text{MeV}}\right).$$

- A detailed analysis of the generic (and the most important from an experimental point of view) subprocesses $1 \to 2$, $1 \to 3$, and $2 \to 2$ shows (see Appendix I) that $\mathfrak{D} \neq 0$ if in both vertices of the macrodiagram there are at least two interacting WPs $\varkappa$ (no matter in or out) with $\sigma_\varkappa \neq 0$.
- The same requirement unavoidably leads to the vanishing of the non-diagonal terms, when the mean distance between $\mathcal{S}$ and $\mathcal{D}$ becomes large enough in comparison with the coherence lengths L_{ij}^{coh}.
- As a result, the range of applicability of the standard QM formula for the neutrino oscillations probability is limited by rather restrictive conditions,

$$\left\langle \left(\frac{2\pi\mathfrak{D}L}{E_\nu L_{ij}} \right)^2 \right\rangle \ll 1, \quad \left\langle \left(\frac{\pi\mathfrak{n}}{2\mathfrak{D}L_{ij}} \right)^2 \right\rangle \ll 1, \quad \text{and} \quad \langle |\Theta_{ij}| \rangle \ll 1.$$

The angle brackets symbolize an averaging over the phase subspace of the process (93) which provides the main contribution into the measured count rate.

The obtained formulas (starting from the relation (150)) were derived under a number of assumptions and simplifications, which are not necessarily adequate to fully represent the real-life experimental conditions. Our consideration suggests that in the analysis and interpretation of real data one should take into account the operating times of the source and detector, their geometry and dimensions, explicit form of the distribution functions of in-packets, and other technical details.

20 Further developments (summary of some results).

Here we'll take a very brief look at some of the more complex aspects of the theory.

It's not part of the course!

The interested listener (reader) can find details and proofs in the works cited below.

20.1 Extended Grimus-Stockinger theorem.

Recall that the important tool for studying the long baselines (LBL) asymptotics of the macroscopic amplitude $\mathcal{A}_{\beta\alpha}$ (105) is the Grimus-Stockinger (GS) theorem (see Sect. **18.1**, p. 599) used in most analyses of neutrino oscillations based on QFT approaches with external wave packets. Recall that the GS theorem, roughly speaking, states that the spatial part of the "dressed" neutrino propagator

$$\mathfrak{J}(\mathbf{X},\kappa) = \int \frac{d\mathbf{q}}{(2\pi)^3} \frac{\Phi(\mathbf{q}) e^{i\mathbf{q}\mathbf{X}}}{\mathbf{q}^2 - \kappa^2 - i0} \tag{151}$$

behaves as $1/L$ for $\kappa^2 \ (\equiv s) = q_0^2 - m_i^2 > 0$ and $L \equiv |\mathbf{X}| \to \infty$, which leads to the classical inverse-square law (ISL) for the detected number of neutrino-induced events. It was shown[a] that the classical ISL is violated at **finite** L. This is a consequence of an extension of the GS theorem, which allows one to compute corrections to the long-distance asymptotics of the propagator (151).

◦ The extended GS ("ExGS") theorem states that for any Schwartz function $\Phi(\mathbf{q})$[b] the integral $\mathfrak{J}(\mathbf{X},\kappa)$ may be represented by the asymptotic series in inverse powers of L of the following form:

[a] VN & D. S. Shkirmanov, "The extended Grimus-Stockinger theorem and the violation of the inverse square law in quantum field theory," Eur. Phys. J. C **73** (2013) 2627, arXiv:1309.1011 [hep-ph].

[b] That is, the function $\Phi(\mathbf{q}) \in C^\infty(\mathbb{R}^3)$ which goes to zero faster than any power of $1/|\mathbf{q}|$, as do all its derivatives. The positive function in the integrand of the WP dressed neutrino propagator belongs to this class.

$$\mathfrak{J}(\mathbf{X},\kappa)=\frac{\Phi(\kappa\mathbf{l})e^{-i\kappa L}}{4\pi L}\left[1+\sum_{a\geq 1}\frac{\mathcal{D}_a(\kappa)}{L^a}\right], \tag{152}$$

where

$$\mathcal{D}_a(\kappa)=\frac{(-i)^a}{\Phi(\kappa\mathbf{l})}\sum_{b=0}^{a}\sum_{c=0}^{\left[\frac{a-b}{2}\right]}\left(\frac{\kappa}{4}\right)^b c_{abc}\left[(\mathbf{l}\times\boldsymbol{\nabla}_{\mathbf{q}})^{2(b+c)}\,(\mathbf{l}\boldsymbol{\nabla}_{\mathbf{q}})^{a-b-2c}\,\Phi(\mathbf{q})\right]_{\mathbf{q}=\kappa\mathbf{l}},\quad \mathbf{l}=\frac{\mathbf{X}}{|\mathbf{X}|}, \tag{153}$$

and c_{abc} are recursively defined positive rational numbers that are trivially computed using Maple® or any other computer algebra system.[a] As an illustration, the first 125 coefficients are given in Appendix K, p. 918. Obviously, such a number is unlikely to be needed in real-world applications.

◦ The range of applicability of the leading (GS) approximation is defined by explicit form of the function $\Phi(\mathbf{q})$, but in the most general case it can be written as

$$L\gg\frac{q_0}{\Sigma_{\text{LBL}}^2}\approx 20\left(\frac{1\,\text{eV}}{\Sigma_{\text{LBL}}}\right)^2\left(\frac{q_0}{1\,\text{MeV}}\right)\ \text{cm}. \tag{154}$$

where Σ_{LBL} is an effective energy dimension parameter that depends on momenta, masses, and momentum spreads ($\sigma_{\varkappa}$ in the CRGP model) of the external (in and out) wave packets.

◦ A trivial but important consequence of the ExGS theorem is that virtual neutrinos are exactly on mass-shell, and both energies and momenta of different mass eigenfields ν_i not coincide. We have already seen this, but the theorem ensures that a key QM "equal-momentum assumption" doesn't hold at long but finite distances either, and not only for $L\to\infty$. Surprisingly, in the ultrarelativistic limit (but only in this limit) the oscillation phases remain unchanged (corrections are $\sim m_i^4/q_0^4$).

[a] Equivalent but recursive-free formulation of the theorem is given by S. E. Korenblit and D. V. Taychenachev, "Extension of Grimus–Stockinger formula from operator expansion of free Green function," Mod. Phys. Lett. A **30** (2015) 1550074, arXiv:1401.4031 [math-ph].

◦ Another potentially falsifiable prediction is that $|\mathfrak{J}(\mathbf{X},\kappa)|^2$ is given by a series in powers of $1/L^2$,

$$|\mathfrak{J}(\mathbf{X},\kappa)|^2 \propto 1+\sum_{n\geq 1}\frac{\mathfrak{C}_n}{L^{2n}}.$$

◦ A critical property of this series is that the leading ISLV correction is **negative**.

The proof of this property is not very simple and one of the most complicated steps in this proof is the proper integration with respect to q_0, which is required to obtain the modified ("wave-packet dressed") $4d$ neutrino propagator. But within the framework of the CRGP model, the proof is relatively simple. Using third order saddle-point asymptotic expansion it is proved[a] that

$$\mathfrak{C}_1=-\frac{q_0^2}{\Sigma_{\mathsf{LBL}}^4},\qquad \frac{1}{\Sigma_{\mathsf{LBL}}^4}\equiv\frac{1}{8}\left[\rho^2-\frac{2\mathfrak{e}}{\mathfrak{r}}+\frac{\left(v_1^2+v_2^2\right)^2}{\mathfrak{r}^2}\right]>0, \tag{155}$$

$$\mathfrak{r}=\widetilde{\Re}_{00}-2\widetilde{\Re}_{03}+\widetilde{\Re}_{33},\quad \rho^2=\widetilde{\Re}_{11}^2+2\widetilde{\Re}_{12}^2+\widetilde{\Re}_{22}^2,$$

$$\mathfrak{e}=v_1^2\widetilde{\Re}_{11}+2v_1v_2\widetilde{\Re}_{12}+v_2^2\widetilde{\Re}_{22},\quad v_i=\widetilde{\Re}_{0i}-\widetilde{\Re}_{3i}\quad(i=1,2),\quad \widetilde{\Re}^{\mu\nu}=\widetilde{\Re}_s^{\mu\nu}+\widetilde{\Re}_d^{\mu\nu}.$$

The purely transversal term $\rho^2/8$ in Eq. (155) is the first-order contribution; the second- and third-order corrections are not in general small and describe nontrivial effects of the in-in, out-out, and in-out WP overlaps in time and space in both source and detector vertices.

It should be pointed out that the value of Σ_{LBL} (a function of the masses, momenta, and momentum spreads of the external WPs) may generally differ from any of $\sigma_{\varkappa}$ **by orders of magnitude**.

[a] VN & D. S. Shkirmanov, "Reactor antineutrino anomaly reanalysis in context of inverse-square law violation," Universe **7** (2021) 246. A detailed statistical analysis shows that the available at the time (2021) reactor data are generally consistent with ISLV at $\Sigma_{\mathsf{LBL}}=(0.66-1.18)$ eV, regardless of the models of the reactor antineutrino spectra. Note: This in no way proves the relevance of ISLV to RAA! So far, it's just a hint...

20.2 Off-shell neutrinos at short baselines.

Well, how do virtual neutrinos behave at short baseline (SBL) for which neither GS nor ExGS theorem is applicable? The answer is based on the study of the SBL asymptotics of the WP dressed 4D neutrino propagator[a]

$$\int \frac{d^4q}{(2\pi)^4} \frac{\widetilde{\delta}_s(q-q_s)\widetilde{\delta}_d(q+q_d)(\hat{q}+m)e^{-iqX}}{q^2-m_j^2+i0} \tag{156}$$

(here and below $dq \equiv d^4q$). The following lemma holds:
The integral

$$J(X) = \int \frac{dq\, e^{-iqX}}{q^2-m^2+i0} \exp\left\{-\frac{1}{4}\left[\widetilde{\Re}_s^{\mu\nu}\,(q-q_s)_\mu\,(q-q_s)_\nu + \widetilde{\Re}_d^{\mu\nu}\,(q+q_d)_\mu\,(q+q_d)_\nu\right]\right\}, \tag{157}$$

can be split into two therms, $J(X) = J_g(X) + J_v(X)$), which are given by the initial segments of the formal asymptotic expansions

$$J_g = -8i\pi^2\sqrt{\frac{\pi|\mathcal{R}|}{\mathcal{G}}}\exp(\Omega)\sum_{a,b,c\geq 0} f_{abc}(i\delta)^a\eta^b\Delta^c, \tag{158a}$$

$$J_v = \frac{4i\pi^2}{E_{\mathbf{p}}}\sqrt{|\mathcal{R}|}\exp\left(\Omega_c\right)\sum_{a,b\geq 0}\left[\frac{\kappa^{2a}}{\kappa_-{}^{2b+1}}\left(\mathcal{A}_{ab}^- + \frac{i\mathcal{B}_{ab}^-\kappa}{\kappa_-}\right) - \frac{\kappa^{2a}}{\kappa_+{}^{2b+1}}\left(\mathcal{A}_{ab}^+ + \frac{i\mathcal{B}_{ab}^+\kappa}{\kappa_+}\right)\right]. \tag{158b}$$

The coefficient functions f_{abc}, $\mathcal{A}^\pm$, and $\mathcal{B}^\pm$ are listed in Appendix J, p. 905; other notations are listed below.

[a] VN & D. S. Shkirmanov, "Virtual neutrino propagation at short baselines," Eur. Phys. J. C **82** (2022) 736, arXiv:2208.02621 [hep-ph].

List of notation:

$$\Omega = \Omega_c - \frac{1}{4\mathcal{G}}\left(\mathcal{P}p - m^2 - 2i\mathcal{R}^{\mu\nu}p_\mu X_\nu\right)^2,$$

$$\Omega_c = -i\mathcal{P}X + \mathcal{R}^{\mu\nu}\left(\frac{1}{4}Y_\mu Y_\nu - X_\mu X_\nu\right) - \frac{1}{4}\left(\widetilde{\Re}_s^{\mu\nu}q_{s\mu}q_{s\nu} + \widetilde{\Re}_d^{\mu\nu}q_{d\mu}q_{d\nu}\right),$$

$$\delta = \Sigma^2\frac{\rho_{\mu\nu}p^\mu X^\nu}{\rho^{\mu\nu}p_\mu p_\nu}, \quad \eta = \frac{\Sigma^2}{E_{\mathbf{p}}^2}, \quad \Delta = \frac{\mathcal{P}p - m^2}{\rho^{\mu\nu}p_\mu p_\nu},$$

$$\kappa = \frac{1}{E_{\mathbf{p}}\sqrt{\widetilde{\Re}_{00}}}, \quad \kappa_\pm = \frac{X_0}{\sqrt{\widetilde{\Re}_{00}}} + \frac{i}{2}\sqrt{\widetilde{\Re}_{00}}\,(\mathcal{P}_0 \pm E_{\mathbf{p}}),$$

$$\rho^{\mu\nu} = |\mathcal{R}|^{-1/4}\mathcal{R}^{\mu\nu}, \quad \Sigma \equiv \Sigma_{\mathsf{SBL}} = |\mathcal{R}|^{1/8},$$

$$\mathcal{R} = ||\mathcal{R}_{kn}||, \quad \mathcal{G} = \mathcal{R}_{\mu\nu}p^\mu p^\nu, \quad p = (p_0, \mathbf{p}) = \left(\sqrt{\mathcal{P}_0^2 + m^2}, \boldsymbol{\mathcal{P}}\right).$$

The 4-vector $\mathcal{P} = (\mathcal{P}_0, \boldsymbol{\mathcal{P}})$ is the stationary point of the numerator of the integrand in Eq. (157):

$$\mathcal{P}_\mu = \mathcal{R}_{\mu\nu}Y^\nu \quad (\text{recall that } Y^\mu = \widetilde{\Re}_s^{\mu\nu}q_{s\nu} - \widetilde{\Re}_d^{\mu\nu}q_{d\nu}), \tag{159}$$

where $\mathcal{R}$ is the tensor inverse of $\widetilde{\Re}$:[a] $\mathcal{R}_{\mu\lambda}\widetilde{\Re}^{\lambda\nu} = \delta_\mu^\nu$. In the exact energy-momentum conservation limit $\mathcal{P} = q_s = -q_d$ and $\mathcal{P} \simeq q_s \simeq -q_d$ even otherwise. So, within the saddle-point approximation, it is natural to interpret $\mathcal{P}$ as the 4-momentum of the virtual neutrino. It should be remarked that $\mathcal{P}$ is independent of the neutrino mass and is determined only by the momenta, masses and momentum spreads of the external wave packets (from both vertices of the macrodiagram).

[a] It may be expedient to recall that the tensors $\widetilde{\Re}_{s,d}$ are inverse of $\Re_{s,d}$. Since these tensors are symmetric and positive definite, the same is true for the tensors $\widetilde{\Re} \equiv \widetilde{\Re}_s + \widetilde{\Re}_d$ and $\mathcal{R}$.

20.3 Count rate in the SBL and LBL modes.

A fairly general (although not the most general) expression for the number of (UR) neutrino-induced events, valid for the two limiting cases, SBL and LBL, is

$$\frac{N_{\beta\alpha}}{\tau_d} = \sum_{\text{spins}} \int d\mathbf{x} \int d\mathbf{y} \int d\mathfrak{P}_s \int d\mathfrak{P}_d \int d|\mathbf{q}| \frac{\mathcal{P}_{\alpha\beta}\left(|\mathbf{q}|, |\mathbf{y}-\mathbf{x}|\right)}{4(2\pi)^3 |\mathbf{y}-\mathbf{x}|^2},$$

$$\mathcal{P}_{\alpha\beta}\left(|\mathbf{q}|, |\mathbf{y}-\mathbf{x}|\right) = \sum_{ij} V_{\beta j} V_{\alpha i} V_{\beta i}^* V_{\alpha j}^* \exp\left(i\varphi_{ij} - \mathcal{A}_{ij}^2 - \mathcal{C}_{ij}^2 - \Theta_{ij}\right) S_{ij},$$

$$S_{ij} = \frac{\exp(-\mathcal{B}_{ij}^2)}{4\mathfrak{D}\tau_d} \sum_{l,l'=1}^{2} (-1)^{l+l'+1} \mathsf{lerf}\left[2\mathfrak{D}\left(x_l^0 - y_{l'}^0 + |\mathbf{y}-\mathbf{x}|\right) + i\mathcal{B}_{ij}\right],$$

$$\mathfrak{D} = 1/\sqrt{2\widetilde{\Re}^{\mu\nu} l_\mu l_\nu},$$

$$d\mathfrak{P}_s = (2\pi)^4 \delta_s(q - q_s) |M_s|^2 \prod_{a\in I_s} \frac{d\mathbf{p}_a f_a(\mathbf{p}_a, s_a, x)}{(2\pi)^3 2E_a} \prod_{b\in F_s} \frac{d\mathbf{p}_b}{(2\pi)^3 2E_b},$$

$$d\mathfrak{P}_d = (2\pi)^4 \delta_d(q + q_d) |M_d|^2 \prod_{a\in I_d} \frac{d\mathbf{p}_a f_a(\mathbf{p}_a, s_a, y)}{(2\pi)^3 2E_a} \prod_{b\in F_d} \frac{[d\mathbf{p}_b]}{(2\pi)^3 2E_b}.$$

The ingredients are listed at p. 647. These formulas do not take into account the inverse-square law violation corrections, for which we unfortunately do not have enough time to discuss.[a]

[a] VN & D. S. Shkirmanov, "Virtual neutrino propagation at short baselines," Eur. Phys. J. C **82** (2022) 736, arXiv:2208.02621 [hep-ph].

Table below shows ingredients of the equations shown in previous page in the leading order for the off-mass-shell (short distances) and on-mass-shell (long distances) regimes. Here

$$L = |\mathbf{y} - \mathbf{x}|, \quad \Delta m^2_{ij} = m^2_i - m^2_j, \quad \text{and} \quad \mathcal{Q}^4 = \left(\mathcal{R}^{00}\mathcal{R}^{\mu\nu} - \mathcal{R}^{0\mu}\mathcal{R}^{0\nu}\right) l_\mu l_\nu.$$

Last column shows the order of magnitude (OoM) of the quantity.

Quantity	Off-shell regime	On-shell regime	OoM
φ_{ij}	$\dfrac{\Delta m^2_{ij} L}{2\lvert\mathbf{q}\rvert}$	$\dfrac{\Delta m^2_{ij} L}{2E_\nu}$	$\dfrac{\lvert\Delta m^2_{ij}\rvert L}{E_\nu}$
$\mathcal{A}^2_{ij}$	$\left(\dfrac{\Delta m^2_{ij} L}{2\lvert\mathbf{q}\rvert^2}\right)^2 \dfrac{\mathcal{Q}^4}{2\mathcal{R}^{\mu\nu} l_\mu l_\nu}$	$\left(\dfrac{\Delta m^2_{ij} L}{2E^2_\nu}\right)^2 \dfrac{1}{2\widetilde{\Re}^{\mu\nu} l_\mu l_\nu}$	$\left(\dfrac{\Delta m^2_{ij}}{E^2_\nu}\Sigma L\right)^2$
$\mathcal{B}_{ij}$	$\dfrac{\Delta m^2_{ij}}{4\lvert\mathbf{q}\rvert}\sqrt{\dfrac{\widetilde{\Re}^{\mu\nu} l_\mu l_\nu}{2}}\,\dfrac{\mathcal{R}^{0\mu} l_\mu}{\mathcal{R}^{\mu\nu} l_\mu l_\nu}$	$\dfrac{\Delta m^2_{ij}}{4E_\nu}\sqrt{\dfrac{\widetilde{\Re}^{\mu\nu} l_\mu l_\nu}{2}}\,\dfrac{Y_k l_k}{Y^\mu l_\mu}$	$\dfrac{\lvert\Delta m^2_{ij}\rvert}{\Sigma E_\nu}$
$\mathcal{C}^2_{ij}$	$\left(\dfrac{\Delta m^2_{ij}}{2\lvert\mathbf{q}\rvert}\right)^2 \dfrac{1}{8\mathcal{R}^{\mu\nu} l_\mu l_\nu}$	0	$\left(\dfrac{\Delta m^2_{ij}}{\Sigma E_\nu}\right)^2$
Θ_{ij}	$\dfrac{m^2_i + m^2_j}{4\lvert\mathbf{q}\rvert}\left[\widetilde{\Re}^{0\mu}_s \left(q - q_s\right)_\mu + \widetilde{\Re}^{0\mu}_d \left(q + q_d\right)_\mu\right]$	$\dfrac{m^2_i + m^2_j}{4q_0}\left[\widetilde{\Re}^{\mu k}_s l^k \left(q_0 l - q_s\right)_\mu + \widetilde{\Re}^{\mu k}_d l^k \left(q_0 l + q_d\right)_\mu\right]$	$\dfrac{m^2_i + m^2_j}{\Sigma E_\nu}$

Evidently, $E_\nu \simeq q_0 \simeq |\mathbf{q}|$ in the UR approximation. As can be seen, the listed structures (except for $\mathcal{C}_{ij}$), related to the SBL and LBL modes, they have the same order of magnitude and have a certain analytical similarity, but are not identical and do not coincide with each other in any approximation. This clearly indicates the existence of a transition region between SBL and LBL.

21 Intermediate conclusions about the QFT approach.

- The standard QM neutrino oscillation theory has a limited range of applicability.
- The QFT modifications of the QM theory are numerous and drastically depend upon:
  - momentum spreads of the external "in" and "out" wave packets (determined by the environment and "prehistory" of their creation).
  - reaction types in the neutrino production and absorption regions ["source" and "detector", respectively] and phase-space domains of these reactions;
  - time interval of steady-state operation of the source "machine " and detector exposure time;
  - dimensions of the source and detector and distance between them.

- Essentially all QFT effects are decoherent and thus lead to a smoothing, distortion or vanishing of the interference (oscillating) terms and to a general suppression of the neutrino event rate in the detector. This suppression is potentially measurable in the dedicate experiments.

  The QFT predicted effects are usually small. But "small" does not mean "uninteresting".

  Modern physics thrives in large part on the discovery of very small effects.

- An effect that perhaps is already being observed is the inverse-square law violation. However, the data are not yet accurate enough to draw any unambiguous conclusions.

Part VI

Neutrino oscillations in matter

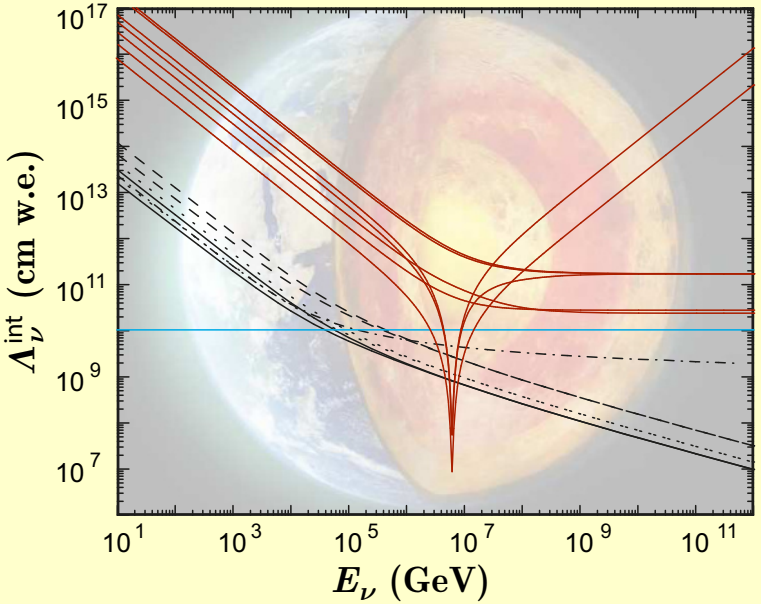

22 Neutrino refraction.

It has been noted by Lincoln Wolfenstein[a] that neutrino oscillations in a medium are affected by interactions even if the thickness of the medium is negligible in comparison with the neutrino mean free path. The effect of the medium arises in this case from the coherent forward scattering of ν_e as a result of its CC interactions with electrons.

Let's forget about inelastic collisions for a while and consider the simplified case where an ultrarelativistic neutrino moves in the external (effective) potential W formed by the background matter.

If the neutrino momentum in vacuum was $\mathbf{p}$ then its energy was $\simeq p = |\mathbf{p}|$. When the neutrino enters into the medium, its energy becomes $E = p + W$.

Let's now introduce the index of refraction $n = p/E$ which is a positive value in the absence of inelastic collisions. Therefore

$$W = (1 - n)E \simeq (1 - n)p. \tag{160}$$

In the last step, we took into account that neutrino interaction with matter is very weak, $|W| \ll E$, and thus $E \simeq p$ is a good approximation.

The natural generalization of Eq. (50) for the time evolution of neutrino flavor states in matter then follows from this simple consideration and the quantum-mechanical correspondence principle.

[a] L. Wolfenstein, "Neutrino oscillations in medium," Phys. Rev. D **17** (1978) 2369–2374.

This is the famous Wolfenstein equation:

$$i\frac{d}{dt}|\boldsymbol{\nu}(t)\rangle_f = \left[\mathbf{V}\mathbf{H}_0\mathbf{V}^\dagger + \mathbf{W}(t)\right]|\boldsymbol{\nu}(t)\rangle_f, \tag{161}$$

where

$$\mathbf{W}(t) = \text{diag}\left(1-n_{\nu_e}, 1-n_{\nu_\mu}, 1-n_{\nu_\tau}, \ldots\right)p \tag{162}$$

is the interaction Hamiltonian.

It will be useful for the following to introduce the *time-evolution operator* for the flavor states defined by

$$|\boldsymbol{\nu}(t)\rangle_f = \mathbf{S}(t)|\boldsymbol{\nu}(0)\rangle_f.$$

Taking into account that $|\boldsymbol{\nu}(t)\rangle_f$ must satisfy Eq. (161) for any initial condition $|\boldsymbol{\nu}(t=0)\rangle_f = |\boldsymbol{\nu}(0)\rangle_f$, the Wolfenstein equation can be immediately rewritten in terms of the evolution operator:

$$i\dot{\mathbf{S}}(t) = \left[\mathbf{V}\mathbf{H}_0\mathbf{V}^\dagger + \mathbf{W}(t)\right]\mathbf{S}(t), \quad \mathbf{S}(0) = \mathbf{1}. \tag{163}$$

This equation (or its equivalent (161)) cannot be solved analytically in the general case of a medium with a varying (along the neutrino pass) density. But for a medium with a slowly (adiabatically) varying density distribution the approximate solution can be obtained by a diagonalization of the effective Hamiltonian. Below we will consider this method for a rather general 2-flavor case but now let us illustrate (without derivation) the simplest situation with a matter of constant density.

22.1 Matter of constant density.

In the 2-flavor case, the transition probability is given by the formula very similar to that for vacuum:

$$P_{\alpha\alpha'}(L) = \frac{1}{2}\sin^2 2\theta_{\mathsf{m}}\left[1-\cos\left(\frac{2\pi L}{L_{\mathsf{m}}}\right)\right],$$

$$L_{\mathsf{m}} = L_{\nu}\left[1-2\kappa\left(L_{\nu}/L_0\right)\cos 2\theta + \left(L_{\nu}/L_0\right)^2\right]^{-1/2}.$$

The L_{m} is called the oscillation length in matter and is defined through the following quantities:

$$L_{\nu} \equiv L_{23} = \frac{4\pi E}{\Delta m^2}, \quad L_0 = \frac{\sqrt{2}\pi A}{G_F N_A Z \rho} \approx 2R_{\oplus}\left(\frac{A}{2Z}\right)\left(\frac{2.5\ \mathsf{g/cm}^3}{\rho}\right),$$

$$\kappa = \mathsf{sign}\left(m_3^2 - m_2^2\right), \quad \Delta m^2 = \left|m_3^2 - m_2^2\right|.$$

The parameter θ_{m} is called the mixing angle in matter and is given by

$$\sin 2\theta_{\mathsf{m}} = \sin 2\theta\left(\frac{L_{\mathsf{m}}}{L_{\nu}}\right),$$

$$\cos 2\theta_{\mathsf{m}} = \left(\cos 2\theta - \kappa\frac{L_{\nu}}{L_0}\right)\left(\frac{L_{\mathsf{m}}}{L_{\nu}}\right).$$

The solution for antineutrinos is the same but with the replacement

$$\kappa \longmapsto -\kappa.$$

The closeness of the value of L_0 to the Earth's diameter is even more surprising than that for L_{ν}. The matter effects are therefore important for atmospheric neutrinos.

23 Propagation of high-energy mixed neutrinos through matter.

"The matter doesn't matter"

Lincoln Wolfenstein, lecture given at 28th SLAC Summer Institute on Particle Physics "Neutrinos from the Lab, the Sun, and the Cosmos," Stanford, CA, Aug. 14-25, 2000.

When neutrinos propagate through vacuum there is a phase change $\exp\left(-im_i^2 t/2p_\nu\right)$. For two mixed flavors there is a resulting oscillation with length

$$L_{\text{vac}} = \frac{4\pi E_\nu}{\Delta m^2} \approx D_\oplus \left(\frac{E_\nu}{10\ \text{GeV}}\right)\left(\frac{0.002\ \text{eV}^2}{\Delta m^2}\right).$$

In matter there is an additional phase change due to refraction associated with forward scattering $\exp\left[ip_\nu(\text{Re}\, n - 1)t\right]$.

The characteristic length (for a normal medium) is

$$L_{\text{ref}} = \frac{\sqrt{2}A}{G_F N_A Z \rho} \approx D_\oplus \left(\frac{A}{2Z}\right)\left(\frac{2.5\ \text{g/cm}^2}{\rho}\right).$$

It is generally believed that the imaginary part of the index of refraction n which describes the neutrino absorption due to inelastic interactions *does not affect the oscillation probabilities* or at the least inelastic interactions can be someway *decoupled* from oscillations.

The conventional arguments are

- $\mathrm{Re}\, n - 1 \propto G_F$ while $\mathrm{Im}\, n \propto G_F^2$;
- Only Δn may affect the oscillations and $\Delta \mathrm{Im}\, n$ is all the more negligible.

It will be shown that these arguments do not work for sufficiently high neutrino energies and/or for thick media $\Longrightarrow$ in general absorption cannot be decoupled from refraction and mixing.[a] By using another cant phrase of Wolfenstein, one can say that

"In some circumstances the matter could matter,"

23.1 Generalized MSW equation.

Let

$f_{\nu_\alpha A}(0)$ be the amplitude for the ν_α zero-angle scattering from particle A of the matter background ($A = e, p, n, \ldots$),

$\rho(t)$ be the matter density (in g/cm^3),

$Y_A(t)$ be the number of particles A per amu in the point t of the medium, and

$N_0 = 6.02214199 \times 10^{23}$ cm^{-3} be the reference particle number density (numerically equal to Avogadro's number).

Then the index of refraction of ν_α for small $|n-1|$ (for normal media $|n-1| \lll 1$) is given by

$$n_\alpha(t) = 1 + \frac{2\pi N_0 \rho(t)}{p_\nu^2} \sum_A Y_A(t) f_{\nu_\alpha A}(0),$$

where p_ν is the neutrino momentum.

[a] $p_\nu \mathrm{Im}\, n \propto \sigma^{\mathrm{tot}}(p_\nu)$ grows fast with energy while $p_\nu\, (\mathrm{Re}\, n - 1)$ is a constant or decreasing function of E_ν.

Since the amplitude $f_{\nu_\alpha A}(0)$ is in general a complex number, the index of refraction is also complex. Its real part is responsible for neutrino refraction while the imaginary part – for absorption. From the optical theorem of quantum mechanics we have

$$\mathsf{Im}\left[f_{\nu_\alpha A}(0)\right] = \frac{p_\nu}{4\pi}\sigma^{\mathsf{tot}}_{\nu_\alpha A}\left(p_\nu\right).$$

This implies that

$$p_\nu \mathsf{Im}\left[n_\alpha(t)\right] = \frac{1}{2}N_0\rho(t)\sum_A Y_A(t)\sigma^{\mathsf{tot}}_{\nu_\alpha A}\left(p_\nu\right) = \frac{1}{2\Lambda_\alpha\left(p_\nu,t\right)},$$

where

$$\Lambda_\alpha\left(p_\nu,t\right) = \frac{1}{\Sigma^{\mathsf{tot}}_\alpha\left(p_\nu,t\right)} = \frac{\lambda^{\mathsf{tot}}_a\left(p_\nu,t\right)}{\rho(t)}.$$

is the mean free path [in cm] of ν_α in the point t of the medium. Since the neutrino momentum, p_ν, is an extrinsic variable in Eq. (164), we will sometimes omit this argument to simplify formulas.

The generalized MSW equation for the time-evolution operator

$$\mathbf{S}(t) = \begin{pmatrix} S_{\alpha\alpha}(t) & S_{\alpha\beta}(t) \\ S_{\beta\alpha}(t) & S_{\beta\beta}(t) \end{pmatrix}$$

of two mixed stable neutrino flavors ν_α and ν_β propagating through an absorbing medium can be written as

$$\boxed{i\frac{d}{dt}\mathbf{S}(t) = \left[\mathbf{V}\mathbf{H}_0\mathbf{V}^T + \mathbf{W}(t)\right]\mathbf{S}(t), \quad \left(\mathbf{S}(0) = \mathbf{1}\right).} \tag{164}$$

Here

$$\mathbf{V}=\begin{pmatrix}\cos\theta & \sin\theta\\ -\sin\theta & \cos\theta\end{pmatrix}$$ is the vacuum mixing matrix ($0\le\theta\le\pi/2$),

$$\mathbf{H}_0=\begin{pmatrix}E_1 & 0\\ 0 & E_2\end{pmatrix}$$ is the vacuum Hamiltonian for ν mass eigenstates,

$$E_i=\sqrt{p_\nu^2+m_i^2}\simeq p_\nu+m_i^2/2p_\nu$$ is the energy of the ν_i eigenstate,

$$\mathbf{W}(t)=-p_\nu\begin{pmatrix}n_\alpha(t)-1 & 0\\ 0 & n_\beta(t)-1\end{pmatrix}$$ is the interaction Hamiltonian.

23.2 Master equation.

It is useful to transform MSW equation into the one with a traceless Hamiltonian. For this purpose we define the matrix

$$\widetilde{\mathbf{S}}(t)=\exp\left\{\frac{i}{2}\int_0^t \mathrm{Tr}\left[\mathbf{H}_0+\mathbf{W}(t')\right]dt'\right\}\mathbf{S}(t).$$

The master equation (ME) for this matrix then is

$$\boxed{i\frac{d}{dt}\widetilde{\mathbf{S}}(t)=\mathbf{H}(t)\widetilde{\mathbf{S}}(t),\quad \widetilde{\mathbf{S}}(0)=\mathbf{1}.} \tag{165}$$

The effective Hamiltonian is defined by

$$\mathbf{H}(t) = \begin{pmatrix} q(t) - \Delta_c & \Delta_s \\ \Delta_s & -q(t) + \Delta_c \end{pmatrix},$$

$$\Delta_c = \Delta \cos 2\theta, \quad \Delta_s = \Delta \sin 2\theta, \quad \Delta = \frac{m_2^2 - m_1^2}{4p_\nu},$$

$$q(t) = q_R(t) + iq_I(t) = \frac{1}{2} p_\nu \left[n_\beta(t) - n_\alpha(t) \right].$$

The Hamiltonian for antineutrinos is of the same form as $\mathbf{H}(t)$ but

$$\mathrm{Re}\left[f_{\overline{\nu}_\alpha A}(0)\right] = -\mathrm{Re}\left[f_{\nu_\alpha A}(0)\right] \quad \text{and} \quad \mathrm{Im}\left[f_{\overline{\nu}_\alpha A}(0)\right] \neq \mathrm{Im}\left[f_{\nu_\alpha A}(0)\right].$$

The neutrino oscillation probabilities are

$$P\left[\nu_\alpha(0) \to \nu_{\alpha'}(t)\right] \equiv P_{\alpha\alpha'}(t) = \left|S_{\alpha'\alpha}(t)\right|^2 = A(t) \left|\widetilde{S}_{\alpha'\alpha}(t)\right|^2, \tag{166}$$

where

$$A(t) = \exp\left[-\int_0^t \frac{dt'}{\Lambda(t')}\right], \quad \frac{1}{\Lambda(t)} = \frac{1}{2}\left[\frac{1}{\Lambda_\alpha(t)} + \frac{1}{\Lambda_\beta(t)}\right].$$

Owing to the complex potential q, the Hamiltonian $\mathbf{H}(t)$ is non-Hermitian and the new evolution operator $\widetilde{\mathbf{S}}(t)$ is nonunitary. As a result, there are no conventional relations between $P_{\alpha\alpha'}(t)$. Since

$$q_I(t) = \frac{1}{4}\left[\frac{1}{\Lambda_\beta(t)} - \frac{1}{\Lambda_\alpha(t)}\right],$$

the matrix $\mathbf{H}(t)$ becomes Hermitian when $\Lambda_\alpha = \Lambda_\beta$. If this is the case at any t, the ME reduces to the standard MSW equation and inelastic scattering results in the common exponential attenuation of the probabilities. We'll consider the more general and more interesting case when $\Lambda_\alpha \neq \Lambda_\beta$.

23.3 Examples.

$\boxed{\nu_\alpha - \nu_s}$ This is the extreme example. Since $\Lambda_s = \infty$, we have $\Lambda = 2\Lambda_\alpha$ and $q_I = -1/4\Lambda_\alpha$. So $q_I \neq 0$ at any energy. Even without solving the evolution equation, one can expect the penetrability of active neutrinos to be essentially modified in this case because, roughly speaking, they spend a certain part of life in the sterile state. In other words, sterile neutrinos "tow" their active companions through the medium as a tugboat. On the other hand, the active neutrinos "retard" the sterile ones, like a bulky barge retards its tugboat. As a result, the sterile neutrinos undergo some absorption.

$\boxed{\nu_{e,\mu} - \nu_\tau}$ Essentially at all energies, $\sigma^{\mathsf{CC}}_{\nu_{e,\mu}N} > \sigma^{\mathsf{CC}}_{\nu_\tau N}$. This is because of large value of the τ lepton mass, m_τ, which leads to several consequences:

1. high neutrino energy threshold for τ production;
2. sharp shrinkage of the phase spaces for CC $\nu_\tau N$ reactions;
3. kinematic correction factors ($\propto m_\tau^2$) to the nucleon structure functions (the corresponding structures are negligible for e production and small for μ production).

The neutral current contributions are canceled out from q_I. Thus, in the context of the master equation, ν_τ can be treated as (almost) sterile within the energy range for which $\sigma^{\mathsf{CC}}_{\nu_{e,\mu}N} \gg \sigma^{\mathsf{CC}}_{\nu_\tau N}$ (see Figures at pp. 660–661).

$\boxed{\overline{\nu}_e - \overline{\nu}_\alpha}$ A similar situation, while in quite a different and narrow energy range, holds in the case of mixing of $\overline{\nu}_e$ with some other flavor. This is a particular case for a normal C asymmetric medium, because of the W boson resonance formed in the neighborhood of $E_\nu^{\mathsf{res}} = m_W^2/2m_e \approx 6.33$ PeV through the reactions $\overline{\nu}_e e^- \to W^- \to$ hadrons and $\overline{\nu}_e e^- \to W^- \to \overline{\nu}_\ell \ell^-$ $(\ell = e, \mu, \tau)$. Let's remind that $\sigma^{\mathsf{tot}}_{\overline{\nu}_e e} \approx 250\ \sigma^{\mathsf{tot}}_{\overline{\nu}_e N}$ just at the resonance peak [see Figure at p. 414 and Table at p. 415, Sect. **10.8**].

23.4 Total cross sections.

According to Albright and Jarlskog[a]

$$\frac{d\sigma^{\mathsf{CC}}_{\nu,\overline{\nu}}}{dxdy} = \frac{G_F^2 m_N E_\nu}{\pi}\,(A_1F_1 + A_2F_2 \pm A_3F_3 + A_4F_4 + A_5F_5\,),$$

where $F_i = F_i(x, Q^2)$ are the nucleon structure functions and A_i are the kinematic factors $i = 1, \ldots, 5$). These factors were calculated by many authors[b] and the most accurate formulas were given by Paschos and Yu:

$$A_1 = xy^2 + \frac{m_l^2 y}{2m_N E_\nu}, \quad A_2 = 1 - y - \frac{m_N}{2E_\nu}xy - \frac{m_l^2}{4E_\nu^2}, \quad A_3 = xy\left(1 - \frac{y}{2}\right) - \frac{m_l^2 y}{4m_N E_\nu},$$

$$A_4 = \frac{m_l^2}{2m_N E_\nu}\left(xy + \frac{m_l^2}{2m_N E_\nu}\right), \quad A_5 = -\frac{m_l^2}{2m_N E_\nu}.$$

The contributions proportional to m_ℓ^2 must vanish as $E_\nu \gg m_\ell$. However they remain surprisingly important even at very high energies.

[a] C. H. Albright and C. Jarlskog, Nucl. Phys. B **84** (1975) 467–492; see also I. Ju, Phys. Rev. D **8** (1973) 3103–3109 and V. D. Barger *et al.*, Phys. Rev. D **16** (1977) 2141–2157.

[b] See previous footnote and also the more recent papers: S. Dutta, R. Gandhi & B. Mukhopadhyaya, Eur. Phys. J. C **18** (2000) 405–416, hep-ph/9905475; N. I. Starkov, J. Phys. G **27** (2001) L81–L85; E. A. Paschos and J. Y. Yu, Phys. Rev. D **65** (2002) 033002, hep-ph/0107261.

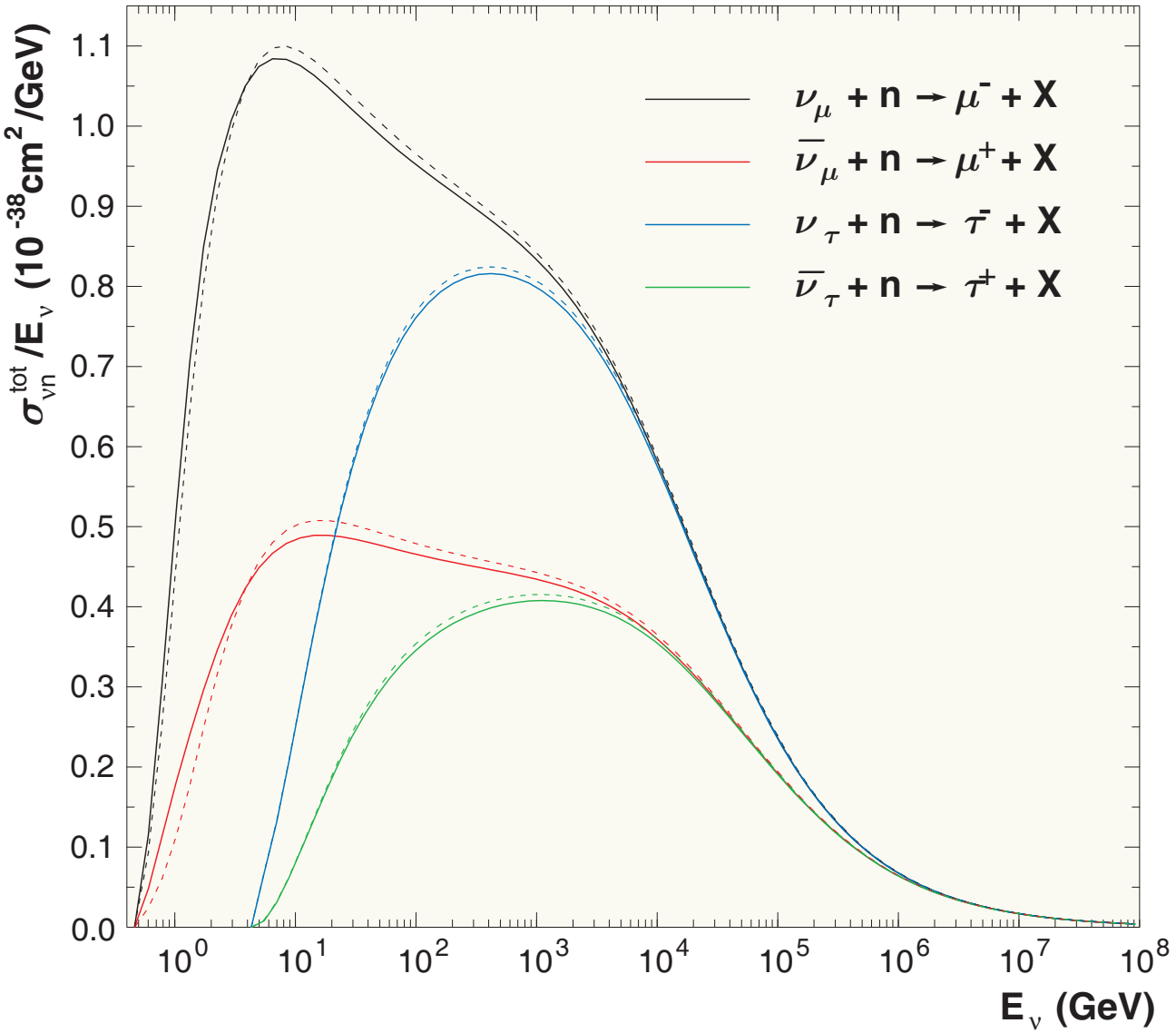

Total inelastic νn cross sections evaluated with the MRST 2002 NNLO PDF model modified according to Bodek–Yang prescription (solid lines) and unmodified (dashed lines).

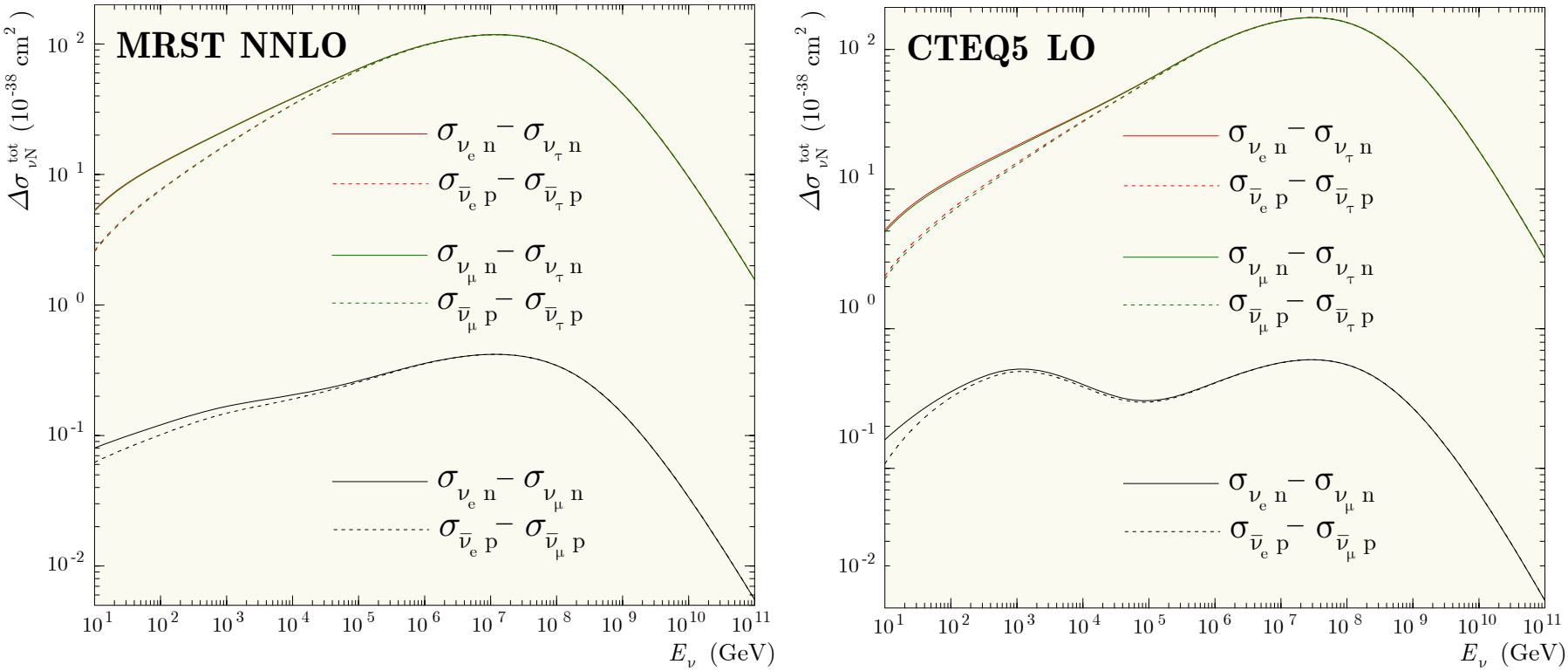

Differences between the total neutrino cross sections for proton and neutron targets evaluated with the MRST 2002 NNLO (*left panel*) and CTEQ 5-DIS LO (*right panel*) PDF models.

23.5 Indices of refraction.

For $E_\nu \ll \min\left(m_{W,Z}^2/2m_A\right)$ and for an electroneutral nonpolarized cold medium, the q_R is energy independent. In the leading orders of the standard electroweak theory it is

$$q_R = \begin{cases} \frac{1}{2}V_0 Y_p \rho & \text{for } \alpha = e \text{ and } \beta = \mu \text{ or } \tau, \\ -\frac{1}{2}a_\tau V_0 \left(Y_p + b_\tau Y_n\right)\rho & \text{for } \alpha = \mu \text{ and } \beta = \tau, \\ \frac{1}{2}V_0 \left(Y_p - \frac{1}{2}Y_n\right)\rho & \text{for } \alpha = e \text{ and } \beta = s, \\ \frac{1}{4}V_0 Y_n \rho & \text{for } \alpha = \mu \text{ or } \tau \text{ and } \beta = s, \end{cases}$$

where

$$V_0 = \sqrt{2}G_F N_0 \simeq 7.63 \times 10^{-14} \text{ eV}$$

$$\left(L_0 = \frac{2\pi}{V_0} \simeq 1.62 \times 10^4 \text{ km} \sim D_\oplus\right),$$

$$a_\tau = \frac{3\alpha r_\tau \left[\ln(1/r_\tau) - 1\right]}{4\pi \sin^2\theta_W} \simeq 2.44 \times 10^{-5},$$

$$b_\tau = \frac{\ln(1/r_\tau) - 2/3}{\ln(1/r_\tau) - 1} \simeq 1.05,$$

α is the fine-structure constant, θ_W is the weak-mixing angle and $r_\tau = (m_\tau/m_W)^2$.

Notes:

- For an isoscalar medium the $|q_R|$ is of the same order of magnitude for any pair of flavors but $\nu_\mu - \nu_\tau$.
- For an isoscalar medium $q_R^{(\nu_\mu - \nu_\tau)}/q_R^{(\nu_e - \nu_\mu)} \approx -5 \times 10^{-5}$.
- For certain regions of a neutron-rich medium the value of $q_R^{(\nu_e - \nu_s)}$ may become vanishingly small. In this case, the one-loop radiative corrections must be taken into account.
- For very high energies the q_R have to be corrected for the gauge boson propagators and strong-interaction effects.

One can expect $|q_R|$ to be either an energy-independent or decreasing function for any pair of mixed neutrino flavors. On the other hand, there are several cases of much current interest when $|q_I|$ either increases with energy without bound (mixing between active and sterile neutrino states) or has a broad or sharp maximum (as for $\nu_\mu - \nu_\tau$ or $\overline{\nu}_e - \overline{\nu}_\mu$ mixings, respectively).

Numerical estimations suggest that for every of these cases there is an energy range in which q_R and q_I are comparable in magnitude. Since $q_R \propto \rho$ and $q_I \propto$ and are dependent upon the composition of the medium (Y_A) there may exist some more specific situations, when

$$|q_R| \sim |q_I| \sim |\Delta|$$

or even

$$|q_R| \sim |\Delta_c| \quad \text{and} \quad |q_I| \sim |\Delta_s| \,.$$

If this is the case, the refraction, absorption and mixing become interestingly superimposed.

23.6 Eigenproblem and mixing matrix in matter.

23.6.1 Eigenvalues.

The matrix $\mathbf{H}(t)$ has two complex instantaneous eigenvalues, $\varepsilon(t)$ and $-\varepsilon(t)$, with $\varepsilon = \varepsilon_R + i\varepsilon_I$ satisfying the characteristic equation

$$\varepsilon^2 = (q - q_+)(q - q_-),$$

where

$$q_\pm = \Delta_c \pm i\Delta_s = \Delta e^{\pm 2i\theta}.$$

The solution is

$$\varepsilon_R^2 = \frac{1}{2}\left(\varepsilon_0^2 - q_I^2\right) + \frac{1}{2}\sqrt{\left(\varepsilon_0^2 - q_I^2\right)^2 + 4q_I^2\left(\varepsilon_0^2 - \Delta_s^2\right)},$$
$$\varepsilon_I = \frac{q_I\left(q_R - \Delta_c\right)}{\varepsilon_R} \quad \text{(provided } q_R \neq \Delta_c\text{)},$$

with

$$\varepsilon_0 = \sqrt{\Delta^2 - 2\Delta_c q_R + q_R^2} \geq |\Delta_s|, \qquad \text{sign}\left(\varepsilon_R\right) \stackrel{\text{def}}{=} \text{sign}(\Delta) \equiv \zeta.$$

(At that choice $\varepsilon = \Delta$ for vacuum and $\varepsilon = \zeta\varepsilon_0$ if $q_I = 0$.)

In the vicinity of the MSW resonance, $q_R = q_R(t_\star) = \Delta_c$

$$\lim_{q_R \to \Delta_c \pm 0} \varepsilon_R = \Delta_s \sqrt{\max\left(1 - \Delta_I^2/\Delta_s^2, 0\right)},$$

$$\lim_{q_R \to \Delta_c \pm 0} \varepsilon_I = \pm\zeta \Delta_I \sqrt{\max\left(1 - \Delta_s^2/\Delta_I^2, 0\right)},$$

where $\Delta_I = q_I(t_\star)$. Therefore the resonance value of $|\varepsilon_R|$ (which is inversely proportional to the neutrino oscillation length in matter) is always smaller than the conventional MSW value $|\Delta_s|$ and *vanishes* if $\Delta_I^2 < \Delta_s^2$ (ε_I remains finite in this case). In neutrino transition through the region of resonance density $\rho = \rho(t_\star)$, ε_I undergoes discontinuous jump while ε_R remains continuous. The corresponding cuts in the q plane are placed outside the circle $|q| \leq |\Delta|$. If $\Delta_I^2 > \Delta_s^2$, the imaginary part of ε vanishes while the real part remains finite.

A distinctive feature of the characteristic equation is the existence of two mutually conjugate "super-resonance" points $q_\pm$ in which ε vanishes giving rise to the total degeneracy of the levels of the system (impossible in the "standard MSW" solution). Certainly, the behavior of the system in the vicinity of these points must be dramatically different from the conventional pattern.

The "super-resonance" conditions are physically realizable for various meaningful mixing scenarios.

Some useful relations:

$$\varepsilon_R^2 = \frac{2q_I^2\left(\varepsilon_0^2 - \Delta_s^2\right)}{\sqrt{\left(\varepsilon_0^2 - q_I^2\right)^2 + 4q_I^2\left(\varepsilon_0^2 - \Delta_s^2\right)} - \varepsilon_0^2 + q_I^2},$$

$$\varepsilon_I = \frac{\sqrt{\left(\varepsilon_0^2 - q_I^2\right)^2 + 4q_I^2\left(\varepsilon_0^2 - \Delta_s^2\right)} - \varepsilon_0^2 + q_I^2}{2q_I\left(q_R - \Delta_c\right)},$$

$$\frac{\partial \varepsilon_R}{\partial q_R} = \frac{\partial \varepsilon_I}{\partial q_I} = \frac{q_I\varepsilon_I + \left(q_R - \Delta_c\right)\varepsilon_R}{\varepsilon_R^2 + \varepsilon_I^2},$$

$$\frac{\partial \varepsilon_I}{\partial q_R} = -\frac{\partial \varepsilon_R}{\partial q_I} = \frac{q_I\varepsilon_R - \left(q_R - \Delta_c\right)\varepsilon_I}{\varepsilon_R^2 + \varepsilon_I^2},$$

$$\mathrm{Re}\left[\frac{q(t) - \Delta_c}{\varepsilon}\right] = \left(\frac{q_R - \Delta_c}{\varepsilon_R}\right)\left(\frac{\varepsilon_R^2 + q_I^2}{\varepsilon_R^2 + \varepsilon_I^2}\right),$$

$$\mathrm{Im}\left[\frac{q(t) - \Delta_c}{\varepsilon}\right] = \left(\frac{q_I}{\varepsilon_R}\right)\left(\frac{\varepsilon_R^2 - \varepsilon_0^2 + \Delta_s^2}{\varepsilon_R^2 + \varepsilon_I^2}\right),$$

$$\left(q_R - \Delta_c\right)^2 = \varepsilon_0^2 - \Delta_s^2.$$

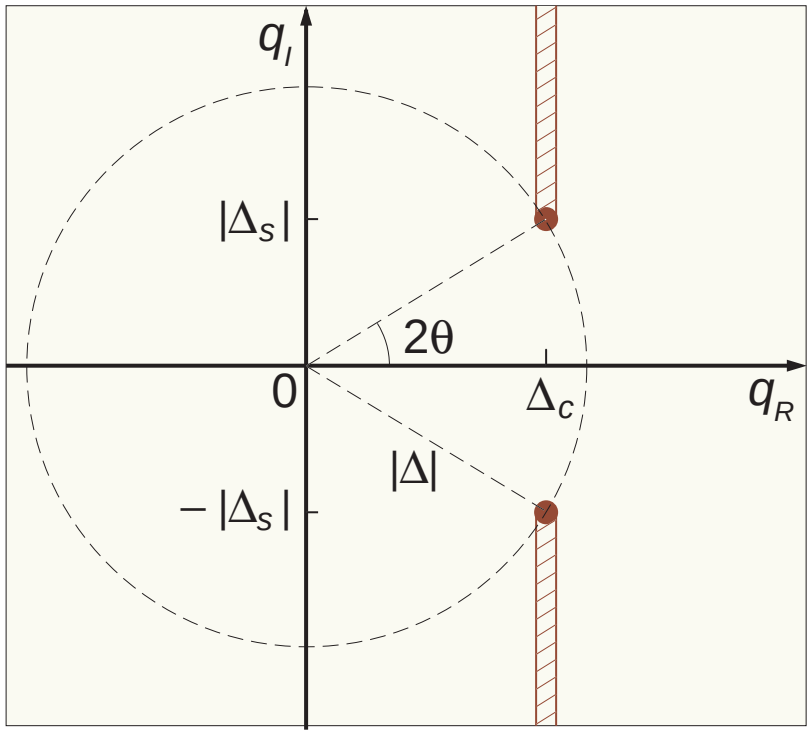

Zeros and cuts of ε in the q plane for $\Delta_c > 0$. The cuts are placed outside the circle $|q| \leq |\Delta|$ parallel to axis $q_R = 0$. The MSW resonance point is $(\Delta_c, 0)$ and the two "super-resonance" points are $(\Delta_c, \pm\Delta_s)$.

23.6.2 Eigenstates.

In order to simplify the solution to the eigenstate problem we'll assume that the phase trajectory $q = q(t)$ does not cross the points $q_\pm$ at any t. In non-Hermitian quantum dynamics one has to consider the two pairs of instantaneous eigenvectors $|\Psi_\pm\rangle$ and $|\overline{\Psi}_\pm\rangle$ which obey the relations

$$\mathbf{H}|\Psi_\pm\rangle = \pm\varepsilon|\Psi_\pm\rangle \quad \text{and} \quad \mathbf{H}^\dagger|\overline{\Psi}_\pm\rangle = \pm\varepsilon^*|\overline{\Psi}_\pm\rangle. \tag{167}$$

and (for $q \neq q_\pm$) form a complete bi-orthogonal and bi-orthonormal set,

$$\langle\overline{\Psi}_\pm|\Psi_\pm\rangle = 1, \quad \langle\overline{\Psi}_\pm|\Psi_\mp\rangle = 0, \quad |\Psi_+\rangle\langle\overline{\Psi}_+| + |\Psi_-\rangle\langle\overline{\Psi}_-| = \mathbf{1}.$$

Therefore, the eigenvectors are defined to the accuracy of a very general gauge transformation $|\Psi_\pm\rangle \longmapsto e^{if_\pm}|\Psi_\pm\rangle$, $|\overline{\Psi}_\pm\rangle \longmapsto e^{-if_\pm^*}|\overline{\Psi}_\pm\rangle$, with arbitrary complex functions $f_\pm(t)$ such that $\mathrm{Im}\,(f_\pm)$ vanish as $q = 0$.[a] Thus it is sufficient to find any particular solution of Eqs. (167). Taking into account that $\mathbf{H}^\dagger = \mathbf{H}^*$, we may set $|\overline{\Psi}_\pm\rangle = |\Psi_\pm^*\rangle$ and hence the eigenvectors can be found from the identity

$$\mathbf{H} = \varepsilon|\Psi_+\rangle\langle\Psi_+^*| - \varepsilon|\Psi_-\rangle\langle\Psi_-^*|.$$

Setting $|\Psi_\pm\rangle = (v_\pm, \pm v_\mp)^T$ we arrive at the equations

$$v_\pm^2 = \frac{\varepsilon \pm (q - \Delta_c)}{2\varepsilon}, \quad v_+v_- = \frac{\Delta_s}{2\varepsilon},$$

a particular solution of which can be written as

$$v_+ = \sqrt{\left|\frac{\varepsilon + q - \Delta_c}{2\varepsilon}\right|}\, e^{i(\varphi-\psi)/2}, \quad v_- = \zeta\sqrt{\left|\frac{\varepsilon - q + \Delta_c}{2\varepsilon}\right|}\, e^{i(-\varphi-\psi)/2}.$$

[a] For our purposes, the class of gauge functions can be restricted without loss of generality by the condition $f_\pm|_{q=0} = 0$.

where

$$\varphi = \arg(\varepsilon + q - \Delta_c) = -\arg(\varepsilon - q + \Delta_c) = \arctan\left(\frac{q_I}{\varepsilon_R}\right), \quad \psi = \arg(\varepsilon) = \arctan\left(\frac{\varepsilon_I}{\varepsilon_R}\right).$$

We have fixed the remaining gauge ambiguity by a comparison with the vacuum case.

23.6.3 Mixing angle in matter.

It is useful to define the complex mixing angle in matter $\Theta = \Theta_R + i\Theta_I$ by the relations

$$\sin\Theta = v_+ \text{ and } \cos\Theta = v_- \quad \text{or, equivalently,} \quad \sin 2\Theta = \frac{\Delta_s}{\varepsilon} \text{ and } \cos 2\Theta = \frac{\Delta_c - q}{\varepsilon}.$$

The real and imaginary parts of Θ are found to be

$$\mathrm{Re}(\Theta) \equiv \Theta_R = \frac{1}{2}\arctan\left[\frac{(q_I - \Delta_s)\,\varepsilon_R - (q_R - \Delta_c)\,\varepsilon_I}{(q_R - \Delta_c)\,\varepsilon_R + (q_I - \Delta_s)\,\varepsilon_I}\right],$$

$$\mathrm{Im}(\Theta) \equiv \Theta_I = \frac{1}{4}\ln\left[\frac{\varepsilon_R^2 + \varepsilon_I^2}{(q_R - \Delta_c)^2 + (q_I - \Delta_s)^2}\right].$$

$$\cos\Theta = \cos\Theta_R \cosh\Theta_I - i\sin\Theta_R \sinh\Theta_I,$$
$$\sin\Theta = \sin\Theta_R \cosh\Theta_I + i\cos\Theta_R \sinh\Theta_I.$$

Having regard to the prescription for the sign of ε_R, one can verify that $\Theta = \theta$ if $q = 0$ (vacuum case) and $\Theta = 0$ if $\Delta_s = 0$ (no mixing or $m_1^2 = m_2^2$). It is also clear that Θ becomes the standard MSW mixing angle with $\mathrm{Im}(\Theta) = 0$ when $q_I = 0$ ($\Lambda_\alpha = \Lambda_\beta$).

23.6.4 Mixing matrix in matter.

In order to build up the solution to ME for the nondegenerated case one has to diagonalize the Hamiltonian. Generally a non-Hermitian matrix cannot be diagonalized by a single unitary transformation. But in our simple case this can be done by a complex orthogonal matrix (extended mixing matrix in matter)

$$\mathbf{U}_f = \mathbf{U}\exp(i\mathbf{f}),$$

where $\mathbf{f} = \mathrm{diag}\,(f_-, f_+)$ and

$$\mathbf{U} = (|\Psi_-\rangle, |\Psi_+\rangle) = \begin{pmatrix} v_- & v_+ \\ -v_+ & v_- \end{pmatrix}$$

$$= \begin{pmatrix} \cos\Theta & \sin\Theta \\ -\sin\Theta & \cos\Theta \end{pmatrix}.$$

Properties of $\mathbf{U}$:

$$\mathbf{U}^T\mathbf{H}\mathbf{U} = \mathrm{diag}\,(-\varepsilon, \varepsilon),$$
$$\mathbf{U}^T\mathbf{U} = \mathbf{1}, \quad \mathbf{U}|_{q=0} = \mathbf{V}.$$

From CE it follows that

$$\frac{\partial\varepsilon}{\partial q} = \frac{(q-\Delta_c)}{\varepsilon}$$

and thus

$$\frac{\partial v_\pm}{\partial q} = \pm\frac{\Delta_s^2 v_\mp}{2\varepsilon^2}.$$

We therefore have

$$i\mathbf{U}^T\dot{\mathbf{U}} = -\Omega\begin{pmatrix} 0 & -i \\ i & 0 \end{pmatrix} = -\Omega\boldsymbol{\sigma}_2,$$

$$\Omega = \frac{\dot{q}\Delta_s}{2\varepsilon^2} = \frac{i}{4}\frac{d}{dt}\ln\left(\frac{q-q_+}{q-q_-}\right).$$

Properties of $\mathbf{U}_f$:

$$\mathbf{U}_f^T\mathbf{H}\mathbf{U}_f = \mathrm{diag}\,(-\varepsilon, \varepsilon),$$
$$\mathbf{U}_f^T\mathbf{U}_f = \mathbf{1}, \quad \mathbf{U}_f|_{q=0} = \mathbf{V},$$
$$i\mathbf{U}_f^T\dot{\mathbf{U}}_f = -\Omega e^{-i\mathbf{f}}\boldsymbol{\sigma}_2 e^{i\mathbf{f}} - \dot{\mathbf{f}}.$$

23.7 Adiabatic solution.

Formal solution to ME in the most general form:

$$\widetilde{\mathbf{S}}(t) = \mathbf{U}_f(t) \exp\left[-i\mathbf{\Phi}(t)\right] \mathbf{X}_f(t) \mathbf{U}_f^T(0). \tag{168}$$

Here $\mathbf{\Phi}(t) = \mathrm{diag}\left(-\Phi(t), \Phi(t)\right)$ and $\Phi(t) = \Phi_R(t) + i\Phi_I(t)$ is the complex dynamical phase, defined by

$$\Phi_R(t) = \int_0^t \varepsilon_R(t')dt', \quad \Phi_I(t) = \int_0^t \varepsilon_I(t')dt',$$

and $\mathbf{X}_f(t)$ must satisfy the equation

$$i\dot{\mathbf{X}}_f(t) = \left[\Omega(t) e^{-i\mathbf{f}(t)} \mathbf{F}(t) e^{i\mathbf{f}(t)} + \dot{\mathbf{f}}(t)\right] \mathbf{X}_f(t), \quad \mathbf{X}_f(0) = \mathbf{1},$$

where

$$\mathbf{F}(t) = e^{i\mathbf{\Phi}(t)} \boldsymbol{\sigma}_2 e^{-i\mathbf{\Phi}(t)} = \begin{pmatrix} 0 & -ie^{-2i\Phi(t)} \\ ie^{2i\Phi(t)} & 0 \end{pmatrix}.$$

It can be proved now that the right side of Eq. (168) is gauge-invariant i.e. it does not depend on the unphysical complex phases $f_\pm(t)$. This crucial fact is closely related to the absence of the Abelian topological phases in the system under consideration.

Finally, we can put $f_\pm = 0$ in Eq. (168) and the result is

$$\widetilde{\mathbf{S}}(t) = \mathbf{U}(t) \exp\left[-i\mathbf{\Phi}(t)\right] \mathbf{X}(t) \mathbf{U}^T(0), \tag{169a}$$

$$i\dot{\mathbf{X}}(t) = \Omega(t)\mathbf{F}(t)\mathbf{X}(t), \quad \mathbf{X}(0) = \mathbf{1}. \tag{169b}$$

These equations, being equivalent to the ME, have nevertheless a restricted range of practical usage on account of poles and cuts as well as decaying and increasing exponents in the "Hamiltonian" $\Omega\mathbf{F}$.

23.7.1 Adiabatic theorem.

The adiabatic theorem of Hermitian quantum mechanics can almost straightforwardly be extended to ME under the following requirements:

(a) the potential q is a sufficiently smooth and slow function of t;
(b) the imaginary part of the dynamical phase is a bounded function i.e. $\lim_{t\to\infty} |\Phi_I(t)|$ is finite;
(c) the phase trajectory $q = q(t)$ is placed far from the singularities for any t.

The first requirement breaks down for a condensed medium with a sharp boundary or layered structure (like the Earth, see next slide). If however the requirement (a) is valid inside each layer (t_i, t_{i+1}), the problem reduces to Eqs. (169) by applying the rule

$$\widetilde{\mathbf{S}}(t) \equiv \widetilde{\mathbf{S}}(t,0) = \widetilde{\mathbf{S}}\,(t,t_n)\ldots\widetilde{\mathbf{S}}\,(t_2,t_1)\,\widetilde{\mathbf{S}}\,(t_1,0),$$

where $\widetilde{\mathbf{S}}\,(t_{i+1},t_i)$ is the time-evolution operator for the i-th layer.

- The requirement (b) alone is not too restrictive considering that for many astrophysical objects (like stars, galactic nuclei, jets and so on) the density ρ exponentially disappears to the periphery and, on the other hand, $\varepsilon_I \to 0$ as $\rho \to 0$. In this instance, the function $\Phi_I(t)$ must be t independent for sufficiently large t.
- But, in the case of a steep density profile, the requirements (a) and (b) may be inconsistent.
- The important case of violation of the requirement (c) is the subject of a special study which is beyond the scope of our lectures.

It is interesting to note in this connection that, in the Hermitian case, a general adiabatic theorem has been proved without the traditional gap condition.[a]

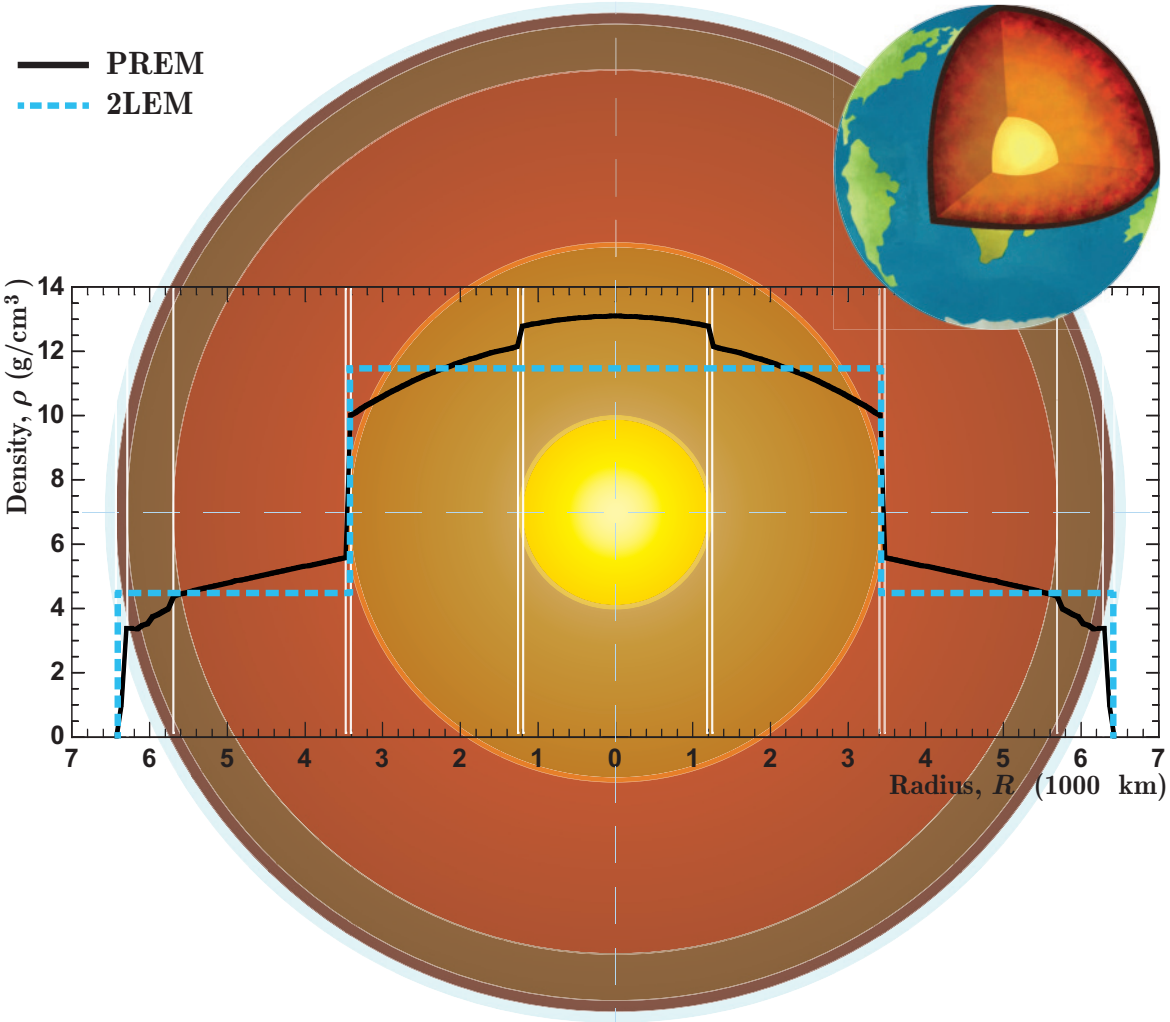

◁ Density profiles in Earth according to the Preliminary Reference Earth Model (PREM, see Sect. **5.1**, p. 197) and (super)simplified Two-Layer Earth Model (2LEM).

To ensure good accuracy, it is usually necessary to break down the PREM layers into dozens of sublayers with mean densities estimated using, e.g., Simpson's quadrature rule

$$\begin{aligned}\langle \rho_i \rangle &= \frac{1}{t_{i+1} - t_i} \int_{t_i}^{t_{i+1}} \rho(t')dt' \\ &\approx \frac{1}{6}\left[\rho\left(t_i\right) + \rho\left(t_{i+1}\right)\right] \\ &\quad + \frac{2}{3}\rho\left(\frac{t_i + t_{i+1}}{2}\right).\end{aligned}$$

[a] J. E. Avron & A. Elgart, "Adiabatic theorem without a gap condition," Commun. Math. Phys. **203** (1999) 445–467, math-ph/9805022.

23.7.2 The solution.

Presume that all necessary conditions do hold for $0 \le t \le T$. Then, in the adiabatic limit, we can put $\Omega = 0$ in Eq. (169b). Therefore $\mathbf{X} = \mathbf{1}$ and Eq. (169a) yields

$$\begin{aligned}
\widetilde{S}_{\alpha\alpha}(t) &= v_+(0)v_+(t)e^{-i\Phi(t)} + v_-(0)v_-(t)e^{i\Phi(t)},\\
\widetilde{S}_{\alpha\beta}(t) &= v_-(0)v_+(t)e^{-i\Phi(t)} - v_+(0)v_-(t)e^{i\Phi(t)},\\
\widetilde{S}_{\beta\alpha}(t) &= v_+(0)v_-(t)e^{-i\Phi(t)} - v_-(0)v_+(t)e^{i\Phi(t)},\\
\widetilde{S}_{\beta\beta}(t) &= v_-(0)v_-(t)e^{-i\Phi(t)} + v_+(0)v_+(t)e^{i\Phi(t)},
\end{aligned}$$

Taking into account Eq. (166) we obtain the survival and transition probabilities:

$$\begin{aligned}
P_{\alpha\alpha}(t) &= A(t)\left\{\left[I_+^+(t)e^{\Phi_I(t)} + I_-^-(t)e^{-\Phi_I(t)}\right]^2 - I^2(t)\sin^2\left[\Phi_R(t) - \varphi_+(t)\right]\right\},\\
P_{\alpha\beta}(t) &= A(t)\left\{\left[I_+^-(t)e^{\Phi_I(t)} - I_-^+(t)e^{-\Phi_I(t)}\right]^2 + I^2(t)\sin^2\left[\Phi_R(t) - \varphi_-(t)\right]\right\},\\
P_{\beta\alpha}(t) &= A(t)\left\{\left[I_-^+(t)e^{\Phi_I(t)} - I_+^-(t)e^{-\Phi_I(t)}\right]^2 + I^2(t)\sin^2\left[\Phi_R(t) + \varphi_-(t)\right]\right\},\\
P_{\beta\beta}(t) &= A(t)\left\{\left[I_-^-(t)e^{\Phi_I(t)} + I_+^+(t)e^{-\Phi_I(t)}\right]^2 - I^2(t)\sin^2\left[\Phi_R(t) + \varphi_+(t)\right]\right\},
\end{aligned} \tag{170}$$

where we have denoted for compactness ($\varsigma, \varsigma' = \pm$)

$$I_\varsigma^{\varsigma'}(t) = |v_\varsigma(0)v_{\varsigma'}(t)|, \quad \varphi_\pm(t) = \frac{\varphi(0) \pm \varphi(t)}{2},$$

$$I^2(t) = 4I_+^+(t)I_-^-(t) = 4I_+^-(t)I_-^+(t) = \frac{\Delta_s^2}{|\varepsilon(0)\varepsilon(t)|}.$$

23.7.3 Limiting cases.

MSW limit.

In the event that the conditions

$$\left|\frac{1}{\Lambda_\beta(t)}-\frac{1}{\Lambda_\alpha(t)}\right| \ll 4\varepsilon_0(t) \quad \text{and} \quad t \ll \min\left[\Lambda_\alpha(t),\Lambda_\beta(t)\right]$$

are satisfied for any $t\in[0,T]$, the formulas (170) reduce to the standard MSW adiabatic solution

$$\left.\begin{aligned} P_{\alpha\alpha}(t) = P_{\beta\beta}(t) &= \frac{1}{2}\left[1+J(t)\right]-I_0^2(t)\sin^2\left[\Phi_0(t)\right],\\ P_{\alpha\beta}(t) = P_{\beta\alpha}(t) &= \frac{1}{2}\left[1-J(t)\right]+I_0^2(t)\sin^2\left[\Phi_0(t)\right],\end{aligned}\right\} \qquad \text{(MSW)}$$

where

$$J(t)=\frac{\Delta^2-\Delta_c\left[q_R(0)+q_R(t)\right]+q_R(0)q_R(t)}{\varepsilon_0(0)\varepsilon_0(t)},$$

$$I_0^2(t)=\frac{\Delta_s^2}{\varepsilon_0(0)\varepsilon_0(t)}, \quad \Phi_0(t)=\int_0^t \varepsilon_0(t')dt'.$$

Needless to say either of the above conditions or both may be violated for sufficiently high neutrino energies and/or for thick media, resulting in radical differences between the two solutions. These differences are of obvious interest to high-energy neutrino astrophysics.

Below, we consider a few illustrations of the "classical" MSW for the 3ν oscillations in Earth.

Numerical examples: 3ν MSW in Earth.

Here we present, without written explanations, some numerical results obtained for 3ν oscillations in the Earth. Of course, at the energies in question ($E_\nu < 1$ TeV), the absorption effect is completely insignificant.

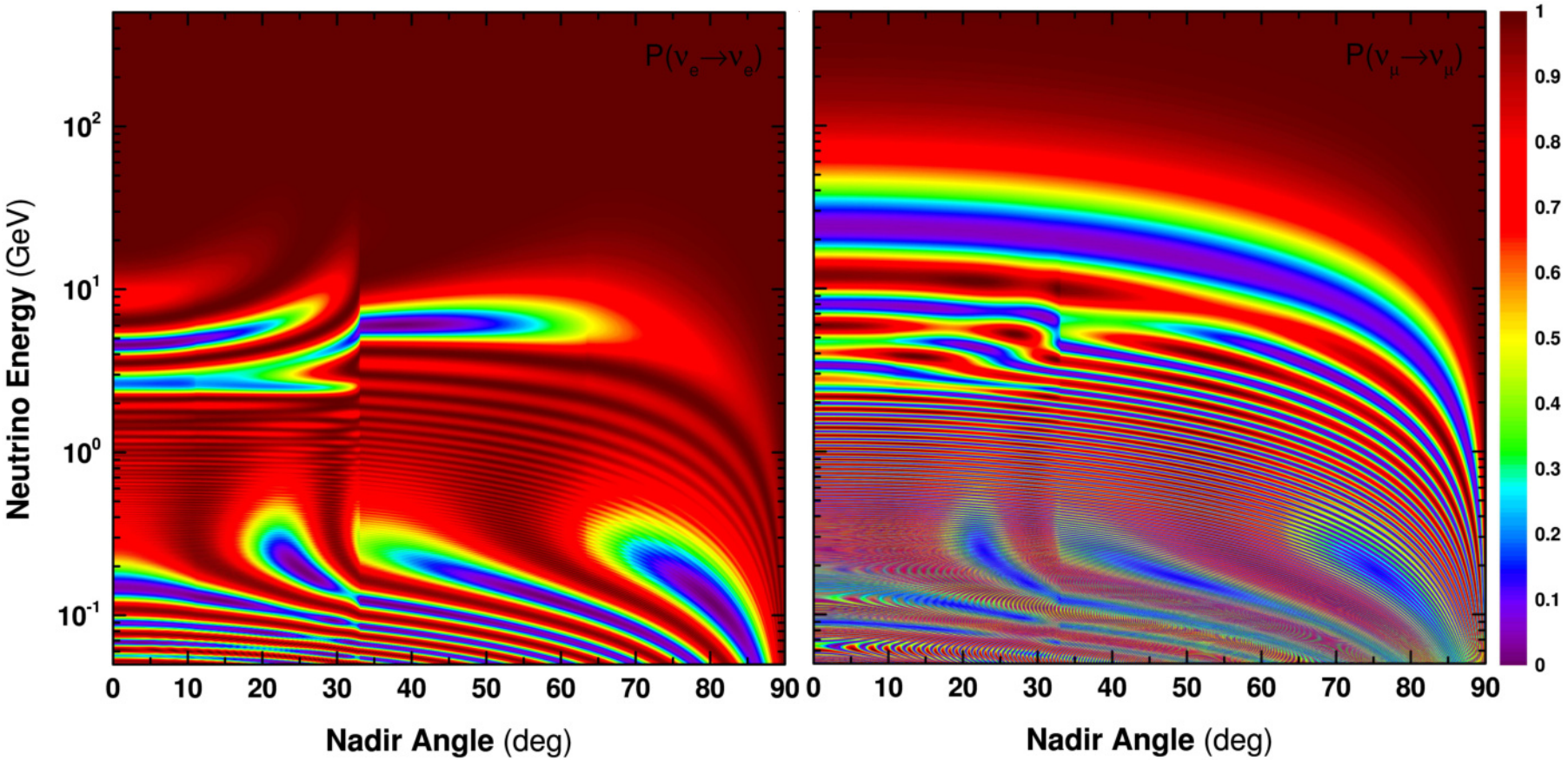

Survival probabilities in Earth for electron (*left panel*) and muon (*right panel*) neutrinos vs. nadir angle and neutrino energy.

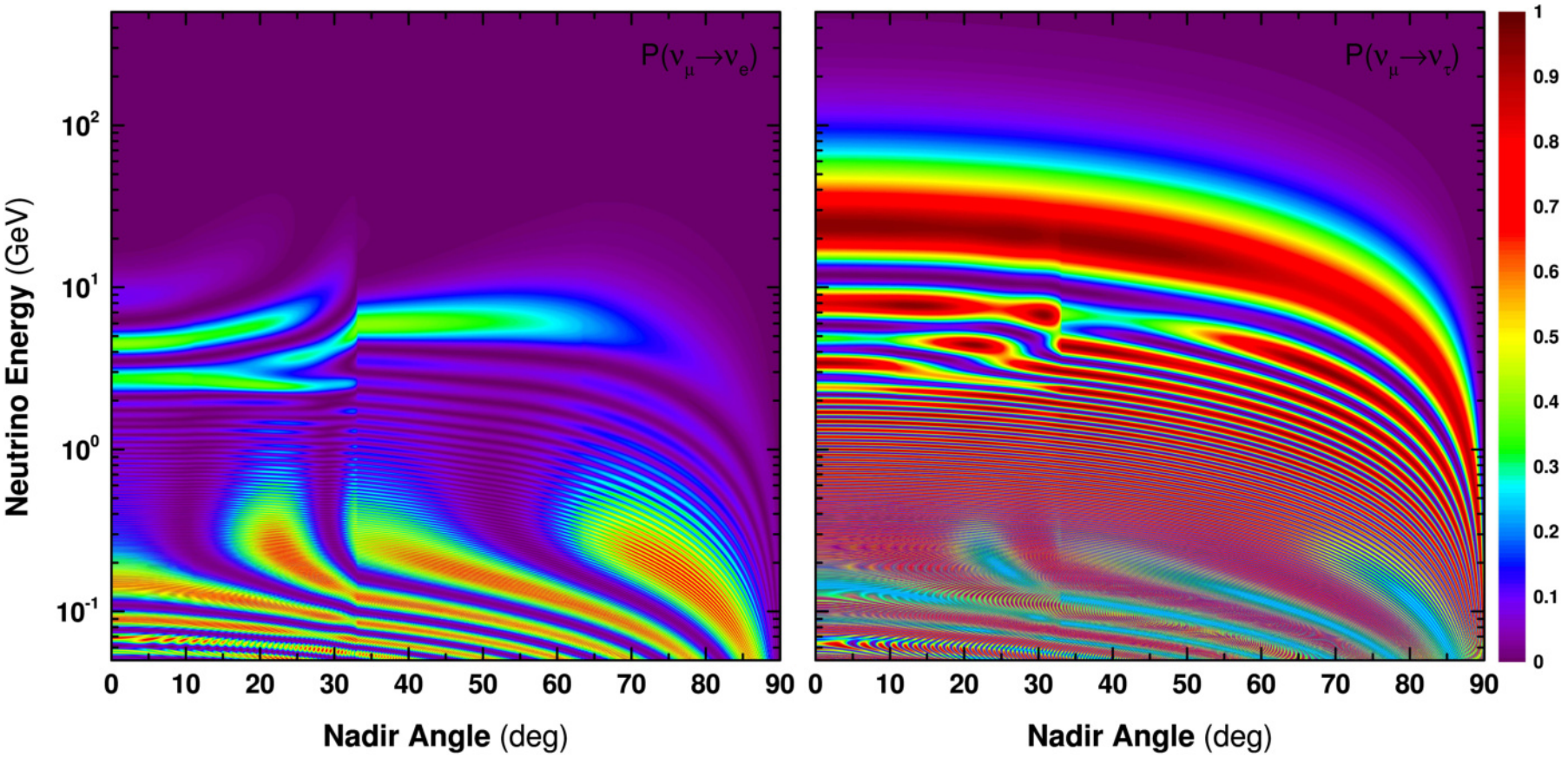

Transition probabilities $P_{\mu e}$ (*left panel*) and $P_{\mu\tau}$ (*right panel*) in Earth vs. nadir angle and neutrino energy.

The calculations were performed with somewhat outdated values of the oscillation parameters, but this will not have a qualitative effect on the neutrino oscillation patterns. The density distribution in the Earth is taken according to the PREM model (see Sect. **5.1**, p. 197).

Diagrams of this kind are called oscillograms. More such oscillograms can be found on the web page ⟨ http://theor.jinr.ru/NeutrinoOscillations/ ⟩.

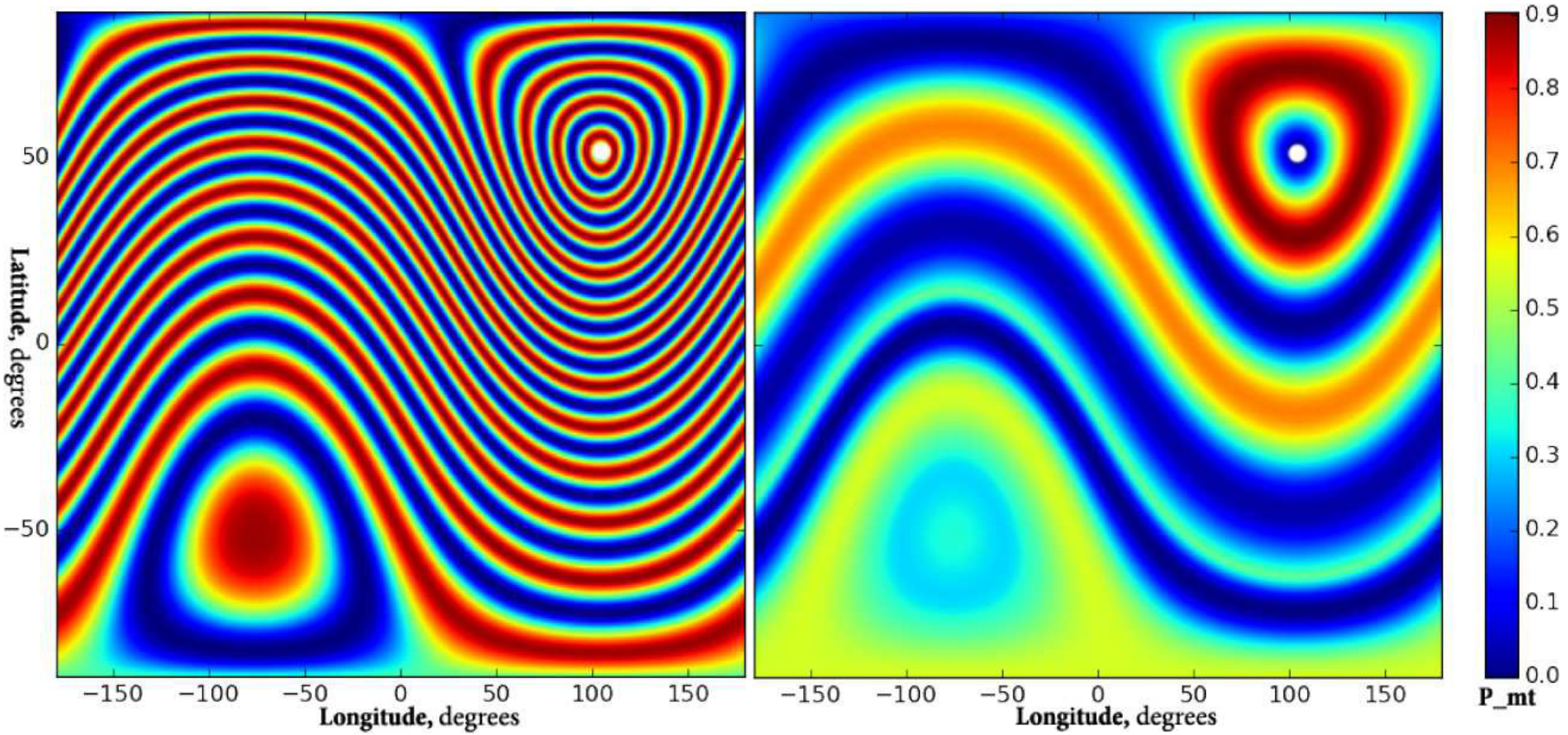

Transition probability $P_{\mu\tau}$ in Earth vs. longitude and latitude for neutrino energies $E_\nu = 1$ GeV (*left panel*) and 5 GeV (*right panel*). The reference point is the NT telescope at lake Baikal (position is shown by white point). That is, it is assumed that neutrinos come to the reference point from all the points shown on the oscillogram.

Calculations are made by I. Shandrov (2016) using so-called Multi-Model Earth Density Approach (MMEDA), which is a combination of CRUST 1.0 for the Earth's crust and PREM for the rest of the Earth.

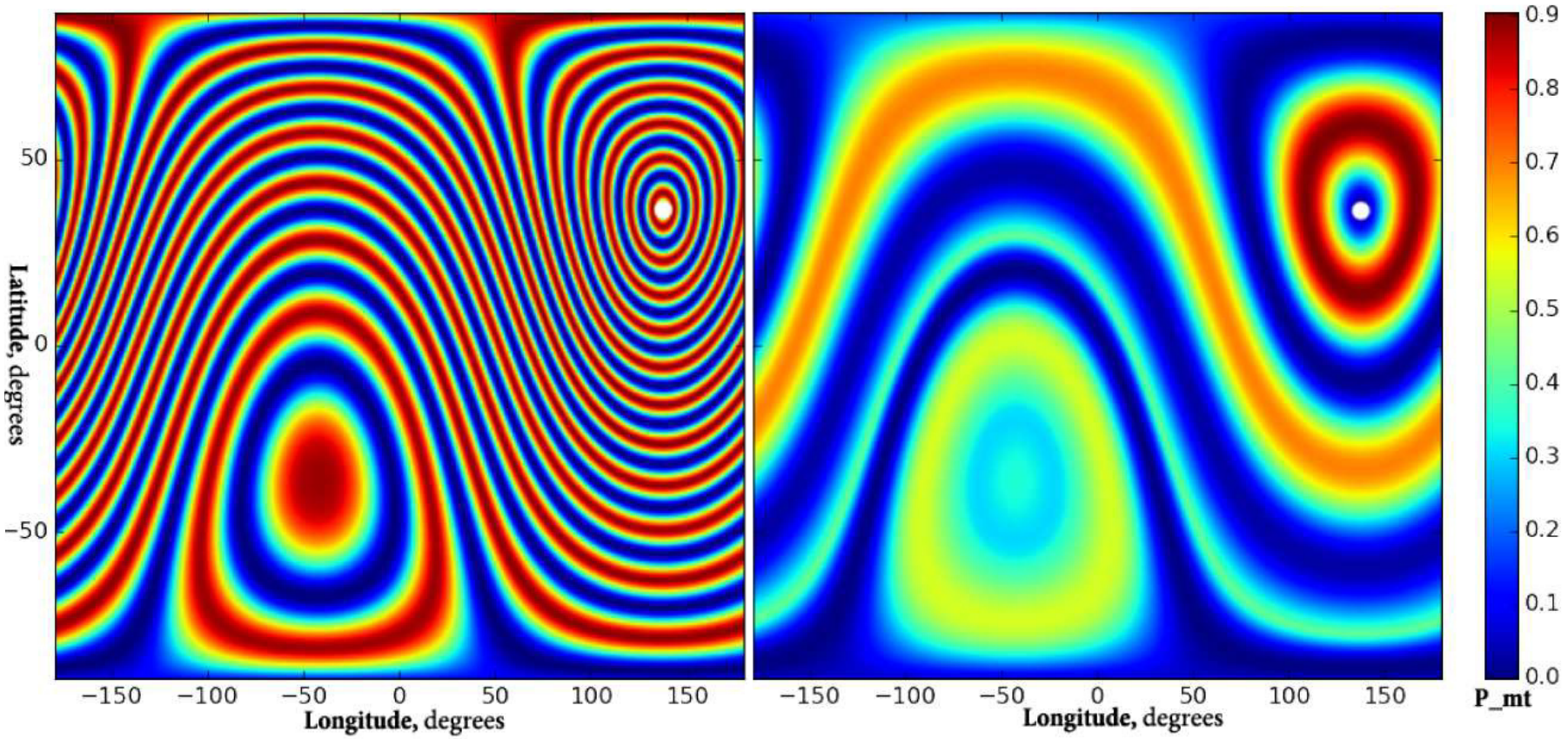

Transition probability $P_{\mu\tau}$ in Earth vs. longitude and latitude for neutrino energies $E_\nu = 1$ GeV (*left panel*) and 5 GeV (*right panel*). The reference point is the Underground neutrino detector Super-Kamiokande at Kamioka (position is shown by white point).

Classical limit.

It is perhaps even more instructive in the context of the neutrino absorption effect, to examine the distinctions between the general adiabatic solution (170) and its "classical limit", in which one can neglect neutrino mixing.

$$\left.\begin{aligned} P_{\alpha\alpha}(t) &= \exp\left[-\int_0^t \frac{dt'}{\Lambda_\alpha(t')}\right], \quad P_{\alpha\beta}(t) = 0, \\ P_{\beta\beta}(t) &= \exp\left[-\int_0^t \frac{dt'}{\Lambda_\beta(t')}\right], \quad P_{\beta\alpha}(t) = 0, \end{aligned}\right\} \qquad (\Delta_s = 0)$$

which takes place either in the absence of mixing or for $m_1^2 = m_2^2$.

Note:

Considering that $\Omega \propto \Delta_s$, the classical limit is the exact solution to the master equation (for $\Delta_s = 0$). Therefore it can be derived directly from Eq. (165). To make certain that the adiabatic solution has correct classical limit, the following relations are useful:

$$\lim_{\Delta_s \to 0} \varepsilon(t) = \zeta\zeta_R \left[q(t) - \Delta_c\right] \quad \text{and} \quad \lim_{\Delta_s \to 0} |v_\pm(t)|^2 = \frac{1}{2}\left(\zeta\zeta_R \pm 1\right),$$

where $\zeta_R = \text{sign}\left[q_R(t) - \Delta_c\right]$.

We have already discussed an example of an oscillogram calculated for the 3ν oscillation in Earth in Sect. **7.14**, p. 336. In the calculation shown at p. 337, the neutrino regeneration, which is not considered in this section, is also taken into account.

23.8 Matter of constant density and composition.

In this simple case, the adiabatic approximation becomes exact and thus free from the above-mentioned conceptual difficulties. For definiteness sake we assume $\Lambda_\alpha < \Lambda_\beta$ (and thus $q_I < 0$) from here. The opposite case can be considered in a similar way. Let's denote

$$\frac{1}{\Lambda_\pm} = \frac{1}{2}\left(\frac{1}{\Lambda_\alpha} + \frac{1}{\Lambda_\beta}\right) \pm \frac{\xi}{2}\left(\frac{1}{\Lambda_\alpha} - \frac{1}{\Lambda_\beta}\right), \quad I_\pm^2 = \frac{1}{4}\left(1 + \frac{\varepsilon_0^2 + q_I^2 - \Delta_s^2}{\varepsilon_R^2 + \varepsilon_I^2}\right) \pm \frac{\xi}{2}\left(\frac{\varepsilon_R^2 + q_I^2}{\varepsilon_R^2 + \varepsilon_I^2}\right),$$

$$L = \frac{\pi}{|\varepsilon_R|} \quad \text{and} \quad \xi = \left|\frac{q_R - \Delta_c}{\varepsilon_R}\right|.$$

As can be easily verified,

$$I_\pm^\pm = \begin{cases} I_\pm & \text{if} \quad \mathsf{sign}\,(q_R - \Delta_c) = +\zeta, \\ I_\mp & \text{if} \quad \mathsf{sign}\,(q_R - \Delta_c) = -\zeta, \end{cases} \qquad I_+^- = I_-^+ = \sqrt{I_+ I_-} = \frac{I}{2} = \left|\frac{\Delta_s}{2\varepsilon}\right|, \quad \text{and} \quad \mathsf{sign}(\varphi) = -\zeta.$$

By applying the above identities, the neutrino oscillation probabilities can be written as

$$\boxed{\begin{aligned} P_{\alpha\alpha}(t) &= \left(I_+ e^{-t/2\Lambda_+} + I_- e^{-t/2\Lambda_-}\right)^2 - I^2 e^{-t/\Lambda} \sin^2\left(\frac{\pi t}{L} + |\varphi|\right), \\ P_{\beta\beta}(t) &= \left(I_- e^{-t/2\Lambda_+} + I_+ e^{-t/2\Lambda_-}\right)^2 - I^2 e^{-t/\Lambda} \sin^2\left(\frac{\pi t}{L} - |\varphi|\right), \\ P_{\alpha\beta}(t) &= P_{\beta\alpha}(t) = \frac{1}{4} I^2 \left(e^{-t/2\Lambda_-} - e^{-t/2\Lambda_+}\right)^2 + I^2 e^{-t/\Lambda} \sin^2\left(\frac{\pi t}{L}\right). \end{aligned}}$$

$$P_{\alpha\alpha}(t) - P_{\beta\beta}(t) = -\zeta \mathsf{Re}\left(\frac{q - \Delta_c}{\varepsilon}\right)\left(e^{-t/2\Lambda_-} - e^{-t/2\Lambda_+}\right) + I^2 e^{-t/\Lambda} \sin\varphi \sin\left(\frac{2\pi t}{L}\right).$$

23.8.1 Case $|q| \gtrsim |\Delta_s|$.

Let's examine the case when Λ_+ and Λ_- are vastly different in magnitude. This will be true when $\Lambda_\beta \gg \Lambda_\alpha$ and the factor ξ is not too small. The second condition holds if q_R is away from the MSW resonance value Δ_c and the following dimensionless parameter

$$\varkappa = \frac{\Delta_s}{|q|} \approx 0.033 \times \sin 2\theta \left(\frac{\Delta m^2}{10^{-3}\ \text{eV}^2}\right)\left(\frac{100\ \text{GeV}}{E_\nu}\right)\left(\frac{V_0}{|q|}\right)$$

is sufficiently small. In fact we assume $|\varkappa| \lesssim 1$ and impose no specific restriction for the ratio q_R/q_I. This spans several possibilities:

⋆ small Δm^2, ⋆ small mixing angle, ⋆ high energy, ⋆ high matter density.

The last two possibilities are of special interest because the inequality $|\varkappa| \lesssim 1$ may be fulfilled for a wide range of the parameters Δm^2 and θ by changing E_ν and/or ρ. In other words, this condition is by no means artificial or too restrictive. After elementary while a bit tedious calculations we obtain

$$\xi = 1 - \frac{1}{2}\varkappa^2 + \mathcal{O}\left(\varkappa^3\right), \quad I^2 = \varkappa^2 + \mathcal{O}\left(\varkappa^3\right), \quad I_+ = 1 + \mathcal{O}\left(\varkappa^2\right), \quad I_- = \frac{1}{4}\varkappa^2 + \mathcal{O}\left(\varkappa^3\right);$$

$$\Lambda \approx 2\Lambda_\alpha, \quad \Lambda_+ \approx \left(1 + \frac{\varkappa^2}{4}\right)\Lambda_\alpha \approx \Lambda_\alpha, \quad \Lambda_- \approx \left(\frac{4}{\varkappa^2}\right)\Lambda_\alpha \gg \Lambda_\alpha.$$

Due to the wide spread among the length/time scales $\Lambda_\pm$, Λ and L as well as among the amplitudes $I_\pm$ and I, the regimes of neutrino oscillations are quite diverse for different ranges of variable t.

With reference to Figures at pp. 682–685, one can see a regular gradation from slow (for $t \lesssim \Lambda_\mu$) to very fast (for $t \gtrsim \Lambda_\mu$) neutrino oscillations followed by the asymptotic nonoscillatory behavior:

$$P_{\mu\mu}(t) \simeq \frac{\varkappa^4}{16} e^{-t/\Lambda_-}, \quad P_{ss}(t) \simeq e^{-t/\Lambda_-}, \quad P_{\mu s}(t) = P_{s\mu}(t) \simeq \frac{\varkappa^2}{4} e^{-t/\Lambda_-}.$$

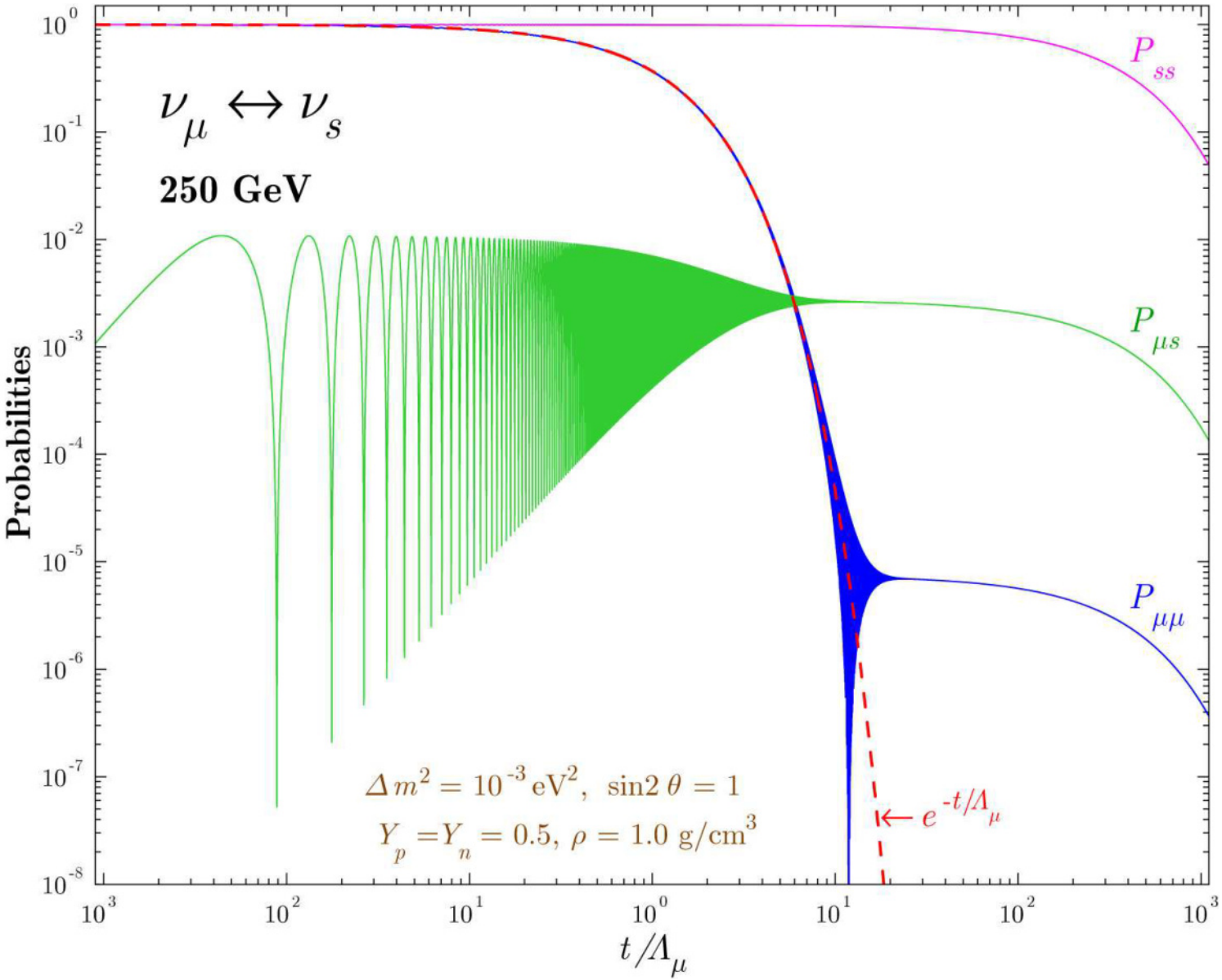

Survival and transition probabilities for $\nu_\mu \leftrightarrow \nu_s$ oscillations ($E_\nu = 250$ GeV, $\rho = 1$ g/cm^3).

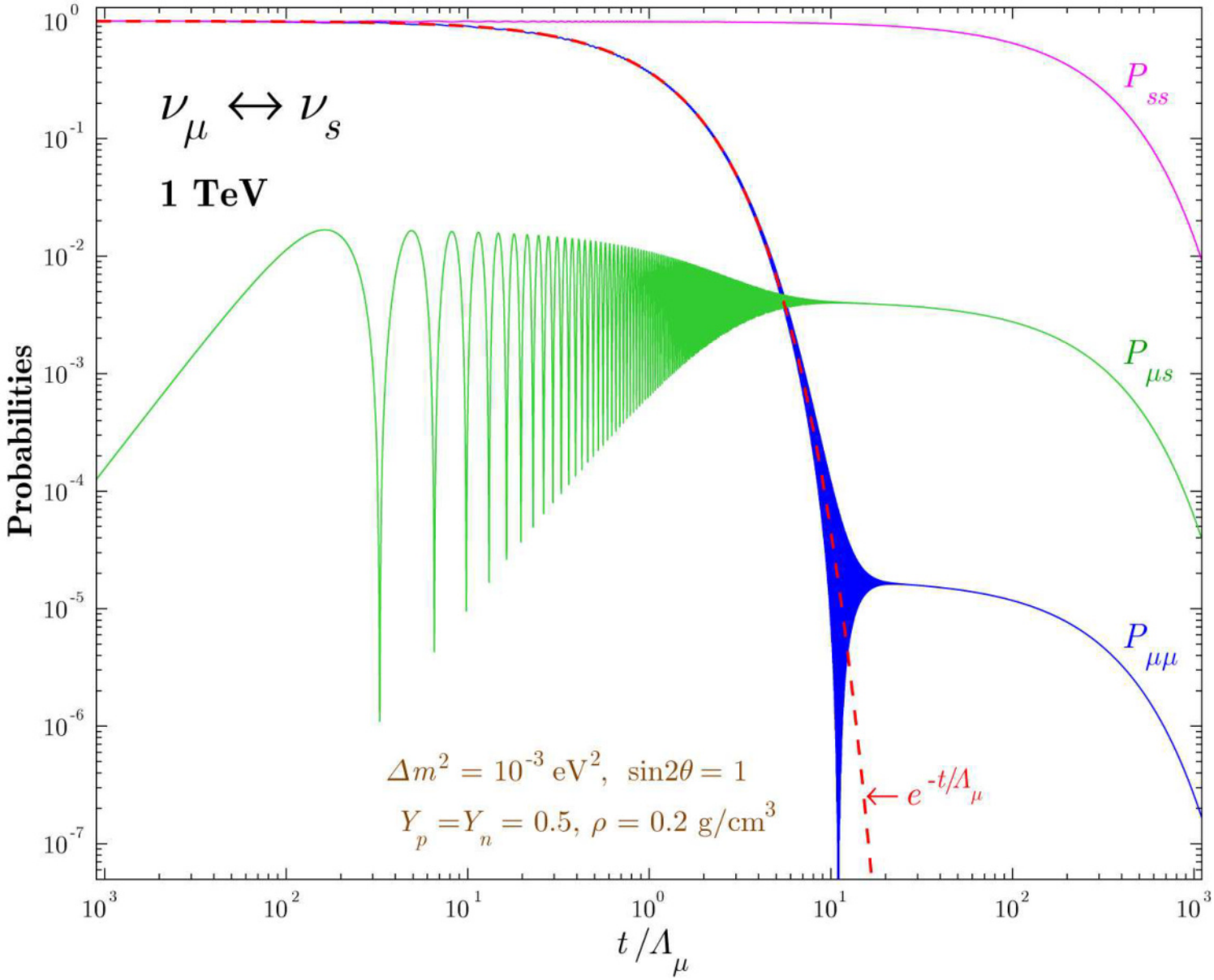

Survival and transition probabilities for $\nu_\mu \leftrightarrow \nu_s$ oscillations ($E_\nu = 1000$ GeV, $\rho = 0.2$ g/cm^3).

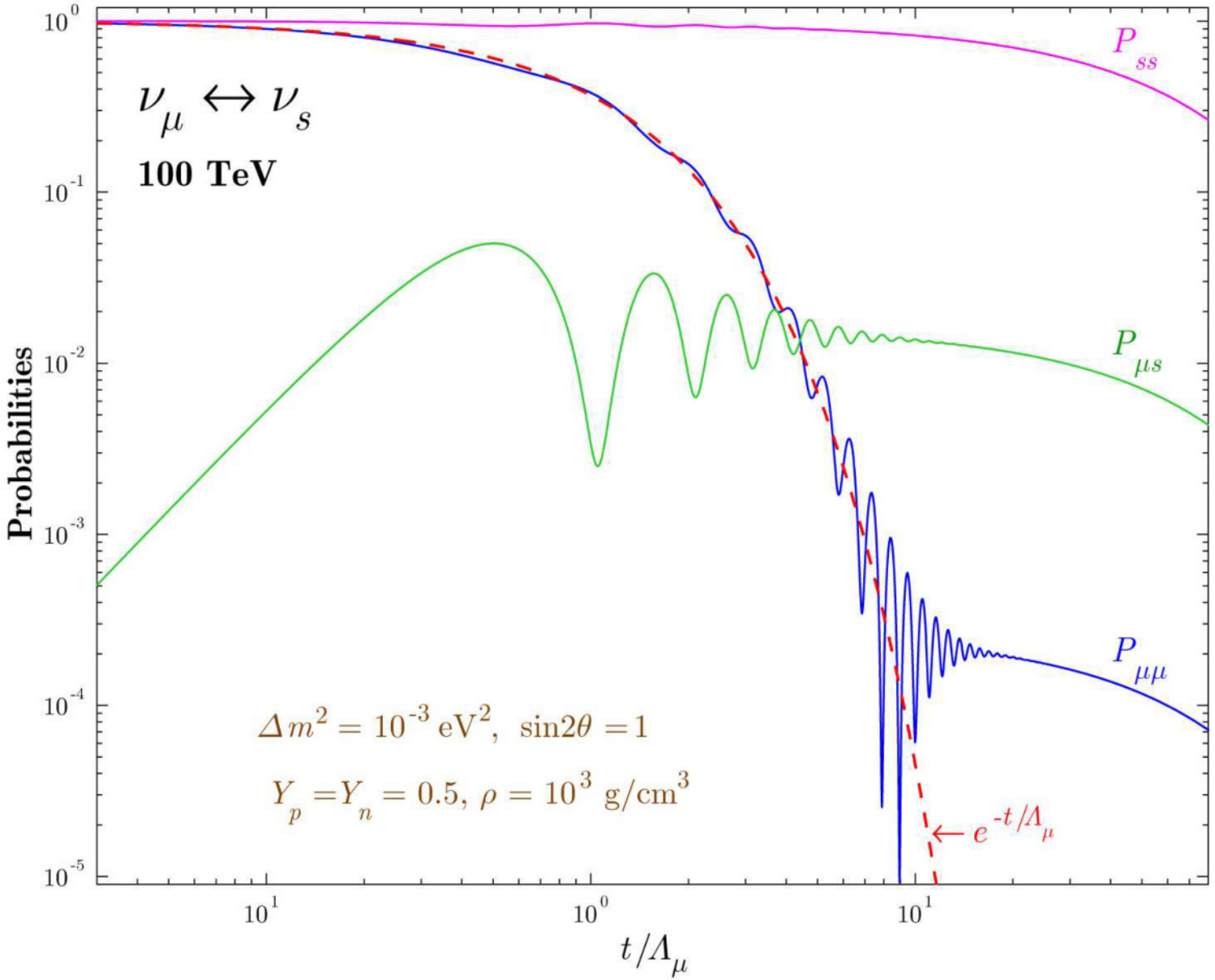

Survival and transition probabilities for $\nu_\mu \leftrightarrow \nu_s$ oscillations ($E_\nu = 100$ TeV, $\rho = 10^{-3}$ g/cm^3).

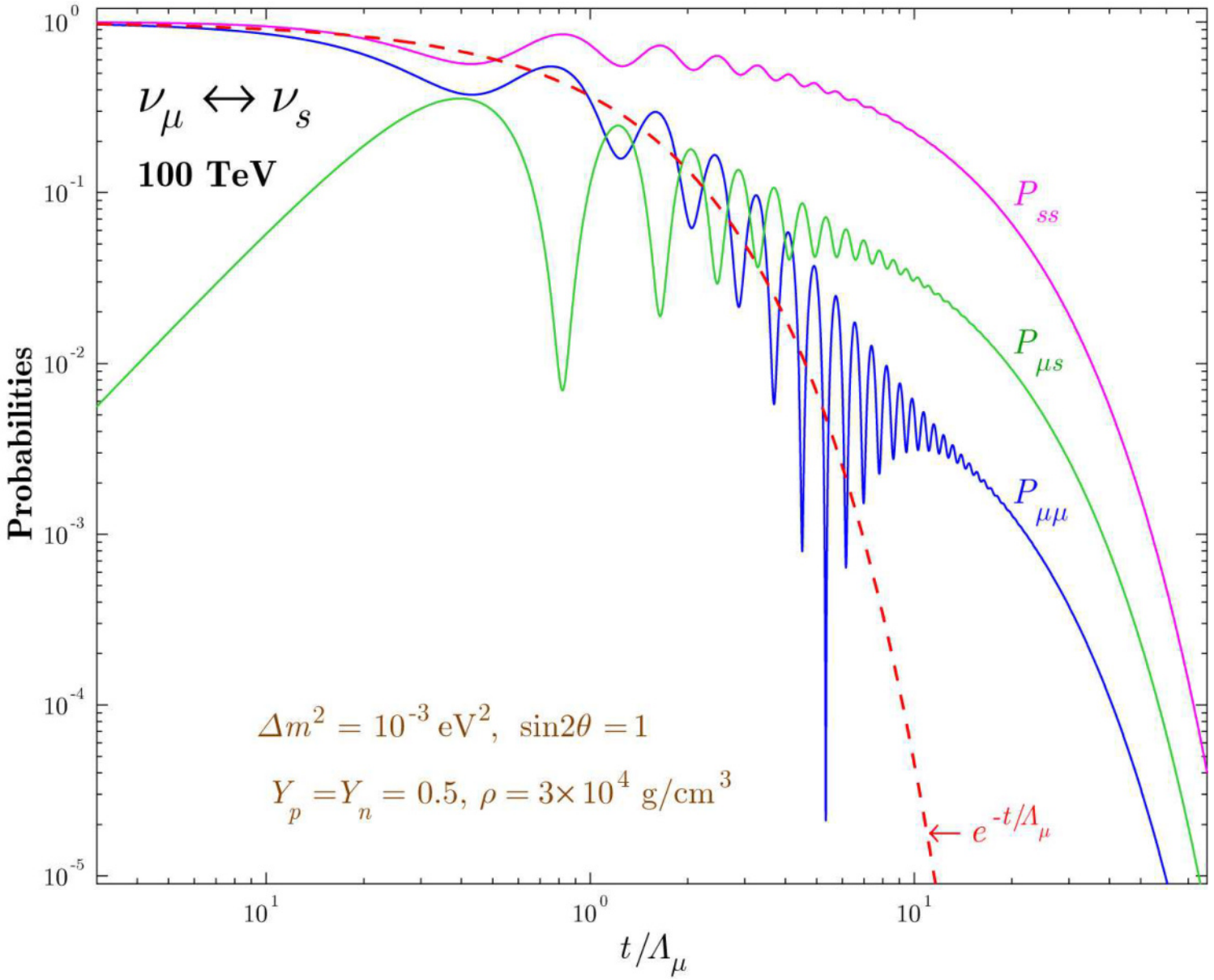

Survival and transition probabilities for $\nu_\mu \leftrightarrow \nu_s$ oscillations ($E_\nu = 100$ TeV, $\rho = 3 \times 10^{-4}$ g/cm^3).

The mechanism under discussion may be released in the Thorne–Żytkow objects (TŻO) – binaries with a neutron star submerged into a red supergiant core. Figure shows an artistic view of how a TŻO could be formed (a supergiant consumes a neutron star).[a]

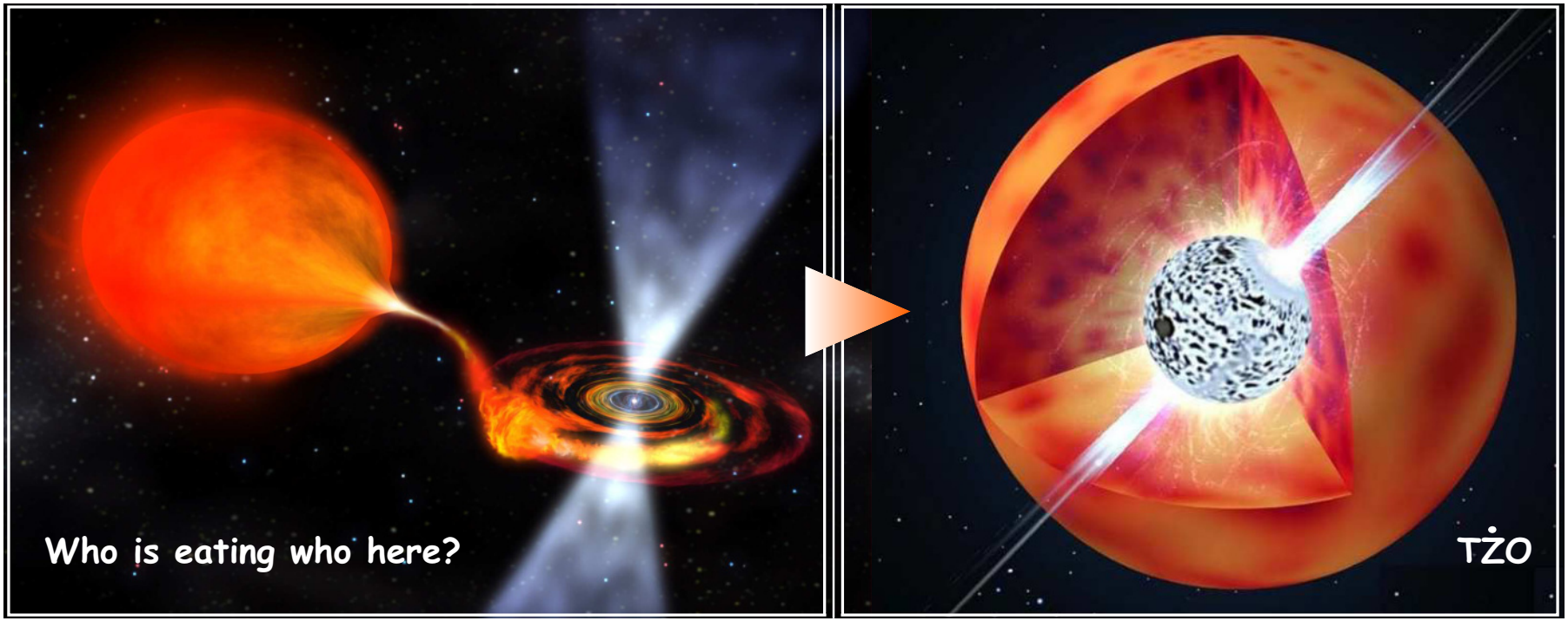

The very bright red star HV 2112 in the Small Magellanic Cloud (see next slide) could be a massive supergiant-like star with a degenerate neutron core (TŻO)... but it is not. With its luminosity of over $10^5 L_\odot$, it could also be a super asymptotic giant branch star (SAGB), a star with an oxygen/neon core supported by electron degeneracy and undergoing thermal pulses with third dredge up.

[a] See, e.g., URLs: ⟨ http://astrofishki.net/universe/hv-2112-neveroyatnyj-obekt-torna-zhitkov/ ⟩ and ⟨ http://www.decifrandoastronomia.com.br/2017/01/uma-estrela-dentro-de-outra-conheca-hv.html ⟩.

Both TŻO and SAGB stars are expected to be rare. Calculations performed by Ch. A. Tout *et al.* [a] indicate that HV 2112 is likely a genuine TŻO. But a much more likely explanation is that HV 2112 is

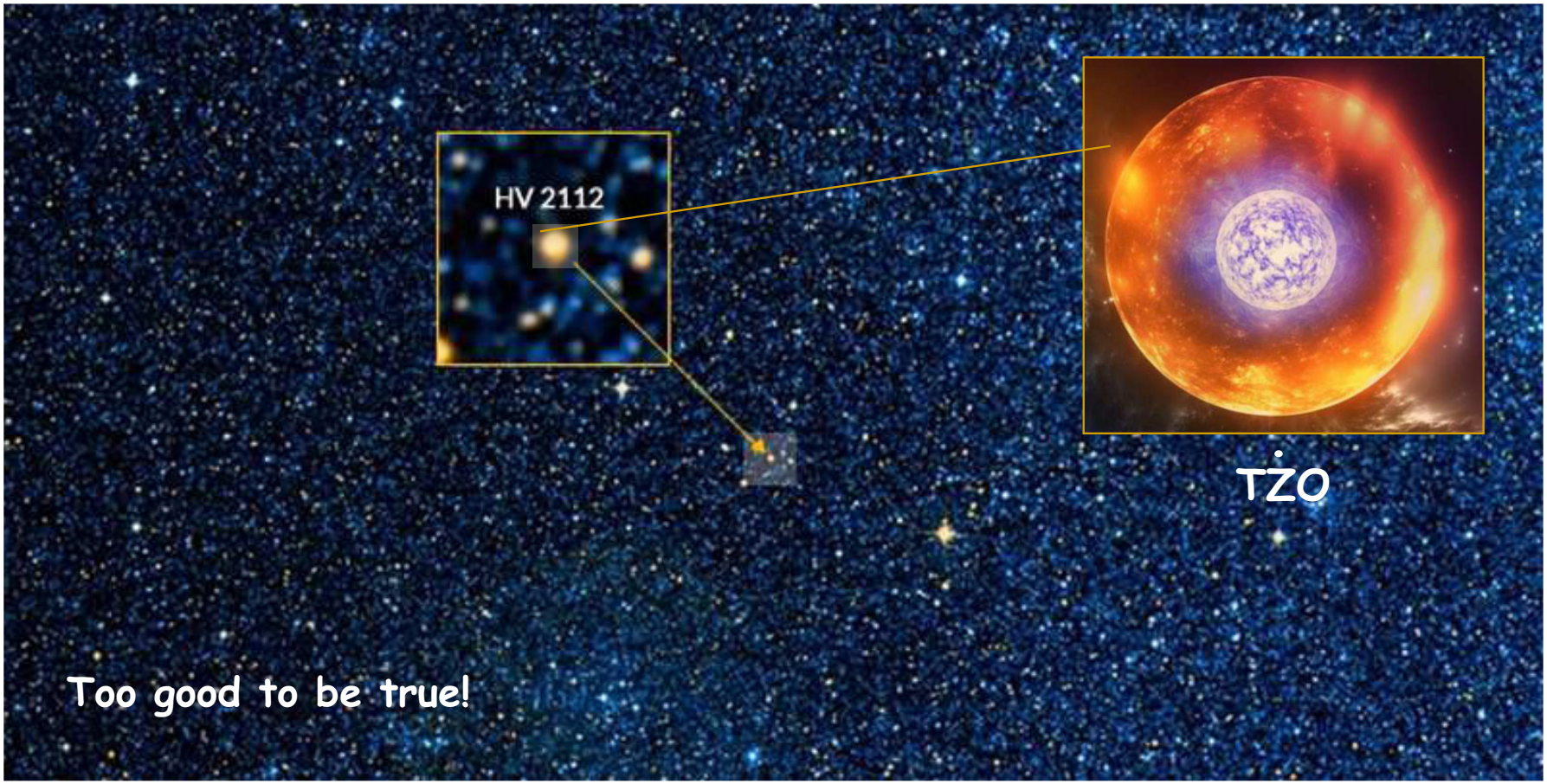

an intermediate mass ($\sim 5M_\odot$) AGB star. A new TŻO candidate (HV 11417) is recently suggested.[b]

[a] Ch. A. Tout, A. N. Żytkow, R. P. Church, & H. H. B. Lau, "HV 2112, a Thorne–Żytkow object or a super asymptotic giant branch star," Mon. Not. Roy. Astron. Soc. **445** (2014) L36–L40, arXiv:1406.6064 [astro-ph.HE].

[b] E. R. Beasor, B. Davies, I. Cabrera-Ziri, & G. Hurst, "A critical re-evaluation of the Thorne–Żytkow object candidate HV 2112," Mon. Not. Roy. Astron. Soc. **479** (2018) 3101–3105, arXiv:1806.07399 [astro-ph.SR].

23.8.2 Degenerate case.

The consideration must be completed for the case of degeneracy. Due to the condition $q_I < 0$, the density and composition of the "degenerate environment" are fine-tuned in such a way that

$$q = q_{-\zeta} = \Delta_c - i\,|\Delta_s|.$$

The simplest way is in coming back to the master equation. Indeed, in the limit of $q = q_{-\zeta}$, the Hamiltonian reduces to

$$\mathbf{H} = |\Delta_s| \begin{pmatrix} -i & \zeta \\ \zeta & i \end{pmatrix} \equiv |\Delta_s|\,\mathbf{h}_\zeta.$$

Considering that $\mathbf{h}_\zeta^2 = \mathbf{0}$, we promptly arrive at the solution of ME: $\widetilde{\mathbf{S}}(t) = \mathbf{1} - it\,|\Delta_s|\,\mathbf{h}_\zeta$ and thus

$$P_{\alpha\alpha}(t) = (1 - |\Delta_s|\,t)^2\, e^{-t/\Lambda}, \quad P_{\beta\beta}(t) = (1 + |\Delta_s|\,t)^2\, e^{-t/\Lambda}, \quad P_{\alpha\beta}(t) = P_{\beta\alpha}(t) = (\Delta_s t)^2\, e^{-t/\Lambda}.$$

Since $1/\Lambda_\beta = 1/\Lambda_\alpha - 4\,|\Delta_s|$, the necessary condition for complete degeneration is $4\Lambda_\alpha\,|\Delta_s| \leq 1$ and

$$1/\Lambda = 1/\Lambda_\alpha - 2\,|\Delta_s| \geq 2\,|\Delta_s|.$$

The equality holds only for $\nu_\beta = s$. The degenerate solution must be compared with the standard MSW solution

$$\left.\begin{aligned} P_{\alpha\alpha}(t) = P_{ss}(t) &= \frac{1}{2}\,[1 + \cos(2\Delta_s t)], \\ P_{\alpha s}(t) = P_{s\alpha}(t) &= \frac{1}{2}\,[1 - \cos(2\Delta_s t)], \end{aligned}\right\} \quad \text{(MSW)}$$

and with the classical penetration coefficient $\exp(-t/\Lambda_\alpha)$ (with $1/\Lambda_\alpha$ numerically equal to $4\,|\Delta_s|$) relevant to the transport of unmixed active neutrinos through the same environment.

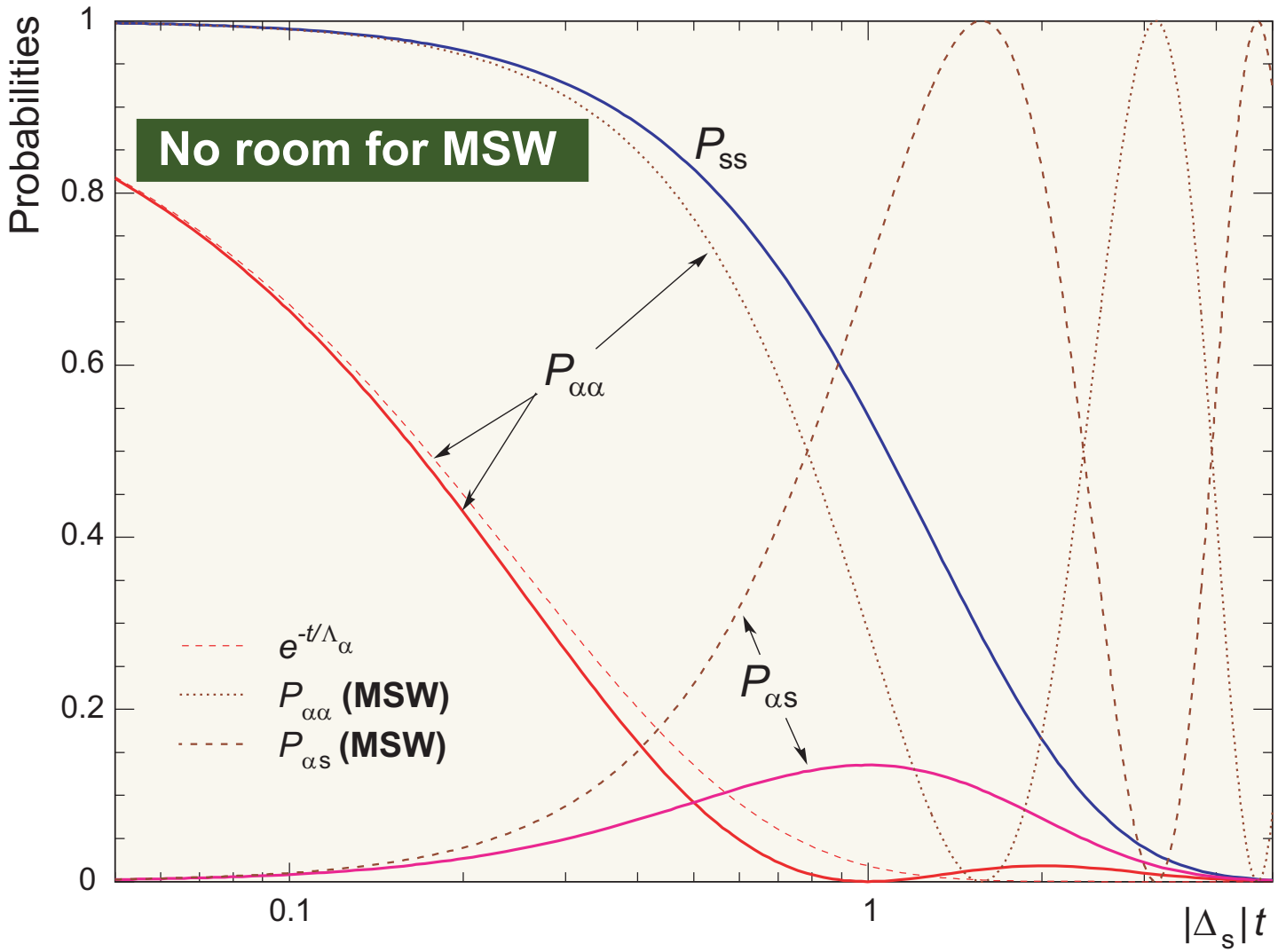

Survival and transition probabilities for $\nu_\alpha \leftrightarrow \nu_s$ oscillations in the case of degeneracy ($q = q_{-\zeta}$). The standard MSW probabilities (dotted and dash-dotted curves) together with the penetration coefficient for unmixed ν_α (dashed curve) are also shown.

23.9 Conclusions.

We have considered, on the basis of the MSW evolution equation with complex indices of refraction, the conjoint effects of neutrino mixing, refraction and absorption on high-energy neutrino propagation through matter. The adiabatic solution with correct asymptotics in the standard MSW and classical limits has been derived. In the general case the adiabatic behavior is very different from the conventional limiting cases (classical absorption and standard MSW).

- A remarkable example (albeit with defiantly unrealistic parameters) is given by the active-to-sterile neutrino mixing. It has been demonstrated that, under proper conditions, the survival probability of active neutrinos propagating through a very thick medium of constant density may become many orders of magnitude larger than it would be in the absence of mixing. The quantitative characteristics of this phenomenon are highly responsive to changes in density and composition of the medium as well as to neutrino energy and mixing parameters.
- Considering a great variety of latent astrophysical sources of high-energy neutrinos, the effect may open a new window for observational neutrino astrophysics.
- In the very distant future it may become an additional (to seismology and the standard MSW effect) spectroscopic tool for neutrino tomography of the Earth and the Sun (being sensitive to the density and chemical composition of the medium).

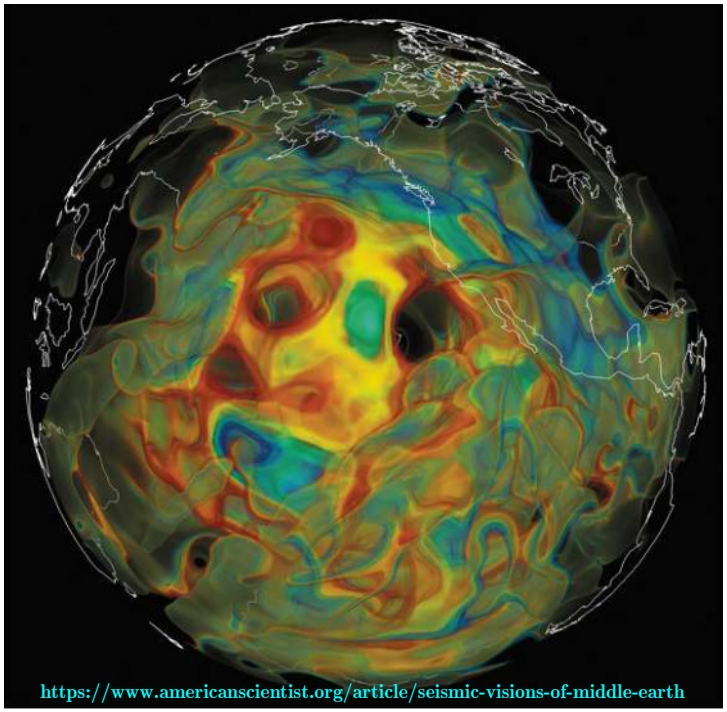

The mantle below the Pacific. Warm (cold) colors denote slower (faster) than average seismic wave speeds. *Image by Ebru Bozdag (Univ. of Nice) & David Pugmire (Oak Ridge National Lab.).*

Part VII

Solar Neutrinos

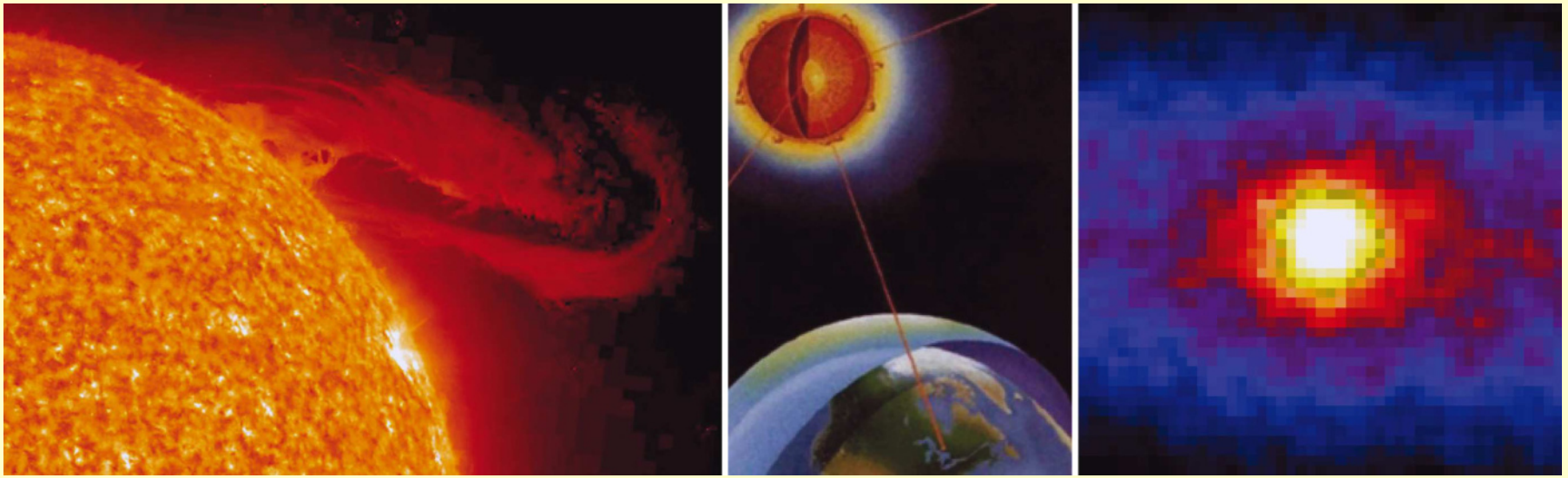

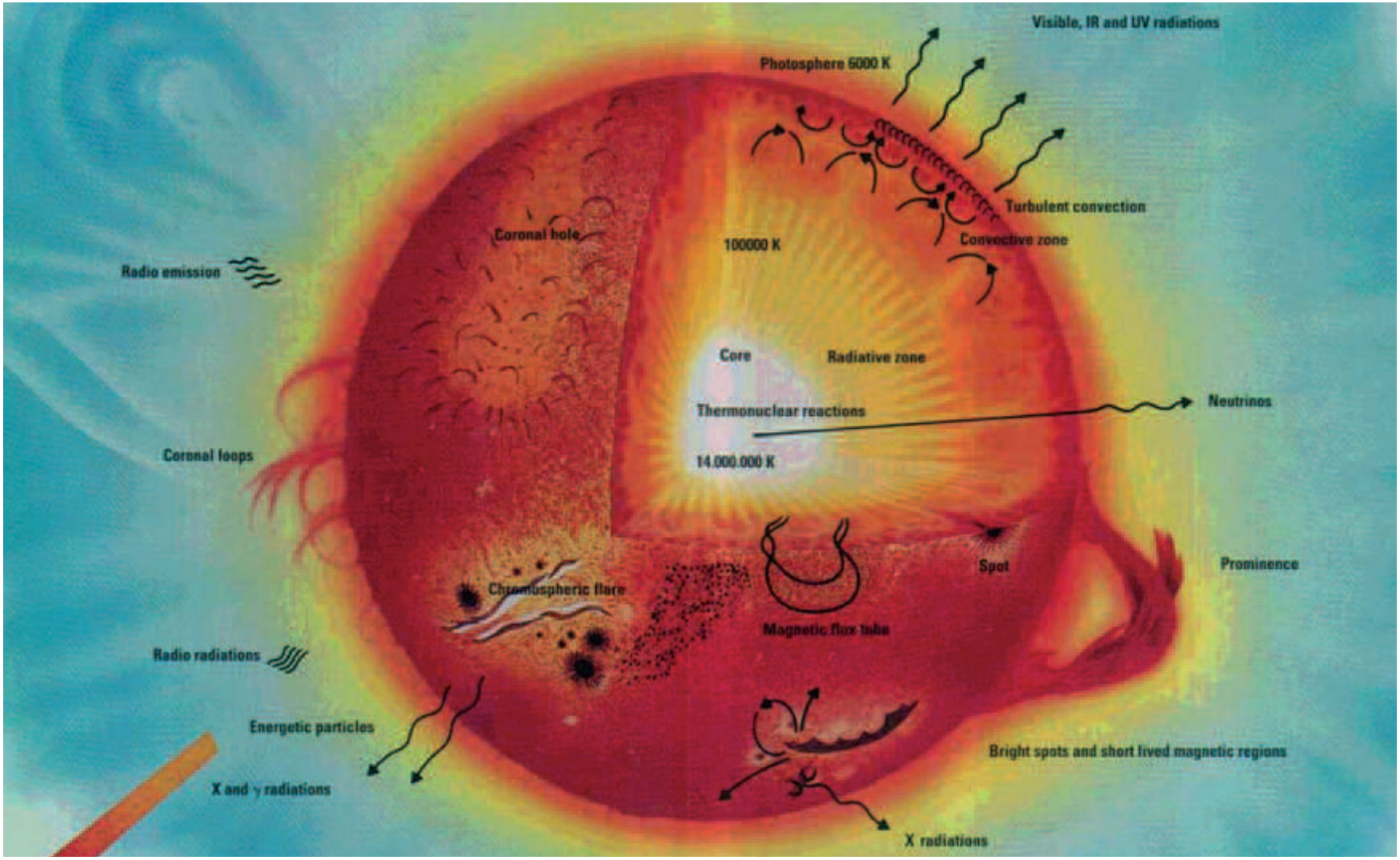

A cutaway view of the Sun, showing the three internal (thermonuclear, radiative, and convective) zones, the solar surface (photosphere), the lower (chromosphere) and upper atmosphere (corona), and a number of phenomena associated with the solar activity cycle (filaments, prominences, flares). [By Calvin J. Hamilton, NASA/ESA.] More details are shown in next slide.

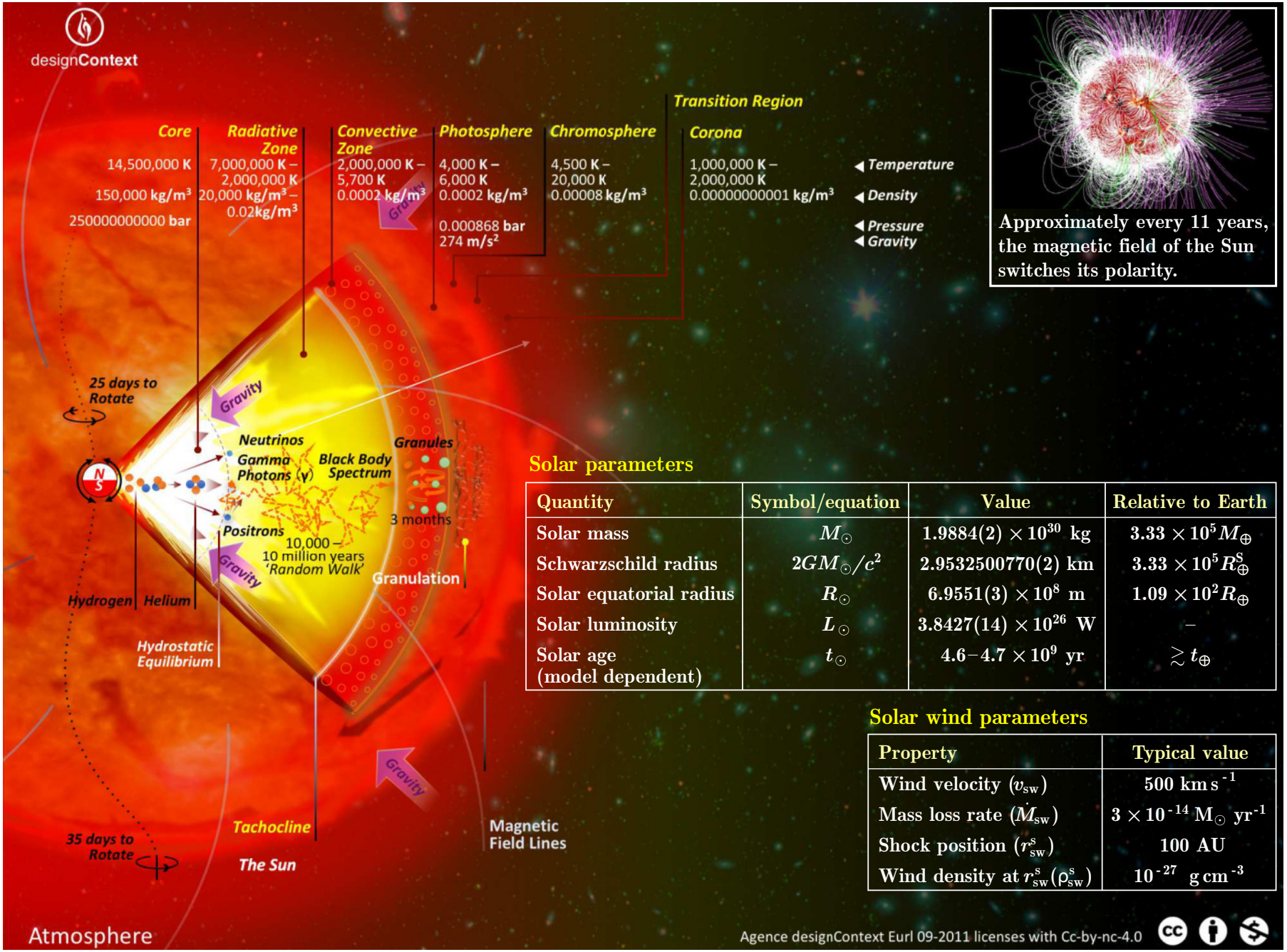

Solar parameters

Quantity	Symbol/equation	Value	Relative to Earth
Solar mass	$M_\odot$	$1.9884(2) \times 10^{30}$ kg	$3.33 \times 10^5 M_\oplus$
Schwarzschild radius	$2GM_\odot/c^2$	2.9532500770(2) km	$3.33 \times 10^5 R^S_\oplus$
Solar equatorial radius	$R_\odot$	$6.9551(3) \times 10^8$ m	$1.09 \times 10^2 R_\oplus$
Solar luminosity	$L_\odot$	$3.8427(14) \times 10^{26}$ W	–
Solar age (model dependent)	$t_\odot$	$4.6–4.7 \times 10^9$ yr	$\gtrsim t_\oplus$

Solar wind parameters

Property	Typical value
Wind velocity (v_{sw})	500 km s^{-1}
Mass loss rate ($\dot{M}_{sw}$)	3×10^{-14} $M_\odot$ yr^{-1}
Shock position (r^s_{sw})	100 AU
Wind density at r^s_{sw} (ρ^s_{sw})	10^{-27} g cm^{-3}

24 Basic equations of stellar structure.

$$\begin{aligned}
\text{Continuity equation:} \quad & \frac{dm}{dr} = 4\pi r^2 \rho, \\
\text{Hydrostatic equation:} \quad & \frac{dp}{dr} = -\frac{Gm\rho}{r^2}, \\
\text{Energy equation:} \quad & \frac{dL}{dr} = 4\pi r^2 \left[\epsilon\rho - \rho \frac{d}{dt}\left(\frac{u}{\rho}\right) + \frac{p}{\rho}\frac{d\rho}{dt} \right], \\
\text{Energy transfer equation:} \quad & \frac{dT}{dr} = \nabla \frac{T}{p}\frac{dp}{dr}.
\end{aligned}$$

Here

r is distance to the center and t is time [all following variables are functions of r and t],
p is pressure [in general, $p = p_{\text{gas}} + p_{\text{rad}} + B^2/8\pi$],
m is the mass of the sphere interior to r ("shell mass"),
ρ is density,
T is temperature,
L is the flow of energy per unit time through the sphere of radius r,
ϵ is the rate of nuclear energy generation per unit mass and time,
u is the internal energy per unit volume.

The temperature gradient is characterized by $\nabla = d\ln T/d\ln p$ and is determined by the mode of energy transport. Since $d\ln T/d\ln p = (p/T)(dT/dp)$, we see that the energy transfer equation is in a sense simply an identity. Let's shortly explain the physical meaning of the first three equations.

1. Continuity equation follows from the definition of the shell mass [here and hereafter we assume spherical symmetry and therefore $\rho = \rho(r)$ etc.]:

$$m = m(r) = \int_{V(r)} \rho(\mathbf{r}) d\mathbf{r} = 4\pi \int_0^r \rho(R) R^2 dR, \quad \Longrightarrow \quad \boxed{\frac{dm}{dr} = 4\pi r^2 \rho.}$$

2. Hydrostatic equation follows from the hydrostatic equilibrium between the gravity and pressure gradient. Let $dV = d\sigma dr$ be a cylindric volume of the radial extend dr and surface $d\sigma$ with the axis directed to the center. The gravity and pressure forces are, respectively,

$$dF_g = -\frac{Gm}{r^2} \rho dV < 0 \quad \text{and} \quad dF_p = p d\sigma - (p + dp) d\sigma = -dp d\sigma > 0.$$

The hydrostatic equilibrium condition $dF_g + dF_p = 0$ then yields

$$-\frac{Gm}{r^2} \rho d\sigma dr - dp d\sigma = 0, \quad \Longrightarrow \quad \boxed{\frac{dp}{dr} = -\frac{Gm\rho}{r^2}.}$$

3. Energy equation. Consider the net energy per second passing outward through a shell at radius r. If no energy is created in the shell, the amount of incoming energy equals the amount of outgoing energy, and $dL/dr = 0$. However, if additional energy is created or absorbed within the shell, then dL/dr will be non-zero. Let ε be the energy released per second by a unit mass of matter. Then

$$\frac{dL}{dr} = 4\pi r^2 \rho \varepsilon.$$

The total rate ε has three components: a) ϵ, the total rate of energy created by nuclear reactions, b) ϵ_{i}, the energy input (e.g. into neutrinos), and c) $\epsilon_{\mathbf{g}}$, the energy produced or lost by gravitational expansion or contraction. The right-hand side of the 3rd equation is the sum of these contributions.

25 Auxiliary equations.

In addition to the basic differential equations, we need auxiliary ones:

$$\begin{aligned} \text{Equation of state:} \quad & \rho = \rho\left(p, T, \{X_i\}\right), \\ \text{Equation for opacity:} \quad & \kappa = \kappa\left(p, T, \{X_i\}\right), \\ \text{Equation for NRR:} \quad & \epsilon = \epsilon\left(p, T, \{X_i\}\right). \end{aligned}$$

These equations link the thermal quantities and the chemical abundances X_i.

The opacity κ enters the basic equations through the temperature gradient:

$$\nabla = \nabla_{\text{rad}} + \nabla_{\text{conv}},$$

in which

$$\nabla_{\text{rad}} = \frac{3}{16\pi a \tilde{c} G} \frac{\kappa p}{T^4} \frac{L}{m},$$

$\tilde{c}$ is the speed of light, a is the radiation density constant, and κ is the opacity, defined such that

$$\frac{1}{\kappa r} = \lambda_\gamma = \text{mean free path of a photon.}$$

In making *"standard"* solar evolutionary models (SSM), the chemical abundance distributions are obtained by the time evolution equations:

$$\frac{\partial X_i}{\partial t} = \left(\frac{\partial X_i}{\partial t}\right)_{\text{nuclear}} + \left(\frac{\partial X_i}{\partial t}\right)_{\text{diffusion}}.$$

Example: Equation of state in SSM

The sophisticated SSM of Bahcall & Pinsonneault[a] uses a quasi-polytropic model with $\gamma = \gamma(r)$. Three regions clearly emerge. In two region the SSM output is approximated by a straight line, indicating polytropic behavior. Of these regions the outermost one ($\gamma \approx 1.667 \approx 5/3$) represents the convective zone where the heat transport is achieved by adiabatic convection. The Sun's inner region constitutes the radiative zone ($\gamma \approx 1.264$) where heat transport is achieved by e/m waves.

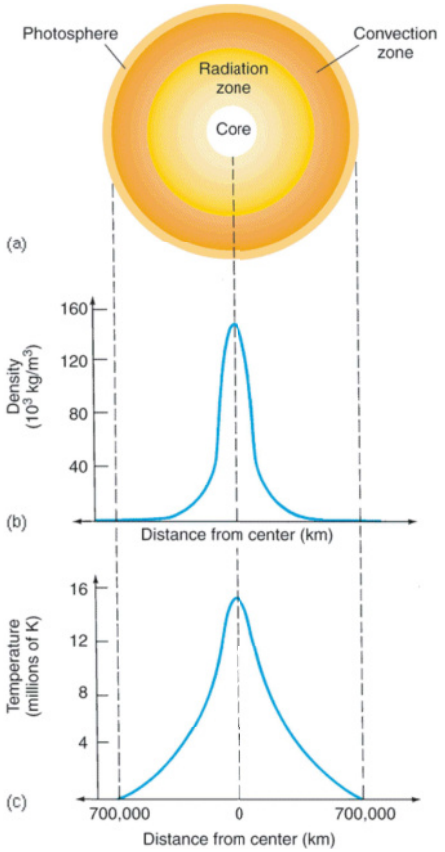

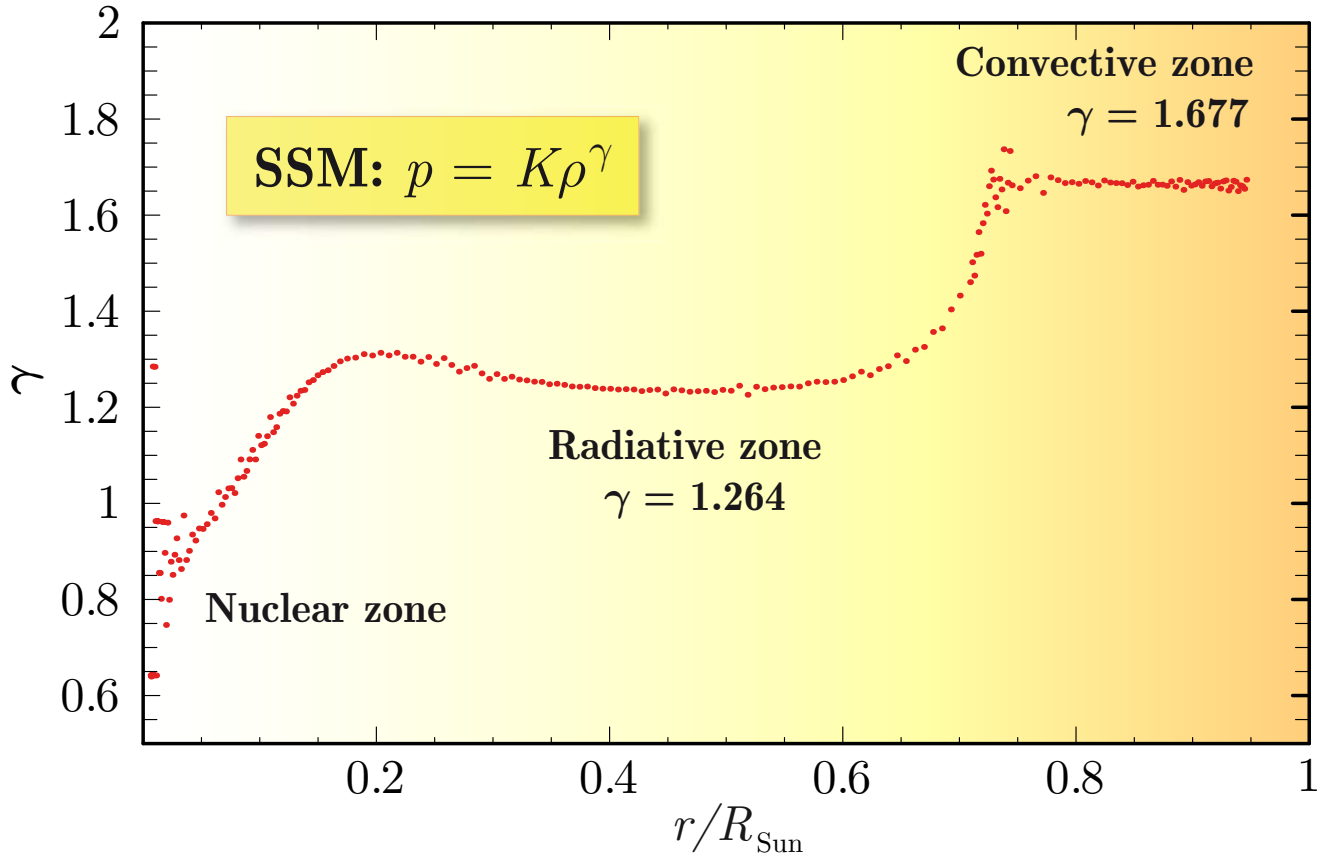

[a] J. N. Bahcall & M. H. Pinsonneault, "Solar models with Helium and heavy-element diffusion," Rev. Mod. Phys. **67** (1995) 781–808, hep-ph/9505425.

26 Helioseismology in a few images.

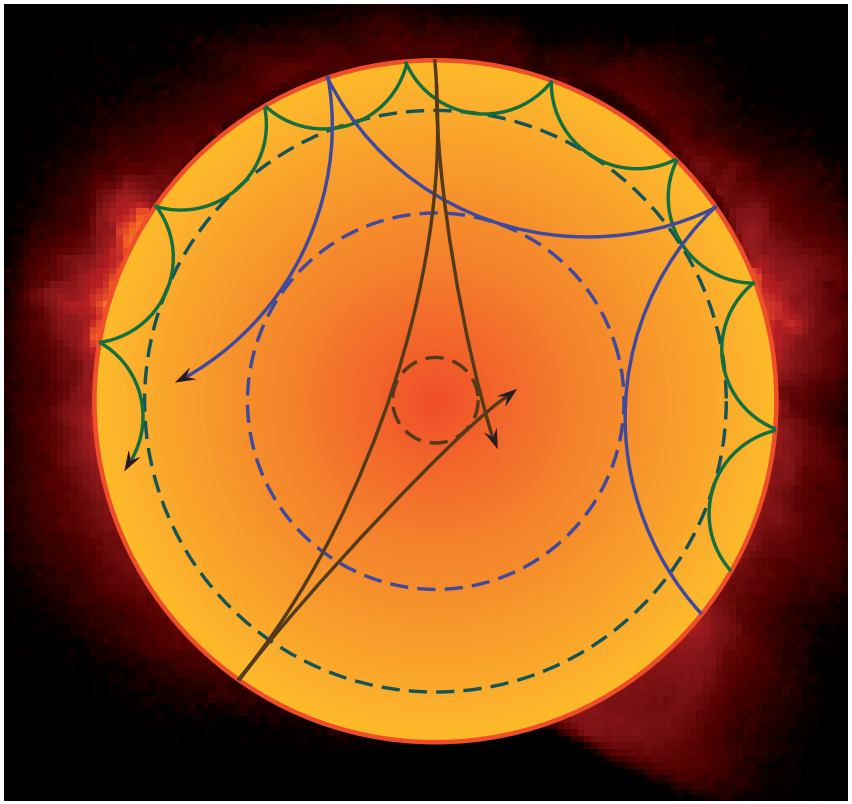

Solar oscillations consist of a reach spectrum of internal acoustic and gravity wave, stochastically exited by turbulent convection.

◁ Propagation of sound rays in a cross section of the solar interior. The ray paths are bent by the increase in sound speed with depth until they reach the inner turning point (indicated by the dotted circles), where they undergo total internal refraction. At the surface the waves are reflected by the rapid decrease in density.

The raw data of helioseismology consist of measurements of the photospheric Doppler velocity and/or (in some cases) intensity in a particular wavelength band taken at a cadence of about one minute and generally collected with as little interruption as possible over periods of months or years.

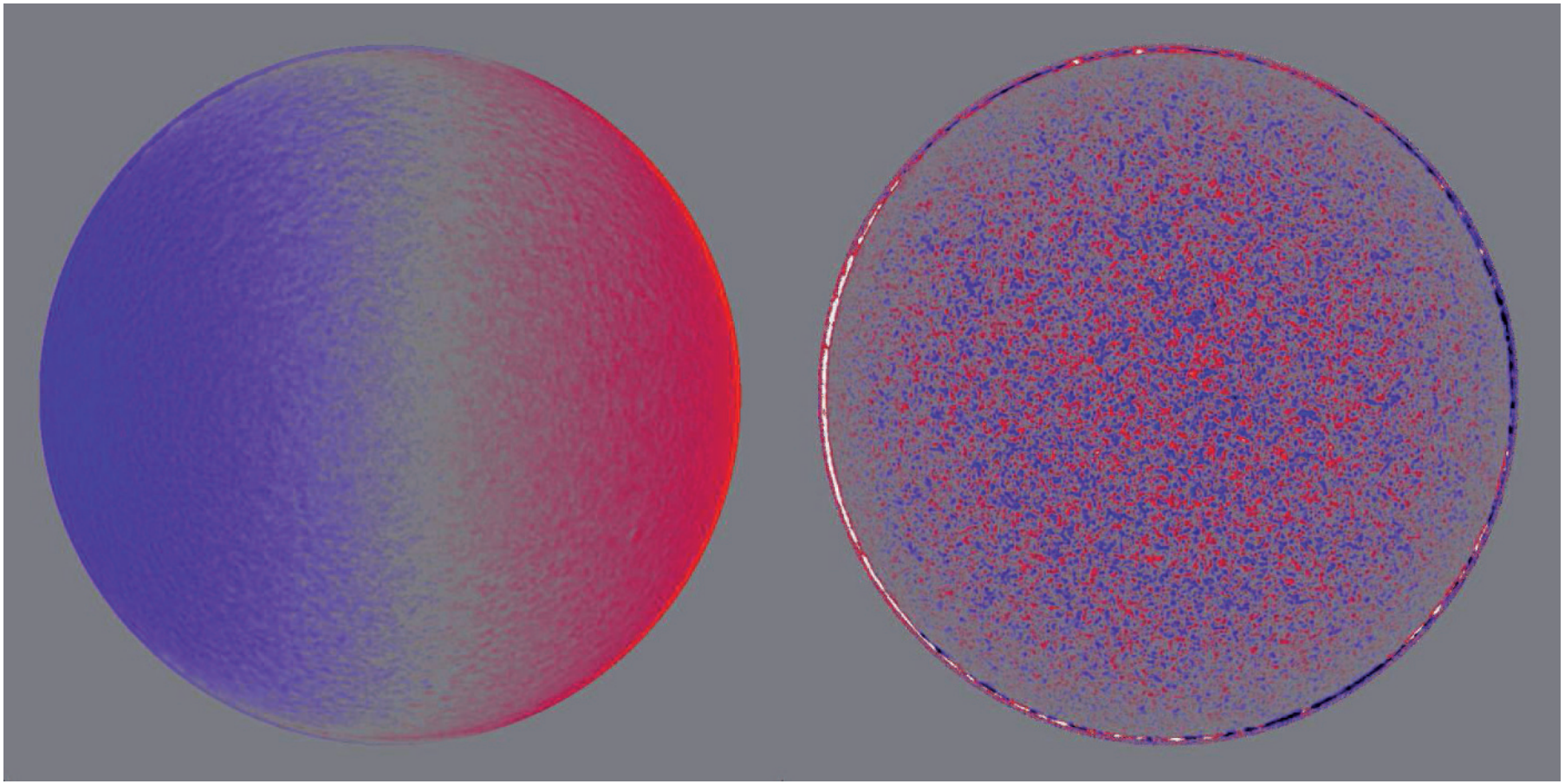

A typical single Doppler velocity image (dopplergram) of the Sun from one GONG (**G**lobal **O**scillation **N**etwork **G**roup] instrument (*left*), and the difference between that image and one taken a minute earlier (*right*), with red corresponding to motion away from, and blue to motion towards, the observer.

The shading across the first image comes from the solar rotation. After removing the rotation, the mottling associated primarily with solar oscillations becomes apparent.

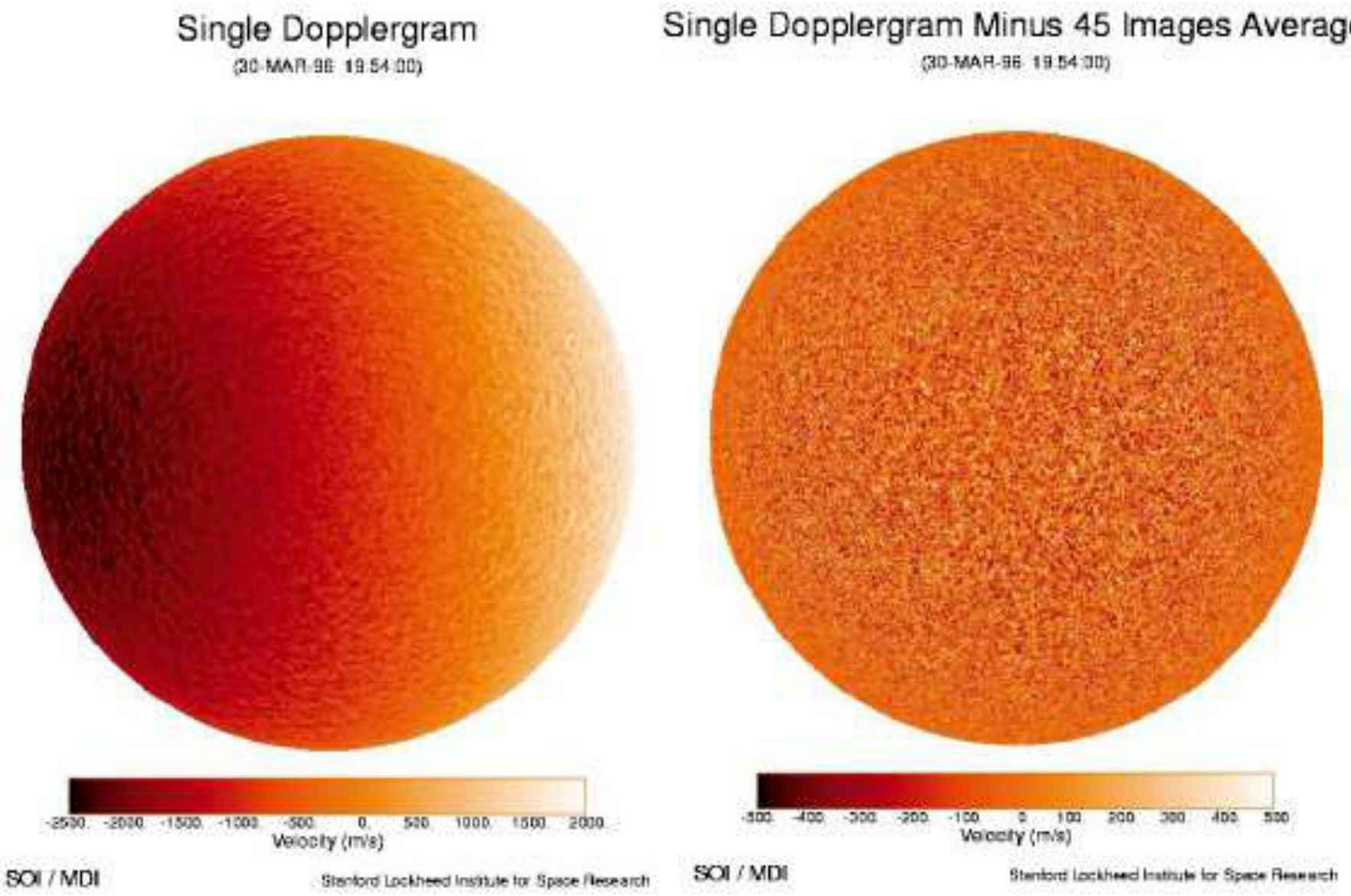

Similar dopplergrams from SOI/MDI.

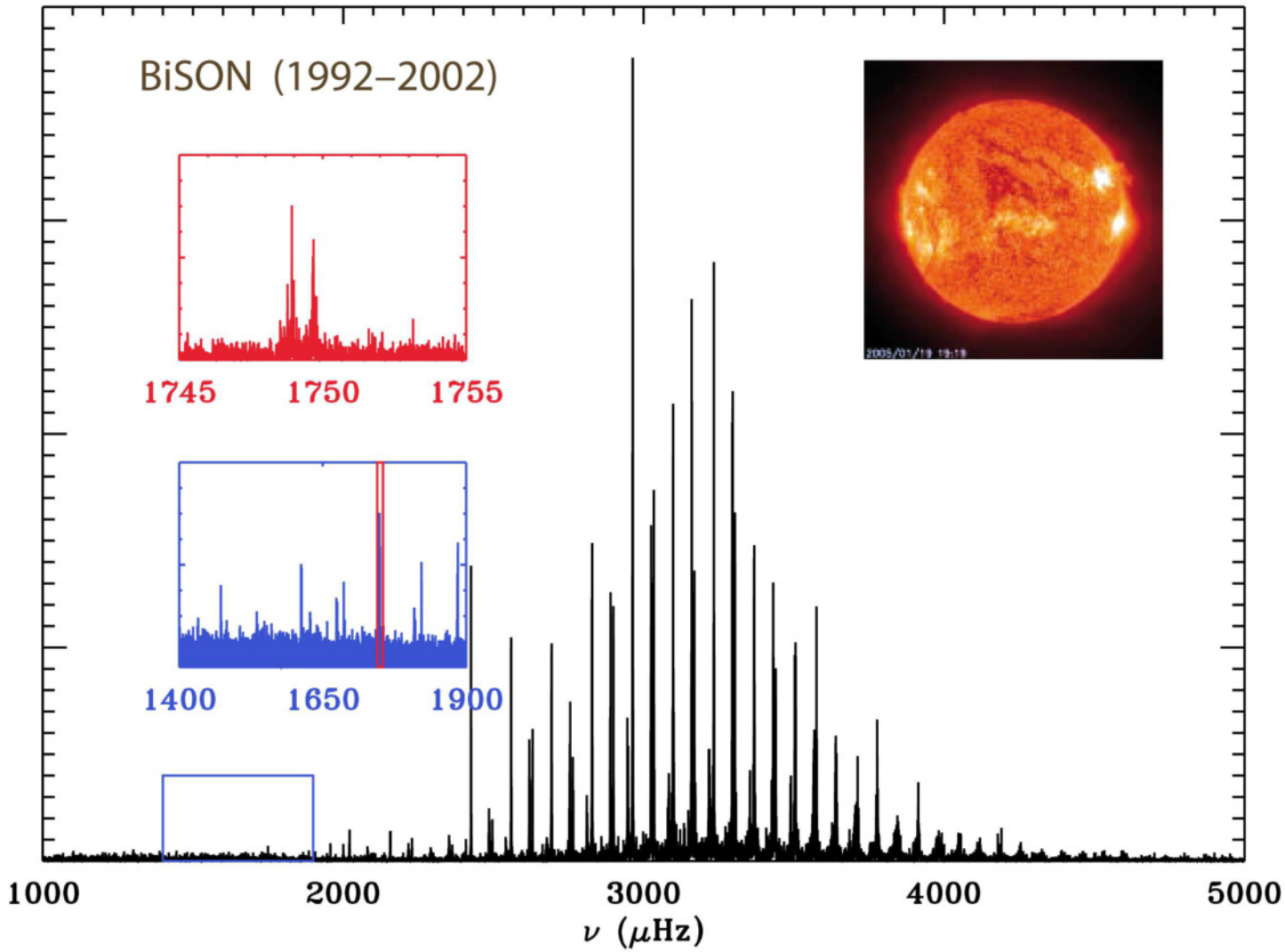

Power spectrum from 10 years of BiSON (**B**irmingham **I**ntegrated **S**olar **N**etwork) data, 1992–2002; the insets show the low-frequency end of the 5-minute band (blue) and a single, rotationally split $l = 1$ peak (red).

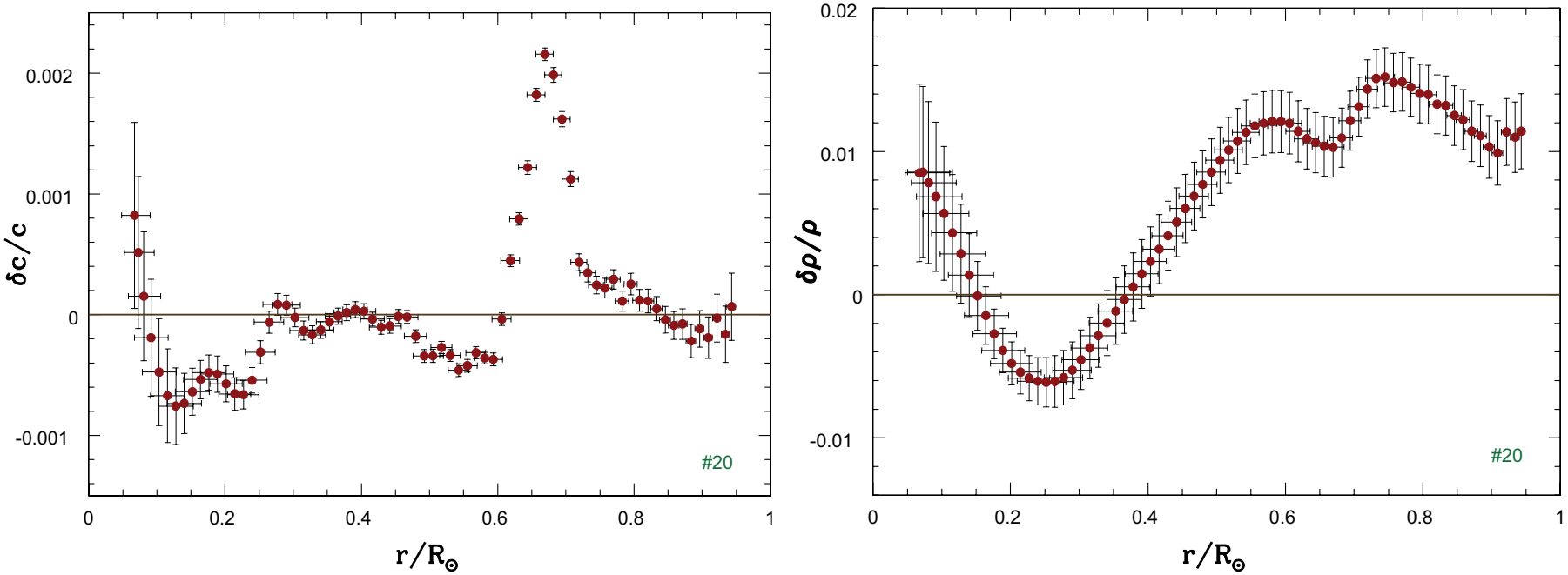

Fractional difference plots [(Sun-SSM)/SSM] for the sound speed (*left panel*) and density (*right panel*) for a SSM.[a] The data were determined by BPB00[b] using the SOHO/MDI (**SO**lar and **H**eliospheric **O**bservatory/**M**ichelson **D**oppler **I**mager) ESA-NASA solar frequency data set.[c] Vertical error bars indicate 1σ errors in the inversion results due to errors in the data. Horizontal error bars are a measure of the resolution of the inversion.

[a] R. A. Winnick *et al.*, "Seismic test of solar models, solar neutrinos, and implications for metal rich accretion," ApJ **576** (2002) 1075–1084, astro-ph/0111096.

[b] S. Basu, M. H. Pinsonneault & J. N. Bahcall, "How much do helioseismological inferences depend upon the assumed reference model?" ApJ **529** (2000) 1084–1100, astro-ph/9909247.

[c] E. J. Rhodes, Jr. *et al.*, "Measurements of frequencies of solar oscillation for the MDI medium-l program," Solar Phys. **175** (1997) 287–310.

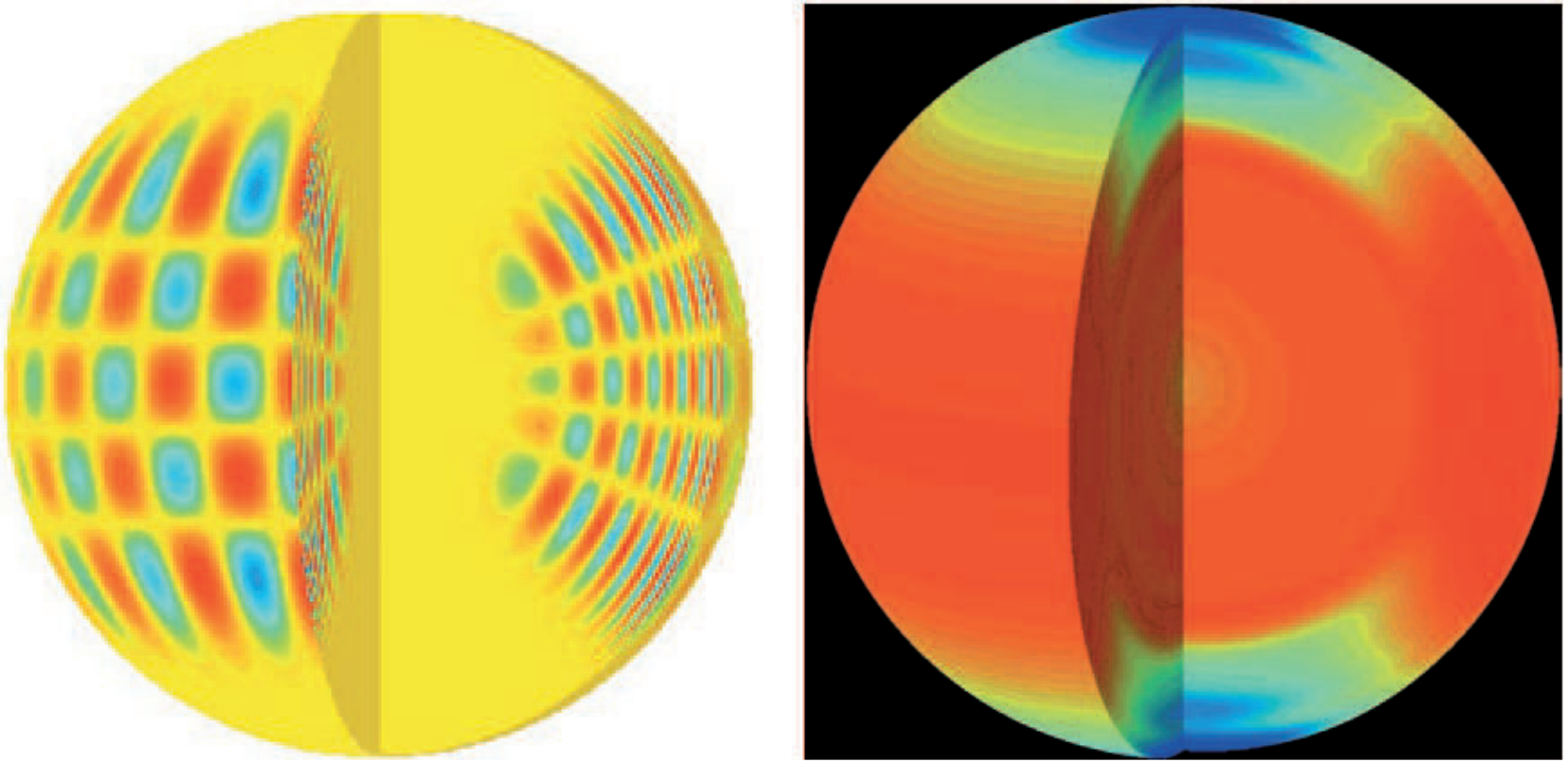

Left: A global acoustic p-mode wave is visualized: The radial order is $n = 14$, the angular degree is $l = 20$, the angular order is $m = 16$, and the frequency is $\nu = 2935.88 \pm 0.1$ μHz with SoHO/MDI (Michelson Doppler Image). The red and blue zones show displacement amplitudes of opposite sign. Right: The internal rotation rate is shown with a color code, measured with SoHO/MDI during May 1996 – April 1997. The red zone shows the fastest rotation rates ($P \approx 25$ days), dark blue the slowest ($P \approx 35$ days). Note that the rotation rate varies in latitude differently in the radiative and convective zones. (Courtesy of SoHO/MDI and NASA.)

27 Solar fusion.

Certain physical investigations in the past year make it probable to my mind that some portion of sub-atomic energy is actually being set free in a star. . . . If five per cent of a star's mass consists initially of Hydrogen atoms, which are gradually being combined to form more complex elements, the total heat liberated will more than suffice for our demands, and we need look no further for the source of a star's energy. . .

Sir Arthur Eddington, Nature (1920)

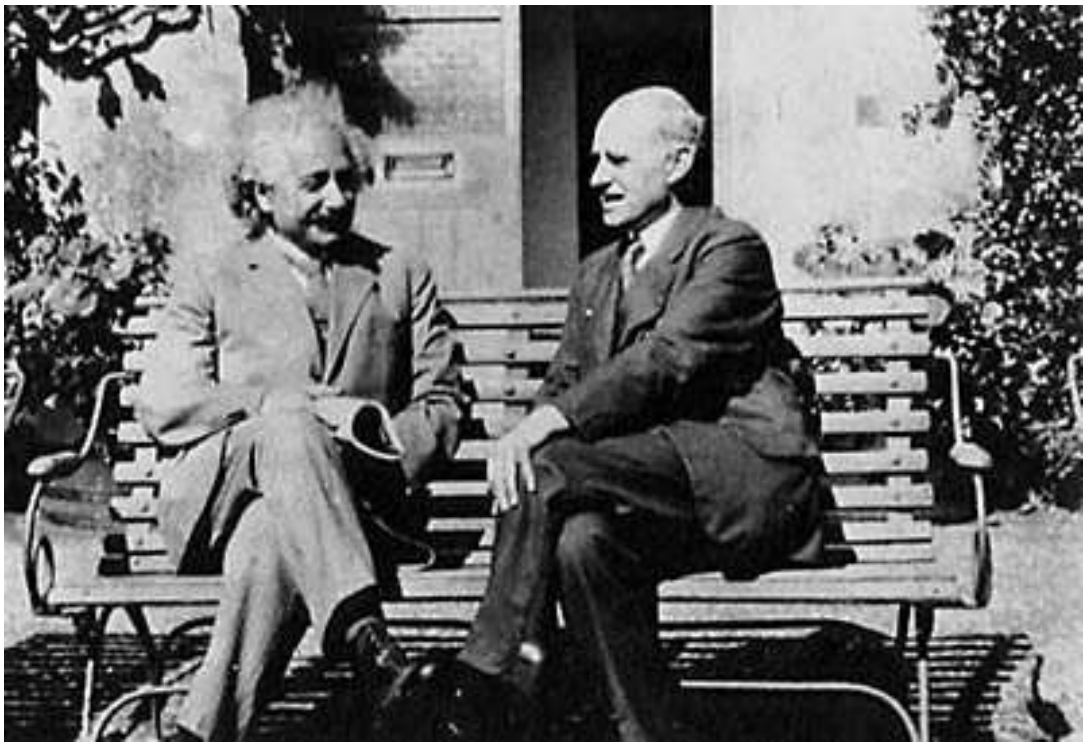

28 The pp fusion step by step.

There is convincing evidence that the general fusion reaction on the Sun is "burning" of Hydrogen to produce Helium:

$$4\,{}^1\mathrm{H} + 2\,e^- \;\rightarrow\; {}^4\mathrm{He} + 2\,\nu_e + 6\,\gamma.$$

In this reaction, the final particles have less internal energy than the starting particles.

Since energy is conserved, the extra energy is released as

- ⋆ energy of motion of the nuclei and electrons in the solar gas,
- ⋆ the production of lots of low energy photons and, finally,
- ⋆ the energy of the electron neutrinos, which easily shoot out of the Sun with almost no interaction with it.

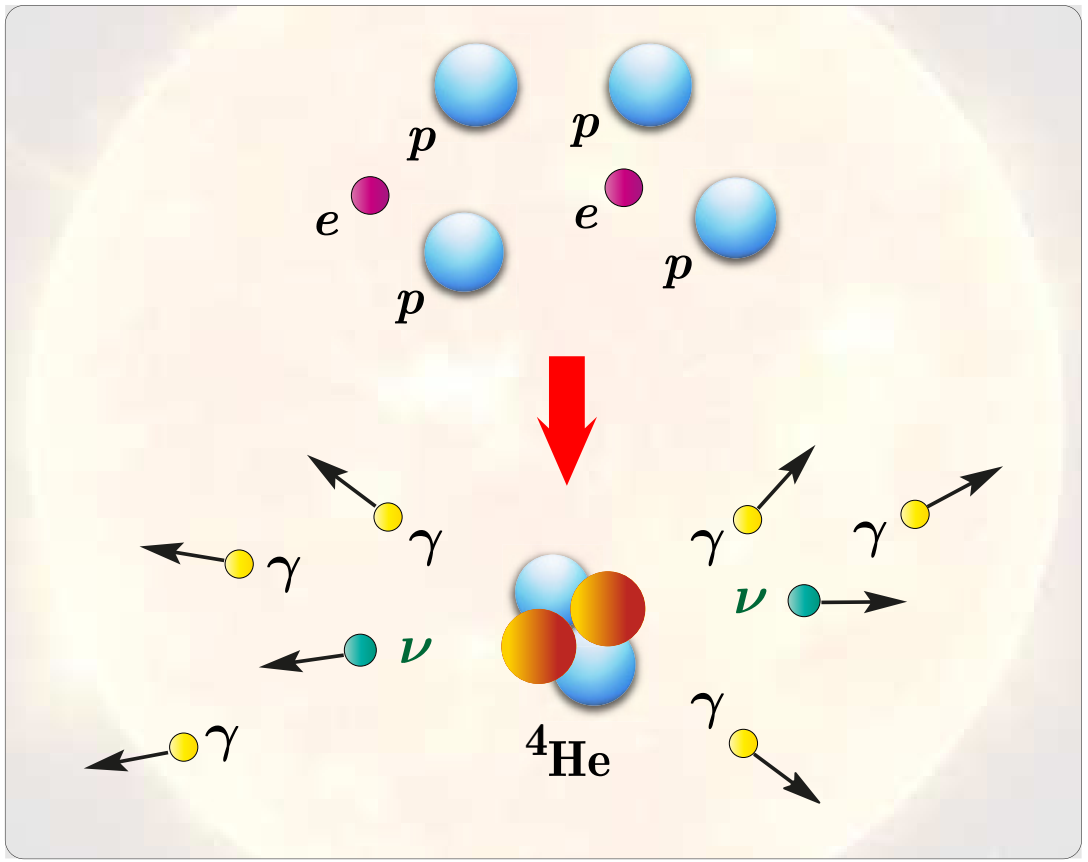

△ A reaction that never takes place in the Sun, already because the probability of a simultaneous collision of six particles is vanishingly small. The Hydrogen to Helium fusion can only occur in stages.

As a result of the fusion, the solar plasma gets hotter and is saturated with lots of photons.

The energy release in the reaction $4\,{}^1\mathrm{H} + 2\,e^- \rightarrow {}^4\mathrm{He} + 2\,\nu_e + 6\,\gamma$ is

$$Q = (4 \times 1.007825u - 4.002603u) \times 931 \text{ MeV}/u = 26.732 \text{ MeV}$$

each time the reaction happens. Here $1.007825u$ is the mass of a Hydrogen atom and $4.002603u$ is the mass of a Helium atom. Binding energies, neutrinos (small mass), and photons (zero mass) do not enter into the calculation.

The luminosity sum rule:

Thus, the generation of $Q = 26.732$ MeV in the Sun is accompanied by the production of two ν_es. If the Sun is approximately in a steady state with a nuclear energy production rate that equals its luminosity, then the total solar neutrino flux at Earth is (Dar & Nussinov, 1991)

$$\Phi_\nu \approx \frac{2S_\odot}{Q - 2\langle E_\nu \rangle} \approx 6.54 \times 10^{10} \text{ cm}^{-2}\,\text{s}^{-1},$$

where $S_\odot = L_\odot/4\pi d_\odot^2 = 1.366$ kW m^{-2} is the measured solar constant which yields a solar luminosity $L_\odot = 4\pi d_\odot^2 \approx 3.846 \times 10^{33}$ erg s^{-1} for an average distance $d_\odot \approx 1.496 \times 10^{13}$ cm of the Earth from the Sun, and

$$\langle E_\nu \rangle = \frac{1}{\Phi_\nu} \sum_i E_\nu^{(i)} \Phi_\nu^{(i)}$$

is the mean energy of solar neutrinos which has been approximated by

$$\langle E_\nu^{(pp)} \rangle \approx 0.265 \text{ MeV},$$

the mean energy of the pp solar neutrinos that dominate the solar neutrino flux.

The fusion reaction as given above is a summary. Really it may only occur in several steps since the temperature in the Sun is too low and, as a result,

---

an inelastic collision of *two* nuclei in the Sun is *nearly impossible*.

The two nuclei have to get within $r_p \sim 10^{-13}$ cm for the strong interactions to hold them together but they repel each other. For example, the potential energy for Coulomb interaction of two protons is

$$U_{\text{Coulomb}} = \frac{e^2}{r_p} \approx 2 \times 10^{-6} \text{ erg} \approx 1.2 \text{ MeV}.$$

Since $T_\odot \lesssim 1.5 \times 10^7$ K (the helioseismology confirms this!)

$$\langle E_p^{\text{kin}} \rangle = \frac{3}{2} k T_\odot \lesssim 2 \text{ keV}.$$

Assuming Maxwellian distribution, the fraction of protons with $E_p^{\text{kin}} > U_{\text{Coulomb}}$ is

$$\exp\left(-E_p^{\text{kin}} / \langle E_p^{\text{kin}} \rangle\right) < e^{-600} \sim 10^{-260}.$$

Considering that the number of protons in the Sun is about 10^{57} we can conclude that

the classical probability of the fusion is ZERO.

Let's estimate the quantum probability.[a] The nucleus wave function can be written

$$\psi \propto \exp\left(i\int p dx\right).$$

$$E_p^{\text{kin}} = p^2/2m = E_0 - U, \qquad \Rightarrow \qquad p = \sqrt{2m\,(E_0 - U)}.$$

The repulsion energy of two nuclei with charges $Z_1 e$ and $Z_2 e$ is $U = Z_1 Z_2 e^2/r$ and the classical turning point ($p = 0$) is given by $r_1 = Z_1 Z_2 e^2/E_0$. In quantum theory

$$p = i\sqrt{2m\,(U - E_0)} \quad \text{for} \quad r < r_1$$

and thus the probability of the barrier penetration (tunnel effect) can be estimated as

$$\psi^2(r) \propto \exp\left[-2\int_r^{r_1} \sqrt{2m\,[U(r') - E_0]}\; dr'\right].$$

where $r \sim r_p$ is the radius of nuclear interaction. Considering that usually $r_p \ll r_1$, for rough estimation we can put $r = 0$.

It is assumed here that one of the nuclei is in rest ($m_2 = \infty$). To take into account its finite mass one have to replace m with the effective dynamic mass of the colliding particles:

$$m \longmapsto M = \frac{m_1 m_2}{m_1 + m_2} = \frac{A_1 A_2}{A_1 + A_2} m_p = A m_p.$$

[a] Here we follow the wonderful book by Ya. B. Zeldovich, S. I Blinnikov, & N. I. Shakura, "Physical principles of structure and evolution of stars," [Я. В. Зельдович, С. И.Блинников, Н. И. Шакура, «Физические основы строения и эволюции звезд», Изд. МГУ, Москва, 1981], which is highly recommended to (Russian-speaking) students for further reading.

Than the barrier penetration probability is given by

$$\psi^2(r) \approx \psi^2(0) = e^{-2\pi\eta} \quad \text{(Gamow factor)},$$

where ($\hbar = c = 1 \Longrightarrow e^2/\hbar c = \alpha$)

$$\eta = \frac{r_1}{\pi}\sqrt{2ME_0}\int_0^1 \sqrt{\frac{1}{x} - 1}\, dx = \frac{1}{2\pi}\sqrt{\frac{E_G}{E}} \quad \text{(Sommerfeld parameter)}$$

and

$$E_G = 2\left(\pi Z_1 Z_2 \alpha\right)^2 M \quad \text{(Gamow energy)}.$$

In thermal equilibrium with the temperature T the number of particles with energy E_0 is proportional to $exp\left(-E_0/kT\right)$. Therefore the full probability is proportional to

$$\int e^{-\chi(E_0)} dE_0, \quad \text{where} \quad \chi = \sqrt{\frac{E_G}{E_0}} + \frac{E_0}{kT}.$$

The integral can be evaluated by using the saddle-point technique considering that the function χ has a sharp minimum (and thus $e^{-\chi}$ has a sharp maximum, – *Gamow's peak*). The minimum is given by

$$\frac{d\chi}{dE_0} = -\frac{1}{2E_0}\sqrt{\frac{E_G}{E_0}} + \frac{1}{kT} = 0.$$

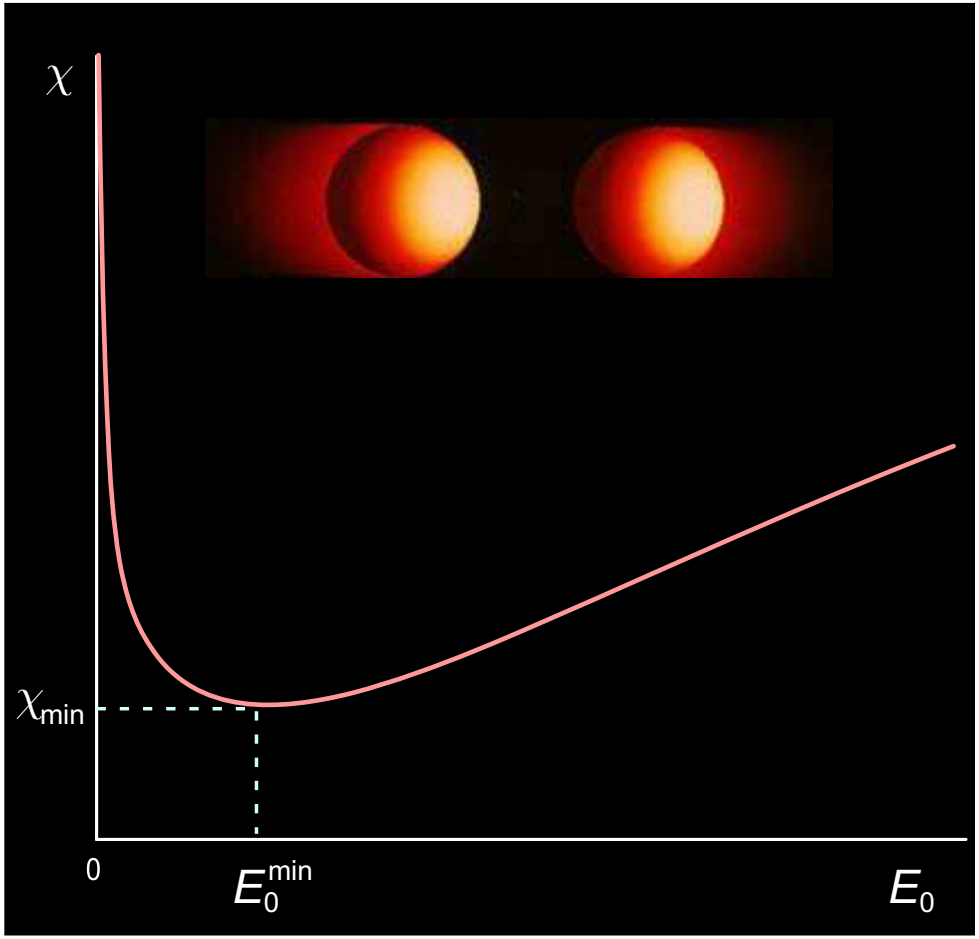

Gamow's peak is given by

$$E_0^{\min} = E_G^{1/3} \left(kT/2\right)^{2/3}$$
$$\simeq 0.122 \left(AZ_1^2 Z_2^2 T_9^2\right)^{1/3} \text{ MeV},$$
$$\chi_{\min} = 3\left(\frac{E_G}{4kT}\right)^{1/3}$$
$$\simeq 4.25 \left(\frac{AZ_1^2 Z_2^2}{T_9}\right)^{1/3},$$

where $T_9 = T/(10^9 \text{ K})$. Now one can approximate $\chi(E_0)$ by

$$\chi(E_0) \simeq \chi_{\min} + \kappa \left(1 - E_0/E_0^{\min}\right)^2,$$
$$\kappa = (3/8)\left(2E_G/kT\right)^{1/3}.$$

Finally, the full probability is estimated by $C(T)\exp\left[-\chi_{\min}(T)\right]$.

Example: for the pp fusion in the center of the Sun ($T_9 \simeq 0.015$)

$$E_0^{\min} \simeq 5.9 \text{ keV}, \quad \chi_{\min} \simeq 13.7, \quad \exp\left(-\chi_{\min}\right) \simeq 1.15 \times 10^{-6}.$$

28.1 The pp I branch.

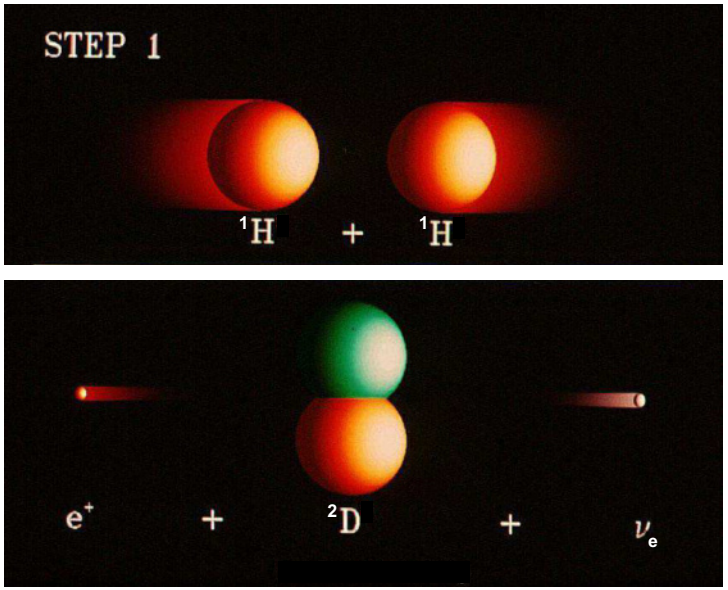

Note: the secondary positron very quickly encounters a free electron in the Sun and both particles annihilate, their mass energy appearing as two 511 KeV γs: $e^+e^- \to \gamma\gamma$.

$$\mathbf{p} + \mathbf{p} \to \mathbf{d} + \mathbf{e}^+ + \nu_\mathbf{e}$$

The energy liberation in this reaction is $Q = 1.442$ MeV, including in average ~ 0.26 MeV taking away by neutrinos ($E_\nu \leq 420$ keV). The number of Deuterium nuclei generated in 1 cm^3 per 1 s is

$$\frac{d[\mathrm{D}]}{dt} = C_{11}\frac{n_p^2}{2N_A T_9^{2/3}}\exp\left(-\frac{3.38}{T_9^{1/3}}\right) \left[\mathrm{cm}^{-3}\mathrm{s}^{-1}\right],$$

$$C_{11} \approx 4.2 \times 10^{-15}.$$

By introducing the weight concentrations (abundances) for the chemical elements

$$X(i) = \frac{m_\mathrm{H} n_i A_i}{\rho} = \frac{n_i A_i}{N_A \rho},$$

we can write the reaction rate:

$$\dot{X}(\mathrm{D}) = C_{11}\rho\left[X(\mathrm{H})\right]^2 T_9^{-2/3} e^{-3.38/T_9^{1/3}} \left[\mathrm{s}^{-1}\right].$$

The characteristic time is $t_{11} \approx 1.3 \times 10^{10}$ yr at $\rho = 100$ g/cm^3 and $T = 1.3 \times 10^7$ K.
The reaction is very rare. That's why the Sun is still burning after $\sim 4.6 \times 10^9$ years!

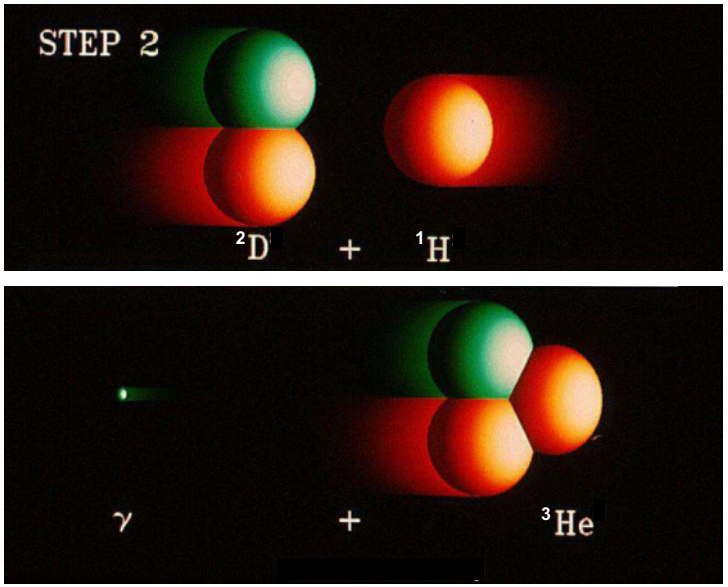

$$\mathbf{p} + \mathbf{d} \rightarrow {}^{\mathbf{3}}\mathrm{He} + \gamma$$

The energy liberation: $Q = 5.494$ MeV; the reaction rate:

$$\dot{X}({}^3\mathrm{He}) = C_{12}\rho X({}^1\mathrm{H}) X({}^2\mathrm{D}) T_9^{-2/3} e^{-3.72/T_9^{1/3}},$$

$$C_{12} \approx 3.98 \times 10^3 \ \mathrm{s}^{-1} \approx 10^{18} C_{11},$$

and $t_{12} \approx 6$ s.

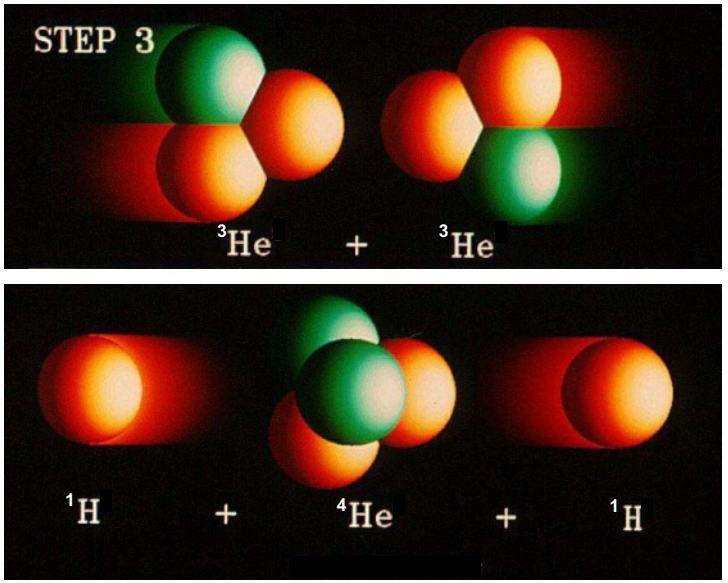

$${}^{\mathbf{3}}\mathrm{He} + {}^{\mathbf{3}}\mathrm{He} \rightarrow \mathbf{2p} + {}^{\mathbf{4}}\mathrm{He}$$

The energy liberation: $Q = 12.859$ MeV; the reaction rate:

$$\dot{X}({}^4\mathrm{He}) = C_{33}\rho \left[X({}^3\mathrm{He})\right]^2 T_9^{-2/3} e^{-12.28/T_9^{1/3}},$$

$$C_{33} \approx 1.3 \times 10^{10} \ \mathrm{s}^{-1} \approx 3 \times 10^6 C_{12}$$

$$\approx 3 \times 10^{24} C_{11},$$

and $t_{33} \approx 10^6$ yr.

• Even at temperatures in the Sun's core, 1.5×10^7 K, the average lifetime of a proton against pp fusion is about $\sim 10^{10}$ yr. It is an extremely slow reaction, and it is this time scale that sets the stellar clock, so to speak, by determining how long the star will remain a stable main sequence object.

• In contrast, the deuteron created will only last about a few seconds before it hits into another proton and fusion creates a ^{3}He nucleus. Therefore it cannot accrue and its stationary concentration is given by $X(\mathrm{D}) = (t_{12}/t_{11})X(\mathrm{H}) \approx 10^{-17}X(\mathrm{H})$.

• The ^{3}He nucleus will last about 250,000 years before it hits another ^{3}He nucleus which has enough energy to penetrate the Coulomb barrier.

28.2 The pep fusion.

The Deuterium can also be produced in the reaction

$$^1\mathrm{H} + ^1\mathrm{H} + e^- \rightarrow ^2\mathrm{D} + \nu_e \quad (E_\nu = 1.44 \text{ MeV})$$

which has a characteristic time scale $\sim 10^{12}$ yr that is rather larger than the age of the Universe at this time. So it is *insignificant* in the Sun as far as energy generation is concerned. Nevertheless, the pep fusion accounts for about 0.25% of the deuterons created in the pp chain.

Enough pep fusions happen to produce a detectable number of neutrinos, so the reaction must be accounted for by those interested in the *solar neutrino problem*.

28.3 The pp II branch.

The ^{3}He does not always have to hit another ^{3}He nucleus. It could hit a ^{4}He forming stable ^{7}Be. But ^{7}Be has an affinity for electron capture, and can absorb free electrons. The electron turns one of the Be protons into a neutron, changing the ^{7}Be into ^{7}Li, while tossing out a neutrino. The ^{7}Li will then quickly fuse with a free proton, resulting in unstable ^{8}Be which immediately falls apart into two stable ^{4}He nuclei.

$^3\text{He}+^4\text{He} \to {}^7\text{Be}+\gamma$	$+1.586$ MeV	$(9.7\times10^5$ yr)
$^7\text{Be}+e^- \to {}^7\text{Li}(+\gamma)+\nu_e$	$+862/384$ keV	$(142$ d)
$^7\text{Li}+^1\text{H} \to {}^4\text{He}+{}^4\text{He}$	$+17.348$ MeV	$(9.5$ min)

$\sim 14\,\%$ of ^{3}He goes out this way avoiding the pp I chain,

$\sim 99.89\,\%$ of ^{7}Be goes the ^{7}Li route.

$\sim 90\%$ of ^{7}Li nuclei are in the ground state and thus $E_\nu = 862$ keV; the rest lithium is created in an excited state and $E_\nu = 384$ keV.

Note: Fusion with ^{4}He is less likely, because there is more ^{3}He around deep inside the stellar core. But in heavier stars, where the temperatures exceed about 2.4×10^7 K, the pp II chain can rival the pp I chain for energy production inside the star. This is because at higher temperatures the ^{3}He gets used up faster, driving down its abundance compared to ^{4}He.

28.4 The pp III branch.

The ^{7}Be has two ways to go – it can either absorb an electron, as in pp II (99.89%), or absorb a proton, as in pp III (0.11%). Absorbing a proton raises the nucleus from beryllium to boron, and the ^{7}Be becomes ^{8}B. But ^{8}B is unstable and takes < 1 s, fairly independent of temperature, to spit out a positron and a neutrino to become beryllium again, only this time it's ^{8}Be. But ^{8}Be falls apart into two ^{4}He nuclei, and once again we have turned Hydrogen into Helium.

$^7\text{Be} + ^1\text{H} \rightarrow ^8\text{B} + \gamma$	$+135$ keV	(66 years)
$^8\text{B} \rightarrow ^8\text{Be} + e^+ + \nu_e$	14.02 MeV	(0.9 s)
$^8\text{Be} \rightarrow ^4\text{He} + ^4\text{He}$	$+18.074$ MeV	(9.7×10^{-17} s)

$\sim 0.11\,\%$ of ^{7}Be goes this route.

Of course, $e^+e^- \rightarrow \gamma\gamma$.

Note: In low mass stars the internal temperature is not high enough to finish the pp cycle. They produce the first stage of pp fusion up to ^{3}He, but are unable to force the last stage of ^{3}He fusion, either with another ^{3}He or an ^{4}He. So they fuse Hydrogen into ^{3}He instead of ^{4}He. This fact is confirmed by the observation that low mass stars are often anomalously rich in ^{3}He compared to ^{4}He.

28.5 The pp IV branch (hep reaction).

The pp chain involves one more process, so-called "hep reaction",

$$^3\text{He} + {}^1\text{H} \to {}^4\text{Li} \to {}^4\text{He} + e^+ + \nu_e.$$

In fact, it is a sub-branch of the pp I chain. The low-energy cross section of this reaction is very uncertain. While the probability of the pp IV branch is roughly estimated to be $\approx 3 \times 10^{-5}\%$, the hep produces highest-energy solar neutrinos,[a]

$$E_\nu \leq 18.77 \text{ MeV},$$

The maximum neutrino energy is equal to the maximum energy of the ^{4}Li β-decay. The hep reaction can at some level influence the electron energy spectrum produced by solar neutrino interactions and potentially can be measured in the high-threshold detectors like Hyper-Kamiokande and DUNE "Module of Opportunity".[b] However, the neutrino flux from the hep branch is so faint that no experiment has so far (fall 2022) been able to observe it.

- The best upper limit for the hep flux today (according to Borexino) is 2.2×10^5 cm^{-2}s^{-1}.
- The observation of hep neutrinos will have a big impact on astroparticle physics, specifically on understanding of stellar evolution and the physics of massive neutrinos, since this process is driven by a much larger fusion core than any other reaction producing neutrinos in the Sun (see Figure at p. 719). A precise interpretation of the observed solar neutrino spectrum requires an accurate estimate of the hep rate. This is an interesting but challenging task.[c]

[a] Except for the immeasurable heep (pp V) branch, which is very briefly discussed below, see p. 723.

[b] S. Parsa *et al.*, "SoLAr: Solar neutrinos in liquid argon," arXiv:2203.07501 [hep-ex].

[c] For a short review, see, e.g., K. Kubodera & T.-S. Park, "The solar hep process," Ann. Rev. Nucl. Part. Sci. **54** (2004) 19–37, nucl-th/0402008.

28.6 The full pp chain.

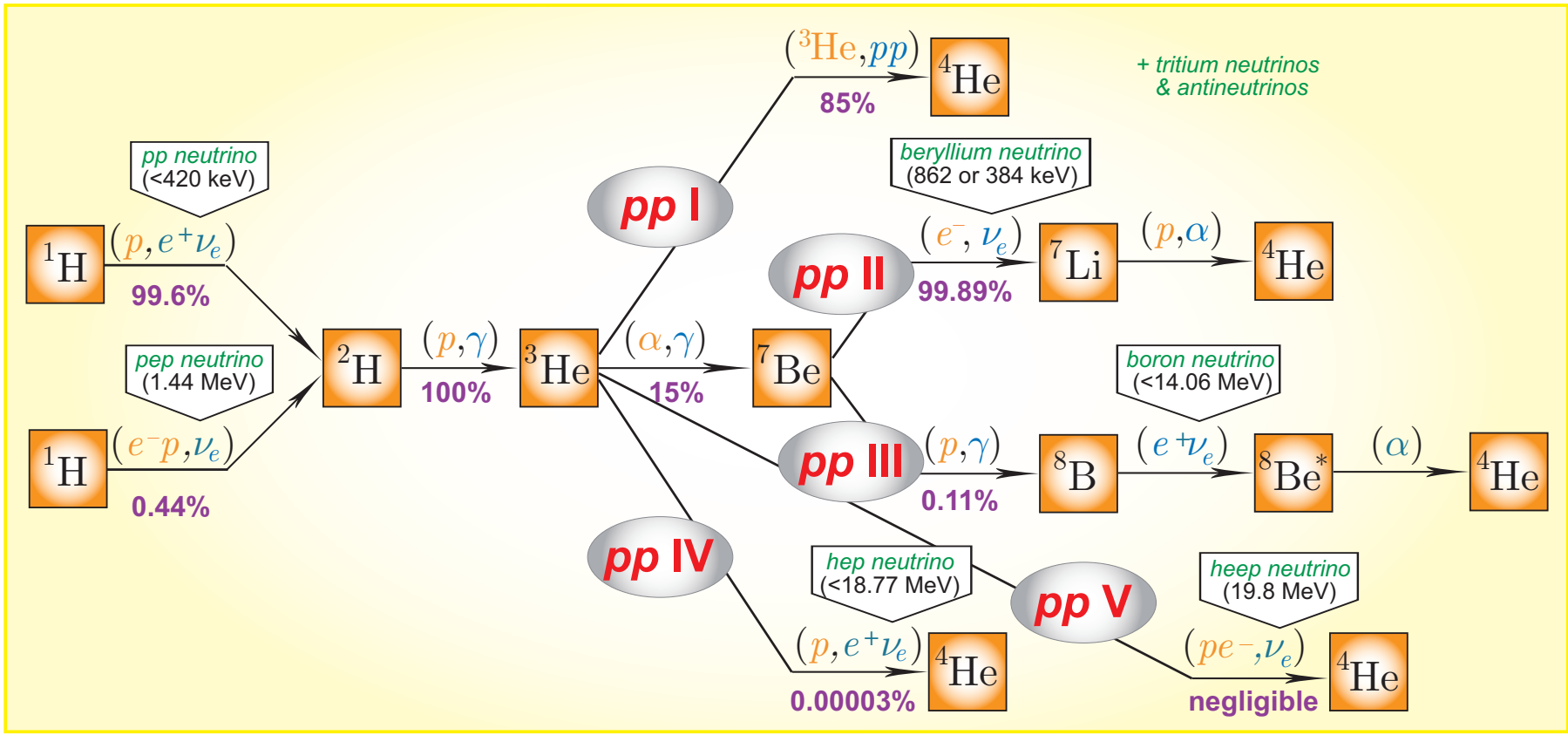

The diagram shows the full pp chain responsible for production of about 98.4% of the solar energy. The neutrinos export 3%, 4%, and 28% of the energy in pp I, pp II, pp III, respectively. Of course, all the chains are active simultaneously in a H-burning star containing significant ^{4}He. The details depend on density, temperature and composition but in the Sun the pp I strongly dominates.

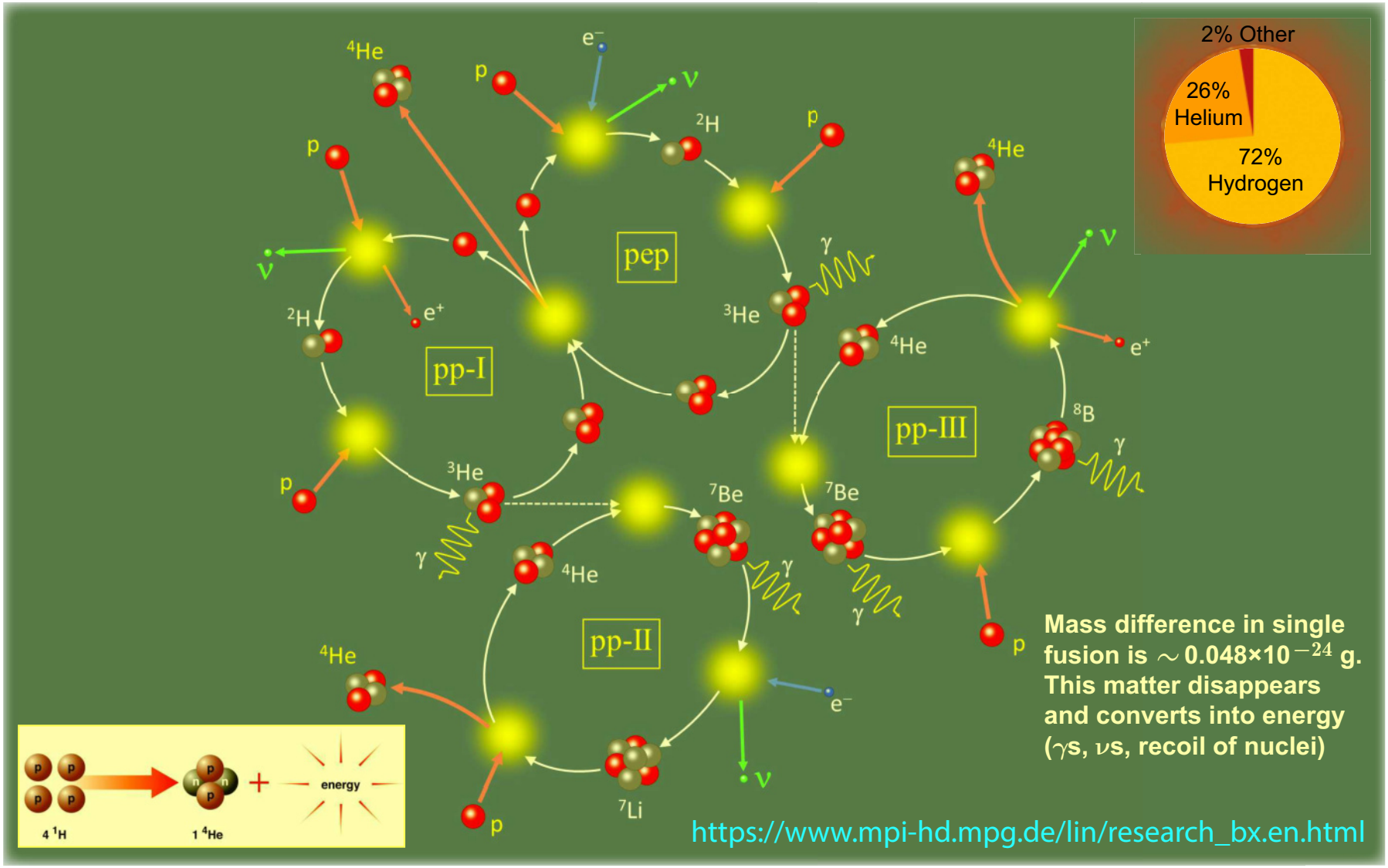

The main part of the pp chain consists of four intertwined branchs. But it is a **quantum relativistic machine** that converts matter into energy. Therefore it is not a Perpetuum Mobile.

Neutrino production profiles.

The rates of the solar neutrino production reactions strongly depend on temperature and thus on distance from the center of the Sun.

Figure shows the normalized flows (i.e. production profiles normalized to unity when integrated over the relative solar radius $R/R_\odot$) of the pp-chain and CNO neutrinos produced within the solar core, calculated with the "BSB(GS98)" model as functions of $R/R_\odot$ (cf. p. 190).

[Figure is taken from J. N. Bahcall, A. M. Serenelli & S. Basu, "10,000 standard solar models: A Monte Carlo simulation," ApJ Suppl. Ser. **165** (2006) 400–431, astro-ph/0511337.]

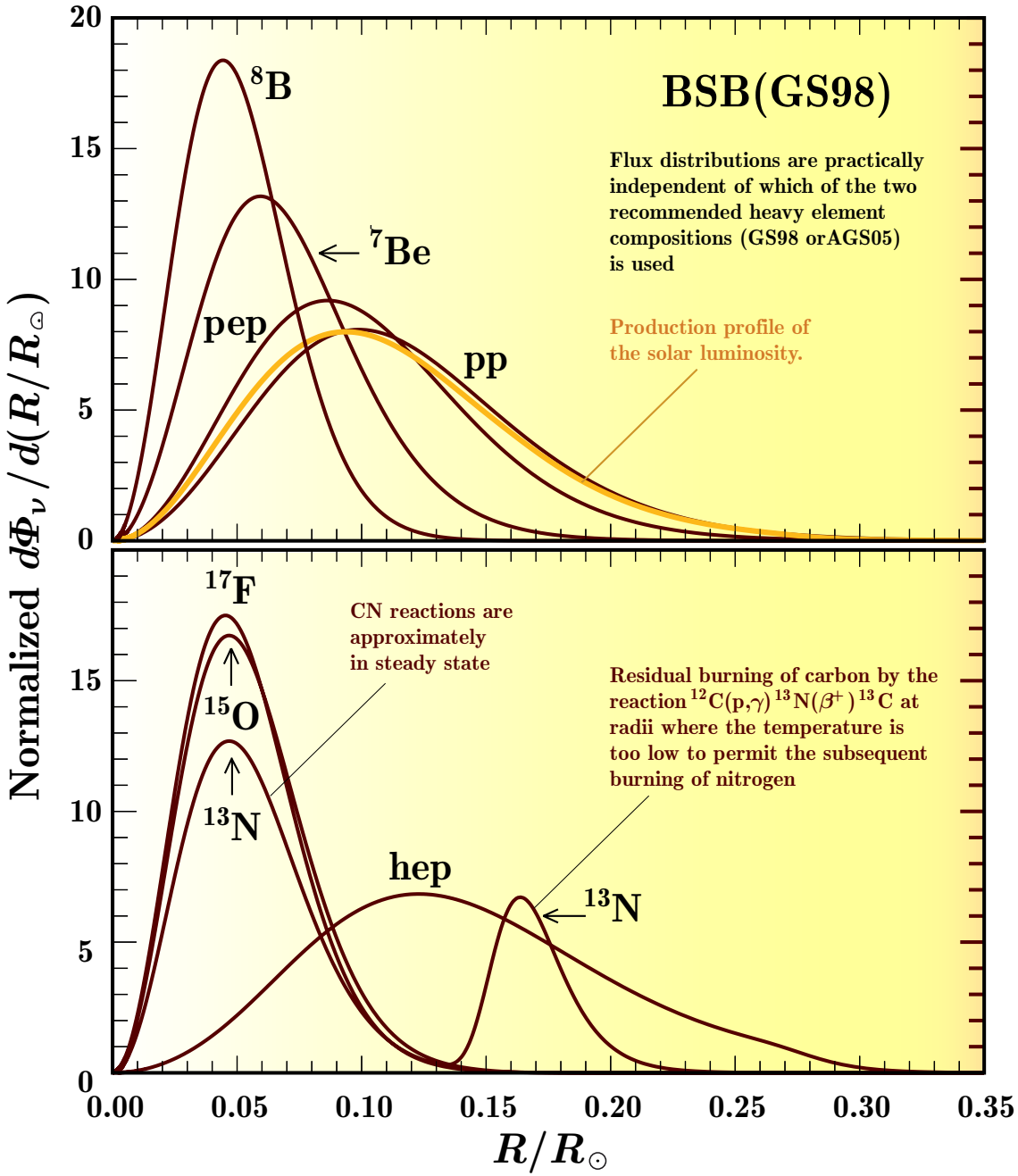

BSB(GS98) is a SSM which uses the same input quantities as the above-mentioned BS05(OP) model, but with improved low-temperature opacities and with the old (high) GS98 metallicities. Very similar results are obtained within solar seismic models (e.g. by Couvidat *et al.*, 2003).

The neutrino flux vanishes at the Sun's center because the neutrino radiation field here is nearly uniform in all directions (neutrino flows crossing a unit area from inside outwards and from outside inwards are the same). With increasing radius, the inward neutrino flux, emerging from the lower-temperature layers, becomes smaller than the outward flux, originating in the high-temperature central regions. The flux from the outer regions of the Sun is obviously zero because the nuclear reactions do not occur below a threshold temperature. Therefore there must be a maximum at some intermediate value of R. This behavior can be seen in the figure on the previous slide.

The ^{8}B, ^{7}Be, ^{15}O, and ^{17}F neutrinos are produced very close to the Sun's center (the inner 10% in radius or 20% in mass) because of the strong temperature dependence of the relevant reaction rates.

The pp, pep, and hep neutrinos appear in broader regions. The ^{13}N neutrino production profile has two peaks. Why? The inner peak at $R \approx 0.047 R_\odot$ corresponds to the region in which the CN reactions operate at quasi-steady state. The outer peak ($R \approx 0.164 R_\odot$) represents the residual burning of ^{12}C by the reaction

$$^{12}\mathrm{C}\,(p,\gamma)\,^{13}\mathrm{N}\,\left(e^{+}\nu_e\right)\,^{13}\mathrm{C}$$

in the (comparatively) low-temperature regions, where the subsequent burning of nitrogen becomes ineffective.

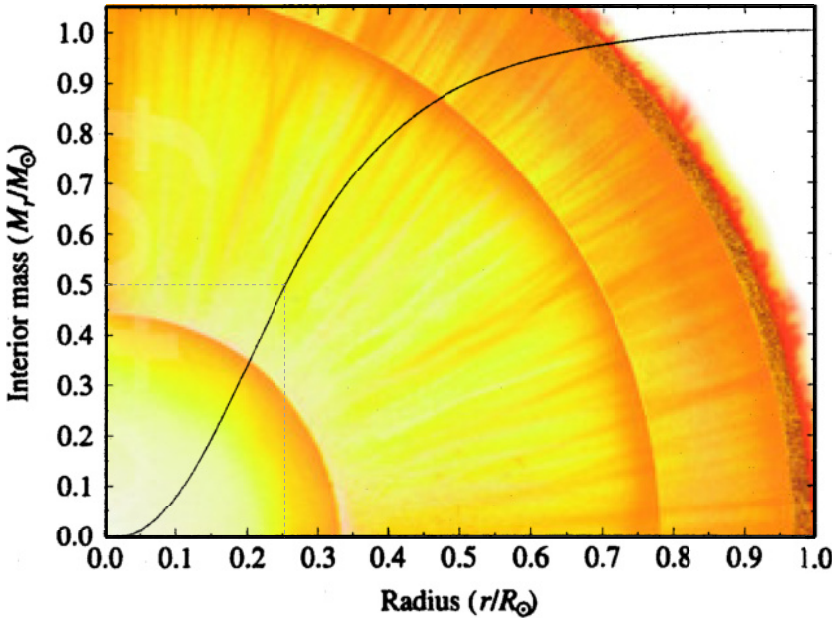

Note that almost half of the solar mass is contained within a radius of $0.25 R_\odot$.

28.7 Training.

- Estimate the characteristic times t_{11}, t_{12}, etc. for several values of the temperature.
- Why $d\,\text{Flux}/d(R/R_\odot) \to 0$ at large $R/R_\odot$?
- Why $d\,\text{Flux}/d(R/R_\odot) \to 0$ at $R/R_\odot \to 0$?
- Why is the fusion ${}^2\text{H} + {}^2\text{H} \to {}^4\text{He}$ forbidden?
- Offer some endothermic reaction(s) in the Sun with ν_e production.
- Offer some reaction(s) in the Sun with production of $\overline{\nu}_e$.
- Are neutrinos generated in powerful solar flares?

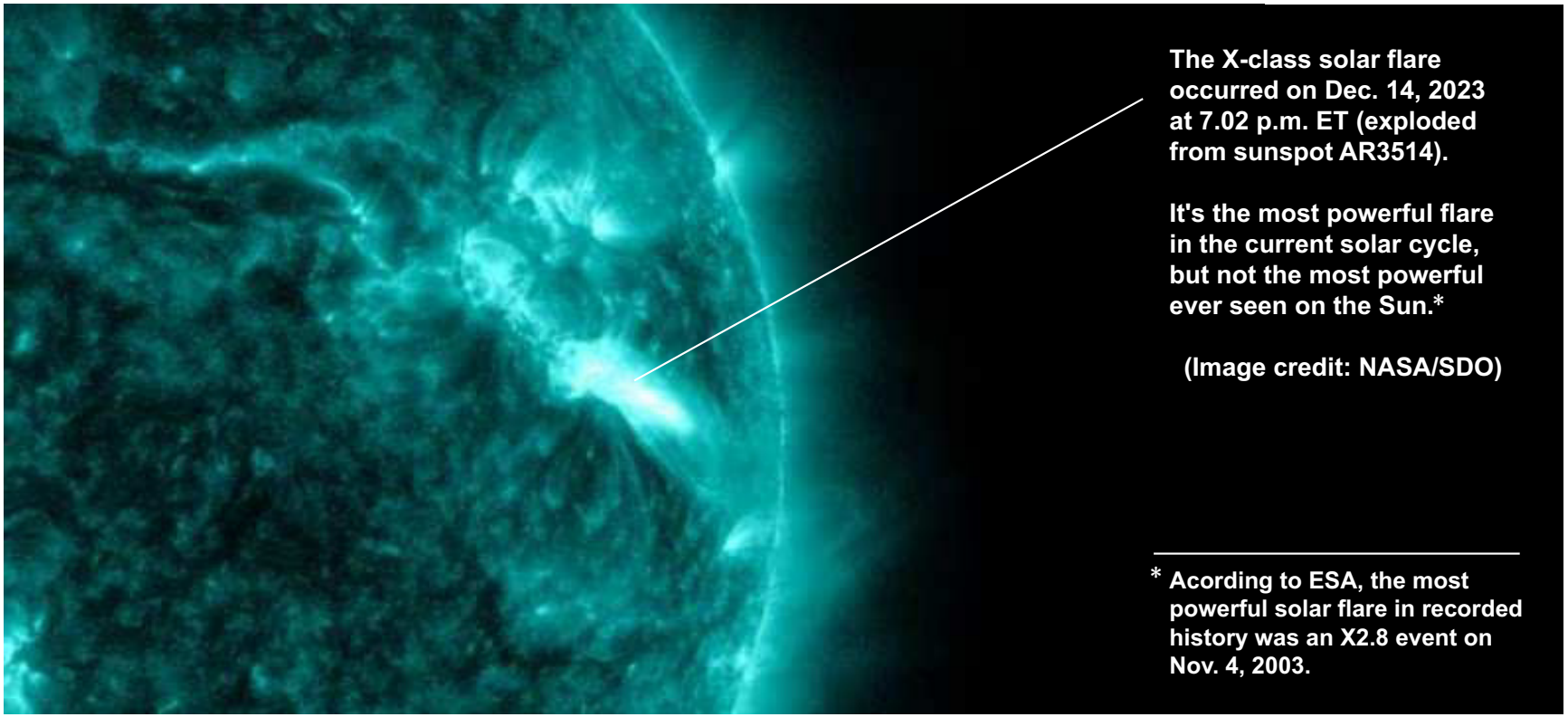

28.8 The full pp chain is not full (?)

In fact there must be a lot of other contributions into the pp chain. Let's consider some (*training*) examples.[a]

28.8.1 Tritium neutrinos.

$$^3\mathrm{He} + e^- \to {}^3\mathrm{H} + \nu_e \quad (E_e > 18.6\ \mathrm{keV},\ t \approx 1.4 \times 10^{11}\ \mathrm{yr}), \tag{171}$$
$$E_\nu = (2.5 - 3.0)\ \mathrm{keV}, \quad F_\nu(1\ \mathrm{a.u}) \approx 8.1 \times 10^4\ \mathrm{cm}^{-2}\mathrm{s}^{-1}.$$

This is an example of endothermal reaction. The chain (171) is completed with the fusion reaction

$$^3\mathrm{H} + p \to {}^4\mathrm{He} + \gamma \quad (E_\gamma = 19.8\ \mathrm{MeV}).$$

28.8.2 Tritium antineutrinos.

In principle, the capture (171) can be followed by the Tritium β-decay with production of *antineutrinos*:

$$E_{\overline{\nu}} < 18.6\ \mathrm{keV}, \quad F_{\overline{\nu}}(1\ \mathrm{a.u.}) \approx 10^3\ \mathrm{cm}^{-2}\mathrm{yr}^{-1}.$$

Alas! Both the energy and flux are very small. This does not allow detecting the solar antineutrinos in the current experimental setups.

[a] B. I. Goryachev, "The extreme energies lines in the solar neutrino spectrum," arXiv:1005.3458 [astro-ph.SR].

28.8.3 The pp V branch (hep reaction).

It is believed that neutrinos with maximum energy are produced in the hep-reaction $E_\nu^{\max} \approx 18.8$ MeV. But, in fact, the most energetic solar neutrinos are produced in the reaction

$$^3\mathrm{He} + e^- + p \to {}^4\mathrm{He} + \nu_e \quad E_\nu = 19.8 \text{ MeV}. \tag{172}$$

Estimated flux is $F_\nu(1 \text{ a.u.}) \approx 2.5 \times 10^{-4}$ cm^{-2}s^{-1}.

28.9 K-shell electron screening.

All our estimations implicitly assume that all the nuclei in the solar core are "bare". But even a comparatively small fraction of ions in the solar plasma affects the ν flux.

Example: Screening in $^7\mathrm{Be} + {}^1\mathrm{H} \to {}^8\mathrm{B} + \gamma$.[a]

Figure shows the predicted enhancement factor

$$\gamma(E) = \sigma_{\text{screened}}(E)/\sigma_{\text{bare}}(E)$$

(vs. the center-of-mass energy) due to K-shell electron.

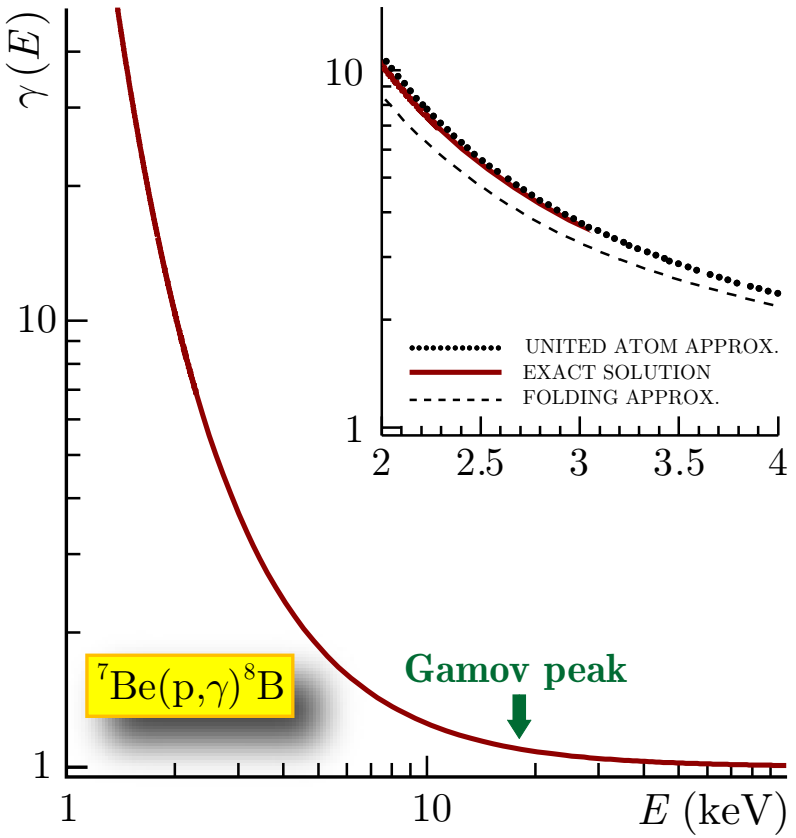

[a] V. B. Belyaev, D. E. Monakhov, D. V. Naumov & F. M. Penkov, "Electron screening in the $^7\mathrm{Be} + p \to {}^8\mathrm{B} + \gamma$," Phys. Lett. A **247** (1998) 241–245, astro-ph/9803003.

29 An excursus: chemical composition of the Sun.

The matter that formed the Sun had already been cycled through one or more generations of stars. We can see elements up to and beyond ^{56}Fe in the photosphere.

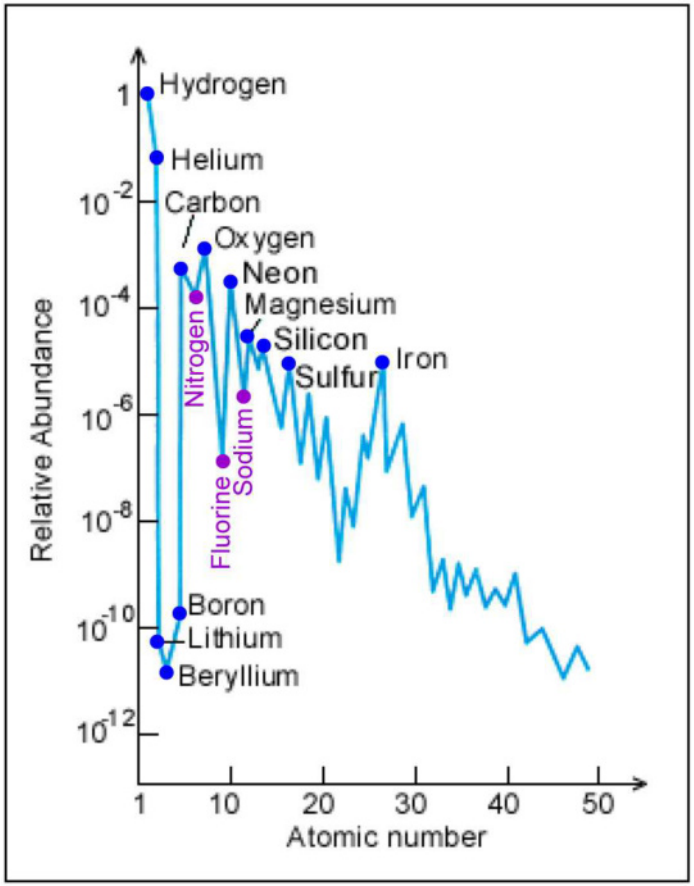

ELEMENTAL ABUNDANCE IN THE SUN

Element	% by mass	% by number
Hydrogen	73.4	92.0
Helium	25.0	7.8
Oxygen	0.80	0.06
Carbon	0.20	0.02
Neon	0.16	0.01
Iron	0.14	0.003
Nitrogen	0.09	0.008
Silicon	0.09	0.004
Magnesium	0.06	0.003
Sulfur	0.05	0.002

Present-day solar abundance curve is shown in the figure (the ordinate compares all elements to Hydrogen) and the relative abundances (by mass and by number) are shown in the table.

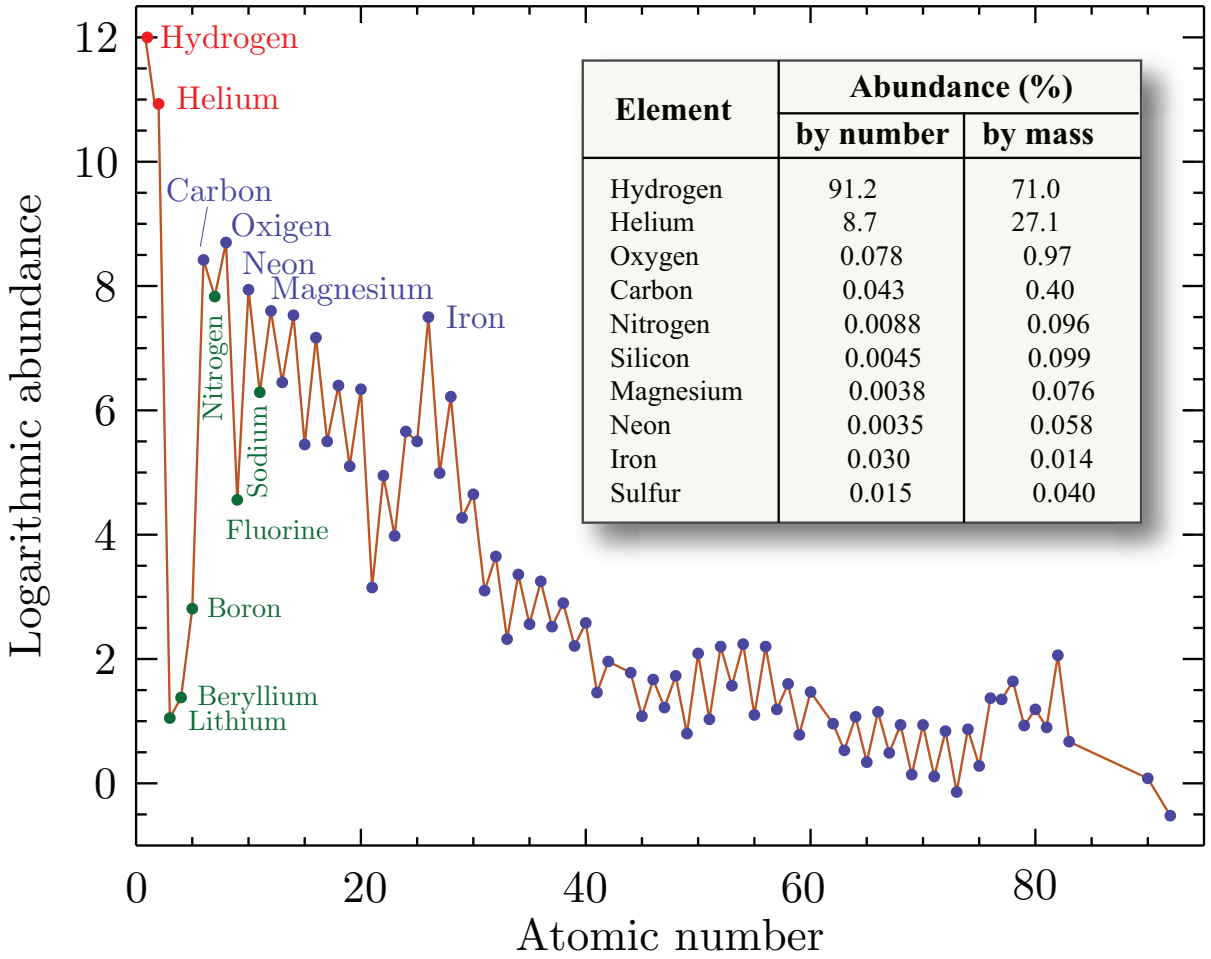

Element	Abundance (%)	
	by number	by mass
Hydrogen	91.2	71.0
Helium	8.7	27.1
Oxygen	0.078	0.97
Carbon	0.043	0.40
Nitrogen	0.0088	0.096
Silicon	0.0045	0.099
Magnesium	0.0038	0.076
Neon	0.0035	0.058
Iron	0.030	0.014
Sulfur	0.015	0.040

[Upadated] present-day solar photospheric elemental abundances vs. Z according to M. Asplund *et al.*, Ann. Rev. Astron. Astrophys. **47** (2009) 481–522, arXiv:0909.0948 [astro-ph.SR]. The logarithmic abundance ϵ_H of Hydrogen is defined to be $\log \epsilon_H = 12$ that is $\log \epsilon_X = \log(n_X/n_H) + 12$, where n_X and n_H are the number densities of elements X and H, respectively. The insert shows the relative abundances of the ten most prevalent elements. Find ten differences with the previous slide.

Comments:

- The general trend is towards ever decreasing abundances as the atomic number increases.
- There is a distinct zig-zag (up-down) pattern to the whole curve. For example,
  - between Carbon and Oxygen there is a decrease (the element is Nitrogen);
  - between Neon and Magnesium the decrease element is Sodium;
  - the largest drop is between Oxygen and Neon, the element that thus decreases notably is Fluorine.

  The reason for this fluctuating pattern is just this: elements with *odd* numbers of nucleons are less stable, resulting in one unpaired (odd) proton or neutron – those that pair these particles result in offsetting spins in opposite directions that enhance stability.

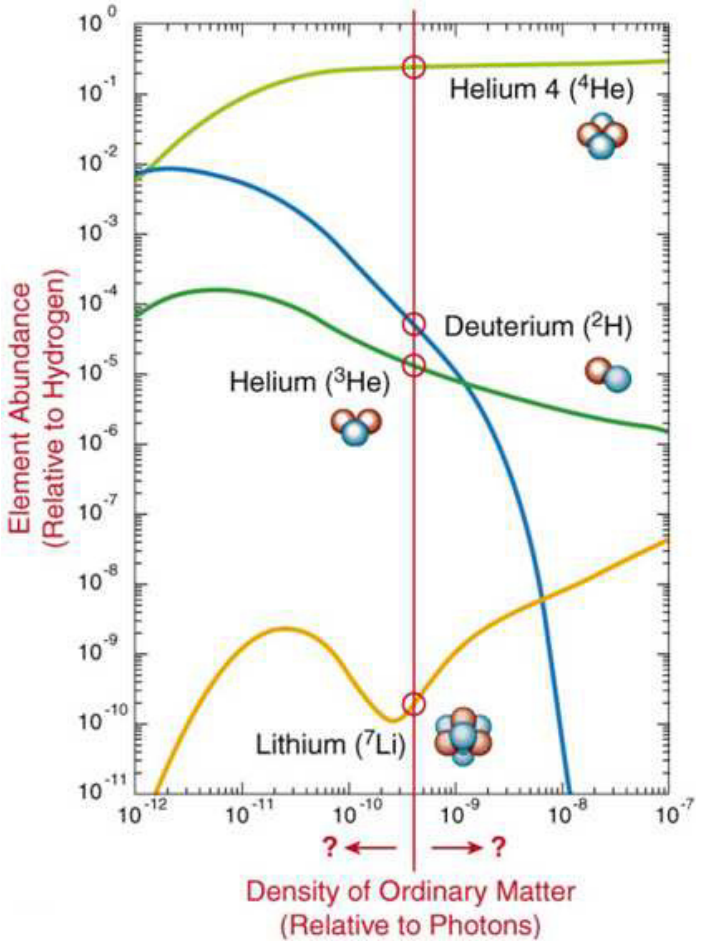

- There is a huge drop in abundance for the Lithium-Beryllium-Boron triplet. This results from two factors:
  - at the Big Bang, nuclear processes that could fuse the proper H or He isotopes into Li and/or the other two were statistically very rare and hence inefficient, and
  - some of the Li-Be-B that formed and survived may be destroyed in processes with stars.

30 The CNO cycle.

The presence of the "impurities" in the solar core opens the door to another fusion reaction. The most important (after the pp) is the CNO bi-cycle, which is responsible for as much as 1.6% of the Sun's total output. The main CNO reactions ("cycle I") are

$^{12}\mathrm{C}+^{1}\mathrm{H} \rightarrow {}^{13}\mathrm{N}+\gamma$	$+1.944$ MeV	$(1.3\times10^{7}$ years$)$
$^{13}\mathrm{N}\rightarrow {}^{13}\mathrm{C}+e^{+}+\nu_e$	$+2.221$ MeV	$(7$ min$)$
$^{13}\mathrm{C}+^{1}\mathrm{H} \rightarrow {}^{14}\mathrm{N}+\gamma$	$+7.551$ MeV	$(2.7\times10^{6}$ years$)$
$^{14}\mathrm{N}+^{1}\mathrm{H} \rightarrow {}^{15}\mathrm{O}+\gamma$	$+7.293$ MeV	$(3.2\times10^{8}$ years$)$
$^{15}\mathrm{O}\rightarrow {}^{15}\mathrm{N}+e^{+}+\nu_e$	$+2.761$ MeV	$(82$ s$)$
$^{15}\mathrm{N}+^{1}\mathrm{H} \rightarrow {}^{12}\mathrm{C}+{}^{4}\mathrm{He}$	$+4.966$ MeV	$(1.1\times10^{5}$ years$)$

- The cycle uses carbon, nitrogen, and oxygen as catalysts to suck up four protons and build a ^{4}He nucleus out of them. The relative abundances of C, N, and O do not change.
- The cycle does not start until the pp fusion has begun, and provides the energy necessary to allow a low level of proton fusions onto the heavier nuclei.
- The cycle timescale is determined by the slowest reaction ($^{14}\mathrm{N}+{}^{1}\mathrm{H}$) while the approach to equilibrium is determined by the second slowest reaction ($^{12}\mathrm{C}+{}^{1}\mathrm{H}$).

The second minor branch ("cycle II") is a similar type of cycle, and it joins onto the first. Starting with ^{14}N, the process steps through two of the last-three reactions given above until ^{15}N is produced. It then proceeds as follows to convert ^{15}N back into ^{14}N, with the production of ^{17}F (fluorine-17) occurring in one of the steps:

$$
\begin{aligned}
^{15}\mathrm{N} + ^{1}\mathrm{H} &\rightarrow ^{16}\mathrm{O} + \gamma && +12.128 \text{ MeV} \\
^{16}\mathrm{O} + ^{1}\mathrm{H} &\rightarrow ^{17}\mathrm{F} + \gamma && +0.601 \text{ MeV} \\
^{17}\mathrm{F} &\rightarrow ^{17}\mathrm{O} + e^{+} + \nu_e && +2.726 \text{ MeV} \\
^{17}\mathrm{O} + ^{1}\mathrm{H} &\rightarrow ^{14}\mathrm{N} + ^{4}\mathrm{He} && +1.193 \text{ MeV}
\end{aligned}
$$

The latter cycle is much less frequent, with the first reaction having a probability of about 4×10^{-4} relative to the last reaction of the cycle I.

The fractions of the nuclear energy loss from the core through neutrino emission in the first and second branches of the CNO process are 6% and 4%, respectively.

Note: The CNO cycle lacks significance at the low temperatures in the Sun. For abundances characteristic of the Sun, the CNO process becomes important for core temperatures of roughly 1.5×10^7 K (1.3 keV), and it provides virtually all of the conversion of Hydrogen into Helium in the later stages of the solar lifetime when the temperature exceed 2.5×10^7 K (2.2 keV).

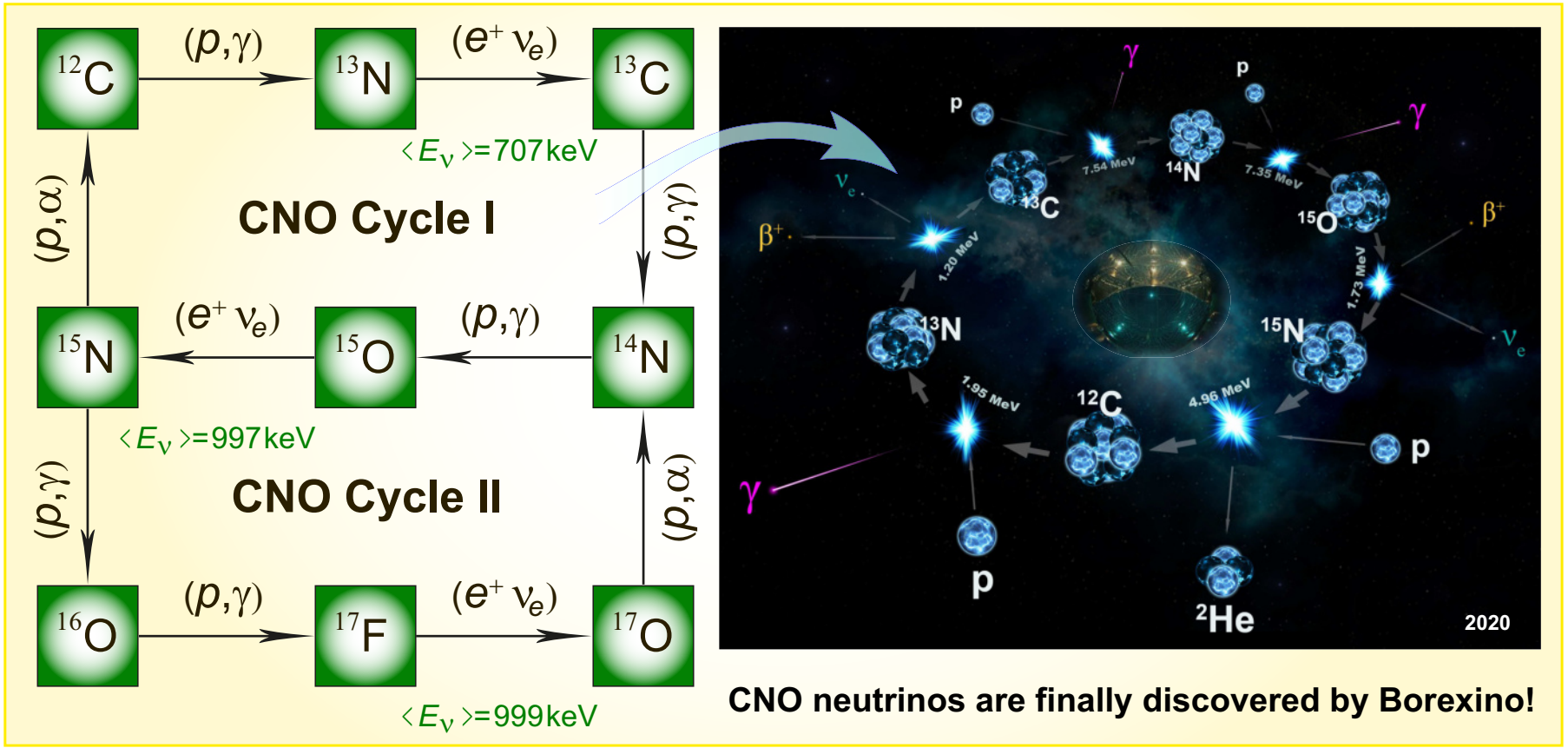

The full CNO bi-cycle (Carl von Weizsacker, Hans Bethe) responsible for production of about 1.5–1.6% of the solar energy. The cycle I fully dominates (cycle II occurs 0.04% of the time).

- The CNO cycles III and IV are only essential for the Hydrogen burning in massive stars. The full net includes ^{18}F, ^{18}O, and ^{19}F (see next slide).
- Recently, there has been strong experimental evidence for the presence of the CNO neutrinos.[a]

[a] N. Agostini *et al.* (The Borexino Collaboration) "Experimental evidence of neutrinos produced in the CNO fusion cycle in the Sun," Nature **587** (2020) 577–582, arXiv:2006.15115 [hep-ex].

30.1 The full CNO poly-cycle.

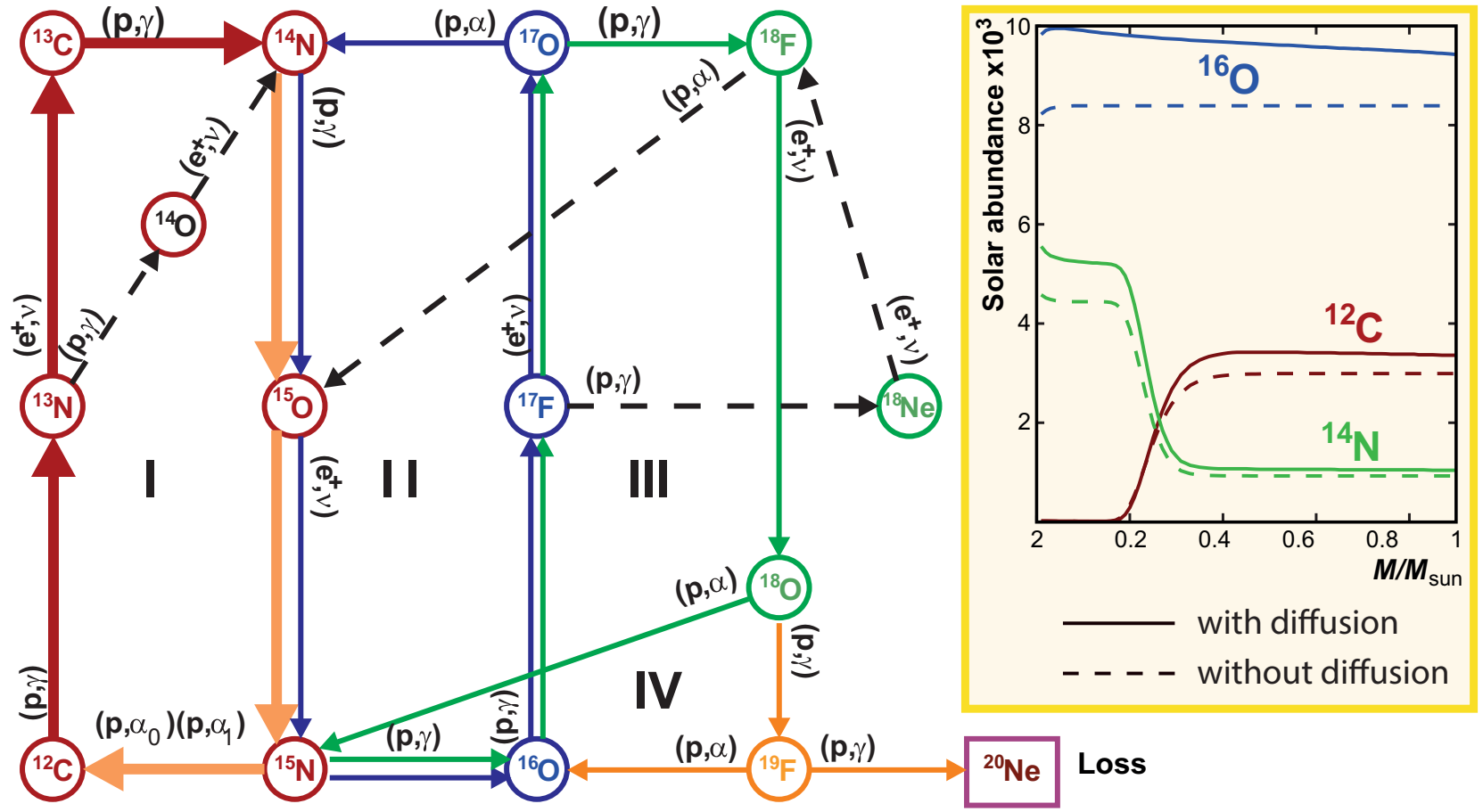

The full CNO poly-cycle. The widths of the arrows illustrate the significance of the reactions in determining the nuclear fusion rates in the poly-cycle. Certain "Hot CNO" processes are indicated by dashed lines. The insert shows the abundances of ^{12}C, ^{14}N, and ^{16}O, in the interior of the sun.

[From A. Kopylov, I. Orekhov, V. Petukhov, A. Solomatin, and M. Arnoldov, "Lithium experiment on solar neutrinos to weight the CNO cycle," Yad. Fiz. **67** (2004) 1204–1209 [Phys. Atom. Nucl. **67** (2004) 1182–1187], hep-ph/0310163.]

30.2 CNO electron capture.

An additional (minor) contribution to the CNO neutrino flux usually not included into the solar models is electron capture (EC) on those isotopes.[a] The relevant reactions are

$$^{13}\mathrm{N} + e^- \to {}^{13}\mathrm{C} + \nu_e, \quad {}^{15}\mathrm{O} + e^- \to {}^{15}\mathrm{N} + \nu_e, \quad {}^{17}\mathrm{F} + e^- \to {}^{17}\mathrm{O} + \nu_e.$$

At solar temperatures and densities one must take into account the contribution from both bound (mainly K-shell) and continuum electrons.

Таблица 1: Neutrino fluxes and energies from the CNO β^+ decays and electron capture.

	Mean β^+ decay flux ($\mathrm{cm}^{-2}\mathrm{s}^{-1}$)	$\langle E_\nu \rangle$ (MeV)	EC flux ($\mathrm{cm}^{-2}\mathrm{s}^{-1}$)	E_ν (MeV)	(EC/β^+ decay)$_{\mathrm{lab}}$
^{13}N	$5.48 \times 10^8 \left(^{+0.21\%}_{-0.17\%}\right)$	0.707	4.33×10^5	2.220	1.96×10^{-3}
^{15}O	$4.80 \times 10^8 \left(^{+0.25\%}_{-0.19\%}\right)$	0.997	1.90×10^5	2.754	9.94×10^{-4}
^{17}F	$5.63 \times 10^6 \left(^{+0.25\%}_{-0.25\%}\right)$	0.999	3.32×10^5	2.761	1.45×10^{-3}

The flux of the CNO EC neutrinos is of the same order as the boron neutrino flux, though at lower neutrino energies. So the rate of these neutrinos on current detectors is expected to be small but not fully negligible.

[a] J. N. Bahcall, "Line versus continuum solar neutrinos," Phys. Rev. D **41** (1990) 2964–2966; L. C. Stonehill, J. A. Formaggio, & R. G. H. Robertson, "Solar neutrinos from CNO electron capture," Phys. Rev. C **69** (2004) 015801, hep-ph/0309266.

31 Solar neutrino spectrum.

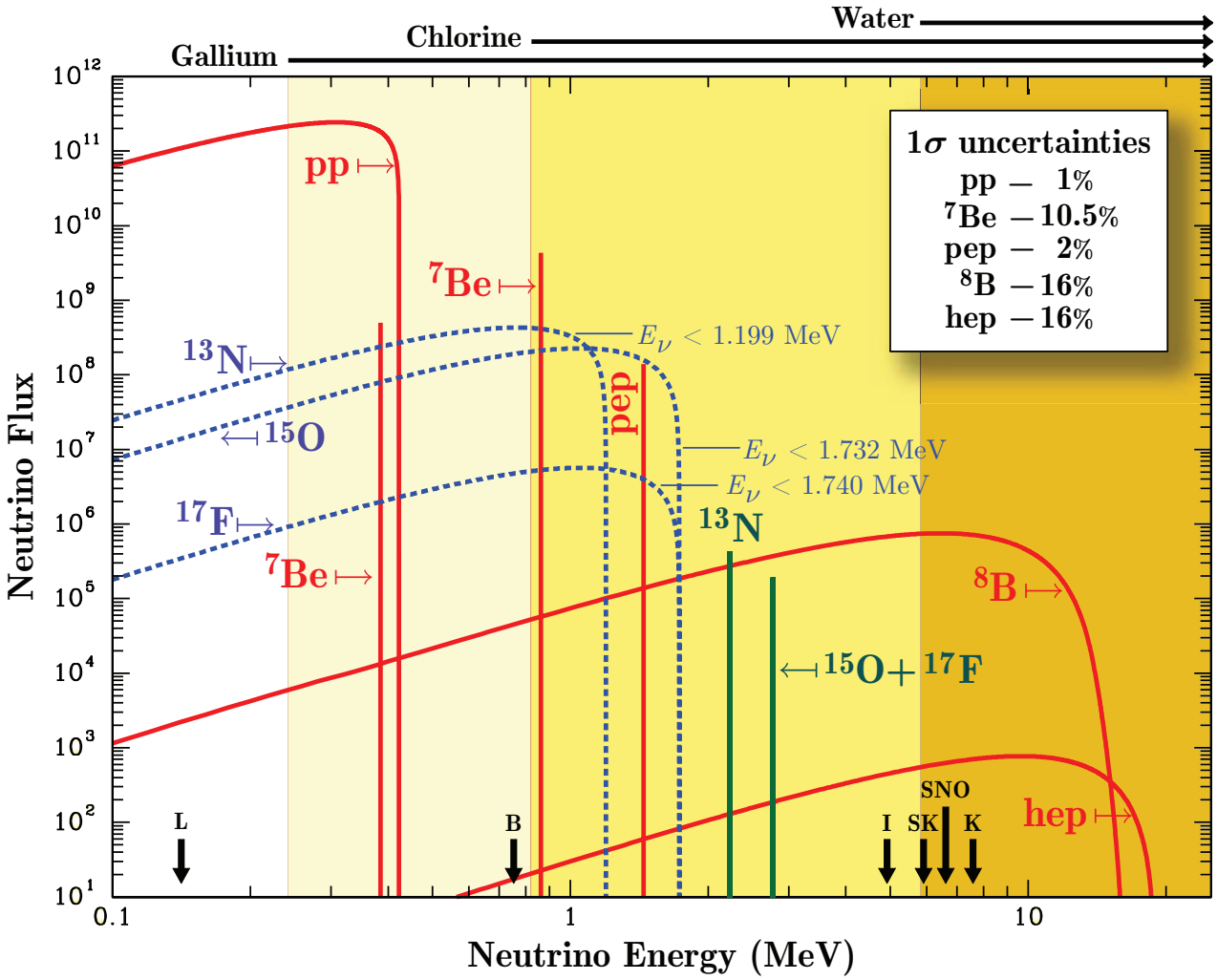

The predicted electron neutrino energy spectrum at 1 a.u. from the pp chain and CNO bi-cycle reactions (including CNO electron capture). Line fluxes are in $\mathrm{cm}^{-2}\mathrm{s}^{-1}\mathrm{MeV}^{-1}$ and spectral fluxes are in $\mathrm{cm}^{-2}\mathrm{s}^{-1}$.

Also shown the uncertainties of the pp cycle neutrino flux calculation (on 1σ level) and the threshold neutrino energies for several detectors; cf. Figure at p. 189.

[The combined data are taken from J. N. Bahcall, A. M. Serenelli & S. Basu, "New solar opacities, abundances, helioseismology, and neutrino fluxes," ApJ **621** (2005) L85–L88 and L. C. Stonehill, J. A. Formaggio & R. G. H. Robertson, "Solar neutrinos from CNO electron capture," Phys. Rev. C **69** (2004) 015801.]

Comparison between the "Standard Solar Models" of Bahcall & Pinsonneault (1995) [BP95] and of Dar & Shaviv (1996) [DS96].[a]

Parameter/Effect	**BSP98**	**DS96**
$M_\odot$	1.9899×10^{33} g	1.9899×10^{33} g
$L_\odot$	3.844×10^{33} erg s^{-1}	3.844×10^{33} erg s^{-1}
$R_\odot$	6.9599×10^{10} cm	6.9599×10^{10} cm
$t_\odot$	4.566×10^{9} **y**	4.57×10^{9} **y**
Rotation	Not Included	Not Included
Magnetic Field	Not Included	Not Included
Mass Loss	Not Included	Not Included
Angular Momentum Loss	Not Included	Not Included
Premain Sequence Evolution	Not Included	Included
Initial Abundances :		
^{4}He	Adjusted	Adjusted
C, N, O, Ne	Adjusted	Adjusted
All Other Elements	Adjusted	Meteoritic

[a] From A. Dar and G. Shaviv, "The solar neutrino problem: An update," Phys. Rept. **311** (1999) 115–141, astro-ph/9808098.

Continued

Parameter/Effect	BSP98	DS96
Photospheric Abundances :		
^{4}He	Predicted	Predicted
C, N, O, Ne	Photospheric	Photospheric
All Other Elements	Meteoritic	Predicted
Radiative Opacities	OPAL 1996	OPAL 1996
Equation of State	Straniero 1996?	Dar – Shaviv 1996
Partial Ionization Effects	Not Included	Included
Diffusion of Elements :		
H, ^{4}He	Included	Included
Heavier Elements	Approximated by Fe	All Included
Partial Ionization Effects	Not Included	Included
Nuclear Reaction Rates :		
$S_{11}(0)$ eV · b	4.00×10^{-19}	4.07×10^{-19}
$S_{33}(0)$ MeV · b	5.3	5.6
$S_{34}(0)$ keV · b	0.53	0.45
$S_{17}(0)$ eV · b	19	17
Screening Effects	Included	Included
Nuclear Equilibrium	Imposed	Not Assumed

The table in next slide summarizes the predicted capture rates for the chlorine and gallium detectors published during 20 years (till 2010).[a] The list is certainly incomplete, but rather representative. The quoted errors are combinations of (usually 3σ) uncertainties from all known sources added quadratically. he recent SSM calculations by Bahcall *et al*. (2006) and Peña-Garay & Serenelli (2008) use the two solar abundances determinations with high and low metallicity, labelled as CS98 and AGS05, respectively. The SSM and seismic model (SeSM) by Turck-Chièze & Couvidat (2010) use the most recent AGSS09 abundances model.

It is seen that the predictions of different models for the gallium target are more robust than those for the chlorine one: the former vary from model to model within 22% (9% for the most recent models that is within the quoted model uncertainties), while the disagreement between the chlorine predictions is as large as 78% (29% for the recent models). Essentially all these models are based on the same physical principles and the disagreement between the output values is mainly due to the input nuclear-physics and astrophysical parameters. The most non-traditional approach has been adopted by Dar and Shaviv (1994, 1996) whose model predicted the lowest solar neutrino flux. The authors have demonstrated that it is possible to "tweak" the standard solar model enough to significantly reduce the high-energy neutrino flux without any major disruption of our understanding of how the Sun shines and how neutrinos behave. However the model of Dar and Shaviv was met with a hostile reception from the solar neutrino community (headed by Bahcall). The main source of uncertainties in the modern solar models is the choice of the input chemical composition of the Sun. The consistency between the different chlorine predictions is much less satisfactory. The "terms-of-trade" between the low (AGS05), high (GS98), or medium (AGSS09, L10) metallicities (LZ, HZ, MZ) is not a matter of majority vote and in any case, today, there is no generally accepted criterion of the optimal model choice.

[a] V. A. Naumov, "Solar neutrinos. Astrophysical aspects," Phys. Part. Nucl. Lett. **8** (2011) 683–703.

Predicted capture rates for chlorine and gallium targets.

Year	Authors	^{37}Cl (SNU)	^{71}Ga (SNU)	
1990	Sackmann *et al.*	7.68	125.0	
1992	Bahcall & Pinsonneault	8.0 ± 3.0	131.5^{+21}_{-17}	
1993	Turck-Chièze & Lopes	6.4 ± 1.4	122.5 ± 7	
1993	Schramm & Shi	4.7	117	a
1994	Shi *et al.*	7.3	129	
1994	Castellani *et al.*	7.8	130	
1994	Dar & Shaviv	4.2 ± 1.2	116 ± 6	
1995	Bahcall & Pinsonneault	$9.3^{+1.2}_{-1.4}$	137^{+7}_{-8}	
1996	Dar & Shaviv	4.1 ± 1.2	115 ± 6	
1996	Christensen-Dalsgaard *et al.*	8.2	132	
1997	Morel *et al.*	8.93	144	b
1998	Bahcall *et al.*	$7.7^{+1.2}_{-1.0}$	129^{+8}_{-6}	
1998	Brun *et al.*	7.18	127.2	
1999	Brunet *et al.*	7.25 ± 0.94	127.1 ± 8.9	c
2001	Bahcall *et al.*	$8.0^{+1.4}_{-1.1}$	128^{+9}_{-7}	
2001	Turck-Chièze *et al.*	7.44 ± 0.96	127.8 ± 8.6	
2003	Couvidat *et al.*	6.90 ± 0.90	126.8 ± 8.9	d
2004	Bahcall & Peña-Garay	8.5 ± 1.8	131^{+12}_{-10}	e
2004	Turck-Chièze *et al.*	7.60 ± 1.10	123.4 ± 8.2	
2006	Bahcall *et al.* (GS98)	8.12	126.08	
2006	Bahcall *et al.* (AGS05)	6.58	118.88	
2008	Peña-Garay & Serenelli (GS98)	$8.46^{+0.87}_{-0.88}$	$127.9^{+8.1}_{-8.2}$	
2008	Peña-Garay & Serenelli (AGS05)	$6.86^{+0.69}_{-0.70}$	$120.5^{+6.9}_{-7.1}$	
2010	Turck-Chièze & Couvidat (SSM)	6.315	120.9	
2010	Turck-Chièze & Couvidat (SeSM)	7.67 ± 1.1	123.4 ± 8.2	

Footnotes to Table at p. 736:

[a] The quoted numbers are corrected according to Shi *et al.* (1994).
[b] Several models; the quoted numbers are for the model "D11" preferred by the authors.
[c] Several models; the quoted numbers are for the reference model "BTZ" as cited by Couvidat *et al.* (2003).
[d] Several models; the quoted numbers are for the model "Seismic$_2$" provided minimal predicted rate.
[e] Several models; the quoted numbers are for the model "BP04" preferred by the authors.

SSM neutrino fluxes from the GS98-SFII (HZ) and AGSS09-SFII (MZ) SSMs, with associated uncertainties (averaging over asymmetric uncertainties).[a] The solar values come from a luminosity constrained analysis of the Borexino data (before 2012). [See p. 787 for the newer Borexino results.]

Reaction	$E_\nu^{\max}$ (MeV)	GS98-SFII	AGSS09-SFII	Solar	Units
$p + p \to {}^2\mathrm{H} + e^+ + \nu$	0.42	$5.98(1 \pm 0.006)$	$6.03(1 \pm 0.006)$	$6.05(1^{+0.003}_{-0.011})$	$10^{10}/\mathrm{cm}^2\mathrm{s}$
$p + e^- + p \to {}^2\mathrm{H} + \nu$	1.44	$1.44(1 \pm 0.012)$	$1.47(1 \pm 0.012)$	$1.46(1^{+0.010}_{-0.014})$	$10^{8}/\mathrm{cm}^2\mathrm{s}$
${}^7\mathrm{Be} + e^- \to {}^7\mathrm{Li} + \nu$	0.86 (90%)/0.38 (10%)	$5.00(1 \pm 0.07)$	$4.56(1 \pm 0.07)$	$4.82(1^{+0.05}_{-0.04})$	$10^{9}/\mathrm{cm}^2\mathrm{s}$
${}^8\mathrm{B} \to {}^8\mathrm{Be} + e^+ + \nu$	~ 15	$5.58(1 \pm 0.14)$	$4.59(1 \pm 0.14)$	$5.00(1 \pm 0.03)$	$10^{6}/\mathrm{cm}^2\mathrm{s}$
${}^3\mathrm{He} + p \to {}^4\mathrm{He} + e^+ + \nu$	18.77	$8.04(1 \pm 0.30)$	$8.31(1 \pm 0.30)$	—	$10^{3}/\mathrm{cm}^2\mathrm{s}$
${}^{13}\mathrm{N} \to {}^{13}\mathrm{C} + e^+ + \nu$	1.20	$2.96(1 \pm 0.14)$	$2.17(1 \pm 0.14)$	≤ 6.7	$10^{8}/\mathrm{cm}^2\mathrm{s}$
${}^{15}\mathrm{O} \to {}^{15}\mathrm{N} + e^+ + \nu$	1.73	$2.23(1 \pm 0.15)$	$1.56(1 \pm 0.15)$	≤ 3.2	$10^{8}/\mathrm{cm}^2\mathrm{s}$
${}^{17}\mathrm{F} \to {}^{17}\mathrm{O} + e^+ + \nu$	1.74	$5.52(1 \pm 0.17)$	$3.40(1 \pm 0.16)$	≤ 59.0	$10^{6}/\mathrm{cm}^2\mathrm{s}$
χ^2/P^{agr}		3.5/90%	3.4/90%		

[a] W. C. Haxton, R. G. Hamish Robertson & A. M. Serenelli, "Solar Neutrinos: Status and Prospects," Ann. Rev. Astron. Astrophys. **51** (2013) 21–61, arXiv:1208.5723 [astro-ph.SR].

Part VIII

Solar neutrino experiments

32 Current status of the solar neutrino problem.

Experimental status on fall 2005

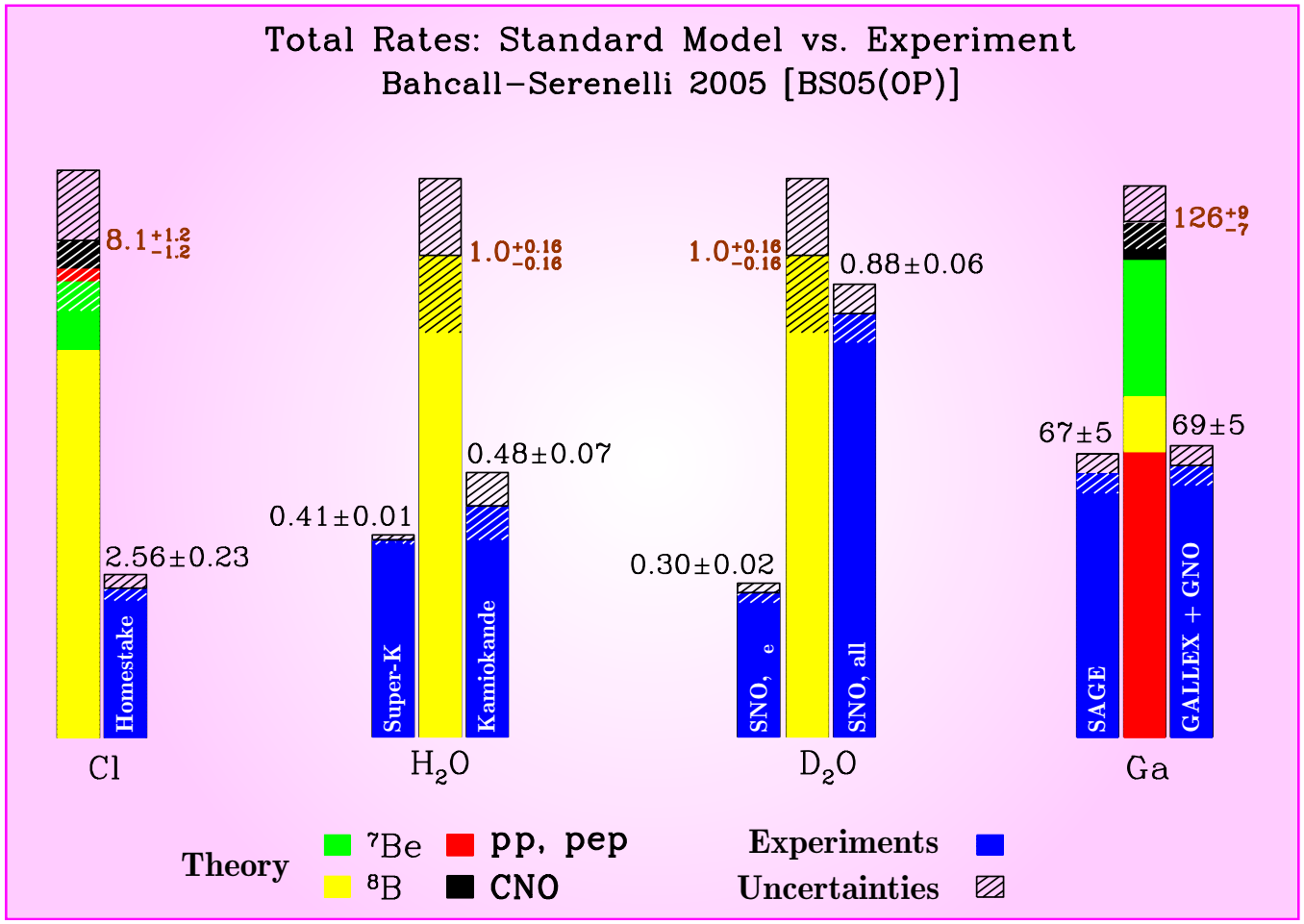

[Borrowed from John Bahcall's Home Page, URL: ⟨ http://www.sns.ias.edu/~jnb/ ⟩ (modified & updated).]

Experimental status on fall 2012

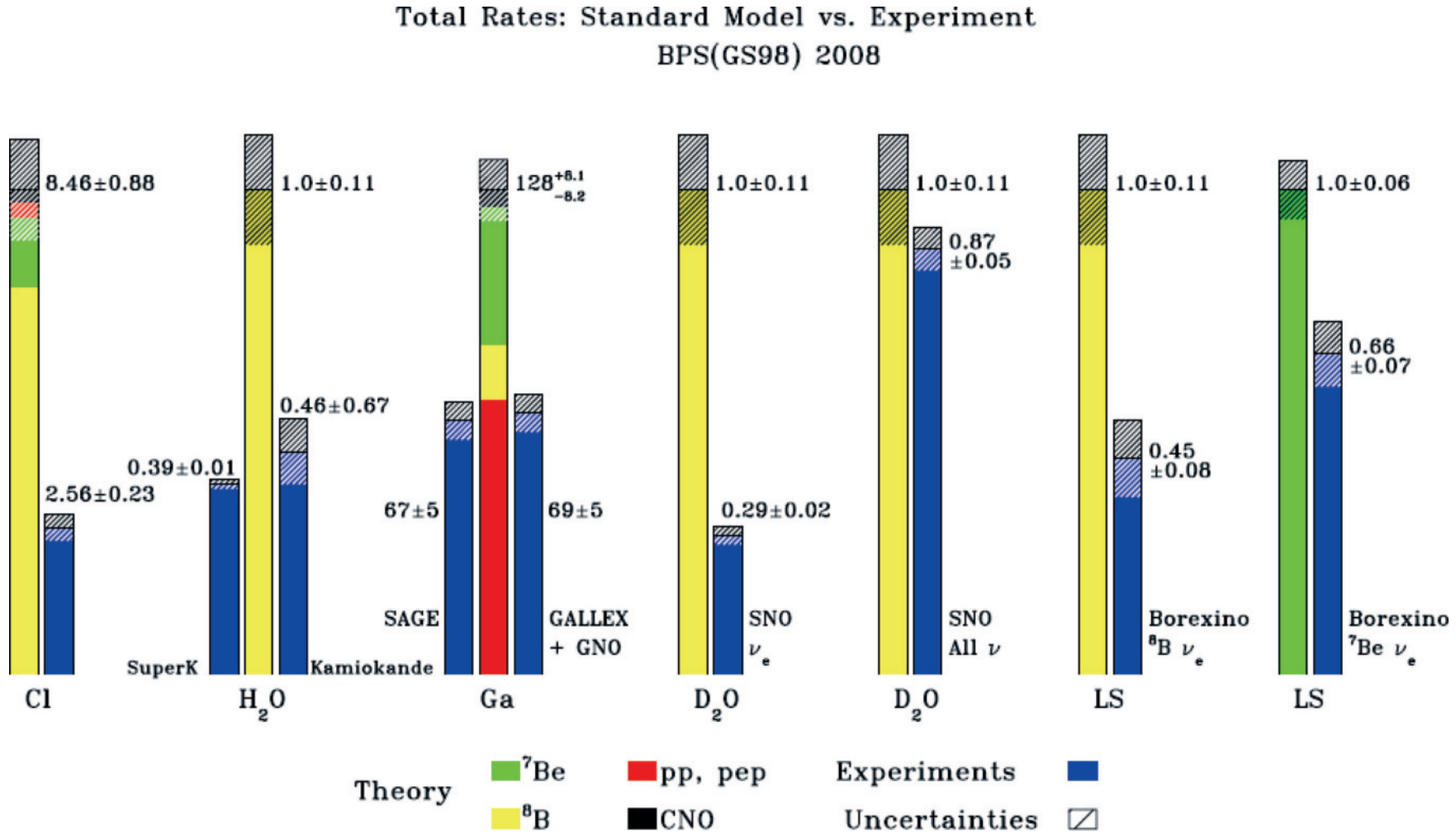

[Borrowed from the lecture by Carlos Pena Garay, "Solar neutrinos: status and prospect" given on the Vth International Pontecorvo Neutrino Physics School, September 6–16, 2012, Alushta, Crimea, Ukraine,
URL: ⟨ http://pontecorvosch.jinr.ru/Lectures/Pena-Garay-Solar.pdf ⟩.]

Experimental status on fall 2018

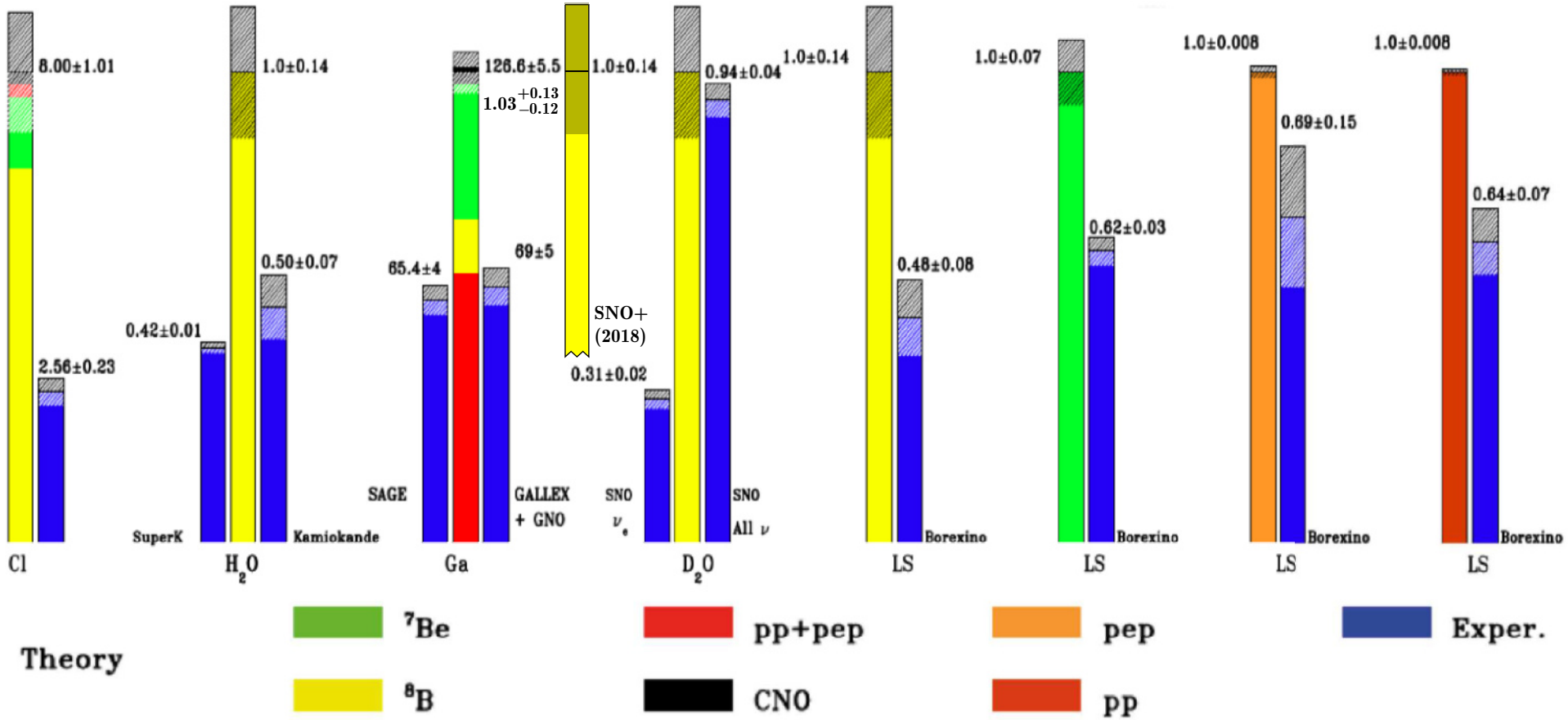

< http://theor.jinr.ru/~neutrino15/talks/Smirnov.pdf >

[From O. Smirnov, "Solar- and geo-neutrinos," lecture on the VIth International Pontecorvo Neutrino Physics School, August 27 – September 4, 2015, Horný Smokovec. The SNO+ data are from M. Anderson *et al.* (SNO+ Collaboration), "Measurement of the ^{8}B solar neutrino flux in SNO+ with very low backgrounds," Phys. Rev. D **99** (2019) 012012, arXiv:1812.03355 [hep-ex].]

Main news come from SNO (Sect. **37**, p. 780) and Borexino (Sect. **38**, p. 783). Some progress in theory is mostly due to the refinement of the input data.

Experiment	Measured flux (SNU / 10^{10} count/m^{2}s)	Ratio experiment/theory	Threshold energy	Years of running
Homestake	$2.56 \pm 0.16 \pm 0.16$	$0.33 \pm 0.03 \pm 0.05$	814 keV	1970-1995
Kamiokande	$2.80 \pm 0.19 \pm 0.33$	$0.54 \pm 0.08^{+0.10}_{-0.07}$	7.5 MeV	1986-1995
SAGE	$75 \pm 7 \pm 3$	$0.58 \pm 0.06 \pm 0.03$	233 keV	1990-2006
GALLEX	$78 \pm 6 \pm 5$	$0.60 \pm 0.06 \pm 0.04$	233 keV	1991-1996
Super-K	$2.35 \pm 0.02 \pm 0.08$	$0.465 \pm 0.005^{+0.016}_{-0.015}$	5.5 (6.5) MeV	from 1996
GNO	$66 \pm 10 \pm 3$	$0.51 \pm 0.08 \pm 0.03$	233 keV	from 1998
SNO (CC)	$1.68 \pm 0.06^{+0.08}_{-0.09}$		1.44 MeV	from 1999
SNO (ES)	$2.35 \pm 0.22 \pm 0.15$		6.75 MeV	
SNO (NC)	$4.94 \pm 0.21^{+0.38}_{-0.34}$		2.22 MeV	
SNO+ (ES)	$2.53^{+0.31\ +0.13}_{-0.28\ -0.10}$		6 MeV	69.2kt-days exp.

- The values are given in SNU (defined as 10^{-36} capture per second per target atom) for the radiochemical experiments and in units of 10^{10} counts/m^{2}s for the water-Cherenkov experiments.
- The first and errors for the relative values correspond to experimental and theoretical errors, respectively, with the statistical and systematic errors added quadratically. The models by Bahcall and Pinsonneault BP98 and BP00 were used in the calculations.

[The data (partially obsolete!) are borrowed from the *Ultimate Neutrino Page* maintained by Juha Peltoniemi and Juho Sarkamo, of Oulu University, URL: ⟨ http://cupp.oulu.fi/neutrino/ ⟩ (last modified 10.4.2005) and from the SNO+ paper cited at p. 741.]

33 Homestake Cl–Ar experiment.

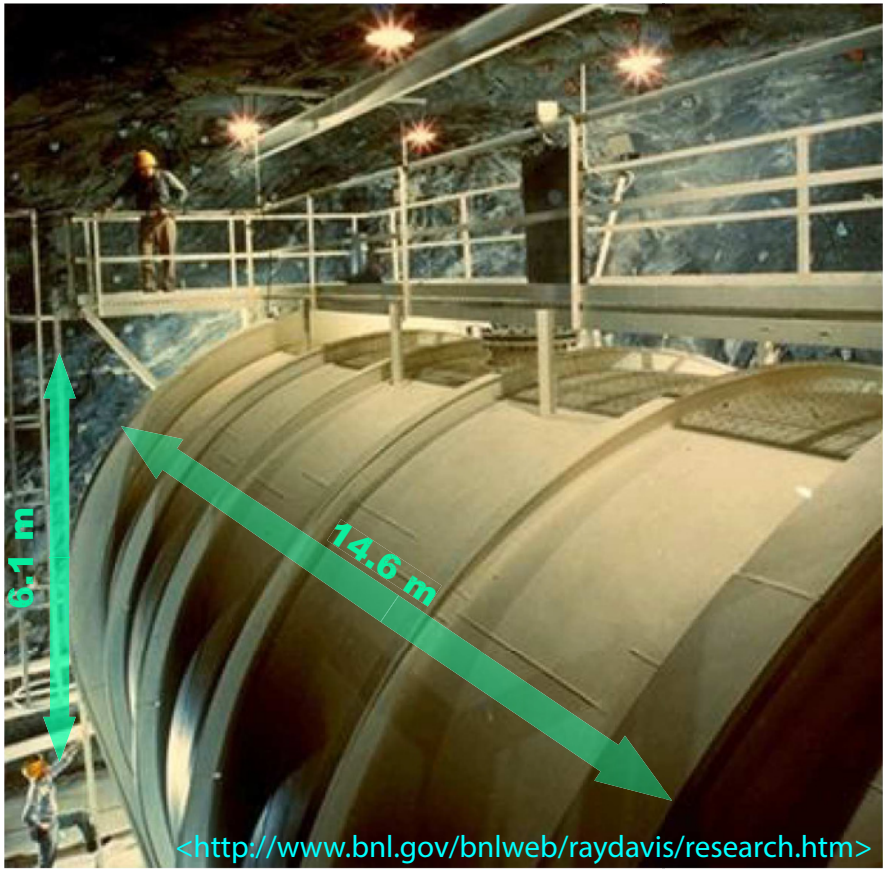

The Homestake Neutrino Trap.

The neutrino trap is a tank 20 feet (6.1 m) in diameter and 48 feet (14.6 m) long filled with 100,000 gallons (378,520 liters) of regular cleaning fluid, tetrachloroethylene (C_2Cl_4). On the average each molecule of C_2Cl_4 contains one atom of the desired isotope, ${}^{37}_{17}Cl$. The other three chlorine atoms ${}^{35}_{17}Cl$ contain two less neutrons. When a neutrino of the right energy reacts with an atom of ${}^{37}_{17}Cl$, it produces an atom of ${}^{37}_{18}Ar$ and an electron (Bruno Pontecorvo, 1946, Louis Alvarez, 1949):

$$\nu_e + {}^{37}_{17}Cl \to {}^{37}_{18}Ar + e^- \quad (E_\nu^{\text{th}} \approx 814 \text{ keV}).$$

Then the radioactive argon decays back to the Chlorine isotope from which it was created by the K-orbital electron capture,

$$e^- + {}^{37}_{18}Ar \to {}^{37}_{17}Cl + \nu_e \quad (T_{1/2} \approx 35.04 \text{ days}).$$

The idea is to tell that the reaction happened by seeing the Auger electron accompanying the K-capture. The argon-37 is allowed to build up for several months, then is removed by purging the tank with Helium gas. The Argon atoms are adsorbed in a cold trap and assayed for radioactivity.

The chlorine-argon experiment has been run by Raymond Davis, Jr., Kenneth C. Hoffman and Don S. Harmer of Brookhaven National Laboratory. The detector is located nearly a mile underground, in a rock cavity at the 4,850 foot level (1.48 km) below the surface in the Homestake Gold Mine in Lead, South Dakota.[a]

Suggested in 1964 by John Bahcall and Raymond Davis, the experiment (based on the Pontecorvo-Alvarez method) was begun on 1967 and continued to measure the solar neutrino flux until the late 1990s.

The first results of the experiment showed that the Sun's output of neutrinos from the isotope Boron-8 was less than expected.

The Homestake mine itself ceased operating at the end of 2001.

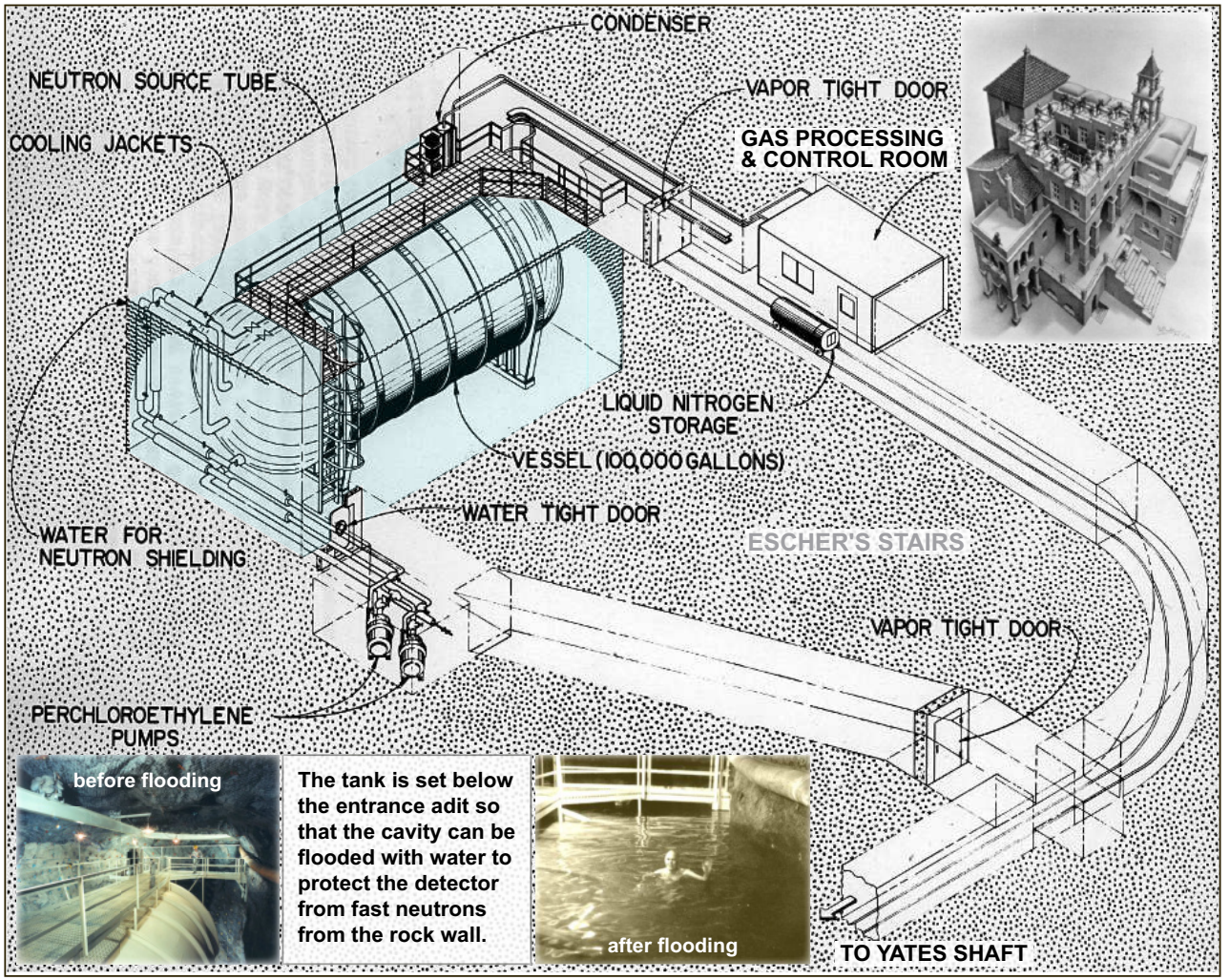

[a] For years, the Homestake mine was the largest and deepest (2,438 m) gold mine in North America.

Deep-mine location shields the solar-neutrino detector from the intense flux of cosmic-ray (atmospheric) muons. Being very penetrating, the muons can knock protons out of atomic nuclei well below the earth's surface.

The atmospheric muons provide one of the most serious background effect. If a muon-induced proton entered the neutrino detector, it could mimic the entry of a solar neutrino by converting an atom of ^{37}Cl into an atom of radioactive ^{37}Ar (via the $^{37}\mathrm{Cl}(p,n)^{37}\mathrm{Ar}$ reaction).

Figure on the right shows the ^{37}Ar production rate in 3.8×10^5 liters of perchloroethylene as a function of the depth below the surface. The corresponding background effect is about 0.2 atoms per day in 10^5 gal ($\approx 3.785 \times 10^5$ liters).

Other sources of the background are estimated to be on the same level or less, in particular,
- fast neutrons from (α, n) reactions and spontaneous fission of U in the rock wall: 0.1–0.3;
- internal contamination (U, Th, Ca): $\lesssim 0.1$;
- atmospheric neutrino interactions: $\lesssim 0.01$.

[From R. Davis, Jr. and D. S. Harmer, "Solar neutrino detection by the ^{37}Cl – ^{37}Ar method," in Proc. of the Informal Conference on Experimental Neutrino Physics (CERN, January 20–22, 1965), CERN 65–32, pp. 201–212.]

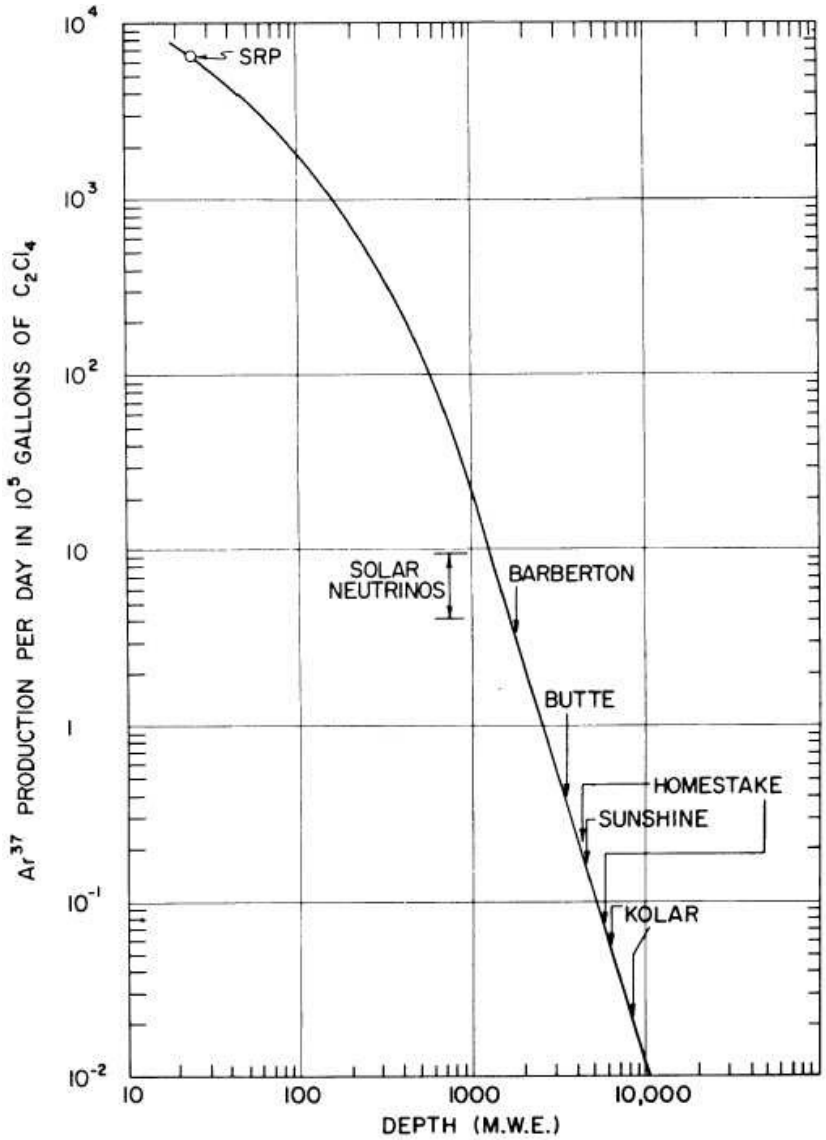

Figure on the right shows the argon extraction system which is deep underground next to the 100,000-gallon neutrino trap. Helium is circulated through the tank to sweep up any atoms of ^{37}Ar that have been formed from ^{37}Cl.

The efficiency of the extraction is determined by previously inserting in the tank a small amount of ^{36}Ar, a rare, nonradioactive isotope of argon. The Helium and argon pass through the apparatus at left, where the argon condenses in a charcoal trap cooled by liquid nitrogen.

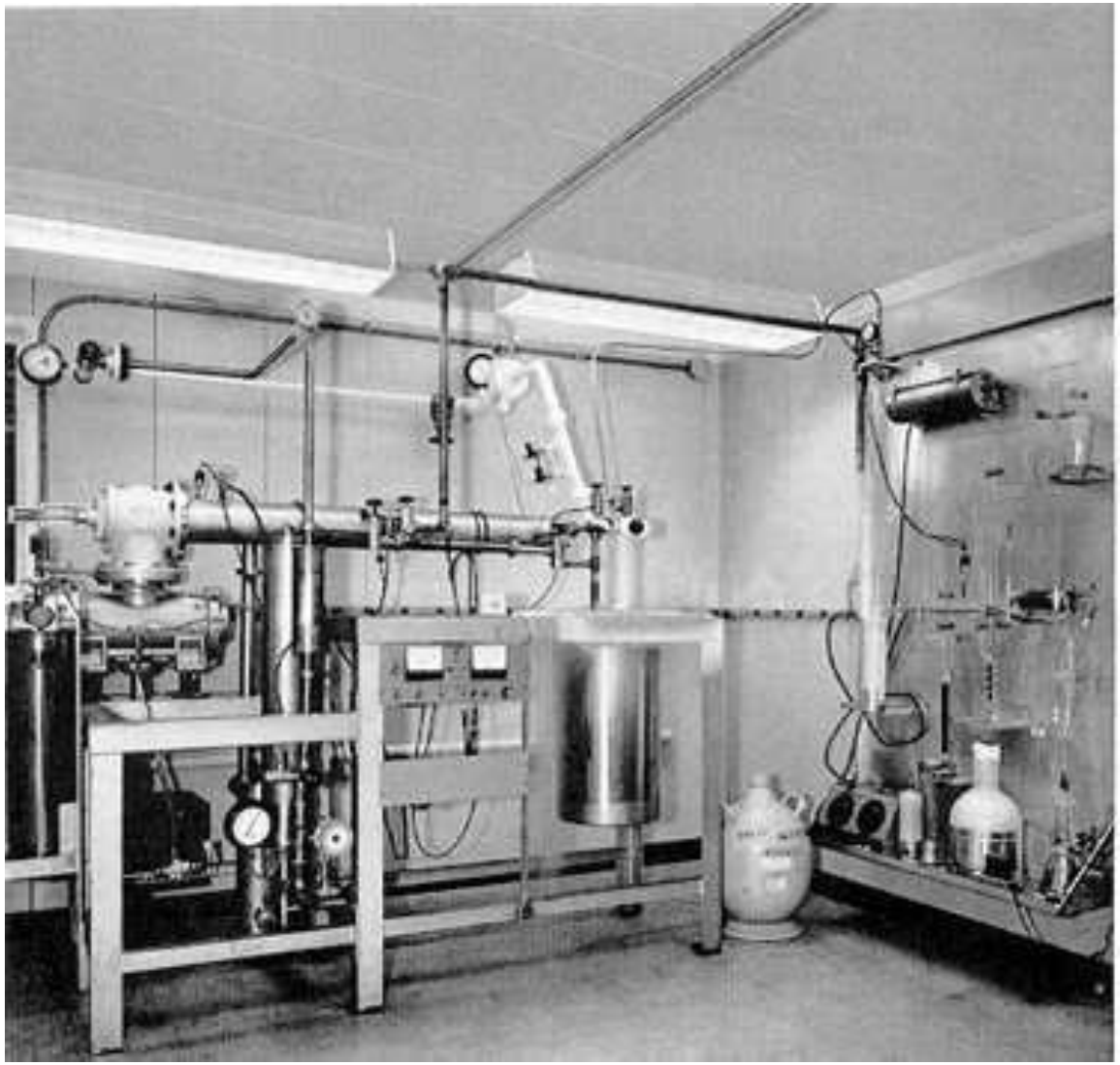

This argon fraction is purified in the apparatus at the right. The purified sample is then shipped to Brookhaven, where the content of ^{37}Ar is determined in shielded counters.

[From J. N. Bahcall, "Neutrinos from the Sun," Sci. Am. **221** (1969) 28–37.]

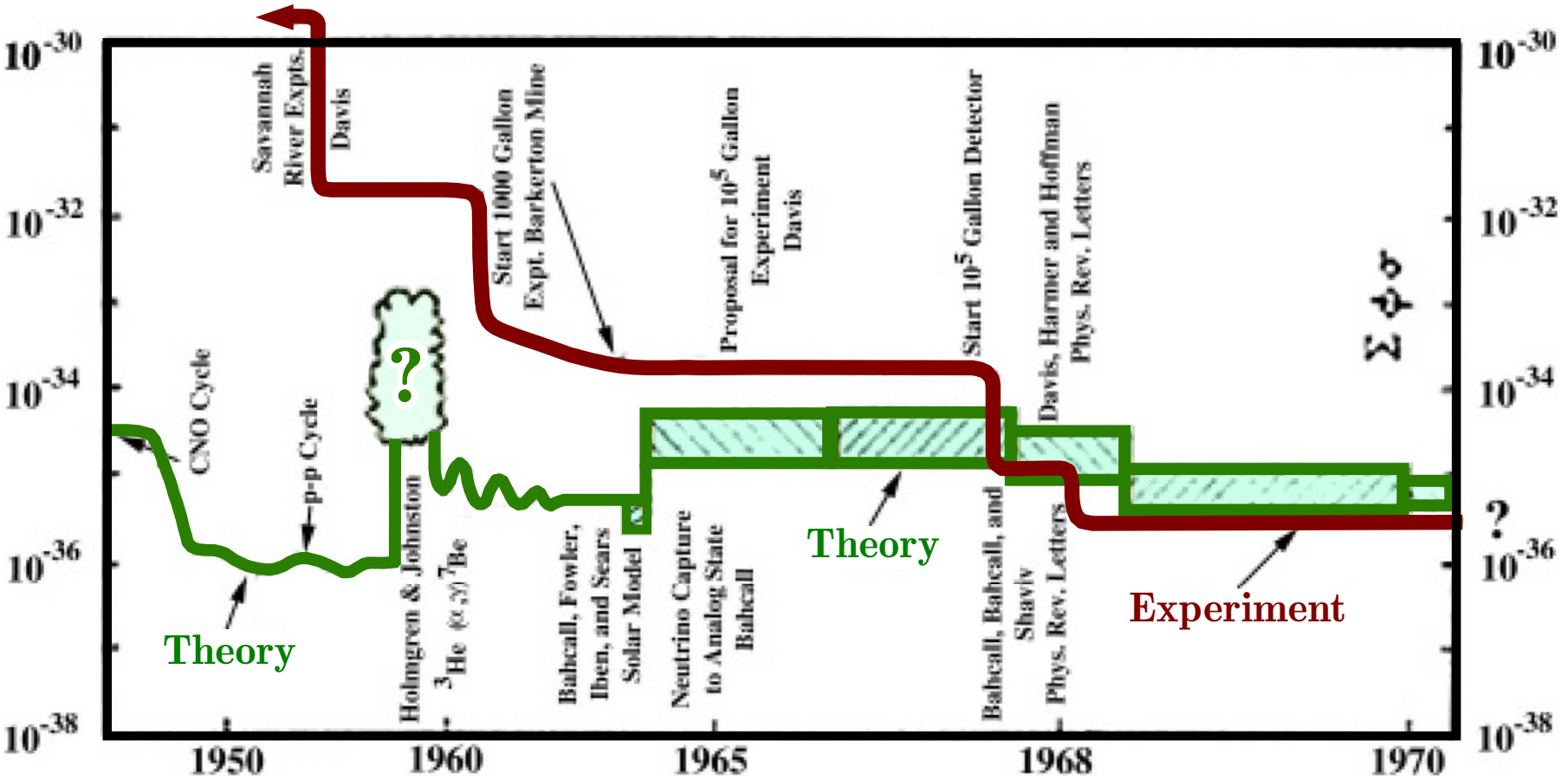

This figure is an overall pictorial history of the subject as it looked in 1970. It shows some of the principal events in the development of the solar neutrino problem. The experimental upper limit is indicated by the thin curve and the range of theoretical values (after 1964) by the cross-hatched region. The units are captures per target atom per second (10^{-36} captures/atom/s $\equiv$ 1 SNU). A few of the major events are indicated on the figure at the period corresponding to the time they occurred.

[Figure is adapted from J. N. Bahcall and R. Davis, Jr., "An account of the development of the solar neutrino problem," in Essays in Nuclear Astrophysics, edited by C. A. Barnes *et al.* (Cambridge University Press, 1982), pp. 243–285.]

Figure shows the observed (Davis & coauthors) and predicted (Bahcall & co-authors) neutrino capture rates published within the period from 1964 to 1980. The earliest observational upper limits of 4000 and 160 SNU (obtained in 1955 and 1964, respectively) are not shown since these would not fit conveniently in the plot [see previous slide].

The theoretical uncertainties are more "experimental" than "theoretical" since the basic theory has not changed since 1964. What have changed are the best estimates for many different input parameters. The error bars shown for the theoretical points represent the range of capture rates that were obtained from standard solar models when the various nuclear and atomic parameters were allowed to vary over the range conventionally regarded as acceptable at the time the calculations were made.

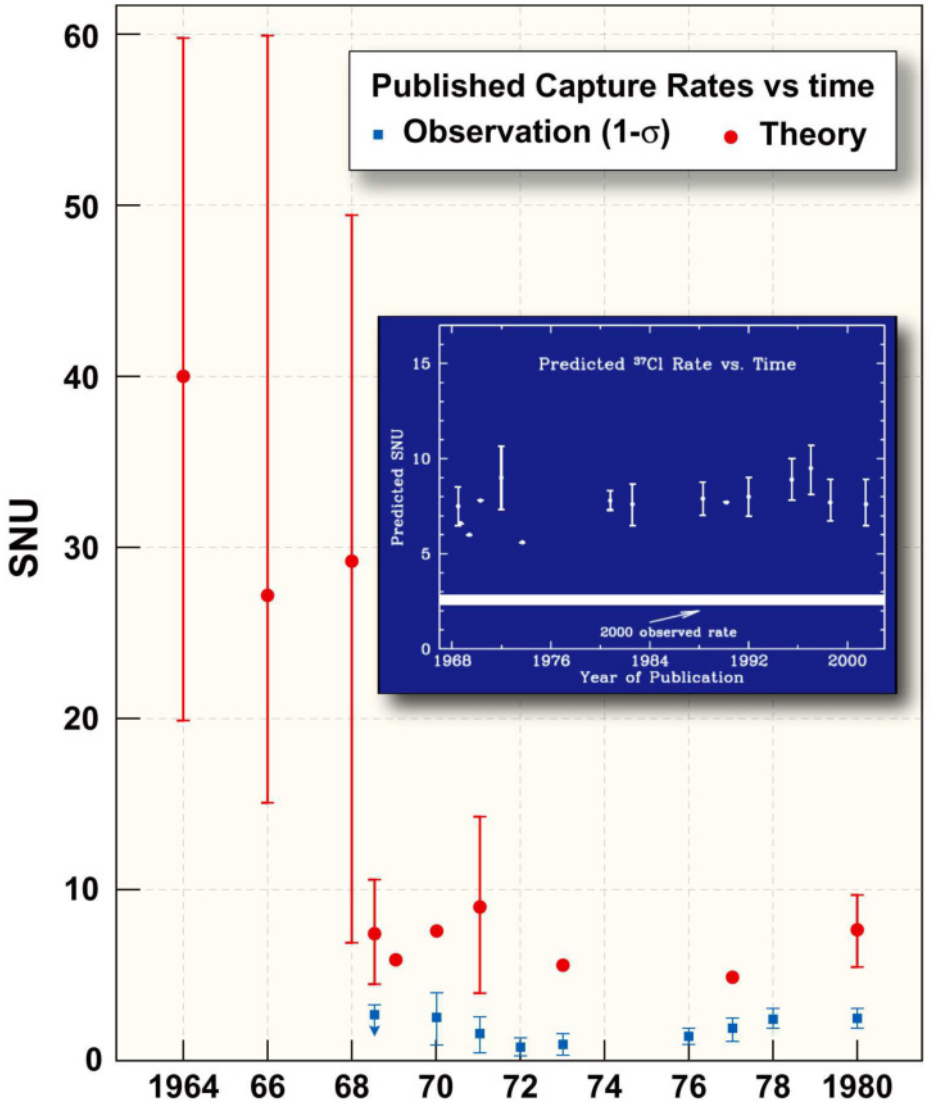

[Figure is adapted from J. N. Bahcall and R. Davis, Jr., "An account of the development of the solar neutrino problem;" see Ref. in previous page.]

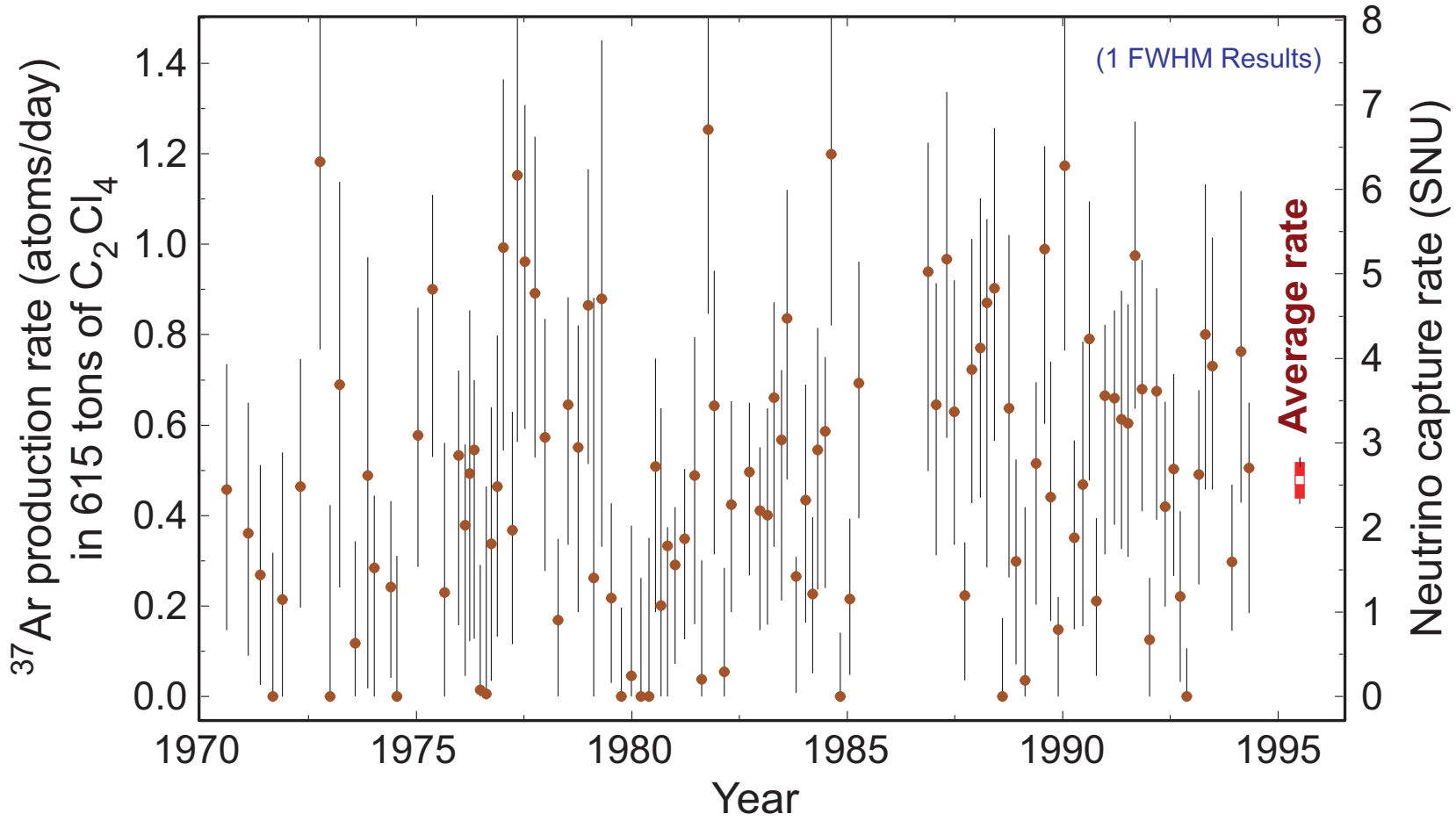

The final Homestake chlorine experiment one-FWHM (full width at half maximum) results for 108 individual solar neutrino observations (no. 18 to 133). All known sources of nonsolar ^{37}Ar production are subtracted. The errors of individual measurements are statistical errors only and are significantly non-Gaussian for near zero rates. The error of the cumulative result is the combination of the statistical and systematic errors in quadrature.

[From B. T. Cleveland *et al.*, "Measurement of the solar electron neutrino flux with the Homestake chlorine detector," ApJ **496** (1998) 505–526 (2960 citations in InSPIRE on December 26, 2023!).]

33.1 Solar neutrino puzzle # I.

The average over 1970–1995 runs solar ν induced ^{37}Ar production rate in the Homestake detector is $0.478 \pm 0.030\,(\text{stat}) \pm 0.029\,(\text{syst})$ day^{-1}. Since the detector contains 2.16×10^{30} ^{37}Cl atoms, this gives a neutrino capture rate of

$$\boxed{\langle \sigma \Phi_{\nu_e} \rangle = 2.56 \pm 0.16\,(\text{stat}) \pm 0.16\,(\text{syst})\ \text{SNU}.}$$

This measurement has to be compared with the SSM predictions for the chlorine detector:

$$\langle \sigma \Phi_{\nu_e} \rangle_{\text{theor}} = \begin{cases} 7.63\ \text{SNU} & \text{(Sackman, Boothroyd \& Fowler, 1990)} \\ 6.36\ \text{SNU} & \text{(Turck-Chièze \& Lopes, 1993)} \\ (4.2 \pm 1.2)\ \text{SNU} & \text{(Dar \& Shaviv, 1994)} \\ (9.3 \pm 1.3)\ \text{SNU} & \text{(Bahcall \& Pinsonneault, 1995)} \\ (4.1 \pm 1.2)\ \text{SNU} & \text{(Dar \& Shaviv, 1996)} \\ (7.7 \pm 1.2)\ \text{SNU} & \text{(Bahcall, Basu \& Pinsonneault, 1998)} \\ (8.1 \pm 1.2)\ \text{SNU} & \text{(Bahcall \& Serenelli, 2005),} \\ 6.315\ \text{SNU} & \text{(Turck-Chièze \& Couvidat, 2010) [SSM],} \\ (7.67 \pm 1.1)\ \text{SNU} & \text{(Turck-Chièze \& Couvidat, 2010) [SeSM].} \end{cases}$$

The observed flux is much lower than that predicted (except for the Dar & Shaviv results). This discrepancy between observation and prediction has existed since the early 1970s when the observations of the Homestake detector were first reported.

This is "The Solar Neutrino Puzzle, Number I".

33.2 Solar neutrino puzzle # II.

There are hints that the observed neutrino flux measured at Homestake shows significant correlation with certain parameters of solar activity, particularly those associated with the heliomagnetic field.

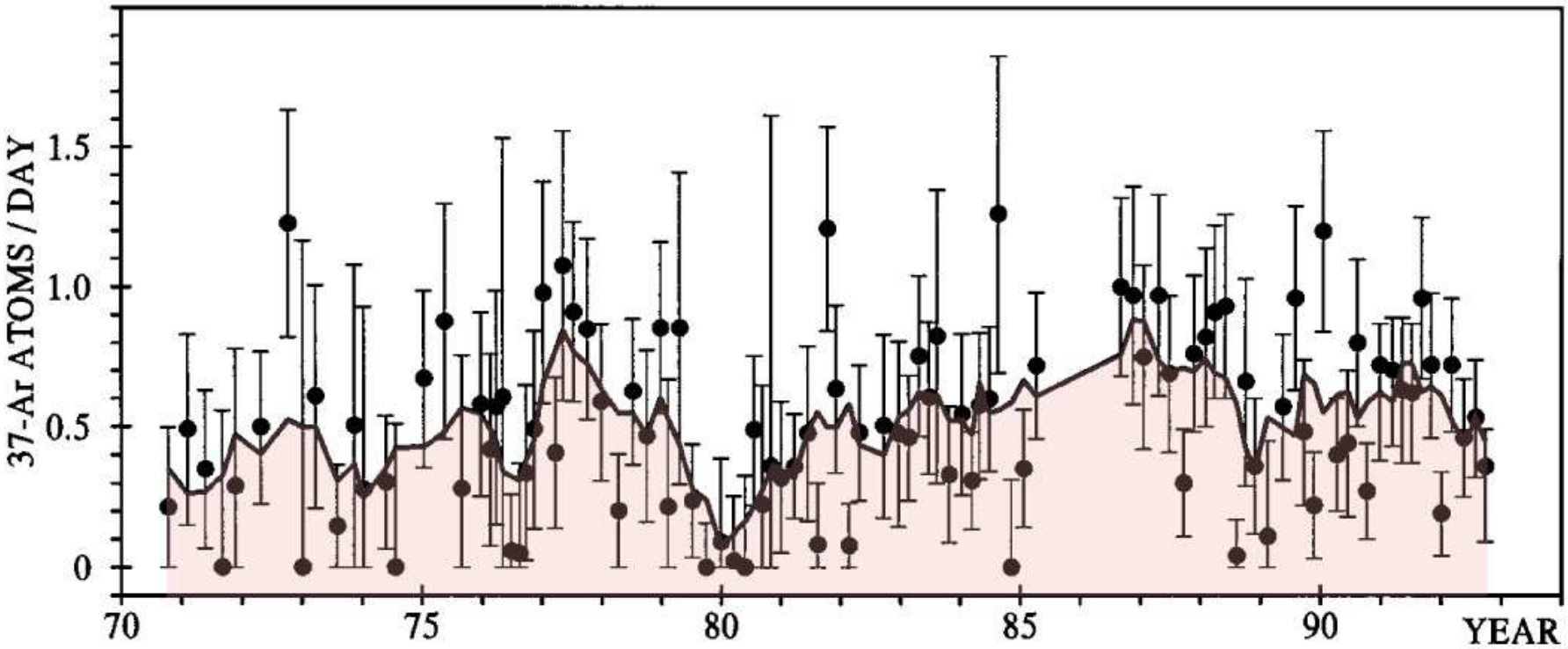

△ Homestake neutrino data with error bars and 5-point running-averaged values (solid line) from runs No. 18 to No. 126. The 5-point running-average values (Q5) are used to illustrate better the long-term behaviour considering that the original neutrino data are very scattered. Other choices for the smoothing, for instance 3- or 7-point running averages, do not alter qualitatively the results.

[This and next figures are borrowed from S. Massetti, M. Storini & N. Iucci, "Correlative analyses for Homestake neutrino data," Nuovo Cim. **20 C** (1997) 1021–1026.]

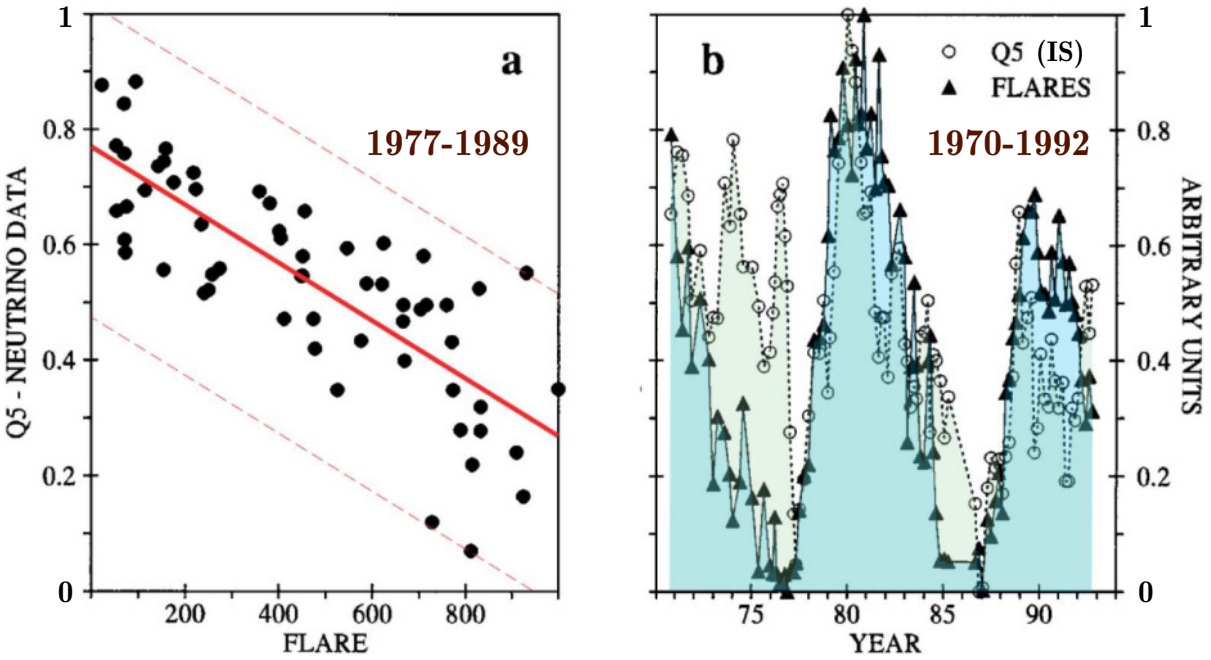

◁ Scatter plot of solar flares counts vs. 5-point running averages of Homestake neutrino values in the period 1977–1989 (a) and the above data sets plotted as a function of time in the period 1970–1992 (b); the neutrino data in (b) are reported with an inverted scale and both data sets are normalized in a way that minimum/maximum = 0/1.

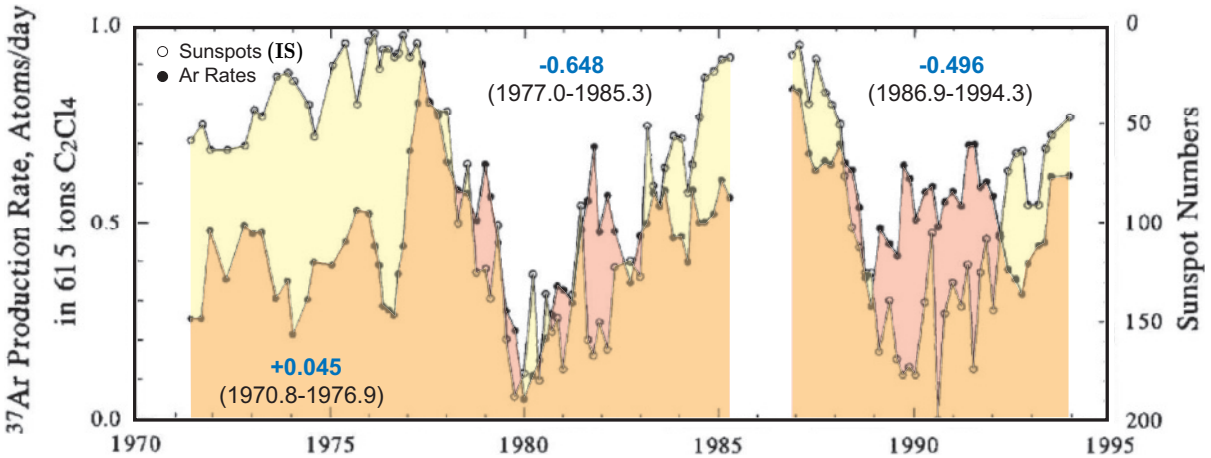

◁ The plot shows the 5-point running averages of the Homestake data compared to sunspot numbers; the sunspots are plotted on an inverted scale (IS) as a function of time.

[Top figures are borrowed from S. Massetti *et al.* (see footnote at p. 751); bottom figure is from R. Davis Jr., "A review of measurements of the solar neutrino flux and their variation," Nucl. Phys. B (Proc. Suppl.) **48** (1996) 284–298.]

Some of the conclusions of the authors are:

The Homestake data:

(i) Exhibit a clear modulation of the neutrino signal, almost on the long term.

(ii) Are badly correlated with geomagnetic indices, supporting the hypothesis that the source of the modulation is on the Sun.

(iii) Are correlated with cosmic-rays intensity only in the period 1970–1982, whereas over the total period the correlation is near zero.

(iv) Are better correlated with flare counts than with sunspot numbers. Note that flare phenomena are intimately related to the toroidal component of the heliomagnetic field. The best correlated period (1977–1989) corresponds to that characterized by a reinforcement of the interplanetary magnetic-field intensity, suggesting again an enhancement of the global heliomagnetic field.

More or less similar conclusions were found in the regression analyses reported by many authors. These results suggest a pulsating character of the Homestake data and their anticorrelation with the solar magnetic activity (sunspot or flare numbers).

This is "The Solar Neutrino Puzzle, Number II".

To solve the solar neutrino puzzles, a huge number of new, sometimes very unexpected ideas have been put forward. Below, we briefly consider a list (perhaps incomplete) of these solutions, focusing mainly on the puzzle #I. Although the generally accepted solution is no longer in doubt today, some of the hypotheses listed below are still the subject of research, if not as alternatives to the basic solution, then as potential sources of correction and simply as interesting possibilities.

Let's divide the proposed solutions into 3 classes:

- Astrophysics and/or Nuclear Physics,
- Nonstandard Neutrino Properties,
- Exotics and Science Fiction.

33.3 Solutions.

33.3.1 Astrophysics and/or Nuclear Physics.

- Models with convective mixing of the solar core [*Ezer & Cameron, 1968; Shaviv & Salpeter, 1968; Bahcall, Bahcall & Ulrich, 1968*].
- Models with turbulent diffusion of ^{3}He [*Schatzman, 1969*].
- A secular instability such that the presently observed solar luminosity does not equal the current energy-generation rate [*Fowler, 1968, 1972; Sheldon, 1969*].
- An overabundance of ^{3}He in the present-day Sun [*Kocharov & Starbumov, 1970*].
- Models with the strong central magnetic field (the energy density of the Sun's central magnetic field $|\mathbf{B}|^2/8\pi$ is a few percent of the gas pressure) [*Abraham & Iben, 1971; Bahcall & Ulrich, 1971; Bartenwerfer, 1973; Parker, 1974; Ulrich, 1974*].
- Models with low heavy elements ("low Z") abundances in the solar interior [*Bahcall & Ulrich, 1971; Schatzman, 1981; Maeder, 1990*].
- An instability of the Sun that makes now a special time [*Fowler, 1972; Dilke & Gough, 1972*].
- A low-energy resonance in the ^{3}He+^{3}He $\rightarrow$ ^{4}He+2^1H reaction [*Fowler, 1972; Fetisov & Kopysov 1972*].

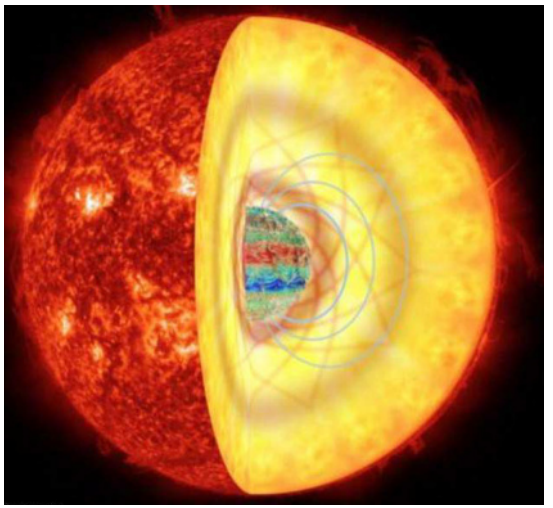

- Helium core (the Sun is assumed to be in a later stage of stellar evolution, such that Hydrogen is burned-out and the core is made of Helium) [*Prentice, 1973*].

- Models with a rapidly rotating solar interior (the rotation is lowering the central pressure and temperature) [*Demarque, Mengel & Sweigert, 1973; Roxburgh, 1974; Rood & Ulrich 1974*].
- Rotation plus magnetic fields [*Snell, Wheeler & Wilson, 1976*].
- A half-solar mass core of large heavy element abundance that survived the big bang and subsequently accreted another half solar mass at the time of the formation of the solar system [*Hoyle, 1975*].
- A departure from the Maxwellian distribution [*Clayton* et al., *1975*].
- A fractionation of the primordial Hydrogen and Helium [*Wheeler & Cameron, 1975*].
- Mixing of ^{3}He due to rapid filamental flow downward [*Cummings & Haxton, 1996*].
- Temporal and spatial variations in temperature [*Dar & Shaviv, 1998*].
- Collective plasma processes [*Salpeter & Van Horne, 1969; . . . ; Tsytovich* et al., *1995, Dar & Shaviv, 1998*].
- A new solar model in which the Sun is formed by accretion of fresh SN debris on the collapsed core of a supernova; neutron emission from the SN remnant at the solar core; neutron decay major elements are iron, nickel, oxygen, silicon [*Manuel, Miller & Katragada, 2003*].

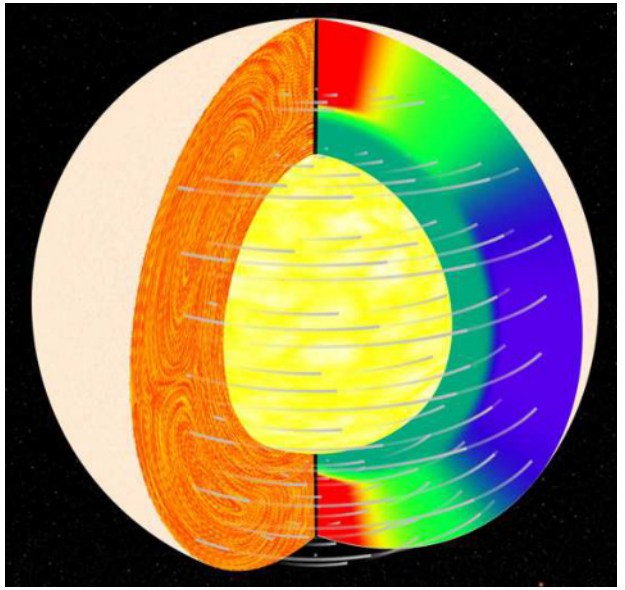

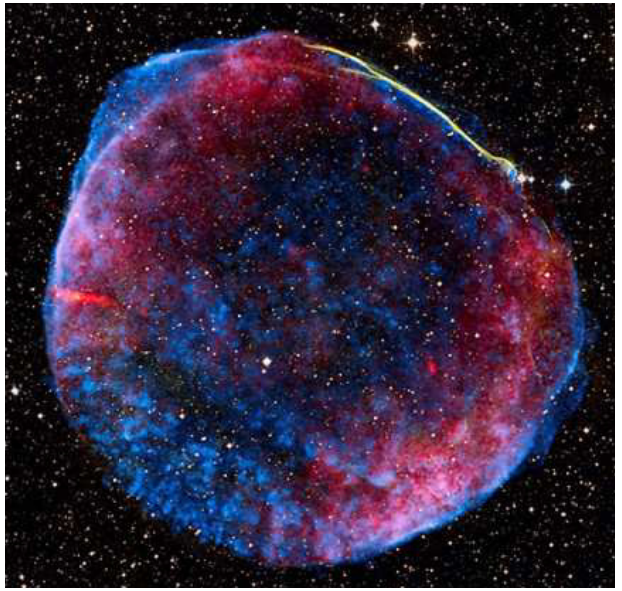

33.3.2 Nonstandard Neutrino Properties.

- Vacuum neutrino oscillations [*Gribov & Pontecorvo, 1969, Bilenky & Pontecorvo, 1977,...*].
- An appreciable (anomalous) magnetic moment for the neutrino [*Cisneros 1971; Okun, Voloshin & Vysotsky, 1986*].
- Neutrino instability [*Bahcall, Cabibbo & Yahil, 1972*].
- Goldstone neutrinos resulting from a spontaneous breakdown of supersymmetry [*Das, 1984*].

- **Matter enhanced neutrino oscillations [*Wolfenstein 1978; ...; Mikheev & Smirnov, 1985.*]**
- Matter-induced neutrino decay $\nu \to \overline{\nu}$ + Majoron [*Berezhiani & Vysotsky, 1987*].
- Resonant neutrino spin–flavor precession in the solar magnetic field [*Akhmedov, 1987; Lim & Marciano, 1988*].
- Nonstandard (in particular, flavor-changing) neutrino interactions with matter [*Roulet, 1991; Guzzo, Masiero & Petcov, 1991; Barger, Phillips & Whisnant, 1991*].
- A nonstandard (strong enough) $\nu_e\gamma$ interaction that would cause the neutrinos to disappear before they leave the Sun or make them lose energy towards detection thresholds [*Dixmier, 1994*]

33.3.3 Exotics and Science Fiction.

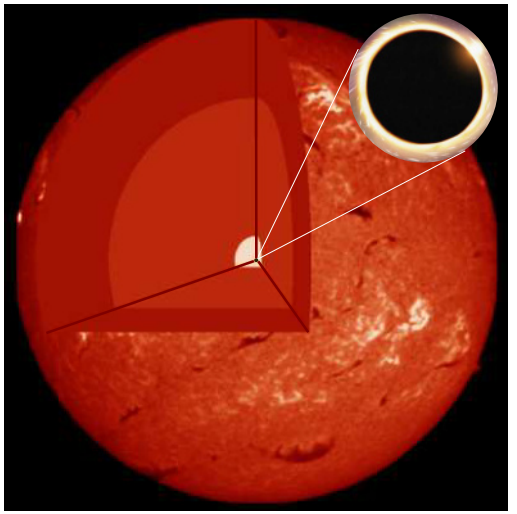

- Quark catalysis [*Libby & Thomas, 1969; Salpeter, 1970*].
- Accretion onto a central black hole (the model assumes that the Sun's energy did not come from fusion, rather from release of energy from accretion onto a black hole at the center of the Sun) [*Clayton, Newman & Talbot, 1975*].
- Multiplicative mass creation [*Maeder, 1977*].
- WIMPs as a source of solar energy [*Faulkner & Gilliland, 1985; Spergel & Press, 1985; Press & Spergel, 1985; Faulkner, Gough & Vahia, 1986; Gilliland* et al., *1986*].
- Violation of equivalence principle (gravitational forces may induce neutrino mixing and flavor oscillations if the equivalence principle is not true) [*Gasperini, 1988, 1989; Halprin & Leung, 1991; ...; Gago, Nunokawa & Zukanovich, 2000; Pantaleone, Kuo & Mansour, 2000*].
- Daemon[a] catalysis (it is assumed that daemons are capable of catalyzing proton-fusion reactions, which may account for the observed solar neutrino deficiency) [*Drobyshevski, 1996, 2002*].

[a] **Daemon** = **Da**rk **E**lectric **M**atter **O**bject, a hypothetical Planckian particle carrying a negative electric charge of up to $Z = 10$ (something like a negatively charged Planckian black hole). [Etymology: "Dæmon" is the Latin version of the Greek "$\delta\alpha\iota\mu\omega\nu$" ("godlike power," "fate," "god" in classical mythology).]

34 Ga-Ge detector SAGE.

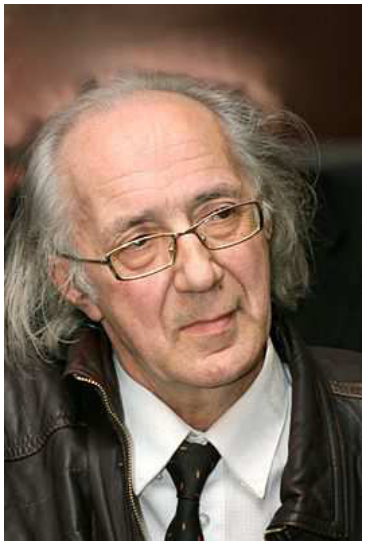

These solar neutrino experiments are based on the reaction (originally proposed by V. A. Kuzmin in 1965)

$$\nu_e + {}^{71}_{31}\mathrm{Ga} \to {}^{71}_{32}\mathrm{Ge} + e^- \quad (E_\nu^{\mathrm{th}} \approx 232.696 \pm 0.15 \text{ keV}).^{\mathrm{a}}$$

Then the radioactive germanium decays back to gallium:

$${}^{71}_{32}\mathrm{Ge} \to {}^{71}_{31}\mathrm{Ga} + e^+ + \nu_e \quad (T_{1/2} \approx 11.4 \text{ days}).$$

Backgrounds for the gallium experiments are caused by ^{71}Ge production through non-neutrino mechanisms

$$p + {}^{71}_{31}\mathrm{Ga} \to {}^{71}_{32}\mathrm{Ge} + n \quad (E_p^{\mathrm{th}} \approx 1.02 \text{ MeV}).$$

Like in the chlorine experiment, the protons may be produced by cosmic muon interactions, fast neutrons or residual radioactivity. Radon gas and its daughter products are also a large cause of background; the radon half-life is about 3.8 days.

In the SAGE (Soviet–American Gallium solar neutrino Experiment), the ^{71}Ge atoms are chemically extracted from a 50-metric ton target of gallium metal and concentrated in a sample of germane gas (GeH_4 – the germanium analogue of methane) mixed with xenon. The ^{71}Ge atoms are then individually counted by observing their decay back to ^{71}Ga in a small proportional counter.

The SAGE group regularly performs solar neutrino extractions, every four weeks, reducing the statistical error, and explores further possibilities for reducing the systematic uncertainties.

[a] This is the weighted average of all the available measurements for the neutrino energy threshold of this reaction computed (including estimates of systematic errors) by G. Audi and A. H. Wapstra.

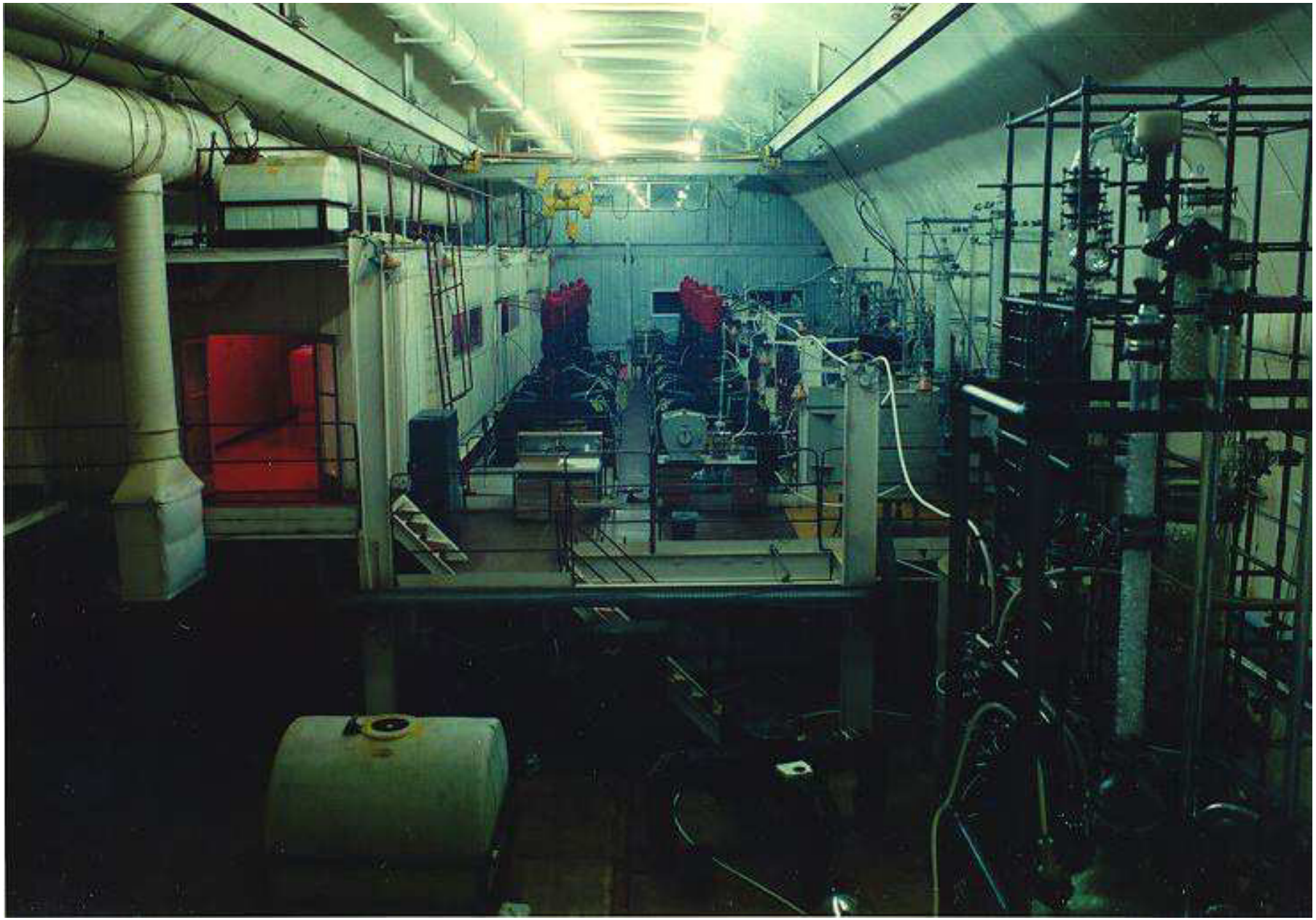

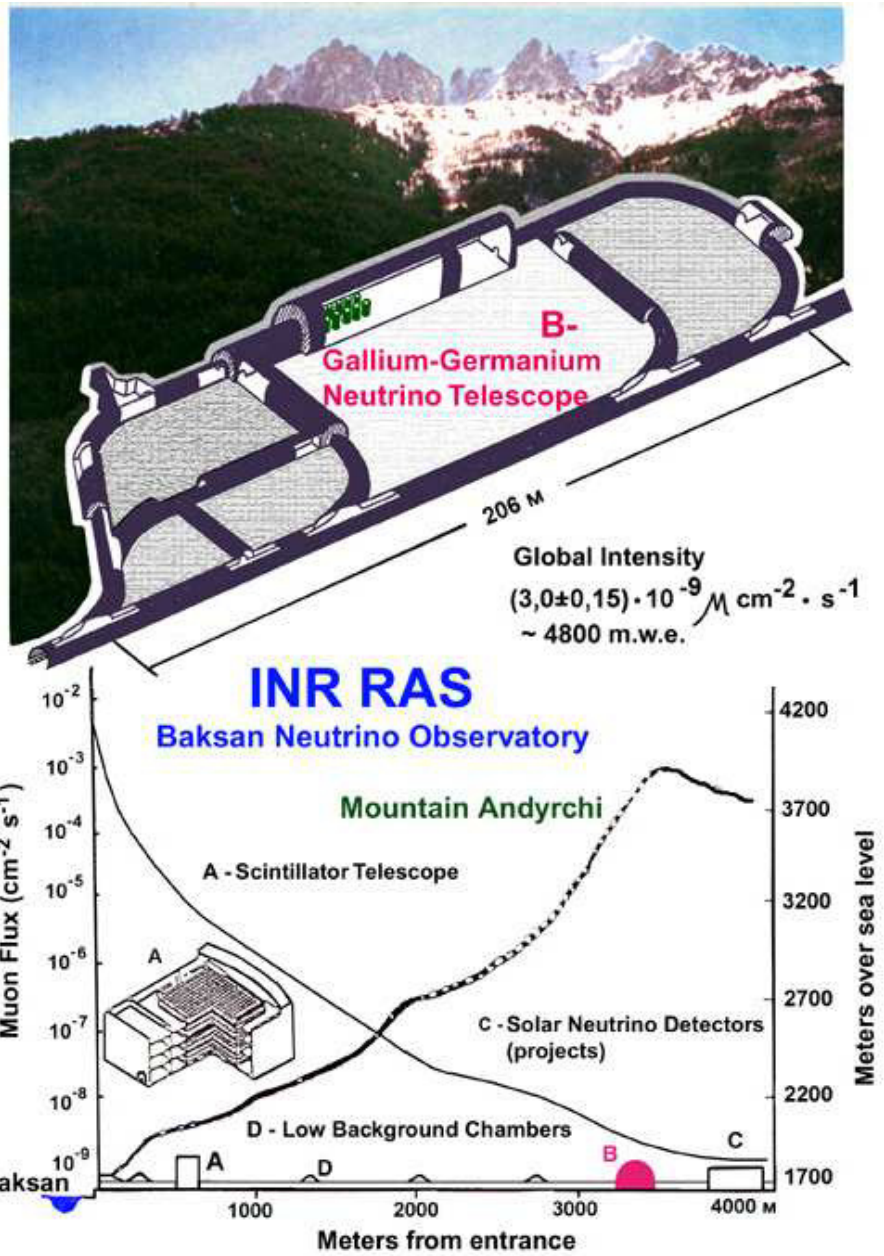
B-
Gallium-Germanium
Neutrino Telescope
206 м
Global Intensity
(3,0±0,15)·10 -9 м cm-2 · s-1
~ 4800 m.w.e.
INR RAS
Baksan Neutrino Observatory
Mountain Andyrchi
A - Scintillator Telescope
C - Solar Neutrino Detectors
(projects)
D - Low Background Chambers
Muon Flux (cm-2 s-1)
Meters over sea level
Baksan
Meters from entrance
1000
2000
3000
4000 м
4200
3700
3200
2700
2200
1700

To check the response of the SAGE experiment to low-energy neutrinos, a source of ^{51}Cr was produced by irradiating 512.7 g of 92.4%-enriched ^{50}Cr in a high-flux fast neutron reactor. This source, which mainly emits monoenergetic 747-keV neutrinos, was placed at the center of a 13.1 ton target of liquid gallium and the cross section for the production of ^{71}Ge by the inverse beta decay reaction $^{71}\text{Ga}(\nu_e, e^-)^{71}\text{Ge}$ was measured to be

$$\sigma\,(\text{Ga-Ge}) = (5.55 \pm 0.60\,(\text{stat}) \pm 0.32\,(\text{stat})) \times 10^{-45}\ \text{cm}^2.$$

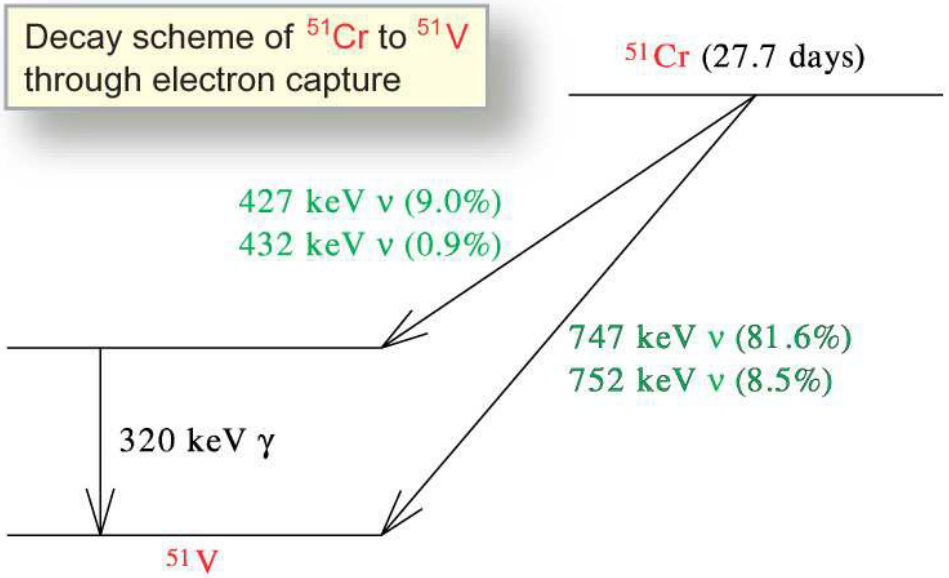

[From J. N. Abdurashitov *et al.*, "Measurement of the response of a gallium metal solar neutrino experiment to neutrinos from a ^{51}Cr source," Phys. Rev. C **59** (1999) 2246–2263.]

The ratio of this result to the theoretical cross section of Bahcall and of Haxton are

$$0.95 \pm 0.12\,(\text{exp})\,^{+0.035}_{-0.027}\,(\text{theor}) \quad \text{and} \quad 0.87 \pm 0.11\,(\text{exp}) \pm 0.09\,(\text{theor}),$$

respectively. This relatively good agreement between prediction and observation implies that the overall experimental efficiency is correctly determined and provides considerable evidence for the reliability of the solar neutrino measurement.

BUT! The remaining small discrepancy might be a hint to something interesting...

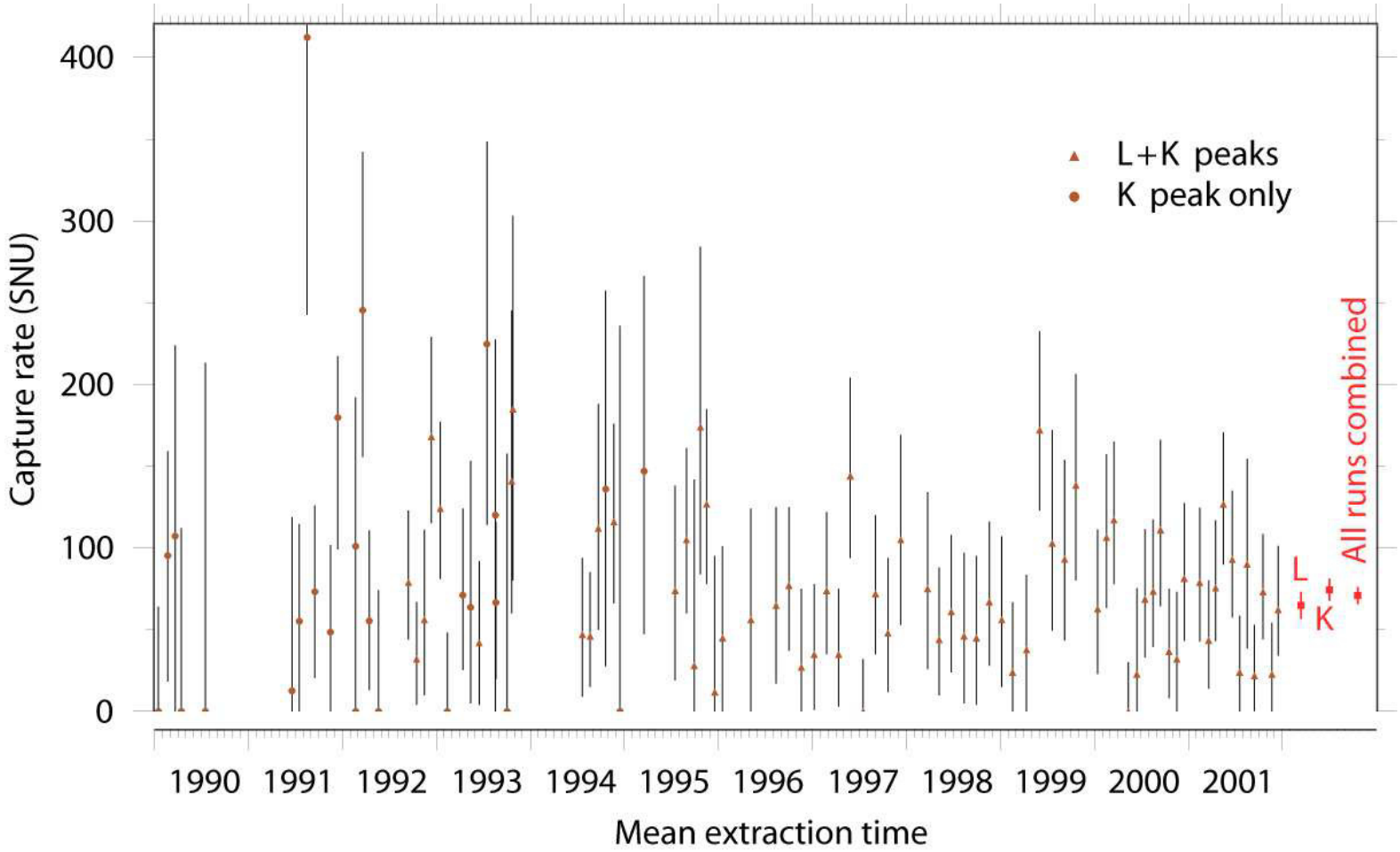

The capture rate from all SAGE extractions versus time: the triangles are for the L and K peaks and the circles are for the K peak alone; the vertical bars near each point correspond to a statistical error of 68%. The average rates for the L, K, and $L+K$ peaks are also shown.

[This and next figures are borrowed from J. N. Abdurashitov *et al.*, "Solar neutrino flux measurements by the Soviet-American Gallium Experiment (SAGE) for half the 22-Year Solar Cycle," Zh. Eksp. Teor. Fiz. **122** (2002) 211–226 [JETP **95** (2002) 181–193], astro-ph/0204245.]

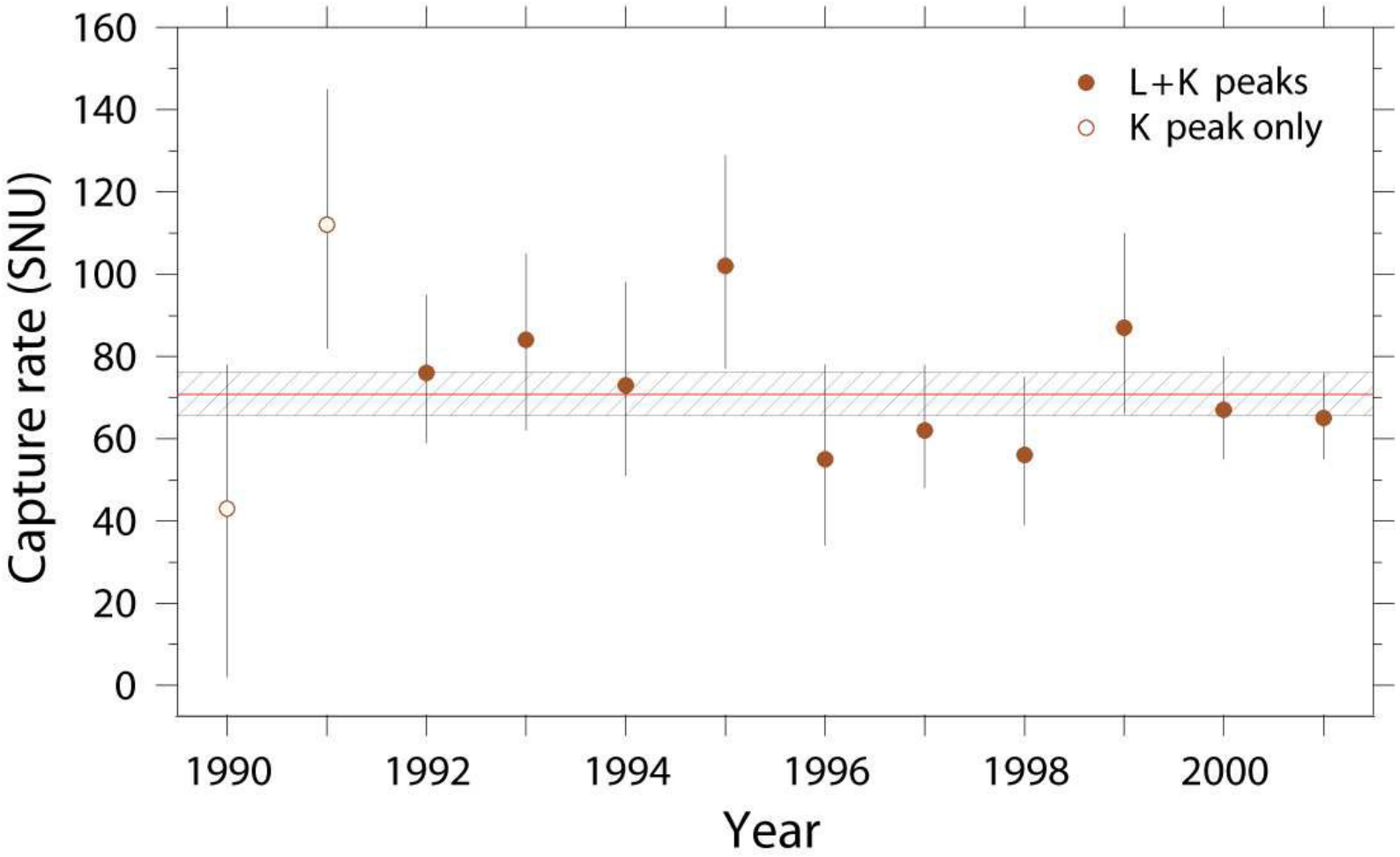

Results of the measurements combined by years; open and filled symbols refer to K and $K+L$ peaks, respectively; the hatched region corresponds to the SAGE result of

$$70.8^{+5.3}_{-5.2}\,(\text{stat})\ ^{+3.7}_{-3.2}\,(\text{syst})\ \text{SNU}.$$

The data shown have a statistical error of 68%. The neutrino capture rate was constant during the entire data acquisition period with a 83% probability.

35 Ga-Ge detectors GALLEX and GNO.

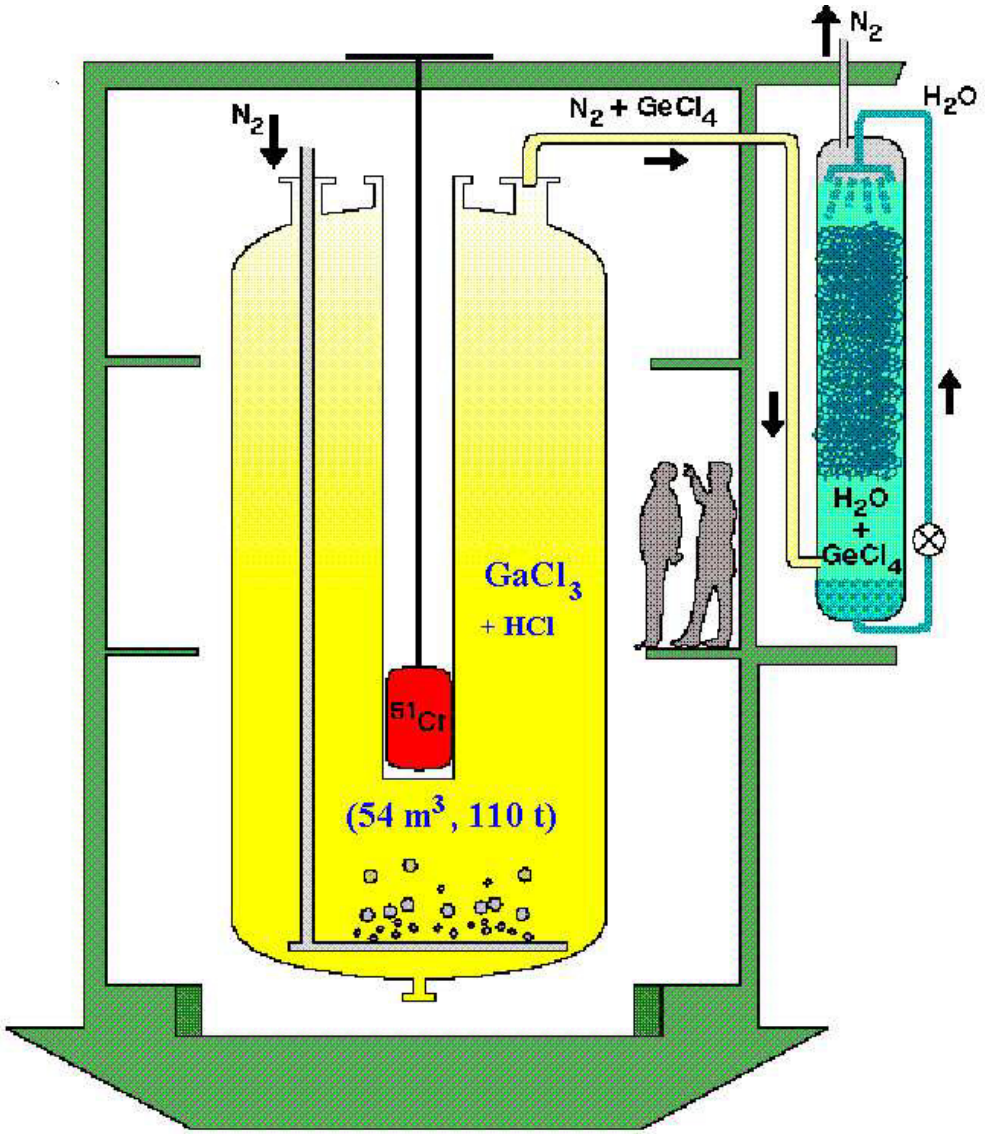

Figure on the left shows a scheme of the GALLEX detector tank with the absorber system and the Chromium source inserted inside the thimble.
The experimental procedure for GALLEX is as follows: 30.3 tons of gallium in form of a concentrated $GaCl_3$-HCl solution are exposed to solar neutrinos. In $GaCl_3$-HCl solution, the neutrino induced ^{71}Ge atoms (as well as the inactive Ge carrier atoms added to the solution at the beginning of a run) form the volatile compound $GeCl_4$, which at the end of an exposure is swept out of the solution by means of a gas stream (nitrogen). The nitrogen is then passed through a gas scrubber where the $GeCl_4$ is absorbed in water.
The $GeCl_4$ is finally converted to GeH_4, which together with xenon is introduced into a proportional counter in order to determine the number of ^{71}Ge atoms by observing their radioactive decay.

[From URL: ⟨http://www.mpi-hd.mpg.de/nuastro/gallex/detector.htm⟩.]

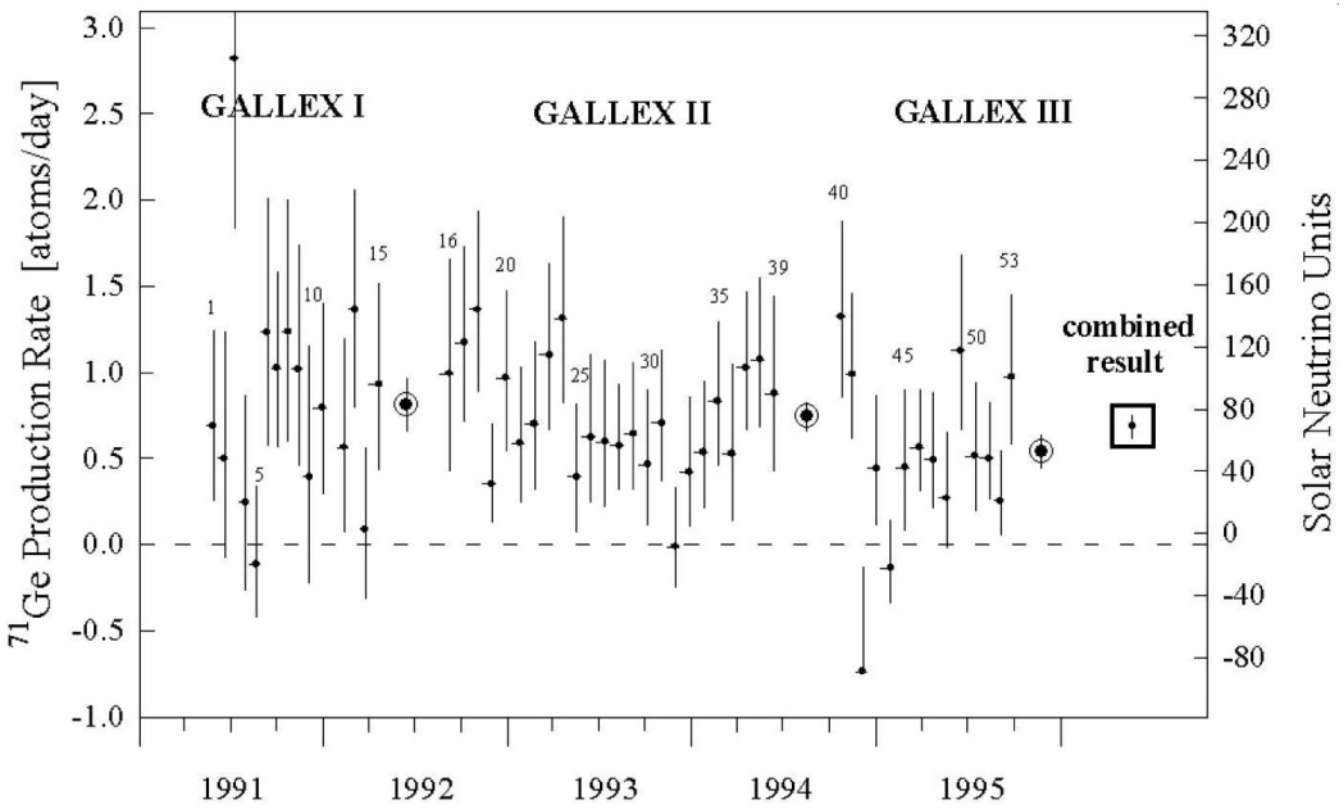

GALLEX I, II, and III single-run overview.

Results for the 14 solar neutrino runs of GALLEX III (labels 40–53), shown together with the earlier results from GALLEX I (labels 1–15) and from GALLEX II (labels 16–39).

The left hand scale is the measured ^{71}Ge production rate; the right hand scale, the net solar neutrino production rate (SNU) after subtraction of side reaction contributions.

Error bars are $\pm 1\sigma$, statistical only. The label "combined" applies to the mean global value for the total of all 53 runs. The visibility is enhanced by a square box, but its error is the small bar inside the box. Horizontal bars represent run duration; their asymmetry reflects the "mean age" of the ^{71}Ge produced.

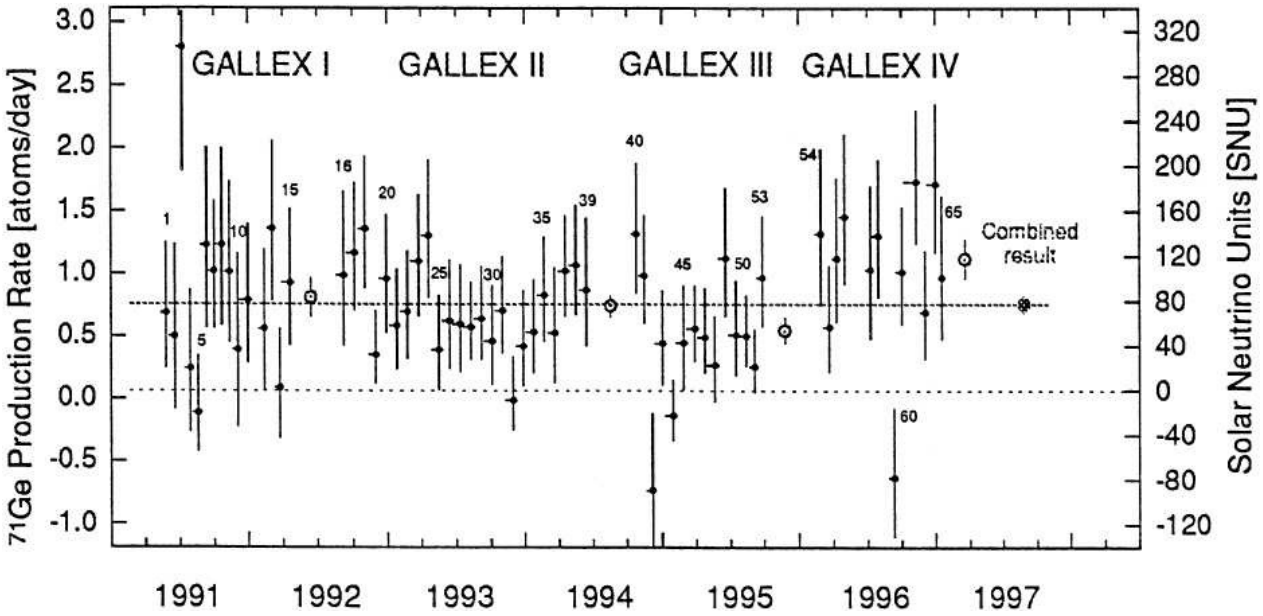

Summary of the results of GALLEX individual solar runs closed points. The left hand scale is the measured ^{71}Ge production rate; the right hand scale, the net solar neutrino production rate SNU after subtraction of side reaction contributions.

Error bars are $\pm 1\sigma$ statistical only. Open circles are the combined results for each of the measuring periods, GALLEX I, II, III and IV. The label "combined" applies to the mean global value for the total of all 65 runs. Horizontal bars represent run duration; their asymmetry reflects the "mean age" of the ^{71}Ge produced. The combined result which comprises 65 solar runs, is $77.5 \pm 6.2^{+4.3}_{-4.7}\,(1\sigma)$ SNU. The GALLEX experimental program to register solar neutrinos has now been completed.

In April 1998, GALLEX was succeeded by a new project, the Gallium Neutrino Observatory (GNO), with newly defined motives and goals.

[From W. Hampel *et al.* (GALLEX Collaboration), "GALLEX solar neutrino observations: Results for GALLEX IV," Phys. Lett. B **447** (1999) 127–133.]

36 Water-Cherenkov neutrino detectors (Kamiokande and Super-Kamiokande).

Super-Kamiokande (SK), as well as its precursor Kamiokande (K), is an underground ring-imaging water-Cherenkov neutrino detector located in the Kamioka mine, Japan (137.32° E longitude, 36.43° N latitude). SK is a cylindrical tank (41.4 m in height, 39.3 m in diameter) filled with 50 kton of ultra-pure water, and situated under about 1 km of rock (2700 m.w.e.). The rock provides a shield against the cosmic-ray muons: the muon count rate in the detector is reduced to 2.2. Hz.

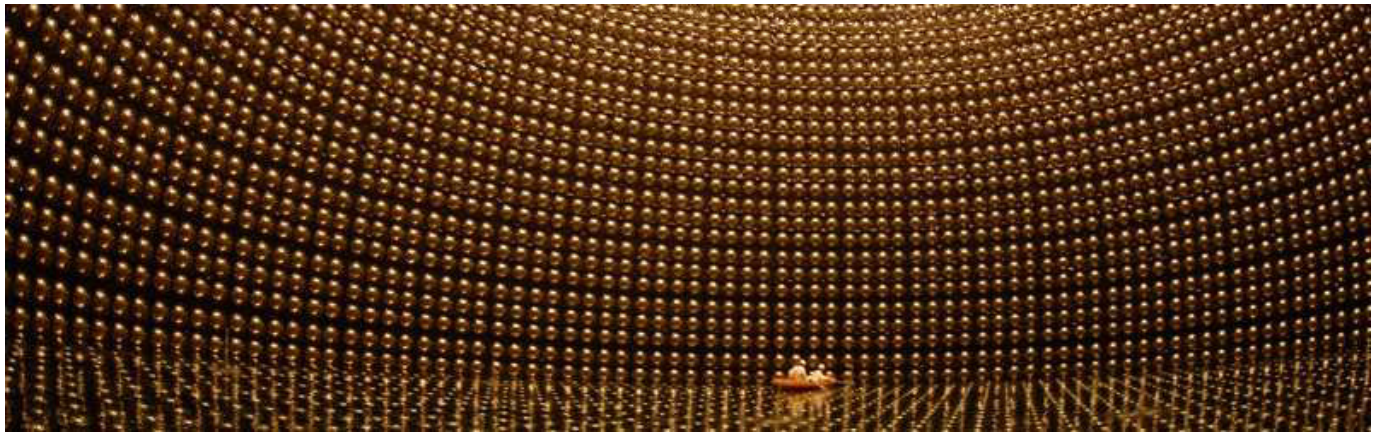

The outer walls of the tank are constructed from 5 cm thick stainless steel sheets, which are attached to the rock cavity and backed by concrete. About 2 m in from the walls is a 1 m wide structure of stainless beams that provide the backbone for the mounting PMTs. The structure divides the whole detector tank into an inner detector (ID) and outer detector (OD).

The 11,146 inward-facing ID PMTs that are used in event detection are mounted on the inside of the steel beam structure and are surrounded with black polyethylene sheets to minimize light reflection within the ID region. They provide a photo-coverage of 40%.

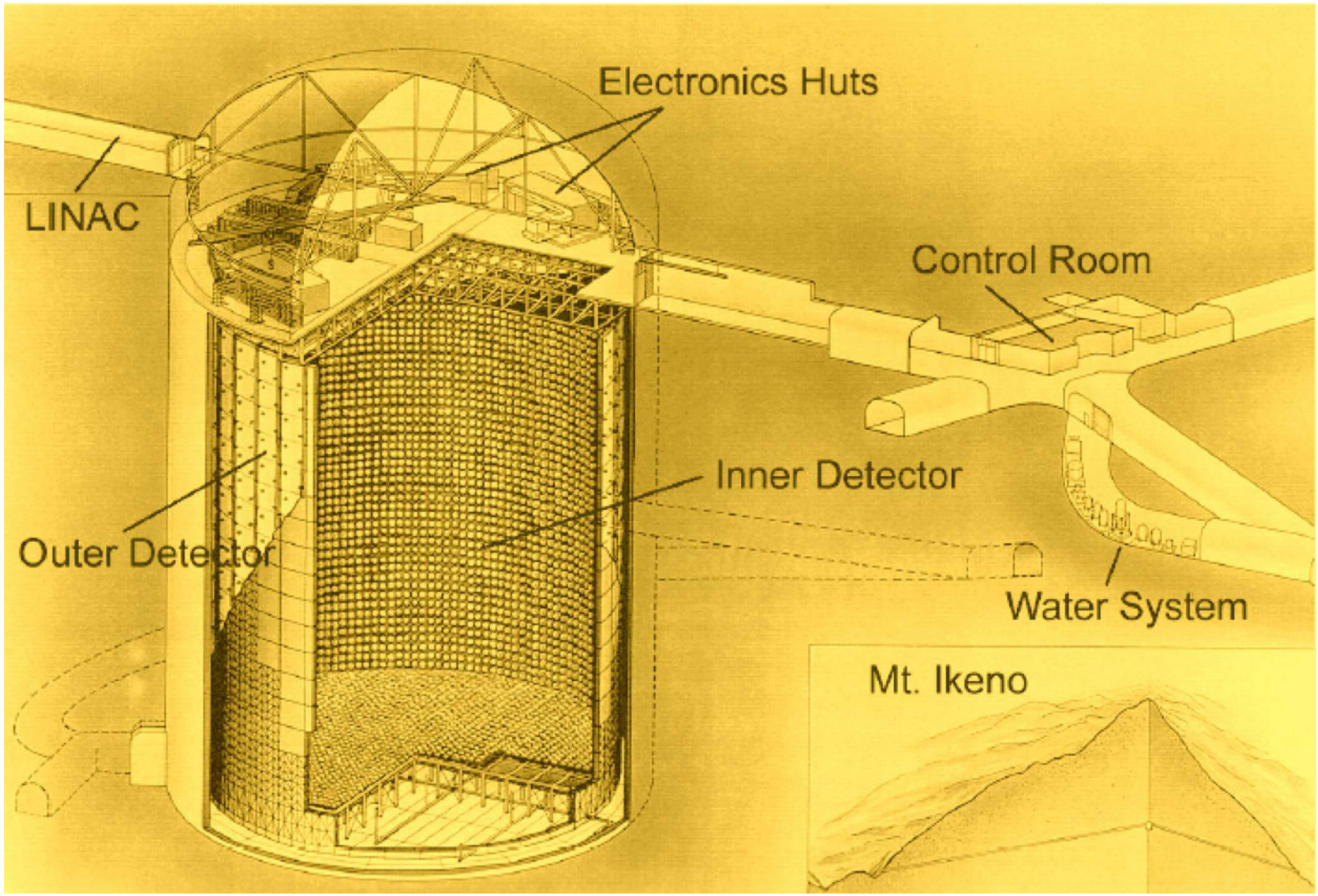

[This and next figures are borrowed from D. Turčan, "Solar neutrino at Super-Kamiokande solving the solar neutrino puzzle via neutrino flavor oscillations," Ph. D. Thesis, Faculty of the Graduate School, Maryland University, 2003.]

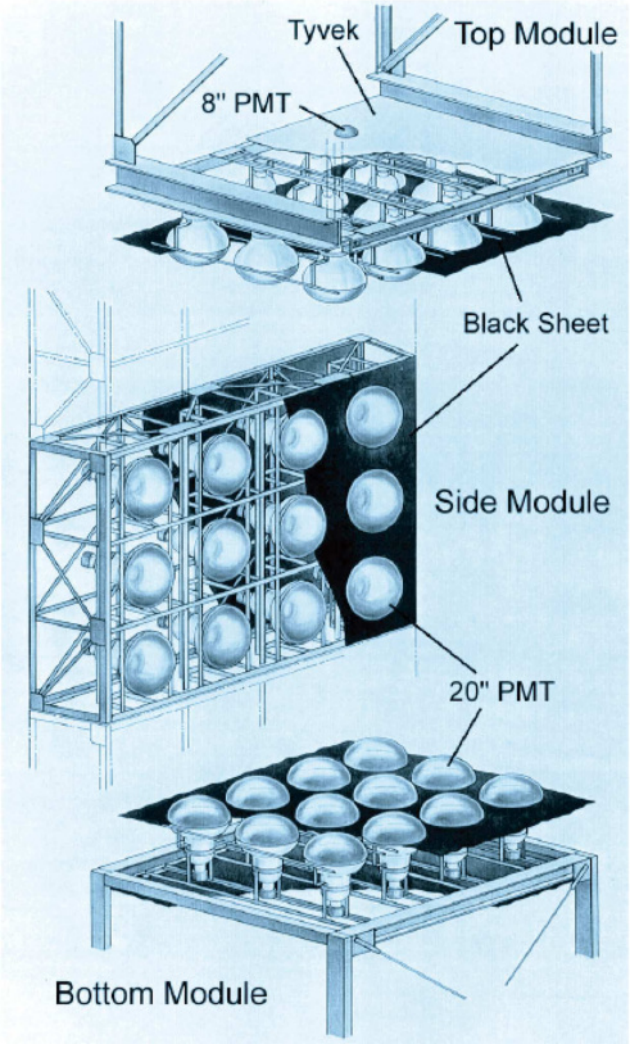

The entire ID region is a volume of 32.5 kt while the region actually used in the analysis is 2 m inside the PMT structure and represents a fiducial volume of 22.5 kt. There are at the least two reasons for excluding the 10 kt volume:

1) It is necessary to reduce the background from radioactive decays of radon which is particularly prominent near the PMTs and beams. The radon is still the main source of background in the fiducial volume, but the 2 m reduction brings the background to a manageable level.

2) There is a need for multiple PMT hits: if an event happens very near a PMT, all the light will be collected by that same PMT, and there will not be sufficient information for reconstructing that event. The PMTs used in SK's ID are 50 cm in diameter; they are largest PMTs in the world, designed and constructed especially for the SK experiment.

The OD, which surrounds the steel structure, has 1885 outward-facing 20 cm PMTs.

The top of the tank is a flat sheet that covers the entire are of the detector. It is under a dome, which lined with a polyurethane material ("Mineguard"), to reduce the radon emanation and erosion from the rock walls.

36.1 Cherenkov method of particle detection.

In a transparent medium with an index of refraction $n > 1$ the light velocity is $v_c = c/n < c$.

When a charged particle traverses the medium with velocity $v > v_c$, the Cherenkov light is emitted in a cone of half angle $\theta_C = \arccos(c/nv)$ from the direction of the particle's track.

This may easily be understood from the Huygens principle:

$$\frac{AB}{v} = \frac{AC}{v_c}$$

$$\Downarrow$$

$$\cos\theta_C = \frac{AC}{AB} = \frac{v_c}{v}.$$

The refractive index of pure water is about 4/3 for a wavelength region 300 to 700 nm (where the PMTs are sensitive). Therefore the Cherenkov light is emitted by ultrarelativistic particles under about 42°.

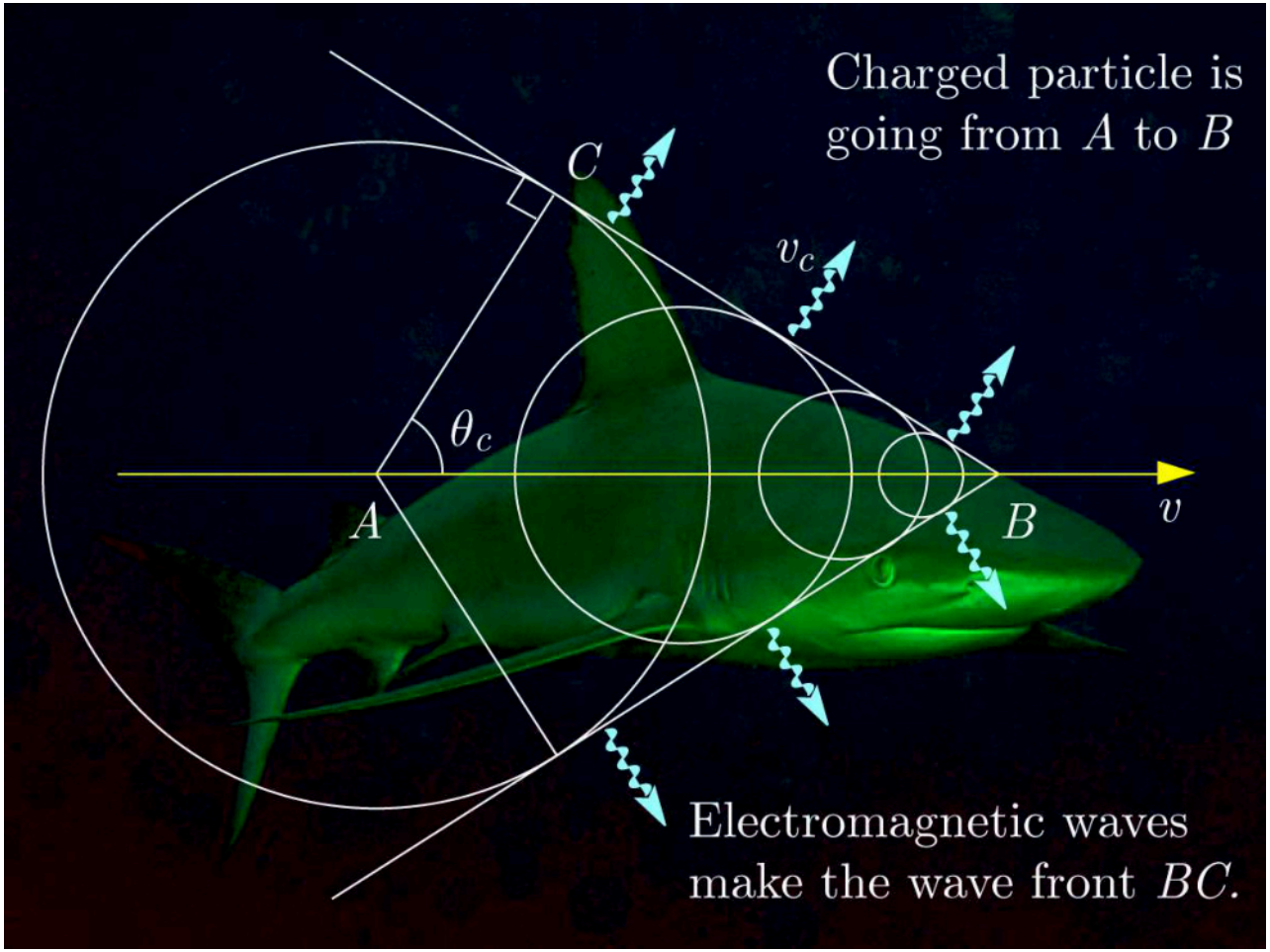

Cherenkov cone construction using Huygens' principle.

The number of photons produced along a flight path dx in a wave length bin $d\lambda$ for a particle carrying charge ze is

$$\frac{d^2N_\gamma}{d\lambda dx} = \frac{2\pi\alpha z^2 \sin^2\theta_C}{\lambda^2},$$

where $\alpha \approx 1/137$ is the fine structure constant. The number of Cherenkov photons emitted per unit path length with wavelength between λ_1 and λ_2 is

$$\frac{dN_\gamma}{dx} = 2\pi\alpha z^2 \int_{\lambda_1}^{\lambda_2} \left[\frac{d^2N_\gamma}{d\lambda dx}\right] \frac{d\lambda}{\lambda^2} \approx 2\pi\alpha z^2 \sin^2\theta_C \left(\frac{1}{\lambda_1} - \frac{1}{\lambda_2}\right)$$

(neglecting the dispersion of the medium). In particular, for the optical range (400–700 nm)

$$\frac{dN_\gamma}{dx} = \frac{491.3\, z^2 \sin^2\theta_C}{1 \text{ cm}}.$$

A single charged particle emits about 214 (380) photons per 1 cm of the path length in water within the optical range (the PMT sensitive range).

For $v \approx c$ the Cherenkov light yield is independent of the energy of the charged particle. This means the light output of a single particle does not allow its energy to be measured.

The energies E_C and momenta p_C of some particles with $v = v_c$ in water (Cherenkov thresholds) are shown in Table assuming $n(H_2O) = 1.33$).

Particle	E_C (MeV)	p_C (MeV/c)
$e^{\pm}$	0.775	0.583
$\mu^{\pm}$	160.3	120.5
$\pi^{\pm}$	211.7	159.2
p	1423	1070

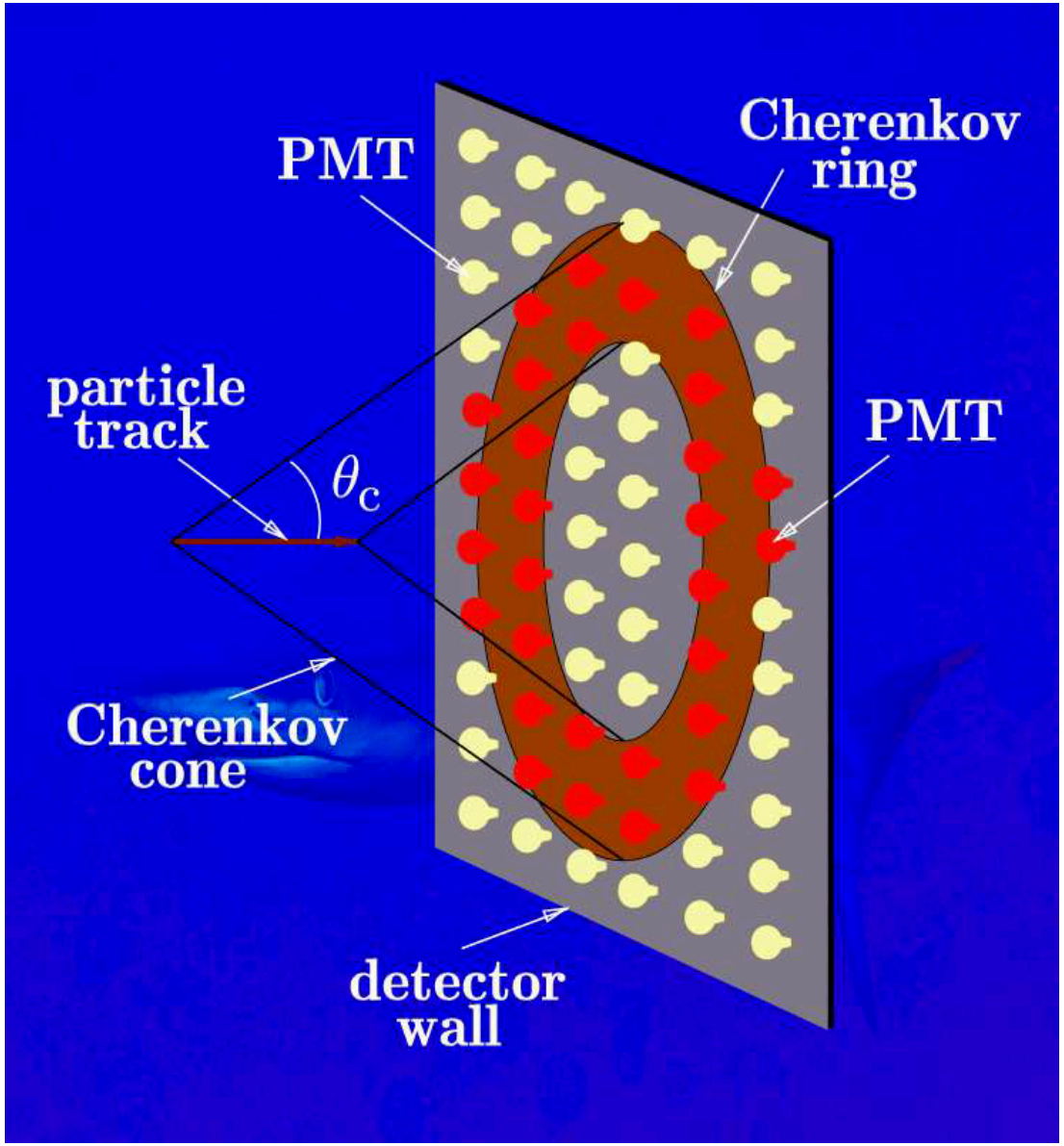

Cherenkov ring.

36.2 Solar event reconstruction method.

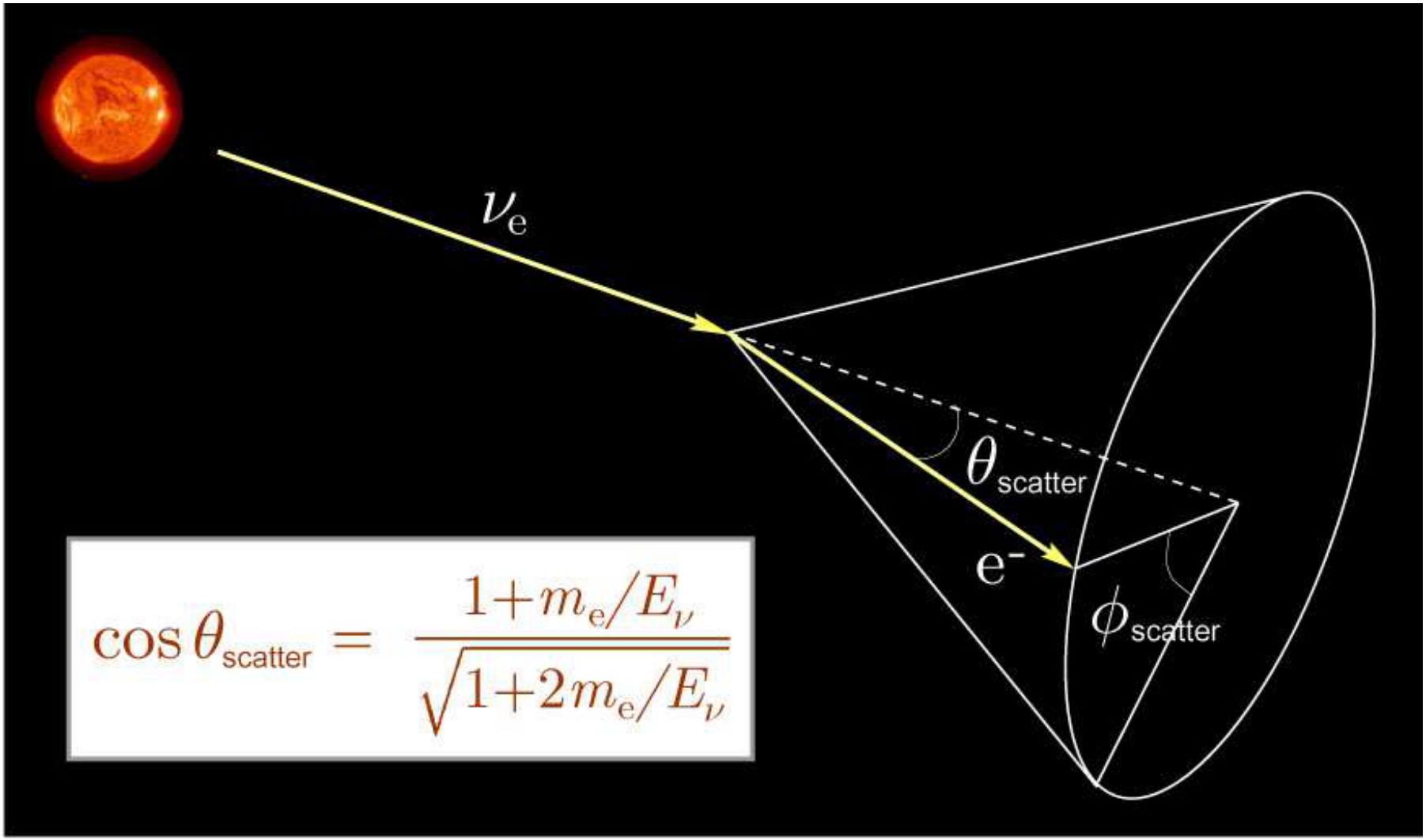

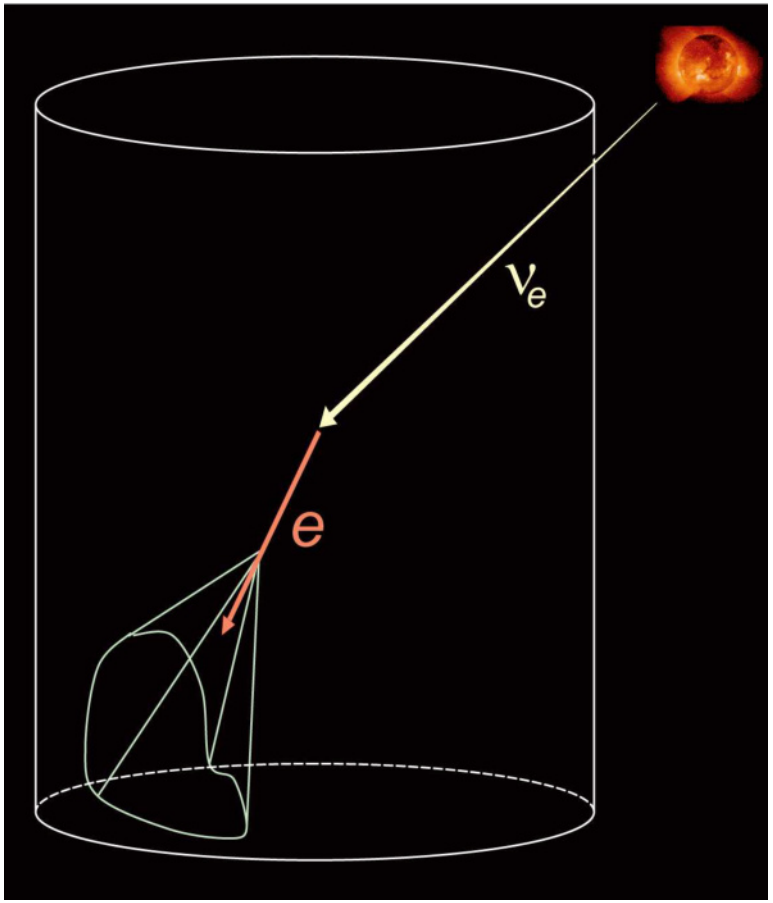

Super-Kamiokande uses elastic scattering of neutrinos from electrons. Cherenkov radiation emitted by the electron is detected by phototubes. The image looks like a diffuse ring on the detector walls.

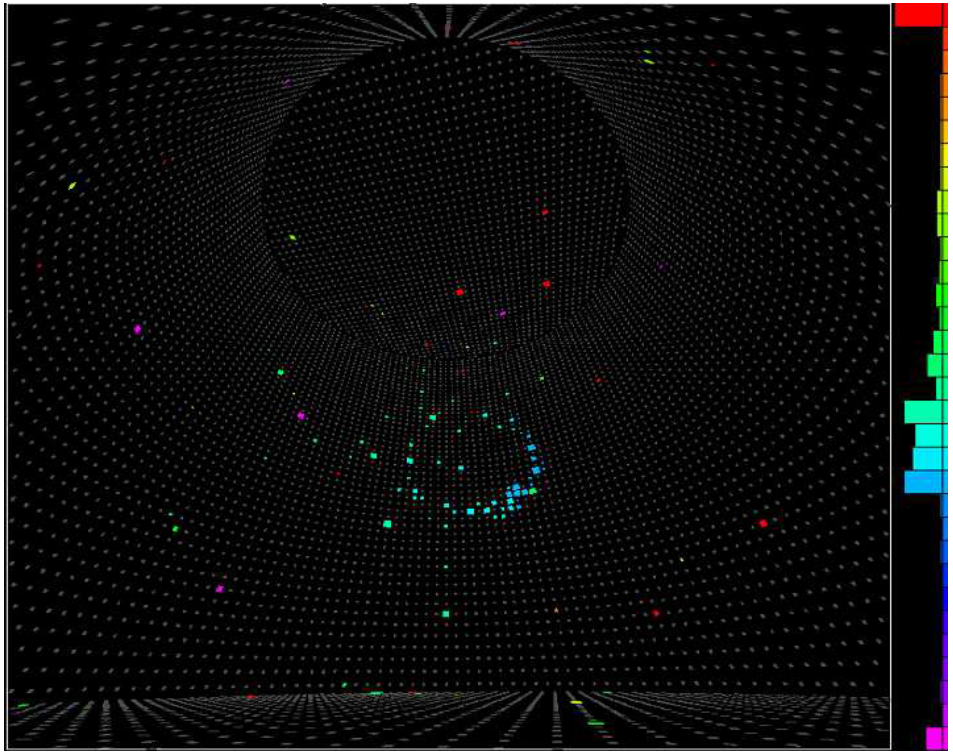

A real event recorded in the Super-Kamiokande detector on 1998-03-12 14:08:40. It is about 12.5 MeV and has an unusually nice, well-defined ring. The color scale is time. This event was found by Mark Vagins.
[From I. Semeniuk, "Feature – Astronomy and the New Neutrino," Sky & Telescope, September 2004, pp. 42–48; see also Tomasz Barszczak, URL: ⟨ http://www.ps.uci.edu/~tomba/sk/tscan/pictures.html ⟩.]

Angular distribution of solar neutrino event candidates in Super-Kamiokande-I. ▷

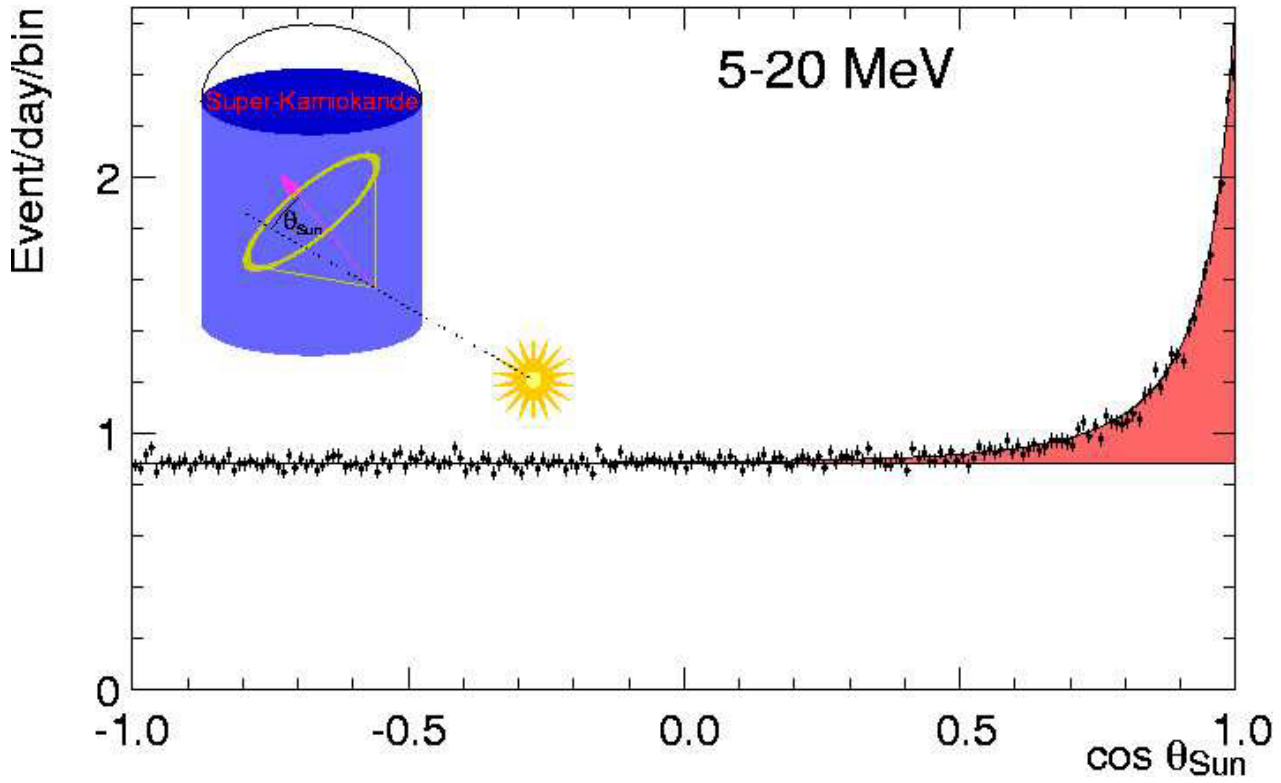

The angular deviation between the true solar and reconstructed direction of events with total energies ranging between 5 and 20 MeV is shown. From the strong forward peak due to elastic scattering of solar ^8B neutrinos off electrons $22,400 \pm 200\,(\text{stat})$ neutrino interactions were observed in 22,500 metric tons of water of the SK tank during 1496 live days. The observed solar neutrino interaction rate is $0.465 \pm 0.005^{+0.016}_{-0.015}$ of the rate expected by the standard solar model (SSM). Assuming only solar ν_e the observed rate corresponds to a ^{8}B flux of

$$\Phi\left(^8\text{B}\right) = (2.35 \pm 0.02\,(\text{stat}) \pm 0.08\,(\text{syst})) \times 10^6\ \text{cm}^{-2}\text{s}^{-1}.$$

All uncertainties given for the time variation data are only statistical and based on an asymmetric Gaussian approximation of the underlying likelihood functions obtained by an unbinned maximum likelihood fit to the $\cos(\theta_{\text{Sun}})$ distributions.

36.3 Seasonal variation of the solar neutrino flux.

Time variation of the SN flux scaled by the SSM prediction.

▷

The curves represent the expected flux modulation due to the eccentricity of the Earth's orbit. The SK data are as of December 2002. The top two panels show the Super-Kamiokande-I rate as a function of time. The topmost panel uses bins of 10 days width, the middle panel displays 45 day bins. The lower left panel combines the 10-day bins into 12 bins to show the yearly cycle assuming asymmetric Gaussians for the probability density functions.

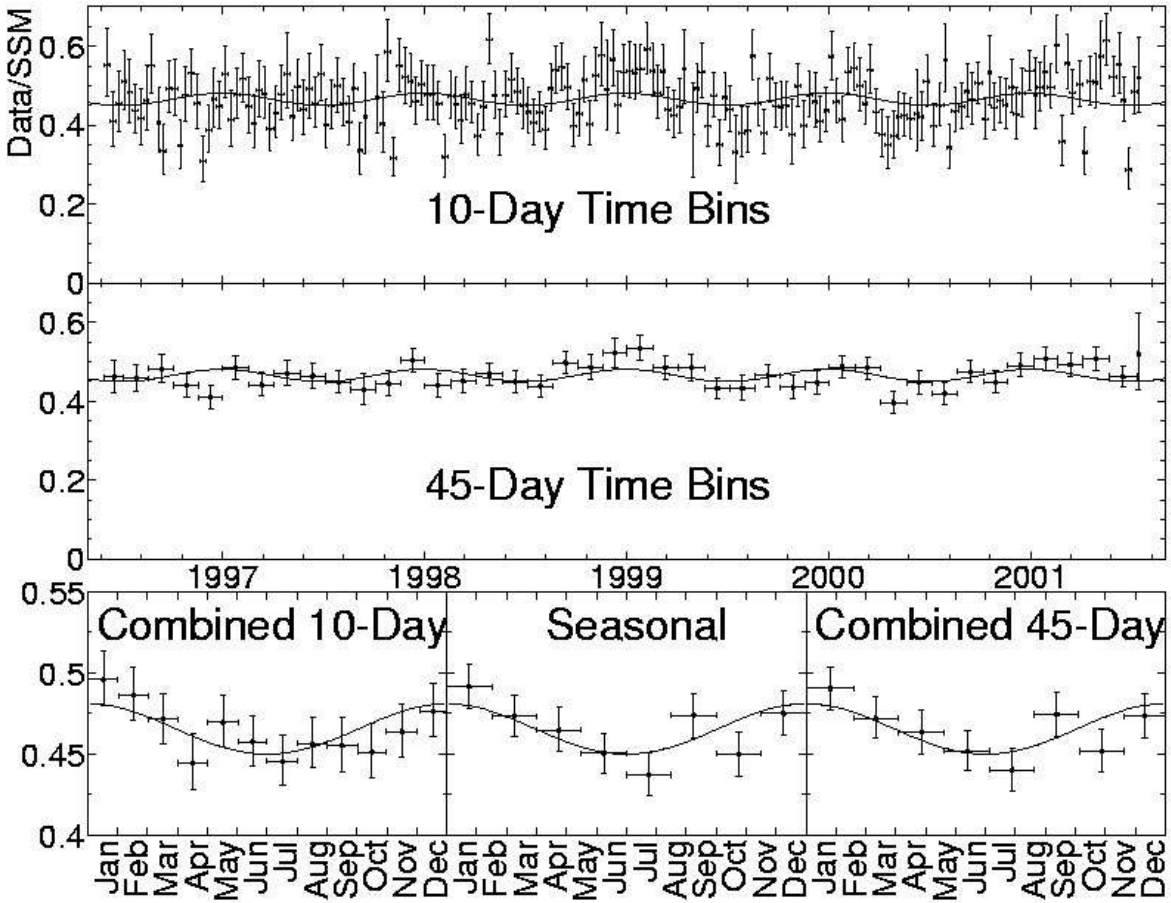

The lower right panel shows the yearly variation data in 8 bins obtained from a similar combination of the 45-day data bins. The middle right panel is the yearly variation data in those same 8 bins, but resulting directly from a maximum likelihood fit to the $\cos(\theta_{\mathsf{Sun}})$ distribution.

36.4 Possible signatures of the solar neutrino oscillations.

1. Reduction of the event rate.

Because of the oscillation, the number of ν_e reduces while the number of ν_μ and ν_τ increases.

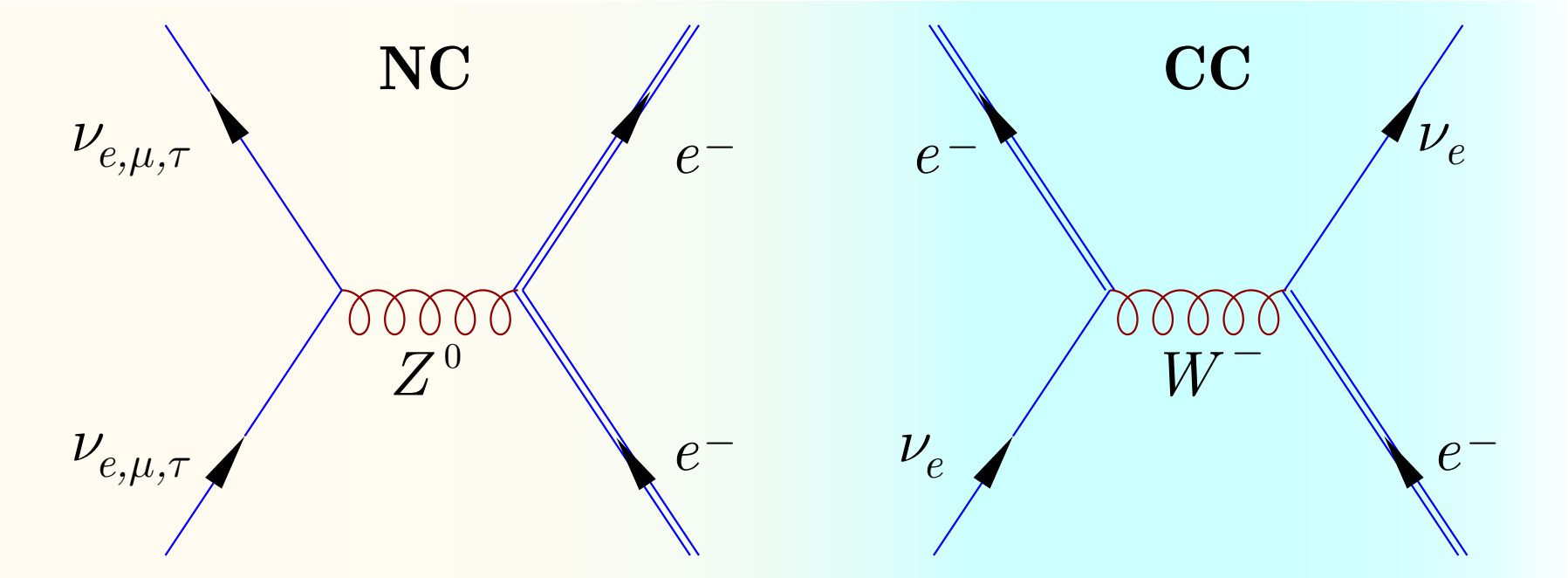

Interaction cross sections at $E_\nu = 10$ MeV are

$$\sigma\left(\nu_e + e^- \to \nu_e + e^-\right) \approx 9.5 \times 10^{-44}\ \text{cm}^2,$$
$$\sigma\left(\nu_{\mu,\tau} + e^- \to \nu_{\mu,\tau} + e^-\right) \approx 1.6 \times 10^{-44}\ \text{cm}^2,$$

Due to the difference of the cross sections, the observed number of events is essentially reduced.

2. Day/Night event rate difference.

When the neutrino goes through the Earth, the oscillation probability is affected by the MSW effect.

3. Gradual change of the oscillation effect.

Transition from the matter effect dominant region to the vacuum oscillation dominant region could be observed by lowering the energy threshold. It would be a crucial test for the MSW effect. SK4 needs to reduce background events and systematic uncertainties. Study is going on and collecting data with the SK4 detector (see 2312.12907 [hep-ex] for the present-day status). The issue was resolved in the Borexino experiment in 2018, see p. 789. The most recent combined Borexino+SK+KamLAND analysis is also provided in 2312.12907 [hep-ex]. We'll discuss all of this next year...

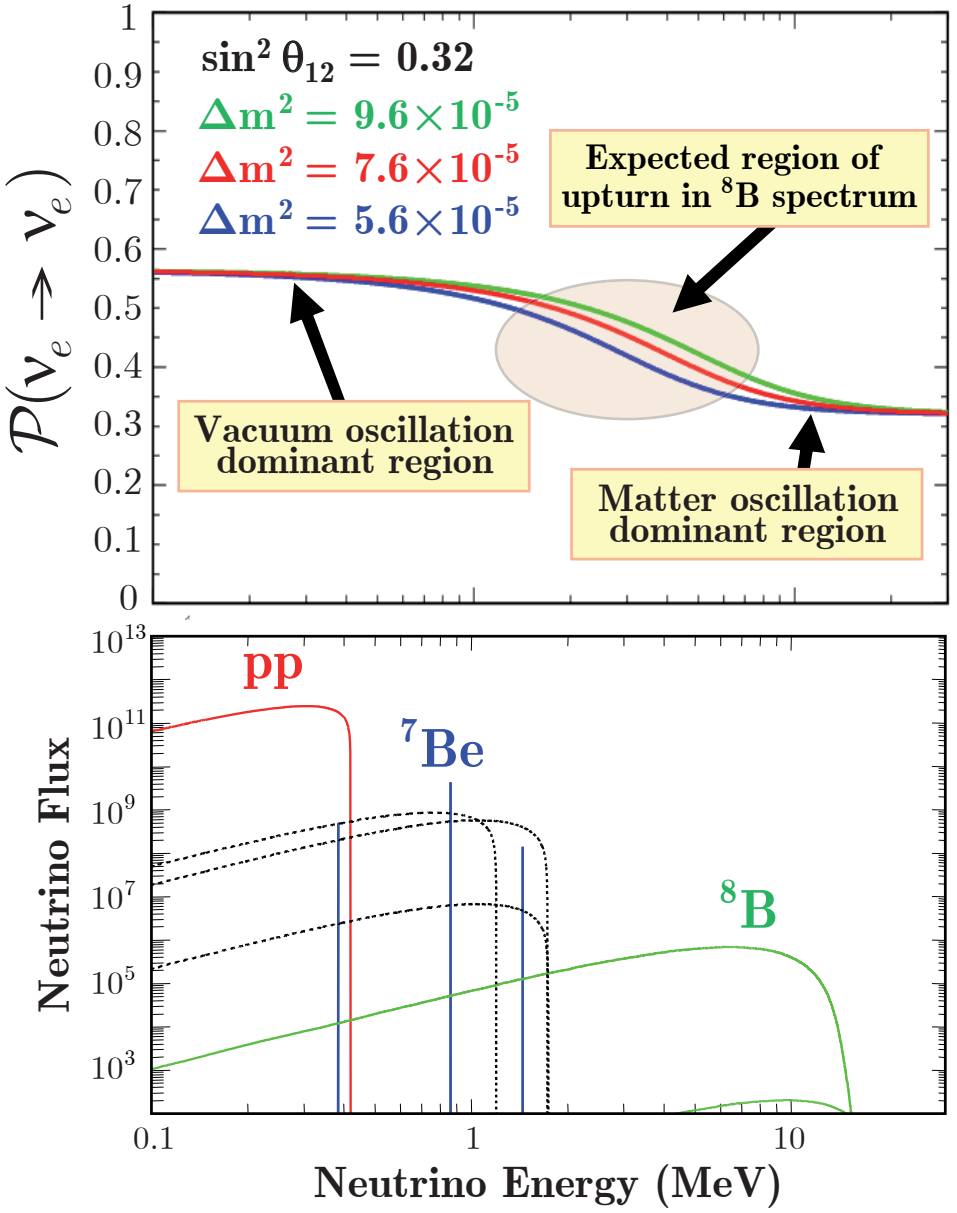

Figure is borrowed from a Yoshinari Hayato's report.

37 D_2O detector SNO.

SNO is a 1 ktonne water Cherenkov detector, located at a depth of 2092 m (6010 m of water equivalent) in the International Nickel Company (INCO) Creighton Mine near Sudbury, Ontario in Canada.[a]

The detector consists of a 5.5 cm thick, 12 m diameter acrylic vessel (AV), holding the 1000 t ultra-pure D_2O target, surrounded by 7 kt of ultra-pure H_2O shielding.

The AV is surrounded by a 17.8 m diameter geodesic sphere, holding 9456 inward-looking and 91 outward-looking 20 cm photomultiplier tubes (PMTs).

Figure shows a view of the SNO detector after installation of the bottom PMT panels, but before cabling (photo by Ernest Orlando, Lawrence Berkeley National Laboratory).

[From The Sudbury Neutrino Observatory webpage, URL: ⟨ http://www.sno.phy.queensu.ca/sno/ ⟩.]

[a] The Creighton Mine is very widely famed, being, indeed, the greatest nickel ore deposit known in the World.

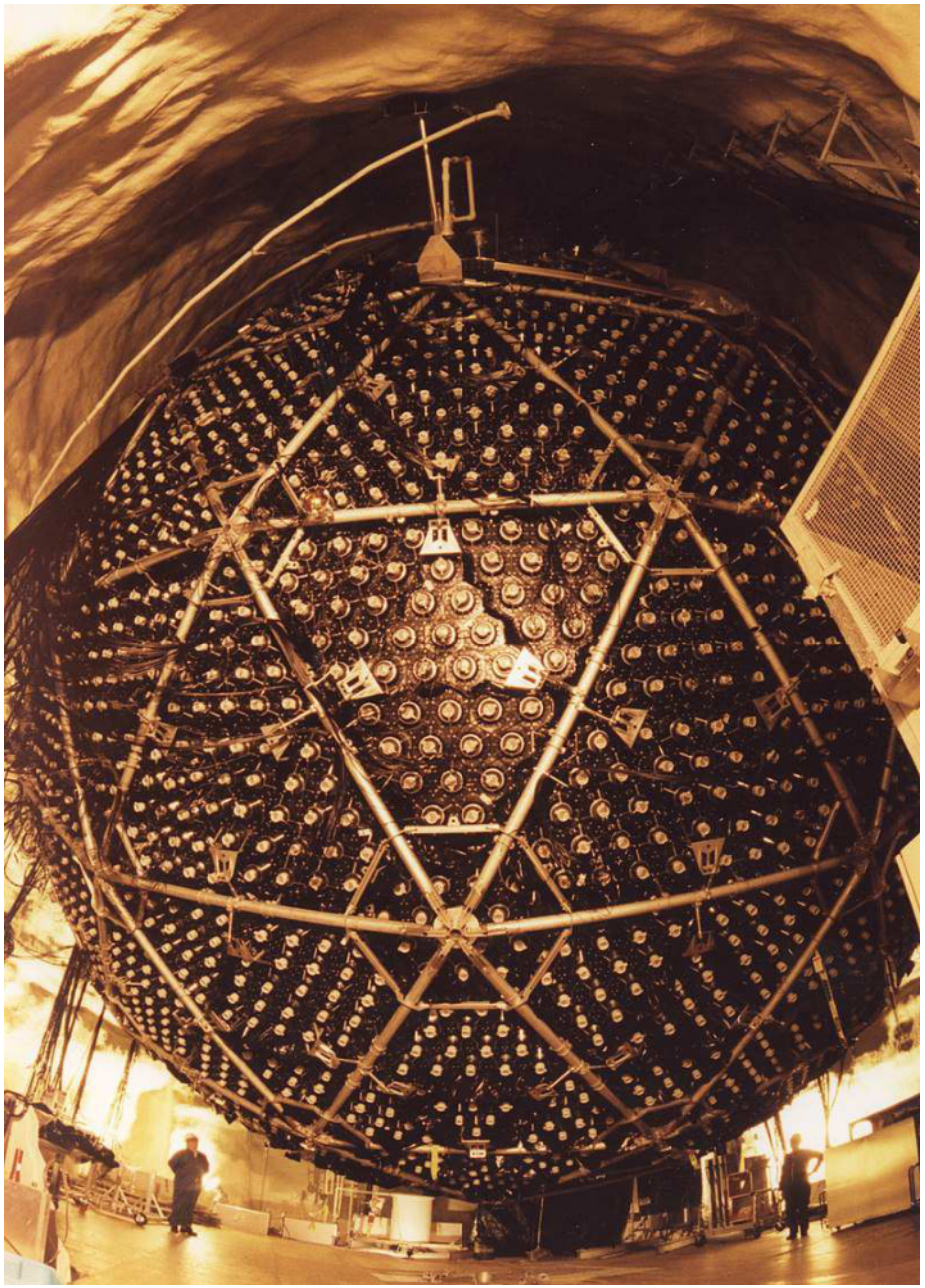

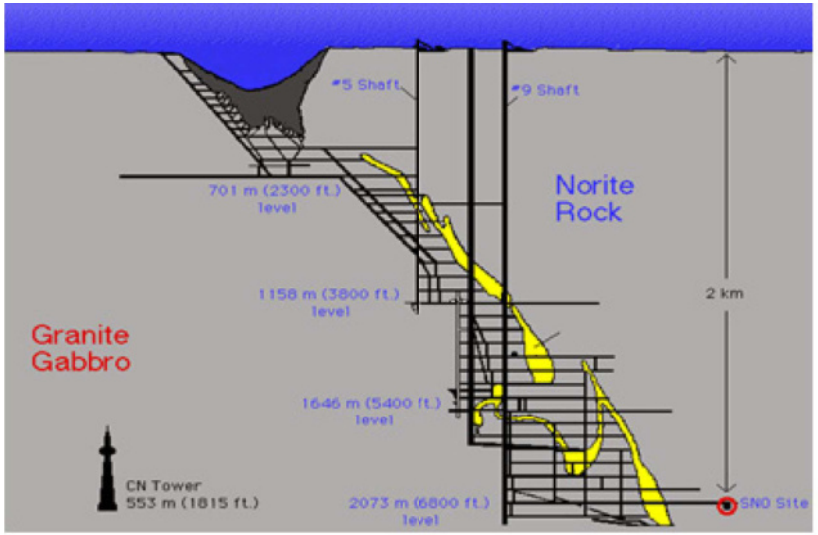

Sudbury Neutrino Observatory

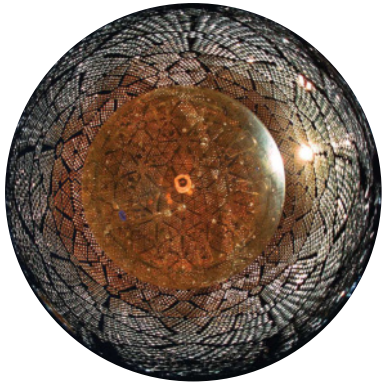

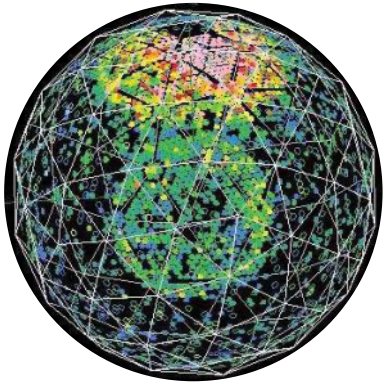

1000 tonnes D_2O

Support Structure for 9500 PMTs, 60% coverage

12 m Diameter Acrylic Vessel

1700 tonnes Inner Shielding H_2O

5300 tonnes Outer Shield H_2O

Urylon Liner and Radon Seal

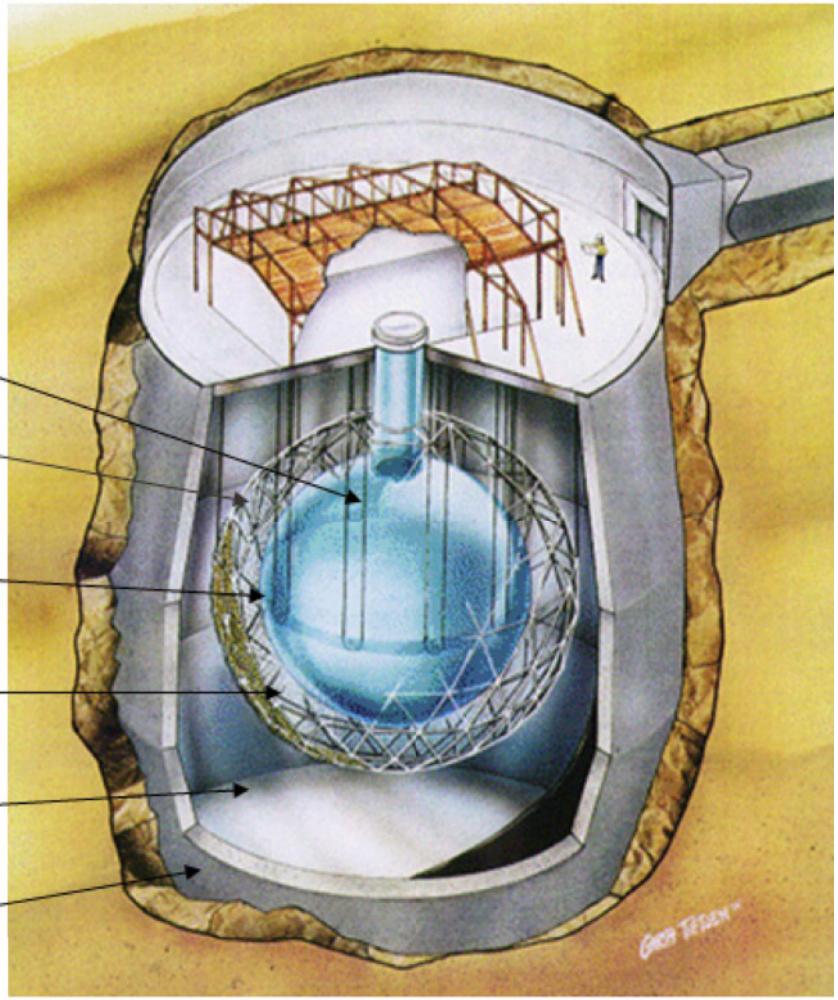

Unique signatures in SNO

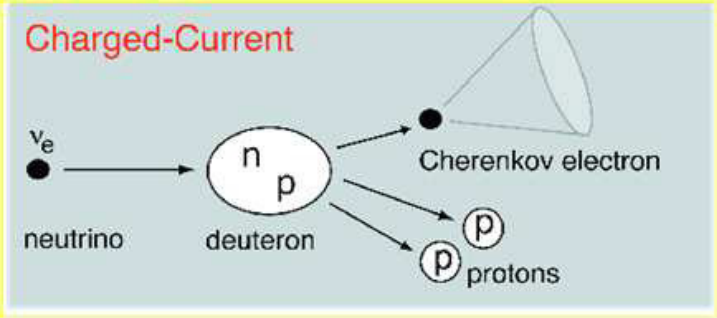

Charged Current (CC) interaction:

$$\nu_e + d \to e^- + p + p$$

$E_\nu^{\text{th}} = 1.44$ MeV. Allows detecting of ν_e only.

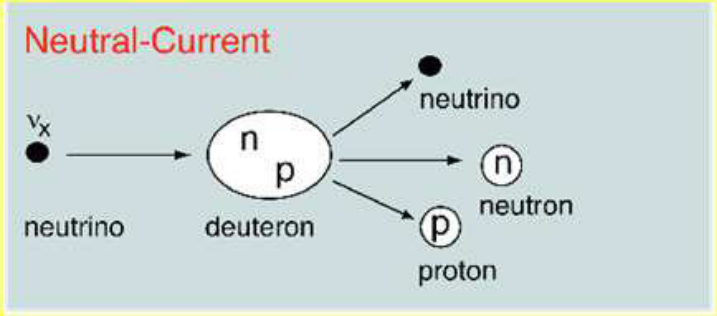

Neutral Current (NC) interaction:

$$\nu_\alpha + d \to \nu_\alpha + n + p$$

$E_\nu^{\text{th}} = 2.22$ MeV. Equally sensitive to all neutrinos.

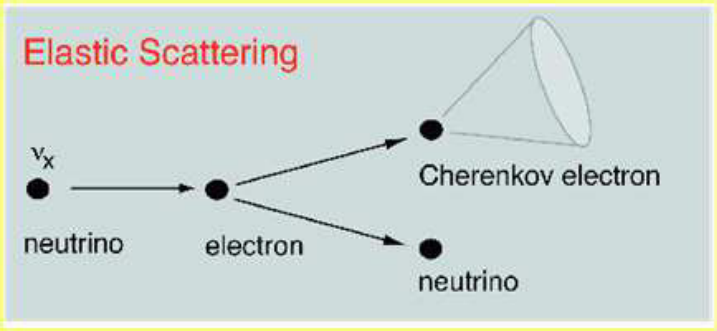

Elastic Scattering (ES):

$$\nu_\alpha + e^- \to \nu_\alpha + e^-$$

$E_\nu^{\text{th}} = 6.75$ MeV. Sensitive to all active neutrinos but enhanced for ν_e.

38 BOREXINO.

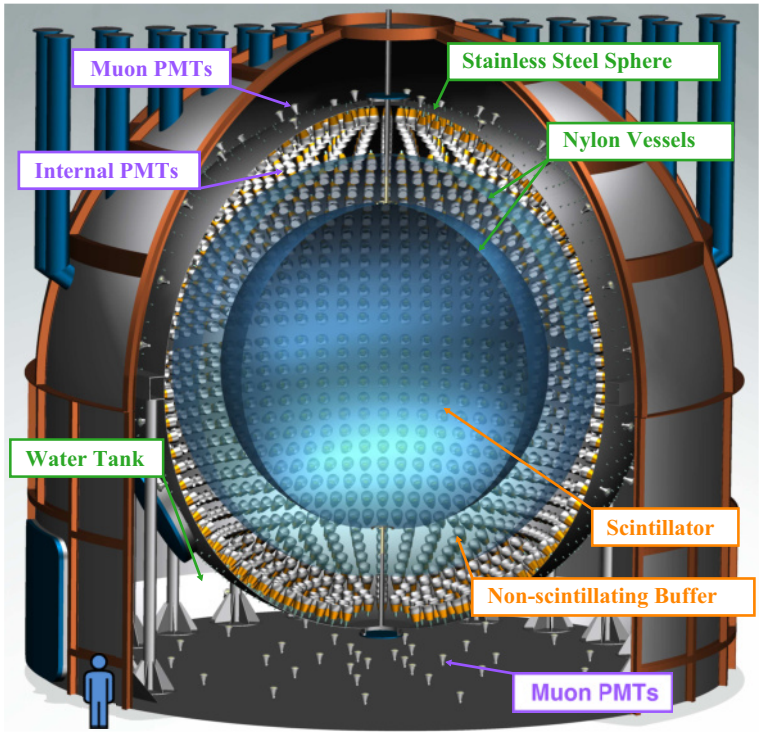

Borexino (the small Boron Experiment) is a part of the *Laboratori Nazionali del Gran Sasso* (LNGS), inside the Gran Sasso mountain, Abruzzo, Italy. The mountain shields the LNGS experiments from outside radiation, allowing to study rare interactions involving neutrinos and other particles. The experiment uses boron-loaded scintillators to measure the flux of solar neutrinos due to ^{7}Be electron captures. It is a multipurpose experiment performed by an international collaboration. Its physics program is centered on solar neutrino physics, but also includes other relevant topics in low-background neutrino detection and underground physics.

The Borexino detector is a real time detector for low energy (sub-MeV) solar neutrinos, with the specific goal of measuring the ^{7}Be neutrino flux from the Sun. The very low energy experimental threshold (250 keV) requires extreme radiopurity of the detector.

A Borexino prototype, called Counting Test Facility (CTF) was built and operated in LNGS Hall C. CTF demonstrated the achievement of ultralow count rates (radiopurities of $\sim 10^{-16}$ gr/gr of ^{238}U equivalent) on the several-ton scale. The Borexino detector was built on the CTF experience. The first data acquisition (DAQ) run with the full detector was started on May 16, 2007. By now (2021), Borexino has completed its main tasks and solved many other burning problems in neutrino physics.

[For more detail, see M. Agostini *et al.* (Borexino Collaboration). "Comprehensive measurement of pp-chain solar neutrinos," Nature **562** (2018) 505–510 and references therein; see also PoS(EPS-HEP2019)40.]

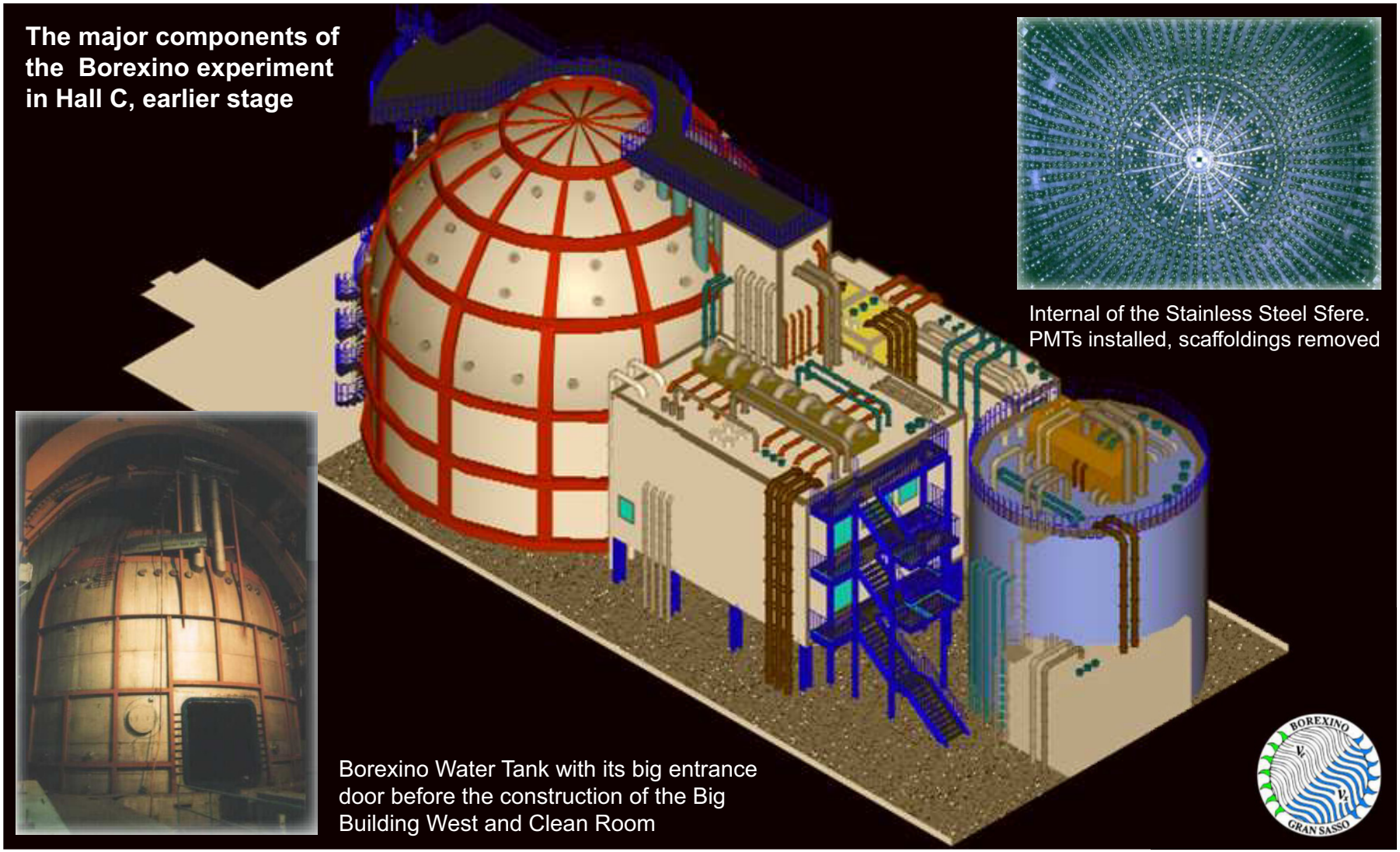

From left to right: the Borexino water tank; the "Big Building" (East and West) which house the control room, DAQ, and portions of the purification system; the purification skids; the CTF detector. [From Ch. Ghiano, "Measurement of the neutrino charged current interaction rate on ^{13}C in Borexino," (Ph.D. Thesis, Thesis, Universitá degli Studi dell'Aquila, 2011).]

Modern view of the Borexino complex at Hall C.

Modern view of the Borexino neutrino detector.

[From G. D. Orebi Gann, "Neutrino detection gets to the core of the Sun," Nature **587** (2020) 550–551.]

Results of the Borexino Phase-I–III solar neutrino analyses.

The rates and fluxes are integral values without any threshold; the first error is statistical, the second systematic. The rate-to-flux conversion uses the global-fit oscillation parameters by Capozzi *et al.* (2018). The last two columns show the fluxes as predicted by the HZ- and LZ-SSM. The fluxes of *pp*, ^{7}Be, *pep*, CNO, ^{8}B, and *hep* νs are normalized to 10^{10}, 10^{9}, 10^{8}, 10^{8}, 10^{6}, and 10^{3}, respectively.[a]

Solar neutrinos	Rate (cpd/100 ton)	Flux ($cm^{-2}s^{-1}$)	HZ-SSM Flux ($cm^{-2}s^{-1}$)	LZ-SSM Flux ($cm^{-2}s^{-1}$)
Phase-II (12/2011 – 05/2016)				
pp	$134 \pm 10^{+6}_{-10}$	$(6.1 \pm 0.5^{+0.3}_{-0.5})$	5.98(1.0 ± 0.006)	6.03(1.0 ± 0.006)
^{7}Be	$48.3 \pm 1.1^{+0.4}_{-0.7}$	$(4.99 \pm 0.11^{+0.06}_{-0.08})$	4.93(1.0 ± 0.06)	4.50(1.0 ± 0.06)
pep (HZ)	$2.43 \pm 0.36^{+0.15}_{-0.22}$	$(1.27 \pm 0.19^{+0.08}_{-0.12})$	1.44(1.0 ± 0.01)	1.46(1.0 ± 0.009)
pep (LZ)	$2.65 \pm 0.36^{+0.15}_{-0.24}$	$(1.39 \pm 0.19^{+0.08}_{-0.13})$	1.44(1.0 ± 0.01)	1.46(1.0 ± 0.009)
CNO	<8.1 (95% C.L.)	<7.9 (95% C.L.)	4.88(1.0 ± 0.11)	3.51(1.0 ± 0.10)
Phase-I + II (01/2008 – 12/2016)				
$^{8}B_{HER\text{-}I}$	$0.136^{+0.013+0.003}_{-0.013-0.013}$	$(5.77^{+0.56+0.15}_{-0.56-0.15})$	5.46(1.0 ± 0.12)	4.50(1.0 ± 0.12)
$^{8}B_{HER\text{-}II}$	$0.087^{+0.080+0.005}_{-0.010-0.005}$	$(5.56^{+0.52+0.33}_{-0.64-0.33})$	5.46(1.0 ± 0.12)	4.50(1.0 ± 0.12)
$^{8}B_{HER}$	$0.223^{+0.015+0.006}_{-0.016-0.006}$	$(5.68^{+0.39+0.03}_{-0.41-0.03})$	5.46(1.0 ± 0.12)	4.50(1.0 ± 0.12)
Phase-I (part) + II + III (part) (11/2009 – 10/2017)				
hep	<0.002 (90% C.L.)	<180 (90% C.L.)	7.98(1.0 ± 0.30)	8.25(1.0 ± 0.12)
Phase-III (07/2016 – 02/2020)				
CNO	$7.2\ ^{+3.0}_{-1.7}$	$(7.0\ ^{+3.0}_{-2.0})$	4.88(1.0 ± 0.11)	3.51(1.0 ± 0.10)

[a] Borrowed from S. Kumaran, L. Ludhova, Ö. Penek, & G. Settanta, "Borexino results on neutrinos from the Sun and Earth," Universe **7** (2021) 231, arXiv:2105.13858 [hep-ex]. Abbreviations used here and on the next three slides: HZ = High Metallicity, LZ = Low Metallicity, cpd = counts per day, HER = High Energy Range.

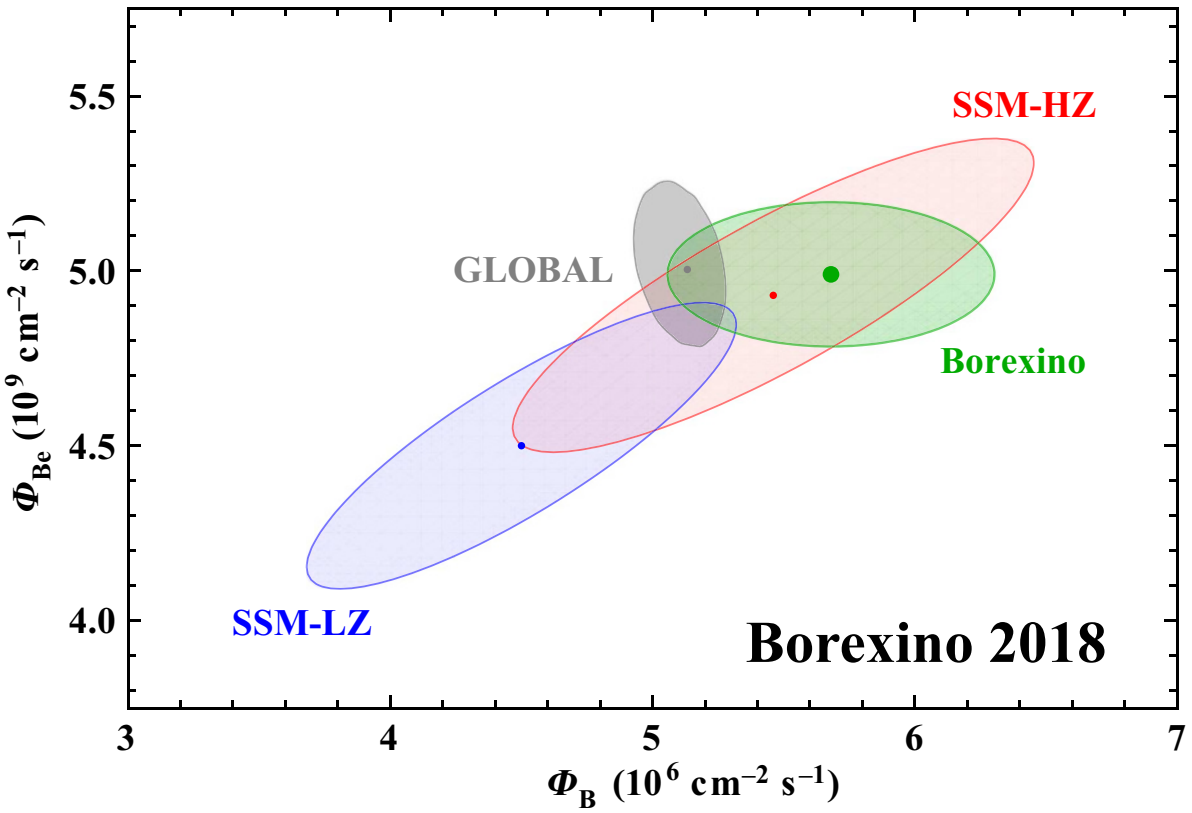

The Borexino results are compatible with the temperature profiles predicted by both HZ- and LZ-SSMs. However, the ^{7}Be and ^{8}B solar ν_e fluxes measured by Borexino provide an interesting hint in favor of the HZ-SSM prediction. However, this hint weakens when the Borexino data are combined with data of all other solar ν_e experiments + KamLAND reactor $\overline{\nu}_e$ data.

Borexino results and analysis in the $\Phi_{^7\mathrm{Be}} - \Phi_{^8\mathrm{B}}$ space at 68.27 % C.L.

Allowed contours in the $\Phi_{^7\mathrm{Be}} - \Phi_{^8\mathrm{B}}$ space are obtained by combining these new results with all solar and KamLAND data in a global analysis, and leaving free the oscillation parameters θ_{12} and Δm^2_{12} (grey ellipse, marked as GLOBAL). The theoretical predictions for the low-metallicity (LZ, blue) and the high-metallicity (HZ, red) SSMs are also shown. The fit returns the following numbers:

$$\tan^2\theta_{12} = 0.47 \pm 0.03 \quad \text{and} \quad \Delta m^2_{12} = (7.5 \pm 10^5) \pm 0.03.$$

[From M. Agostini *et al.* (Borexino Collaboration). "Comprehensive measurement of pp-chain solar neutrinos," Nature **562** (2018) 505–510; see also reference in footnote of p. 787.]

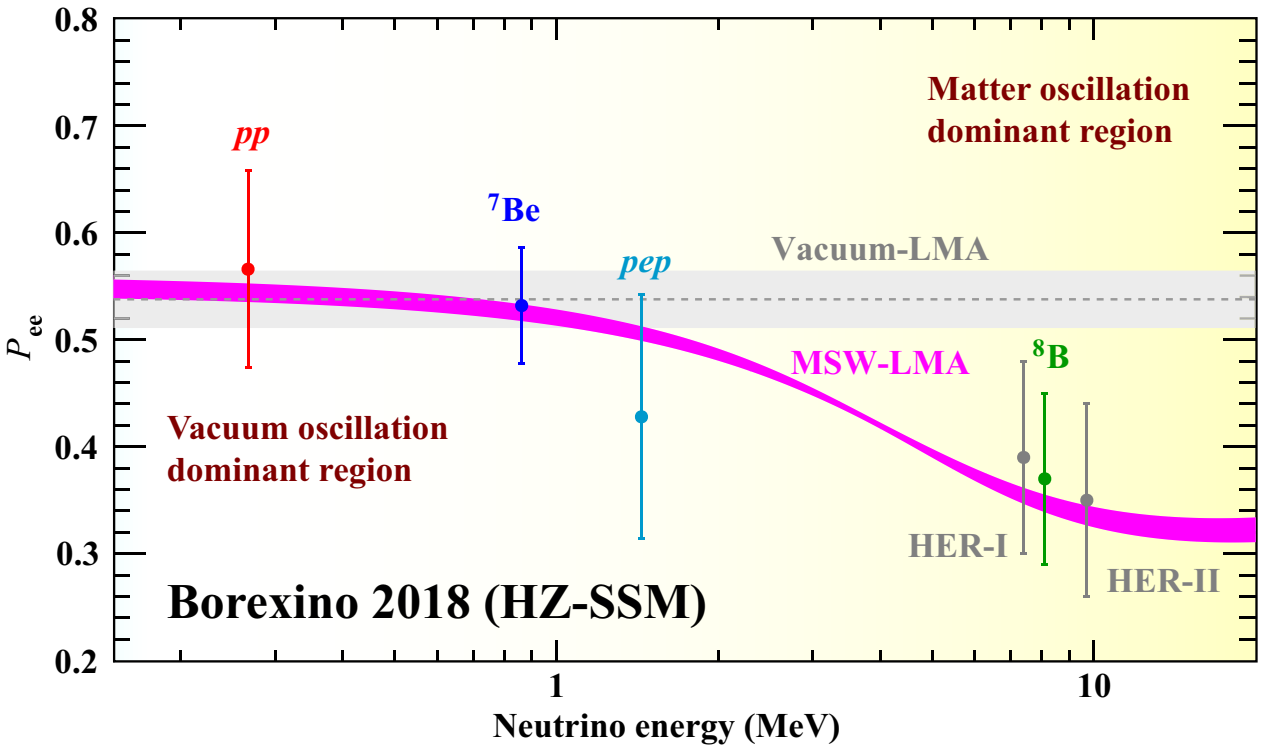

Measured solar neutrino survival probabilities are

0.57 ± 0.09	(pp, 0.267 MeV)
0.53 ± 0.05	(^{7}Be, 0.862 MeV)
0.43 ± 0.11	(pep, 1.44 MeV)
0.39 ± 0.09	(^{8}B$_{\text{HER-I}}$, 7.4 MeV)
0.37 ± 0.08	(^{8}B$_{\text{HER}}$, 8.1 MeV)
0.35 ± 0.09	(^{8}B$_{\text{HER-II}}$, 9.7 MeV)

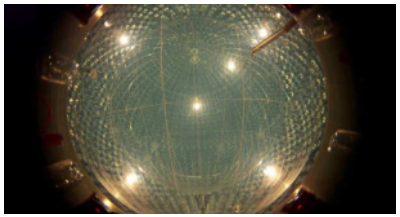

Electron neutrino survival probability $P_{ee} \equiv \mathcal{P}(\nu_e \to \nu_e)$ vs. neutrino energy.

The pink band is the $\pm 1\sigma$ prediction of MSW-LMA while the grey band represents the vacuum-LMA solution. Data points show the Borexino 2018 results for pp, ^{7}Be, pep, and ^{8}B (green for the HER range, and grey for the separate HER-I and HER-II sub-ranges), assuming HZ-SSM. The ^{8}B and pp data points are set at the mean energy of neutrinos that produce scattered electrons above the detection threshold. The quoted error bars include experimental and theoretical uncertainties.

Borexino data disfavors the vacuum-LMA hypothesis at 98.2 % C.L. and are in excellent agreement with the expectations from the MSW-LMA paradigm. It's actually a Nobel result.

[From M. Agostini *et al.* (Borexino Collaboration). "Comprehensive measurement of pp-chain solar neutrinos," Nature **562** (2018) 505–510; see also reference in footnote of p. 787.]

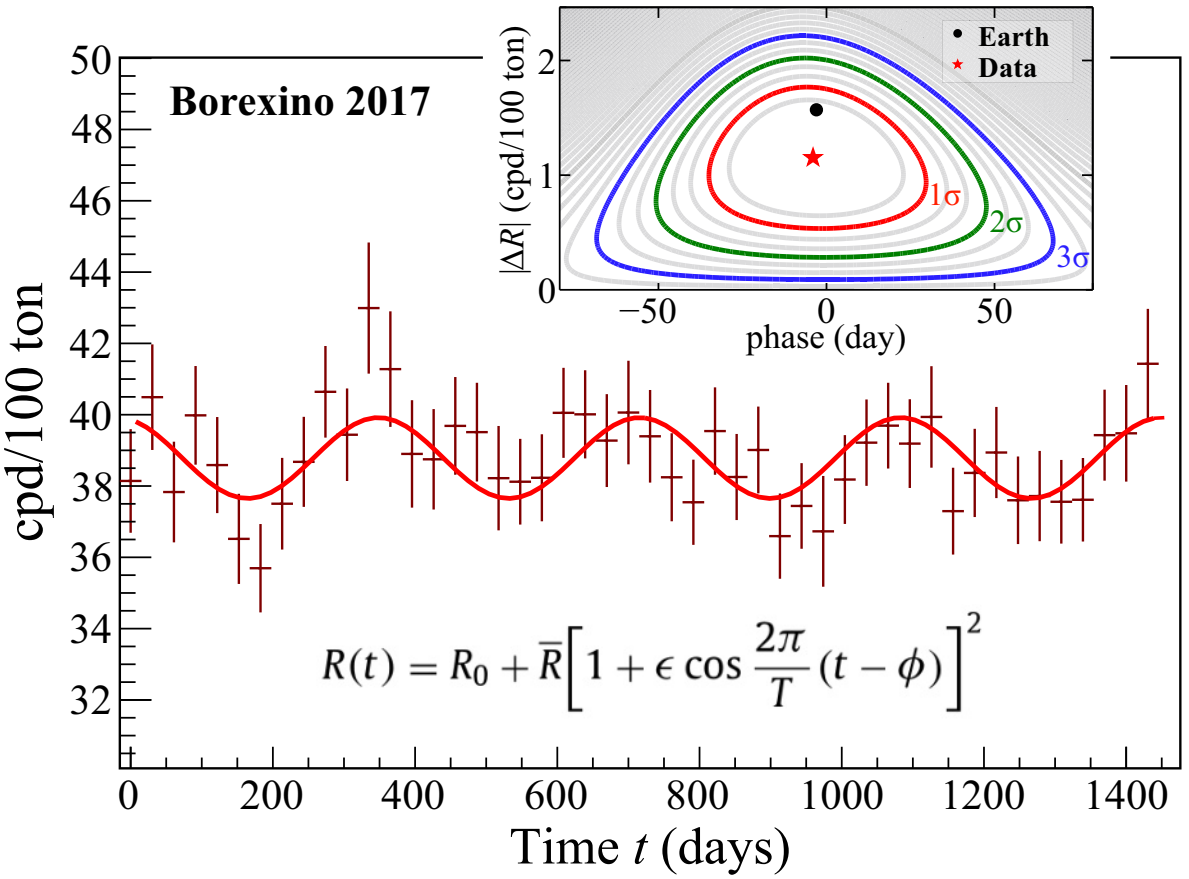

Borexino was able to measure the annual modulation of solar neutrinos with high significance, confirming the solar origin of the measured ^{7}Be signal. The fit values for the modulation periodicity and its amplitude obtained with three different analytical approaches are well consistent with each other and with the expectations. Borexino rejected the hypothesis of no modulation with a confidence level of 99.99%.

Borexino Phase-II rate of β-like events passing selection cuts in 30.43-days long bins starting from Dec. 11, 2011. The red line is resulting function from the fit with the equation shown in the figure, where $\epsilon = 0.0167$ is the Earth orbital eccentricity, $T = 1$ year is the period, ϕ is the phase relative to the perihelion, $\overline{R}$ is the average neutrino interaction rate, and R_0 is the time-independent background rate. Insert shows the amplitude and phase. The red star indicates the best-fit results, while the black point the expected values. Confidence contours of 1, 2, and 3σ are indicated with colored solid lines.

[From M. Agostini *et al.* (Borexino Collaboration), "Seasonal modulation of the ^{7}Be solar neutrino rate in Borexino," Astropart. Phys. **92** (2017) 21–29; 1701.07970 [hep-ex]; see also reference in footnote of p. 787.]

Part IX

Neutrino anomalies (?)

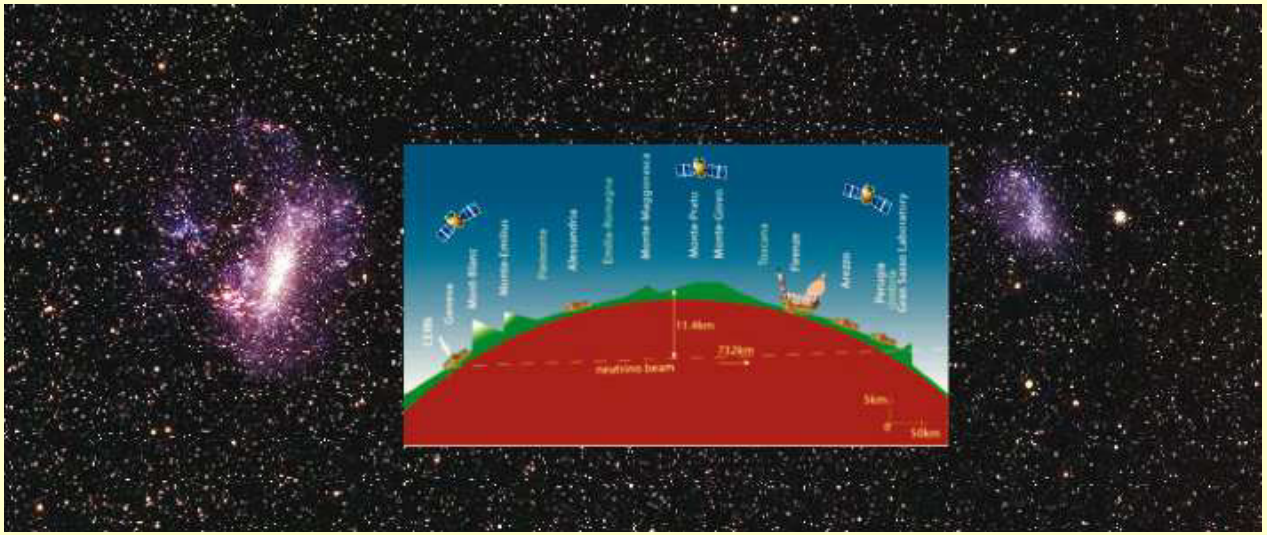

This chapter is not yet complete.

Although the neutrino oscillation phenomenon has been very well established by a number of experiments, there are several experiments whose results are inconsistent with this standard picture and hint either at the existence of an additional, sterile, neutrino, or at entirely new physics beyond the Standard Model. Let's list some "neutrino anomalies," both hitherto unexplained and seemingly closed, but which have not lost their propaedeutic significance:

- ⋆ LSND (vs. KARMEN) anomaly.
- ⋆ KARMEN time anomaly.
- ⋆ MiniBooNE anomaly (+ new data from MicroBooNE).
- ⋆ Reactor antineutrino anomaly (essentially all reactor data + new fantastic results of NEUTRINO-4).
- ⋆ Gallium anomaly (GALLEX, SAGE + recent confirmation from BEST).
- ⋆ GSI (Darmstadt) anomaly (vs. Two-Body-Weak-Decays experiment).
- ⋆ ANITA anomaly (although perhaps this is not a problem of the Standard Model, but of, say, glaciology or the theory of radio emissions from extensive air showers).
- ⋆ OPERA neutrino anomaly (seems to have dissolved into thin air... it's a pity).

Some of these anomalies have already been discussed in the lectures with varying degrees of detail, while others have not been mentioned at all. In this chapter we intend to add some details and fill in some gaps.[a]

[a] For a recent review, see G. Karagiorgi *et al.*, Snowmass Neutrino Frontier: NF02 Topical Group Report "Understanding experimental neutrino anomalies," arXiv:2209.05352 [hep-ex] (September 12, 2022).

Every science is made up entirely of anomalies rearranged to fit.
Raphael Aloysius Lafferty

Любая наука состоит исключительно из аномалий, перестроенных так, чтобы соответствовать реальности.
Рафаэль Алоизиус Лафферти

Through every rift of discovery some seeming anomaly drops out of the darkness, and falls, as a golden link into the great chain of order.
Edwin Hubbel Chapin

Через каждый разлом открытия какая-то кажущаяся аномалия выпадает из темноты и, как золотое звено, попадает в великую цепь порядка.

Эдвин Хаббел Чапин

Our most exciting discoveries come from studying anomalies. The once-in-1000 occurrence is worth getting detail on.
Michael J. Silverstein

Наши самые захватывающие открытия связаны с изучением аномалий. То, что случается один раз из 1000, заслуживает подробного рассмотрения.
Майкл Дж. Сильверстайн

Don't sweep "problems" under the rug. "Problems" are often clues!
Adam Riess

Не заметайте «проблемы» под ковер. «Проблемы» часто служат подсказками!
Адам Рисс

39 Neutrino velocity measurements.

39.1 Tests of Lorentz invariance.

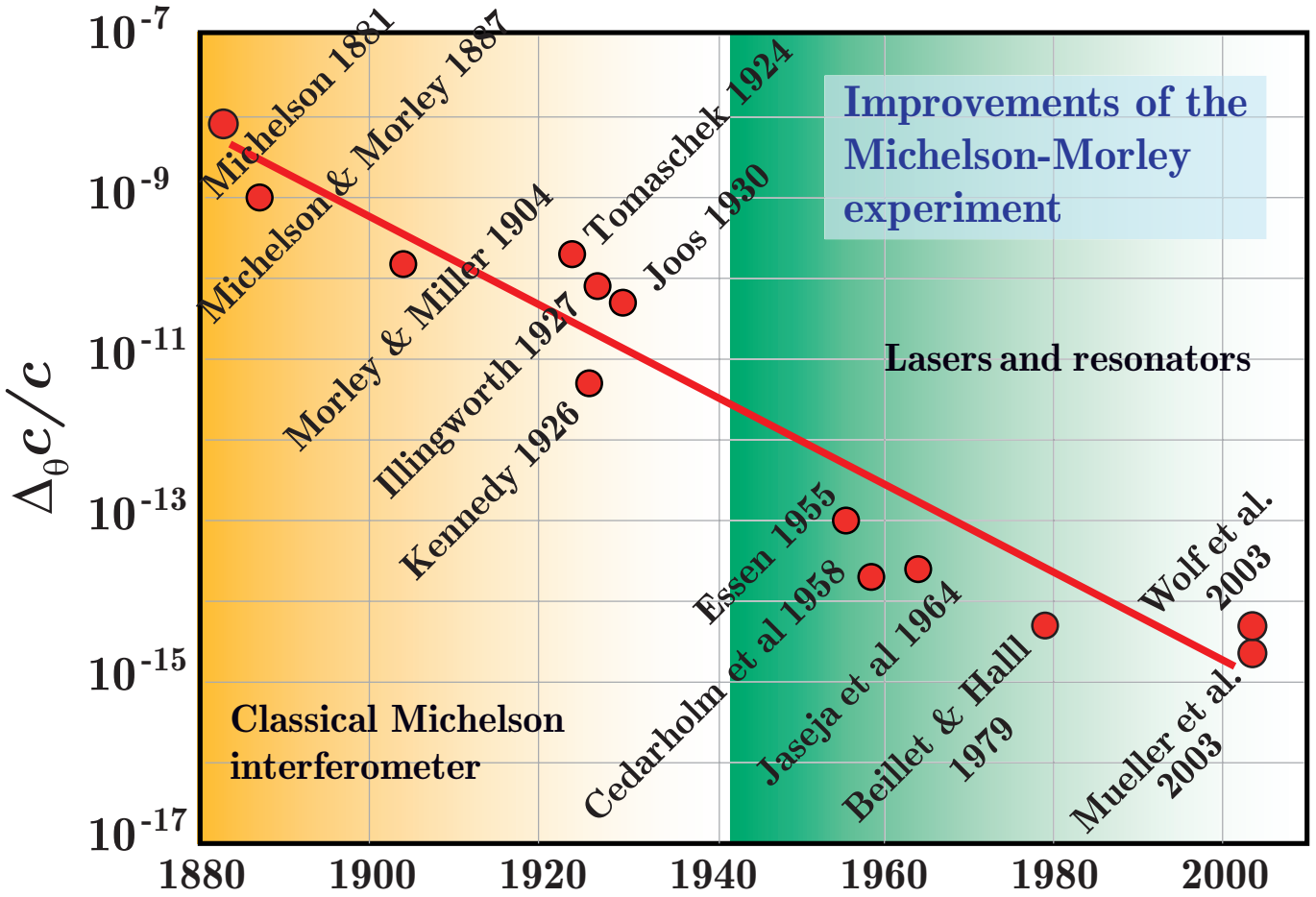

[Figure is taken from S. Herrmann *et al.*, "Test of Lorentz invariance using a continuously rotating optical resonator," Lect. Notes Phys. **702** (2006) 385–400.]

The constancy of c, i.e. its independence on laboratory velocity and orientation has been verified experimentally at improved precision by numerous repetitions of the Michelson-Morley experiment, providing a firm experimental basis for special relativity so far.

- The best current limit for a possible anisotropy of the speed of light is

$$\boxed{\Delta_\theta c/c < 10^{-17}.}$$

[Ch. Eisele *et al.*, "Laboratory test of the isotropy of light propagation at the 10^{-17} level," Phys. Rev. Lett. **103** (2009) 090401; S. Herrmann *et al.*, "Rotating optical cavity experiment testing Lorentz invariance at the 10^{-17} level," Phys. Rev. D **100** (2009) 105011, arXiv:1002.1284 [physics.class-ph].]

The sensitivity of the next-generation Michelson-Morley type experiments to violation of the Lorentz invariance is expected to be in the 10^{-19} to 10^{-20} regime.

[M. Nagel *et al.*, "Electromagnetic cavity tests of Lorentz invariance on Earth and in space," arXiv:1112.3857 [physics.class-ph].]

- The relativistic relation $\boxed{v = p/\sqrt{p^2 + m^2}}$ (173)

is confirmed in the accelerator experiments for $1 - v$ down to 2×10^{-7}.

The relation (173) has been tested in the SLAC accelerator by comparison of relative velocities of γ quanta with mean energies ~ 15 GeV and electrons with energies in the interval 15–20.5 GeV by using a time-of-flight technique with 1-psec sensitivity and a flight path of about 1 km. At such energies, the expected value of $v_\gamma - v_e = 1 - v_e$ was $(3.1 - 5.8) \times 10^{-10}$. No significant difference in v_γ and v_e was observed to within 2×10^{-7}.

[Z. G. T. Guiragossian *et al.*, "Relative velocity measurements of electrons and gamma rays at 15 GeV," Phys. Rev. Lett. **34** (1975) 335–338.]

The accuracy of the earlier experiments was order of magnitude lower.

39.2 Accelerator measurements of neutrino velocity.

In all ν experiments it is assumed that the relation (173) holds for muons, pions, and kaons.

- FNAL 1976 [345 m (decay pipe) + 550 m (shield), $\langle E_\nu^{(\pi)} \rangle = 25$ GeV, $\langle E_\nu^{(K)} \rangle = 75$ GeV]:

$$|v_\nu - v_\mu| < 4 \times 10^{-4} \text{ (99\% C.L.)}$$

[J. Alspector *et al.*, "Experimental comparison of neutrino and muon velocoties," Phys. Rev. Lett. **36** (1976) 837–839.]

- FNAL 1979 [345 m (decay pipe) + 550 m (shield), $E_\nu^{(\pi,K)} = 30$ to 200 GeV]:

$$|v_\nu - \overline{v}_\nu| < 7 \times 10^{-5}, \quad |v_\nu^{(K)} - v_\nu^{(\pi)}| < 5 \times 10^{-5}, \quad |v_{\nu,\overline{\nu}} - 1| < 4 \times 10^{-5} \text{ (95\% C.L.)}.$$

[G. R. Kalbfleisch *et al.*, "Experimental comparison of neutrino, antineutrino, and muon velocoties," Phys. Rev. Lett. **43** (1979) 1361–1364.]

- FNAL Tevatron – FMMF (1995) [Hadron & muon shield is located 542 m downstream of the neutrino target, the FMMF (E733) detector is located 1599 m downstream of the neutrino target; wide band neutrino beam]

  There were some time anomalies but there is no definite conclusions concerning v_ν.
  Seems to be in agreement with the FNAL 1979 limits.

  [E. Gallas *et al.* (FMMF Collaboration), "Search for neutral weakly interacting massive particles in the Fermilab Tevatron wideband neutrino beam," Phys. Rev. Lett. **52** (1995) 6; E. Gallas, PhD, Michigan State University, 1993; FERMILAB-THESIS-1993-36, UMI-94-06493.]

- FNAL-SOUDAN (MINOS experiment) 2007 [734 km, $\langle E_\nu \rangle \sim 3$ GeV, $E_\nu \lesssim 120$ GeV]:

$$\delta t = (126 \pm 32\,(\text{stat}) \pm 64\,(\text{syst}))\ \text{ns}\ (68\%\ \text{C.L.}),$$
$$\Downarrow\ (?)$$
$$(v_\nu - 1) = (5.1 \pm 2.8\,(\text{stat}) \pm 0.30\,(\text{syst})) \times 10^{-5}\ (68\%\ \text{C.L.}).$$

The measurement is consistent with the speed of light to less than 1.8σ.
The corresponding 99% confidence limit on the speed of the neutrino is

$$-2.4 \times 10^{-5} < (v_\nu - 1) < 12.6 \times 10^{-5}\ (99\%\ \text{C.L.}).$$

This measurement has implicitly assumed that the m_2 and m_3 neutrino mass eigenstates that comprise the beam are traveling at the same velocity. This assumption is borne out in observing that the arrival times at the far detector match the expectation distribution. Indeed, if the two eigenstates were to travel at velocities differing by as little as $\delta v/v \gtrsim 4 \times 10^{-7}$, the short ~ 1 ns $[\sim 29.4$ cm, VN$]$ bunches would separate in transit and thus decohere, changing or destroying oscillation effects at the far detector.

[P. Adamson *et al.* (MINOS Collaboration), "Measurement of neutrino velocity with the MINOS detectors and NuMI neutrino beam," Phys. Rev. D **76** (2007) 072005.]

A few details:

⋆ MINOS measures the absolute transit time of an ensemble of neutrinos, to < 100 ns accuracy, by comparing ν arrival times at the near detector (ND) and far detector (FD). The distance between front face of the ND and the center of the FD is 734298.6 ± 0.7 m.

⋆ The beam flavor content: $93\%\ \nu_\mu$, $6\%\ \overline{\nu}_\mu$, $1\%\ \nu_e + \overline{\nu}_e$ at ND. After oscillating, the beam at FD is approximately $60\%\ \nu_\mu$.

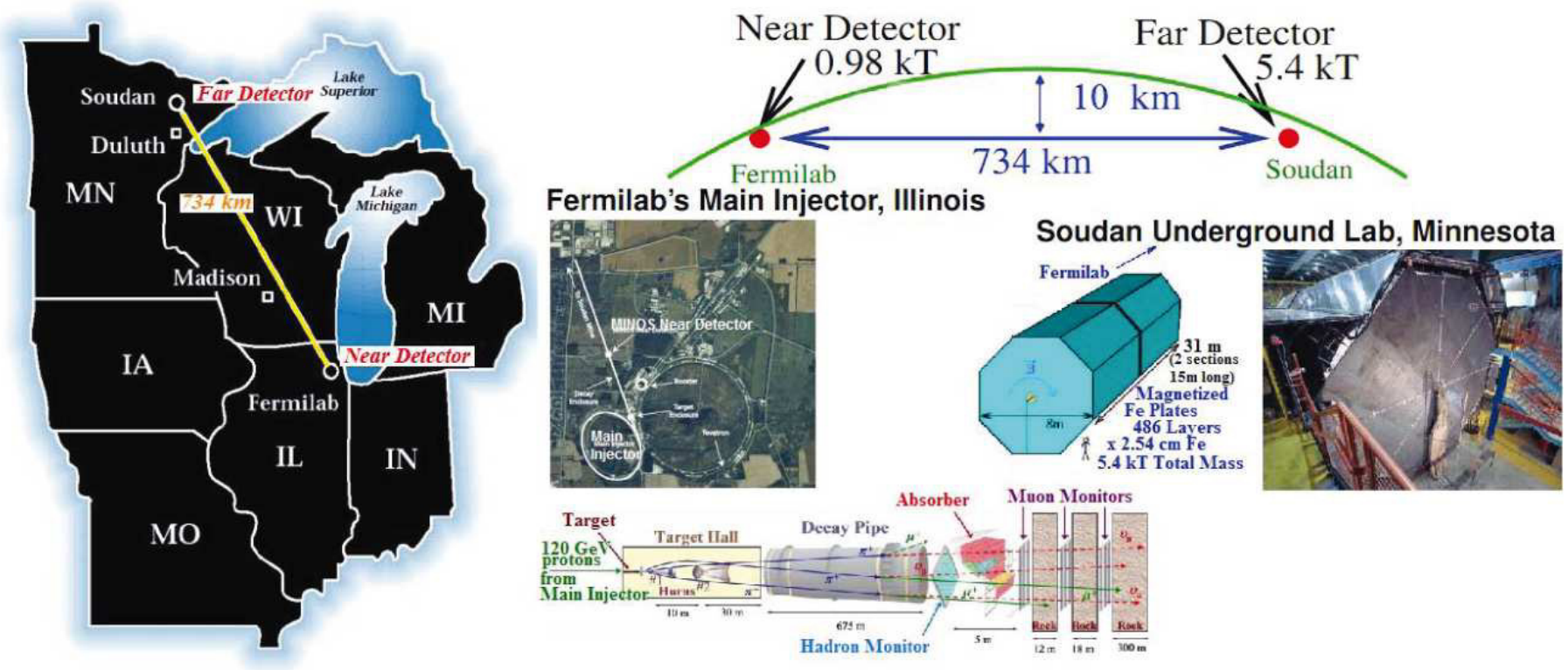

Schematic layout of the MINOS experiment.

[Borrowed from G. Brunetti, "Neutrino velocity measurement with the OPERA experiment in the CNGS beam," Ph.D. thesis, in joint supervision of the Université Claude Bernard, Lyon-I and Universitá degli Studi di Bologna (May 2011), N° d'ordre 88-2011, LYCEN–T 2011-10; URLs: ⟨ http://amsdottorato.cib.unibo.it/3917/ ⟩, ⟨ http://tel.archives-ouvertes.fr/tel-00633424 ⟩.]

- CERN-LNGS (OPERA experiment) 2011 [730 km, $\langle E_\nu \rangle \sim 17$ GeV, $E_\nu \lesssim 350$ GeV]:

$$\delta t = \left(57.8 \pm 7.8\,(\text{stat})\ {}^{+8.3}_{-5.9}\,(\text{syst})\right)\ \text{ns},$$

$$\Downarrow\ (?)$$

$$(v_\nu - 1) = \left(2.37 \pm 0.32\,(\text{stat})\ {}^{+0.34}_{-0.24}\,(\text{syst})\right) \times 10^{-5}.$$

[T. Adam *et al.* (OPERA Collaboration) arXiv:1109.4897v2 [hep-ex] (November 17, 2011).]

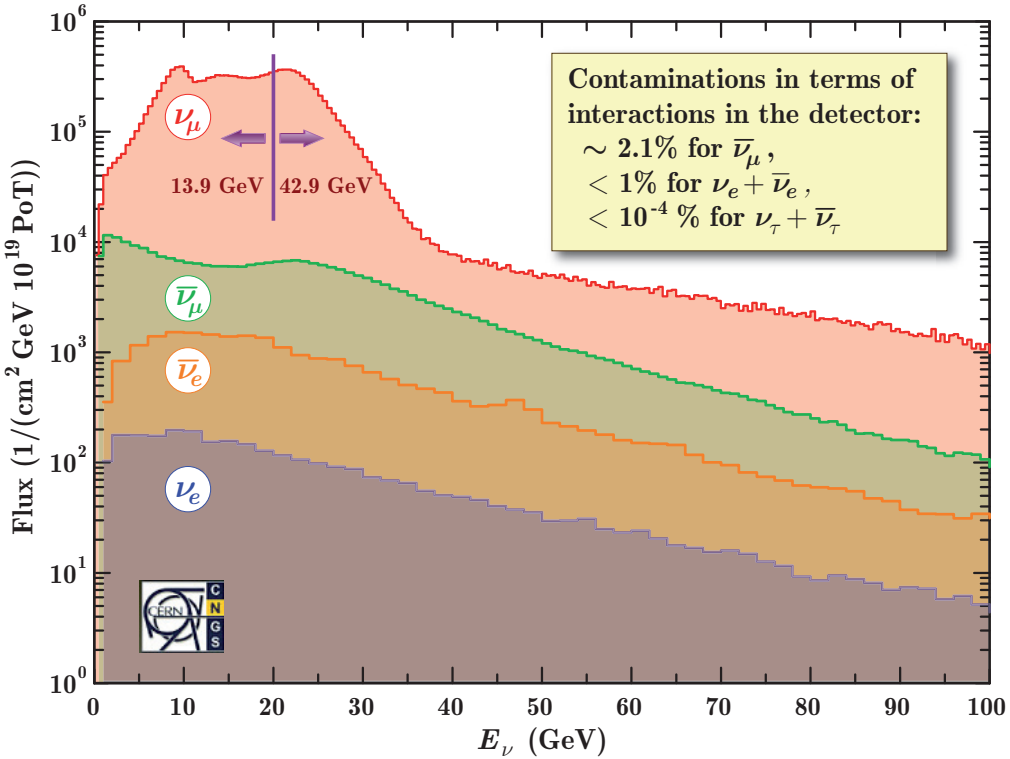

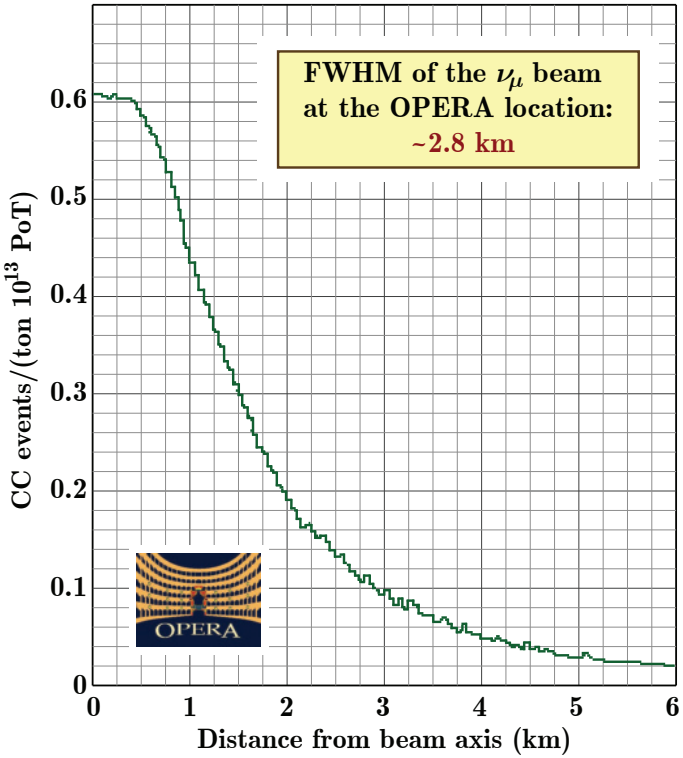

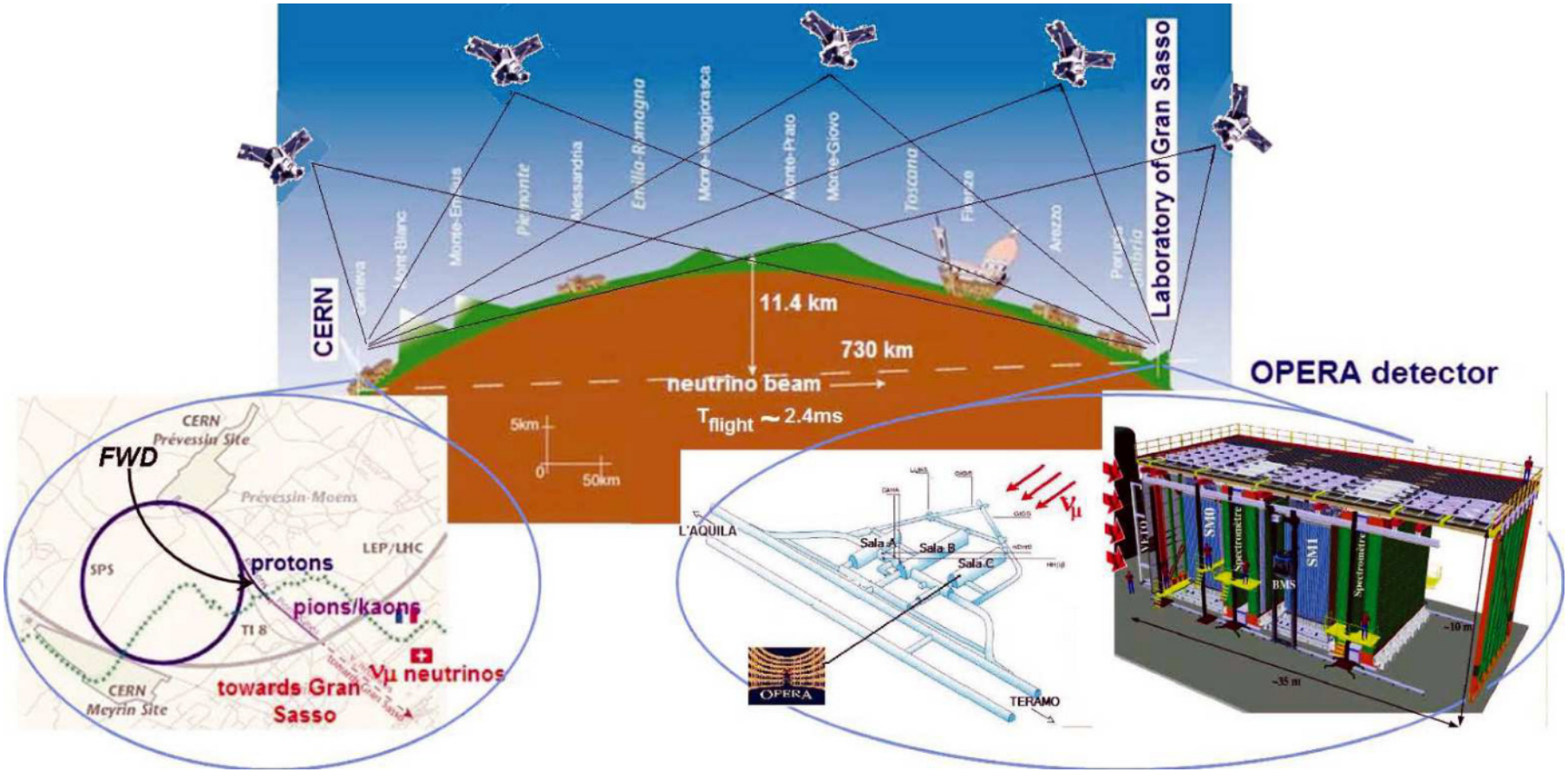

Schematic layout of the OPERA experiment.

[Borrowed from G. Brunetti, "Neutrino velocity measurement with the OPERA experiment in the CNGS beam," PhD thesis, in joint supervision of the Université Claude Bernard, Lyon-I and Universitá degli Studi di Bologna (May 2011), N° d'ordre 88-2011, LYCEN–T 2011-10; URLs: ⟨ http://amsdottorato.cib.unibo.it/3917/ ⟩, ⟨ http://tel.archives-ouvertes.fr/tel-00633424 ⟩.]

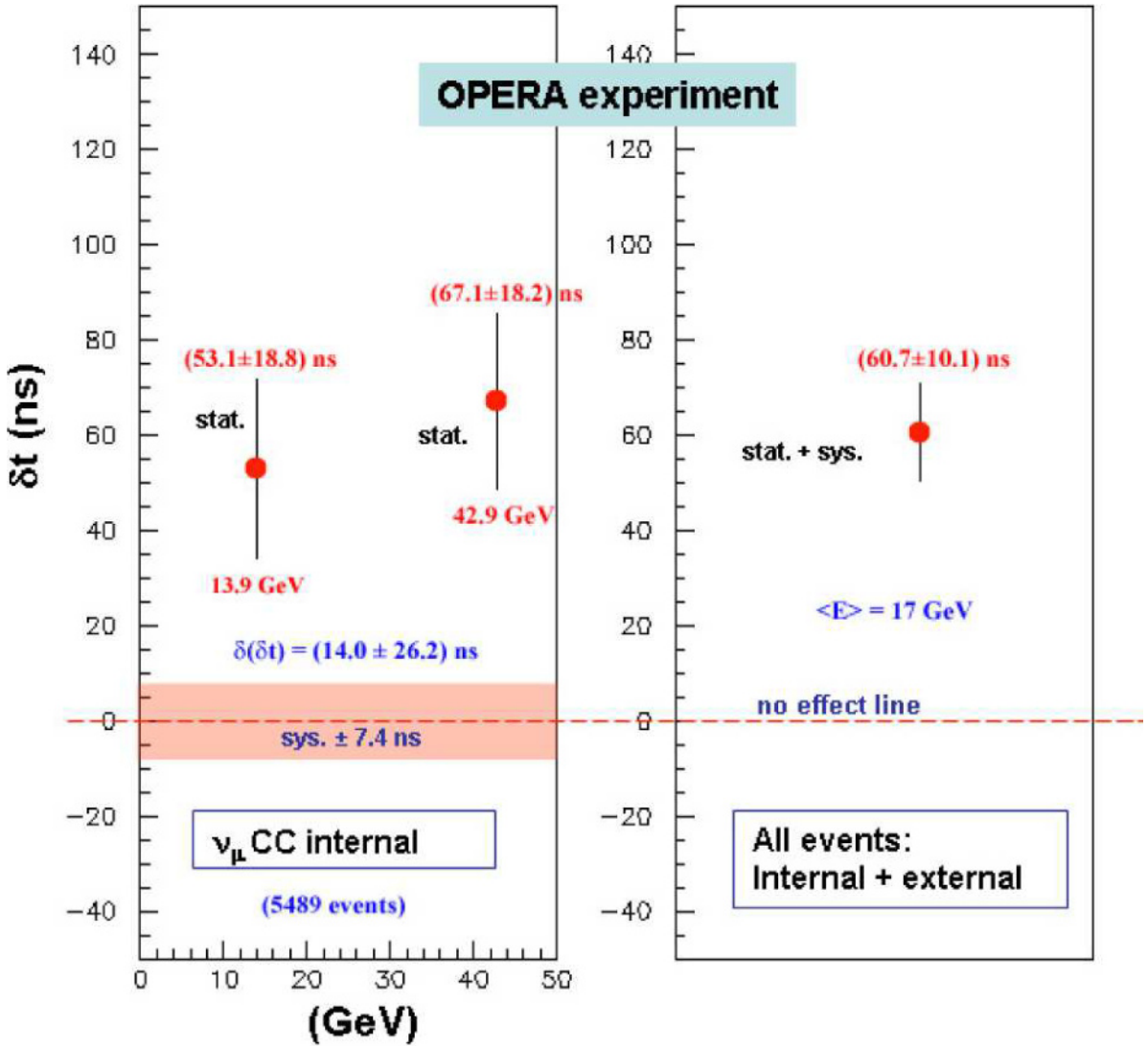

◁ Summary of the results for the measurement of δt.

The *left panel* shows δt vs. neutrino energy for ν_μ CC internal events. The errors attributed to the two points are just statistical in order to make their relative comparison easier since the systematic error (represented by a band around the no-effect line) cancels out.

The *right panel* shows the global result of the analysis including both internal and external events (for the latter the neutrino energy cannot be measured).

The error bar in the *right panel* includes statistical and systematic errors added in quadrature.

The result provides no clues on a possible energy dependence of δt in the domain explored by the OPERA, within the statistical accuracy of the measurement.

39.3 Astrophysical constraint.

The ν burst from SN 1987A (Kamiokande-II, IMB, BUST) [$\approx$ 51 kps, $\langle E_{\overline{\nu}} \rangle \sim 15$ MeV, $E_{\overline{\nu}} \lesssim 40$ MeV] provides the constraint:

$$|v_\nu - 1| < 2 \times 10^{-9}.$$

[K. Hirata *et al.* (Kamiokande-II Collaboration), "Observation of a neutrino burst from the supernovae SN1987A," Phys. Rev. Lett. **58** (1987) 1490–1493; R. M. Bionta *et al.*, "Observation of a neutrino burst in coincidence with supernova 1987A in the Large Magellanic Cloud," Phys. Rev. Lett. **58** (1987) 1494–1496; E. N. Alekseev *et al.*, "Possible detection of a neutrino signal on 23 February 1987 at the Baksan underground scintillation telescope of the Institute of Nuclear Research," Письма в ЖЭТФ **45** (1987) 461–464 [JETP Lett. **45** (1987) 589–592].]

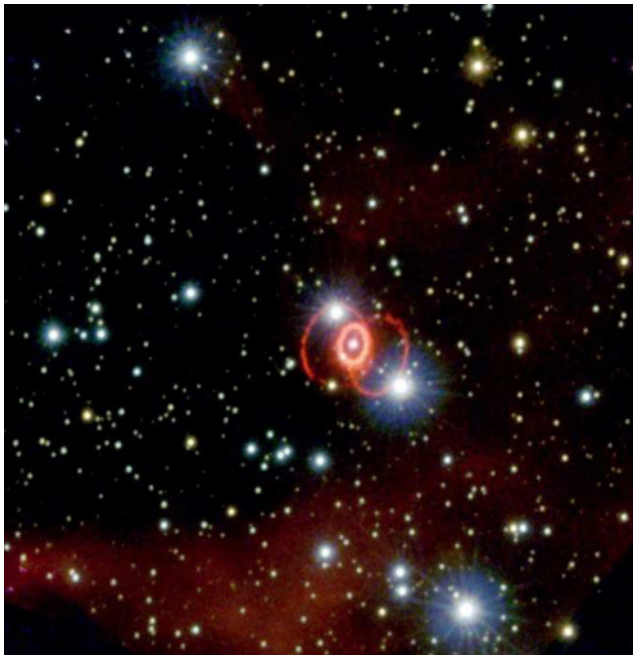

Arguments: [M. J. Longo, "Test of relativity from SN1987A," Phys. Rev. D **36** (1987) 3276–3277.]

The arrival time of the antineutrinos is known to be within a few seconds of 7:35:40 UT on February 23, 1987. The arrival time of the first light from Shelton's SN is less well known. The last confirmed evidence of no optical brightening was at approximately 2:20 UT [I. Shelton, IUA Circular No. 4330,1987]. The earliest observations of optical brightening were at 10:38 UT by Garradd and by McNaught [G. Garradd, IUA Circular No. 4316, 1987; R. H. McNaught, *ibid*].

Standard SN theory expects that the neutrinos and antineutrinos are emitted in the first few second of the collapse, while the optical outburst begins ~ 1 h later, when the cooler envelope is blown away. Altogether this leads to an uncertainty of about 3 h: $|v_\nu - 1|_{\max} \sim 3 \text{ h}/(1.6 \times 10^5 \times 365 \times 24 \text{ h}) \approx 2 \times 10^{-9}$. However Longo's limit is generally not robust.

39.4 A possible explanation (excluded).

This section is excluded from the lectures[a] because the "anomaly" turned out to be an experimental artifact (see Part "Neutrino Chronicles," after 2011, (p. 58). However, who knows if future experiments will resuscitate the problem.

In February 2012, the OPERA collaboration announced two possible sources of error that could have significantly influenced the results. A link from a GPS receiver to the OPERA master clock was loose, which increased the delay through the fiber. The glitch's effect was to decrease the reported flight time of the neutrinos by 73 ns, making them seem faster than light. A clock on an electronic board ticked faster than its expected 10 MHz frequency, lengthening the reported flight-time of neutrinos, thereby somewhat reducing the seeming faster-than-light effect. OPERA stated the component had been operating outside its specifications.
In March 2012 an LNGS seminar was held, confirming the fiber cable was not fully screwed in during data gathering. LVD researchers compared the timing data for cosmic high-energy muons hitting both the OPERA and the nearby LVD detector between 2007–2008, 2008–2011, and 2011–2012. The shift obtained for the 2008–2011 period agreed with the OPERA anomaly. The researchers also found photographs showing the cable had been loose by October 13, 2011. Correcting for the two newly found sources of error, results for neutrino speed appear to be consistent with the speed of light.

[a] However, those who are interested can take a look at eprint D. V. Naumov & VN, "Neutrino velocity anomalies: A resolution without a revolution," arXiv:1110.0989 [hep-ph] (unpublished).

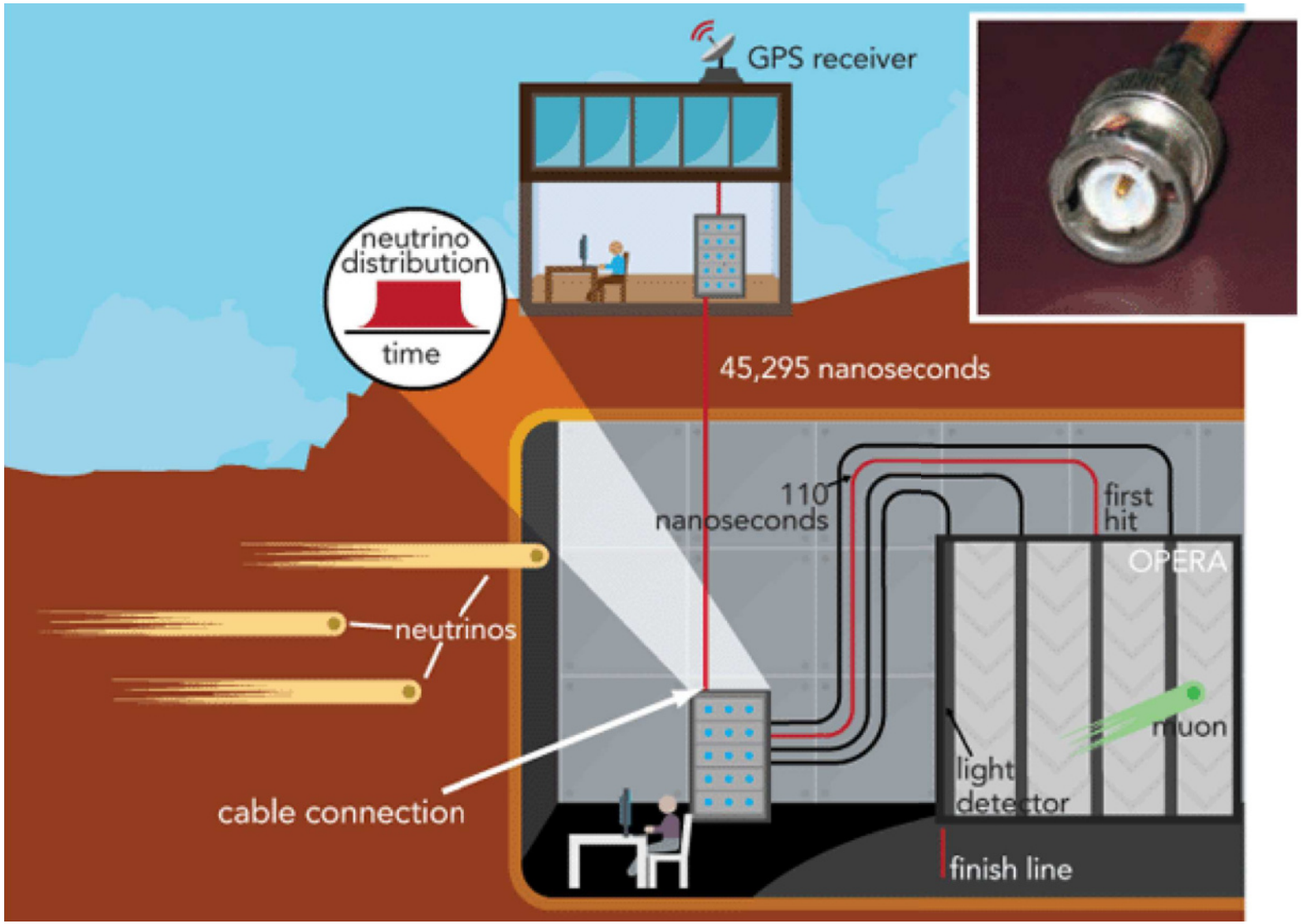

A loose plug (like the one shown) in OPERA's detector may have skewed neutrino measurements by tens of nanoseconds.

[From E. Cartlidge, "Loose cable may unravel faster-than-light result," Science **335**, Iss. 6072 (2012) 1027.]

40 GSI anomaly.

Here we'll briefly review the following papers:[a]

Experiment

[1] Yu. A. Litvinov *et al.*, "Measurement of the β^+ and orbital electron-capture decay rates in fully-ionized, Hydrogen-like, and Helium-like ^{140}Pr ions," Phys. Rev. Lett. **99**, 262501 (2007), arXiv:0711.3709 [nucl-ex].

[2] Yu. A. Litvinov *et al.*, "Observation of non-exponential orbital electron capture decays of Hydrogen-Like ^{140}Pr and ^{142}Pm ions," arXiv:0801.2079 [nucl-ex].

Theory

[3] H. J. Lipkin, "New method for studying neutrino mixing and mass differences," arXiv:0801.1465 [hep-ph].

[4] A. N. Ivanov, R. Reda & P. Kienle, *"On the time-modulation of the K-shell electron capture decay of H-like $^{140}\mathrm{Pr}^{58+}$ ions produced by neutrino–flavour mixing,"* arXiv:0801.2121 [nucl-th].

[5] M. Faber, "Kinematics and quantum field theory of the neutrino oscillations observed in the time-modulated orbital electron capture decay in an ion storage ring," arXiv:0801.3262 [nucl-th].

[6] C. Giunti, "Comment on the neutrino-mixing interpretation of the GSI time anomaly," arXiv:0801.4639 [hep-ph].

[7] H. J. Lipkin, "Simple quantum mechanics explains GSI Darmstadt oscillations even with undetected neutrino; Momentum conservation requires; Same interference producing oscillations in initial and final states," arXiv:1003.4023 [hep-ph].

[a] For a more detailed bibliography on the GSI anomaly, see pp. 993–994.

40.1 Sketch of GSI facilities.

The **G**esellschaft für **S**chwer**I**onenforschung mbH (Institute for Heavy Ion Research) in the Arheilgen suburb of Darmstadt is a federally and state co-funded center.[a] GSI performs basic and applied research in physics and related natural science disciplines.

Main fields of study

- plasma physics
- atomic physics
- nuclear reactions
- nuclear structure
- biophysics research
- medical research

[a] URL: ⟨http://www.gsi.de/⟩.

The elements discovered at GSI:

✓	Bohrium	$^{[270]}_{107}$Bh	(1981)
✓	Hassium	$^{[269]}_{108}$Hs	(1984)
	Meitnerium	$^{[270]}_{109}$Mt	(1982)
✓	Darmstadtium	$^{[281]}_{110}$Ds	(1994)
✓	Roentgenium	$^{[280]}_{111}$Rg	(1994)
	Ununbium	$^{[285]}_{112}$Uub	(1996)

First experiments to synthesize 4 of these 6 elements were performed at JINR (marked).

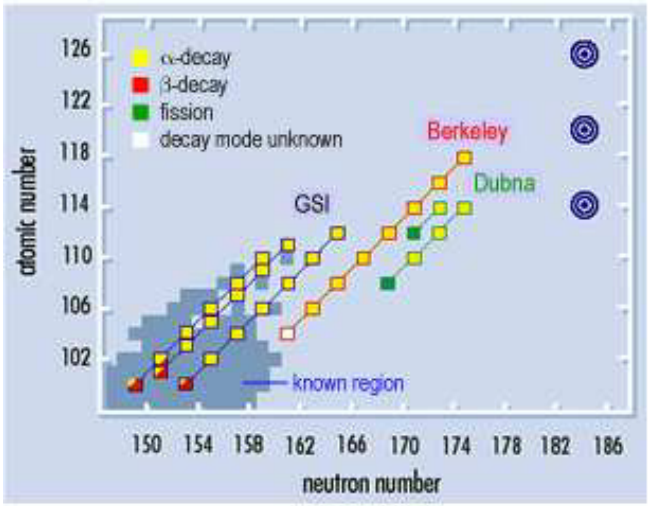

Decay chains of the elements 110, 111, and 112 produced at GSI together with the new Berkeley and Dubna data.

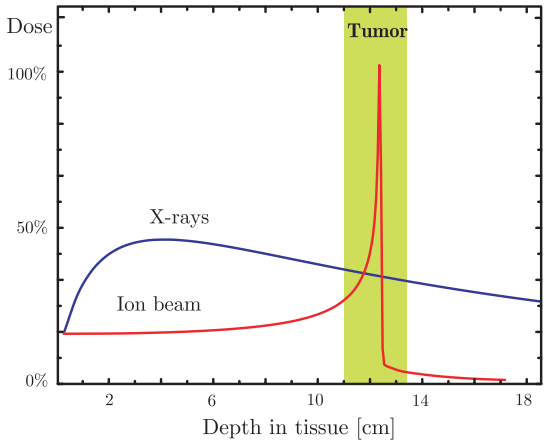

Another important discovery done at the GSI is the application of heavy ion beams for cancer treatment (from 1997). In stead of using X-rays, carbon ions are used to irradiate the patient. The technique allows tumors which are close to vital organs to be treated, which is not possible with X-rays. This is due to the fact that the Bragg peak of carbon ions is much sharper than the peak of X-ray photons.

The chief tool is the heavy ion accelerator facility consisting of

- **UNILAC**, the Universal Linear Accelerator (kinetic energy of 2–20 MeV per nucleon),
- **SIS 18**, the heavy-ion synchrotron (1–2 GeV/u),
- **ESR**, the Experimental Storage-cooler Ring (0.5–1.0 GeV/u), and
- **FRS**, the in-flight Fragment Separator.

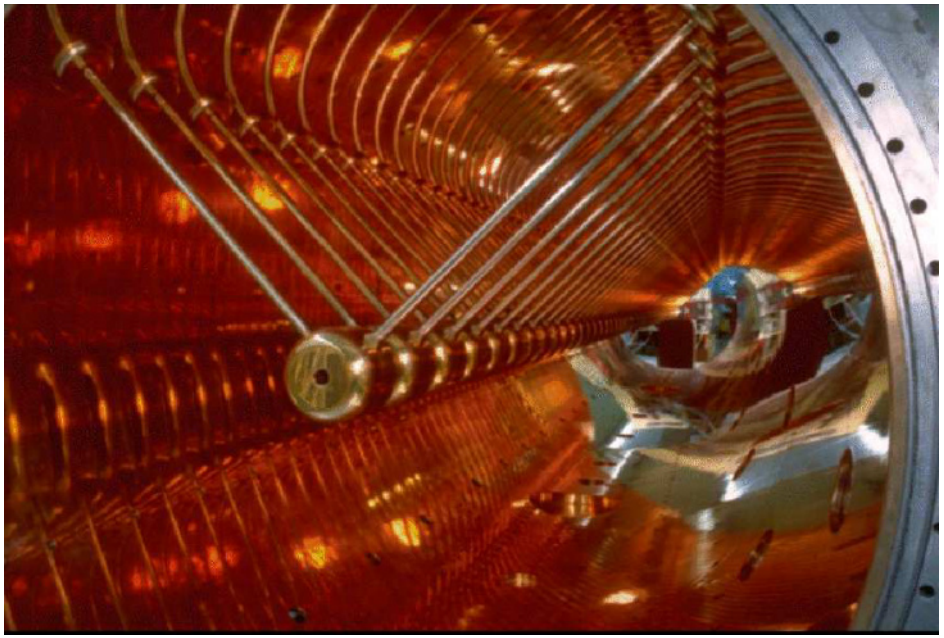

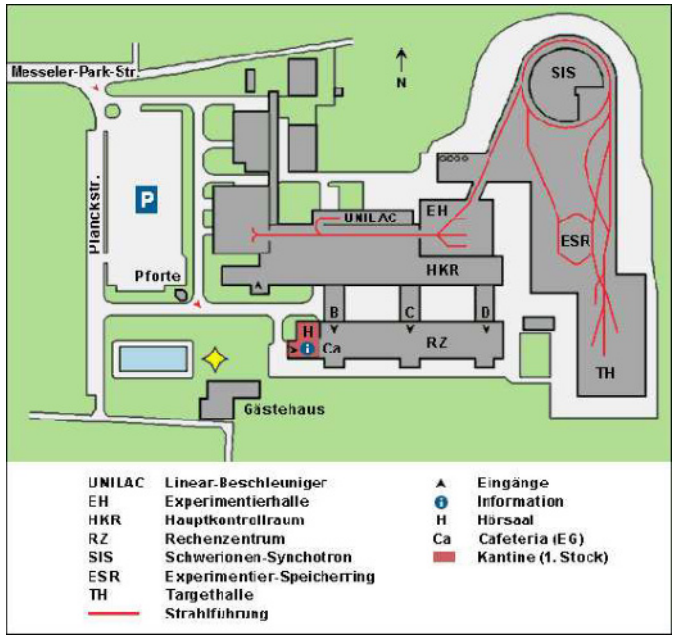

The UNILAC was commissioned in 1975, the SIS 18 and the ESR were added in 1990 boosting the ion acceleration from 10% of light speed to 90%.

Storage rings are used to accumulate ions up to the highest possible currents. A high brilliance of the circulating ion beams, which means very small diameters and angular divergences and an extremely small velocity distribution is obtained and preserved by applying special techniques like *electron*, *stochastic*, or *laser* cooling.

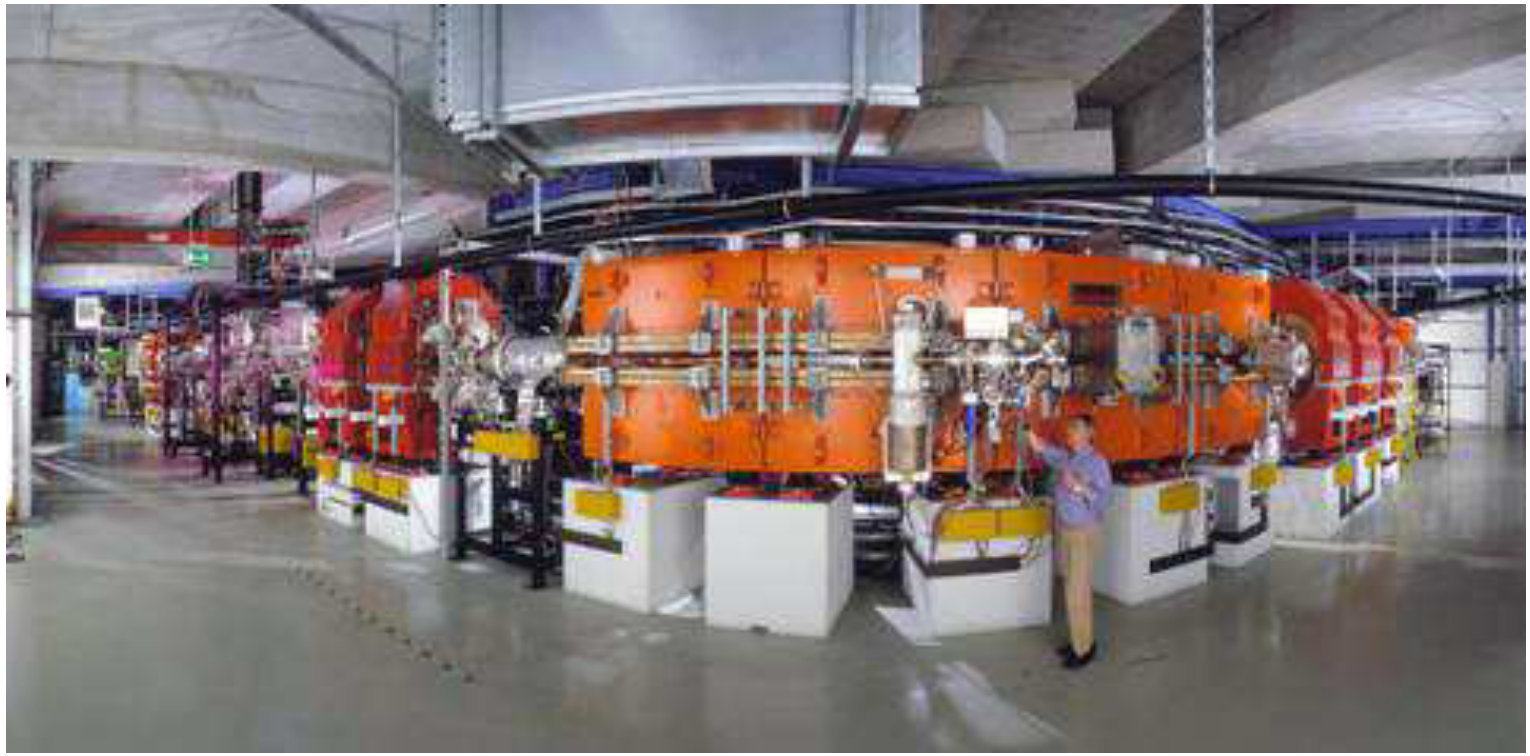

The ESR is worldwide the only storage ring which fulfills these requirements for all ions from Helium ($Z = 2$) up to even bare uranium with ($Z = 92$) at ion velocities $v = (0.1 - 0.9)c$. Therefore, the ESR provides unique possibilities especially for experiments with the heaviest available ions.

The ESR has a circumference of 108.36 m and a magnetic rigidity of 10 T m.

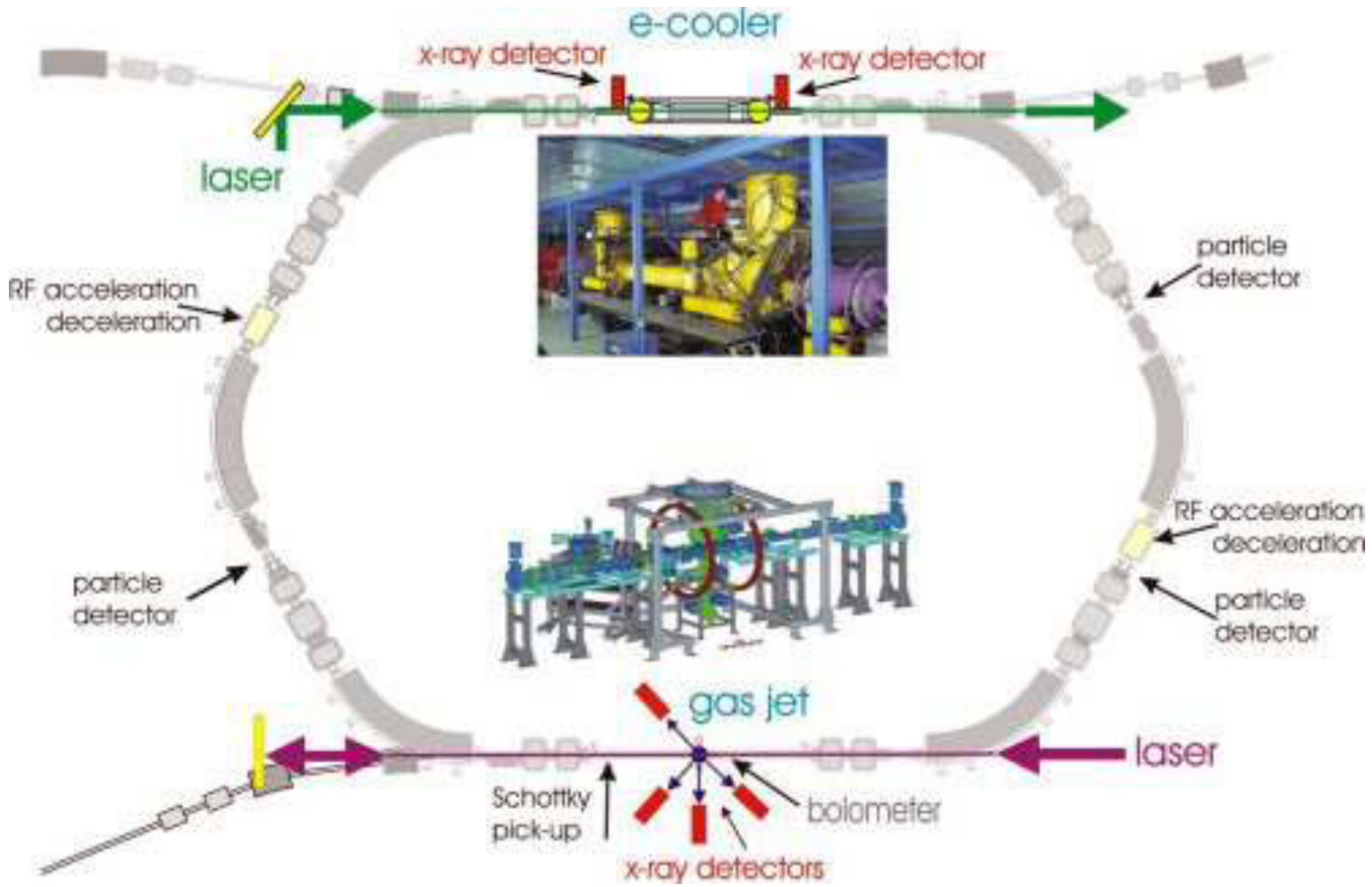

The ultrahigh vacuum inside the ring of about 10^{-11} Torr is essential for keeping the number of collisions between the stored ions and the atoms of the rest gas as small as possible. Such collisions could change the charge state of the ions and lead to drastic intensity losses of the stored beams.

Таблица 2: Beam properties.

Particle energy	3 – 560 MeV/u for U
	3 – 830 MeV/u for Ne
Energy definition	$\sim 10^{-4}$ with e-cooling
Cycle length	field ramp 1.5 s
Storage time	minutes to hours
Fast extraction	~ 0.5 μs
Slow extraction	to some 10 s
Beam emittance	0.1π mm $\cdot$ mrad
	with e-cooling
Part. number/cycle	typically 10^8 with cool.

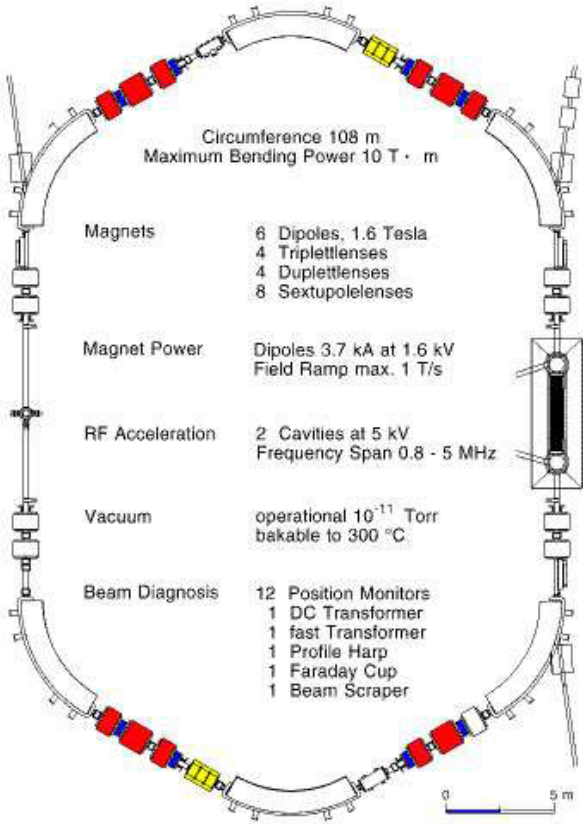





40.2 Measurement of the β^+ and orbital EC decay rates in H-like and He-like ^{140}Pr ions.

In the experiment [1], it has been selected the praseodymium nucleus

$$\boxed{^{140}\text{Pr}} \qquad (Z = 59, \quad A_r = 140.90765(2)\ \text{u} \approx 131.25463\ \text{GeV}/c^2).$$

The neutral atom decays with 99.4% to the ground state of cerium

$$\boxed{^{140}\text{Ce}} \qquad (Z = 58, \quad A_r = 140.116(1)\ \text{u} \approx 130.517\ \text{GeV}/c^2)$$

via a pure Gamow-Teller β decay with a change of the nuclear angular momentum by one unit $\Delta I = 1$ and no parity change ($1^+ \to 0^+$ transition).

A proton in ^{140}Pr can be converted into a neutron by a weak decay in two ways:

- either via the electron capture decay (whereby a "monochromatic" ν_e is emitted)

$$p + e^- \to n + \nu_e \qquad (\varepsilon)$$

- or via a three-body β^+ decay in which the e^+ and the ν_e share the decay energy

$$p \to e^+ + n + \nu_e \qquad (\beta^+).$$

Memento:

Beta plus decay or Positron emission (β^+):

$$(Z, A) \to (Z-1, A) + e^+ + \nu_e \qquad \text{(e.g., } {}^{11}\text{C} \to {}^{11}\text{B} + e^+ + \nu_e\text{)}.$$

(Only allowed when $M(Z, A) > M(Z-1, A) + m_e + m_\nu$).

Example of isotopes which undergo β^+ decay are
carbon-11, potassium-40, nitrogen-13, oxygen-15, fluorine-18, iodine-121.

Electron capture or Inverse Beta Decay (ε)

is a decay mode for isotopes that will occur when there are too many protons in the nucleus of an atom or ion and insufficient energy to emit a positron:

$$(Z, A) + e^- \to (Z-1, A) + \nu_e \qquad \text{(e.g., } {}^{40}_{19}\text{K} + e^- \to {}^{40}_{18}\text{Ar} + \nu_e\text{)}.$$

However, it continues to be a viable decay mode for radioactive isotopes that can decay by β^+ mode. If the energy difference between the parent atom and the daughter atom is less than 1.022 MeV, β^+ decay is forbidden and e-capture is the sole decay mode.

Most probable are K-electron capture (also K-capture) or L-electron capture (L-capture).
In general, the atom/ion moves into an excited state with the inner shell missing an electron. When transiting to the ground state, the atom/ion will emit an X-ray γ.

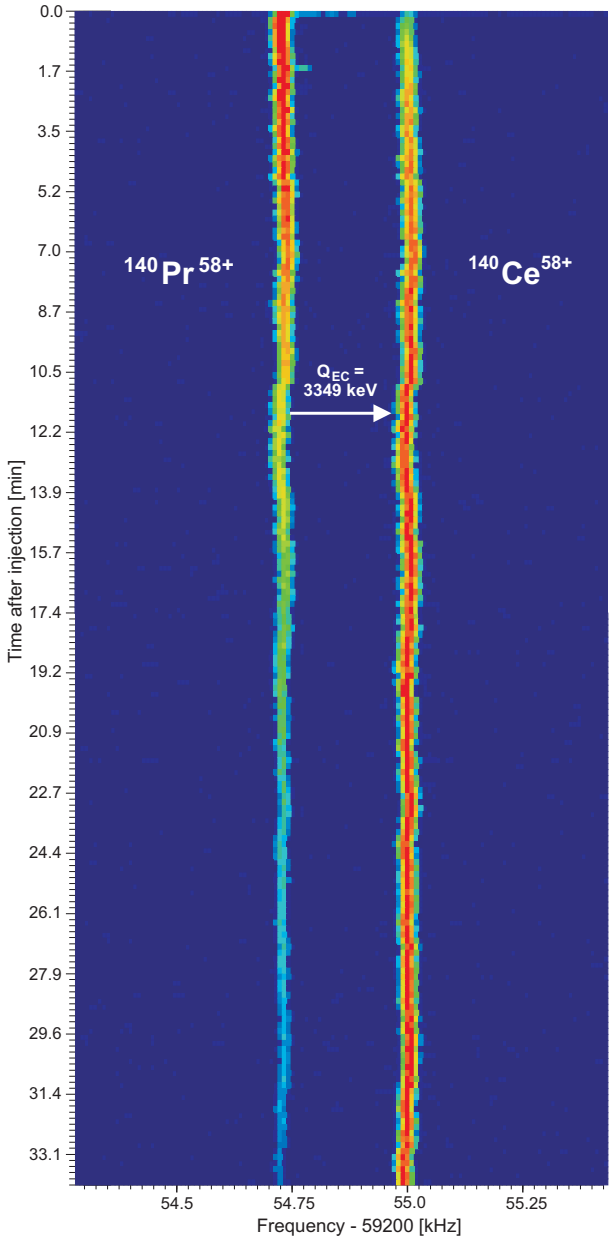

Radioactive ^{140}Pr ions have been produced via the projectile fragmentation of samarium ^{152}Sm accelerated by the SIS to 508 MeV/u. The ions were separated in-flight in the FRS and subsequently injected into the ESR.
Stochastic pre-cooling (to 400 MeV/u) and electron cooling were applied to the ^{140}Pr^{59+}, ^{140}Pr^{58+} and ^{140}Pr^{57+} ions coasting in the ESR.
The cooling forces all stored ions to the same mean velocity and reduces the initial velocity spread, caused by the fragmentation reaction, to $\delta v/v \approx 5 \times 10^{-7}$.

Schottky frequency spectra at the 31st harmonics of the revolution frequency taken subsequently as a function of time. In the ε decay of H-like ^{140}Pr, the mass changes by $Q_\varepsilon = 3.349$ MeV/c^2 which leads to a small change in the frequency (270 Hz). The intensity of the frequency lines is proportional to the number of stored ions.
It can be seen that the intensity of the line corresponding to the parent ions ^{140}Pr^{58+} decreases in the course of time and that the intensity of the line corresponding to the daughter ions ^{140}Ce^{58+}increases.

Decay curves of the parent ions have been fitted with an exponential function:

$$N_{\mathrm{Pr}}(t) = N_{\mathrm{Pr}}(0) \cdot e^{-\lambda t}. \tag{174}$$

- For H-like and He-like ^{140}Pr ions, $\lambda = \lambda_{\varepsilon} + \lambda_{\beta+} + \lambda_{\mathrm{loss}}$.
- The bare $^{140}\mathrm{Pr}^{59+}$ nuclei can only decay via the β^+-decay mode $\Longrightarrow \lambda = \lambda_{\beta+} + \lambda_{\mathrm{loss}}$.
- The growth of the number of daughter ions from the ε decay of $^{140}\mathrm{Pr}^{58+} \rightarrow {}^{140}\mathrm{Ce}^{58+}$ and $^{140}\mathrm{Pr}^{57+} \rightarrow {}^{140}\mathrm{Ce}^{57+}$ is determined solely by the ε rate of ^{140}Pr λ_{ε}, whereas the loss of stable ^{140}Ce ions is determined only by λ_{loss}.

Therefore, one can fit the number of ^{140}Ce daughters as a function of time t by using:

$$N_{\mathrm{Ce}}(t) = N_{\mathrm{Pr}}(0)\frac{\lambda_{\varepsilon}}{\lambda - \lambda_{\mathrm{loss}}}\left(e^{-\lambda_{\mathrm{loss}} t} - e^{-\lambda t}\right) + N_{\mathrm{Ce}}(0)e^{-\lambda_{\mathrm{loss}} t} \tag{175}$$

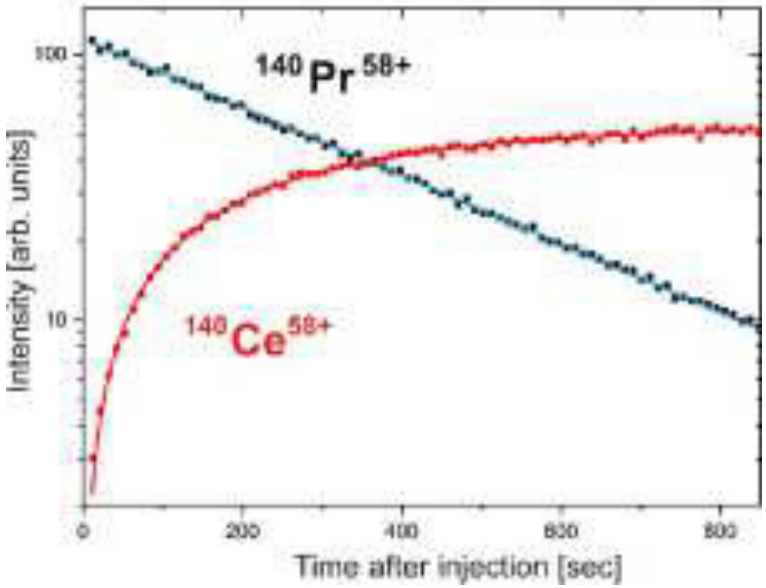

An example: the decay and growth curves of $^{140}\mathrm{Pr}^{58+}$ and $^{140}\mathrm{Ce}^{58+}$ ions as a function of time after injection. The data points are shown in the laboratory frame and can be converted to the rest-frame of the ions using the Lorentz factor $\gamma = 1.43$.
The lines represent the best fits according to Eqs. (174) and (175).

The mean loss constant has been determined to be $\lambda_{\text{loss}} = 0.0003(1)\ \text{s}^{-1}$, which is within the error bars the same for the studied charge states of ^{140}Ce and ^{140}Pr.

Таблица 3: Measured β^+ and ε decay constants obtained for H-like, and He-like ^{140}Pr ions. The quoted values are given in the rest frame of the ions.

Ion	λ_{β^+} (1/s)	λ_{ε} (1/s)
$^{140}Pr^{59+}$	0.00158(8)	—
$^{140}Pr^{58+}$	0.00161(10)	0.00219(6)
$^{140}Pr^{57+}$	0.00154(11)	0.00147(7)

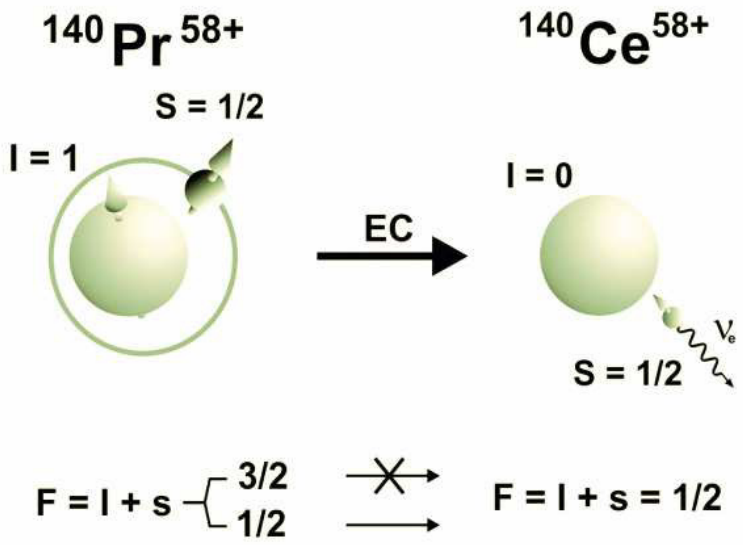

- The measured β^+ decay rate is within the errors independent on the degree of ionization. [This is expected, since the electron screening modifies the β^+ rate by less than 3% in fully-ionized ions compared to neutral atoms.]
- The striking result is–in spite of the fact that the number of orbital electrons is reduced from two in $^{140}Pr^{57+}$ ions to only one in $^{140}Pr^{58+}$ ions – that the ε rate increases by a factor of 1.49(8).
- Moreover, the half-lifes $T_{1/2} = \ln(2)/\lambda$ are different for neutral atoms and ions:

$$T_{1/2}\left(^{140}Pr^{0+}\right) = 3.04(9)\ \text{min}, \quad \text{while} \quad T_{1/2}\left(^{140}Pr^{58+}\right) = 3.39(1)\ \text{min}.$$

The K-shell ε to β^+ decay ratio $\lambda_\varepsilon/\lambda_{\beta+}$ for neutral atom $^{140}Pr^{0+}$ and ions $^{140}Pr^{58+}$ and $^{140}Pr^{57+}$. Comparison of measurements and theoretical predictions.

EXPERIMENT			THEORY		
$^{140}Pr^{0+} \rightarrow {}^{140}Ce^{0+}$					
Biryukov & Shimanskaya	(1960)	0.76(?)			
Biryukov & Shimanskaya	(1962,1970)	0.74(3)			
Evans *et al.*	(1972)	0.90(8)			
Campbell *et al.*	(1977)	0.73(3)	Bambynek *et al.* [b]	(1977)	0.85(1)
$^{140}Pr^{57+} \rightarrow {}^{140}Ce^{57+}$					
Litvinov *et al.* [a]	(2007)	1.36(9)	Ivanov *et al.* [c]	(2007)	1.40(4)
$^{140}Pr^{58+} \rightarrow {}^{140}Ce^{58+}$					
Litvinov *et al.* [a]	(2007)	0.95(8)	Ivanov *et al.* [c]	(2007)	0.94(3)

[a] Yu. A. Litvinov *et al.*, "Measurement of the β^+ and orbital electron-capture decay rates in fully-ionized, Hydrogen-like, and Helium-like ^{140}Pr ions," Phys. Rev. Lett. **99** (2007) 262501, arXiv:0711.3709 [nucl-ex].

[b] W. Bambynek *et al.*, "Orbital electron capture by the nucleus," Rev. Mod. Phys. **49** (1977) 77.

[c] A. N. Ivanov, M. Faber, R. Reda & P. Kienle, "Weak decays of H-like $^{140}Pr^{58+}$ and He-like $^{140}Pr^{57+}$ ions," Phys. Rev. C **78** (2008) 025503, arXiv:0711.3184 [nucl-th].

40.3 Non-exponential orbital EC decays.

Ref. [2] reports the results of the first experiments which used time-resolved single-particle decay spectroscopy for studying the time evolution of two-body weak decays, i.e. EC and β_b^+-decays of radioactive ions in the ESR.

The physics motivation was the question:

whether or not the electron neutrinos generated in such decays as coherent superposition of mass eigenstates would affect the exponential decay.

H-like praseodymium ^{140}Pr ($Z = 59$) and promethium ^{142}Pm ($Z = 61$) ions have been selected for these studies.

This choice has many advantages (see next slide).

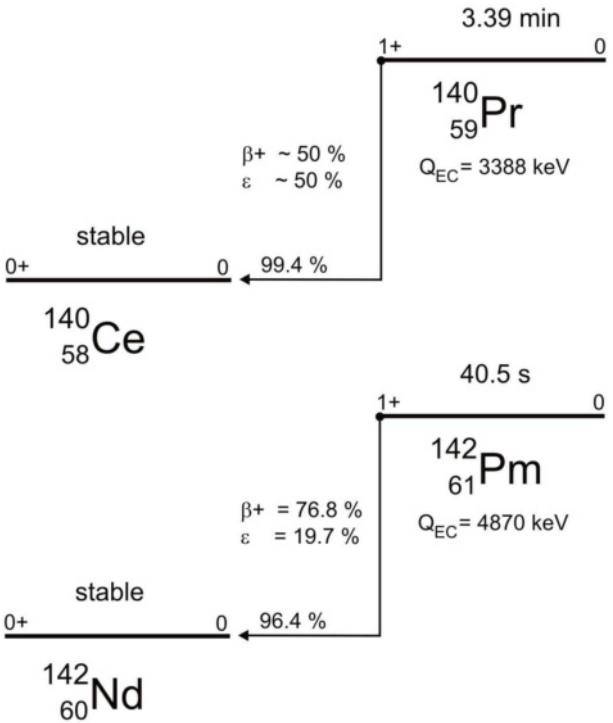

Decay schemes of neutral $^{140}_{59}$Pr (*top panel*) and $^{142}_{61}$Pm (*bottom panel*) atoms. The final state cerium and neodymium atoms are stable.

- Both nuclei decay to stable daughter nuclei via either the three-body positron emission (β^+ mode) or the two-body ε-decay.
- Both systems decay mainly by a single allowed Gamow-Teller ($1^+ \to 0^+$) transition.
- The weak transitions to excited states can be safely neglected in the present context.

- These nuclides have quite different decay energies (Q_ε values) and lifetimes, thus allowing a detailed comparison of their time evolutions.
- Both Q_ε-values are sufficiently large to be easily resolved by SMS.
- Furthermore, their half-lives are much larger than the time needed for the preparation of the ions.

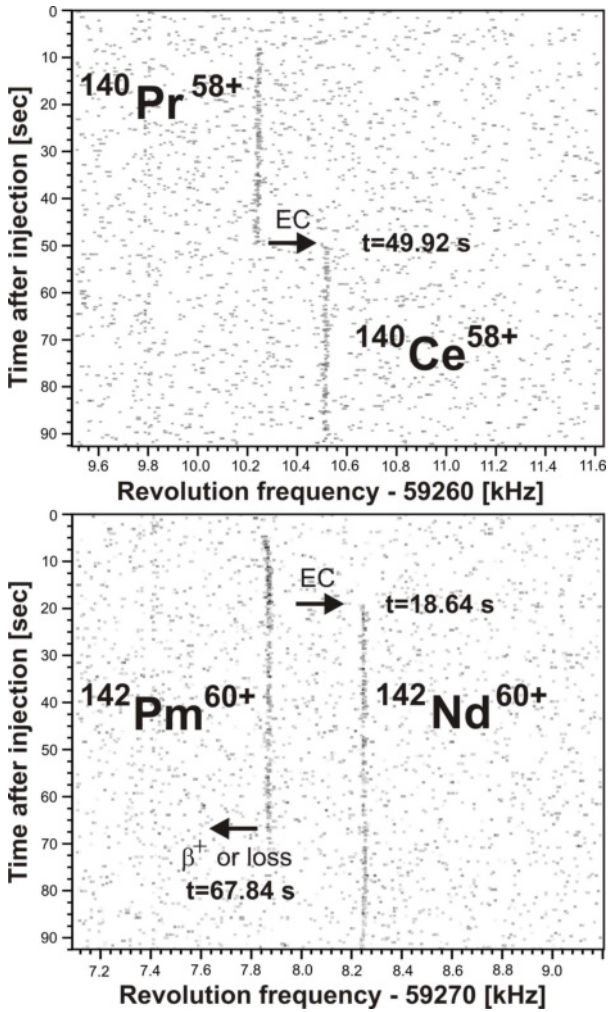

The figure illustrates two out of many thousand runs.
Top panel: a series of consecutive frequency spectra of a single parent ^{140}Pr^{58+} ion decaying to the daughter ^{140}Ce^{58+} ion 49.92 s after the injection into the ESR.
Left panel: two injected ^{142}Pm^{60+} ions decay 18.64 s and 67.84 s after the injection. The first ion decays by EC to a ^{142}Nd^{60+} ion. The second ion decays by β^+-decay or is lost due to atomic charge exchange reactions. The frequency differences between parent and daughter ions correspond to $Q_\varepsilon(^{140}\text{Pr}^{58+}) = 3.35$ MeV and $Q_\varepsilon(^{140}\text{Pr}^{58+}) = 4.83$ MeV.

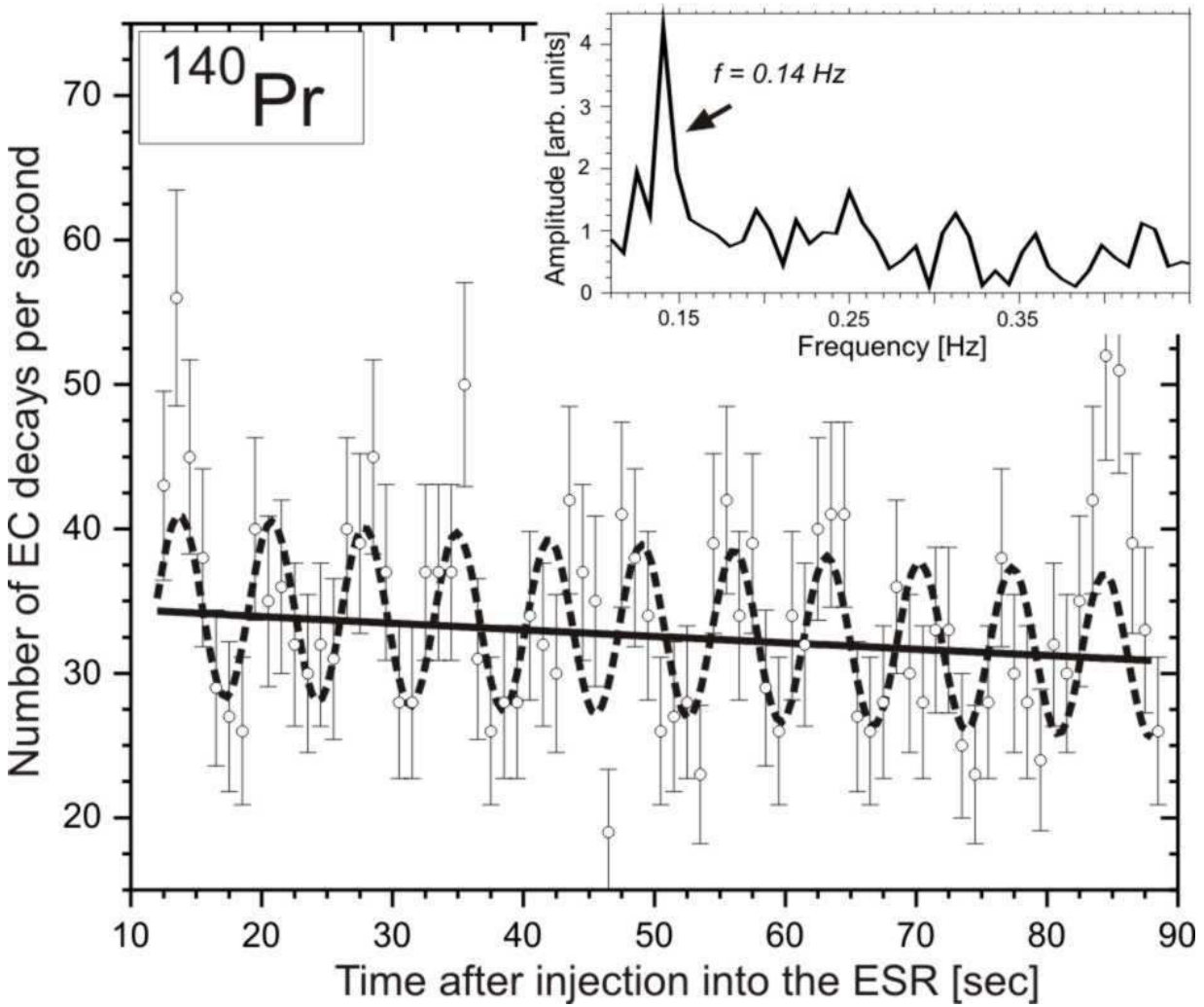

Number of EC-decays of H-like ^{140}Pr ions per second as a function of the time after the injection into the ring. The solid and dashed lines represent the fits according to Eq. (176) (without modulation) and Eq. (177) (with modulation), respectively. The inset shows the Fast Fourier Transform of the data. A clear frequency signal is observed at 0.14 Hz (lab frame).

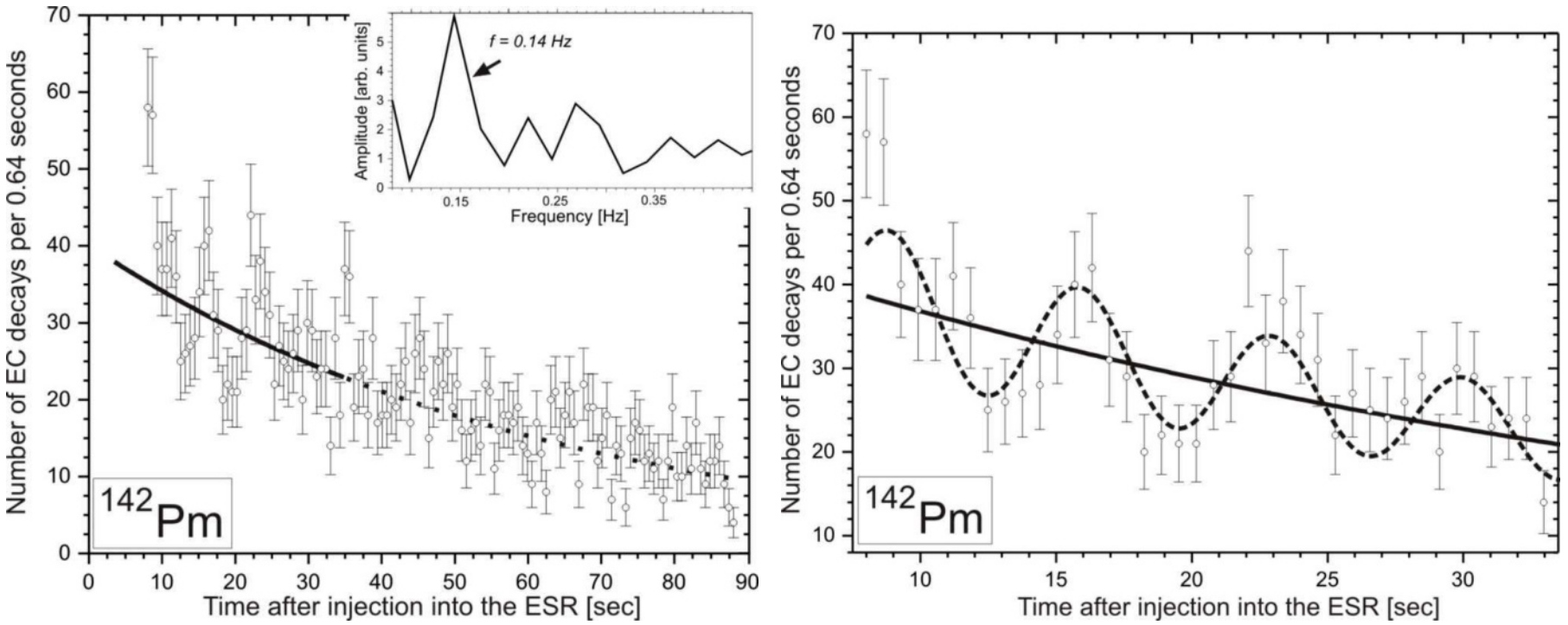

Left panel: Number of EC-decays of H-like ^{142}Pm ions per 0.64 seconds as a function of the time after the injection into the ring. The solid line represents the exponential decay fit according to Eq. (176) until 33 s after injection (continued as a dotted line). The inset shows the Fast Fourier Transform spectrum obtained from the data until 33 s. The reduced resolution compared to the figure in previous slide is explained by a smaller number of points used for the FFT. A clear FFT peak is observed at about 0.14 Hz (laboratory frame).

Right panel: A zoom to the first 33 sec after injection of the data presented the *left panel*. The solid line represents the exponential decay fit according to Eq. (176). The dashed line shows the fit according to Eq. (177).

The data were fitted with the exponential decay function:

$$\frac{dN_\varepsilon(t)}{dt} = N(0)\lambda_\varepsilon e^{-\lambda t}, \tag{176}$$

where $N(0)$ is the number of parent ions at the time $t = 0$ (the time of injection) and

$$\lambda = \lambda_\varepsilon + \lambda_{\beta+} + \lambda_{\text{loss}}.$$

The ratio of $\lambda_\varepsilon/\lambda_{\beta+}$ is 0.95(8) for the H-like ^{140}Pr and is expected to be about 0.32 for the H-like ^{142}Pm.

It is clear to see from the data that the expected exponential decrease of the EC-decays as a function of time shows a superimposed *periodic time modulation*. To account for this modulation the data were fitted with the function:

$$\frac{dN_\varepsilon(t)}{dt} = N(0)e^{-\lambda t}\lambda_\varepsilon[1 + a\cos(\omega t + \phi)] \tag{177}$$

with an amplitude a, an angular frequency ω, and a phase ϕ of the modulation. For the case of ^{142}Pm ions only the first 33 seconds after the injection were fitted with Eq. (177) due to the short half-life of the mother nuclei and, thus, the fast damping of the modulation amplitude.

The fits were done with the MINUIT package using the χ^2 minimization and the maximum likelihood methods which yielded consistent results.

The fit parameters obtained for ^{140}Pr and ^{142}Pm EC-decay data illustrated in figures. The fits are done according to Eq. (176) and Eq. (177) which is indicated in the first column. The corresponding χ^2/DoF are given in the last column.

Fit parameters of ^{140}Pr data

Eq.	$N_0\lambda_\varepsilon$	λ	a	ω	χ^2/DoF
(176)	34.9(18)	0.00138(10)	–	–	107.2/73
(177)	35.4(18)	0.00147(10)	0.18(3)	0.89(1)	67.18/70

Fit parameters of ^{142}Pm data

Eq.	$N_0\lambda_\varepsilon$	λ	a	ω	χ^2/DoF
(176)	46.8(40)	0.0240(42)	–	–	63.77/38
(177)	46.0(39)	0.0224(41)	0.23(4)	0.89(3)	31.82/35

From the angular frequency ω one can extract the periods of the modulation:

$$T(^{140}\text{Pr}) = 7.06(8)\ \text{s} \quad \text{and} \quad T(^{142}\text{Pm}) = 7.10(22)\ \text{s} \quad \text{(lab. frame)}$$

The amplitudes a agree within the error bars. The average value is $\langle a \rangle = 0.20(2)$.

The observed periodic modulations of the expected exponential decrease of the number of EC-decays per time unit still suffer from restricted statistics.

However, the "zero hypothesis" of a pure exponential decay can be already rejected according to the χ^2/DoF-values on the 99% C.L. (one-sided probabilities $p = 0.006$) for both investigated nuclear systems.

Explanations/Questions	**Objections**
1. Finding of nearly the same oscillation period of about 7 sec might suggest a technical artefact as their common origin, such as periodic instabilities in the storage ring or of the recording systems.	The complete and uninterrupted information upon the status of each stored ion during the whole observation time. Parent and daughter ions from both systems coast on different orbits in the ESR and have different circulation times.
2. Binning effects. 3. A variance of the delay between the decay of the mother and the "re-appearance" of the daughter ion.	Both effects lead to an uncertainty of the decay time that is much smaller than the observed period.

Explanations/Questions	Objections
4. It is very probable that the H-like ^{140}Pr and ^{142}Pm ions with nuclear spin $I = 1^+$ are produced in a coherent superposition of the two $1s$ hyperfine states with total angular momenta $F = 1/2$ and $F = 3/2$. This could lead to well-known quantum beats with a beat period $T = h/\Delta E$, where ΔE is the hyperfine splitting.	Those beat periods should be at least 12 orders of magnitude shorter than the observed ones. The weak decay conserves the F quantum number, and since the final state (fully ionized daughter nuclei with $I = 0^+$ and emitted ν_e) has $F = 1/2$, the EC-decay from the $F = 3/2$ state is *not* allowed.
5. A hypothetical mechanism which transfers the parent ions periodically within 7 s from the $F = 1/2$ ground state to the $F = 3/2$ state and back in both nuclides could generate the observed modulations.	Yet unknown. [But Ch. Weinheimer, L. Grigorenko & E. Kolomeitsev have some ideas...]
6. What is the effect of the continuous monitoring of the state of the ion?	**?** The same question remains in the "neutrino" explanation (see below).

Thus, we may try to interpret the modulations as due to the properties of the electron neutrino generated in the EC-decay as a coherent superposition of the mass eigenstates: $\nu_e = \sum_i V_{ei}^* \nu_i$.

40.4 Suggesting considerations.

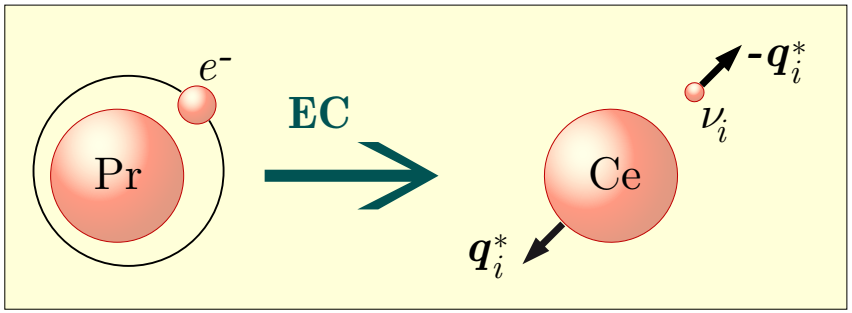

Exact kinematics of EC decay in the rest-frame of the mother ion prescribes that the 4-momenta of the i-th neutrino p_i^* and the daughter ion p_d are different in each i-th "sub-process":

$$E_i^* = \frac{M_m^2 - M_d^2 + m_i^2}{2M_m}, \quad E_{d(i)}^* = \frac{M_m^2 + M_d^2 - m_i^2}{2M_m},$$

$$\mathbf{p}_i^* = -\mathbf{p}_{d(i)}^* \equiv \mathbf{q}_i^*, \quad |\mathbf{q}_i^*| = \sqrt{(E_i^*)^2 - m_i^2}.$$

The difference between the energies is

$$\delta E_{ji}^* = E_j^* - E_i^* = E_{d(i)}^* - E_{d(j)}^* = \frac{m_j^2 - m_i^2}{2M_m} = \frac{\Delta m_{ij}^2}{2M_m}.$$

The difference between the momenta is *much larger*:

$$\delta q_{ji}^* = |\mathbf{q}_j^*| - |\mathbf{q}_i^*| \approx \left(\frac{M_m^2 + M_d^2}{M_m^2 - M_d^2}\right) \delta E_{ji}^*.$$

Current "LMA solution" to the solar neutrino problem, together with the KamLAND data yields

$$\Delta m^2_{12} = (8.0 \pm 0.3) \times 10^{-5}\ \text{eV}^2.$$

The masses of $^{140}\text{Pr}^{58+}$ (mother) and $^{140}\text{Ce}^{58+}$ (daughter) ions are, respectively,

$$M_m = 130322.600\ \text{MeV} \quad \text{and} \quad M_d = 130319.252\ \text{MeV} \quad (Q_\varepsilon = 3348 \pm 6\ \text{keV}).$$

Therefore

$$\delta E^*_{21} = \frac{8.0 \times 10^{-5}\ \text{eV}^2}{2 \cdot 130322.6 \times 10^6\ \text{eV}} \approx 3.1 \times 10^{-16}\ \text{eV},$$

$$\delta q^*_{21} \approx 3.8925 \times 10^4 \cdot \delta E^*_{21} \approx 1.2 \times 10^{-11}\ \text{eV}.$$

Corresponding time interval δt_{21} can be estimated by using the uncertainty relation:

$$\delta t^*_{21} \cdot \delta E^*_{21} \sim \frac{\hbar}{2} \quad \Longrightarrow \quad \delta t^*_{21} \sim 1.1\ \text{s}.$$

Moreover, we may construct a "period" in the lab frame using the factor $\gamma = 1.43$:

$$T_{21} = 2\pi \cdot \gamma \cdot \delta t^*_{21} \approx 9.6\ \text{s},$$

which is close (to a miracle) to the observed period of 7 s.

The next two ideas are:

- The initial and final states must be described by *wave packets*, rather than by plane-wave functions.
- We have to sum the amplitudes of the ith sub-process rather than the probabilities.

Recently, these ideas were realized within a quantum-mechanical (QM) approach by Ivanov, Reda, and Kienle [4] and quantum field theoretical approach by Faber [5] (see Refs. at p. 805.

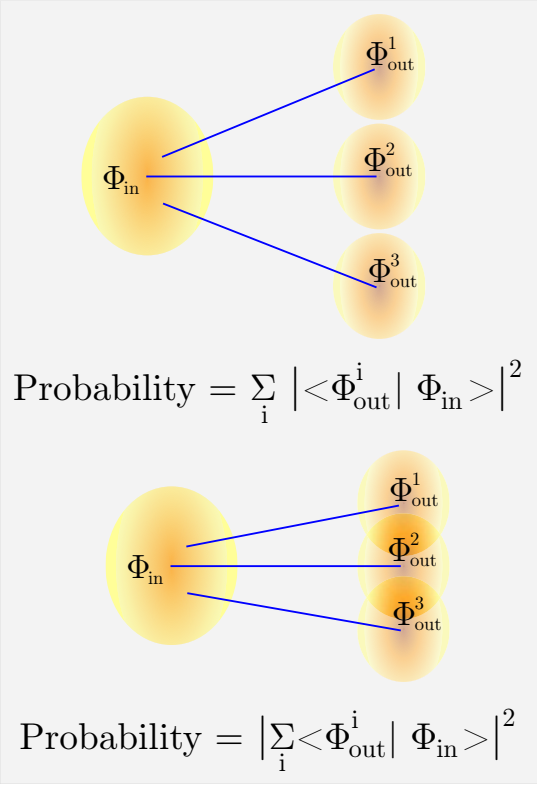

Resume of QM approach.

Neglecting the $e3$ mixing, Ivanov *et al.* obtained

$$\lambda_\varepsilon(t) = \lambda_\varepsilon(0)\left[1 + a\cos\left(\frac{\Delta m^2_{21}}{4M_d}\ t\right)\right],$$

where the amplitude of the time-modulation of the rate of the EC-decay is

$$a = \sin 2\theta_{12}\exp\left[-\left(\delta|\Delta\mathbf{q}_{21}|\right)^2\right].$$

and $\delta|\Delta\mathbf{q}_{21}|$ is an *input parameter*. Using the experimental value $\sin 2\theta^{\rm exp}_{12} = 0.925(32)$ and setting $\delta|\Delta\mathbf{q}_{21}| = 1.238(43)$, they fit the experimental data $a^{\rm exp} = 0.20(2)$.

The origin of M_d here is *puzzled*!

In the lab frame the period of modulation of the rate of the EC-decay $\lambda_\varepsilon(t)$ is defined by

$$T_{21} = \frac{8\pi\gamma M_d}{\Delta m^2_{12}},$$

For the experimental value of the period of 7.06(8) s the authors get

$$\boxed{\Delta m^2_{12} = 4.44(5) \times 10^{-4}\ \text{eV}^2.}$$

This value is by a factor of 5.5 larger than

$$\Delta m^2_{12} = 0.80(3) \times 10^{-4}\ \text{eV}^2,$$

obtained as a best-fit of the global analysis of the solar ν and KamLAND data.

Resume of QM approach.

$$\boxed{\Delta m^2_{12} = 0.775(26) \times 10^{-4}\ \text{eV}^2\ \ (!!!)}$$

BUT! It seems that this value has been obtained by using the experimental period of modulations in the *rest frame of the mother nucleus*... After the Lorentz transformation, the resulting Δm^2_{12} will be *decreased* by the factor of 1.43.

Part X

APPENDICES

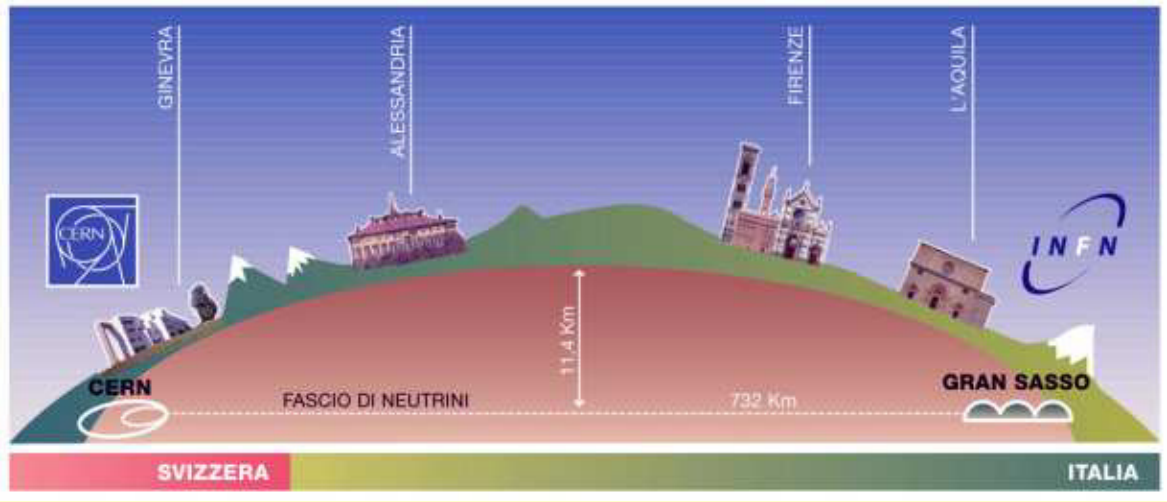

A Some details on QES kinematics (Sect. 9.1, p. 372).

Let's prove the statement at p. 373 that Eq. (18) has two solutions as $\zeta \leq 1$ and only one solution as $\zeta > 1$.

- $\zeta < 1$: It is obvious that $P_\ell^+(0) > 0$. Thus, according to Eq. (20), p. 373, $P_\ell^-(0) > 0$. Since

$$P_\ell^+(\theta) = P_\ell^-(\theta) = \frac{m_\ell^2}{\sqrt{s}} \frac{E_\nu}{E_\ell^*} \sqrt{1-\zeta^2} \quad \text{if and only if} \quad \sin\theta = \zeta,$$

  both $P_\ell^+(\theta)$ and $P_\ell^-(\theta)$ are positive for $0 \leq \theta < \arcsin\zeta$. It is also clear that $\cos\theta > 0$ (otherwise $P_\ell^\pm(\theta)$ would be negative at $\sin\theta = \zeta$). Therefore, there are two *physical* solutions, $P_\ell^+(\theta) > 0$ and $P_\ell^-(\theta) > 0$, for $0 \leq \theta < \min(\arcsin\zeta, \pi/2) \equiv \theta_\ell(E_\nu)$ and there is no physical solution for $\theta \geq \theta_\ell(E_\nu)$.

- $\zeta > 1$: The signs of the *formal* solutions $P_\ell^+(\theta)$ and $P_\ell^-(\theta)$ are opposite. Since, according to Eq. (19a), p. 373, $P_\ell^+(\theta) \geq P_\ell^-(\theta)$, we have $P_\ell^+(\theta) \geq 0$ and thus $P_\ell^-(\theta) \leq 0$. So for any θ there is the only *physical* solution, $P_\ell^+(\theta)$.

- $\zeta = 1$: In this special case $P_\ell^* = m_\ell E_\nu/\sqrt{s}$ and $E_\ell^* = m_\ell(E_\nu + M_i)/\sqrt{s}$; therefore

$$P_\ell^-(\theta) = 0, \quad P_\ell^+(\theta) = \frac{2m_\ell(E_\nu + M_i)E_\nu\cos\theta}{s + E_\nu^2\sin^2\theta},$$

$$E_\ell^-(\theta) = m_\ell, \quad E_\ell^+(\theta) = m_\ell + \frac{2m_\ell E_\nu^2\cos^2\theta}{s + E_\nu^2\sin^2\theta}.$$

  The case is only possible for $0 \leq \theta \leq \pi/2$ since $P_\ell^-(\theta) < 0$ as $\theta > \pi/2$. The two solutions are different everywhere except for the angle $\theta = \pi/2$.

One more useful identity can be found from Eq. (20):

$$P_\ell^+ \frac{\partial P_\ell^-}{\partial \theta} + P_\ell^- \frac{\partial P_\ell^+}{\partial \theta} = 0.$$

It is therefore clear that $P_\ell^+(\theta)$ ($P_\ell^-(\theta)$ is a monotonically decreasing (increasing) function of θ within the two-branch region $\zeta < 1$, $\theta > \theta_\ell(E_\nu)$. From this it follows that the scattering angle θ is a single-valued function of P_ℓ the for any ζ. Of course this trivial fact immediately follows from Eq. (18), p. 373.

Taking into account the conditions $\zeta \geq \sin\theta$ and $\sin\theta \geq 0$ we have

$$\begin{aligned} P_\ell &= P_\ell^+(\theta), \quad E_\ell = E_\ell^+(\theta), \quad 0 \leq \theta \leq \pi, && \text{if} \quad \zeta > 1, \\ P_\ell &= P_\ell^\pm(\theta), \quad E_\ell = E_\ell^\pm(\theta), \quad 0 \leq \theta < \arcsin\zeta, && \text{if} \quad \zeta \leq 1. \end{aligned}$$

The asymptotic value of $\arcsin\zeta$ at $E_\nu \to \infty$ is given by

$$\arcsin\zeta \to \arcsin\left(\frac{M_i}{m_\ell}\right) \quad \text{if} \quad M_i \leq m_\ell.$$

The condition $\zeta = 1$ defines the neutrino energy at which the second solution, P_ℓ^-, disappears.

The condition $\zeta = 1$ can be rewritten in terms of the neutrino energy as

$$\left(E_\nu - \epsilon_\nu^-\right)\left(E_\nu - \epsilon_\nu^+\right) = 0, \tag{178}$$

with

$$\epsilon_\nu^\pm = \frac{M_f^2 - (M_i \mp m_\ell)^2}{2\,(M_i \mp m_\ell)} \quad \text{and} \quad \epsilon_\nu^+ - \epsilon_\nu^- = m_\ell\left(1 + \frac{M_f^2}{M_i^2 - m_\ell^2}\right).$$

In general, Eq. (178) may have 0, 1 or 2 solutions. The latter possibility is in fact excluded since ϵ_ν^- is either negative or, as in the case of e^+ production, positive but is below the reaction threshold,

$$E_\nu^{\text{th}} = \left[(M_f + m_\ell)^2 - M_i^2\right]/(2M_i).$$

The nontrivial solutions, ϵ_ν^+, together with the thresholds and the differences $\epsilon_\nu^+ - E_\nu^{\text{th}}$ are

Reaction	E_ν^{th} (MeV)	ϵ_ν^+ (MeV)	$\epsilon_\nu^+ - E_\nu^{\text{th}}$
$\nu_e + n \to e^- + p$	0	–	–
$\overline{\nu}_e + p \to e^+ + n$	1.8060638	1.8060648	0.94537 eV
$\nu_\mu + n \to \mu^- + p$	110.16137	110.89578	734.41 keV
$\overline{\nu}_\mu + p \to \mu^+ + n$	113.04730	113.82083	773.53 keV
$\nu_\tau + n \to \tau^- + p$	3453.6527	–	–
$\overline{\nu}_\tau + p \to \tau^+ + n$	3463.4511	–	–

The same but for the isoscalar nucleon ($M_i \approx M_f \approx (M_i + M_f)/2$):

ℓ	E_ν^{th} (MeV)	ϵ_ν^+ (MeV)	$\epsilon_\nu^+ - E_\nu^{\text{th}}$
e	0.51114	0.51114	0.0757 eV
μ	111.603	112.357	753.8 keV
τ	3458.55	–	–

The IN approximation is appropriate at $E_\nu > (40 - 50)$ MeV for $e^\pm$ production and slightly above the reaction thresholds for $\mu^\pm$ and $\tau^\pm$ productions.

The exact kinematics suggests that the condition $\zeta = 1$ is never satisfied for electron production (the reaction with no threshold, $\zeta > 1$) and for $\tau^{\pm}$ production ($\zeta < 1$) while for production of e^+ and $\mu^{\pm}$ the values of ϵ_ν^+ are slightly above the reaction thresholds. However the two-branch energy gap

$$\epsilon_\nu^+ - E_\nu^{\mathsf{th}} = \frac{m_\ell \left(M_f - M_i + m_\ell\right)^2}{2M_i \left(M_i - m_\ell\right)}$$

for e^+ and $\mu^{\pm}$ production is extremely narrow since both $m_{e,\mu}$ and $m_n - m_p$ are small in comparison with the nucleon mass.

For better understanding the behavior of the parameter ζ let us investigate the derivative

$$\frac{d\zeta}{ds} = \frac{1}{2\zeta}\left(\frac{d\zeta^2}{ds}\right) = \frac{M_i^2\,\Xi}{m_\ell^2 \left(s - M_i^2\right)^3 \zeta},$$

$$\Xi = \left(m_\ell^2 + M_f^2 - M_i^2\right) s + \left(M_f^2 - m_\ell^2\right)\left(m_\ell^2 - M_f^2 + M_i^2\right).$$

Since $s \geq \max\left[M_i^2, \left(M_f + m_\ell\right)^2\right]$, we have

- $M_f < M_i - m_\ell$:

$$\Xi < -\left(M_i^2 - M_f^2\right)^2 + m_\ell^2\left(2M_f^2 - m_\ell^2\right) < -M_f\left(M_i - M_f\right)^2\left(2M_i + M_f\right) - m_\ell^4;$$

- $M_f > M_i - m_\ell$:

$$\Xi > 2m_\ell\left(M_f + m_\ell\right)\left[M_f\left(M_f + m_\ell\right) - M_i^2\right] > 2m_\ell M_i\left(M_f + m_\ell\right)\left(M_f - M_i\right);$$

- $M_f = M_i - m_\ell$:

$$\Xi = -2M_i^2\left(M_i - M_f\right)^2.$$

Therefore $d\zeta/ds < 0$ for the e^- production and $d\zeta/ds > 0$ for the rest QE reactions.

Since ζ vanishes on the thresholds of these 5 reactions, $d\zeta/ds \to \infty$ as $E_\nu \to E_\nu^{\text{th}}$. This behavior is clearly seen in Figure at p. 375.

Let us consider the kinematics of the thresholdless reaction $\nu_e + n \to e^- + p$ with more details. Since

$$\frac{dE_e^*}{d\sqrt{s}} = \frac{E_p^*}{\sqrt{s}} > 0 \quad \text{and} \quad \frac{dE_\nu^*}{d\sqrt{s}} = \frac{E_n^*}{\sqrt{s}} > 0,$$

we have

$$E_e^* \geq \frac{m_n^2 - m_p^2 + m_e^2}{2m_n} \simeq 1.292578811 \text{ MeV}, \quad P_e^* \gtrsim 1.187282648 \text{ MeV}/c \quad \text{and} \quad E_\nu^* \geq 0.$$

$$\frac{dQ_\pm}{d\sqrt{s}} = \frac{2\left(E_e^* \pm P_e^*\right)\left(E_n^* P_e^* \pm E_p^* E_\nu^*\right)}{\sqrt{s} P_e^*}.$$

According to the last equation, $dQ_+^2/d\sqrt{s} > 0$ that is Q_+^2 is a monotonically increasing function of neutrino energy. Let us prove that the same is also true for Q_-^2. Indeed, after some manipulations we can find that

$$\frac{dQ_-^2}{d\sqrt{s}} = \frac{\left(E_e^* - P_e^*\right) A_+ A_-}{8s\sqrt{s} P_e^* \left(E_n^* P_e^* + E_p^* E_\nu^*\right)}, \quad \text{where} \quad A_\pm = \left(m_n \pm m_p\right) s + m_n \left(m_p^2 - m_e^2 \pm m_p m_n\right).$$

Taking into account that $s \geq m_n^2$ we have

$$A_\pm \geq m_n \left[\left(m_n \pm m_p\right)^2 - m_e^2\right]$$

and therefore $dQ_-^2/d\sqrt{s} > 0$.

Finally,

$$\frac{d\left(Q_+^2 - Q_-^2\right)}{d\sqrt{s}} = \frac{4\left[E_e^* E_p^* E_\nu^* + \left(P_e^*\right)^2 E_n^*\right]}{\sqrt{s} P_e^*} > 0.$$

Several important facts follow from the above consideration:

- at $E_\nu = 0$

  $$Q_-^2 = Q_+^2 = -m_e^2 \simeq -0.2611199 \text{ MeV}^2$$

  and, at very low energies, the Q^2 interval linearly squeezes when energy decreases:

  $$Q_+^2 - Q_-^2 \sim 2\sqrt{\left(m_n^2 - m_p^2 + m_e^2\right)^2 - 4m_e^2 m_n^2}\left(\frac{E_\nu}{m_n}\right)$$
  $$\simeq 4.7491306 \times 10^{-6}\left(\frac{E_\nu}{1 \text{ MeV}}\right) \text{ MeV}^2;$$

- Q_-^2 is *negative at all energies* while Q_+^2 changes its sign at

  $$s = m_n^2\left(1 + \frac{m_e^2}{m_n^2 - m_p^2}\right) \quad \text{or} \quad E_\nu = \frac{m_n m_e^2}{2\left(m_n^2 - m_p^2\right)} \simeq 50.5091 \text{ keV};$$

- the asymptotic behavior of the lower bound at high energies is given by

  $$Q_-^2 \sim -\frac{m_e^2\left(m_n^2 - m_p^2\right)}{s} \simeq -\frac{6.341723 \times 10^{-4} \text{ MeV}^2}{s}.$$

To obtain the latter formula we took into account that

$$P_e^* = \frac{\sqrt{s}}{2}\left[1 - \frac{m_p^2 + m_e^2}{s} - \frac{2m_e^2 m_p^2}{s^2} + \mathcal{O}\left(\frac{1}{s^3}\right)\right] \quad \text{and} \quad E_e^* - P_e^* = \frac{m_e^2}{\sqrt{s}}\left[1 + \frac{m_p^2}{s} + \mathcal{O}\left(\frac{1}{s^2}\right)\right].$$

It is useful to investigate the behavior of Q_-^2 for all QE reactions. It can be shown that

$$\frac{dQ_-^2}{d\sqrt{s}} = \frac{(E_\ell^* - P_\ell^*)\, A_+ A_-}{8s\sqrt{s}P_\ell^* \left(E_i^* P_\ell^* + E_f^* E_\nu^*\right)},$$

where

$$A_\pm = (M_i \pm M_f)\, s + M_i \left[M_f\, (M_f \pm M_i) - m_\ell^2\right].$$

For the threshold value $s = s^{\text{th}} = (M_f + m_\ell)^2$ we obtain

$$A_\pm = A_\pm^{\text{th}} = \pm M_f\, (m_\ell + M_f \pm M_i)^2 \quad \text{and} \quad A_-^{\text{th}} A_+^{\text{th}} = -M_f \left[(m_\ell + M_f)^2 - M_i^2\right]^2.$$

By using these relations one can prove that

- $Q_-^2 < 0$ for e^- production,
- $Q_-^2 > 0$ for e^+, μ^+ and τ^+ production,
- Q_-^2 changes its sign for μ^- and τ^- production at

$$s = m_n \left(1 + \frac{m_\ell^2}{m_n^2 - m_p^2}\right) \quad \text{or} \quad E_\nu = \frac{m_\ell^2 m_n}{2\,(m_n^2 - m_p^2)}.$$

These features are illustrated in the figure at next slide.
Unfortunately it is seen no observational consequences of these nontrivial facts.

The kinematic boundaries for the Bjorken variable $y = (pq)/(pk) = 1 - E_\ell/E_\nu$ are

$$y_{\min} \le y \le y_{\max}, \quad y_{\min,\max} = 1 - \frac{1}{\sqrt{s}} \left[E_\ell^* \left(1 + \frac{M_i}{E_\nu}\right) \pm P_\ell^*\right].$$

At high energies, $E_\ell^* \approx P_\ell^* \approx \sqrt{s}/2$ and thus $y_{\min} \to 0$, $y_{\max} \to 1$, $y_{\max} - y_{\min} = 2P_\ell^*/\sqrt{s} \to 1$.

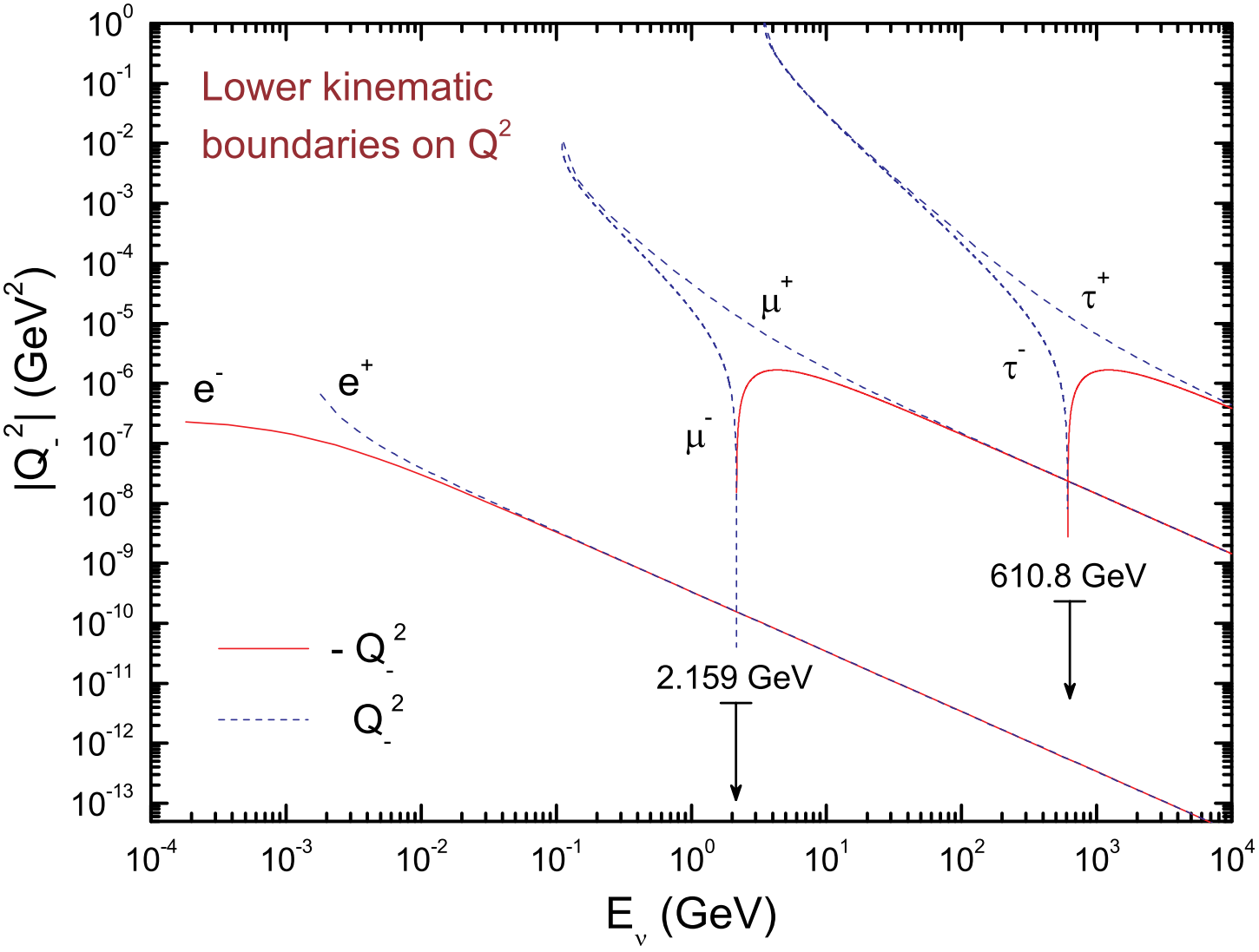

Absolute value of the lower kinematic boundary Q^2_- vs (anti)neutrino energy for the six $\Delta Y = 0$ QE reactions. The energies at which the Q^2_- changes its sign are also shown.

B Some details on DIS kinematics (Sect. 9.3, p. 380).

Nachtmann and Feynman variables. The Nachtmann variable[a] is defined by

$$x_N = \frac{Q^2}{2M^2x}\left(\sqrt{1+\frac{4M^2x^2}{Q^2}}-1\right) = \frac{2x}{1+\sqrt{1+4M^2x^2/Q^2}},$$

where x is the standard Bjorken scaling variable. Clearly $x_N \approx x$ when $Q^2 \gg 4M^2x^2$ but in general case $x_N < x$. How to use the Nachtmann variable? The recipe is

$$\frac{d\sigma}{dxdy} = K\sum_{i=1}^{5} A_i\left(x,y,E_\nu\right)F_i\left(x_N,Q^2\right).$$

However, the Nachtmann variable is not the *fraction of the nucleon momentum carried by the struck parton in the Breit frame*. Let us call the latter Feynman variable, x_F. Under assumption that the struck and final partons are on-shell the Feynman variable is defined by[b]

$$\frac{x_F}{x_N} = \frac{Q^2_{fi}}{Q^2}. \tag{179}$$

[a] O. Nachtmann,"Positivity constraints for anomalous dimensions," Nucl. Phys. B **63** (1973) 237–247; O. Nachtmann, "Is there evidence for large anomalous dimensions?" Nucl. Phys. B **78** (1978) 455–467.

[b] H. Georgi and H. D. Politzer, "Precocious scaling, rescaling and ξ scaling," Phys. Rev. Lett. **36** (1976) 281–1284; erratum – *ibid*. **37** (1976) 68; A. De Rujula, H. Georgi & H. D. Politzer, "Demythification of electroproduction, local duality and precocious scaling," Ann. Phys. **103** (1977) 315–353. For a more recent discussion of the problem see, e.g., S. R. Kelner & D. A. Timashkov,"Proton structure functions in the quasielastic limit," Yad. Fiz. **64** (2001) 1802–1808 [Phys. Atom. Nucl. **64** (2001) 1722–1728].

Here

$$2Q_{fi}^2 = Q^2 + m_f^2 - m_i^2 + \sqrt{Q^4 + 2\left(m_f^2 + m_i^2 + 2k_T^2\right)Q^2 + \left(m_f^2 - m_i^2\right)^2},$$

m_i and m_f are the masses of the struck and final partons, and k_T is the transverse momentum of the struck parton in the Breit frame. For NC scattering $m_f = m_i$. Thus

$$x_F = \frac{x_N}{2}\left[1 + \sqrt{1 + \frac{4(m_i^2 + k_T^2)}{Q^2}}\right]$$

and neglecting k_T^2/Q^2 or taking some "effective" value for k_T^2, x_F may be used the same way as x_N. Well, but how to use the Feynman variable for CC scattering? In general this is not a trivial question, because x_F is now different for different quark transitions and well above the t quark production threshold all transitions (with electric charge change of ± 1) become possible.

Let us write the $1/Q^2$ expansion

$$\frac{Q_{fi}^2}{Q^2} = 1 + \frac{m_f^2 + k_T^2}{Q^2} - \frac{2\left(m_i^2 + k_T^2\right)\left(m_f^2 + k_T^2\right)}{Q^4} + \ldots.$$

We can slightly simplify our life by neglecting the $\mathcal{O}\left(k_T^2/Q^2\right)$ and $\mathcal{O}\left(m_{i,f}^4/Q^4\right)$. It would be nice to write

$$\frac{d\sigma}{dxdy} = K\sum_{i=1}^{5} A_i\left(x, y, E_\nu\right) F_i\left(x'_F, Q^2\right), \quad \text{where} \quad x'_F = x_N\left(1 + \frac{m_f^2}{Q^2}\right) \approx x_F.$$

But which f must be used in every PDF $q\left(x'_F, Q^2\right)$? Another problem is in bad behavior of x'_F for small Q^2. Indeed, x'_F behaves like $\left(m_f^2/M^2\right)x^{-1}$ as $Q^2 \to 0$. Therefore it can be large.

Derivation of Eq. (179). Here we will follow the Kelner–Timashkov approach (see Ref. at p. 839). We mark the physical values in the Breit frame (BF) with tilde over the symbol. Thus $\tilde{q} = \left(\tilde{q}^0, 0, 0, \tilde{q}^3\right)$, $\tilde{p}_N = \left(\tilde{p}^0, 0, 0, \tilde{p}^3\right)$ and $\tilde{p}^3 \to -\infty$. Let k_i and k_f are the 4-momenta of initial (struck) and final partons. By definition,

$$\tilde{k}_i^3 = x_F \tilde{p}^3 \tag{180}$$

and thus

$$\tilde{k}_i^0 = \sqrt{\left(x_F \tilde{p}^3\right)^2 + k_T^2 + m_i^2}, \tag{181}$$

where $k_T^2 = \tilde{k}_T = \left(\tilde{k}_i^1\right)^2 + \left(\tilde{k}_i^2\right)^2$ (that is k_T is the part of $\tilde{k}_i$ transverse to $\tilde{p}_N$ and $\tilde{q}$). From the conservation law

$$\tilde{q} + \tilde{k}_i = \tilde{k}_f$$

we have

$$2\tilde{q}\tilde{k}_i = 2\left(\tilde{q}^0 \tilde{k}_i^0 - \tilde{q}^3 \tilde{k}_i^3\right) = Q^2 + m_f^2 - m_i^2. \tag{182}$$

Velocity of the BF in the lab. frame is $\mathbf{v}_{\mathrm{BF}} = -\tilde{\mathbf{p}}_N / \tilde{p}^0$. Therefore

$$|\mathbf{v}_{\mathrm{BF}}| = -\frac{\tilde{p}^3}{\tilde{p}^0}, \quad \sqrt{1 - |\mathbf{v}_{\mathrm{BF}}|^2} = \frac{\tilde{p}^0}{M},$$

and Lorentz transformation of q can be written as

$$\tilde{q}^0 = \frac{1}{M}\left(q^0 \tilde{p}^0 + q^3 \tilde{p}^3\right),$$
$$\tilde{q}^3 = \frac{1}{M}\left(q^3 \tilde{p}^0 + q^0 \tilde{p}^3\right).$$

Substituting these equations into Eq. (182), taking into account Eqs. (180) and (181) and finding the limit as $\tilde{p}^3 \to -\infty$ we arrive at the following *exact* equation for x_F:

$$\left(q^0 + q^3\right) M x_F + \frac{\left(m_i^2 + k_T^2\right)\left(q^0 - q^3\right)}{M x_F} = Q^2 + m_f^2 - m_i^2.$$

Its solution yields Eq. (179).

Useful formulas:

$$q^3 = \nu\sqrt{1 + \frac{2Mx}{\nu}} = \nu\sqrt{1 + \frac{4M^2x^2}{Q^2}}.$$

Here we assume that $q^0 = \nu \geq 0$. This is true if $M' \geq M$ In fact we *must* assume that $m_p = m_n$ to have x varying between 0 and 1. This approximation seems natural if we neglect the transverse momentum k_T (which may be much larger then the $n - p$ mass difference) and light quark masses.

Threshold Conditions. We define the differential cross sections for the inclusive CC DIS reaction

$$\nu N \to lX \tag{183}$$

by

$$\frac{d\sigma^{\text{DIS}}_{\nu N \to lX}}{dy} = \int_{x^-}^{1} dx\, \theta\left(W^2 - M_h^2\right) \frac{d^2\sigma_{\nu N \to lX}}{dxdy},$$

where

$$W^2 = p_X^2 = (q+p)^2 = Q^2\left(\frac{1}{x} - 1\right) - M^2$$

and M_h is the total mass of the hadron system h.

Let us find out the points of intersection between the curves

$$(1-x)Q^2 = \left(M_h^2 - M^2\right) x$$

and

$$\left(Q^2 + m_\ell^2\right)^2 + \frac{2Q^2 E_\nu}{Mx}\left(Q^2 + m_\ell^2\right) - 4Q^2 E_\nu^2 = 0.$$

The solution is

$$x = x_h^{\pm}\left(E_\nu\right) = \frac{a_h\left(E_\nu\right) \pm \sqrt{b_h\left(E_\nu\right)}}{2c_h\left(E_\nu\right)},$$

where

$$a_h\left(E_\nu\right) = 1 - \frac{\left(M_h^2 - M^2 - m_\ell^2\right)\left[\left(M_h^2 - M^2\right)E_\nu + m_\ell^2 M\right]}{2M\left(M_h^2 - M^2\right)E_\nu^2},$$

$$b_h\left(E_\nu\right) = \left[1 - \frac{\left(M_h - m_\ell\right)^2 - M^2}{2ME_\nu}\right]\left[1 - \frac{\left(M_h + m_\ell\right)^2 - M^2}{2ME_\nu}\right],$$

$$c_h\left(E_\nu\right) = 1 + \frac{\left(M_h^2 - M^2 - m_\ell^2\right)^2}{4\left(M_h^2 - M^2\right)E_\nu^2}.$$

Clearly $b_h\left(E_\nu\right) \geq 0$ (and thus the solution does exist) at

$$E_\nu \geq E_\nu^h = \frac{\left(M_h + m_\ell\right)^2 - M^2}{2M},$$

where E_ν^h is exactly the *threshold neutrino energy* for the reaction (183).

Clearly, for the quasielastic threshold ($M_h = M$) the solution degenerates to $x_h^{\pm} = 1$ providing no additional cutoff for the physical region

$$y^- \leq y \leq y^+, \quad x^- \leq x \leq 1.$$

For very high neutrino energies we have

$$x_h^- \approx \frac{m_\ell^2}{2ME_\nu} \approx x^-, \quad x_h^+ \approx 1 - \frac{M_h^2 - M^2}{2ME_\nu}.$$

We assume from here that $M_h > M$.

Let us now *define* the differential and total cross sections for the inclusive reaction (183) by

$$\frac{d\sigma^{\mathsf{DIS}}_{\nu N \to lhX}}{dy} = \int_{x^-}^{x_h^+} dx\, \theta\left(y - y_h^{\mathsf{min}}\right) \theta\left(y^+ - y\right) \frac{d^2\sigma_{\nu N \to l + \mathsf{anything}}}{dxdy},$$

$$y^-\left(x_h^-, E_\nu\right) \leq y \leq y^+\left(x_h^+, E_\nu\right), \qquad E_\nu \geq E_\nu^h,$$

and

$$\begin{aligned}\sigma^{\mathsf{DIS}}_{\nu N \to lhX} &= \int dy \int_{x^-}^{x_h^+} dx\, \theta\left(y - y_h^{\mathsf{min}}\right) \theta\left(y^+ - y\right) \frac{d^2\sigma_{\nu N \to l + \mathsf{anything}}}{dxdy} \\ &= \int_0^1 dy' \int_{x^-}^{x_h^+} dx\, \left(y^+ - y_h^{\mathsf{min}}\right) \frac{d^2\sigma_{\nu N \to l + \mathsf{anything}}}{dxdy},\end{aligned} \tag{184}$$

where

$$y_h^{\mathsf{min}} = y_h^{\mathsf{min}}\left(x, E_\nu\right) = \mathsf{max}\left[y^-\left(x, E_\nu\right), \frac{M_h^2 - M^2}{2M(1-x)E_\nu}\right],$$

$$y^{\pm}\left(x_h^{\pm}, E_\nu\right) = \frac{M_h^2 - M^2}{2M\left(1 - x_h^{\pm}\right)E_\nu},$$

and the new variable y' in Eq. (184) is defined by

$$y = \left(y^+ - y_h^{\mathsf{min}}\right) y' + y_h^{\mathsf{min}}.$$

For the moment we'll assume that the *minimal* hadron system h of the DIS is $N + 2\pi$. Therefore $M_h = M + 2m_\pi$,

$$y_h^{\mathsf{min}} = \mathsf{max}\left[y^-, \frac{2m_\pi\left(M + m_\pi\right)}{M(1-x)E_\nu}\right],$$

and the *total* CC cross section is

$$\sigma_{\nu N}^{\mathsf{tot}} = \sigma_{\nu N}^{\mathsf{QES}} + \sigma_{\nu N}^{\mathsf{RES}} + \sigma_{\nu N \to \ell + N + 2\pi + X}^{\mathsf{DIS}}.$$

Needless to say that $\sigma_{\nu N \to \ell h X}^{\mathsf{DIS}} = 0$ as $E_\nu \leq E_\nu^h$ and that the corresponding results for the NC inclusive reaction

$$\nu\left(\overline{\nu}\right) N \to \nu\left(\overline{\nu}\right) + h + X$$

can be obtained by putting $m_\ell = 0$ in the above equations.

C Gamma matrices.

Pauli matrices.

$$\sigma_0 \equiv 1 = \begin{pmatrix} 1 & 0 \\ 0 & 1 \end{pmatrix}, \quad \sigma_1 = \begin{pmatrix} 0 & 1 \\ 1 & 0 \end{pmatrix}, \quad \sigma_2 = \begin{pmatrix} 0 & -i \\ i & 0 \end{pmatrix}, \quad \sigma_3 = \begin{pmatrix} 1 & 0 \\ 0 & -1 \end{pmatrix}, \quad \boldsymbol{\sigma} = (\sigma_1, \sigma_2, \sigma_3);$$

$$[\sigma_i, \sigma_j]_+ = 2\delta_{ij}\sigma_0, \quad [\sigma_i, \sigma_j]_- = 2i\epsilon_{ijk}\sigma_k, \quad \sigma_i\sigma_j = \delta_{ij}\sigma_0 + i\epsilon_{ijk}\sigma_k \quad (\epsilon_{123} = 1);$$

$$(\boldsymbol{q\sigma}) = U|\mathbf{q}|\sigma_3 U \text{ and } U(\boldsymbol{q\sigma})U = |\mathbf{q}|\sigma_3, \text{ where } U = U^\dagger = \frac{(\boldsymbol{q\sigma} + |\mathbf{q}|\sigma_3)}{\sqrt{2|\mathbf{q}|\,(|\mathbf{q}| + q^3)}}.$$

Dirac matrices.

$$\gamma = \left(\gamma^0, \boldsymbol{\gamma}\right), \quad \boldsymbol{\gamma} = \left(\gamma^1, \gamma^2, \gamma^3\right), \quad [\gamma^\mu, \gamma^\nu]_+ = 2g^{\mu\nu}, \quad \gamma_\mu\gamma^\mu = 4, \quad \gamma_0^\dagger = \gamma_0, \quad \gamma_k^\dagger = -\gamma_k, \quad \sigma^{\mu\nu} = \frac{i}{2}[\gamma^\mu, \gamma^\nu]_-;$$

$$\gamma^5 = i\gamma^0\gamma^1\gamma^2\gamma^3 = \frac{i}{4!}\epsilon_{\mu\nu\lambda\rho}\gamma^\mu\gamma^\nu\gamma^\lambda\gamma^\rho \quad (\epsilon_{0123} = 1), \quad [\gamma^5, \gamma^\mu]_+ = 0, \quad \gamma_5^2 = 1, \quad \gamma_5^\dagger = \gamma_5.$$

Block structure (Dirac representation).

$$\gamma^0 = \gamma_0 = \begin{pmatrix} 1 & 0 \\ 0 & -1 \end{pmatrix}, \quad \gamma^k = -\gamma_k = \begin{pmatrix} 0 & \sigma_k \\ -\sigma_k & 0 \end{pmatrix}, \quad \gamma^5 = \gamma_5 = \begin{pmatrix} 0 & 1 \\ 1 & 0 \end{pmatrix};$$

$$\sigma^{k0} = \begin{pmatrix} 0 & -\sigma_k \\ -\sigma_k & 0 \end{pmatrix}, \quad \sigma^{kl} = -i\epsilon_{klm}\begin{pmatrix} \sigma_m & 0 \\ 0 & \sigma_m \end{pmatrix}, \quad \gamma^5\gamma^0 = \begin{pmatrix} 0 & -1 \\ 1 & 0 \end{pmatrix}, \quad \gamma^5\gamma^k = \begin{pmatrix} -\sigma_k & 0 \\ 0 & \sigma_k \end{pmatrix}.$$

Specific identities.

$$\gamma^\mu\gamma_\mu = \hat{\gamma} = 4,\ \ \gamma^\mu\gamma^\nu\gamma_\mu = -2\gamma^\nu,\ \ \gamma^\mu\gamma^\nu\gamma^\lambda\gamma_\mu = 4g^{\nu\lambda};$$

$$\gamma^\mu\gamma^\nu\gamma^\lambda\gamma^\rho\gamma_\mu = -2\gamma^\rho\gamma^\lambda\gamma^\nu;$$

$$\gamma^\mu\gamma^\nu\gamma^\lambda = g^{\mu\nu}\gamma^\lambda + g^{\nu\lambda}\gamma^\mu - g^{\mu\lambda}\gamma^\nu - i\epsilon^{\rho\mu\nu\lambda}\gamma_\rho\gamma^5;$$

$$\gamma_0\gamma_\mu^\dagger\gamma_0 = \gamma_\mu,\ \ \gamma_0(\gamma_\mu\gamma_5)^\dagger\gamma_0 = \gamma_\mu\gamma_5;$$

$$\mathrm{Tr}(\gamma^\mu) = \mathrm{Tr}(\underbrace{\gamma^\mu\gamma^\nu\ldots\gamma^\lambda}_{\text{odd number of }\gamma\text{s}}) = \mathrm{Tr}(\underbrace{\gamma^\mu\gamma^\nu\ldots\gamma^\lambda}_{\text{odd number of }\gamma\text{s}}\gamma^5) = 0;$$

$$\mathrm{Tr}(\gamma^\mu\gamma^\nu) = 4g^{\mu\nu},\ \ \mathrm{Tr}(\gamma^\mu\gamma^\nu\gamma^\lambda\gamma^\rho) = 4\left(g^{\mu\nu}g^{\lambda\rho} - g^{\mu\lambda}g^{\nu\rho} + g^{\mu\rho}g^{\nu\lambda}\right),$$

$$\mathrm{Tr}(\gamma^5) = \mathrm{Tr}(\gamma^\mu\gamma^\nu\gamma^5) = 0,\ \ \mathrm{Tr}(\gamma^\mu\gamma^\nu\gamma^\lambda\gamma^\rho\gamma^5) = 4i\epsilon^{\mu\nu\lambda\rho};$$

$$\hat{a}\hat{b} = (ab) - ia_\mu b_\nu\sigma^{\mu\nu},\ \ \hat{a}^2 = a^2;$$

$$\mathrm{Tr}(\hat{a}\hat{b}) = 4(ab),\ \ \mathrm{Tr}(\hat{a}\hat{b}\hat{c}\hat{d}) = 4\left[(ab)(cd) - (ac)(bd) + (ad)(bc)\right],$$

$$\mathrm{Tr}(\hat{a}\hat{b}\hat{c}\hat{d}\gamma^5) = 4i\epsilon_{\mu\nu\lambda\rho}a^\mu b^\nu c^\lambda d^\rho;$$

$$\gamma_\mu\hat{a}\gamma^\mu = -2\hat{a},\ \ \gamma_\mu\hat{a}\hat{b}\gamma^\mu = 4(ab),\ \ \gamma_\mu\hat{a}\hat{b}\hat{c}\gamma^\mu = -2\hat{c}\hat{b}\hat{a};$$

$$\epsilon_{\mu\nu\lambda\rho}\gamma^\rho\gamma_5 = \gamma_\mu\sigma_{\nu\lambda} - i\left(g_{\mu\nu}\gamma_\lambda - g_{\mu\lambda}\gamma_\nu\right),$$

$$\epsilon_{\mu\nu\lambda\rho}\sigma^{\lambda\rho}\gamma_5 = 2\left(g_{\mu\nu} - \gamma_\mu\gamma_\nu\right).$$

Complete set of 4×4 matrices. $\Gamma_A^2 = 1$, $A = 1..16$, $\mathrm{Tr}\Gamma_A = 0$ for $A \neq 1$, $\mathrm{Tr}\Gamma_1 = 4$, $\Gamma_1 = 1$.

$$\Gamma_2 = \gamma^0 = \begin{pmatrix} 1 & 0 \\ 0 & -1 \end{pmatrix}$$

$$\Gamma_3 = i\gamma^1 = i\begin{pmatrix} 0 & \sigma_1 \\ -\sigma_1 & 0 \end{pmatrix} \qquad \Gamma_4 = i\gamma^2 = i\begin{pmatrix} 0 & \sigma_2 \\ -\sigma_2 & 0 \end{pmatrix} \qquad \Gamma_5 = i\gamma^3 = i\begin{pmatrix} 0 & \sigma_3 \\ -\sigma_3 & 0 \end{pmatrix}$$

$$\Gamma_6 = \sigma^{10} = \begin{pmatrix} 0 & -\sigma_1 \\ -\sigma_1 & 0 \end{pmatrix} \qquad \Gamma_7 = \sigma^{20} = \begin{pmatrix} 0 & -\sigma_2 \\ -\sigma_2 & 0 \end{pmatrix} \qquad \Gamma_8 = \sigma^{30} = \begin{pmatrix} 0 & -\sigma_3 \\ -\sigma_3 & 0 \end{pmatrix}$$

$$\Gamma_9 = i\sigma^{12} = \begin{pmatrix} \sigma_3 & 0 \\ 0 & \sigma_3 \end{pmatrix} \qquad \Gamma_{10} = i\sigma^{23} = \begin{pmatrix} \sigma_1 & 0 \\ 0 & \sigma_1 \end{pmatrix} \qquad \Gamma_{11} = i\sigma^{31} = \begin{pmatrix} \sigma_2 & 0 \\ 0 & \sigma_2 \end{pmatrix}$$

$$\Gamma_{12} = i\gamma^5\gamma^0 = \begin{pmatrix} 0 & -i \\ i & 0 \end{pmatrix}$$

$$\Gamma_{13} = \gamma^5\gamma^1 = \begin{pmatrix} -\sigma_1 & 0 \\ 0 & \sigma_1 \end{pmatrix} \qquad \Gamma_{14} = \gamma^5\gamma^2 = \begin{pmatrix} -\sigma_2 & 0 \\ 0 & \sigma_2 \end{pmatrix} \qquad \Gamma_{15} = \gamma^5\gamma^3 = \begin{pmatrix} -\sigma_3 & 0 \\ 0 & \sigma_3 \end{pmatrix}$$

$$\Gamma_{16} = \gamma^5 = \begin{pmatrix} 0 & 1 \\ 1 & 0 \end{pmatrix}$$

D Spin pseudovector (Sect. 10.6, p. 404).

Let's denote $\mathcal{P} = \mathcal{P}\boldsymbol{\xi}$, where $\boldsymbol{\xi} = \left(\xi_1, \xi_2, \xi_3\right)$ is a unit pseudovector one which does not change sign under an inversion of the coordinate system (unlike velocity and momentum). For understanding its transformation properties we introduce the axial 4-vector $s = (s_0, \mathbf{s})$ whose spatial component, $\mathbf{s}$, coincides with the vector $\boldsymbol{\xi}$ in the lepton rest frame (LRF). We will mark that frame by symbol *; then, by definition, $\mathbf{s}^\star = \boldsymbol{\xi}^\star$. Since the scalar product of a polar and an axial 4-vectors must vanish,

$$sp = s_0 E_\ell - \mathbf{s}\mathbf{p}_\ell = 0 \quad \Longrightarrow \quad s_0 = \frac{\mathbf{s}\mathbf{p}_\ell}{E_\ell}; \quad \Longrightarrow \quad s_0^\star = 0 \quad \text{and} \quad s^2 = \left(s^\star\right)^2 = -\left(\boldsymbol{\xi}^\star\right)^2 = -1.$$

Let's now represent the pseudovector $\mathbf{s}$ in the form $\mathbf{s} = \boldsymbol{\xi} + \alpha\left(\boldsymbol{\xi}\mathbf{p}_\ell\right)\mathbf{p}_\ell$, where α is an unknown function. According to the above relations it satisfies the equation

$$m_\ell^2 P_\ell^2 \alpha^2 + 2m_\ell^2 \alpha - 1 = 0$$

which has two solutions,

$$\alpha_\pm = \frac{\pm 1}{m_\ell\left(E_\ell \pm m_\ell\right)}.$$

Only one of these solutions (namely α_+) provides the condition $\mathbf{s}^\star = \boldsymbol{\xi}^\star$. Indeed,

$$\alpha_-\left(\boldsymbol{\xi}\mathbf{p}_\ell\right)\mathbf{p}_\ell = -\left(\boldsymbol{\xi}\mathbf{n}_\ell\right)\left(\frac{E_\ell}{m_\ell} + 1\right)\mathbf{n}_\ell,$$

(where $\mathbf{n}_\ell = \mathbf{p}_\ell/|\mathbf{p}_\ell|$); this quantity does not vanish in LRF, while (as it should be)

$$\alpha_+\left(\boldsymbol{\xi}\mathbf{p}_\ell\right)\mathbf{p}_\ell = \left(\boldsymbol{\xi}\mathbf{n}_\ell\right)\left(\frac{E_\ell}{m_\ell} - 1\right)\mathbf{n}_\ell \to 0 \quad \text{as} \quad |\mathbf{p}_\ell| \to 0.$$

Finally we arrive at the well-known formula for the components of the spin 4-vector:

$$\mathbf{s} = \boldsymbol{\xi} + \frac{(\boldsymbol{\xi}\mathbf{p}_\ell)\,\mathbf{p}_\ell}{m_\ell\,(E_\ell + m_\ell)}, \quad s_{_0} = \frac{(\boldsymbol{\xi}\mathbf{p}_\ell)}{m_\ell}.$$

An obvious while very important feature of the vector $\boldsymbol{\xi}$ is in its invariance relative to Lorentz boosts. Indeed, the boost from LRF to laboratory frame (LF) gives

$$s_{_3} = \frac{E_\ell}{m_\ell}\,\xi^\star_{_3}, \quad s_{_{1,2}} = \xi^\star_{_{1,2}}.$$

On the other hand,

$$s_{_3} = \xi_{_3} + \frac{\xi_{_3} P_\ell^2}{m_\ell\,(E_\ell + m_\ell)} = \frac{E_\ell}{m_\ell}\,\xi_{_3}, \quad s_{_{1,2}} = \xi_{_{1,2}}.$$

Therefore $\boldsymbol{\xi} = \boldsymbol{\xi}^\star$. This *does not mean* at all that $\boldsymbol{\xi}$ is invariant relative to *any* Lorentz transformation. Let us consider, for example, a spatial rotation given by a 3×3 matrix $\mathbf{T}$. Under such a transformation,

$$\mathbf{s} \mapsto \mathbf{s}' = \mathbf{T}\mathbf{s} = \mathbf{T}\boldsymbol{\xi} + \frac{(\boldsymbol{\xi}\mathbf{p}_\ell)\,\mathbf{T}\mathbf{p}_\ell}{m_\ell\,(E_\ell + m_\ell)}.$$

On the other hand,

$$\mathbf{s}' = \boldsymbol{\xi}' + \frac{(\boldsymbol{\xi}'\mathbf{p}'_\ell)\,\mathbf{p}'_\ell}{m_\ell\,(E'_\ell + m_\ell)}.$$

Since $E'_\ell = E_\ell$, $\mathbf{p}'_\ell = \mathbf{T}\mathbf{p}_\ell$, and $\boldsymbol{\xi}\mathbf{p}'_\ell = \boldsymbol{\xi}\mathbf{T}\mathbf{p}_\ell = \mathbf{T}^T\boldsymbol{\xi}\mathbf{p}_\ell$, we have

$$\boldsymbol{\xi} \mapsto \boldsymbol{\xi}' = \mathbf{T}\boldsymbol{\xi}.$$

Therefore $\boldsymbol{\xi}$ and $\mathbf{p}_\ell$ are transformed similar way and thus $\boldsymbol{\xi}\mathbf{p}_\ell$ is invariant. It is also clear that vector $\boldsymbol{\xi}$ will be (in general) transformed by a superposition of a spatial rotation and a Lorentz boost.

E Some slightly outdated results to see rapid progress.

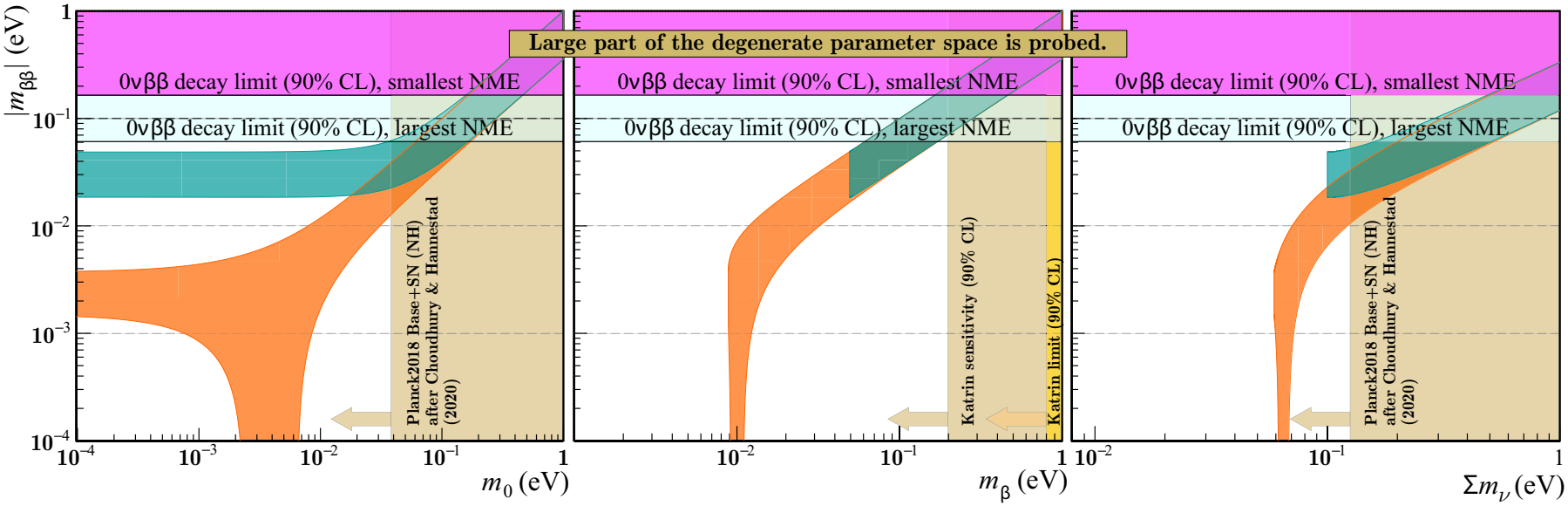

△ The 2022 status for the maximally allowed parameter space for $|m_{\beta\beta}|$ as a function of m_0, m_β, and $\sum m_\nu$, assuming the central values of the neutrino oscillation parameters from the global fit of Zyla *et al.* (2020) [close to NuFIT 5.1]. The orange and green areas show the parameter space allowed assuming normal and inverted ordering, respectively. The shaded areas are explaned in the legends. The $m_{\beta\beta}$ upper limits are mainly from the KamLAND-Zen experiment (cf. the Figure at p. 852).

The figure is very informative. Note in particular that measurement of $\sum m_\nu$ below 100 meV would disfavor the inverted ordering hypothesis. Moreover, any measurement of $\sum m_\nu$ would naturally set a lower bound on $m_{\beta\beta}$, even in the case of the normal ordering. This is already qualitatively visible in the figure, but a proper estimation needs to take into account all uncertainties on the oscillation parameters and the anticipated 20 meV accuracy of the measurement on $\sum m_\nu$.

[Borrowed from M. Agostini *et al.*, "Toward the discovery of matter creation with neutrinoless double-beta decay," Rev. Mod. Phys. **95** (2023) 025002, arXiv:2202.01787v2 [hep-ex]; figure is updated and slightly modified.]

The 2015 status for the maximally allowed parameter space for $m_{\beta\beta}$ as a function of the lightest neutrino mass m_0. In the case of normal (inverted) mass ordering the ranges are shown by green (blue) color. The light (dark) colored regions are computed by taking into account (without taking account) the current 1σ uncertainties of the relevant mixing parameters. Also shown are the limits on $m_{\beta\beta}$ coming from KamLAND-Zen and EXO-200 (light brown band), GERDA (light violet band), and the bounds on m_0 obtained by *Planck* 2013 and 2018.

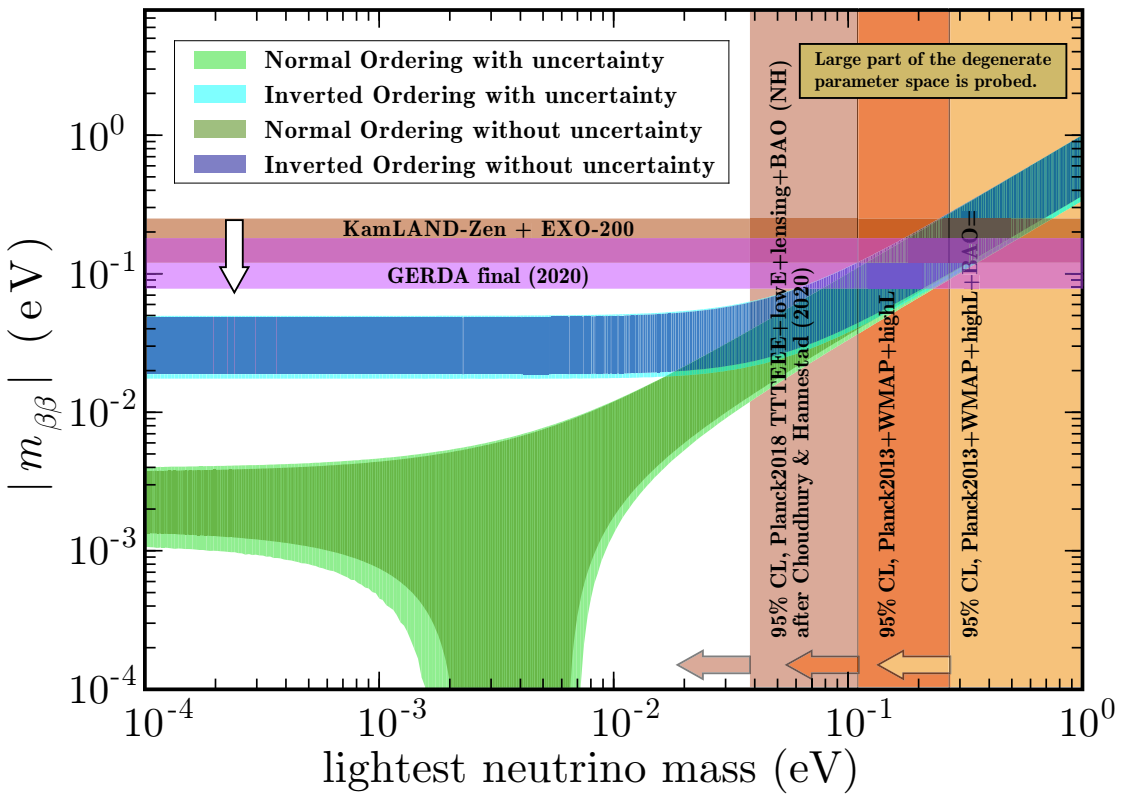

The $0\nu\beta\beta$ bounds span broad bands because of the nuclear matrix element (NME) uncertainty. The KamLAND-Zen+EXO-200 limits are out of date, more recent once can be found on p. 851.

It is remarkable that the effect of the 1σ uncertainties of the mixing parameters is quite small. In contrast, variation over the Majorana phases gives much larger impact on allowed region of $m_{\beta\beta}$, not only producing sizeable width but also creating a down-going branch at 10^{-3} eV $\lesssim m_0 \lesssim 10^{-2}$ eV for the case of the normal mass ordering due to the strong cancellation of the three mass terms.

[From H. Minakata, H. Nunokawa, and A. A. Quiroga, "Constraining Majorana CP phase in the precision era of cosmology and the double beta decay experiment," PTEP **2015** (2015) 033B03, arXiv:1402.6014 [hep-ph]; partially updated.]

[Is very likely excluded.] The only evidence for the $(\beta\beta)_{0\nu}$ decay has been obtained by the Heidelberg-Moscow (HM) (**sub**)collaboration in the Gran Sasso laboratory. The HM best value of the effective neutrino mass is $|m_{\beta\beta}| = 0.4$ eV. Allowing conservatively for an uncertainty of the nuclear matrix element of $\pm 50\%$ the 3σ confidence range may widen to $(0.1 - 0.9)$ eV.

The bars in the figure denote allowed ranges of $|m_{\beta\beta}|$ in different neutrino mass scenarios, allowed by the neutrino oscillation experiments of that time (2005). All models except the *degenerate* one are excluded by the new $(\beta\beta)_{0\nu}$ decay result. Also shown is the exclusion line from WMAP, plotted for $\sum_k m_k < 1.0$ eV. WMAP does not rule out any of the neutrino mass schemes and HM result. *Planck*-2018 is in strong contradiction with HM, see p. 143).

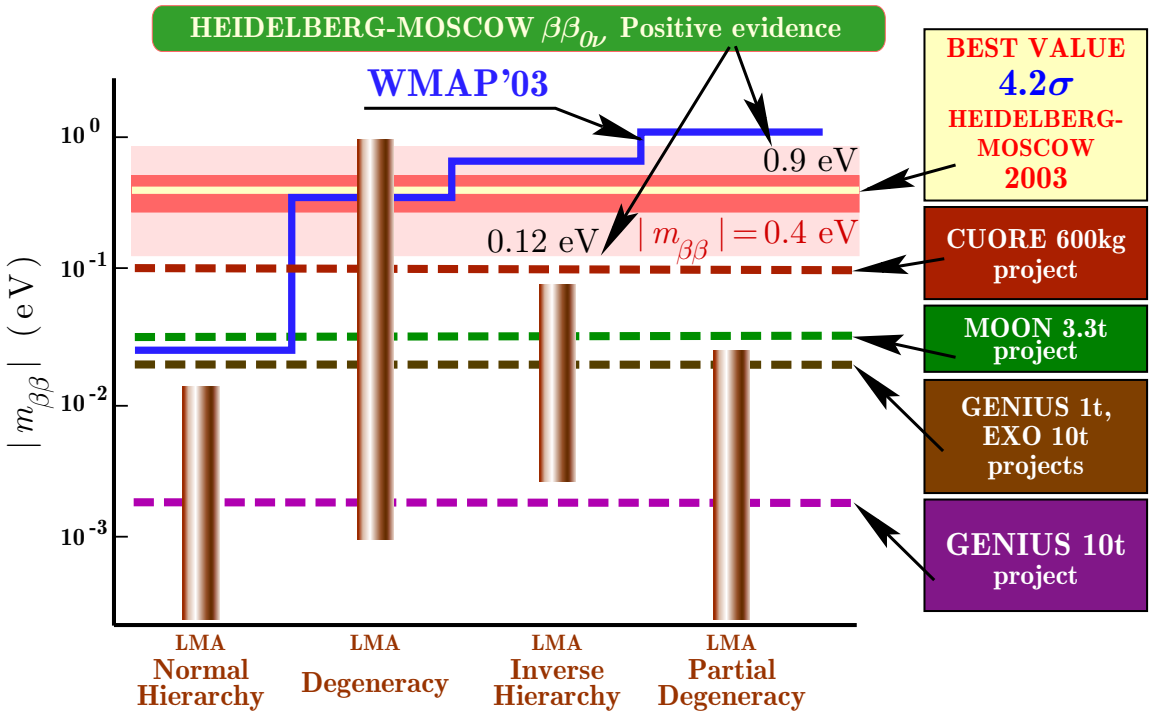

Further shown are the expected sensitivities for the future potential $(\beta\beta)_{0\nu}$ decay experiments CUORE, MOON, EXO, and GENIUS. The current state is discussed below.

[From H. V. Klapdor-Kleingrothaus, "First evidence for neutrinoless double beta decay and world status of double beta experiments," in Proceedings of the XI International Workshop "Neutrino Telescopes," February 22–25, 2005, Venice, Italy, ed. M. Baldo-Ceolin, Padova University (2005) pp. 215–237, hep-ph/0512263.]

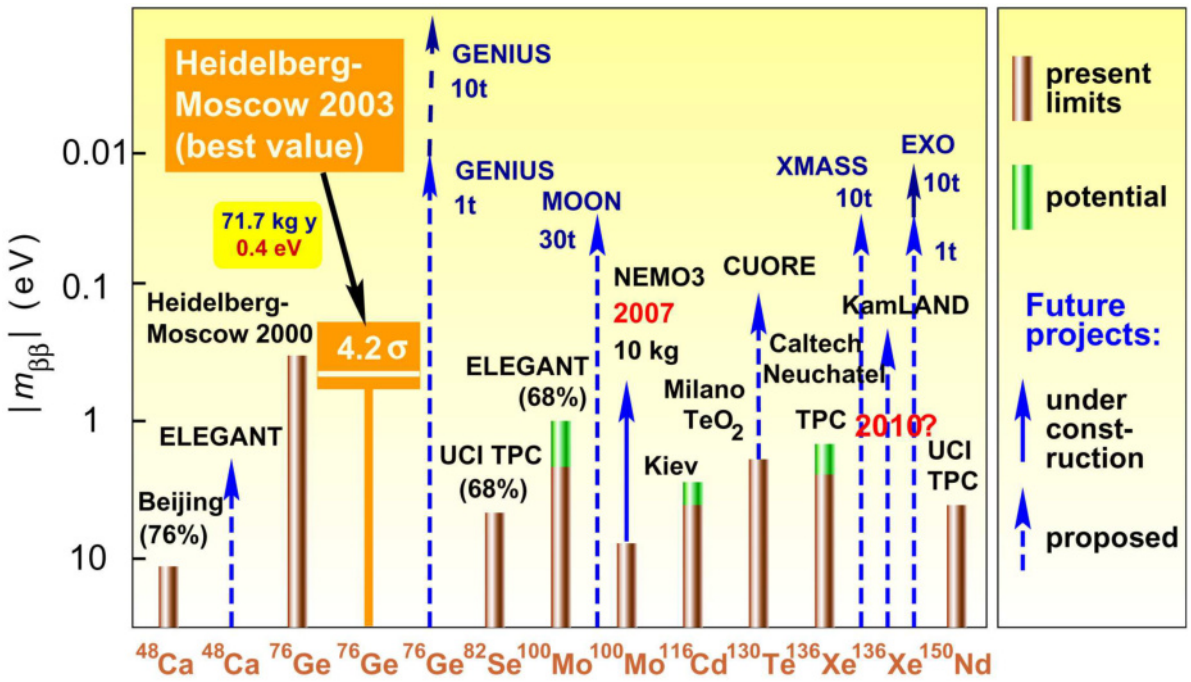

The $|m_{\beta\beta}|$ limits: the state of art in 2005.

◁ Figure (also of historical interest) shows the HM-2000 and HM-2003 results in comparison with the potential of the most promising other $(\beta\beta)_{0\nu}$ experiments as well as the expected potential of several projects (many of which are already in operation). Given are limits for $|m_{\beta\beta}|$, except for the HM-2003 experiment where the measured *value* is given (confidence range and best value).

[The histogram is built by combining the data from papers H. V. Klapdor-Kleingrothaus *et al.*, "Latest results from the Heidelberg-Moscow double beta decay experiment," Eur. Phys. J. A **12** (2001) 147–154, hep-ph/0103062 and H. V. Klapdor-Kleingrothaus, "First evidence for neutrinoless double beta decay and world status of double beta experiments," in Proceedings of the XI International Workshop on Neutrino Telescopes, Venice, Febuary 22–25, 2005, edited by M. Baldo-Ceolin, pp. 215–237, hep-ph/0512263.]

New approaches and considerably enlarged experiments are required to fix the $(\beta\beta)_{0\nu}$ half life with higher accuracy. This will, however, only marginally improve the precision of the deduced effective neutrino mass $|m_{\beta\beta}|$ (or its upper limit), because of the uncertainties in the nuclear matrix elements, which probably hardly can be reduced to less than 50%.

Current (2019) state of the art of $(\beta\beta)_{0\nu}$ experiments:

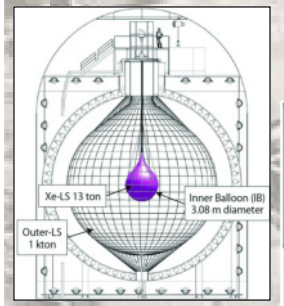

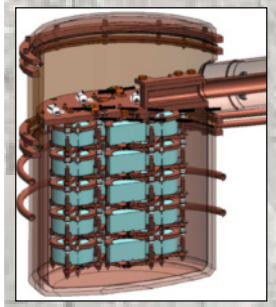

$T^{0\nu}_{1/2}$ $(10^{25}$ yr) (sensitivity)	$T^{0\nu}_{1/2}$ $(10^{25}$ yr) (lower limit)	isotope	experiment	year	status
5.6 (8.0)	>10.7 (>4)	Xe-136	KamLAND-Zen (phase I+II) (KLZ-800)	2016 (2019)	completed running
11	>9	Ge-76	Gerda (phase I+II)	2018	running
4.8	>2.7	Ge-76	Majorana Demonstrator	2018	running
5.0	>3.5	Xe-136	EXO-200 (phase I+II)	2019	completed
1.5	>2.3	Te-130	CUORE	2019	running
0.5	>0.35	Se-82	CUPID-0	2019	completed
		Te-130	SNO+		commissioning

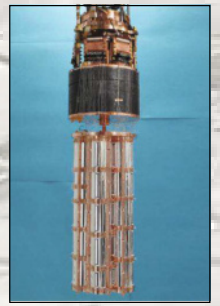

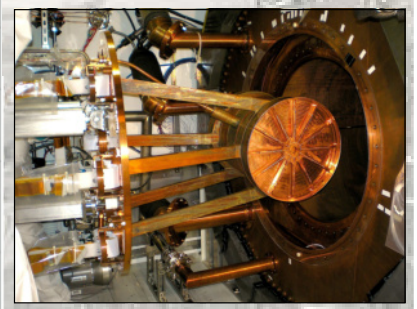

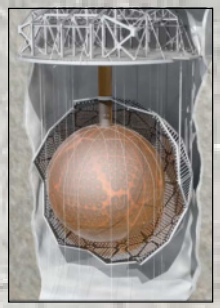

Andrea Pocar (University of Massachusetts, Amherst) believes that the progress is defined by detector technology, rather than by choice of isotope. And also, let's add, by a piece of luck (NH/IH dilemma, mass of the lightest neutrino, balance of the Majorana phases, nuclear physics uncertainties).

[Table is borrowed from report by A. Pocar, "Neutrinoless double beta decay experiments," on the Internat. Workshop on Next generation Nucleon Decay and Neutrino Detectors (NNN19), Univ. de Medellin, Colombia, November 7–9, 2019.]

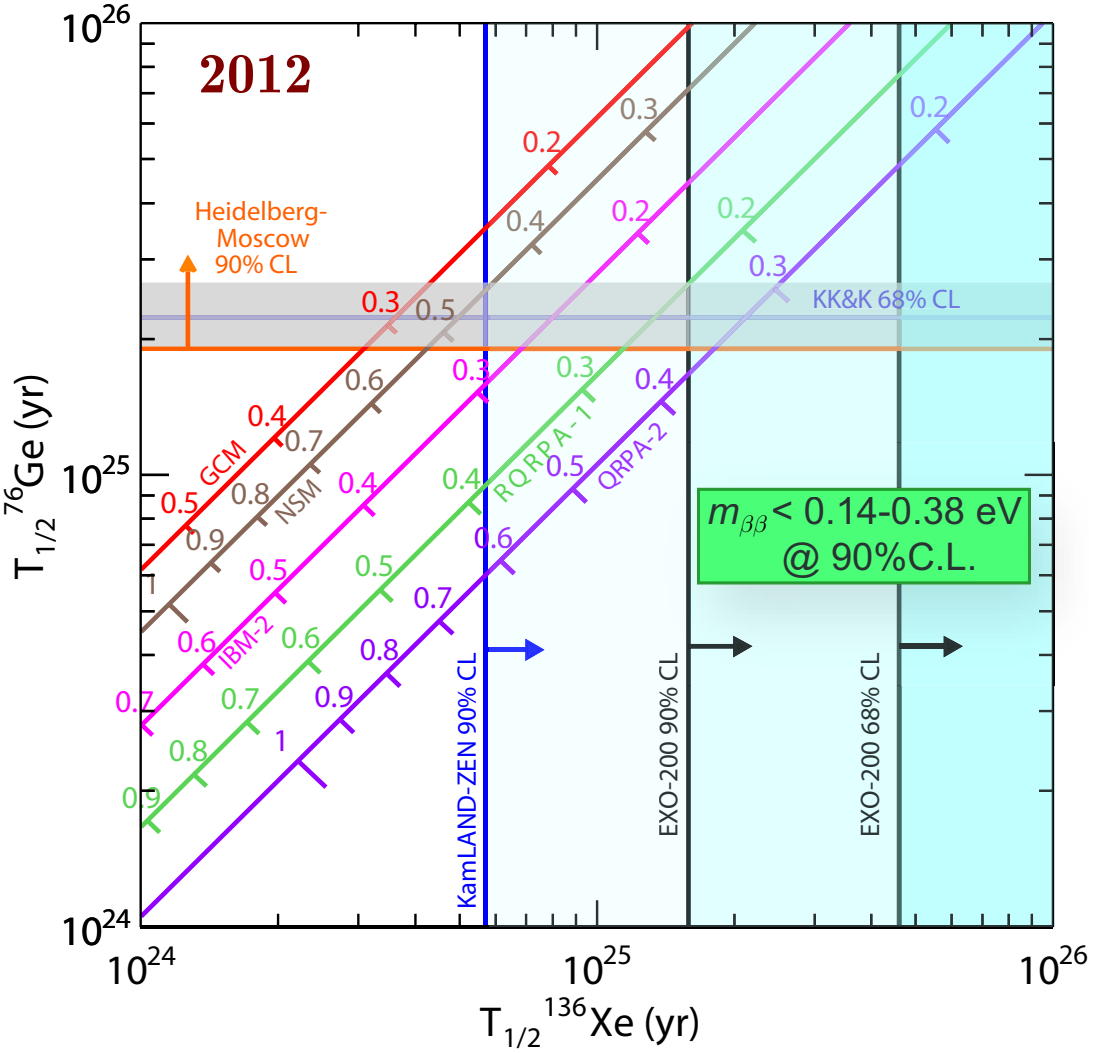

◁ Relation between the $T_{1/2}^{0\nu\beta\beta}$ in ^{76}Ge and ^{136}Xe for several nuclear matrix element (NMA) calculations (GCM, IBM-2, NSM, RQRPA-1, QRPA-2)[a] and excluded regions after the ^{136}Xe experiments KamLAND-Zen and EXO-200.

For each NMA $|m_{\beta\beta}|$ is also shown (eV). The Klapdor *et al.* claim is represented by the gray band, along with the best limit for ^{76}Ge. The EXO-200 result contradicts this claim at the 68% C.L. (90% C.L.) for the nominal values of all (most) matrix element calculations considered and provides upper bounds to $m_{\beta\beta}$ between 140 and 380 meV at 90% C.L.

[From M. Auger *et al.* (EXO Collaboration), "Search for neutrinoless double-beta decay in ^{136}Xe with EXO-200," Phys. Rev. Lett. **109** (2012) 032505, arXiv:1205.5608 [hep-ex].]

[a] Glossary: **GCM** – Generator-Coordinate Method, **IBM** – Interacting Boson Model, **NSM** – Nuclear Shell Model (NSM), **(R)QRPA** – (Relativistic) Quasiparticle Random Phase Approximation.

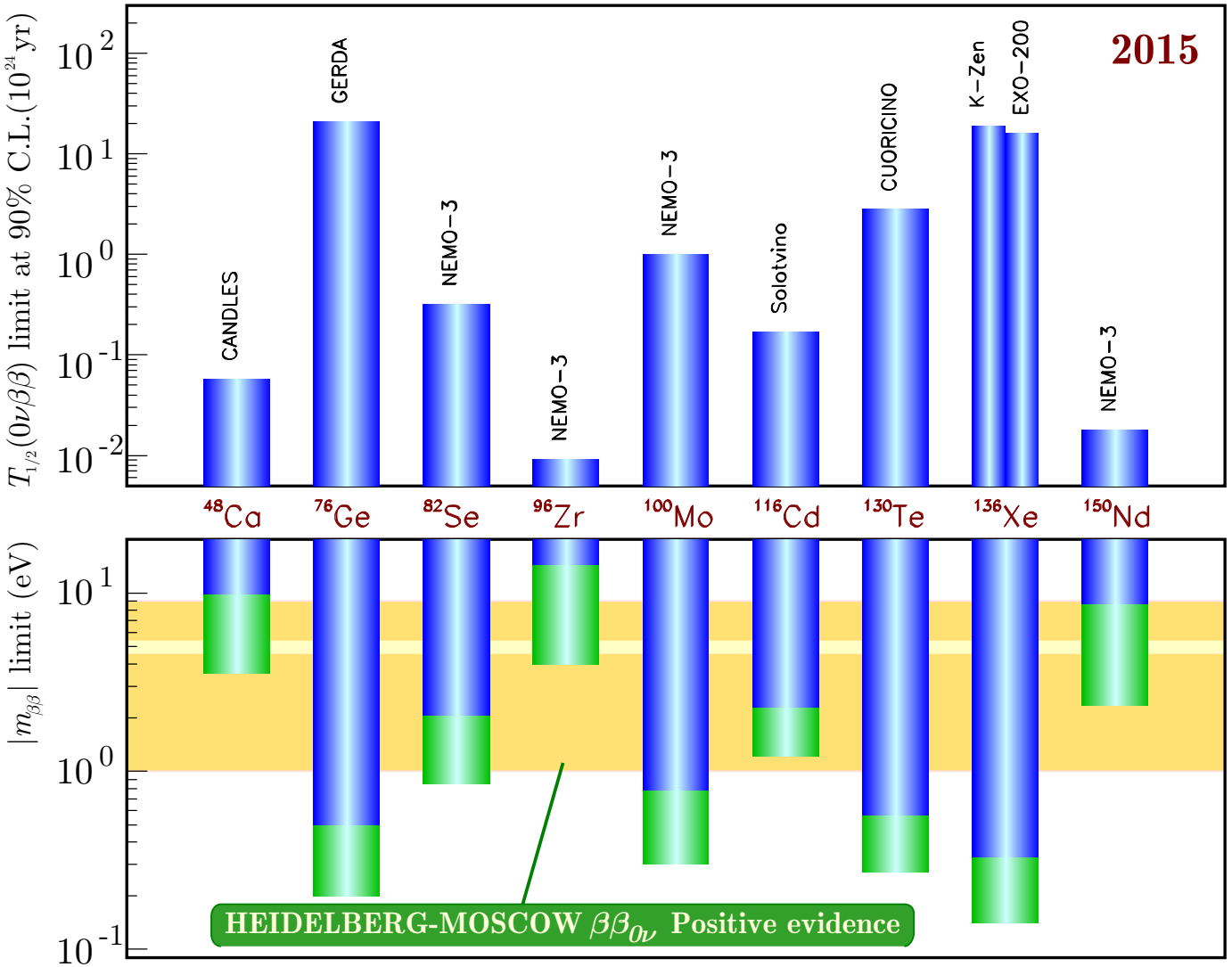

The $0\nu\beta\beta$ half-life limits (90% C.L.) obtained in a variety of experiments (*top panel*) and corresponding minimal and maximal upper limits on the effective Majorana neutrino mass $|m_{\beta\beta}|$ (*bottom panel*) – status on 2015 (data are now somewhat obsolete).

[Adapted from X. Sarazin, "Review of double beta experiments," J. Phys. Conf. Ser. **593** (2015) 012006.]

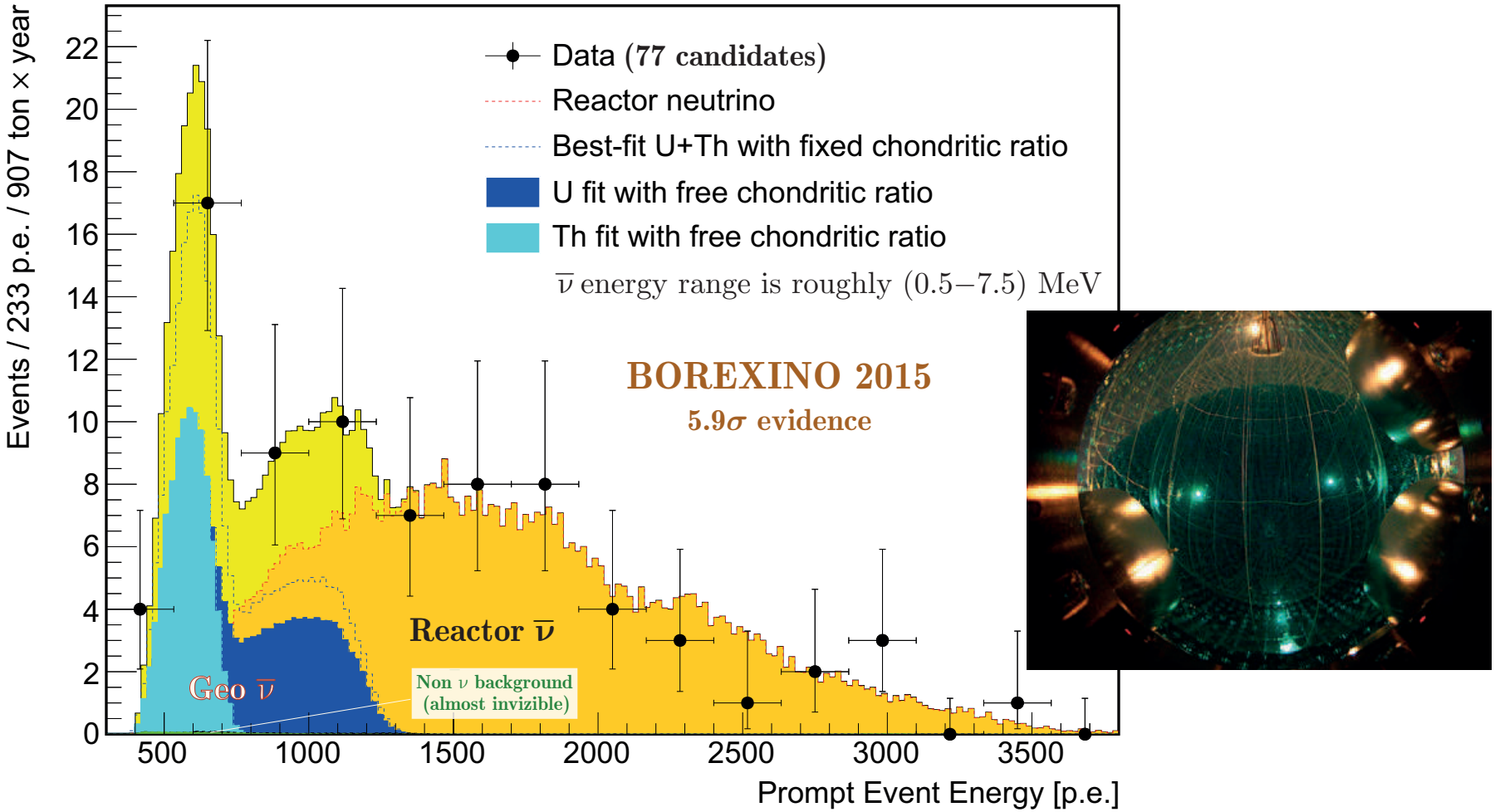

Borexino 2015 result: the prompt light yield spectrum, in units of photoelectrons (p.e.), of geo-$\overline{\nu}_e$ candidates and the best-fit. The best-fit shows the geo- and reactor $\overline{\nu}_e$ spectra (dotted lines) assuming the chondritic ratio. Colored areas show the result of a separate fit with U (blue) and Th (light blue) set as free and independent parameters; cf. with the Borexino 2019 analysis, pp.214, 215.

[M. Agostini *et al.* (Borexino Collaboration), "Spectroscopy of geo-neutrinos from 2056 days of Borexino data," Phys. Rev. D **92** (2015) 031101(R), arXiv:1506.04610 [hep-ex].]

F Multi-packet states (Sect. 17.6, p. 555).

- The multi-packet state can be written in two forms:

$$| \{\mathbf{p}, s, x\}_n\rangle = \left(\prod_{i=1}^{n} 2E_{\mathbf{p}_i}\right)^{1/2} A^\dagger_{\mathbf{p}_1 s_1}(x_1) A^\dagger_{\mathbf{p}_2 s_2}(x_2) \cdots A^\dagger_{\mathbf{p}_n s_n}(x_n)|0\rangle \tag{185a}$$

and

$$| \{\mathbf{p}, s, x\}_n\rangle = (\pm 1)^{n(n-1)/2} \left(\prod_{i=1}^{n} 2E_{\mathbf{p}_i}\right)^{1/2} A^\dagger_{\mathbf{p}_n s_n}(x_n) \cdots A^\dagger_{\mathbf{p}_2 s_2}(x_2) A^\dagger_{\mathbf{p}_1 s_1}(x_1)|0\rangle, \tag{185b}$$

where the sign "+" ("−") is for bosons (fermions). Let us check the equivalence of these definitions. It is evident for $n = 1, 2$. For $n \geq 2$ we obtain after n successive permutations:

$$| \{\mathbf{p}, s, x\}_{n+1}\rangle = (\pm 1)^{n} \left(\prod_{i=1}^{n+1} 2E_{\mathbf{p}_i}\right)^{1/2} A^\dagger_{\mathbf{p}_{n+1} s_{n+1}}(x_{n+1}) A^\dagger_{\mathbf{p}_1 s_1}(x_1) \cdots A^\dagger_{\mathbf{p}_n s_n}(x_n)|0\rangle.$$

Assuming validity of Eq. (185b), the right-hand part of the last equality can be written as

$$(\pm 1)^{n+n(n-1)/2} \left(\prod_{i=1}^{n+1} 2E_{\mathbf{p}_i}\right)^{1/2} A^\dagger_{\mathbf{p}_{n+1} s_{n+1}}(x_{n+1}) A^\dagger_{\mathbf{p}_n s_n}(x_n) \cdots A^\dagger_{\mathbf{p}_1 s_1}(x_1)|0\rangle.$$

Since $(-1)^{n+n(n-1)/2} = (-1)^{-n+n(n-1)/2} = (-1)^{n(n+1)/2} = (-1)^{(n+1)[(n+1)-1]/2}$, the equality (185b) is proved by induction on n.

• Let's now prove Eq. (63), p. 556. It is obviously satisfied for $n = 1$.

By direct calculation one checks that

$$\begin{aligned} M_2 &\equiv \langle \mathbf{q}_1, r_1, y_1; \mathbf{q}_2, r_2, y_2 | \mathbf{p}_1, s_1, x_1; \mathbf{p}_2, s_2, x_2 \rangle \\ &= \exp\left[i\left(q_1 y_1 + q_2 y_2 - p_1 x_1 - p_2 x_2\right)\right] \\ &\quad \times \left[\delta_{s_1 r_1}\delta_{s_2 r_2}\mathcal{D}(\mathbf{p}_1, \mathbf{q}_1; x_1 - y_1)\mathcal{D}(\mathbf{p}_2, \mathbf{q}_2; x_2 - y_2)\right. \\ &\quad \left. \pm\delta_{s_1 r_2}\delta_{s_2 r_1}\mathcal{D}(\mathbf{p}_1, \mathbf{q}_2; x_1 - y_2)\mathcal{D}(\mathbf{p}_2, \mathbf{q}_1; x_2 - y_1)\right] \\ &= \exp\left[i\sum_{i=1}^{2}\left(q_i y_i - p_i x_i\right)\right] |\mathbb{D}_2|, \end{aligned}$$

that is, Eq. (63) is satisfied also for $n = 2$. Now we calculate the matrix element $M_{n+1} \equiv \langle \{\mathbf{q}, r, y\}_{n+1} \,|\, \{\mathbf{p}, s, x\}_{n+1} \rangle$ for $n \geq 2$. According to Eq. (185b),

$$\begin{aligned} M_{n+1} &= \left(\prod_{i=1}^{n+1} 4E_{\mathbf{q}_i}E_{\mathbf{p}_i}\right)^{1/2} \langle 0|A_{\mathbf{q}_{n+1}r_{n+1}}(y_{n+1})\cdots A_{\mathbf{q}_2 r_2}(y_2)A_{\mathbf{q}_1 r_1}(y_1) \\ &\quad \times A^\dagger_{\mathbf{p}_1 s_1}(x_1)A^\dagger_{\mathbf{p}_2 s_2}(x_2)\cdots A^\dagger_{\mathbf{p}_{n+1}s_{n+1}}(x_{n+1})|0\rangle \\ &= \left(\prod_{i=1}^{n+1} 4E_{\mathbf{q}_i}E_{\mathbf{p}_i}\right)^{1/2} \langle 0|A_{\mathbf{q}_1 r_1}(y_1)\cdots A_{\mathbf{q}_n r_n}(y_n)A_{\mathbf{q}_{n+1}r_{n+1}}(y_{n+1}) \\ &\quad \times A^\dagger_{\mathbf{p}_{n+1}s_{n+1}}(x_{n+1})A^\dagger_{\mathbf{p}_n s_n}(x_n)\cdots A^\dagger_{\mathbf{p}_1 s_1}(x_1)|0\rangle. \end{aligned}$$

Then, after successive permutations of the operator $A^{\dagger}_{\mathbf{p}_{n+1}s_{n+1}}(x_{n+1})$ with the operators $A_{\mathbf{q}_n r_n}(y_n)$, …, $A_{\mathbf{q}_1 r_1}(y_1)$, by applying Eq. (63) for the n-packet matrix elements, and taking into account the (anti)commutation relation (61c), p. 551, we obtain

$$
\begin{aligned}
M_{n+1} = & \left(\prod_{i=1}^{n+1} 4E_{\mathbf{q}_i} E_{\mathbf{p}_i} \right)^{1/2} \sum_{j=1}^{n+1} (\pm 1)^{n+j+1} \delta_{s_{n+1} r_j} \exp\left[i(q_j y_j - p_{n+1} x_{n+1}) \right] \\
& \times \left(4E_{\mathbf{q}_j} E_{\mathbf{p}_{n+1}} \right)^{-1/2} \mathcal{D}\left(\mathbf{p}_{n+1}, \mathbf{q}_j; x_{n+1} - y_j \right) \\
& \times \langle 0 | A_{\mathbf{q}_1 r_1}(y_1) \cdots A_{\mathbf{q}_{j-1} r_{j-1}}(y_{j-1}) A_{\mathbf{q}_{j+1} r_{j+1}}(y_{j+1}) \cdots \\
& \cdots A_{\mathbf{q}_n r_n}(y_n) A_{\mathbf{q}_{n+1} r_{n+1}}(y_{n+1}) A^{\dagger}_{\mathbf{p}_n s_n}(x_n) \cdots A^{\dagger}_{\mathbf{p}_1 s_1}(x_1) | 0 \rangle .
\end{aligned}
$$

The right-hand part of this relation can be rewritten in compact form as

$$
\exp\left[i \sum_{i=1}^{n+1} (q_i y_i - p_i x_i) \right] \sum_{j=1}^{n+1} (\pm 1)^{n+j+1} \delta_{s_{n+1} r_j} \mathcal{D}\left(\mathbf{p}_{n+1}, \mathbf{q}_j; x_{n+1} - y_j \right) |\mathbb{D}^{(j)}_{n+1}|,
$$

where $|\mathbb{D}^{(j)}_{n+1}|$ is the minor of order n of $|\mathbb{D}_{n+1}|$ obtained after deleting from the latter the $(n+1)$-th row and j-th column. The sum over j in the last expression just represents the minor expansion of $|\mathbb{D}_{n+1}|$ over the bottom [$(n+1)$-th] row, hence

$$
M_{n+1} = \exp\left[i \sum_{i=1}^{n+1} (q_i y_i - p_i x_i) \right] |\mathbb{D}_{n+1}|.
$$

This completes the proof by induction.

G Gaussian integration in Minkowski spacetime.

We are frequently dealing with the Gaussian integrals

$$\mathcal{G}(A,B) = \int dx \exp\left(-A_{\mu\nu}x^\mu x^\nu + B_\mu x^\mu\right), \tag{186}$$

where $A = ||A_{\mu\nu}||$ is a symmetric and positive-definite matrix and B_μ are some complex constants. While these integrals are well known we reconsider this issue here, because there is some confusion in the literature concerning the correct definition of the matrix inverse to A in Minkowski space. In our case $A_{\mu\nu}$ and B_μ form, respectively, a tensor and 4-vector, though this fact is not used below. Moreover, the main steps of the subsequent derivation are not affected by the space-time dimension and signature.

The matrix A can always be diagonalized by an orthogonal transformation $O = ||O_{\mu\nu}||$:

$$A_{\mu\nu} = \sum_\alpha a_\alpha O_{\mu\alpha}O_{\nu\alpha}, \quad \sum_\alpha O_{\mu\alpha}O_{\nu\alpha} = \delta_{\mu\nu}, \tag{187}$$

where $a_\alpha > 0$ are the eigenvalues of A. Taking this into account, the quadratic form in the integrand of Eq. (186) can be rewritten as

$$\begin{aligned} -A_{\mu\nu}x^\mu x^\nu + B_\mu x^\mu &= -\sum_\alpha a_\alpha \left(O_{\mu\alpha}x^\mu\right)\left(O_{\nu\alpha}x^\nu\right) + B_\mu x^\mu \\ &= \sum_\alpha \left(-a_\alpha y_\alpha^2 + \sum_\mu B_\mu O_{\mu\alpha} y_\alpha\right), \end{aligned} \tag{188}$$

where $y_\alpha = O_{\mu\alpha}x^\mu$ (and thus $x^\mu = \sum_\alpha O_{\mu\alpha}y_\alpha$).

The Jacobian of this transformation is $|O| = 1$, hence $dx = dy$. Substituting Eq. (188) into (186) reduces it to the standard Gaussian quadratures:

$$\mathcal{G}(A,B) = \prod_\alpha \sqrt{\frac{\pi}{a_\alpha}} \exp\left[\frac{1}{4a_\alpha}\left(\sum_\mu B_\mu O_{\mu\alpha}\right)^2\right].$$

According to Eq. (187)

$$\sum_\alpha a_\alpha^{-1} O_{\mu\alpha} O_{\nu\alpha} = \left(A^{-1}\right)_{\mu\nu} \stackrel{\text{def}}{=} \widetilde{A}^{\mu\nu} \quad \text{and} \quad \prod_\alpha a_\alpha = |A|.$$

Therefore, for the 4D Minkowski space-time

$$\mathcal{G}(A,B) = \frac{\pi^2}{\sqrt{|A|}} \exp\left[\frac{1}{4}\sum_{\mu\nu}\left(A^{-1}\right)_{\mu\nu} B_\mu B_\nu\right] = \frac{\pi^2}{\sqrt{|A|}} \exp\left(\frac{1}{4}\widetilde{A}^{\mu\nu} B_\mu B_\nu\right). \tag{189}$$

Note that $\widetilde{A} = gA^{-1}g$ and thus $|\widetilde{A}| = 1/|A| = \prod_\alpha a_\alpha^{-1}$. Therefore the matrix $\widetilde{A}$ is positive-definite and of course symmetric.

H Stationary point (Sect. 18.1.1).

H.1 General case.

Here we describe a method for solving Eq. (110) in the most general case, i.e., for arbitrary configuration of the external momenta. The general solution is of interest both from a methodological point of view and for the practical summation of the diagrams with non(sub)relativistic and (ultra)relativistic neutrinos.[a] Although the proposed algorithm is somewhat cumbersome, it can easily be used in (semi)numerical analysis.

It is convenient to work with Eq. (110) written in the form

$$m_j \left[R - (\mathbf{Rl}) \frac{(1-v_j)^2}{v_j} \right] = \left[Y_0 - \frac{(\mathbf{Yl})}{v_j} \right] \sqrt{1-v_j^2}, \tag{190}$$

in which the unknown quantity is the virtual neutrino velocity v_j. Squaring both parts of the above equation we obtain the fourth-order algebraic equation

$$v^4 + c_3 v^3 + c_2 v^2 + c_1 v + c_0 = 0, \tag{191}$$

whose coefficients have the form

$$c_0 = \frac{(\mathbf{Rl})^2 - (\boldsymbol{\eta}\mathbf{l})^2}{(\mathbf{Rl})^2 + \eta_0^2}, \qquad c_1 = -2\frac{R(\mathbf{Rl}) + 2(\mathbf{Rl})^2 - \eta_0(\boldsymbol{\eta}\mathbf{l})}{(\mathbf{Rl})^2 + \eta_0^2},$$

$$c_2 = \frac{R^2 + 6(\mathbf{Rl})^2 + 4R(\mathbf{Rl}) + (\boldsymbol{\eta}\mathbf{l})^2 - \eta_0^2}{(\mathbf{Rl})^2 + \eta_0^2}, \qquad c_3 = -2\frac{R(\mathbf{Rl}) + 2(\mathbf{Rl})^2 + \eta_0(\boldsymbol{\eta}\mathbf{l})}{(\mathbf{Rl})^2 + \eta_0^2}.$$

Here $\eta_\mu = Y_\mu/m_j$; hereinafter in this section it is assumed that $m_j > 0$ (the case of a massless neutrino is trivial), and the index j, numbering the neutrino eigenfields, is omitted in order not to overload the formulas. All other notations are the same as in the main text.

[a] The case is of interest, in particular, for studying the relic neutrinos and mixing with heavy sterile neutrinos.

The solution of Eq. (191) can be found by the Descartes-Euler method.[a] Following this method, we transform Eq. (191) to the so-called "depressed" form:

$$\left(v+\frac{c_3}{4}\right)^4+\widetilde{c}_2\left(v+\frac{c_3}{4}\right)^2+\widetilde{c}_1\left(v+\frac{c_3}{4}\right)+\widetilde{c}_0=0; \tag{192}$$

the explicit form of the coefficients c_i and $\widetilde{c}_i$ we will not need for the following. Solutions of this equation are constructed from the roots of the cubic equation

$$z^3+a_2z^2+a_1z+a_0=0, \tag{193}$$

in which

$$a_0=-\frac{\widetilde{c}_1^2}{64},\quad a_1=\frac{\widetilde{c}_2^2-4\widetilde{c}_0}{16},\quad a_2=\frac{\widetilde{c}_2}{2}.$$

Equation (193) can also be identically transformed to the "depressed cubic" form (the Cardano form):

$$\left(z+\frac{a_2}{3}\right)^3+\mathfrak{p}\left(z+\frac{a_2}{3}\right)+\mathfrak{q}=0.$$

The following notations are used here:

$$\mathfrak{p}=a_1-\frac{a_2^2}{3}=-\frac{\left[R^2+4R(\mathbf{Rl})-\eta_0^2+(\boldsymbol{\eta}\mathbf{l})^2\right]^2}{48\left[(\mathbf{Rl})^2+\eta_0^2\right]^2},$$

$$\mathfrak{q}=a_0-\frac{a_1a_2}{3}+2\left(\frac{a_2}{3}\right)^3=-\frac{A}{864\left[(\mathbf{Rl})^2+\eta_0^2\right]^3},$$

[a] See, e.g., G. A. Korn & Th. M. Korn, "Mathematical handbook for scientists and engineers," 2nd enlargend and revised edition, McGraw-Hill Book Company, New York, San Francisco, Toronto, London, Sydney, 1968; Russian translation: Г. Корн, Т. Корн. «Справочник по математике для научных работников и инженеров». Москва, «Наука», 1973.

$$A = A_0 + A_1(\mathbf{Rl}) + A_2(\mathbf{Rl})^2 + A_3(\mathbf{Rl})^3,$$

$$A_0 = R^6 - 3\left[\eta_0^2 - (\boldsymbol{\eta}\mathbf{l})^2\right]R^4 + 3\left[\eta_0^4 + 16\eta_0^2(\boldsymbol{\eta}\mathbf{l})^2 + (\boldsymbol{\eta}\mathbf{l})^4\right]R^2 - \left[\eta_0^2 - (\boldsymbol{\eta}\mathbf{l})^2\right]^3,$$

$$A_1 = 12R\left\{R^4 - 2\left[\eta_0^2 - (\boldsymbol{\eta}\mathbf{l})^2\right]R^2 + \left[\eta_0^2 - 7\eta_0(\boldsymbol{\eta}\mathbf{l}) + (\boldsymbol{\eta}\mathbf{l})^2\right](\eta l)^2\right\},$$

$$A_2 = 48R^2\left[R^2 - \eta_0^2 + (\boldsymbol{\eta}\mathbf{l})^2\right] + 54(\eta l)^4,$$

$$A_3 = 64R^3.$$

The number of real roots is determined by the sign of the function

$$\mathfrak{B} = \frac{\mathfrak{q}^2}{4} + \frac{\mathfrak{p}^3}{27} = \frac{\left[\eta_0(\boldsymbol{\eta}\mathbf{l})R - (\eta l)^2(\mathbf{Rl})\right]^2 B}{27648\left[(\mathbf{Rl})^2 + \eta_0^2\right]^6},$$

obviously coinciding with the sign of the polynomial

$$B = B_0 + B_1(\mathbf{Rl}) + B_2(\mathbf{Rl})^2 + B_3(\mathbf{Rl})^3,$$

whose coefficients have the form

$$B_0 = R^6 - 3\left[\eta_0^2 - (\boldsymbol{\eta}\mathbf{l})^2\right]R^4 + 3\left[\eta_0^4 + 7\eta_0^2(\boldsymbol{\eta}\mathbf{l})^2 + (\boldsymbol{\eta}\mathbf{l})^4\right]R^2 - \left[\eta_0^2 - (\boldsymbol{\eta}\mathbf{l})^2\right]^3,$$

$$B_1 = 6R\left\{2R^4 - 4\left[\eta_0^2 - (\boldsymbol{\eta}\mathbf{l})^2\right]R^2 + \left[2\eta_0 - (\boldsymbol{\eta}\mathbf{l})\right]\left[\eta_0 - 2(\boldsymbol{\eta}\mathbf{l})\right](\eta l)^2\right\},$$

$$B_2 = 48R^2\left[R^2 - \eta_0^2 + (\boldsymbol{\eta}\mathbf{l})^2\right] + 27(\eta l)^4,$$

$$B_3 = 64R^3.$$

Namely, for $B < 0$ there are three different real roots, for $B > 0$ there is one real and a pair of mutually conjugate complex roots; at $B = 0$ two or all three real roots may coincide (case of degeneracy). The following useful identity linking A and B can be proved:

$$A = B + 27\left[\eta_0(\boldsymbol{\eta}\mathbf{l})R - (\eta l)^2(\mathbf{Rl})\right]^2. \tag{194}$$

H.1.1 Ferro-Tartaglia-Cardano solution in terms of radicals.

The roots of the depressed cubic equation (193) are

$$z_0 = a + (A_+ + A_-), \quad z_\pm = a - \frac{1}{2}(A_+ + A_-) \pm i\frac{\sqrt{3}}{2}(A_+ - A_-),$$

where

$$a = \frac{a_2}{3} = -\frac{C_0 + C_1(\mathbf{Rl}) + C_2(\mathbf{Rl})^2 + C_3(\mathbf{Rl})^3}{12\left[(\mathbf{Rl})^2 + \eta_0^2\right]^2},$$

$$\begin{aligned} A_\pm^3 &= -\frac{\mathfrak{q}}{2} \pm \sqrt{\mathfrak{B}} \\ &= \frac{A/18 \pm i^\delta \left|\eta_0(\boldsymbol{\eta}\mathbf{l})R - (\eta l)^2(\mathbf{Rl})\right| \sqrt{|B|/3}}{96\left[(\mathbf{Rl})^2 + \eta_0^2\right]^3}; \end{aligned}$$

$$\begin{aligned} C_0 &= -\eta_0^2\left[2R^2 - 2\eta_0^2 - (\boldsymbol{\eta}\mathbf{l})^2\right], \\ C_1 &= -2\eta_0\left[4\eta_0 - 3(\boldsymbol{\eta}\mathbf{l})\right]R, \\ C_2 &= R^2 - 2(\eta l)\left[5\eta_0 - (\boldsymbol{\eta}\mathbf{l})\right], \\ C_3 &= 4R; \end{aligned}$$

$\delta = 0$ at $B \geq 0$ and $\delta = 1$ at $B < 0$.

The expression for $A_\pm$ is somewhat simplified by taking into account the identity (194):

$$A_\pm = \frac{1}{12\left[(\mathbf{Rl})^2 + \eta_0^2\right]}\left[3\sqrt{3}\left|\eta_0(\boldsymbol{\eta}\mathbf{l})R - (\eta l)^2(\mathbf{Rl})\right| \pm i^\delta\sqrt{|B|}\right]^{2/3}.$$

H.1.2 Viète solution in trigonometric form.

For completeness, we also give a more compact trigonometric form of the solution (the Viet form) which may turn out to be more convenient for numerical calculations and in any case is useful to control the accuracy of calculations by comparison with the canonical solution. The explicit form of the trigonometric solution depends on the sign of the function B.

Case $B < 0$. As already noted, in this case (sometimes called "irreducible"), Eq. (193) has three real roots:

$$z_0 = a + \zeta_0 \cos\frac{\alpha}{3}, \quad z_\pm = a - \zeta_0 \cos\left(\frac{\alpha \pm \pi}{3}\right),$$

where

$$\zeta_0 = \frac{\left|R^2 + 4R(\mathbf{Rl}) - \eta_0^2 + (\boldsymbol{\eta}\mathbf{l})^2\right|}{6\left[(\mathbf{Rl})^2 + \eta_0^2\right]}, \quad \cos\alpha = -\frac{A}{\left|R^2 + 4R(\mathbf{Rl}) - \eta_0^2 + (\boldsymbol{\eta}\mathbf{l})^2\right|^3}.$$

Case $B \geq 0$. In this case Eq. (193) has one real and two complex roots. Let's introduce notations:

$$\tan\alpha' = \sqrt[3]{\tan\frac{\beta}{2}}, \quad \sin\beta = -\frac{4}{\cos\alpha} = \frac{4}{A}\left|R^2 + 4R(\mathbf{Rl}) - \eta_0^2 + (\boldsymbol{\eta}\mathbf{l})^2\right|^3, \quad |\beta| \leq \frac{\pi}{2}$$

(in all cases the real value of the cube root is chosen). Then the roots are

$$z_0 = a - \zeta_0 \operatorname{cosec} 2\alpha', \quad z_\pm = a + \frac{\zeta_0}{2}\left(\operatorname{cosec} 2\alpha' \pm i\sqrt{3}\cot 2\alpha'\right), \quad |\alpha'| \leq \frac{\pi}{4}.$$

H.1.3 Roots of Eq. (191).

The roots of the depressed fourth-degree equation (192) are given by combinations

$$\Xi_n = \pm\sqrt{z_-} \pm \sqrt{z_0} \pm \sqrt{z_+},$$

in which four of eight possible combinations of signs are chosen so that the following condition is satisfied:

$$-\sqrt{z_-}\sqrt{z_0}\sqrt{z_+} = \frac{\widetilde{c}_1}{8} = \frac{D_0 + D_1(\mathbf{Rl}) + D_2(\mathbf{Rl})^2 + D_3(\mathbf{Rl})^3 + D_4(\mathbf{Rl})^4}{8\left[(\mathbf{Rl})^2 + \eta_0^2\right]^3}.$$

The notation used here is:

$$\begin{aligned}
D_0 &= \eta_0^3(\boldsymbol{\eta}\mathbf{l})\left(R^2 + \eta_0^2\right), \\
D_1 &= \eta_0^2\left[R^2 - 3\eta_0^2 + 4\eta_0(\boldsymbol{\eta}\mathbf{l}) - 2(\boldsymbol{\eta}\mathbf{l})^2\right] R, \\
D_2 &= \eta_0\left\{2\left[3\eta_0 - (\boldsymbol{\eta}\mathbf{l})\right] R^2 - (\eta l)\left[6\eta_0^2 - 3\eta_0(\boldsymbol{\eta}\mathbf{l}) + (\boldsymbol{\eta}\mathbf{l})^2\right]\right\}, \\
D_3 &= \left[9\eta_0^2 - 8\eta_0(\boldsymbol{\eta}\mathbf{l}) + (\boldsymbol{\eta}\mathbf{l})^2\right] R, \\
D_4 &= 2(\eta l)^2.
\end{aligned}$$

All four roots of Eq. (191) can now be found by the formula

$$v_n = \Xi_n - c_3/4 \quad (n = 1, 2, 3, 4).$$

The only real nonnegative root of interest corresponding to the stationary point, must satisfy the condition of positivity of the second derivative (112).

H.2 Stationary point in ultrarelativistic case.

Consider configurations of the external WP momenta for which the following conditions are satisfied:

$$q_s^0 \sim -q_d^0 \sim |\mathbf{q}_s| \sim |\mathbf{q}_d|. \tag{195}$$

This case is realized in all modern neutrino experiments and is therefore of most practical interest.

In the plane-wave limit ($\sigma_\varkappa = 0$, $\forall\varkappa$) and in the massless neutrino approximation ($m_j = 0$),[a] the energy-momentum conservation in each vertex of the macrodiagram requires strict equalities

$$q_s^0 = -q_d^0, \quad \mathbf{q}_s = -\mathbf{q}_d = q_s^0\mathbf{l}.$$

Thus, according to Eqs. (108) and (111), the root of Eq. (110) is

$$q_0 = \lim_{\sigma_\varkappa = 0,\, \forall\varkappa} \frac{Y_0 - (\mathbf{Yl})}{R} = q_s^0 \qquad [\mathrm{PW}_0\text{-limit}] \tag{196}$$

and is nothing but the energy of the real massless neutrino ($q_j = E_0 l$, $q_j^2 = 0$).

In the more general case $\sigma_\varkappa \neq 0$, under the conditions (195) and under the natural additional assumption that the neutrino masses m_j are small compared to the minimum absolute energy transfers $|q_s^0| \sim |q_d^0|$ in the vertices of the diagram, i.e.,

$$m_j \ll \min(q_s^0) \quad \text{and} \quad m_j \ll \min|q_d^0|, \tag{197}$$

the solution (110) can be found as a series in powers of the dimensionless parameter $r_j = m_j^2/2E_\nu^2$.

[a] Hereinafter we will call this special (in fact model) case "PW_0-limit".

- In inequalities (197), it is assumed that the minimum is taken over the entire set of the most probable momenta $\mathbf{p}_\varkappa$ of external packets in the source and detector, which is determined by the conditions of the particular experiment.[a]
- In the definition of the parameter r_j there is a representative (effective) energy of the virtual neutrino,

$$E_\nu = \frac{(Yl)}{R} = \frac{\left(\widetilde{\Re}_s^{\mu\nu} q_{s\nu} - \widetilde{\Re}_d^{\mu\nu} q_{d\nu}\right) l_\mu}{\left(\widetilde{\Re}_s^{\mu\nu} + \widetilde{\Re}_d^{\mu\nu}\right) l_\mu l_\nu}, \tag{198}$$

which coincides with the energy transfer q_s^0 in the PW_0-limit and is close to it in magnitude at sufficiently small $\sigma_\varkappa$ Let's consider this variable in more detail. We introduce the 4-vectors

$$\Delta_s = (\Delta_s^0, \boldsymbol{\Delta}_s) = q_s - \frac{1}{2}\left(q_s^0 + |q_d^0|\right) l \quad \text{and} \quad \Delta_d = (\Delta_d^0, \boldsymbol{\Delta}_d) = -q_d - \frac{1}{2}\left(q_s^0 + |q_d^0|\right) l,$$

$l = (1, \mathbf{l})$, $|\mathbf{l}| = 1$. In the component-wise notation

$$\Delta_s^0 = -\Delta_d^0 = \frac{1}{2}\left(q_s^0 - |q_d^0|\right), \quad \boldsymbol{\Delta}_s = \mathbf{q}_s - \frac{1}{2}\left(q_s^0 + |q_d^0|\right)\mathbf{l}, \quad \boldsymbol{\Delta}_d = -\mathbf{q}_d - \frac{1}{2}\left(q_s^0 + |q_d^0|\right)\mathbf{l}.$$

Clearly $|\Delta_{s,d}^0| \ll |q_{s,d}^0|$ and $|\boldsymbol{\Delta}_{s,d}^0| \ll |\mathbf{q}_{s,d}| \sim |q_{s,d}^0|$. Then, according to Eq. (198),

$$E_\nu = \frac{q_s^0 + |q_d^0|}{2} + \frac{\left(\widetilde{\Re}_s^{\mu\nu} \Delta_{s\nu} + \widetilde{\Re}_d^{\mu\nu} \Delta_{d\nu}\right) l_\mu}{\left(\widetilde{\Re}_s^{\mu\nu} + \widetilde{\Re}_d^{\mu\nu}\right) l_\mu l_\nu} \approx \frac{q_s^0 + |q_d^0|}{2}.$$

[a] Actually, this is not a very strict definition, but its physical meaning is clear if the momentum distributions of wave packets in the source and detector (understood as macroscopic devices) are narrow enough.

- According to definition (198), E_ν is a rotation-invariant function of momenta, masses, and momentum dispersions of all external wave packets. Due to the approximate energy-momentum conservation, $E_\nu > 0$ and is transformed as zero component of a 4-momentum.

So let's write the quantities q_0 and $|\mathbf{q}_j| = \sqrt{q_0^2 - m_j^2}$ (naturally treated as energy and 3-momentum value of the virtual neutrino ν_j) as a power series

$$q_0 \equiv E_j = E_\nu \left(1 - \sum_{n=1}^{\infty} C_n^E r_j^n\right), \quad |\mathbf{q}_j| \equiv P_j = E_\nu \left(1 - \sum_{n=1}^{\infty} C_n^P r_j^n\right). \tag{199}$$

It is convenient to rewrite Eq. (110) in the following form:

$$q_0|\mathbf{q}_j| - \mathfrak{m}\,(q_0 - |\mathbf{q}_j|)^2 - E_\nu\,[(\mathfrak{n}+1)|\mathbf{q}_j| - \mathfrak{n}q_0] = 0. \tag{200}$$

This equation contains dimensionless rotationally invariant functions

$$\mathfrak{n} = \frac{(\mathbf{Yl})}{(Yl)} \quad \text{and} \quad \mathfrak{m} = \frac{(\mathbf{Rl})}{R}.$$

From Eq. (200) we see that the coefficients C_n^E and C_n^P for all $n \geq 1$ are expressed only through these two functions. The coefficients are easily found for any finite order on r_j using the standard recurrence procedure, i.e., by substituting the series (199) into Eq. (200), decomposing the resulting series into a series on powers of r_j and equating the factors at each power of r_j to zero. Let us write out here the first three pairs:

$$\begin{aligned}
C_1^E &= \mathfrak{n}, & C_1^P &= \mathfrak{n}+1,\\
C_2^E &= \mathfrak{n}\left(2\mathfrak{n}+\frac{3}{2}\right) - \mathfrak{m}, & C_2^P &= (\mathfrak{n}+1)\left(2\mathfrak{n}+\frac{1}{2}\right) - \mathfrak{m},\\
C_3^E &= \mathfrak{n}\left(7\mathfrak{n}^2+9\mathfrak{n}+\frac{5}{2}\right) - (5\mathfrak{n}+2)\mathfrak{m}, & C_3^P &= (\mathfrak{n}+1)\left(7\mathfrak{n}^2+5\mathfrak{n}+\frac{1}{2}\right) - (5\mathfrak{n}+3)\mathfrak{m}.
\end{aligned} \tag{201}$$

It is easy to prove that the coefficients satisfy the symmetry relation $C_n^P = (-1)^n C_n^E\big|_{\mathfrak{n} \longmapsto -(\mathfrak{n}+1)}$ for all n.

Thus, the quantities E_j and $\mathbf{p}_j = P_j\mathbf{l}$ are naturally interpreted as, respectively, effective (or the most probable) energy and momentum of the virtual massive neutrino ν_j. With their help we can also determine the effective velocity of the neutrino $\mathbf{v}_j = v_j\mathbf{l} = \mathbf{p}_j/E_j$, for which we find:

$$v_j = 1 - r_j - \left(2\mathfrak{n} + \frac{1}{2}\right) r_j^2 - \left(7\mathfrak{n}^2 + 5\mathfrak{n} + \frac{1}{2} - 2\mathfrak{m}\right) r_j^3 + \mathcal{O}\left(r_j^4\right). \tag{202}$$

As one would expect, $0 < 1 - v_j \ll 1$, i.e., neutrinos are ultrarelativistic. Since, in addition[a],

$$R = R^{\mu\nu} l_\mu l_\nu = \mathfrak{F} E_\nu^{-2}, \tag{203}$$

where

$$\mathfrak{F} = \left[R^{\mu\nu} q_\mu q_\nu\right]_{q = E_\nu l} > 0, \tag{204}$$

we see that the second derivative (112b) at the point $q_0 = E_j$ is positive and hence the function $F_j(q_0)$ has at this point *absolute minimum*.

Note again that the quantities E_j, $\mathbf{p}_j$, and $\mathbf{v}_j$ are uniquely determined not only by the most probable momenta $\mathbf{p}_\varkappa$ of the external (in and out) WPs in the source and detector, but also their masses and momentum dispersions. In the following, it will be shown by a simple example that the functions $\mathfrak{n}$ and $\mathfrak{m}$ can vary by orders of magnitude in different kinematic regions of the reaction (93). Therefore, the smallness of the parameter r_j generally speaking does not guarantee that the corrections $\propto r_j^2$ (and higher powers) in Eqs. (199) and (202) are small throughout the whole phase space of the reaction. For now we just impose additional conditions

$$|\mathfrak{n}| r_j \ll 1 \quad \text{and} \quad |\mathfrak{m}| r_j \ll |\mathfrak{n}|, \quad \forall j, \tag{205}$$

guaranteeing that the $\mathcal{O}\left(r_j^2\right)$ corrections can be neglected.

[a] Recall that the quadratic forms $\widetilde{\mathfrak{R}}_s^{\mu\nu} q_\mu q_\nu$ and $\widetilde{\mathfrak{R}}_d^{\mu\nu} q_\mu q_\nu$ are positive for arbitrary 4-vector $q \not\equiv 0$.

Particular configurations of external momenta. To illustrate the above results, let us consider a special (simplest) configuration of external momenta,

$$q_s^0 = -q_d^0 \equiv \mathcal{E} > 0, \quad \mathbf{q}_s = -\mathbf{q}_d \equiv \mathcal{P}\mathbf{l}, \quad \mathcal{P} > 0, \tag{206}$$

corresponding to the exact conservation of energy and momentum, tranported from S to D. We will call the variable $\mathcal{Q}^2 = \mathcal{E}^2 - \mathcal{P}^2$ the neutrino virtuality. The ultrarelativistic conditions are now given by the following inequalities:

$$|\mathcal{Q}^2| \ll \mathcal{E}^2 \quad \text{and} \quad m_j^2 \ll \mathcal{E}^2.$$

Note that the virtuality in general does not have to coincide with m_j^2 even in order of magnitude and thus the two conditions are independent.

It is not difficult to show that for the configuration (206)

$$E_\nu = \mathcal{E}\left[1 + \mathfrak{n}_0\left(1 - \frac{\mathcal{P}}{\mathcal{E}}\right)\right], \quad \mathfrak{n} = \mathfrak{n}_0 - \left(1 - \frac{\mathcal{P}}{\mathcal{E}}\right)\left(\mathfrak{n}_0^2 - \frac{\mathscr{R}}{R}\right)\left[1 + \mathfrak{n}_0\left(1 - \frac{\mathcal{P}}{\mathcal{E}}\right)\right]^{-1},$$

where

$$\mathfrak{n}_0 = \frac{(\mathbf{Rl}) - \mathscr{R}}{R} = \mathfrak{m} - \frac{\mathscr{R}}{R} \quad \text{and} \quad \mathscr{R} = R_{kn} l_k l_n. \tag{207}$$

By decomposing E_ν and $\mathfrak{n}$ by the small parameter $\mathcal{Q}^2/\mathcal{E}^2$, we obtain

$$E_\nu = \mathcal{E}\left[1 + \mathfrak{n}_0 \frac{\mathcal{Q}^2}{2\mathcal{E}^2}\left(1 + \frac{\mathcal{Q}^2}{2\mathcal{E}^2} + \frac{\mathcal{Q}^4}{8\mathcal{E}^4} + \dots\right)\right],$$

$$\mathfrak{n} = \mathfrak{n}_0 + \left(\mathfrak{m} - \mathfrak{n}_0 - \mathfrak{n}_0^2\right)\frac{\mathcal{Q}^2}{2\mathcal{E}^2}\left[1 - (2\mathfrak{n}_0 - 1)\frac{\mathcal{Q}^2}{4\mathcal{E}^2} + \left(2\mathfrak{n}_0^2 - 2\mathfrak{n}_0 + 1\right)\frac{\mathcal{Q}^4}{8\mathcal{E}^4} + \dots\right],$$

where, as usual, dots denote corrections of the next orders of smallness. Hence

$$E_\nu \to \mathcal{E} \text{ and } \mathfrak{n} \to \mathfrak{n}_0 \text{ as } \mathcal{Q}^2 \to 0.$$

Re-expanding the above expressions for E_j and P_j in two small (independent) parameters $\mathcal{Q}^2/\mathcal{E}^2$ and $m_j^2/\mathcal{E}^2$ we find:

$$E_j = \mathcal{E} + \frac{\mathcal{Q}^2 - m_j^2}{2\mathcal{E}} \left[\mathfrak{n}_0 \left(1 + \frac{\mathcal{Q}^2}{4\mathcal{E}^2} \right) + \left(4\mathfrak{n}_0^2 + 3\mathfrak{n}_0 - 2\mathfrak{m} \right) \frac{m_j^2}{4\mathcal{E}^2} + \dots \right],$$

$$P_j = \mathcal{P} + \frac{\mathcal{Q}^2 - m_j^2}{2\mathcal{E}} \left[(\mathfrak{n}_0 + 1) \left(1 + \frac{\mathcal{Q}^2}{4\mathcal{E}^2} \right) + \left(4\mathfrak{n}_0^2 + 5\mathfrak{n}_0 - 2\mathfrak{m} + 1 \right) \frac{m_j^2}{4\mathcal{E}^2} + \dots \right].$$

This shows, in particular, that the effective energy (momentum) of the neutrino can be either bigger or smaller than the transferred energy $\mathcal{E}$ (transferred momentum $\mathcal{P}$);

- Naturally, $E_j = \mathcal{E}$ and $P_j = \mathcal{P}$ for $\mathcal{Q}^2 = m_j^2$ (and only in this case).

In other words, even with the precise balance of the transferred 4-momenta at the vertices of the macrodiagram, the effective 4-momentum of the virtual neutrino $(E_j, P_j \mathbf{l})$ generally does not coincide with the 4-vector $(\mathcal{E}, \mathcal{P}\mathbf{l})$.

The expansion for the effective neutrino velocity has the form

$$v_j = 1 - \frac{m_j^2}{2\mathcal{E}^2} \left[1 - \mathfrak{n}_0 \frac{\mathcal{Q}^2}{\mathcal{E}^2} + (4\mathfrak{n}_0 + 1) \frac{m_j^2}{4\mathcal{E}^2} + \dots \right],$$

so that the main correction to the ultrarelativistic limit, $v_j \to 1$, does not depend on the neutrino virtuality.

H.3 Stationary point in nonrelativistic case.

Let's now consider the opposite case, corresponding to the following configuration of external momenta:

$$q_s^0 \sim -q_d^0 \sim m_j \gg |\mathbf{q}_s| \sim |\mathbf{q}_d|. \tag{208}$$

This case is of potential interest for experiments to study (so far hypothetical) heavy neutrinos. And, of course, it is important for studying the relic neutrinos.

As in the general case, we'll use Eq. (190) written in terms of the virtual neutrino velocity. Let's introduce the dimensionless 4-vector $\varrho_j = (\varrho_j^0, \boldsymbol{\varrho}_j)$ with components

$$\varrho_j^\mu = \frac{1}{\mathscr{R}}\left(R_0^\mu - \frac{1}{m_j}Y^\mu\right). \tag{209}$$

It is easy to see that these components are small in absolute value when conditions (208) are satisfied. Indeed, by substituting into the definition (209) the expression for the 4-vector Y, which in a component-wise notation has the form

$$Y^\mu = \widetilde{\mathfrak{R}}_s^{\mu 0} q_s^0 - \widetilde{\mathfrak{R}}_d^{\mu 0} q_d^0 + \widetilde{\mathfrak{R}}_s^{\mu k} q_s^k - \widetilde{\mathfrak{R}}_d^{\mu k} q_d^k,$$

we obtain:

$$\varrho_j^\mu = \frac{1}{m_j \mathscr{R}}\left[\widetilde{\mathfrak{R}}_s^{\mu 0}\left(m_j - q_s^0\right) + \widetilde{\mathfrak{R}}_d^{\mu 0}\left(m_j + q_d^0\right) - \widetilde{\mathfrak{R}}_s^{\mu k} q_s^k + \widetilde{\mathfrak{R}}_d^{\mu k} q_d^k\right]. \tag{210}$$

Since all the terms in Eq. (210) contain small multipliers ($1 - q_s^0/m_j$, q_s^k/m_j, etc.) we conclude that $|\varrho_{j\mu}| \ll 1$.

Taking this into account, we'll search for the solution of Eq. (190) as the double power series

$$v_j = \bar{v}_j \left[1 + \sum_{n=1}^{\infty} \sum_{m=0}^{\infty} C_{nm}^{(v)} (\boldsymbol{\varrho}_j \mathbf{l})^n \varrho_{j0}^m \right], \tag{211}$$

in which

$$\bar{v}_j = \frac{(\boldsymbol{\varrho}_j \mathbf{l})}{1 + \varrho_{j0}}.$$

Let's write out the first six dimensionless coefficient functions $C_{nm}^{(v)}$:

$$\begin{aligned}
C_{10}^{(v)} &= -\frac{1}{2} C_{11}^{(v)} = 3 C_{12}^{(v)} = \frac{3(\mathbf{Rl})}{2\mathscr{R}}, \\
C_{20}^{(v)} &= \frac{9(\mathbf{Rl})^2}{2\mathscr{R}^2} - \frac{R_{00}}{2\mathscr{R}} + \frac{1}{2}, \\
C_{21}^{(v)} &= -\frac{18(\mathbf{Rl})^2}{\mathscr{R}^2} + \frac{3R_{00}}{2\mathscr{R}} + \frac{3}{2}, \\
C_{30}^{(v)} &= \frac{3(\mathbf{Rl})}{8\mathscr{R}} \left[\frac{45(\mathbf{Rl})^2}{\mathscr{R}^2} - \frac{10R_{00}}{\mathscr{R}} - \frac{23}{3} \right].
\end{aligned} \tag{212}$$

From Eqs. (211) and (212) we find

$$\begin{aligned}
E_j &= m_j + \frac{m_j \bar{v}_j^2}{2} \left(1 + \frac{3}{4} \delta_j + \ldots \right), \\
P_j &= m_j \bar{v}_j \left(1 + \frac{1}{2} \delta_j + \ldots \right).
\end{aligned}$$

Here the function

$$\delta_j = (\boldsymbol{\varrho}_j \mathbf{l})^2 \left[1 + \frac{3(\mathbf{R}\mathbf{l})}{\mathscr{R}} (\boldsymbol{\varrho}_j \mathbf{l}) - \varrho_{j0} \right]$$

defines the value of the basic relativistic corrections, and the dots denote the higher order corrections on $(\boldsymbol{\varrho}_j \mathbf{l})$ and ϱ_{j0}. As we see, the nonrelativistic relation between effective velocity, energy and momentum remains valid up to the second order by $(\boldsymbol{\varrho}_j \mathbf{l})$ and that the relativistic corrections to E_j and P_j are positive. It can be proved that the function $\mathscr{R}$ is positive. Given this fact, it is easy to see that the second derivative (112b) is positive at the stationary point. Indeed, by substituting Eqs. (211) and (212) into Eq. (112b) we obtain

$$\left. \frac{d^2 F_j(q_0)}{dq_0^2} \right|_{q_0 = E_j} = 2R + \frac{2\mathscr{R}}{\bar{v}_j^2} \left[1 - \frac{6(\mathbf{R}\mathbf{l})}{\mathscr{R}} (\boldsymbol{\varrho}_j \mathbf{l}) + \varrho_{j0} + \dots \right] > 0. \tag{213}$$

The peculiarity arising here at $\bar{v}_j = 0$ should not be perplexing, since it only confirms the intuitive expectation that the amplitude of the process with a neutrino at rest in the intermediate state should be zero. Nevertheless, this case requires a more detailed investigation of the conditions of applicability of the saddle-point method and GS theorem.

Particular configurations of external momenta. Let's turn to the special case of the exact balance of the energy-momentum transfer in the macrodiagram vertices. We'll use notation (206) and, according to Eq. (208), we'll assume that

$$0 \le \mathcal{E}/m_j - 1 \ll 1 \quad \text{and} \quad 0 \le \mathcal{P}/m_j \ll 1.$$

It is clear that in the discussed nonrelativistic case the small neighborhood of this particular configuration of 4-momenta gives the main contribution to the amplitude. We have

$$\varrho_j^\mu = \frac{1}{\mathscr{R}}\left[R_k^\mu l_k \frac{\mathcal{P}}{m_j} - R_0^\mu\left(\frac{\mathcal{E}}{m_j} - 1\right)\right]$$

and therefore

$$\varrho_{j0} = \frac{(\mathbf{Rl})}{\mathscr{R}}\frac{\mathcal{P}}{m_j} - \frac{R_{00}}{\mathscr{R}}\left(\frac{\mathcal{E}}{m_j} - 1\right), \quad (\boldsymbol{\varrho}_j\mathbf{l}) = \frac{\mathcal{P}}{m_j} - \frac{(\mathbf{Rl})}{\mathscr{R}}\left(\frac{\mathcal{E}}{m_j} - 1\right).$$

As we can see, the sign of the parameter ϱ_{j0} can be arbitrary, while the value $\boldsymbol{\varrho}_j\mathbf{l} \sim \mathcal{P}/m_j$ is non-negative provided that $\mathcal{E}/m_j - 1 \sim \mathcal{P}^2/m_j^2$. By substituting the found relations in Eq. (211), considering Eqs. (212), and rearranging the obtained expression in powers of of the two small independent parameters $\mathcal{P}/m_j$ and $\mathcal{E}/m_j - 1$, we arrive at the following expression for the effective velocity of the virtual neutrino:

$$v_j = \bar{v}_j\left\{1 + \frac{(\mathbf{Rl})}{2\mathscr{R}}\frac{\mathcal{P}}{m_j} + \left[\frac{R_{00}}{\mathscr{R}} - \frac{3(\mathbf{Rl})^2}{2\mathscr{R}^2}\right]\left(\frac{\mathcal{E}}{m_j} - 1\right) + \ldots\right\}, \quad \bar{v}_j = (\boldsymbol{\varrho}_j\mathbf{l}). \tag{214}$$

If $(\mathbf{Rl}) > 0$ then, according to the GS theorem, only the kinematic region is allowed in which $\mathscr{R}\mathcal{P} > (\mathbf{Rl})\,(\mathcal{E} - m_j)$. From Eq. (214) we find the effective energy and momentum of the virtual neutrino in the leading order by $\mathcal{P}/m_j$ and $\mathcal{E}/m_j - 1$:

$$E_j \approx m_j + \frac{m_j\bar{v}_j^2}{2}, \quad P_j \approx m_j\bar{v}_j.$$

These simple formulas fully satisfy intuitive expectations only when $|\mathcal{E}/m_j - 1| \lesssim \mathcal{P}^2/m_j^2$. In this (and only this) special case

$$\bar{v}_j \approx \frac{\mathcal{P}}{m_j}, \quad E_j \approx m_j + \frac{\mathcal{P}^2}{2m_j} \quad \text{and} \quad P_j \approx \mathcal{P}.$$

I Inverse overlap tensors and related quantities.

I.1 General formulas.

Consider the general properties of the tensors

$$\Re^{\mu\nu}_{s,d} = \sum_{\varkappa} T^{\mu\nu}_{\varkappa} = \sum_{\varkappa} \sigma^2_{\varkappa} \left(u^{\mu}_{\varkappa} u^{\nu}_{\varkappa} - g^{\mu\nu}\right) \quad \text{and} \quad \widetilde{\Re}^{\mu\nu}_{s,d} = \left(\Re^{-1}_{s,d}\right)_{\mu\nu}.$$

The explicit form of the matrices $\Re_{s,d} = ||\Re^{\mu\nu}_{s,d}||$ reads

$$\Re_{s,d} = \sum_{\varkappa} \sigma^2_{\varkappa} \begin{pmatrix} \Gamma^2_{\varkappa} - 1 & -\Gamma_{\varkappa} u_{\varkappa 1} & -\Gamma_{\varkappa} u_{\varkappa 2} & -\Gamma_{\varkappa} u_{\varkappa 3} \\ -\Gamma_{\varkappa} u_{\varkappa 1} & 1 + u^2_{\varkappa 1} & u_{\varkappa 1} u_{\varkappa 2} & u_{\varkappa 1} u_{\varkappa 3} \\ -\Gamma_{\varkappa} u_{\varkappa 2} & u_{\varkappa 2} u_{\varkappa 1} & 1 + u^2_{\varkappa 2} & u_{\varkappa 2} u_{\varkappa 3} \\ -\Gamma_{\varkappa} u_{\varkappa 3} & u_{\varkappa 3} u_{\varkappa 1} & u_{\varkappa 3} u_{\varkappa 2} & 1 + u^2_{\varkappa 3} \end{pmatrix}$$

$$= \sum_{\varkappa} (\sigma_{\varkappa} \Gamma_{\varkappa})^2 \begin{pmatrix} \mathbf{v}^2_{\varkappa} & -v_{\varkappa 1} & -v_{\varkappa 2} & -v_{\varkappa 3} \\ -v_{\varkappa 1} & 1 - v^2_{\varkappa 2} - v^2_{\varkappa 3} & v_{\varkappa 1} v_{\varkappa 2} & v_{\varkappa 1} v_{\varkappa 3} \\ -v_{\varkappa 2} & v_{\varkappa 2} v_{\varkappa 1} & 1 - v^2_{\varkappa 3} - v^2_{\varkappa 1} & v_{\varkappa 2} v_{\varkappa 3} \\ -v_{\varkappa 3} & v_{\varkappa 3} v_{\varkappa 1} & v_{\varkappa 3} v_{\varkappa 2} & 1 - v^2_{\varkappa 1} - v^2_{\varkappa 2} \end{pmatrix}.$$

As above, the index $\varkappa$ ranges over the sets of initial ($I_{s,d}$) and final ($F_{s,d}$) WP states; $u_{\varkappa i}$ and $v_{\varkappa i}$ ($i = 1, 2, 3$) are the components of the vectors $\mathbf{u}_{\varkappa} = \mathbf{p}_{\varkappa}/m_{\varkappa}$ and $\mathbf{v}_{\varkappa}$, respectively ($u_{\varkappa i} = \Gamma_{\varkappa} v_{\varkappa i}$). Clearly, $|T_{\varkappa}| = |T_{\varkappa}|_{\mathbf{v}_{\varkappa}=0} = 0$ while $|\Re_{s,d}| \geq 0$, as judged by strength of positivity of $\Re^{\mu\nu}_{s,d} x_{\mu} x_{\nu}$ and assuming that $\sigma_{\varkappa} > 0$ for all $\varkappa$. Moreover, all principal minors of $|\Re_{s,d}|$ are positive.

Although there are perfectly general expressions for the inverse overlap tensors $\widetilde{\Re}_{s,d}$ and determinants $|\Re_{s,d}|$ (see p. 578), they are too complicated for use in the analysis of particular processes. Therefore, below we'll take a bit different approach and detail a few of the most important special cases.

We will use the following notation:

$$\omega_i = \sum_\varkappa \sigma_\varkappa^2 \left(1 + u_{\varkappa i}^2\right), \quad \omega = \sum_\varkappa \sigma_\varkappa^2 \mathbf{u}_\varkappa^2, \quad \upsilon_i = \sum_\varkappa \sigma_\varkappa^2 \Gamma_\varkappa u_{\varkappa i}, \quad w_i = \sum_\varkappa \sigma_\varkappa^2 u_{\varkappa j} u_{\varkappa k}. \tag{215}$$

Here and below in this Section, the indices s and d are omitted for short. The spatial indices denoted by i, j, k range over 1,2,3, and (if not stipulated otherwise) $i \neq j \neq k$. With this notation, the determinants of $\Re_s$ and $\Re_d$ are given by

$$\begin{aligned} |\Re_{s,d}| = \omega \prod_i \omega_i + 2\omega \prod_i w_i + \sum_i \upsilon_i w_i \left(\upsilon_i w_i - \upsilon_j w_j - \upsilon_k w_k\right) \\ + \sum_i \left[w_i \omega_i \left(2\upsilon_j \upsilon_k - \omega w_i\right) - \upsilon_i^2 \omega_j \omega_k\right]. \end{aligned} \tag{216}$$

The matrices inverse to $\Re_{s,d}$ are straightforwardly (but not trivially) determined through the adjuncts $\mathfrak{A}_{s,d}^{\mu\nu}$ of $|\Re_{s,d}|$:

$$\Re_{s,d}^{-1} = |\Re_{s,d}|^{-1} ||\mathfrak{A}_{s,d}^{\mu\nu}||, \tag{217}$$

$$\begin{aligned} \mathfrak{A}_{s,d}^{00} &= \prod_i \omega_i - \sum_i w_i^2 \omega_i + 2 \prod_i w_i, \\ \mathfrak{A}_{s,d}^{0i} &= \upsilon_i \omega_j \omega_k - \upsilon_j w_k \omega_k - \upsilon_k w_j \omega_j + w_i \left(\upsilon_j w_j + \upsilon_k w_k - \upsilon_i w_i\right), \\ \mathfrak{A}_{s,d}^{ii} &= \omega \left(\omega_j \omega_k - w_i^2\right) + 2 w_i \upsilon_j \upsilon_k - \upsilon_j^2 \omega_k - \upsilon_k^2 \omega_j, \\ \mathfrak{A}_{s,d}^{jk} &= \left(\upsilon_j \upsilon_k - \omega w_i\right) \omega_i + \upsilon_i \left(\upsilon_i w_i - \upsilon_j w_j - \upsilon_k w_k\right) + \omega w_j w_k. \end{aligned} \tag{218}$$

The elements of the matrices $\widetilde{\Re}_s$ and $\widetilde{\Re}_d$ are given by

$$\widetilde{\Re}^{\mu\nu}_{s,d} = |\Re_{s,d}|^{-1}\widetilde{\mathfrak{A}}^{\mu\nu}_{s,d},$$

where

$$\widetilde{\mathfrak{A}}^{00}_{s,d} = \mathfrak{A}^{00}_{s,d}, \quad \widetilde{\mathfrak{A}}^{0i}_{s,d} = \widetilde{\mathfrak{A}}^{i0}_{s,d} = -\mathfrak{A}^{0i}_{s,d}, \quad \widetilde{\mathfrak{A}}^{ij}_{s,d} = \widetilde{\mathfrak{A}}^{ji}_{s,d} = \mathfrak{A}^{ij}_{s,d}.$$

The positive-definiteness of the quadratic forms $\Re^{\mu\nu}_{s,d}q_\mu q_\nu$ provides a set of strict inequalities, in particular,

$$\widetilde{\Re}^{\mu\mu}_{s,d} > 0, \quad \widetilde{\Re}^{00}_{s,d}\widetilde{\Re}^{ii}_{s,d} - \left(\widetilde{\Re}^{0i}_{s,d}\right)^2 > 0, \quad \widetilde{\Re}^{jj}_{s,d}\widetilde{\Re}^{kk}_{s,d} - \left(\widetilde{\Re}^{jk}_{s,d}\right)^2 > 0. \tag{219a}$$

The left parts of these inequalities correspond to the principal minors of the matrix $\widetilde{\Re}_{s,d}$ of the 1-st and 2-nd orders. It is assumed here that there is no summation in repeating indices but, of course, the sums of the corresponding minors are also positive. One more useful set of inequalities is

$$\omega\omega_i > \upsilon_i^2.$$

Similar inequalities are valid also for adjuncts $\mathfrak{A}^{\mu\nu}_{s,d}$ and $\widetilde{\mathfrak{A}}^{\mu\nu}_{s,d}$ (since $|\widetilde{\Re}_{s,d}| > 0$), and for the elements of the matrix $||R^{\mu\nu}|| = ||\widetilde{\Re}^{\mu\nu}_s + \widetilde{\Re}^{\mu\nu}_d||$:

$$R_{\mu\mu} > 0, \quad R_{00}R_{ii} - R^2_{0i} > 0, \quad R_{jj}R_{kk} - R^2_{jk} > 0. \tag{219b}$$

These inequalities lead to important corollaries, in particular, to the positivity of the functions $\mathscr{R}$ and $\mathfrak{m} - \mathfrak{n}_0 - \mathfrak{n}_0^2$ which enter the amplitude.

Indeed, in the coordinate frame where the z axis is directed along the unit vector $\mathbf{l}$ we have

$$\mathscr{R} = R_{33}, \quad \mathfrak{m} - \mathfrak{n}_0 - \mathfrak{n}_0^2 = \frac{R_{00}\mathscr{R} - (\mathbf{Rl})^2}{R^2} = \frac{R_{00}R_{33} - R_{03}^2}{(R_{00} - 2R_{03} + R_{33})^2}.$$

Since these quantities are rotation invariant, from Eqs. (219b) it follows that

$$\mathscr{R} > 0 \quad \text{and} \quad \mathfrak{m} - \mathfrak{n}_0 - \mathfrak{n}_0^2 > 0.$$

From the last inequality it is seen that

$$\Theta_j \approx \frac{m_j^4 R\left(\mathfrak{m} - \mathfrak{n}_0 - \mathfrak{n}_0^2\right)}{4E_\nu^2} = \frac{m_j^4\left[R_{00}\mathscr{R} - (\mathbf{Rl})^2\right]}{4RE_\nu^2} > 0.$$

(see (122)). This leads to a suppression of the probability (133).

The functions $\mathfrak{n}$ and $\bar{\mathfrak{m}}$ can be now constructed from the tensor components $R^{0i} = \widetilde{\Re}_s^{0i} + \widetilde{\Re}_d^{0i}$ and 4-vector $Y = Y_s + Y_d$, where $Y_s^\mu = \widetilde{\Re}_s^{\mu\nu} q_{s\nu}$ and $Y_d^\mu = -\widetilde{\Re}_d^{\mu\nu} q_{d\nu}$.

> Note that for computing the functions $\mathfrak{n}$ and $\bar{\mathfrak{n}}$ we actually only need to know the inner product $Yl = (Y_s + Y_d)l = E_\nu R$ and zero-component $Y^0 = Y_s^0 + Y_d^0$. Moreover, it is sufficient to calculate these quantities in the PW_0 limit, in which the calculations are essentially simplified.

From here on we will use the symbol $[\![f]\!]$ to indicate that the function f is calculated in the PW_0 limit. In these terms

$$Y_{s,d}l \to \widetilde{\Re}_{s,d}^{\mu\nu} q_\mu l_\nu \Big|_{q=E_\nu l} = E_\nu^{-1}\left[\!\!\left[\widetilde{\Re}_{s,d}^{\mu\nu} q_\mu q_\nu\right]\!\!\right] \quad \text{and} \quad Y_{s,d}^0 \to \left[\!\!\left[\widetilde{\Re}_{s,d}^{0\mu} q_\mu\right]\!\!\right].$$

To illustrate the general formulas, we consider below a few simple types of processes in the source and detector of interest for applications of the theory to real neutrino experiments.

I.2 Two-particle decay in the source.

Let us investigate the simplest process – the leptonic decay $a \to \ell \nu_*$ in the source, where a is a charged meson ($\pi^\pm$, $K^\pm$, $D_s^\pm$, ...), ℓ is a charged lepton and ν_* denotes a virtual neutrino or antineutrino. Forasmuch as such decays provide the main source of accelerator, atmospheric and astrophysical neutrinos of high energies, we will study this example circumstantially.

Assuredly, the formulas of this Section can be straightforwardly translated to *any* 2-body decay $a \to b \nu_*$, for example, to an electron capture decay of relativistic ions (e.g., $^{140}\mathrm{Pr}^{57+} \to {}^{140}\mathrm{Ce}^{57+} \nu_*$) in a gedanken experiment capable of detecting the electron-capture neutrino interactions. With certain stipulations, they can also be applied to the sequential processes of emission and resonant absorption (by induced orbital e-capture) of Mössbauer antineutrinos, e.g., $^3\mathrm{H} \to {}^3\mathrm{He} + \overline{\nu}_*$, $\overline{\nu}_* + {}^3\mathrm{He} \to {}^3\mathrm{H}$).

Arbitrary momenta.

In the considered case, the determinant of the matrix $\Re_s$ can readily be obtained from Eq. (216) written in the proper frame of the meson wave packet:[a]

$$\boxed{|\Re_s| = \sigma_a^2 \sigma_\ell^2 \sigma_2^4 |\mathbf{u}_\ell^\star|^2.} \tag{220}$$

Here $\sigma_2^2 = \sigma_a^2 + \sigma_\ell^2$ and $\mathbf{u}_\ell = \mathbf{p}_\ell / m_\ell = \Gamma_\ell \mathbf{v}_\ell$.

[a] We use the star superscript to denote the meson proper frame. The subscripts a and ℓ indicate the corresponding particles and should not be confused with Lorentz indices. A similar index convention is used in the subsequent text.

Since $|\Re_s|$ is a Lorentz invariant, Eq. (220) can be transformed to the laboratory frame just by substitution

$$|\mathbf{u}_\ell^\star| = \frac{\sqrt{(E_\ell \mathbf{p}_a - E_a \mathbf{p}_\ell)^2 - |\mathbf{p}_a \times \mathbf{p}_\ell|^2}}{m_a m_\ell} = (u_a u_\ell)\mathrm{V}_{a\ell}, \quad \mathrm{V}_{a\ell} = \frac{\sqrt{(\mathbf{v}_a - \mathbf{v}_\ell)^2 - |\mathbf{v}_a \times \mathbf{v}_\ell|^2}}{1 - \mathbf{v}_a \mathbf{v}_\ell}.$$

Here $\mathrm{V}_{a\ell}$ is the relative velocity of the meson and lepton in the lab. frame.

Notice that the kinematic variables in this formula are not in general constrained by the energy-momentum conservation. By adopting that the virtual neutrino is on-mass-shell and neglecting both the neutrino masses and the smearing of the meson and lepton momenta, one may use the standard 2-particle kinematics, according to which

$$|\mathbf{v}_\ell^\star| = \mathrm{V}_{a\ell} = \frac{m_a^2 - m_\ell^2}{m_a^2 + m_\ell^2} \quad \text{and} \quad |\mathbf{u}_\ell^\star| = \frac{m_a^2 - m_\ell^2}{2 m_a m_\ell}.$$

In a little bit more complicated way one can calculate the adjuncts $\mathfrak{A}_s^{\mu\nu}$ defined by Eqs. (218):

$$\begin{aligned}
\mathfrak{A}_s^{00} &= \sigma_2^2 \left[\sigma_2^2 \left(\sigma_a^2 \Gamma_a^2 + \sigma_\ell^2 \Gamma_\ell^2\right) + \sigma_a^2 \sigma_\ell^2 \left|\mathbf{u}_a \times \mathbf{u}_\ell\right|^2\right], \\
\mathfrak{A}_s^{0i} &= \sigma_2^2 \left\{\sigma_a^2 \left[\sigma_a^2 \Gamma_a + \sigma_\ell^2 \Gamma_\ell (u_a u_\ell)\right] u_{ai} + \sigma_\ell^2 \left[\sigma_\ell^2 \Gamma_\ell + \sigma_a^2 \Gamma_a (u_a u_\ell)\right] u_{\ell i}\right\}, \\
\mathfrak{A}_s^{ii} &= \sigma_2^2 \left\{\sigma_a^2 \left[\sigma_a^2 u_{ai} + \sigma_\ell^2 (u_a u_\ell) u_{\ell i}\right] u_{ai} + \sigma_\ell^2 \left[\sigma_\ell^2 u_{\ell i} + \sigma_a^2 (u_a u_\ell) u_{ai}\right] u_{\ell i}\right. \\
&\qquad \left. + \sigma_a^2 \sigma_\ell^2 \left[\left(\Gamma_\ell \mathbf{u}_a - \Gamma_a \mathbf{u}_\ell\right)^2 - \left|\mathbf{u}_a \times \mathbf{u}_\ell\right|^2\right]\right\}, \\
\mathfrak{A}_s^{jk} &= \sigma_2^2 \left[\sigma_a^4 u_{aj} u_{ak} + \sigma_\ell^4 u_{\ell j} u_{\ell k} + \sigma_a^2 \sigma_\ell^2 (u_a u_\ell) \left(u_{aj} u_{\ell k} + u_{\ell j} u_{ak}\right)\right], \quad j \neq k.
\end{aligned} \tag{221}$$

No kinematic constraints were imposed for derivation of these formulas.

Using Eqs. (221) and taking into account Eq. (217), we obtain (for arbitrary q)

$$\widetilde{\Re}_s^{\mu\nu} q_\mu q_\nu = \frac{1}{|\Re_s|} \left[\mathfrak{A}_s^{00} q_0^2 + \sum_i \left(-2\mathfrak{A}_s^{0i} q_0 + \mathfrak{A}_s^{ii} q_i \right) q_i + 2 \sum_{j<k} \mathfrak{A}_s^{jk} q_j q_k \right] \frac{A_2}{\sigma_a^2 \sigma_\ell^2 \sigma_2^2 |\mathbf{u}_\ell^\star|^2} - \frac{q^2}{\sigma_2^2}, \quad (222)$$

where we have defined the Lorentz-invariant function

$$\begin{aligned} A_2 = & \left[\sigma_2^2 \left(\sigma_a^2 \Gamma_a^2 + \sigma_\ell^2 \Gamma_\ell^2 \right) + \sigma_a^2 \sigma_\ell^2 \left(\Gamma_\ell \mathbf{u}_a - \Gamma_a \mathbf{u}_\ell \right)^2 \right] q_0^2 \\ & - 2 \left\{ \sigma_a^2 \left[\sigma_a^2 \Gamma_a + \sigma_\ell^2 \Gamma_\ell (u_a u_\ell) \right] \mathbf{u}_a \mathbf{q} + \sigma_\ell^2 \left[\sigma_\ell^2 \Gamma_\ell + \sigma_a^2 \Gamma_a (u_a u_\ell) \right] \mathbf{u}_\ell \mathbf{q} \right\} q_0 \\ & + \sum_i \left[\sigma_a^4 u_{ai}^2 + \sigma_\ell^4 u_{\ell i}^2 + 2\sigma_a^2 \sigma_\ell^2 (u_a u_\ell) u_{ai} u_{\ell i} \right] q_i^2 \\ & + 2 \sum_{j<k} \left[\sigma_a^4 u_{aj} u_{ak} + \sigma_\ell^4 u_{\ell j} u_{\ell k} + \sigma_a^2 \sigma_\ell^2 (u_a u_\ell) \left(u_{aj} u_{\ell k} + u_{ak} u_{\ell j} \right) \right] q_j q_k. \end{aligned}$$

By applying the identities

$$\begin{aligned} (u_a q) (u_\ell q) &= \Gamma_a \Gamma_\ell q_0^2 - \left[\Gamma_a (\mathbf{u}_\ell \mathbf{q}) + \Gamma_\ell (\mathbf{u}_a \mathbf{q}) \right] q_0 + (\mathbf{u}_a \mathbf{q}) (\mathbf{u}_\ell \mathbf{q}), \\ (\mathbf{u}_a \mathbf{q}) (\mathbf{u}_\ell \mathbf{q}) &= \sum_i \left[(u_{ai} q_i) (u_{\ell i} q_i) + (u_{aj} q_j) (u_{\ell k} q_k) + (u_{ak} q_k) (u_{\ell j} q_j) \right], \end{aligned}$$

we arrive at the compact formula for the function A_2:

$$A_2 = \sigma_a^4 (u_a q)^2 + \sigma_\ell^4 (u_\ell q)^2 + 2\sigma_a^2 \sigma_\ell^2 (u_a u_\ell) (u_a q) (u_\ell q). \quad (223)$$

Now we can write out the 4-vector Y_s whose components are defined by

$$Y_s^0 = \widetilde{\Re}_s^{0\nu} q_{s\nu} = \frac{1}{|\Re_s|}\left[\mathfrak{A}^{00}\left(E_a - E_\ell\right) - \mathfrak{A}^{0i}\left(p_a - p_\ell\right)_i\right],$$
$$Y_s^i = \widetilde{\Re}_s^{i\nu} q_{s\nu} = \frac{1}{|\Re_s|}\left[\mathfrak{A}^{ij}\left(p_a - p_\ell\right)_j - \mathfrak{A}^{i0}\left(E_a - E_\ell\right)\right].$$

After elementary manipulations with Eqs. (221), we arrive at the expression:

$$Y_s^\mu = \frac{1}{|\mathbf{u}_\ell^\star|^2}\left\{\left[\frac{(p_a p_\ell)}{m_a^2} - 1\right]\frac{p_a^\mu}{\sigma_\ell^2} - \left[\frac{(p_a p_\ell)}{m_\ell^2} - 1\right]\frac{p_\ell^\mu}{\sigma_a^2}\right\}. \tag{224}$$

Even simpler:

$$(\mathbf{Rq}) = \frac{1}{\sigma_2^2|\mathbf{u}_\ell^\star|^2}\left\{\left[\frac{\sigma_a^2\Gamma_a}{\sigma_\ell^2} + \Gamma_\ell(u_a u_\ell)\right](\mathbf{u}_a\mathbf{q}) + \left[\frac{\sigma_\ell^2\Gamma_\ell}{\sigma_a^2} + \Gamma_a(u_a u_\ell)\right](\mathbf{u}_\ell\mathbf{q})\right\}.$$

PW$_0$ limit.

In the PW$_0$ limit ($q \to p_a - p_\ell = p_\nu = E_\nu l$, $p_\nu^2 = 0$ in this instance) we have

$$u_a u_\ell = \frac{E_\ell^\star}{m_\ell}, \quad u_a q = E_\nu^\star, \quad u_\ell q = \frac{m_a E_\nu^\star}{m_\ell},$$

where

$$E_\ell^\star = \frac{m_a^2 + m_\ell^2}{2m_a} \quad \text{and} \quad E_\nu^\star = \frac{m_a^2 - m_\ell^2}{2m_a}$$

are, respectively, the lepton and neutrino energies in the meson rest frame.

By applying the above relations to Eqs. (223) and (222), we obtain

$$\boxed{\left[\!\left[\widetilde{\Re}^{\mu\nu}_{s}\, q_\mu q_\nu\right]\!\right] = \frac{m_\ell^2}{\sigma_\ell^2} + \frac{m_a^2}{\sigma_a^2}.} \tag{225}$$

The shape of the effective neutrino wave packet.

To illustrate Eq. (225) let us consider the special but quite realistic case when one can neglect the contributions into the full function $\mathfrak{D}$ caused by the reaction in the detector. For this we have to assume that the parameters $\sigma_\varkappa$ for all $\varkappa \in D$ are large enough in comparison with σ_a and σ_ℓ.). Then from Eq. (225) we obtain:

$$\mathfrak{D}^2 \approx E_\nu^2 \left[2\left(\frac{m_\ell^2}{\sigma_\ell^2} + \frac{m_a^2}{\sigma_a^2}\right)\right]^{-1} \ll E_\nu^2, \quad \sigma_j^2 \approx \frac{m_j^2}{2}\left(\frac{m_\ell^2}{\sigma_\ell^2} + \frac{m_a^2}{\sigma_a^2}\right)^{-1} \ll m_j^2. \tag{226}$$

So, in this simplest case, the effective wavepacket of virtual neutrino with a given mass definitely defined by the mass and momentum spreads of the packets of a and ℓ and the values of σ_j for all three known neutrino are *mightily small* for any values of σ_a and σ_ℓ allowed by the CRGP approximation.

Moreover, taking into account that the masses of the known neutrinos are many orders of magnitude smaller than the masses of all other known (massive) elementary particles, we can conclude that $\sigma_j^2 \lll \sigma_{a,\ell}^2$.

While the estimations were done neglecting the detector contributions, they partially explain the success of the standard quantum-mechanical assumptions that the light neutrinos have definite momenta in spite of the fact that they are produced in the processes with the particles having comparatively large momentum spreads. From (226) it in particular follows that $\sigma_j = 0$ as $m_j = 0$ that is the massless neutrinos can be treated as plane waves. With obvious limitations this remarkable fact can be used in the analyses of the processes in which the light massive (or massless) neutrinos participate as external wavepackets. From the conditions of applicability of the CRGP approximation for unstable particles

$$(\sigma_\varkappa/\sigma_\varkappa^{\max})^4 \ll 1, \quad \sigma_\varkappa^{\max} = \sqrt{m_\varkappa \Gamma_\varkappa}$$

(where $\Gamma_\varkappa = 1/\tau_\varkappa$ is the full decay width of the particle $\varkappa$) it follows the important limitation:

$$\sigma_j^2 \ll \frac{m_j^2}{2}\left(\frac{m_\ell}{\Gamma_\ell} + \frac{m_a}{\Gamma_a}\right)^{-1}.$$

Therefore, for the two-particle decays of *any* mesons with a muon in the final state ($\pi_{\mu 2}$, $K_{\mu 2}$, etc.) we obtain the upper limit

$$\frac{\sigma_j^2}{m_j^2} \ll \frac{\Gamma_\mu}{m_\mu} \approx 1.4 \times 10^{-18} \quad \Longrightarrow \quad \frac{\sigma_j^{\max}}{\sigma_\mu^{\max}} \approx \frac{m_j}{m_\mu} \lll 1.$$

This leads to the lower limit for the effective transversal and longitudinal dimensions of the neutrino wavepacket:

$$d_j^\perp \gg 2.5\left(\frac{0.1\ \text{eV}}{m_j}\right)\ \text{km} \quad \text{and} \quad d_j^\parallel = \frac{d_j^\perp}{\Gamma_j} \gg 2.5 \times 10^{-5}\left(\frac{1\ \text{GeV}}{E_\nu}\right)\left(\frac{0.1\ \text{eV}}{m_j}\right)\ \text{cm}.$$

Some conclusions.

- The size $d_j^{\perp}$ is on no account the size of the neutrino wave packet at rest, since all our estimations were performed in the ultrarelativistic approximation and are therefore valid only for such frames in which the neutrinos remain ultrarelativistic. The Lorentz invariance of the effective neutrino wave function $\psi_y^j(\mathbf{p}_j, x)$ also takes place up to the same reserve requirement. The explicit form of the effective wave packet of the nonrelativistic neutrino requires a special consideration, beyond the scope of the present consideration.
- The limitations for the characteristics of the neutrino wavepackets created in $a_{\tau 2}$ decays depend on the type of the decaying particle. For example, in the case of a D_s meson decay we obtain $\sigma_j^2/m_j^2 \ll 2.2 \times 10^{-13}$.
- The effective dimensions $d_j^{\perp}$ and $d_j^{\parallel}$ define (on the order of magnitude) the allowed transversal and longitudinal quantum deviations of the center of the neutrino packet from the "classical trajectory" $\overline{\mathbf{L}}_j = \mathbf{v}_j T$.
- The transversal deviations $\delta\mathbf{L}_j^{\perp} \sim d_j^{\perp}$ can be huge, wittingly larger than the dimensions of the present-day neutrino detectors and the natural widening of the accelerator neutrino beams even in the distances of about $\sim 10^3$ km from the source. This fact should not cause bewilderment and confusion if we remind ourselves that the standard quantum-mechanical description of the massive neutrino as a state with definite momentum implicates, as a direct consequence of the Heisenberg uncertainty relation, that its "dimensions" (both transversal and longitudinal) are *infinitely large*. Such description does not lead to unphysical results since the neither transversal dimensions nor transversal quantum fluctuations enter the transition amplitude and thus do not affect the observables.

The effects of noncollinearity of the momentum transfers in the source and detector vertices are defined by the functions $\mathfrak{n}$ and $\mathfrak{m}$ discussed below.

Contributions to functions $\mathfrak{n}$ and $\mathfrak{m}$.

From general formula (224) we find the 4-vector Y_s in the PW$_0$-approximation:

$$Y_s = \frac{1}{m_a E_\nu^\star}\left[\left(\frac{m_\ell^2}{\sigma_\ell^2}+\frac{m_a^2}{\sigma_a^2}\right)p_a - \frac{m_a^2}{\sigma_a^2}\,p_\nu\right] = \frac{1}{m_a E_\nu^\star}\left[\left(\frac{m_\ell^2}{\sigma_\ell^2}+\frac{m_a^2}{\sigma_a^2}\right)p_\ell - \frac{m_\ell^2}{\sigma_\ell^2}\,p_\nu\right].$$

The scalar products required to calculate $a_{\ell 2}$ contributions to the functions $\mathfrak{n}$ and $\mathfrak{m}$ have the form

$$Y_s l = \left[\!\left[\widetilde{\Re}_s^{\mu\nu} q_\mu q_\nu\right]\!\right]\frac{1}{E_\nu} = \left(\frac{m_\ell^2}{\sigma_\ell^2}+\frac{m_a^2}{\sigma_a^2}\right)\frac{1}{E_\nu},$$

$$\mathbf{Y_s l} = Y_s^0 - Y_s l = \frac{\Gamma_a}{E_\nu^\star}\left[\left(\frac{m_\ell^2}{\sigma_\ell^2}+\frac{m_a^2}{\sigma_a^2}\right)\left(1-\frac{m_a E_\nu^\star}{E_a E_\nu}\right) - \frac{m_a^2}{\sigma_a^2}\frac{E_\nu}{E_a}\right].$$

Hence we find:

$$\frac{\mathbf{Y_s l}}{Y_s l} = \Gamma_a\left[1-\left(\frac{m_a^2\sigma_\ell^2}{m_a^2\sigma_\ell^2+m_\ell^2\sigma_a^2}\right)\frac{E_\nu}{E_a}\right]\frac{E_\nu}{E_\nu^\star} - 1 \equiv \mathfrak{n}_s\left(E_a, E_\nu\right).$$

Since for a fixed value of E_ν the function $\mathfrak{n}_s$ depends linearly on E_a, the following inequality holds:

$$\mathfrak{n}_s \geq \mathfrak{n}_s\left(E_a^{\min}, E_\nu\right),$$

in which

$$E_a^{\min} = \frac{m_a}{2}\left(\frac{E_\nu}{E_\nu^\star}+\frac{E_\nu^\star}{E_\nu}\right)$$

is the minimum energy of particle a required to produce a massless neutrino with energy E_ν in the $a_{\ell 2}$-decay.

Thus, the absolute minimum of the function $\mathfrak{n}_s$ is negative:

$$\mathfrak{n}_s^{\min} = \mathfrak{n}_s\left(m_a, E_\nu^\star\right) = -\frac{\left(m_a^2 - m_\ell^2\right)\sigma_\ell^2}{2\left(m_a^2\sigma_\ell^2 + m_\ell^2\sigma_a^2\right)}, \quad |\mathfrak{n}_s^{\min}| < \frac{1}{2}\left(1 - \frac{m_\ell^2}{m_a^2}\right).$$

The function $\mathfrak{n}_s$ increases with E_ν and can be arbitrarily large at $E_\nu \gg E_\nu^\star$;

$$\mathfrak{n}_s \geq \mathfrak{n}_s\left(E_a^{\min}, E_\nu\right) = \frac{1}{2}\left(1 - 2|\mathfrak{n}_s^{\min}|\right)\left(\frac{E_\nu}{E_\nu^\star}\right)^2\left[1 + \mathcal{O}\left(\frac{E_\nu^\star}{E_\nu}\right)\right].$$

If $|Y_s^0| \gg |Y_d^0|$ and $Y_s l \gg Y_d l$, then the function $\mathfrak{n}_s$ can serve as an estimate for the full function $\mathfrak{n}$. As is well known, the neutrino energy distribution in the $a_{\ell 2}$-decay is uniform (i.e., independent of E_ν) within kinematic boundaries $E_\nu^\star \Gamma_a(1 - |\mathbf{v}_a|) \leq E_\nu \leq E_\nu^\star \Gamma_a(1 + |\mathbf{v}_a|)$, where it follows that the average neutrino energy is $\overline{E}_\nu = \Gamma_a E_\nu^\star$. Therefore, at high energies of decaying mesons, $\Gamma_a \gg 1$, to within $\mathcal{O}(\Gamma_a^{-2})$ we have

$$\mathfrak{n}_s\left(E_a, \overline{E}_\nu\right) \approx \Gamma_a^2\left(1 - |\mathfrak{n}_s^{\min}|\right) = \left(1 - |\mathfrak{n}_s^{\min}|\right)\left(\frac{\overline{E}_\nu}{E_\nu^\star}\right)^2, \quad \mathfrak{n}_s r_i\big|_{E_\nu = \overline{E}_\nu} \approx \frac{\left(1 - |\mathfrak{n}_s^{\min}|\right)}{2}\left(\frac{m_i}{E_\nu^\star}\right)^2 \ll 1.$$

Under the same assumptions and holding only the leading in Γ_a and $E_\nu/E_\nu^\star$ terms, one can estimate the $a_{\ell 2}$-decay contribution to the function $\mathfrak{m}$:

$$\mathfrak{m}_s \approx \Gamma_a^2\left\{1 + \frac{\sigma_\ell^4 m_a^4}{\left(m_\ell^2\sigma_a^2 + m_a^2\sigma_\ell^2\right)^2}\left[1 + \frac{2\sigma_a^2 E_\nu^\star}{m_a\left(\sigma_a^2 + \sigma_\ell^2\right)}\right]\left(\frac{E_\nu}{E_a}\right)^2\right\}\left(\frac{E_\nu}{E_\nu^\star}\right)^2.$$

From this we see that $\mathfrak{m}_s \gg \mathfrak{n}_s$; nevertheless, inequalities (205) assumed in Appendix H.2, p. 870 remain valid at $E_\nu \sim \overline{E}_\nu$.

I.3 Quasielastic scattering in detector.

As the simplest (and most important) example of a reaction in the detector vertex of the diagram consider the quasielastic scattering of a virtual neutrino $\nu_* a \to b\ell$, in which the target particle a may be an electron, nucleon, or nucleus, and ℓ a charged lepton.

Since in a typical neutrino experiment the target particles have very small (thermal) velocities with respect to the lab. system, we will assume that the latter coincides with the proper frame of the wave packet describing the state of the particle a. Of course, if necessary, all formulas can be transformed to any other frame of reference, since we are dealing only with with vectors and tensors, the laws of transformation of which are well known.

Arbitrary momenta.

In the proper frame of the packet a, the determinant of the matrix $\Re_d$ has the form

$$\begin{aligned} |\Re_d| = \sigma_3^2 \Big\{ \left(\sigma_3^2 + \sigma_a^2\right) \sigma_b^2 \sigma_\ell^2 \left(u_b u_\ell\right)^2 \mathrm{V}_{b\ell}^2 + 2\sigma_a^2 \sigma_b^2 \sigma_\ell^2 \left(u_b u_\ell\right) \left(\mathbf{u}_b \mathbf{u}_\ell\right) + \\ + \sigma_a^2 \left[\sigma_b^2 \left(\sigma_a^2 + \sigma_b^2\right) \mathbf{u}_b^2 + \sigma_\ell^2 \left(\sigma_a^2 + \sigma_\ell^2\right) \mathbf{u}_\ell^2 \right] \Big\} . \end{aligned} \tag{227}$$

Here $\mathrm{V}_{b\ell}$ is the relative velocity of particles b and ℓ, and $\sigma_3^2 \equiv \sigma_a^2 + \sigma_b^2 + \sigma_\ell^2$. The important conclusion that follows from this formula is that the determinant $|\Re_d|$ remains *nonnegative* even if one (but only one!) of the particles a, b or ℓ is described by a plane wave. If, for example, one neglects the terms proportional to σ_ℓ^2, the formula for the determinant (227) becomes formally the same as one for the two-particle decay (see Eq. (220)):

$$|\Re_d| \approx \sigma_a^2 \sigma_b^2 \left(\sigma_a^2 + \sigma_b^2\right)^2 |\mathbf{u}_b|^2 . \tag{228}$$

This important property makes it possible to greatly simplify the analysis of multi-packet in- and out-states by neglecting the contributions of packets of very large spatial dimensions (characterized by very small values of $\sigma_\varkappa$ parameters) in those kinematic regions in which the determinants $|\Re_s|$ and $|\Re_d|$ calculated in this approximation do not turn to zero.[a] In particular, it simplifies the accounting of radiative corrections in the precision calculations.

Let's return to the general case. According to Eq. (218), the algebraic adjuncts $\mathfrak{A}_d^{\mu\nu}$ have the form

$$\begin{aligned}
\mathfrak{A}_d^{00} &= \sigma_3^2\left[\sigma_3^2\left(\sigma_a^2+\sigma_b^2\Gamma_b^2+\sigma_\ell^2\Gamma_\ell^2\right)+\sigma_b^2\sigma_\ell^2\left|\mathbf{u}_b\times\mathbf{u}_\ell\right|^2\right],\\
\mathfrak{A}_d^{0i} &= \sigma_3^2\sigma_b^2\left[\left(\sigma_a^2+\sigma_b^2\right)\Gamma_b+\sigma_\ell^2(u_bu_\ell)\right]u_{bi}+\sigma_3^2\sigma_\ell^2\left[\left(\sigma_a^2+\sigma_\ell^2\right)\Gamma_\ell+\sigma_b^2(u_bu_\ell)\right]u_{\ell i},\\
\mathfrak{A}_d^{ii} &= \sigma_b^2\left(\sigma_3^2\sigma_b^2-\sigma_a^2\sigma_\ell^2\mathbf{u}_\ell^2\right)u_{bi}^2+\sigma_\ell^2\left(\sigma_3^2\sigma_\ell^2-\sigma_a^2\sigma_b^2\mathbf{u}_b^2\right)u_{\ell i}^2+\\
&\quad+2\sigma_b^2\sigma_\ell^2\left[\sigma_a^2\Gamma_b\Gamma_\ell+\left(\sigma_b^2+\sigma_\ell^2\right)(u_bu_\ell)\right]u_{bi}u_{\ell i}+\sigma_3^{-2}|\Re_d|,\\
\mathfrak{A}_d^{jk} &= \sigma_b^2\left(\sigma_3^2\sigma_b^2-\sigma_a^2\sigma_\ell^2\mathbf{u}_\ell^2\right)u_{bj}u_{bk}+\sigma_\ell^2\left(\sigma_3^2\sigma_\ell^2-\sigma_a^2\sigma_b^2\mathbf{u}_b^2\right)u_{\ell j}u_{\ell k}+\\
&\quad+\sigma_b^2\sigma_\ell^2\left[\sigma_a^2\Gamma_b\Gamma_\ell+\left(\sigma_b^2+\sigma_\ell^2\right)(u_bu_\ell)\right]\left(u_{pj}u_{\ell k}+u_{bk}u_{\ell j}\right),\quad j\neq k.
\end{aligned}\tag{229}$$

For an arbitrary 4-vector q we have:

$$|\Re_d|\widetilde{\Re}_d^{\mu\nu}q_\mu q_\nu=\mathfrak{A}_d^{00}q_0^2+\sum_i\left(-2\mathfrak{A}_d^{0i}q_0+\mathfrak{A}_d^{ii}q_i\right)q_i+2\sum_{j<k}\mathfrak{A}_d^{jk}q_jq_k.$$

[a] A similar caveat must be taken into account in the general case, i.e., when discarding the contributions of WPs with very small values of $\sigma_\varkappa$ one should cut out the neighborhoods of the phase space within which the determinants $|\Re_s|$ and $|\Re_d|$ calculated in this approximation are zero. As a rule, such regions are located near the kinematic boundaries of phase space and do not contribute to the experimentally measured characteristics. Recall that the approximate formula (228) is applicable only when $|\mathbf{u}_b|\neq 0$, which is possible at the kinematic boundary. However, the value of $|\mathbf{u}_\ell^\star|$ in Eq. (220) is always nonzero.

By substituting the expressions (229), we obtain:

$$
\begin{aligned}
|\Re_d|\widetilde{\Re}_d^{\mu\nu} q_\mu q_\nu &= \mathfrak{A}_d^{00} q_0^2 + \sum_i \left(-2\mathfrak{A}_d^{0i} q_0 + \mathfrak{A}_d^{ii} q_i\right) q_i + 2\sum_{j<k} \mathfrak{A}_d^{jk} q_j q_k \\
&= \sigma_3^2 \left[\sigma_3^2 \left(\sigma_a^2 + \sigma_b^2 \Gamma_b^2 + \sigma_\ell^2 \Gamma_\ell^2\right) + \sigma_b^2 \sigma_\ell^2 \left|\mathbf{u}_b \times \mathbf{u}_\ell\right|^2\right] q_0^2 + \sigma_3^{-2} |\Re_d| \mathbf{q}^2 \\
&\quad - 2\sigma_3^2 \sigma_b^2 \left[\left(\sigma_a^2 + \sigma_b^2\right) \Gamma_b + \sigma_\ell^2 \Gamma_\ell (u_b u_\ell)\right] (\mathbf{u}_b \mathbf{q})\, q_0 \\
&\quad - 2\sigma_3^2 \sigma_\ell^2 \left[\left(\sigma_a^2 + \sigma_\ell^2\right) \Gamma_\ell + \sigma_b^2 \Gamma_b (u_b u_\ell)\right] (\mathbf{u}_\ell \mathbf{q})\, q_0 \\
&\quad + \sigma_3^2 \left[\sigma_b^4 (\mathbf{u}_b \mathbf{q})^2 + \sigma_\ell^4 (\mathbf{u}_\ell \mathbf{q})^2 + 2\sigma_b^2 \sigma_\ell^2 (u_b u_\ell) (\mathbf{u}_b \mathbf{q}) (\mathbf{u}_\ell \mathbf{q})\right] \\
&\quad + \sigma_a^2 \sigma_b^2 \sigma_\ell^2 \left\{[(\mathbf{u}_b \times \mathbf{u}_\ell)\mathbf{q}]^2 - (\mathbf{u}_b \times \mathbf{u}_\ell)^2 \mathbf{q}^2\right\}.
\end{aligned}
$$

Using Eq. (229), we also find the components of the 4-vector Y_d:

$$
Y_d^0 = \frac{\sigma_3^2}{|\Re_d|} \left(c_a^0 m_a - c_b^0 E_b - c_\ell^0 E_\ell\right), \quad \mathbf{Y}_d = \frac{\sigma_3^2}{|\Re_d|} \left(c_b \mathbf{u}_b + c_\ell \mathbf{u}_\ell\right).
$$

The coefficient functions appear here are given by the following formulas:

$$
\begin{aligned}
c_a^0 &= \sigma_a^2 \left(\sigma_3^2 + \sigma_b^2 \Gamma_b^2 + \sigma_\ell^2 \Gamma_\ell^2\right) + \sigma_b^2 \sigma_\ell^2 \left[(\Gamma_b \Gamma_\ell - 1)^2 - (\mathbf{u}_b \mathbf{u}_\ell)^2\right] + \left(\sigma_b^2 \Gamma_b + \sigma_\ell^2 \Gamma_\ell\right)^2, \\
c_b^0 &= \sigma_3^2 \left[\sigma_a^2 + \sigma_b^2 + \sigma_\ell^2 \Gamma_\ell^2 (1 - \mathbf{v}_b \mathbf{v}_\ell)\right], \qquad c_\ell^0 = c_b^0\big|_{b \leftrightarrow \ell}, \\
c_b &= \sigma_b^2 \left\{\left[m_a \sigma_\ell^2 \Gamma_\ell - m_\ell \left(\sigma_b^2 + \sigma_\ell^2\right)\right] (u_b u_\ell) + m_a \sigma_b^2 \Gamma_b - m_b \left(\sigma_b^2 + \sigma_\ell^2\right)\right\} + \\
&\quad + \sigma_a^2 \left\{m_b \sigma_\ell^2 \mathbf{u}_\ell^2 + \sigma_b^2 \left[\Gamma_b (m_a - m_\ell \Gamma_\ell) - m_b\right]\right\}, \qquad c_\ell = c_b\big|_{b \leftrightarrow \ell}.
\end{aligned}
$$

As it should be, the obtained expressions for the convolution $|\Re_d|\widetilde{\Re}_d^{\mu\nu} q_\mu q_\nu$ and the components of the 4-vector Y_d are all symmetric with respect to the index replacement $b \leftrightarrow \ell$, and their non-covariant form is related to the use of a special (laboratory) reference frame.

PW_0 limit.

In the PW_0 limit, the kinematics of the $2 \to 2$ reaction allows us to write down the quantities $|\Re_d|$, $\widetilde{\Re}_d^{\mu\nu} q_\mu q_\nu$, and $\mathbf{Y}_d \mathbf{l}$ in terms of any two independent invariant variables; we will use the standard pair of variables: $s = (p_a + p_\nu)^2 = m_a (2E_\nu + m_a)$ and $Q^2 = -(p_\nu - p_\ell)^2$. To write the expressions of the previous section through these variables, we take into account the exact kinematic relations

$$E_b = \frac{1}{m_a}\left(E_b^* E_a^* - E_\nu^* P_\ell^* \cos\theta_*\right), \quad \mathbf{p}_b \mathbf{p}_\nu = \frac{E_\nu}{m_a}\left(E_b^* E_\nu^* - E_a^* P_\ell^* \cos\theta_*\right),$$
$$E_\ell = \frac{1}{m_a}\left(E_\ell^* E_a^* + E_\nu^* P_\ell^* \cos\theta_*\right), \quad \mathbf{p}_\ell \mathbf{p}_\nu = \frac{E_\nu}{m_a}\left(E_\ell^* E_\nu^* + E_a^* P_\ell^* \cos\theta_*\right),$$
$$|\mathbf{u}_b \times \mathbf{u}_\ell| = \frac{E_\nu P_\ell^* \sin\theta_*}{m_b m_\ell}, \quad (\mathbf{u}_b \times \mathbf{u}_\ell)\, \mathbf{p}_\nu = 0,$$
$$u_b u_\ell = \frac{s - m_b^2 - m_\ell^2}{2 m_b m_\ell}, \quad \mathrm{V}_{b\ell} = \frac{2\sqrt{s} P_\ell^*}{s - m_b^2 - m_\ell^2},$$

in which $P_\ell^* = |\mathbf{p}_\ell^*|$ is the absolute value of the lepton momentum, $E_\nu = |\mathbf{p}_\nu| = \left(s - m_a^2\right)/2m_a$ and $\mathbf{p}_\nu = E_\nu \mathbf{l}$ is the energy and momentum of the massless neutrino in lab. frame, and

$$E_\nu^* = \frac{s - m_a^2}{2\sqrt{s}}, \quad E_\ell^* = \frac{s + m_\ell^2 - m_b^2}{2\sqrt{s}}, \quad E_a^* = \frac{s + m_a^2}{2\sqrt{s}} \quad \text{and} \quad E_b^* = \frac{s - m_\ell^2 + m_b^2}{2\sqrt{s}}$$

are the energies of the particles ν^*, ℓ, a, and b in the center-of-mass frame (CMF), defined by the conditions

$$E_\nu^* + E_a^* = E_b^* + E_\ell^*, \quad \mathbf{p}_\nu^* + \mathbf{p}_a^* = \mathbf{p}_\ell^* + \mathbf{p}_b^* = 0.$$

The lepton scattering angle θ_* in CMF is related to the variable Q^2,

$$Q^2 = 2E_\nu^* \left(E_\ell^* - P_\ell^* \cos\theta_*\right) - m_\ell^2.$$

The kinematically allowed region of the phase space is given by the inequalities

$$s \geq s_{\text{th}} = \max\left[m_a^2, (m_b + m_\ell)^2\right], \tag{230}$$

$$Q_-^2 \leq Q^2 \leq Q_+^2, \quad Q_\pm^2 = 2E_\nu^* \left(E_\ell^* \pm P_\ell^*\right) - m_\ell^2. \tag{231}$$

The kinematic formulas given here have already been discussed in Sect. **9.1**, p. 372. For more details, see Appendix A, p. 831.

Now, after elementary, albeit rather cumbersome algebraic transformations, we find:

$$[\![|\Re_d|]\!] = \frac{\sigma_3^2}{4m_a^2 m_b^2 m_\ell^2} \sum_{k,l=0}^{2} A_{kl} s^k Q^{2l},$$

$$\left[\!\left[|\Re_d| \widetilde{\Re}_d^{\mu\nu} q_\mu q_\nu\right]\!\right] = \frac{\sigma_3^2}{4m_a^2 m_b^2 m_\ell^2} \sum_{k,l=0}^{2} B_{kl} s^k Q^{2l},$$

$$[\![|\Re_d| \mathbf{Y}_d \mathbf{q}]\!] = \frac{\sigma_3^2}{8m_a^2 m_b^2 m_\ell^2} \sum_{k,l=0}^{3} C_{kl} s^k Q^{2l}.$$

Explicit formulas for the coefficients A_{kl}, B_{kl}, and C_{kl} are given in Appendix J, p. 905. Additional results relevant to the example in question are also presented there.

Thus, the quadratic form $\widetilde{\Re}_d^{\mu\nu} q_\mu q_\nu$ and the scalar product $\mathbf{Y}_d\mathbf{q}$ are rational functions of two invariant variables s and Q^2:

$$\left[\!\left[\widetilde{\Re}_d^{\mu\nu} q_\mu q_\nu\right]\!\right] = \frac{\sum_{k,l} B_{kl} s^k Q^{2l}}{\sum_{k,l} A_{kl} s^k Q^{2l}} \equiv \mathfrak{F}_d(s, Q^2),$$

$$[\![\mathbf{Y}_d\mathbf{q}]\!] = \frac{1}{2} \frac{\sum_{k,l} C_{kl} s^k Q^{2l}}{\sum_{k,l} A_{kl} s^k Q^{2l}} \equiv \mathfrak{n}_d(s, Q^2)\mathfrak{F}_d(s, Q^2).$$

Here we introduced the function[a]

$$\mathfrak{n}_d = \frac{[\![\mathbf{Y}_d\mathbf{l}]\!]}{[\![Y_d l]\!]} = \frac{1}{2} \frac{\sum_{k,l} C_{kl} s^k Q^{2l}}{\sum_{k,l} B_{kl} s^k Q^{2l}}.$$

It is also useful to introduce the function $\mathfrak{D}_d$ by the following definition:

$$\frac{\mathfrak{D}_d^2}{E_\nu^2} = \frac{1}{2\mathfrak{F}_d} = \frac{1}{2} \frac{\sum_{k,l} A_{kl} s^k Q^{2l}}{\sum_{k,l} B_{kl} s^k Q^{2l}}.$$

Although neither $\mathfrak{D}_d$ nor $\mathfrak{n}_d$ make obvious physical sense by themselves, they are useful for illustrating the behavior of the functions $\mathfrak{D}$ and $\mathfrak{n}$ of interest in the particular case where one can neglect the corresponding contributions to $\mathfrak{D}$ and $\mathfrak{n}$ due to the reaction in the source vertex.

[a] It should be noted that, unlike $\mathfrak{F}_d$, the function $\mathfrak{n}_d$ is not a relativistic invariant, in spite of the fact that it is expressed (in lab. frame) in terms of two invariants.

This limiting case (just the opposite of the one considered for $a_{\ell 2}$-decay) is realized under the conditions

$$\left[\!\left[\widetilde{\Re}_d^{\mu\nu} q_\mu q_\nu\right]\!\right] \gg \left[\!\left[\widetilde{\Re}_s^{\mu\nu} q_\mu q_\nu\right]\!\right] \quad \text{и} \quad [\![|\mathbf{Y}_d \mathbf{l}|]\!] \gg [\![|\mathbf{Y}_s \mathbf{l}|]\!] \,.$$

In the simplest particular case, when

$$\frac{\sigma_a}{m_a} = \frac{\sigma_b}{m_b} = \frac{\sigma_\ell}{m_\ell} = \lambda = \text{const},$$

(these relations describe a kind of scaling of effective packet sizes) one can show, that the functions $\lambda^2 \mathfrak{F}_d$ (and hence $\mathfrak{D}_d/\lambda$) and $\mathfrak{n}_d$ do not depend on the parameter λ and are determined solely by kinematics. This "refined" (although certainly not very realistic) case is illustrated by the Figures in next two slides for six quasielastic neutrino and antineutrino scattering reactions on free nucleons.

The domains of the functions $\mathfrak{F}_d$ and $\mathfrak{n}_d$ are bounded by the kinematic conditions (230) and (231), and differences in the shape of the surfaces depicted in different panels are mainly due to different reaction thresholds (230), i.e., essentially the masses of the final leptons. Therefore, the differences are leveled out at sufficiently high energies, i.e., at $s \gg \max(s_{\mathsf{th}})$. The tendency of the function $\mathfrak{F}_d$ to zero at $E_\nu \to 0$ for the threshold-free reaction $\nu n \to p e^-$ is irrelevant for our problem limited to consideration of ultrarelativistic neutrinos.

In the nonrelativistic limit ($E_\nu \sim m_j$, see Appendix H.3, p. 876) the formulas for the dispersion are strongly modified.

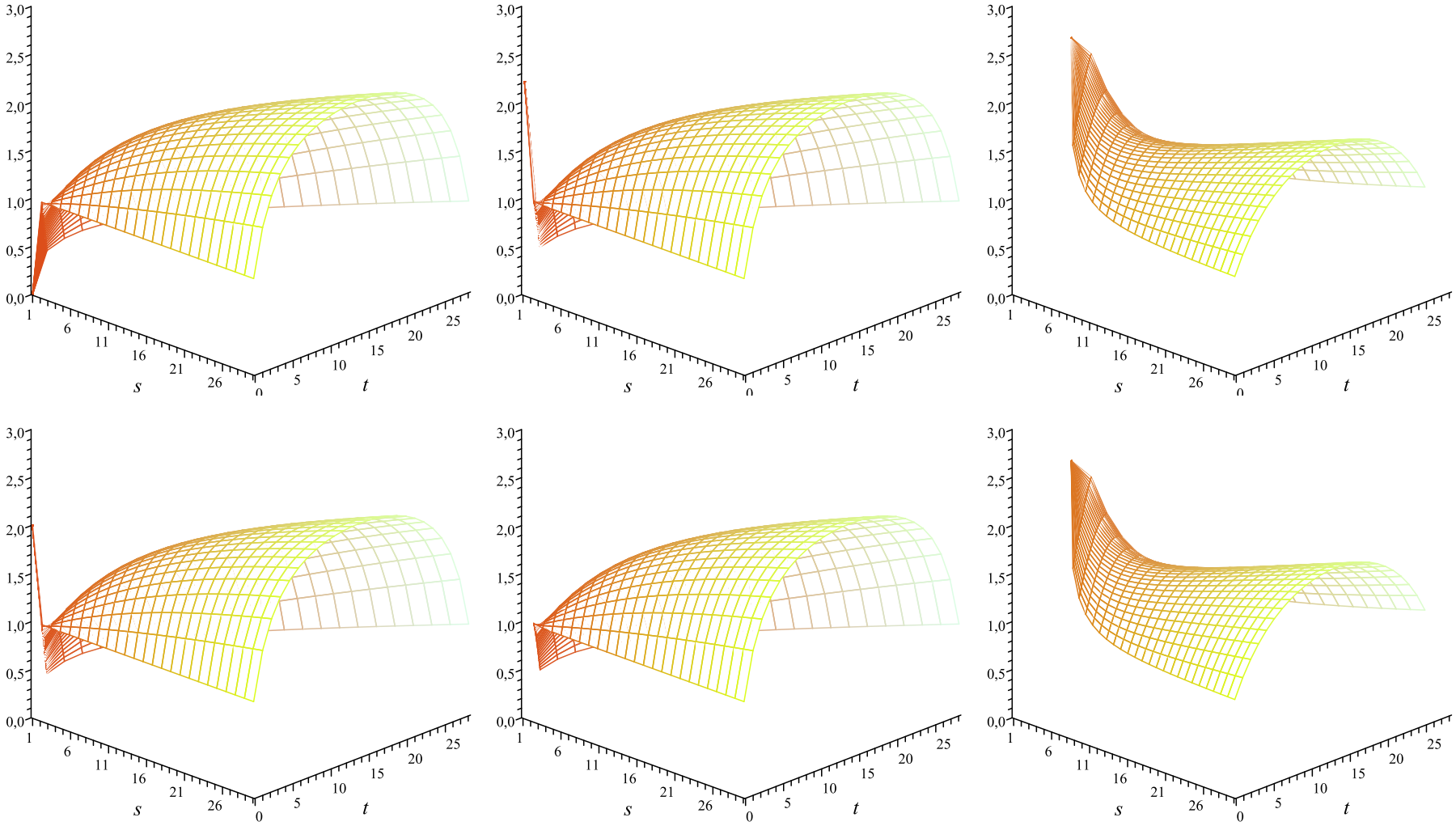

△ Function $\lambda^2\mathfrak{F}_d$ vs. s and $t = Q^2$ (both variables are in GeV^2) for quasielastic reactions $\nu n \to p e^-$ (top left), $\nu n \to p \mu^-$ (top mid), $\nu n \to p \tau^-$ (top right), $\overline{\nu} p \to n e^+$ (bottom left), $\overline{\nu} p \to n \mu^+$ (bottom mid), and $\overline{\nu} p \to n \tau^+$ (bottom right). The calculations are performed in the PW$_0$ limit with a toy "σ-scaling" model in which $\sigma_p/m_p = \sigma_n/m_n = \sigma_\ell/m_\ell = \lambda$, $\lambda = \text{const}$.

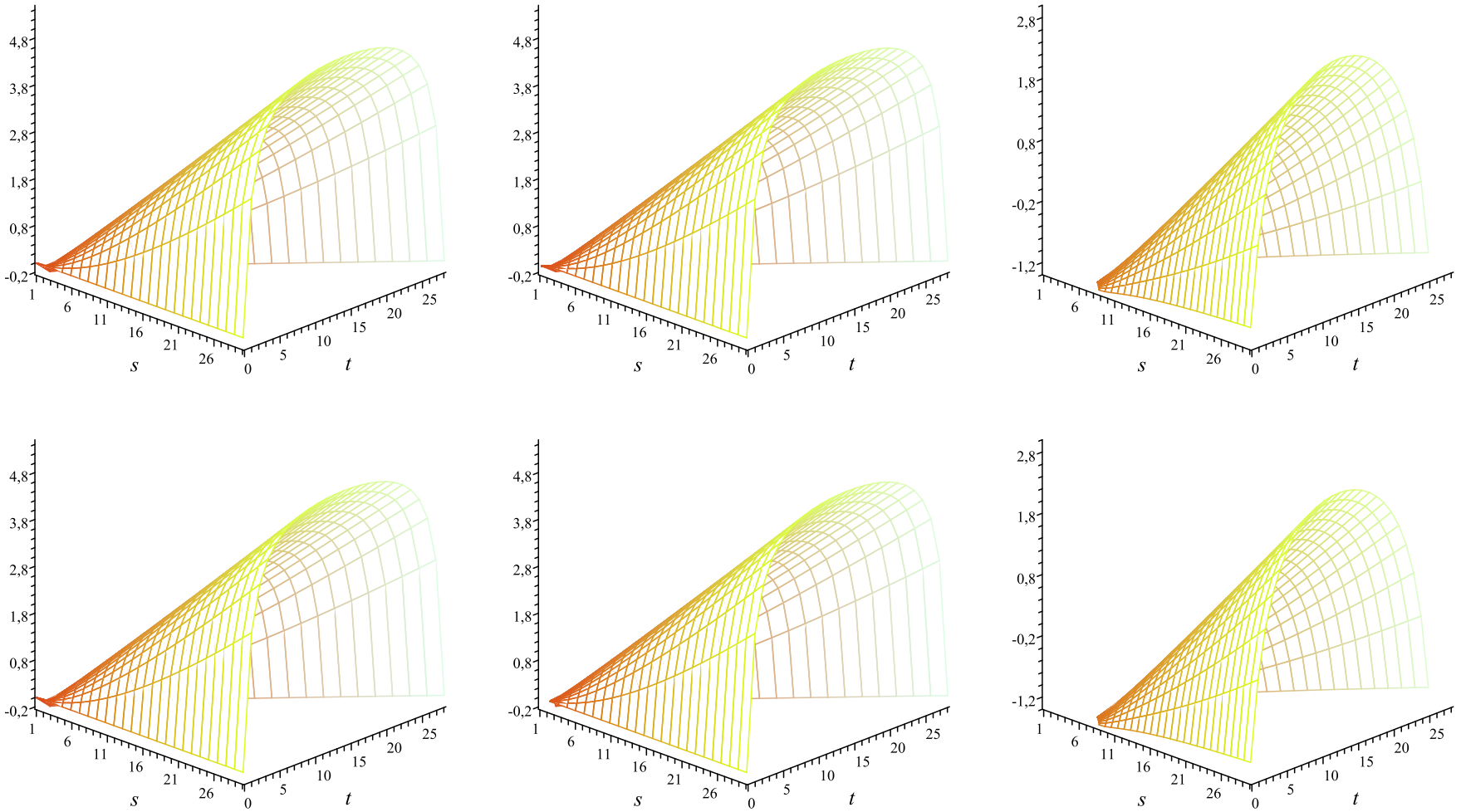

△ Function $\mathfrak{n}_d$ vs. s and $t = Q^2$ (both variables are in GeV^2) for quasielastic reactions $\nu n \to p e^-$ (top left), $\nu n \to p \mu^-$ (top mid), $\nu n \to p \tau^-$ (top right), $\overline{\nu} p \to n e^+$ (bottom left), $\overline{\nu} p \to n \mu^+$ (bottom mid), and $\overline{\nu} p \to n \tau^+$ (bottom right). The calculations are performed in the PW$_0$ limit with the "σ-scaling" model.

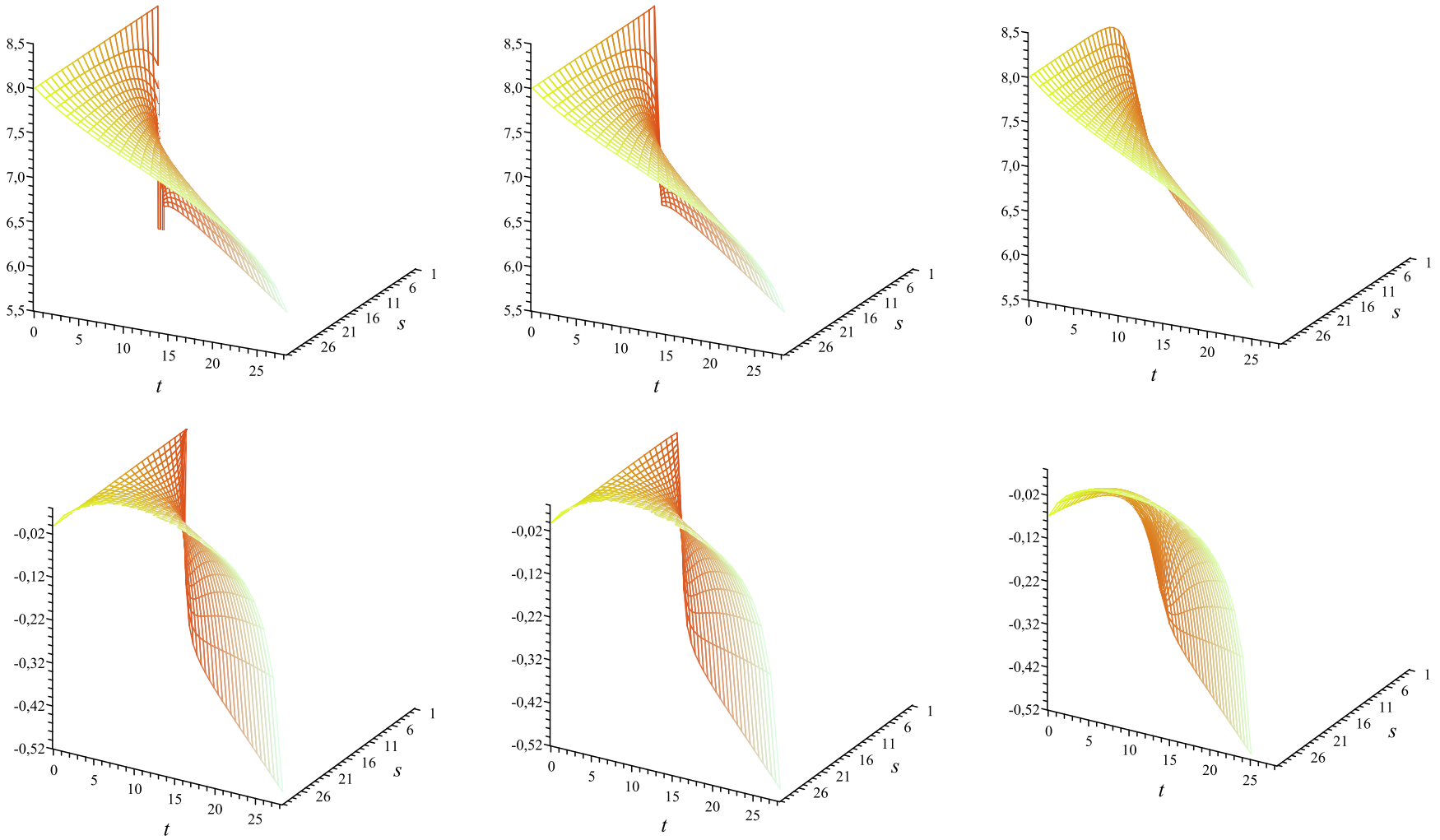

△ Functions $\lg(\mathfrak{F}_d)$ (*top panels*) and $\mathfrak{n}_d$ (*bottom panels*) vs. s and $t = Q^2$ (both variables are in GeV^2) for quasielastic reactions $\nu n \to p e^-$, $\nu n \to p \mu^-$, and $\nu n \to p \tau^-$ (from left to right). Calculations are done in the PW$_0$ limit with $\sigma_p/m_p = \sigma_n/m_n = 10^{-3}$, $\sigma_\ell/m_\ell = 10^{-4}$.

In the general case, the behavior of the functions $\mathfrak{F}_d$ and $\mathfrak{n}_d$ becomes much more involved. $\sigma_p/m_p = \sigma_n/m_n = 10\sigma_\ell/m_\ell = 10^{-3}$. Figures in previons slide show examples of the functions $\lg(\mathfrak{F}_d)$ and $\mathfrak{n}_d$ for the reactions $\nu n \to p e^-$, $\nu n \to p \mu^-$, and $\nu n \to p \tau^-$, assuming that

$$\sigma_p/m_p = \sigma_n/m_n = 10\sigma_\ell/m_\ell = 10^{-3}.$$

Of course, this assumption, adopted here for illustrative purposes only, It is, of course, accepted here solely for illustrative purposes, and is completely arbitrary and, moreover, completely unrealistic. In the more realistic situation, $\sigma_\varkappa/m_\varkappa \lll 1$, even the function $\lg(\mathfrak{F}_d)$ varies very much within its domain and the details of its behavior are difficult to reproduce on a two-dimensional graph. To better understand the properties of the functions $\mathfrak{F}_d$ and $\mathfrak{n}_d$, Appendix J, p. 905 contains the most important limit cases, asymptotics, and inequalities.

I.4 Three-particle decay in the source.

The general formulas describing the three-particle decay $a \to b + \ell + \nu_*$ formally coincide with the formulas for scattering $2 \to 2$ when considered in the rest frame of the particle a. The main difference is caused by kinematics. So we will consider this case briefly.

Similar to the $2 \to 2$ scattering case, the functions $|\Re_s|$ and $\widetilde{\Re}_s^{\mu\nu} q_\mu q_\nu$ can be written in terms of two independent invariant variables, which can be, for example, any pair of invariants

$$s_1 = (p_b + p_\ell)^2 = (p_a - p_\nu)^2\,, \quad s_2 = (p_\nu + p_\ell)^2 = (p_a - p_b)^2\,, \quad s_3 = (p_\nu + p_b)^2 = (p_a - p_\ell)^2\,,$$

related by the identity $s_1 + s_2 + s_3 = m_a^2 + m_b^2 + m_\ell^2$. The physical domain for these variables is given by the conditions

$$(m_b + m_\ell)^2 \le s_1 \le m_a^2, \quad m_\ell^2 \le s_2 \le (m_a - m_\ell)^2\,, \quad m_b^2 \le s_3 \le (m_a - m_b)^2\,.$$

For certainty, we will use the pair (s_1, s_2). The domain for this pair is the Dalitz diagram

$$s_1^- \le s_1 \le s_1^+, \quad m_\ell^2 \le s_2 \le (m_a - m_\ell)^2,$$

where

$$s_1^\pm = m_b^2 + m_\ell^2 - \frac{\left(s_2 + m_b^2\right)\left(s_2 - m_a^2 + m_\ell^2\right) \mp \left(s_2 - m_b^2\right)\sqrt{\left(s_2 - m_a^2 - m_\ell^2\right)^2 - 4m_a^2 m_\ell^2}}{2s_2}.$$

Using the results of the previous section, we find, for example,

$$[\![|\Re_s|]\!] = \frac{\sigma_3^2}{4m_a^2 m_b^2 m_\ell^2} \sum_{k,l=0}^{2} A'_{kl} s_1^k s_2^l,$$

$$\left[\!\left[|\Re_s| \widetilde{\Re}_d^{\mu\nu} q_\mu q_\nu\right]\!\right] = \frac{\sigma_3^2}{4m_a^2 m_b^2 m_\ell^2} \sum_{k,l=0}^{2} B'_{kl} s_1^k s_2^l.$$

Hence, the quadratic form $\widetilde{\Re}_s^{\mu\nu} q_\mu q_\nu$ is a rational function of the variables s_1 and s_2,

$$\left[\!\left[\widetilde{\Re}_s^{\mu\nu} q_\mu q_\nu\right]\!\right] = \frac{\sum_{k,l} B'_{kl} s_1^k s_2^l}{\sum_{k,l} A'_{kl} s_1^k s_2^l} \equiv \mathfrak{F}_s(s_1, s_2).$$

The non-zero coefficients A'_{kl} and B'_{kl} are written out in Appendix J, p. 905. There are also formulas for the function $\mathfrak{F}_s(s_1, s_2)$ in the case of a strong parameter hierarchy $\sigma_\varkappa$.

J More formulas for the $2 \to 2$ and $1 \to 3$ processes.

Here, we have collected some cumbersome formulas and technical details useful for practical calculations of the amplitudes for the macrodiagrams which include the virtual neutrino quasielastic scattering in the detector vertex and 3-particle decay in the source vertex.

J.1 Coefficients A_{kl}, B_{kl}, and C_{kl} $(2 \to 2)$.

The coefficients A_{kl}, B_{kl} $(0 \le k,l \le 2)$, and C_{kl} $(0 \le k,l \le 3)$, involved into the functions $[\![|\Re_d|]\!]$, $\left[\!\left[|\Re_d|\widetilde{\Re}_d^{\mu\nu}q_\mu q_\nu\right]\!\right]$, and $[\![|\Re_d|\mathbf{Y}_d\mathbf{q}]\!]$ defined at p. 897 are

$$
\begin{aligned}
A_{00} &= \sigma_b^2 m_a^2 m_\ell^2 \left[\sigma_a^2\left(\sigma_a^2+\sigma_b^2\right)\left(m_a^2-2m_b^2\right)+\sigma_\ell^2\left(\sigma_b^2+\sigma_\ell^2\right)\left(m_\ell^2-2m_b^2\right)-3\sigma_a^2\sigma_\ell^2 m_b^2\right] \\
&\quad +\sigma_3^2 m_b^2\left[\sigma_b^2 m_b^2\left(\sigma_a^2 m_\ell^2+\sigma_\ell^2 m_a^2\right)+\sigma_a^2\sigma_\ell^2\left(m_b^4-4m_a^2 m_\ell^2\right)\right], \\
A_{01} &= \sigma_a^2\left\{\sigma_b^2\left[2\sigma_a^2 m_\ell^2\left(m_a^2+m_b^2\right)+\sigma_\ell^2\left(m_b^2+m_\ell^2\right)\left(m_a^2+2m_b^2\right)\right]\right. \\
&\quad \left.+2\left[\sigma_b^4 m_\ell^2\left(m_a^2+m_b^2\right)+\sigma_\ell^2 m_b^4\left(\sigma_a^2+\sigma_\ell^2\right)\right]\right\}, \\
A_{02} &= \sigma_3^2\sigma_a^2\left(\sigma_b^2 m_\ell^2+\sigma_\ell^2 m_b^2\right), \\
A_{10} &= -\sigma_\ell^2\left\{\sigma_b^2\left[\sigma_a^2\left(m_a^2+m_b^2\right)\left(2m_b^2+m_\ell^2\right)+2\sigma_\ell^2 m_a^2\left(m_b^2+m_\ell^2\right)\right]\right. \\
&\quad \left.+2\left[\sigma_b^4 m_a^2\left(m_b^2+m_\ell^2\right)+\sigma_a^2 m_b^4\left(\sigma_a^2+\sigma_\ell^2\right)\right]\right\}, \\
A_{11} &= -\sigma_a^2\sigma_\ell^2\left[\sigma_b^2\left(m_a^2+m_b^2+m_\ell^2\right)+2\sigma_3^2 m_b^2\right], \\
A_{12} &= -\sigma_a^2\sigma_b^2\sigma_\ell^2,
\end{aligned}
$$

$$
\begin{aligned}
A_{20} &= \sigma_3^2\sigma_\ell^2\left(\sigma_a^2 m_b^2+\sigma_b^2 m_a^2\right),\\
A_{21} &= \sigma_a^2\sigma_b^2\sigma_\ell^2,\\
A_{22} &= 0;
\end{aligned}
$$

$$
\begin{aligned}
B_{00} &= m_a^2 m_\ell^2\left\{\sigma_b^2\left(m_a^2+m_\ell^2\right)\left[\sigma_a^2\left(m_a^2+m_b^2\right)+\sigma_b^2\left(m_a^2+m_\ell^2\right)\right.\right.\\
&\qquad \left.\left.+\sigma_\ell^2\left(m_b^2+m_\ell^2\right)\right]+m_b^2\left(\sigma_a^4 m_a^2+\sigma_\ell^4 m_\ell^2+\sigma_a^2\sigma_\ell^2 m_b^2\right)\right\},\\
B_{01} &= m_a^2\left\{2\sigma_\ell^4 m_b^2 m_\ell^2+\sigma_\ell^2\left(m_b^2+m_\ell^2\right)\left[\sigma_b^2\left(m_a^2+2m_\ell^2\right)+\sigma_a^2 m_b^2\right]\right.\\
&\qquad \left.+\sigma_b^2 m_\ell^2\left[\sigma_a^2\left(2m_a^2+m_b^2+m_\ell^2\right)+2\sigma_b^2\left(m_\ell^2+m_a^2\right)\right]\right\},\\
B_{02} &= \sigma_3^2 m_a^2\left(\sigma_b^2 m_\ell^2+\sigma_\ell^2 m_b^2\right),\\
B_{10} &= -m_\ell^2\left\{\sigma_\ell^2\left[\sigma_b^2 m_a^2\left(m_a^2+m_b^2+2m_\ell^2\right)+\sigma_a^2 m_b^2\left(m_a^2+m_b^2\right)\right]\right.\\
&\qquad \left.+\sigma_a^2\sigma_b^2\left(m_a^2+m_b^2\right)\left(m_\ell^2+2m_a^2\right)+2m_a^2\left[\sigma_a^4 m_b^2+\sigma_b^4\left(m_\ell^2+m_a^2\right)\right]\right\},\\
B_{11} &= -\left[2\sigma_3^2\sigma_b^2 m_a^2 m_\ell^2+\left(m_a^2+m_b^2+m_\ell^2\right)\left(\sigma_a^2\sigma_b^2 m_\ell^2+\sigma_b^2\sigma_\ell^2 m_a^2+\sigma_\ell^2\sigma_a^2 m_b^2\right)\right],\\
B_{12} &= -\left(\sigma_a^2\sigma_b^2 m_\ell^2+\sigma_b^2\sigma_\ell^2 m_a^2+\sigma_\ell^2\sigma_a^2 m_b^2\right),\\
B_{20} &= \sigma_3^2 m_\ell^2\left(\sigma_a^2 m_b^2+\sigma_b^2 m_a^2\right),\\
B_{21} &= \sigma_a^2\sigma_b^2 m_\ell^2+\sigma_b^2\sigma_\ell^2 m_a^2+\sigma_\ell^2\sigma_a^2 m_b^2,\\
B_{22} &= 0;
\end{aligned}
$$

$$
\begin{aligned}
C_{00} &= m_a^2 m_\ell^2 \left\{ \sigma_a^2 \left[\sigma_b^2 \left(m_a^4 + m_a^2 m_\ell^2 - m_a^2 m_b^2 + m_\ell^2 m_b^2 \right) + \sigma_\ell^2 m_b^2 \left(m_b^2 - 2 m_a^2 \right) \right] \right. \\
&\quad \left. + \left(\sigma_b^2 m_a^2 + \sigma_\ell^2 m_b^2 + \sigma_b^2 m_\ell^2 \right) \left[\sigma_b^2 m_a^2 + \left(2 m_\ell^2 - m_b^2 \right) \left(\sigma_\ell^2 + \sigma_b^2 \right) \right] \right\}, \\
C_{01} &= m_a^2 \left\{ \sigma_a^2 \left[\sigma_b^2 \left(2 m_a^2 m_\ell^2 + m_b^2 m_\ell^2 + m_\ell^4 \right) + \sigma_\ell^2 m_b^2 \left(m_\ell^2 + m_b^2 \right) \right] \right. \\
&\quad + \sigma_\ell^4 m_b^2 \left(3 m_\ell^2 - m_b^2 \right) + \sigma_b^4 m_\ell^2 \left(2 m_a^2 - m_b^2 + 3 m_\ell^2 \right) \\
&\quad \left. + \sigma_b^2 \sigma_\ell^2 \left(m_b^2 + m_\ell^2 \right) \left(m_a^2 - m_b^2 + 3 m_\ell^2 \right) \right\}, \\
C_{02} &= m_a^2 \sigma_3^2 \left(m_b^2 \sigma_\ell^2 + \sigma_b^2 m_\ell^2 \right), \\
C_{10} &= -m_\ell^2 \left\{ \sigma_a^2 \left[\sigma_b^2 \left(2 m_a^4 - 2 m_a^2 m_b^2 + m_a^2 m_\ell^2 + m_b^2 m_\ell^2 \right) + \sigma_\ell^2 m_b^2 \left(m_b^2 - 3 m_a^2 \right) \right] \right. \\
&\quad + \sigma_b^4 \left[2 m_a^2 \left(m_a^2 - m_b^2 \right) + m_\ell^2 \left(3 m_a^2 - m_b^2 \right) \right] - \sigma_\ell^4 m_b^2 \left(m_a^2 + m_b^2 \right) + \\
&\quad \left. + \sigma_b^2 \sigma_\ell^2 \left[m_a^2 \left(2 m_a^2 + 4 m_\ell^2 - 3 m_b^2 \right) - m_b^2 \left(m_b^2 + m_\ell^2 \right) \right] \right\}, \\
C_{11} &= -\sigma_a^2 \left[\sigma_b^2 m_\ell^2 \left(3 m_a^2 + m_b^2 + m_\ell^2 \right) + \sigma_\ell^2 m_b^2 \left(m_a^2 + m_b^2 + m_\ell^2 \right) \right] - \\
&\quad - \sigma_b^4 m_\ell^2 \left(m_a^2 - m_b^2 - m_\ell^2 \right) + \sigma_\ell^4 m_b^2 \left(m_a^2 + m_b^2 + m_\ell^2 \right) + \\
&\quad + \sigma_b^2 \sigma_\ell^2 \left[\left(m_b^2 + m_\ell^2 \right)^2 - m_a^2 \left(m_a^2 - m_b^2 + 3 m_\ell^2 \right) \right], \\
C_{12} &= -\sigma_a^2 \left(\sigma_b^2 m_\ell^2 + \sigma_\ell^2 m_b^2 \right) - \sigma_b^2 \sigma_\ell^2 \left(m_a^2 - m_b^2 - m_\ell^2 \right) + \sigma_b^4 m_\ell^2 + \sigma_\ell^4 m_b^2, \\
C_{20} &= m_\ell^2 \left\{ \sigma_a^2 \left[\sigma_b^2 \left(m_a^2 - m_b^2 \right) - \sigma_\ell^2 m_b^2 \right] + \sigma_b^4 \left(m_a^2 - m_b^2 \right) - \sigma_\ell^2 m_b^2 \left(\sigma_b^2 + \sigma_\ell^2 \right) + 2 \sigma_b^2 \left(\sigma_\ell^2 m_a^2 - \sigma_\ell^2 m_b^2 \right) \right\}, \\
C_{21} &= \sigma_a^2 \left(\sigma_b^2 m_\ell^2 + \sigma_\ell^2 m_b^2 \right) - 2 \sigma_b^2 \sigma_\ell^2 \left(m_b^2 + m_\ell^2 \right) - \sigma_b^4 m_\ell^2 - \sigma_\ell^4 m_b^2, \\
C_{22} &= -\sigma_b^2 \sigma_\ell^2, \quad C_{3k} = \delta_{k1} \sigma_b^2 \sigma_\ell^2 .
\end{aligned}
$$

J.2 Low-energy limits of functions $\mathfrak{F}_d$ and $\mathfrak{n}_d$.

The limits of the functions $\mathfrak{F}_d$ and $\mathfrak{n}_d$ at the kinematic threshold of the quasielastic reaction $\nu + b \to b + \ell$ in the detector are as follows:[a]

$$\mathfrak{F}_d(s_{\text{th}}, Q^2_{\text{th}}) = \frac{(m_b + m_\ell)^2}{\sigma_b^2 + \sigma_\ell^2} + \frac{m_a^2}{\sigma_a^2}, \quad \mathfrak{n}_d(s_{\text{th}}, Q^2_{\text{th}}) = -\frac{\left(\sigma_b^2 + \sigma_\ell^2\right)\left[(m_b + m_\ell)^2 - m_a^2\right]}{2\left[\sigma_a^2 (m_b + m_\ell)^2 + \sigma_b^2 m_a^2 + \sigma_\ell^2 m_a^2\right]}.$$

Here it is assumed that $m_a < m_b + m_\ell$. The thresholds s and Q^2 are

$$s_{\text{th}} = (m_b + m_\ell)^2 \quad \text{and} \quad Q^2_{\text{th}} = m_\ell \left(m_b - \frac{m_a^2}{m_b + m_\ell} \right).$$

For the thresholdless reaction ($m_a > m_b + m_\ell$, $s_{\text{th}} = m_a^2$, $Q^2_{\text{th}} = -m_\ell^2$) we find

$$\mathfrak{F}_d(s_{\text{th}}, Q^2_{\text{th}}) = 0, \quad \mathfrak{n}_d(s_{\text{th}}, Q^2_{\text{th}}) = 1 - \frac{\sigma_3^2\left[2\sigma_a^2 m_b^2 + \sigma_b^2\left(m_a^2 + m_b^2 - m_\ell^2\right)\right]}{2\left[\sigma_a^2\sigma_b^2\left(m_a^2 + m_b^2 - m_\ell^2\right) + \sigma_a^4 m_b^2 + \sigma_b^4 m_a^2\right]}.$$

Thus, the exact vanishing function $\mathfrak{F}_d$ is possible only for a threshold-free reaction (e.g., $\nu n \to pe$) at $E_\nu = 0$. Of course, this formal limit goes far beyond the ultrarelativistic approximation $E_\nu^2 \gg \max(m_j^2)$ used in the formulas for the functions $\mathfrak{F}_d$ and $\mathfrak{n}_d$ and has no practical value now, since all current neutrino experiments work exclusively with ultrarelativistic neutrinos and antineutrinos.

[a] All formulas are written in the PW_0-limit, assuming the exact energy-momentum conservation in the reaction $2 \to 2$ plus $m_j = 0$, $\forall j$. In addition, it is assumed, unless otherwise specified, that all momentum spreads $\sigma_\varkappa$ are non-zero.

It is pertinent to recall here that a more general analysis covering the nonrelativistic case (see p. 876 in Appendix F) is of potential interest in the context of studying the detection of relic ($C\nu B$) neutrinos, as well as for accelerator and astrophysics experiments searching for hypothetical superheavy neutrinos and keV-mass sterile neutrinos.

It is interesting to note that the limit $\mathfrak{F}_d$ at $E_\nu = \max(m_j) \equiv m_\nu$ and $Q^2 = -m_\ell^2$ (for a thresholdless reaction), which is given by the expression

$$\frac{4m_a^2 m_\ell^2 m_\nu^2}{\sigma_3^2 \sigma_a^2 \sigma_b^2 \sigma_\ell^2} \left[\frac{\sigma_a^2 \sigma_b^2 \left(m_a^2 + m_b^2 - m_\ell^2 \right) + \sigma_b^4 m_a^2 + \sigma_a^4 m_b^2}{\left(m_a^2 - m_b^2 \right)^2 - 2m_\ell^2 \left(m_a^2 + m_b^2 \right)^2 + m_\ell^4} \right] \left(\frac{m_a^2}{\sigma_a^2} + \frac{m_b^2}{\sigma_b^2} + \frac{m_\ell^2}{\sigma_\ell^2} \right)^{-1},$$

can still be large in magnitude if at least two of the three parameters σ_a, σ_b, and σ_ℓ are small compared to m_ν.

J.3 High-energy asymptotics of functions $\mathfrak{F}_d$ and $\mathfrak{n}_d$.

Assuming that $\sigma_{a,b,\ell} \neq 0$ and $Q^2 < \infty$, the asymptotic behavior of the functions $\mathfrak{F}_d(s, Q^2)$ and $\mathfrak{n}_d(s, Q^2)/s$ at high energies is independent of the variable s, viz:

$$\mathfrak{F}_d(s, Q^2) \underset{s \to \infty}{\sim} \frac{m_a^2}{\sigma_a^2} + \frac{m_b^2}{\sigma_b^2} + \frac{m_\ell^2}{\sigma_\ell^2} - \left(\frac{m_a^2}{\sigma_a^2} + \frac{m_b^2}{\sigma_b^2} \right)^2 \left(\frac{Q^2}{\sigma_3^2} + \frac{m_a^2}{\sigma_a^2} + \frac{m_b^2}{\sigma_b^2} \right)^{-1},$$

$$\mathfrak{n}_d(s, Q^2) \underset{s \to \infty}{\sim} \frac{s}{2\sigma_a^2} \left[\frac{m_a^2}{\sigma_a^2} + \frac{m_b^2}{\sigma_b^2} + \frac{m_\ell^2}{\sigma_\ell^2} + \frac{\sigma_3^2 m_\ell^2}{\sigma_\ell^2 Q^2} \left(\frac{m_a^2}{\sigma_a^2} + \frac{m_b^2}{\sigma_b^2} \right) \right]^{-1}.$$

These asymptotics satisfy the following inequalities:

$$\frac{m_\ell^2}{\sigma_\ell^2} < \mathfrak{F}_d(s,Q^2) < \frac{m_a^2}{\sigma_a^2} + \frac{m_b^2}{\sigma_b^2} + \frac{m_\ell^2}{\sigma_\ell^2},$$
$$\frac{\sigma_b^2\sigma_l^2\left(m_b^2 - m_a^2\right)}{2\sigma_3^2\left(\sigma_a^2 m_b^2 + \sigma_b^2 m_a^2\right)} < \mathfrak{n}_d(s,Q^2) < \frac{s}{2m_a^2}\left[1 + \frac{\sigma_a^2}{m_a^2}\left(\frac{m_b^2}{\sigma_b^2} + \frac{m_\ell^2}{\sigma_\ell^2}\right)\right]^{-1},$$

($s \to \infty$, $Q^2 < \infty$), and their limiting values at the kinematic boundaries are:

$$\lim_{s\to\infty} \mathfrak{F}_d(s,Q_-^2) = \frac{m_\ell^2}{\sigma_\ell^2}, \qquad \lim_{s\to\infty} \mathfrak{n}_d(s,Q_-^2) = \frac{\sigma_b^2\left(m_a^2 - m_b^2\right) - \sigma_\ell^2 m_b^2}{2\left(\sigma_a^2 m_b^2 + \sigma_b^2 m_a^2\right)},$$
$$\lim_{s\to\infty} \mathfrak{F}_d(s,Q_+^2) = \frac{m_b^2}{\sigma_b^2}, \qquad \lim_{s\to\infty} \mathfrak{n}_d(s,Q_+^2) = \frac{\sigma_\ell^2\left(m_a^2 - m_\ell^2\right) - \sigma_b^2 m_\ell^2}{2\left(\sigma_a^2 m_\ell^2 + \sigma_\ell^2 m_a^2\right)}.$$

These quantities, as we see, are symmetric with respect to the index replacement $b \longleftrightarrow \ell$. The thresholds $\mathfrak{n}_d(s,Q_\pm^2)$ become zero at specific relations between the parameters $\sigma_\varkappa$ and the masses. In these exotic cases, the NLO ($\propto 1/s$) corrections must be taken into account.

In the particular case where the target particle a is a nucleon, it follows from dynamical considerations that at high neutrino energy, the mean scattering angle in CIF, $\langle\theta_*\rangle$, is equal by the order of magnitude to the inverse Lorentzian factor of the lepton, $\mathit{\Gamma}_\ell^* = E_\ell^*/m_\ell$. Therefore, $\langle Q^2\rangle \sim m_\ell^2$ and $\langle\theta\rangle \sim m_\ell/\sqrt{s}$, where θ is the scattering angle of the lepton in lab. frame (coinciding with the nucleon rest frame). It can be shown that the corresponding asymptotics of the functions $\mathfrak{F}_d$ and $\mathfrak{n}_d$ are

$$\mathfrak{F}_d\left(s,m_\ell^2\right) \underset{s\to\infty}{\sim} \frac{m_\ell^2}{\sigma_\ell^2}\left[1 + \frac{\sigma_\ell^2}{\sigma_3^2}\left(\frac{m_a^2}{\sigma_a^2} + \frac{m_b^2}{\sigma_b^2}\right)\left(\frac{m_a^2}{\sigma_a^2} + \frac{m_b^2}{\sigma_b^2} + \frac{m_\ell^2}{\sigma_3^2}\right)^{-1}\right] < 2\frac{m_\ell^2}{\sigma_\ell^2},$$

$$\mathfrak{n}_d\left(s, m_\ell^2\right) \underset{s\to\infty}{\sim} \frac{\sigma_b^2\sigma_\ell^2 s}{2\left[\left(\sigma_b^2 m_a^2 + \sigma_a^2 m_b^2\right)\left(\sigma_a^2 + \sigma_b^2 + 2\sigma_\ell^2\right) + \sigma_a^2\sigma_b^2 m_\ell^2\right]} < \frac{E_\nu}{2m_a}.$$

Since at high energies a significant contribution to the counting rate of quasielastic events gives only a narrow region of angles close to $\theta = \langle\theta\rangle$, we can conclude that the effective asymptotic value of $\mathfrak{F}_d$ is practically a constant, which is mainly determined by the magnitude of the momentum dispersion of the lepton wave packet, σ_ℓ. At the same time, an arbitrary[a] variations of the parameters σ_a and σ_b can change the asymptotic only within factor of 2.

The asymptotic behavior of $\mathfrak{F}_d(s, Q^2)$ changes dramatically if one (and only one) of the parameters $\sigma_\varkappa$ turns to zero. Moreover, in the case $\sigma_a = 0$ or $\sigma_b = 0$, the asymptotics does not depend on s:

$$\mathfrak{F}_d(s, Q^2) \underset{s\to\infty}{\longrightarrow} \begin{cases} \dfrac{Q^2}{\sigma_b^2 + \sigma_\ell^2} + \dfrac{m_\ell^2}{\sigma_\ell^2}, & \text{for } \sigma_a = 0, \\ \dfrac{Q^2}{\sigma_a^2 + \sigma_\ell^2} + \dfrac{m_\ell^2}{\sigma_\ell^2}, & \text{for } \sigma_b = 0, \end{cases}$$

and at $\sigma_\ell = 0$ it grows quadratically with s:

$$\mathfrak{F}_d(s, Q^2) \underset{s\to\infty}{\sim} \frac{\left(\dfrac{Q^2}{\sigma_a^2 + \sigma_b^2} + \dfrac{m_a^2}{\sigma_a^2} + \dfrac{m_b^2}{\sigma_b^2}\right) s^2}{\left(Q^2 + m_a^2 + m_b^2\right)^2 - 4m_a^2 m_b^2}, \quad \text{for } \sigma_\ell = 0.$$

[a] Not violating, of course, the conditions of applicability of the CRGP model.

J.4 Other variables.

Some properties of the function $\mathfrak{F}_d$ become more transparent being rewritten in terms of the variables E_ν and θ_*. Consider the asymptotic expansion of $\mathfrak{F}_d$ for $E_\nu \to \infty$ and a fixed value of the angle θ_*. For not too small values of $\sin\theta_*$ it can be written as

$$\begin{aligned}\mathfrak{F}_d(E_\nu,\theta_*) = \frac{m_a^2}{\sigma_a^2} + \frac{m_b^2}{\sigma_b^2} + \frac{m_\ell^2}{\sigma_\ell^2} - \frac{a_1\sigma_3^2}{2m_a E_\nu \sin^2\theta_*}\left\{\left[\left(\frac{m_b^2}{\sigma_b^2}+\frac{m_\ell^2}{\sigma_\ell^2}\right)\cos\theta_*\right.\right.\\ \left.+\left(\frac{m_b^2\sigma_\ell^2 - m_\ell^2\sigma_b^2}{m_\ell^2\sigma_b^2 + m_b^2\sigma_\ell^2}\right)\left(\frac{2m_a^2}{\sigma_a^2}+\frac{m_b^2}{\sigma_b^2}+\frac{m_\ell^2}{\sigma_\ell^2}\right)\right]^2\\ \left.+\left(\frac{4m_a m_b m_\ell}{\sigma_a\sigma_b\sigma_\ell}\right)^2\left(\frac{m_b^2}{\sigma_b^2}+\frac{m_\ell^2}{\sigma_\ell^2}\right)^{-2}\left(\frac{m_a^2}{\sigma_a^2}+\frac{m_b^2}{\sigma_b^2}+\frac{m_\ell^2}{\sigma_\ell^2}\right)\right\}\\ +\frac{1}{\sin^4\theta_*}\cdot\mathcal{O}\left(\frac{m_a^2}{E_\nu^2}\right).\end{aligned}$$

For $\sin\theta_* = 0$ we obtain:

$$\mathfrak{F}_d(E_\nu,0) = \frac{m_\ell^2}{\sigma_\ell^2}\left[1 - \frac{m_a^2 - m_b^2}{m_a E_\nu} + \mathcal{O}\left(\frac{m_a^2}{E_\nu^2}\right)\right],$$

$$\mathfrak{F}_d(E_\nu,\pi) = \frac{m_b^2}{\sigma_b^2}\left[1 - \frac{m_a^2 - m_\ell^2}{m_a E_\nu} + \mathcal{O}\left(\frac{m_a^2}{E_\nu^2}\right)\right].$$

As noted above, at high energies $\langle\theta_*\rangle \sim \Gamma_\ell^* = E_\ell^*/m_\ell$.

It can be proved that the corresponding asymptotic expansion has the form

$$\mathfrak{F}_d(E_\nu, \theta_* = 1/\Gamma_\ell^*) = \frac{m_\ell^2}{\sigma_\ell^2}\left[b_0 - \frac{b_1\sigma_3^2}{m_a(b_0-1)^2E_\nu} + \mathcal{O}\left(\frac{m_a^2}{E_\nu^2}\right)\right],$$

where

$$\begin{aligned}
b_0 &= 1 + \frac{\sigma_\ell^2\left(m_b^2\sigma_a^2 + m_a^2\sigma_b^2\right)}{\sigma_3^2\left(m_b^2\sigma_a^2 + m_a^2\sigma_b^2\right) + m_\ell^2\sigma_a^2\sigma_b^2},\\
b_1 &= 8\sigma_\ell^2\left(m_b^2\sigma_a^2 + m_a^2\sigma_b^2\right)^3\left[m_b^2\left(m_a^2 - m_b^2 + \frac{1}{3}m_\ell^2\right)\sigma_a^2 + m_a^2\left(m_a^2 - m_b^2 + \frac{4}{3}m_\ell^2\right)\sigma_b^2\right]\\
&\quad + 2\sigma_\ell^2\left(m_b^2\sigma_a^2 + m_a^2\sigma_b^2\right)\left[m_b^2\sigma_a^4 + \left(m_a^2 + m_b^2 + m_\ell^2\right)\sigma_a^2\sigma_b^2 + m_a^2\sigma_b^4\right]\\
&\quad \times\left[m_b^2\left(m_a^2 - m_b^2 - m_\ell^2\right)\sigma_a^2 + m_a^2\left(m_a^2 - m_b^2 + m_\ell^2\right)\sigma_b^2\right],
\end{aligned}$$

and $\sigma_3^2 = \sigma_a^2 + \sigma_b^2 + \sigma_\ell^2$. It is therefore seen that the effective asymptotic (high-energy) value of $\mathfrak{F}_d(E_\nu, \theta_*)$ is practically constant ($\propto m_\ell^2/\sigma_\ell^2 \gg 1$) and, given that $1 < b_0 < 2$ (since $\partial b_0/\partial\sigma_\ell^2 > 0$), its magnitude is determined mainly by the momentum dispersion of the lepton wave packet.

J.5 Strong hierarchy limit for $\mathfrak{F}_d$.

The function $\mathfrak{F}_d(s,Q^2)$ is greatly simplified in the case of a strong hierarchy between the parameters σ_a, σ_b and σ_ℓ. By calculating the corresponding consecutive limits, we find:

$$\mathfrak{F}_d(s,Q^2) \approx \begin{cases} \dfrac{\left(Q^2+m_\ell^2\right)^2}{\left(s-Q^2-m_b^2\right)^2-4m_a^2m_\ell^2}\left(\dfrac{m_a}{\sigma_a}\right)^2, & \text{for } \sigma_\ell \gg \sigma_a \gg \sigma_b, \\ \dfrac{\left(Q^2+m_\ell^2\right)^2}{\left(s-m_b^2-m_\ell^2\right)^2-4m_b^2m_\ell^2}\left(\dfrac{m_b}{\sigma_b}\right)^2, & \text{for } \sigma_\ell \gg \sigma_b \gg \sigma_a, \\ \dfrac{\left(s-m_a^2\right)^2}{\left(Q^2+m_a^2+m_b^2\right)^2-4m_a^2m_b^2}\left(\dfrac{m_b}{\sigma_b}\right)^2, & \text{for } \sigma_a \gg \sigma_b \gg \sigma_\ell, \\ \dfrac{\left(s-m_a^2\right)^2}{\left(s-Q^2-m_b^2\right)^2-4m_a^2m_\ell^2}\left(\dfrac{m_\ell}{\sigma_\ell}\right)^2, & \text{for } \sigma_a \gg \sigma_\ell \gg \sigma_b, \\ \dfrac{\left(s-Q^2-m_a^2-m_\ell^2\right)^2}{\left(s-m_b^2-m_\ell^2\right)^2-4m_b^2m_\ell^2}\left(\dfrac{m_\ell}{\sigma_\ell}\right)^2, & \text{for } \sigma_b \gg \sigma_\ell \gg \sigma_a, \\ \dfrac{\left(s-Q^2-m_a^2-m_\ell^2\right)^2}{\left(Q^2+m_a^2+m_b^2\right)^2-4m_a^2m_b^2}\left(\dfrac{m_a}{\sigma_a}\right)^2, & \text{for } \sigma_b \gg \sigma_a \gg \sigma_\ell. \end{cases}$$

In particular, we see that neither the largest nor the smallest of the three parameters $\sigma_\varkappa$ affects the shape and the value of the function $\mathfrak{F}_d(s,Q^2)$. This nontrivial (and unexpected) property can be generalized to the processes with an arbitrary number of particles in the initial and final states.

Namely, in the case of a strong hierarchy between the momentum dispersions, $\sigma_\varkappa$, the only significant parameter is the second largest momentum dispersion after the largest. This fact is very useful in the analysis of multi-particle processes (with more than two external wave packets), since it allows to consider the packets with very small (compared to the others) spreads $\sigma_\varkappa$ as plane waves. In particular, the calculation of radiative corrections becomes much simpler with the plane-wave photons as the outer lines of the Feynman macrodiagrams, since it can be done using standard QFT methods.

Recall that taking into account the loop electroweak corrections does not lead to additional computational complications associated with the wave-packet formalism, since the loops are all formally included in the corresponding matrix elements and are in no way related to the characteristics of the external incoming and outgoing states. By convention, gauge bosons also cannot appear as the external lines of the macrodiagrams.

J.6 Coefficients A'_{kl} and B'_{kl} $(1 \to 3)$.

The coefficients A'_{kl} and B'_{kl} $(0 \leq k, l \leq 2)$, appearing in the expressions for the functions $|\Re_s|$ and $\mathfrak{F}_s(s, Q^2)$ for 3-particle decay (see p. 903) have the form

$$
\begin{aligned}
A'_{00} &= \sigma_\ell^2 \left[\sigma_a^2 m_b^2 \left(\sigma_a^2+\sigma_\ell^2\right)\left(m_a^2-m_\ell^2\right)^2 + \sigma_b^2 m_a^2 \left(\sigma_b^2+\sigma_\ell^2\right)\left(m_b^2-m_\ell^2\right)^2\right] \\
&\quad + \sigma_a^2\sigma_b^2 m_\ell^2 \left\{\sigma_\ell^2\left[m_\ell^2\left(m_a^2+m_b^2+m_\ell^2\right) - 7m_a^2 m_b^2\right] + \left(\sigma_a^2+\sigma_b^2\right)\left(m_\ell^4 - 4m_a^2 m_b^2\right)\right\}, \\
A'_{01} &= -\sigma_a^2\left\{\sigma_b^2\left[\sigma_\ell^2\left(m_b^2+m_\ell^2\right)\left(m_a^2+2m_\ell^2\right) + 2m_\ell^4\left(\sigma_a^2+\sigma_b^2\right)\right] + 2\sigma_\ell^2 m_b^2\left(m_\ell^2+m_a^2\right)\left(\sigma_a^2+\sigma_\ell^2\right)\right\}, \\
A'_{02} &= \sigma_3^2\sigma_a^2\left(\sigma_b^2 m_\ell^2 + \sigma_\ell^2 m_b^2\right), \\
A'_{10} &= -\sigma_b^2\left\{\sigma_a^2\left[\sigma_\ell^2\left(m_\ell^2+m_a^2\right)\left(m_b^2+2m_\ell^2\right) + 2m_\ell^4\left(\sigma_a^2+\sigma_b^2\right)\right] + 2\sigma_\ell^2 m_a^2\left(\sigma_b^2+\sigma_\ell^2\right)\left(m_\ell^2+m_b^2\right)\right\}, \\
A'_{11} &= \sigma_a^2\sigma_b^2\left[\sigma_\ell^2\left(m_a^2+m_b^2+m_\ell^2\right) + 2\sigma_3^2 m_\ell^2\right],
\end{aligned}
$$

$$
\begin{aligned}
A'_{12} &= -\sigma_a^2\sigma_b^2\sigma_\ell^2,\\
A'_{20} &= \sigma_3^2\sigma_b^2\left(\sigma_a^2 m_\ell^2+\sigma_\ell^2 m_a^2\right),\\
A'_{21} &= -\sigma_a^2\sigma_b^2\sigma_\ell^2,\\
A'_{22} &= 0;
\end{aligned}
$$

$$
\begin{aligned}
B'_{00} &= m_a^2 m_b^2\left\{\sigma_\ell^2\left(m_a^2+m_b^2\right)\left[\sigma_a^2\left(m_a^2+m_\ell^2\right)+\sigma_b^2\left(m_b^2+m_\ell^2\right)+\sigma_\ell^2\left(m_a^2+m_b^2\right)\right]+\right.\\
&\quad \left.+m_\ell^2\left(\sigma_a^4 m_a^2+\sigma_b^4 m_b^2+\sigma_a^2\sigma_b^2 m_b^2\right)\right\},\\
B'_{01} &= -m_a^2\left\{\sigma_a^2\left[\sigma_b^2 m_\ell^2\left(m_b^2+m_\ell^2\right)+\sigma_\ell^2 m_b^2\left(2m_a^2+m_b^2+m_\ell^2\right)\right]\right.\\
&\quad \left.+2m_b^2\left[\sigma_b^4 m_\ell^2+\sigma_\ell^4\left(m_a^2+m_b^2\right)\right]+\sigma_b^2\sigma_\ell^2\left(m_b^2+m_\ell^2\right)\left(m_a^2+2m_b^2\right)\right\},\\
B'_{02} &= \sigma_3^2 m_a^2\left(\sigma_b^2 m_\ell^2+\sigma_\ell^2 m_b^2\right),\\
B'_{10} &= -m_b^2\left\{2\sigma_a^4 m_a^2 m_\ell^2+\sigma_a^2\left(m_a^2+m_\ell^2\right)\left[\sigma_b^2 m_\ell^2+\sigma_\ell^2\left(2m_a^2+m_b^2\right)\right]\right.\\
&\quad \left.+\sigma_\ell^2 m_a^2\left[2\sigma_\ell^2\left(m_a^2+m_b^2\right)+\sigma_b^2\left(m_a^2+2m_b^2+m_\ell^2\right)\right]\right\},\\
B'_{11} &= 2\sigma_3\sigma_\ell^2 m_a^2 m_b^2+\left(m_a^2+m_b^2+m_\ell^2\right)\left(\sigma_a^2\sigma_b^2 m_\ell^2+\sigma_b^2\sigma_\ell^2 m_a^2+\sigma_\ell^2\sigma_a^2 m_b^2\right),\\
B'_{12} &= -\left(\sigma_a^2\sigma_b^2 m_\ell^2+\sigma_b^2\sigma_\ell^2 m_a^2+\sigma_\ell^2\sigma_a^2 m_b^2\right),\\
B'_{20} &= \sigma_3^2 m_b^2\left(\sigma_a^2 m_\ell^2+\sigma_\ell^2 m_a^2\right),\\
B'_{21} &= \sigma_a^2\sigma_b^2 m_\ell^2+\sigma_b^2\sigma_\ell^2 m_a^2+\sigma_\ell^2\sigma_a^2 m_b^2,\\
B'_{22} &= 0.
\end{aligned}
$$

J.7 Strong hierarchy limit for $\mathfrak{F}_s$.

Similar to the $2 \to 2$ scattering case, the function $\mathfrak{F}_s(s_1, s_2)$ becomes especially simple when there is a strong hierarchy between the parameters σ_a, σ_b, and σ_ℓ:

$$\mathfrak{F}_s(s_1,s_2) \approx \begin{cases} \dfrac{\left(s_1+s_2-m_a^2-m_b^2\right)^2}{\left(s_2-m_a^2-m_\ell^2\right)^2-4m_a^2m_\ell^2}\left(\dfrac{m_a}{\sigma_a}\right)^2, & \text{for } \sigma_\ell \gg \sigma_a \gg \sigma_b, \\ \dfrac{\left(s_1+s_2-m_a^2-m_b^2\right)^2}{\left(s_1-m_b^2-m_\ell^2\right)^2-4m_b^2m_\ell^2}\left(\dfrac{m_b}{\sigma_b}\right)^2, & \text{for } \sigma_\ell \gg \sigma_b \gg \sigma_a, \\ \dfrac{\left(s_1-m_a^2\right)^2}{\left(s_1+s_2-m_\ell^2\right)^2-4m_a^2m_b^2}\left(\dfrac{m_b}{\sigma_b}\right)^2, & \text{for } \sigma_a \gg \sigma_b \gg \sigma_\ell, \\ \dfrac{\left(s_1-m_a^2\right)^2}{\left(s_2-m_a^2-m_\ell^2\right)^2-4m_a^2m_\ell^2}\left(\dfrac{m_\ell}{\sigma_\ell}\right)^2, & \text{for } \sigma_a \gg \sigma_\ell \gg \sigma_b, \\ \dfrac{\left(s_2-m_b^2\right)^2}{\left(s_1-m_b^2-m_\ell^2\right)^2-4m_b^2m_\ell^2}\left(\dfrac{m_\ell}{\sigma_\ell}\right)^2, & \text{for } \sigma_b \gg \sigma_\ell \gg \sigma_a, \\ \dfrac{\left(s_2-m_b^2\right)^2}{\left(s_1+s_2-m_\ell^2\right)^2-4m_a^2m_b^2}\left(\dfrac{m_a}{\sigma_a}\right)^2, & \text{for } \sigma_b \gg \sigma_a \gg \sigma_\ell. \end{cases}$$

These formulas show that neither the largest nor the smallest of the parameters affect the value and shape of the function $\mathfrak{F}_s(s_1, s_2)$.

K Coefficients c_{abc}, f_{abc}, F_{abc}, $\mathcal{A}^{\pm}_{ab}$, $\mathcal{B}^{\pm}_{ab}$ (Sect. 20, p. 641).

Coefficients c_{abc} (Sect. 20.1, p. 641).

The first 125 nonzero coefficients c_{abc} in Eq. (153).

$c_{000} = 1$
$c_{100} = 1$
$c_{110} = 2$
$c_{200} = 1$
$c_{201} = 1/2$
$c_{210} = 4$
$c_{220} = 2$
$c_{300} = 1$
$c_{301} = 3/2$
$c_{310} = 6$
$c_{311} = 3/2$
$c_{320} = 6$
$c_{330} = 4/3$
$c_{400} = 1$
$c_{401} = 3$
$c_{402} = 3/8$
$c_{410} = 8$
$c_{411} = 6$
$c_{420} = 12$
$c_{421} = 2$
$c_{430} = 16/3$
$c_{440} = 2/3$
$c_{500} = 1$
$c_{501} = 5$
$c_{502} = 15/8$
$c_{510} = 10$
$c_{511} = 15$
$c_{512} = 5/4$
$c_{520} = 20$
$c_{521} = 10$
$c_{530} = 40/3$
$c_{531} = 5/3$
$c_{540} = 10/3$
$c_{550} = 4/15$
$c_{600} = 1$
$c_{601} = 15/2$
$c_{602} = 45/8$
$c_{603} = 5/16$
$c_{610} = 12$
$c_{611} = 30$
$c_{612} = 15/2$
$c_{620} = 30$
$c_{621} = 30$
$c_{622} = 15/8$
$c_{630} = 80/3$
$c_{631} = 10$
$c_{640} = 10$
$c_{641} = 1$
$c_{650} = 8/5$
$c_{660} = 4/45$
$c_{700} = 1$
$c_{701} = 21/2$
$c_{702} = 105/8$
$c_{703} = 35/16$
$c_{710} = 14$
$c_{711} = 105/2$
$c_{712} = 105/4$
$c_{713} = 35/32$
$c_{720} = 42$
$c_{721} = 70$
$c_{722} = 105/8$
$c_{730} = 140/3$
$c_{731} = 35$
$c_{732} = 7/4$
$c_{740} = 70/3$
$c_{741} = 7$
$c_{750} = 28/5$
$c_{751} = 7/15$
$c_{760} = 28/45$
$c_{770} = 8/315$
$c_{800} = 1$
$c_{801} = 14$
$c_{802} = 105/4$
$c_{803} = 35/4$
$c_{804} = 35/128$
$c_{810} = 16$
$c_{811} = 84$
$c_{812} = 70$
$c_{813} = 35/4$
$c_{820} = 56$
$c_{821} = 140$
$c_{822} = 105/2$
$c_{823} = 7/4$
$c_{830} = 224/3$
$c_{831} = 280/3$
$c_{832} = 14$
$c_{840} = 140/3$
$c_{841} = 28$
$c_{842} = 7/6$
$c_{850} = 224/15$
$c_{851} = 56/15$
$c_{860} = 112/45$
$c_{861} = 8/45$
$c_{870} = 64/315$
$c_{880} = 2/315$
$c_{900} = 1$
$c_{901} = 18$
$c_{902} = 189/4$
$c_{903} = 105/4$
$c_{904} = 315/128$
$c_{910} = 18$
$c_{911} = 126$
$c_{912} = 315/2$
$c_{913} = 315/8$
$c_{914} = 63/64$
$c_{920} = 72$
$c_{921} = 252$
$c_{922} = 315/2$
$c_{923} = 63/4$
$c_{930} = 112$
$c_{931} = 210$
$c_{932} = 63$
$c_{933} = 7/4$
$c_{940} = 84$
$c_{941} = 84$
$c_{942} = 21/2$
$c_{950} = 168/5$
$c_{951} = 84/5$
$c_{952} = 3/5$
$c_{960} = 112/15$
$c_{961} = 8/5$
$c_{970} = 32/35$
$c_{971} = 2/35$
$c_{980} = 315/35$
$c_{990} = 4/2835$

Coefficients f_{abc} (Sect. 20.2, p. 644).

Several lower-order coefficient functions f_{abc} in Eq. (153) are:

$$
\begin{aligned}
f_{000} &= 1,\\
f_{001} &= \frac{1}{2}\theta_1 - \frac{1}{2}\omega_1,\\
f_{002} &= \frac{1}{8}\theta_1^2 + \frac{1}{4}\theta_2 - \frac{1}{2}\omega_2 + \frac{3}{8}\omega_1^2 - \frac{1}{4}\omega_1\theta_1,\\
f_{010} &= 3\omega_1 - \theta_1 - \frac{1}{\varrho}\Big(\frac{1}{2}\theta_2 - \omega_2 + \frac{1}{4}\theta_1^2\\
&\quad - \frac{1}{2}\omega_1\theta_1 + \frac{3}{4}\omega_1^2\Big),\\
f_{011} &= -\frac{3}{2}\theta_2 + 9\omega_2 - \frac{3}{4}\theta_1^2 + \frac{9}{2}\omega_1\theta_1 - \frac{45}{4}\omega_1^2\\
&\quad - \frac{1}{\varrho}\Big(\theta_3 - 3\omega_3 + \frac{3}{4}\theta_1\theta_2 - \frac{3}{4}\omega_1\theta_2\\
&\quad - \frac{3}{2}\theta_1\omega_2 + \frac{9}{2}\omega_1\omega_2 + \frac{1}{8}\theta_1^3 - \frac{3}{8}\omega_1\theta_1^2\\
&\quad + \frac{9}{8}\omega_1^2\theta_1 - \frac{15}{8}\omega_1^3\Big),\\
f_{020} &= -30\omega_2 + \frac{105}{2}\omega_1^2 + \frac{3}{2}\theta_1^2 + 3\theta_2 - 15\omega_1\theta_1\\
&\quad - \frac{1}{\varrho}\Big(36\omega_3 - 3\theta_1\theta_2 - 4\theta_3 - \frac{1}{2}\theta_1^3 + 9\omega_1\theta_2\\
&\quad + \frac{105}{2}\omega_1^3 - 90\omega_1\omega_2 + \frac{9}{2}\omega_1\theta_1^2 - \frac{45}{2}\omega_1^2\theta_1 + 18\theta_1\omega_2\Big)\\
&\quad - \frac{1}{\varrho^2}\Big(\frac{45}{4}\omega_1^2\omega_2 - \frac{3}{8}\omega_1\theta_1^3 - \frac{9}{16}\omega_1^2\theta_1^2\\
&\quad + \frac{15}{8}\omega_1^3\theta_1 - \frac{105}{32}\omega_1^4 - \frac{9}{2}\omega_2^2 + 9\omega_4\\
&\quad - \frac{9}{8}\theta_2^2 - \frac{9}{8}\omega_1^2\theta_2 - 3\theta_1\theta_3 + \frac{9}{4}\omega_1\theta_1\theta_2\\
&\quad + \frac{9}{8}\theta_1^2\theta_2 - \frac{9}{32}\theta_1^4 + \frac{9}{4}\theta_1^2\omega_2 - \frac{9}{2}\omega_1\theta_1\omega_2\\
&\quad - \frac{1}{2}\omega_2\theta_2 - 9\omega_1\omega_3\Big),\\
f_{100} &= \omega_1 - \theta_1,\\
f_{101} &= -\theta_2 + 2\omega_2 - \frac{3}{2}\omega_1^2 + \omega_1\theta_1 - \frac{1}{2}\theta_1^2,\\
f_{110} &= 3\theta_2 - 18\omega_2 + \frac{3}{2}\theta_1^2 - 9\omega_1\theta_1 + \frac{45}{2}\omega_1^2\\
&\quad + \frac{1}{\varrho}\Big(2\theta_3 - 6\omega_3 + \frac{3}{2}\theta_1\theta_2 - \frac{3}{4}\omega_1\theta_1^2\\
&\quad - \frac{3}{2}\omega_1\theta_2 - 3\theta_1\omega_2 + 9\omega_1\omega_2 + \frac{9}{4}\omega_1^2\theta_1\\
&\quad - 6\omega_3 + \frac{1}{4}\theta_1^3 - \frac{15}{4}\omega_1^3\Big),\\
f_{200} &= \theta_2 + \frac{1}{2}\theta_1^2 - 2\omega_2 + \frac{3}{2}\omega_1^2 - \omega_1\theta_1.
\end{aligned}
$$

The functions ϱ, θ_s, ω_s $(s = 0, 1, \ldots)$ are rotation invariants:

$$\varrho = \frac{1}{E_{\boldsymbol{p}}^2}\rho^{\mu\nu}p_\mu p_\nu = \rho^{\mu\nu}v_\mu v_\nu, \quad \theta_s = \mathrm{Tr}\,\boldsymbol{\rho}^s, \quad \omega_s = \mathbf{v}^T\rho^s\mathbf{v}, \quad v = (1, \mathbf{v}), \quad \mathbf{v} = \frac{\mathbf{p}}{E_{\mathbf{p}}}, \quad \boldsymbol{\rho} = ||\rho_{kn}||.$$

Coefficients F_{abc} (Sect. 20.2, p. 644).

Several lower-order coefficient functions F_{abc} in Eq. (153) are:

$$
\begin{aligned}
F_{000} &= 0,\\
F_{001} &= \frac{1}{2}\theta_1 - \frac{1}{2}\omega_1,\\
F_{002} &= \frac{1}{4}\theta_2 - \frac{1}{2}\omega_2 + \frac{1}{4}\omega_1^2,\\
F_{010} &= 3\omega_1 - \theta_1 - \frac{1}{\varrho}\Big(\frac{1}{2}\theta_2 - \omega_2 + \frac{1}{4}\theta_1^2\\
&\quad - \frac{1}{2}\omega_1\theta_1 + \frac{3}{4}\omega_1^2\Big),\\
F_{011} &= -\frac{3}{2}\theta_2 + 9\omega_2 - \frac{1}{4}\theta_1^2 + \frac{5}{2}\omega_1\theta_1 - \frac{39}{4}\omega_1^2\\
&\quad - \frac{1}{\varrho}\Big(\theta_3 - 3\omega_3 + \frac{1}{2}\theta_1\theta_2 - \frac{1}{2}\omega_1\theta_2\\
&\quad - \theta_1\omega_2 + 4\omega_1\omega_2 + \frac{1}{2}\omega_1^2\theta_1 - \frac{3}{2}\omega_1^3\Big),\\
F_{020} &= -30\omega_2 + 48\omega_1^2 + \theta_1^2 + 3\theta_2 - 12\omega_1\theta_1\\
&\quad - \frac{1}{\varrho}\Big(36\omega_3 - \frac{5}{2}\theta_1\theta_2 - 4\theta_3 - \frac{1}{4}\theta_1^3\\
&\quad + \frac{15}{2}\omega_1\theta_2 + \frac{201}{4}\omega_1^3 - 87\omega_1\omega_2\\
&\quad + \frac{13}{4}\omega_1\theta_1^2 - \frac{81}{4}\omega_1^2\theta_1 + 17\theta_1\omega_2\Big)\\
&\quad - \frac{1}{\varrho^2}\Big(\frac{21}{2}\omega_1^2\omega_2 - \frac{1}{2}\omega_1\theta_1^3 - \frac{1}{4}\omega_1^2\theta_1^2\\
&\quad + \frac{3}{2}\omega_1^3\theta_1 - 3\omega_1^4 - 4\omega_2^2 + 9\omega_4 - \theta_2^2\\
&\quad - \frac{3}{4}\omega_1^2\theta_2 - 3\theta_1\theta_3 + 2\omega_1\theta_1\theta_2\\
&\quad + \frac{5}{4}\theta_1^2\theta_2 - \frac{1}{4}\theta_1^4 + 2\theta_1^2\omega_2 - 4\omega_1\theta_1\omega_2 - 9\omega_1\omega_3\Big),\\
F_{100} &= \omega_1 - \theta_1,\\
F_{101} &= -\theta_2 + 2\omega_2 - \omega_1^2,\\
F_{110} &= 3\theta_2 - 18\omega_2 + \frac{1}{2}\theta_1^2 - 5\omega_1\theta_1 + \frac{39}{2}\omega_1^2\\
&\quad + \frac{1}{\varrho}\Big(2\theta_3 - 6\omega_3 + \theta_1\theta_2 - \omega_1\theta_2\\
&\quad - 2\theta_1\omega_2 + 8\omega_1\omega_2 + \omega_1^2\theta_1 - 3\omega_1^3\Big),\\
F_{200} &= \theta_2 - 2\omega_2 + \omega_1^2.
\end{aligned}
$$

These functions are obtained from the equality

$$\sum_{abc} f_{abc}(i\delta)^a\eta^b\Delta^c = \exp\left[\sum_{abc} F_{abc}(i\delta)^a\eta^b\Delta^c\right].$$

It is proved that $F_{200} > 0$ and therefore $f_{200} = F_{200} + \frac{1}{2}(\theta_1 - \omega_1)^2 > 0$.

Coefficients $\mathcal{A}_{ab}^{\pm}$ and $\mathcal{B}_{ab}^{\pm}$ (Sect. 20.2, p. 644).

The lowest-order real dimensionless coefficient functions $\mathcal{A}_{ab}^{\pm}$ and $\mathcal{B}_{ab}^{\pm}$ are found to be

$$
\begin{aligned}
\mathcal{A}_{00}^{\pm} &= 1, \\
\mathcal{A}_{10}^{\pm} &= 3\omega_1 - \theta_1, \\
\mathcal{A}_{01}^{\pm} &= -\frac{1}{2}\Big(1 + \zeta_0 + \omega_1 \pm \omega_1^0\Big), \\
\mathcal{A}_{11}^{\pm} &= \frac{3}{4}\omega_1\Big(4\theta_1 - 2 - 15\omega_1\Big) + \frac{1}{2}\Big(\theta_1 - \theta_2\Big) - \frac{1}{4}\theta_1^2 + 6\omega_2 + \frac{1}{2}\Big(\theta_1 - 3\omega_1\Big)\zeta_0 - 3(\omega_1^0)^2 + \omega_0^0 \pm 3\Big(2\omega_2^0 - 5\omega_1\omega_1^0 + \omega_1^0\theta_1\Big), \\
\mathcal{B}_{00}^{\pm} &= \omega_1^0 \pm \frac{1}{2}\Big(3\omega_1 - \theta_1\Big), \\
\mathcal{B}_{10}^{\pm} &= 3\Big(5\omega_1\omega_1^0 - 2\omega_2^0 - \omega_1^0\theta_1\Big) \pm \frac{3}{4}\Big[35\omega_1^2 - 20\omega_2 + \theta_1\Big(3\theta_1 - 10\omega_1\Big) + 2\Big(\theta_2 - \theta_1^2\Big)\Big], \\
\mathcal{B}_{01}^{\pm} &= \frac{3}{2}\omega_1^0\Big(\theta_1 - \zeta_0\Big) + 3\omega_2^0 - \frac{3}{2}\omega_1^0 - 9\omega_1\omega_1^0 \pm \frac{3}{4}\Big[\theta_1\Big(1 + \zeta_0 + \omega_1\Big) - \omega_1\Big(3 + 3\zeta_0 + 5\omega_1\Big) + 2\omega_0^0 + 2\omega_2 - 6(\omega_1^0)^2\Big].
\end{aligned}
$$

The new rotation invariants ω_s^0 and ζ_0 figuring here are defined as

$$
\omega_0^0 = \rho_{0k}\rho_{0k}, \quad \omega_1^0 = \rho_{0k}v_k, \quad \omega_2^0 = \rho_{0k}\rho_{kn}v_n, \quad \zeta_0 = \rho_{00} - \widetilde{\rho}_{00}^{-1}, \quad \widetilde{\rho}^{\mu\nu} = |\widetilde{\Re}|^{-1/4}\widetilde{\Re}^{\mu\nu},
$$

and the functions ω_s and θ_s were defined at p. 919.

L Complex error function and related formulas.

The Gauss error function and complementary error function of complex argument were studied in a number of works. Here we reproduce the well-known power series and asymptotic expansion:

$$\mathrm{erf}(z) = \frac{2}{\sqrt{\pi}} \int_0^z dt e^{t^2} = \frac{2}{\sqrt{\pi}} \sum_{n=0}^{\infty} \frac{(-1)^n z^{2n+1}}{(2n+1)n!} = \frac{2}{\sqrt{\pi}} e^{-z^2} \sum_{n=0}^{\infty} \frac{2^n z^{2n+1}}{(2n+1)!!}, \tag{232}$$

$$\mathrm{erfc}(z) = 1 - \mathrm{erf}(z) \sim \frac{e^{-z^2}}{\sqrt{\pi} z} \left[1 + \sum_{n=1}^{\infty} \frac{(-1)^n (2n-1)!!}{(2z^2)^n} \right] \quad \left(z \to \infty, \ \ |\arg z| < \frac{3\pi}{4} \right). \tag{233}$$

Using these formulas, one obtains the expansions

$$\mathrm{Ierf}(z) = z\,\mathrm{erf}(z) + \frac{e^{-z^2}}{\sqrt{\pi}} = \frac{1}{\sqrt{\pi}} \left[1 + z^2 - \frac{z^4}{6} + \frac{z^6}{30} - \frac{z^8}{168} + \mathcal{O}\left(z^{10}\right) \right], \tag{234a}$$

$$= \frac{e^{-z^2}}{\sqrt{\pi}} \left[1 + 2z^2 + \frac{4z^4}{3} + \frac{8z^6}{15} + \frac{16z^8}{105} + \mathcal{O}\left(z^{10}\right) \right], \tag{234b}$$

which are useful for, respectively, small $|z|$ (234a) and intermediate $|z|$ (234b).[a] To obtain the asymptotics of $\mathrm{erfc}(z)$ [and thus of $\mathrm{Ierf}(z)$] at large $|z|$ and $|\arg z| > 3\pi/4$, one has to apply Eq. (233) to $\mathrm{erfc}(-z)$ and then use the rule $\mathrm{erfc}(z) = 2 - \mathrm{erfc}(-z)$. As a result, we find:

$$\mathrm{Ierf}(z) \sim \pm z + \frac{e^{-z^2}}{2\sqrt{\pi} z^2} \left[1 - \frac{3}{2z^2} + \frac{15}{4z^4} - \frac{105}{8z^6} + \mathcal{O}\left(\frac{1}{z^8}\right) \right] \quad (z \to \infty). \tag{235}$$

[a] In practice, Eqs. (234a) and (234b) are fruitful for $|z| \lesssim 1$ and $1 \lesssim |z| \lesssim 4.5$, respectively.

The upper (lower) sign in Eq. (235) must be taken for $|\arg z| < 3\pi/4$ ($|\arg z| > 3\pi/4$).

The subsequent formulas can be used for numerical evaluation of the error function with high accuracy. They are based on the following integral representation of $\mathrm{erfc}(z)$:

$$\mathrm{erfc}(z) = \frac{2z}{\pi}\int_0^\infty \frac{dt\, e^{-t^2}}{t^2+z^2} = \frac{z}{\pi}\int_{-\infty}^\infty \frac{dt\, e^{-t^2}}{t^2+z^2}.$$

From this equation one obtains

$$\begin{aligned}
\mathrm{Re}\left[\mathrm{erfc}(a+ib)\right] &= +\frac{r}{\pi}\exp\left[-r^2\cos(2\omega)\right]\left[r^2\cos(2ab+\omega)\mathscr{I}_0(a,b)+\cos(2ab-\omega)\mathscr{I}_2(a,b)\right],\\
\mathrm{Im}\left[\mathrm{erfc}(a+ib)\right] &= -\frac{r}{\pi}\exp\left[-r^2\cos(2\omega)\right]\left[r^2\sin(2ab+\omega)\mathscr{I}_0(a,b)+\sin(2ab-\omega)\mathscr{I}_2(a,b)\right],
\end{aligned}$$

where

$$\mathscr{I}_n(a,b) = \int_{-\infty}^\infty \frac{dt\, t^n e^{-t^2}}{(t^2+a^2-b^2)^2+4a^2b^2} = \int_{-\infty}^\infty \frac{dt\, t^n e^{-t^2}}{\left[t^2+r^2\cos(2\omega)\right]^2+r^2\sin(2\omega)}, \qquad (236)$$

$$r=\sqrt{a^2+b^2}, \quad \cos\omega = \frac{a}{r}, \quad \sin\omega = \frac{b}{r};$$

all the quantities now being real. Note that the integrands in Eqs. (236) are positive and nonsingular (except for the trivial case $r=0$), and quickly decay for large value of $|t|$.

These properties allow accurate numerical integration based on standard quadrature rules.

M Spatial integration (Sect. 19.1, p. 618).

The integration over $\mathbf{x}$ and $\mathbf{y}$ in the event rate integral is performed over the explored volume of the source and over the detector fiducial volume, respectively. Here we restrict ourselves to the simplest (while not very realistic) example of homogeneous source and detector. It implies that the density functions $\overline{f}_a(\mathbf{p}_a, s_a; \mathbf{x})$ do not depend of $\mathbf{x}$ within the source and detector volumes (and vanish outside these volumes). Thus our concern is only with the L-dependent factor $e^{\Phi_{ij}}/L^2$. Below we will also assume that the detector dimensions are negligibly small in comparison with these of the source, which are in turn small in comparison with the mean distance between the source and detector.

We place the origin of the coordinate system at an internal point of the detector (point O_d in Figure) and direct the z-axis along the unit vector $-l$ that is to the interior of the source. Then $\mathbf{x} = Ll$, $L = O_sO_d$, and the source volume integral we are interested in can be written as

$$\mathcal{J}_{ij} \equiv \int_{\mathrm{V}_s} \frac{d\mathbf{x}}{L^2}\, e^{\Phi_{ij}(L)} = \int_{\Omega_s} d\mathbf{\Omega} \int_{L^N_{\mathbf{\Omega}}}^{L^F_{\mathbf{\Omega}}} dL\, e^{\Phi_{ij}(L)}.$$

Here V_s is the explored volume of the source, Ω_s is the solid angle under which this volume is seen from the origin O_d, $L^N_{\mathbf{\Omega}}$ and $L^F_{\mathbf{\Omega}}$ are, respectively, the distances from O_d to the near and far boundaries of the source for the given direction $\mathbf{\Omega} = (\sin\phi\sin\theta, \cos\phi\sin\theta, \cos\theta)$.

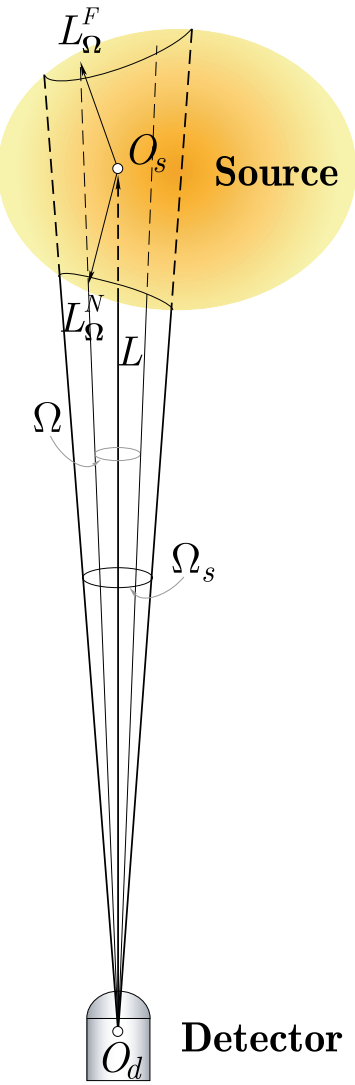

We may define the conventional distance between the source and detector as

$$\overline{L} = \frac{1}{2\Omega_s} \int_{\Omega_s} d\mathbf{\Omega} \left(L^F_{\mathbf{\Omega}} + L^N_{\mathbf{\Omega}} \right).$$

By way of avoiding misapprehension, we remark that, depending on the angular resolution of the detector, the solid angle Ω_s can be either smaller than or equal to the overall solid angle of the whole source machine; for instance, only a segment of the sun or atmosphere could be considered as the neutrino source. [Figure schematically illustrates the first possibility while the above equation for $\mathcal{J}_{ij}$ is valid in both cases.] Next, the smallness of Ω_s does not yet ensure the smallness of the source itself; a collimated accelerator beam provides a good counter-example.

The elementary integration over L yields

$$\mathcal{J}_{ij} = \frac{E_\nu L_{ij}}{4\sqrt{\pi} D} \int_{\Omega_s} d\mathbf{\Omega} \left[\mathrm{erf}\left(\frac{2\pi D L^F_{\mathbf{\Omega}}}{E_\nu L_{ij}} - \frac{iE_\nu}{2D} \right) - \mathrm{erf}\left(\frac{2\pi D L^N_{\mathbf{\Omega}}}{E_\nu L_{ij}} - \frac{iE_\nu}{2D} \right) \right]$$
$$\times \exp\left[-\frac{2E_\nu^2 + (\Delta E_{ij})^2}{8D^2} \right] \quad (i \neq j), \tag{237a}$$

$$\mathcal{J}_{jj} = \int_{\mathrm{V}_s} \frac{d\mathbf{x}}{L^2} = \int_{\Omega_s} d\mathbf{\Omega} \left(L^F_{\mathbf{\Omega}} - L^N_{\mathbf{\Omega}} \right). \tag{237b}$$

These formulas may be of some utility in processing the data from "short baseline" neutrino experiments, in which the distance from the source (e.g., the pion decay channel of a neutrino factory) to detector is comparable in magnitude with the longitudinal dimension of the source.

In case of an "ideal" experiment, for which we accept that

$$r_N = \max_{\mathbf{\Omega} \in \Omega_s} \left(\overline{L} - L^N_{\mathbf{\Omega}} \right) \ll \overline{L} \quad \text{and} \quad r_F = \max_{\mathbf{\Omega} \in \Omega_s} \left(L^F_{\mathbf{\Omega}} - \overline{L} \right) \ll \overline{L}, \tag{238}$$

we can try to apply the following expansion of the probability integral:

$$\mathrm{erf}(z+\delta) \approx \mathrm{erf}(z) + \frac{2\delta}{\sqrt{\pi}} e^{-z^2} [1 - z\delta + \frac{2}{3}(2z^2-1)\delta^2 + \ldots]. \tag{239}$$

The $\mathcal{O}(\delta^2)$ and $\mathcal{O}(z^2\delta^2)$ terms of this expansion can be neglected by assuming that $|\delta| \ll 1$ and $|z\delta| \ll 1$. In our case, the first condition reads

$$\frac{2\pi D r_{N,F}}{E_\nu L_{ij}} \ll 1, \tag{240}$$

while the second one is found to be unnecessary owing to an approximate cancellation of the second-order terms. Indeed, by applying Eq. (239) we obtain

$$\mathcal{J}_{ij} \approx \int_{\Omega_s} d\boldsymbol{\Omega} \left(L^F_{\boldsymbol{\Omega}} - L^N_{\boldsymbol{\Omega}}\right) e^{\Phi_{ij}(\overline{L})} \left\{1 - \Delta_{\boldsymbol{\Omega}} \left[\frac{2i\pi\overline{L}}{L_{ij}} - \left(\frac{2\pi D\overline{L}}{E_\nu L_{ij}}\right)^2\right]\right\},$$

$$\Delta_{\boldsymbol{\Omega}} = 2\left(1 - \frac{L^N_{\boldsymbol{\Omega}} + L^F_{\boldsymbol{\Omega}}}{2\overline{L}}\right) = \frac{L^F_{\boldsymbol{\Omega}} - \overline{L}}{\overline{L}} - \frac{\overline{L} - L^N_{\boldsymbol{\Omega}}}{\overline{L}}.$$

Evidently $|\Delta_{\boldsymbol{\Omega}}| \ll 1$. Then by assuming that

$$\max_{\boldsymbol{\Omega}\in\Omega_s} \Delta_{\boldsymbol{\Omega}} \left[\left(\frac{2\pi D\overline{L}}{E_\nu L_{ij}}\right)^4 + \left(\frac{2\pi\overline{L}}{L_{ij}}\right)^2\right]^{1/2} \ll 1, \tag{241}$$

we arrive at the result (already valid for any i and j)

$$\mathcal{J}_{ij} \approx e^{\Phi_{ij}(\overline{L})} \int_{\Omega_s} d\boldsymbol{\Omega} \left(L^F_{\boldsymbol{\Omega}} - L^N_{\boldsymbol{\Omega}}\right) \approx \mathrm{V}_s \frac{e^{\Phi_{ij}(\overline{L})}}{\overline{L}^2}. \tag{242}$$

suspected from the mean-value theorem but supplemented with the nontrivial sufficient conditions for its validity (238), (240), and (241). The volume V_s in Eq. (242) has been estimated (with the same accuracy) to be

$$\mathrm{V}_s = \int_{\mathrm{V}_s} d\mathbf{x} = \frac{1}{3} \int_{\Omega_s} d\mathbf{\Omega} \left[\left(L^F_{\mathbf{\Omega}} \right)^3 - \left(L^N_{\mathbf{\Omega}} \right)^3 \right] \approx \overline{L}^2 \int_{\Omega_s} d\mathbf{\Omega} \left(L^F_{\mathbf{\Omega}} - L^N_{\mathbf{\Omega}} \right).$$

Now, supposing that the fiducial volume of the detector V_d is small enough in comparison with V_s (that is usually the case) and the geometry of the detector is not too bizarre, the integration over $\mathbf{y}$ trivially yields

$$\int_{\mathrm{V}_d} d\mathbf{y} \int_{\mathrm{V}_s} d\mathbf{x} \, \frac{e^{\Phi_{ij}(L)}}{L^2} \approx \mathrm{V}_s \mathrm{V}_d \, \frac{e^{\Phi_{ij}(\overline{L})}}{\overline{L}^2}, \tag{243}$$

where $\overline{L}$ still has a meaning of the conventional distance between the source and detector.

To illustrate significance of the conditions (238), (240), and (241), let us consider the simple case of a spheroidal source of radius r, those angular dimension θ_s is no larger than the angular resolution of the detector. Simple geometric consideration suggests that $\Delta_{\mathbf{\Omega}} = 2(1 - \cos\theta)$ and, of course, $r_N = r_F = r$. Hence

$$\max_{\mathbf{\Omega} \in \Omega_s} \Delta_{\mathbf{\Omega}} = \Delta_{\mathbf{\Omega}_s} = 2\left(1 - \cos\theta_s\right) \approx \theta_s^2 \approx \left(r/\overline{L} \right)^2. \tag{244}$$

To simplify further, we suppose that $2\pi\overline{L} \gg |L_{ij}|$ (which is always true for the solar and astrophysical neutrinos detected at earth) and $2\pi\overline{L} \lesssim |L_{ij}| E_\nu / D$ (which may be doubtful for the distant astrophysical neutrino sources but acceptable for sun).

Then the condition (240) is automatically fulfilled while (241) is transformed to

$$\frac{2\pi r^2}{\overline{L}|L_{ij}|} \ll 1. \tag{245}$$

The latter is certainly not satisfied for sun with the currently accepted value of Δm^2_{12}. Indeed, the regions of effective neutrino production in the solar interior are the relatively narrow concentric spherical layers with typical radius from about $0.1R_\odot$ for ^{8}B, ^{7}Be, and CNO neutrinos to about $0.3R_\odot$ for pp, pep, and hep neutrinos (here $R_\odot$ is the solar radius). So the left part of the inequality (245) can roughly be estimated as

$$\frac{2\pi r^2}{\overline{L}|L_{12}|} \approx 26 \left(\frac{r}{0.2R_\odot}\right)^2 \left(\frac{|\Delta m^2_{12}|}{8\times 10^{-5}\ \text{eV}^2}\right)\left(\frac{1\ \text{MeV}}{E_\nu}\right).$$

Consequently (that is not a novelty) the approximation (243) is fully inapplicable to the solar neutrino oscillation studies.

To summarize: although our consideration is highly simplified in several respects,[a] it demonstrates that the integration over the source volume must be under careful control even in the long baseline neutrino oscillation experiments.

[a] A more sophisticated analysis must take into account the spatial distribution of colliding and/or decaying particles in the source and, what is very important for astrophysical applications (in particular, for the solar neutrino experiments), the background matter effects caused by the virtual neutrino forward scattering in the source.

N Simple examples with pion decay.

Why is it possible to neglect the neutrino mass?

Consider decay $\pi \to \mu\nu_i$, where ν_i is the mass eigenstate with mass m_i ($i = 1, 2, 3$). Then in the pion rest frame ($\mathbf{p}^\star_\mu + \mathbf{p}^\star_{\nu_i} = 0$)

$$E^\star_\nu = \frac{m^2_\pi - m^2_\mu + m^2_i}{2m^2_\pi} \quad \text{and} \quad E^\star_\mu = \frac{m^2_\pi + m^2_\mu - m^2_i}{2m^2_\pi}.$$

$\Longrightarrow$ The final states are different for the pion decay modes with different ν-species.
$\Longrightarrow$ The full pion decay width in the muon mode is

$$\Gamma(\pi \to \mu\nu_\mu) = \sum_i \Gamma(\pi \to \mu\nu_i) \propto \sum_i |\langle \mu, \nu_i | \pi \rangle|^2.$$

In the Standard Model (somehow extended by a Dirac or Majorana neutrino mass term)

$$\langle \mu, \nu_i | \pi \rangle = V^*_{\mu i}\, M_i,$$

where $M_i = \text{const}$ in the pion rest frame. Since $m_i \lll m_{\mu,\pi}$, it can be approximated (with very good precision) as $M_i \approx \langle \mu, \nu_0 | \pi \rangle$, where ν_0 is a **fictitious massless** neutrino. So, due to unitarity of $\mathbf{V}$,

$$\Gamma(\pi \to \mu\nu_\mu) \propto \sum_i |V_{\mu i}|^2 \, |\langle \mu, \nu_0 | \pi \rangle|^2 = |\langle \mu, \nu_0 | \pi \rangle|^2,$$

$$\Downarrow$$

$$\boxed{\Gamma(\pi \to \mu\nu_\mu) \approx \Gamma(\pi \to \mu\nu_0).}$$

This result is almost model-independent and almost exact: the ν mass corrections are practically unmeasurable. **Homework:** Estimate the order of magnitude of the ν mass correction.

Overlap of pion and muon wave packets.

Let's discuss the simplest example of the WP overlaping , when the states I_s and F_s contain only one packet each. For certainty, we consider the $\pi_{\mu 2}$ decay in the source and write the two-packet overlap integral corresponding to this process[a]

$$\mathsf{V}_{\pi\mu} = \int dx |\psi_\pi(\mathbf{p}_\pi, x_\pi - x)||\psi_\mu(\mathbf{p}_\mu, x_\mu - x)|.$$

Here and until the end of this section, π and μ are not Lorentz indices, but particle labels. In CIF of pion and muon ($\mathbf{p}^*_\pi = -\mathbf{p}^*_\mu \equiv \mathbf{p}_*$) it has the form

$$\mathsf{V}_{\pi\mu} = \int dx |\psi_\pi(\mathbf{p}_*, x^*_\pi - x)\psi_\mu(-\mathbf{p}_*, x^*_\mu - x)|.$$

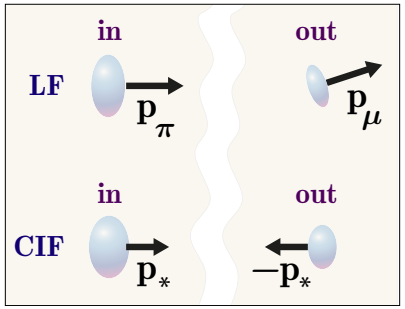

After replacing the integration variable $x \longmapsto x + (x^*_\pi + x^*_\mu)/2$ we have

$$\mathsf{V}_{\pi\mu} = \int dx \left| \psi_\pi\left(\mathbf{p}_*, x + \frac{x^*_\mu - x^*_\pi}{2}\right) \psi_\mu\left(-\mathbf{p}_*, x + \frac{x^*_\pi - x^*_\mu}{2}\right)\right|.$$

Calculation of this integral in the CRGP model boils down to the sequential calculation of four standard Gaussian quadratures, which results in

$$\mathsf{V}_{\pi\mu} = \frac{\pi^2 m_\pi m_\mu}{\sigma_\pi\sigma_\mu\,(\sigma^2_\pi + \sigma^2_\mu)\,(E^*_\pi + E^*_\mu)|\mathbf{p}_*|}\exp\left(-\mathfrak{S}_s\right),$$
$$\mathfrak{S}_s = \frac{\sigma^2_\pi\sigma^2_\mu}{\sigma^2_\pi + \sigma^2_\mu}|\mathbf{b}^*_{\pi\mu}|^2, \quad |\mathbf{b}^*_{\pi\mu}| = \left|\mathbf{n}_* \times (\mathbf{x}^*_\mu - \mathbf{x}^*_\pi)\right|. \tag{246}$$

[a] Note that the definition of $\mathsf{V}_{\pi\mu}$ is not the same as in 18.2.2.

Here $E_\pi^* = \sqrt{\mathbf{p}_*^2 + m_\pi^2}$ and $E_\mu^* = \sqrt{\mathbf{p}_*^2 + m_\mu^2}$ are the energies of pion and muon, $\mathbf{n}_* = \mathbf{p}_*/|\mathbf{p}_*|$ is the unit vector, and $|\mathbf{b}_{\pi\mu}^*|$ is the classical impact parameter in CIF of pion and muon.
Using Eq. (246) and identity[a]

$$|\mathbf{b}_{\pi\mu}^*|^2 = \left(1 + \frac{\sigma_\pi^2}{\sigma_\mu^2}\right)\left|\mathbf{b}_\pi^{(\pi)}\right|^2 + \left(1 + \frac{\sigma_\mu^2}{\sigma_\pi^2}\right)\left|\mathbf{b}_\mu^{(\mu)}\right|^2 \tag{247}$$

we find

$$\mathfrak{S}_s = \left(\frac{1}{\sigma_\pi^2} + \frac{1}{\sigma_\mu^2}\right)^{-1} |\mathbf{b}_{\pi\mu}^*|^2 = \sigma_\pi^2\left|\mathbf{b}_\pi^{(\pi)}\right|^2 + \sigma_\mu^2\left|\mathbf{b}_\mu^{(\mu)}\right|^2. \tag{248}$$

Corollaries:

- If vectors $\mathbf{n}_*$ and $\mathbf{x}_\mu^* - \mathbf{x}_\pi^*$ are collinear, then, as seen from Eq. (248), $\mathfrak{S}_s = 0$ at *any* distance between the centers of the pion and muon wave packets.
- If this distance is large enough, viz,

$$|\mathbf{x}_\mu^* - \mathbf{x}_\pi^*|^2 \gg \frac{1}{\sigma_\pi^2} + \frac{1}{\sigma_\mu^2} \tag{249}$$

  (so that the condition (90) is obviously fulfilled), the function $\mathfrak{S}_s$ is small in magnitude only at sufficiently small angles α_* between vectors $\mathbf{n}_*$ and $\mathbf{x}_\mu^* - \mathbf{x}_\pi^*$, namely at $\alpha_*^2 \ll \rho_*^{-2}$, where

$$\rho_* = \left(\frac{1}{\sigma_\pi^2} + \frac{1}{\sigma_\mu^2}\right)^{-1/2} |\mathbf{x}_\mu^* - \mathbf{x}_\pi^*|.$$

[a] From Eq. (247) it follows in particular that $\left|\mathbf{b}_\pi^{(\pi)}\right| = \left|\mathbf{b}_\mu^{(\mu)}\right| = 0$ as $|\mathbf{b}_{\pi\mu}^*| = 0$. The indices (π) and (μ), as usual, mark the CIF of the corresponding particle.

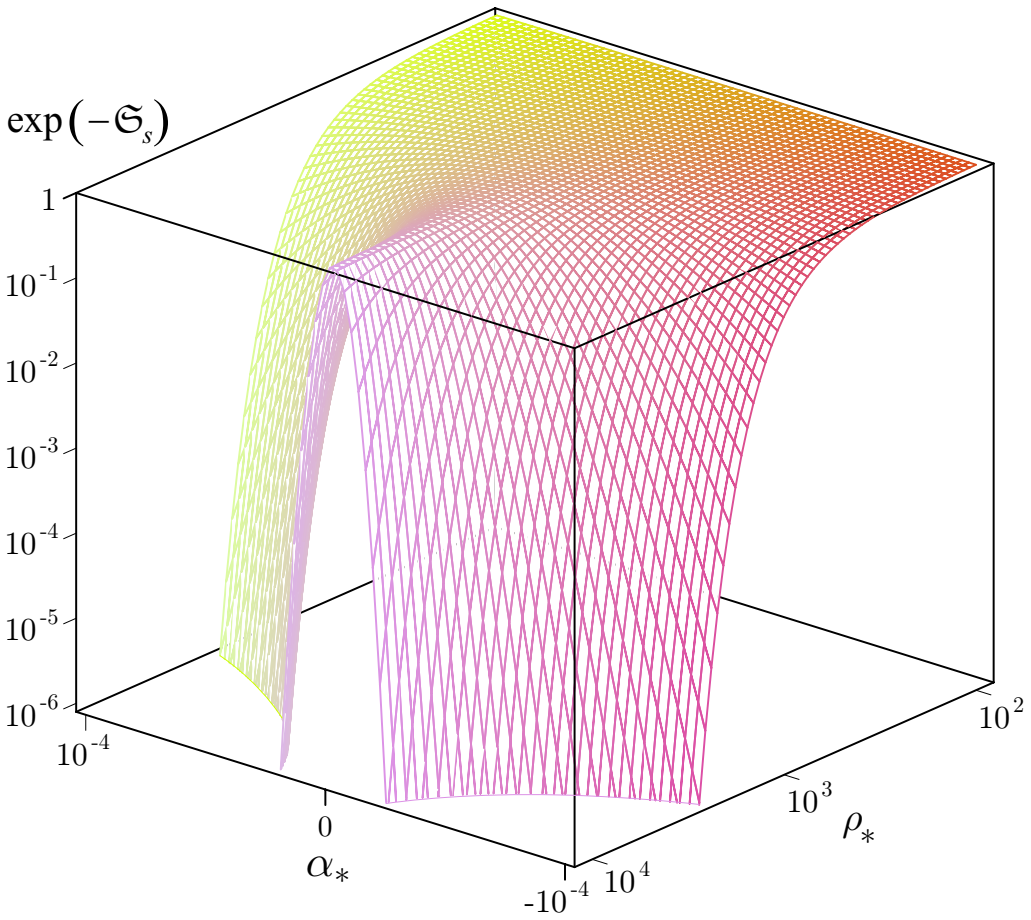

◁ Figure shows the geometric suppression factor $\exp(-\mathfrak{S}_s)$ for $\pi_{\mu 2}$ decay as a function of $\rho_* \propto |\mathbf{x}^*_\mu - \mathbf{x}^*_\pi|$ and α_* – the angle between vectors $\mathbf{n}_*$ and $\mathbf{x}^*_\mu - \mathbf{x}^*_\pi$.

As $|\alpha_*|$ increases, the function $\mathfrak{S}_s$ increases and the suppression factor $\exp(-\mathfrak{S}_s)$ decreases rapidly, excluding the possibility of $\pi_{\mu 2}$ decay with

$$\alpha_*^2 \gg \rho_*^{-2}.$$

In every experiment, we always see that the muon born in the $\pi_{\mu 2}$-decay escapes from the very point (more precisely, from the spatial region surrounding that point, limited by the resolution of the instrument) where the pion disappeared.

In the CIF of the pion and muon, this just means that the impact parameter $|\mathbf{b}^*_{\pi\mu}| \approx \alpha_* \rho_*$ is zero or very small; the same is true for $\left|\mathbf{b}^{(\pi)}_\pi\right|$ and $\left|\mathbf{b}^{(\mu)}_\mu\right| = 0$ (see the footnote on the previous slide).

Thereby we get an explanation of the "obvious" experimental fact, unexplainable in the framework of the theory with plane waves. We however leave open the question of the possibility of experimental measurement of the impact parameter $|\mathbf{b}^*_{\pi\mu}|$, which would allow us to check the above constructions.

O Some details on MSW with absorption (Sect. 23.8, p. 680).

Here we consider the case of matter with constant density and provide formulas for the two specific but potentially interesting cases: $|q| \gg |\Delta|$ and $q_I^2 \gg \varepsilon_0^2$.

Case $|q| \gg |\Delta|$

Notation. $x = \Delta/|q| \ll 1$, $r = q_R/|q| \leq 1$, $s = \sin 2\theta$, $c = \cos 2\theta$.

$$\begin{aligned}
\varepsilon_R^2 = |q|^2 \big[& r^2 - 2crx + (c^2 + s^2 r^2)x^2 - 2cs^2(1-r^2)rx^3 + s^2(1-r^2)(c^2 + r^2 - 5c^2r^2)x^4 \\
& -2cs^2 r(1-r^2)(1 - 3c^2 - 3r^2 + 7c^2r^2)x^5 + \mathcal{O}(x^6)\big] , \\
\varepsilon_I^2 = q_I^2 \big[& 1 - s^2x^2 - 2cs^2x^3 + s^2(c^2 + r^2 - 5c^2r^2)x^4 \\
& -2cs^2 r(1 - 3c^2 - 3r^2 + 7c^2r^2)x^5 + \mathcal{O}(x^6)\big] , \\
|\varepsilon|^2 = |q|^2 \big[& 1 - 2crx + s^2x^2 - 2cs^2rx^3 + s^2(c^2 + r^2 - 5c^2r^2)x^4 \\
& -4cs^2 r(1-r^2)(1 - 3c^2 - 3r^2 + 7c^2r^2)x^5 + \mathcal{O}(x^6)\big] ;
\end{aligned}$$

$$\begin{aligned}
\varepsilon_R = \zeta|q| \big| & r - cx + \tfrac{1}{2}s^2 rx^2 - \tfrac{1}{2}cs^2(1-2r^2)x^3 + \tfrac{1}{8}s^2(1-5c^2)(3-4r^2)rx^4 \\
& -\tfrac{1}{8}cs^2(3-7c^2)(1-8r^2+8r^4)x^5 + \mathcal{O}(x^6)\big| , \\
\varepsilon_I = \zeta\zeta_R q_I \xi ;
\end{aligned}$$

$$\xi = 1 - \tfrac{1}{2}s^2x^2 - cs^2rx^3 - \tfrac{1}{8}s^2(1-5c^2)(1-4r^2)x^4 - \tfrac{1}{2}cs^2(3-7c^2)(1-2r^2)rx^5 + \mathcal{O}(x^6);$$
$$I^2 = s^2x^2\left\{1 + 2crx + \left[1 - 2c^2 - 2(1-3c^2)r^2\right]x^2 + \left[2 - 3c^2 - (3-5c^2)r^2\right]x^3 + \mathcal{O}(x^4)\right\};$$

$$\begin{aligned} a_1 &= 1 + \tfrac{1}{2}s^2(1-2r^2)x^2 + cs^2(3-4r^2)rx^3 + \tfrac{1}{2}s^2\left[1 - 4c^2 - 6(1-5c^2)(1-r^2)r^2\right]x^4 \\ &\quad + 2cs^2\left[4 - 9c^2 - (3-7c^2)(5-4r^2)r^2\right]rx^5 + \mathcal{O}(x^6), \\ a_2 &= 1 + \tfrac{1}{2}s^2(1-2r^2)x^2 + cs^2(3-4r^2)rx^3 \\ &\quad + \tfrac{3}{8}s^2(1-5c^2)\left[1 - 8r^2(1-r^2)\right]x^4 + \tfrac{1}{2}cs^2(3-7c^2)\left[5 - 4r^2(5-4r^2)\right]rx^5 + \mathcal{O}(x^6); \end{aligned}$$

$$\begin{aligned} I_+ &= 1 + \tfrac{1}{4}s^2(1-2r^2)x^2 + \tfrac{1}{2}cs^2(3-4r^2)rx^3 - \tfrac{1}{16}s^2\left[3(1-5c^2) + 2(11-59c^2)(1-r^2)r^2\right]x^4 \\ &\quad + \tfrac{1}{4}cs^2\left[2(7-17c^2) - (11-27c^2)(5-4r^2)r^2\right]rx^5 + \mathcal{O}(x^6), \\ I_- &= \tfrac{1}{4}s^2x^2\left[1 + 2crx + \mathcal{O}(x^2)\right]; \end{aligned}$$

$$\begin{aligned} I_+^2 &= 1 + \tfrac{1}{2}s^2(1-2r^2)x^2 + cs^2(3-4r^2)rx^3 + \tfrac{1}{16}s^2\left[7 - 31c^2 - 48(1-5c^2)(1-r^2)r^2\right]x^4 \\ &\quad + \tfrac{1}{4}cs^2\left[31 - 71c^2 + (3-7c^2)(5-4r^2)r^2\right]rx^5 + \mathcal{O}(x^6), \\ I_-^2 &= \tfrac{1}{16}s^4x^4\left[1 + 4crx + \mathcal{O}(x^2)\right]. \end{aligned}$$

Case $q_I^2 \gg \varepsilon_0^2$

Notation. $x_s = \Delta_s^2/q_I^2$, $x = \varepsilon_0^2/q_I^2 \geq x_s$, $\zeta_I = \mathsf{sign}\,(q_I)$.

$$
\begin{aligned}
\varepsilon_R &= |q_I|\,(x-x_s)^{-1/2}\left(1+\tfrac{1}{2}x_s-\tfrac{1}{2}x_sx+\tfrac{7}{8}x_s^2+\ldots\right),\\
\varepsilon_I &= \zeta_R q_I\left(1-\tfrac{1}{2}x_s+\tfrac{1}{2}x_sx-\tfrac{5}{8}x_s^2-\tfrac{1}{2}x_sx^2+\tfrac{7}{4}x_s^2x-\tfrac{21}{16}x_s^3+\ldots\right),\\
\varepsilon_R^2 &= q_I^2(x-x_s)\left(1+x_s-x_sx+2x_s^2+\ldots\right),\\
\varepsilon_I^2 &= q_I^2\left(1-x_s+x_sx-x_s^2-x_sx^2+3x_s^2x-2x_s^3+\ldots\right),\\
|\varepsilon|^2 &= q_I^2\left(1+x-2x_s+2x_sx-2x_s^2-2x_sx^2+6x_s^2x-4x_s^3+\ldots\right),\\
|\varepsilon| &= |q_I|\left(1+\tfrac{1}{2}x-x_s-\tfrac{1}{8}x^2+\tfrac{3}{2}x_sx-\tfrac{3}{2}x_s^2+\tfrac{1}{16}x_s^3+\ldots\right),\\
a_1|\varepsilon|^2 &= q_I^2\left(1+x-\tfrac{3}{2}x_s+x_sx-x_s^2-x_sx^2+3x_s^2x-2x_s^3+\ldots\right),\\
a_2|\varepsilon|^2 &= q_I^2\left(1+x-\tfrac{3}{2}x_s+x_sx-\tfrac{9}{8}x_s^2-x_sx^2+\tfrac{25}{8}x_s^2x-\tfrac{35}{16}x_s^3+\ldots\right),\\
I_+^2 &= 1+\tfrac{1}{2}x_s-\tfrac{3}{2}x_sx+\tfrac{31}{16}x_s^2+\tfrac{5}{2}x_sx^2-\tfrac{71}{8}x_s^2x+\tfrac{217}{32}x_s^3+\ldots,\\
I_-^2 &= \tfrac{1}{16}x_s^2\left(1-2x+\tfrac{7}{2}x_s+\ldots\right),\\
I_+ &= 1+\tfrac{1}{4}x_s-\tfrac{3}{4}x_sx+\tfrac{15}{16}x_s^2+\tfrac{5}{4}x_sx^2-\tfrac{17}{4}x_s^2x+\tfrac{101}{32}x_s^3+\ldots,\\
I_- &= \tfrac{1}{4}x_s\left(1-x+\tfrac{7}{4}x_s+x^2-5x_sx+\tfrac{37}{8}x_s^2+\ldots\right),\\
\tan\varphi &= \zeta_I\,(x-x_s)^{-1/2}\left(1-\tfrac{1}{2}x_s+\tfrac{1}{2}x_sx-\tfrac{5}{8}x_s^2+\ldots\right),\\
\varphi &= \tfrac{\pi}{2}-\zeta_I\,(x-x_s)^{1/2}\left(1+\tfrac{1}{2}x_s-\tfrac{1}{3}x^2+\tfrac{1}{6}x_sx+\tfrac{13}{24}x_s^2+\ldots\right).
\end{aligned}
$$

P Neutrino (astro)physics toolkit (booklet).

- **Accelerator $\nu/\overline{\nu}$s** [ANL, BNL, CERN, FNAL, IHEP, KEK, LAMPF, J-PARC,...]

  Examples of the LBL experiments

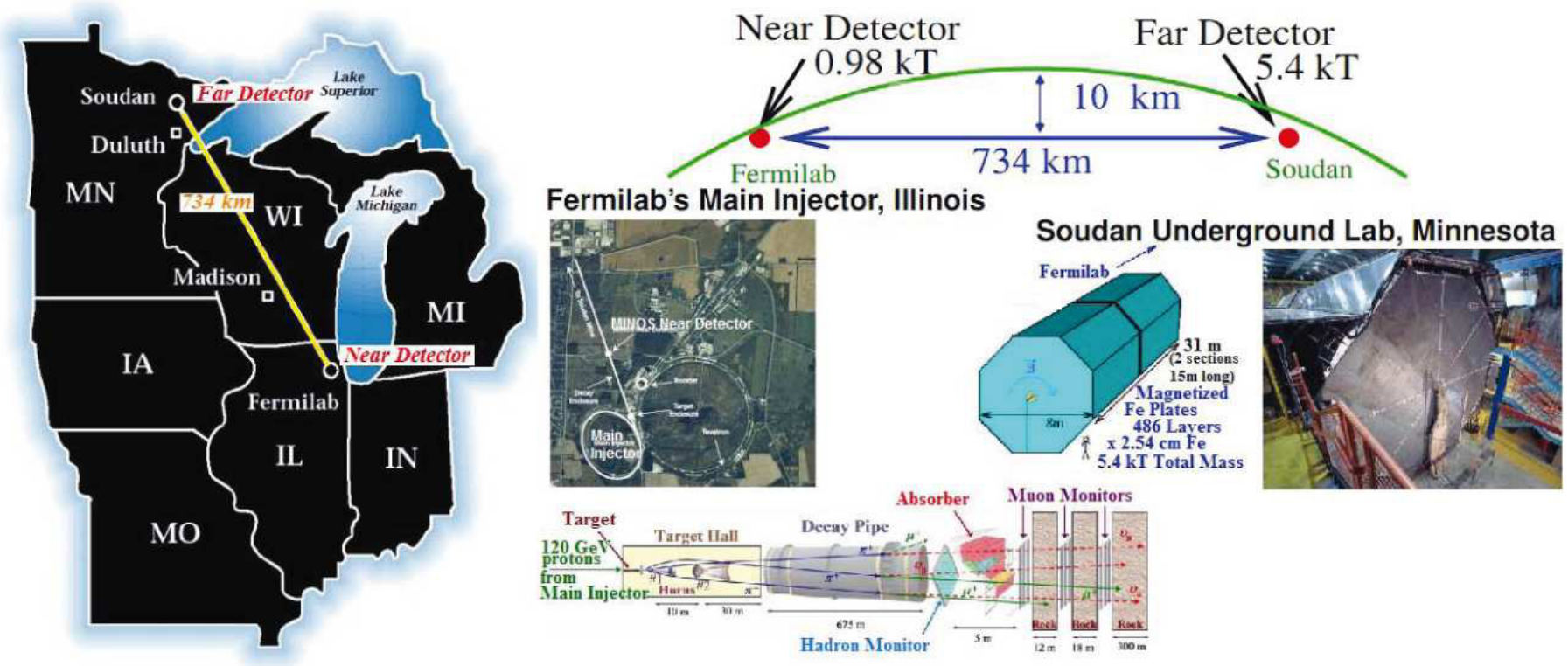

Schematic layout of the MINOS experiment [FNAL – SOUDAN].

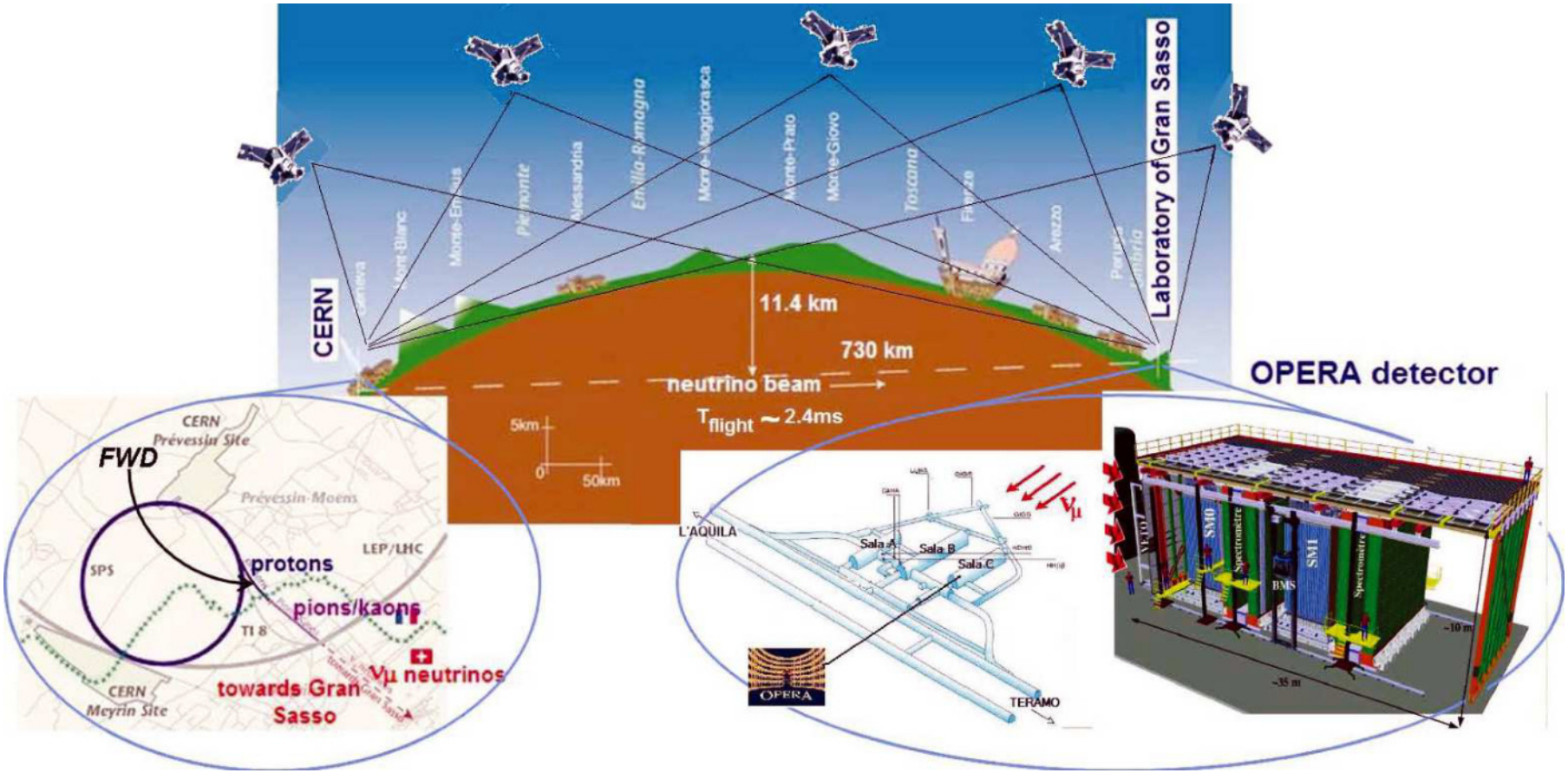

Schematic layout of the OPERA experiment [CERN – LNGS].

[Figures in this and previous slides are borrowed from G. Brunetti, "Neutrino velocity measurement with the OPERA experiment in the CNGS beam," Ph.D. thesis, in joint supervision of the Université Claude Bernard, Lyon-I and Universitá degli Studi di Bologna (May 2011), N° d'ordre 88–2011, LYCEN–T 2011–10; see URLs ⟨ http://amsdottorato.cib.unibo.it/3917 ⟩ and ⟨ http://tel.archives-ouvertes.fr/tel-00633424 ⟩.]

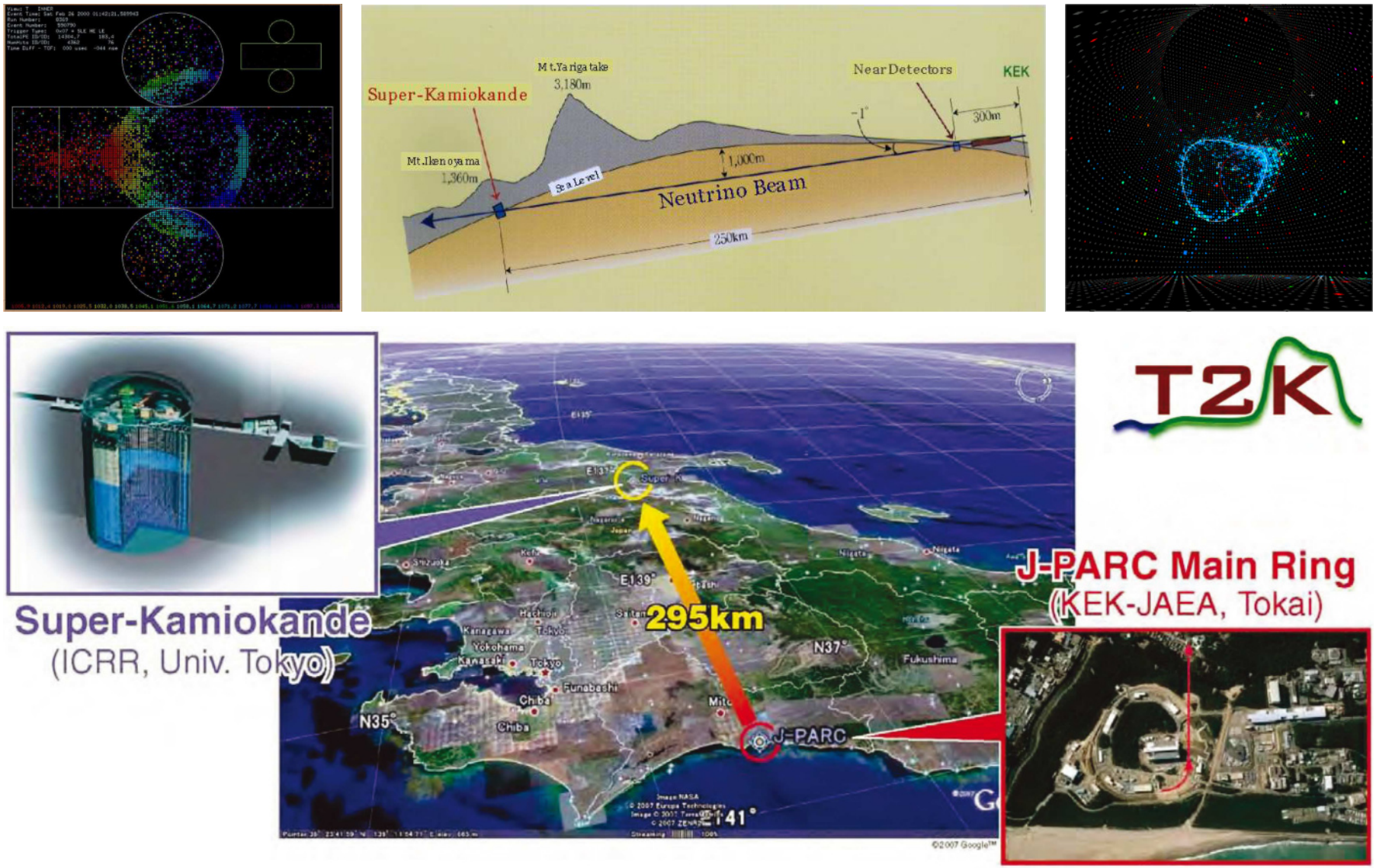

Schematic layouts of the K2K [KEK (Tsukuba) – Super-Kamiokande] and T2K [J-PARC (Tokai) – Super-Kamiokande] experiments. [From relevant websites].

- **Reactor $\overline{\nu}$s** [Angra, Braidwood, Bugey, CHOOZ & Double CHOOZ, Daya Bay, Gosgen, JOYO, KASKA, KNPP-GEMMA, KamLAND, Krasnoyarsk, Kuo-Sheng, Palo Verde, RENO, Rovno, Savannah River Site, SONGS, TEXONO,...]

  Examples of the reactor antineutrino experiments

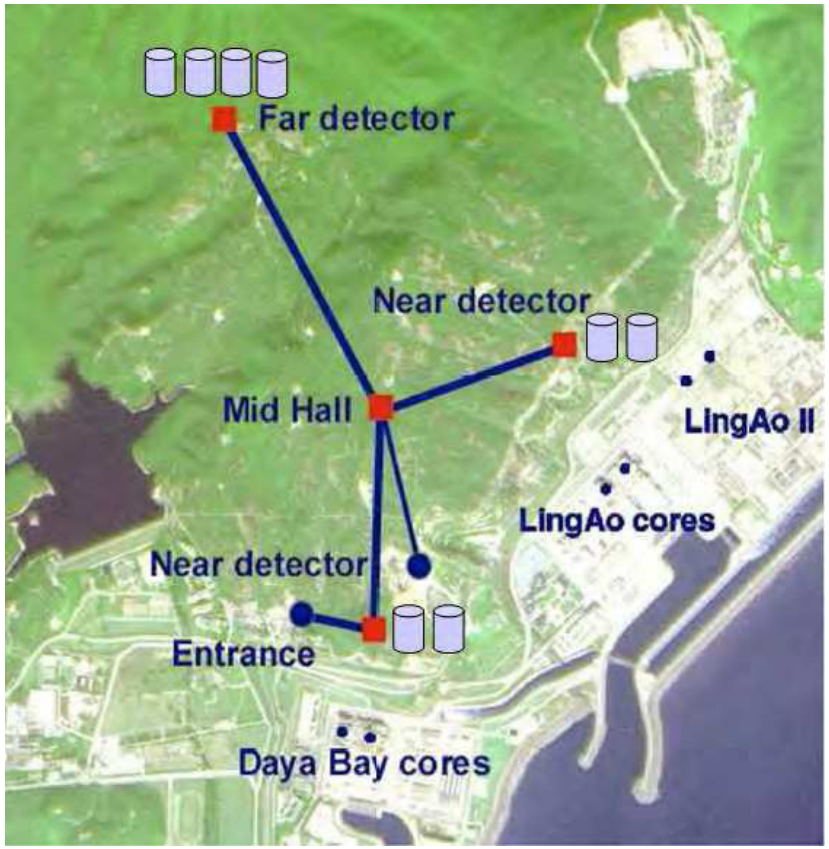

Default configuration of the Daya Bay experiment (*left panel*) and the power stations around the KamLAND experiment (*right panel*). [From Daya Bay & KamLAND Proposals.]

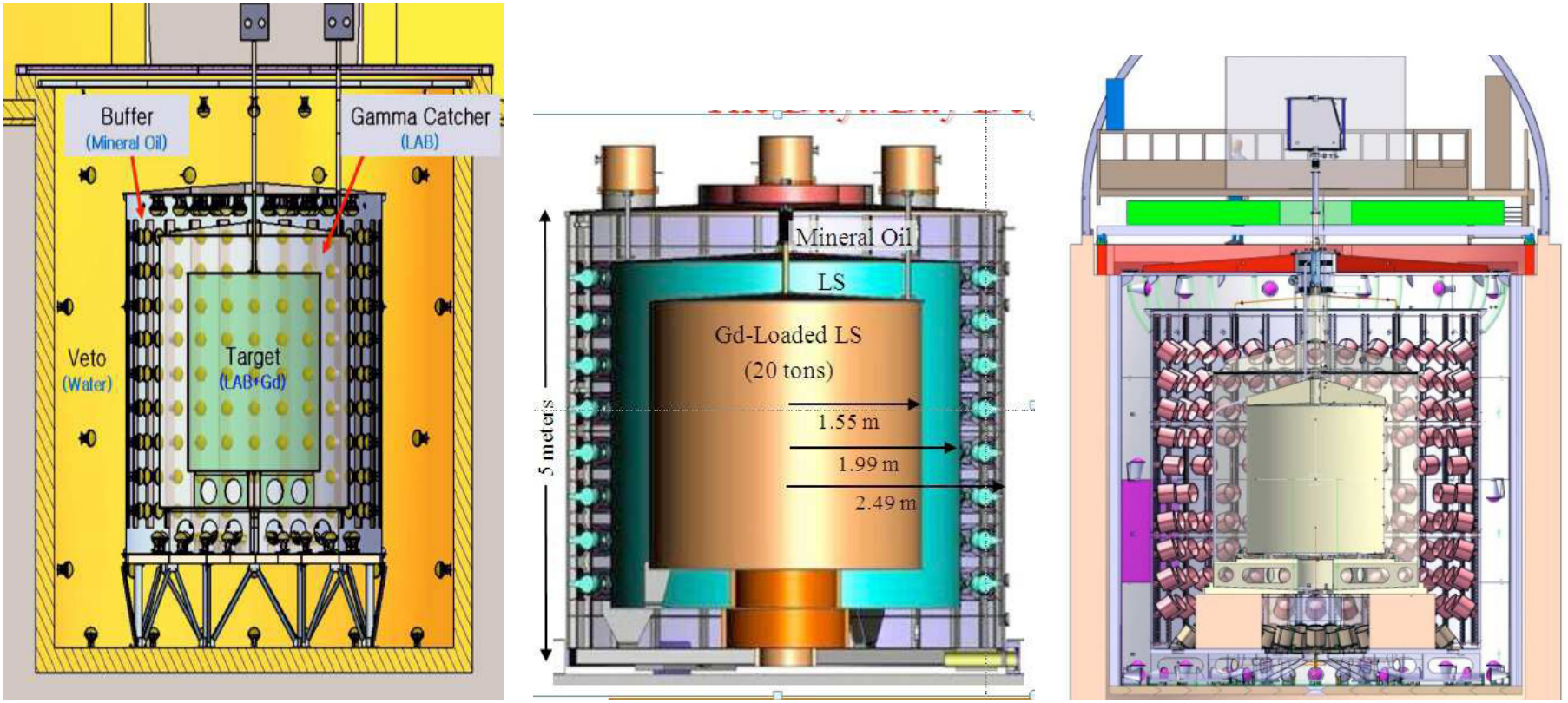

The Daya Bay (*left panel*), Reno (*middle panel*), and Double Chooz (*right panel*) detector layouts. The common design is an evolution of the CHOOZ detector.

[From T. Lasserre, "Oscillation parameters with forthcoming reactor neutrino experiments," in: Proceedings of the Workshop 'European Strategy for Future Neutrino Physics,' Geneva, Switzerland, October 1–3, 2009, edited by A. Blondel, & F. Dufour, CERN-2010-003, pp. 33–40.]

Underground Laboratories for terrestrial and extraterrestrial neutrinos

[BNO, DUSEL, Homestake, Gran Sasso, Kamioka, KGF, Modane, Mont Blanc, Pyhäsalmi, SOUDAN, SNOLAB,...]

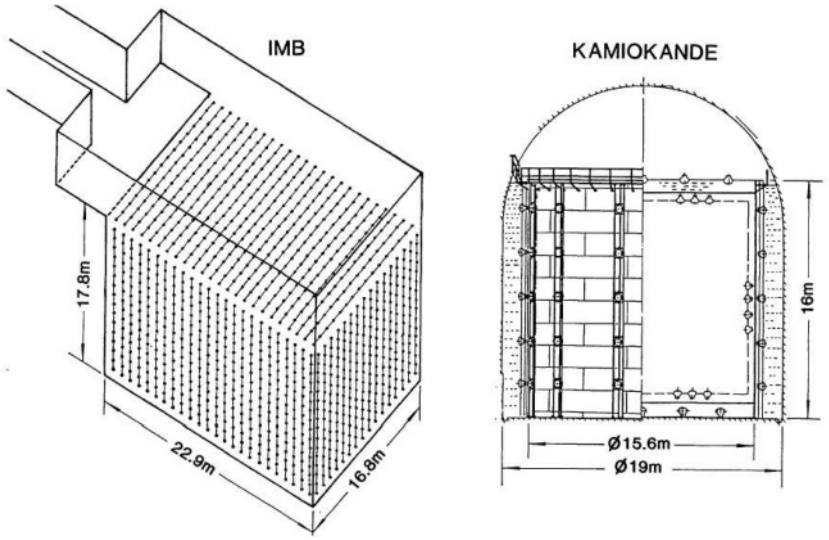

Water Cherenkov detectors.

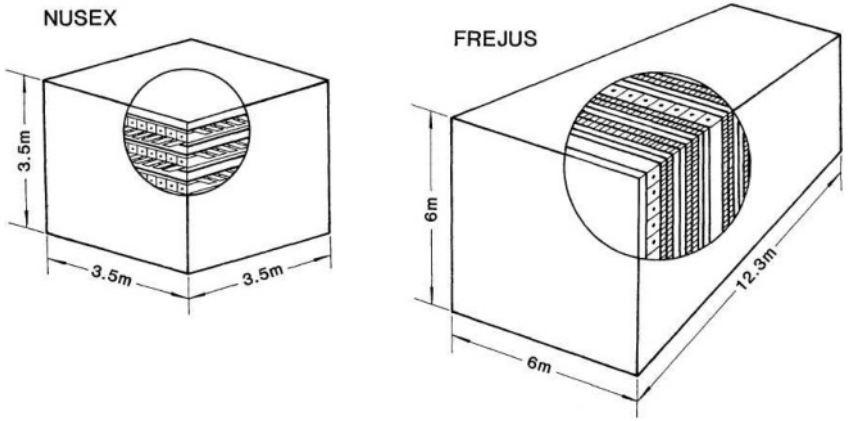

Tracking calorimeter detectors.

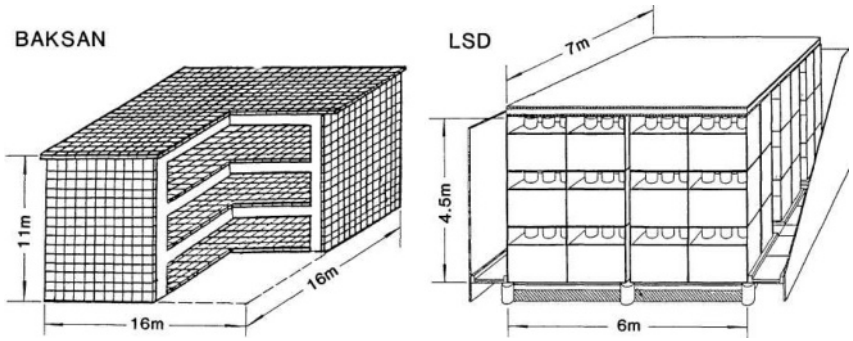

Liquid scintillator detectors.

Figures show the park of underground detectors (as it was on 1989) capable to catch atmospheric neutrinos. Of those shown, only the Baksan Underground Scintillation Telescope (BUST) is still in operation.

[Borrowed from A. M. Bakich, "Aspects of neutrino astronomy," Space Sci. Rev. **49** (1989) 259–310.]

Modern park – a few examples.

Gran Sasso underground laboratory (INFN) is the largest underground laboratory for astroparticle physics in the World. Most important experiments relevant to neutrino physics and astrophysics are GALLEX/GNO, Borexino, OPERA, ICARUS, LVD, CRESST, CUORE, XENON, GERDA, DAMA.

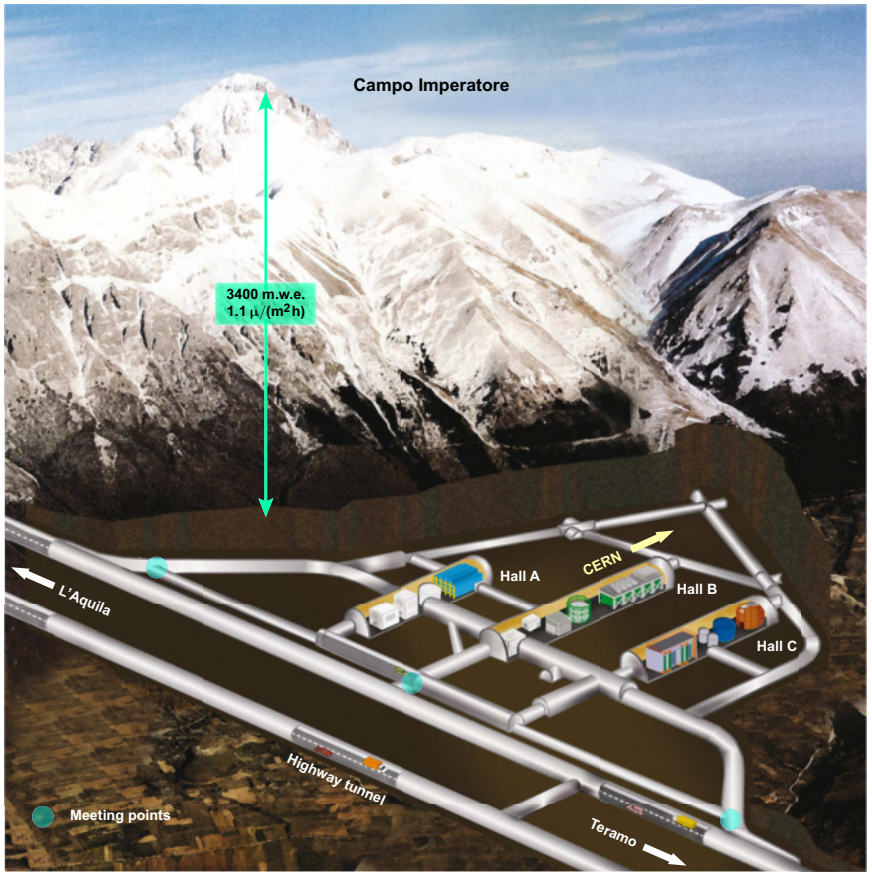

Super-Kamiokande (Kamioka Observatory in Mozumi mine).

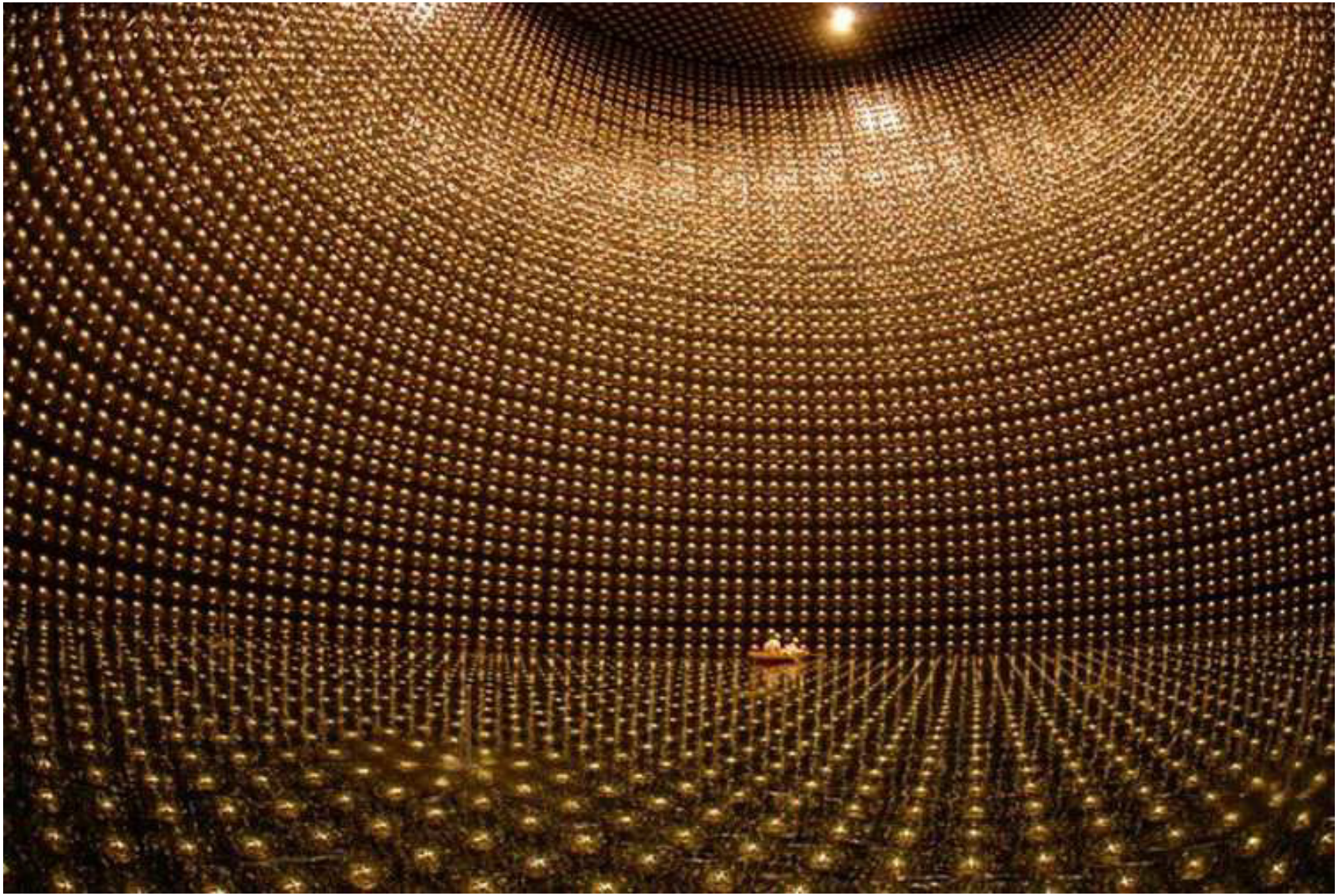

Inside of the Super-Kamiokande detector during water filling.

Super-Kamiokande detects about 2 Hz of comic ray muons. Some interesting images are shown here.

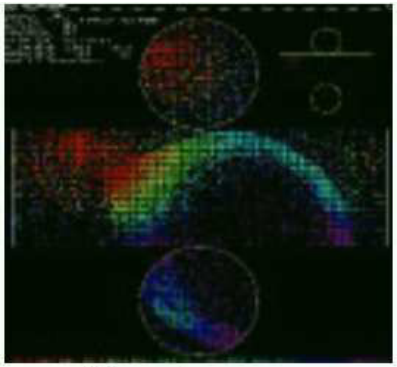
Stopping muon

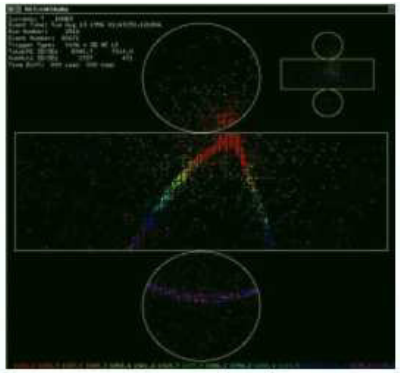
Corner edge clipping muon

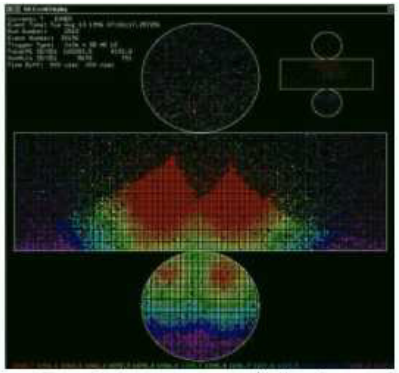
Double muon (Timing distribution)

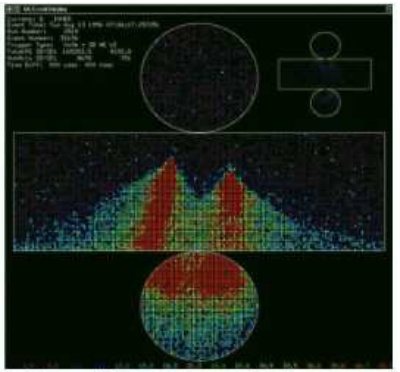
Double muon (Charge distribution)

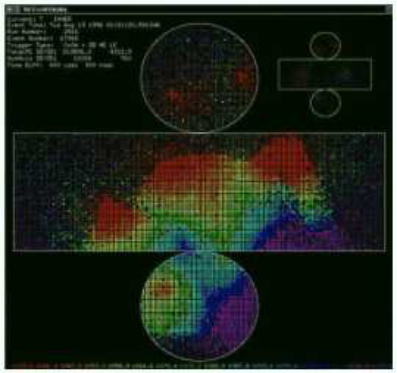
Triple muons

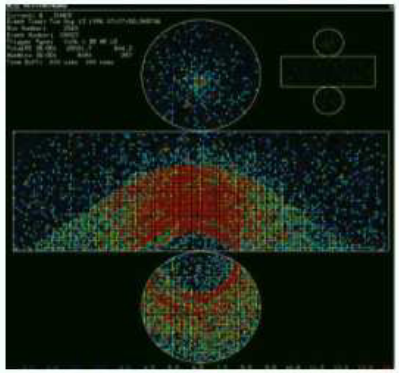
Stopping muon entering from the top (Charge distribution)

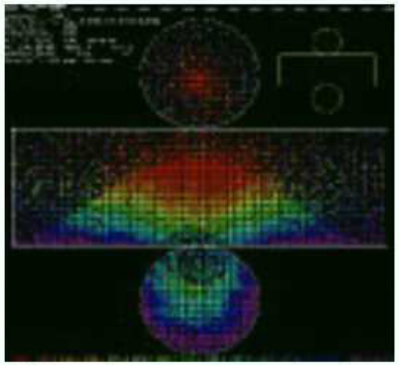
Stopping muon entering from the top (Timing distribution)

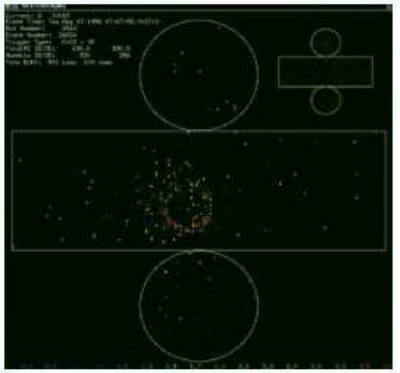
An electron emitted from muon decay

Cosmic ray Muon Events.

[From ⟨ http://www-sk.icrr.u-tokyo.ac.jp/sk/detector/eventdisplay-e.html ⟩ (UC).]

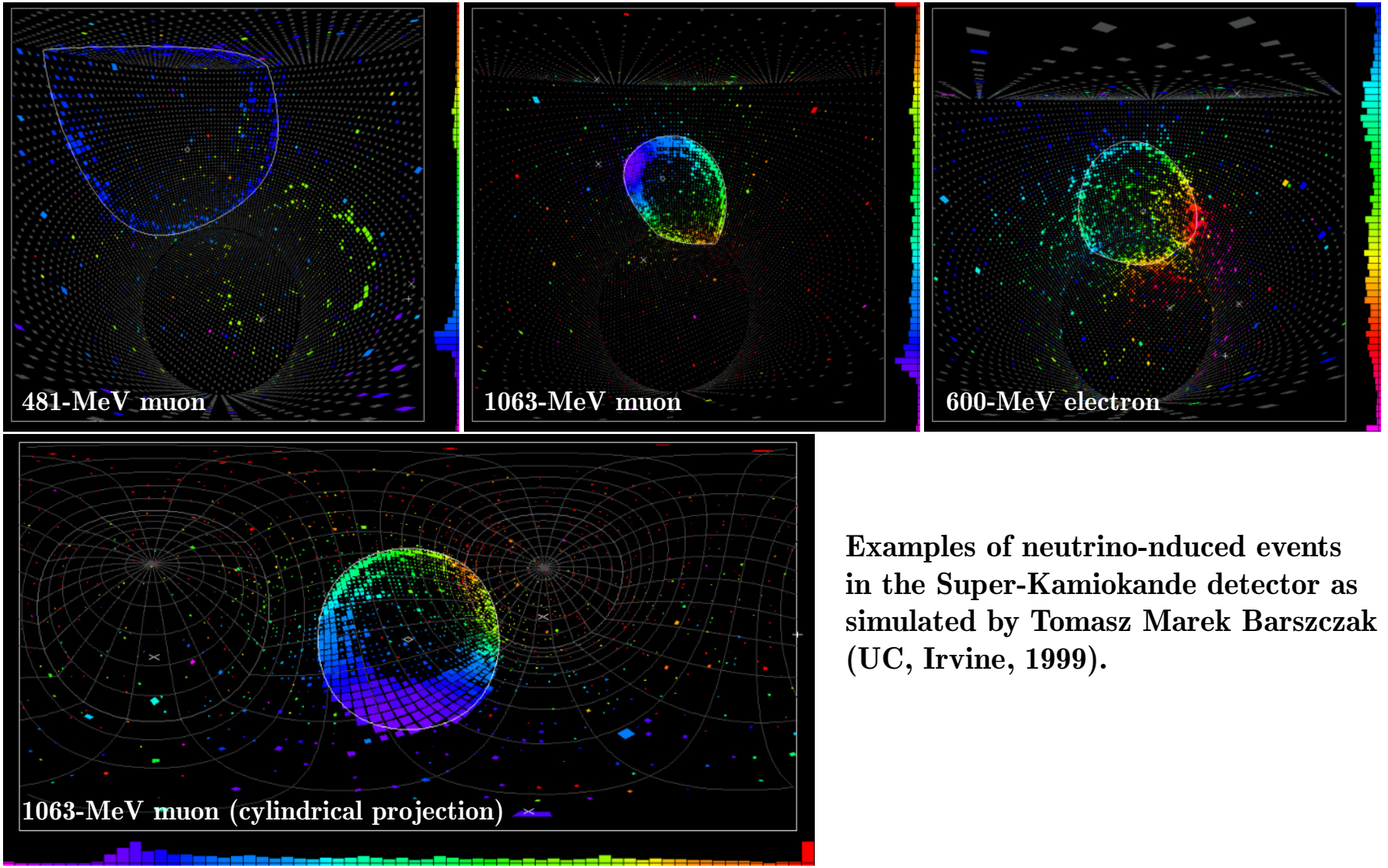

Examples of neutrino-nduced events in the Super-Kamiokande detector as simulated by Tomasz Marek Barszczak (UC, Irvine, 1999).

Simulated events.

[From Tomasz Barszczak's webpage ⟨ http://www.ps.uci.edu/~tomba/sk/tscan/pictures.html ⟩ (UC).]

Figures in this and next slides show two real (not Monte Carlo) events recorded in the Super-Kamiokande-I detector.

[From Tomasz Barszczak's webpage ⟨http://www.ps.uci.edu/~tomba/sk/tscan/pictures.html⟩ (UC).]

A real multiple ring event (found by Brett Michael Viren, State University of New York at Stony Brook) ▷

This event recorded on 24/09/1997, 12:02:48 was one of the close candidates for decay $p \to e^+ + \pi^0$ but did not pass analysis cuts.

The π^0 meson would decay immediately into two gammas which make overlapping fuzzy rings. Positron and π^0 would fly in opposite directions.

Time color scale spans 80 ns.

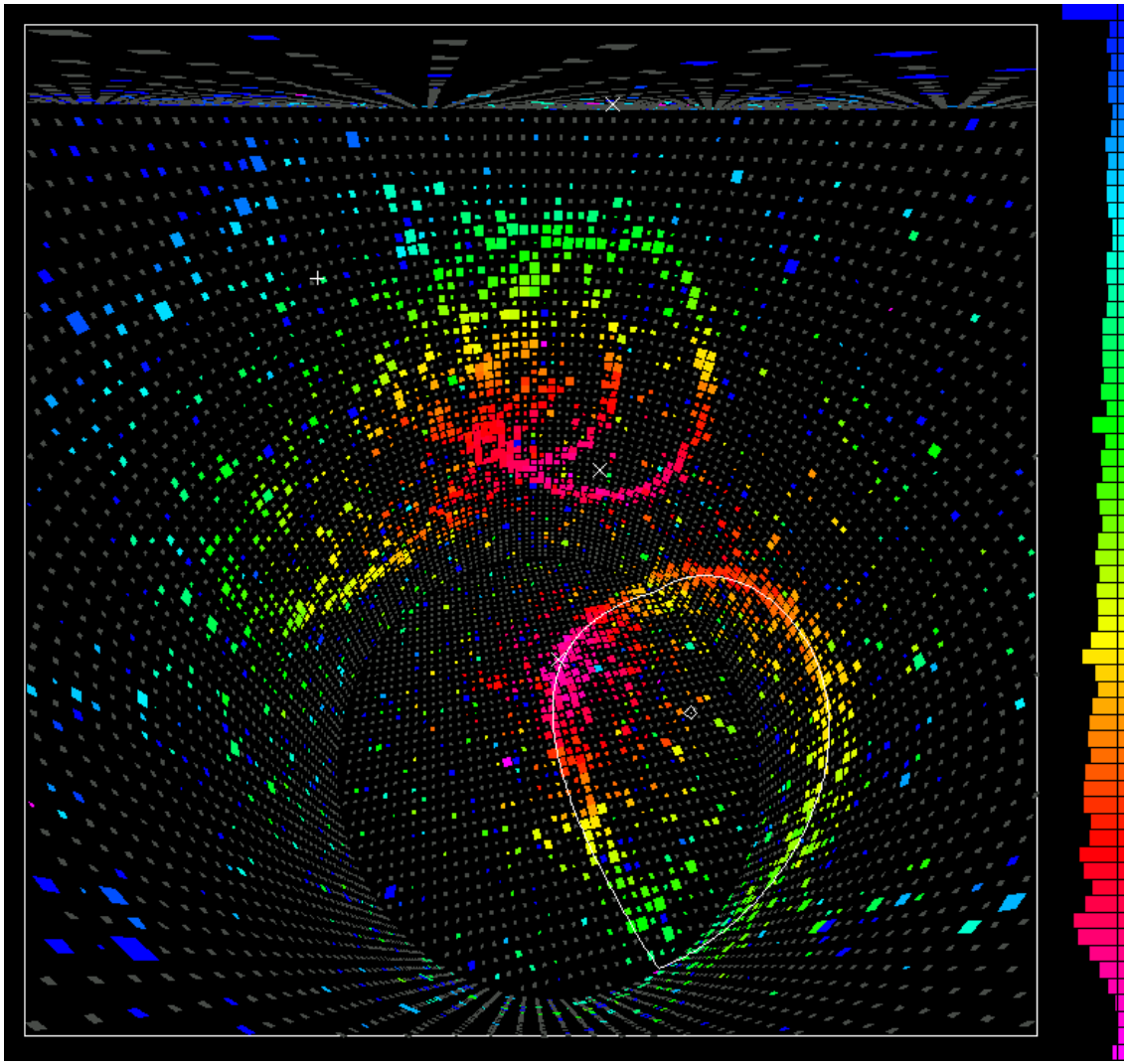

Multiple ring event recorded in the Super-Kamiokande detector on 24/09/1997, 12:02:48.

An upward-going through-going muon event recorded on 30/05/1996, 17:12:56. ▷

The muon entered through the flat circular part of the detector near the bottom of the picture where purple earliest PMT hits can be seen. It exited through the cylindrical side wall in the middle of the picture.

Time color scale spans 262 ns.

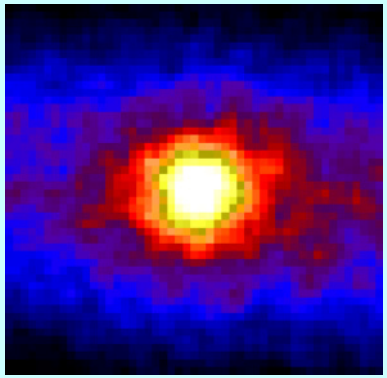

The Sun in neutrino light.

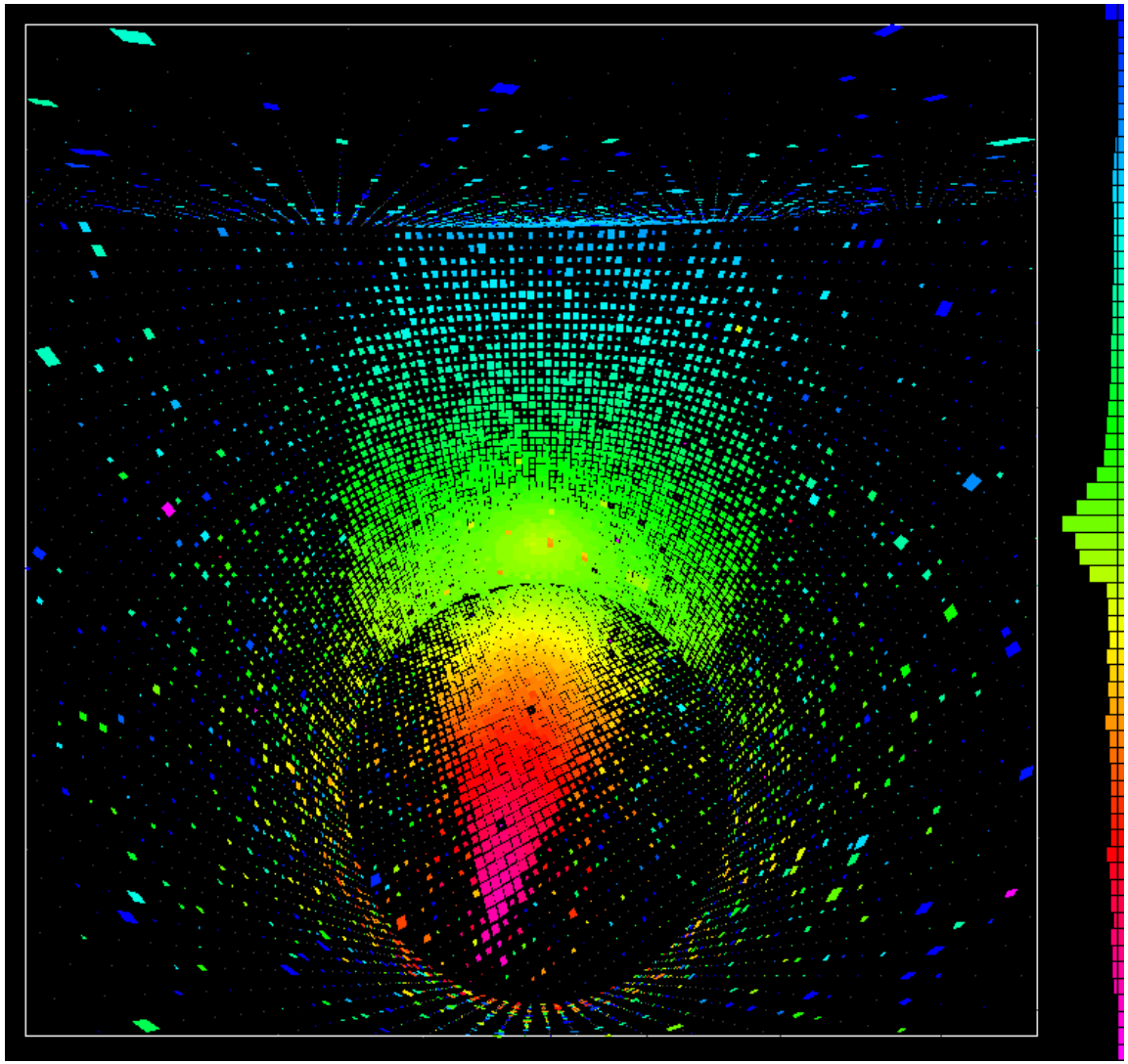

Through-going muon event recorded in the Super-Kamiokande detector on 30/05/1996, 17:12:56.

Hyper-Kamiokande project.

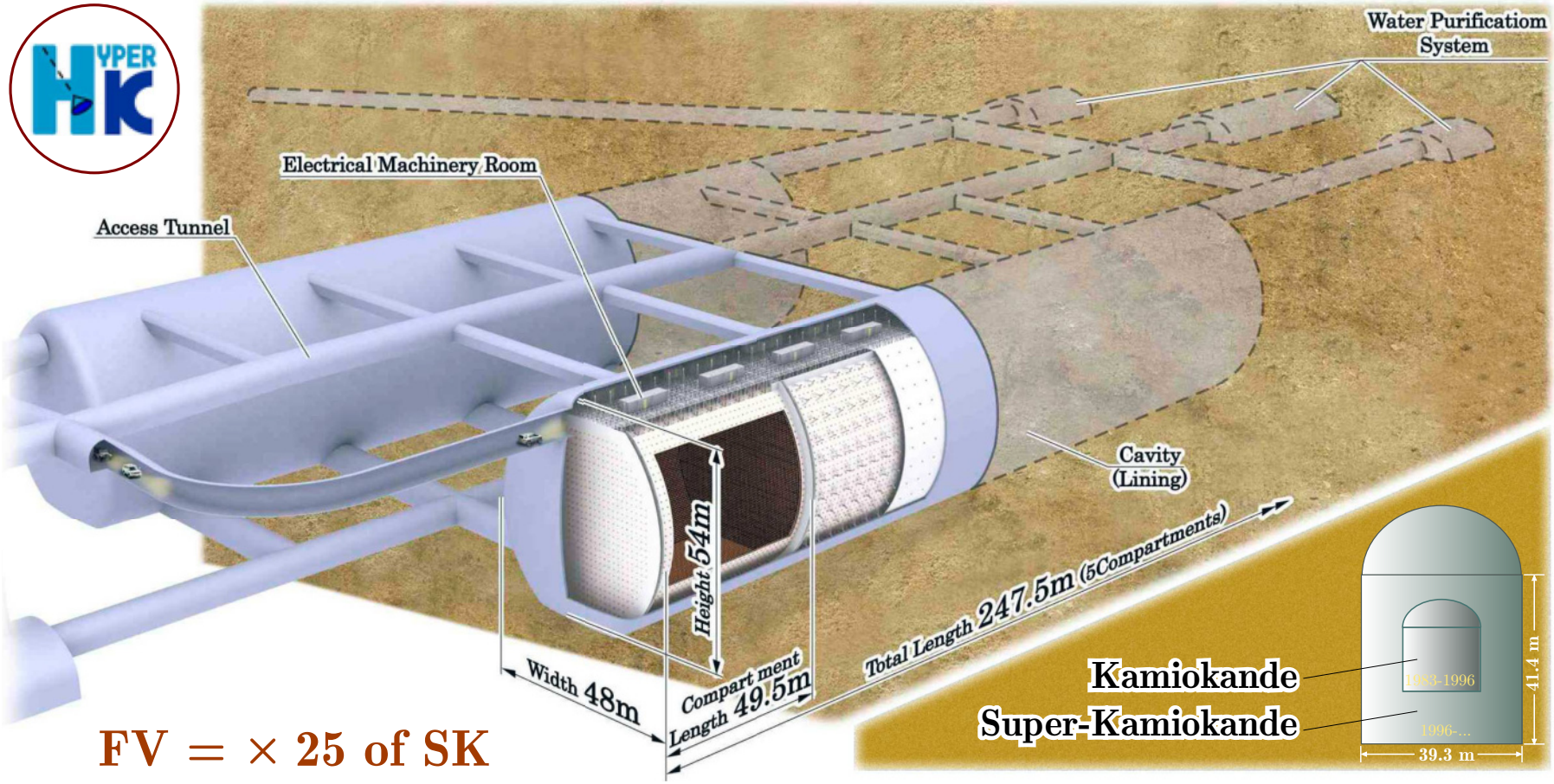

Schematic view of the Hyper-Kamiokande detector, a megaton water Cherenkov detector, proposed as a successor to Super-Kamiokande; to be located at Tochibora mine in Kamioka town, a few kilometers from the Super-Kamiokande position, 648 m rock (1,750 m w.e.) overburden.

[From K. Abe *et al.*, "Letter of intent: The Hyper-Kamiokande experiment – Detector design and physics potential," arXiv:1109.3262 [hep-ex].]

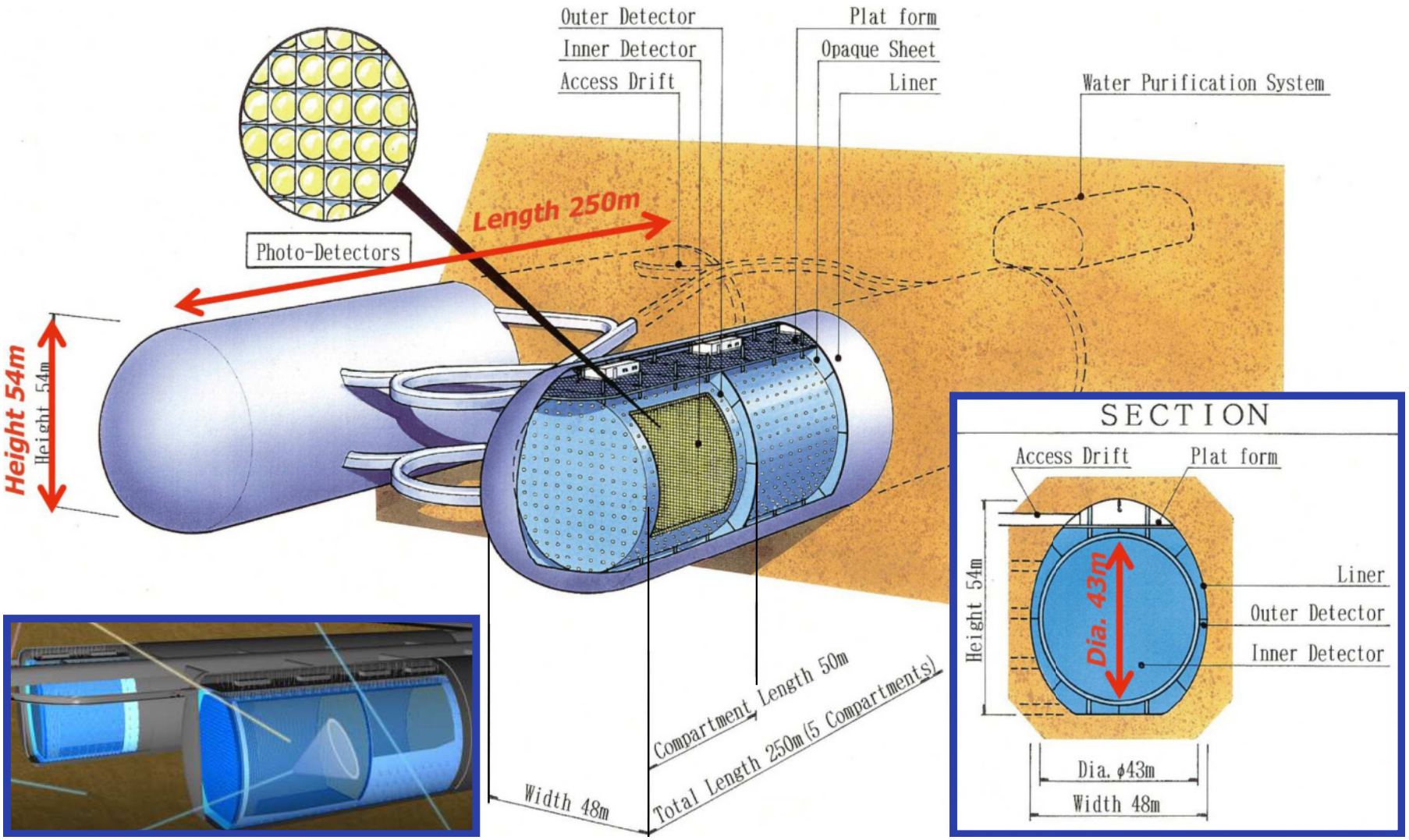

Yet another view of the Hyper-Kamiokande detector (note small differences in dimensions).

[From H. Aihara, "Large water Cherenkov detectors – Technical issues," in Proceedings of the workshop "European Strategy for Future Neutrino Physics," (CERN, Geneva, Switzerland, October 1–3, 2009), edited by A. Blondel & F. Dufour, CERN-2010-003, pp. 177–183.]

Parameters of the baseline design.

Detector type		Ring-imaging water Cherenkov detector
Candidate site	Address	Tochibora mine, Kamioka town, Gifu, Japan
	Latitude	$36^\circ 21' 08.928''$ N
	Longitude	$137^\circ 18' 49.688''$ E
	Altitude	508 m
	Overburden	648 m rock (1,750 m w.e.)
	Cosmic-ray muon flux	$\sim 2.3 \times 10^{-6}$ sec^{-1}cm^{-2}
	Off-axis angle for the J-PARC ν	2.5° (same as Super-Kamiokande)
	Distance from the J-PARC	295 km (same as Super-Kamiokande)
Detector geometry	Total volume	0.99 Megaton
	Inner volume	0.74 Megaton
	Fiducial volume	0.56 Megaton
	Outer volume	0.20 Megaton
PM tubes		99,000 20-inch $\varnothing$ PMTs
		20% photo-coverage
	Outer detector	25,000 8-inch $\varnothing$ PMTs
Water quality	light attenuation length	> 100 m @ 400 nm
	Rn concentration	< 1 mBq/m^3

Hyper-Kamiokande project timeline

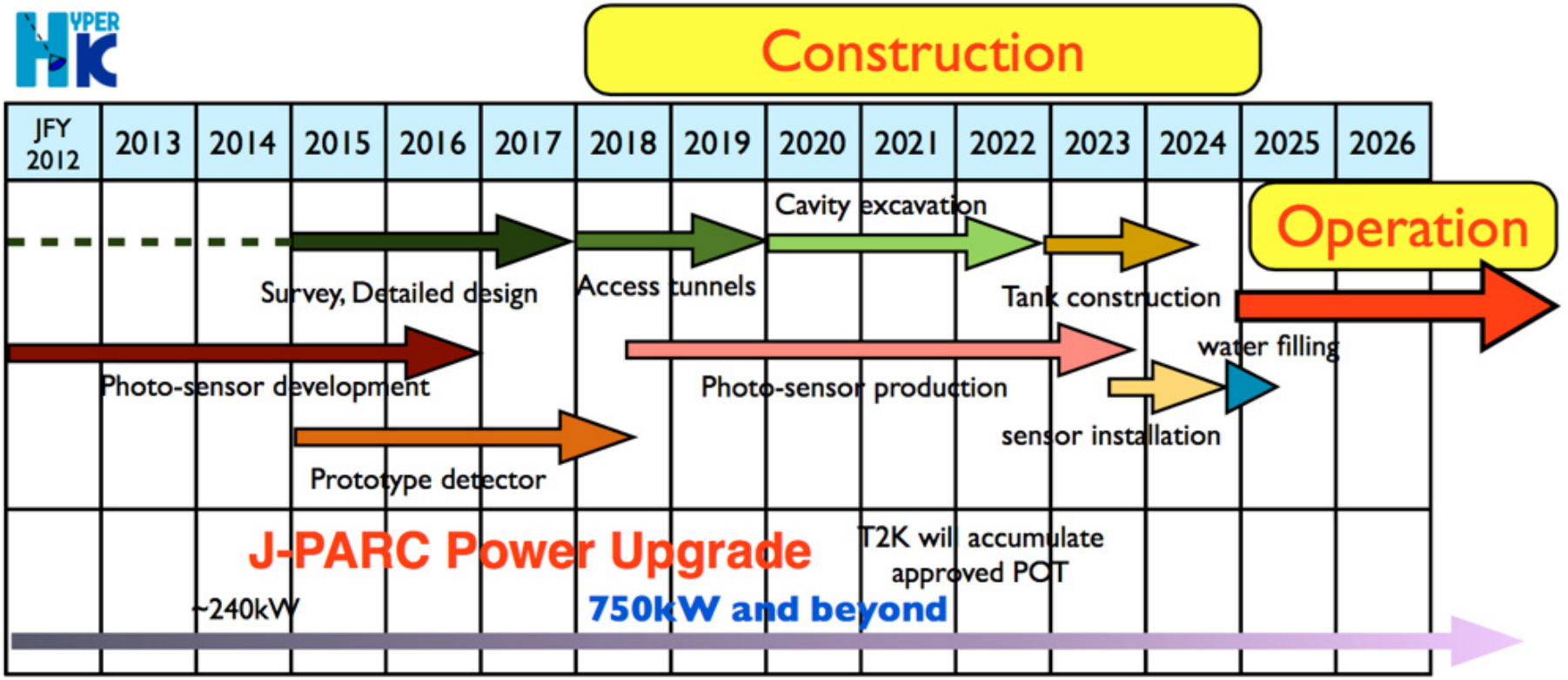

[See, e.g., F. Di Lodovico, "The Hyper-Kamiokande Experiment," talk at EPCP-2015, Nagoya, May 25–29, 2015.]

MEMPHYS project (stalled for some reason).

The MEMPHYS (MEgaton Mass PHYSics) is a project for a Megaton scale water Cherenkov detector in a large international underground laboratory in the Fréjus tunnel.[a]

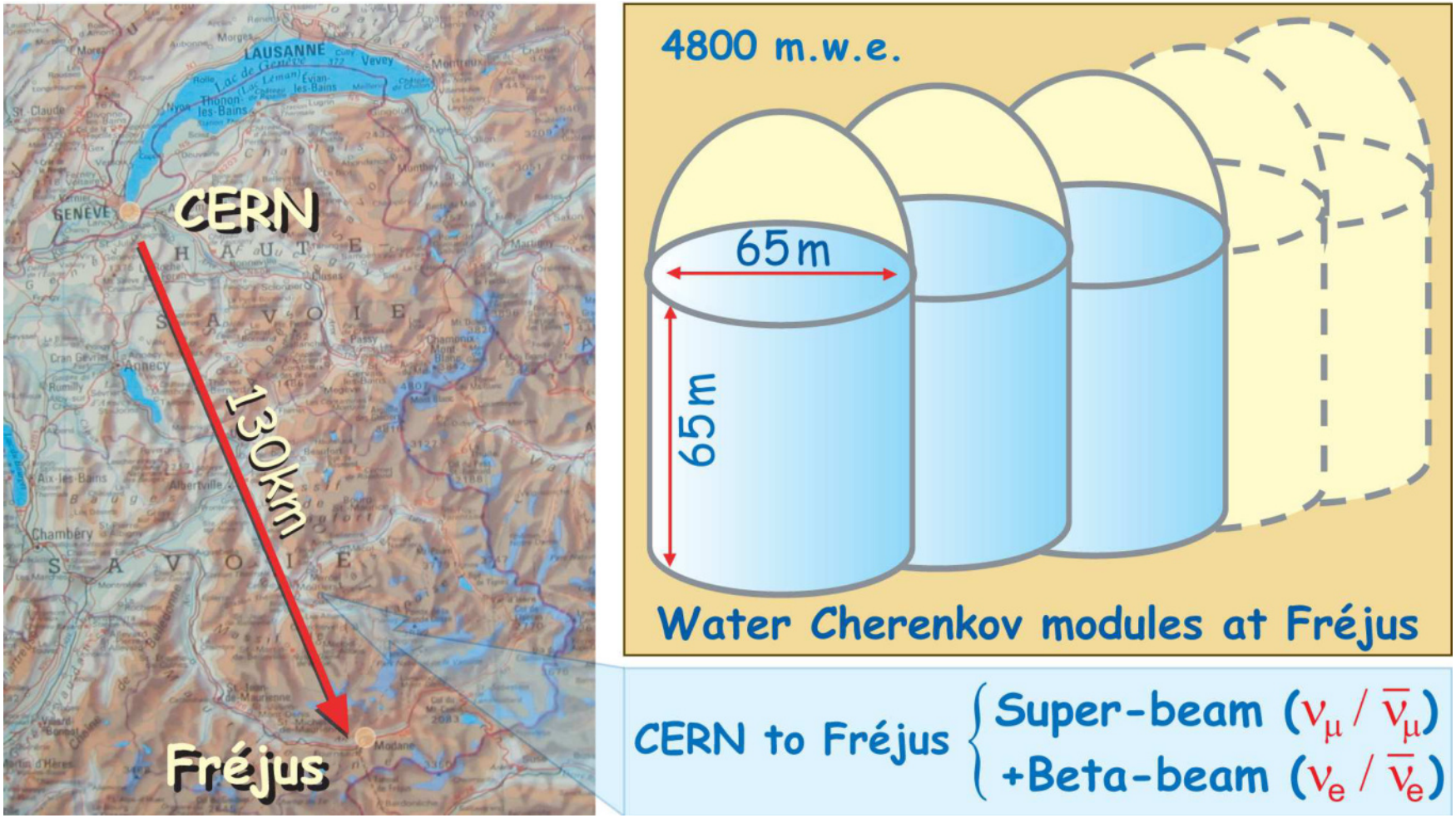

[a] For more details, see L. Agostino *et al.* (MEMPHYS Collaboration), "Study of the performance of a large scale water-Cherenkov detector (MEMPHYS)," JCAP01(2013)024, arXiv:1206.6665 [hep-ex] and refs. therein.

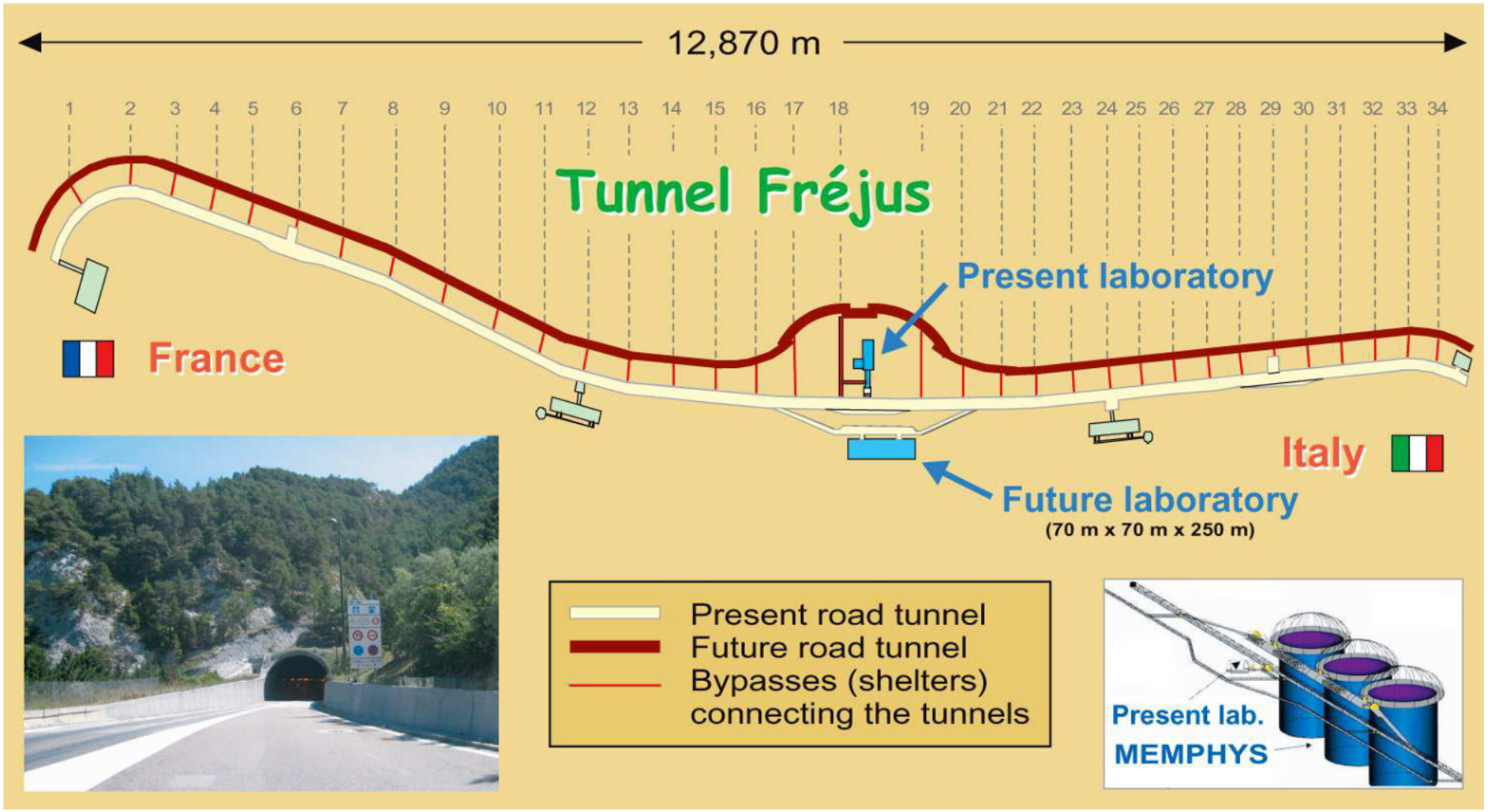

A preliminary investigation shows the feasibility to excavate in the middle of the Fréjus tunnel at a depth of 4800 m.w.e. up to five shafts of about $250,000$ m^3 each to place 3 to 4 water Cherenkov modules and a liquid argon detector (of about 100 kt total mass).

Main results of the preliminary study are

1. the best site (rock quality) is found in the middle of the mountain, at a depth of 4800 m.w.e.;
2. of the two considered shapes : "tunnel" and "shaft", the "shaft (= well) shape" is strongly preferred;
3. Cylindrical shafts are feasible up to a diameter $\oslash = 65$ m and a full height $h = 80$ m (volume $\approx 250,000$ m^3);
4. with "egg shape" or an "intermediate shape" the volume of the shafts could be still increased (to $\oslash = 70$ m);
5. the estimated cost is $\sim 80 \times 10^6$ Euros $\times$ Number of shafts.

Detector basic unit:

a cylinder (*a la* SK) 65 m diameter and 65 m height $\Rightarrow$ 215 kt of water ($\sim 4 \times$ SK) taking out 4 m from outside for veto and fiducial cut $\Rightarrow$ 146 kt fiducial target.

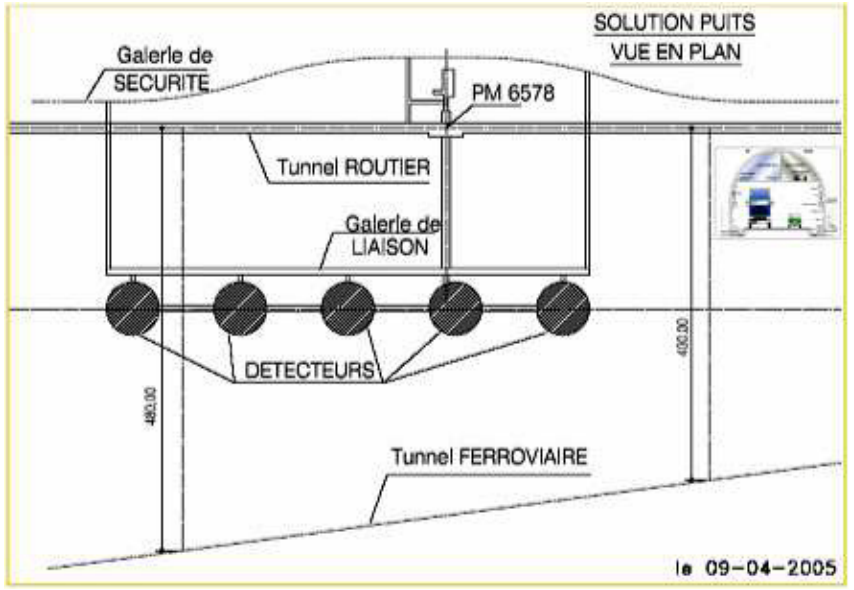

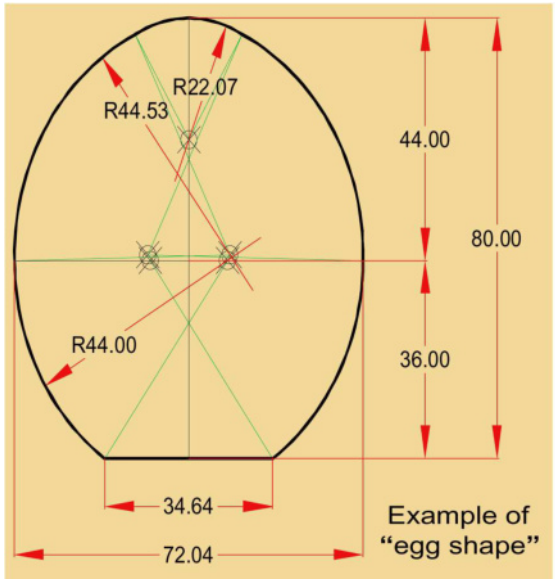

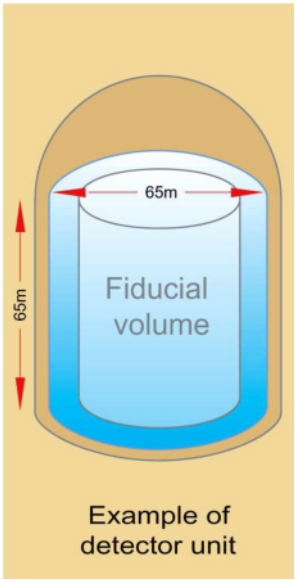

Mechanics and photoelectronics is under R&D to minimize the cost to quality ratio.

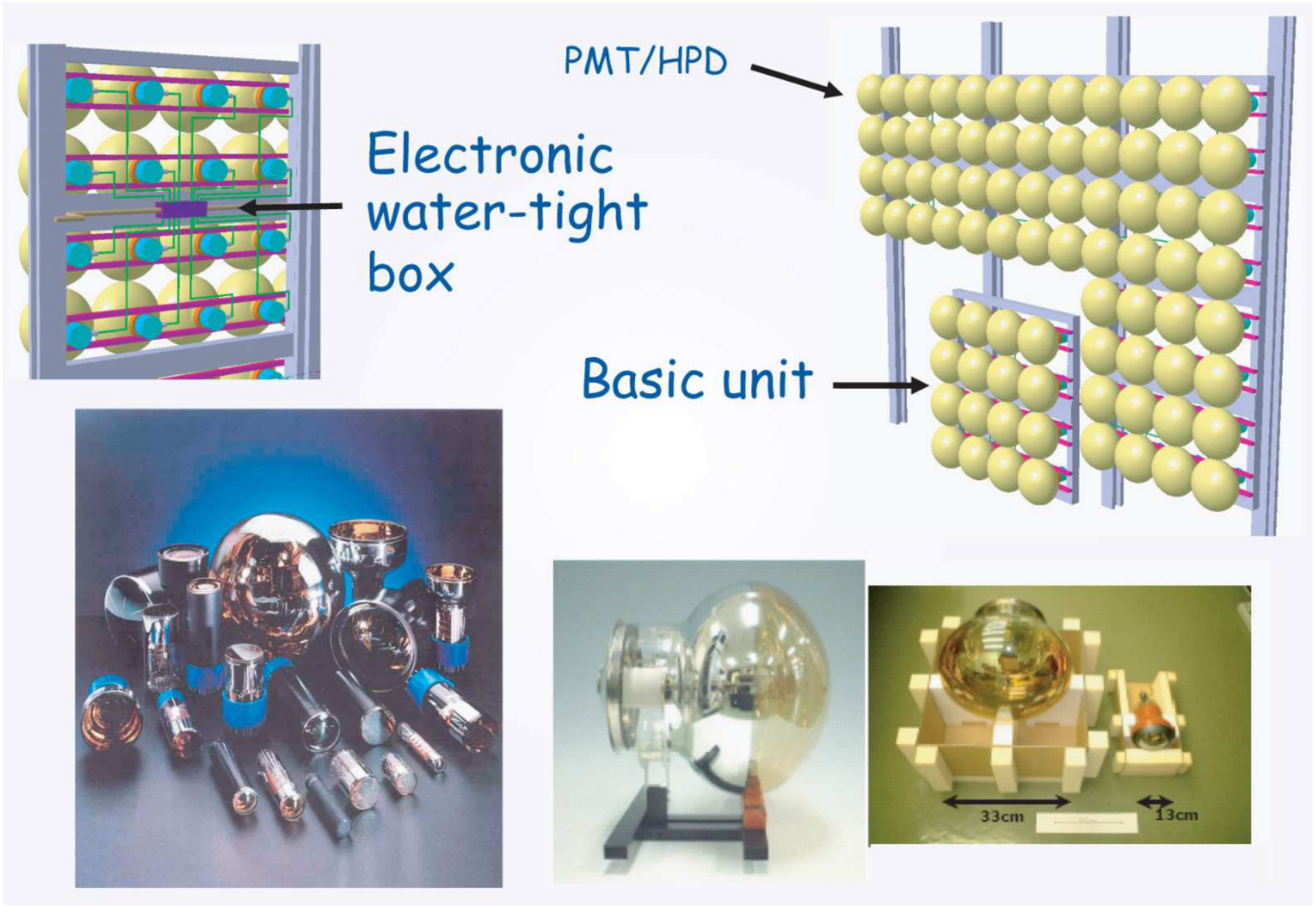

Physics goals and potential[a]

- ⋆ proton decay (for 5 Megaton $\times$ years):
  - $\tau\left(p \to e^+\pi^0\right) \approx 10^{35}$ years,
  - $\tau\left(p \to \nu K^+\right) \approx 2 \times 10^{34}$ years,
  - complementarity with liquid argon detector.
- ⋆ Neutrino bursts from supernova explosions (collapse studies and explosion alerts):
  - $\sim 200,000$ events from a SN at 10 kpc,
  - ~ 30 events from Andromeda,
  - ~ 2 events at 3 Mpc.
- ⋆ Relic neutrinos from past supernovae explosions (for 5 Megaton $\times$ years):
  - ~ 100 events with pure water,
  - $2000/4000$ events with gadolinium loaded water.
- ⋆ Solar and atmospheric neutrinos.

- ⋆ Neutrino SPL super-beam (SB) and beta-beam (βB) from CERN.

[a] For more details see J. E. Campagne, M. Maltoni, M. Mezzetto & T. Schwetz, "Physics potential of the CERN-MEMPHYS neutrino oscillation project," JHEP04(2007)003, hep-ph/0603172; see also Ref. at p. 952.

Underwater/ice neutrino telescopes

[AMANDA, ANTARES, Baikal NT, IceCube, NEMO, NESTOR $\longmapsto$ Baikal-GVD, IceCube-Gen2 (+Radio Extension), KM3NET/ARCA+ORCA (Super-ORCA), P-ONE,..., $\longmapsto$ PLEνM or other NT multi/global network $\longmapsto$ Synergies between NTs, γ & GW detectors (+ CR, DM, Cosmology,...).]

In 1960, Moisey Markov (JINR, Dubna)[a] and Frederick Reines (Case Western Reserve University)[b] independently suggested to catch high-energy cosmic neutrinos via their charged current interactions using the ocean as a detector medium by observing the Cherenkov light of the produced muons and, simultaneously, as a screen for the cosmic-ray and solar light backgrounds.

Perhaps the idea of Reines was a natural development of the earlier note concerning experimental search for nucleon decay:*"Higher sensitivity could be obtained both by using larger counters and by going deep underground or in the ocean to eliminate cosmic rays,"* [c]

Up-going (neutrino induced) muons can be identified in a background of down-going cosmic-ray muons which are more than 10^5 times more frequent for a depth of about 1–2 km. The Earth is therefore also serves as a part of the detector, being the natural filter and "discriminator". This makes neutrino detection possible over the hemisphere of sky faced by the bottom of the detector.

[a] M. A. Markov, "On high energy neutrino physics," in Proceedings of the 10th Annual International Conference on High Energy Physics, "ICHEP 60" (University of Rochester, NY, USA, August 25 – September 1, 1960), edited by E. C. G. Sudarshan, J. H. Tinlot & A. C. Melissinos; see URL: ⟨ http://inspirehep.net/record/1341439/files/C60-08-25-p578.pdf ⟩. See also M. A. Markov and I. M. Zheleznykh, "On high energy neutrino physics in cosmic rays," Nucl. Phys. **27** (1961) 385–394.

[b] F. Reines, "Neutrino interactions," Ann. Rev. Nucl. Sci. **10** (1960) 1–26. Kenneth Greisen (Cornell University) in the same journal volume [K. Greisen, "Cosmic ray showers," Ann. Rev. Nucl. Sci. **10** (1960) 63–108] also mentioned the idea of neutrino astronomy as a "fanciful proposal".

[c] F. Reines, C. L. Cowan & H. W. Krusenot, "Conservation of the number of nucleons," Phys. Rept. **109** (1958) 609–610.

It was thought that the ocean, a deep lake, or Antarctic ice could be a rather inexpensive target, the detector can be build modular and enlarged when necessary. The detector can take the advantage of the rising cross section for neutrino-nucleon interactions with energy. As the range of the final state muon or τ lepton increases with energy, the effective detector volume is growing as well with energy. Furthermore, it is expected that the energy spectra from many point astrophysical sources fail off less step that from atmospheric neutrinos. Thus the deep underwater detectors can be used as telescopes for high-energy neutrino astronomy.

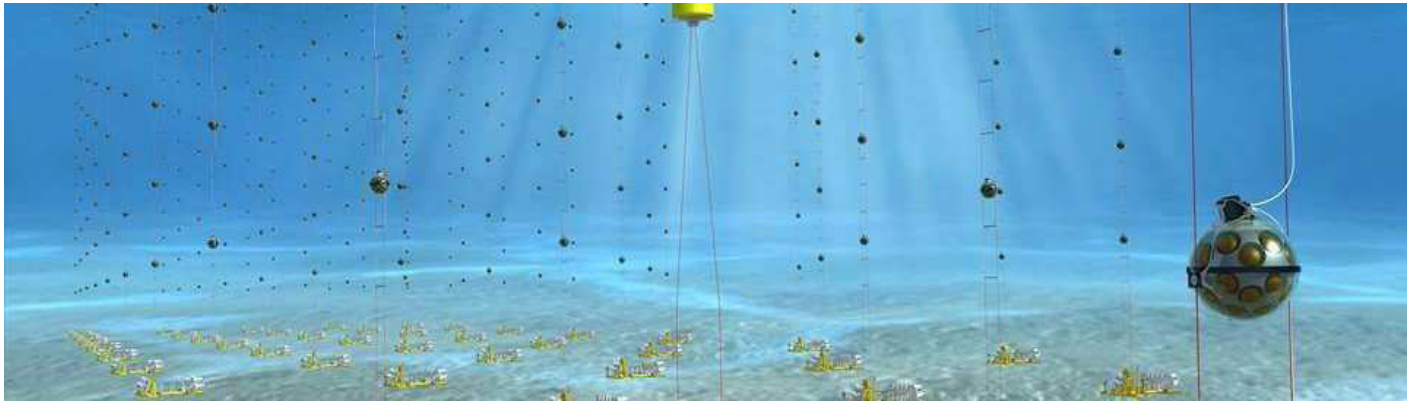

The optical requirements on the detector medium are severe. A large absorption length is needed because it determines the required spacing of the optical sensors and, to a significant extent, the cost of the detector. A long scattering length is needed to preserve the geometry of the Cerenkov pattern. Nature has been kind and offered ice and water as the natural Cerenkov media. Their optical properties are, in fact, complementary. Water and ice have comparable attenuation lengths, with the roles of scattering and absorption reversed. Optics seems, at present, to drive the evolution of ice and water detectors in predictable directions: towards very large telescope area in ice exploiting the long absorption length, and towards lower threshold and good muon track reconstruction in water exploiting the long scattering length.

Figure in the next slide shows a map of present-day underwater/ice Cherenkov NT projects.

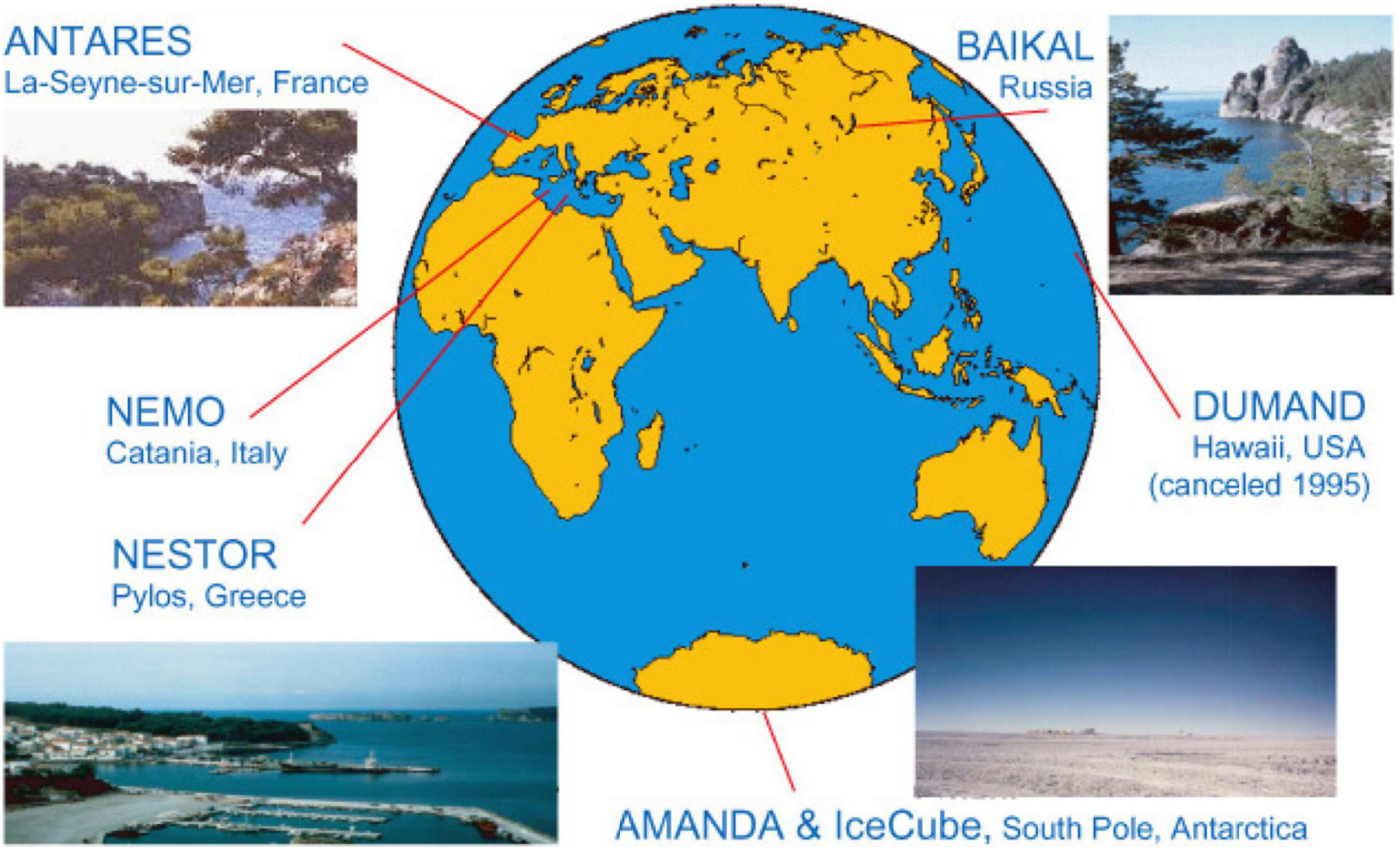

A bit obsolete map of underwater/ice Cherenkov neutrino telescope projects.

[From Francis Halzen's webpage ⟨ http://icecube.wisc.edu/~halzen/ ⟩].

DUMAND Project

The DUMAND (Deep Underwater Muon and Neutrino Detector) proposal aimed for a $250 \times 250 \times 500$ m^3 array of 756 detector modules to be located at a depth of about 4.5–4.8 km in the Pacific Ocean ~ 30 km due west from the Kona Coast of the Island of Hawaii.

The expanded schematic diagram in next slide shows the underwater location of the detector, the full array of 36 strings with optical sensors and a single PMT module.

The enclosed target mass of the detector was planned to be of about 30 Mtons and its effective area of about 10^5 m^2. The angular resolution was estimated at 15 to 45 mrads, depending on the muon energy.

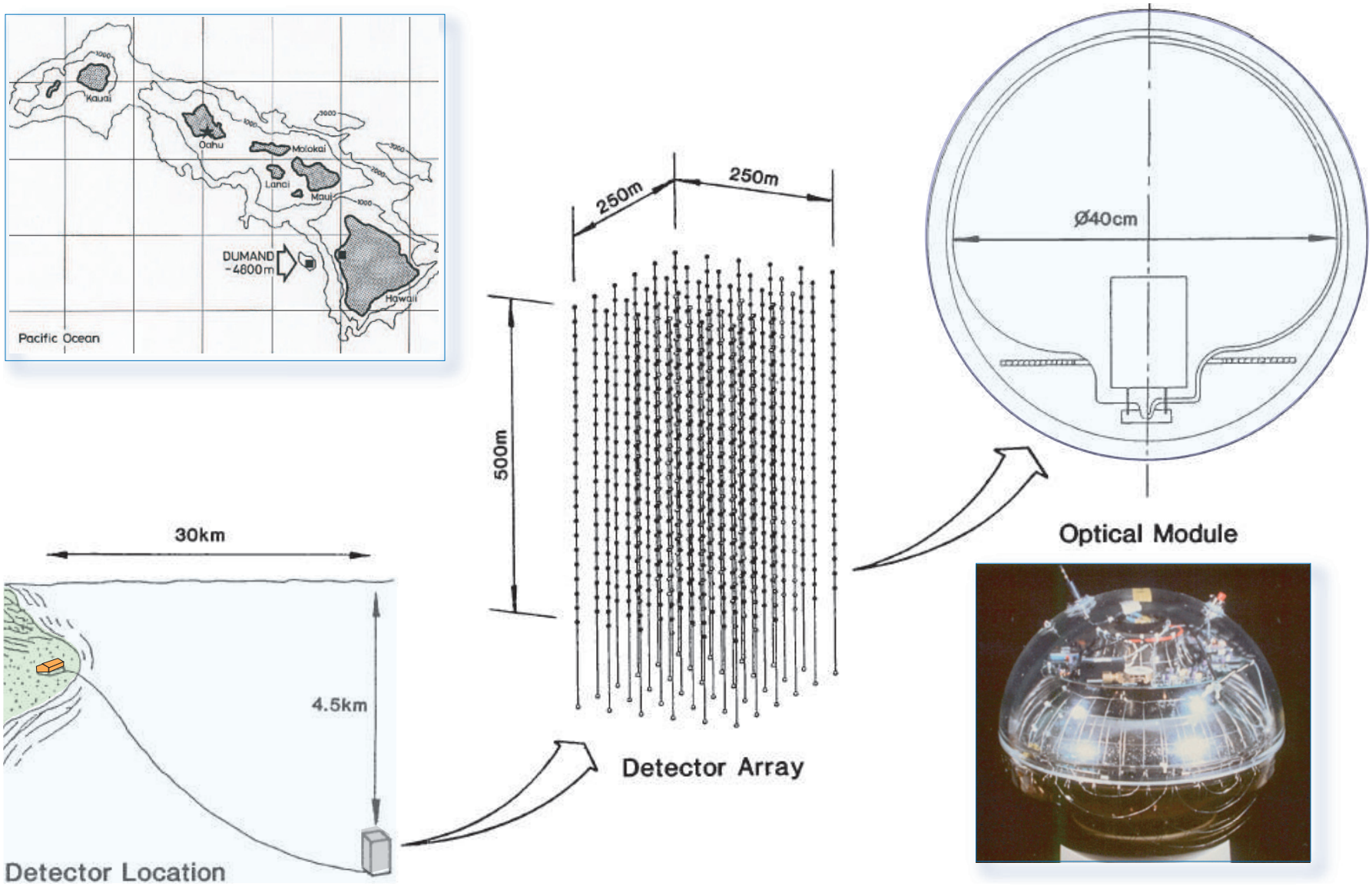

Proposed configuration of the DUMAND detector.

In the middle of 90s, the DUMAND Collaboration intended to deploy a prototype 9-string array in two phases: first 3 strings (the triad) as a demonstration, and the remaining 6 strings (complete octagon + center string) after about 1 year of testing and operation. The effective detection area of the full 9-string array was estimated as $\sim 2 \times 10^4$ m^2.

▷

The Island of Hawaii was selected for the deployment due to a variety of compelling reasons: exceptional water clarity, proximity of an abyssal plain (4.8 km) with appropriate seabed characteristics to a suitable shore site (30 km away), presence of an active particle physics group at the nearby University of Hawaii in Honolulu, and pre-existing laboratory infrastructure at the shore site (due to an ocean thermal energy research project).

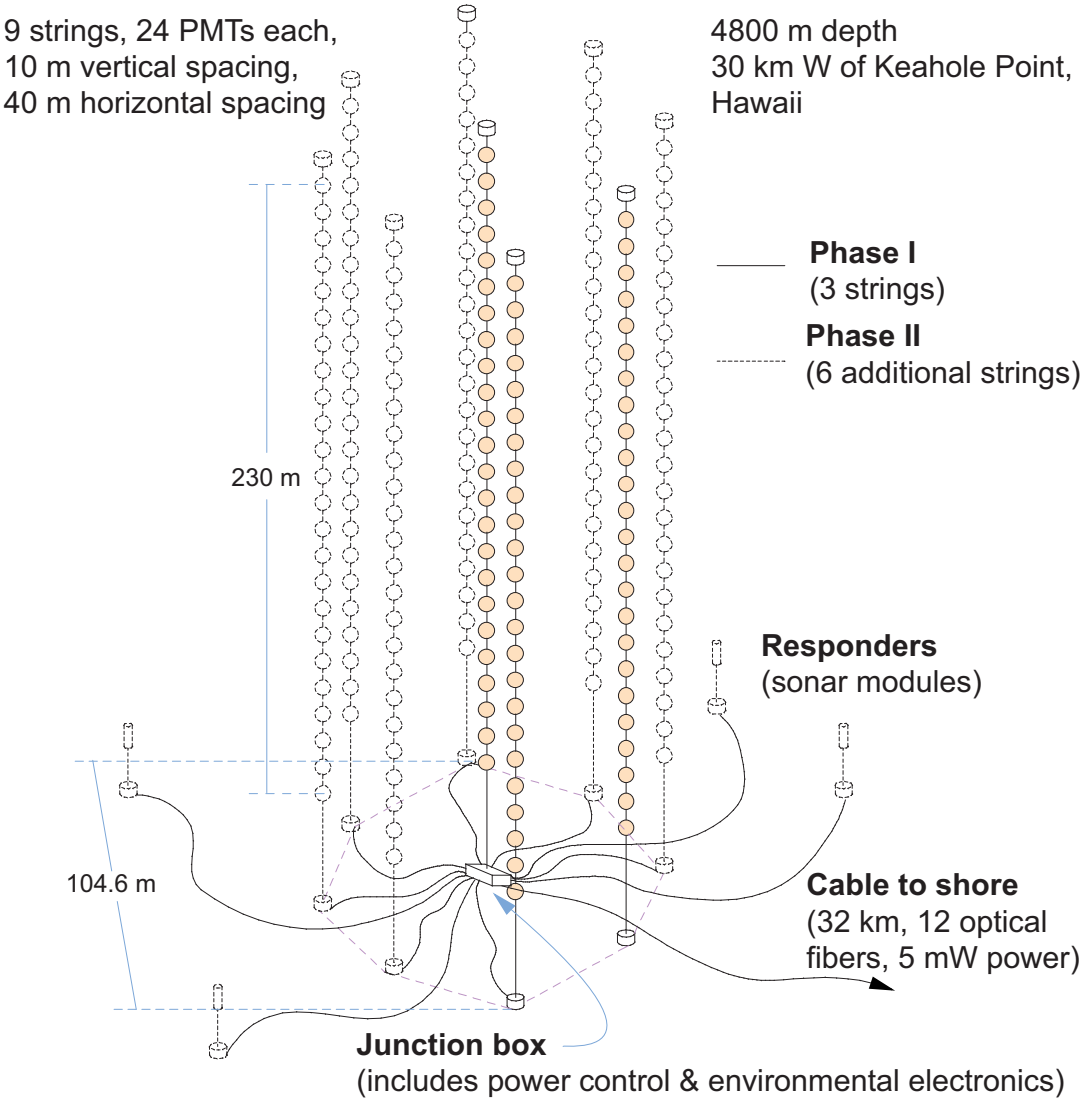

A sketch of the DUMAND-II underwater neutrino detector.

[From R. J. Wilkes, "DUMAND and AMANDA: High-energy neutrino astrophysics," astro-ph/9412019.]

Baikal neutrino telescope

The Lake Baikal neutrino experiment exploits the deep water of the great Siberian lake as a detection medium for high-energy neutrinos via muons and electrons generated in neutrino interactions.

Left panel: Space image of Baikal, early spring. *Right panel*: Ice campus of the Baikal NT collaboration with Khamar-Daban mountain at skyline.

The neutrino telescope NT 200, put into operation at April, 1998, was located in the southern part of the lake (51.50° N, 104.20° E) at a distance of 3.6 km from the nearest shore and at a depth of about 1.1 km.

The distance to the opposite shore is more than 30 km. This asymmetry allows to study the asymmetry in the azimuth distribution of muons arriving at large zenith angles. The absorption length of water at the site is about 20 m for wavelengths between 470 and 500 nm, and seasonal variations are less than 20%. Light scattering is subjected strongly to seasonal and year-to-year variations.

Figure in p. 965 [a] shows the layout of the Baikal NT 200 and the preceding array NT 96 (on the right) which took data between April 1996 and March 1997.[b] The NT 200 consisted of 192 optical modules (OMs) at 8 strings arranged at an umbrella-like frame. Pairs of OMs are switched in coincidence with a 15 ns time window and define a channel. The array is time-calibrated by two nitrogen lasers. Of these, one (fiber laser) is mounted just above the array. Its light is guided via optical fibers to each OM pair. The other (water laser) is arranged 20 m below the array. Its light propagates directly through water. The expansion on the left of the figure shows two pairs of optical modules ("svjaska") with the electronics module, which houses parts of the readout and control electronics. Three underwater electrical cables connect the detector with the shore station.

[a] Description of the telescope and figures in pp. 965 and 968 are from Ch. Spiering *et al.* (Baikal Collab.), "The Baikal deep underwater neutrino experiment: Results, status, future," Prog. Part. Nucl. Phys. **40** (1998) 391–401, astro-ph/9801044; V. A. Balkanov *et al.* (Baikal Collab.), "The Lake Baikal neutrino experiment: Selected results," Yad. Fiz. **63** (2000) 1027 [Phys. Atom. Nucl. **63** (2000) 951], astro-ph/0001151.

[b] Various stages of the stepwise increasing detector are NT 36 (1993–1995), NT 72 (1995–1996), NT 96 (1996–1997) and NT 144 (1997–1998).

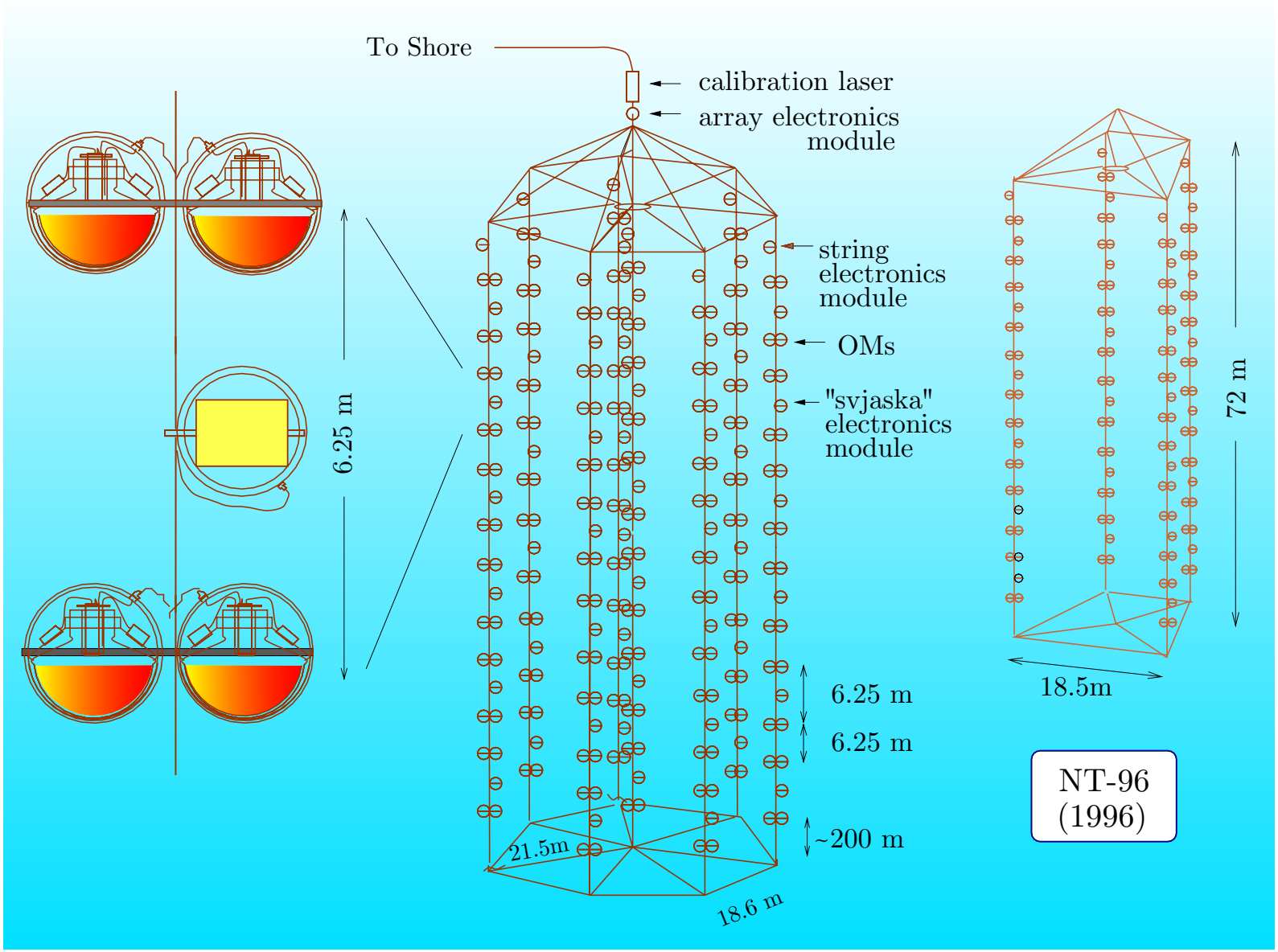

Baikal NT 200 and NT 96 schematic view (see text for description and references).

Figure in p. 967 shows an overall view of the NT 200 telescope. Here,
$1-3$ are cables to shore; $4-6$ are the string stations for shore cables;
7 is the string with the telescope; 8 is the hydrometric string;
$9-14$ are the ultrasonic emitters.

The insert at the left bottom of the figure shows two pairs of optical modules (OM) together with the electronic module controlling the OMs. Shown are two pairs of OMs directed face to face.

Figure in p. 968 displays three neutrino candidates separated during 18 days of the NT 96 exposition (the time period between April 16 and May 17, 1996).

(a) A "gold plated" 19-hit neutrino event. Hit channels are in color. The thick line gives the reconstructed muon path, thin lines pointing to the channels mark the path of the Cherenkov photons as given by the fit to the measured times. The areas of the ellipses are proportional to the measured amplitudes. The fake probability of this event was estimated to be $< 1\%$.

(b) An unambiguous 14-hit neutrino candidate.

(c) An ambiguous event reconstructed as a neutrino event (dashed line) but with a second solution above the horizon (solid line). This event is assigned to the sample of downward going muons.

Figure in p. 969 shows NT 200+ – a 2008 upgrade of the NT 200 by three sparsely instrumented distant outer strings which increase the fiducial volume for high-energy cascades to a few dozen Mtons. Correspondingly, the NT 200+ sensitivity is about 4 times better than that of NT 200, with a moderate 20% increase of optical modules only. A prototype string of 140 m length with 12 optical modules was deployed in March 2003, electronics, data acquisition and calibration systems for NT 200+ have been tested. The full NT 200+ was deployed in 2005.

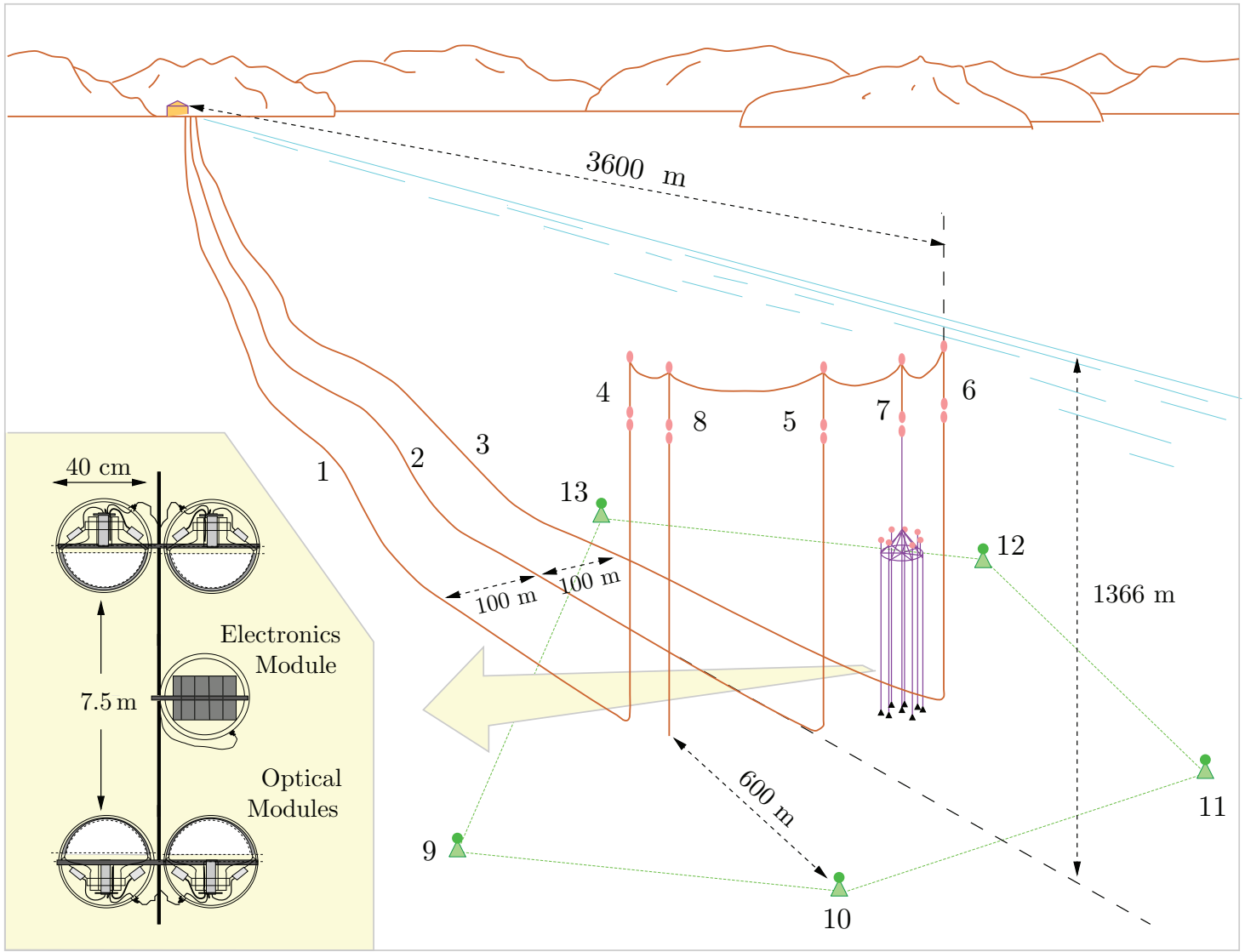

Overall view of the NT 200 complex in Lake Baikal.

[From V. A. Balkanov *et al.* (Baikal Collaboration) "In-situ measurements of optical parameters in Lake Baikal with the help of a neutrino telescope," Appl. Opt. **33** (1999) 6818–6825, astro-ph/9903342.]

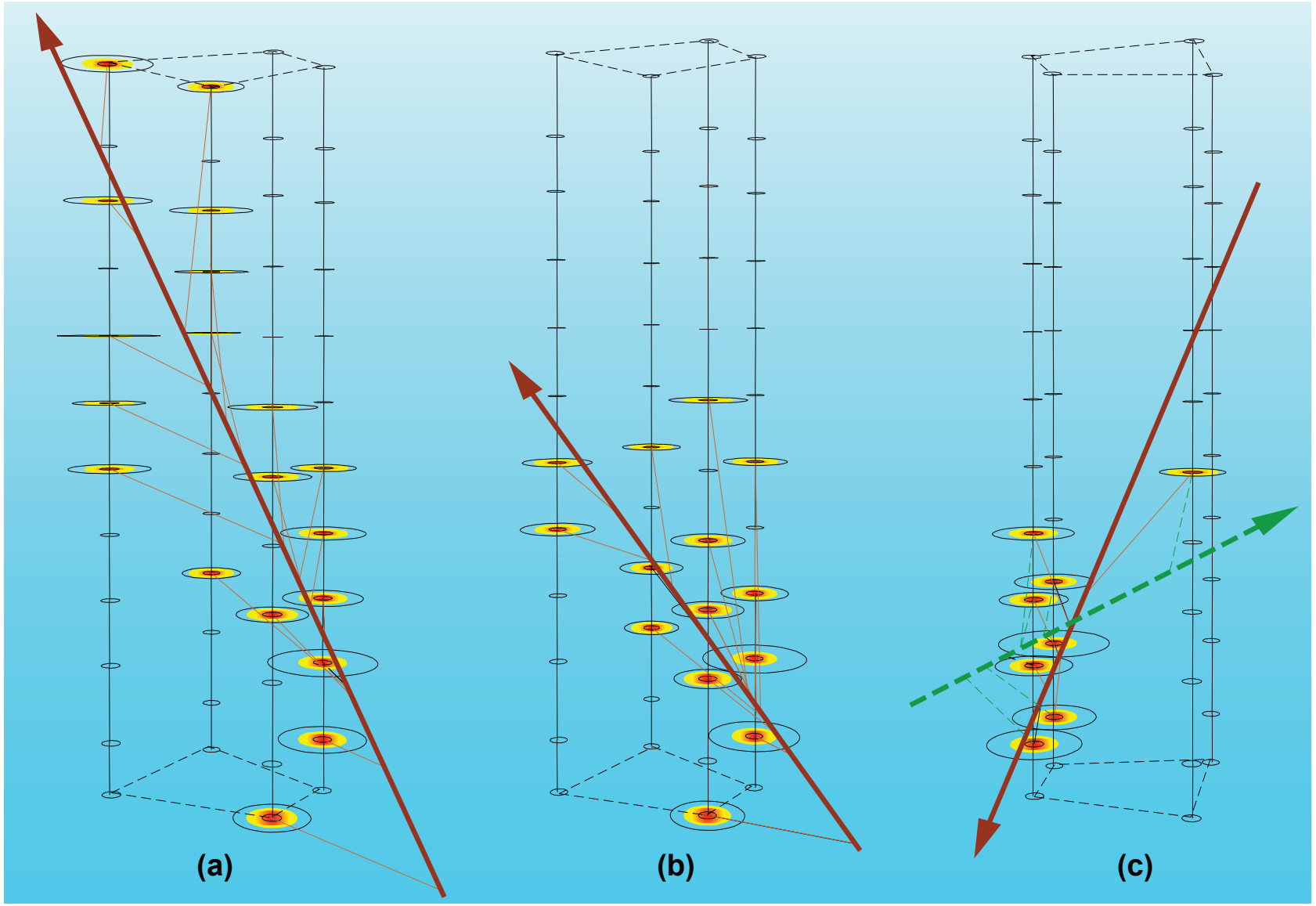

Three neutrino candidates recorded in NT 96 (see text for details and reference).

Since 2005, the upgraded 10-Mton scale detector NT 200+ is in operation. The most recent milestone of the ongoing km^3-telescope research and development work (R&D) was the installation of a "new technology" prototype string in spring 2008, as a part of NT 200+.

Figure on the right gives a sketch of the upgraded Baikal telescope NT 200+ as of 2008. The old compact NT 200 (center) surrounded by three external long strings at 100 m radius from the center and the new technology km^3-prototype string. Also indicated are the external laser and central control and readout unit (DAQ-center) about 20 m below surface.

[From A. Avrorin *et al.*, "The Baikal neutrino telescope – results and plans," Nucl. Instrum. Meth. A **630** (2011) 115–118.]

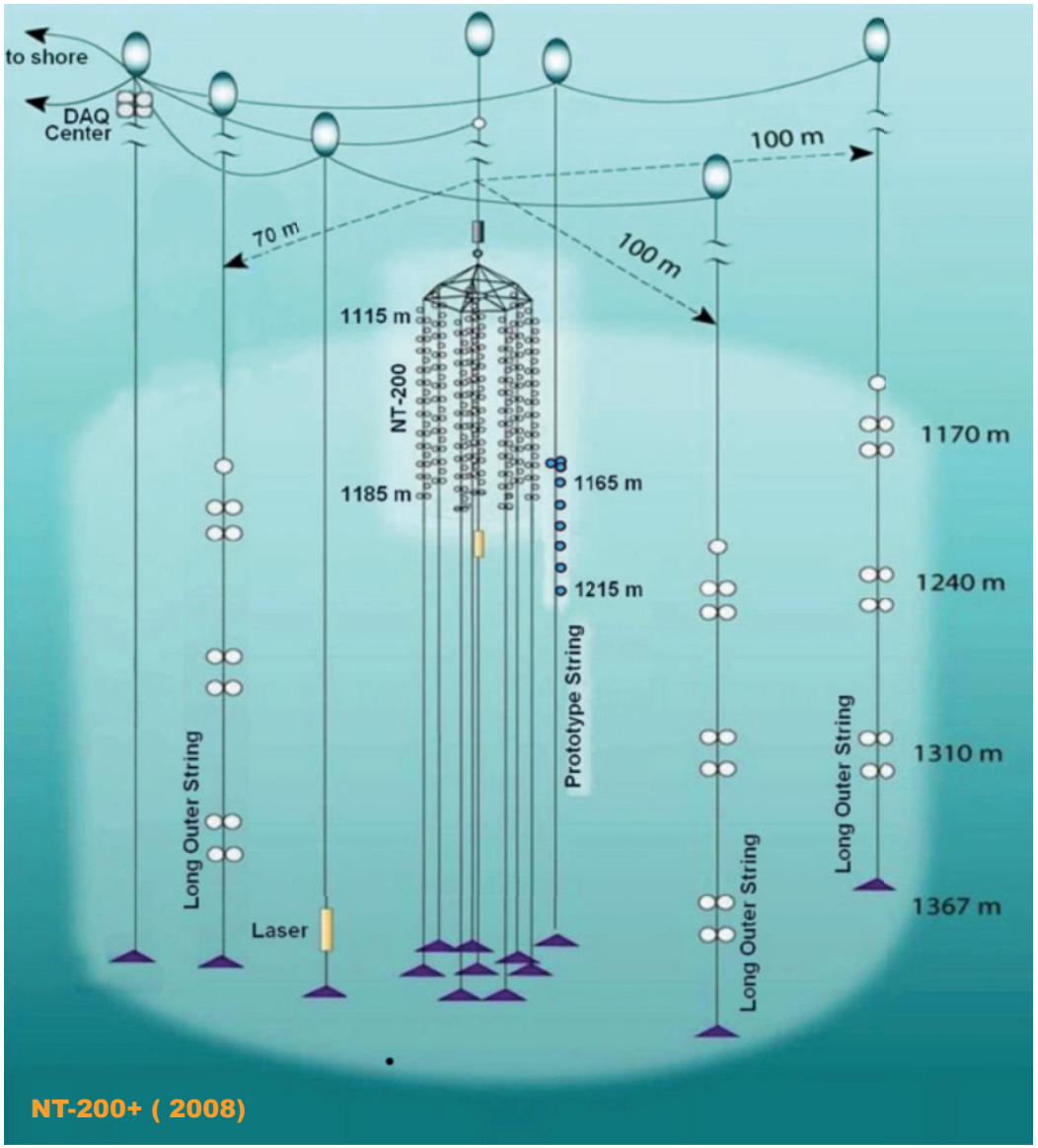

Baikal-GVD (Gigaton Volume Detector)

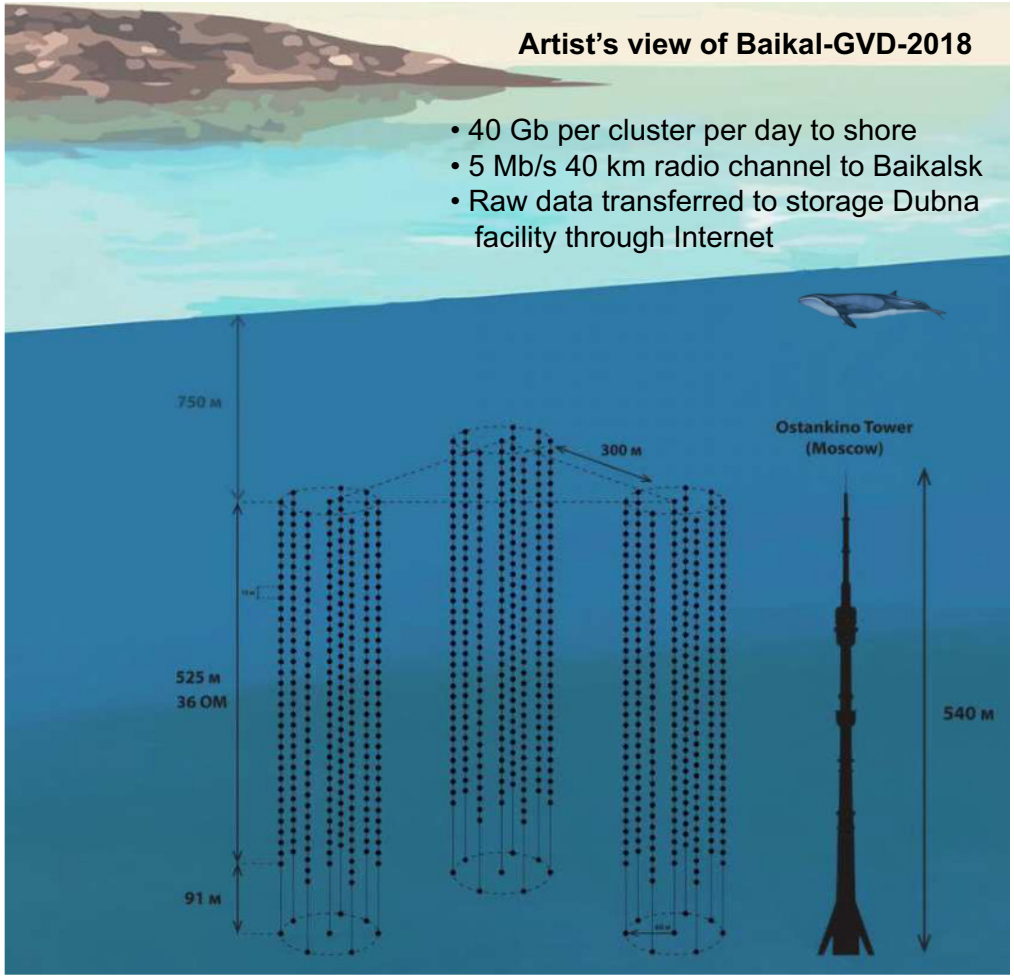

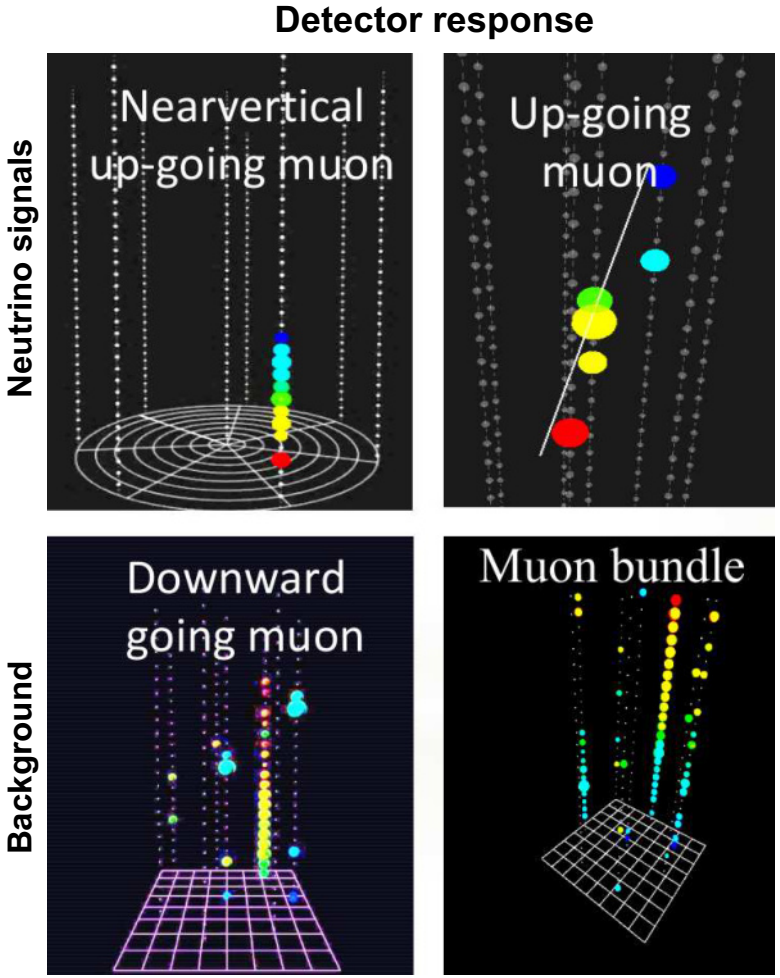

[Adapted from O. V. Suvorova, "Baikal-GVD neutrino experiment," (The 9th international workshop in air shower detection at high altitudes, INR RAS, Moscow, September 17–18, 2018); for more detail, see A. D. Avrorin *et al.*, "High-energy neutrino astronomy and the Baikal-GVD neutrino telescope," Phys. Atom. Nucl. **84** (2021) 513–518, arXiv:2011.09209v1 [astro-ph.HE].]

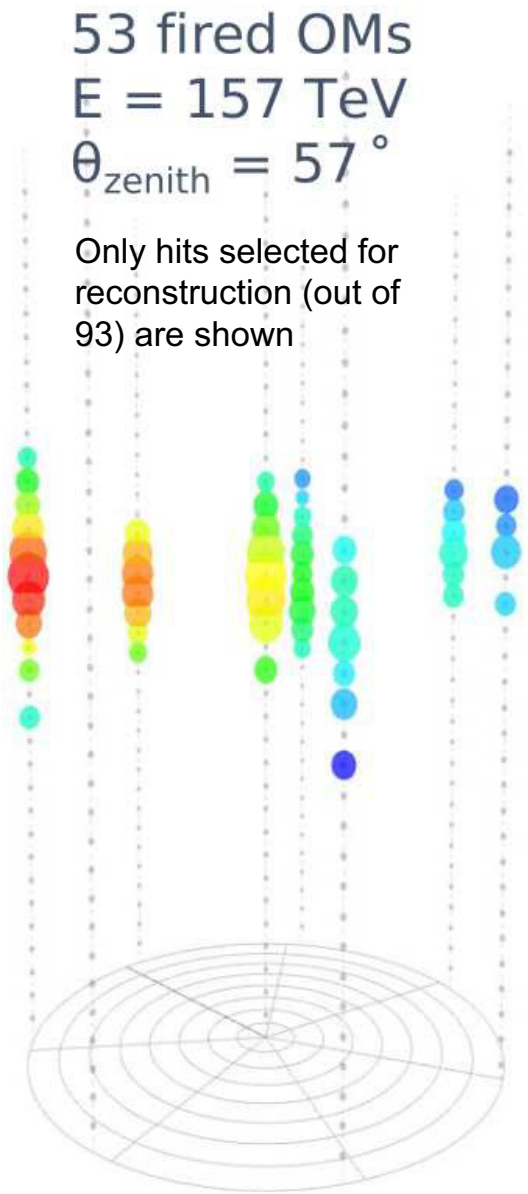

2016, 2018 and 2019 (4 months) data were processed, full exposition: 1364 days

7 candidates with E > 100 TeV and number of hits >19 + 1 upgoing cascade with E = 71 ТэВ

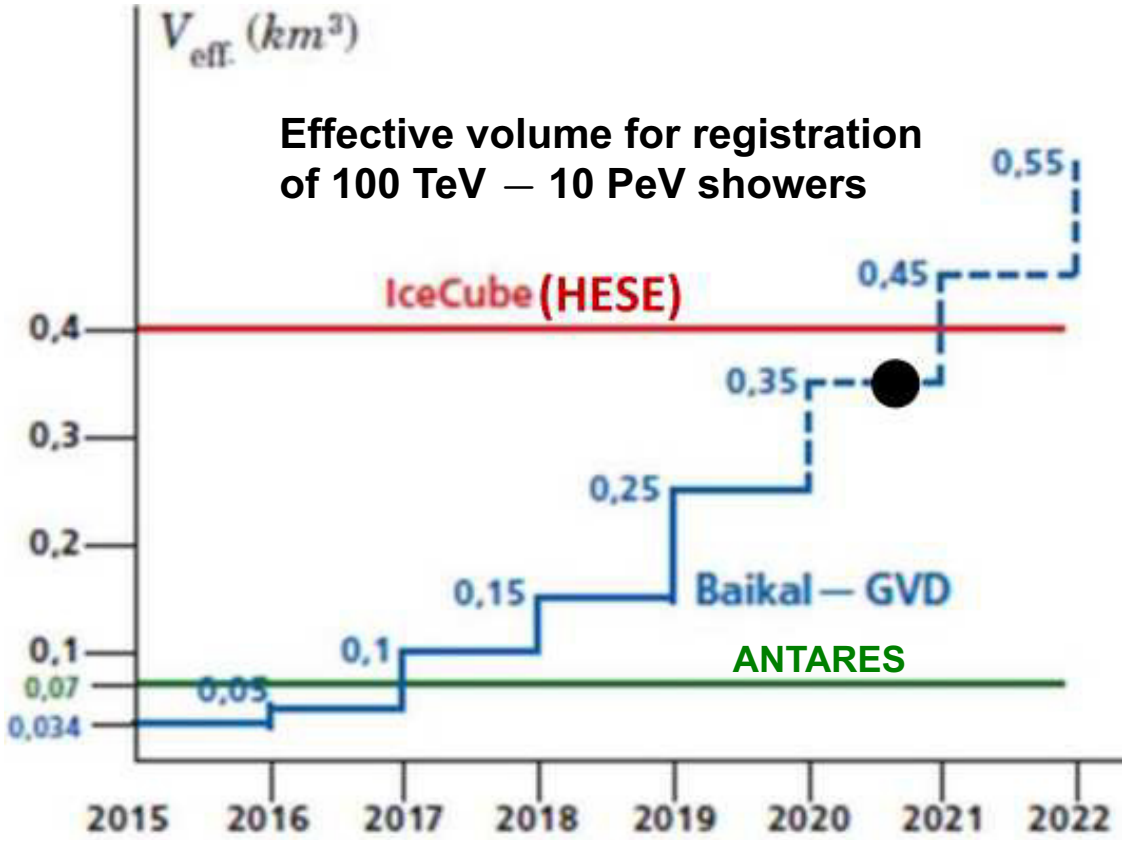

[From G. B. Safronov (for the Baikal-GVD Collaboration), "Status of Baikal-GVD experiment," (ICHEP 2020, Prague (virtual), July 28 – August 6, 2020).]

Detector construction status

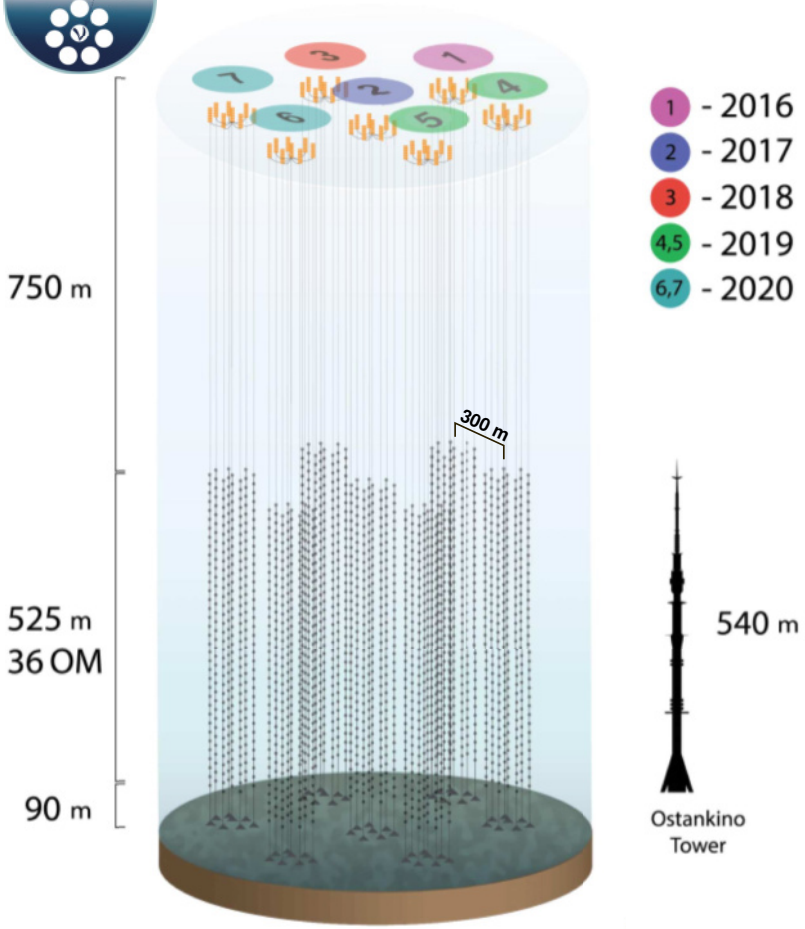

Deployment schedule

Year	Total number of clusters	Total number of strings	Number of OMs
2016	1	8	288
2017	2	16	576
2018	3	24	864
2019	5	40	1440
2020	**7**	**56**	**2016**
2021	9	72	2592
2022	11	88	3168
2023	13	104	3744
2024	15	120	4320

[From G. B. Safronov (for the Baikal-GVD Collaboration), "Status of Baikal-GVD experiment," (ICHEP 2020, Prague (virtual), July 28 – August 6, 2020); Г. В. Домогацкий. «Глубоководный нейтринный телескоп Baikal-GVD». (36-я Всероссийская конференция по космическим лучам «ВККЛ-2020», НИИЯФ МГУ, Москва (дистанционная), 28 сент. – 2 окт., 2020). See also nice animation @ ⟨ https://www.youtube.com/watch?v=XehDQTNCUiY ⟩.]

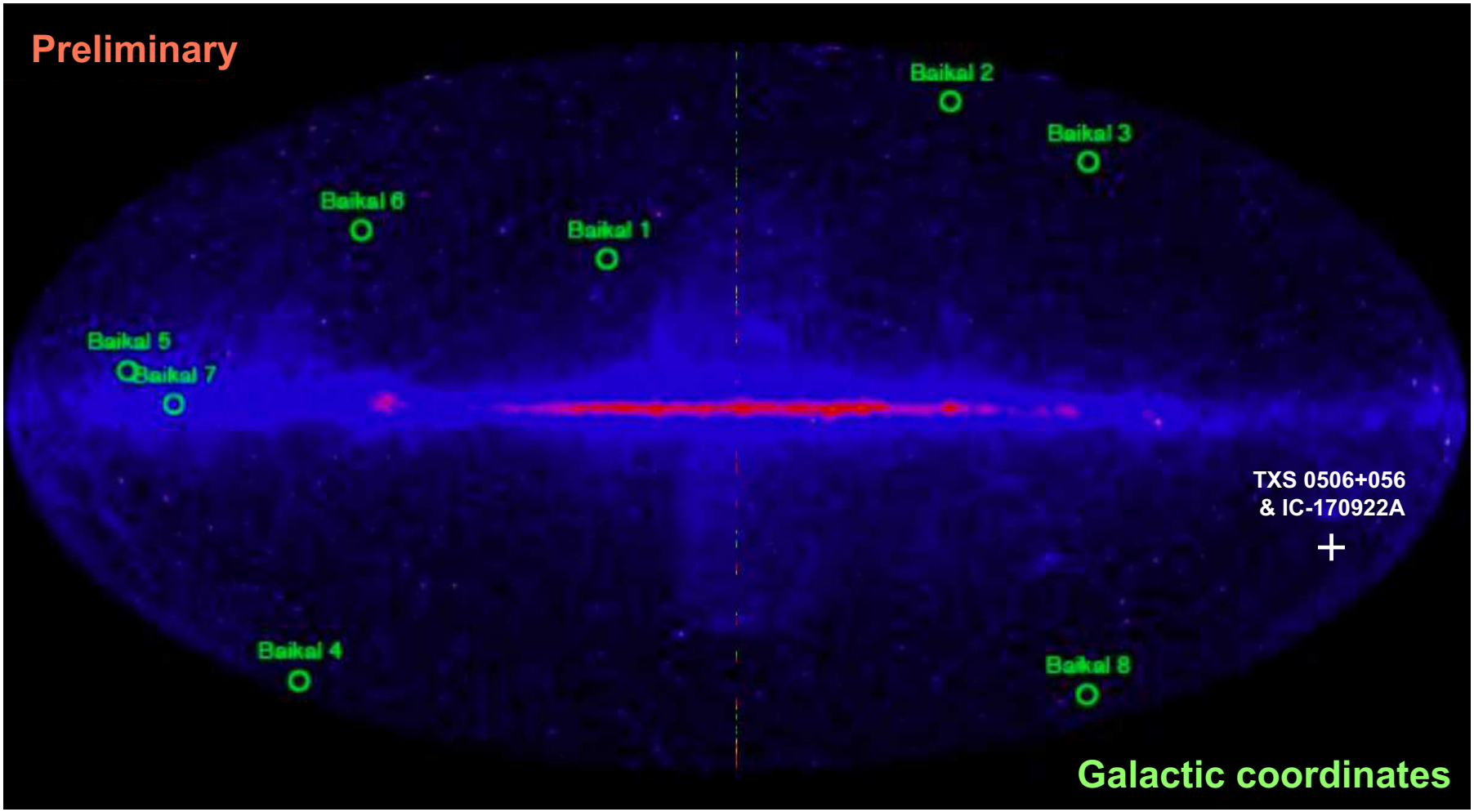

Baikal-GVD events on the background of the Fermi-LAT γ-ray skymap (Fourth Fermi Large Area Telescope catalog, 4FGL) for $E_\gamma > 10$ GeV (credits to D. Semikoz and A. Neronov)
[From G. B. Safronov (for the Baikal-GVD Collaboration), "Status of Baikal-GVD experiment," (ICHEP 2020, Prague (virtual), July 28 – August 6, 2020).]

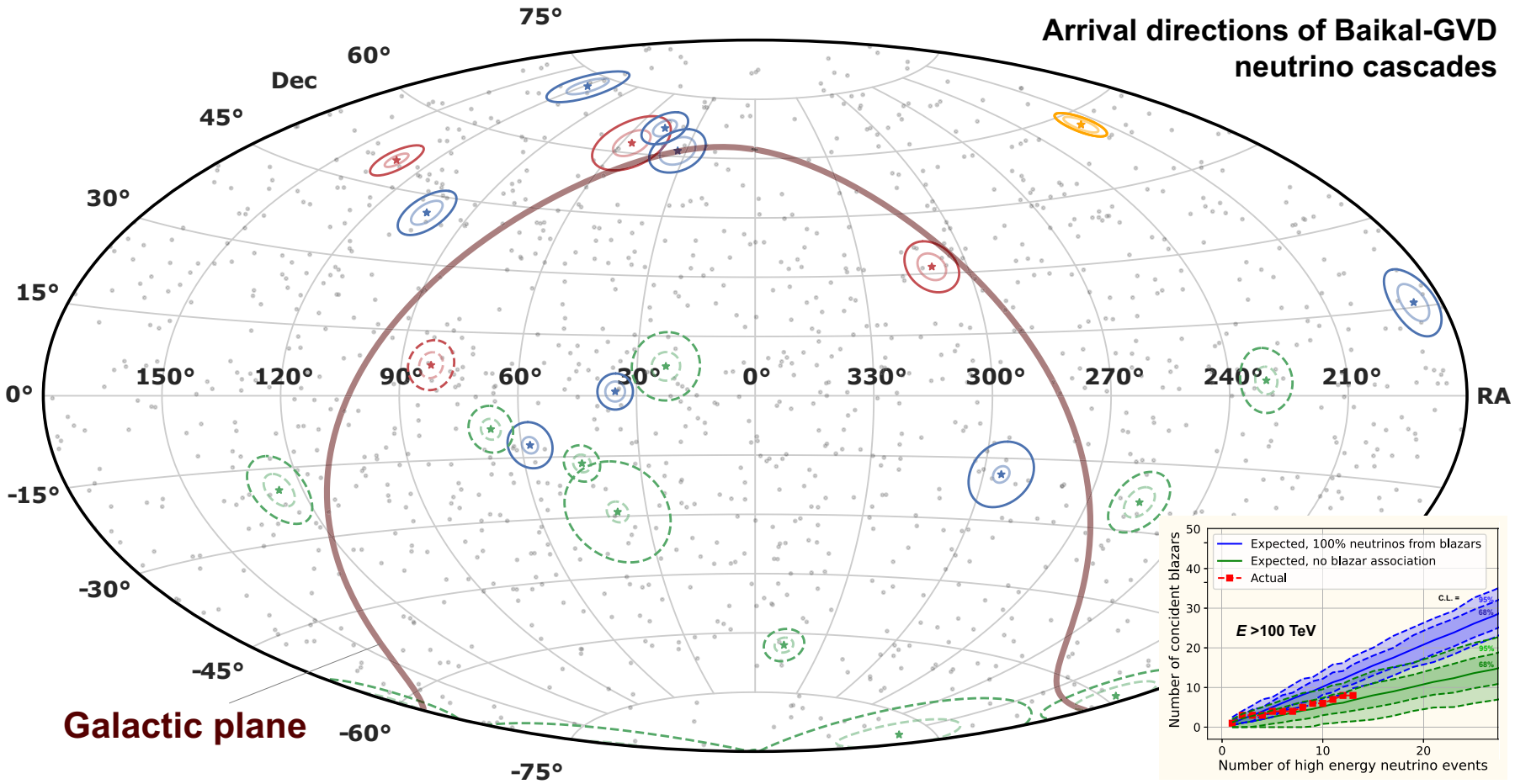

Directions of arrival of high-energy Baikal-GVD neutrino-induced cascades (stars) and their 50% and 90% C.L. uncertainty regions (ellipses) on the sky map in equatorial coordinates. Colour represents energies of the events: below 100 TeV (green), 100–200 TeV (blue), 200–1000 TeV (red), and 1 PeV (orange). Dashed/solid ellipses show events below/above the horizon. Positions of blazars from the 8 GHz VLBI sample with flux densities above 0.33 Jy [1 Jy (Jansky) $= 10^{-26}$ W/m^2] are shown as grey dots. The insert is self-explanatory.

[Adapted from V. A. Allakhverdyan *et al.* (Baikal-GVD Collaboration), "Search for directional associations between Baikal Gigaton Volume Detector neutrino-induced cascades and high-energy astrophysical sources," Mon. Not. Roy. Astron. Soc. **526** (2023) 942–951, arXiv:2307.07327 [astro-ph.HE].]

AMANDA

The AMANDA (Antarctic Muon And Neutrino Detector Array) detector is located at the South Pole station, Antarctica. The detector uses the 2.8 km thick ice sheet at the South Pole as a neutrino target, Cherenkov medium and cosmic ray flux attenuator. The detector consists of vertical strings of optical modules (OMs) – photomultiplier tubes sealed in glass pressure vessels – frozen into the ice at depths of 1500–2000 m below the surface.

Construction of the South Pole Station as of February, 2002.

Two more fine photos of the Amundsen-Scott South Pole Station are shown in pp. 976 and 977.
[From Francis Halzen's webpage ⟨ http://icecube.wisc.edu/~halzen/ ⟩.]

Amundsen-Scott South Pole Station.

One another vie of the South Pole Station.

Figure on the right shows the configuration of the AMANDA detector. The shallow array, AMANDA-A, was deployed at depths of 800 to 1000 m in 1993–1994 in an exploratory phase of the project. Studies of the optical properties of the ice carried out with AMANDA-A showed a high concentration of air bubbles at these depths, leading to strong scattering of light and making accurate track reconstruction impossible. Therefore, a deeper array of 10 strings with 302 OMs was deployed in the austral summers of 1995–1996 and 1996–1997 at depths of 1500–2000 m. This detector is referred to as AMANDA-B10. It was augmented by 3 additional strings in 1997–1998 and 6 in 1999–2000, forming the AMANDA-II array. This detector has been calibrated and in operation since January 2000.

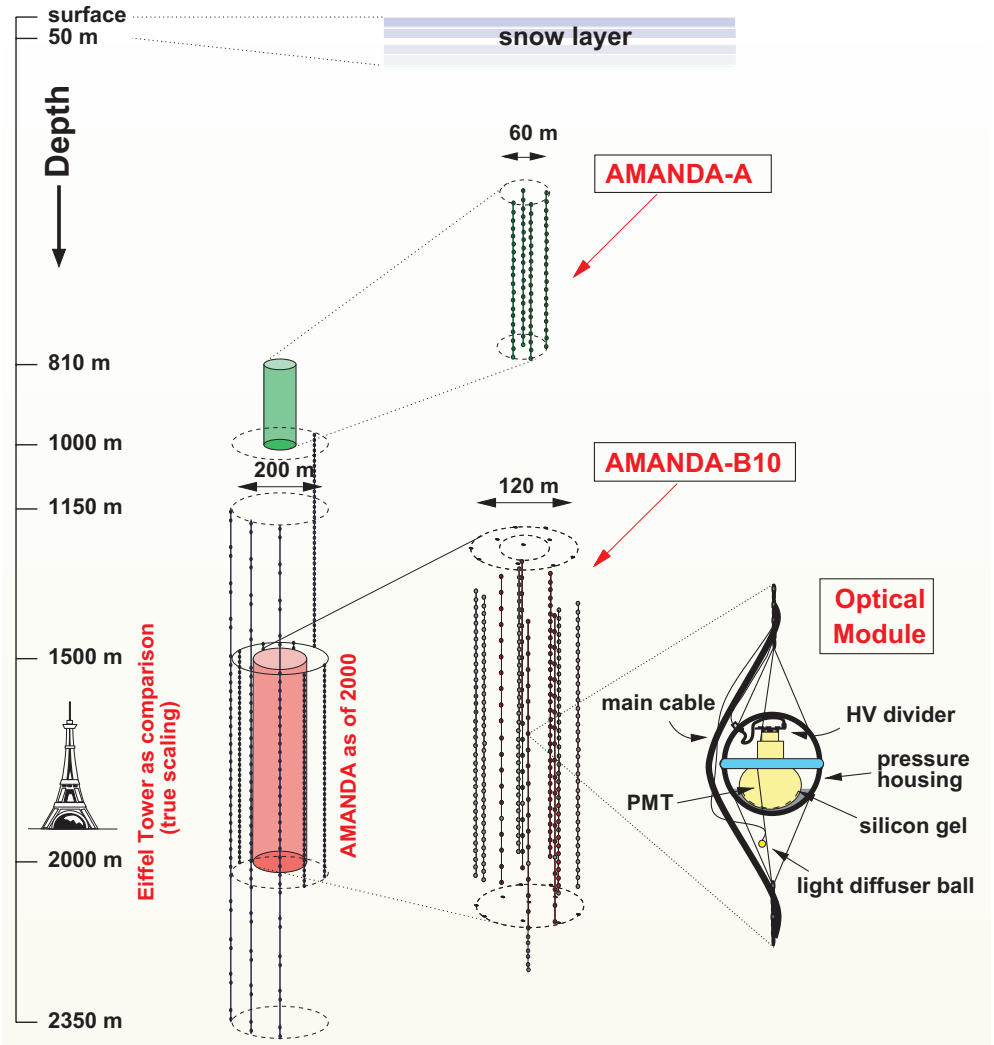

Schematic view of the AMANDA-II array.

[From J. Ahrens *et al.*, Phys. Rev. D **66** (2002) 012005, astro-ph/0205109.]

Figure on the right is an artistic view of a neutrino induced event in the AMANDA detector while Figure in p. 980 displays three real neutrino candidates. Let us describe these in some detail.

(a) Event display of an upgoing muon event. The gray scale indicates the flow of time, with early hits at the bottom and the latest hits at the top of the array. The arrival times match the speed of light. The sizes of the ellipses correspond to the measured amplitudes.

(b) The upgoing muon event has a smooth distribution of hits along the extended uniform track. The track-like hit topology of this event can be used to distinguish it from background events.

(c) A background event with a poor smoothness value and a large deviation from a straight line.

Two more neutrino candidates (both were recorded on May 11, 2000) are shown in p. 981.[a]

[a] Figures are borrowed from URL: ⟨ http://amanda.physics.wisc.edu/ ⟩. In this site, there a lot of nice animated images relevant to the subject.

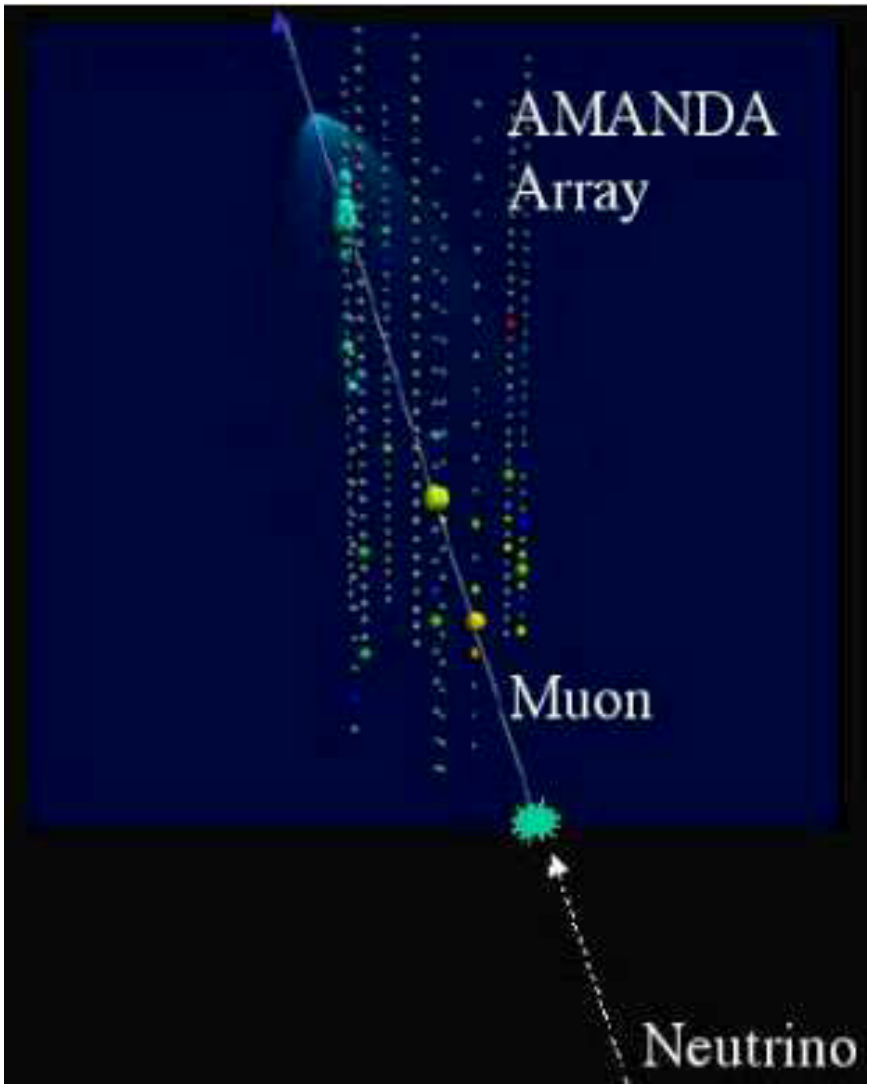

Artistic view of a ν induced event in the AMANDA detector.

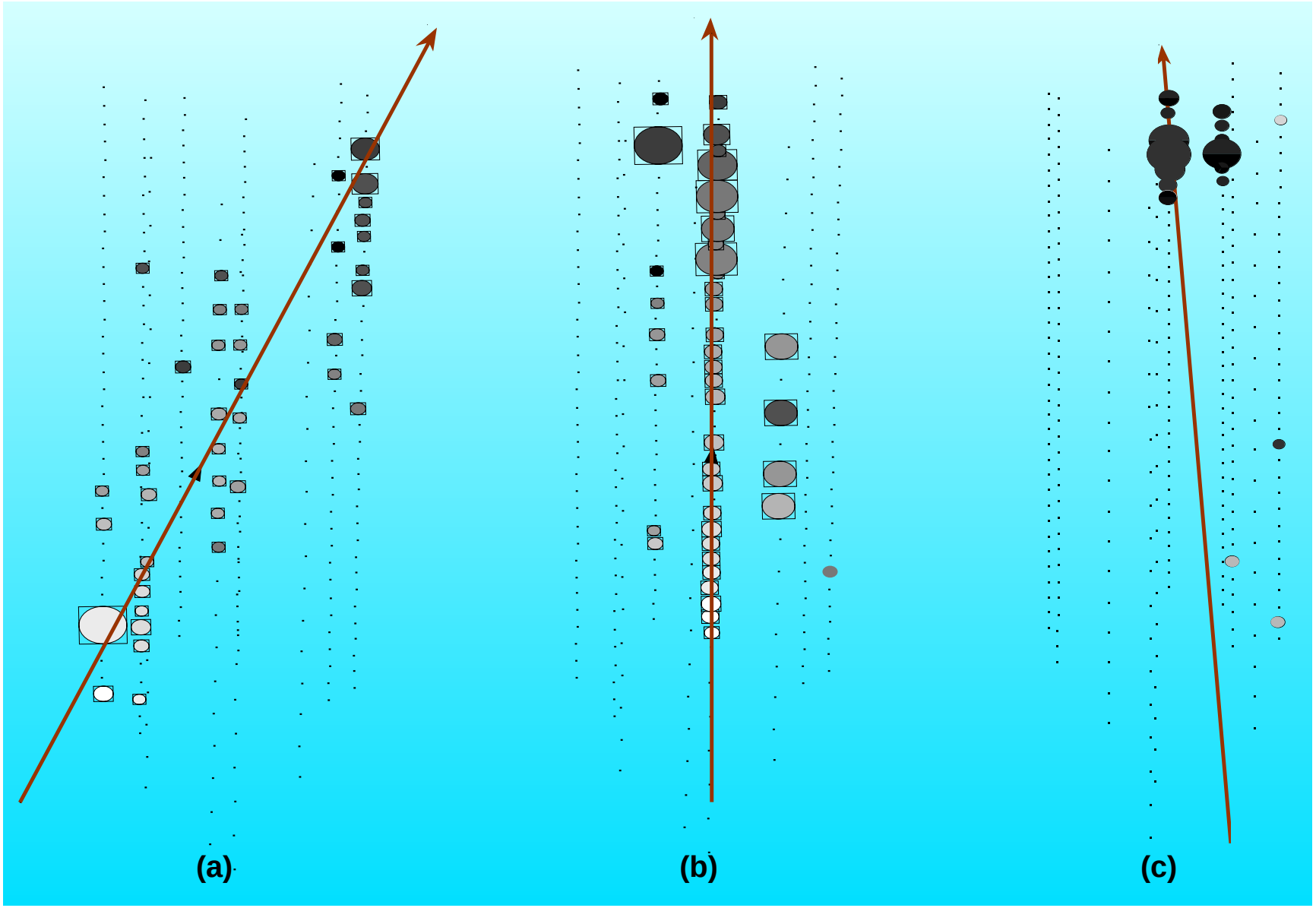

Three neutrino candidates recorded in AMANDA-B10 (see text).

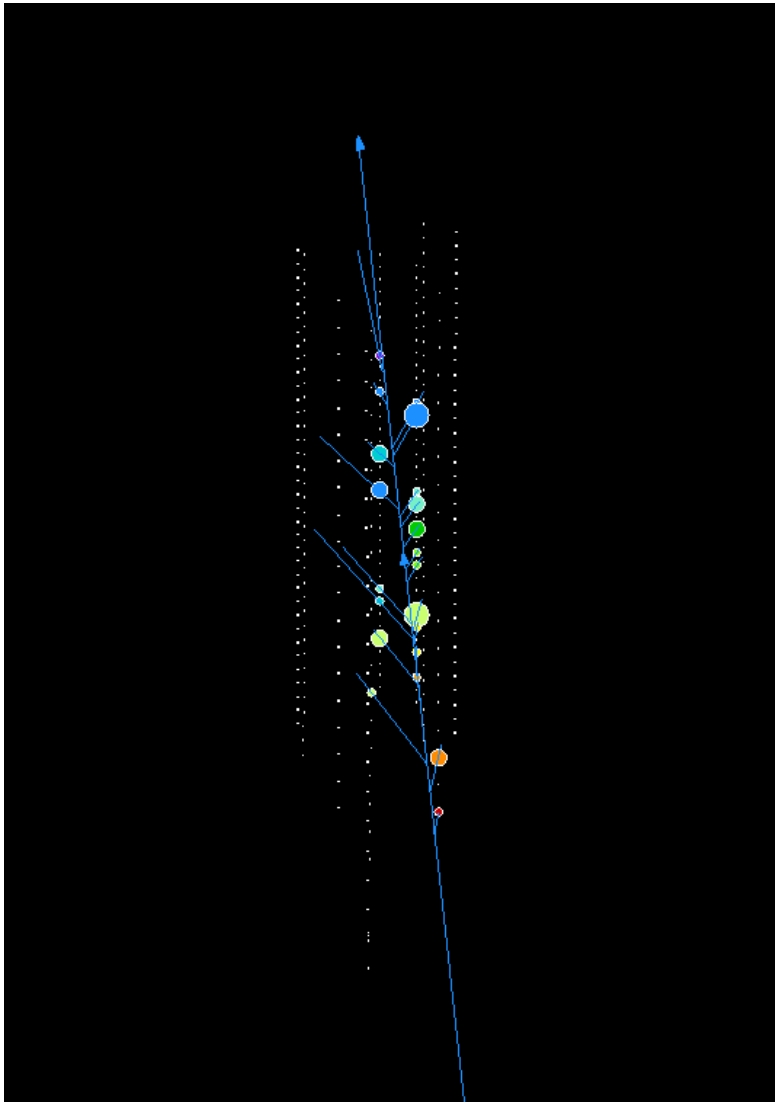

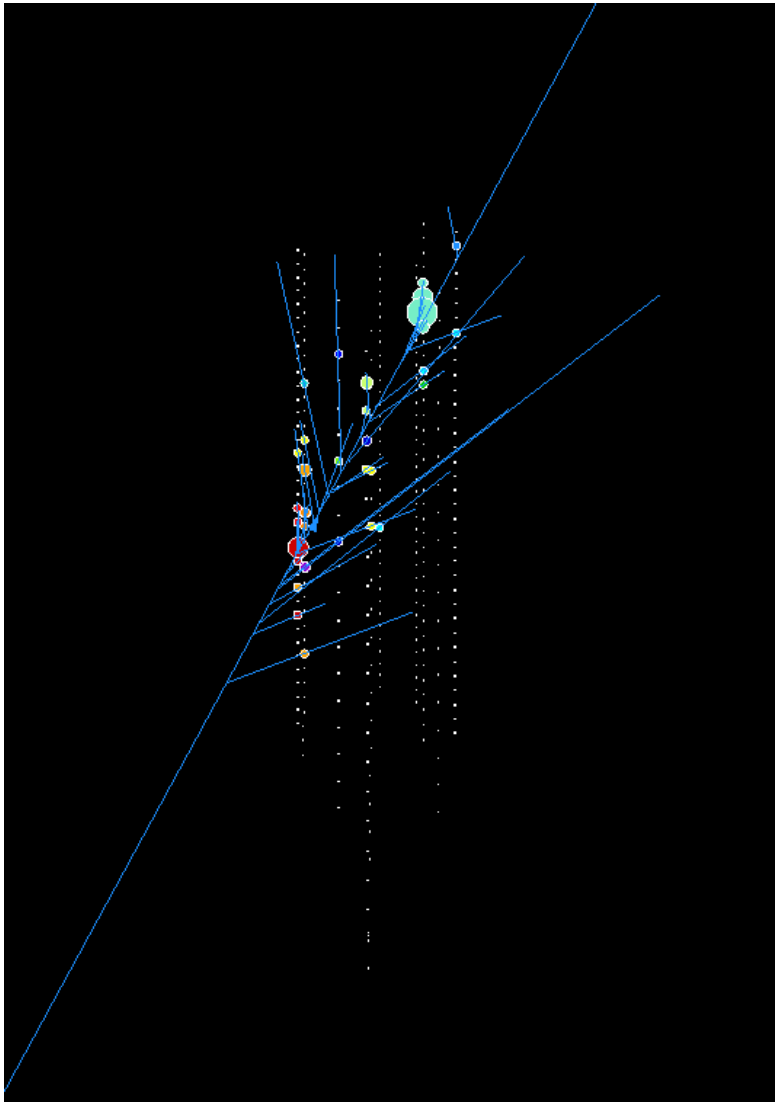

Two more neutrino candidates in AMANDA, #910225 and #10604848 (recorded on May 11, 2000).

[From URL: ⟨ http://amanda.physics.wisc.edu/ ⟩.]

IceCube

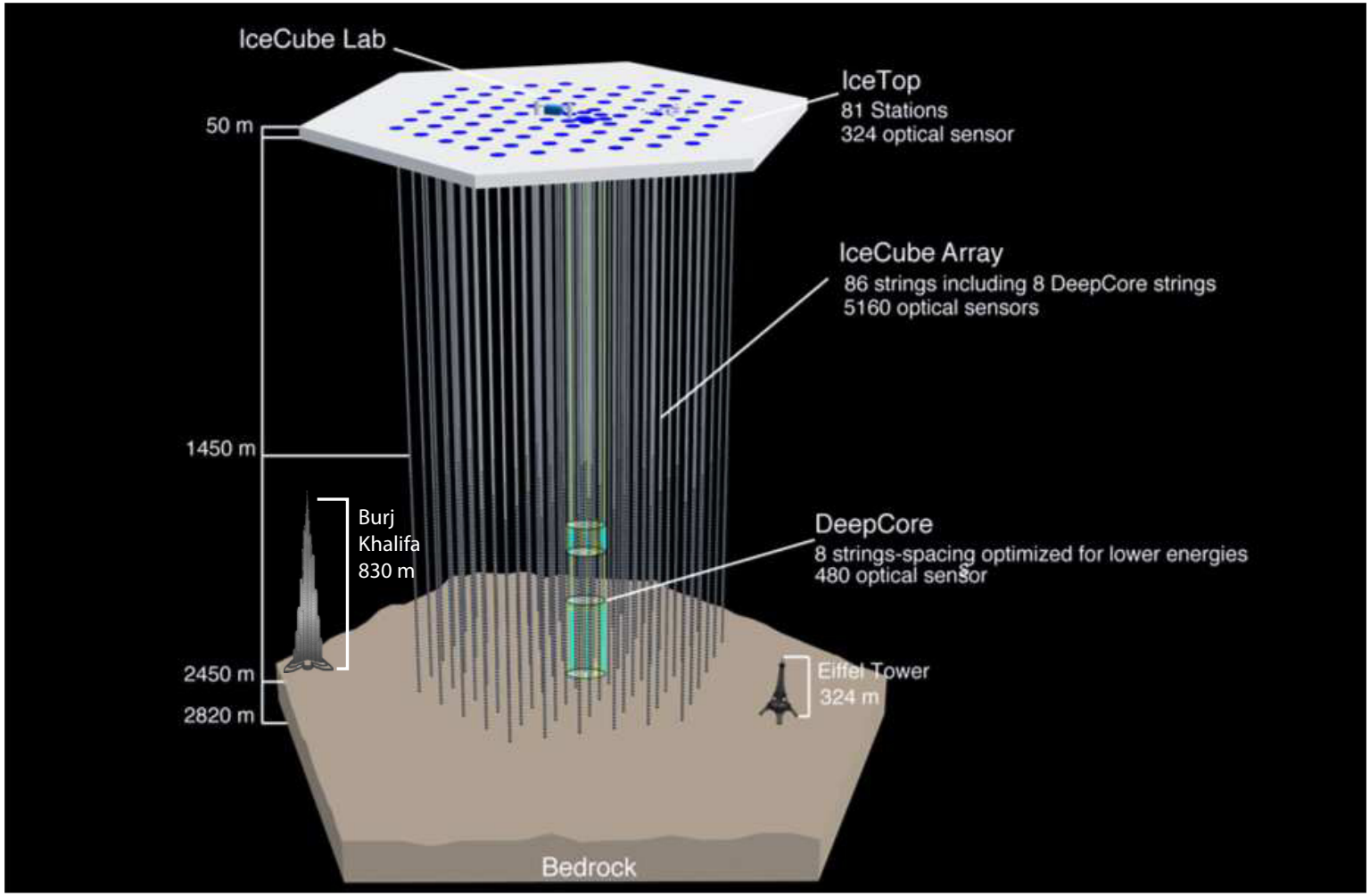

The IceCube Neutrino Telescope is made up of 86 strings with a total of 5,160 Digital Optical Modules that are used to sense and record neutrino events. Although the telescope is 2,820 m tall, the average hole is 2,452 m deep (almost three times as big as the tallest building in the world).

[Adapted from an image by Danielle Vevea & Jamie Yang, see IceCube NO webpage ⟨ http://icecube.wisc.edu/ ⟩.]

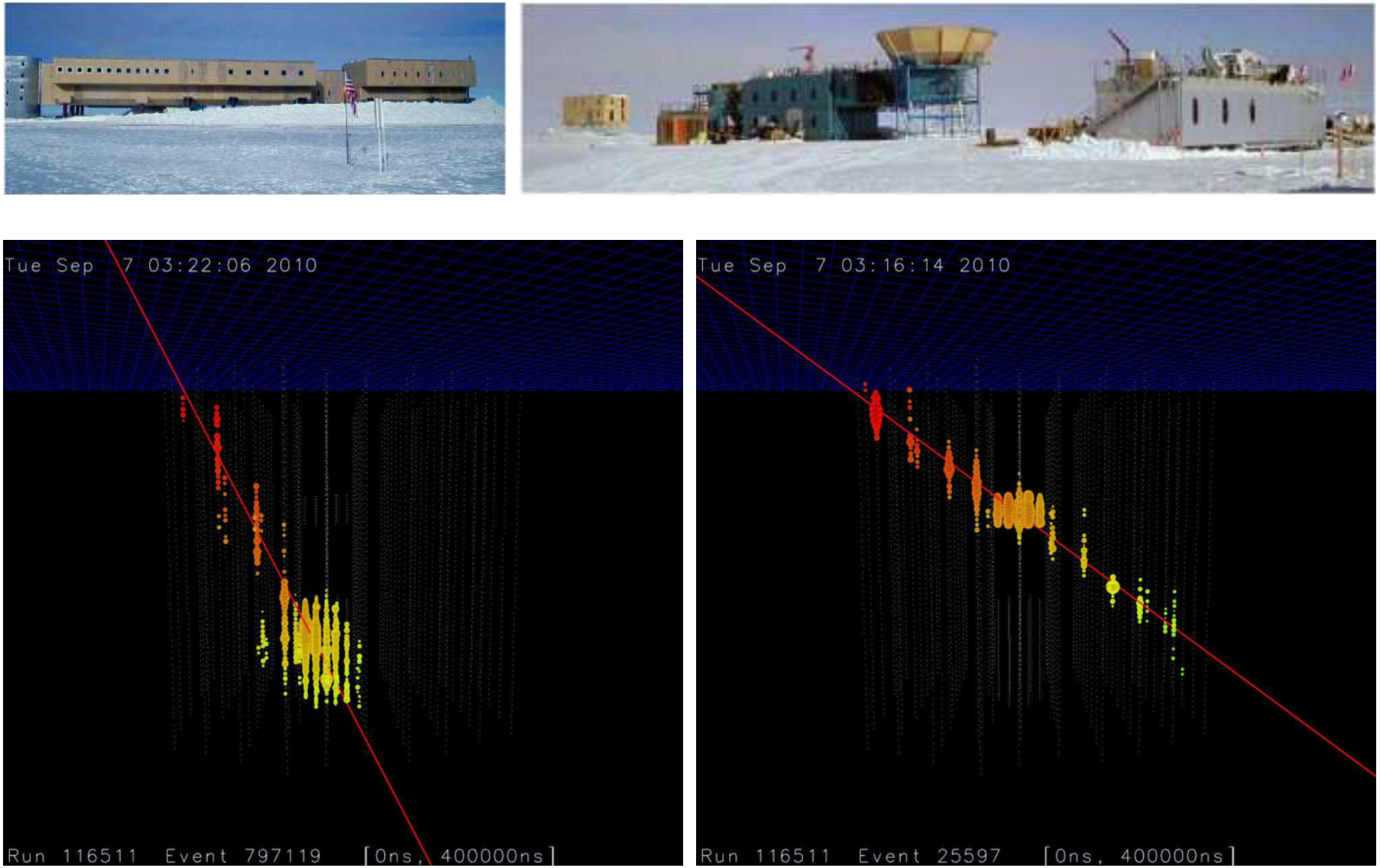

Two typical neutrino events captured by the IceCube Telescope. [From http://icecube.wisc.edu/].

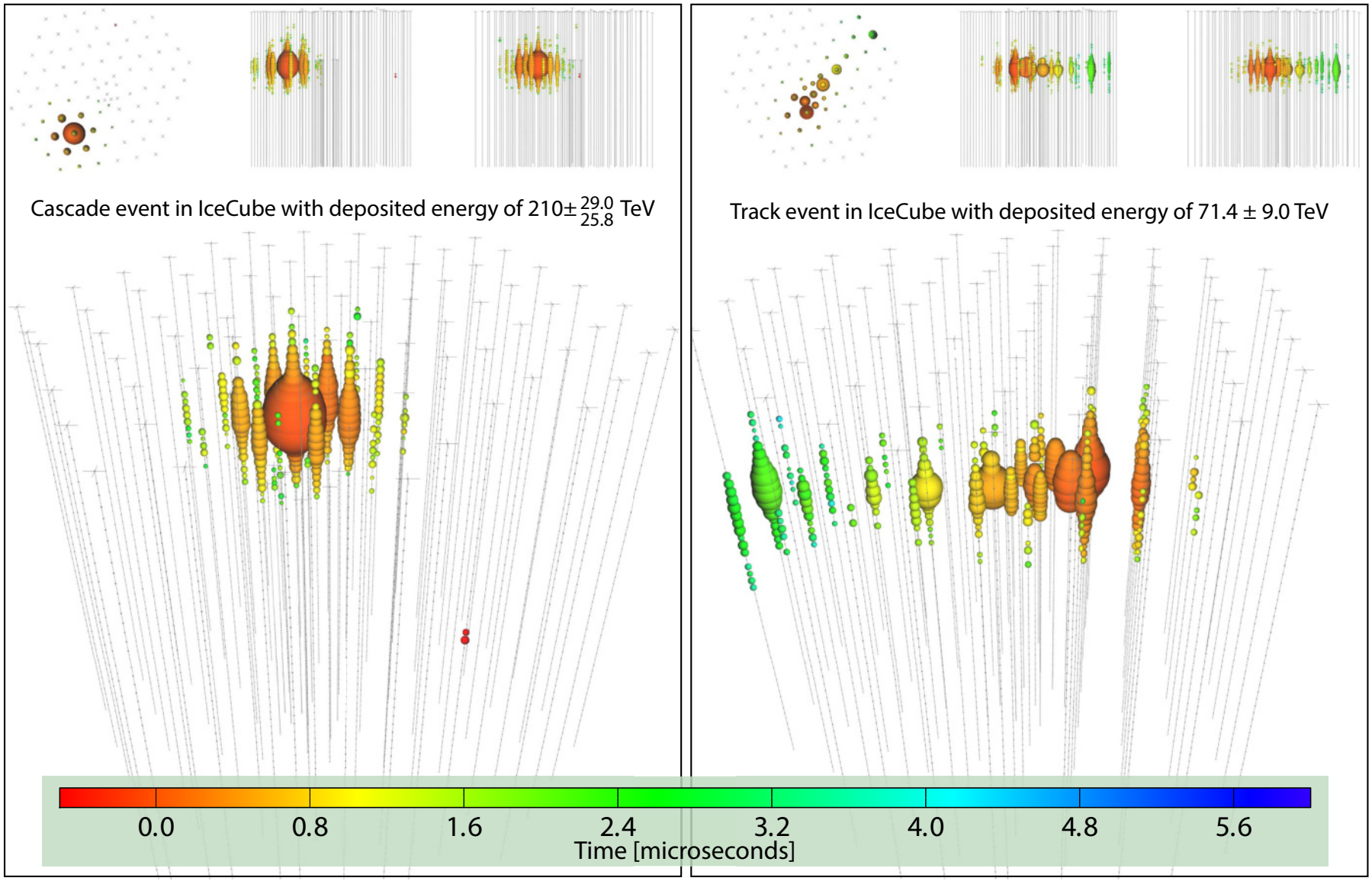

[From M. G. Aartsen *et al.* (IceCube Collaboration), "Evidence for high-energy extraterrestrial neutrinos at the IceCube Detector," Science **342**, Iss. 6161 (2013) 1242856, arXiv:1311.5238 [astro-ph.HE].]

Enabling multimessenger astronomy with IceCube real-time neutrino alerts.

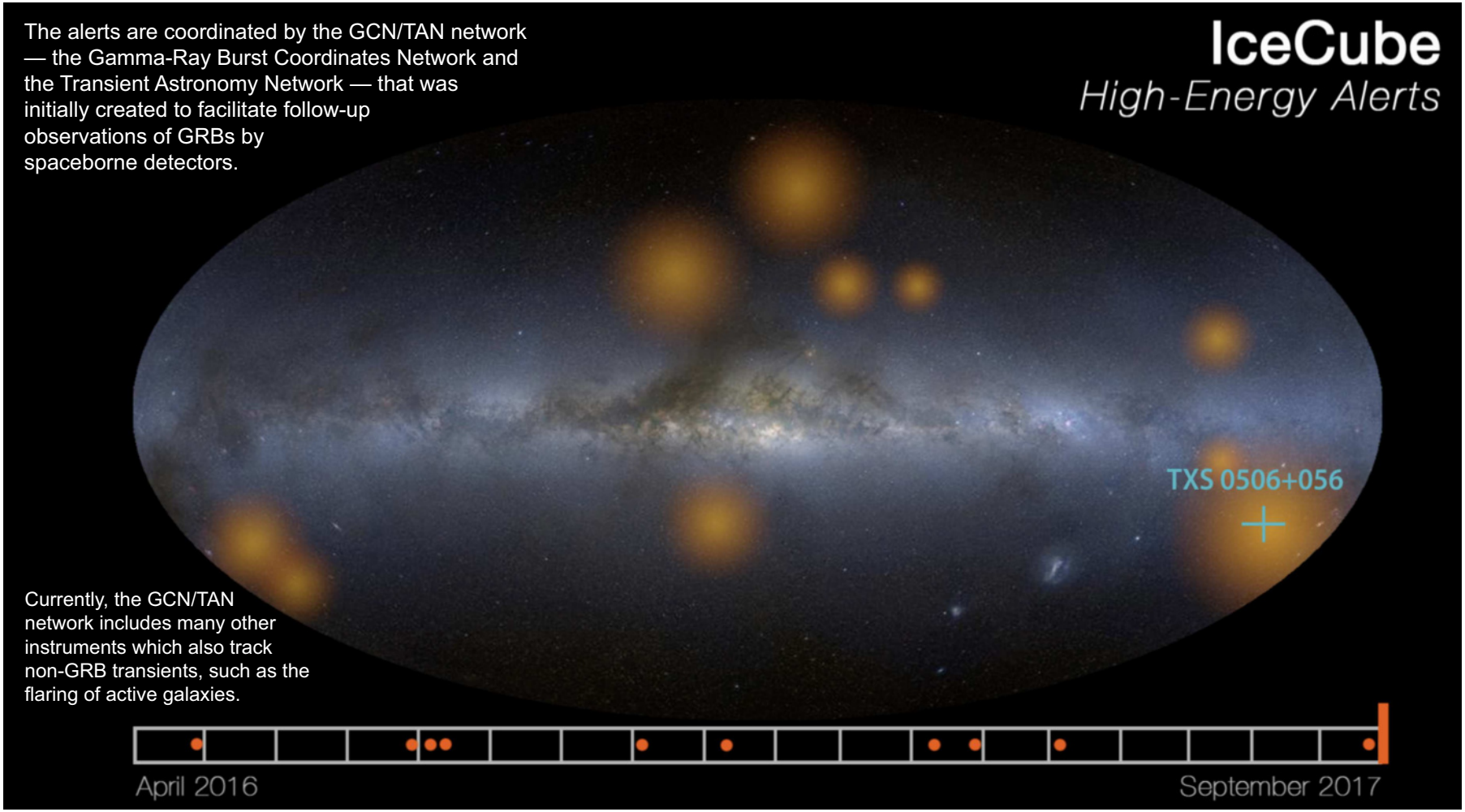

IceCube real-time alerts trigger on a series of neutrino signatures with a high chance of identifying a neutrino of astrophysical origin, thus pointing to interesting regions of the sky, and notify the international community when an interesting cosmic phenomenon could be observed.

[From URL ⟨https://icecube.wisc.edu/science/data/realtime_alerts⟩.]

KM3 projects (ANTARES, NEMO, NESTOR) – a bit obsolete

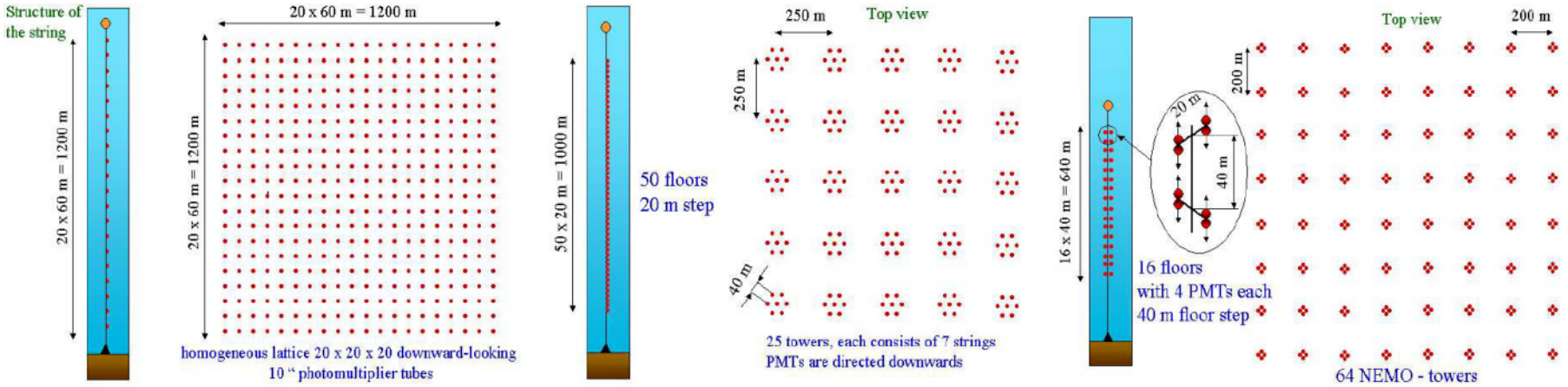

Future KM3 neutrino telescope geometries. *Left panel*: schematic view of a homogeneous detector with 8000 PMTs (not quite optimal to be built); *Middle panel*: the layout of a NESTOR-like detector with 8750 PMTs; *Right panel*: the layout of a NEMO-like detector with 4096 PMTs.

These three designs have very different degrees of homogeneity. One more difference may be due to various numbers of downward-looking and upward-looking PMTs (down-down, up-down, etc.).

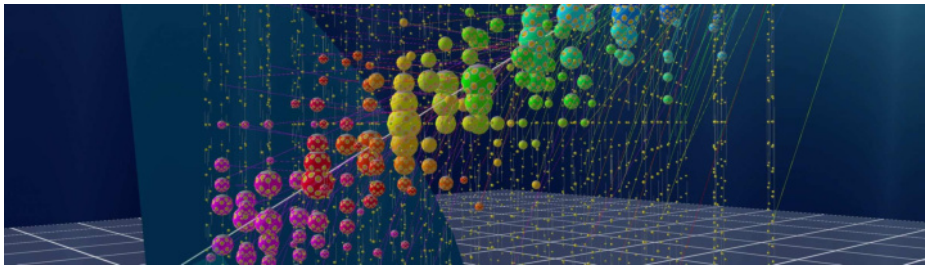

[From D. Zaborov, "Comparison of different KM3 designs using Antares tools," in Proceedings of the Workshop on Technical Aspects of a Very Large Volume Neutrino Telescope in the Mediterranean Sea 'VLVνT', Amsterdam, October 5–8, 2003, edited by E. de Wolf (NIKHEF, Amsterdam, The Netherlands), pp. 104–108.]

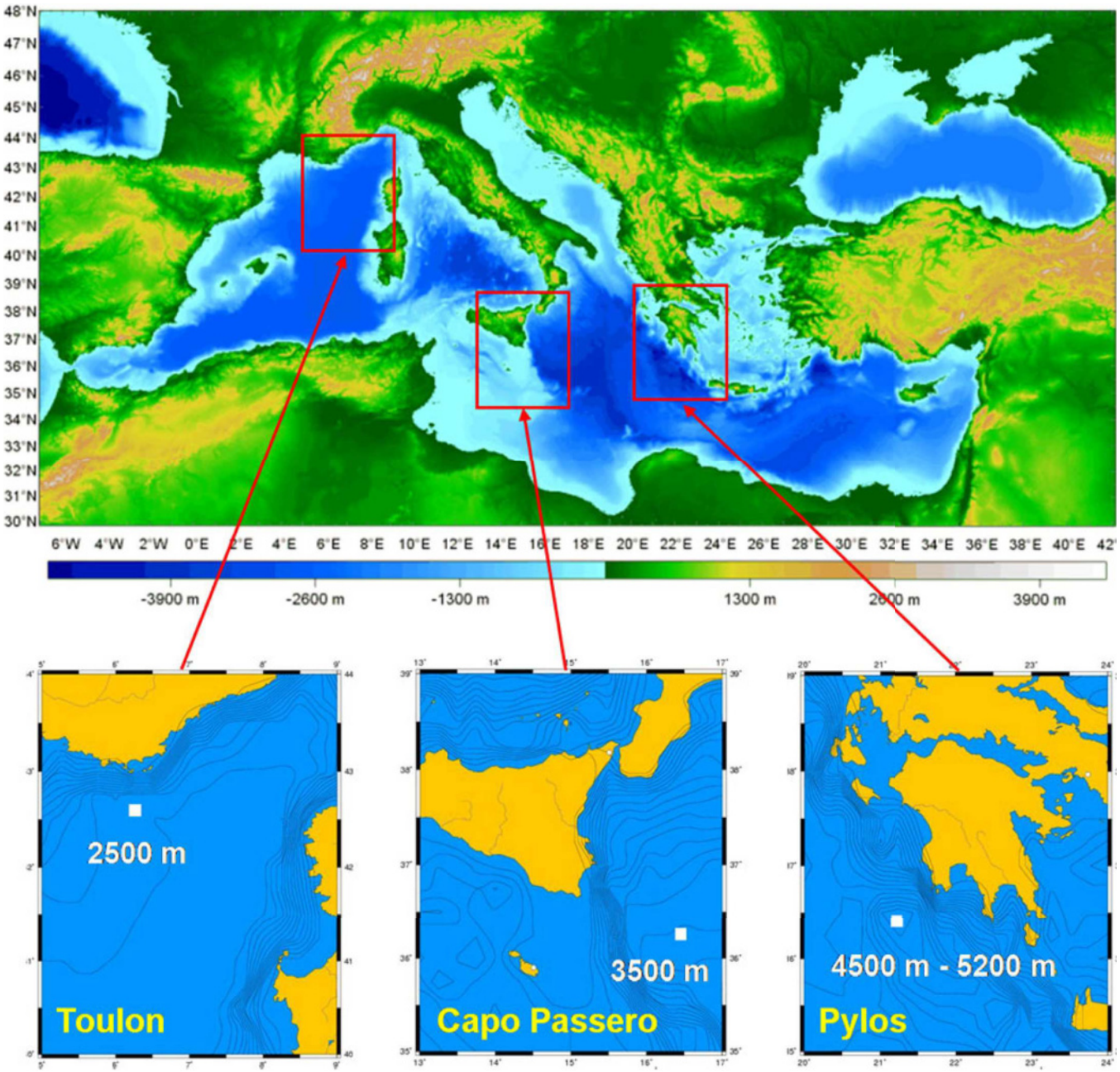

Locations of the sites of the three Mediterranean neutrino telescope projects.

[From P. Bagley *et al.*, "KM3NeT. Conceptual Design Report for a Deep-Sea Research Infrastructure Incorporating a Very Large Volume Neutrino Telescope in the Mediterranean Sea,"]

KM3NeT ARCA/ORCA (**A**strophysics/**O**scillation **R**esearch with **C**osmics in the **A**byss)

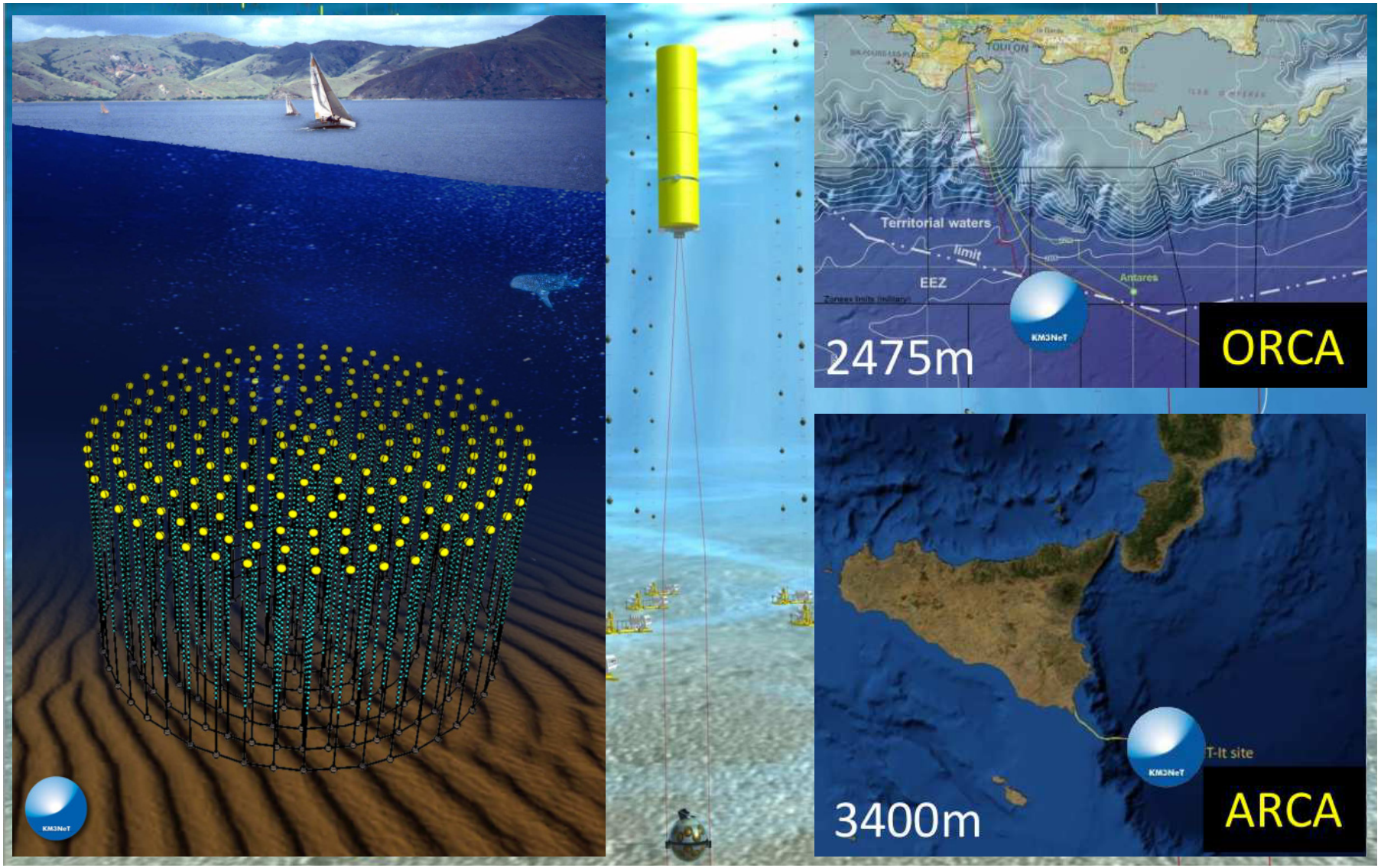

[From A. Heijboer, "Neutrino Mass Hierarchy and other physics in H_20 (ORCA & PINGU) Report in the Neutrino Oscillation Workshop 'NOW-2016'," (Otranto, Lecce, September 4–11, 2016).]

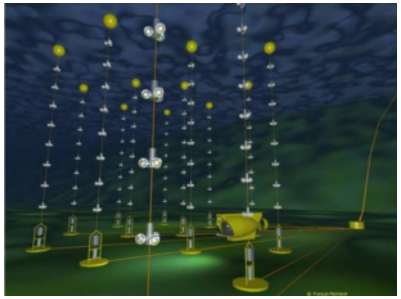

ORCA

200 m

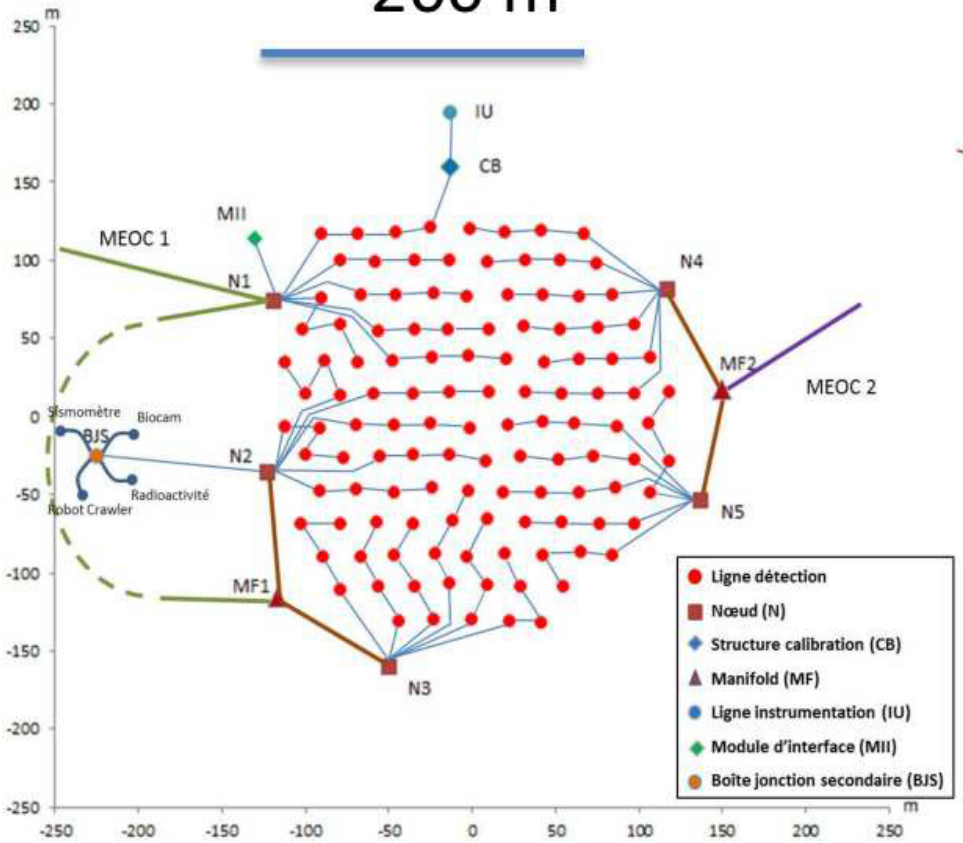

ARCA

200 m

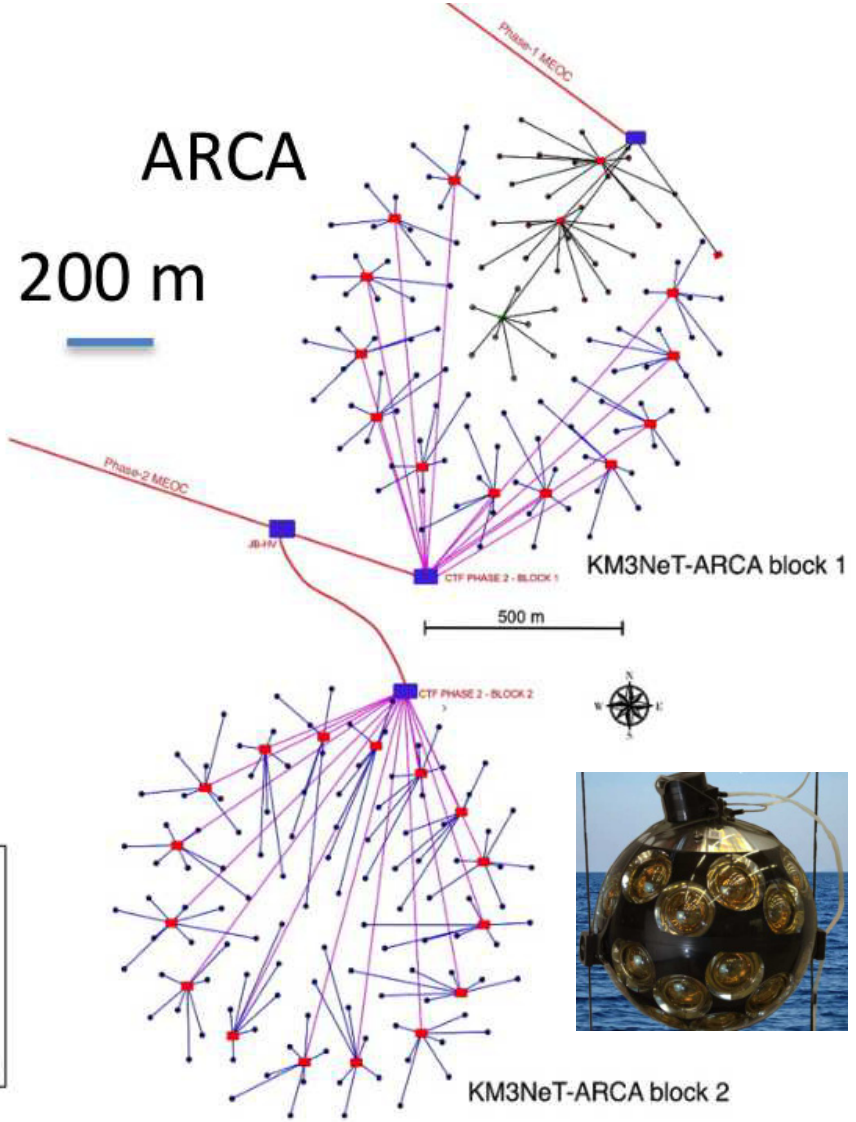

[From D.Samtleben, "Neutrinos in the Mediterranean Sea," Report in The XXIX International Conference on Neutrino Physics and Astrophysics, Virtual (June 22 – July 2, 2020.]

Selected References

References to the ANITA puzzle (see p. 357).

[1] P. W. Gorham *et al.* (ANITA Collaboration), "Characteristics of four upward-pointing cosmic-ray-like events observed with ANITA," Phys. Rev. Lett. **117** (2016) 071101, arXiv:1803.05088 [astro-ph.HE].

[2] P. W. Gorham *et al.* (ANITA Collaboration), "Observation of an unusual upward-going cosmic-ray-like event in the third flight of ANITA," Phys. Rev. Lett. **121** (2018) 161102, arXiv:1803.05088 [astro-ph.HE].

[3] P. Motloch *et al.*, "Can transition radiation explain the ANITA event 3985267?" Phys. Rev. D **95** (2017) 043004, arXiv:1606.07059 [astro-ph.HE].

[4] J. F. Cherry & I. M. Shoemaker, "A sterile neutrino origin for the upward directed cosmic ray showers detected by ANITA," Phys. Rev. D **99** (2019) 063016, arXiv:1802.01611 [hep-ph].

[5] L. A. Anchordoqui *et al.*, "Upgoing ANITA events as evidence of the CPT symmetric Universe," LHEP **1** (2018) 13–16, arXiv:1803.11554 [hep-ph].

[6] C. Deaconu (for the ANITA Collaboration), "Recent results from ANITA," arXiv:1810.00820 [astro-ph.HE].

[7] A. Romero-Wolf *et al.* (ANITA Collaboration), "Upward-pointing cosmic-ray-like events observed with ANITA," PoS(ICRC2017)935, arXiv:1810.00439 [astro-ph.HE].

[8] G.-y. Huang, "Sterile neutrinos as a possible explanation for the upward air shower events at ANITA," Phys. Rev. D **98** (2018) 043019, arXiv:1804.05362 [hep-ph].

[9] A. Connolly *et al.*, "On ANITA's sensitivity to long-lived, charged massive particles," arXiv:1807.08892 [astro-ph.HE].

[10] D. B. Fox *et al.*, "ANITA anomalous events as signatures of a beyond Standard Model particle, and supporting observations from IceCube," arXiv:1809.09615 [astro-ph.HE].

[11] J. H. Collins *et al.*, "R-parity violating supersymmetric explanation of the anomalous events at ANITA," Phys. Rev. D **99** (2019) 043009, arXiv:1810.08479 [hep-ph].

[12] A. Romero-Wolf *et al.*, "Comprehensive analysis of anomalous ANITA events disfavors a diffuse tau-neutrino flux origin," Phys. Rev. D **99** (2019) 063011, arXiv:1811.07261 [astro-ph.HE].

[13] P. Dasgupta & P. Jain, "General treatment of reflection of spherical electromagnetic waves from a spherical surface and its application to ANITA observations," Astropart. Phys. **128** (2021) 102530, arXiv:1811.00900 [physics.class-ph].

[14] L. A. Anchordoqui & I. Antoniadis, "Supersymmetric sphaleron configurations as the origin of the perplexing ANITA events," Phys. Lett. B **790** (2019) 578–582, arXiv:1812.01520 [hep-ph].

[15] B. Chauhan & S. Mohanty, "A leptoquark resolution to flavor and ANITA anomalies," Phys. Rev. D **99** (2019) 095018, arXiv:1812.00919 [hep-ph].

[16] L. Heurtier *et al.*, "A dark matter interpretation of the ANITA anomalous events," Phys. Rev. D **99** (2019) 095014, arXiv:1902.04584 [hep-ph].

References to current experimental results on $0\nu\beta\beta$ decay (see pp. 468, 469).

[17] S. Umehara *et al.*, "Neutrino-less double-β decay of ^{48}Ca studied by CaF_2(Eu) scintillators," Phys. Rev. C **78** (2008) 058501 arXiv:0810.4746 [hep-ex].

[18] J. Argyriades *et al.*, "Measurement of the two neutrino double beta decay half-life of Zr-96 with the NEMO-3 detector," Nucl. Phys. A **847** (2010) 168–179, arXiv:0906.2694 [nucl-ex].

[19] S. Di Domizio "CUORICINO: Final results," J. Phys. Conf. Ser. **375** (2012) 042014.

[20] R. Arnold *et al.*, "Results of the search for neutrinoless double-β decay in ^{100}Mo with the NEMO-3 experiment," Phys. Rev. D **92** (2015) 072011, arXiv:1506.05825 [hep-ex].

[21] R. Arnold *et al.*, "Measurement of the $2\nu\beta\beta$ decay half-life of ^{150}Nd and and a search for $0\nu\beta\beta$ decay processes with the full exposure from the NEMO-3 detector," Phys. Rev. D **94** (2016) 072003, arXiv:1606.08494 [hep-ex].

[22] R. Arnold *et al.*, "Measurement of the double-beta decay half-life and search for the neutrinoless double-beta decay of ^{48}Ca with the NEMO-3 detector," Phys. Rev. D **93** (2016) 112008, arXiv:1604.01710 [hep-ex].

[23] R. Arnold *et al.*, "Measurement of the $2\nu\beta\beta$ decay half-life of ^{48}Cd and search for the $0\nu\beta\beta$ with the NEMO-3 detector," Phys. Rev. D **95** (2017) 012007, arXiv:1610.03226 [hep-ex].

[24] A. S. Barabash *et al.*, "Final results of the Aurora experiment to study 2β decay of ^{116}Cd with enriched $^{116}CdWO_4$ crystal scintillators," Phys. Rev. D **98** (2018) 092007, arXiv:1811.06398 [nucl-ex].

[25] R. Arnold *et al.*, "Final results on ^{82}Se double beta decay to the ground state of ^{82}Kr from the NEMO-3 experiment," Eur. Phys. J. C **78** (2018) 821, arXiv:1806.05553 [hep-ex].

[26] G. Anton *et al.*, "Search for neutrinoless double-β decay with the complete EXO-200 dataset," Phys. Rev. Lett. **123** (2019) 161802, arXiv:1906.02723 [hep-ex].

[27] M. Agostini *et al.*, "Final results of GERDA on the search for neutrinoless double-β decay," Phys. Rev. Lett. **125** (2020) 252502, arXiv:2009.06079 [nucl-ex].

[28] D. Q. Adams *et al.*, "Search for Majorana neutrinos exploiting millikelvin cryogenics with CUORE," Nature **604**, No. 7904 (2022) 53–58, arXiv:2104.06906 [nucl-ex].

[29] S. Ajimura *et al.*, "Low background measurement in CANDLES-III for studying the neutrino-less double beta decay of ^{48}Ca," Phys. Rev. D **103** (2021) 092008 arXiv:2008.09288 [hep-ex].

[30] O. Azzolini *et al.*, "Final result on the neutrinoless double beta decay of ^{82}Se with CUPID-0," Phys. Rev. Lett. **129** (2022) 111801, arXiv:2206.05130 [hep-ex].

[31] D. Q. Adams *et al.*, "New direct limit on neutrinoless double beta decay half-life of ^{128}Te with CUORE," Phys. Rev. Lett. **129** (2022) 222501, arXiv:2205.03132 [nucl-ex].

[32] C. Augier *et al.*, "Final results on the $0\nu\beta\beta$ decay half-life limit of ^{128}Mo from the CUPID-Mo experiment," Eur. Phys. J. C **82** (2022) 1033, arXiv:2202.08716 [nucl-ex].

[33] I. J. Arnquist *et al.*, "Final result of the Majorana Demonstrator's search for neutrinoless double-β in ^{76}Ge," Phys. Rev. Lett. **130** (2023) 062501, arXiv:2207.07638 [nucl-ex].

[34] S. Abe *et al.*, "Search for the Majorana nature of neutrinos in the inverted mass ordering region with KamLAND-Zen," Phys. Rev. Lett. **130** (2023) 051801, arXiv:2203.02139 [hep-ex].

References on GSI anomaly (see 40.3, p. 818).

[35] A. N. Ivanov, M. Faber, R. Reda & P. Kienle, "Weak decays of H-like $^{140}Pr^{58+}$ and He-like $^{140}Pr^{57+}$ ions," Phys. Rev. C **78** (2008) 025503, arXiv:0711.3184 [nucl-th].

[36] Z. Patyk, J. Kurcewicz, F. Bosch, H. Geissel, Y. A. Litvinov & M. Pfutzner, "Orbital electron capture decay of Hydrogen- and Helium-like ions," Phys. Rev. C **77** (2008) 014306.

[37] N. Winckler *et al.*, "Orbital electron capture decay of hydrogen- and helium-like $^{142}Pr^{57+}$ ions Phys. Lett. B **679** (2009) 36–40.

[38] Yu. A. Litvinov *et al.*, "Measurement of the β^+ and orbital electron-capture decay rates in fully-ionized, Hydrogen-like, and Helium-like ^{140}Pr ions," Phys. Rev. Lett. **99** (2007) 262501, arXiv:0711.3709 [nucl-ex].

[39] H. J. Lipkin, "New method for studying neutrino mixing and mass differences," arXiv:0801.1465 [hep-ph]; H. J. Lipkin, "Simple quantum mechanics explains GSI Darmstadt oscillations even with undetected neutrino; Momentum conservation requires Same interference producing oscillations in initial and final states," arXiv:1003.4023 [hep-ph].

[40] Yu. A. Litvinov *et al.*, "Observation of non-exponential orbital electron capture decays of Hydrogen-like ^{140}Pr and ^{142}Pm ions," Phys. Lett. B **664** (2008) 162–168, arXiv:0801.2079 [nucl-ex].

[41] A. N. Ivanov, R. Reda & P. Kienle, "On the time-modulation of the K-shell electron capture decay of H-like $^{140}Pr^{58+}$ ions produced by neutrino-flavour mixing," arXiv:0801.2121 [nucl-th].

[42] A. N. Ivanov, E. L. Kryshen, M. Pitschmann & P. Kienle, "Time modulation of the β^+-decay rate of H-Like $^{140}Pr^{58+}$ ions," Phys. Rev. Lett. **101** (2008) 182501.

[43] M. Faber, "Kinematics and quantum field theory of the neutrino oscillations observed in the time-modulated orbital electron capture decay in an ion storage ring," arXiv:0801.3262 [nucl-th].

[44] C. Giunti, "Comment on the neutrino-mixing interpretation of the GSI time anomaly," arXiv:0801.4639 [hep-ph].

[45] M. Peshkin, "Unitarity constraint upon kinetically analyses of the GSI time-modulated radioactive decay experiment," arXiv:0803.0935 [hep-ph].

[46] A. N. Ivanov, R. Reda & P. Kienle, "Reply on 'Comment on neutrino-mixing interpretation of the GSI time anomaly' by C. Giunti, arXiv:0801.4639 [nucl-th]," arXiv:0803.1289 [nucl-th].

[47] H. Kleinert & P. Kienle, "Neutrino-pulsating vacuum and neutrino mass difference," Electron. J. Theor. Phys. **6** (2009) 107–122, arXiv:0803.2938 [nucl-th].

[48] P. M. Walker, "A neutrino's wobble?" Nature **453**, No. 7197 (2008) 864–865.

[49] H. Burkhardt, J. Lowe, G. J. Stephenson Jr., T. Goldman & B. H. J. McKellar, "Oscillations in the GSI electron capture experiment," arXiv:0804.1099 [hep-ph].

[50] A. N. Ivanov, E. L. Kryshen, M. Pitschmann & P. Kienle, "Neutrino masses from the Darmstadt oscillations," arXiv:0804.1311 [nucl-th].

[51] M. Peshkin, "Comment on 'New method for studying neutrino mixing and mass differences'," arXiv:0804.4891 [hep-ph].

[52] C. Giunti, "Rates of processes with coherent production of different particles and the GSI time anomaly," Phys. Lett. B **665** (2008) 92–94, arXiv:0805.0431 [hep-ph].

[53] H. J. Lipkin, "The GSI method for studying neutrino mass differences – for pedestrians," arXiv:0805.0435 [hep-ph].

[54] A. N. Ivanov, E. L. Kryshen, M. Pitschmann & P. Kienle, "On the time-modulation of the β^+-decay rate of H-like $^{140}Pr^{58+}$ ion," Phys. Rev. Lett. **101** (2008) 182501, arXiv:0806.2543 [nucl-th].

[55] A. N. Ivanov, E. L. Kryshen, M. Pitschmann & P. Kienle, "Comments on 'Rates of processes with coherent production of different particles and the GSI time anomaly' by C. Giunti, Phys. Lett. B **665** (92) 2008, 0805.0431," arXiv:0807.2750 [nucl-th].

[56] H. Kienert, J. Kopp, M. Lindner & A. Merle, "The GSI anomaly," J. Phys. Conf. Ser. **136** (2008) 022049, arXiv:0808.2389 [hep-ph].

[57] A. Gal, "Neutrinos do not oscillate yet at GSI," Nucl. Phys. A **842** (2010) 102–112, arXiv:0809.1213 [nucl-th], 1004.4098 [nucl-th].

[58] A. G. Cohen, S. L. Glashow & Z. Ligeti, "Disentangling neutrino oscillations," Phys. Lett. B **678** (2009) 191–196, arXiv:0810.4602 [hep-ph].

[59] M. Faber, A. N. Ivanov, P. Kienle, E. L. Kryshen, M. Pitschmann & N. I. Troitskaya, "Can the 'Darmstadt oscillations' be treated as two closely spaced mass-eigenstates of the H-like mother ions?" arXiv:0811.0922 [nucl-th].

[60] M. Peshkin, "Comment on 'The GSI method for studying neutrino mass differences – for pedestrians'," arXiv:0811.1765 [hep-ph].

[61] G. Lambiase, G. Papini & G. Scarpetta, "Spin-rotation coupling in non-exponential decay of Hydrogenlike heavy ions," arXiv:0811.2302 [nucl-th].

[62] C. Giunti, "The GSI time anomaly: facts and fiction," Nucl. Phys. B (Proc. Suppl.) **188** (2009) 43–45, arXiv:0812.1887 [hep-ph].

[63] P. A. Vetter, R. M. Clark, J. Dvorak, K. E. Gregorich, H. B. Jeppesen, S. J. Freedman, D. Mittelberger & M. Wiedeking, "Search for oscillation of the electron-capture decay probability of ^{142}Pm," Phys. Lett. B **670** (2008) 196–199, arXiv:0807.0649 [nucl-ex].

[64] Yu. A. Litvinov *et al.*, "Comment on the paper 'Search for oscillation of the electron-capture decay probability of ^{142}Pm' at arXiv:0807.0649v1," arXiv:0807.2308 [nucl-ex].

[65] T. Faestermann, F. Bosch, R. Hertenberger, L. Maier, R. Kruecken & G. Rugel, "Could the GSI oscillations be observed in a standard electron capture decay experiment?" Phys. Lett. B **672** (2009) 227–229, arXiv:0807.3297 [nucl-ex].

[66] C. Giunti, "Comment on 'A neutrino's wobble?'," arXiv:0807.3818 [hep-ph].

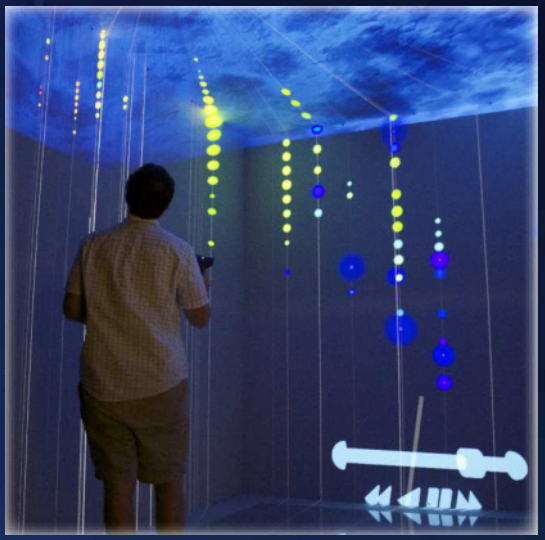

THE END